AD-A050 748 ADVISORY GROUP FOR AEROSPACE RESEARCH AND DEVELOPMENT--ETC F/G 20/6
OPTICAL FIBRES, INTEGRATED OPTICS AND THEIR MILITARY APPLICATIO--ETC(U)
OCT 77 H HODARA

UNCLASSIFIED AGARD-CP-219 NL

1 OF 6
AD
A050748

(2)

B.S.

AGARD-CP-219

AGARD-CP-219

AD A050748

AGARD

ADVISORY GROUP FOR AEROSPACE RESEARCH & DEVELOPMENT

7 RUE ANCELLE 92200 NEUILLY SUR SEINE FRANCE

AGARD CONFERENCE PROCEEDINGS No. 219

Optical Fibres, Integrated Optics and Their Military Applications

Edited by
Dr.H.Hodara

NORTH ATLANTIC TREATY ORGANIZATION

DISTRIBUTION AND AVAILABILITY
ON BACK COVER

14 AGARD-CP-219

NORTH ATLANTIC TREATY ORGANIZATION

ADVISORY GROUP FOR AEROSPACE RESEARCH AND DEVELOPMENT

(ORGANISATION DU TRAITE DE L'ATLANTIQUE NORD)

9 AGARD Conference Proceedings, No.219

6 OPTICAL FIBRES, INTEGRATED OPTICS AND THEIR MILITARY APPLICATIONS,

Editor: Dr H.Hodara
Tetra Tech. Inc.
630 North Rosemead Blvd.
Pasadena, California, USA

10 H. Hodara

11 Oct 77

12 565p.

Papers presented at the Electromagnetic Wave Propagation Panel/Avionics Panel Joint Symposium held in London, 16–20 May 1977.

400 043 JOB

THE MISSION OF AGARD

The mission of AGARD is to bring together the leading personalities of the NATO nations in the fields of science and technology relating to aerospace for the following purposes:

– Exchanging of scientific and technical information;

– Continuously stimulating advances in the aerospace sciences relevant to strengthening the common defence posture;

– Improving the co-operation among member nations in aerospace research and development;

– Providing scientific and technical advice and assistance to the North Atlantic Military Committee in the field of aerospace research and development;

– Rendering scientific and technical assistance, as requested, to other NATO bodies and to member nations in connection with research and development problems in the aerospace field;

– Providing assistance to member nations for the purpose of increasing their scientific and technical potential;

– Recommending effective ways for the member nations to use their research and development capabilities for the common benefit of the NATO community.

The highest authority within AGARD is the National Delegates Board consisting of officially appointed senior representatives from each member nation. The mission of AGARD is carried out through the Panels which are composed of experts appointed by the National Delegates, the Consultant and Exchange Program and the Aerospace Applications Studies Program. The results of AGARD work are reported to the member nations and the NATO Authorities through the AGARD series of publications of which this is one.

Participation in AGARD activities is by invitation only and is normally limited to citizens of the NATO nations.

The content of this publication has been reproduced directly from material supplied by AGARD or the authors.

Published October 1977

ISBN 92-835-0206-X

Printed by Technical Editing and Reproduction Ltd
Harford House, 7–9 Charlotte St, London W1P 1HD

AVIONICS PANEL

Chairman:	Mr J.N.Bloom, Canada
Deputy Chairman:	Ir. H.A.Timmers, Netherlands

ELECTROMAGNETIC WAVE PROPAGATION PANEL

Chairman:	Mr P.Halley, France
Deputy Chairman:	Dr H.Albrecht, Germany
NATO DRG Panel IV Representative:	Dr M.Hartl

PROGRAM COMMITTEE

Dr H.Hodara (Chairman), USA	Dr C.Sandbank, UK
Ing. Gen. J.Bertrais, France	Dr E.Spitz, France
Mr L.Dworkin, USA	Mr T.Sueta, USA
Mr P.Halley, France	Mr M.Treheux, France
Mr R.Payne, USA	Dr M.Vogel, Germany
Mr B.Rubin, USA	Mr D.Williams, USA

PANEL EXECUTIVE

CDR D.G.Carruthers, US Navy
AGARD

THEME

Rapid developments in laser semiconductors and low loss optical fibres are responsible for new applications in the areas of communication, imaging and data transmission in general. Optical fibres provide a high degree of communication security, freedom from electronic interference, large length-bandwidth product, and system miniaturization through their small size. The combination of all these features leads to new concepts and unique applications in military hardware.

The purpose of this conference is to review and present the latest developments in fibre and integrated optics, stressing their military applications and emphasizing the topics of major interest to the Avionics and Electromagnetic Wave Propagation Panels: End Devices, Coupling and Propagation Mechanisms, Optical Cables and Systems.

CONTENTS

EDITOR'S INTRODUCTION

Recent world conferences of Fiber Optics have been dominated by the telecommunication industry stressing telephone applications. Unlike those, this meeting emphasizes the development of complete systems and devices for military applications.

The meeting covers three major areas:

Overview and Complete Systems: Session 1 and 2, respectively

Integrated Optics: Session 3

Components: Fiber Propagation, Session 4; Sources and Detectors, Session 5; Couplers, Session 6

The outstanding results of the Conference are presented in the Session Summaries of these Proceedings. Among the most promising developments, we note:

- marine application of optical fibers in underwater cables,
- operational fiber-optic systems with high data rate,
- use of large-diameter wide-bandwidth fibers supporting a few lower order modes,
- a novel injection laser, capable of fine tuning and coupling into a single mode fibre,
- a long-life, stress-free double heterostructure GaInAsP/InP diode laser operating CW, at room temperature, between 1.10 and 1.31 μm.

Review and Assessment of Fiber Optics for Military Applications

By

Henry F. Taylor
Naval Electronics Laboratory Center
San Diego, CA 92152

SUMMARY

Component technology, system design considerations, and military applications of optical fiber communications are reviewed in this paper.

The basic components include optical transmission lines, transmitters, receivers, repeaters, connectors, and bus couplers. Characteristics of these devices which have a particular bearing on military usage, such as environmental and radiation effects, are emphasized. Recent results representative of the state-of-the-art in component technology are indicated.

Factors which affect the selection of components for a particular system are discussed. The most important of these are cable length, analog or digital signal bandwidth, system environment, reliability requirements, and cost constraints. Some of the options available in selecting components to meet these system criteria include compound glass or silica fibers, fibers with step index or graded index profile, single fiber or multifiber cables, light-emitting diode or injection laser sources, and PIN or avalanche photodiode detectors.

Some of the military systems applications which are being actively pursued include digital point-to-point links and multiterminal busses for ships, aircraft, and land bases, secure systems for voice and video, tactical land-line telemetry links, and undersea cables for transmitting sonar signals. Some systems which have been successfully demonstrated are described. In each application area, the proven or anticipated benefits of using fiber optics are discussed.

INTRODUCTION

The technology of optical fiber communications (which includes transmitters, receivers, and connectors, as well as the optical transmission lines) has evolved rapidly during the 1970's (Gloge, D., 1976, Campbell, L. L., 1976; Campbell, J. R. and Bryant, J. F., 1977; Barnoski, M. K., 1976; Personick, S. D., 1975; DiDomenico, M., 1974; Miller, S. E., et al., 1973; Maurer, R. D., 1973). The most important barriers which were perceived at the beginning of the decade – the high attenuation of fibers, problems associated with cabling of glass and silica fibers, and the reliability of injection laser light sources – have by now been largely overcome. The emphasis has therefore shifted from research to engineering and manufacturing. Industrial efforts in these areas are accelerating, as the potential market for components now appears much larger than many had anticipated a few years ago. The introduction of standard lines of components and of MIL-qualified components over the next few years can be confidently anticipated. It is also expected that the cost of components will continue to drop fairly rapidly, making fiber optics communication cost-effective for an increasing number of civilian and military applications.

This paper reviews the basic components, discusses system design considerations, and describes some present and anticipated military applications for fiber optics communication.

COMPONENTS

The basic components for fiber optics communications are the optical transmission lines, transmitters, receivers, repeaters, connectors and splicers, and bus couplers. The transmission lines, transmitters, receivers, and connectors are now available commercially, with several manufacturers for each component. Facilities for the testing of components have been assembled at several military and industrial laboratories. Strong efforts are underway toward standardization of military component types, in cooperation with the appropriate industrial committees.

Fiber Optics Transmission Lines (Maurer, R. D., 1973; French, W. G., et al., 1975)

An optical transmission line consists of a jacketed cable containing the fibers, and often, in addition to the fibers, strength members, electrical conductors, and additional material for protecting the fibers against crushing.

Conceptually, the simplest type of optical fiber consists of a dielectric cylinder of refractive index n_1 surrounded by a second medium of index n_0. A light ray entering the cylinder at an angle θ to the axis, in a plane containing the axis, will be confined to the cylinder by total internal reflection if

$$n_0 \sin\theta < \sqrt{n_1^2 - n_0^2}$$

However, in practice, if the fiber material is uniform and is surrounded by air, minute irregularities at the glass-air interface cause much of the light to be lost by scattering at each encounter with the surface. The surface scattering problem can be eliminated if the fiber consists of a core of high-index material surrounded by a cladding of lower index. The condition for confinement becomes

$$n_0 \sin\theta < \sqrt{n_1^2 - n_2^2}$$

where n_1 and n_2 are the core and cladding refractive indices and n_0 is the index of the medium in which the incident ray propagates. (Usually, this medium is air, so $n_0 = 1.00$.) If the cladding is several wavelengths thick, the light will propagate in the core and cladding and not contact the surface. Two important fiber parameters are the acceptance angle θ_a, the angle of the most oblique ray which is totally reflected, and the numerical aperture, abbreviated NA, which are given by

$$\sin\theta_a = NA = \sqrt{n_1^{\,2} - n_2^{\,2}}\ .$$

The ray-tracing analysis of fiber propagation is accurate only in fibers which support at least several guided modes. Only one guided mode of a given polarization will exist in a circular, step-index fiber if $v \leqslant 2.405$

$$v = \left(\frac{2\pi a}{\lambda}\right)\sqrt{n_1^{\,2} - n_2^{\,2}}\ .$$

where a is the fiber radius and λ is the optical wavelength (Snitzer, E., 1961). If $(n_1 - n_2)/n_1 \ll 1$, the modes are essentially plane polarized. For large v, the number of guided modes of a particular polarization is approximately $v^2/2$.

The initial distribution of power among the modes depends upon the spatial and angular distribution of the incident light beam. In particular, an input beam which propagates nearly parallel to the axis and fills the entire fiber core excites primarily low-order modes, while a beam which propagates at a large angle to the axis excites higher-order modes.

Power in a particular mode propagates along the fiber axis with a velocity V_g, known as the group velocity, which is given by

$$V_g = \frac{1}{\left(\dfrac{\partial\beta}{\partial\omega}\right)}$$

where β is the mode propagation constant and ω is the radian frequency of the light wave. In a step-index fiber, V_g decreases with increasing mode order. This is explained by noting that rays incident at a large angle to the fiber axis, which excite primarily higher-order modes, travel a longer path in the fiber than a paraxial ray, which excites low-order modes. Thus, the component of velocity along the axis is lower for high-angle rays (or high-order modes). The transit time t_0 for a paraxial ray is

$$t_0 = n_1 L/c$$

where L is the fiber length and c is the speed of light in vacuum. The difference in transit time Δt between a ray entering at an angle θ and a paraxial ray is

$$\Delta t = (n_2 L/c)\left\{\sec[\sin^{-1}(\sin\theta/n_1) - 1]\right\} \tag{1}$$

Assuming that the incident cone of light fills the numerical aperture of the fiber, this formula gives the pulse broadening due to the difference in mode (or ray) propagation velocities ("intermode dispersion") expected from a temporally narrow incident pulse, with θ replaced by θ_a. This behavior does not hold for long fibers, because high-angle rays usually suffer greater attenuation than paraxial rays, and because of mode conversion. Mode conversion is caused by inhomogeneities in the refractive index of the fiber and by bends in the fiber axis. For sufficiently long fibers, it is predicted (Personick, S. D., 1971) and observed (Cohen and Personick, 1975) that pulse spreading due to intermode dispersion is proportional to $\sqrt{L}$, rather than to L. The transition from L to $\sqrt{L}$ dependence is typically found to occur at lengths of the order of 1 km. A reduction in pulse spreading by a factor of five or more below that predicted by (1) has been observed in long fibers.

Intermode dispersion limits the information capacity of a step-index multimode fiber to a value which is unacceptably low for many wideband, long distance systems. Intermode dispersion can be eliminated by using a single-mode fiber. Extremely low (<50 ps/km) pulse dispersion is possible, but the spatial and angular tolerances for coupling hardware even using laser sources are so severe (~1 μm, ~1 mrad) that practical single-mode systems are still some years in the future. A more satisfactory solution, at least for the present, is the graded-index fiber. In a fiber with a parabolic index distribution, the rays which must travel the greatest distance in the fiber also have a higher average speed. The net result is that the transit time for all rays is, to first order, the same. As a consequence, pulse dispersion for a graded-index fiber with a nearly-parabolic profile in the core is much lower (Cohen, L. G., et al., 1975; Olshanski, R., and Keck, D. B., 1976) (<1ns/km) than for a step-index fiber (~30–50 ns/km for NA ~ 0.15). Refractive index profiles for step multimode, step single-mode, and graded-index fibers are illustrated in Fig. 1.

Another source of pulse spreading in fibers, known as material dispersion, results from the fact that the group velocity depends upon wavelength in any material medium. The spread in group velocities for a light source with a wavelength spread $\Delta\lambda$ is

$$\Delta Vg = \left(\frac{\partial Vg}{\partial\lambda}\right)\Delta\lambda$$

In fused silica at 8000 Å, for example, $\dfrac{\partial Vg}{\partial\lambda} = 9$ ps/Å. For light-emitting diode sources, where $\Delta\lambda$ is relatively large (~400Å), material dispersion can be the dominant source of pulse distortion in graded-index fibers.

Step-index or graded-index glass or silica fibers are produced either by drawing from a preform or from the melt using a double crucible arrangement. One of the earlier preform techniques employs a rod of high-index glass inserted in a hollow tube of lower refractive index. One end of the rod and tube is heated to softening and drawn to a fiber. The ratio of rod and tube diameters is maintained in the fiber as the ratio of core to cladding diameters. A newer method utilizes ion exchange in a hot salt solution to produce a nearly-parabolic index profile in a glass rod preform, which is subsequently drawn into a graded-index fiber.

The major innovation in low-loss technology occurred when techniques for depositing a layer of higher-index doped silica inside a hollow cylinder of pure silica were devised. A preform of this type is then collapsed and drawn into a fiber. The core index can be graded by varying the concentration of the dopant as a function of time during deposition.

The double crucible method employs an inner crucible containing high-index glass and an outer crucible containing glass of lower index. The contents of both crucibles are heated to melting, and the fiber material is drawn from the two crucibles through concentric orifices. By providing a mixing region in which both components are in contact in the molten state, a graded-index profile can be obtained.

Finally, it is possible to draw a glass or silica fiber of uniform composition from a preform or melt, and coat this fiber with a polymer or plastic of lower refractive index. Most commonly, silica is used for this type of step-index fiber. These "plastic-clad" silica fibers are presently produced less expensively than other silica fibers.

Glass purification is the key to minimizing optical absorption in fibers. By reducing concentrations of transition metal and hydroxyl ions to a few parts per billion, fibers with losses of 0.5 dB/km at a wavelength of 1.05 μm and 1 dB/km at 0.8 μm have been produced (Horiguchi, M., and Osanai, H., 1976). An attenuation curve for one of these fibers is illustrated in Fig. 2. The losses in those fibers are close to the theoretical limit from Rayleigh scattering, which is proportional to λ^{-4}, over the wavelength range from 0.4 μm to 1.1 μm. Fibers with losses of less than 10 dB/km are now produced in quantity by several manufacturers.

The effect of ionizing radiation on fiber attenuation is of particular interest from the standpoint of military applications. It has been found that most compound glass fibers and some doped silica fibers are quite susceptible to transient and permanent coloration by X-rays, gamma rays, and slow neutrons (Evans, B. D. and Sigel, G. H., 1975; Sigel, G. H. and Evans, B. D., 1974; Mattern, P. L., et al., 1974; Maurer, R. D., et al., 1973). Increases in attenuation of 1 dB/km-rad or more at near-infrared wavelengths are observed. Recent data indicates that even pure silica and germania-doped silica fibers are strongly affected at low doses (Sigel, G. H., 1977).

Glass and silica fibers in the as-drawn condition are generally very strong, with tensile strengths of several hundred thousand psi in lengths of a few meters. However, they possess tiny surface flaws, known as Griffith microcracks, as a result of thermal stresses during cooling and mechanical contact with the drawing apparatus. When a fiber is subjected to tension in the presence of water vapor, these cracks have a tendency to propagate in from the surface, causing the fiber to break (Maurer, R. D., 1975; Kurkjian, C. R., et al., 1976). In order to protect fibers against the tendency of cracks to form and grow, polymer coatings or buffers are applied. Thin coatings can be applied by dipping as a part of the drawing process, while thicker buffers are applied by extrusion. Although the strength of buffered fibers is now adequate for use in some general purpose cables, further progress in fiber strength is needed for cables which are subjected to severe tensile loads, such as those for undersea deployment.

Fiber bundles, which have been manufactured in large quantities for several years, are adequate as transmission lines for some short-distance communications applications. These bundles typically contain a few hundred fibers, protected only by a silicone lubricant, and enclosed in a polyvinyl chloride (PVC) jacket. The diameter of the optical surface for a commonly used variety is 1.2 mm. Losses are nominally quoted at 500 dB/km for these bundles, although at least one manufacturer routinely produces bundles with losses less than 100 dB/km.

As dictated by the requirements for installation and use, it has usually proven expedient to incorporate the fibers into a cable designed to protect them against breakage. In addition to buffered fibers and a protective jacket, the cables usually contain strength members of Kevlar, steel, or S-glass, and some also incorporate copper conductors for electrical power transmission and additional material for providing crush resistance. The cabling operation is accomplished using equipment for producing electrical cables, with relatively minor modifications. Cables for general purpose use are now produced by several manufacturers. Further progress is needed in high-strength optical fiber technology before cables suitable for most undersea applications can be manufactured (Wilkins, G. and Eastley, R., 1977; Putnam, W. H., 1976; Wilkins, G. A., 1976; Frieberger, R. J., 1976). The cross section of two types of undersea cable designed for high strength are illustrated in Fig. 3.

Transmitters

A transmitter for fiber optics communications consists of a light source, generally a light-emitting diode (LED) or injection laser diode (ILD), and an electronic driver, in a package containing suitable electrical and optical connectors.

The technology for producing semiconductor light sources has evolved rapidly over the past few years, in part because they are the preferred type of light emitter for use in fiber optics communications. The LED and ILD are both pn junction diodes which emit light generated by electron-hole recombination when passing current in the forward-biased condition. The laser is designed such that a resonant optical cavity is formed by cleaved surfaces of the crystal, which serve as mirrors situated on either side of the recombination region. In the LED, the emission spectrum is essentially that of the spontaneous emission of the material modified by its absorption, and typically has a spectral width of 300–500 Å. In the injection laser, the cavity resonance causes substantial narrowing of the emission spectrum to a width of 50Å or less, as well as the improved directionality and phase coherence characteristic of stimulated emission. Both LED's and ILD's have the advantages of small size, light weight, low drive voltage (~1.5V), and relatively good power conversion efficiency (1–10%). In addition, both can be modulated by varying the drive current (direct modulation), with cutoff frequencies of 1 GHz for experimental LED's (Heinen, J., et al., 1976) and lasers (Chown, M., et al., 1973). Cutoff frequencies for commercial LED's are generally below 50 MHz, however. Most LED's display good linearity of output power as a function of drive current, and in some injection lasers the variation of power with changes in drive current is close to linear above the threshold current (Dixon, R. W., et al., 1976) which marks the onset of stimulated laser emission.

A major milestone in laser technology occurred in 1970 with the announcement of the first ILD to operate continuously at room temperature (Hayashi, M. B., et al., 1970), and another was the introduction about 2 years ago of a commercial CW room temperature device. Operating lifetimes of several thousand hours are now routinely achieved for ILD's under CW, room temperature operation, and some manufacturers expect that 10^5-10^6 hours are reasonable goals. Some such devices have been operated continuously at temperatures as high as 60–80°C, but the threshold current increase and operating life drops considerably at these temperatures. Reliable operation at the higher temperatures (e.g., > 125°C) required of most military equipment may not be readily obtained. The maximum ambient temperature of an ILD transmitter can, however, be extended by the use of thermoelectric cooling.

The great improvement in injection lasers has been based upon the technology for growing multiple layers in the gallium-aluminum arsenide ($Ga_xAl_{1-x}As$) alloy system by liquid-phase epitaxy (Panish, M. B., 1975). By growing several layers of different doping levels and aluminum concentration, it is possible to produce "double heterostructure" (DH) devices in which carrier recombination occurs in a narrow (<1 μm) layer and the stimulated optical emission is also closely confined. One such ILD is illustrated in Fig. 4. The electrical current density needed to reach the threshold for stimulated emission in DH lasers is much lower than in conventional diffused-junction gallium arsenide ILD's. Lower current densitites mean less heating of the material and much slower thermal degradation of the device properties. The same heterostructure growth techniques have also made it possible to increase the radiance of LED's. High-radiance LED's can be designed for emission either perpendicular (Burrus, C. A., et al., 1975) or parallel (Wittke, J. P., et al., 1976) to the junction plane.

The primary advantages for ILD's over LED's for use in fiber communications are improved efficiency for coupling to fibers, relatively narrow spectral width, and wider modulation bandwidths. The improved coupling efficiency, particularly for use with single fibers as opposed to bundles, results from the narrow beam divergence and the small emitting area of the laser. The use of a narrow stripe electrode for current injection makes it possible to achieve beam widths of less than 20 μm parallel to the junction, while typical widths perpendicular to the junction are 1-2 μm. Coupling efficiencies for both lasers and LED's can be improved by the use of a lens (Wittmann, L., 1975), but the improvement is generally greater for the laser because of its higher radiance. For coupling to single, multimode fibers, losses in the 3-6 dB range can be expected for injection lasers, and 10-20 dB with LED's. The reduction in spectral width is important for long distance, wideband systems, and amounts to a reduction in material dispersion of from 3.5 ns/km for an LED with 400 Å spectral width to 0.4 ns/km for a laser with 50 Å spectral width at a wavelength near 0.8 μm.

In spite of the attractive features of injection lasers, LED's will also undoubtedly be used in many systems because of their lower cost, simpler circuit requirements, improved linear dynamic range, and the possibility of continuous operation at low drive currents at temperatures well in excess of 100°C without external cooling.

Gallium aluminum arsenide ILD's and LED's are usually designed to have a central wavelength in the 8000 Å - 8600 Å range. This fortunately coincides with a low-loss "window" in the transmission of typical silica fibers. However, even lower fiber losses are almost always observed at wavelengths in the 1.0-1.2 μm spectral range. Efficient ILD's have been produced in $Ga_xIn_{1-x}As$ (Mabbitt, A. W., and Mobsby, C. D., 1975) and $Ga_xIn_{1-x}As_yP_{1-y}$ (Hsieh, J. J., 1976; Pearsall, T. P., et al., 1976), which emit in that spectral range. Reported operating lifetimes for these laboratory devices remain lower than in gallium aluminum arsenide, and silicon photodetectors do not perform as well at those wavelengths. Nevertheless, quaternary alloy ILD's appear promising for use in long-distance systems, as there is good reason to believe that long lifetimes will be readily achieved (Wieder, H. H., 1977).

Digital and analog transmitter modules designed for fiber communications are now available commercially, both for use with single fibers and with bundles. These modules contain driving electronics as well as an injection diode source and are supplied with optical and electrical connectors. Although present commercial modules use LED sources, experimental versions using lasers are also being produced. The digital modules generally use TTL-compatible interfaces and have maximum data rates in the 10-20 Mb/s range; the analog modules generally have bandwidths of 5-10 MHz for video or 4 kHz for voice.

Receivers

A receiver for fiber optics communications consists of a photodiode detector and associated amplifiers and/or threshold circuits, in a package with suitable electrical and optical connectors (Personick, S. D., 1975; Goell, J. E., 1974; Barnoski, M. K., 1976).

Silicon PIN and silicon avalanche photodiodes (APD's), which have been commercial products for a number of years, are presently the preferred type of photodetector for optical fiber communications. Both are operated as backbiased diodes and are designed so that as much of the incident light as possible is absorbed in a region of intrinsic silicon. The photo-generated carriers are swept out of the intrinsic region toward the contacts by the applied field. In the avalanche device, electrons from the intrinsic region enter a pn junction region with high electric fields in which carrier multiplication takes place, as illustrated in Fig. 5. The electrons and holes in this region acquire enough energy from the field to produce additional carriers by ionization, so that the avalanche device is characterized by internal gain.

Some of the PIN diodes will respond at frequencies to several gigahertz, while APD's have cutoff frequencies as high as 1 GHz.

The sensitivity of a receiver, which includes a detector and its following amplifiers, is determined by the efficiency of the detector in converting photons to electrons ("quantum efficiency") and by the various noise factors which can limit the ability of the receiver to restore the original analog or digital signal. The detector quantum efficiency q is defined as the average number of photoelectrons generated directly by the absorption of a photon ("primary" photoelectrons) n_e to the average number of incident photons n_p;

$$q = n_e/n_p$$

For a detector with internal gain G, the average number of collected electrons n_e' is

$$n_e' = G\, n_e$$

In terms of the incident optical power P, the photon energy hν, electronic charge e, and photocurrent I, the quantum efficiency can be written

$$q = h\nu I/ePG$$

Typical values of quantum efficiency for silicon PIN photodiodes are in the 80%-90% range, and for avalanche photodiodes, in the 30%-50% range, at wavelengths near 0.8 μm. At 0.63 μm, the quantum efficiencies are roughly half these figures. Gains for silicon avalanche photodiodes usually lie in the 50-200 range for optimum performance.

The principal sources of noise which limit the performance of a receiver using a PIN photodiode are dark-current shot noise and amplifier noise (including thermal noise). Assuming that the receiver is designed such that the bandwidth of the preamplifier equals the signal bandwidth, the dark-current noise is proportional to the bandwidth, while thermal noise is proportional to the square of the bandwidth. Thermal noise therefore tends to dominate at high bandwidths ($\gtrsim$1 MHz for PIN receivers). Thermal noise can be significantly reduced by using a high-impedance FET preamplifier with a bandwidth substantially less than that of the signal. The signal is integrated at the preamplifier input and is differentiated after amplification to restore the received waveform.

In the APD receiver, the carrier multiplication boosts the signal level internally, prior to the preamplifier. The increase in signal level with respect to amplifier noise gives an improved sensitivity in the receiver, even though carrier multiplication introduces some additional noise. The net result, taking into account the somewhat lower efficiency of the avalanche device, is a 10–20 dB improvement in sensitivity for the APD receiver as compared with one which uses a PIN photodiode. A comparison of the performance of well-designed digital receivers using PIN and APD detectors (Personick, S. D., 1975) is illustrated in Fig. 6.

Against this improved sensitivity must be weighed the disadvantages of the avalanche photodiode receiver. First, the device must be biased in the 150–400 V range for optimum gain, and the voltage must be compensated for ambient temperature variations. The PIN device needs only a few volts of bias for optimum performance and need not be temperature compensated. The net result is that, even neglecting the cost of high-voltage DC power supply, the avalanche receiver is several times more expensive than a PIN receiver of a given bandwidth.

Receivers for fiber optics communications are sold commercially, with typical sensitivities of -37 dBm for a 10 Mb/s data rate and an error rate of 10^{-8}, using a silicon PIN detector.

Repeaters

Repeaters for optical fiber communications typically consist of a receiver to detect and amplify an incoming signal, an equalizer and signal regenerator, and a transmitter to launch the regenerated signal into the next section of transmission line (Goell, J. E., 1974; Barnoski, M. K., 1976). Optical power gains in the 35–60 dB range are typically needed to offset line and coupling losses for a section of the system. Digital repeaters with data rates as high as 800 Mb/s have been demonstrated in the laboratory (Nawata, K., and Takano, K., 1976).

For either land or undersea systems, electrical power for a repeater must usually be supplied through conductors contained within the cable. Electrical power consumption, which, for the optical repeater, includes power dissipated by electronic components such as amplifiers as well as that required to drive the light source, is an important consideration in repeater design.

Connectors and Splicers

Connectors for large (~1 mm diameter) fiber bundles have not proven particularly difficult to fabricate, since the mechanical tolerances for such connectors (~0.1–0.2 mm) can easily be maintained by standard machining and casting equipment. Those tolerances are also compatible with those required for standard electrical connectors, and modified SMA rf connectors are frequently used for fiber bundles. Pressure-tight connectors for aircraft bulkheads have also been produced.

Field installation of connectors and splicing for large bundles requires that the fiber ends be cemented or epoxied in a fitting and polished. Portable air-driven repair kits for accomplishing this have been demonstrated, but further work in manufacturing methods for repair and termination equipment is needed. Typical losses for bundle splice connectors, which includes "packing fraction" and Fresnel losses, are in the neighborhood of 3 dB, with ±0.2 dB tolerance about this figure allowed for the Navy standard.

Connectors for single multimode fibers (~30–85 μm core diameter) are considerably more difficult to produce, since the mechanical tolerances (~5 μm) are difficult to achieve with modern machine tools. One approach is to lay the fibers end-to-end in a groove or other fixture which provides axial alignment and clamp them in place by applying lateral pressure (Dalgleish, J. F., and Lukas, H. H., 1975). Special alignment fixtures have also been fabricated for use as connectors for multifiber cables (Thiel, F. L., et al., 1974; Auracher, F., and Zeitler, H. H., 1976).

It is often necessary to provide mechanical termination of the cable strength member at the connector in order to provide adequate protection for the fibers. At present, installation of field terminations or splices for single-fiber cables is more difficult and time-consuming than would normally be acceptable in an operational environment.

Nevertheless, if sufficient care is taken, single-fiber connections with losses in the 0.5–1.5 dB range can be obtained repeatably. It is anticipated that, as standard cable configurations are more clearly defined and fiber diameter and core concentricity hold to tighter tolerances, further engineering efforts and perhaps some novel approaches will yield improved cable connectors which are amenable to simple amenable to simple installation and maintenance and to reliable operation.

Bus Couplers

The need for special couplers to perform the function of signal distribution is a unique feature of the multiterminal bus. Two generic types of optical bus coupler have been proposed and demonstrated: the "star" (or "radial arm") coupler and "Tee" coupler. The star coupler (Hudson, M. C., and Thiel, F. L., 1974) is an optical mixer which is linked to the terminals by sections of transmission line in radial fashion. Spatial mixing in the coupler causes a portion of the light from each transmitter to be received at every terminal. The trend in star couplers for military use is towards couplers with 3, 4, 8, or 16 ports. The optical Tee coupler, on the other hand, provides a means for signals to be injected into and removed from a fiber optics trunk line at each terminal. Hybrid systems utilizing a combination of both generic types of coupler have also been proposed.

From a systems standpoint, the star couplers offer the advantage that the loss, in dB, increases only as log N for an N-terminal system. By contrast, the loss is proportional to N for a system using Tee couplers. As a result, the number of terminals which can be implemented without repeaters is much larger in a star system. Using available technology, a star system with over a hundred terminals can be designed, while the present limit for a repeaterless system using Tee couplers is about ten terminals. On the other hand, the Tee coupler seems to offer some advantages in terms of cable cost and ease of installation and maintenance and system modification.

Both star and Tee couplers have been built for single-fiber and multifiber bundle transmission lines. One design for the star coupler uses a polished glass cylinder with a mirror at one end as the mixing block. Bundle versions of the Tee coupler have used bifurcated fiber bundles (Biard, J. R., and Shaunfield, J. E., 1974), branching glass structures (Milton, A. F., and Lee, A. B., 1976), and glass blocks with internal mirrors (Taylor, H. F., et al., 1975) to provide access to the transmission line. Tee couplers for single fiber links have also been made by cementing or fusing two parallel fibers together (Barnoski, M. K., and Friedrich, H. R., 1976). The fibers have part or all of the cladding removed to promote efficient power transfer, and are separated at the ends to provide four coupling ports. Branching multimode waveguide structures (Witte, H. H., 1976) and mechanical arrangements for causing mode conversion (Jeunhomme, L., and Pocholle, J. P., 1976) have also been used for tapping single fibers.

Further work is needed in the coupler technology to meet requirements of future multiplexed systems, but there seem to be no serious barriers to achieving efficient operation of either star (radial arm) or Tee couplers and systems based on these approaches.

SYSTEM DESIGN CONSIDERATIONS

Three of the key parameters which must be considered in the design of a fiber optics communications link are the length, signal bandwidth, and fiber attenuation. Connector attenuation also becomes very important if several serial feed-throughs are needed. As an example of how these parameters interact, Table 1 gives the maximum allowable fiber attenuation for a particular length of the fiber transmission line and signal bandwidth. It is assumed in that example that the receiver incorporates a silicon PIN photodiode, that the transmitter power level is +3 dBm, and that a 10 dB margin is allowed for coupling, connection, and splicing losses. A signal-to-noise ratio of 30 dB for the analog signals and an error rate of 10^{-9} for digital signals are assumed. According to the table, attenuation factors in the 500 to 1000 dB/km range for aircraft applications (maximum distance approximately 50 m) and in the 80–180 dB/km range for shipboard application (maximum distance approximately 300 m) will be needed.

TABLE 1

Maximum fiber attenuation (in dB/km) for various cable lengths and signal bandwidths

		length (m) 50	300	1000
Bandwidth Requirement	4 kHz analog	1400 dB/km	230 dB/km	70 dB/km
	5 MHz analog	800	130	40
	2 Mbit/sec PCM	1000	160	50
	10 Mbit/sec PCM	800	130	40
	50 Mbit/sec PCM	600	100	30

In the transmitters and receivers, superior performance is generally achieved with ILD sources and APD detectors, while cost considerations tend to favor the use of LED sources and PIN photodiodes. For example, the power coupled into a fiber of NA $\sim$ 0.2 from an ILD source is 0 dB/m or greater, while if an LED is used, the power coupled into the fiber is of the order of -10 dBm. At the receiver end, the replacement of a PIN photodiode with an APD gives an improvement of 10–15 dB in the power budget for the system.

For long distance communications links, dispersion in the transmission line tends to limit the signal bandwidth. Material dispersion is of the order of 3 ns/km for LED sources, and only about 0.4 ns/km for typical ILD's. The intermode dispersion is of the order of 1 ns/km for the better quality of graded index fibers, compared with 30 ns/km for conventional step index fibers (NA = 0.14), and 100 ns/km for plastic-clad silica fibers. For longer distances ($\gtrsim$1 km), the intermode dispersion is less than these figures would indicate, due to mode conversion. In the examples given in Table 1, based on these figures, it is seen that graded index fibers would be necessary for the 50 Mb/s, 1 km system but that either LED's or ILD's could be used in that system.

Environmental constraints could also have a strong influence on the choice of components. For example, a requirement for hardness to ionizing radiation might affect the type of fibers used, or a requirement for high temperature (>80°C) operation could rule out the use of ILD's in some systems.

COMPARISON WITH ELECTRICAL SIGNAL TRANSMISSION

The great majority of present-day military systems use coaxial or wire-pair cable for signal transmission. These electrical transmission media have undeniable advantages in comparison with fiber optics. First, a fiber optics system will have extra components – transmitters for converting electrical signals to light, and receivers for performing the reverse conversion – and these components can increase the costs and complexity of a system. Second, terminating and splicing fiber optics cables, particularly in single fiber systems, remains a rather difficult procedure which one cannot expect untrained personnel to perform. Also, some types of optical fiber are quite sensitive to ionizing radiation. And, finally, the most important factor is that the cost of present fiber transmission lines, connectors, transmitters and receivers is presently so high that, in many instances, optical systems are simply too expensive, even though the fibers might offer other attractive features for use in such systems.

The advantages of using fibers for communications have been described many times. The fiber optics transmission line can be much smaller in size and lighter in weight than an electrical line of equivalent bandwidth. These attributes can translate into both cost and performance improvements in military systems. A properly jacketed optical cable will neither emit nor pick up electromagnetic radiation. This insures immunity from intercept to meet TEMPEST requirements, or from pick-up by other transmission lines of classified information being transmitted over the fiber optics cable. Since the fibers will not pick up electromagnetic radiation, crosstalk, interference (EMI), and the transient effects associated with electromagnetic pulse (EMP) can be reduced or eliminated. The electromagnetic compatibility (EMC) of interconnected electronic systems and subsystems is greatly enhanced by the use of an insulating transmission medium. Silica fibers can be expected to survive fire damage and continue transmitting at temperatures approaching 1000°C (although the jacket material would not survive at those temperatures) as compared with the 300°C rating for high temperature electrical cable. Finally, the fibers can be used in hazardous areas containing flammable or explosive fumes without danger from electrically induced sparking.

In most cases life-cycle costs will probably be the deciding factor as to whether to use fiber optics or electrical cables. This is illustrated by recent studies comparing the costs associated with both transmission media to a given level of system performance for the A-7 aircraft (Greenwell, R. A., 1976; Uhlhorn, R. W., et al., 1976).

SYSTEMS APPLICATIONS

Fiber optics is now being given serious consideration for use in a variety of military systems, including aircraft, shipboard, mobile and fixed land-based and undersea systems (Albares, D. J., et al., 1975; Dworkin, L., et al., 1976, 1977). Examples illustrating the use of fiber optics in each of these types of platforms and environments are given below, and the rationale for using fiber optics in each case is discussed.

Aircraft Applications

The Navy and the Air Force have recently concluded tests to show the feasibility of using fiber optics for signal transmission in an aircraft environment. The Navy test involved the installation and flight testing of fiber optics links to replace wire-pair and coaxial cables in the navigation and weapons delivery system of an A-7 aircraft (Greenwell, R. A., and Holma, R. A., 1977; Harder, R. D., et al., 1977; Ellis, J. R., and Williams, D. N., 1976). A total of 115 wire signal links were replaced by 13 fiber optic channels, 12 digital and 1 analog, carrying multiplexed signals. A block diagram of the system is given in Fig. 7, and a photograph of the fiber optics hardware in Fig. 8. Fiber bundle transmission lines, LED transmitters, and silicon PIN receivers were used. The digital channels used a return-to-zero Manchester format with a maximum data rate of 10 Mb/s. Special pressure bulkhead connectors were developed for and used in the demonstration. The aircraft was flown for approximately 100 hours and all of the weapons systems on board the aircraft were demonstrated using the fiber optics links. The performance of the fiber optics was satisfactory during the entire testing cycle, and Navy technicians performed the nominal maintenance required during the course of the program. Improved EMC and immunity from cross talk, EMI and EMP are seen as the primary advantages for using fiber optics in systems such as those employed in the A-7 demonstration. These factors enhance the ability to use fiber optics for multiplexing to reduce the size, weight and space of cabling on the aircraft.

In an Air Force demonstration (Biard, J. R., and Shaunfield, J. E., 1977; Stewart, L. L., 1977) two wideband fiber optics links have been flown on an operational aircraft for over 300 hours. Additional flight testing is planned. The two data transfer requirements met by fiber optics during these tests were a 30-meter link operating at 160 MHz carrier frequency with a 20 MHz bandwidth and a video link 20 meters in length, operating with a 20 MHz bandwidth. The advantages of using fiber optics in these systems are, primarily, improved bandwidth and EMC, and reduced EMI susceptibility.

Both the Air Force and the Navy have developed laboratory models of fiber optics multiterminal data busses. The Air Force version operates at 10 Mb/s with eight terminals, using a radial arm (star) coupler with a maximum distance from the coupler to remote terminals of about 30 meters (Shaunfield, J. E., 1976). For the Navy data bus, eight terminals were demonstrated with a 5 Mb/s data rate, using optical "Tee" couplers (Altman, D. E., 1975). The Air Force bus was successfully built and tested to the format requirements in MIL-STD-1553.

A final aircraft application being pursued is for the Navy P-3C weapon system. Interfaces have been developed for a 10 Mb/s intercomputer channel, a 30 MHz video channel and a 40 kHz acoustic channel with 48 dB dynamic range. Maximum distance is of the order of 10 meters in this system, so that once again simple components similar to those for the A-7 demonstration can be used.

Shipboard Applications

One of the earliest deployments of fiber optics on board a ship was the six-station telephone system on board the cruiser, USS LITTLE ROCK (Eastley, R. A., and Putnam, W. H., 1974). The remote terminals were connected to a central switching station by maximum runs of 30 meters of fiber optics bundles, as illustrated in Fig. 10. The rationale for developing this system was to meet TEMPEST requirements, and the need for messengers to travel from one compartment of the ship to another to convey classified information was eliminated by the use of fiber optics in this system. It was successfully deployed in the Mediterranean for over 3 years.

A fiber optics data link interface to connect Naval Intelligence Processing System (NIPS) computers with various system peripherals is under development. This project is designed to show the feasibility of employing fiber optics for the transfer of high-speed digital data as well as video information in intraship communications. The fiber optic link connects several interactive display terminals, teletypewriters, and line-printers connected to the multiplexer unit in the Compartmented Mode Processing System (CMPS). Fiber optics is being used here both for improved bandwidth and for meeting TEMPEST requirements on board the ship.

Another application for fiber optics is a system for sending analog signals from a sonar array on a submarine to a computer for processing (Allard, F. C., 1976). A 55-channel converter within the pressure hull translates the electrical output from the hydrophones to light signals. In this case, plastic fibers and a red LED are used for the signal transmission. Laboratory tests and sea trials have demonstrated the superior crosstalk and EMI immunity of the fiber optics cables over that of the conventional twisted shielded pairs, in addition to substantial volume and weight savings. Eventually an even greater payoff is expected to be achieved by running fiber optics cables through pressure barriers so that the signals can be transmitted through the hull in optical form. This could reduce the number and diameter of hull penetrations and result in a significant savings in the cost and weight of the pressure hull design.

Data bussing using fiber optics is an attractive possibility for ships as well as aircraft (Altman, D. E., 1976). Because of the greater distances involved, a different selection of components is mandated. The fiber optics replacement for the electrical version of the Shipboard Data Multiplexing (SDMS) system is now under development. This system would employ graded index fibers used in conjunction with star (radial) couplers and ILD's in the transmitters and APD's in the receivers. The initial plan is to maintain the signal format of the present system which employs five channels multiplexed at frequencies from 41 to 83 MHz with a 1.2 Mb/s data rate per channel.

Fixed Land-Based Systems

A system to interconnect a satellite antenna to a computer processing center in which the bandwidth of fiber optics makes it cost-effective in comparison with electrical transmission is under development (Eppes, T. A., et al., 1977). The length is 1.8 km and the system uses eighteen 20 Mb/s single-fiber channels. These channels are contained in three cables, each of which contains eight graded index fibers (six for signal transmission, plus two spares). LED's are used in the transmitters and APD's in the receivers. The data format is base-band non-return-to-zero. Maximum allowable loss in the system is 28 dB, with a minimum of -17.5 dBm of optical power, at a wavelength centered near 8400 Å, coupled into a specified fiber. The bit error rate is less than 1×10^{-8} with an input to the optical receiver of -45.5 dBm.

In another land-based application, illustrated by a block diagram in Fig. 10, several fiber links were installed at the NORAD Cheyenne Mountain complex. The data rates in this case were less than 10 Mb/s and the maximum length was about 200 meters. The chief advantage of fiber optics in this case was immunity from RFI, crosstalk problems, and EMP.

Mobile Land-Based Systems

The Army has a large effort in the development of tactical land-based fiber optics systems. The main advantages in these systems are immunity from EMP effects, reduction in cable size, weight, and volume, and elimination of crosstalk. Two areas of interest are local distribution, with a one-for-one replacement of existing facilities with fiber optics on the loop side of a switch, and long haul, between switching facilities. Cables for both system types are under development.

For the local distribution system, illustrated in Figs. 11 and 12, channel bandwidths are 4 kHz analog and 16 kb/s to 576 kb/s digital, with the possibility of multiplexing of several channels per fiber. Cable runs in this system range from about 75 m to 3.2 km, with individual cable sections of 75 m, 300 m, and 1 km length. Both LED's and ILD's are being considered for use in the transmitters, and the receivers will contain PIN detectors. Plastic-clad silica fibers will probably be used based on considerations of ionizing radiation vulnerability and cost. Maximum allowable fiber attenuation is about 10 dB/km. A laboratory demonstration has been carried out using LED's and PIN detectors, with bidirectional operation over twelve channels in each direction (Slayton, I. B., 1975). A 334 m length of six-fiber cable was used, with four multiplexed channels per fiber. Channel bandwidths were 4 kHz and 32 kb/s.

For long-haul transmission, the lengths increase to 8 km at a maximum data rate of 20 Mb/s in a system without repeaters and 64 km at a 2.304 Mb/s data rate with repeaters. Length and bandwidth requirements dictate theuse of ILD sources, APD photodetectors, and graded-index fibers with a loss of less than 5 dB/km. Other land-based applications which are being pursued involve surveillance and weapons support systems.

Undersea Systems

Fiber optics may in the future replace electrical signal cables in a number of sonar telemetry systems, including sonobuoy (Redfern, J., 1976), torpedo, bottom-laid, moored, and towed array surveillance systems. Undersea applications of fiber optics differ somewhat from other long-run single-fiber applications because of the severe environmental and mechanical conditions to which the cables are subjected. These include pressures of 10,000 psi, and mechanical tension as high as 30,000 lbs. Problems peculiar to undersea cables include maintenance of the loss characteristics under the pressure of the ocean environment and in protection of the fibers from moisture while in a submerged cable. Another key area is that of fiber strength – the typical designs for most of the undersea cable types require that the fibers withstand stretching of 1-2% of their total length without breakage. Since fibers tend to degrade much more rapidly when subjected to both humidity or moisture and tension, this has proven a particular difficulty.

To date, prototype cables for a number of undersea applications have been produced. These include a large (1.7 cm diameter) cable for a towed applications, a 1.5 mm diameter cable for sonobuoy use, and a 1 mm diameter cable for a guided torpedo. Samples of length in the 300-500 meter range of each of these cables have been tested and results have generally been encouraging. For example, attenuation of the fibers was in the 3-10 dB/km range for most of the cables tested.

Improved bandwidth and reduced size and weight are the prime advantages for using fiber optics in undersea cables. The non-inductive nature of the optical cable eliminates impedance changes experienced during reeling and unreeling of electrical cables. Short circuits which can occur at pinholes in the jacket of electrical cables are also eliminated. In some cases, such as the towed array cable, the immunity of the cable to EMI in the region in which it emerges from the water and is coiled on the deck of a ship is also a significant advantage.

CONCLUSIONS

Based on the progress achieved during the past few years, fiber optics is being seriously considered for signal transmission in virtually every military environment. The most important research issues have been resolved, but significant engineering advances are still needed in areas such as field connectors for single fiber systems, fiber strength improvement for undersea applications, and operating life for ILD and LED sources. Assuming that the cost of components, and particularly the fibers, continues to drop, guided optical communication will be cost-effective for an increasing number of applications. The early adoption of standards for these components is also important from the standpoint of fostering their widespread use in military systems.

ACKNOWLEDGEMENTS

The author greatly appreciates the efforts of several individuals who have provided information for and critically reviewed this manuscript: L. V. Dworkin, U.S. Army Electronics Command; K. C. Trumble, U.S. Air Force Avionics Laboratory, and D. J. Albares, R. A. Eastley, R. J. Kochanski, W. H. Putnam, and D. N. Williams of the U.S. Naval Electronics Laboratory Center.

REFERENCES

Albares, D. J., Dworkin, L. V., and Trumble, K. C., Jan. 1975, "Prospective Applications for Fiber Optic Transmission in the Military," Williamsburg, VA, Topical Meeting on Fiber Optic Transmission.

Allard, F. C., Feb. 1976, "A Fiber Optics Sonar Link," Electro-Optics System Design, p. 32–35.

Altman, D. E., 1975, "Eight-Terminal Bidirectional Fiber Optic Trunk Data Bus," Naval Electronics Laboratory Center Technical Report 1969.

Altman, D. E., 1976, "A Study of the Application of Fiber Optics Technology to the Shipboard Data Multiplex System," Naval Electronics Laboratory Center Technical Report 1995.

Auracher, F., and Zeitler, K.-H., 1976, "Multiple Fiber Connectors for Multimode Fibers," Opt. Comm. 18, 556.

Barnoski, M. K., Ed. 1976, "Fundamentals of Optical Fiber Communications," New York, Academic Press.

Barnoski, M. K., and Friedrich, H. R., 1976, "Fabrication of an Access Coupler with Single-Strand Multimode Fiber Waveguides," Appl. Opt. 15, 2629.

Biard, J. R., and Shaunfield, J. E., 1974, "Optical Couplers," Air Force Avionics Laboratory Technical Report 74–314.

Biard, J. R., and Shaunfield, J. E., 1977, "Wideband Fiber Optic Data Link," Air Force Avionics Laboratory Technical Report (to be published).

Burrus, C. A., et al., 1975, "Direct Modulation Efficiency of LED's for Optical Fiber Transmission Applications," Proc. IEEE 63, 329.

Campbell, J. R., and Bryant, J. F., 1977, "Fiber Optic Technology Summary for the Defense Communications System," Naval Electronics Laboratory Center Technical Note 3236.

Campbell, L. L., 1976, "Status of Fiber Optic Research in the U.S.A.," Opt. Eng. 15, 473.

Chown, M., et al., 1973, "Direct Modulation of Double-Heterostructure Lasers at Rates up to 1 Gbit/s," Electron. Lett. 9, 34.

Cohen, L. G., et al., 1975, "Transmission Properties of a Low-Loss, Near-Parabolic Index Fiber," Appl. Phys. Lett. 26, 472.

Cohen, L. G., and Personick, S. D., 1975, "Length Dependence of Pulse Dispersion in a Long Multimode Optical Fiber," Appl. Opt. 14, 1357.

Dalgleish, J. F., and Lukas, H. H., 1975, "Optical-Fibre Connector," Electron. Lett. 11, 24.

DiDomenico, M., Jr., 1974, "A Review of Fiber Optical Transmission Systems," Optical Engineering 13, 423.

Dixon, R. W., et al., 1976, "Improved Light-Output Linearity in Stripe-Geometry Double-Heterostructure (Al, Ga)As Lasers," Appl. Phys. Lett. 29, 372.

Dworkin, L., et al., 1976, "The Role of Fiber Optics in the Army Wescon Conference, Session 14.

Dworkin, L, et al., 1977, "Progress Towards Practical Military Fiber Optics Communications Systems," Williamsburg, VA, Topical Meeting on Fiber Optic Transmission.

Eastley, R. A., and Putnam, W. H., 1974, "Telephone System – Fiber Optic Modem S202," Naval Electronics Laboratory Center Technical Document 260.

Ellis, J. R., and Williams, D. N., 1976, "Fiber Optics Application to A-7 Aircraft," Society of Photo-Optical Instrumentation Engineers, Vol. 77.

Eppes, T. A., et al., 1977, "A Two Kilometer Optical Fiber Digital Transmission System For Field Use at 20 mb/s," this meeting, paper No.

Evans, B. D., and Sigel, G. H., 1975, "Radiation Resistant Fiber Optic Materials and Waveguides," IEEE Trans. Nucl. Science NS-22, 2462.

Frieberger, R. J., 1976, "300 Meter Sonobuoy Cable/500 Meter Tow Cable," Report N00123-75-C-1023.

French, W. G., et al., 1975, "Glass Fibers for Optical Communication," Ann. Rev. Mater. Sci. 5, 373.

Gardner, W. B., 1975, "Microbending Loss in Optical Fibers," Bell Syst. Tech. J. 54, 457.

Gloge, D., 1976, "Optical Fiber Technology," New York, IEEE Press.

Goell, J. E., 1974, "An Optical Repeater with a High-Impedance Input Amplifier," Bell Syste. Tech. J. 53, 629.

Greenwell, R. A., 1976. "Results of A-7 ALOFT "Bottoms Up" Model and Weight Sensitivity Analysis," Naval Electronics Laboratory Center Technical Report 1998; and "A-7 ALOFT Life-Cycle Cost and Measures of Effectiveness Models," Naval Electronics Laboratory Center Technical Report 1982.

Greenwell, R. A., and Holma, G., 1977, "A-7 ALOFT Economic Analysis and EMI-EMP Test Results," this meeting, paper no. 14.

Harder, R. D., et al., 1977, "A-7 ALOFT Demonstration Final Report," Naval Electronics Laboratory Center Technical Report 2024.

Hayashi, M. B., et al., 1970, "Junction Lasers which Operate Continuously at Room Temperature," Appl. Phys. Lett. 17, 109.

Heinen, J., et al., 1976, "Light Emitting Diodes with a Modulation Bandwidth of more than 1 GHz," Electron. Lett. 12, 553.

Horiguchi, M., and Osanai, H., 1976, "Spectral Losses of Low-OH-Content Optical Fibers," Electron. Lett. 12, 310.

Hseih, J. J., 1976, "Room-Temperature Operation of GaInAsP/InP Double-Heterostructure Diode Lasers Emitting at 1.1μm," Appl. Phys. Lett. 28, 283.

Hudson, M. C., and Thiel, F. L., 1974, "The Star Coupler: A Unique Interconnection Component for Multimode Optical Waveguide Communications Systems," Appl. Opt. 13, 2540.

Jeunhomme, L., and Pocholle, J. P., 1976, "Directional Coupler for Multimode Optical Fibers," Appl. Phys. Lett. 29, 485.

Kurkjian, C. R., 1976, "Strength of 0.04 - 50 m Lengths of Coated Fused Silica Fibers," Appl. Phys. Lett. 28, 588.

Mabbitt, A. W., and Mobsby, C. D., 1975, "High-Speed High-Power 1.06 m Gallium Indium-Arsenide Light-Emitting Diodes," Electron. Lett. 11, 157.

Mattern, P. L., et al., 1974, "The Effect of Radiation on the Absorption and Luminescence of Fiber Optic Waveguides and Materials," SAND-74-8622.

Maurer, R. D., 1973, "Glass Fibers for Optical Communications," Proc. IEEE 61, 452.

Maurer, R. D., et al., 1973, "Effect of Neutron and Gamma Radiation on Glass Optical Waveguides," Appl. Opt. 12, 2024.

Maurer, R. D., 1975, "Strength of Optical Fiber Waveguides," Appl. Phys. Lett. 27, 220.

Miller, S. E., et al., 1973, "Research toward Optical Fiber Transmission Systems," Proc. IEEE, 1703.

Milton, A. F., and Lee, A. B., 1976, "Optical Access Couplers and a Comparison of Multiterminal Fiber Communication Systems," Appl. Opt. 15, 244.

Nawata, K., and Takano, K., 1976, "800 Mb/s Optical-Repeater Experiment," Electron. Lett. 12, 178.

Olshansky, R., and Keck, D. B., 1976, "Pulse Broadening in Graded-Index Optical Fibers," Appl. Opt. 15, 483.

Panish, M. B., 1975, "Heterostructure Injection Lasers," IEEE Trans. Micro. Theory Tech., MTT-23, 20.

Pearsall, T. P., et al., 1976, "Efficient Lattice-Matched Double-Heterostructure LED's at 1.1 μm from $Ga_xIn_{1-x}As_yP_{1-2}$," Appl. Phys. Lett. 28, 499.

Personick, S. D., 1971, "Time Dispersion in Dielectric Waveguides," Bell Syst. Tech. J. 50, 843.

Personick, S. D., 1973, "Receiver Design for Digital Fiber Optic Communication Systems," Bell Syst. Tech. J. 52, 843.

Personick, S. D., 1975, "Optical Fibers, a New Transmission Medium," Communications Society 14, 20.

Putnam, W. H., 1976, "Fiber Optic Tow Cable Environmental Tests," Naval Electronics Laboratory Center Technical Report 2006.

Redfern, J., 1976, "Preliminary Analysis of the Requirements for a Fiber Optic Cable for Sonobuoy Applications," Naval Undersea Center Technical Note TN-1654.

Slayton, I. B., 1975, "26 Pair Cable System," RDT and ECOM Report 75-0363.

Shaunfield, J. E., 1976, "EMI/EMP Resistant Data Bus," Air Force Avionics Laboratory Technical Report TR-76-99.

Sigel, G. H., and Evans, B. D., 1974, "Effect of Ionizing Radiation on Transmission of Optical Fibers," Appl. Phys. Lett. 24, 140.

Sigel, G. H., 1977, Private Communication.

Snitzer, E., 1961, "Cylindrical Dielectric Waveguide Modes," J. Opt. Soc. Amer. 51, 491.

Stewart, L. L., 1977, "Flight Operational Wideband Fiber Optics Data Links," Air Force Avionics Laboratory Technical Report (to be published).

Taylor, H. F., et al., 1975, "Data Bussing with Fiber Optics," Nav. Res. Rev. 28, No. 2, 12.

Thiel, F. L., et al., 1974, "In-Line Connectors for Multimode Optical Waveguide Bundles," Appl. Opt. 13, 240.

Uhlhorn, R. W., et al., 1976, "A-7 ALOFT Economic Analysis," McDonnell Aircraft Company.

Wieder, H. H., 1977, Private Communication.

Wilkins, G. A., 1976, "Fiber Optic Cables for Undersea Communications," to appear in Fiber Optics and Integrated Optics.

Wilkins, G. and Eastley, R., 1977, "Recent Progress in Optical Fiber Cables for Use in the Ocean," this meeting, paper no. 4.

Witte, H. H., 1976, "Optical Tapping Element for Multimode Fiber," Opt. Commun. 18, 559.

Wittke, J. P., et al., 1976, "High Radiance LED for Single-Fiber Optical Links," RCA Review 37, 159.

Wittmann, L., 1975, "Contact-Banded Epoxy-Resin Lenses to Fibre Endfaces," Electron. Lett. 11, 477.

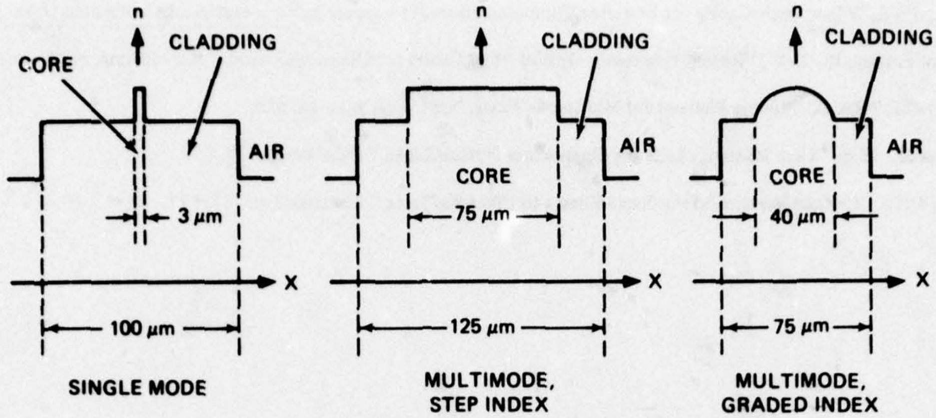

Fig. 1. Refractive index profiles for three types of optical fibers for signal transmission. Typical core and cladding dimensions are indicated.

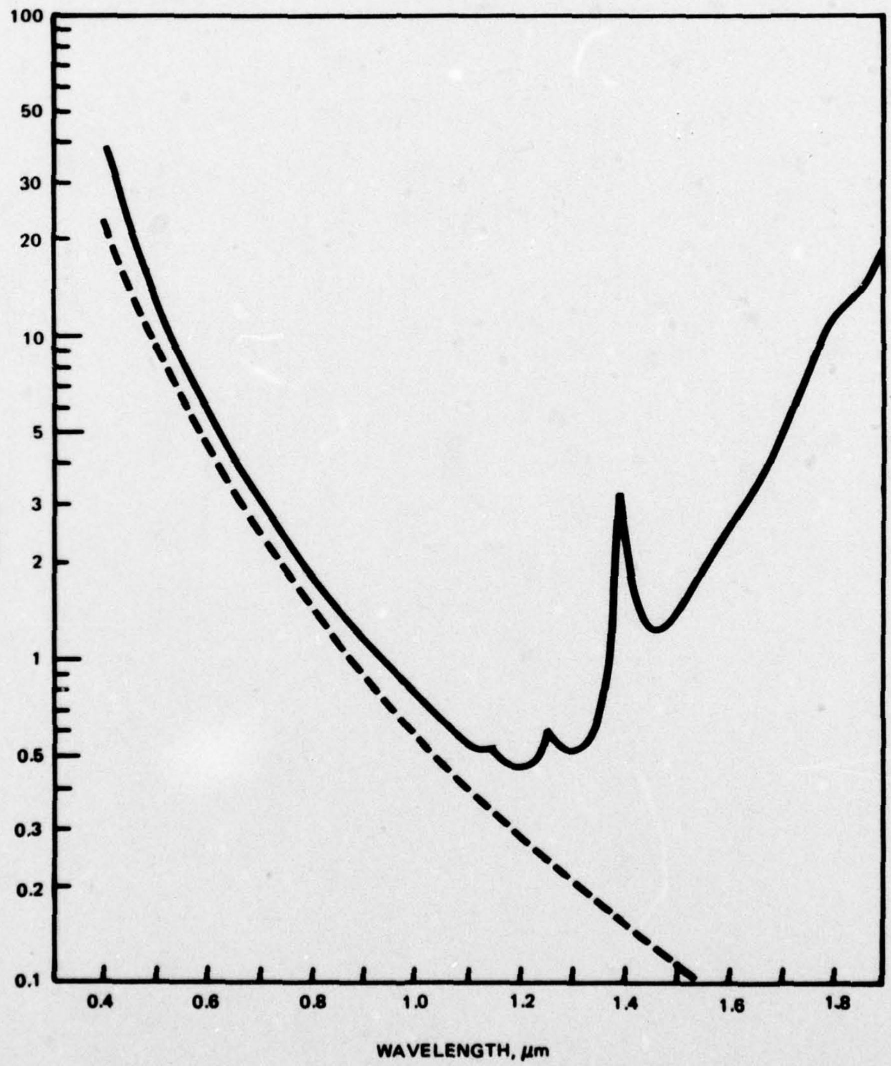

Fig. 2. Spectral loss characteristics for a low-loss fiber with a phosphosilicate core and a borosilicate cladding. The dashed line represents a theoretical minimum loss due to Rayleigh scattering for this type of fiber.

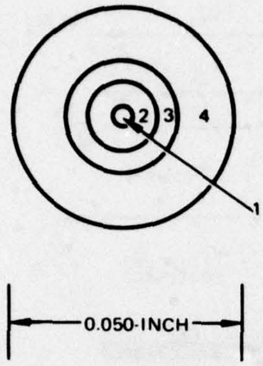

NUC/AIRLOG CABLE UNIT

1. 0.005-INCH-DIAMETER, STEP INDEX, OPTICAL FIBER (ITT #SCVD 259).
2. TEFLON (PFA) BUFFER, ADDED BY ITT TO 0.015-INCH DIAMETER.
3. LOW SHORE, LOW MODULUS, ELASTOMER #240-1, ADDED BY AIR LOGISTICS TO 0.025-INCH DIAMETER.
4. LOADBEARING STRUCTURE, ADDED BY AIR LOGISTICS TO FINAL DIAMETER OF 0.050-INCH. THIS STRUCTURE CONTAINS 9840 PARAXIAL, HTS-901 S-GLASS FILAMENTS IN A POLYAMIDE-MODIFIED, AMINE-CURED, EPOXY RESIN SYSTEM (AIR LOGISTICS #380-4). THE S-GLASS VOLUME FRACTION IN THE MATRIX IS APPROXIMATELY 0.64.

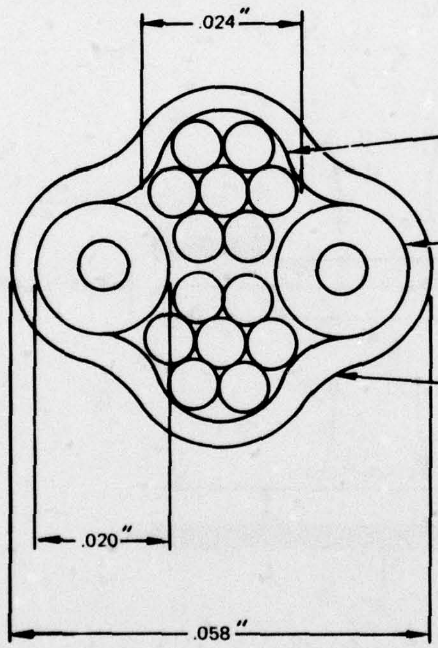

STRANDED STEEL WIRE

- SEVEN (7) STRANDS .0081-INCH DIA.
- 0.33-INCH LAY
- WT (2 WIRES) 8.4 lb/km
- TENSILE STRENGTH: 300 000 psi
- YOUNG'S MODULUS: 30 700 000 psi

OPTICAL FIBER

- WT (2 FIBERS) 2.13 lb/km
- TENSILE STRENGTH $>$100 000 psi (PROOF TEST)
- COATING MATERIALS: SILICONE RTV/PFA

PLASTIC JACKET

- WT 1.32 lb/km
- MATERIAL: HIGH DENSITY POLYETHELENE

NOTE:

1. TOTAL CABLE WEIGHT: 3.6 lb (300 METRES)
2. CABLE BREAKING STRENGTH: 180 lb
3. CABLE ELEMENTS ARE STRANDED: LAY LENGTH 2.0-INCH, LAY ANGLE 2°

Fig. 3. Two types of fiber optics cable for undersea use

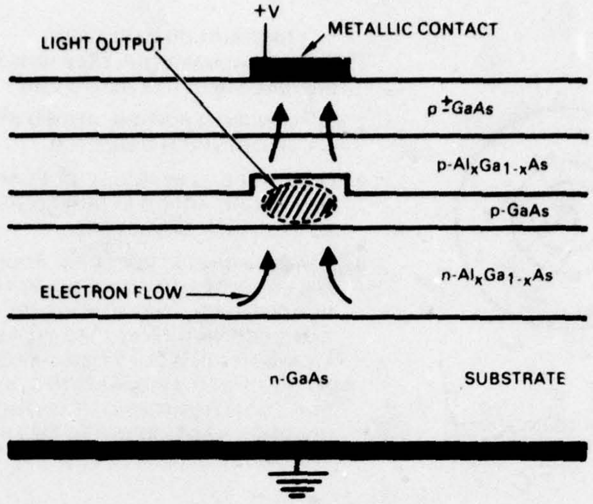

Fig. 4. Schematic diagram of a $Ga_xAl_{1-x}As$ double-heterostructure injection laser designed for operation in a single transverse mode. The refractive index of the P-GaAs layer exceeds that of the adjacent layer to provide for waveguiding in the vertical direction, and the step in that layer confines the beam in the horizontal direction. The light is generated by the recombination of the injected electrons and holes in the pn junction region.

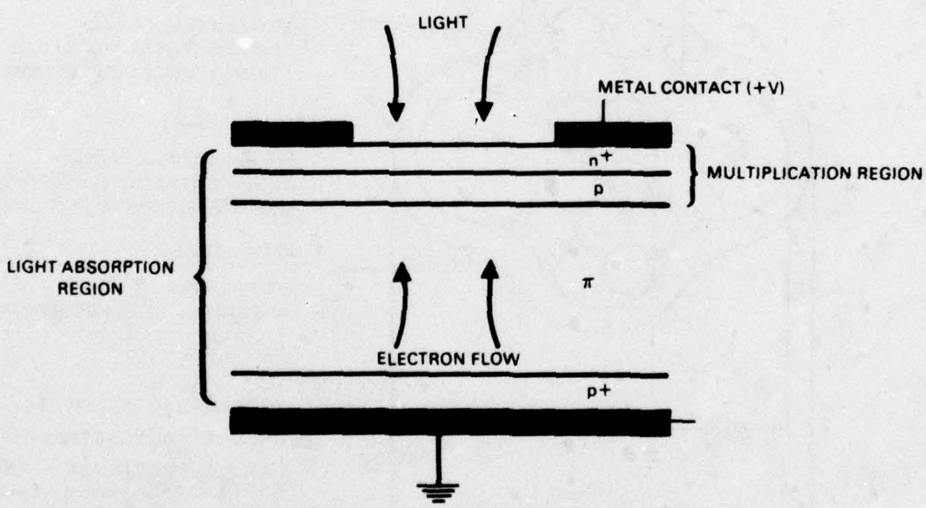

Fig. 5. Schematic diagram of a silicon avalanche photodiode. The incident light is absorbed primarily in the wide intrinsic (π) region, creating electron-hole pairs. Carrier multiplication occurs in the high-field depletion region of the pn^+ junction.

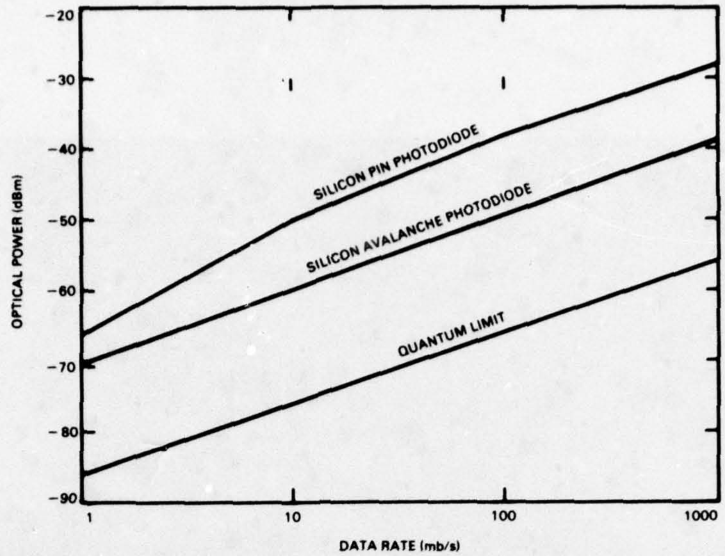

Fig. 6. Comparison of state-of-the-art receiver performance with the quantum limit. The internal gain of the silicon avalanche photodiode gives an improvement of about 10 dB in sensitivity in comparison with the silicon PIN photodiode for data rates between 10 Mb/s and 1 Gb/s. The avalanche photodiode sensitivity is nearly 20 dB less than the quantum limit, which assumes a noiseless receiver with unity quantum efficiency.

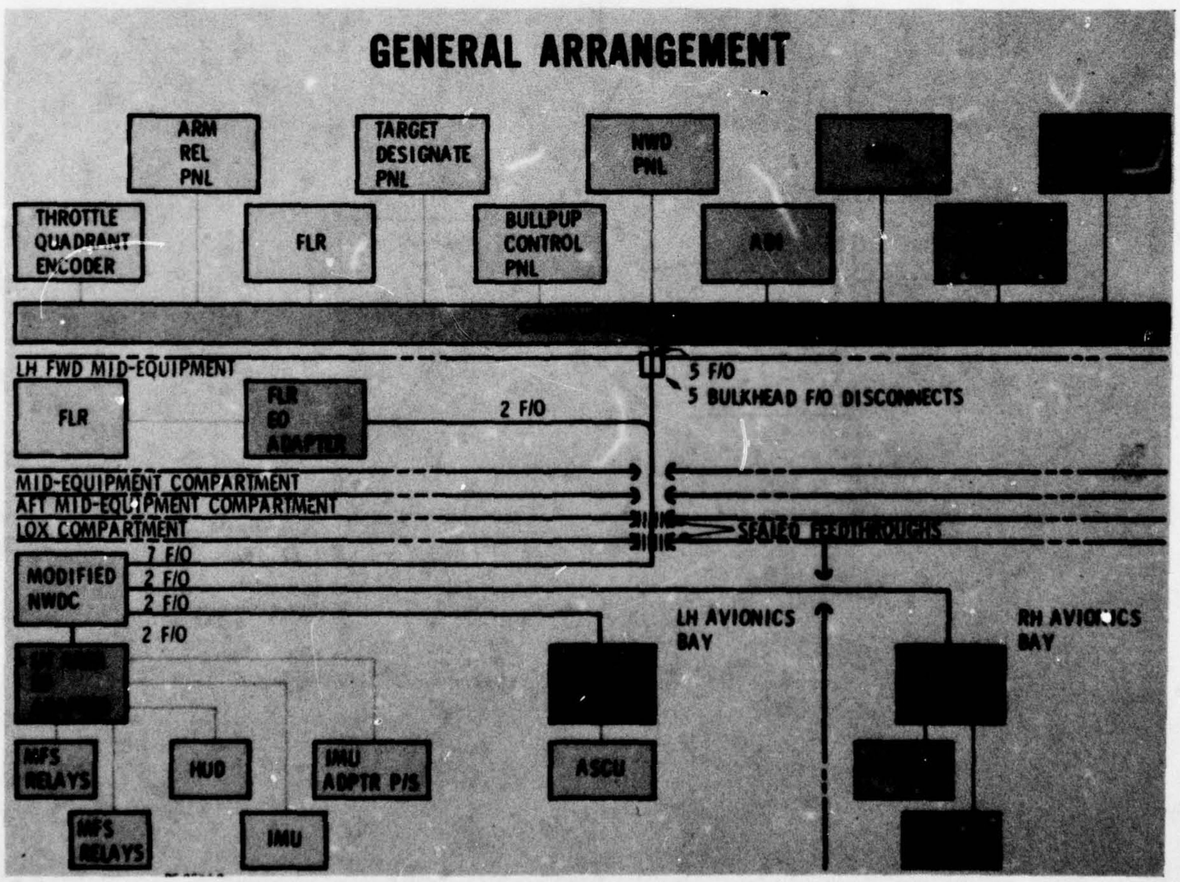

Fig. 7. Block diagram of A-7 demonstration.

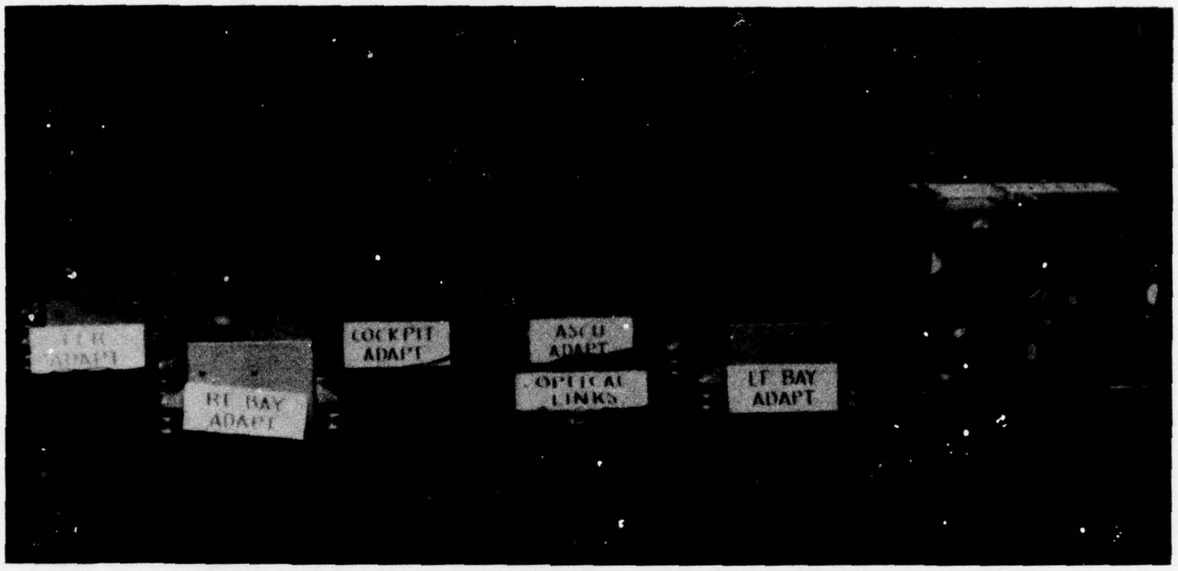

Fig. 8. Fiber optics hardware for A-7 system.

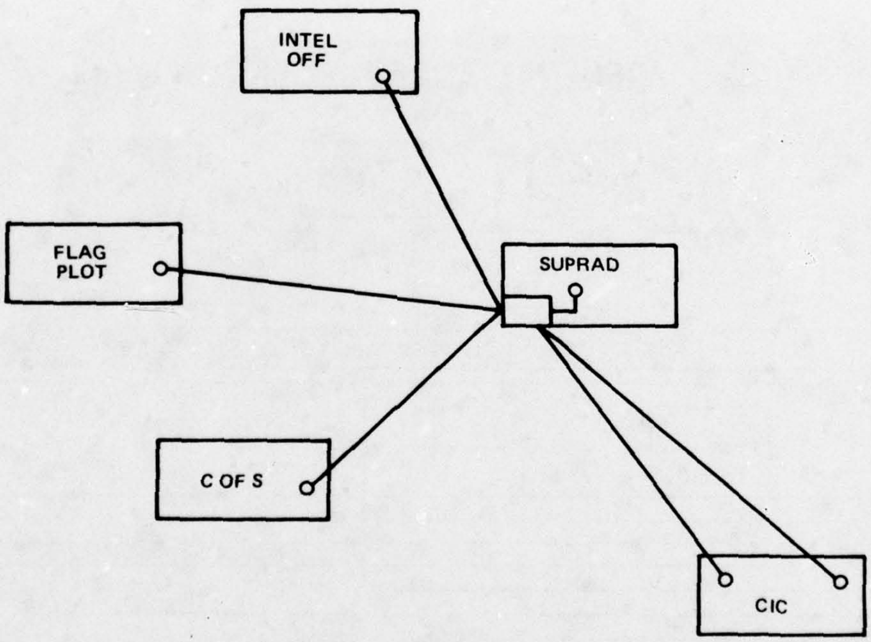

Fig. 9. Schematic of the telephone system installed on the USS LITTLE ROCK.

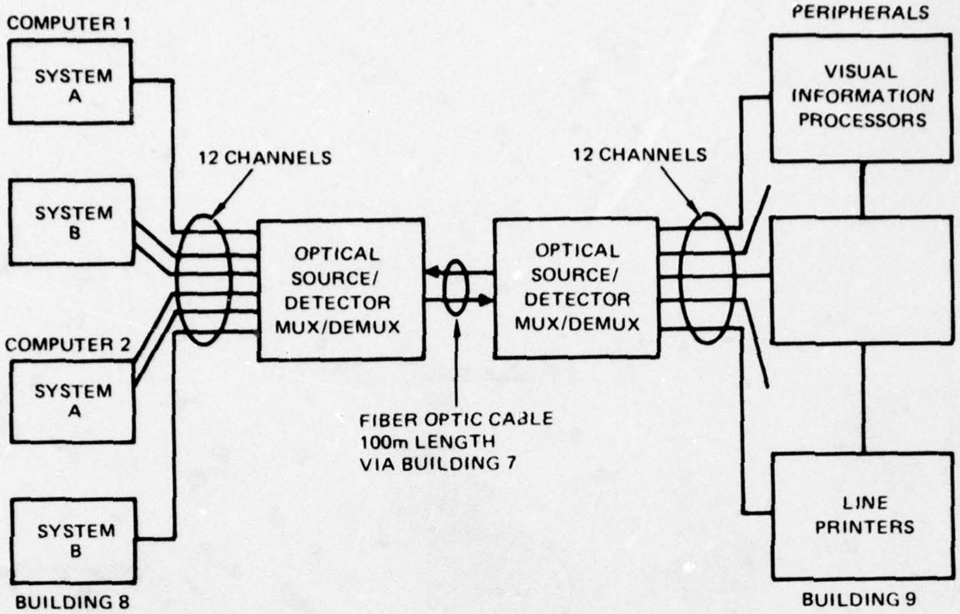

Fig. 10. NORAD fiber optics system.

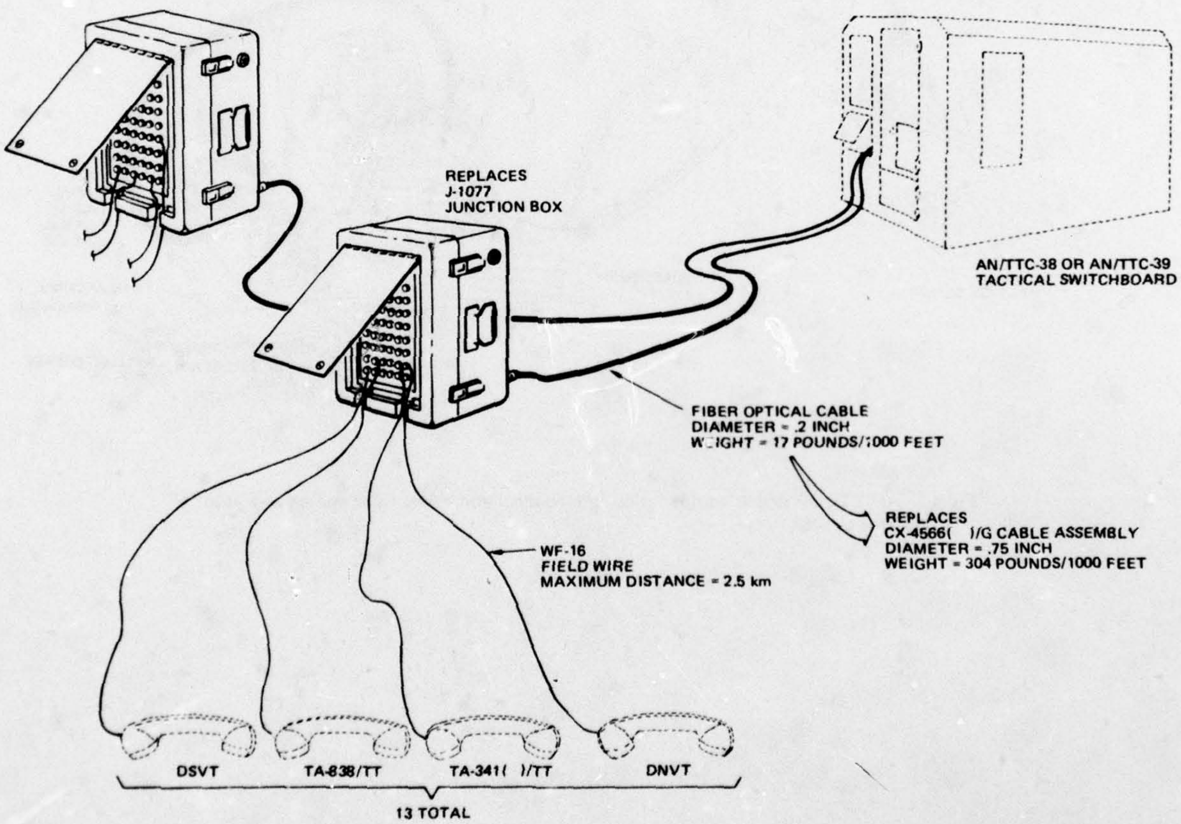

Fig. 11. Tactical fiber optics link system diagram.

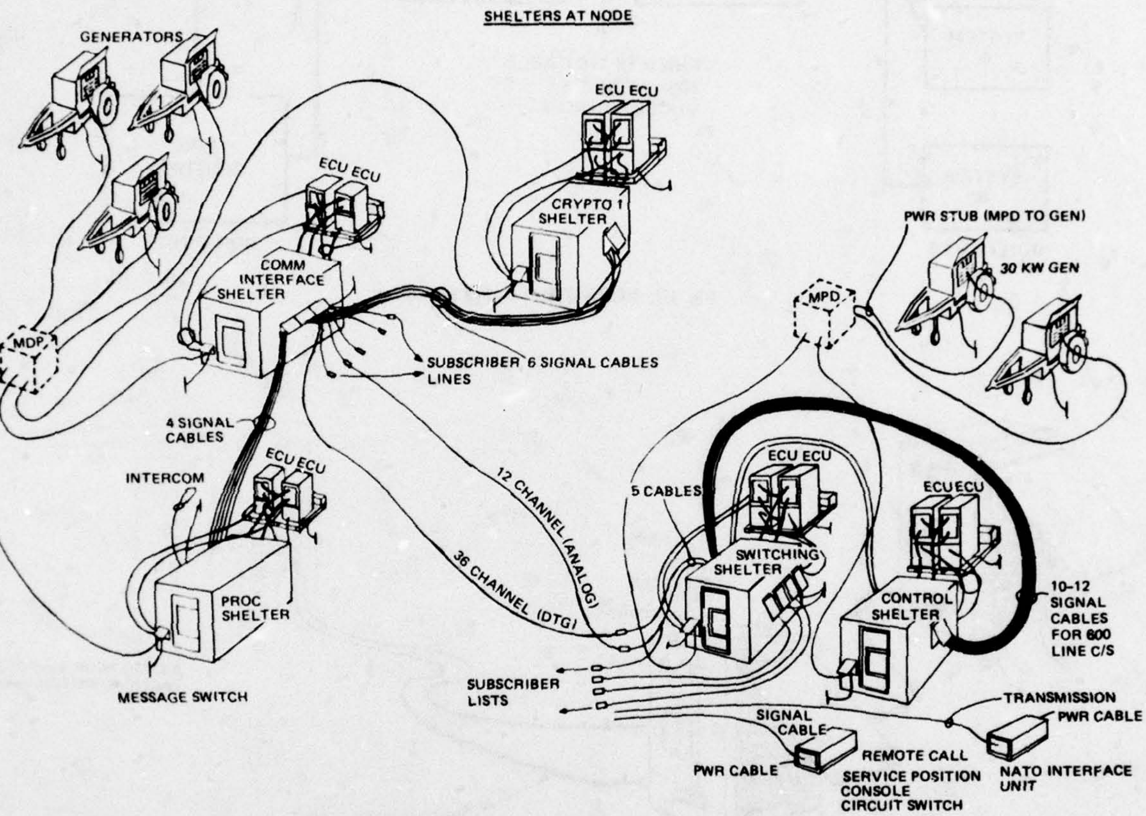

Fig. 12. AN/TTC-39 switch configuration interconnect and signal cable replaceable with fiber optics.

REVIEW OF INTEGRATED OPTICS

H. Kogelnik
Bell Telephone Laboratories
Holmdel, New Jersey 07733

ABSTRACT

A tutorial introduction and a review is given of the field of integrated optics and optical guided-wave devices. Device principles and potential applications are discussed. The properties of dielectric waveguides are reviewed briefly and new materials and new fabrication techniques are mentioned. An illustration is given of recent work on devices. This includes a discussion of work on guided-wave modulators and switches with focus on devices made by titanium diffusion in lithium niobate. Mention is made of an experimental 4 x 4 switching network which was recently demonstrated in the laboratory. Other devices discussed are corrugated waveguide filters in which rejection bandwidth from 0.1 to 6 Å have been obtained. The paper concludes with a discussion of the use of guided-wave techniques in semiconductor junction lasers.

I. INTRODUCTION

The purpose of this paper is to give the reader a brief tutorial introduction to and a review of the growing research field of "integrated optics", and to give an illustration of recent work. In the limited space and time available, it is impossible to aim for completeness, and we refer the reader interested in more completeness and more detail to a series of recent review articles (Miller, S. E., 1969; Goell, J. E., et al., 1970; Goell, J. E., et al., 1970; Tien, P.K., 1971; Miller, S.E., 1972; Taylor, H. F., et al., 1974; Chang, W. S., et al., 1974; Tien, P. K., 1974; Kogelnik, H., 1975; Conwell, E.M., 1976; Tien, P. K., 1977) and recent monographs on the subject. (Barnoski, M. K., 1973; Tamir, T., 1975)

Historically, there was early relevant work in the seven years before 1969, but the coining of the term "Integrated Optics" by S. E. Miller (Miller, S. E., 1969) in that year marks also the beginning of considerable research interest in this subject; and there are now research activities in a still increasing number of university, industrial and governmental laboratories. One main impetus for this stems from the promise of optical-fiber transmission systems (Miller, S. E. et al., 1973) which, in turn, is based on the recent achievement of low transmission losses in optical fibers. We should point out that a majority of fiber systems under study today are multimode fiber systems in which light propagates in mixtures of hundreds of electromagnetic modes. Integrated optics has, so far, not offered much for multimode systems, as most integrated optical circuits and devices are single-mode structures. Creative thought is needed here. However, single-mode fiber systems are attracting increasing interest for higher transmission speeds and longer transmission distances. These systems are more compatible with integrated optics, and here integrated optics techniques may one day provide compact circuits and devices for repeaters, and may offer such possibilities as wavelength multiplexing or switching of optical signals. Fiber losses of the order of 1 db/km have now been achieved throughout the near-infrared region from 0.8 to about 1.6 μm marking this as spectral region of principal interest to integrated optics.

The name integrated optics now covers all exploration of guided-wave techniques used to construct new or improved optical devices. Waveguides are used to confine the light to very small cross-sections over relatively long lengths. One aims for compact and miniaturized devices of better reliability, better mechanical and thermal stability, and for lower power consumption and lower drive voltages in active devices. There is, of course, also the hope that one will be able to combine several guided-wave devices on a common substrate or chip and form more complicated optical circuits in analogy with the integrated circuits of electronics. However, some of the new guided-wave devices, lasers or modulators, for example, may well be able to compete on their individual merits with their bulk-optical counterparts.

The waveguides used in integrated optics are dielectric waveguides, usually in the form of a planar film or strip of higher refractive index than the surrounding. The devices of interest are often the counterparts of familiar microwave or optical devices. They are couplers, junctions, directional couplers, filters, wavelength multiplexers and demultiplexers, and active devices such as modulators, switches and lasers and detectors. In the following, we will first discuss briefly the characteristics of the dielectric waveguides used in integrated optics and of the materials employed to fabricate them. This will be followed by an illustration of recent work on devices and circuits.

II. DIELECTRIC WAVEGUIDES

Dielectric waveguides are used to confine and guide the light in the devices of integrated optics. We distinguish between planar film guides which confine the light in only one dimension, and strip guides which confine the light in two dimensions. Figure 1 shows schematically sideviews of a film waveguide where n_f, n_s and n_c are the refractive indices of the film, substrate and cover materials, respectively. The film acts as a waveguide if

$$n_f > n_s, n_c. \tag{1}$$

The guide supports guided modes where the light is confined in and near the film, and radiation modes where the light is spread out far away from the film. Figures 1a and 1b show the simple ray pictures corresponding to the radiation modes, and Figure 1c shows the ray picture of a guided mode. In the latter case, the ray angle θ exceeds the critical angle θ_c for total internal reflection at the film-substrate interface given by

$$\sin \theta_c = n_s/n_f, \tag{2}$$

and the rays are trapped inside the film. The guide will support only one single guided mode when the film height h is very small, i.e., approximately given by

$$h \approx \frac{\lambda}{2} (n_f^2 - n_s^2)^{-1/2}, \tag{3}$$

where λ is the wavelength. For more detail on the theory of dielectric waveguides, the reader is referred to review texts such as (Kogelnik, H., 1975).

Strip guides confining the light in two dimensions can be made in various cross-sections, some of which are shown in Figure 2. In every one of these cases, the guide index n_f is larger than that of the surrounding.

Strip guides can be used to form various circuit patterns. The example of a directional coupler circuit is shown in Figure 3 where the dark areas indicate the strip regions of higher refractive index. Practical index differences $n_f - n_s$ depend on the fabrication technology used and are typically in the range of 10^{-3} to 10^{-2}. Typical dimensions of single-mode strip guides are heights of 0.5 μm and widths of 2-3 μm.

To define circuit patterns one has to use photolithographic techniques that often strain the state of the art known in electronic integrated circuits, and the employment of electron-beam exposure is often necessary. (Zernike, F., 1975)

III. MATERIALS

New materials and new fabrication techniques are, and have been, of central importance to integrated optics. A considerable number of new materials and techniques have been found and explored for the fabrication of dielectric guides and integrated optical devices. (Zernike, F., 1975; Hammer, J. M., 1975; Garmire, E., 1975) Materials allowing guide losses of 1 db/cm or better are usually desired. A low-loss waveguide material useful for passive devices such as directional couplers or corrugated waveguide filters has been a film of glass produced by RF-sputtering on a glass substrate of lower index. (Goell, J. E., et al., 1969) Other materials examples are the electrooptic crystals $LiNbO_3$ and $LiTaO_3$ which are of interest for modulators and switches. It has been found (Schmidt, R. V., et al., 1974; Hammer, J. M., et al., 1974) that low-loss waveguides can be made in these ferroelectric materials by in-diffusion of the metals Ti and Nb, respectively. GaAs and related III-V semiconductor compounds are of particular interest to integrated optics, as these materials are suitable for the fabricatoon of efficient, electrically pumped junction lasers as well as for modulators and detectors. (Garmire, E., 1975) In these materials, waveguides are made by epitaxial growth of heterostructures with suitable refractive index. To form the waveguides for GaAs lasers, e.g., the addition of Al is used to lower the index in the substrate and cover layers.

To be of use in transmission systems, junction lasers must be capable of operating continuously at room temperature with a long device life. In the GaAlAs materals system, cw room temperature operation was demonstrated about seven years ago (Hayashi, I., et al., 1970; Alferov, Zh.I., et al., 1971) and good progress has been made since in improving device life. The GaAlAs system can provide lasers in the wavelength range of 0.75 to 0.9 μm. Several other materials systems show promise for the spectral range from 1.0 μm to 1.6 μm. Recently, cw laser operation at room temperature was demonstrated in GaAsSb/AlGaAsSb system (Nahory, R. E., et al., 1976) at 1.0 μm, in the GaInAsP/InP system (Hsieh, J. J., et al., 1976) at 1.1 μm, and the InGaAs/InGaP system (Nuese, C. J., et al., 1976) at 1.06 to 1.12 μm.

IV. DIFFERENT TYPES OF INTEGRATION

We have indicated before that the confinement of light provided by waveguiding can lead to considerable improvements in integrated optics devices, such that they can compete well with their bulk-optical counterparts on their individual merits. Examples for this are the low drive powers offered by guided-wave lasers and modulators. As guided-wave devices are essentially made of waveguides, they can also be connected by waveguides, i.e., the devices are suitable for integration, which is an additional benefit. Depending on the application one has in mind, one can think of several kinds of integration. For optical communications, it may be advantageous to have several kinds of devices, e.g., a laser, a modulator and a detector, all on one chip, and all in one materials system. This is called monolithic integration. GaAs and its relatives are suitable materials for monolothic integration. In the first experimental demonstrations of this, combinations of a laser and an absorption modulator (Reinhardt, F. K., et al., 1974) and of a laser and a phase modulator (Reinhardt, F. K., et al., 1975) were reported. Other interesting possibilities are laser-filter-modulator or filter-detector combinations: In all these cases, the integration is serial and multi-functional, i.e., the optical signal is processed sequentially by devices of different kinds.

When several devices of the same kind are made on one chip, we call this monofunctional integration. Here one has more freedom to optimize the materials choice for each given device. We shall mention later two experimental cases where monofunctional integration was already demonstrated in the laboratory. (Schmidt, R. V., 1976; Aiki, K., et al., 1976) One has the simplest case of monofunctional integration when devices of one kind are arranged unconnected and in parallel on one chip. This may be many lasers on a chip, or many modulators etc. There are also interesting cases of monofunctional chips where the devices are interconnected, e.g., many interconnected switches can form a switching network, (Schmidt, R. V., 1976) many interconnected filters on a chip can form a wavelength multiplexing circuit, etc.

V. MODULATORS AND SWITCHES

Considerable progress was made in recent years in guided-wave modulator and switching devices. (Hammer, J.M., 1975; Kaminow, I. P., 1975) To illustrate this work, we consider devices where waveguides were made by diffusion of Ti into $LiNbO_3$. This technique allows the fabrication of embedded strip guides in relatively simple photolithographic steps, as sketched in Figure 4. This way, a phase modulator of the geometry shown in Figure 5 was constructed. (Kaminow, I. P., et al., 1975) The waveguide was about 5 μm wide, the metal electrodes plated on the crystal surface were about 9 μm apart and 30 mm long. For this modulator, the required drive voltage was only 0.3 volts and the drive power was as low as 1.7 μW/MHz of bandwidth to achieve a modulation index of 1 rad at $\lambda = 0.63$ μm.

Using the same diffusion technique, a switched directional coupler of the geometry shown in Figure 6 was demonstrated. (Schmidt, R. V., et al., 1976) Here, a pair of guides is used, each about 3 μm wide and spaced as close as 3 μm over a 3 mm interaction length to allow the coupling and exchange of light between the two waveguides. The two electrode pairs are split in the middle to permit the application of voltages of reversed polarity. With this switching device, light entering one guide can be switched from one guide to the other with conversion ratios of 400:1 (i.e., 26 db).

By connecting several such switches, one can build switching networks such as that shown in Figure 7. By application of proper voltages light entering any of the input guides can be switched to any of the output guides. An experimental 4×4 switching network in which five switches of the kind described above were integrated on a $LiNbO_3$ chip was recently demonstrated. (Schmidt, R. V., 1976)

VI. FILTERS

Filters are needed for applications such as wavelength multiplexing of transmission channels. One way to make a guided-wave filter device is to machine a corrugation of a very short period Λ into the surface of a film guide as shown in Figure 8. Such a periodic guide of length L provides a band rejection filter with a fractional bandwidth of approximately

$$\Delta\lambda/\lambda \approx \Lambda/L \tag{4}$$

centered at a wavelength λ_o given by

$$\lambda_o = 2N\Lambda, \tag{5}$$

where N is the effective index of the guided mode. (Kogelnik, H., 1975) Figure 8, taken from (Flanders, D.C., 1974), shows the response of a corrugated glass guide at 0.57 μm.

The filter was fabricated by means of a holographic exposure of masking photoresist using a UV laser and by subsequent ion-beam etching. It was L = 0.57 mm long, and had corrugations with a period of Λ = 2000 Å and a depth of 460 Å. The response was measured with a tunable dye laser. In subsequent filter experiments (Schmidt, R. V., et al., 1974) bandwidths as narrow as 0.1Å were achieved.

VII. LASERS

The confinement of the light in double heterostructure junction lasers has, of course, been vital for the cw room temperature operation of these devices. Several other guided-wave techniques are under exploration to further improve the performance of junction lasers. One example is the use of various strip waveguides (Lee, T.P., et al., 1975; Lee, T. P., et al., 1976) in efforts to obtain single transverse mode output. Another example is the exploitation of distributed feedback structures (DFB), where a periodic waveguide similar to a corrugated waveguide filter is superimposed on the gain medium. DFB promises simple, compact, low-loss laser resonators, spectrally pure laser output and possibly smaller sensitivity of the laser wavelength to variations in temperature. Figure 9 shows a side view of a separate confinement GaAlAs heterostructure DFB junction laser that has been fabricated with the help of molecular beam epitaxy. (Casey, H. C., et al., 1976) GaAlAs junction lasers of somewhat similar geometry were recently demonstrated in cw operation at room temperature. (Nakamura, M., et al., 1975; Aiki, K., et al., 1976) Our final example of current research (Aiki, K., et al., 1976) is the monolithic integration on a GaAs chip of six DFB junction lasers with slightly different corrugation periods. Each of these lasers operates at a different wavelength, separated by about 20 Å from each other as sketched in Figure 10. The output from the six lasers is combined into a single multimode waveguide on the same chip.

REFERENCES

Aiki, K., Nakamura, M and Umeda, J., October, 1976, "Frequency Multiplexing Light Source with Monolithically Integrated Distributed-Feedback Diode Lasers", Applied Physics Letters, Vol. 29, NO. 8.

Aiki, K., Nakamura, M. and Umeda, J., October, 1976, "Lasing Characteristics of Distributed-Feedback GaAs-GaAlAs Diode Lasers with Separate Optical and Carrier Confinement", IEEE J. of Quantum Electronics, QE-12, 10.

Alferov, Zh. I., Andreev, V. M., Garbuzov, D. Z., Zhilgoev, Ju. V., Morozov, E. P., Portnoy, E. L., and Trofim, V. G., March, 1971, "Translation in Soviet Physics Semiconductor", 4, 1573-1575.

Barnoski, M. K., 1973, "Introduction to Integrated Optics", Plenum Press, New York.

Casey, Jr., H. C., Somekh, S. and Illgems, M., "Room-Temperature Operation of Low-Threshold Separate Confinement Heterostructure Injection Laser with Distributed Feedback", Appl. Phys. Lett. 27, 142-144, August, 1976.

Chang, W. S., Muller, W. M. and Rosenbaum, F. J., 1974, "Integrated Optics", Laser Applications, Vol. 2, Academic Press, New York.

Conwell, E. M., May, 1976, "Integrated Optics", Physics Today, 48-59.

Flanders, D. C., Kogelnik, H., Schmidt, R. V. and Shank, C. V., February, 1974, "Grating Filters for Thin-Film Optical Waveguides", Appl. Phys. Lett. 24, 194.

Garmire, E., 1975, "Semiconductor Components for Monolithic Applications", Integrated Optics, T. Tamir, Ed., Springer, Heidelberg.

Goell, J. E. and Standley, R. D., October, 1970, "Integrated Optical Circuits", Proc. IEEE 58, 1504-1512.

Goell, J. E. and Standley, R. D., December, 1969, "Sputtered Glass Waveguide for Integrated Optical Circuits", BSTJ 48, 10, 3445.

Goell, J. E., Standley, R. D. and Li, T., August, 1970, "Optical Waveguides Bring Laser Communication Closer", Electronics 20, 60-67.

Hammer, J. M., 1975, "Modulation and Switching of Light in Dielectric Waveguides", Integrated Optics, T. Tamir, Ed., Springer, Heidelberg.

Hammer, J. M. and Phillips, W., June, 1974, "Low-Loss Single-Mode Optical Waveguides and Efficient High Speed Modulators of $LiNb_xTa_{1-x}O_3$ on $LiTaO_3$", Appl. Phys. Lett. 24, 545.

Hayashi, I., Panish, M. B., Foy, P. W. and Sumski, S., August 1970, "Junction Lasers which Operate Continuously at Room Temperature", Appl. Phys. Lett. 17, 109-111.

Hsieh, J. J., Rossi, J. A. and Donnelly, J. P., June, 1976, "Room Temperature cw Operation of GaInAsP/InP Double Heterosturcture Diode Lasers Emitting at 1.1 μm", Appl. Phys. Lett. 28, 709-711.

Kaminow, I. P., January, 1975, "Optical Waveguide Modulators", IEEE Transactions on MIcrowave Theory and Technology, MTT-23, 57-70.

Kaminow, I. P., Stulz, L. W. and Turner, E. H., November, 1975, "Efficient Strip-Waveguide Modulator", Appl. Phys. Lett. 27, 555-557.

Kogelnik, H., January, 1975, "An Introduction to Integrated Optics", IEEE Transactions on Microwave Theory and Technology, MTT-23, 2-16.

Kogelnik, H., 1975, "Theory of Dielectric Waveguides", Integrated Optics, T. Tamir, Ed., Springer, Heidelberg.

Lee, T. P., Burrus, C. A., Miller, B. I. and Logan, R. A., September, 1972, "$Al_xGa_{1-x}As$ Double Heterostructure Rib-Waveguide Injection Laser", IEEE J. Quantum Electronics QE-11, 432-435.

Lee, T. P and Cho, A. Y., August, 1976, "Single-Transverse-Mode Injection Lasers with Embedded Stripe Layer Grown by Molecular Beam Epitaxy", Appl. Phys. Lett. 29, 164.

Miller, S. E., September, 1969, "Integrated Optics: An Introduction" Bell System Tech. J. 48, 2059.

Miller, S. E.,February, 1972, "A Survey of Integrated Optics, IEEE J. Quantum Electronics QE-8, 199-205.

Miller, S. E., Marcatili, E. A. J. and Li, T., December, 1973, "Research Toward Optical-Fiber Transmission Systems", Proc. IEEE, 61, 1703-1753.

Nahory, R. E., Pollack, M. A., Beebe, E. D., DeWinter, J. C. and Dixon, R. W., January, 1976, "Continuous Operation of 1.0 μm Wavelength $GaAs_{1-x}Sb_x/Al_yGa_{1-y}As_{1-x}Sb_x$ Double-Heterostructure Injection Lasers at Room Temperature", Appl. Phys. Lett. 28, 19-21.

Nakamura, M., Aiki, K., Umeda, J and Yariv, A., October, 1975, "CW Operation of Distributed Feedback GaAs-GaAlAs Diode Lasers at Temperatures up to 300 K", Appl. Phys. Lett. 27, 403-405.

Nuese, C. J., Olsen, G. H., Ettenberg, M., Gannon, J. J., and Zamerowski, T. J., December, 1976, "CW Room Temperature $In_xGa_{1-x}Ga/In_yGa_{1-y}P$ 1.06 μm Lasers", Appl. Phys. Lett. 29, 807-809.

Reinhardt, F. K. and Logan, R. A., November, 1974, "Monolithically Integrated AlGaAs Double Heterostructure Optical Components", Appl. Phys. Lett., 25 622-624.

Reinhardt, F. K. and Logan, R. A., November, 1975, "Integrated Electro-Optic Intracavity Frequency Modulation of Double-Heterostructure Injection Laser", Appl. Phys. Lett. 27, 532.

Schmidt, R. V. and Buhl, L. L., October, 1976, "Experimental 4 x 4 Optical Switching Network", Electronics Letters, 12, 575-577.

Schmidt, R. V., Flanders, D. C., Shank, C. V. and Standley, R. D., December, 1974, "Narrow-band Grating Filters for Thin-Film Optical Waveguides", Appl. Phys. Lett. 25, 651.

Schmidt, R. V. and Kamonow, I. P., October, 1974, "Metal-Diffused Optical Waveguides in $LiNbO_3$", Appl. Phys. Lett. 25, 458-460.

Schmidt, R. V. and Kogelnik, H., May, 1976, "Electro-Optically Switched Coupler with Stepped $\Delta\beta$ Reversal using Ti-Diffused $LiNbO_3$ Waveguides", Appl. Phys. Lett. 28, 503-506.

Tamir, T., Ed., 1975, "Integrated Optics", Topics in Applied Physics 7, Springer, Heidelberg.

Taylor, H. F. and Yariv, A., August, 1974, "Guided Wave Optics", Proc. IEEE, 62 1044.

Tien, P. K., 1974, "Integrated Optics", Scientific American 230, 28.

Tien, P. K., April, 1977, "Integrated Optics and New Wave Phenomena in Optical Waveguides", Rev. Mod. Physics 49.

Tien, P. K., November, 1971, "Light Waves in Thin Films and Integrated Optics", Appl. Opt. 10, 2395.

Zernike, F., 1975, "Fabrication and Measurement of Passive Components", Integrated Optics, T. Tamir, Ed., Springer, Heidelberg.

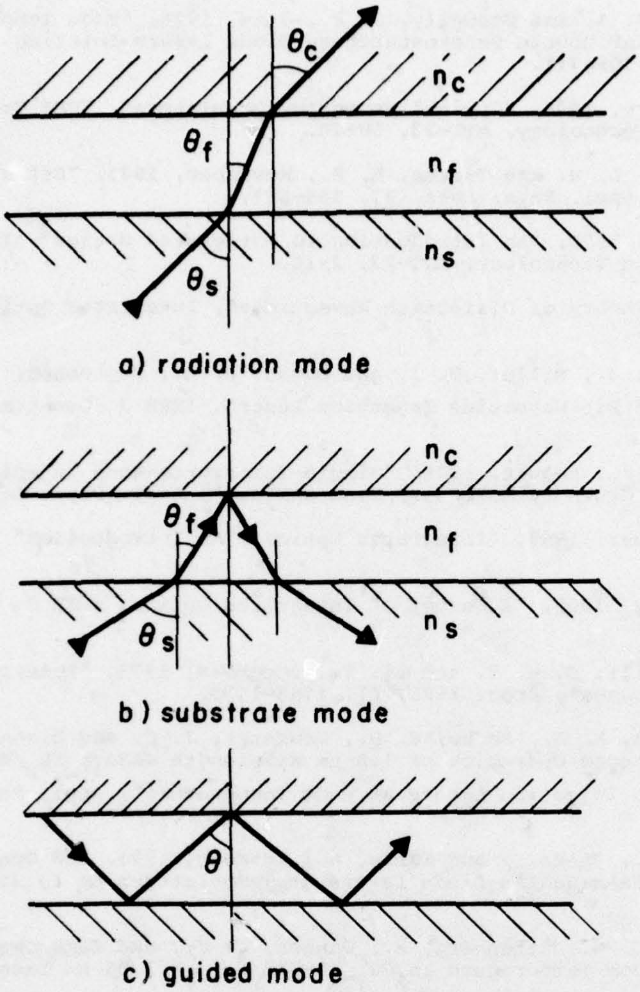

Figure 1 - Ray pictures in a dielectric slab waveguide corresponding to radiation modes (a), substrate modes (b) and guided modes (c).

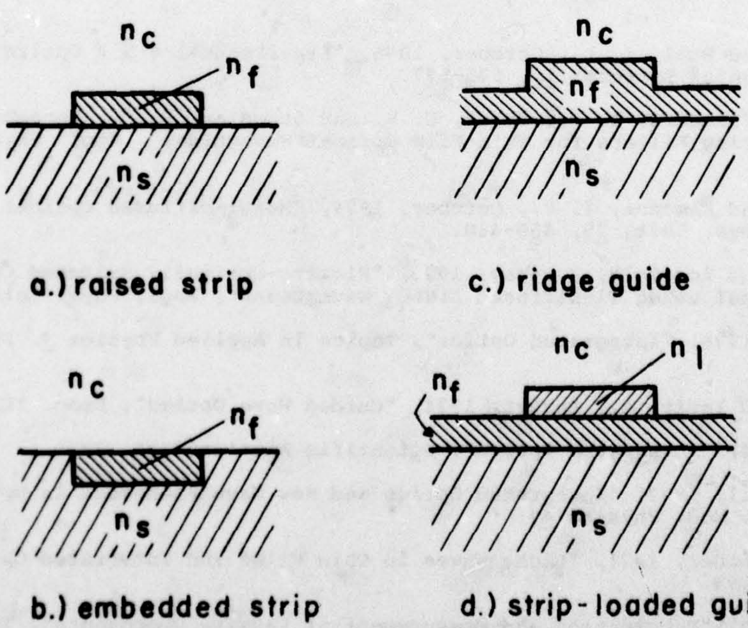

Figure 2 - Cross-sections of various strip guides.

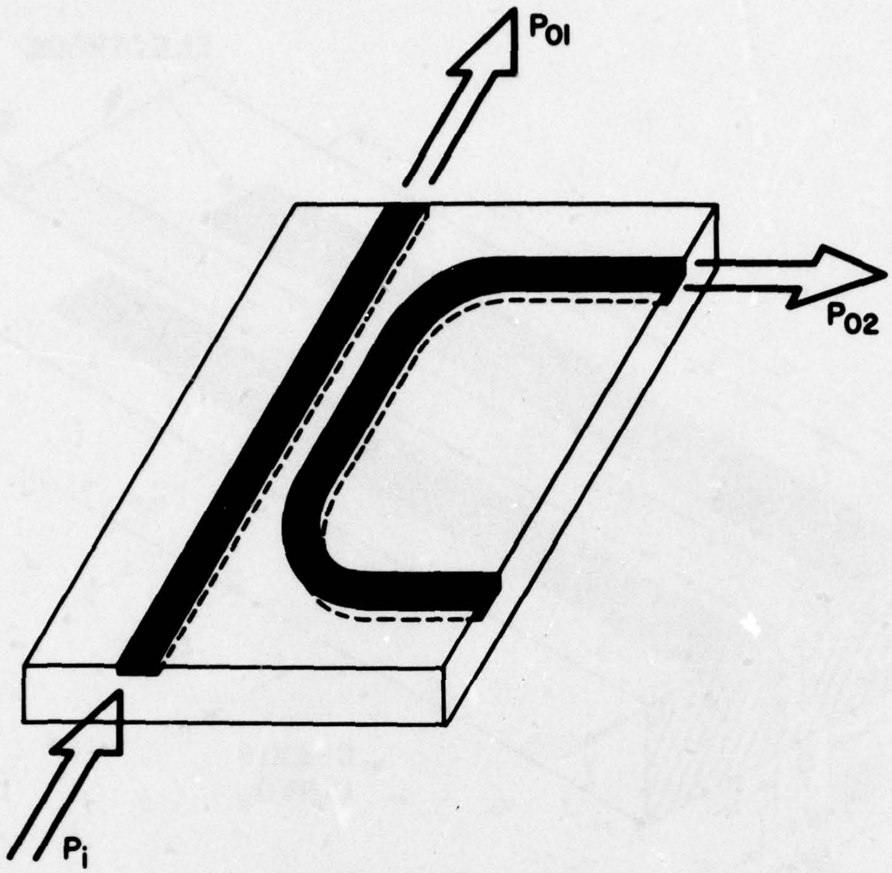

Figure 3 - Optical directional coupler made of strip guides.

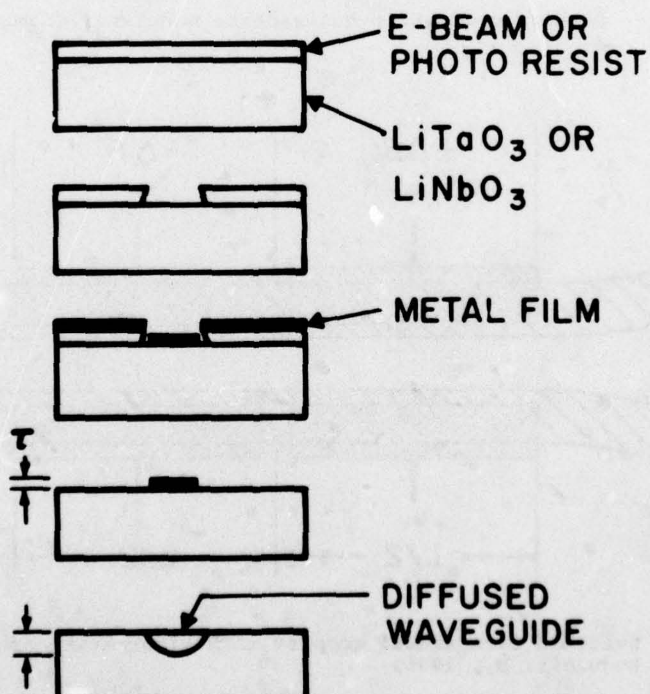

Figure 4 - Fabrication sequence for diffused strip guide.

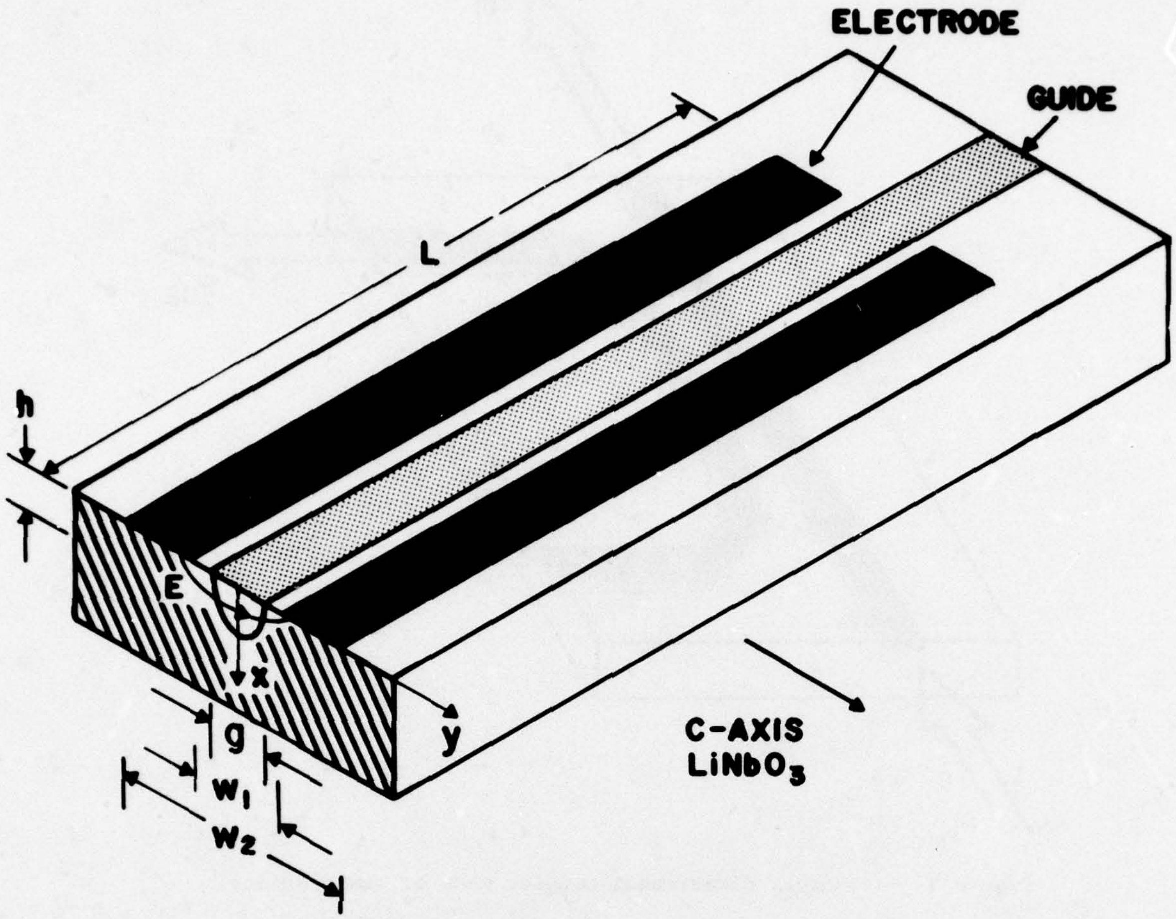

Figure 5 - Schematic of strip-guide phase modulator (Kaminow, et. al., 1975).

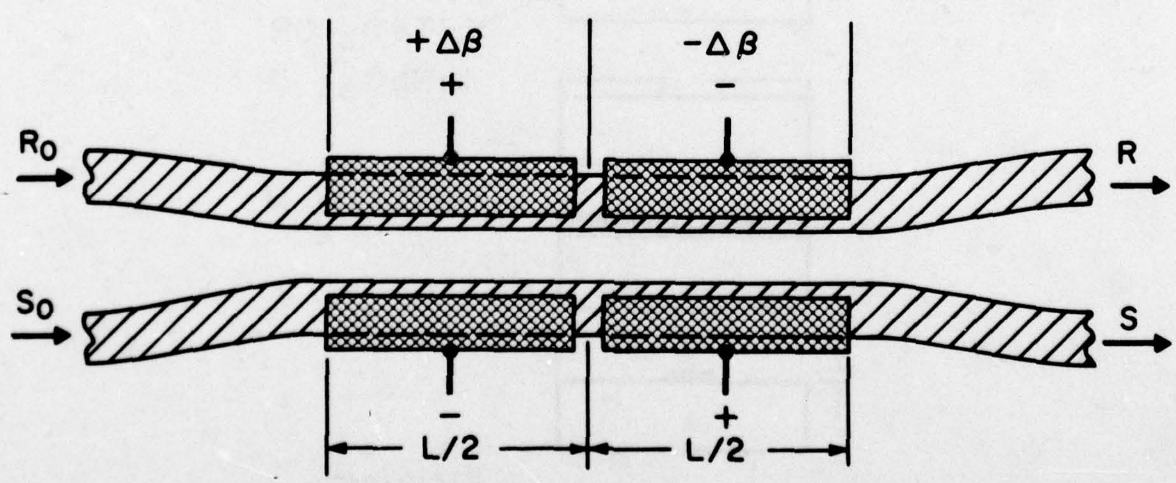

Figure 6 - Switched directional coupler with alternating $\Delta\beta$ (Schmidt, R. V. and Kogelnik, H., 1976).

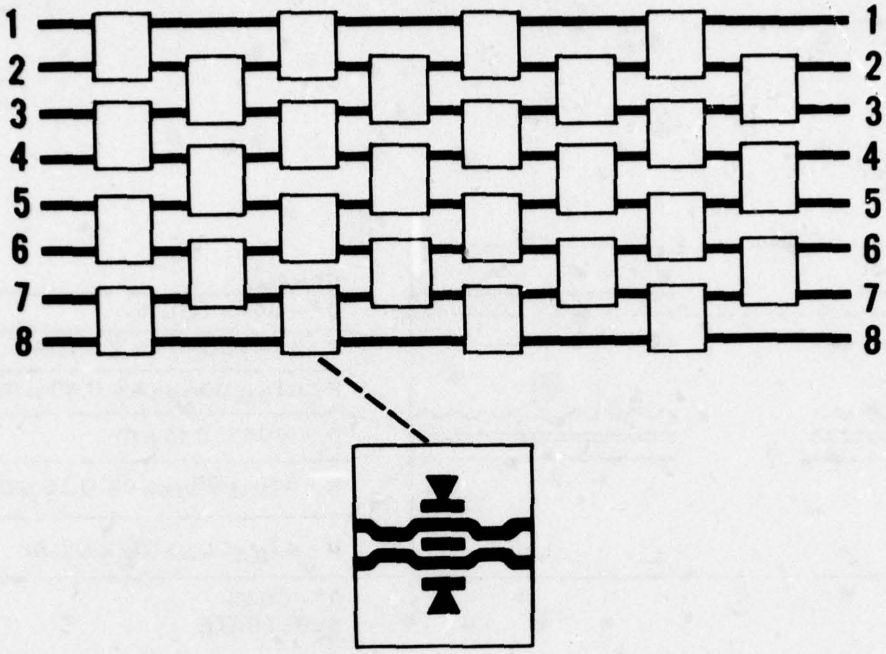

Figure 7 - Optical switching network.

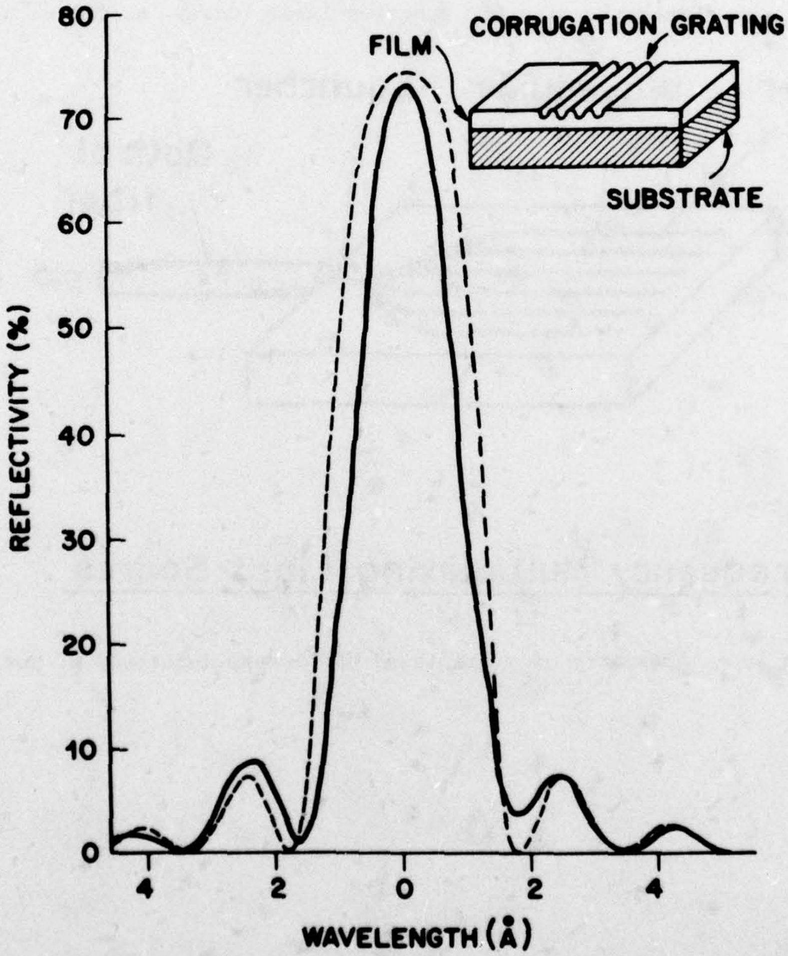

Figure 8 - Frequency response of a corrugated waveguide filter (Flanders, et al., 1974).

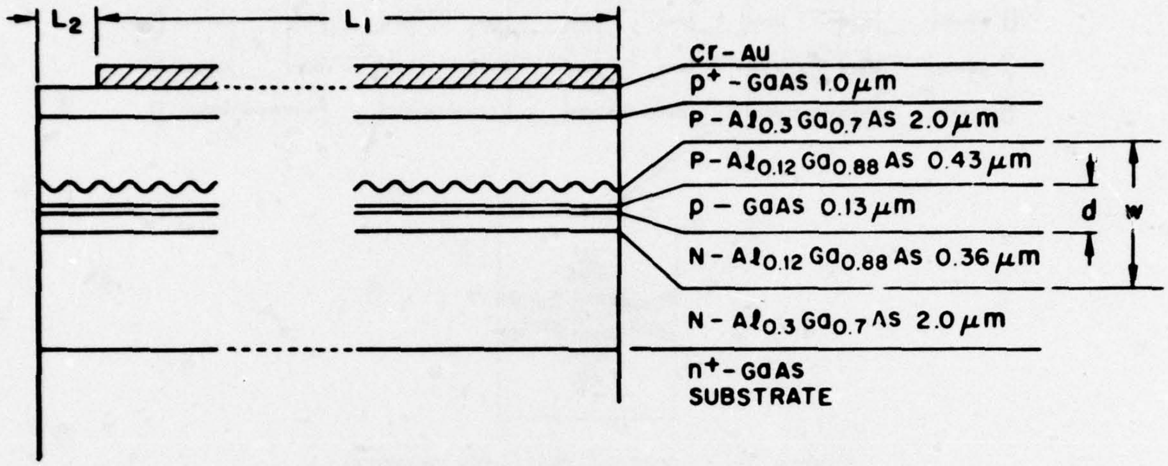

Figure 9 - Schematic of a DFB junction laser (Casey, H. C., et al., 1976).

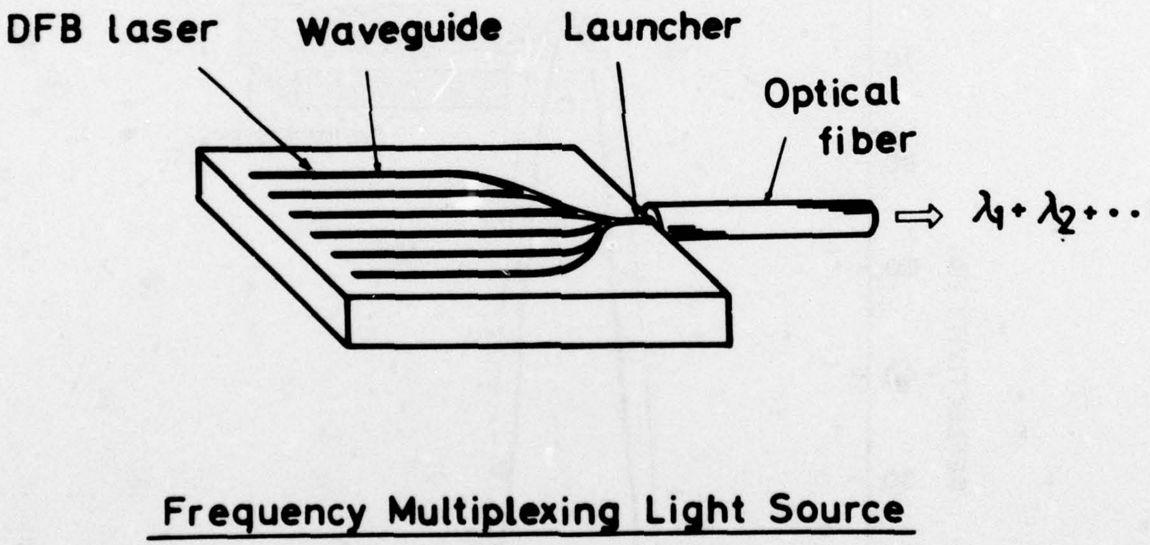

Figure 10 - Schematic of multiplexed DFB lasers (courtesy M. Nakamura)

L'AVENIR DES FIBRES OPTIQUES POUR LES APPLICATIONS AERONAUTIQUES MILITAIRES

P. LECAT
SERVICE TECHNIQUE DES
TELECOMMUNICATIONS DE L'AIR
129, rue de la Convention
75731 PARIS CEDEX 15
FRANCE

R E S U M E

Compte tenu de l'évolution des technologies en matière d'électronique embarquée, dont l'aboutissement est l'interconnexion des équipements par bus numérique, les systèmes de bord vont être à l'avenir particulièrement vulnérables aux perturbations électromagnétiques ramenées par les câblages en cas de foudroiement ou s'ils sont soumis à une impulsion électromagnétique d'origine nucléaire.

Les fibres optiques, étant intrinsèquement insensibles à ces phénomènes, paraissent donc une solution attrayante à ce problème.

L'état actuel de la technique montre la faisabilité d'interconnexions par fibres optiques, en particulier pour la réalisation de bus numériques.

Les travaux a effectuer dans l'avenir pour introduire ces liaisons au stade opérationnel relèvent donc maintenant plus du développement et de l'industrialisation que de la recherche.

1. L'EVOLUTION DES MATERIELS DE BORD

Les possibilités ouvertes par l'évolution des technologies électroniques, jointes au besoin de matériels de plus en plus performants ont conduit à la réalisation d'équipements de bord utilisant des composants élémentaires d'encombrement, de poids et de consommation d'énergie réduits. Un des exemples les plus frappants à cet égard est l'évolution des dispositifs transmettant les ordres des commandes de vol à bord d'un avion.

Certes, les dispositifs d'entrée d'ordres sont toujours des commandes manuelles à la disposition du pilote, le système de commande agissant toujours finalement sur une gouverne, ou un robinet de débit de carburant, mais la chaîne de transmission s'est grandement modifiée depuis que le premier avion a pris l'air.

Les premiers dispositifs comportaient une transmission par câbles et tringleries.

La vitesse des avions allant croissant, les efforts nécessaires pour braquer les gouvernes s'accrurent eux aussi. Il devint donc nécessaire de venir en aide au pilote par utilisation de servocommandes hydrauliques.

L'avènement des composants semi-conducteurs permit de rendre ces systèmes plus souples d'emploi, par introduction de la fonction pilote automatique, et exploitation des possibilités de modification des caractéristiques dynamiques de réponse de l'avion à une sollicitation. Cette étape a conduit à introduire des liaisons filaires pour transmettre les ordres sous forme de signaux électriques analogiques.

La dernière étape est la généralisation des techniques logiques qui permet l'intégration des fonctions à bord de l'avion. Les ordres sont alors traités et transmis sous forme numérique.

L'évolution qui vient d'être évoquée a donc conduit, pour remplir une même fonction, à passer de dispositifs de transmission mécaniques, d'abord purement passifs, puis comportant une amplification, à des dispositifs électriques mettant en jeu des énergies de plus en plus faibles.

2. EFFET DES PERTURBATIONS ELECTROMAGNETIQUES SUR LES LIAISONS FILAIRES -

Essayons maintenant d'examiner de plus près les perturbations électriques les plus importantes auxquelles aura à faire face un avion et leur effet sur les lignes de transmissions à bord.

On prendra comme cas d'étude une liaison telle que celles représentées à la figure 1. Ce peut être le cas de la transmission des commandes de vol depuis un calculateur situé dans une soute à équipement jusqu'à une servocommande située dans la queue de l'appareil.

Les deux avions représentent respectivement le cas d'un chasseur et celui d'un gros porteur (AWACS par exemple).

Les perturbations envisagées sont l'impulsion électromagnétique dûe à une explosion nucléaire à haute altitude et le foudroiement de l'avion en vol. On trouve à la figure 2 les caractéristiques temporelles des deux phénomènes (LANDT, J.A, 1974; STEVENS, D.J, 1974; ROBB, J.D, 1974)

Le couplage de l'avion au phénomène perturbateur va s'effecuter, soit par effet d'antenne dans le cas de l'impulsion électromagnétique (LANDT, J.A, 1974), soit par excitation directe en courant dans le cas de la foudre.

Les câblages seront alors le siège de courants et tensions que l'on peut approximer par des sinusoïdes amorties de fréquence

. fo $\simeq$ 10 MHz pour l'avion 1,

. fo $\simeq$ 3 MHz pour l'avion 2,

et ayant une période d'amortissement de l'ordre d'une dizaine de microsecondes.

En admettant une atténuation de 20 dB au niveau de la peau de l'appareil, on est conduit à estimer des valeurs crêtes des courants en court-circuit et surtensions en circuit ouvert telles que celles indiquées au tableau en figure 3.

On voit immédiatement apparaître le problème posé par les surtensions au niveau des équipements d'extrémité. Dans des conditions où une lampe avait des chances de résister, un étage d'entrée à transistors sera certainement mis hors service.

En outre, les évaluations faites ci-dessus supposent que la peau de l'avion apporte une atténuation importante et qu'elle est donc correctement métallisée. Là encore l'évolution technologique s'effectue dans un sens défavorable avec l'apparition des matériaux composites utilisés pour gagner du poids dans la réalisation des structures d'avions.

4. LES MOYENS DE PROTECTION - INTERET DES LIAISONS OPTIQUES -

Il convient bien sûr de noter qu'avec l'apparition des transmissions numériques, les problèmes de compatibilité électromagnétique ont conduit à prendre des précautions qui vont dans le bon sens. En effet, les signaux numériques comportant des fronts raides se sont avérés être d'importants générateurs de parasites. Ils ont donc nécessité l'emploi de paires bifilaires torsadées blindées qui minimisent l'interaction de signaux véhiculés en mode différentiel sur de tels câbles avec l'environnement.

Mais hélas, si l'on se réfère aux amplitudes des signaux perturbateurs que l'on risque de recueillir sur une paire bifilaire, même si l'on escompte un affaiblissement de 60 dB pour le passage au mode différentiel, on voit que l'on recueillera encore plusieurs volts, voire plusieurs dizaines de volts au niveau du récepteur.

De tels niveaux sont inacceptables pour des circuits logiques qui risquent alors de changer d'état de manière intempestive.

Quelles sont donc les solutions envisageables ?

On peut songer à utiliser des câbles surblindés pour obtenir une atténuation supplémentaire des perturbations. Ces câbles devront en outre être à haut isolement pour supporter des surtensions de plusieurs dizaines de kilovolts pendant plusieurs microsecondes.

Dans ce cas il faut également découpler les équipements d'extrémités par des transformateurs à haut isolement également, faute de quoi les surtensions en mode commun détruiraient ces équipements (voir fig. 4).

La solution relative à la protection d'une liaison filaire cumule donc isolement et blindage, sources de poids et d'encombrement, et ne devrait donc être considérée que comme un pis-aller par les avionneurs.

Ces inconvénients des liaisons filaires ayant été mis en évidence, les liaisons par fibres optiques apparaissent comme une alternative séduisante. Déjà mieux que compétitives avec les liaisons filaires non protégées si l'on considère leur poids linéique, elles apportent en outre, et l'isolement, et le blindage ..... ou plus exactement elle rendent ce dernier inutile.

5. FAISABILITE DES LIAISONS PAR FIBRES OPTIQUES -

Sans revenir sur la possibilité de réaliser des liaisons point à point qui ne posent pas de problèmes techniques particuliers, examinons le cas d'un bus optique, avec comme objectif un débit numérique de 3 Mbits par seconde un taux d'erreur de 10^{-9} entre un ensemble de 19 terminaux, dans le cas de l'avion 2.

L'architecture générale du système est représentée à la figure 5, la longueur maximale des liaisons est de 50 m si le coupleur central (fibre mélangeuse) est correctement placé dans l'avion.

Pour des raisons de synchronisation, on suppose le signal codé biphase. On trouve à la figure 6 l'allure temporelle du signal ainsi que sa densité spectrale.

La réalisatin de ce bus peut se faire de la façon suivante (fig.7)

- émission par diode électroluminescente

- transmission par faisceau de fibres multimodes, le couplage entre émetteur et faisceau, entre deux faisceaux, entre faisceau et récepteur s'effectuant par fibre mélangeuse.

- réception par photodiode PIN.

Considérons le bilan énergétique d'une telle liaison.

Pour une probabilité d'erreur de 10^{-9} le rapport S/B en sortie de la diode PIN doit être d'environ 17 dB si l'on décode le signal bibphase par intégration (THOMSON-CSF, 1974).

Pour passer correctement ce signal biphase à 3 M bits/S, il faut une bande passante de 5 à 6 MHz.

La puissance équivalente de bruit de la photodiode étant d'environ 0,4 $pW/\sqrt{Hz}$, la puissance optique du signal reçu doit être :

$$Po \simeq 10 \text{ nW}$$

Le bilan des pertes s'établit comme suit dans le cas le plus défavorable (D'AURIA, L. et JACQUES, A., 1976).

- couplage diode électroluminescente - monofibre :	6 dB
- couplage monofibre faisceau :	1 dB
- porte due au taux de remplissage :	3 dB
- couplage faisceau - monofibre :	1 dB
- couplage monofibre - photodiode :	1 dB
- 50 m de faisceau à 100 dB/Km :	5 dB
- coupleur 19 voies :	20 dB
- raccordements au coupleur :	5 dB
- 30% fibres cassées par tronçon :	3 dB
Pertes totales	45 dB

D'où la puissance nécessaire au niveau de la diode émettrice:

$$Pi = 0{,}3 \text{ m W}$$

Une puissance de 1mW pouvant être obtenue sous faible courant au niveau de cette diode, on ne rencontrera pas de problème de durée de vie pour ces composants.

La liaison est tolérante au niveau de la précision d'ajustement des connecteurs ainsi qu'au niveau des cassures de fibres (2 fibres sur un faisceau de 7 fibres; 5 sur un faisceau de 19).

Il apparaît néanmoins qu'un poste important au bilan des pertes est dû aux connexions (5 dB par raccordement entre deux faisceaux).

Il en résulte par exemple qu'on ne peut effectuer de franchissement de cloisons étanches en sectionnement comme il est d'usage à moins d'augmenter la puissance d'émission, ce qui se fera évidemment au détriment de la durée de vie de la diode électroluminescente.

7. LE DEVELOPPEMENT DES TRANSMISSIONS PAR FIBRES OPTIQUES -

Ceci nous amène tout naturellement à évoquer les travaux nécessaires au développement des systèmes à fibres optiques en tant que moyens opérationnels de transmission à bord d'avions.

7.1. Travaux sur les connexions

Le premier axe d'effort consiste à réduire les pertes au niveau des connexions, par exemple en connectant les faisceaux fibre à fibre. Cette solution permettrait de s'affranchir des pertes dans la fibre mélangeuse ainsi que des pertes dues au taux de remplissage. Le problème auquel on se heurte dans ce cas est celui des tolérances mécaniques, en particulier en ce qui concerne la reproductibilité du diamètre des fibres, condition essentielle de l'alignement des coeurs dans un faisceau multifibre.

7.2. Normalisation

La remarque formulée ci-dessus soulève le problème de la concurrence entre câble monofibre et faisceau multifibre dans les applications embarquées.

Si l'on considère que, les fibres étant fragiles, elles doivent de toute façon être protégées par une enveloppe mécanique résistante, alors le monofibre s'impose. Si par contre l'on considère, comme cela paraît être le cas, que la principale source de cassures est la torsion des fibres lors des manipulations, alors le faisceau de fibres apporte une redondance qui permet d'utiliser un gainage mécaniquement moins résistant, donc plus léger.

De toute manière, il semble souhaitable que le nombre de fibres dans un faisceau reste inférieur ou égal à 19.

En outre et ceci est un problème connexe du précédent, le développement des fibres se fait de manière anarchique : diversité de cotes - diamètre de coeur et de gaine, diversité de formules conduisant à une diversité d'indices de réfraction, qui nuisent à la compatibilité des composants. Une telle anarchie ne peut que freiner l'essor des systèmes d'interconnexion par fibres optiques.

Il paraîtrait donc souhaitable dans ce domaine d'élaborer une norme définissant le nombre de fibres d'un faisceau, les diamètres et indices de réfraction du coeur et de la gaine des fibres, de même qu'ont été adoptées pour les câbles coaxiaux les impédances normalisées de 50 et 75 Ω.

7.3 Equipements d'extrémités

Le troisième axe d'effort concerne l'adaptation entre les liaisons optiques et les équipements connectés.

Cette adaptation consiste pour le fabricant de composants, à développer des émetteurs et récepteurs, intégrant ou non les composants optoélectroniques, mais d'emploi analogue à celui des amplificateurs de ligne pour les transmissions sur paires bifilaires.

De tels émetteurs devraient par exemple admettre comme entrée des signaux logiques au standard TTL, accompagnés en parallèle par un signal d'horloge de synchronisation, les récepteurs associés restituant ces deux signaux.

Pour le fabricant d'équipements, cette organisation implique la transmission séquentielle de l'information.

7.4. Problèmes de montage et de maintenance

Le quatrième axe d'effort concerne l'adaptation des liaisons optiques aux techniques de montage et de maintenance usuelles en aéronautique. Il conviendra donc autant que faire se peut de minimiser la remise en cause des méthodes de travail.

Cela implique au niveau des opérations de câblage la possibilité de couper, de conditionner les extrémités de câble optique et de monter les connecteurs dans les conditions rencontrées dans un atelier de câblage.

Il convient donc de développer des outils simples d'emploi, ne demandant si possible pas plus de dextérité de la part du câbleur que le maniement du fer à souder.

Cela implique également :

- soit d'incorporer aux récepteurs une commande automatique de gain leur assurant une dynamique de fonctionnement compatible avec la dynamique des atténuations dans les réseaux d'interconnexion complexes,

- soit d'inclure dans ces réseaux des dispositifs égaliseurs de puissance optique (PORTER D.R et REESE J.R, 1976).

Cela implique enfin un effort au niveau des connecteurs qui devront supporter le montage et le démontage dans une soute d'avion sans nécessiter l'ambiance dépoussiérée d'une salle blanche.

8. CONCLUSION

Les fibres optiques abordent maintenant ce qui peut être considéré comme une phase de développement précédant leur introduction opérationnelle à bord des avions militaires.

L'état de la technique permet dores et déjà de répondre à des besoins ponctuels portant sur des liaisons point à point.

On peut donc espérer voir le problème de la protection des liaisons à bord d'avion contre les perturbations électromagnétiques résolu de manière plus légère que ne le permettent les technologies filaires actuelles.

Toutefois les problèmes de protection au niveau des alimentations et des circuits internes des équipements restera justiciable des méthodes de protection classiques.

On peut espérer que le gain de poids apporté par les liaisons optiques augmentera la marge de manoeuvre pour les protections classiques restant à mettre en oeuvre.

REFERENCES

1. D'AURIA, L., JACQUES, A., 1976, " Deuxième Colloque Européen sur les transmissions par Fibres Optiques ", Communication XIII.3 -

2. LANDT, J.A, 1974, "Peak curent estimates : cylinders in free space with extension to other structures", PEM 32.

3. PORTER,J.D, REESE, I.R, 1976, " Deuxième Colloque Européen sur les Transmissions par Fibres Optiques", Communication XIII.4 -

4. ROBB, J.D, 1974, " Coordination of Lightning and EMP protection in airborne systems design ", PEM 29.

5. STEVENS, D.J, 1974, " Summary of EMP control management for the B1 aircraft", PEM 25.

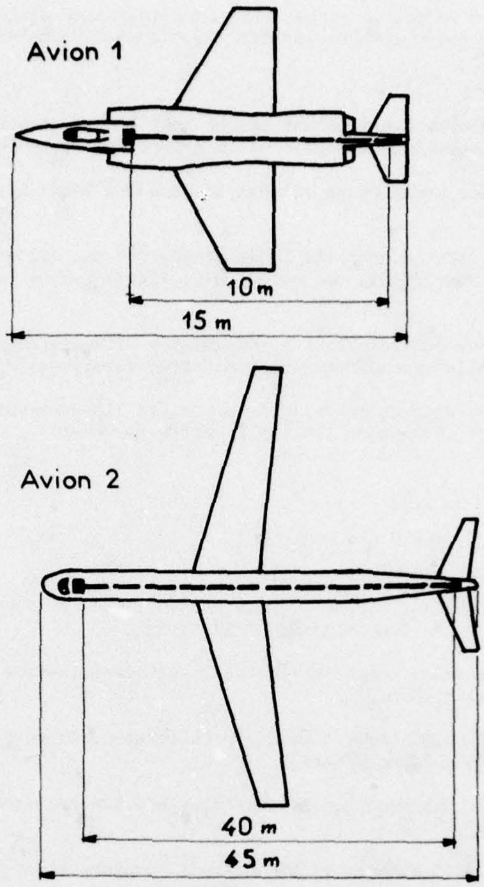

Fig.1 Exemples de liaisons

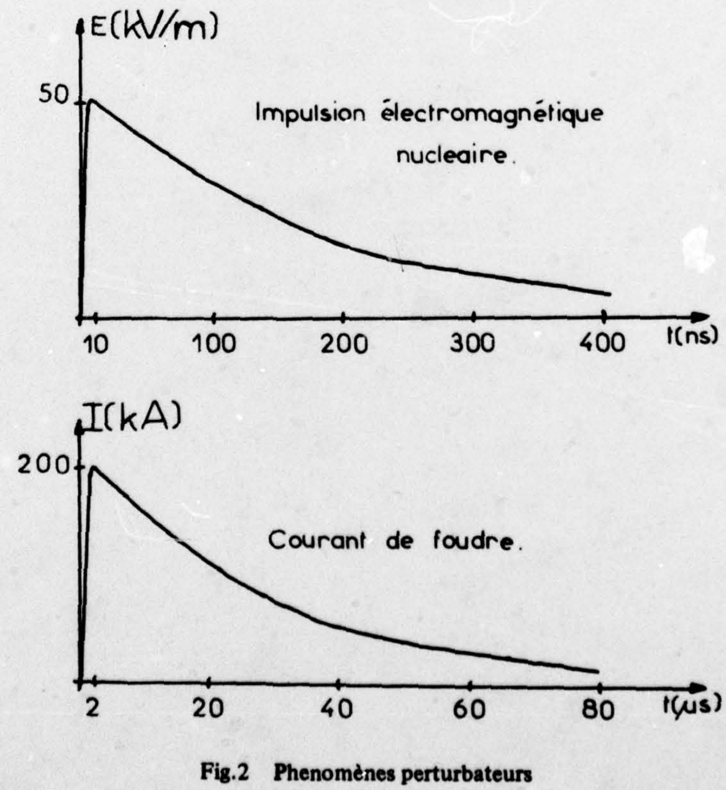

Fig.2 Phenomènes perturbateurs

	Avion 1		Avion 2	
	IEM	Foudre	IEM	Foudre
Courant total sur structure	1,6 kA	200 kA	5 kA	200 kA
Effet mode commun (paire non blindée) V_{co}	50 kV	130 kV	200 kV	780 kV
I_{cc}	100 A	520 A	300 A	1,6 kA
Tension sur blindage : V_{co}	50 kV	130 kV	200 kV	780 kV
Courant sur blindage : I_{cc}	100 A	520 A	300 A	1,6 kA
Effet mode commun (paire blindée) V_{co}	5 kV	13 kV	20 kV	78 kV
I_{cc}	10 A	52 A	30 A	160 A

Fig.3 Courants et tensions induits

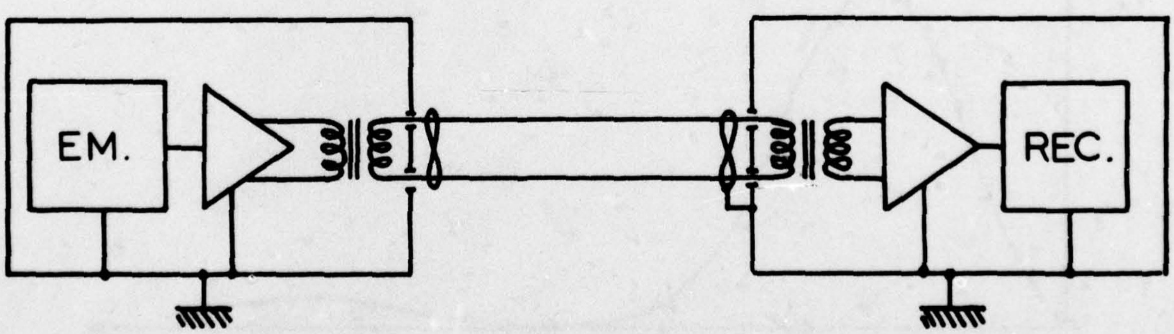

Fig.4 Liaison électrique protégée

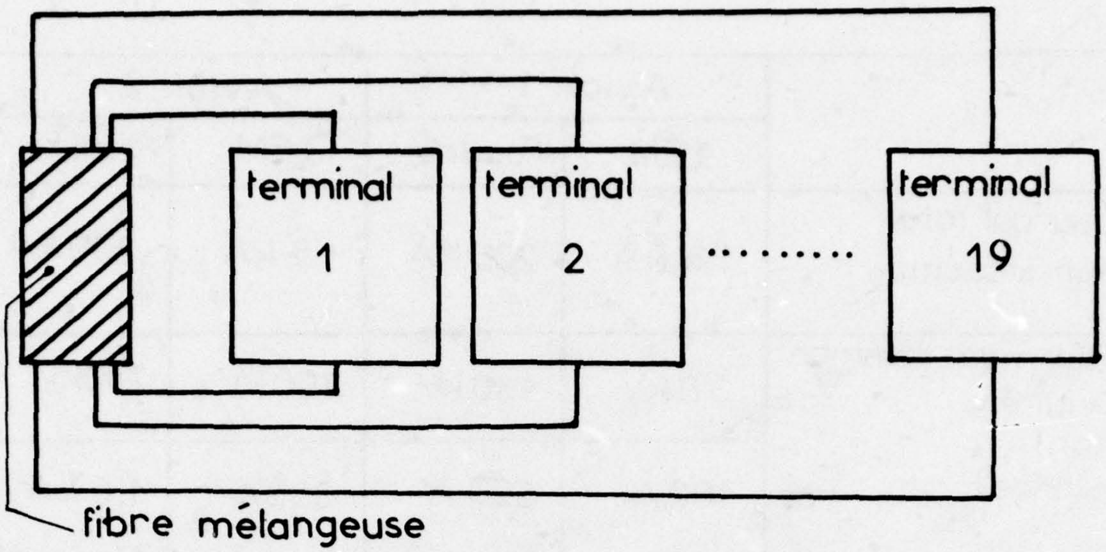

Fig.5 Organisation d'un bus optique

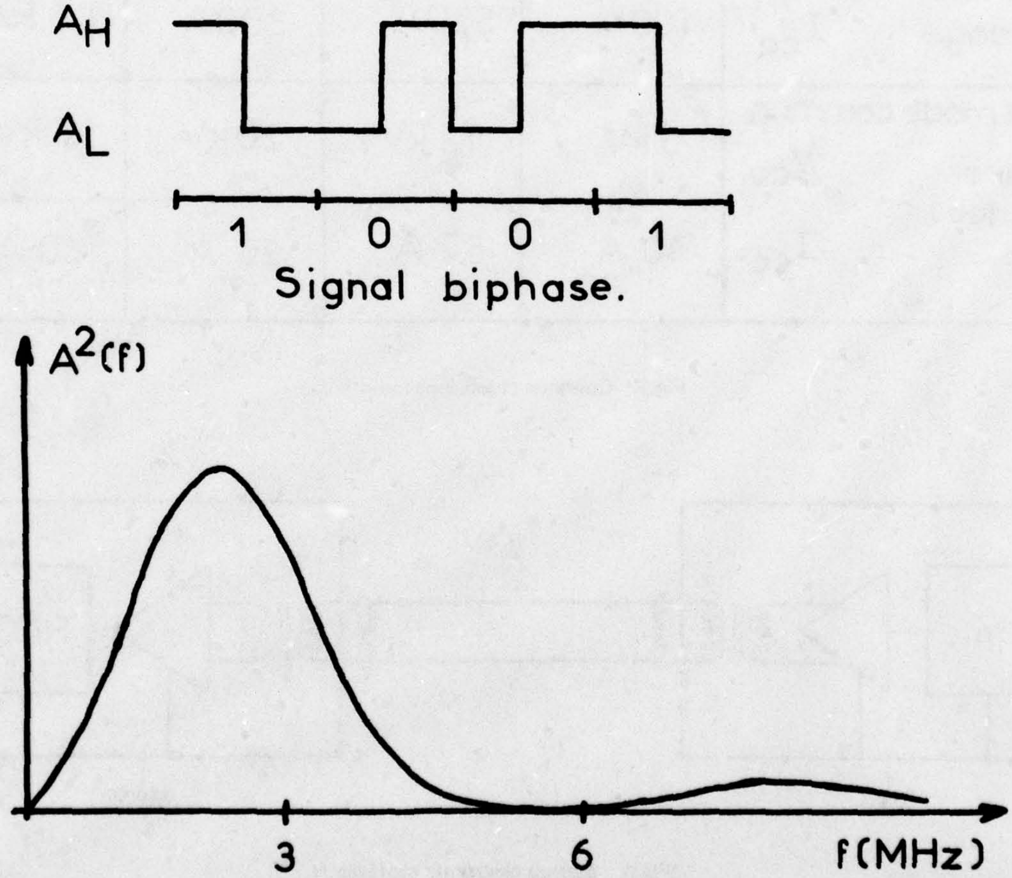

Fig.6 Densité spectrale d'un signal biphase à 3 Meb/s

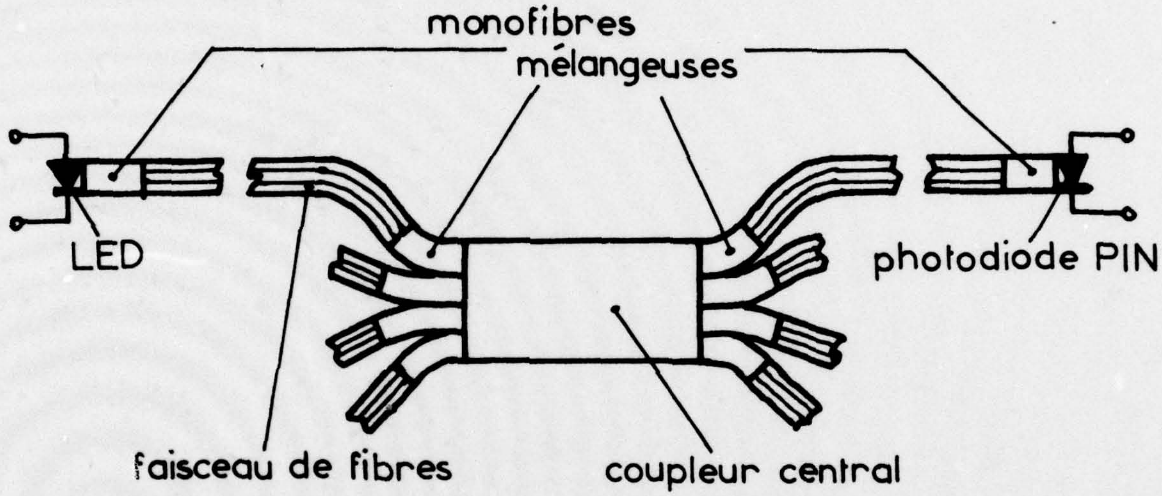

Fig.7 Realisation d'un bus optique

RECENT PROGRESS IN OPTICAL FIBER CABLES FOR USE IN THE OCEAN

G. A. Wilkins
Naval Undersea Center
Hawaii Laboratory
Kailua, Hawaii, USA

R. A. Eastley
Naval Electronics Laboratory Center
San Diego, California, USA

SUMMARY

Physical and optical test results are given for several undersea, low loss, optical and electro-optical cable units. Diameters for these cables range from 1.0 mm to 17.5 mm, and all were designed to operate in environments of high tensile, bending and hydrostatic stresses. Design constraints necessary to isolate the optical fibers from such stresses are described. Design details and rationales are given for each cable unit. Continuing technical problems and probable solutions are discussed.

1. INTRODUCTION

The last decade has seen a rapid increase in the degree of sophistication required of cable-controlled systems which must carry out search, recovery, inspection and general work operations on or near the deep sea floor. This sophistication has precipitated a serious conflict between the simultaneous needs for higher information bandwidth and reduced cable diameter. Much higher (multi-megahertz) bandwidth is required to support such tools as search and mapping sonars, chemical/magnetic/nuclear sensors, and high resolution, real-time television (even stereo TV). Much smaller cable diameter is needed to reduce drag and to improve system depth performance in a towing mode or in the face of ocean currents.

While cable bandwidth and diameter are the chief protagonists in this conflict, other cable parameters---strength, flexibility, air weight, in-water weight, payload capacity, power transfer and operational safety factors---play important roles. If these "secondary" parameters are critical, then bandwidth is normally sacrificed and system sensor performance is degraded. If bandwidth requirements cannot be relaxed, then system compromises may take several forms. The cable's diameter may grow beyond desirable limits, so that storage volume, handling system dimensions and sensitivity to currents are pushed to *their* limits. Additional electrical conductors may be required, adding weight but not strength to the cable, so that the system's safety factor (ratio of cable strength to maximum static cable tension) is reduced below a safe level.

The problem is not limited to the deep sea search or work system (Sigel, G.H., 1976). It will be encountered whenever high frequency information must be transmitted through a cable which has an overly constrained diameter. Other examples are numerous; the data link between a deep sonobuoy and its surface transmitter, a video data tether between a diver and a remote monitoring station, and the monitor/control link for a wire-guided torpedo. In many undersea systems, the need for data at high (to megahertz) rates is stymied by conventional cables which are diameter-limited to much lower bandwidths.

As an illustration, consider a typical tether cable (Fig. 1), commonly used to tow instrumentation packages at depths to 6 km. The cable's rated breaking strength is 15,400 kg*. Its weight in air is 1050 kg/km, which corresponds to an over-the-side weight of about 5100 kg for tethered operations to 6 km. System safety factor *with no payload*, is 3, which is uncomfortably less than the value of 5 normally required for lifting and towing operations at sea. Addition of any payload weight will further reduce this safety factor. Cables of this type are often used to support deep tow operations at a safety factor which approaches 2. The incidence of cable failures is high.

Telemetry attenuation for the cable in Fig. 1 is about 5.9 dB/km at a frequency of 1.0 MHz. If an 8-km cable length is needed to ensure package deployment to a depth of 6 km, then the highest frequency that can be passed through the cable and reconstructed (60 dB total attenuation) is 1.6 MHz. This is insufficient to transmit real-time television without severely degraded resolution, and will certainly not allow real-time stereo TV. It has marginal capability for support of today's high resolution, high-search-rate sonars. If there is a requirement to simultaneously operate two or more such sensor systems, the cable is totally inadequate. In fact, a usable bandwidth of 30 to 50 MHz will be needed to simultaneously transmit data from all of the sensors that should be included in an effective deep sea search or mapping system.

The historical approach to the bandwidth problem for a coaxial cable has been to increase the diameter of the dielectric spacer, while maintaining constant coverage by the shield conductor. (The latter step controls radiation leakage, but adds dead weight to the cable.) Assume, for example, that the dielectric O.D. of the cable in Fig. 1 is increased from 0.706 cm to 2.54 cm (i.e., a type SD transoceanic telephone cable). The limiting frequency for 60 dB attenuation over an 8-km length becomes 33 MHz---but the cable's diameter, storage volume, drag cross section and weight must all rise. A much

---

* This paper will use those units which are normally measured in the laboratory or the field---e.g., kg rather than newtons, and kg/cm^2 rather than N/m^2 or pascals.

longer cable will be needed to compensate for the effects of current drag, so that part of the additional bandpass is lost. The dead weight due to additional copper in the cable will undoubtedly reduce the system's safety factor. Finally, a larger handling system and ship will be required to carry and deploy the new cable. In summary, a conventional approach which narrowly focused on the need for greater cable bandwidth has forced the entire system to grow to monstrous proportions and cost.

Some of this penalty can be alleviated through use of special cable materials; e.g., lightweight loadbearing and electrical elements (Wilkins, G.A., 1975a, 1975b, 1975c and 1976a). Substitution of DuPont's KEVLAR-29 or KEVLAR-49 for steel tension members can reduce cable weight and increase the system safety factor. This approach does nothing, however, to alleviate the basic dependence of bandwidth on cable diameter. This is the primary role for the fiber optic data link, and the reason why our laboratories formed a technical partnership to attack the bandwidth/diameter constraint through the use of optical fiber technology.

The program goal has been the development of a family of reliable, fiber optic, undersea cables. These range from a miniature data link for tethering of self-powered systems, to optical units that can be assembled into larger, relatively conventional, electromechanical cables to support system data transmission functions. Sponsorship has also been by partnership---the Defense Advanced Research Projects Agency because of its interest in deep ocean work cables, the Naval Air Systems Command in sonobuoy technology, and the Naval Electronic Systems Command in general undersea cable technology. All fiber manufacturing and cable assembly phases of the program have been carried out by private industry, as identified in Section 6.

2. DESIGN CONSTRAINTS ON THE OPTICAL FIBER

We have found four properties of the optical fiber---four modes of response to a local environment---to be of dominant importance in the design of fiber optic cables. These are contamination by water, microbending, curvature of the symmetry axis, and axial (tensile) strain. The design of an effective optical fiber cable must accommodate each of these properties (Wilkins, G.A., 1976b).

2.1. Water Contamination

A glass fiber will weaken and ultimately fail if it is simultaneously exposed to a humid environment and to tensile stress. The mechanism (Gulati, S.T., 1975) is probably an interaction of the hydroxyl ion with the walls of minute cracks or crazing in the fiber surface. The result---analogous with stress corrosion in metals---is that these cracks propagate into the fiber cross section until the unit fails.

If the fiber is not under tensile stress, this weakening is much less evident and may not exist at all. The design constraint, therefore, has two components. The fiber must be protected from direct exposure to water molecules. In undersea applications, this is a difficult or impossible task, since the cable may be required to operate for years in a high pressure (to 700 kg/cm^2) environment. Second, the fiber should be maintained at as low a tensile stress as possible.

Many coating materials have been evaluated for their ability to provide short term (to hundreds of hours) isolation of optical fibers from water at high pressure. These include ethylene vinyl acetate (EVA), fluorocarbon resins (TEFLON^R), polyvinylidene fluoride (KYNAR^R), and polyester elastomers (HYTREL^R). The material must have extremely low permeability, and must form a smooth, intimate, continuous coating on the fiber. Best results are obtained if the coating is applied by extrusion (actually "pulltrusion"), as an in-line step in the fiber drawing process. The coating must be applied before the fiber can be contaminated by atmospheric water or dust, and before it can contact any external surface.

2.2 Fiber Microbends

This "buffering" layer has a second critical function; it must stiffen and isolate the optical fiber to reduce its tendency to conform to adjacent roughened surfaces. Examples of such surfaces include a storage reel or deployment sheave, the insulation around adjacent conductors within a cable, and crossovers due to improper winding of the optical cable unit on a storage reel. Such "microbending" has two serious impacts. First, it increases radiation losses in the fiber's higher order modes which, in order to remain in phase while transiting the outside of the bend, would have to exceed the speed of light in the medium. Second, it increases mode coupling, which converts lower order modes into higher (more lossy) orders. These effects can drastically increase the fiber's optical attenuation. Olshansky (1975) has shown that, for the case of a 125-μm fiber passing over a single 12-μm bump, the additional attenuation can be 0.15 dB. Multiple microbends of this type in an actual cable can increase fiber attenuation by hundreds of dB. One of our early attempts to strengthen a poorly buffered fiber with a matrix of 9-μm S-Glass filaments in epoxy resulted in more than 1400 dB/km of *additional* attenuation.

The fiber buffering annulus can give almost complete protection against microbends. To do so, it must have sufficient rigidity (compressive modulus) to support the fiber against localized bending or buckling. It must also be sufficiently plastic to transmit external anisotropic stresses to the fiber as though they were radially isotropic. The buffer's composition must be uniform, and its outer surface smooth and circular. Gloge (1975) recommends a compound buffering jacket, with a hard inner structure and a soft outer shell. Our own experience, described below and in the section on experimental cables, is somewhat different.

Two DuPont materials---TEFLON PFA and HYTREL---have shown the greatest promise in satisfying the several functions we require of the fiber buffer. Both have been applied over an initial coating of silicone RTV (SYLGARD[R]). Of the two buffering materials, HYTREL is preferred because of (1) its lower melt temperature, and (2) TEFLON's tendency at high temperature to chemically react with the walls of the extrusion cavity. This reaction produces tiny carbon-like flakes, which flow through the die, become fixed within the buffer annulus, and may act as local microbend centers. The two buffering materials, compared in Table 1, have been applied by ITT (Roanoke, Virginia) under contracts with our laboratories.

2.3. Effects of Optical Fiber Curvature

In general use, any optical fiber will be stored on a reel, or assembled as a helix in a cable structure, or both. These operations will impose a curvature on the fiber and, therefore, will also induce radiation losses and mode coupling. The radius of this type of bend is large compared to the fiber radius, so that the relative induced attenuation should be much less than it is for microbending. *However*, the entire cable is involved in the "macrobend", so that total attenuation impact may be quite large. This may cause serious operational problems, since the attenuation of the stored fiber may be much greater than that of the same fiber after unreeling and deployment.

Gloge (1972) predicts that, at a wavelength of 1000 nm, a step index fiber will almost immediately lose one-half of its transmission modes if the radius of curvature is equal to the diameter of the optical core divided by the relative index difference between core and cladding. For a core diameter of 0.1 mm, and relative index difference of 0.01, this critical radius is 1 cm. In the case of the graded index fiber, the corresponding radius is twice as great. Mode coupling will tend to replenish these high-loss modes, so that bending attenuation will continue to reduce the intensity of the transmitted light.

The onset of curvature-induced attenuation will be extremely rapid. As Gallawa (1976) points out, not only will the optical power loss in bending be an exponential function of the bending attenuation coefficient, but that coefficient will *itself* be an exponential function of the fiber radius of curvature. This means that a relatively small change in the fiber's radius of curvature can increase bending losses from negligible to dominant levels.

The fiber's curvature is also constrained by its strength or, more realistically, by its allowable strain. If an optical fiber of (cladding) diameter d is wrapped around a cylinder of radius R, then the relative tensile strain on the fiber's outermost surface will be ε compared to that of the (neutral) axis of fiber symmetry, where;

$$1 + \varepsilon = (R + d)/(R + d/2) \qquad (1)$$

If the cylinder radius is 1 cm and the fiber diameter 125 μm, this surface strain will be more than 0.6%. Such a value is small compared to reported average fiber breaking strains of 4--6%. It is quite large compared to the "weak link" breaking strains we have encountered in kilometer lengths of production optical fibers.

Two years ago, the strongest optical fibers available had approximately a 50% probability of breakage when 1 kilometer was exposed to a proof strain of 0.25%. We have recently been able to purchase (at a fixed price) kilometer-length optical fibers, both step and graded index, which have survived a manufacturer's proof test to a stress of 7000 kg/cm^2. This is equivalent to a proof strain of 1%. It seems reasonable that, within one or two years, very long fibers can be purchased to specifications of 2% (or even higher) demonstrated survival strain.

Until this capability is well established, however, we have arbitrarily imposed a minimum fiber radius of curvature of 5 cm in the design of all optical cables. This is equivalent to a differential bending strain of 0.125% for a fiber with an overall diameter of 125 μm. Love's (1976) criterion of proof testing states that the ability of a brittle material to survive for very long periods (e.g., 20 years) at a given strain level can be verified by subjecting it for a short period to a strain three times greater. In our case, the ratio of proof strain to bending strain is 8/1, which should leave an adequate margin for residual (assembly) tensile strains.

2.4. Fiber Tensile Strain and Strain Relief

In treating the tensile properties of optical fibers, the literature normally focuses on the need for higher fiber ultimate strength. We find that fiber strain---i.e., the highest achievable strain-to-break in a long fiber---is a more meaningful property in cable design. The two parameters are, of course related via the fiber's tensile modulus. But expressing the need in terms of strain allows the materials scientist the potentially useful freedom to adjust strength *and* modulus, rather than strength alone.

The optical fiber should never be expected to carry an appreciable load. First of all, it cannot. Even if we were able to increase the minimum strength of long optical fibers by a factor of 10 (to 70,000 kg/cm^2), a 125-μm fiber could survive a load no greater than 8.6 kg. This is negligible compared to the strength required in most undersea cables. Other cable elements must carry the tensile load. These elements will have two primary functions; to provide the strength necessary to absorb the design cable relief with an acceptable safety factor, and, while so doing, to provide adequate strain relief for the optical fiber(s). The question of "How?" this is to be done is a proper subject for cable design. We are proceeding along three principal paths.

2.4.1. Fibers With Higher Ultimate Strain

As stated earlier, it is now possible to buy, at a fixed (but high) price, very long optical fibers that have been proof tested to 1% strain. This strain level allows the full strength of such high-modulus loadbearing materials as boron and graphite to be achieved in a cable. At this strain, steel wires will be loaded to their yield stress. When 2% fibers are available, the ultimate stress of KEVLAR-49 can be achieved. At 4% strain, the same will be true for KEVLAR-29 and S-Glass. (Note that fiber strength is not mentioned in this projection.)

We believe that optical fiber "strength" objectives should be threefold. First, the minimum or weak-link strain of the optical fiber must be increased toward the limits just given. Second, these limits must be achievable over longer fiber lengths, with a goal of 10 kilometers or the projected distance between signal repeaters, whichever is greater. Finally, these fiber strain properties must show little or no degradation with age or (normal) cable usage.

2.4.2. Higher-Modulus Loadbearing Elements

For any given cable load, the strain on the optical fiber will decrease as the tensile modulus of the loadbearing section is increased. This factor, considered alone, would indicate a favored position for such loadbearing materials as graphite and boron, since their tensile modulus can be as much as 65% greater than that of steel and 5 times greater than glass. But boron and graphite, in addition to being expensive and difficult to process, are extremely stiff. Although one of our contractors has built prototype, optical fiber, cable units using both material, results to date have been unsatisfactory. The cable units are so stiff that they fail, under pure bending loads, at sheave/cable diameter ratios of 50/1.

The development work reported here has concentrated primarily on (stranded) steel and HTS 901 S-Glass tension members. These materials have given the best compromise between the conflicting needs for high modulus and flexibility. They also give the optical cable unit sufficient usable tensile strength that it can readily be handled by modern high speed cabling machinery when the unit is to be assembled into a more complex cable structure.

Our program has made little use of KEVLAR to date, primarily because of its low rigidity in compression. One cable unit (reported later in this paper) *did* use KEVLAR-49, but only to furnish handling strength while the unit was assembled as the optical core of a larger electromechanical cable. During this assembly, the unit was maintained under constant and controlled tension. We are planning to make use of "hybrid" loadbearing structures; especially composites of KEVLAR-49 and S-Glass, with the first material supplying the modulus and the second a predictable degree of stiffness.

2.4.3. Strain Relief Through Cable Geometry

The third design path assembles the optical fiber as a helical element in the cable structure, and offers two potential gains. First, it allows the fiber to cycle around the cable axis of symmetry (the neutral or unstrained axis during bending). When the cable is then bent around a sheave or reel, the fiber alternates between the axially-compressed and axially-tensioned sides of the helix. If the fiber is loosely held in the structure, the average effect (over one helix cycle) is as though it is continuously on the neutral axis. When applied to KEVLAR-49---another non-yielding material---this helix structure gave nearly a 1000/1 increase in flexure lifetime (Wilkins, 1975a).

In addition, the helical optical fiber is given a measure of strain relief when the cable is subjected to tensile loading. This advantage is rather limited, especially if the design goal is a cable with a diameter only a few times greater than that of the optical fiber. Consider the best possible helix---an optical fiber contained within a hollow tube. Except for its ends, which are fixed to the ends of the tube, the fiber has total freedom of motion. Along the tube, the fiber axis is defined by the helix mean pitch diameter D, and by the helix angle Θ. Relative to the length of the tube (Z), the fiber length is defined by;

$$\lambda = Z/\cos\Theta \tag{2}$$

If the tube ends are gripped and stretched, the fiber helix will begin to collapse. The fiber will experience no tensile strain until the tube has suffered an absolute strain of δ (that is, a relative strain of $\sigma = \delta/Z$), where;

$$\sigma = \delta/Z = (1 - \cos\Theta)/\cos\Theta \tag{3}$$

In terms of the minimum required strain relief σ, this defines a minimum value for the fiber helix angle Θ.

$$\Theta \geq \mathrm{Cos}^{-1}(1/1+\sigma) \tag{4}$$

The maximum allowable value for Θ is set by ρ, the minimum allowable radius of curvature for the optical fiber.

$$\rho = D/2\mathrm{Sin}^2\Theta \tag{5}$$

so that;

$$\Theta \leq \mathrm{Sin}^{-1}(D/2\rho)^{\frac{1}{2}} \tag{6}$$

Equations (6) and (4) define the upper and lower bounds, respectively, for the optical fiber's helix angle in the cable structure. These limits are plotted in Fig. 2, corresponding to our own design constraints of a minimum fiber strain relief of 0.5% and a 5-cm minimum radius of fiber curvature. Note how confining the allowed Θ--D space is. The full story is even worse, since the non-zero cross section of the fiber must be considered. For the geometrical constraints just stated, and a 125-μm fiber buffered to a diameter of 0.05 cm, no helix with an overall diameter less than 0.149 cm is allowed. Cable diameter is now 11.9-times greater than that of the optical fiber---a factor of 142 growth in cross sectional area---just to achieve a 0.5% strain relief.

We have concluded that the fiber helix is only a partial solution for tensile strain relief of the miniature optical cable unit; i.e., any cable with an outer diameter less than about 10 times the diameter of the bare fiber. The helix has considerable value, however, in relieving the fiber from bending stresses, and certain design criteria can be applied toward that application. One of these is that the fiber helix should pass through at least one full cycle within the arc length of a cable bend. Assume that the cable makes a 90-deg bend around a 5-cm-radius sheave, so that the contact arc length (L) is 3.93 cm. If the mean pitch diameter (D) of the optical fiber in its helix is 0.10 cm, then the minimum helix angle required to give this cycle length is;

$$\Theta \geq \mathrm{Tan}^{-1}(\pi D/L) = 4.57 \text{ deg} \tag{7}$$

As Equation (6) and Fig. 2 verify, this helix angle can be increased to as much as 5.74 deg without violating the radius of curvature limitation. At the larger angle, the helix cycle length will be 3.13 cm.

3. EXPERIMENTAL CABLES

Although several cables have been designed, built and tested during the past two years of our program, only four will be reported here. The smallest is a single-fiber optical cable unit, without conductors, intended to model both a miniature data link for use with an undersea, self-powered, instrument package, and an optical data link in a more complex cable. The largest is a complete electromechanical cable, investigated as a potential replacement for the type of conventional cable described in Fig. 1. Designs and design philosophies for these four cables are described below. Test results will be given in Section 4.

3.1. Single-Fiber Miniature Cable

This cable, illustrated in Fig. 3, was fabricated to explore minimum diameter limits for a simple optical cable which combined (a) low additional attenuation due to cabling stresses, (b) sensibly high tensile strength and modulus, and (c) the flexibility and flexure resistance to allow reeling and loaded flexure with a 5-cm curvature radius. When used with a self-powered instrument package, it could serve as the entire support cable. Alternatively, it might be assembled into a more complex electromechanical cable of arbitrary dimensions and performance.

As shown in Fig. 3, the optical fiber is coincident with the cable axis. The fiber could have been assembled as a helix, but the gains would have been minor compared with the complexity and risk of such an operation. In the limiting helix, the manufacturer's TEFLON buffer would have been tangent to the unit's outside surface. This would have forced the loadbearing structure to also be a helix, resulting in considerable rotational torque under tensile loading. The largest helix angle that could have been chosen without violating our 5-cm radius of curvature constraint was 5.41 deg; corresponding to a helix length of 2.95 cm, and a theoretical strain relief of 0.45%. Actual strain relief would have been less, since radial shrinkage of the fiber helix would have been resisted by a central core.

The loadbearing S-Class filaments in the cable are paraxial, and occupy a 64% volume fraction within their annulus. This is reasonably close to the $\pi/4$ theoretical limit for squarecentered packing. Ideally, these filaments would have been incorporated as a two-layer contrahelix, to improve flexibility while maintaining a zero-torque configuration. We may attempt to do this in the future, but the required tooling costs are currently beyond the level of available funds.

A concerted effort was made to fabricate the cable with a void-free construction. The cable's weight is 2.09 kg/km in air and 0.84 kg/km in seawater. Its average breaking strength of 255 kg corresponds to a (cable only) safety factor of 51 for operations to a depth of 6 km. The cable can carry a package with an in-water weight of 46 kg to this depth, while maintaining a system safety factor of 5. The 8 km of cable necessary to support this operation---including storage reel---can easily be carried by one man!

Why did we choose S-Glass with its low modulus and 4.5% breaking strain? First, the choice of loadbearing material is relatively unimportant if the optical unit is to be assembled into a larger cable. There, cable strain will be determined by total cable load and by the tensile modulus of other parts of the structure. Second, major increases are being achieved in strain-to-break for long lengths of optical fiber. As this improvement continues, the optical fiber will be able to survive a much larger fraction (perhaps all) of the S-Glass breaking strain. Finally, experience gained in assembly of S-Glass/epoxy matrices can be translated into similar structures where the loadbearing filaments are graphite, boron, KEVLAR, steel or hybrid composites of these materials.

Trial runs have been made in which the S-glass filaments were replaced with filaments of graphite, boron or steel. The results to date have been mixed and generally less than satisfactory. We have not yet solved problems with bonding of the epoxy resin to these materials, and with breakup of the graphite and boron filaments as they pass through the closing die. Work in this area is continuing under contract.

A slightly smaller version of the cable unit in Fig. 3 has just been completed, but has not yet been fully tested. An informal report on its performance should be ready in time for the NATO Conference in May, 1977. The new unit has a diameter of 0.102 cm, a breaking strength of 145 kg, and an attenuation (850 nm) of 3.8 dB/km. Diameter reduction was achieved by deleting the second buffer annulus, and replacing the TEFLON PFA with HYTREL. (The second buffer had been specified during an early program stage when the quality of the initial fiber coating---then, polyvinylidene fluoride---was so poor, due to localized "bumping" and incomplete wetting of the fiber surface, that additional protection against microbends and water intrusion was needed.)

3.2. Two-Fiber Miniature Cable (Freiburger, R.J., 1976)

In this design, shown in Fig. 4, an attempt was made to increase the cable's tensile modulus (decrease fiber strain under load) by incorporating stranded steel wires as the loadbearing structure. The optical fibers have no protective buffering beyond that supplied by the manufacturer. The helical geometry gives the optical fibers a strain relief of 0.1%---somewhat academic because of the presence of the steel wires---and a radius of curvature of 9.8 cm. Assembly of internal components and final jacketing were carried out as separate and independent processes. Planned cable dimensions were 0.147 cm (major axis) and 0.128 cm (minor axis). The dimensions shown in Fig. 4 apparently resulted from an over-expansion of the outer jacket after it emerged from the extrusion die. Due to equipment limitations, no void filling agents were employed.

The cable's breaking strength is 122 kg. Its weight in air is 7.58 kg/km, which corresponds to an in-water weight of approximately 5.55 kg/km. This gives a safety factor (cable alone) of 3.66 for tethered operations to a depth of 6 km. The actual safety factor will be somewhat less due to compression of internal voids at high pressure, since this effect will increase the cable's specific gravity.

This stranded steel cable is far more flexible than the S-Glass-armored unit described earlier. It can easily be wound around a forefinger, and readily accepts axial twisting. (The latter feature is especially important if the cable is to be stored by winding on a mandrel, then deployed by pulling it from the end of a storage cannister.) As will be seen later, its greatest single fault is the lack of any void-filling agent. This makes the cable highly susceptible to radial compression at high pressure, with resultant microbending of the optical fibers.

3.3. Six-Fiber, Deep Sea, Work Cable (Freiburger, R.J. 1976)

Here, the conventional deep sea cable described earlier (Fig. 1) was used as a model, and was modified to accept a multi-fiber optical data link. In addition, several physical design constraints were imposed. The cable was to have a breaking strength at least as great as the original unit, but was to be torque balanced. (The 2J69RC armor has a torque mismatch of about 2/1.) The new cable was to be more flexible, with a longer life under loaded flexure. Finally, it was to have the same (or lower) conductor resistance and the same (or higher) voltage rating as the model cable.

The cable's 6-fiber optical core is shown in Fig. 5, and the final cable in Fig. 6. A 1420-Denier KEVLAR-49 yarn was used as the loadbearing member in the core unit. This maintained flexibility and low weight, and gave the optical unit a safe handling tension of at least 15 kg (1% strain) during following assembly operations. Note that the core has space available for up to 12 optical fibers. If all of these fibers were graded index, the cable *could* have a bandpass of more than 1000 MHz over an 8-km length. In addition, the coaxial configuration for the electrical section allows emergency signals to be transmitted over this length at frequencies to about 1 MHz.

The cable's weight is 1040 kg/km in air and approximately 822 kg/km in seawater. At its measured breaking strength of 16,800 kg, this corresponds to a (cable only) safety factor of 3.41 at a 6-km operating depth. Again, equipment limitations precluded void filling of the cable's optical core.

3.4. Three-Fiber, Deep Ocean, Work Cable

The last experimental cable reported here (Fig. 7) was actually the first cable fabricated under our program. Again, it departed from the conventional deep sea cable of Fig. 1 as a model, and attempted to improve that design while adding optical conductors.

The two power conductors were reconfigured to allow reduction of cable diameter with no sacrifice of electrical performance.

The optical section consists of three, S-Glass-ruggedized, step index, optical fibers, each having the cross section shown in Fig. 3. These subunits were joined in a no-helix configuration, then molded to a diameter of 0.305 cm with the same thermosetting epoxy resin used in the S-glass matrix. A bedding jacket of high density polyethylene was extruded over this core to a uniform diameter of 0.457 cm. Serving of the electrical conductors and extrusion of the electrical jacket were performed as an in-line process, to maintain precise positioning of the copper wires and to minimize any contamination which might reduce the effectiveness of the insulation between the two wire groups. All internal voids were filled. Finally, the armor package was assembled in a torque-balanced configuration. The cable's design breaking strength is 17,600 kg. With an air weight of 859 kg/km and in-water weight of 685 kg/km, it has a (cable only) safety factor of 4.28 for tethered operations to 6 km.

The three-fiber work cable was fabricated early in our learning curve and, as a result, suffers from several critical deficiencies. The most serious of these are:

- Fibers And Fiber Buffering. The optical fibers predated the results of recent strength improvements, and had "weak link" breaking strains of about 0.25% in kilometer lengths. The initial buffering jacket (polyvinylidene fluoride) did not completely wet the fiber, and tended to form localized bumps on the fiber surface; it actually served as a *source* for microbends with amplitudes that were often greater than the diameter of the fiber. Addition of a second buffering jacket did not fully compensate for this effect. In a relaxed or loosely coiled state, the ruggedized fibers showed little increase in attenuation. Under tensile or bending stress, major attenuation increases (10's of dB/km) were measured. In full awareness of these deficiencies, we decided to proceed with cable assembly to determine what additional problems might be encountered there. The rationale was that this tension and bending sensitivity might work to our advantage, by helping to identify marginal deficiencies in the cable assembly operations.

- Fiber Geometry. The three optical units should have been assembled as a helix. While this would have given little benefit in tensile strain relief, it would have helped to cancel the effects of bending stress. Equipment and funding limitations at the time prevented this design feature.

- Conductor Geometry. Cabling equipment limitations initially made it impossible to maintain the conductor geometry shown in Fig. 7; especially the spacing between wire groups so critical to insulation resistance. The conductor helix angle (14.75 deg) was reduced to 3.5 deg to keep the wires from migrating and birdcaging as they passed through the jacket extrusion die. This change increased the conductor helix length from 6.67 cm to 28.7 cm, and made the conductor wires much more sensitive to tensile and flexure fatigue.

4. PRELIMINARY RESULTS OF CABLE TESTS

Tests of the experimental cables described in the previous section are still in progress, and results presented here should be regarded as preliminary. Environmental test data given below will be limited primarily to the cables described in Fig. 3, 4 and 6, since deficiencies of the cable in Fig. are so clear that it has been assigned a much lower test priority. For convenience, test results for the two miniature cables will be described jointly.

4.1. Results of Miniature Cable Tests (Stephens, D.H., 1976)

The two cables illustrated in Fig. 3 and 4 have been subjected to a series of environmental tests---including attenuation before and after cabling, tensile cycling, tensile stress/strain, flexure fatigue under load, pressurization and temperature.

4.1.1. Attenuation

Optical fiber attenuation was measured at wavelengths of 850 and 1060 nm, both before and after the fibers were assembled into cables. The results are given in Table 2. Within measurement error (equivalent to about 0.2 dB/km), the fibers appear to have suffered no attenuation increases due to either cabling or in-cable stresses. We are attempting to measure fiber attenuation *while* the cables are under various stresses, but measurements are handicapped by the difficulty of uniformly stressing long cable lengths. When such tests are run on short samples, the fixed measurement error dominates any attenuation changes.

4.1.2. Cable Performance Under Tensile Stress

Short lengths of both cables have been tab-terminated and subjected to both tensile cycling and pull to failure. The test samples (25-cm gauge length) show no apparent change of physical or optical properties after 100 cycles between 0 and 40% of short term ultimate stress. The results of pull-to-break testing (same gauge) are given in Table 3 and Fig. 8. Note that the S-Glass cable has much higher ultimate strain than the cable with steel wires. This factor---for identical cable geometry and tension members whose *sole* function is to carry a useful load with minimum strain on the optical fiber---gives steel a decided advantage over S-Glass. The latter material gains its very high useful strength because a moderate (700,000 kg/cm^2) tensile modulus remains effective over a much greater elongation than is the case with steel. It is worth noting that, in the destructive tensile tests we have run with the S-Glass cable, the optical fiber always survived both ultimate strain and the rather explosive rupture of the loadbearing matrix.

If we define "tensile modulus" as the ratio of tensile load per unit of relative strain per unit of total cable cross section, then the two cables have almost identical moduli until a stress is reached where the steel begins to yield. This comparison is made in Fig. 9. For steel, the combination of stranding and grouping at the cable core sharply reduces its contribution of strength and modulus to the cable cross section. The penalties which result are summarized below. (The high value shown for the tensile modulus of the S-Glass filaments is probably caused by an axial stiffening of the loadbearing structure by the epoxy resin matrix.)

Conditions of Mean Value Comparison	Strength (kg/cm^2) Steel	S-Glass	Modulus (kg/cm^2) Steel	S-Glass
Filaments or Wires Only	26,800	42,000	2,110,000	917,000
Loadbearing Section Only	20,500	26,900	1,460,000	587,000
Total Cable Cross Section	6,200	20,200	430,000	440,000

We are left with a dilemma. For maximum flexibility, the loadbearing structure should be at or near the cable core. For maximum strength and modulus efficiency, it should be near the cable's outer surface, where the ratio of available area to radius is greatest. The two constraints are in conflict. One possible resolution, considered but not yet tried by our group, is to keep the loadbearing structure in the outer annulus, but add flexibility by giving its filaments or wires a helix geometry. If this is done, a contrahelix structure is needed (in most applications) to ensure that the cable generates little or no torque when under load. The contrahelix will give some degree of rotational stiffness, but not enough to interfere with a cannister mode of storage and deployment.

4.1.3. Cable Performance Under Loaded Flexure

Samples of both miniature optical cables have been subjected to a series of flexure tests at loads corresponding to 20%, 30% and 40% of ultimate tensile stress. The test fixture is described in Fig. 10. It allows four parameters to be varied; sheave radius, tensile load, flexure amplitude and flexure rate. Four test sections are simultaneously cycled. In our tests, sheave radius was 5 cm, flexure amplitude was ± 28 deg, and the cycle rate was approximately 1/sec. Continuity of the optical fiber(s) and physical condition of the cable structure were periodically checked.

The results are summarized in Table 4. Note that "failure" of a test sample means that three test sections from the same gauge length survived. In terms of long term flexure capability (e.g., 100,000 cycles), the S-Glass cable has a degradation threshold at slightly more than 20% of ultimate stress. The corresponding value for the steel cable is about 40%. These two stress levels represent approximately equal absolute loads. We had expected that the steel cable would have a much shorter optical flexure life, due to the steel wires bearing on the buffered fibers, and that the polyethylene jacket would show early symptoms of erosion. Neither of these occurred.

4.1.4. Attenuation Response to Pressure and Temperature

The greatest deficiency shown by the two miniature cables was in their response to hydrostatic pressurization. This test was made with the cables in water at a pressure equivalent to a 5-km depth, and with the cable ends carried out of the test chamber through squeeze-type stuffing tubes.

Test Conditions	Attenuation Increase (dB/km) Steel Cable	S-Glass Cable
Cable Interior Not Flooded	53	12.5
Cable Interior Flooded	0	----

For the steel cable, "flooded" means that the cable jacket was repeatedly punctured so that water could flow among its interior elements. This relieved high bearing stresses on the optical fibers, caused by external pressure which forced the jacket into internal voids. (This pressure probably caused the buffered optical fibers to conform to the ridges and channels of the steel loadbearing structure, so that they were distorted into a cyclic microbending shape.) The reason for the pressure response by the S-Glass cable is not yet known. It may be due to compression of residual voids within either the buffer layer(s) or the loadbearing structure. For both cables, this tentative explanation leads to the (less tentative) conclusion that internal cable voids *must* be eliminated.

For both cables, attenuation (at 850 nm) increased less than 1 dB/km when their temperature was reduced to 0°C. At 70°C, the steel cable unit showed an attenuation increase of 2 dB/km. At 63°C, the epoxy matrix in the S-Glass cable softened and, since the cable unit was not constrained by a storage reel, the loadbearing structure buckled.

4.2. Test Results For The Deep Ocean Work Cables (Putnam, W.H., 1976)

Optical and environmental tests of the two electromechanical cables (Fig. 6 and 7) have been completed. Mechanical stress tests are continuing, and results should be available in time for the NATO Conference. The six-fiber cable showed optical attenuation values of 6 to 14 dB/km at 850 nm. (The history of its attenuation changes during cabling is shown in Table 5.) During tensile testing, the cable's optical attenuation increased as much as 10 dB/km at a load of 6900 kg. Attenuation increased by 1.6 dB/km when the cable was cooled to $1^{o}C$, and by 0.4 dB/km when it was pressurized to 700 kg/cm^2. The three-fiber cable had optical attenuation values of 120 to 570 dB/km at ambient temperature and pressure (no load). Its attenuation increased by more than 100 dB/km in response to pressurization and reduced temperature.

Measurements of absolute attenuation were based on the dual-length technique, in which power transmission is normalized to the power transmitted by a 1-meter segment of the same optical fiber). During environmental tests, attenuation changes were measured by monitoring cable transmission using a 850-nm LED source. In both techniques, the launch numerical aperture was 0.1, the source size was equal to the core diameter, input power was measured through a beamsplitter, and light was stripped from the fiber cladding.

A few measurements have been made of optical fiber survivability during destructive tensile testing of the work cables. A typical result is given in Fig. 11, for a straight-pull test and a cable gauge length of 2.4 m. As the figure shows, all optical fibers fail before the cable breaks, but *none* of them fail before the cable has passed the classic yield point (defined here as the load at which cable strain has deviated by 0.2% from a straight load/strain curve.) In the test represented by Fig. 11, "strain" is based on a measurement which is averaged over the entire cable gauge length. The cable yields, however, at a highly localized point. Therefore, we conclude that the optical fibers broke at a point in the cable which saw a much higher strain than the value of 1.9% indicated by the figure.

5. CONCLUSIONS AND RECOMMENDATIONS

Many of our conclusions have already been stated during earlier discussions of cable design, cable tests and test interpretation. The following points are sufficiently important to be reemphasized here.

- Optical fibers can be incorporated into cable structures with little or no excess loss. However, further development work is required if cable attenuation levels of 5 dB/km are to be routinely achieved; especially with graded index fibers.

- Optical fibers are needed with higher minimum strain-to-break in lengths of many (at least 10) kilometers. Today, we are on the threshold of fibers with 1% minimum strain over such lengths. When this parameter reaches 2% over similar lengths, the full capabilities of steel and KEVLAR-49 can be utilized. At 4% minimum strain, almost all candidate tension members can be used, and the cable designer will have a complete family of loadbearing materials with which to tailor cable strength, weight, diameter, stiffness and flexure performance.

- The fiber must be isolated, via buffering jackets, from external anisotropic stress. This jacket must be applied with extreme care---in choice of material, in uniformity of coverage, and with regard to its many functions. It must not be so non-uniform that it serves as a source (rather than a solution) of microbends. The initial buffer jacket should be applied as an in-line step in the fiber drawing process, before the fiber can be contaminated by water vapor or dust, and before it can contact any external surface.

- If the cable is to be subjected to tensile, bending or pressure stresses, it must be fabricated without internal voids. These become localized discontinuities within the cable; i.e., points of origin for local strain or microbending of the optical fiber.

5.1. Power Transmission in the Optical Cable

The deep sea work cables in Fig. 6 and 7 allow telemetry bandwidth to be increased by nearly two orders of magnitude. Yet, neither cable's performance was meaningfully improved in such critical parameters as strength, diameter, weight and safety factor. This is primarily due to the presence of the electrical conductors, which were ignored during redesign of the cable. In the conventional deep sea cable (Fig. 1), these conductors have two important functions---transmission of power and data. In the electro-optical cable, the data role is removed; *but the cross section and weight of copper in the cable remain essentially unchanged.* Therefore, changes in cable weight, diameter and safety factor are relatively minor. To achieve the full impact of fiber optic telemetry, a number of additional design options should be considered. (1) Use such lightweight conductor materials as high strength aluminum or copper-clad aluminum. (2) Employ the conductor in a dual mode; e.g., copper-clad steel, which can serve as both the conductor and the tension member. At 40% conductivity, this material is available at a tensile strength which approaches that of improved cabling steel. (3) Incorporate insulation materials which have much higher resistance and breakdown levels to transmit power at higher voltages. Where the conventional undersea work cable is used at an operating voltage of 600 VRMS, levels to 3000 VRMS can be employed. (4) Redefine the undersea system's power transmission requirement so that it is equal to *average* payload power rate, rather than peak power load. Use a recharging sys m in the payload to smooth power peaks and valleys by storing and dispensing energy. (5) Substitute such lightweight materials as KEVLAR-49 for steel in the cable's armor package. This last recommendation should be treated with extreme caution until the minimum strain-at-break for long optical fibers has been increased to a value of at least 2%.

6. ACKNOWLEDGEMENTS AND REFERENCES

All fiber and cable fabrications discussed in this paper have been performed by U.S. companies under contract to the Navy. Specifically:

- o Corning Glass Works (Corning, New York) fabricated and buffered the optical fibers used in the cable shown in Fig. 7.
- o Air Logistics Corporation (Pasadena, California) applied secondary buffer layers and S-Glass loadbearing structures to the cables described in Fig. 3 and 7.
- o Simplex Wire and Cable Company (Portsmouth, New Hampshire) completed fabrication of the cable in Fig. 7.
- o ITT (Roanoke, Virginia) fabricated and buffered the optical fibers used in the cables in Fig. 3, 4, 5 and 6. With ITT, Cable-Hydrospace (San Diego, California), it was also responsible for fabrication of the cables in Fig. 4, 5 and 6.
- o Tension Member Technology (Westminster, California) performed tensile tests on the cables in Fig. 6 and 7.

6.1. References

FREIBURGER, R.J., 1976, "Final Report on 300-Meter Sonobuoy Cable and 500-Meter Tow Cable", ITT (Roanoke, Va.) Report No. N00123-75-C-1023, 15 July, 1976.

GALLAWA, R.L., 1976, "A User's Mannual For Optical Waveguide Communications", U.S. Department of Commerce, Office of Telecommunications Report No. OT76-83, March, 1976.

GLOGE, D., 1972, "Bending Loss in Multimode Fibers With Graded and Ungraded Core Index", Applied Optics, Vol. 11, No. 11, pp 2506-2513.

GLOGE, D., 1975, "Optical-Fiber Packaging and its Influence on Fiber Straightness and Loss", BSTJ, Vol. 54, No. 2, pp 245-262.

GULATI, S.T., JUSTICE, B., SNOWDEN, W.E., AND JENKINS, D.M., 1975, "Water Integrity of Optical Fibers", Corning Glass Works (Corning, New York) Final Technical Report, Navy Contract N00123-75-C-1061.

OLSHANSKY, R., 1975, "Distortion Losses in Cabled Optical Fibers, Applied Optics, Vol. 14, No. 1, pp 20-21.

PUTNAM, W.H., 1976, "Fiber Optic Undersea Tow Cable Optical and Environmental Tests", NELC TR 2006, Naval Electronics Laboratory Center, San Diego, California, December, 1976.

SIGEL, G.H., Jr., "Fiber Optics For Naval Applications: An Assessment of Present and Near-Term Capabilities", NRL Report 8062, Naval Research Laboratory, Washington, D.C., September, 1976.

STEPHENS, D.H., 1976, "Fiber Optic Sonobuoy Cable Environmental Tests", NELC TN 3276, Naval Electronics Laboratory Center, December, 1976.

WILKINS, G.A., 1975a, "Performance Characteristics of KEVLAR-49 Tension Members", The Proceedings of the International Conference on Composite Materials, Vol II, pp 1278-1308, April, 1975.

WILKINS, G.A., ROE, N., JUSTICE, R., AND RUPRECHT, A., 1975b, "Designs For Neutrally Buoyant Multiconductor Cables", Proceedings of MTS-IEEE Ocean '75 Symposium, pp 121-127, September, 1975.

WILKINS, G.A., HIGHTOWER, J.D., AND ROSENCRANTZ, D.M., 1975c, "Lightweight Cables For Deep Tethered Vehicles", Proceedings of MTS-IEEE Ocean '75 Symposium, pp 138-147, September, 1975.

WILKINS, G.A, GIBSON, P.T., AND THOMAS, G.L., 1976a, "Production and Performance of a KEVLAR-Armored Deep Sea Cable", Proceedings of MTS-IEEE Ocean '76 Symposium, pp 9A1--10, September, 1976.

WILKINS, G.A., 1976b, "Fiber Optic Cables For Undersea Communication", Fiber and Integrated Optics, Vol. 1, No. 1 (in publication).

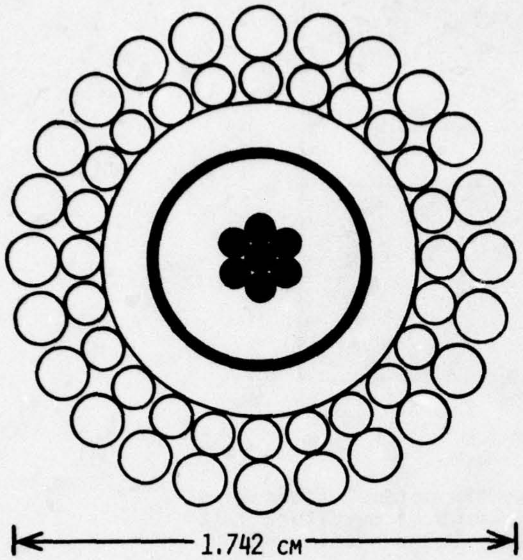

ELECTRICAL SECTION. CENTER CONDUCTOR IS 7 COPPER WIRES, EACH 0.098 CM, AS A LEFT HAND LAY OF UNSTATED HELIX ANGLE. SHIELD CONDUCTOR IS A #33 AWG COPPER BRAID. INSULATOR AND FINAL JACKET ARE HIGH DENSITY POLYETHYLENE, EXTRUDED TO DIAMETERS OF 0.706 CM AND 1.092 CM, RESPECTIVELY.

ARMOR SECTION. A CONTRAHELIX OF GALVANIZED, IMPROVED PLOW STEEL, 24 WIRES IN EACH LAYER. INNER ARMOR WIRES ARE 0.146 CM, AS 19.9-DEGREE (RH) HELIX. OUTER WIRES ARE 0.185 CM, AS 18.6-DEGREE (LH) HELIX.

Figure 1. Conventional deep ocean support cable (U. S. Steel Type 2J69RC coax).

Table 1. Critical physical properties for two DuPont fiber buffering materials---TEFLON PFA and HYTREL.

PARAMETER	TEFLON PFA	HYTREL POLYESTER ELASTOMER
SPECIFIC GRAVITY	2.15	1.25
MELTING TEMPERATURE (^{o}C)	305	218
MELT INDEX (GM/600-SEC)	9--12	12.5
ULTIMATE TENSILE STRENGTH (KG/CM^2)	280	400
TENSILE MODULUS---0-5% RELATIVE STRAIN INTERVAL (KG/CM^2)	---	2800
FLEXURAL MODULUS (KG/CM^2)	6600	5200
ULTIMATE ELONGATION (%)	300	350
HARDNESS (DUROMETER)	60	72
WATER ABSORPTION PER ASTM D570 (%)	0.03	"LOW"
CHEMICAL RESISTANCE	EXCELLENT	EXCELLENT

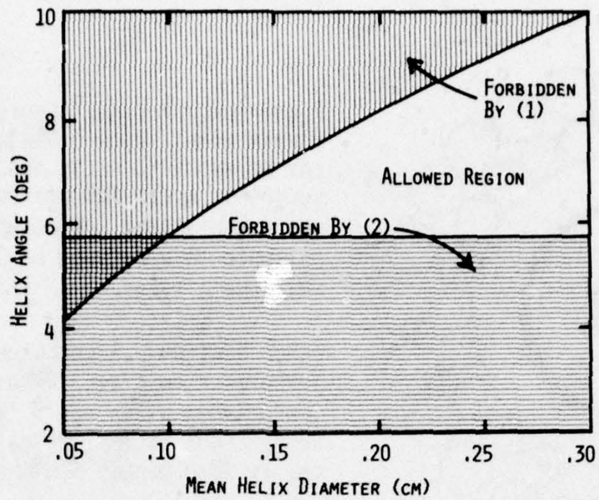

Figure 2 Geometrical constraints on the optical fiber in a helix. (1) The fiber's radius of curvature will be not less than 5 cm. (2) Fiber strain relief will be not less than 0.5%.

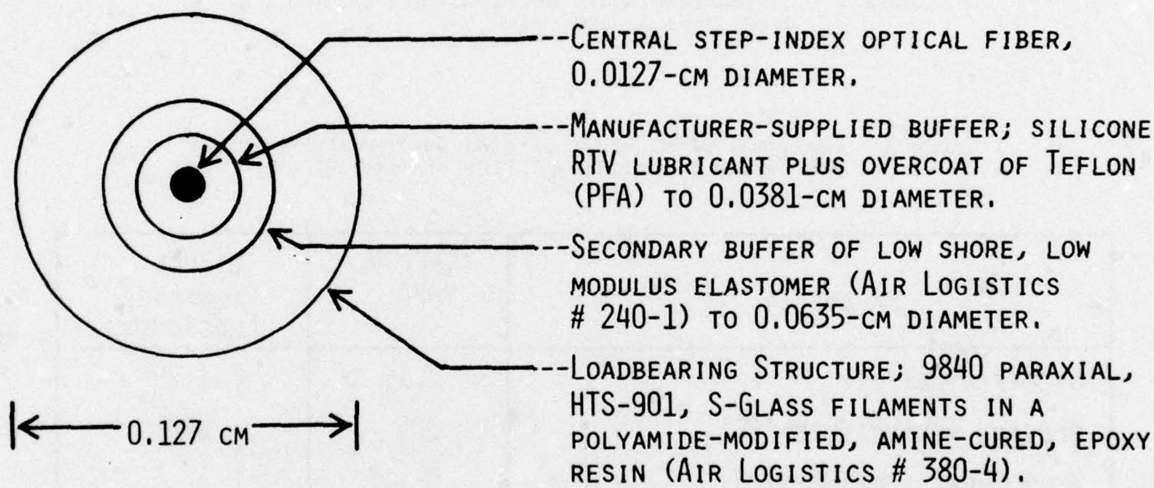

Figure 3. A lightweight, miniature, optical cable.

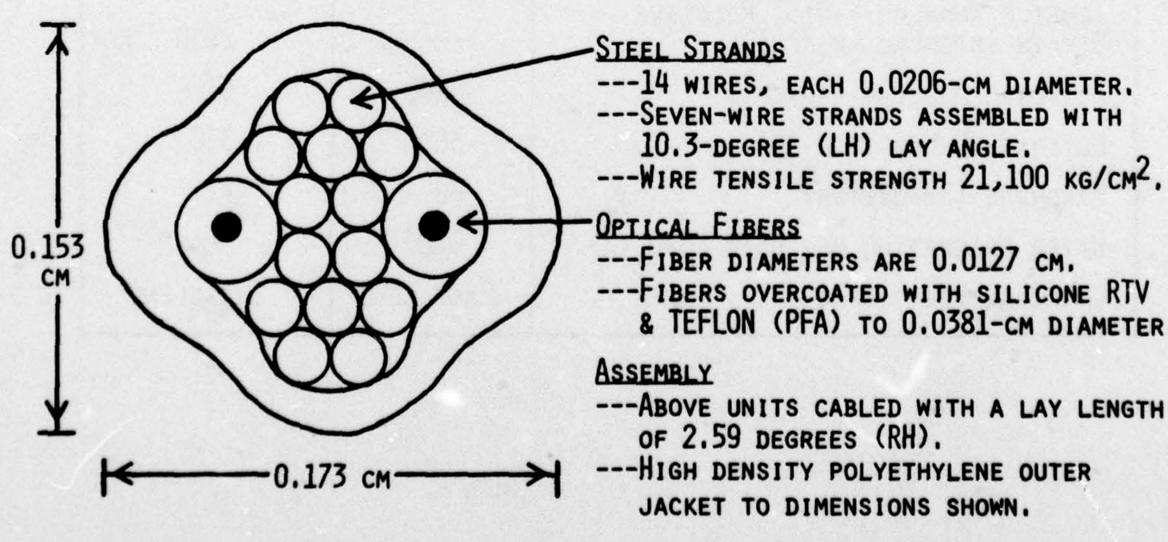

Figure 4. A twin-fiber, miniature, optical cable.

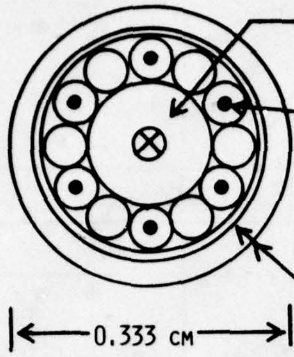

Figure 5. A six-fiber optical core for a deep ocean work cable.

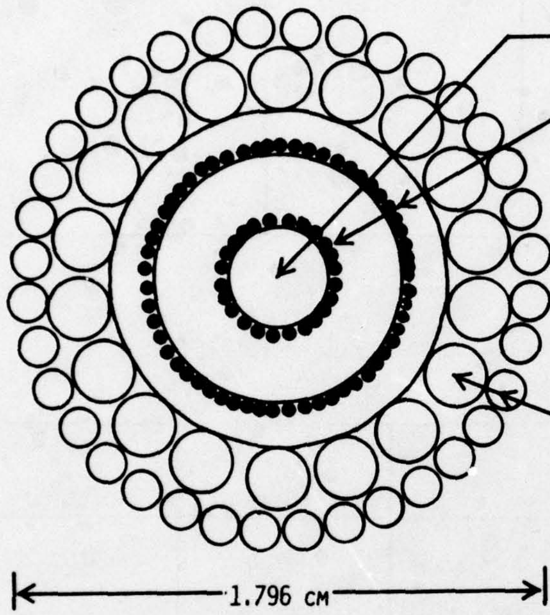

Figure 6. A six-fiber, deep ocean, electro-optical cable.

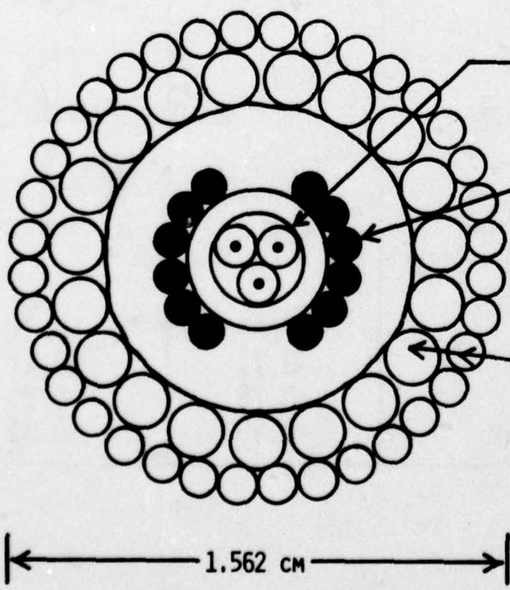

Figure 7. A three-fiber, deep ocean, electro-optical cable.

Table 2. Attenuation history for the cables in Fig. 3 and 4.

Test Subject	Attenuation (dB/km at 0.13 NA)	
	850 nm	1060 nm
Single-Fiber Cable (Fig. 3)		
As Manufactured/Buffered	7.3	5.0
After Cabling	7.75	5.0
Two-Fiber Cable (Fig. 4)		
As Manufactured/Buffered (Tested as One Fiber)	5.6	2.8
After Cabling		
Fiber A	4.8	1.8
Fiber B	4.8	3.7

Table 3. Summary of tensile tests for the miniature cables in Fig. 3 and 4.

Tensile Test Parameter	Fig. 3 Cable	Fig. 4 Cable
Mean Load at Break (kg)	255.4	122.5
Coef. of Variation (%)	1.2	1.3
Mean Load; 0.2% Strain Offset (kg)	*****	108.9
Coef. of Variation (%)	*****	5.3
Ultimate Strain at Break (%)	4.58	1.93
Coef. of Variation (%)	7.5	8.1
Initial Tensile Modulus (kg/cm^2)	434,000	418,000
Coef. of Variation (%)	7.1	9.8
Correlation of:		
Yield Load to Ultimate Load	*****	+0.39
Ultimate Load to Ultimate Strain	-0.11	+0.21
Ultimate Load to Tensile Modulus	+0.25	-0.05
Ultimate Strain to Tensile Modulus	-0.99	-0.51

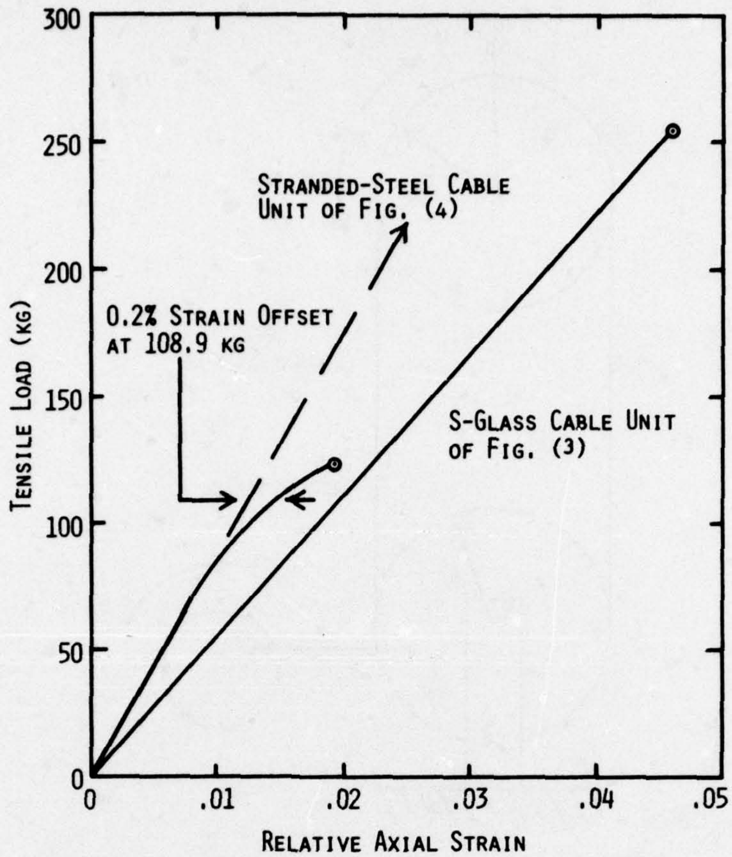

Figure 8 Typical load/strain curves for the miniature cables in Fig. 3 and 4.

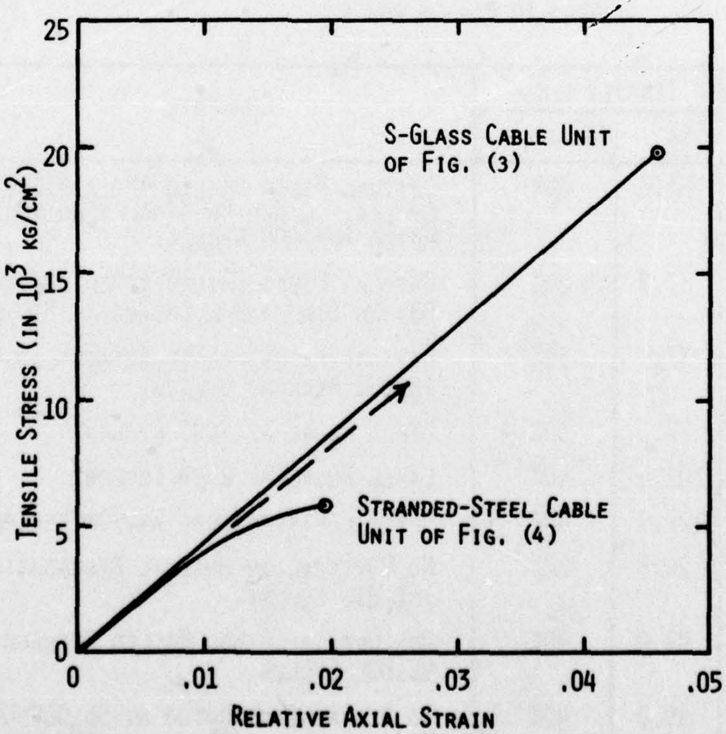

Figure 9. Typical stress/strain curves for the miniature cables in Fig. 3 and 4.

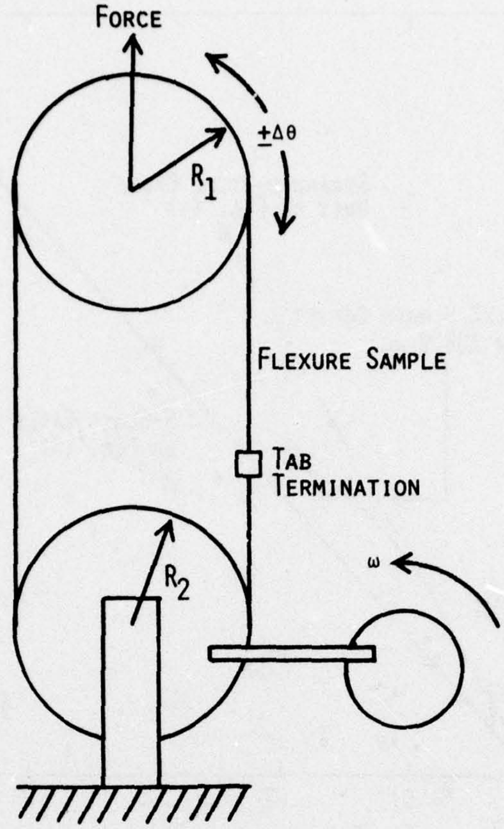

Figure 10. Fixture used for loaded flexure tests.

Table 4. Summary of flexure test results for the miniature cables in Fig. 3 and 4.

CABLE UNIT FROM FIG #	TENSILE LOAD		COMMENTS
	KG	RELATIVE	
3	51.3	20%	OPTICAL FIBER FAILED AFTER 418,000 FLEXURE CYCLES. CABLE PHYSICAL STRUCTURE UNDAMAGED AFTER 907,000 CYCLES.
3	51.3	20%	OPTICAL FIBER FAILED AFTER 197,600 CYCLES; BUT NO STRUCTURAL DAMAGE AT 310,000 CYCLES.
3	77.1	30%	OPTICAL FIBER FAILED BETWEEN 15,000 AND 16,000 FLEXURE CYCLES.
3	77.1	30%	CABLE BROKE AT 9691 CYCLES.
3	102.5	40%	CABLE BROKE AT 2340 CYCLES.
3	102.5	40%	OPTICAL FIBER BROKE AT 100 CYCLES.
4	24.5	20%	NO PHYSICAL OR OPTICAL DEGRADATION AFTER 101,850 CYCLES.
4	49.0	40%	ONE OPTICAL FIBER FAILED BETWEEN 90,000 AND 95,000 CYCLES.
4	49.0	40%	NO DEGRADATION NOTED AT 55,000 CYCLES. BOTH OPTICAL FIBERS BROKEN AT 155,000 CYCLES, BUT NO OTHER DAMAGE VISIBLE.

Table 5. Attenuation history for the optical cable in Fig. 6. (From Freiburger, R.J., 1976)

Fiber #	Fiber Type	Fiber Attenuation (dB/km at 820 nm)				
		Before Cabling	As Optical Sub-bundle	Before 2nd Conductor	After Coax Jacketing	After Cable Armoring
1	Graded	5.3	6.8	7.2	15.6	15.4
2	Graded	12.3	17.3	12.7	16.1	11.4
3	Step	6.8	8.0	6.6	7.4	7.4
4	Step	7.3	8.0	8.8	6.2	7.2
5	Step	6.6	5.7	10.2	15.7	12.2
6	Step	10.1	9.1	9.8	14.5	13.7

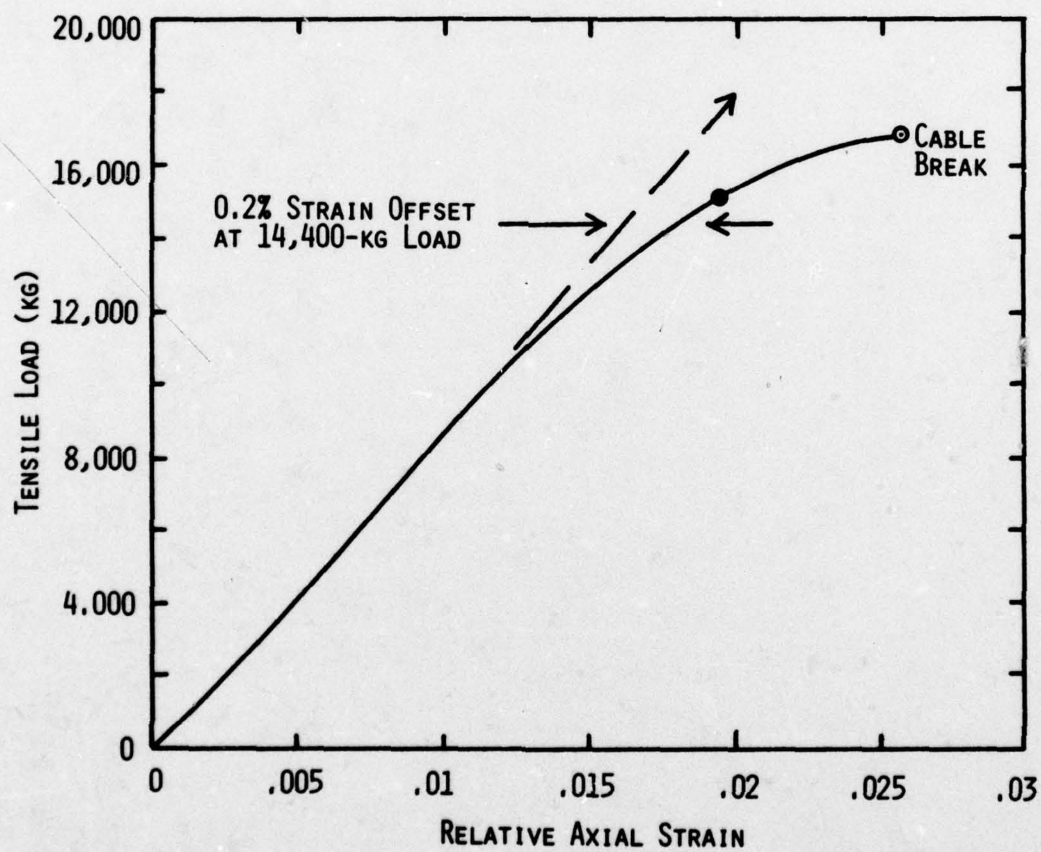

Figure 11. Typical load/strain curve for the 6-fiber, deep ocean work cable in Fig. 6. The solid circle represents the load and strain at which all optical fibers broke.

FIBRE-OPTICS FOR DEFENCE APPLICATIONS IN THE UK

B. Ellis
Space Department
Royal Aircraft Establishment
Farnborough
Hants

and

W. S. Nicol
DCVD
Ministry of Defence
Empress State Building
London

ABSTRACT

The Philosophy underlying the choice of particular types of fibre-optic systems for military applications is discussed. Some existing and planned systems are described together with details of supporting component development.

1. INTRODUCTION

The idea of using optical fibres to transmit data over appreciable distances was conceived a little over 10 years ago by Kao and Hockham (1966), working in Standard Telephone Laboratories at Harlow in the United Kingdom. In the intervening decade the development of fibre-optics has been vigorously pursued in several countries. While the long distance civil telecommunications applications have been well to the fore in stimulating this activity it is nevertheless the case that the advantages of fibre-optics for military systems were appreciated at an early stage. This is important since the justification for the military use of fibre-optics is generally quite different from that of civil applications for which lower overall system cost is the sole motivation. Many benefits are sought by military users and the potential advantages have been listed too frequently in the past to require repetition here. It is, however, worth noting that although the particular advantages stressed for any given application depend upon the nature of the application (the strongest advantages for avionics may differ from those for naval systems, for example) it is usually an advantage stemming from the good electromagnetic compatibility of optical fibres which is most important. The attractions of a transmission medium which does not appreciably radiate or pick up electromagnetic radiation are obvious; in addition ground loop problems are often solved by the isolation achieved with a fibre-optic link.

Two other general observations concerning military applications should be noted. Firstly, the severity of the environmental constraints of many military applications far exceeds that applying to civil uses. Secondly, many military applications cover only quite modest distances and often involve only moderate data rates. It is thus clear that, while many aspects of fibre-optic development are common to both the military and civil fields, there are also many areas in which the separate development of components for military applications has been, and will continue to be, essential. Before considering in detail the military applications of fibre-optics within the UK it is therefore instructive to review the developments which have led to our present capability and to outline the philosophy underlying our plans for the future.

2. COMPONENT DEVELOPMENT IN THE UK

2.1 Components for Bundle Systems

In the UK, as elsewhere, the first interest was in systems employing fibre bundles, due to the earlier availability of fibres in bundle form and to the simpler launching requirements of bundles. Thus MOD funded component development was originally concerned principally with fibre bundles and led to the availability of fibre bundles with high numerical aperture and quite low loss (NA - 0.48, 100 dB/km, Pilkington), low loss connectors (1.5-2 dB, Plessey Co) and a high power high radiance source designed especially for bundle systems (launching 2.5 mW into a 400 μm diameter bundle of NA 0.5 at 200 mA drive. A number of prototype systems using fibre bundles have been built, providing much valuable information and making a useful foundation for the use of bundles in some of the simpler current and future systems.

2.2 Single Multimode Fibre Components

Attention has now turned to single multimode fibre systems. Among the reasons for this are the far lower connector loss possible with single fibres, the possibility of active branching and the likelihood of greater strength in a properly protected single fibre. Until comparatively recently the choice of fibre core size has been largely constrained by factors stemming from the fibre manufacturing process. However, the advent of plastic clad silica (PCS) fibre has made the manufacture of large core fibres simple and it is now possible to consider the use of fibres with cores 200 μm or more in diameter. Since, as noted earlier, many applications involve relatively short distances and low data rates the use of large core fibre of relatively high NA imposes no disadvantages. The upper limit to the core diameter is set in practice by the increasing stiffness of the fibre. Connector problems are greatly eased by the use of large core sizes, making PCS fibre of considerable interest for some applications. Development of PCS fibre is being undertaken at STL (with CVD funding) and attenuation as low as 20 dB/km at 820 nm has been achieved.

For applications for which PCS fibre is not suitable the use of doped silica/silica fibre is envisaged and cables incorporating such fibre are being developed at GEC and STL. It is noteworthy that the demountable connector developed by STL, with CVD funding, has been demonstrated in the laboratory to have a loss ~ 1 dB using 85 µm core fibre (Bedgood et al 1976). This connector utilises the watch jewel ferrule technique of which details have been given elsewhere. Thus the anticipated low connector loss with single fibres has already been demonstrated in the laboratory; connectors for field use are currently being developed, although it may be noted that a field-worthy version with a slightly higher loss is already available in a standard military connector shell.

Active branching, in which a fraction of the radiation propagating in a fibre may be coupled out is an important potential advantage obtainable with single fibres. The leaky mode coupler (Stewart and Stewart, 1977) is a device which may function in this way. Not only does this device, development of which is being sponsored by CVD at the Plessey Co, give the possibility of active branching but it is also capable of application as a branching device in a "clip-on" mode with bare fibre; this eliminates the insertion loss associated with more conventional branching devices. The device may also be used to feed power into a fibre.

For many MOD applications an incoherent emitter in the form of a high radiance LED is suitable. The development of such a device for use with bundles has been referred to earlier. In addition to this a very high speed HR LED is being developed, by the Plessey Co, for use with single fibre systems. Already analogue modulation to beyond 1 GHz (3 dB point) has been demonstrated with encouragingly high radiance.

Solid state laser development at STL, under CVD sponsorship, has led to encouragingly long lived devices, having a median life of 25000 hours under moderate (2-3 mW) output powers. These lifetimes are improving with burn-in. Degradation is observed by an increase in threshold current density alone and not by a change in incremental efficiency. For higher laser power applications the technique of bonding optical fibres directly to lasers has been very successful. Lasers are expected to find application in systems having high launched power requirements.

A source module employing either an LED or a laser is under consideration.

It will be apparent that only one type of component is not currently under development and that is the detector. At present commercially available devices have adequate performance to meet systems needs.

3. APPLICATIONS OF FIBRE-OPTICS IN MILITARY SYSTEMS

3.1 Ground Based Systems

The use of fibre-optics in the Army's future battlefield communications system, project Ptarmigan, is being actively considered. In this application high frequency cable up to 2 km in length may be replaced by fibre-optics. The advantage sought is that of reduced electromagnetic interference but savings in cost and weight may also be obtained. Fibre-optic cables for this application must withstand the full rigours of the severe battlefield environment and must, for example, tolerate vehicles of all kinds being driven over them.

3.2 Naval Systems

An experimental 120 m fibre bundle link, using Pilkington fibre, has been installed in HMS Tiger to link the bridge with radar equipment. This has provided valuable experience of installation procedures for bundle systems; in this instance, for example, it was found to be essential to fit the terminating ferrules after the cable had been installed in order to avoid undue stress at the terminations. The link involves 25 bends of 3 inch radius, passes through 3 watertight bulkheads and over 2 expansion joints. It has functioned satisfactorily since its installation in July 1976.

Fibre-optic links are also being considered for underwater applications including a life support system link for divers relaying data on the physiological parameters of divers when working. A short trial link within an underwater vehicle has also been tested.

3.3 Avionic Applications

Future military aircraft will almost certainly incorporate some form of data bus linking the computers, displays, navigation system and various sensors. Such a multiplexed system may be purely electrical but it is clear that fibre-optics could be used to advantage, particularly in alleviating problems with electromagnetic compatibility.

This is especially true in modern aircraft constructed from largely non-metallic materials. As a precursor to a full data bus an experimental point-to-point link has been developed by Marconi-Elliott for MOD to convey 5 M baud signals over distances of up to 30 m; it is termed "Minilink" and uses a fibre bundle in conjunction with a high radiance LED source. Studies of environmental effects on this link are being undertaken at RSRE, Malvern. Some work on optical sensing devices, particularly pressure sensors for engine applications is also underway. Future data highway applications are likely to employ many of the components currently under development and described in section 2.

Fibre-optics is also likely to be employed in the communications systems of future aircraft. Where-ever it is necessary to pass high frequency signals any appreciable distance within an aircraft the use of fibre-optics becomes attractive. Thus optical links are being developed for analogue use in the 225–400 MHz communication band. For this purpose the fast high radiance LED described in section 2.2 will be used. The objective is to launch 100 μW into a fibre of 85 μm core with 0.16 NA at frequencies up to 400 MHz. The required frequency response has already been obtained, indeed modulation to frequencies well beyond 1 GHz has been demonstrated. It is planned to achieve the required launched power by the incorporation of a lens into the LED structure. Not only will this source meet the analogue transmission requirements it will also serve to meet any future high data rate digital needs that may arise.

4. CONCLUSION

Fibre-optics is likely to find widespread application in future military systems. Components for bundle systems have reached an advanced state of development and the development of single fibre components is well in hand.

5. ACKNOWLEDGMENTS

The work described in this paper includes, besides that of RAE and CVD, that of several other parts of the UK MOD whose contributions are gratefully acknowledged.

REFERENCES

BEDGOOD, M., et al 1976, Electrical Communication 51, No 2 (1976).

KAO, K. C., and HOCKHAM, G. A., 1966, Proc. IEE 113, 1151.

STEWART, C., and STEWART, W. J., 1977, This Conference Paper No 45.

A REVIEW OF NASA FIBER OPTICS TASKS*

Alan R. Johnston
Jet Propulsion Laboratory
Pasadena, California 91103

SUMMARY

This paper reports on the status of on-going NASA tasks involving fiber-optic data transmission, and related topics. Ground-based applications, including a multiplexed wideband 2 km prototype link and a building-to-building video link, are described. Possible applications in space and an orbital fiber-optic experiment are also discussed. In connection with the use of fibers in space, the effects to be expected from the space environment are touched on, particularly radiation-darkening of fibers and temperature effects. Laboratory results on performance of fibers at cryogenic temperatures are also presented. Finally, some thoughts on future applications are given.

1. INTRODUCTION

The primary purpose of this paper is to provide an overview of current NASA efforts in fiber optics. On-going NASA tasks related to fiber optics and integrated optics will be reviewed. They involve both ground-based data transmission and applications in space, and range from the investigation of basic system limitations to development of a prototype ground communication link and an orbital experiment. The status of these tasks will be very briefly summarized, and some ideas about their future direction will be indicated. References will be given where available so the reader seeking more detailed information will be able to obtain it from existing reports or from the individuals directly involved.

The second section of this paper discusses ground-based applications. Progress toward demonstrating a prototype 2-km wideband multiplexed data link at Kennedy Space Center will be summarized. Another near-term application involving on-site data transfer is a building-to-building video link experiment at the Jet Propulsion Laboratory.

The third section examines the use of fibers on spacecraft. The first applications being contemplated for fiber optics in space are on board the Shuttle. Both digital data transfer and analog TV transmission by means of fiber optics are possibilities. Results of an initial study of a proposed Shuttle TV link are briefly mentioned.

This study (and others) has shown that space applications may subject fibers and other link components to a unique environment, of which temperature extremes and particle radiation are expected to be the most important. Under worst-case conditions, low temperature extremes of roughly -150°C may occur, with deleterious effects on polymer materials used in fiber bundle or cable fabrication to be expected. Both plastic and plastic-clad fibers which use polymers for optical functions will be directly affected but, in addition, stiffening and embrittlement of the polymer materials used for protective jackets will affect the design of a fiber system.

Depending on the mission, radiation effects in space will also restrict the choice of fiber materials to the radiation hard class, primarily the doped-silica-glass type. Expected dosage and fiber lifetimes to be expected in space will be summarized.

An active data link experiment is being developed at the Jet Propulsion Laboratory for a flight aboard the Shuttle-launched Long Duration Exposure Facility, and a description of the experiment completes the section on fibers in space.

The fourth section treats technology effort related to fiber optics. Laboratory results showing the performance of certain fibers at cryogenic temperatures are presented. Development of long-life CW solid-state lasers by Langley Research Center that are useful for transmitter modules and ultimately for integrated optics devices will then be described. In addition, an interesting investigation of the possible use of fiber waveguides originated by Vali and Shorthill at the University of Utah will be mentioned.

The paper concludes with some remarks, necessarily of a speculative nature, about possible longer-range uses of fiber optics.

*This paper presents the results of one phase of research carried out at the Jet Propulsion Laboratory, California Institute of Technology, under Contract No. NAS 7-100 sponsored by the National Aeronautics and Space Administration. The opinions presented are those of the author and do not necessarily represent an official NASA position.

2. GROUND-BASED APPLICATIONS

There is a great variety of possible ground-based applications for optical fibers. The motivation to pursue these applications results from the promise of lower cost because of the higher information throughput of fibers as compared to a copper transmission line and the greatly decreased bulk which must be housed in conduit. The expected easing of EMI and ground-loop problems is also frequently considered very important for many system applications, such as in a digital computer interconnect.

2.1. Kennedy Space Center Experiment.

An experimental wideband data link is under development at NASA's Kennedy Space Center under the technical direction of Charles Bell (Ref. 1). The link is approximately 2 km (6000 ft) in length (Fig. 1) and connects the Central Information Facility (CIF), which contains a large computing facility and the Flight Crew Training Building (FCTB), in which the shuttle-launch checkout equipment is being developed. Functionally, the experimental link will be a part of the prototype (or serial No. 0) of the complex prelaunch checkout network for the shuttle. This work was preceded by an investigation of a wideband prototype link, also described in Ref. 1. This laboratory prototype link used a 100 MHz bandwidth, and the information (both digital and analog) was transmitted by frequency-domain modulation of the light. Alternative forms of transmitters and receivers were evaluated.

In the present experiment, multiplexing techniques for combining many data channels (both analog and digital) onto one fiber are being emphasized; hence, the acronym MOTS (Multiplexed Optical Transmission System). The aim is to develop a wideband link using modular, interchangeable components such that the changing data needs of different launches might be accommodated by changing plug-in modules at the terminals without affecting the wideband fiber link itself. Even the direction of data transmission on a given fiber could be reversed by changing transmitter and receiver modules. The user of one individual data channel need not be aware of the details of the multiplexed wideband optical link.

A block diagram of the 2-km experiment is shown in Fig. 2. Each fiber will carry one 35- to 50-MHz analog data channel or up to 10 5-MHz multiplexed data channels. The fibers themselves have a 7 dB/km loss and a 600 MHz-km throughput capability, providing for at least a 50-MHz bandwidth over a total length of 12 km for future requirements.

The cable is a 10-fiber cable, utilizing Corning-graded index fiber.

A prototype optical fiber cable made at KSC is compared with samples of the present multichannel wideband cable in Fig. 3. The prototype is very similar to the cable that will be installed in the underground conduit (Ref. 2). If optimum multiplexing were applied, the 10-fiber optical cable would have an information capacity many times that of one of the large 36-pair copper wire cable. Metal armor is used in the fiber cable, and its interior will be kept dry by a slight positive gas pressure.

The cable was obtained from the supplier in 1-km lengths, and will be pulled into subsurface conduit by conventional techniques. The total number of splices required per fiber to make up the run will be determined by the practicalities of pulling the sections of cable into the conduit. A minimum of two splices, up to perhaps five splices per fiber, is expected to be needed. The splices will be of the hot-fusion type, made in place in the manholes by portable equipment supplied with the cable (Ref. 2). The expected loss per splice is 1/2 dB.

Four fibers will be used for data; two in each direction. A separate fiber will be used for wideband analog data, such as multiple FM TV channels, and another for multiplexed digital data. The six remaining fibers can be jumpered (Fig. 2) for experiments with longer fiber runs. A total length up to 12 km can be set up in this way, including repeaters, if desired. Initial tests with the 2-km cable in place are planned for mid 1977.

The present fiber terminals (Ref. 3) use a Burrus-type, high-intensity LED in the transmitter, and an avalanche photodetector in the receiver. Injection-laser sources are being examined for future use in transmitter modules. The present LED transmitters are capable of coupling over 1 mW into a fiber. The Minimum Detectable Power (MDP) of the receiver modules is in the range of 5-8 nW for a 35-MHz bandwidth, allowing over 30 dB for fiber, coupling, and connector losses.

Looking further into the future, this experiment will examine longer links, as mentioned above, and will also evaluate the performance of a fiber link in a real field environment. The experiment is designed to explore the problems of installing and maintaining fiber cables in underground conduits, which at KSC are typically submerged in a very corrosive environment. The Shuttle launch area is located 7 km from the Launch Control Center. At present, there are a total of roughly 12,000 miles of video channel at KSC. The fiber-optic technology may provide a cost-effective alternative for some of these requirements, and the present experiment is expected to help develop the capability to implement these longer links.

2.2. JPL Closed-Circuit TV Link.

An experimental closed-circuit TV link is being implemented at the Jet Propulsion Laboratory in order to evaluate the applicability of fiber optics in the mission control complex. The test link is 700 ft in length and has been set up using a single-fiber waveguide. Fiber-optic cables are not being tested - an unprotected but plastic-sheathed fiber has been placed by hand in a cable tunnel connecting the two buildings. The link uses direct analog transmission of the video signals, so achieving a high signal-to-noise ratio in the delivered signal is the most important requirement. Typically, the video signals being transmitted represent data to be presented in an alphanumeric display.

One reason for selecting this application for an initial experiment was that grounding problems between the two buildings and other interference effects can cause difficulty with video transmission. This type of problem can always be cured, but the promise of inherent immunity to transmission-line interference was of interest. A second reason was that a large number of such circuits are in operation lab-wide, making any potential cost saving that may be possible with fiber links proportionally more important. We hope to gain experience in a user environment with this experiment, enabling us to draw better conclusions about the performance and future cost that can be expected with fiber-optic transmission.

3. SPACE APPLICATIONS

Applications on spacecraft will likely be motivated primarily by potential simplification of EMI problems and secondly by weight considerations. Reduced cost for the link hardware itself is not likely to be a significant factor, as it is for ground-based applications.

3.1. Vehicles.

Since we are now on the eve of the Shuttle era in space transportation, one naturally would look toward Shuttle systems as an area for fruitful application of fiber-optic technology. The Shuttle, like any other large aircraft, contains complex electronic systems which are interconnected with data bussing techniques. Unfortunately, the Shuttle-Orbiter development is too far along to take advantage of fiber optics in any of its basic avionics systems.

On the other hand, Shuttle payloads, which range from the large Spacelab to small probe type spacecraft, remain a possible area for application, both within individual payloads and for interfacing the payload with the Orbiter. An initial unpublished study of the feasibility of using fiber optics for payload interfacing has been made by Rockwell International, but no hardware effort has been undertaken.

The primary motivation for the use of fiber-optic links for such interfacing is the promise of immunity to electromagnetic interference (EMI) effects on the interconnecting line. Although interference always will be possible within the terminal electronic modules of a link, just as in any other electronic equipment, the dielectric fiber waveguide inherently will not couple to any electrostatic or magnetic field along the way. Any simplification of the EMI problem in the payload interface is particularly valuable because the Shuttle payload bay is expected to be an electrically noisy area, and there is a requirement for a short turnaround time for the Orbiter, sharply limiting the time available for troubleshooting. Each payload is likely to present new problems in this area, further emphasizing the value of eliminating any source of possible EMI at the outset. The other potential benefits of fiber optics (decreased weight, and size, and increased bandwidth) are very useful properties, but probably are secondary to the EMI question.

Other potential shuttle applications have also received some attention. We at JPL and Paul Coan of the Shuttle television group at NASA's Johnson Space Center have made a preliminary study of video signal transmission and TV camera control requirements for a CCTV system to be used in the Shuttle payload bay. The purpose of the system is to monitor payload deployment and retrieval activities. A study has been completed on this system (Ref 4). Breadboarding of some of the important components (fibers and connectors), using materials selected to withstand the temperature environment expected in the payload bay, is planned.

A longer-range application selected for study at JPL is the data bus portion of a spacecraft Unified Data System (UDS) being developed for future spacecraft. The fiber links would interconnect elements of a microprocessor-oriented data and control system that is physically distributed among a number of separate packages on the spacecraft.

3.2. Space Environment

Before applying a new technology such as fiber optics on spacecraft, it is necessary to examine the effects that the space environment may have. Two important environmental effects expected are from possible wide-temperature variations and radiation-darkening of fibers. Other environmental conditions (e.g., launch vibration) are similar to those already faced in aircraft systems.

The initial JPL study of the Shuttle Orbiter CCTV system indicated that a worst-case temperature range of +120° to -150°C was possible in the payload bay. In general, fiber cables contain polymer materials in which mechanical properties will be adversely affected by this wide a temperature range. Flexibility is difficult to retain at the low temperature extreme. These considerations are, of course, shared with conventional copper cabling. Polymers which outgas excessively in space must also be avoided. It is likely that the cabling materials that perform satisfactorily are going to be different from those in common use in today's developmental fiber cables. There may also be an effect on cable performance caused by temperature cycling, in which undue compression of the fibers at low temperature occurs as a result of contraction of the jacket. None of these possibilities have been thoroughly studied for fiber cables.

Of even more importance is the fact that in plastic-clad, or in all-plastic fibers, which otherwise would be an attractive choice for space applications, the temperature effects can affect the optical characteristics of the fiber. The effect of low temperature on the plastic-clad, fused-silica type has been investigated at JPL and is discussed in more detail in the following section. Briefly, we find that the transmission of silicone-clad fiber is impaired at lower temperature and ceases entirely at about -80°C. The all-plastic fibers are also not suitable for the entire -150° to +120°C temperature range, but the all-glass, doped-fused-silica chemical-vapor deposited (CVD) type appears to be unaffected.

The terminal electronic packages are also affected by temperature, especially the LED emitter. However, the behavior of components needed for fiber-optic terminals are similar to those widely used in other electronic modules. It is felt that the temperature of the terminal modules will be controlled along with other electronics within an acceptable range by conventional design techniques. Control of the fiber temperature is not assumed, because it would be much more cumbersome and probably is not necessary.

Radiation dosage is an important environmental factor because radiation-induced absorption occurs in all optical fibers. The highest dosages expected in space are large enough to create an important design constraint on the complete link. Radiation effects on the terminal electronics are expected to be similar to the effects on other electronics, so they are not discussed here.

Extensive laboratory investigations of the effect of radiation on fibers have been reported in the literature (Ref. 5, 6, 7, 8). These studies indicate a large variation in sensitivity between different fiber types, the large-aperture lead-glass-type fiber being highly radiation-sensitive, and pure silica types being quite insensitive. The range of sensitivity approaches a factor of 10^6 between softest and hardest glasses. However, laboratory experiments to date use much higher dose rates and shorter exposure times than expected in space.

More recent experiments using plastic-clad fused-silica fibers (Ref. 9, 10) have indicated a short-term saturation of the induced loss that occurs at doses in the neighborhood of 100 rad. As a result, the induced loss for a small dose is much larger than one would predict from data taken at a large total dose. In addition, the induced loss is observed to decay after irradiation with a time constant of the order of 15 minutes, and the rate of decay is unchanged after 2 to 3 hours. The amount of the initial non-linear-induced loss and the degree of post-exposure annealing depend quite strongly on the purity of the fused silica used to fabricate the fibers.

Further investigations are in progress at the Naval Research Laboratory. To date, the indication is still that the final induced loss of high-silica-fiber types will be small, but darkening at low doses is highly non-linear, and the degree of long-term annealing is not known for any dose. More laboratory work is needed on induced loss at the low dose rate and long duration typical of space missions.

To provide a reference for understanding the radiation effects in fibers, the estimated total dose for different mission types is given in Table 1. Note that the radiation exposure on any orbital mission is highly dependent on the specific orbit chosen, and can vary over many orders of magnitude. The numbers shown in Table 1 must be regarded as approximate; they are intended to convey only an idea of the order of magnitude of the expected dose and how much it may vary, depending on the type of mission. The doses shown are unshielded; the dose internal to a spacecraft can be two orders of magnitude smaller for earth orbit, but the Jupiter radiation is harder to shield out. The 10^6 rad dose for Jupiter orbit should be a rough value for the internal dose also.

Table 2 indicates the estimated radiation-induced loss one may expect for different fiber types.

The added loss caused by the radiation is given in dB for a 30-m length of fiber, representing approximately the attenuation margin that would have to be provided in a spacecraft link to allow for radiation effects. The induced loss coefficient is that reported for large dose.

Again, these figures are approximate and are intended to indicate only the order of magnitude of the effects to be expected.

Table 1. Representative Radiation Dose

Type of Mission	No Shielding (Total Dose)
Low Earth Orbit	10^3-10^4 rad/yr
Synchronous Earth Orbit	10^6 rad/yr
Jupiter Orbiter	10^6 rad

Table 2. Radiation-Induced Fiber Loss

Fiber Type	Large Dose Induced-Loss Coefficient	Induced Loss/30 m (dB)		
	dB/km rad	10^2 rads	10^4 rads	10^6 rads
Fused-Silica; Suprasil I	10^{-5} [a]	-	∿0	0.3
Plastic-Clad Fused Silica	10^{-4} [b]	0.3[d]	3[d]	3
Corning-Type B CVD	10^{-3} [a]	3[d]	-	30
Galileo K 2K Glass	2[a]	6	-	-
Pilkington Hytran Glass	10[c]	30	-	-

Notes:

a. Ref 5

b. Ref 9

c. Ref 10

d. Estimated from early results on nonlinear low-dose behavior in Ref 9, 10.

3.3. Orbital Exposure Experiment

A fiber-optic data transmission experiment is currently under development at JPL for a 6-month flight on board the NASA Long-Duration Exposure Facility (LDEF) to be launched in late 1979. The LDEF is a Shuttle-launched vehicle (Ref. 11) which can carry a number of self-contained experiments into low earth orbit for exposure to the space environment. A photograph illustrating the LDEF vehicle and a typical experiment tray is shown in Fig. 4. LDEF will be retrieved by a later Shuttle flight for data recovery and evaluation.

The purpose of the LDEF fiber-optic experiment is to confirm the predicted radiation effects for several types of fiber and to verify the link design approaches and the performance of components used in the experimental fiber-optic links.

The Fiber-Optic Data Transmission Experiment will contain four active 100-m links. Single-fiber-per-channel technology will be used. The fibers for each link will be arranged in a planar helical coil such that one side can be directly exposed to space and, if desired, a known thickness of shielding material may be mounted over the coil. The back side of each coil will be shielded by the experiment tray and other LDEF structure. Up to 8 inactive 100-m fibers may also be carried by the experiment for inspection after retrieval.

Each active link will transmit a digital pseudo-random sequence at a nominal 10-M bit rate. A block diagram illustrating the experimental layout is shown in Fig. 5. Bit-error-detection logic will be provided in each test circuit, and errors will be accumulated and recorded for later analysis (Ref. 12). A variable decision threshold in the fiber link receivers will be used to determine fiber loss. A microprocessor controller will sequence the operation of each link and will transfer the data to the recorder.

The experiment will be battery-powered and self-contained, as required by the LDEF format. In order to conserve battery power, the experiment will be turned on once every 12 hours, the complete data cycle lasting approximately 15 minutes.

Radiation-sensitive fibers of the lead-glass type, which have a known and large radiation-induced attenuation, will be incorporated into the experiment for dosimetry, as suggested in an earlier publication by Sigel (Ref. 4). These dosimeter fibers will allow accurate measurement of the actual radiation dose received by the fibers in the experiment.

4. SUPPORTING TECHNOLOGY INVESTIGATIONS

The tasks described below support future application of fiber optic technology.

4.1. Temperature Effects on Fiber Transmission

Because of the very large worst-case predicted temperature excursions in the Shuttle payload bay, and smaller but still important temperature excursions that are possible on other spacecraft, we are investigating temperature-induced changes in various fiber types at JPL. No change was expected in glass-core glass-clad fibers, but the behavior of plastic-clad fibers was regarded with more uncertainty. The results are still incomplete, but several conclusions can be made. Plastic-clad fibers are indeed changed; the silicone-clad type being unusable below about -50°C. The changes were reversible. The observed transmission changes are not necessarily a consequence of a loss mechanism; they can be caused by changes in refractive index.

Transmission measurements were made on single-fiber samples of different lengths from 1 m to 100 m for temperatures from room temperature down to -110°C. No tests have yet been made at elevated temperatures. Four different types of fiber (as shown in Table 3) were tested. The transmission measurements were made at 0.6 μm. An attempt was made to eliminate cladding modes with mode strippers at both input and output ends of the fiber.

Figure 6 shows relative transmission as a function of temperature for short samples of three types of fiber. For the ITT step index sample, care was taken to eliminate all light propagating in the cladding or plastic jacketing; otherwise, effects dependent on sample length might occur that are dependent on input coupling. We conclude that intrinsic transmission in a glass-core glass-clad fiber is not temperature-dependent.

The behavior of the Corning sample was different at low temperature from the ITT sample, in that it exhibited a larger transmission loss for longer lengths. The ITT fibers showed a larger relative loss for shorter lengths, as might be expected if light propagating in the cladding or jacket is the cause. The difference is not fully understood at present.

For a short fiber length and typical LED excitation, significant, though not critical (1-3 dB), changes in received power can occur in glass-clad fibers, and receiver design should take this possibility into account. We feel the probable reason

Table 3. Typical Characteristics of Tested Fibers

Manufacturer and Designation	Attenuation (dB/km) at λ = 820 nm	Numerical Aperture	Core Index	Core Material	Clad Material	Core Diam (μm)	Sheath Material
ITT Plastic-Clad (PS-05-40)	20	0.25	1.46	Silica	Silicone Polymer	135	Teflon
ITT Step Index CVD (GS-02-10)	8	0.25	1.48	Doped Silica	Doped Silica	50	Teflon
Corning Step Index CVD (79-W-01)	6	0.18	-	Doped Silica	Doped Silica	85	Opaque
DuPont Plastic-Clad (PFX-S120-R)	90	0.4	1.46	Silica	Polymer	200	-

is that some of the light launched in the cladding of a short link reaches the detector, and this portion of the total received power is influenced by temperature changes in the protective polymer sheath materials.

The cause of the dramatic cutoff observed in the silicone-clad, fused-silica fiber at -80°C is the temperature coefficient of the index of refraction of the polymer-cladding compound which directly affects the numerical aperture (NA) of the fiber. The change in index of a silicone compound similar to the cladding on our fiber sample was measured by the minimum deviation method, and the result is shown in Fig. 7. No marked change in slope is observed.

Since the transmission loss is due to the decreasing NA of the fiber, transmission changes should not depend on fiber length - an expectation confirmed by experiment. The possibility of compressive force exerted by the teflon jacket affecting the cladding index was considered, but tests of a special fiber without the teflon jacket yielded the same transmission vs temperature curve.

The DuPont-type of plastic-clad fiber uses a different cladding polymer. Tests of this fiber type, although made with a rather short sample, indicate a quite different temperature dependence (as seen in Fig. 6). It is not known yet whether the observed temperature-induced loss is a consequence of changing fiber NA, or whether a temperature-dependent loss mechanism is effective.

4.2. Laser Development

A group under H. Hendrix at NASA Langley Research Center has been involved for some time in the development of semiconductor light sources which are applicable to fiber-optic data transmission. Most of this work has been concentrated on demonstrating long-life, room-temperature, CW-injection lasers, an important component for fiber-link transmitters, because of their fast response and ability to be efficiently coupled to fibers. Some exploratory study of planar waveguide components has also been done.

Most of this work has been performed under contract. Development work on CW lasers using the GaAlAs system has been supported at RCA Laboratories (Ref. 13), and some effort has also been directed toward planar waveguiding techniques (Ref. 14). More recently, techniques were investigated for fabricating injection lasers that emit at shorter wavelengths so their emission would be visible (Ref. 15). The GaAsP system was also investigated, as well as the more familiar GaAlAs system. Room-temperature CW operation was achieved at 7400Å with GaAlAs, and operation at 6520Å was achieved at 77°K in GaAsP devices. The initial interest in visible-emission lasers was related to instrumentation applications involving interferometry, but the same devices are important because this is the wavelength region for lowest attenuation in the DuPont type of plastic-clad fused-silica fiber. In addition, an investigation of distributed feedback laser techniques has been reported (Ref. 16).

More recently, interest has turned toward the 1.1 μm region, and the InGaAsP system is being examined at RCA as a possible means for achieving a 1.1 μ injection laser to take advantage of the very low fiber attenuation which has been reported there.

4.3. Fiber-Optic Ring Interferometer

An application of fiber optics in a completely different area (rotation sensing) has been under investigation by Vali and Shorthill of the University of Utah Research Institute, under NASA sponsorship. Their ideas may also suggest other interesting uses of fiber waveguides in instrumentation (Ref. 17). Vali and Shorthill recognized that by using a single-mode fiber as the light path, the sensitivity of the well-known ring interferometer to rotation can be increased many-fold (Ref. 18). In fact, if a ring light path set up by mirrors is replaced by a fiber loop of the same area, the rotation-induced path difference between opposite directions of propagation can be multiplied by the number of turns in a fiber coil. With the best fibers available today, a total path length of a kilometer or more seems easily achievable. The immediate application being investigated is that of an accurate, all-solid-state gyro with no moving parts. Vali and Shorthill have reported observing interference fringes through nearly 1 km of Corning single-mode fiber (Ref. 19), and are presently building a breadboard gyro on a rotatable table for evaluation of the concept. In a small parallel task at JPL, W. Goss and R. Goldstein are investigating sensitive AC-detection techniques needed for readout of the very small fringe shifts expected in a high-performance optical gyro.

5. CONCLUSIONS

Recent exploratory work at several laboratories has identified candidate applications for fiber-optic data links, and many others certainly exist. It is not yet possible to say which way the tradeoff between fiber-optic techniques and conventional copper transmission will ultimately go in each of these examples. However, it is possible to make several observations.

The first real applications outside the laboratory are likely to be off-line experiments in situations where there is a special need for the type of performance that fiber links can offer. The direct advantages so often quoted for fiber links are bandwidth, small size and weight, EMI resistance, and low cost. It may well be that this list is in order of increasing importance.

We feel that the strongest near-term motivation for the use of fiber links is likely to be the immunity to EMI problems. Much time is spent in testing and debugging in order to eliminate interference and ground loops in any electronic system. In some instances, such as in the Shuttle-payload interface already mentioned, or as another example, in error-free control signal and data transmission on a large high-power transmitting antenna, the inherent immunity of optical fibers to interconnect-induced EMI takes on a special significance. The first applications are probably going to be of this type.

In almost all cases, fiber-optic transmission is an option. Exceptions may exist where only fibers will work, but usually the same job can be done with other techniques. The problem is to determine which approach is best.

Therefore, in the long term, cost will become the most important parameter determining where fibers are going to be used. Bandwidth, size, and weight all play a part in determining the overall cost. It should be noted that electromagnetic compatibility testing and debugging time are also very significant cost factors.

Fiber is not cheap in its present state of development, and fiber links are not easy to justify now on the basis of cost alone. However, in the future, fiber costs are expected to come down significantly (Ref. 20). Fiber-terminal electronics are not greatly different from what would be used with copper transmission lines. Therefore, there is good reason for optimism on this point.

Environmental effects will have an influence on the design of fiber links to be used in space. Temperature effects on some types of fiber, and radiation darkening on all fibers must be taken into account. More work needs to be done in this area, but initial results indicate that with proper design, fiber links are not likely to be significantly more sensitive than the electronics they interconnect.

In the future, one of the difficult tasks foreseen by NASA is that of handling and transmitting very large amounts of information economically. Where requirements for very large data rates emerge, fiber transmission techniques may become particularly important. Optical links should not be thought of as potentially applicable only in certain unique situations, but rather as devices that can be used in a wide spectrum of specific applications to help solve a great number of information transmission problems.

REFERENCES

1. Charles H. Bell, Fiber Optic Multiplexed Optical Transmission Systems for Space Launch Facilities, p. 151, Proceedings, SPIE Vol. 63, Symposium on Guided Optical Communications, San Diego, August 19, 1975.

2. General Cable Co., Colonia, New Jersey.

3. Harris Electronics, Melbourne, Florida.

4. Fiber Optic Links for the Shuttle Orbiter CCTV System, A. R. Johnston, J. Katz, M. Donovan, and C. Yeh. (Unpublished)

5. G. H. Sigel, B. D. Evans, R. J. Ginther, E. J. Friebele, D. C. Griscom, and J. Babiskim, "Radiation Effects in Fiber-Optic Waveguides," NRL Memorandum Report 2934, Nov. 1974.

6. L. M. Watkins, "Absorption Induced in Fiber Waveguides by Low Rate Electron and Gamma-Ray Radiation," SAND 75-8222, Sandia Corp., Albuquerque, N. Mex., March 1975.

7. P. L. Mattem, L. M. Watkins, G. D. Skoog, J. R. Brandon, and E. H. Barsis, IEEE, Trans-Nuclear Science NS-22, 2468 (1975).

8. B. D. Evans and G. H. Sigel, IEEE Trans-Nuclear Science NS-22, 2462 (1975).

9. Mokhtar S. Maklad, Gary W. Bickel, and George H. Sigel, "Radiation Response of Low Loss Silicon-Clad Silica Fiber," Optical Fiber Transmission II, Williamsburg, Va., Feb. 1977, Technical Digest, Optical Society of America.

10. E. J. Friebele, G. H. Sigel, Jr., and R. E. Jaegar, In Situ Measurement of Growth and Decay of Radiation Damage in Fiber-Optic Waveguides, Optical-Fiber Transmission II, Williamsburg, Va., Feb. 1977, Technical Digest, Optical Society of America.

11. John diBattista, "LDEF - A New Capability for Space Testing and Basic Research," 27th Congress of the International Astronautical Federation. Anaheim, CA, Oct. 10-16, 1976. IAF Preprint No. 76-197.

12. L. A. Bergman and A. R. Johnston, Bit Error Rate Measurement for Evaluation of a Fiber-Optic Link, Vol. 77. Fibers and Integrated Optics, SPIE, Palos Verdes, CA, 1976.

13. See, for example, I. Ladany and H. Kressel (AlGa)A5 Double Heterojunction Lasers: The Effect of Junction Area on Operating Life, Third International GaAs Symposium, 1974 NAS1-11421; I. Ladany and H. Kressel, NASA CR-2556, 1975.

14. Jim Hamner, H. Kressel, I. Ladany, C. C. Neil, and W. Phillips, Efficient Modulation and Coupling of CW Junction Lasers using Electro-Optic Waveguides, Proc. IEEE.

15. I. Ladany, H. Kressel and C. J. Nuese, Room Temperature Operation Visible Emission Semiconductor Diode Lasers, Final Report, NA51-13739B4, RCA Laboratories, inceton, N.J., March 1976.

16. Lawley, Kenneth L., Bellavance, David W., and Keisinger, Axel R., Narrow Spectral Width Semiconductor Laser, NASA CR-145025, 1976, Texas Instruments, Inc., Dallas, Texas.

17. F. P. Kapron, N. F. Borelli and D. B. Keck, IEEE QE-8, 222 (1972).

18. V. Vali and R. W. Shorthill, Fiber Optic Laser Gyroscopes, Vol. 77, Proceedings SPIE Technical Symposium East Session of Fibers and Integrated Optics, Reston, Virginia, March 22-25, 1976.

19. V. Vali and R. W. Shorthill, Ring Interferometer, 950 m long, Appl Optics 16, No. 2, 290-291, February 1977.

20. L. C. Gunderson, Opitcal Waveguide Cost Considerations, Optical Fiber Transmission II, Williamsburg, Va., February 1977, Technical Digest, Optical Society of America.

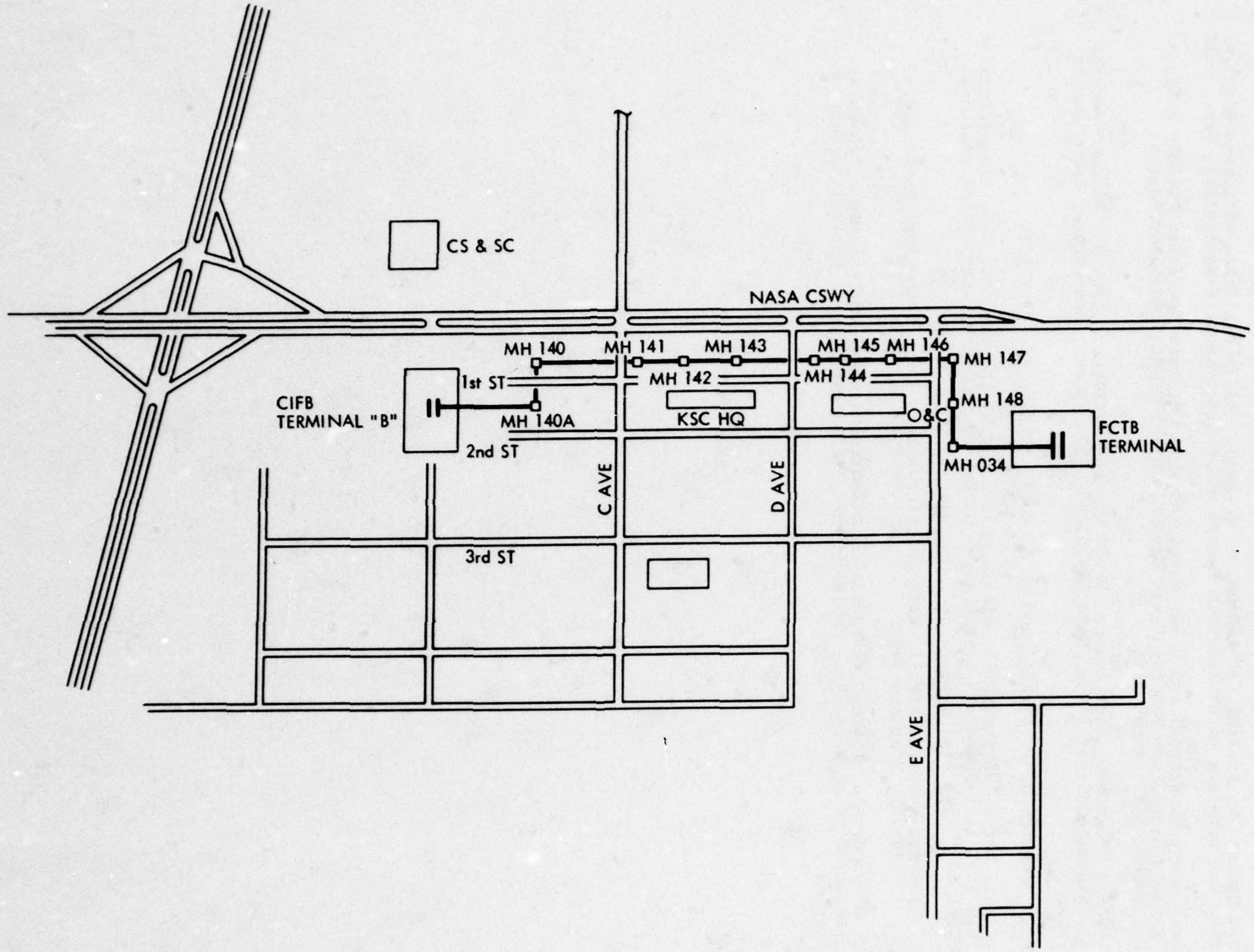

Figure 1. Map Showing Layout of KSC Experimental Fiber Link

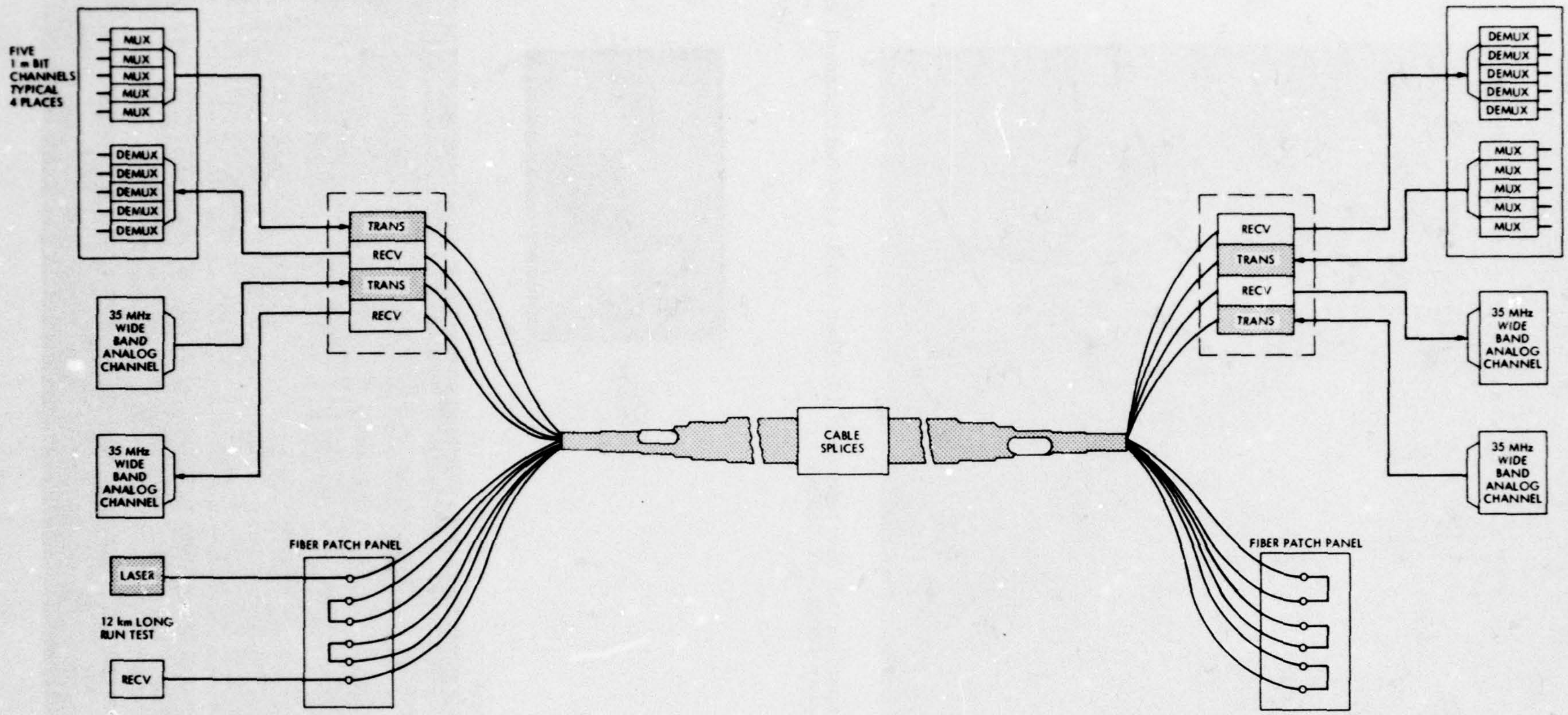

Figure 2. Block Diagram of Multiplexed Optical Transmission System (MOTS) Experiment at Kennedy Space Center

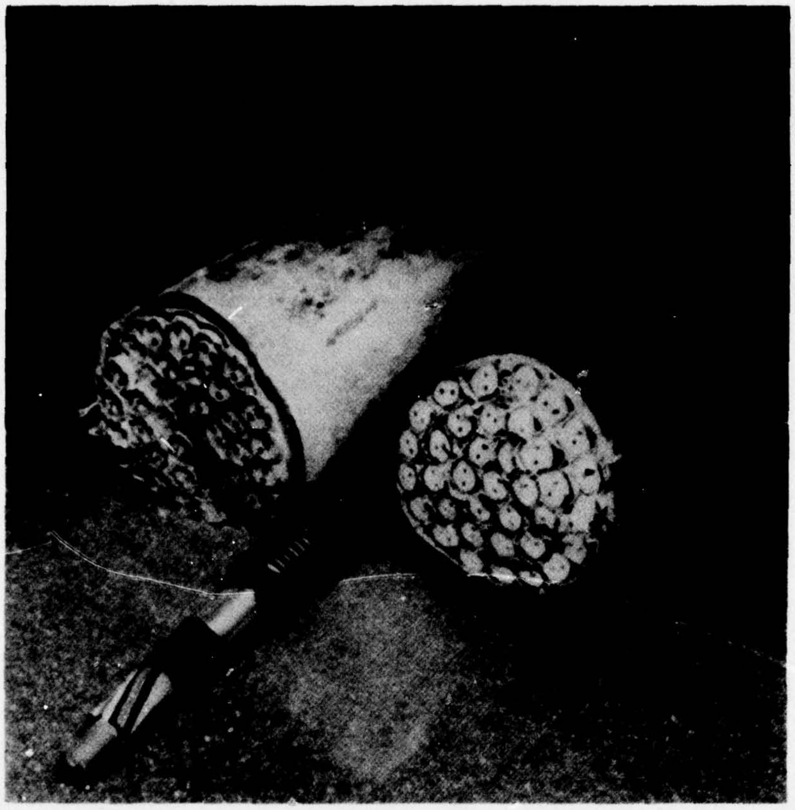

Figure 3. Comparison of Developmental 10-Fiber Cable with Multichannel Wideband Copper Conductor Cables.

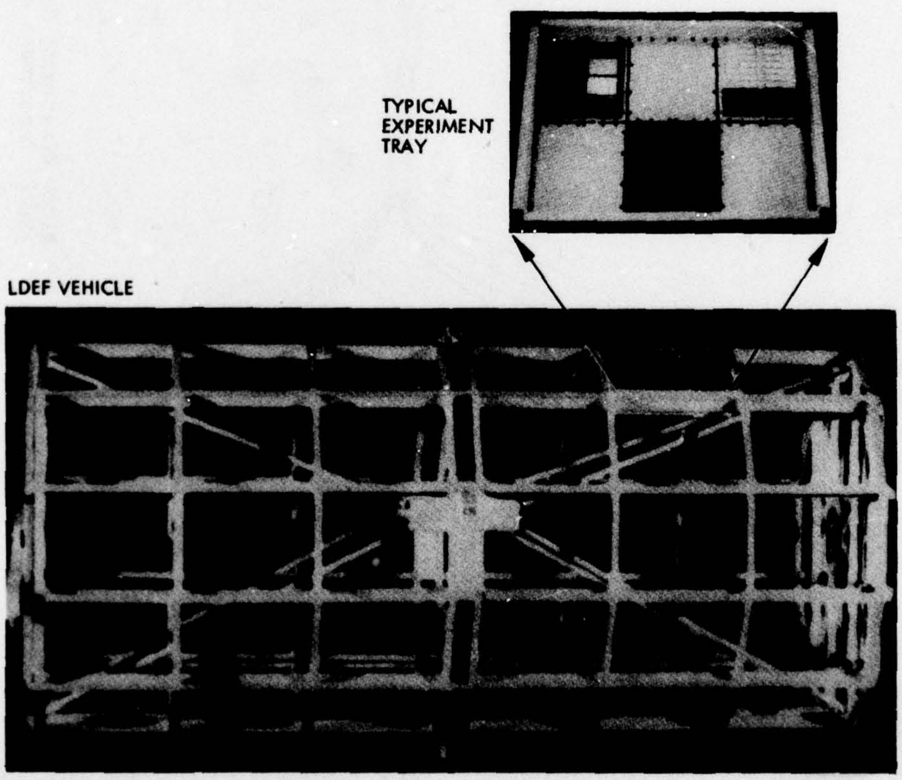

Figure 4. The LDEF Vehicle and a Representative Self-Contained Experiment Tray

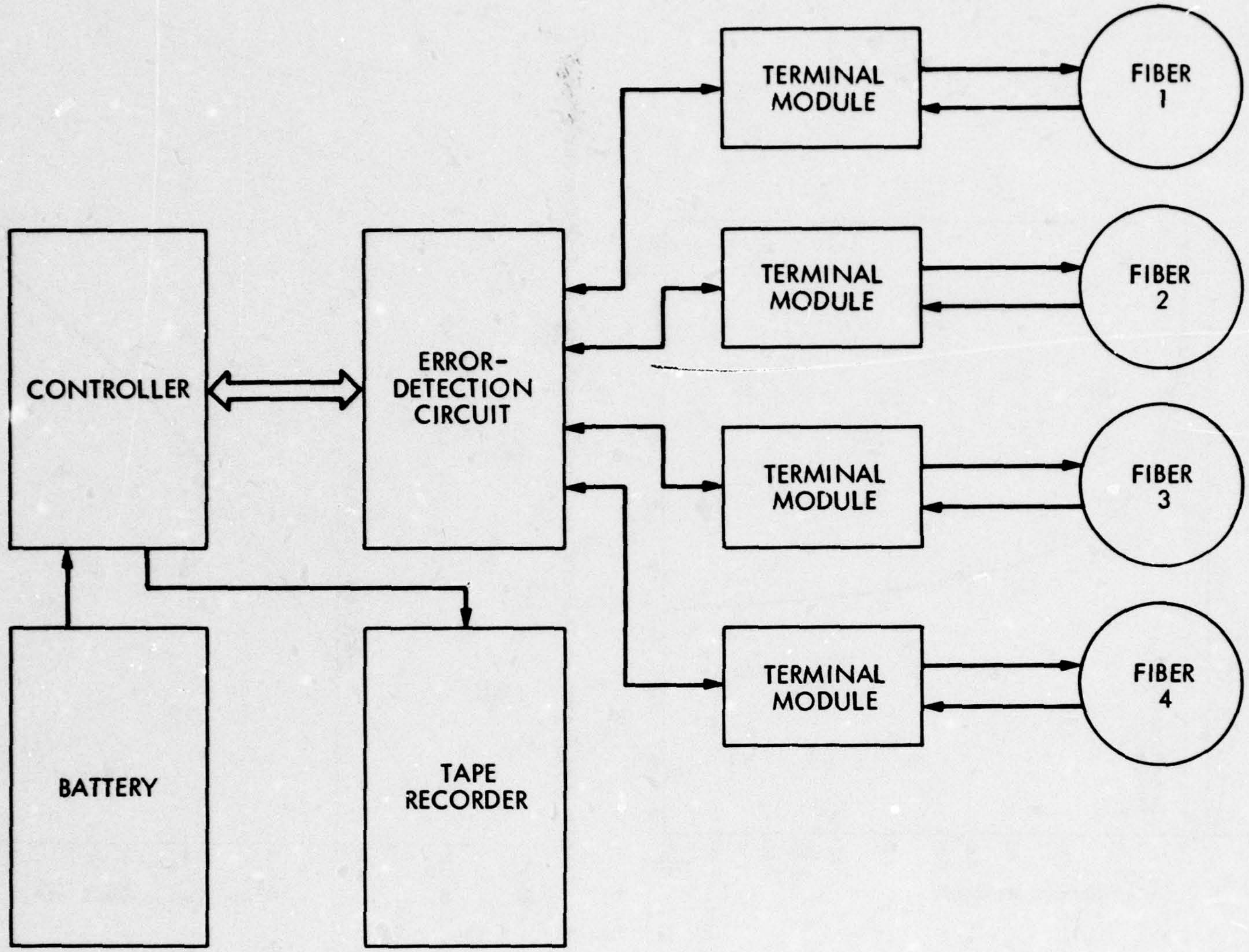

Figure 5. A Functional Block Diagram of the LDEF Experiment

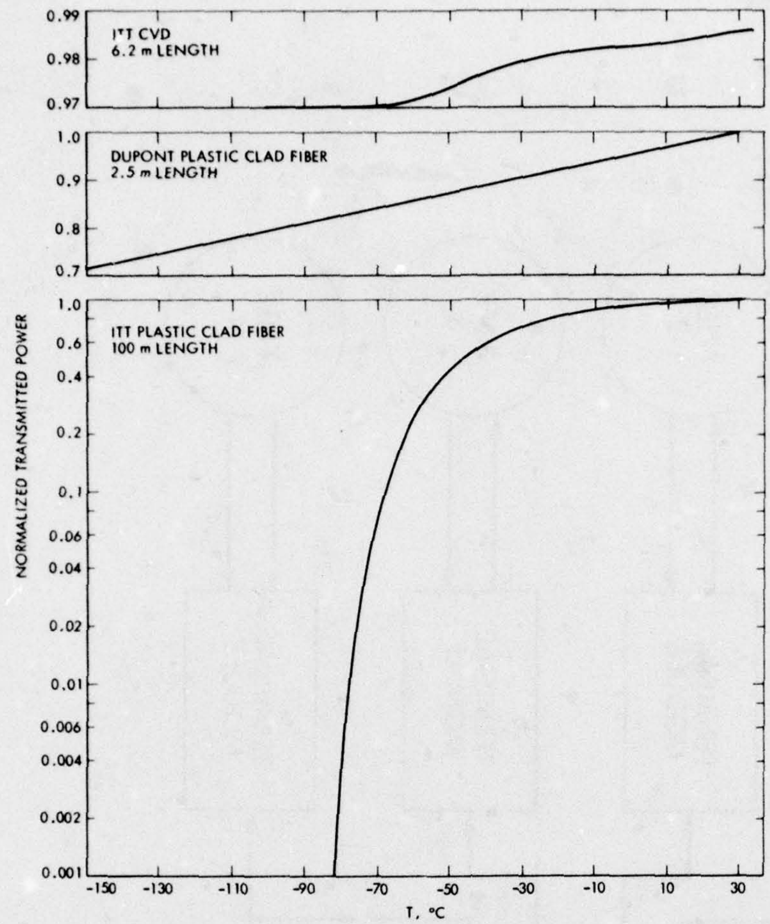

Figure 6. Transmitted Power vs Temperature for Short Samples of Different Fibers

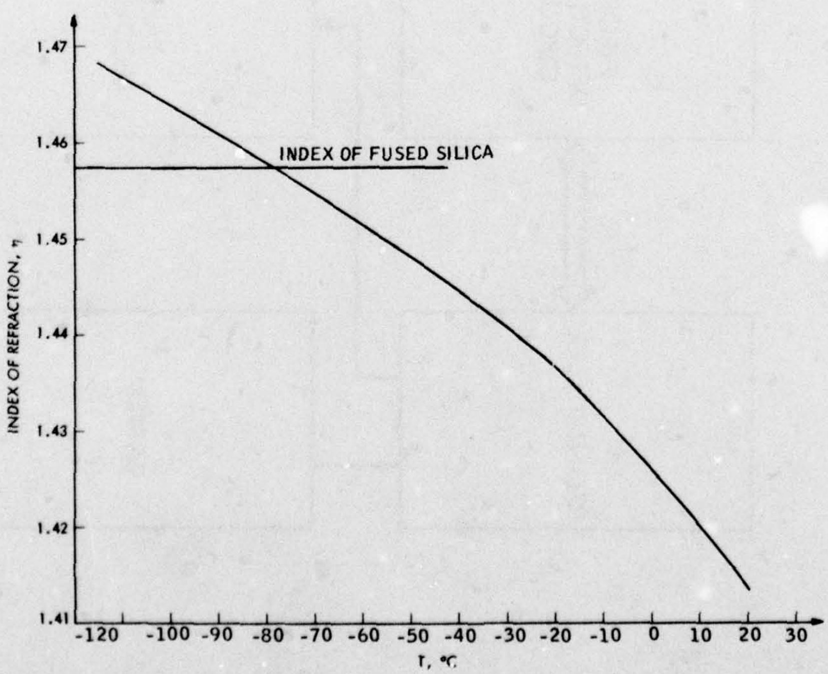

Figure 7. Index of Refraction vs Temperature for Dow Corning Sylgard 184

FUNDAMENTAL MODE SIGNAL TRANSMISSION IN SINGLE- AND MULTIMODE FIBRES

K. Petermann, H.-G. Unger
Institut für Hochfrequenztechnik
Technische Universität Braunschweig
D-3300 Braunschweig
W-Germany

SUMMARY

In single-mode operation of single- and multimode fibres, signals are transmitted with very little distortion. In perfectly straight and uniform fibres, this residual distortion is caused only by material- and mode dispersion. For a suitable choice of the emission wavelength and of the refractive index profile, this dispersion vanishes to first order, so that as far as the fibre is concerned, transmission rates of some 100 Gbit/s would be possible.

The propagation is distorted by random bends as introduced by the cabling process. Therefore a microbending loss occurs, which, however, becomes negligible as long as the fundamental mode spotsize is kept small. In addition, the conversion of energy to higher order modes due to microbending and its reconversion distorts pulses in the fundamental mode. This pulse distortion can be kept small by sufficiently attenuating the higher order modes or by inserting discrete mode filters. Simple analytic design considerations are given.

1. INTRODUCTION

When transmitting high transmission-rates by means of optical fibres, the signal should be guided in the fundamental mode only, thus delay differences between different modes do not occur. The residual pulse distortion in single-mode operation remains quite small.

For studying the transmission properties in the fundamental mode, fibres of most general design will here be considered. Fig. 1a shows a conventional single-mode fibre in form of a cladded-core- or graded-index fibre. Another possibility for a single-mode fibre is the W-fibre as shown in Fig. 1b (Kawakami, S. and Nishida, S., 1974) with a relatively large refractive index difference (n_1-n_2) between core and inner cladding which leads to good confinement of the fundamental mode field within the core.

The W-fibre can be single-moded since the higher order modes are leaky and thus attenuated due to the outer cladding of the higher refractive index n_3. Another possibility for attenuating higher order modes is to insert discrete mode filters (Fig. 1c) into multimode fibres (Furuya, K. et al., 1975). We then gain the advantage of using low-loss multimode fibres for the "fundamental mode transmission".

2. SINGLE-MODE RANGE

To describe a single-mode fibre according to Fig. 1a, the fibre parameter

$$V = ka\sqrt{n_1^2 - n_2^2}$$

is introduced, with k denoting the free space wavenumber. A cladded-core fibre or a fibre with truncated parabolic profile become single-moded for $V < 2.4$ or $V < 3.53$, respectively. A W-fibre of Fig. 1b is described by the W-fibre parameter

$$V_w = ka\sqrt{n_1^2 - n_3^2} ,$$

the refractive index difference ratio

$$\delta = (n_1-n_2)/(n_1-n_3)$$

and the radii ratio c. The single-mode range of a W-fibre can be obtained from Fig. 2 (Petermann, K. and Storm, H., 1976). This diagram gives cutoff-curves of the fundamental HE_{11}-mode and the next higher LP_{11}-mode for small differences between the refractive indices n_1, n_2, and n_3. For a given c, the single-mode range lies in between the corresponding cutoff-curves. In case of c = 1.2, for example, the single-mode range is represented by the shaded area. The fibre transmission line of Fig. 1c also behaves as a single-mode fibre, if the mode filters let pass the fundamental mode, only. The design of such mode filters, however, will not be discussed in the present work.

3. SIGNAL TRANSMISSION

When investigating signal transmission, the dispersion and attenuation characteristics must be studied.

Due to the emission bandwidth of the optical source (usually a laser) material- and mode dispersion occur which lead to broadening of the input pulse. In addition, the transmission is distorted by random bends which are introduced by the cabling process. Due to these random bends, the fundamental mode suffers an additional attenuation, the so-called microbending loss. Due to reconversion from higher order modes, microbending also distorts the pulse shape.

4. MATERIAL- AND MODE DISPERSION

To begin with, a perfectly straight and uniform fibre is considered. The pulse distortion due to its material- and mode dispersion is first considered separately.

4.1. Material Dispersion

Material dispersion occurs since the refractive index of glass or fused silica depends on the frequency $f = c/\lambda$ (λ - light wavelength, c - speed of light) at which light is emitted. When considering a plane wave propagating through a homogeneous medium of refractive index $n_1(f)$, the delay per length τ_M is given by

$$\tau_M = \frac{1}{c}\frac{d(f\cdot n_1(f))}{df} . \tag{1}$$

The delay τ_M also depends on the wavelength $\lambda = c/f$ of the emitted light. When denoting the delay at a wavelength $\lambda_0 = c/f_0$ as τ_{MO}, τ_M may be expanded in terms of ascending powers of $(f-f_0)$:

$$\tau_M = \tau_{MO} + \left.\frac{d\tau_M}{df}\right|_{f=f_o} \cdot(f-f_o) + \frac{1}{2}\left.\frac{d^2\tau_M}{df^2}\right|_{f=f_o} \cdot(f-f_o)^2 . \tag{2}$$

If the optical source emits at the center frequency f_0 with a spectral width Δf, different spectral components have different delays which, to a first order approximation, spread over $(d\tau_M/df)\cdot\Delta f$.

For fused silica, the dispersion coefficient $d\tau_M/df$ is shown in Fig. 3. This coefficient is positive for $\lambda < 1.28$ µm and turns negative for $\lambda > 1.28$ µm. For $\lambda = 1.28$ µm, the dispersion coefficient vanishes, thus the material dispersion is reduced to an effect of second order. A numerical value for this lower dispersion limit has been given by Arnaud (1976). He typically obtains for the minimum pulse broadening:

$$\Delta\tau \approx 0.0018\ (\Delta f\ [\mathrm{THz}])^2\ \mathrm{ns/km} . \tag{3}$$

For a typical spectral width $\Delta\lambda = \Delta f\ (\lambda/f) = 20$ Å, eq. (3) yields a pulse broadening of only

$$\Delta\tau \approx 0.23\ \mathrm{ps/km} \tag{4}$$

In order to make use of this remarkably low dispersion, lasers with fast modulation, fibres with low attenuation and suitable photodetectors at a wavelength of about 1.3 µm are needed. Fibres with an attenuation of less than 1 dB/km are already available for the desired wavelength range (Takata, H. et al., 1976) but lasers and photodetectors are still to be developed.

In the wavelength range of 0.8 - 0.9 µm as it is usually employed, material dispersion is much larger. For the above example, a pulse broadening of about 120 - 200 ps/km is obtained.

4.2 Mode Dispersion

The fundamental mode propagation constant β depends on the fibre parameter V and therefore also on the light wavelength λ. Because of this dependence even in fibres with wavelength independent refractive index a dispersion occurs which is called mode dispersion. The fundamental mode delay τ_m can be written in a form similar to eq. (2), without material dispersion the coefficient $d\tau_m/df$ then describes the magnitude of mode dispersion. In case of small index differences between core and cladding, mode dispersion is usually much smaller than material dispersion and can be neglected as long as emission wavelengths with non-vanishing $d\tau_M/df$ are considered.

For conventional single-mode fibres according to Fig. 1a, the mode dispersion coefficient $d\tau_m/df$ has a positive sign. In the wavelength region of $\lambda = 0.8 \ldots 0.9$ µm, $d\tau_M/df$ according to Fig. 3 is likewise positive; therefore material dispersion and mode dispersion add to a larger dispersion value.

If, however, signals are transmitted in the fundamental mode of a multimode fibre, the dispersion coefficient $d\tau_m/df$ may become negative, as shown in Fig. 4a. In case of a cladded-core fibre, the minimum value of $d\tau_m/df$ is obtained for a fibre parameter $V \approx 4.5$. The magnitude of this minimum strongly depends on the refractive index difference $\Delta = (n_1-n_2)/n_1$, as shown in Fig. 4b.

In such a fibre, material- and mode dispersion have opposite signs, thus, at least in principle, a compensation is possible. For this compensation we must require $d\tau_m/df \approx -d\tau_M/df$. For a wavelength $\lambda = 0.85$ µm this requirement is met according to Figs. 3 and 4 for a relative refractive index difference $\Delta \approx 0.1$. The dispersion then drops to similarly low values as in eqs. (3) and (4).

From the technological point of view, however, the realisation of the above large refractive index difference is quite difficult; furthermore very small core radii are needed. For $\Delta = 0.1$, $V = 4.5$, and $\lambda = 0.85$ µm, the core radius must be made as small as $a = 0.9$ µm.

To facilitate the above compensation a source emitting at a higher wavelength is desired. For a wavelength $\lambda = 1.1$ µm, for example, we obtain from Figs. 3 and 4 a relative refractive index difference

$\Delta \approx 4$ %, the realisation of which might be possible. We then also obtain a larger core radius, $a \approx 1.9$ µm, which is more suitable for splicing and connecting fibres.

The above considerations are restricted to cladded-core fibres with fibre parameter values $V > 4$, which are not single-mode and therefore must be operated by inserting mode filters. Instead of inserting discrete mode filters also a continuous filtering is possible by use of the W-profile according to Fig. 1b. The resulting dispersion coefficient for the fundamental mode in W-fibres is shown in Fig. 4a by the dashed curves. A refractive index difference ratio $\delta = (n_1-n_2)/(n_1-n_3) = 10$ and radii ratios $c = 1.4$ and $c = 2.0$ are assumed. The upper scale denotes the W-fibre parameter V_W as used in Fig. 2.

Values for the material dispersion have only been given here for fused silica; but other glasses have similar properties. The dispersion problem might become more difficult, however, when core and cladding differ in their dispersion characteristics. This particular problem has been analyzed by Jürgensen (1975).

5. MICROBENDING

The above considerations are restricted to perfectly straight and uniform fibres. After cabling, however, the fibre deviates from perfect straightness in that it has random bends, the so-called "microbending". A fibre exhibiting microbending is shown in Fig. 5.

Due to microbending, the fundamental mode propagation is degraded in two respects:
a) The fundamental mode suffers a microbending loss.
b) Pulse distortion occurs due to energy reconversion from higher order modes.

5.1. Microbending Loss

Microbending causes the fundamental mode energy to partly convert to higher order modes and to the radiation field, so that a microbending loss occurs. In order to calculate this loss accurately, interaction between the fundamental mode and higher order modes must be determined. This requires an extensive numerical procedure and general dependencies are difficult to recognize.

For calculating the microbending loss to a good approximation, the large number of higher order modes and radiation modes can be replaced by a single quasi-mode (Petermann, K., 1976a). The microbending loss is then obtained by calculating the coupling between the fundamental mode and the quasi-mode, only.

When applying a simple model for the quasi-mode (Petermann, K., 1976b), the microbending loss $\bar{\gamma}$ with respect to the fundamental mode power is obtained as

$$\bar{\gamma} = (1/2)(kn_1 w_0)^2 \, \phi(1/(kn_1 w_0^2)) \tag{5}$$

with the free space wavenumber k and the refractive index on the fibre axis n_1. w_0 is a spotsize parameter

$$w_0^2 = \int_0^\infty r^3 E_0^2(r)\, dr \Big/ \int_0^\infty r\, E_0^2(r)\, dr \,, \tag{6}$$

where $E_0(r)$ denotes the fundamental mode field and r the radial coordinate. In case of a Gaussian field, for example, w_0 denotes the radius where the intensity has dropped to 1/e of its maximum value. $\phi(\Omega)$ represents the power spectrum of curvature

$$\phi(\Omega) = \lim_{L\to\infty} \frac{1}{L} \left| \int_0^L (1/R)\, e^{-j\Omega z}\, dz \right|^2 \tag{7}$$

with R denoting the local curvature radius of the fibre.

Eq. (5) is already a good approximation for the fundamental-mode microbending loss. By choosing the above mentioned quasi-mode in a more suitable way (Petermann, K., 1976a), the approximation according to eq. (5) can be further improved. For this purpose, effective spotsize parameters w_{01} and w_{02} are introduced:

$$\bar{\gamma} = (1/2)(kn_1 w_{02})^2 \, \phi(1/(kn_1 w_{01}^2)) \,. \tag{8}$$

Fig. 6 shows the spotsize parameters w_0, w_{01}, and w_{02} versus the fibre parameter V for cladded-core fibres and fibres with a truncated parabolic profile.

For large values of the fibre parameter V, the spotsize parameters differ only slightly from each other; therefore eqs. (5) and (8) then yield nearly the same result.

To evaluate eqs. (5) and (8), the power spectrum of curvature must be known. Theoretical considerations (Gloge, D., 1975; Olshansky, R., 1975) indicate that the power spectrum of curvature may be written in form of a power law:

$$\phi(\Omega) = C/\Omega^{2p} \tag{9}$$

with a constant coefficient C. The curvature spectrum is characterized by the parameter p, where $p = 0$ corresponds to a flat power spectrum with zero correlation length, while $p = 1,2$ account for the more realistic situation of larger correlation distances.

It has been shown (Petermann, K., 1977) that eq. (5) yields exact results for $p = 0$, while eq. (8) is exact in case of $p = 1$, independent of any specific refractive index profile. Beyond these special cases, eqs. (5) and (8) represent excellent approximations also for other power spectra as long as w_0, w_{01}, w_{02} do not differ too much from each other. But even in case of some difference between w_0, w_{01}, and w_{02} as, for example, in case of a cladded-core fibre with fibre parameter $V = 1.5$, eq. (8) deviates less than 20 % from exact numerical results for the power spectrum of eq. (9) and $p = 0, 1, 2$. The agreement between eqs. (5), (8) and accurate results still becomes much better for larger V-values. Therefore eqs. (5), (8) represent excellent approximations for the fundamental mode microbending loss in conventional single-mode fibres and multimode fibres of practical interest.

For a W-fibre according to Fig. 1b, this agreement may be not quite as good as shown by Petermann and Storm (1976). Fig. 7 shows the ratio of the accurate microbending loss to the approximate loss according to eq. (5) versus the radii ratio c for curvature power spectra according to eqn. (9). In Fig. 7a, the parameters $V_W = 2.4$ and $\delta = (n_1-n_2)/(n_1-n_3) = 8.75$ are chosen, and $c = 1$ represents the conventional cladded-core fibre.

For $p = 0$, eq. (5) yields exact results; for $p \leq 2$, it deviates by less than 10 % from exact results if only the radii ratio is $c = 1$ or $c > 1.7$. For intermediate values of c, however, the accurate microbending loss is much larger than the value obtained from eq. (5). This large difference is due to the peculiar field distribution in a W-fibre. The field is strongly concentrated within the fibre core, then decays rapidly through the inner cladding but extends far into the outer cladding of refractive index n_3. This peculiar behaviour cannot properly be described by only introducing the spotsize parameter w_0 as in eq. (5).

The fibre parameters of Fig. 7a are indicated by a cross in Fig. 2. It is obvious that this fibre is close to the HE_{11}-fundamental mode cutoff. Fibres of practical interest will be designed closer to the cutoff of the next higher LP_{11}-mode, as, for example, the fibre indicated by a circle in Fig. 2 with parameters $V_W = 3.0$ and $\delta = 5.6$. For those parameters, Fig. 7b shows the ratio of accurate microbending loss to the approximation from eq. (5); under these more practical conditions, the differences are less than about 10 %. The agreement is much better in this case since the fields (in the outer cladding) decay faster and therefore their contribution to the microbending loss becomes smaller.

Fig. 7c shows the spotsize parameter w_0 for the W-fibres according to Figs. 7a and 7b. Accurate values for the microbending loss may now be obtained from eqs. (5), (9), and Fig. 7.

We have thus shown that eq. (5) is in good agreement with accurate numerical results also in case of W-fibres, if the fibre is operated close to the cutoff of the next higher LP_{11}-modes. Otherwise the accurate value for the microbending loss is larger than the value of the approximation.

According to eqs. (5) and (8) the microbending loss essentially depends only on the spotsize parameter w_0 and the wavelength of light $\lambda = 2\pi/k$. For the power spectrum according to eq. (9), this dependence can be written as:

$$\bar{\gamma} \sim w_0^{(2+4p)} \ / \ \lambda^{(2+2p)} \ . \tag{10}$$

For fixed wavelength, the microbending loss $\bar{\gamma}$ increases with the sixth or tenth power of the spotsize parameter for $p = 1$ or $p = 2$, respectively. For the choice of the optimum fundamental mode spotsize, two requirements should be considered:
a) for low microbending loss, the spotsize should be small
b) for low splicing- and connector loss, the spotsize should be large.
In order to meet both requirements as good as possible, we require the microbending loss not to exceed the microbending loss of a typical multimode fibre. This requirement is met for $w_0 \leq 3\lambda$ (Petermann, K., 1977). The proper core radius can then be obtained from Fig. 6.

When considering the dependence of microbending loss on the wavelength of light, not only the wavelength but also the spotsize changes owing to the dependence of spotsize on the fibre parameter V. The relative dependence of microbending loss on wavelength is shown in Fig. 8 for a cladded-core fibre. Curvature spectra according to eq. (9) are assumed. The dependence of the microbending loss on wavelength is in qualitative agreement with the measured attenuation of single-mode fibres (Maslowski, S., 1976).

5.2. Pulse Distortion Due To Microbending

In the preceding chapter, it was assumed that the fundamental mode energy is converted to higher order modes and that no reconversion occurs. If, however, the attenuation of the higher order modes is low enough, the higher order mode energy is partly reconverted into the fundamental mode and distorts signals.

Such signal distortion is more likely to occur in fibres according to Figs. 1b and 1c, since for them the higher order mode attenuation may be quite low. In the W-fibre of Fig. 1b, the higher order modes are continuously attenuated, while in Fig. 1c, higher order modes are attenuated by discrete mode filters.

Pulse distortion due to energy reconversion has been analyzed earlier for millimeter-waveguide applications (Unger 1961). A more general study is possible by applying the time dependent coupled power equations (Marcuse, D., 1974), where we assume for our present problem that coupling takes place from the 2 fundamental HE_{11}-modes to the four LP_{11}-modes only. These LP_{11}-modes then partly reconvert their energy to the HE_{11}-mode, while some of their energy converts also to modes of still higher order.

The pulse distortion due to mode conversion and reconversion can be controlled in two ways:
a) by increasing the attenuation difference between HE_{11}- and LP_{11}-mode
b) by increasing the number of mode filters.
For calculating the pulse distortion, we assume that only the fundamental mode is launched and also that only the fundamental mode is detected by the receiver.

This pulse distortion limits the maximum bit-rate which can be transmitted. When binary PCM-modulation is used, the most critical case for the choice of the decision level in the receiver is to distinguish a single high-level signal from a low-level signal which is preceded by high-level signals. A sequence of high-level signals corresponds to a long rectangular pulse, the output response of which can be deduced from Fig. 9. The solid curve corresponds to the output signal as obtained without reconversion. The dashed curve shows the pulse portion due to reconversion; it adds to the undistorted pulse. This pulse portion yields the distortion; the main pulse is followed by a pulse tail of relative amplitude K. The pulse tail decays exponentially and extends over a time span of $\Delta\tau \cdot L/n$, where $\Delta\tau$ denotes the delay difference per fibre length between the HE_{11}-mode and the LP_{11}-mode. L denotes the total length of the fibre, in which n mode filters are inserted. The rate of decay of the pulse tail from its initial amplitude K depends on the attenuation difference between LP_{11}- and HE_{11}-mode.

For calculating the initial pulse tail amplitude, the attenuation difference

$$\Delta\gamma = \gamma_1 - \gamma_0 - \bar{\gamma}/2 \tag{11}$$

is introduced. γ_0, γ_1, and $\bar{\gamma}$ denote the loss coefficients of the HE_{11}- and LP_{11}-mode and the microbending loss, respectively. The loss coefficients γ are related to the respective modal power P according to $\gamma = -(dP/dz)/P$. γ_1 also includes the loss as arising due to the coupling from the LP_{11}-mode to higher order modes. If this loss contribution just equals $\bar{\gamma}/2$, $\Delta\gamma$ represents the attenuation difference between the HE_{11}- and LP_{11}-mode in the straight fibre.

When transmitting very high bit-rates, the amplitude K should be small; it should not exceed unity. For small K and when no mode filters are inserted, one obtains:

$$K = (\bar{\gamma} \cdot L)^2 \, (\exp(-\Delta\gamma L) + \Delta\gamma L - 1)/(2(\Delta\gamma L)^2) \, . \tag{12}$$

Fig. 10 shows the relation between the relative amplitude K and the attenuation difference $\Delta\gamma$. If, for example, a fibre of length L = 10 km, exhibiting a microbending loss $\bar{\gamma} \triangleq 2$dB/km is considered and if $K < 0.25$ is required, the attenuation difference $\Delta\gamma$ should exceed 11 dB/km.

If, on the other hand, a fibre with $\Delta\gamma = 0$ and n mode filters is considered, one obtains for small K:

$$K = (\bar{\gamma} \cdot L)^2/4n \, . \tag{13}$$

For a fibre transmission line with $\bar{\gamma} \cdot L \triangleq 20$ dB, corresponding to the above example, Fig. 11 shows the relative amplitude K of the pulse tail versus the number of mode filters n. The dashed curve represents the approximation according to eq. (13) while the solid curve represents an exact evaluation of the time dependent coupled-power equations. For keeping the amplitude K below 0.25, 20 - 25 mode filters must be inserted.

The above design considerations must be applied if either the pulse duration of the PCM-signal is small compared to $\Delta\tau \cdot L/n$ (when applying eq. (13)) or small compared to $\Delta\tau/\Delta\gamma$ (when applying eq. (12)). In case of a cladded-core fibre with small microbending loss, which corresponds to a fundamental mode spotsize $w_0 \lesssim 3$ µm, the delay difference between HE_{11}- and LP_{11}-mode is larger than about 6 ns/km. Therefore the above design rules must be applied for bit-rates higher than about 500 Mbit/s.

Finally, it should be noted that the above analysis represents a worst-case calculation, it considers long sequences of high-level signals. When choosing a suitable code for the PCM-modulation, where long sequences of high-level signals do not occur, the transmission characteristics can be improved.

6. CONCLUSIONS

It has been shown that microbending loss becomes negligible, if the fundamental mode spotsize is chosen sufficiently small. Pulse distortion due to microbending also becomes negligible, if the higher order modes are sufficiently attenuated. Under these conditions, the fundamental mode is able to transmit very high bit-rates, especially when the fibres are operated at wavelengths $\lambda > 1$ µm, where material- and mode dispersion compensate each other. In case of this compensation, transmission rates of hundreds of Gbit/s become feasible.

7. REFERENCES

Arnaud, J.A., 1976, "Propagation theory: hamiltonian approach", paper presented at the Seminar on Optical Fibre Propagation, Lannion, France, September 24, 1976.

Furuya, K. et al., 1975, "External higher-index mode filters for band widening of multimode fibres", Appl. Phys. Letters 27, 456-458.

Gloge, D., 1975, "Optical-fiber packaging and its influence on fiber straightness and loss", Bell Syst. Tech. J. 54, 245-262.

Jürgensen, K., 1975, "Dispersion-optimized optical single-mode glass fibre waveguides", Appl. Optics 14, 163-168.

Kawakami, S. and Nishida, S., 1974, "Characteristics of a doubly clad optical fiber with a low index inner cladding", Journ. Quant. Electr. IEEE QE-10, 879-887.

Malitson, I.H., 1965, "Interspecimen Comparison of the refractive index of fused silica", J. Opt. Soc. Am. 55, 1205-1209.

Marcuse, D., 1974, "Theory of dielectric optical waveguides", Academic Press.

Maslowski, S., 1976, "High capacity communications using monomode fibres", 2nd European Conference on Optical Fiber Transmission, Paris, September 27 - 30.

Olshansky, R., 1975, "Distortion losses in cabled optical fibers", Appl. Opt. 14, 20-21.

Petermann, K., 1976a, "Theory of microbending loss in monomode fibres of arbitrary refractive index profile", Arch. Elektr. & Obertr. 30, 337-342.

Petermann, K., 1976b, "Microbending loss in monomode fibres", Electron. Lett. 12, 107-109.

Petermann, K., 1977, "Fundamental mode microbending loss in graded-index and W-fibres", Opt. and Quant. Electron. 9, to be published.

Petermann, K. and Storm, H., 1976, "Microbending loss in single-mode W-fibres", Electron. Lett. 12, 537-538.

Takata, H. et al., 1976, "On ultimate low loss 'window' in doped silica glass optical fiber", Post-deadline paper, 2nd European Conference on Optical Fiber Transmission, Paris, September 27-30.

Unger, H.G., 1961, "Regellose Störungen in Wellenleitern", Arch. Elektr. & Obertr. 15, 393-401.

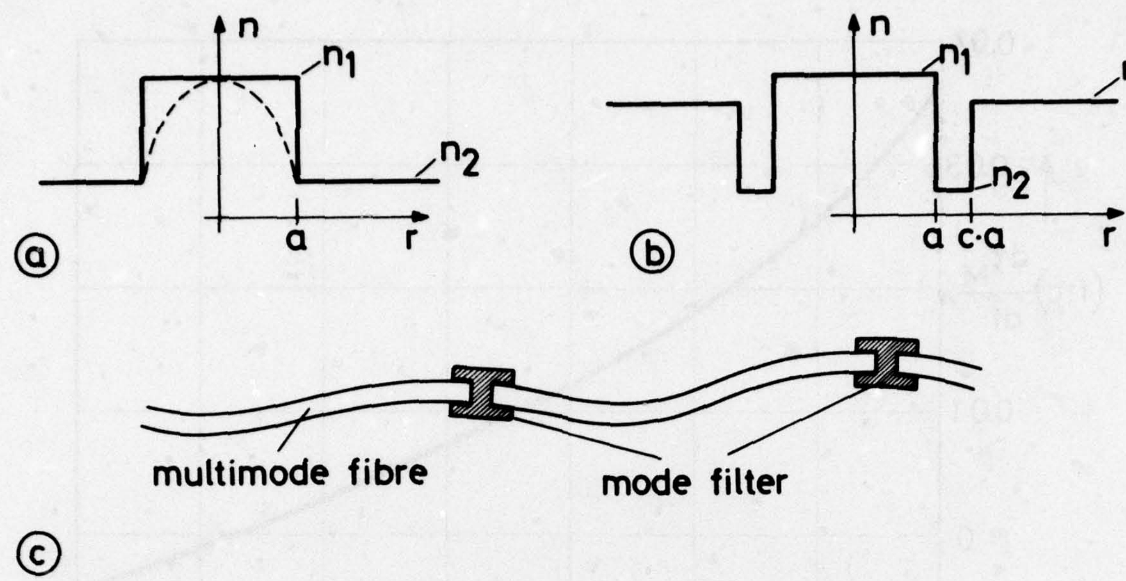

Fig. 1: Several possibilities for fundamental mode fibre transmission
a) conventional cladded-core or graded-index single-mode fibre
b) W-fibre
c) fibre transmission line consisting of a multimode fibre with discrete mode filters

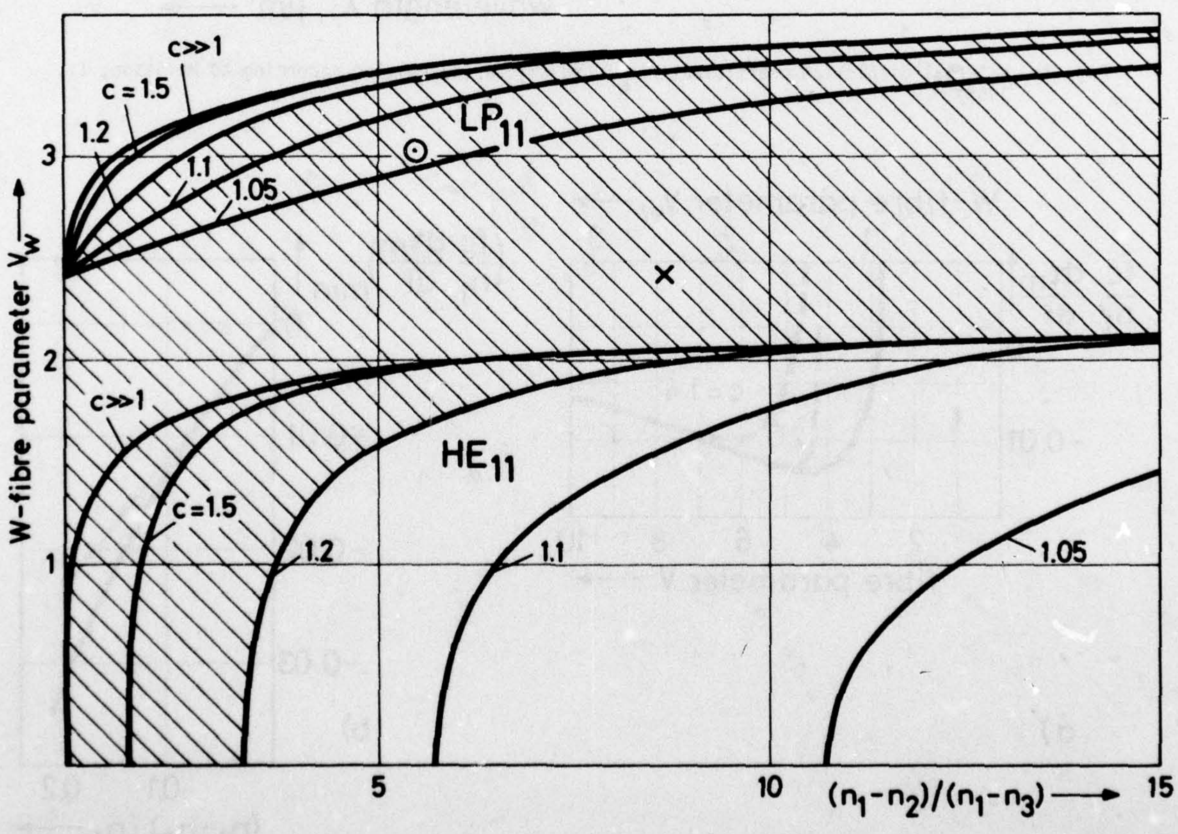

Fig. 2: Cutoff curves of the fundamental HE_{11}-mode and the first higher order LP_{11}-mode in a W-fibre with the radii ratio c. The shaded area shows the single-mode range of a W-fibre with c = 1.2

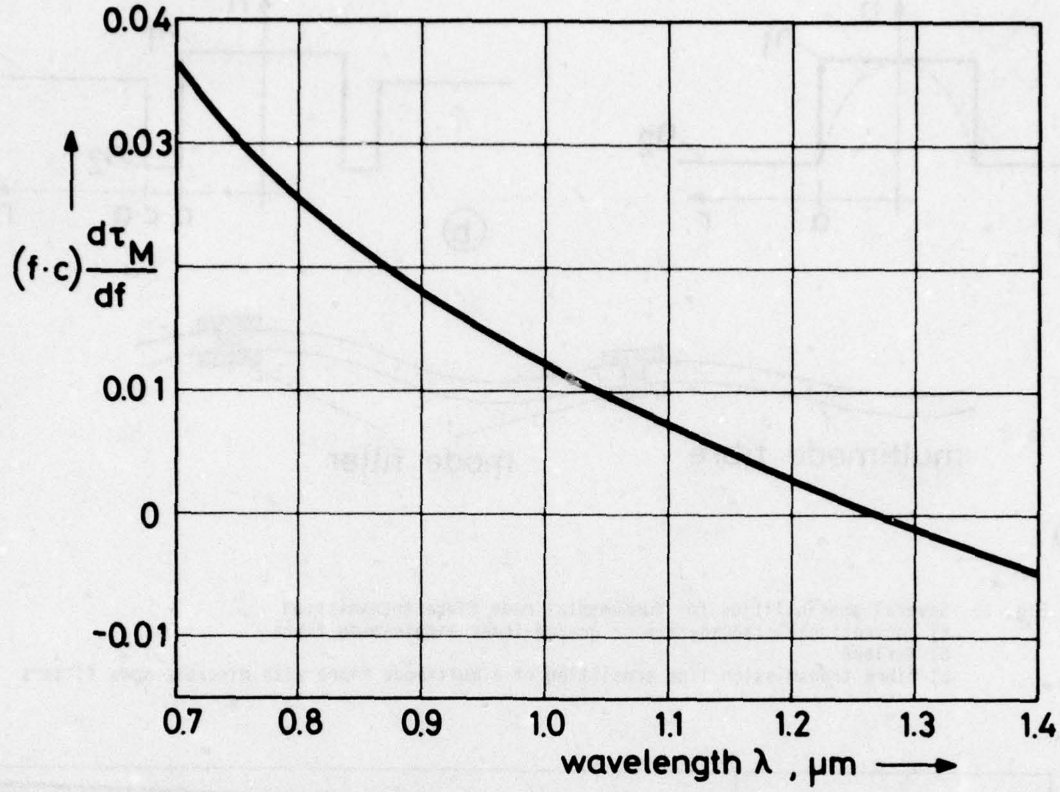

Fig. 3: Material dispersion coefficient for fused silica (calculated according to Malitson, I., 1965)

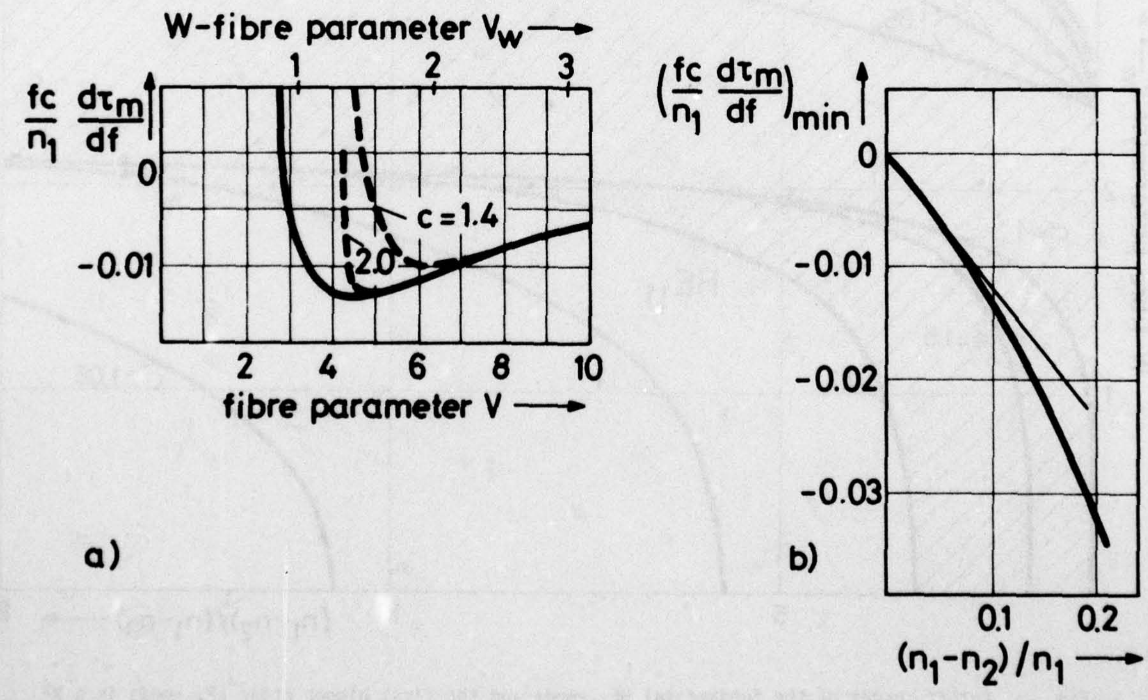

Fig. 4: Fundamental mode dispersion coefficient

a) of a cladded-core fibre (solid curve) and of W-fibres (dashed curves) with refractive index difference ratio $(n_1-n_2)/(n_1-n_3) = 10$. Assumption: $(n_1-n_2)/n_1 = 0.1$

b) Peak of negative dispersion for a cladded-core fibre versus the refractive index difference

(after Kawakami, S. and Nishida, S., 1974)

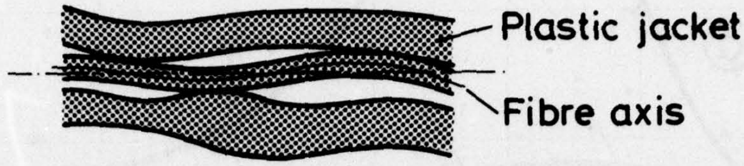

Fig. 5: Microbending

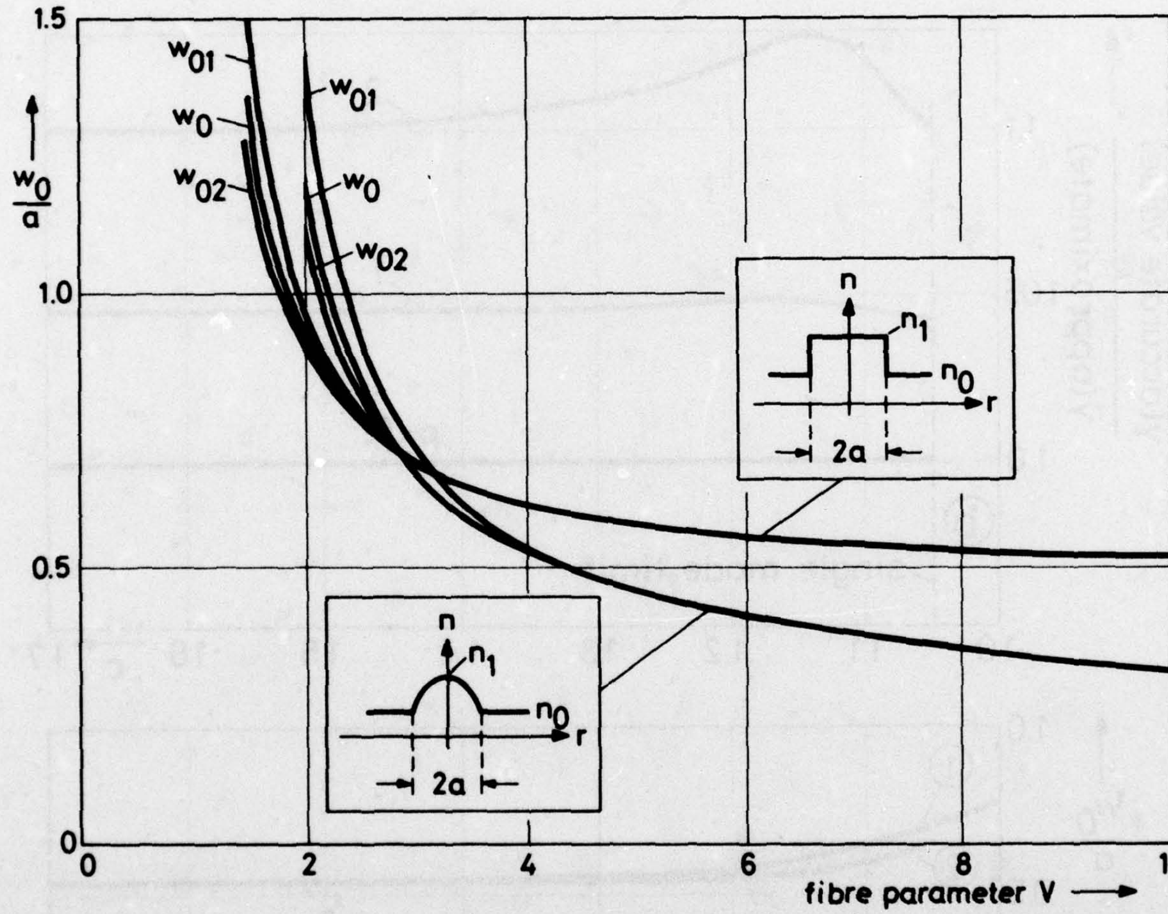

Fig. 6: Fundamental mode spotsize parameters normalized with respect to core radius as used for calculating the microbending loss

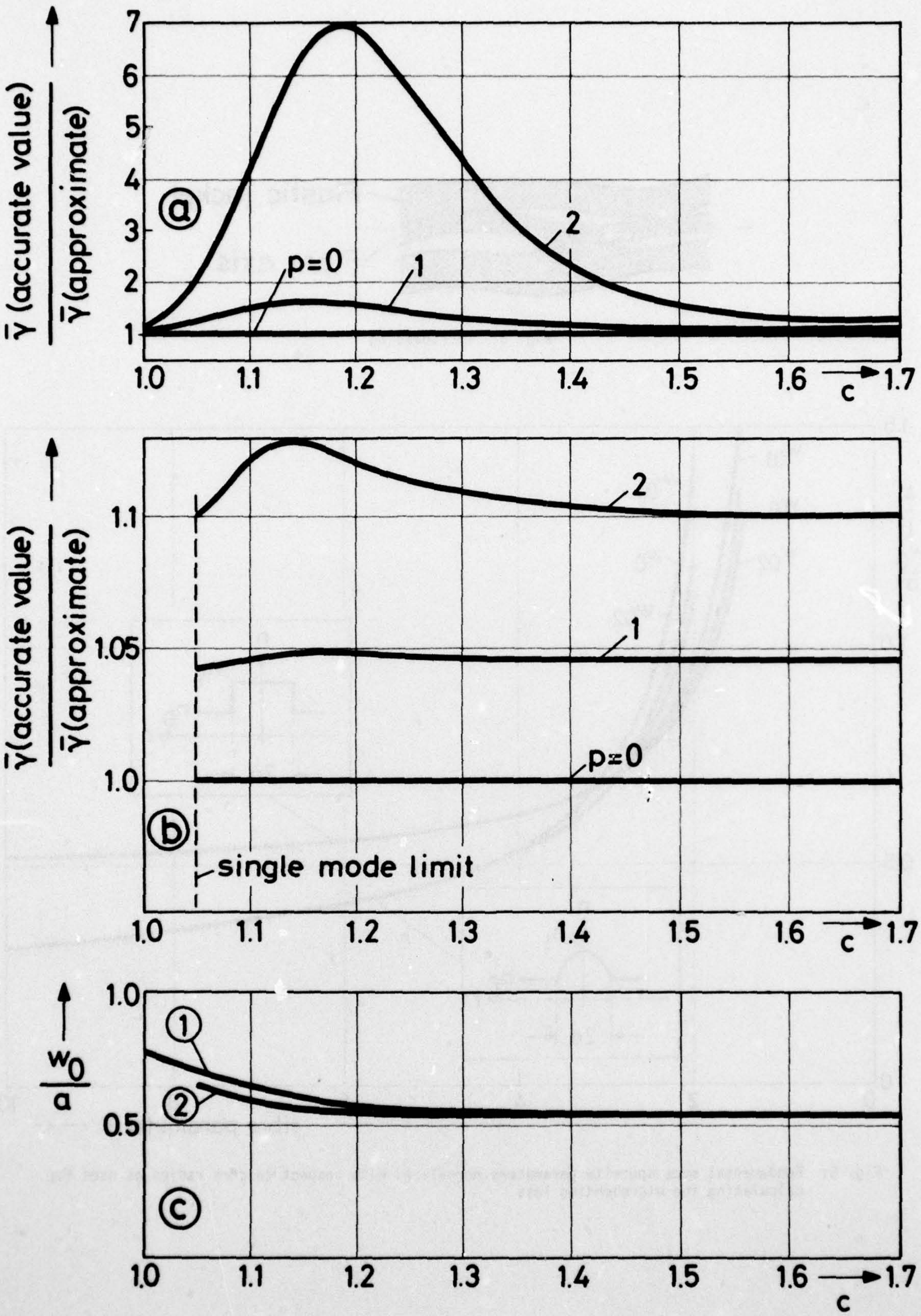

Fig. 7: Ratio of accurate microbending loss in W-fibres to the approximation according to eq. (5)
a) W-fibre parameter $V_W = 2.4$, $\delta = 8.8$
b) W-fibre parameter $V_W = 3.0$, $\delta = 5.6$
c) spotsize parameter w_0 for the fibres according to Figs. 7a (curve 1) and 7b (curve 2)

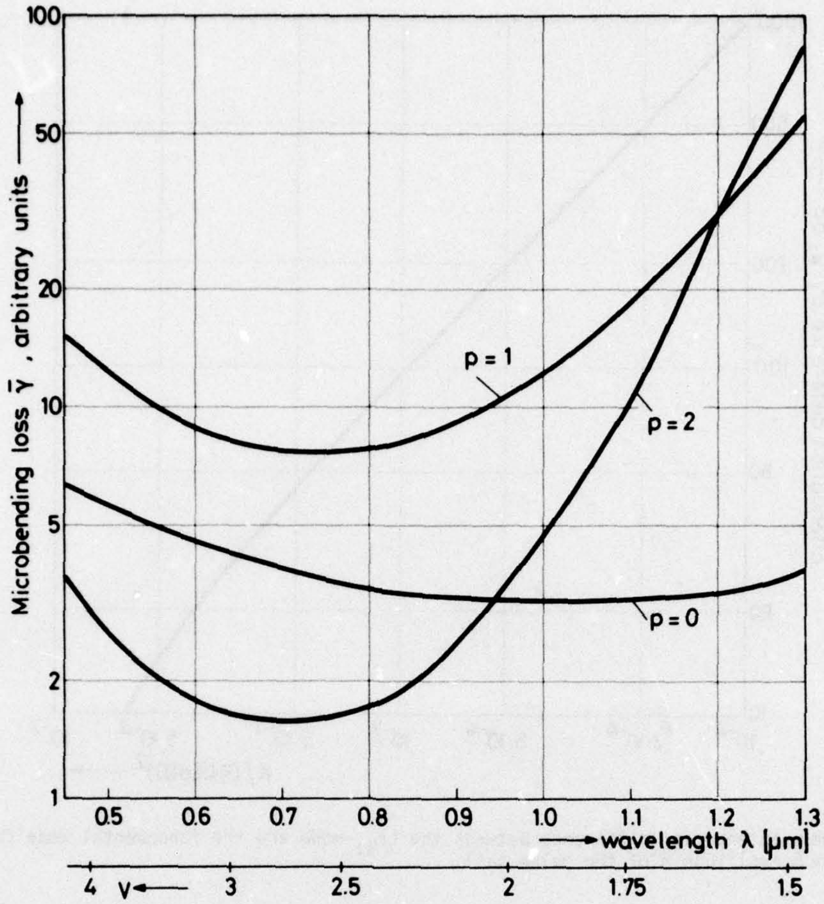

Fig. 8: *Fundamental mode microbending loss of a cladded-core fibre versus wavelength for several curvature power spectra.* Assumption: Fibre parameter V = 2.4 at a wavelength λ = 0.8 μm

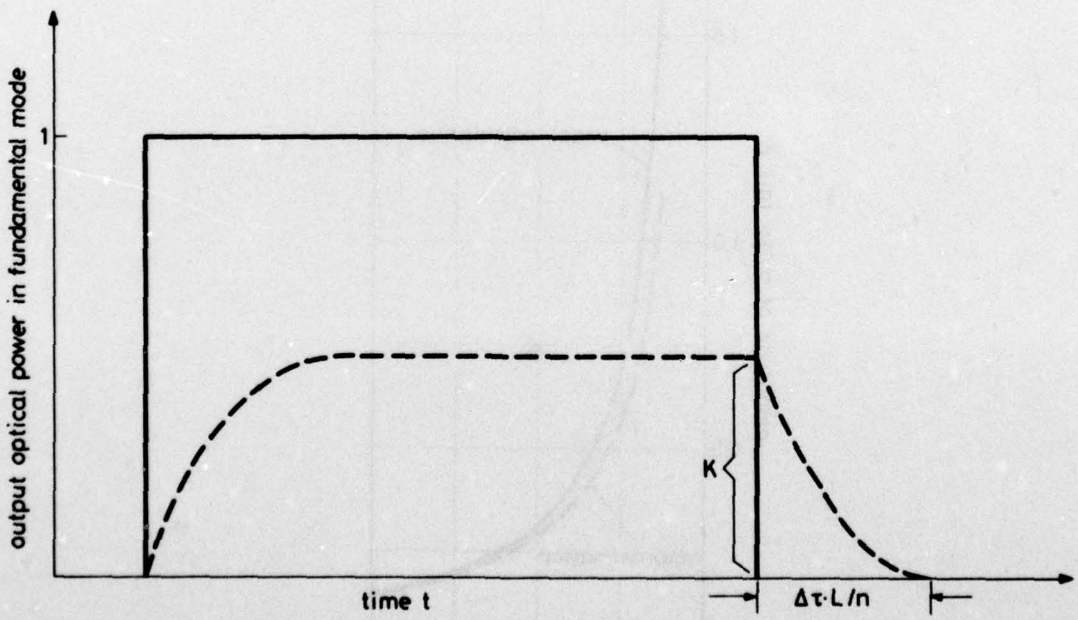

Fig. 9: Output response to a long rectangular input pulse
—— ideal output signal without reconversion
--- pulse contribution arising from reconversion between the first higher order LP_{11}-mode and the fundamental mode

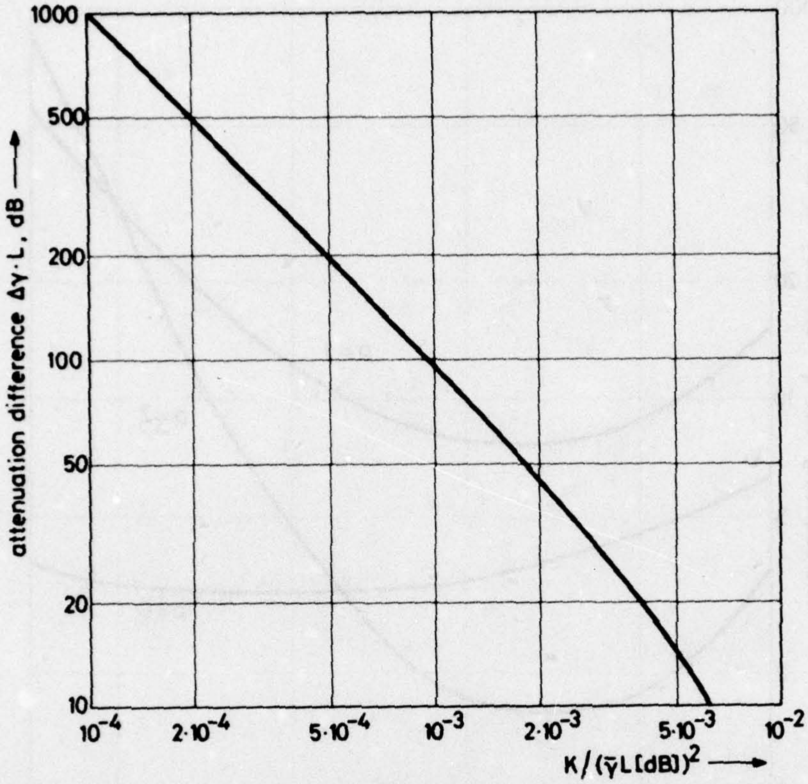

Fig. 10: Minimum attenuation difference between the LP_{11}-mode and the fundamental mode for a given maximum amplitude K of the pulse tail

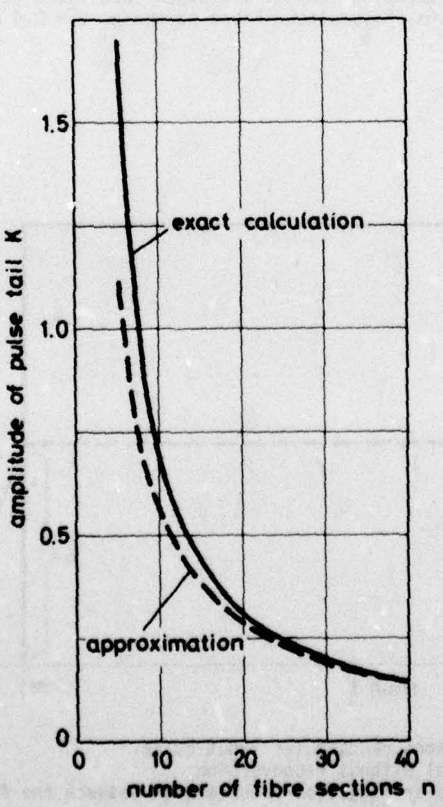

Fig. 11: The amplitude of pulse tail when inserting n mode filters into a fibre transmission line with total microbending loss $(\tilde{\gamma}\cdot L) \triangleq 20$ dB

BEAM EVOLUTION ALONG A MULTIMODE OPTICAL FIBER*

by

S. Y. Shin and L. B. Felsen
Department of Electrical Engineering and Electrophysics
Polytechnic Institute of New York, Farmingdale, NY 11735

ABSTRACT

When a Gaussian beam is injected obliquely across the endface of a multimode optical fiber, the field inside the fiber may be explored either by tracking the beam or by expansion in terms of guided modes. For highly collimated beams and large core radius, direct tracking is preferable until the multiply reflected beam fields can no longer be individually resolved. This paper presents results for the phase and amplitude of the beam field as it progresses down the fiber via successive reflections from the core interface. The analysis is performed by first formulating the fields generated in the fiber by a point source and then converting these fields to beam fields by assigning a complex value to the source coordinates. It is shown that paraxial Gaussian beam fields are calculable completely from corresponding point-source-excited fields in a geometric optical ray bundle. It is found that the beam projection on the fiber cross section refocuses between reflections but that the beam divergence increases when the number of reflections from the fiber wall is sufficiently large. Numerical results are presented for beams injected in a meridional plane.

1. INTRODUCTION

The coupling of Gaussian laser beams into dielectric fibers is of special interest for optical communication. The extensive literature on this subject may be divided into two major categories: a) contributions which treat the problem by guided mode analysis, and b) contributions which employ a ray-optical approach (SNITZER, E., 1961; KAWAKAMI, S. and NISHIZAWA, J., 1968). The latter have been concerned either with the ray-optical interpretation of guided modes (SNYDER, A. W., PASK, C. and MITCHELL, D. J., 1973) or with direct ray tracing. Ray tracing has been used primarily to chart the trajectory of an injected beam, but has not been exploited for quantitative information on the amplitude variation of the beam field, especially in focusing regions where conventional ray optics is inapplicable. Moreover, the usual ray-optical treatment does not account for multiple reflections at the fiber wall, nor for conversion from rays or beams to modes when the latter description is more appropriate. The alternative use of multiply reflected beams or of guided modes is relevant especially for multimode fibers with large core diameter since the spot size of a focused incident beam is then small compared to the fiber cross section. It may therefore be advantageous to track the incident beam directly into the fiber rather than to express the field at the outset in terms of the guided modes. Such beam tracking forms the substance of this paper. Beam coupling to the guided modes is to be presented separately (SHIN, S. Y. and FELSEN, L. B., in preparation).

A new technique has recently been formulated whereby an incident two-dimensional or three-dimensional Gaussian beam is generated from an incident line source (cylindrical wave) or point source (spherical wave) field by assigning complex values to the source coordinates (FELSEN, L. B., 1975). Thus, the Green's function problem, long of interest in radiation and diffraction theory, is also fundamental for the calculation of fields due to Gaussian beams. For the optical fiber, the relevant Green's function is that for a dielectric cylinder with homogeneous or radially inhomogeneous refractive index profile. Of special importance is the construction of high-frequency asymptotic solutions since these describe the parameters for optical propagation. Such solutions can be developed directly by ray-optical methods, without the need for departing initially from an exact formulation of the field problem. Apart from yielding the desired information directly, the ray-optical method is important because it can accommodate geometries, such as non-circular fibers or fibers with anisotropic core, for which exact solutions are not available.

While the complex-source-point technique converts the ray-optical field into a general beam field, it is adequate (for beams that remain well collimated) to consider only the paraxial region surrounding the beam axis since the field elsewhere is very small. Under these conditions, it suffices to restrict the source-excited ray-optical field to the vicinity of a central ray that subsequently becomes the beam axis; i.e., it is adequate to treat a particular thin ray bundle rather than the entire family of rays. It is then found that the real parameters governing the phase and amplitude behavior of the field in the ray bundle also describe the field in the Gaussian beam when the analytic continuation to complex-source-point coordinates is performed. Thus, as in the parallel plane case (FELSEN, L. B. and SHIN, S. Y., 1975), a rigorous link is provided between point-source-excited ray optics and paraxial beam optics, in terms of the conventional ray-optical parameters which have strong physical content. This aspect facilitates examination of the multiply reflected beam field solution with respect to periodic refocusing, beam spreading, and other physical attributes.

2. RAY-OPTICAL FIELDS

As noted in Section I, the paraxial ray bundle emanating from a point source is fundamental for the subsequent construction of the fields excited by a Gaussian beam. Moreover, the three-dimensional

* This research was sponsored in part by the Joint Services Electronics Program under Contract No. F 44620-69-C-0047 and in part by the National Science Foundation under Grant No. ENG-7522625.

fields in the fiber can be easily derived from a knowledge of the two-dimensional fields in the fiber cross section. Therefore, paraxial ray bundles emitted by a line source parallel to the fiber axis (z-axis) are considered first.

2.1 Two-dimensional Problem

(a) General ray-optical fields

The incident field (line source in an unbounded dielectric with constant refractive index) is normalized so that $\overline{G}_{inc}$ is the infinite space Green's function

$$\overline{G}_{inc} = \frac{i}{4} H_o^{(1)}(k\rho) \sim \frac{1}{4}\sqrt{\frac{2}{\pi k\rho}} \exp(ik\rho + i\pi/4), \quad k\rho \gg 1. \tag{1}$$

where k is the wavenumber and ρ is the distance from the source. A time dependence $\exp(-i\omega t)$ is suppressed. Then the field $\overline{G}$ along a ray after s reflections at the walls of a fiber with a radius "a" is given by*:

$$\overline{G} \sim \frac{i}{4}\sqrt{\frac{2}{\pi k}} \left|\frac{L_{fo}}{L-L_{fo}}\right|^{1/2} \frac{1}{L_o^{1/2}} e^{ik\overline{\psi}} e^{-i\frac{\pi}{2}\sigma_f - i\frac{\pi}{4}} \tag{2}$$

where

$$\overline{\psi} = 2s\,L_a - L_o + L. \tag{2a}$$

The lengths L_o, L_{fo}, L_a and L, defined in Fig. 1, are measured from the perpendicular bisector of the central ray (shown dashed) in a ray tube: $L_a = a \sin\gamma_a$ is the half length of the central ray between reflections, L_o locates the source point S. L_{fo} is the distance to a ray tube focus (point of tengency of the central ray with the caustic of the reflected ray family, which is not shown), and L is the distance to an observation point. The orientation of the central ray is fixed by the angle γ_a. Depending on location along the multiply reflected ray, L and L_{fo} may be positive or negative; in regions ①, they are positive, while in regions ②, they are negative. The integer s counts the number of reflections, and σ_f counts the number of times that the central ray passes through a ray tube focus. Focusing need not occur after every reflection. In fact, a real focus $L = L_{fo}$ is possible only when L and L_{fo} have the same algebraic sign, and when $|L_{fo}| < L_a$; otherwise, there will be a virtual focus. The following rule concerning solutions of the equation $L = L_{fo}$ is found to apply:

$$\begin{aligned} &s > (L_a/2L_o) + 1/2 && \text{-- real focus in region 1} \\ &s < (L_a/2L_o) - 1/2 && \text{-- real focus in region 2} \\ &\frac{L_a}{2L_o} - \frac{1}{2} < s < \frac{L_a}{2L_o} + \frac{1}{2} && \text{-- no real focus} \end{aligned} \tag{3}$$

The ray-optical formula in (2) evidently fails when $L \to L_{fo}$ and must then be augmented by a caustic transition function (FELSEN, L. B. and MARCUVITZ, N., 1973). We shall exclude such observation points from our considerations. The focal distance is given by

$$L_{fo} = L_a L_o (L_a - 2s\,L_o)^{-1} \quad \text{or} \quad \frac{1}{L_{fo}} = \frac{1}{L_o} - \frac{2s}{L_a} \tag{4}$$

Thus, the focus moves toward the center of the reflected ray cord (i.e., $L_{fo} \to 0$) as the number s of reflections increases sufficiently. The total field at an observation point $\underset{\sim}{\rho}$, as computed by ray optics, is given by the sum of all fields along rays passing through $\underset{\sim}{\rho}$. This implies inclusion of all rays with such initial angles that they reach $\underset{\sim}{\rho}$ after an appropriate number of reflections.

The ray-optical formula in (2) implies that the wall reflection coefficient is $\Gamma = +1$ so that phase and amplitude of a ray are preserved after reflection. To account for the incidence-angle-dependent reflection coefficient at the wall of a dielectric fiber, the field after every reflection should be multiplied by $\Gamma(\gamma_a)$, where (assuming total reflection and negligible leakage),

$$\Gamma(\gamma_a) = \frac{\sin\gamma_a - i(\cos^2\gamma_a - n^2)^{1/2}}{\sin\gamma_a + i(\cos^2\gamma_a - n^2)^{1/2}} \equiv \exp\left[i\,\theta(\gamma_a)\right] \tag{5}$$

where the relative refractive index n is smaller than unity.

---

* See Appendix A (also FELSEN, L. B. and MARCUVITZ, N., 1973) for the source-excited after a single reflection. Multiple reflections are treated in the same way by calculating the ray tube cross section with reference to every relevant real or virtual focus.

If the ray is to be tracked over many reflections, it is appropriate to employ the modified trajectories and fields obtained when a lateral ray shift on the boundary is included. For the present discussion, the effect of the ray shift can be neglected since its cumulative effect over the range of interest here is not significant. It can be shown that, at a given observation point, the field computed from (2) and (5) with the non-shifted path in Fig. 1 agrees with the field computed with the laterally shifted path in Fig. 2 provided that the number of reflections is not too large and that $L \neq L_{fo}$. This is analogous to the result found previously for the plane stratified layer problem (FELSEN, L. B. and SHIN, S. Y., 1975). It should, however, be emphasized that when the multiply reflected ray fields are to be summed into guided modes, the laterally shifted paths must be utilized in order to furnish the correct asymptotic modal dispersion equation.

(b) Paraxial approximation

The ray-optical fields in (2), with (5), are now expressed so that they describe observation points in the vicinity of the central ray in terms of quantities pertaining to that ray. This is accomplished by expanding the phase along a neighboring ray in terms of the parameters for the central ray (the ray amplitude is insensitive to this correction). Thus, introducing a perpendicular distance d from a point $\bar{\rho}$ on the central ray to an observation point $\rho = (\bar{\rho}, d)$, one finds that, without inclusion of the lateral shift (see Fig. 3),

$$\Psi(\bar{\rho}, d) = 2s L_a - L_o + L + \frac{d^2}{2R}, \qquad R = L - L_{fo}, \tag{6}$$

provided that $d << |R|$. Subject to this modification, the formulas in (2), with (5), describe the field in the paraxial region about the central ray defined by the angle γ_a. Note that R is the radius of curvature of the wavefront, positive for convex and negative for concave curvatures.

2.2 Three-dimensional Problem

For the three-dimensional case, the incident field, due to an oscillating point source at $\underset{\sim}{r}' = (\underset{\sim}{\rho}', z')$, is given by the infinite space Green's function

$$G_{inc} = \frac{e^{ikr}}{4\pi r}, \qquad r = \left[\rho^2 + (z - z')^2\right]^{1/2}, \tag{7}$$

where r is the distance from the source point to the observation point. The ray-optical field after s reflections in the cylindrical waveguide is, in the paraxial approximation:

$$G \sim \left|\frac{L_{fo}/\sin\beta}{R_1/\sin\beta}\right|^{1/2} \left|\frac{L_o/\sin\beta}{R_2/\sin\beta}\right|^{1/2} \frac{e^{ik\psi}}{4\pi L_o/\sin\beta}\, e^{-i(\pi/2)\sigma_f} \tag{8}$$

where the phase function is given by

$$\psi = (2s L_a - L_o + L)/\sin\beta + \frac{d_1^2}{2R_1/\sin\beta} + \frac{d_2^2}{2R_2/\sin\beta}, \tag{9}$$

with

$$R_1 = L - L_{fo}, \qquad R_2 = 2s L_a - L_o + L. \tag{9a}$$

Here, β is the angle between the ray and a line parallel to the positive z axis (see Fig. 4). d_2 is the perpendicular distance from the central ray measured in the plane containing the ray and a line parallel to the z axis, and d_1 is a perpendicular distance from the central ray measured normal to that plane. All the other symbols have been defined previously. The three-dimensional interpretation of various distances D follows from the recognition that lengths D and $D/\sin\beta$ measure, respectively, the cross sectional projection and the actual length along a ray. The third factor in (8) normalizes the incident field to its value at the central plane along the ray cord (see Fig. 1). The first and second factors account for the ray tube cross section spreading in transverse and longitudinal planes, respectively, as sketched in Fig. 5, keeping in mind that the non-spherical wavefront has two different radii of curvature $R_1/\sin\beta$ and $R_2/\sin\beta$. While the transverseely projected ray tube focuses periodically as in the two-dimensional case, the longitudinal projection expands indefinitely.

As in (2), with (6), the boundary reflection coefficient in (8) is $\Gamma = 1$. When the incidence-angle-dependent reflection coefficient $\Gamma(\gamma_a, \beta)$ for the boundary of the dielectric fiber is included, the field in (8) must be multiplied by $[\Gamma(\gamma_a, \beta)]^s$, where

$$\Gamma(\gamma_a, \beta) = \frac{\sin\beta\sin\gamma_a - i(\cos^2\gamma_a + \cos^2\beta - n^2)^{1/2}}{\sin\beta\sin\gamma_a + i(\cos^2\gamma_a + \cos^2\beta - n^2)^{1/2}} \equiv \exp[i\theta(\gamma_a, \beta)] \tag{10}$$

The corresponding laterally shifted path, required in general but not for the present study, is shown in Fig. 6.

3. MULTIPLY REFLECTED BEAM FIELDS

The preceding results for line-source and point-source-excited fields can be converted into excitation by a sheet beam and a rotationally symmetric Gaussian beam, respectively, by assigning a complex value to the source point. For the two-dimensional case (Fig. 7(a)), if the beam axis is inclined at an angle α with respect to the positive x-axis and the beam waist is centered at x_o thereon, one replaces the real source point (x', y') by $(x_o + ib\cos\alpha,\ ib\sin\alpha)$, where b is a positive constant related to the beam width w_0 at the waist by $b = kw_0^2/2$ (FELSEN, L. B., 1976). Thus, the polar source coordinates (ρ', ϕ') are transformed into

$$\rho' = (x'^2 + y'^2)^{1/2} = [(\rho_o\cos\alpha + ib)^2 + \rho_o^2\sin^2\alpha]^{1/2} \tag{11}$$

$$\phi' = \tan^{-1}\frac{y'}{x'} = \tan^{-1}\left(\frac{ib\sin\alpha}{\rho_o + ib\cos\alpha}\right) = \cos^{-1}\left(\frac{\rho_o\sin\alpha}{\rho'}\right) - \left(\frac{\pi}{2} - \alpha\right) \tag{12}$$

where $\rho_o = (x_o^2 + y_o^2)^{1/2} = x_o$. For the three-dimensional case with source point at (ρ', ϕ', z'), if the beam axis is to be inclined at an angle β with respect to a line parallel to the z-axis, if its projection in the x-y plane is to make an angle α with the positive x-axis, and if its waist is to be centered at $(x_o, 0, z_o)$ (Fig. 7(b)), then

$$\rho' = [(\rho_o\cos\alpha + ib_\perp)^2 + \rho_o^2\sin^2\alpha]^{1/2}, \quad b_\perp = b\sin\beta \tag{13}$$

$$\phi' = \tan^{-1}\left(\frac{ib_\perp\sin\alpha}{\rho_o + ib_\perp\cos\alpha}\right) = \cos^{-1}\left(\frac{\rho_o\sin\alpha}{\rho'}\right) - \left(\frac{\pi}{2} - \alpha\right) \tag{14}$$

$$z' = z_o + ib_z, \quad b_z = b\cos\beta \tag{15}$$

This may be shown to be equivalent to the replacement

$$L_o \to L_o + ib \quad \text{(two-dimensional case)} \tag{16a}$$

$$L_o \to L_o + ib_\perp,\ z' \to z_o + ib_z \quad \text{(three-dimensional case)} \tag{16b}$$

where $b_\perp$ and b_z are the transverse and longitudinal projections, respectively, of the beam direction vector $\underset{\sim}{b}$. The focal distance L_f for the two-dimensional case becomes accordingly:

$$L_f = \frac{L_a(L_o + ib)}{L_a - 2s(L_o + ib)} = L_f^r + iL_f^i, \tag{17}$$

where

$$L_f^r = L_a\frac{L_o(L_a - 2sL_o) - 2sb^2}{(L_a - 2sL_o)^2 + 4s^2b^2} \tag{18}$$

$$L_f^i = b\frac{L_a^2}{(L_a - 2sL_o)^2 + 4s^2b^2} \tag{19}$$

For the three-dimensional case,

$$b \to b_\perp \quad \text{in (17) - (19)} \tag{20}$$

From (6), the paraxially approximated phase for the two-dimensional beam becomes

AD-A050 748 ADVISORY GROUP FOR AEROSPACE RESEARCH AND DEVELOPMENT--ETC F/G 20/6
OPTICAL FIBRES, INTEGRATED OPTICS AND THEIR MILITARY APPLICATIO--ETC(U)
OCT 77 H HODARA

UNCLASSIFIED AGARD-CP-219 NL

2 OF 6

AD A050748

$$\psi = 2s\,L_a - (L_o + ib) + L + \frac{d^2}{2(L - L_f^r - i\,L_f^i)}$$

$$= 2s\,L_a - (L_o + ib) + L + \frac{d^2(L - L_f^r + i\,L_f^i)}{2\left[(L - L_f^r)^2 + (L_f^i)^2\right]} \quad . \tag{21}$$

from which one observes that the minimum beamwidth occurs at (the beamwidth w is defined so that the exponential amplitude becomes $\exp(-d^2/w^2)$)

$$L = L_f^r \quad . \tag{22a}$$

rather than at the paraxial ray tube focus $L = L_{fo}$ (Fig. 8). The displacement from the ray tube focus is given by

$$L_f^r - L_{fo} = -2s\,L_a^2\,b^2 \Big/ \left[(L_a - 2s\,L_o)^2 + 4s^2b^2\right](L_a - 2s\,L_o) \tag{22b}$$

and the beamwidth at the minimum by

$$w_s = w_o\,L_a\left[(2s\,L_o - L_a)^2 + 4s^2b^2\right]^{-1/2} \quad , \quad w_o = (2b/k)^{1/2} \quad . \tag{22c}$$

The total paraxial beam field is from (2), for $d << |L - L_f|$.

$$\overline{G}_b \sim \frac{i}{4\pi}\sqrt{\frac{2\pi}{k}}\left(\frac{L_f}{L - L_f}\right)^{1/2} \frac{1}{(L_o + ib)^{1/2}}\, e^{ik\overline{\psi}_b}\, e^{-i\frac{\pi}{4}} \; , \; L_f = L_f^r + i\,L_f^i \quad . \tag{23}$$

with the square roots so defined that $\overline{G}_b \to \overline{G}$ in (2) when $b \to 0$.

Thus, after many reflections, the minimum beamwidth tends to zero, the location of the minimum approaches the center of the reflected beam axis cord (since $L_f^r \to L_{fo} \to 0$), and the field amplitude tends to zero since $L_f \to 0$. The latter circumstance implies a rapid divergence of the beam after many reflections. In (22a), the location of the minimum beamwidth after s reflections has been based on the exponential behavior only, without inclusion of the algebraic terms in (23). One observes that (23) remains valid at the beamwidth minimum so that for the paraxial beam field, the restrictions imposed on the ray-optical formula (2) may be removed. Note, however, that since $L_f \to 0$ as $s \to \infty$, the resulting restriction $d << |L|$ prohibits observation points in the narrow focal region $L \to 0$, which then resembles that for the paraxial ray bundle (see (6)).

For the three-dimensional paraxial beam, and a boundary reflection coefficient $\Gamma = 1$, one has similarly (see (8) and (9)),

$$\psi_b = \left[2s\,L_a + L - (L_o + ib_\perp)\right] \Big/ \sin\beta$$

$$+ \frac{d_1^2}{2(L - L_f^r - i\,L_f^i)/\sin\beta} + \frac{d_2^2}{2(2s\,L_a + L - (L_o + ib_\perp))/\sin\beta} \tag{24}$$

with a consequent displacement of the beamwidth minima along the d_1 direction in the cross section, from the ray focal points $L = L_{fo}$ to

$$L = L_f^r \tag{25a}$$

The normalized minimum beamwidth (at L_f^r) along the d_1 direction and the corresponding normalized beamwidth along the d_2 direction, respectively, are (note the change in (20) for L_f^r and L_f^i in (19))

$$\frac{w_{s1}}{w_o} = \left(\frac{L_f^i}{b\sin\beta}\right)^{1/2} \quad , \quad \frac{w_{s2}}{w_o} = \left[\frac{(2s\,L_a + L_f^r - L_o)^2}{b^2\sin^2\beta} + 1\right]^{1/2} \tag{25b}$$

The paraxial beam field becomes, with the square roots so defined that $G_b \to G$ as $b \to 0$,

$$G_b \sim \left[\frac{L_f}{L-L_f} \right]^{1/2} \left[\frac{L_o + i b_\perp}{2s\,L_a - (L_o + i b_\perp) + L} \right]^{1/2} \frac{e^{ik\psi_b}}{4\pi (L_o + i b_\perp)/\sin\beta} \tag{26}$$

As before, the multiply reflected beam, when projected onto the waveguide cross section, focuses periodically but diverges more strongly after successive focusings; the longitudinally projected beam profile spreads out continuously. This is shown in Fig. 8 for the special case when the beam axis lies in a meridional plane.

The modifications for the indicence- angle dependent reflection coefficient in (5) and (10) follow from Sec. II but do not appreciably affect the observations made above in connection with beam tracking.

The utility of beam tracking becomes questionable when the multiply reflected beams can no longer be individually resolved. It may then be prefereable to employ the guided mode expansion (SHIN, S. Y. and FELSEN, L. B., in preparation). An appropriate criterion defining the limit of resolution in the longitudinal section of Fig. 8 is the equality of the axial beamwidth Q_s after s reflections and the spacing Z_β between successive reflections. Both Q_s and Z_β can be expressed as in the parallel plane geometry (FELSEN, L. B. and SHIN, S. Y., 1975),

$$Q_s = \left(\frac{8}{kb}\right)^{1/2} \frac{R_s}{\sin\beta} \quad , \qquad Z_\beta = 4L_a \cot\beta \quad , \tag{27}$$

where $R_s = (2sL_a + L - L_o)/\sin\beta$ is the total path length along the beam axis after s reflections. From $Q_s = Z_\beta$, one obtains the limiting number of reflections $\bar{s}$, beyond which the multiply reflected beam fields fill the entire longitudinal cross section (see Fig. 8(b)), as the integer closest to $s = s_\ell$, where

$$s_\ell = (2L_a)^{-1}(kw_o L_a \sin\beta\cos\beta + L_o - L) \approx \frac{1}{2} kw_o \sin\beta\cos\beta \ . \tag{28a}$$

The last expression is valid when $\beta \neq 0$, and w_o is defined in (22c). The corresponding axial distance z_ℓ is

$$z_\ell = s_\ell Z_\beta / 2 \tag{28b}$$

The limit of resolution in the transverse cross section (Fig. 8) is somewhat less clearly defined. Here, the degree of collimation of the beam may be taken as an appropriate measure of the utility of beam tracking. Since the angular divergence φ of a Gaussian beam is $\varphi = 2\tan^{-1}(2/kw_s)$, where w_s is the minimum spot size as given in (22c), one may solve for the number of reflections $\bar{s}$ as the integer closest to s_t corresponding to a specified value of $C \equiv \tan(\varphi/2)$, recognizing that $kw_o \gg 1$:

$$s_t = L_a \frac{L_o + \left[L_o^2 + \{(\frac{kw_o}{2}C)^2 - 1\}(L_o^2 + b^2)\right]^{1/2}}{2(L_o^2 + b^2)} \approx Ckw_o L_a\left[4(L_o^2 + b^2)^{1/2}\right]^{-1}, \text{ if } \frac{kw_o}{2}C \gg 1 \tag{29}$$

When C is of the order of unity, the beam is strongly divergent, and s_t may then be taken to define a limit on the utility of the beam tracking procedure. The overall limit is then provided by the smaller of s_ℓ and s_t.

4. INFLUENCE OF FIBER ENDFACE

In the preceding treatment, it has been assumed that the incident beam is launched from inside the fiber. To account for exterior launching across an endface as in Fig. 9, we consider a transmitted ray tube on one side of a dielectric interface (where the wavenumber is k) when a point source is situated on the other side (where the wavenumber is k_o). Since the transmitted wavefront is non-spherical, the family of transmitted rays does not converge on a point but is tangent to a caustic surface (FELSEN, L. B. and MARCUVITZ, N., 1973). Therefore, the field across the endface inside the fiber does not have the form (7) but rather a form similar to (8) which accommodates an astigmatic ray pencil. Moreover, with $\bar{\beta}$ denoting the angle between the incident ray and a line parallel to z (see Fig. 9a), the incident field should be multiplied by the transmission coefficient, $[1 + \Gamma(\bar{\beta})]$; the direction of the transmitted ray pencil is inferred from that of the incident pencil by Snell's law. These considerations lead to the following field across the endface inside the fiber:

$$G_{trans} \sim \frac{e^{ik_o r_i}}{4\pi r_i} \{1+\Gamma(\bar{\beta})\} \sqrt{\frac{r_o^{(1)} r_o^{(2)}}{(r_t+r_o^{(1)})(r_t+r_o^{(2)})}} \; e^{ik\left[r_t + \frac{d_1^2}{r_t+r_o^{(1)}} + \frac{d_2^2}{r_t+r_o^{(2)}}\right]} \tag{30}$$

where

$$r_o^{(1)} = \frac{k}{k_o} r_i \quad , \qquad r_o^{(2)} = \frac{k}{k_o} \frac{\cos^2\beta}{\cos^2\bar{\beta}} r_i \tag{30a}$$

are the distances to the virtual foci of the astigmatic ray pencil, while r_i and r_t are the lengths of the incident and refracted ray segments, respectively, measured along the central ray. The paraxial distances d_1 and d_2 from the central ray are measured perpendicular to the plane of incidence and in the plane of incidence, respectively. The various geometrical quantities are defined in Fig. 9. The tracking of this field between reflections at the fiber wall then proceeds as in (8), provided that in the first factor, L_{fo} is taken from (4) with L_o replaced by $L_o^{(1)}$, *and in the second factor,* L_o *is replaced by* $L_o^{(2)}$.

Conversion of the incident point-source-excited field into a Gaussian beam field is accomplished as before by making the replacements $r_i \to (r_i - ib)$.

5. NUMERICAL RESULTS

The behavior of the beam as it travels between successive reflections at the fiber wall is described by the minimum normalized beamwidth (w_{s1}/w_o) and the corresponding normalized beamwidth (w_{s2}/w_o) in (25b). When the beam axis lies in a meridional plane, one has $L_a = a$ and measures L_o from the cylinder axis (see Fig. 1(a)). Numerical results as a function of fiber radius and of the width, minimum spot location and launching angle of the injected Gaussian beam are presented in Figs. 10-12. One observes from Fig. 10(a) that decreasing the fiber radius or increasing the injected beamwidth via b eventually decreases successive beamwidth minima w_{s1}, and hence increases the rate of beam divergence, in the cross section plane. This behavior is attributed to the greater boundary curvature sampled by the incident and successively reflected beams under these conditions. In the meridional plane, the rate of divergence (essentially linear) decreases with decreasing fiber radius or increasing beamwidth. In the former case, this occurs because the beam travels a shorter distance between reflections (Fig. 10(b)) while in the latter case, the more highly collimated incident beam spreads more slowly. As the waist of the injected beam moves closer to the boundary, the rate of beam divergence in the cross section plane increases (Fig. 11(a)) but is practically unchanged in the meridional plane (Fig. 10(b)). This follows from (25b), with (18)-(20), since the dependence of w_{s1} on L_o occurs in the product (sL_o), whence increasing L_o generates a given w_{s1} after fewer reflections s. Finally, decreasing the injection angle β has the same cross sectional effect as decreasing the beamwidth b since β and b in w_{s1} occur in the combination (b sin β). Thus, the beam diverges more slowly in the cross section plane (Fig. 12). However, since the distance between reflections is now large, the beam may fill a substantial portion of the meridional plane after or even before the first reflection. It should be noted that several of the (w_{s1}/w_o) curves achieve values greater than unity for small values of s, thereby signifying better collimation between initial reflections before broadening occurs.

6. CONCLUSIONS

In this paper, it has been shown how the field associated with a Gaussian beam injected across the endface of a multimode constant index circular fiber can be constructed entirely by the ray-optical method. This method yields the amplitude as well as the phase of the field and can be generalized to other fiber configurations (e.g., non-circular geometry and (or) non-isotropic composition) which have so far defied exact analytical treatment. The ray solutions are converted into beam solutions by the complex-source-point procedure. The linkage between an optical ray bundle and a paraxial Gaussian beam stressed in the analysis has provided not only physical insight but also computational convenience. While the ray-optical formulas fail in the vicinity of the focal regions of the ray bundle, the corresponding beam formulas remain applicable there and can be used to predict the spot size everywhere along the multiply reflected beam. Thus, beam tracking by ray optics and subsequent use of the complex-source-point method is actually simpler than ray optics per se, although the paraxial beam formulas contain, except for the initial spot size, no other parameters than those of the optical ray bundle.

The behavior of the multiply reflected ray bundle and beam have been discussed in some detail. An *obliquely incident, non-meridional ray bundle,* when projected onto a cross sectional plane, is refocused between successive reflections at the curved fiber wall, but the rate of divergence of the bundle is found to increase with the number of reflections. On the other hand, the longitudinally projected ray tube cross section expands continually. When the multiply reflected ray bundle has diverged so much that individual reflections can no longer be resolved, it may be better to express the field in terms of the guided modes (SHIN, S.Y. and FELSEN, L.B., in preparation). These observations remain applicable when the point-source-excited fields are converted into beam fields; the focal regions of the ray bundle locate approximately, *after many reflections, the focal regions of the paraxial beam.* Thus, both the direct beam tracking and the guided mode formulations are useful, depending on the propagation length at which the field is observed. Very highly collimated beams injected into a large diameter fiber may remain resolvable over considerable distances. The output field will then again be a spot located appropriately in the cross section of the fiber endface. These observations are supported by the numerical results.

Only scalar fields have been considered here. Electromagnetic vector beams can be treated in the same manner by looking first at the fields excited by a vector dipole and then assigning complex values to the source coordinates. Moreover, the analysis can be readily extended to graded index fibers by following the procedure employed for the plane parallel configuration (FELSEN, L. B. and SHIN, S. Y., 1975).

7. APPENDIX A

Derivation of the Ray-Optical Formulas

The formula in (2) can be constructed directly by ray-optical methods. First, one determined the ray paths and ray tubes shown in Fig. 1. In cylindrical (ρ, ϕ) coordinates, the ray path can be expressed as $\phi = \phi(\rho, \mu)$, where the ray parameter μ identified the initial ray orientation γ_a via the relation $\mu = a \cos \gamma_a$. On the ray path, the functional dependence of ϕ on ρ is for $\phi > \phi' + 2n\pi$ (see Fig. 13),

$$\phi = \gamma_> - \gamma_< + 2s\gamma_a + \phi' + 2n\pi \tag{31}$$

where (ρ', ϕ') locates the source point x and

$$\gamma_a = \cos^{-1}(\mu/a) \quad , \quad \gamma_> = \cos^{-1}(\mu/\rho_>) \quad , \quad \gamma_< = \cos^{-1}(\mu/\rho_<) \tag{31a}$$

with $\rho_>$ and $\rho_<$ denoting the greater or smaller values, respectively, of the radial coordinate. The ray tube cross section is calculated from Fig. 1(b) as

$$dA = \rho \sin \gamma \, d\phi = (\rho \sin \gamma) \, d\mu \, (d\phi/d\mu)_{\rho = \text{const.}} = \left| \frac{L - L_{fo}}{L_{fo}} \right| d\mu \tag{32}$$

where $\mu = a \cos \gamma_a = \rho \cos \gamma$ characterized the central ray and $d\mu$ is constant along a ray tube. The ray tube cross section is conveniently tracked along ρ = constant contours, for which $d\phi/d\mu$ is then evaluated from (31); this leads to the last equality in (32). The procedure is analogous to that employed in reference [9] for ray tracing in plane stratified media, and remains valid when ϕ in (31) is modified to account for a ray shift upon reflection.

The ray-optical field is calculated from the well-known formula

$$u \sim \hat{u} \, e^{ik(\psi - \hat{\psi})} \sqrt{\frac{d\hat{A}}{dA}} \tag{33}$$

where the caret superscript identifies conditions at an initial reference point along a ray, with ψ_s representing the phase. The initial field can be referred to the source point (or focal point) by the relation

$$\hat{u} \, e^{-ik\hat{\psi}} \sim \frac{1}{4} \sqrt{\frac{2}{\pi k L_o}} \; e^{ikL_o + i\frac{\pi}{4}} \tag{34}$$

which then reduces (33) to (2).

The three-dimensional field in (8) follows from directly analogous considerations.

8. REFERENCES

1. SNITZER, E., 1961, "Cylindrical dielectric waveguide modes," J. Opt. Soc. Am. 51, p. 491-498.
2. KAWAKAMI, S. and NISHIZAWA, J., 1968, "An optical waveguide with the optimum distribution of the refractive index with reference to waveform distortion," IEEE Trans. MTT-16, p. 814-818.
3. SNYDER, A. W., PASK, D. and MITCHELL, D. J., 1973, "Light acceptance property of an optical fiber," J. Opt. Soc. Am. 63, p. 59-64.
4. SHIN, S. Y. and FELSEN, L. B., in preparation, "Guided mode excitation in an optical fiber by a Gaussian beam."
5. FELSEN, L. B., 1976, "Evanescent Waves," J. Opt. Soc. Am. 66, p. 751-760.

8. REFERENCES

1. BATORSKY, D.V. and FELSEN, L.B., 1971, "Ray optical calculation of modes excited by sources and scatterers in weakly inhomogeneous ducts," Radio Science 6, p. 911-923.

2. FELSEN, L.B. and MARCUVITZ, N., 1973, "Radiation and Scattering of Waves," Prentice-Hall, Englewood Cliffs, New Jersey, p. 168-169.

3. FELSEN, L.B. and SHIN, S.Y., 1975, "Rays, beams and modes pertaining to the excitation of dielectric waveguides," IEEE Trans. on Microwave Theory and Techniques (Special Issue on Integrated Optics and Optical Waveguides). MTT-23, p.150-161.

4. FELSEN, L.B., 1976, "Evanescent Waves," Opt. Soc. Am. 66, p. 751-760.

5. KAWAKAMI, S. and NISHIZAWA, J., 1968, "An optical waveguide with the optimum distribution of the refractive index with reference to waveform distortion," IEEE Trans. MTT-16, p. 814-818.

6. SHIN, S.Y. and FELSEN, L.B., in preparation, "Guided mode excitation in an optical fiber by a Gaussian beam."

7. SNITZER, E., 1961, "Cylindrical dielectric waveguide modes," J. Opt. Soc. Am. 51, p. 491-498.

8. SNYDER, A.W., PASK, D. and MITCHELL, D.J., 1973, "Light acceptance property of an optical fiber," J. Opt. Soc. Am. 63, p. 59-64.

9. Reference 7, Sec. 5.8.

10. Reference 7, Sec. 5.5.

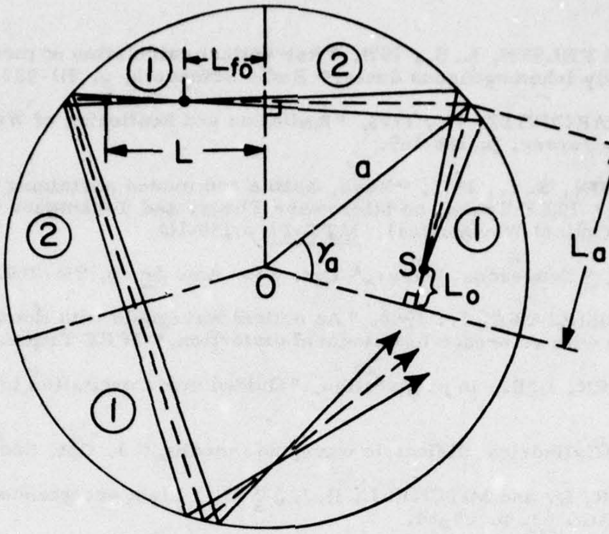

(a) multiply reflected ray

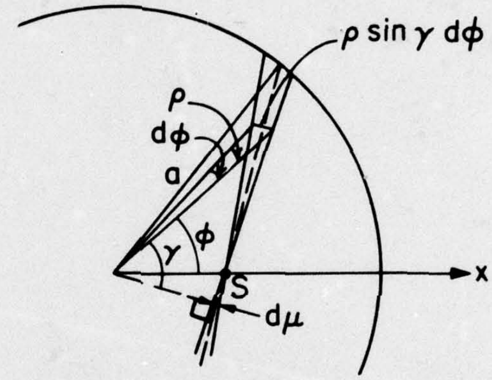

(b) calculation of ray tube cross section

Fig. 1 Ray tube and definition of coordinates (ray shift omitted)

(a) multiply reflected ray
(b) calculation of ray tube cross section

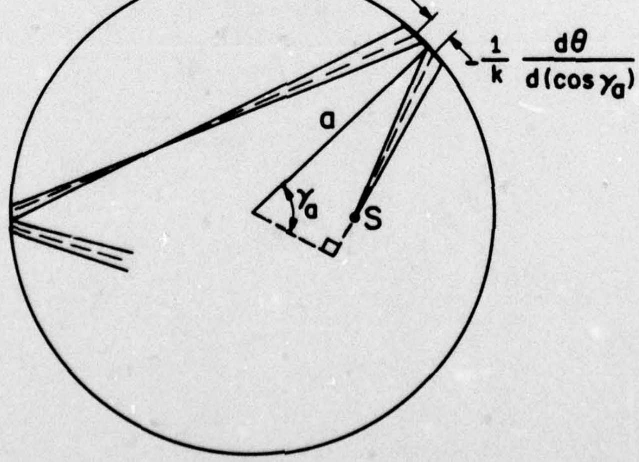

Fig. 2 Ray path with lateral shift on boundary

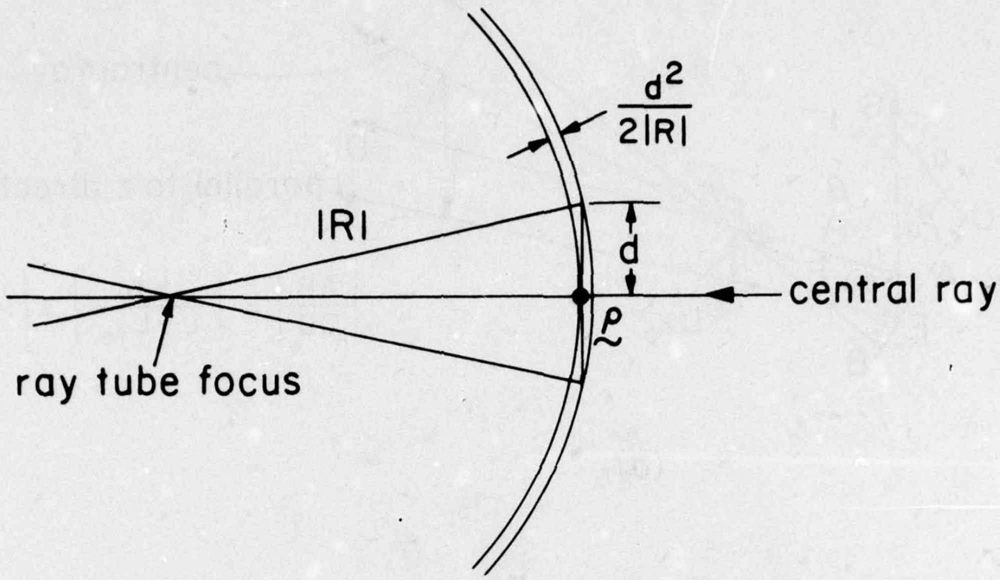

Fig. 3 Parameters for paraxial approximation

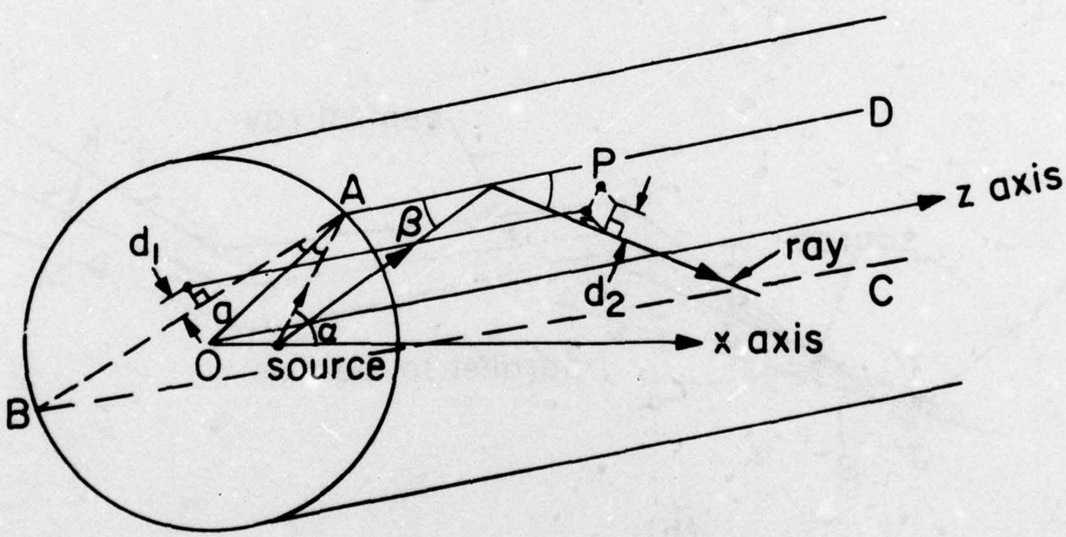

Fig. 4 Three-dimensional geometry. P is a paraxial observation point. Line AB is the projection of the ray on the cross section. d_2 is measured in the plane ABCD containing the ray

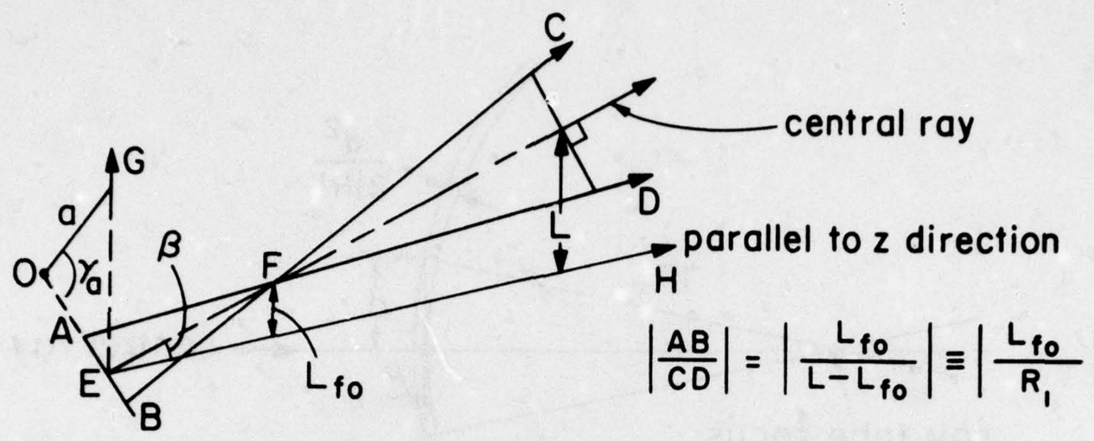

(a)

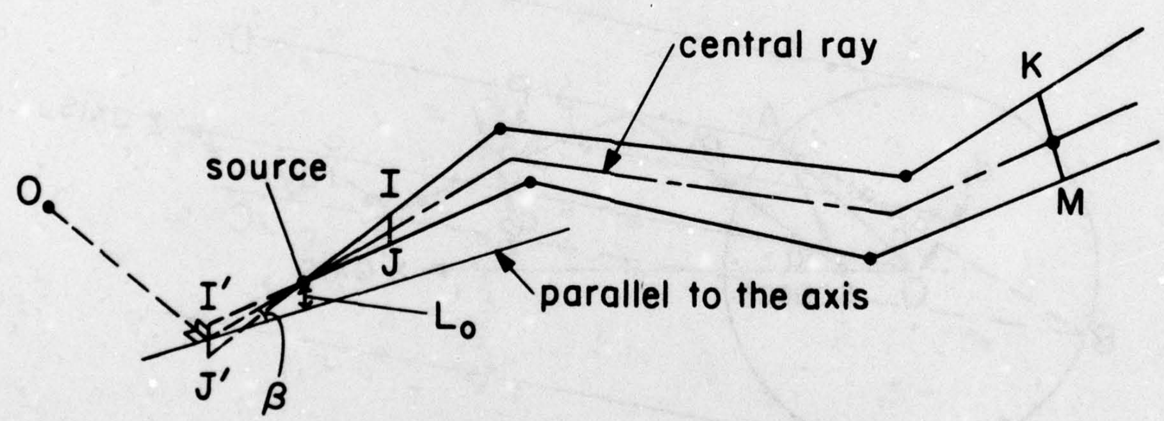

(b)

Fig. 5. Projections of ray tube in three dimensions

(a) Projection of ray tube in the direction of d_1.

Note: AB ∥ CD; lines AB and EG lie in the cross section; point E is at the center of the transversely projected ray path EG′ between reflections.

(b) Projection of ray tube in the direction of d_2.

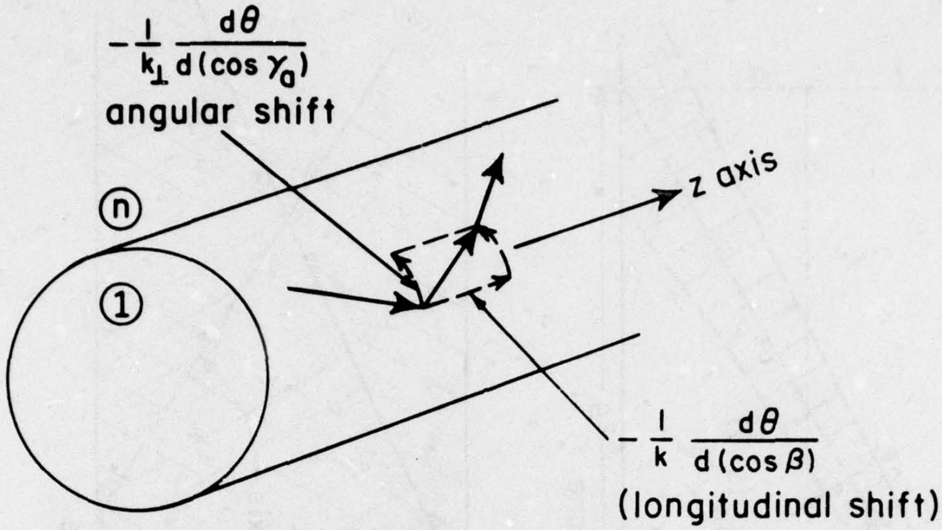

Fig. 6 Ray trajectories with lateral shift. The phase increment $\Delta\psi$ due to the conventional lateral shift $L_z = -d\theta/dk_z$ on a plane boundary is $k_z L_z$, where z is the coordinate along the boundary and k_z is the wavenumber along z. The analog for the curved boundary is $\Delta\psi = k_\phi L_\phi$, where $k_\phi = k\cos\gamma_a$ and $L_\phi = -d\theta/dk_\phi$.

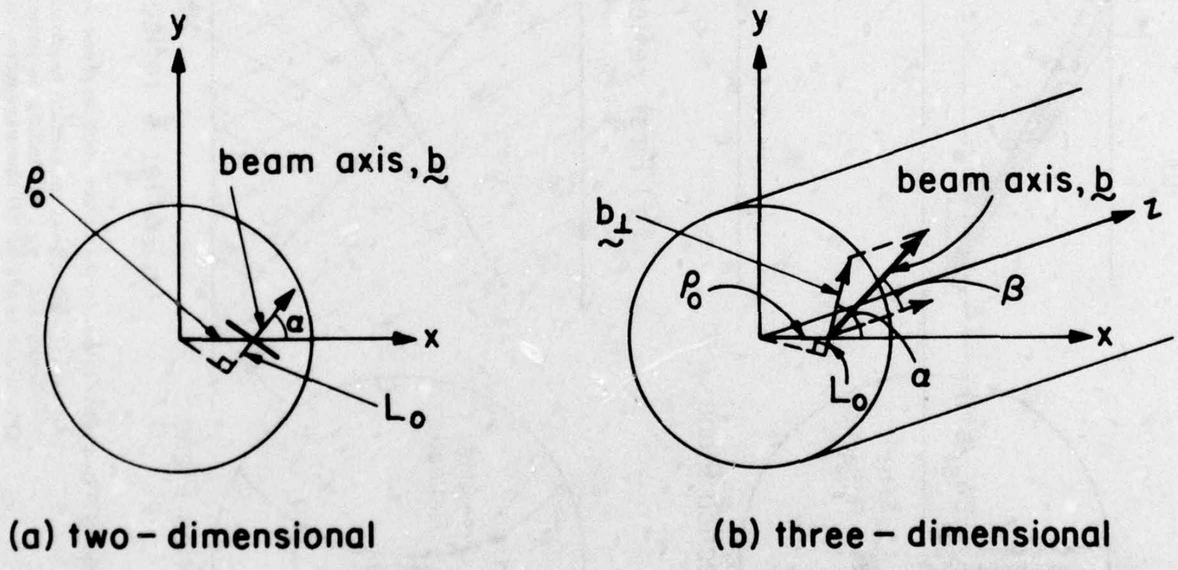

Fig. 7 Coordinates for beam problem

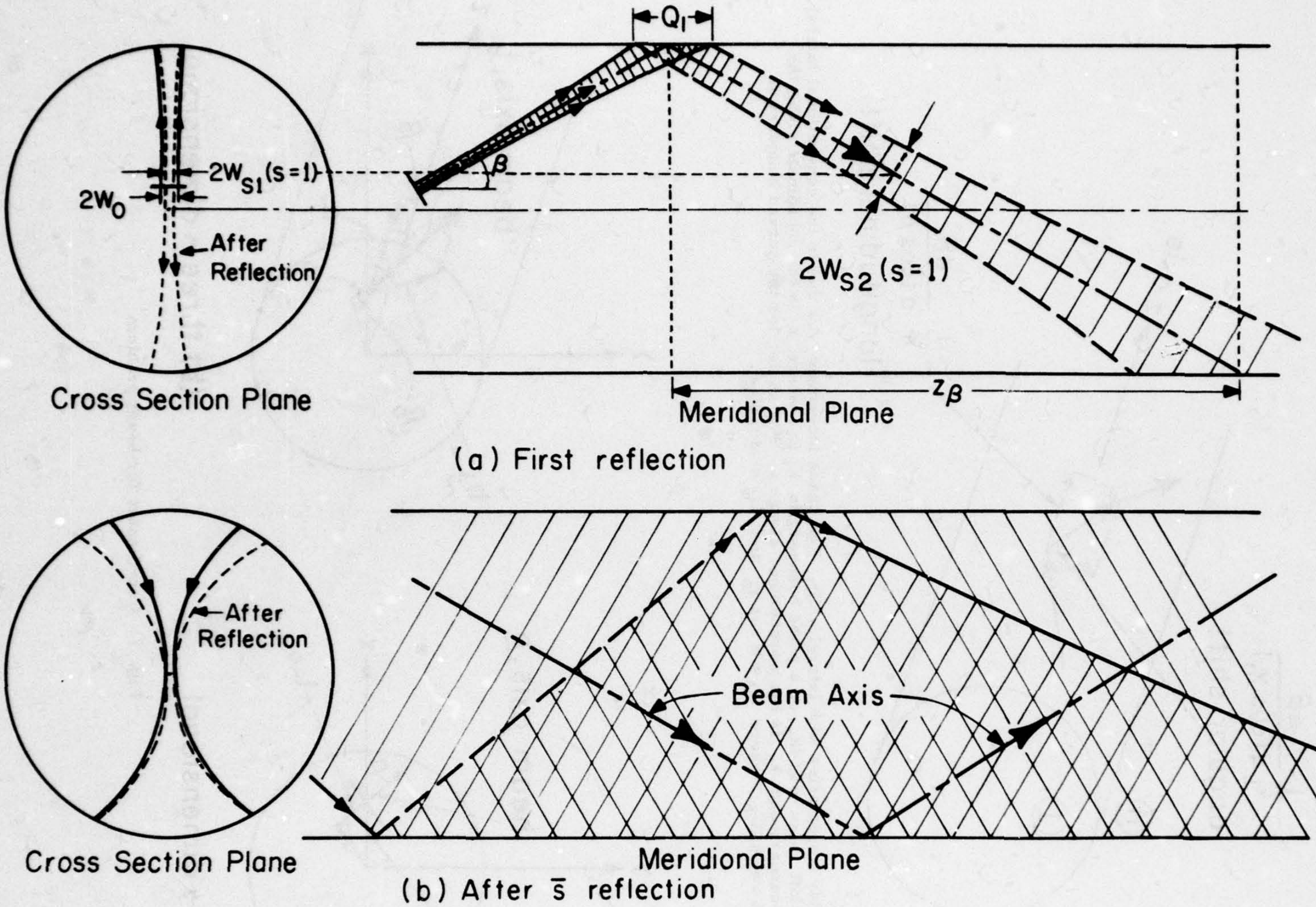

Fig. 8 Beam evolution in the cross section plane and the meridional plane

(a) First reflection: minimum beamwidths for few reflections can be larger than initial beamwidth w_o, depending on parameters involved.
(b) Beam tends to fill the waveguide completely in the meridional plane after $\bar{s}$ reflections.

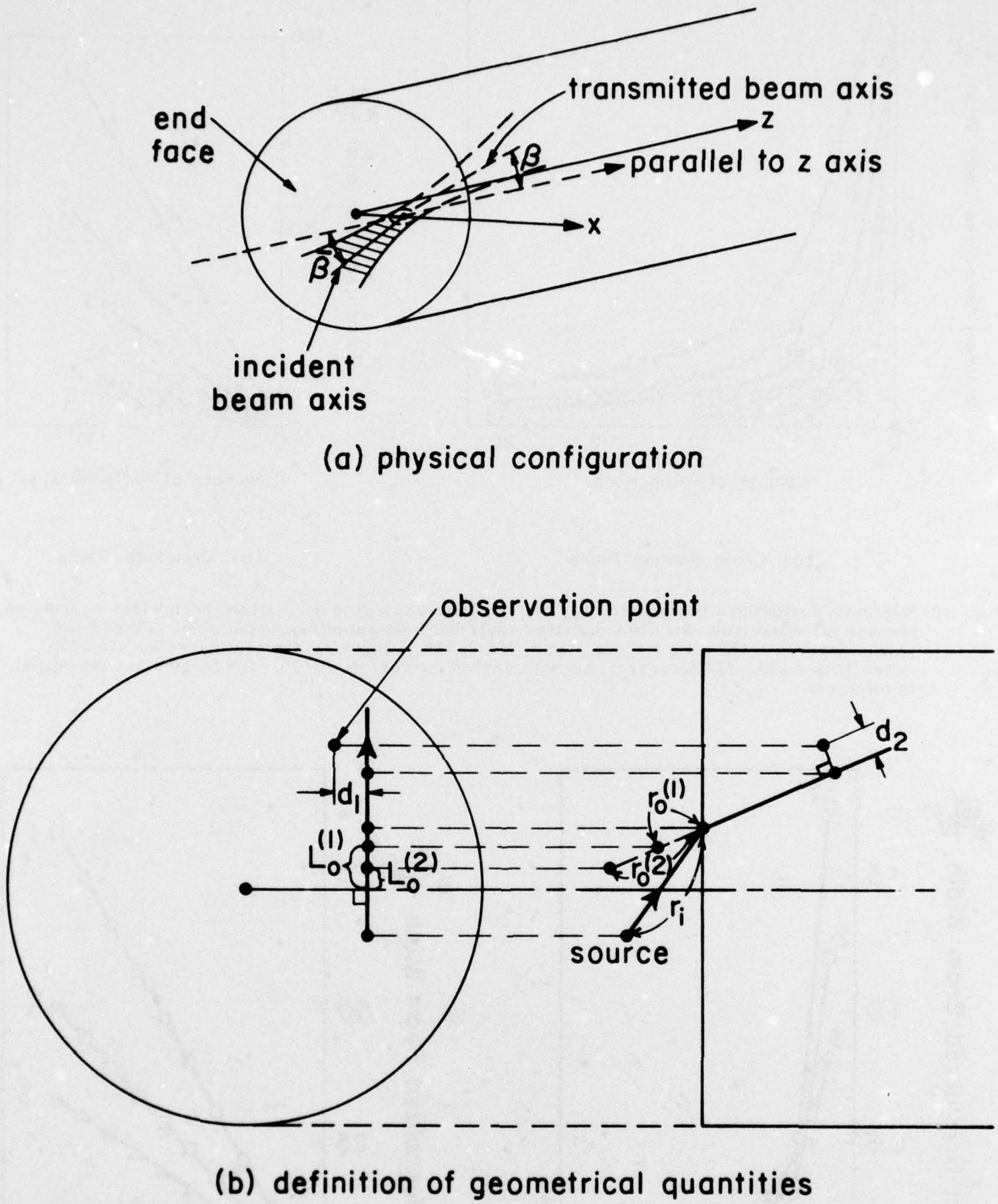

Fig. 9 Beam incident on fiber endface

(a) Physical configuration

(b) Definition of geometrical quantities. The right-hand side of the figure depicts the plane of incidence and the left-hand side depicts the projection on the endface. The distance $L_o^{(1)}$ and $L_o^{(2)}$ show the displacements of the virtual foci for the refracted ray from a horizontal axis through the center of the fiber.

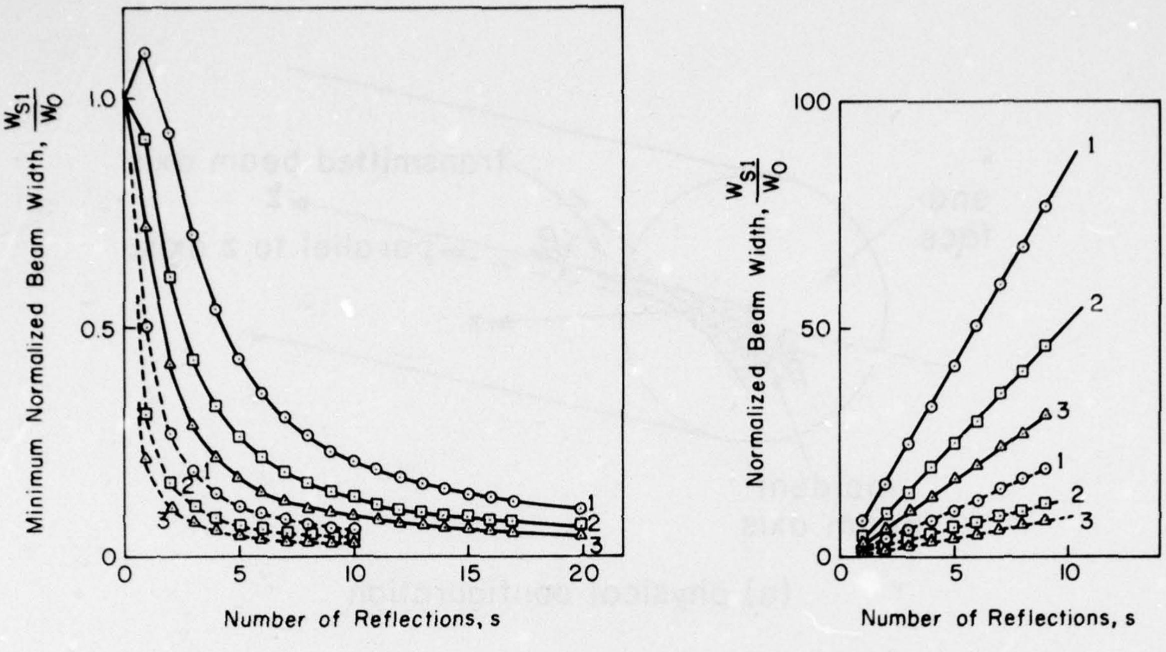

(a) Cross Section Plane

(b) Meridional Plane

Fig. 10 Minimum normalized beamwidth w_{s1}/w_o and corresponding normalized beamwidth w_{s2}/w_o vs. number of reflections, for different fiber radii and initial minimum spot size. Fixed beam parameters: $\beta = 15^o$, $L_a = a$, $L_o = a/9$, $k = 2.54\pi$. Curve 1: a = 450; curve 2: a = 270; curve 3: a = 180. Solid curves: b = 400; dashed curves: b = 1600. All lengths are measured in microns.

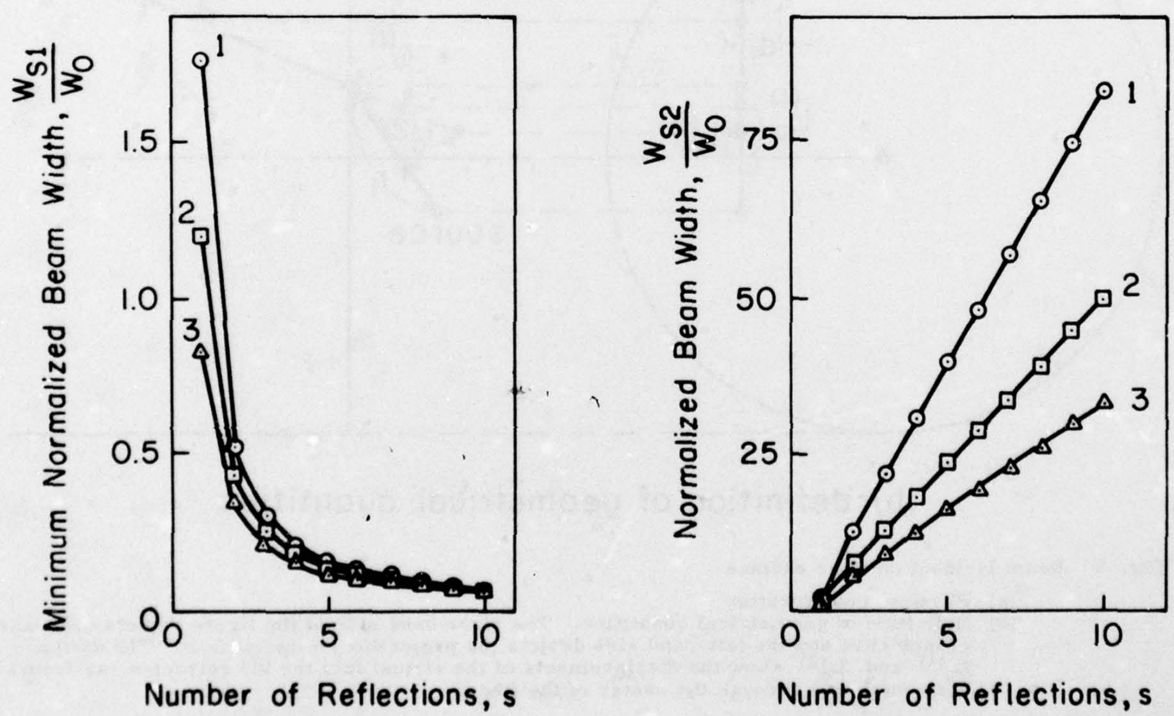

(a) Cross Section Plane

(b) Meridional Plane

Fig. 11 Minimum normalized beamwidth w_{s1}/w_o and corresponding normalized beamwidth w_{s2}/w_o vs. number of reflections. Beam parameters: $\beta = 15^o$, $L_a = a$, $L_o = 2a/3$, b = 400, Curve 1: a = 450; curve 2: a = 270; curve 3: a = 180. All lengths are measured in microns.

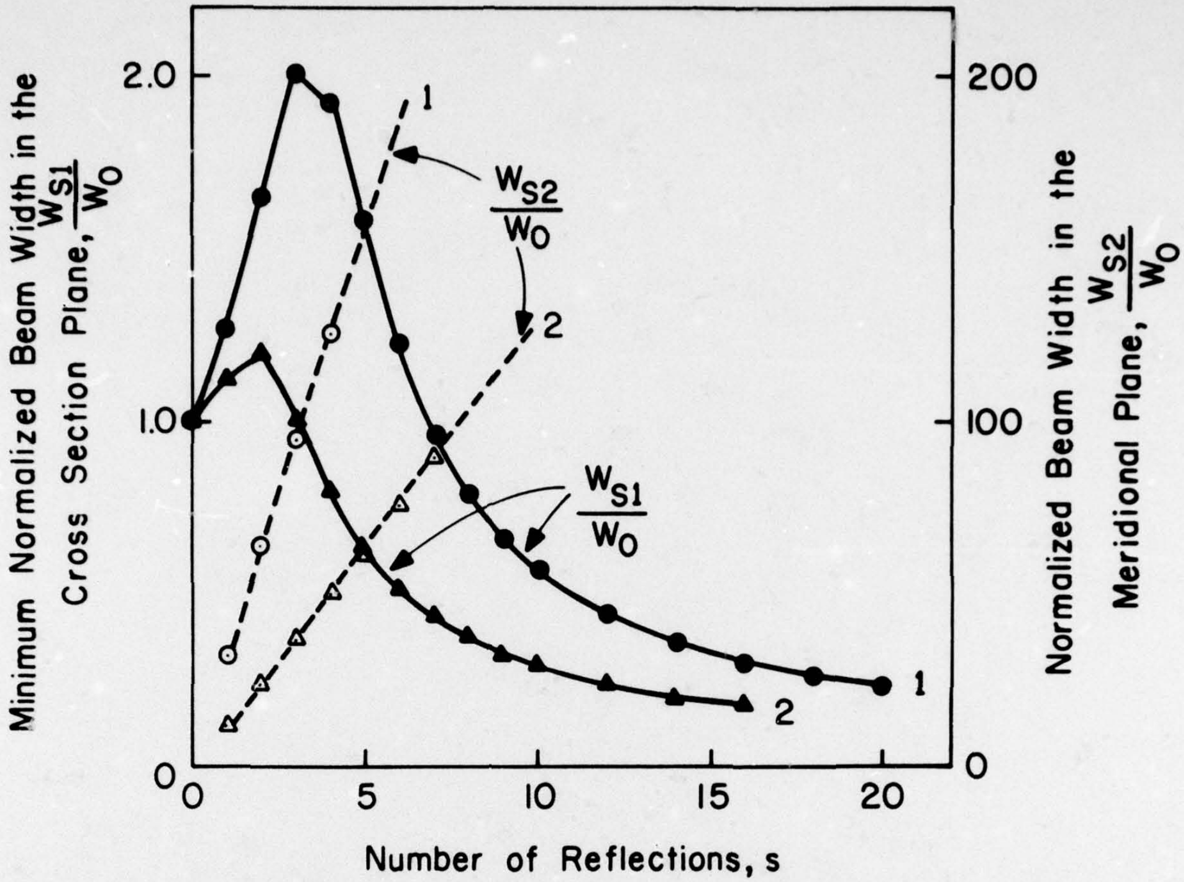

Fig. 12 Minimum normalized beamwidth w_{s1}/w_o and corresponding normalized beamwidth w_{s2}/w_o vs. number of reflections. Beam parameters: $\beta = 1^o$, $L_a = a$, $L_o = a/9$, $b = 1600$, $k = 2.54\pi$. Curve 1: $a = 450$; curve 2: $a = 180$. The solid line indicates w_{s1}/w_o and the dashed line w_{s2}/w_o. All lengths are measured in microns.

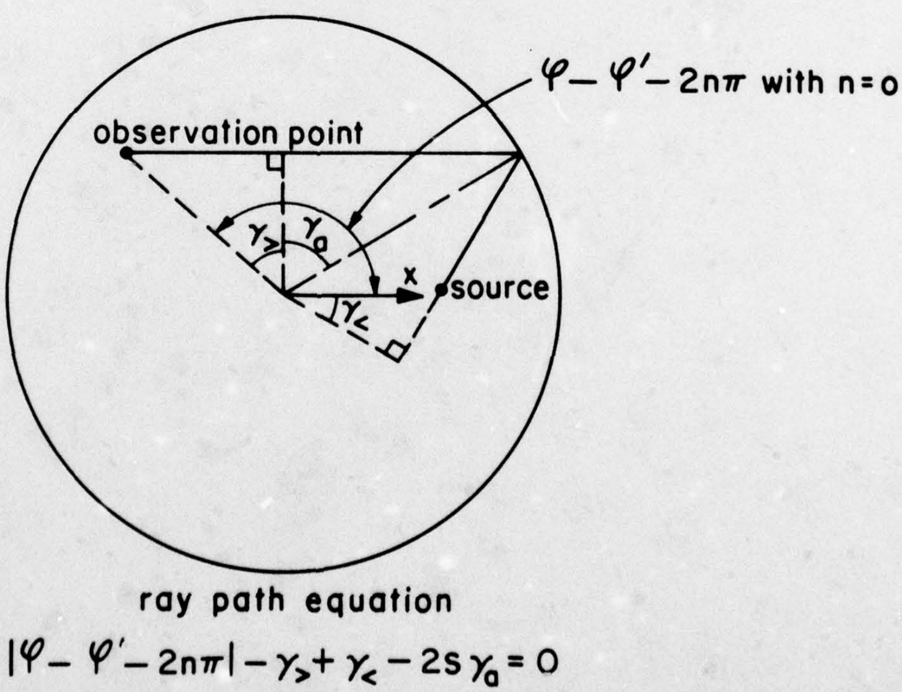

Fig. 13 Ray path and path equation.

TESTING OF TENSILE STRENGTH OF OPTICAL FIBER WAVEGUIDES

by
C.Kao, M.Maklad, J.Goell
ITT Roanoke
Roanoke, VA 24109, USA

Introduction

The tensile strength of an optical fiber waveguide is an important parameter. It determines both the stress levels permitted along the fibers during cabling and during service. In general, strong fibers require less exacting cabling machinery design and allows more flexible choice of strength reinforcing material for making up a cable to meet specific strength requirements.

The tensile strength of an optical fiber waveguide is governed by the existence of a stress concentration along the fiber, such that fracture stress is reached at that point. Current evidences suggest that surface flaws are principally responsible for the development of high stress concentrations and that failure of a uniformly stressed fiber in tension occurs at the deepest surface flaw. Furthermore, in the presence of moisture, the flaws over the fiber surface would enlarge under a stress level well below that of the fracture stress. This effect is known as fatigue or stress corrosion. The stress level, above which crack propagation takes place, is called the fatigue limit. Thus, if the service stress is higher than the fatigue limit, it could lead to premature failure.

The measurement of fiber strength is complicated by the statistical variation of fiber strength along the length of a fiber. If sufficient data can be gathered such that the statistics of the large but rare flaws are characterized, then extrapolation of statistical values of fiber tensile strength of one test gauge length to that of another may be defined with known confidence limits. Otherwise, extrapolation is at best fortuitous. On the other hand, if the nature of the rare flaws are known, then more suitable testing techniques may be evolved. What is desired is to have test procedures which enable reliable long length strength to be predicted, while the procedures should be simple and should not destroy more fiber than necessary. This paper indicates, by way of experimental evidences, how a testing procedure could be developed.

Discussion

If the fibers are made by a consistent process, then the statistics of flaws (conveniently expressed in terms of Weibull Distribution) is well defined. If there is more than one way for the flaws to be formed in that process, then the flaw distribution may be multimodal, and the Weibull probability plot may assume an "S" shape. This situation was commonly found in many fibers. In those cases, the statistics of the rare large flaws are extremely important to be determined accurately; otherwise, extrapolation for long length strength may lead to gross inaccuracies. If the flaws are caused by a single mechanism, then a linear Weibull plot results. In that case, the extrapolation accuracy should improve.

The above argument leads to the following test procedure. From short gauge length tests, the Weibull probability plot is constructed for a particular fiber, using

$$F= 1-\exp[(\sigma/\sigma_o)^m \ (L/L_o) \ (t/t_o)^r].$$

From the plot, the Weibull parameter m is determined. In the case of a non-linear plot, the determination of a valid m is in question.

Extrapolation of long length (L_2) strength from short length tests results at a particular failure probability is given by

$$(\sigma_1/\sigma_2)^m (L_1/L_2)=1$$

This can be substantiated by using a proof test at a stress equal to the expected stress where a given probability of failure will occur. For experimental purposes, the proof stress chosen may be for a 5% probability of failure, for a short gauge length of 2 m, so that by testing a few lengths of 1 km samples the extrapolation validity may be verified.

If m is not well defined, then the choice of proof stress becomes difficult. In such cases, proof tests must be carried out at different stress levels in order to determine the rare flaw distribution.

In the proof tests, it is necessary to take into consideration the stress corrosion effects. If the proof stress is applied over a considerable time, the fiber strength will decrease. The permissible duration can be inferred from the static fatigue failure data.

Sample Preparation and Test

The samples tested were prepared by drawing fibers of long lengths. The fibers were coated on-line with protective claddings to reduce the possibility of damage due to mechanical abrasion.

The tensile strength on short gauge length was obtained by the following technique. A long sample was divided into the number of specimens to be tested of specific gauge length. A specimen was then mounted on the tensile testor (Figure 1) by looping one end around a large diameter spool (d=4") which was attached to a tensile gauge (0-200 lbs.). The other end was threaded around another spool of the same diameter which was attached to a lever which was used to apply the load. The end of the fiber was then wrapped again around the first spool and attached. The load was applied at a known rate and the fracture load values read from the tension gauge.

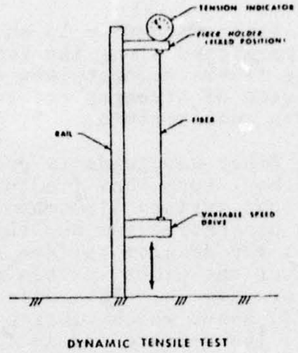

Figure 1

The test for long gauge length tensile strength was as follows. The long length sample was held on a spool and reeled off between two large rollers, as in Figure 2.

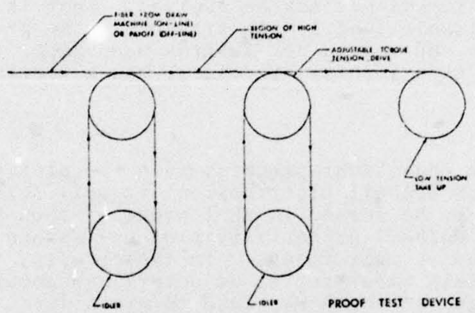

Figure 2

A tension gauge was used to measure the stress developed between the two rollers by a controlled slip clutch on the drive wheel. In this manner, the entire length of the sample can be tested.

Static fatigue tests were performed on short gauge length samples by winding over a series of mandrels of different sizes, simulating different tensile loads. Times to failure were recorded.

Experimental Evidences

A typical Weibull plot for a short (60 cm) length gauge test of a fiber sample (A) made without special precautions is as shown in Figure 3. This also shows an experimental

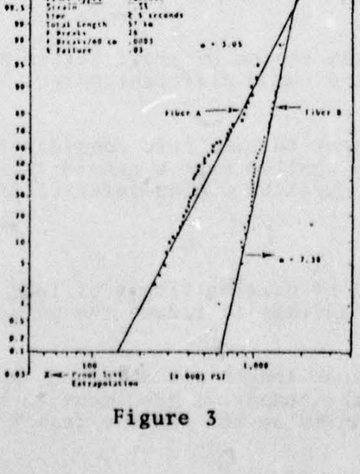

Figure 3

point derived from long length strength tests. This clearly illustrates a non-linear distribution.

A typical Weibull plot for a short length gauge test of a fiber sample made with special precautions is as shown in Figure 4. It can be seen that the m value is greatly improved and that the Weibull plot is linear, except a small tail distribution. Proof test at 500 kpsi confirmed the extent of the tail. Thus, short length test gives a good guide line to expected long length strength but extrapolation using the apparent m value would lead to optimistic estimation unless tail distribution is absent.

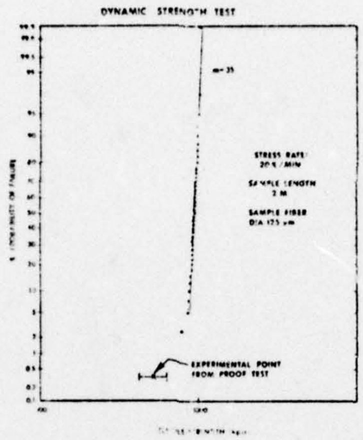

Figure 4

Static fatigue tests showed the time-to-failure for the same fiber (illustrated in Figure 5) at different stress. The n value was calculated from Figure 5 and was found to be 25. If the fiber is subjected even to a proof test load of about 400 kpsi for a duration of 10 seconds, the expected degradation from Figure 5 can be seen to be negligible. At a service load of 100 kpsi, the fiber is expected to last forever.

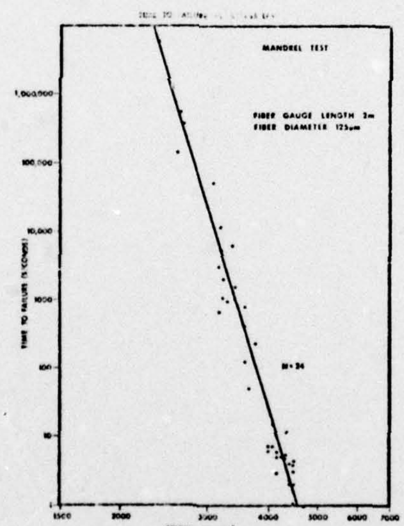

Figure 5

Concluding Remarks

The extrapolation of fiber strength for a long length fiber from short length strength tests is reliable only if the flaw distribution is well characterized. For a fiber with random flaws caused by several mechanisms, the extrapolation is unlikely to be reliable.

The test procedure which could be used to characterize fibers with specified strength is to conduct short length test coupled with proof test at about twice the service strength. For fibers made for high strength, this procedure allows high production yield as well as a guaranteed strength specification. For fibers made without special precautions, this procedure could still be adopted, but the fiber yield may be unacceptably low.

COLOUR MULTIPLEXING TECHNIQUES AND APPLICATIONS IN OPTICAL WAVEGUIDE LINKS.

David A. Kahn
Plessey Radar Research Centre
Havant, Hants., U.K.

SUMMARY

The feasibility of colour multiplexing is established in the paper by a review of the currently available components, namely sources, detectors, waveguides, and colour splitting/combining devices.

Operational systems employing colour multiplexing and developed in the author's laboratory are then described.

Finally, an assessment of the technique and the identification of the most likely application areas is given.

1. INTRODUCTION

Currently available optical fibre waveguides can have low attenutations over a very broad region of the spectrum extending from the visible, i.e. 0.5μm, up to around 1.8μm, almost two octaves of frequency encompassing a total bandwidth of approximately 4.10^{14}Hz. Within such a large bandwidth, a great number of channels can be accommodated by means of frequency division multiplexing (FDM) even where channel separation is extremely large by conventional standards (1). The term "Colour Multiplexing" is adopted to describe the technique and distinguish it from the use of subcarrier FDM with a single optical source.*†

2. SOURCES AND DETECTORS

2.1. Detectors.

The silicon photodiode and its derivatives efficiently detect radiation from the U.V. to about 1.1μm. The germanium photodiode extends the detection capability up to about 1.8μm (2) but generally suffers from a relatively large, noise generating dark current. New mixed crystal photodiode technologies are emerging based upon GaIn As (3), and CuIn As/CdS (4), which detect in the region beyond the silicon cutoff wavelength and yet have low noise, high speed and good quantum conversion efficiencies.

2.2. Sources.

Both semiconductor lasers and light-emitting diodes (LEDs) are potential candidates for colour multiplexing systems. Fast LEDs are available for a range of wavelengths from the visible up to beyond 1μm using such materials as GaAs, GaAlAs, GaP, GaInAs (5), where the central wavelength is to some extent programmable by the choice of the composition ratios. The large fractional bandwidth of the LED (3-5%) would limit the number of channels to a maximum of about 20, other factors notwithstanding.

The range of laser emission wavelengths for devices that can operate CW at normal ambient temperatures is at present more restricted, although all the indications are favourable.§ The associated narrow linewidths are desirable for colour multiplexing on the grounds of efficient spectral filtering and channel isolation.

3. COLOUR MULTIPLEXING TECHNIQUES

Colour Multiplexing and demultiplexing can be accomplished by any one of several passive optical elements including the grating, the prism, and the dichroic filter. Our experience is currently restricted to the dichroic filter techniques which will now be described.

The dichroic filter consists of a multilayer film deposited upon a transparent substrate which separates incident radiation into two colour bands, one of which is transmitted and the other reflected. Ideally, very little radiation is absorbed by such a filter, which is mounted at an angle of 45^0 to the incident radiation in order to separate the incident power from the reflected power. The arrangement is thus very similar to the design of a colour TV camera.

The spectral definition of a dichroic filter is sensitive to the angle of incidence and the operation of such a filter is degraded if used with a highly converging or diverging radiation flux, such as is normally associated with a fibre waveguide. The problem can be easily accommodated by the use of auxiliary lenses such that the radiation incident upon the filter is in the form of a collimated beam of relatively large diameter e.g. 2mm.

* Note, however, that no restriction to the visible region is intended
† Some authors refer to the technique as "Wavelength Multiplexing"
§ E.g. paper 35 of this conference

Whilst the dichroic filter is an efficient method of spatially separating two colour bands, it is by no means adequate by itself to achieve desirable levels of crosstalk rejection. This can be achieved by the addition of further filters in the receive channels. These additional filters can be of the interference type or the absorption type but must efficiently transmit the required channel wavelength whilst attenuating the other channel(s).

Similarly, it may be necessary to add filters at the source channel prior to multiplexing, as for example in the case of a LED, the spectral emission skirts are very broad albeit at low levels, and some devices are known to emit at a wavelength in addition to that specified/expected.

4. OPERATIONAL SYSTEMS

4.1. History.

Our first colour multiplexed link was designed and constructed in 1975 and carried radar video character information. The purpose of the link was to demonstrate that an optical link, in addition to providing the well categorised advantages of electrical isolation, interference immunity and reduced fire hazard, could also by virtue of its superior bandwidth replace several electrical cables. It was not originally envisaged that colour multiplexing would be used; however, when the design authority was offered the option of a dedicated clock channel (1), it was gratefully accepted as a means of considerably simplifying the terminal electronics, reducing design and test costs, and improving the system performance and versatility. The link was installed at the Admiralty Surface Weapons Establishment, U.K., in 1976 and is performing satisfactorily.

During 1976 we constructed for demonstration purposes another link wherein the colour multiplexing was arranged to provide a duplex facility i.e. one colour for each direction. In order to emphasize the versatility of the technique, one channel was designed to carry baseband analogue video for a CCTV system, whilst the other channel carries digital data. No crosstalk is discernable in spite of the adjacence of transmitter and receiver at both terminals.

The experience gained from the production of these two links was used to develop the commercial range of duplex secure communication links (SCL's). (6)

4.2. Technical details.

The terminals are designed as fully integrated units incorporated in a diecast box having a single demountable optical connector. The box also contains two electrical connectors with separate interfaces for full duplex (where applicable) operation, the optical transmitter(s), the optical receiver(s), the optical multiplexer, and the power supply with a power input connector. An outline system block diagram is shown in Fig. 1.

The terminals incorporate low-cost devices of high reliability, wide operating temperature range and long lifetime. The optical transmitters are LEDs operating at 670nm (red) and 900nm respectively. The receivers are p-i-n- silicon photodiodes with low-noise transimpedance amplification (7).

Demountable connectors are provided to enable ease of installation and maintenance. These are based upon the lens coupler (8) within the shell of a standard electrical connector. The lens coupler has a large area interface which ensures that the connector is relatively immune from the effects of dust and grime. It also provides a good interface with the dichroic filter as illustrated in Fig. 2.

5. USEFUL FEATURES OF COLOUR MULTIPLEXING

5.1. Freedom from format requirements.

This is probably the most useful feature of colour multiplexing. Frequently, the situation arises where there is a requirement to transmit two streams of information which are not readily compatible for multiplexing purposes without a significant investment in design analyses and hardware. As examples, one could cite two data streams with unrelated clock rates, or an analogue and a digital signal such as CCTV and Telegraph, or two RF signals where no crossmodulation is to be permitted. In these situations, colour multiplexing offers a simple solution.

5.2. Electrical Isolation

The electrical isolation that exists between terminals of an optical fibre link is well appreciated. However, with the use of colour multiplexing, electrical isolation between information channels can be maintained at both ends if required. This could apply to the earlier example where separation between two RF channels is of paramount importance.

5.3. The power/bandwidth S/N advantage

Whereas using electronic multiplexing, the information channels have to share the total optical power which is limited by radiance considerations, with optical multiplexing, the total optical power is increased in proportion to the number of colour channels. The situation becomes even more interesting if one recalls that the electrical noise power from a photodiode amplifier of low-noise design scales with the cube of bandwidth. Thus if one compares S/N ratios given two similar information sources to be multiplexed and a choice between colour multiplexing and electronic multiplexing, the ratio becomes 8:1 or 9dB. in favour of the former. This assumes that the electronically multiplexed link requires twice the bandwidth and that all LEDs involved deliver equal powers to the receiver. In general, the S/N improvement is given by $30\log_{10}n$ dB where 'n' is the number of colour channels. Alternatively, for a given S/N ratio, the required optical power per colour channel is reduced by $15\log_{10}n$ dB.

5.4 The passive mux/demux element.

The use of a multiplexer that is passive i.e. consumes no power, and consists simply of a multiple film on a glass substrate should ultimately be more reliable and cheaper than alternative solutions employing electronics.

5.5 Reserve capacity.

Any optical waveguide installed is capable of supporting additional communications channels of almost any form by means of colour multiplexing, without prejudice to its original and ongoing functions.

6. SPECIAL APPLICATIONS

6.1. Duplex operation.

This capability has already been described. It should of course result in substantial cost savings because of the halving of the cable requirement and the associated simplification of connectors.

6.2. Bandwidth expansion.

Over longer ranges where the dispersion of the waveguide limits channel capacity using a single carrier, the waveguide capacity can be increased in proportion to the number of colour channels.

6.3. Dedicated clock.

This application has also been mentioned as a means of system simplification and consequent cost reduction. It may be noted that the power needed for a clock channel is minimal, enabling low radiance devices to suffice for this purpose. (1)

6.4. Highway control.

On an optical databus, a design option is to transmit data on one colour channel, whilst using another colour channel for highway control, routing, timing etc.

6.5. Highway multiplexing.

Different elements of a military system e.g. an aeroplane may require different highways with different protocols. Thus one could envisage a weapons highway, a flight-control highway, a communications highway etc. By the use of colour multiplexing, all highways could share the same waveguide.

6.6. Line Integrity Monitor.

A dedicated colour channel could be assigned to monitoring the integrity of a link. This feature could be designed in as part of a damage-adaptive strategy for fighting vehicles, aircraft and ships. In a different field, it is of some significance in the design of secure communications links.

6.7. Instrumentation.

There is currently a considerable interest in the possibilities of using optical (non-electrical) transducers for various instrumentation purposes in aircraft and other environments. The impetus behind this interest is based upon the concept of compatibility with optical fibres and the resultant benefits in terms of interference immunity, lack of spark hazard etc. The use of colour coding enables the outputs from these transducers to be transmitted down a single optical channel which is highly desirable. In these cases, the colour could be a direct analogue of the quantity to be measured or colour channels could represent digital code channels.

7. CONCLUSIONS

In summary, it is evident that the components necessary for the implementation of colour multiplexing are now available, i.e. the sources, the detectors, the filters, and the waveguide. Furthermore, a standard two-colour link for simplex or duplex operation has been developed, based upon the use of the dichroic filter in conjunction with the lens coupler.

Advantages of colour multiplexing include:

(a) Freedom from format constraints.
(b) Significant increase in S/N ratio.
(c) Large reserve capacity for waveguides already installed.
(d) Optical isolation between channels.
(e) Use of simple, passive mux/demux element.

Potential Applications include:

(a) Single fibre duplex operation.
(b) Bandwidth expansion on dispersion limited links.
(c) Provision of a dedicated clock channel.
(d) Provision of a line integrity monitor.
(e) Instrumentation coding.
(f) Highway control.
(g) Highway multiplexing.

It is the view of the author that many of the advantages and applications outlined will introduce substantial cost and reliability benefits over alternative schemes and that the emergence of colour multiplexing should heavily influence the evolution of optical waveguide systems architecture.

8. REFERENCES

1. KAHN, D.A., September 1974. "Optical Waveguide Data Transmission for Avionics". AGARD LS-71(5).
2. CONRADI, J., August 1975, "Planar Germanium Photodiodes", Applied Optics, 14, 8.
3. MABBIT, A.W., and AHMAD, K., 1976. "The Fabrication of Leds and detectors from the GaInAs system", International Electron Devices Meeting, Paper 25. (Washington DC).
4. WAGNER, S., SHAY, J.L., MIGLIORATO, P., KASPER, H.M. October 1974. "$CuInSe_2$/CdS heterojunction photovoltaic detectors", Appl. Phys. Letts., 25, 8.
5. MABBIT, A.W., MOBSBY, C.D., GOODFELLOW, R.C., September 1975. "High Radiance Gallium Indium Arsenide Light Emitting Diodes for Fibre Optic Communication Applications". IEE Conference Publication No. 32.
6. -------. "Secure Communication Links", January 1977. Plessey Publication RSL 2002.
7. KAHN, D.A., October 1970. "Wideband low-noise optical detection using photodiodes". Plessey Technical Note ERL/N 242 U.
8. U.K. Patent 1429843.

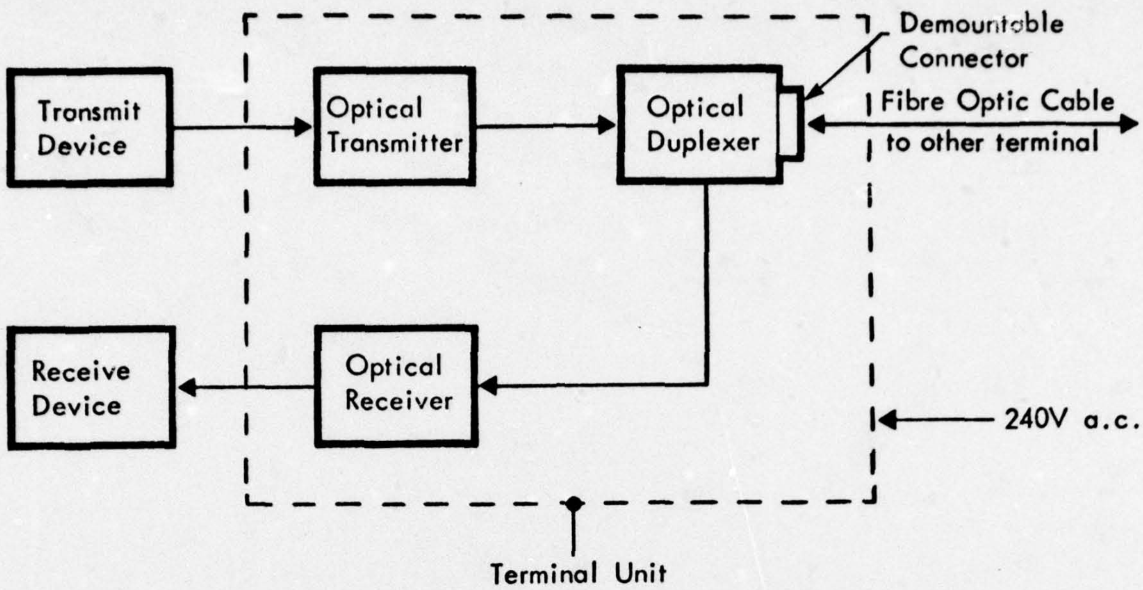

Fig.1 Secure communications link – system block diagram

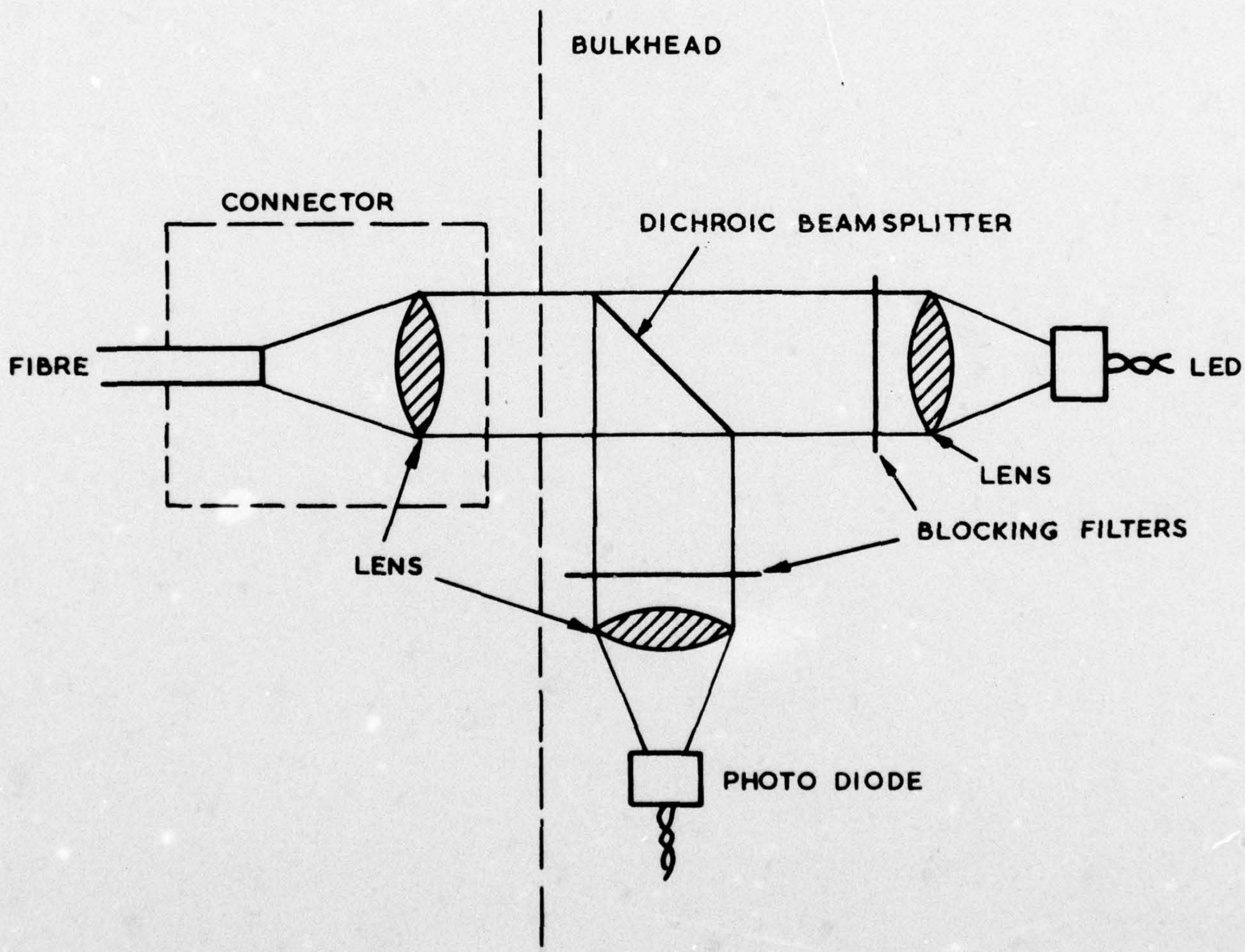

Fig.2 Optical terminal layout

QUESTIONS AND COMMENTS ON SESSION 1

REVIEW AND ASSESSMENT OF FIBER OPTICS FOR MILITARY APPLICATION
H. Taylor

Dr. Sandbank: Please could you enlarge on your point that graded index fibers are needed for shipborne data links - i.e. what is maximum path length, bandwidth, etc.?

Dr. Taylor: Links involved are roughly 1/2 Km long. Dan Altman of NELC showed that graded index fibers are needed for the following reason: In order to minimize the interface with the electronics the electrical carriers (FSK modulated) are directly converted to light signal and their frequency extends from 41 MHz to 83 MHz.

FIBER OPTIC SYSTEMS FOR DEFENSE APPLICATIONS IN THE UK
B. Ellis

Dr. Stringer: You have described high bandwidth and digital optical fibers generally for aircraft application. Do you see any objection to the application of the technology to analogue tasks.

Dr. Ellis: I think fiber-optics is very well suited to the sort of application you have mentioned.

Dr. Magne: About the Army application presentation slide: are the fiber optics cables supposed to be lost after a move of the tactical communications network?

Dr. Ellis: No. It is anticipated that the fiber cables would be recovered.

Dr. Elmer H. Hara: (1) You mentioned 100 μW launched into the fiber. Do you think this could be increased to, say, 0.5 mW in the future? (2) Have you made any measurements on the linearity of the LED?

Dr. Ellis: (1) I would be surprised if we could get much more than 100 μW from a 400 MHz device. It must be realized that 100 μW is already quite an impressive figure for a device of this speed and is quite adequate for most application. (2) Some preliminary measurements of non-linearity have been made but it would be premature to give details.

Dr. P. D. Baker: Reference has been made to the use of fiber optics in avionics; the engine is also part of an aircraft in addition to the fuselage. A fibre optic mounted upon a jet engine experiences the extremes of environmental temperature -50° to greater than 300°C (570°F), and vibration levels in excess of 20g; it should also be capable of providing a hand hold! A fibre optic functioning under these conditions is expected to have a life well in excess of 1000 engine operating hours.

A REVIEW OF NASA FIBER OPTIC TASKS
A. R. Johnston

Dr. H. Beger: (1) Have you observed or do you expect at higher radiation levels disturbances by scintillation effects in the fibers? (2) Shielding of fibers against space radiation may help only against low energy radiation.

Dr. A. R. Jonston: (1) We feel that scintillation errors will be very unlikely. However, the LOEF orbital experiment will be set up to detect errors of this type if they occur. (Comment by Dr. Maklad of ITT Roanoke: The light from scintillation is broad band and can be effectively discriminated against with an appropriate filter.) (2) Yes, shielding cannot be expected to lower the radiation dose on a fiber except for the very low energy portion of the radiation spectrum. For earth orbit applications, significant shielding is expected from typical spacecraft structure.

FUNDAMENTAL MODE SIGNAL TRANSMISSION IN SINGLE AND MULTIMODE FIBRES
H. G. Unger

Dr. Clarricoats: Does your theory apply to moderate v-value fibres?

Dr. Unger: The present theory for fundamental mode propagation in perfect and imperfect fibres, and for signal loss and distortion in this mode applies for any v-values for which the fibre guides this mode. It lumps all higher order modes into a quasi-mode, however, and is hence not suited to study multi-mode signal transmission.

BEAM EVOLUTION ALONG A MULTIMODE OPTICAL FIBER
L. B. Felsen, S. Y. Shin

Dr. Unger: Is the lateral Goos-Hahnchen Shift, which is being contemplated recently related to the lateral component of beam shift that has been discussed in the paper?

Dr. Felsen: The ray and beam shifts in the paper, as developed for curved boundaries, are new but they do relate to the transverse lateral shifts on plane boundaries discussed in some recent literature. However, various published results for both the longitudinal and transverse shifts are not in agreement with one another. The discrepancies can be traced to different ad hoc assumptions built into the analyses, which lead to inconsistencies in some instances and to incorrect models in others. We have recently examined the entire subject of lateral ray and beam shifts within a rigorous framework based on the solution of the electromagnetic boundary value problem when a ray field or beam field impinges upon an interface separating two different media. We have established criteria for conditions that permit the reflected beam to be interpreted as originating from a shifted position on the interface, with a phase center displaced from the location of the shifted image point of the incident beam waist. The simple formulas for the beam shifts, which we have derived, are further justified by the fact that they lead to the correct conversion of multiply reflected ray and beam fields into modal fields when an incident ray or beam is reflected repeatedly at the boundaries of a planar or fiber waveguide; omission of the lateral shifts, or use of shifts different from ours, yields an incorrect dispersion equation for the guided modes. These results are contained in a forthcoming paper by S. Y. Shin and L. B. Felsen, "Lateral Ray and Beam Shifts at an Interface Separating Two Media," to be published in the Special Issue of Radio Science devoted to Integrated Optics and Optical Fiber Communication.

TESTING OF TENSILE STRENGTH OF OPTICAL FIBER WAVEGUIDES
C. K. Kao, M. Maklad, J. E. Goell

Dr. F. S. Stringer: Have you looked at flat cable flexing?

Dr. Maklad: No, we have not studied flat cable flexing. However, the strength of the flat cable is expected to be similar to that of a single fiber. An adverse effect on fiber strength would be possible if fiber crossover is present in the cable configuration.

Dr. Gordon L. Mitchell: How do you grip fibers? We have hard problems with short (high strength) fiber samples pulling out of grips, even when they are cemented in.

Dr. Maklad: Each fiber end is wrapped around the spool once and then taped. This method provided enough traction to prevent fiber slippage.

COLOUR MULTIPLEXING TECHNIQUES AND APPLICATIONS IN OPTICAL WAVEGUIDE LINKS
D. A. Kahn

Dr. Elmer H. Hara: (1) In your duplex link what optical power isolation did you achieve? (2) What coupling efficiency did you achieve from your light source to a fiber using the dichroic filters and lenses?

Dr. Kahn: (1) The crosstalk between the channels was not evident and I would estimate it to be no more than -40 dB (optical) and probably never -60 dB. (2) The additional loss (at a receiver) introduced by the lens, the dichroic filter and the blocking filter is estimated at between 1.5 and 2 dB, largely caused by Fresnel reflections. [A similar figure applies to the transmitter terminal.] None of the components had antireflection coatings. The overall coupling efficiency is otherwise essentially radiance limited.

Dr. A. G. Glowe: Could you comment on the ability of the technique to handle the military temperature range? Presumably the sources would have to be tracked by the dichroic filters.

Dr. Kahn: Dichroic filters are robust elements that can sustain the military temperature range. For most of the system applications which I described, only two or three "colour" channels are required and consequently the band separation can be very large, thus making the effect of source or filter drift of no consequence. For example, on the two systems developed by Plessey, the two wavelengths are 670 nm and 900 nm respectively.

Summary of Session I

OVERVIEW

by
F. S. Stringer

Session Chairman's Comments

1. This session, particulary papers 1-5 inclusive, provided an encouraging indication that optical fibre technology can achieve already most of the capabilities of conventional conductor techniques, but with very attractive and additional advantages. It is noteworthy that cost was considered only fourth in order of importance and cost was mainly relevant to civil aviation needs. Protection from EMI, better handling of multiplex digital systems, with weight and space saving offered the most attractive advantages. Examples shown for aircraft applications were dramatic.

2. New components offer many novel techniques to obtain star and tee joints, couplers and filters. It is evident a lot more work is needed however before rationalized standards can be achieved.

3. Useful information is now available on the subject of performance loss when cables are subjected to radiation from nuclear sources. Only broad information was available to the conference.

4. Marine applications, particularly for underwater purposes, were covered and the presentations pointed to a lot of work which has been done already. Though considerable care is needed to design for high resistance to stress and weight problems, recent advances in high strength cladding are of interest.

5. The presentations on fundamental theory should prove helpful, particularly the methods of using, or in some cases removing, multimodes. The discussion on tensile strength of optical fibres had obvious and useful application to the remote control of equipment and to avionics systems connections which are subject to flexing.

6. Questions were limited to two or three per lecture, not due necessarily to timing, but apparently to a reticence on the part of delegates generally. Those questions which were asked however demonstrated a genuine specialist interest. It was evident from the questions that the conference was not regarded as a forum for elementary education on the subject, but it was of interest to specialists in the field.

7. The interest in colour multiplexing should be intense, since it offers an increase from current state of the art bandwidths of up to 10^6 - 10^7 Hz to a new upper limit of 10^{14} Hz. Silicon detectors were mentioned, also mixed crystal detectors. The potential is available for the application of LEDs for colour systems. Lasers are a suitable alternative and dichroic fibers are an interesting innovation. The integrity of system data transmission may be enhanced considerably by the introduction of colour. It is a pity that the subject was not treated in more depth, but it is to be hoped more will be said about it in the final discussion period.

AN EXPERIMENTAL OPTICAL-FIBER LINK FOR THE COMMAND AND CONTROL SYSTEM 280

Elmer H. Hara and H.Claire Frayn
Communications Research Centre, Department of Communications
Ottawa, Ontario, Canada K2H 8S2

SUMMARY

The development of an experimental optical-fiber link for the Command and Control System (CCS-280) for the DDH-280 Destroyer Escorts of the Canadian Navy is described. The objective of the task was to demonstrate the viability of optical-fiber transmission systems in combat action data systems such as the CCS-280. The experimental optical-fiber link, located between two Situation Display Consoles, consisted of 31 channels transmitting the digital signals between the two Consoles. Single optical fibers were used for each transmission channel, some of which carried time division multiplexed signals at a maximum bit rate of 10 Mb/s. The optical fibers were enclosed in an armoured sheath to form a cable of approximately 2.5 cm in diameter and 4 m in length.

Experimental trials were carried out on a land-based CCS-280 at the Canadian Forces Fleet School in Halifax, Nova Scotia, Canada. When acceptance tests established for the CCS-280 itself were applied to the optical link, the tests were satisfied with zero defects and the optical link performed satisfactorily under simulated combat conditions.

1. INTRODUCTION

The Communications Research Centre (CRC) of the Department of Communications (DOC) was asked early in 1973 by the Action Information Systems Section of the Directorate of Maritime Combat Systems (DMCS-7) of the Department of National Defence (DND) to address a connector breakage problem in the cable system for the Command and Control System 280 (CCS-280) of the DDH-280 class destroyer escorts. Because the cables carrying digital signals were large and stiff, movement during maintenance of the terminals linked by these cables often placed stress on the connectors sufficient to break some connector pins. Such breakage could severely reduce the combat readiness of the destroyer escort. The possibility of using an optical-fiber link to solve the problem was suggested by DND.

After the problem was studied, it was concluded that the breakage could be avoided by conventional remedies such as:

(1) redesign of the cable clamping structure on the connector casing so that the cable is securely clamped and the mechanical strain is borne fully by the protective outer casing of the cable,

(2) development of a cable comprised of much smaller individual coaxial cables (e.g. RG-178u) which would be lighter and more flexible, and

(3) development of a multiplex-demultiplexing system to reduce the number of transmission channels.

These conclusions were discussed with DMCS-7, who confirmed that a new cable clamping design and a multiplexing system were under consideration. Although the new clamping design was well underway, the multiplexing system was not progressing well because of prior commitments to other tasks. It was then pointed out that a major interest of DMCS-7 was to demonstrate the application of optical-fiber links as alternatives to coaxial-cable systems because of the inherent advantages of optical fibers such as the immunity to electromagnetic interference (EMI) and radio frequency interference (RFI) and the elimination of ground loop problems. An optical-fiber solution to this particular problem would serve to alert and inform armed forces personnel of the advantages of optical-communications technology in military systems. In particular, the viability of optical-fiber links in military applications would be demonstrated by a successful operation of such a link in a combat action data system such as the CCS-280 where complex digital signals ranging from near DC to megabit-per-second pulse rates with fast rise and fall times and critical timing relations are required. For these reasons, the CCS-280 Optical Link Task was formally approved by DOC and DND in October 1973. The Task was completed in January 1976 with the installation and successful operation of the experimental optical link in the CCS-280 located at the Canadian Forces Fleet School in Halifax, Nova Scotia, Canada. This report summarizes technical aspects of the Task.

2. OPTICAL-FIBER LINK

Table 1 lists the two major contracts issued for the Task. The prime contractor Litton Systems (Canada) Ltd. who was charged with overall responsibility of the Task while Bell-Northern Research Ltd. (BNR) was contracted to supply the optoelectronic components. The BNR design based on the single-fiber-per-channel approach was chosen over the usual bundled-fiber designs because it would provide a smaller cable and it was felt that the single-fiber design would become the standard in the future.

TABLE 1

TASK CONTRACTS

1. Prime Contract ($97,500.00)

Contractor:

Litton Systems (Canada) Ltd., Rexdale, Ontario Canada

Requirements:

To design, construct and test the optical link by

i) designing and fabricating the multiplexing and demultiplexing units,

ii) testing and debugging the multiplexing and demultiplexing units through a hardwire link,

iii) integrating the optoelectronic units into the system,

iv) testing and debugging the optical link,

v) installing, testing and debugging the optical link at the Canadian Forces Fleet School in Halifax, and

vi) providing technical assistance during the Acceptance Tests.

COMPLETED, January, 1976.

2. Optoelectronic Components Contract ($63,000.00)

Contractor:

Bell-Northern Research Ltd., Ottawa, Ontario, Canada.

Requirements:

To design, construct and test optoelectronic components consisting of 32 sets of

i) transmitter units which contain

a) LED drivers with TTL compatible input,
b) Burrus type LEDs,
c) fiber couplers, and

ii) receivers units which contain

a) fiber couplers,
b) PIN photodiodes, and
c) post detection amplifiers with TTL compatible output.

To design construct and test and optical fiber cable 4 m in length containing a minimum of 31 transmission channels.

COMPLETED October, 1975

2.1 Combat and Control System 280

A block diagram of the CCS-280 display system is shown in Fig. 1. The Situation Display Consoles (c.f. Fig. 2) are connected to the computer through the electronic marker generator (EMG). Each Situation Display Console (SDC) has a large cathode-ray tube (CRT) that displays the combat situation and a small CRT that displays file information. An operator monitors the displays and provides input to the central computer for action. An analogue and digital signal cable system interconnects the SDCs in "daisy-chain" fashion.

For the experiment, the digital signal cable between SDCs No. 5 and No. 6 was replaced by the optical-fiber link. By choosing the last link in the sequence of SDCs, disconnection of the optical-fiber link for fault location was facilitated.

The multiplicity of connections to an SDC is clearly seen in Fig. 3. Each SDC has attached to it an input and an output digital plug along with analogue and other cables. Each digital cable plug combines two 78-pin connectors, and terminates two 1.25" diameter cables and 14 copper wires. Among the 54 lines that are used actively, there are 32 bidirectional data lines. A close-up of the input and output digital plugs is shown in Fig. 4.

2.2 Optical-Fiber Transmission System

Since bidirectional optical-fiber links were impractical to construct, time division multiplexing (TDM) was used to reduce the number of data lines to 10 (5 in each direction). The control lines were not multiplexed because of the random nature of their pulse timing. Table 2 summarizes the functions of the resulting 31 optical transmission lines.

TABLE 2

NUMBER OF OPTICAL TRANSMISSION LINES

Function	Optical Transmission Lines
Output Data/Parity	5
Output Controls	6
Symbology Output	10
Reset, Synchronization	3
Input Data/Parity	5
Input Controls	1
Light-Pen Interrupt	1
Total	31

Examples of the pulse timings for the optical-fiber link are shown in Fig. 5. A clock rate of 10 Mb/s was chosen for the multiplexing and demultiplexing (MUX/DEMUX) system in order to take advantage of the readily available transistor-transistor logic (TTL) technology. Although the maximum bit rate was set at 10 Mb/s, rise and fall times of 10 ns were required to preserve the relative positions of the leading and trailing edges of the critical timing pulses. The stringent timing condition also dictated that the skewness between any two lines be less than 20 ns. The required characteristics of the input and output pulses of the optoelectronic units for data transmission are shown in Fig. 6. Due to the random nature of the control pulses of the CCS-280 where certain logic states are maintained for periods in excess of 100 μs, the optoelectronic system was required to be not only TTL compatible, but also DC coupled. The electronic specifications for the optoelectronic system are listed in Table 3.

TABLE 3

ELECTRONIC SPECIFICATIONS FOR THE OPTOELECTRONIC UNITS

Maximum bit rate	10 Mb/s
Rise and fall times	<10 ns
Error rate	<1 in 10^9 bits
Skewness between any two channels	≤20 ns
DC coupled, TTL compatible	

The general assembly of the optical link is shown in Fig. 7. The optoelectronic components are housed with the MUX/DEMUX system in two cabinets, as shown. The coaxial-cable transmission system is terminated at a junction box (J-box) contained in the coax-fiber-interface cabinet. A functional diagram of the multiplexed optical link is given in Fig. 8.

2.3 Optoelectronic Components

Figure 9 shows a transmitter and receiver pair, along with a short optical fiber used for testing the units. A circuit diagram for the transmitter unit is shown in Fig. 10 and the characteristics are listed in Table 4. A potentiometer (R_1 = 10 kΩ) was

TABLE 4

TRANSMITTER UNIT CHARACTERISTICS

Input	TTL Compatible
Peak emission wavelength	830 nm
LED maximum dc current	60 mA
LED maximum peak current (1 μs pulse, 10^5 pps)	100 mA
Light turn-on and turn-off time (10 - 90%)	<10 ns
Power supply requirements	+12 V ± 0.1 V @ 90 mA (@ max. LED current of 60 mA)

TABLE 4 (continued)

Electrical connector	Mates with edgeboard connector, 0.100" centers (e.g., ITT Cannon G05 D16A2BA3L)
Optical output connector	Single-fiber bulkhead connector jack (BNR C-10)
Dimensions	0.9" x 2" x 2"
Operating ambient temperature range	+10° to +40° C

provided to allow adjustment of the bias current through the light emitting diode (LED). Figure 11 shows the circuit diagram for the receiver unit and Table 5 lists the characteristics. Interstage coupling is DC to provide compatibility with the CCS-280 control signals. Since the optical link was an experimental development, adherance to MIL specifications was not demanded.

TABLE 5

RECEIVER UNIT CHARACTERISTICS

Photodetector	BNR D-5-2
Electrical output	TTL compatible
Output rise and fall time (0.8 - 2.0 V)	<5 ns (output terminated with a TTL gate)
Power supply requirements	+12 V ±25 mV @ 60 mA - 5 V ±50 mV @ 10 mA
Electrical connector	Mates with edgeboard connector, 0.100" centers (e.g., ITT Cannon G05 D16A2BA3L)
Optical input connector	Single-fiber bulkhead connector jack (BNR C-10)
Dimensions	0.9" x 2" x 2"
Operating ambient temperature range	+10° to +40° C

The optical cable is 4 m in length and contains 31 active lines plus 11 spares. The cable could have been 100 meters or longer without an alteration in the basic design of the optical link. The optical fiber characteristics are listed in Table 6 and the

TABLE 6

FIBER CHARACTERISTICS

Fiber attenuation	<50 dB/kM @ 830 nm
Numerical aperature	0.19
Core diameter	60 μm
Fiber O.D.	150 μm
Plastic jacket O.D.	0.9 mm
Tensile strength	60 newtons
Minimum bend radius	3 mm
Minimum recommended bend radius	1 cm

cable characteristics are given in Table 7. The cable fabrication process obviously increased the fiber loss but the performance of the system was not affected.

A total of 34 fibers were terminated with single-fiber bulkhead connectors. The physical dimensions of a connector are given in Fig. 12. The connectors are easily manipulated and no difficulty was encountered by personnel unfamiliar with optical-fiber technology.

2.4 Mechanical Configuration

The cabinet containing the optoelectronic units, MUX/DEMUX system and power supplies is shown in Fig. 13. The plug-in box on the front panel is a termination unit for the coaxial cables. The optical cable is connected to the right of the cabinet and the individual optical fibers can be seen at the centre of the figure.

TABLE 7

ARMOURED CABLE CHARACTERISTICS

Cable attenuation	200 dB/km @ 830 nm
Number of fibers	42
Number of fibers terminated with connector plugs	34
Length of fibers	4.8 m
Length of flexible conduit	4 m
Cable O.D.	2.2 cm (0.85")
Bulkhead mounting hole diameter	1.9 cm (0.75")
Minimum bending radius	15 cm

Figure 14 shows the array of optoelectronic units in position. The layout of the optical fibers from the optical cable on the right to each optoelectronic plug-in unit can be seen. The cage at the lower righthand side of the figure contains the MUX/DEMUX system.

When independent testing of the MUX/DEMUX circuitry was required, the optical-fiber system could be temporarily replaced by a hard-wire (twisted wire pair) cable, 1 m long. Figure 15 shows the test cable interconnecting the two cabinets. The plug to the optoelectronic system is seen disconnected on the lefthand side of the figure. The black cable curving upwards from right to left in the figure is the optical cable.

3. OPTICAL-FIBER LINK PERFORMANCE

The optoelectronic components were first tested independently. Some typical waveforms are shown in Fig. 16. Table 8 lists the results of the acceptance tests for the optoelectronic components. The electronic specifications were easily met by the optical system.

TABLE 8

OPTOELECTRONIC ACCEPTANCE TESTS

Plug-in Units Tx/Rx Serial Numbers	Output Pulse Width (ns)	Transmission Delay (ns)	Error in 10^9 Pulses	Pulse Rise Time (0.7V - 2V) (ns)	Pulse Fall Time (2V - 0.7V) (ns)
1/1	48.5	85	0	4	3
2/2	52	85	0	5.5	3
3/3	54.5	80	0	5	3
5/5	48	94	0	3.5	4
6/6	50	88	0	5	3
7/7	51	86.5	0	3.5	3.5
8/8	54.5	85	0	4.5	4
9/9	55.5	80	0	4	3
10/10	54	82	0	4	4
11/11	54	82	0	4	3
15/15	51	88	0	4	4
16/16	50	81	0	4	3
18/18	48.5	82.5	0	5	3
19/19	50	83	0	3.5	4
20/20	51	85	0	4	5
21/21	46	84	0	4	3
22/22	50	81	0	3.5	3
24/24	51.5	84.5	0	4	4
25/25	52	78	0	4	3
26/26	59	80	0	5.5	4
27/27	53	85	0	4	5
28/28	55	80	0	3.5	3
29/29	53	81	0	4	3
30/30	55	80	0	3.5	3
31/31	45	92	0	4	3
32/32	45.5	93	0	3.5	3.5
33/33	55	86	0	4	3
34/34	52	84	0	5	3
36/36	50	92	0	4	4
37/37	57	83	0	4	3
38/38	56	80	0	4	3.5
40/40	50.5	84	0	3.5	3
41/41	48	87	0	4.5	4
42/42	52	84	0	5	3

The link was installed between SDCs No. 5 and No. 6 at the Canadian Forces Fleet School, Halifax, Nova Scotia, Canada and subjected to a stringent test based upon the original acceptance tests† for the CCS-280 itself. All criteria were met without defects. A combat situation was also simulated and no distinction could be seen between SDC No. 5 and SDC No. 6.

4. CONCLUSIONS

The CCS-280 Optical Link Task has demonstrated that optical-fiber transmission systems can be used effectively in action data systems where complex digital signals ranging from DC to 10 Mb/s, and with fast rise and fall times of about 10 ns, are transmitted. The single-fiber-per-channel design was shown to be satisfactory and no difficulties were experienced in handling the optoelectronic components during installation and tests. Multiplexing of the data lines was accomplished despite the stringent timing requirements imposed by the CCS-280.

The demonstration link was designed to be connected externally to the existing components of the CCS-280, in order to allow the system to be returned conveniently to its original state. A considerable simplification of the cable system could be accomplished by integrating the optical link into the overall system design.

The expected spin-off from contracting the development and installation of the optical link to private industry was also realized. The contract with BNR contributed in part to their development of optoelectronic system components. Experience and familiarity gained by LSL in the application of optical-fiber transmission systems has provided a bisis for their involvement in future optical-link projects. Applications of optical-communications technology to military communication systems are expected to increase in the coming years. In view of their many advantages, such as immunity to EMI and small size, optical-fiber transmission links will no doubt be considered in applications such as the transmission of radar-video and sonar signals, and transducer signals generated by temperature, pressure, rpm and volume sensors, as well as in action data systems.

---

† The CCS-280 Acceptance Tests are considered to be classified information.

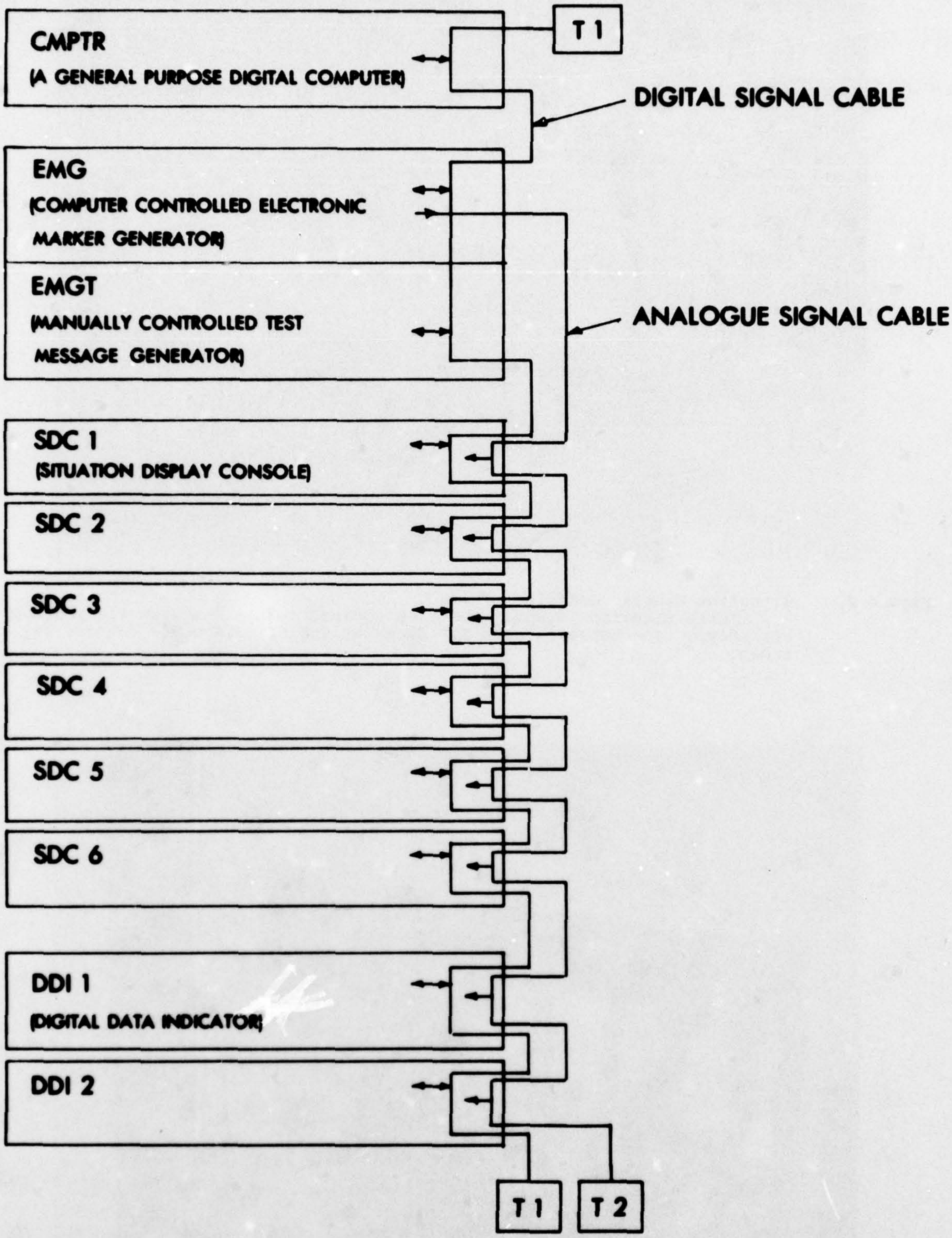

Figure 1 Block Diagram of the CCS-280 Display Subsystem
An analogue and digital signal cable system was used in the CCS-280.

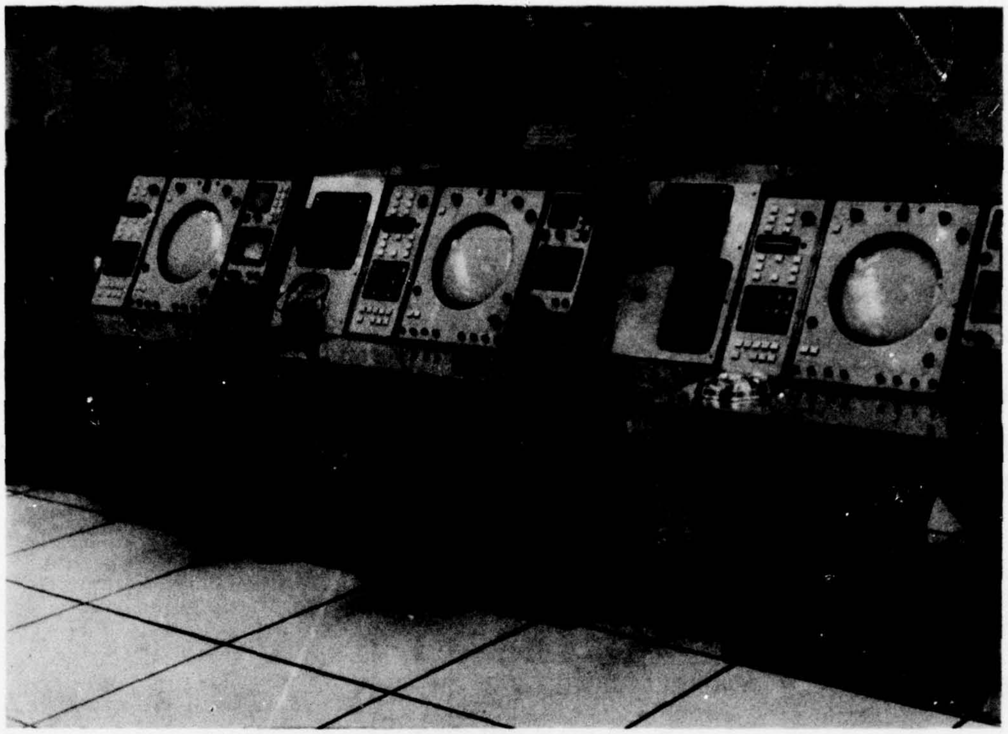

Figure 2 Situation Display Consoles
Three Situation Display Consoles located at the Canadian Fleet School are shown. The consoles have 12" diameter and 5" (diagonal) cathode ray tubes.

Figure 3 SDC Interconnecting Cables
The two digital coaxial-cable plugs are seen on the righthand side. Two grounding straps are located next to the digital plugs. The two analogue-signal cable plugs are on the lefthand side.

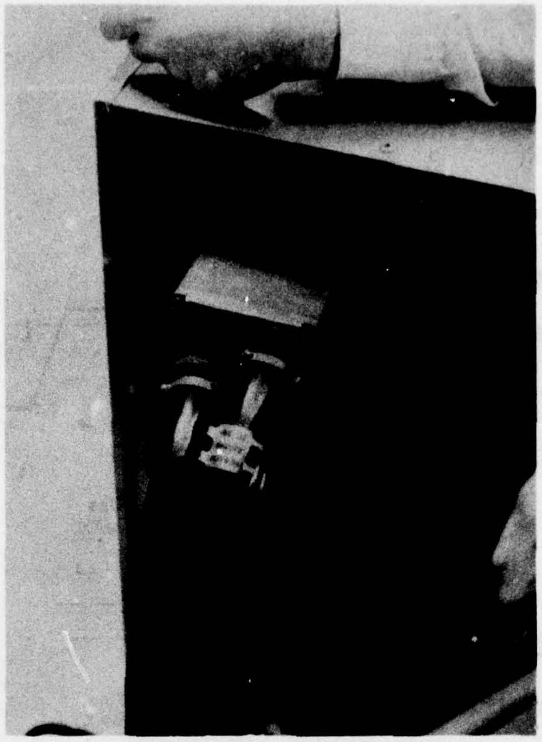

Figure 4 A Close-Up of the CCS-280 Digital Coaxial Cable
Two cables each containing 35 coaxial cables are connected to a single plug. The photograph shows two plugs aligned vertically at the back of the EMG.

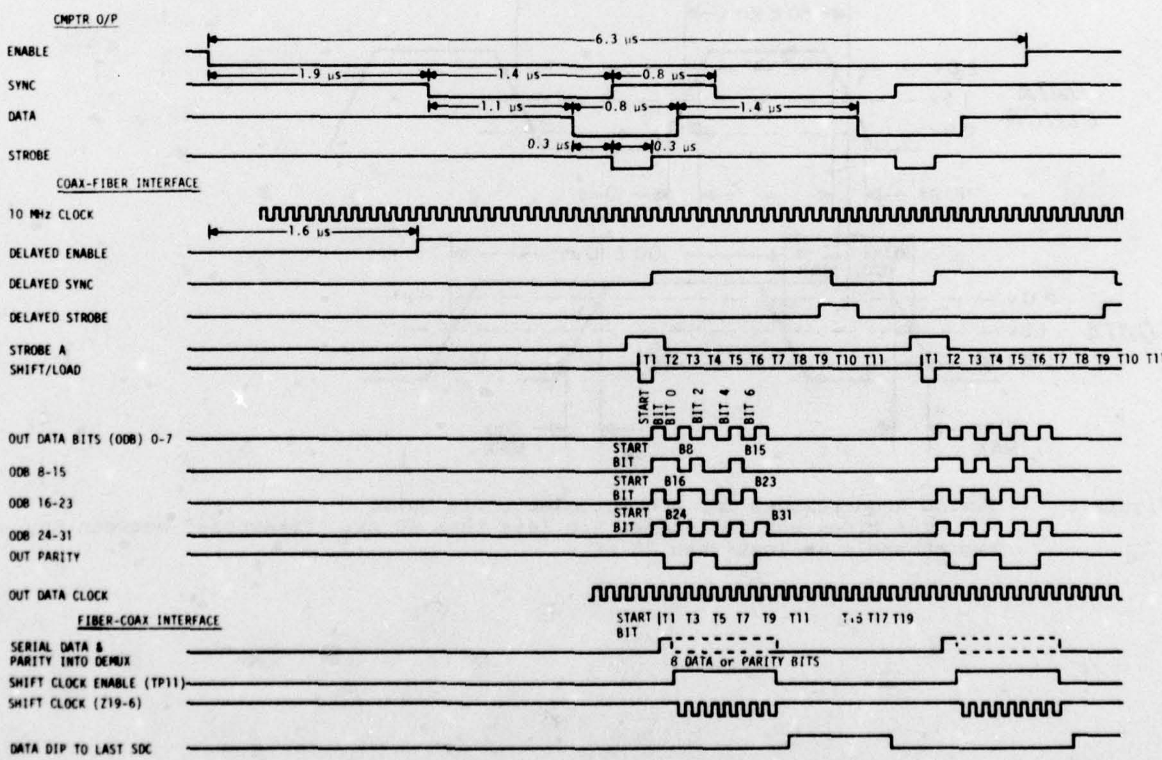

Figure 5 Multiplexing-Demultiplexing System Signals
An example of timing relations between various signals is shown.

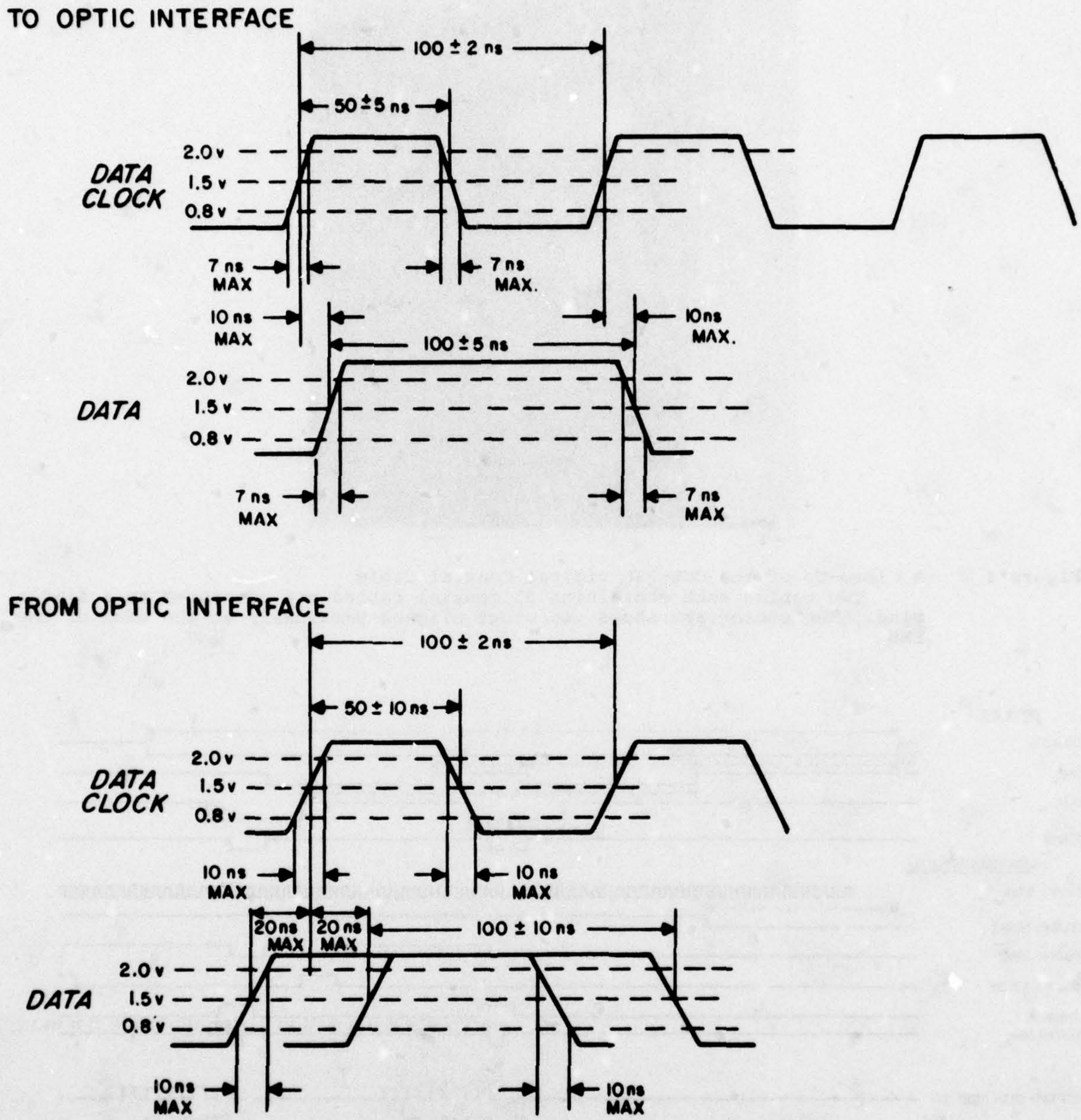

Figure 6 Timing Requirements for the Optoelectronic Units
The rise- and fall-times are less than 10 ns. "Skewness" between any two channels is less than 20 ns.

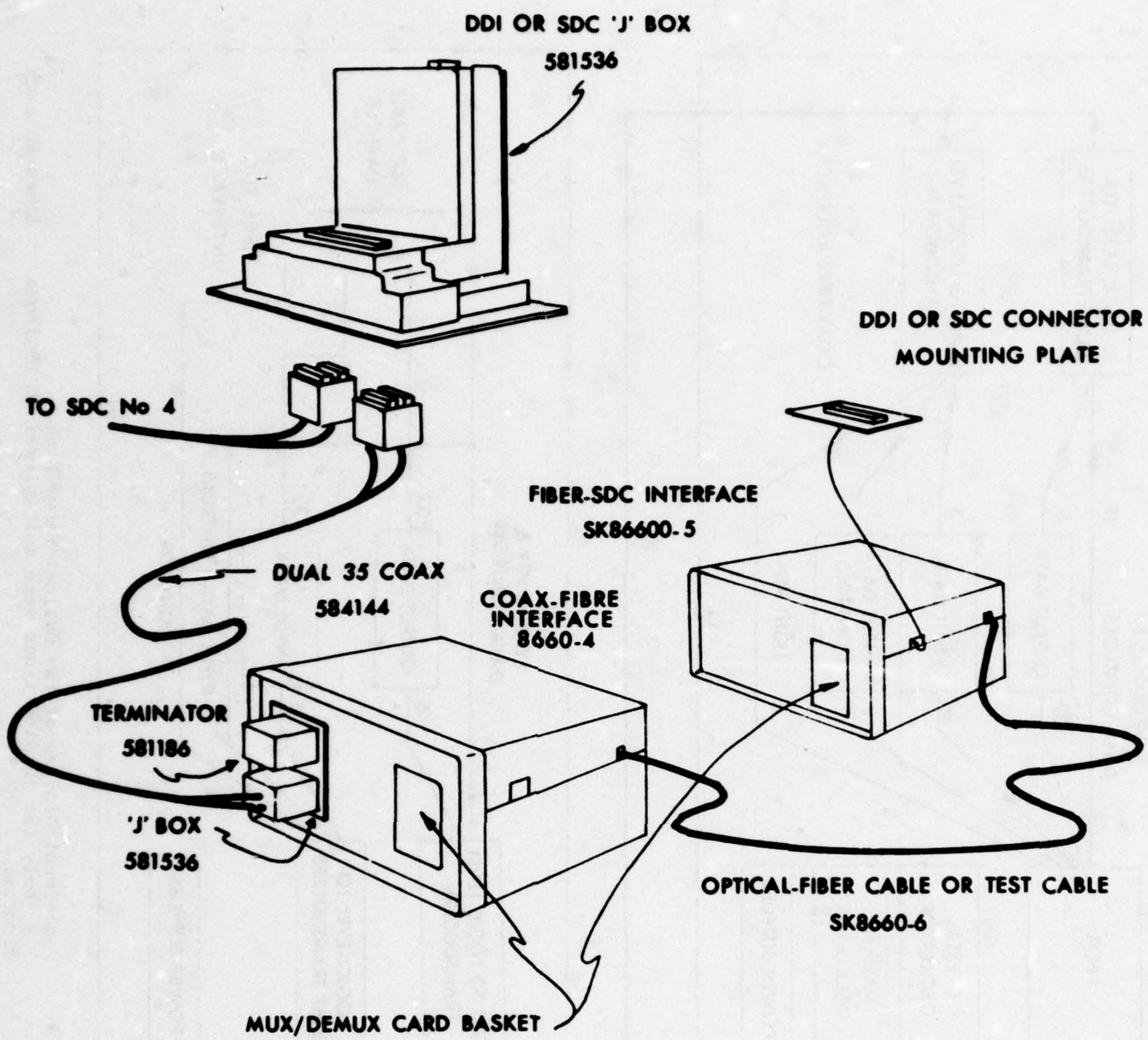

Figure 7 General Assembly of the Optical-Fiber Link
The dimensions are not to scale. The cabinets are approximately 12" x 34" x 56" in size.

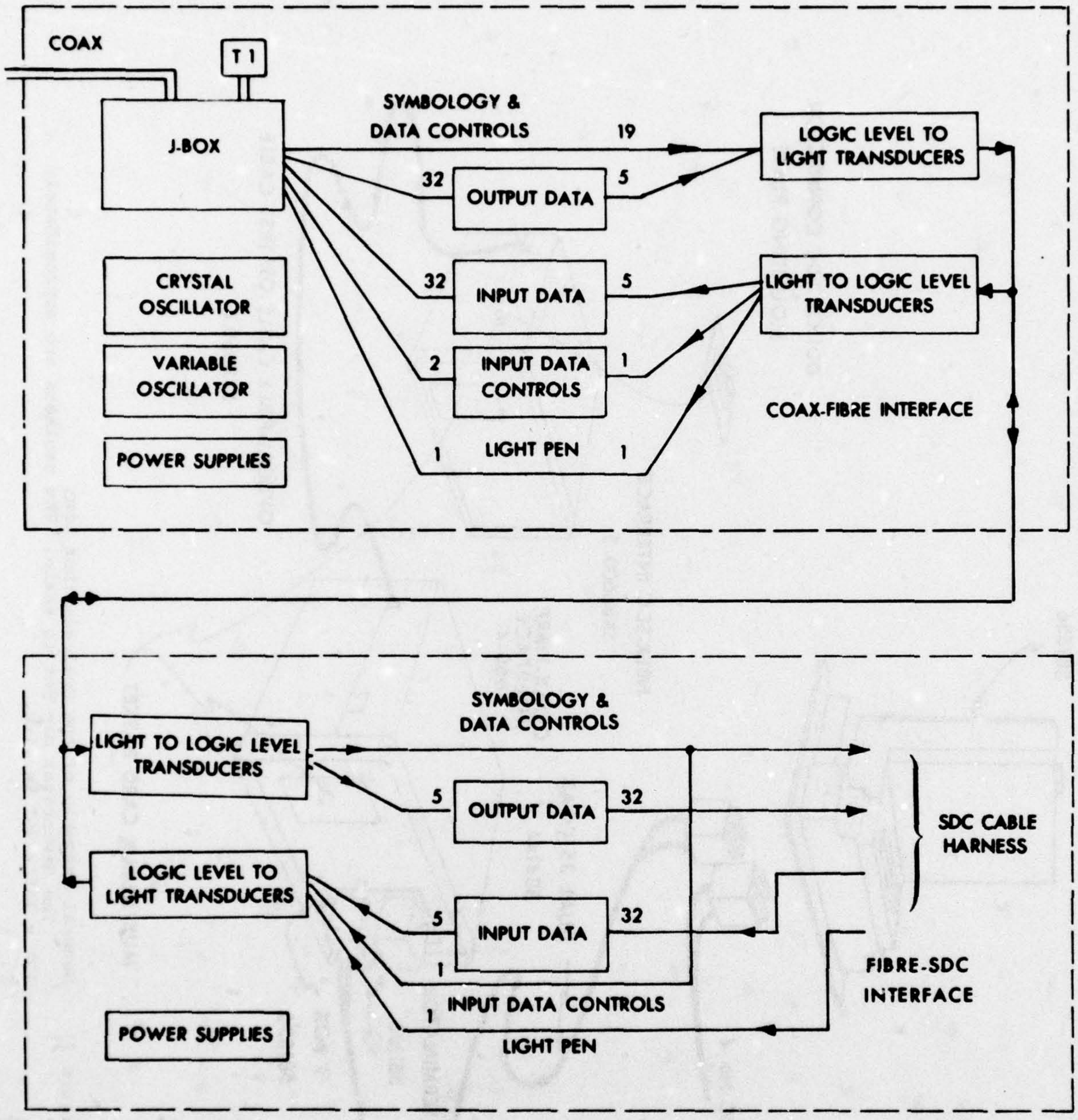

Figure 8 Functional Diagram of the Optical-Fiber Link
Only the 32 data lines were multiplexed to 10 lines, 5 lines in each direction.

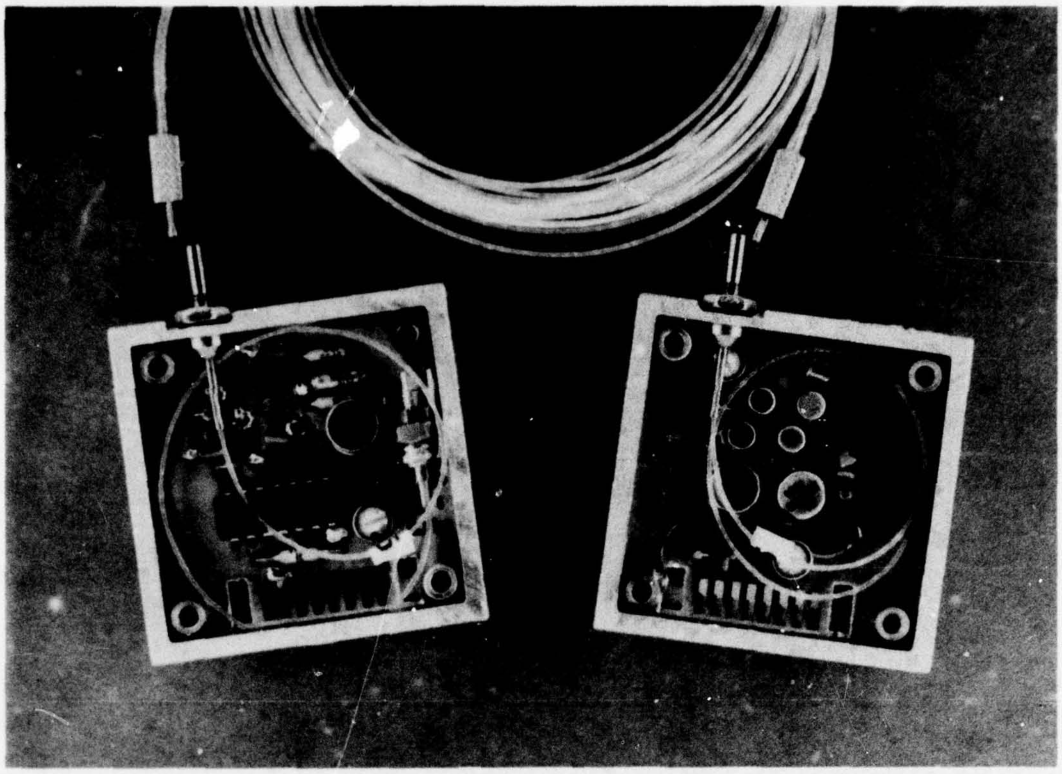

Figure 9 Optoelectronic Plug-In Units
The fiber connectors are disconnected. Dimensions of the cases are 0.9" x 2" x 2". The transmitter is on the lefthand side. A stud-mounted light-emitting-diode (LED) is used in this example. The CCS-280 units used LEDs mounted in TO-18 transistor headers.

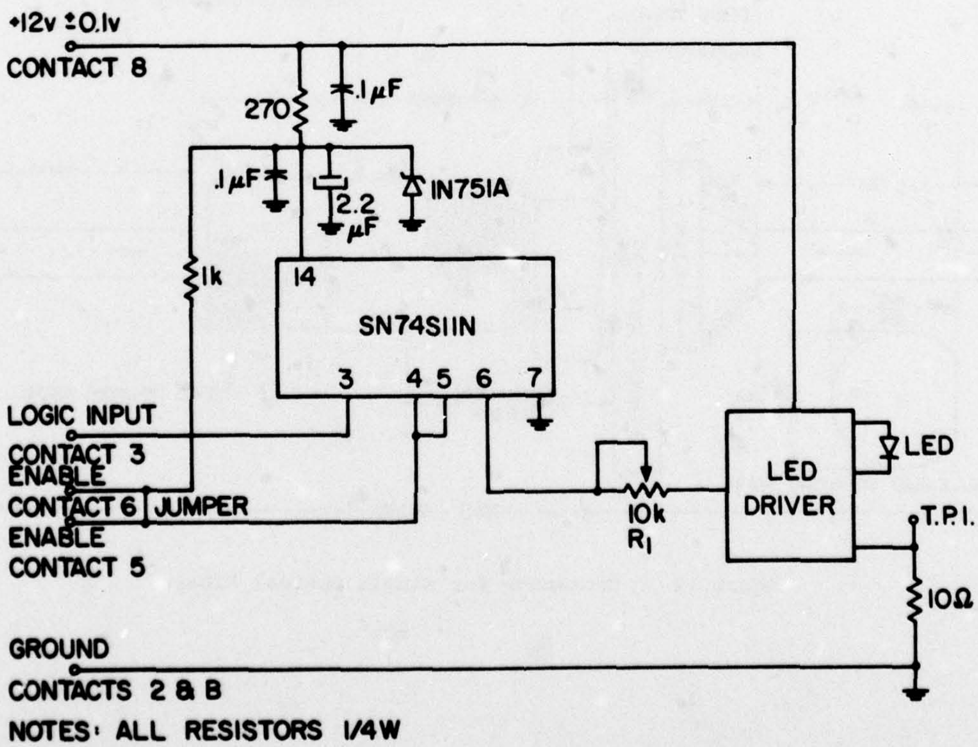

Figure 10 Schematic Diagram of Transmitter Unit

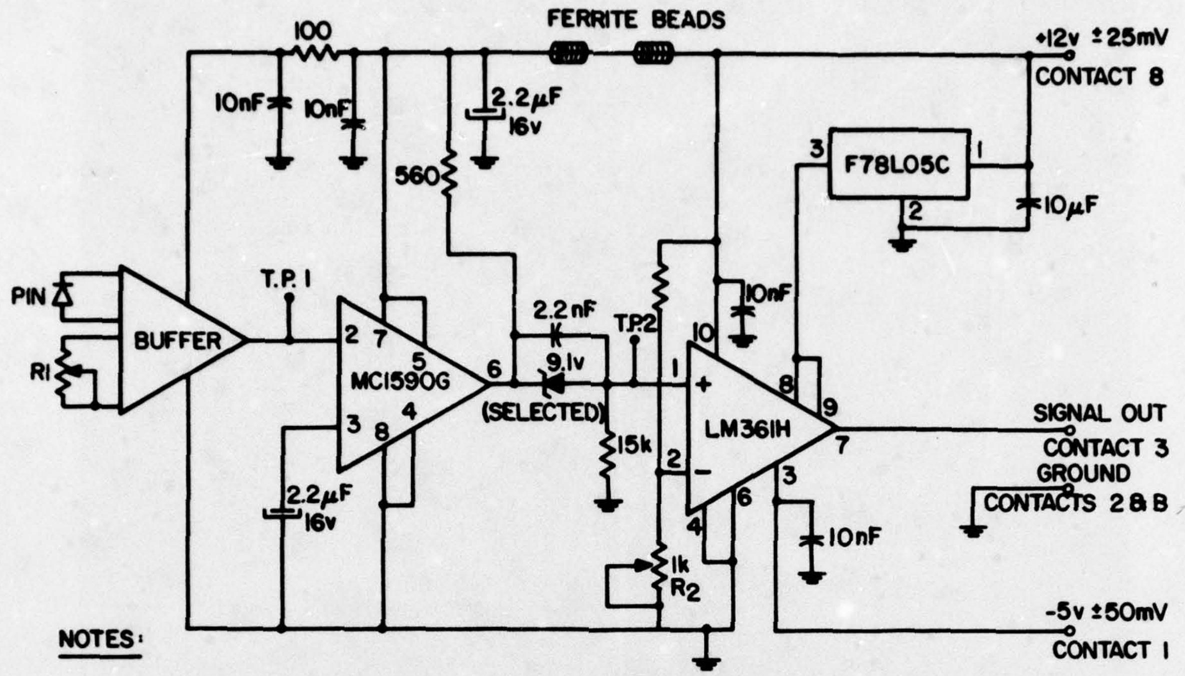

NOTES:

(1) ALL RESISTORS ARE 1/8W UNLESS OTHERWISE SPECIFIED.

(2) 9.1v ZENER SELECTED TO 1% TOLERANCE AT .5 mA ZENER CURRENT.

Figure 11 Schematic Diagram of Receiver Unit

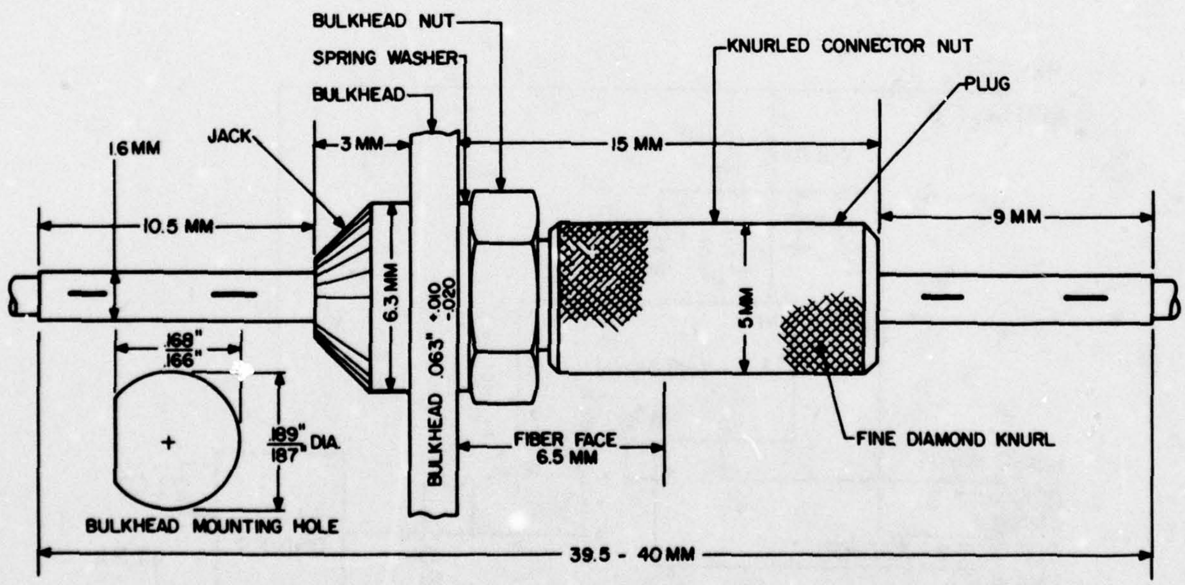

Figure 12 Connector for Single Optical Fibers

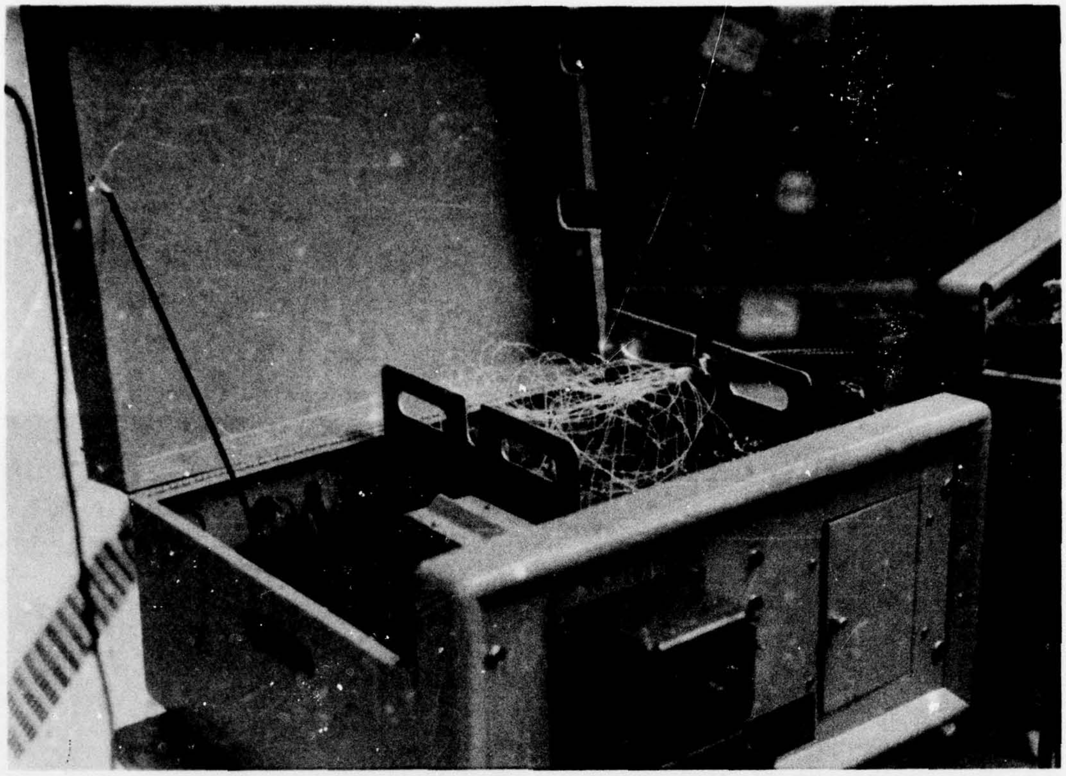

Figure 13 Optical Link Cabinet
The cabinet dimensions are approximately 12" x 34" x 56".

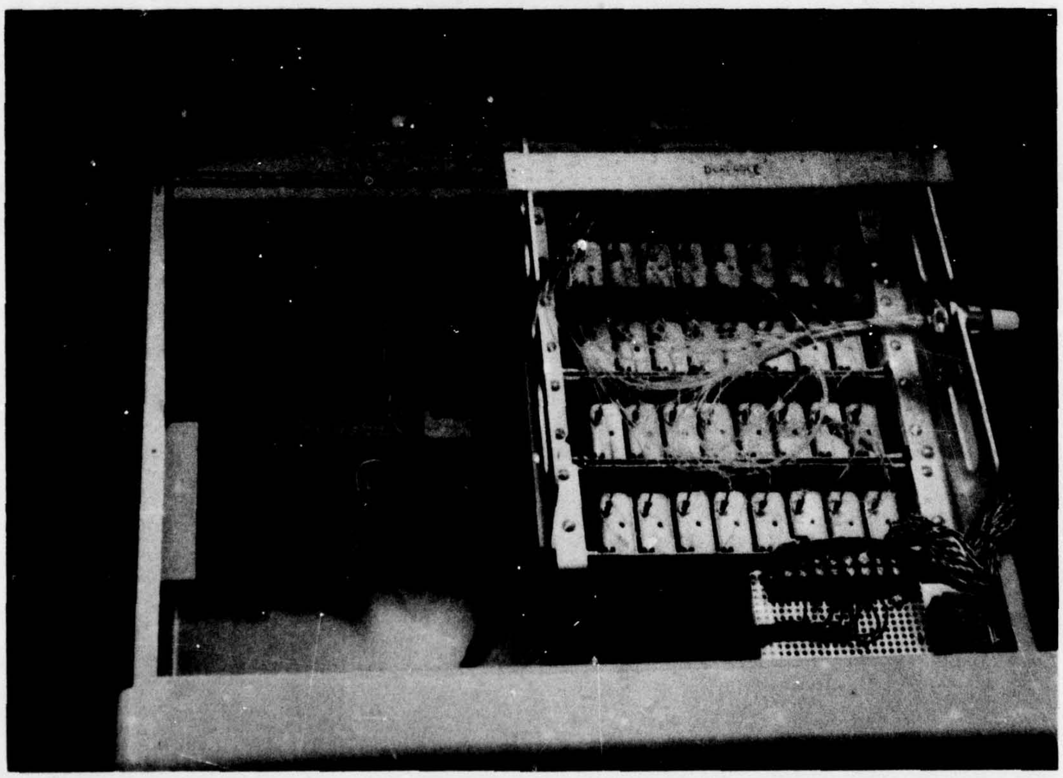

Figure 14 Optoelectronic Plug-In Units
The units are housed in a large cabinet in order to avoid difficulties that may arise in a closely packed system.

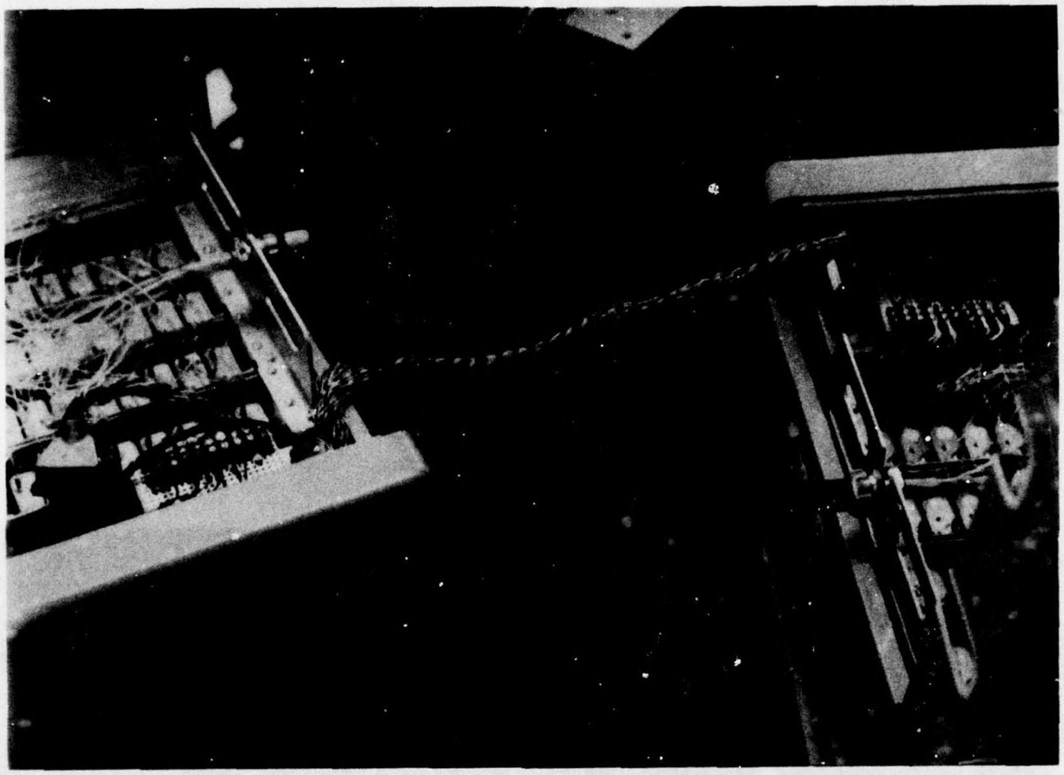

Figure 15 Hard-Wire Test Cable for the MUX/DEMUX System
The cable consists of twisted copper wire pairs.

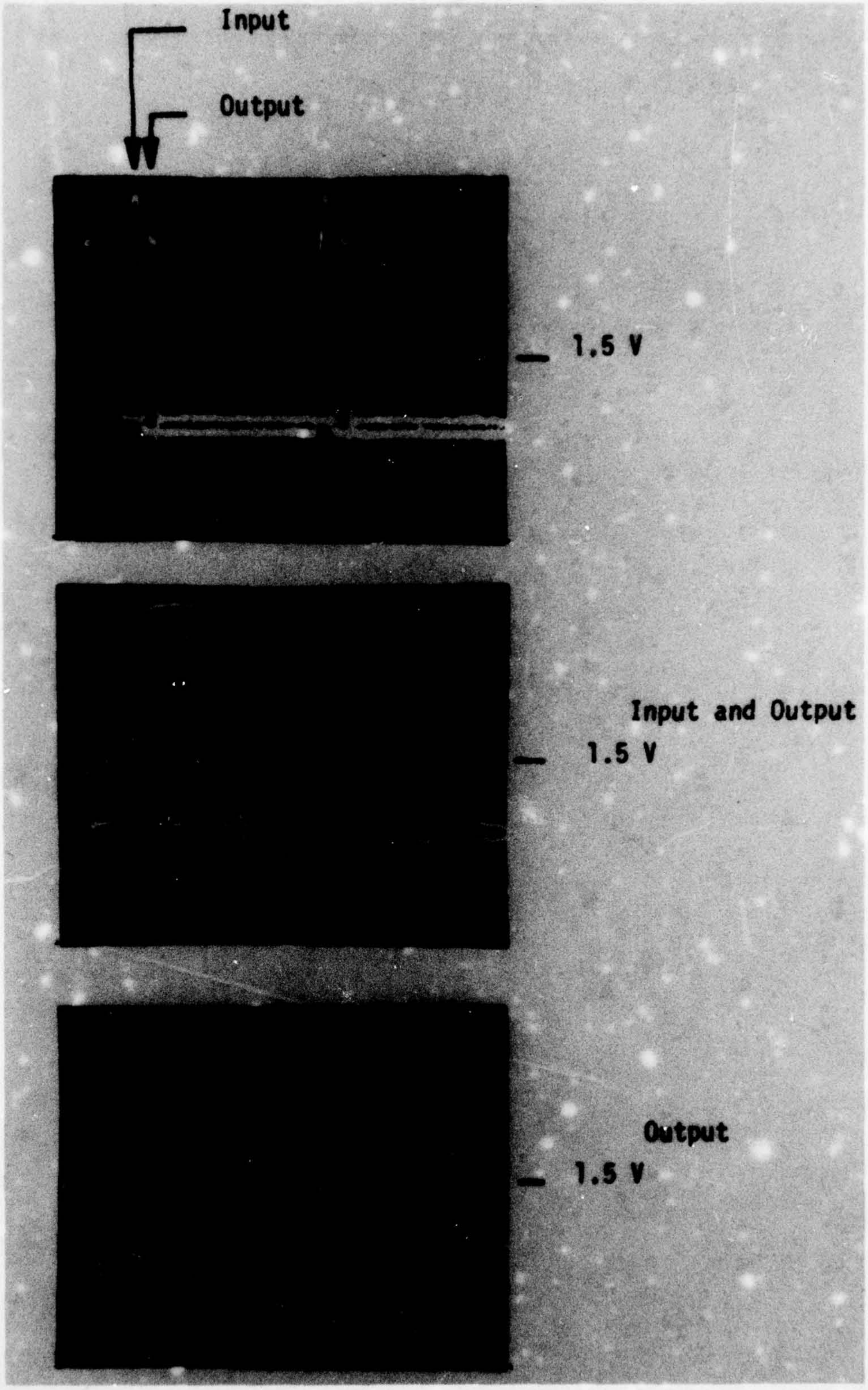

Figure 16 Typical Input and Output Waveforms of the Optoelectronic Units

MULTICHANNEL FIBER OPTIC SONAR LINK (FOSL-1)

Frederick C. Allard
Norman S. Bunker
Naval Underwater Systems Center
New London, Connecticut 06320
U.S.A.

SUMMARY

During the past year, a fiber optic transmission line was designed, built and tested at sea in an operational sonar system. This inboard transmission line conducts 52 channels from a preamplifier bank to a beamforming section. Plastic fiber optics is used in a 61-channel cable. Optical connectors are utilized at two levels. Commercially available electro-optical components are employed in the line driver and line receiver designs to achieve wide dynamic signal range with low distortion at low cost.

The transmission line, designated FOSL-1 (Fiber Optic Sonar Link-No. 1) was designed as an initial step toward a military-qualified subsystem. The utilization of established technologies, the modular construction and ease of maintenance allow for extended "hands off" operation by sonar technicians who are not specially trained for fiber optics.

1. INTRODUCTION

During the past year, the New London Laboratory of the Naval Underwater Systems Center installe fiber optic sonar link onboard a naval vessel for subsequent testing at sea. The link was installed, as shown in figure 1, within the hull connecting a preamplifier cabinet with a beamformer cabinet. Two immediate objectives of this 52-channel installation were to demonstrate:

(a) the specified, stringent performance capability,

(b) the survivability of the link outside the laboratory.

FOSL-1 was less a technological challenge than an engineering challenge, since an implicit objective was to use the minimum number of minimum cost components in constructing a fiber optic link with an extremely wide, linear dynamic signal range. FOSL-1 thus provides a vehicle for assessing the relevance of current fiber optics in an analog sonar system context.

2. LINK DESCRIPTION

FOSL-1 is comprised of 52 parallel channels, each consisting of a line driver, fiber optic bundle, and line receiver as shown in figure 2. The input to each fiber optic channel is a preamplified hydrophone signal. The amplitude of the input analog signal determines the instantaneous output frequency of the voltage controlled oscillator (VCO). The VCO generates a frequency-modulated (FM) square wave which, in turn, modifies the output of a red light-emitting diode (LED). The LED radiates into its assigned fiber optic channel. At the line receiver, 11 m away, a given fiber optic bundle is read out by a hybrid detector/operational amplifier that retrieves the FM signal for subsequent demodulation by a phase locked loop (PLL). The output of the PLL is conditioned by a two-pole active filter to provide a faithful reproduction of the original analog input.

This link operates with an FM bandwidth of 40 kHz for handling an 8.5 kHz analog signal bandwidth while achieving a dynamic signal range in excess of 100 dB. The line driver optical signal is derived from a wideband FM electrical signal; the detector bandwidth and PLL lock range are compatible with a narrowband FM signal. This format provides a maximum signal-to-noise ratio while maintaining low distortion over the range of most-likely occurring signal levels. Total harmonic distortion is 1.0% maximum and decreases as a function of input signal level.

Cost was an important consideration in the design of FOSL-1. The current cost per channel for electro-optical components is $91.00. This figure includes electronic components, card guides, power supplies, enclosures, etc. Last year's cost for the custom connectorized fiber optic cable assembly was $164.00 on a per channel basis. Today's cost for the cable materials and connectors would be about $40.00 per channel.

2.1. Plastic Multichannel Cable.

Having previously demonstrated a multichannel capability in the laboratory (ALLARD, F. C., 1976) a primary concern was survival of the fiber optic cable — particularly with respect to strain relief at connectors — onboard a ship. Plastic fiber optics was chosen for its clearly superior mechanical reliability.

The plastic bundle of choice duPont PFX 0715 (now designated PFX P740), contains 7 polymer-clad methylmethacrylate fibers within a polyethylene jacket. The active diameter of each fiber is 400 μm with a numerical aperture of 0.53. The composite 7-fiber diameter is 1.12 mm, resulting in a packing fraction of 0.78. Attenuation is 470 dB/km at 656 nm.

Sixty-one of the PFX bundles are jacketed within an asbestos tape-wrap sheathed with fluorocarbon tubing to provide a measure of flame and heat resistance. The tape that was chosen was made from selected asbestos fiber in a process designed to meet requirements of the Occupational Safety and Health Act (OSHA).

The 61-channel cable, with an overall diameter of 23 mm, was bifurcated at each end and terminated with pairs of modified electrical connectors as shown in figure 3. While the at-sea test only required an 11 m cable, lengths up to 65 m are possible using the PFX 0715 fibers. The connectors each have a 31-channel capacity and are shown in figure 4, where the mating panel-mount receptacle is shown to the left. These Deutsch connectors are of the miniature bayonet style, utilizing standard inserts. Clearance holes in the No. 16 contacts represent the only accommodation to fiber optics. The contacts utilize a retention clip. Once the optical fiber(s) are epoxied in the contacts and the ends polished, the terminated bundles are attached to the connector shell in exactly the same manner — and with the same plastic tool — as an electrical cable. Although the direct substitution of fiber optics for wire may not yield an optimum connection, it does yield a serviceable connection that proved to be reliable and relatively trouble-free.

The cable mount connector contains seven PFX 0715 fibers in each pin, whereas the panel-mount receptacle contains a single 1 mm diameter Crofon fiber. The jacketed Crofon fibers form flying leads within the transmitter and receiver enclosures at each end of the cable.

The intent of mating a single 1 mm strand to a 7-strand bundle having a combined diameter of 1.1 mm was to minimize the coupling losses inherent in a bundle-to-bundle connection. An empirical analysis verified that a Crofon-to-PFX-to-Crofon configuration reduced transmission loss by 2.5 dB compared to a PFX-to-PFX-to-PFX cable configuration. The total attenuation of the cable assembly — from LED to detector — is 15 dB. This figure includes connector losses but does not include insertion loss at the LED.

2.2. Line Driver.

The fiber optic sonar link was engineered as a retrofit to the host sonar system. In this context, signals are extracted from the sonar preamplifier and conducted via shielded, twisted-pair wires to a fiber optic line driver cabinet shown in figure 5. Fifty-two circuit boards — one for each sonar channel — are contained within a cabinet measuring 61 cm x 33 cm x 13 cm (with no attempt at miniaturization). Note that the optical connectors to the left in figure 5 contain one-third as many conductors as the electrical connectors to the right, for the same channel capacity.

The line driver circuit shown in figure 6 is deceptively simple. Of the 13 components shown, 9 serve the driver function directly, whereas the remaining components provide for power supply decoupling. Functionally the incoming signal determines the frequency generated by an Intersil 8038 voltage controlled oscillator (VCO) chosen for its low distortion and minimal associated external circuitry. The square wave output stage of the VCO has insufficient current sinking capacity to drive the LED directly, however, thus requiring a transistor drive stage. The LED current, limited to 25 mA peak, follows the FM waveform generated by the VCO.

The VCO is the first active element in FOSL-1. Its free-running (i.e., zero voltage input) frequency should be consistent from channel to channel, since this determines the operating point for the phase locked loop in the line receiver. Tests of 60 VCO's using the same external frequency-determining components yielded a 6 kHz spread about a mean free-running frequency of 48 kHz. This amount of variability necessitated a hand selection process to match a VCO to a given circuit board. In this manner the frequency spread was reduced to 2 kHz.

The FM "beta" is 13 at a test frequency of 1 kHz, meaning that the VCO output frequency ranges from 35 to 61 kHz for a maximum amplitude 1 kHz signal.

A simple transistor inverter couples the VCO square wave output to the red LED, a Fairchild FLV104. The domed epoxy encapsulation was ground down and faceted to allow close coupling of the Crofon lead. Output power of the LED's varied almost 300% in a sample of 75 faceted LED's and was attributed to variable conversion efficiency in the LED chip itself.

Variation in chip centering relative to encapsulation was compensated by centering the chip within the AMP plastic connector bushing. The LED was held in place with an electrically insulating, heat-conductive staking compound. The AMP bushing itself was epoxied to the circuit board and provided the receptacle for the plastic AMP ferrules with which the Crofon leads were terminated.

2.3. Line Receiver.

The line receiver accepts optical signals from the fiber optic cable and restores the original analog electrical waveforms, which are then conducted via shielded, twisted-pair wires to the sonar beamforming cabinets. The line receiver cabinet is directly comparable to the line driver cabinet shown in figure 5, containing individual circuit boards for each of the 52 sonar channels.

An individual line receiver board is shown in figure 7. More elaborate than the line driver, it provides additional possibilities for gain and phase variations from channel to channel. Concern for uniformity begins at the detector, a Devar 529-2-5 hybrid detector/transimpedance amplifier. This hybrid is packaged in a TO-5 can which is located within an AMP plastic bushing. The bushing is epoxied to the circuit board and mates with a Crofon lead (also shown in figure 7).

A detector area of 5 mm^2 was chosen to ensure maximum collection efficiency by reducing alignment problems. As with the LED, close coupling of the detector and the Crofon lead is sufficient. No lenses or index matching fluids are used anywhere in FOSL-1.

The decision to operate the detector photoconductively, based on the performance of several hybrid units led to an unexpected engineering challenge. Devar, as it turns out, does not control the frequency response characteristics of this device in the photoconductive mode. Additional frequency rolloff components to correct this situation would have unnecessarily restricted the device bandwidth (HAMSTRA, R. N., and WENDLAND, P., 1972). Subsequent procurements from Devar yielded devices whose frequency response characteristics varied significantly from those of the test sample. The problem was further aggravated by the decision to provide only +15 V power in FOSL-1 for economic reasons.

The output of the Devar unit is coupled to an NE 565A phase locked loop. The phase transfer characteristics of the detector/amplifier — PLL combination are sufficiently variable as to require compensation, particularly at the higher input signal frequencies.

The FM conversion efficiency is also variable from one PLL to the next, mainly because the PLL gain is established by internal components that are loosely specified (20%). A filter-buffer stage serves to control gain and eliminate carrier harmonic feedthrough. This stage, with a nominal gain of 2, has the transfer characteristic of a 2-pole Butterworth filter.

Since one of the performance objectives of FOSL-1 was uniformity of transfer characteristics from channel to channel, a Monte Carlo analysis was used to determine a method for selecting filter components. The characteristics of the overall link were too complicated to allow for accurate modelling, however. The cumulative effects of all the preceding active elements resulted in an alignment procedure, using two interacting adjustments to control gain and phase.

2.4. Link Performance.

FOSL-1, as installed, demonstrated

(a) 100 dB signal dynamic range (min.)

(b) 8.5 kHz signal bandwidth (min.)

(c) 0 dB gain ($\pm$0.1 dB)

(d) 80 dB crosstalk rejection (min.)

(e) 1.0% worst case total harmonic distortion

The construction of FOSL-1 did not meet military qualifications but did conform to good commercial practice. A system check following 2500 hours of operation verified that all channels were operative, with no signs of deterioration.

3. CONCLUSION

FOSL-1, based on materials commercially available in 1976, has provided an engineering exercise leading to several projections:

1. fiber optic links can achieve the requisite sonar performance at affordable cost,

2. fiber optic links can survive the shipboard environment on the same basis as conventional electronics, and

3. the implementation of military-qualified fiber optic links will require straightforward development of manufacturing methods with respect to fiber optic and electro-optic elements.

REFERENCES

1. ALLARD, F. C., February 1976, "A Fiber Optic Sonar Link," Electro-Optical Systems Design, p. 32.

2. HAMSTRA, R. N., Jr., and WENDLAND, P., July 1972, "Noise and Frequency Response of Silicon Photodiode Operational Amplifier Combination," Applied Optics, 11, p. 1539.

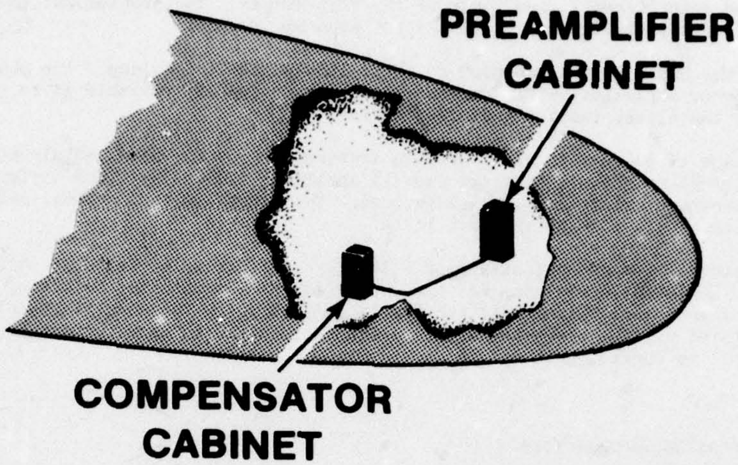

Fig. 1. FOSL-1 installation

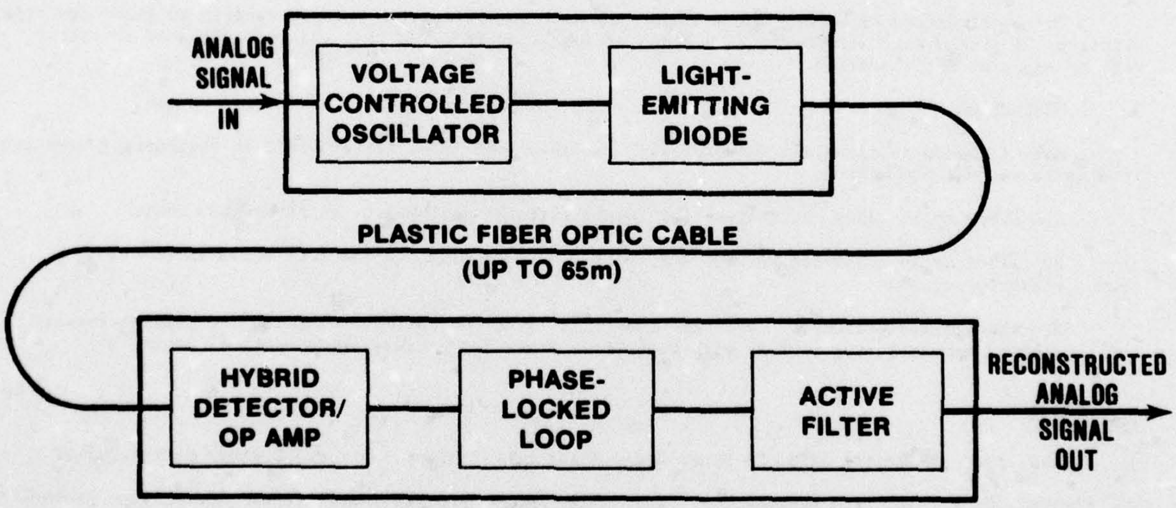

Fig. 2. Block diagram of single fiber optic channel

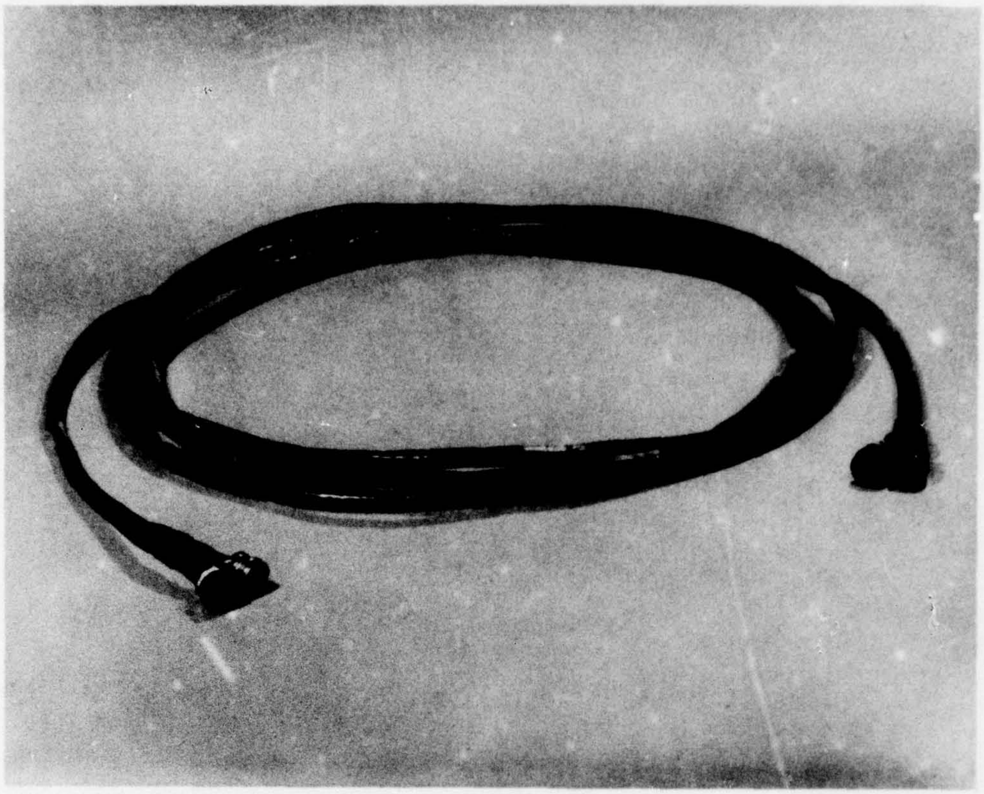

Fig. 3. 61-channel plastic fiber optic cable

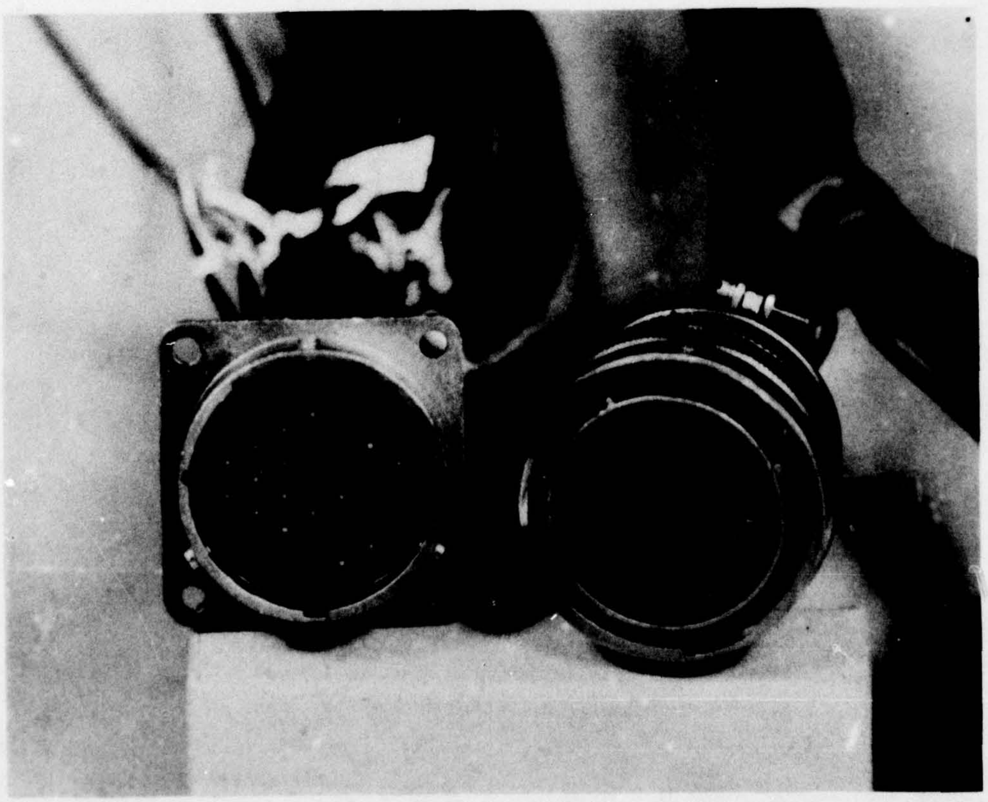

Fig. 4. Fiber optic connector pair

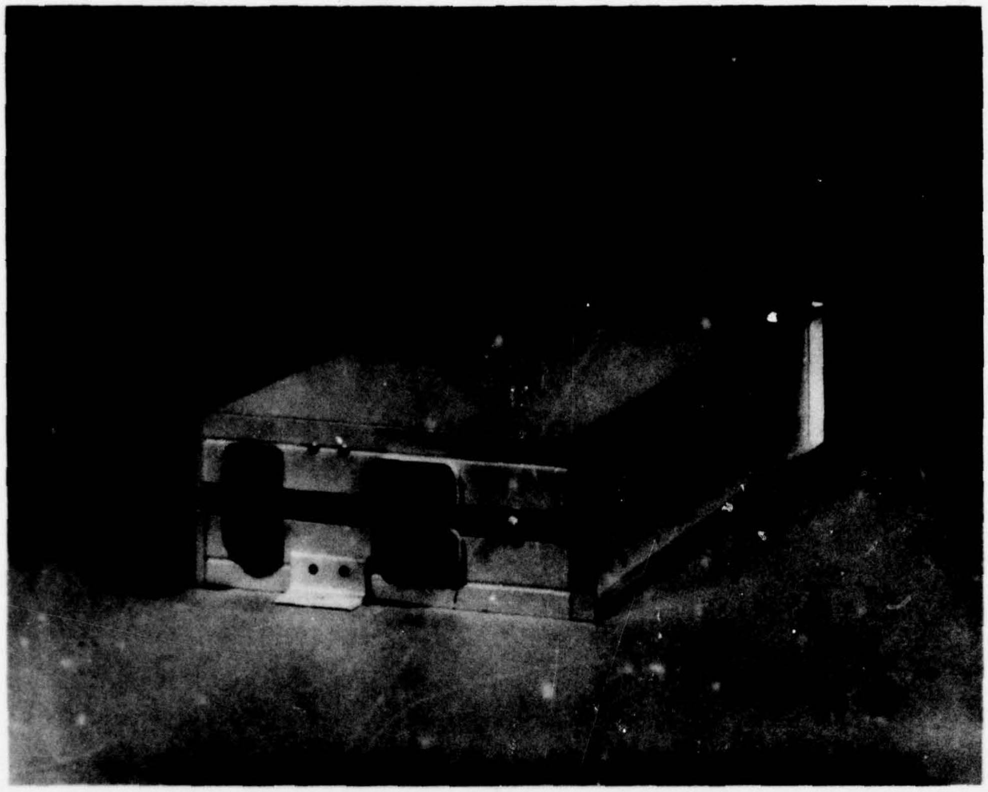

Fig. 5. Fiber optic line driver cabinet

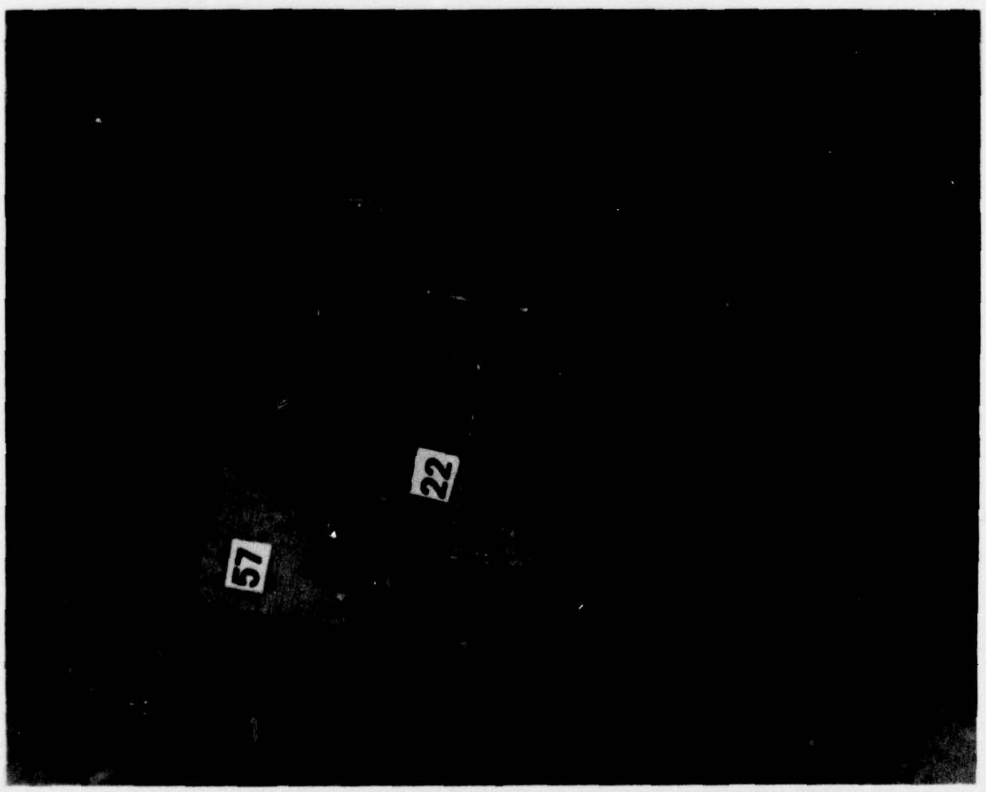

Fig. 6. Fiber optic line driver circuit board

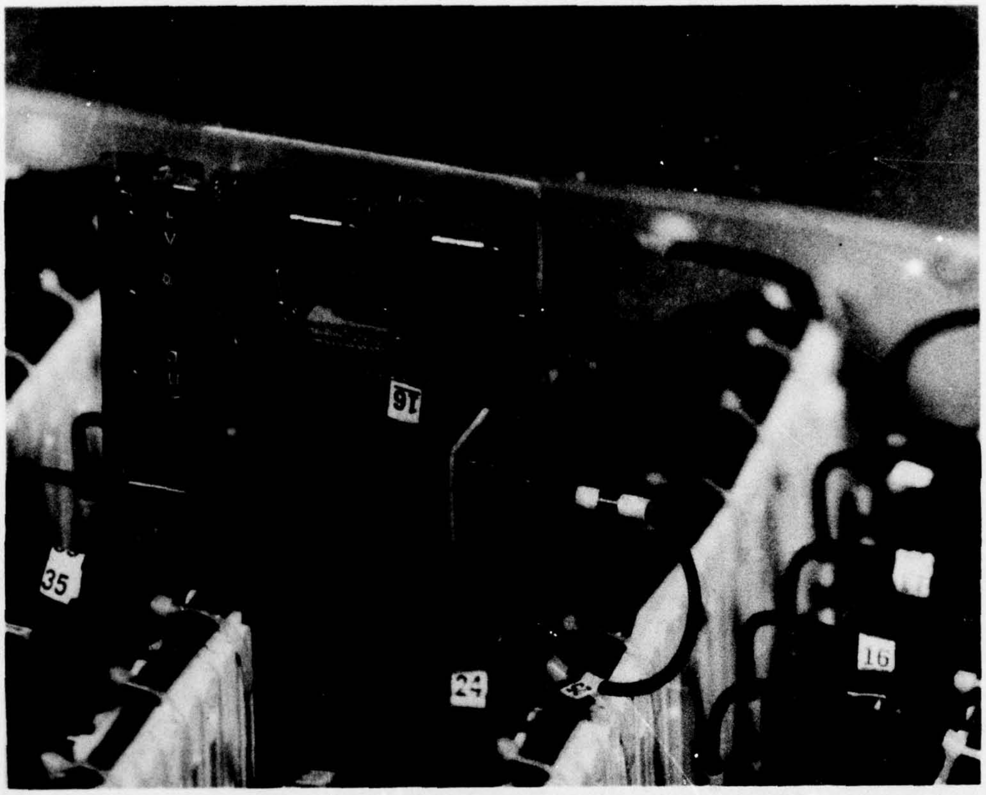

Fig. 7. Fiber optic line receiver circuit board (on extender card)

A TWO KILOMETER OPTICAL FIBER DIGITAL TRANSMISSION SYSTEM FOR FIELD USE AT 20 Mb/s

By

T. A. Eppes
J. E. Goell

ITT ELECTRO-OPTICAL PRODUCTS DIVISION
P. O. Box 7065
Roanoke, Virginia 24019

and

R. J. Gallenberger

NAVAL ELECTRONIC LABORATORY CENTER
271 Catalina Blvd.
San Diego, California 91252

SUMMARY

This paper describes a two-kilometer optical fiber digital transmission system for bit rates up to 20 Mb/s. The system includes a light emitting diode (LED) optical source, an avalanche photodiode (APD) receiver, and multi-fiber graded index cable. The data channel elements are connected via several field installable optical connectors. The design and performance of such components as transmitter modules, receiver modules, optical cable, and field installable optical connectors are discussed.

1. INTRODUCTION

The potential of fiber optics in long distance transmission of digital data is apparent. However, widespread introduction of such systems hinges on the availability of adequate system components capable of being installed and performing in the field. The purpose of the effort discussed here was to design and build such a system.

The fiber optic data transmission system described here operates over 2 km with an NRZ data rate from 100 Kb/s to 20 Mb/s. At least six channels are available per cable. The overall data channel performance is:

o Distance	2 km
o Data Rate	100 Kb/s to 20 Mb/s
o Bit Error Rate	$<10^{-8}$
o Mean Time Between Failure	
$0-30^{o}C$	7000 hours
$70^{o}C$	3000 hours
o Input/Output Electrical Signal	Standard TTL
Data Format	NRZ
o Output Electrical Signal-Digital	
Rise/Fall Time[a]	<15 nsec
Pulse Spread[b]	<20 nsec
o Output Electrical Signal-Analog	
SNR[c]	>30:1
Peak-to-Peak Voltage[d]	3 ± 1V
Rise/Fall Time[a]	<25 nsec
Pulse Spread[b]	<15 nsec
Overshoot	<10%
Droop[e]	<10%
Optical Crosstalk (1 km)	<50 dB

a. 10% to 90% peak-to-peak amplitude.
b. Change from input pulse width to output pulse width measured at 50% points.
c. Ratio of peak-to-peak 10 MHz square wave signal amplitude out of 10 MHz filter to RMS noise out of filter with source constantly on.
d. Measured across 10 K Ω load.
e. Measured for 100 consecutive logic ones at 100 kb/s, NRZ.

The components of the system are:

- o transmitter module
- o receiver module
- o multi-fiber cable
- o buffered fiber
- o one-way optical connector

Figure 1 is a diagram of the data channel configuration. The TTL input to the transmitter module is used to modulate a light emitting diode (LED) operating at 0.82 µm. Six-foot buffered fibers are used to couple light from the transmitter modules to individual fibers of the multi-fiber cable. The buffered fibers have optical connector plugs on each end for mating with the module jacks and multi-fiber cable.

The multi-fiber cable contains up to eight fibers as the core of an external strength member cable. The cable is ruggedized for installation in underground duct systems. After installation, at least 6 of the 8 fibers are guaranteed to be functional. The 2 km distance is traversed using two 1 km cable sections. The two cable sections are joined by five optical connectors.

At the receiving end of the system, the cable fibers are terminated with the optical connector jacks. Similar to the transmitting end, six-foot buffered fibers are used to couple light to the receiver modules. An avalanche photodiode detector (APD) is used to maximize sensitivity in the receiver. The receiver module supplies the required digital and analog outputs.

2. LINK DESIGN

To ensure that acceptable system operation results when the various system components are configured as a data channel, a link budget for both loss and dispersion is presented. These budgets represent worst case levels for each of the components and can thus be used as accept/reject criteria. On average then, the system performance is considerably better than that predicted by the loss and dispersion budgets.

2.1 Loss Budget

The purpose of the loss budget is to identify the required optical power performance of each link component. The loss budget contributors are the transmitter output power, connector losses, cable losses, and receiver sensitivity. The difference between the transmitter output and the receiver sensitivity is the power margin. The link loss is the sum of all connector and cable losses. The difference between the power margin and the link loss equals the excess power margin which provides a measure of the allowable time and temperature degradation.

The average power out of the transmitter module is -17.5 dBm (17.9 µwatts) based on experimental results with ITT 801-E and Bell Northern Research 40-2-10-3 LEDs. In order to achieve the 30:1 peak signal to rms noise ratio, the average power into the receiver detector (RCA C30817) has to be -48.2 dBm (15 nwatts). Thus, the power margin is 30.7 dB.

Connector loss occurs at six interfaces. Four of the six interfaces involve graded index fiber-to-graded index fiber coupling while one interface involves a graded index fiber and step index fiber. In all of these cases, a worst case loss of 2 dB is assumed. At the detector surface, a 1 dB coupling loss is assumed. Hence, the total connector loss is 11 dB. The loss of the two graded index cables when connected is 6.5 dB/km maximum. Over the 2 km link, a loss of 13 is expected. The total link loss is then 24 dB.

Subtracting the link loss of 24 dB from the power margin of 30.7 dB gives an excess power margin of 6.7 dB which allows for time and temperature degradation. Temperature tests over the range of -20°C to +50°CC show that an equivalent optical degradation of 3 dB occurs. An additional degradation in the LED output power of 3.7 dB is therefore possible before the link performance begins to fall below any of the specifications.

2.2 Rise/Fall Time Budget

The rise/fall time budget is derived in much the same manner as the loss budget. Here again, worst case design levels are specified. The rise/fall time budget contributors are the transmitter rise/fall time, the fiber dispersion, and the receiver rise/fall time. The rise/fall time is defined as being measured between the 10% and 90% points of a pulse edge. The overall link rise/fall time (receiver analog output) is to be less than 25 nsec. The expected overall rise time is computed as 1.1 times the square root of the sum of the squares of the budget contributors.

The transmitter rise/fall time equals 12 nsec based on experimental results with the ITT and BNR LEDs. A speed-up network is used for both LEDs and is discussed in more detail in Section 3.

The fiber contribution consists of both material and multimode dispersion. Dispersions are measured between the 50% points of dispersed pulses coming out of the fiber under measurement. The material dispersion amounts to 4 nsec/km while the multimode dispersion is 6 nsec/km. No sub-root length dependence is assumed for the multimode dispersion. Root sum squaring the fiber dispersion over the 2 km gives a fiber dispersion of 14 nsec. The effect on rise/fall time is found by multiplying by 0.7. Hence, the fiber rise/fall time contribution is 10 nsec.

The receiver bandwidth equals to 20 MHz which corresponds to a rise/fall time of 17 nsec. This bandwidth is consistent with the 30:1 SNR sensitivity of -48.2 dBm.

Combining the transmitter, fiber, and receiver rise/fall time effects as described above gives the required analog rise/fall time of 25 nsec.

3. TERMINAL ELECTRONICS

The terminal electronics functions as the electrical-to-optical and optical-to-electrical interfaces. The transmitter module contains a TTL digital input and an optical connector output. The receiver module contains an optical connector input and TTL digital and 3 volt peak-to-peak analog outputs. The outside physical dimensions of each are identical, 51 mm x 63 mm x 127 mm.

3.1 Transmitter Design

The transmitter module is pictured in Figure 2 as viewed from the optical connector end. Two mounting holes are shown for securing the module into a panel assembly. The electrical interfaces consist of the TTL digital input, the +5 Vdc supply, and ground lug.

The digital input consists of four line drivers. Each line driver is capable of delivering up to 80 mA of drive current. Current limiting resistors are used to reduce the current drive per line driver to 60 mA. An RC circuit is employed in parallel with the current limiting resistor to decrease the LED output rise/fall rime. To simplify getting the required optical output power, a four pole switch is used to apply from one to four of the drivers. In almost all cases, two driving can be used to get a peak current of 120 mA. The LED output is coupled into a short graded index fiber "pigtail" which feed the optical connector jack.

The transmitter module specifications are:

Power Supply Voltage	+5 ±0.25 Vdc
Power Supply Current Drain	≤300 mA
Data Input	TTL compatible
Optical Output Rise/Fall Time	≤12 nsec
Peak Optical Output Power	≥35 μwatts
Data Rate	dc to 20 Mb/s (NRZ)

3.2 Receiver Design

Figure 3 is a photograph of the receiver module as viewed from the electrical interface side. The optical interface is physically identical to that of the transmitter module. The receiver module is powered from ± 15 and +5 Vdc supplies and has two outputs, one TTL digital and one 3 Vp-p analog. A block diagram is shown in Fig. 4.

The received optical power is coupled to the detector face through a short, large core, step index "pigtail" fiber. Coupling efficiency between the "pigtail" fiber and the detector is approximately 80% (1 dB loss). The detector is an RCA C30817 silicon APD. The device exhibits high quantum efficiency, 70-75%, at the system operating wavelength of 0.82 μm and a rise/fall time of 2 nsec. The detected photocurrent is first amplified via a bipolar cascode transimpedance amplifier. Additional amplification is achieved via two SN 52733 amplifiers.

The signal is amplified to a peak level of about 1.5 volts, and fed to a clamping circuit prior to presentation to the comparator to eliminate baseline wander during reception of a long string of "1"s or "0"s. The output of the comparator is a 5 volt peak-to-peak signal which is fed to a 50 ohm line driver. The analog output signal is obtained by increasing the output voltage of the last amplifier with a two-stage transistor amplifier.

Automatic gain control (AGC) is obtained by peak detecting the output of the last amplifier and supplying control lines to the amplifiers and to the APD power supply. The APD control is derived from a voltage on the command line to the APD power supply. An optical AGC range of about 25 dB is available.

The receiver module specifications are:

Digital Data Output	TTL Compatible
Total Power Supply Current Drain	≤ 300 mA
Peak-to-Peak Analog Output	$3 \pm 1\ V_{pp}$
Analog Rise/Fall Time	≤ 17 nsec
Digital Rise/Fall Time	≤ 20 nsec
Analog Optical Sensitivity[a]	-48.2 dBm
Digital Optical Sensitivity[b]	-58 dBm
Power Supply Variation Tolerance	±5%

a. Average optical power at detector for 30:1 SNR
b. Average Optical power at detector for 10^{-8} BER

4. FIBER/CABLE DESIGN

Interconnection of the terminal electronics is achieved by using two fiber structures. One is a multi-fiber cable which traverses the 2 km distance. The other is a six foot buffered fiber which is coiled into a one inch diameter and is used to patch any transmitter or receiver to any fiber in the cable. Both fiber structures are capable of being terminated into either plug or jack optical connectors.

4.1 Multi-Fiber Cable

The multi-fiber cable consists of eight graded index fibers in lengths up to 1 km. As shown in Figure 5, the cable is formed around a 2 mm optical fiber bundle. This bundle is composed of eight fibers helically laid around 1 mm filler in the center with polyurethane extruded over it. To provide the necessary tensile strength, Kevlar® 49 strength member yarns are helically laid around the polyurethane cover of the fiber bundle. Finally, the Kevlar® is covered with Teflon® tape with an outer jacket of polyurethane extruded over the tape to form an outer cable diameter of 6.4 mm. The outer jacket and the strength members protect the fiber bundle from damage due to crushing as well as providing the necessary tensile strength. Also, the outer polyurethane jacket provides protection against water and abrasion.

The graded index fibers are fabricated using a chemical vapor deposition (CVD) process. The finished fiber is composed of three basic layers as shown in Figure 6. The core is 50 μm in diameter and consists of doped silica with a refractive index profile which approximates a parabolic distribution from the center of the core to the edge of the cladding. The cladding around the core is a layer of borosilicate which gives a fiber diameter of 125 μm. To protect the glass fiber from abrasion, an outer jacket of Hytrel® is extruded over the glass. In addition to protecting the glass fiber, the Hytrel® jacket helps reduce microbending losses in the cable. The coated fiber has a diameter of about 0.5 mm.

The cable specifications are:

Cable Diameter	6.4 mm
Glass Fiber Diameter	125 μm
Number of Fibers	8
Tensile Strength (2 meter gage length)	150 kg
Attenuation (0.82 μm)	≤ 7 dB/km
Multi-mode Dispersion	≤ 6 nsec/km
Crosstalk	≤ 50 dB
Minimum Bending Radius	5 cm
Operating Temperature Range	$-20^{o}C$ to $+50^{o}C$

4.2 Buffered Fibers

At the two terminals the multi-fiber cables are terminated into junction boxes. The cable strength members are "tied off" and the individual fibers wrapped around a set of spools for storage. Approximately ten feet of fiber is stored on the spools to allow for several re-terminations of each fiber. Each fiber is terminated into a panel mounted connector jack. Six-foot buffered fibers with connector plugs on both ends are used to connect the transmission cable fibers with the transmitter and receiver modules.

The buffered fibers consist of graded index fibers identical to those contained in the cables except that the Hytrel® jacket diameter is increased to about 0.9 mm. No strength member material is used in the buffered fibers. In order to facilitate handling, the buffered fibers are coiled to one inch in diameter, up to the connectors on each end.

5. CONNECTOR DESIGN

Inter-connection of the terminal electronics, buffered fibers and multi-fiber cables is done with single way, single fiber optical connectors manufactured by ITT Leeds (U. K.). A total of five connectors per data channel are used.

5.1 Physical Description

Figure 7 is a photograph of a complete connector. The end-to-end length is 37 mm. The diameter of the main body is about 7.1 mm. Other physical dimensions are shown in Figure 8 with the plug and jack halves identified. The bulk of the connector is identified with the jack portion. Holes in the flange allow the jack to be bulkhead mountable. The plug portion is therefore the demountable half. No provision for terminating a strength member is present; hence, the connector only couples coated fibers.

5.2 Alignment Mechanism

The alignment mechanism used in the connector consists of a jewel bearing located within a precision machined stainless steel ferrule as shown in Figure 9. In the center of the jewel bearing is a precision hole into which the optical fiber is inserted. Jewels are available with hole sizes ranging from 50 μm to 200 μm in 10 μm steps so that a wide range of fiber sizes may be accommodated with the same basic connector design. The jewel bearing is installed in one end of the stainless steel ferrule at the factory.

The ferrules containing the two fibers to be connected are placed in a precision machined sleeve which aligns the two fiber cores. Both of the stainless steel ferrules are spring loaded to insure that the ferrules are abutted. The alignment sleeve and ferrules are then inserted into bulkhead mounting flanges. The connector assembly is completed by screwing a threaded capon each end of the connector.

Assembly of the connector is simple enough to be performed either in the field of at the factory by trained technicians. First, 5 cm of the fiber's protective plastic coating is removed to expose the bare glass. A couple of millimeters from the plastic coating the fiber is scratched using a diamond scribe. The fiber is then broken at the scratch to create a good optical end on the fiber. The fiber end is then positioned to within a few microns of, but recessed from, the end of a proper sized jewel/ferrule with the aid of a microscope. The ferrule is then sealed with epoxy. Once the fibers are installed on the ferrules, the remainder of the assembly process is done by hand.

For graded index fibers (50 μm core diameter) the average connector loss is about 2 dB with a minimum of 1 dB and a maximum of 3 dB. These results were verified in an interchangeability experiment involving 25 different ferrule combinations. Degradation over 50 full mating cycles showed a negligible increase in average loss. With step index fibers or larger core graded index fibers, the loss is expected to reduce to about 1.5 dB.

6. CONCLUSIONS

To verify that the individual component loss and rise/fall time budgets were met, several data channels were configured and the signal output quality evaluated. In all tests, the performance was better than the required specification. The SNR of the analog output varied from 40:1 to 90:1 while the rise time ranged from 15 nsec to 22 nsec. Analog pulse droop and over shoot were about 5-7%. The bit error rate of the digital output was in excess of 10^{-10} at 20 mB/s (NRZ). The digital output rise/fall time was about 6 nsec.

This effort has clearly demonstrated that wideband communication over several kilometers using fiber optic components capable of field operation can be achieved. Moreover, sufficient margin is available to ensure satisfactory operation over extended time and temperature ranges. Another feature evident in this effort is full component interchangeability, whereby field repair by trained technicians is facilitated. As fiber optics becomes a more widely used communications tool, features such as producibility, stability, maintainability, and reliability will become important evaluation criteria to potential users and much of the groundwork in these areas has now been laid.

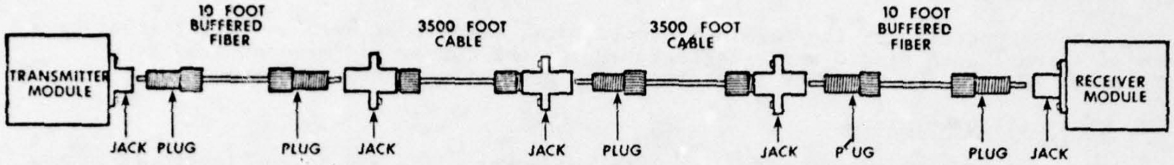

Fig.1 Data channel configuration

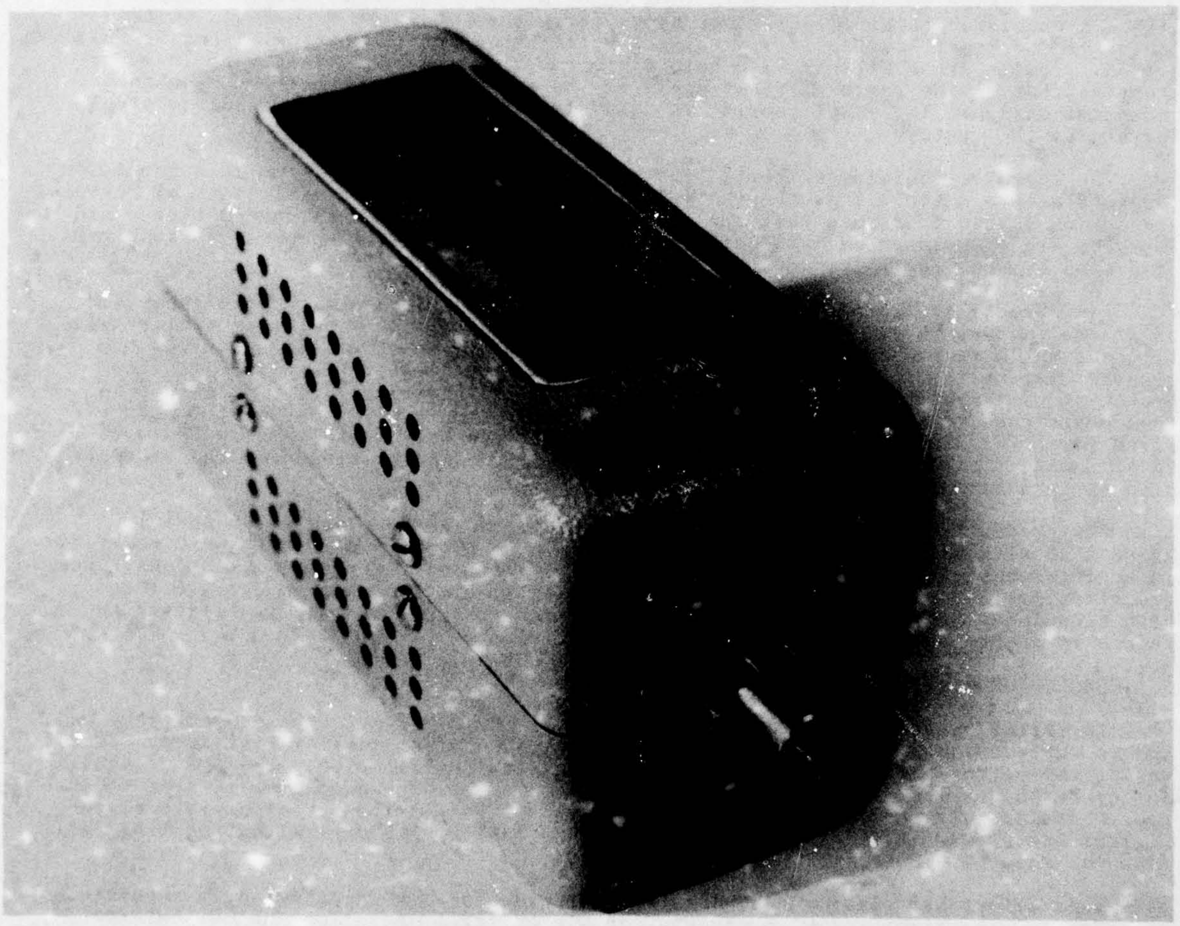

Fig.2 Photograph of the transmitter module

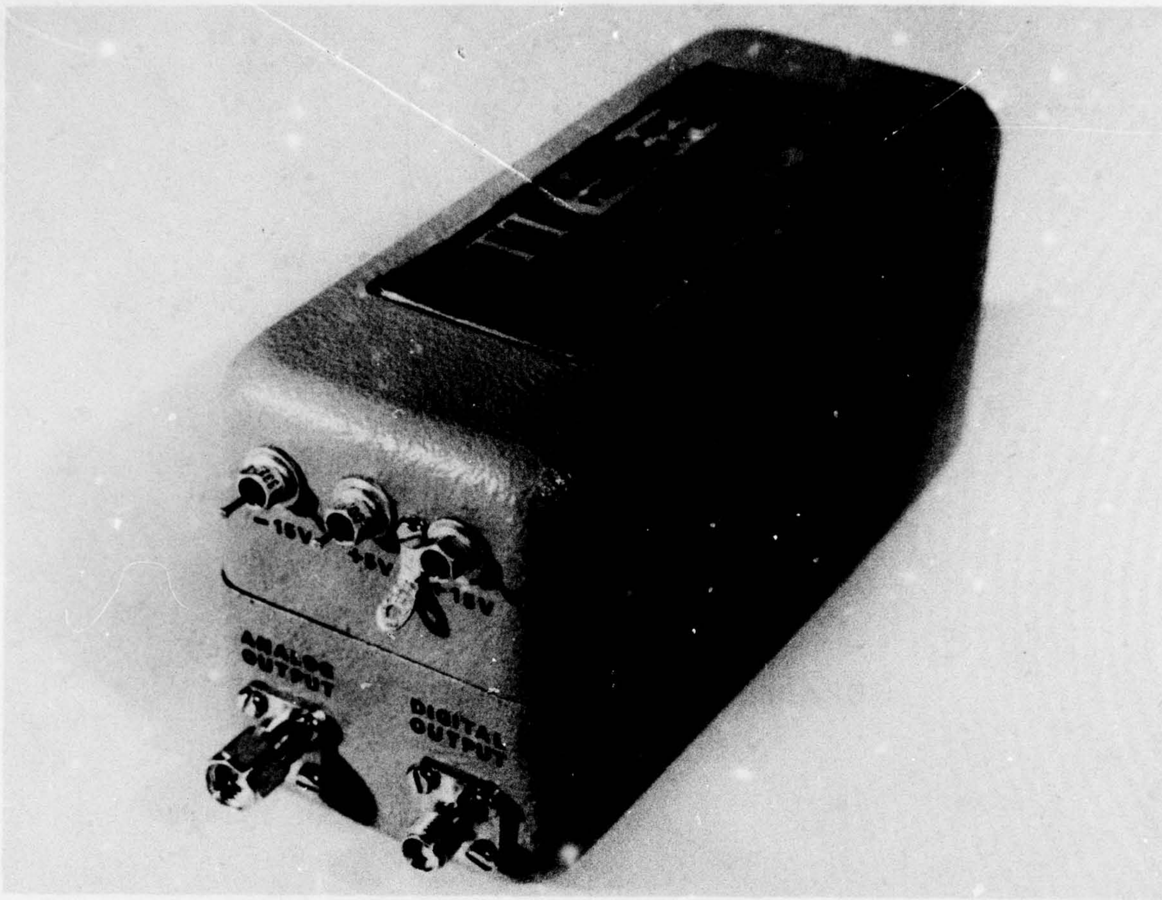

Fig.3 Photograph of the receiver module

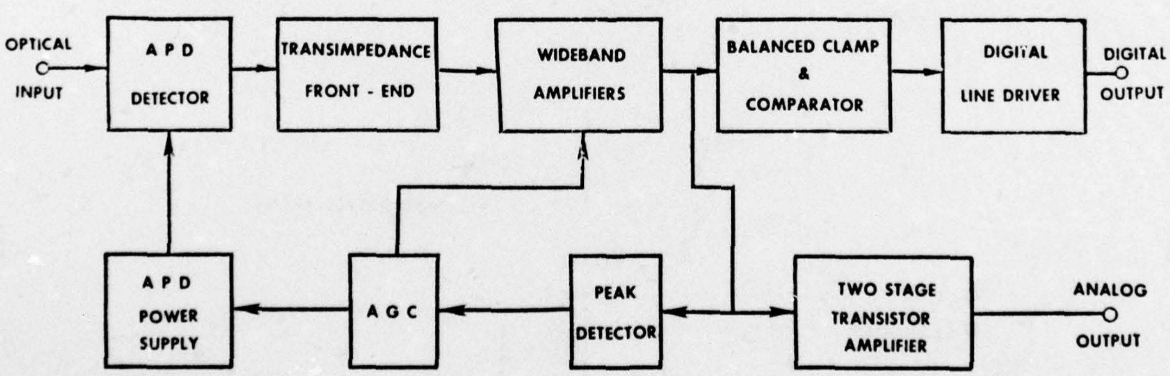

Fig.4 Receiver module block diagram

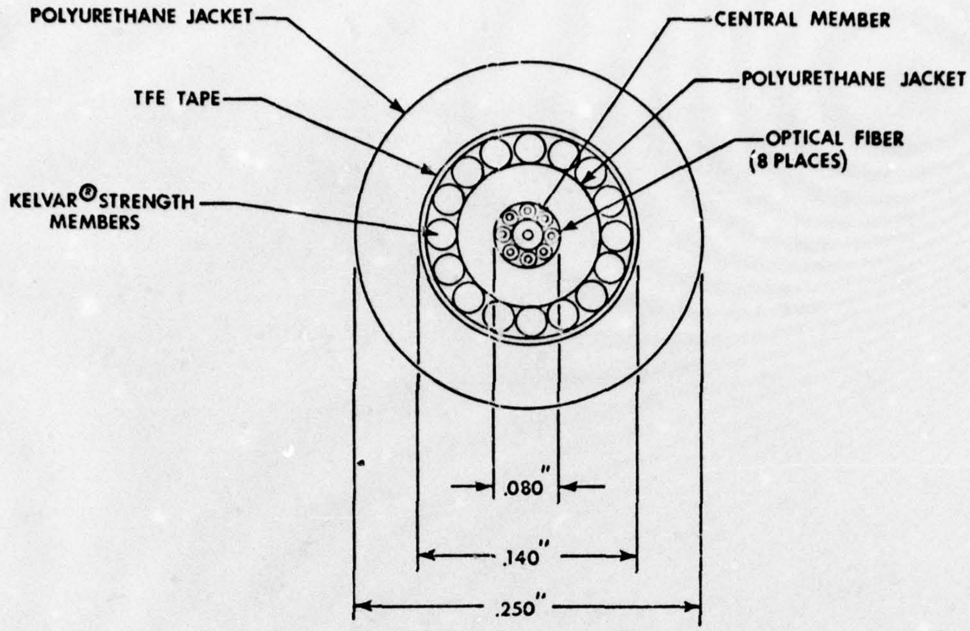

Fig.5 Multi-fiber cable cross section

GRADED INDEX MULTIMODE FIBER

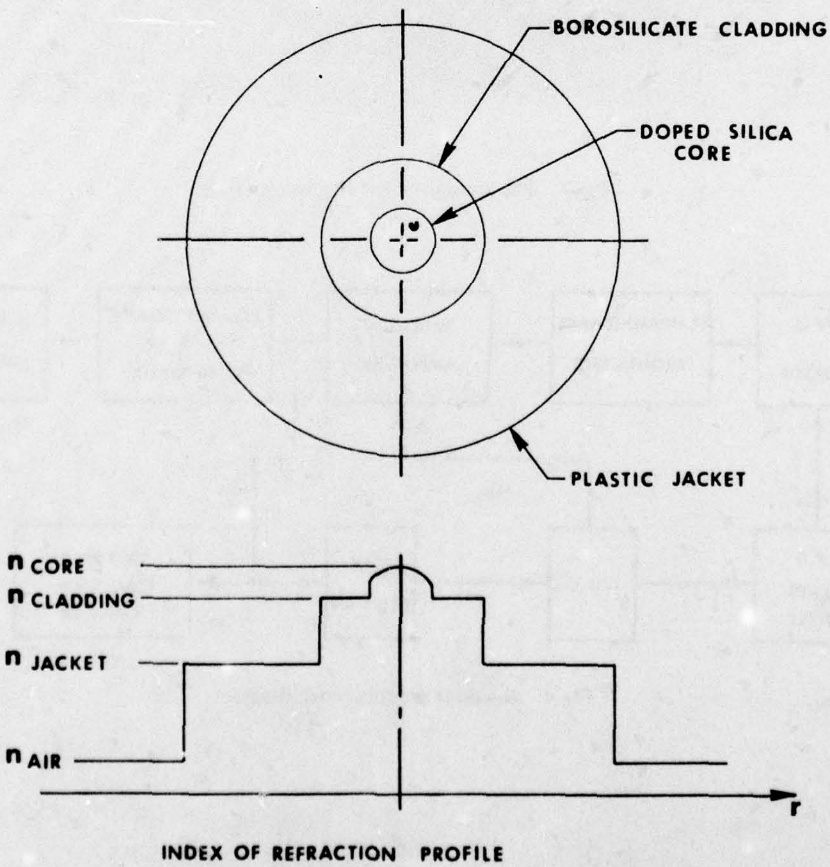

Fig.6 Graded index fiber cross section

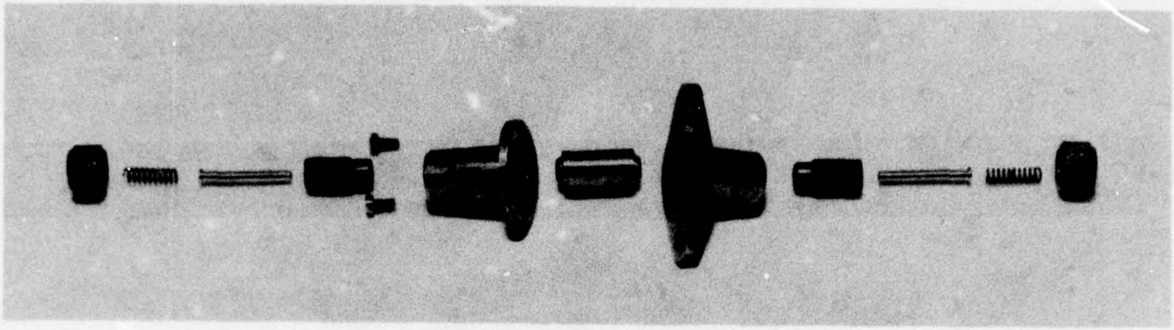

Fig.7 Photograph of the single channel connector

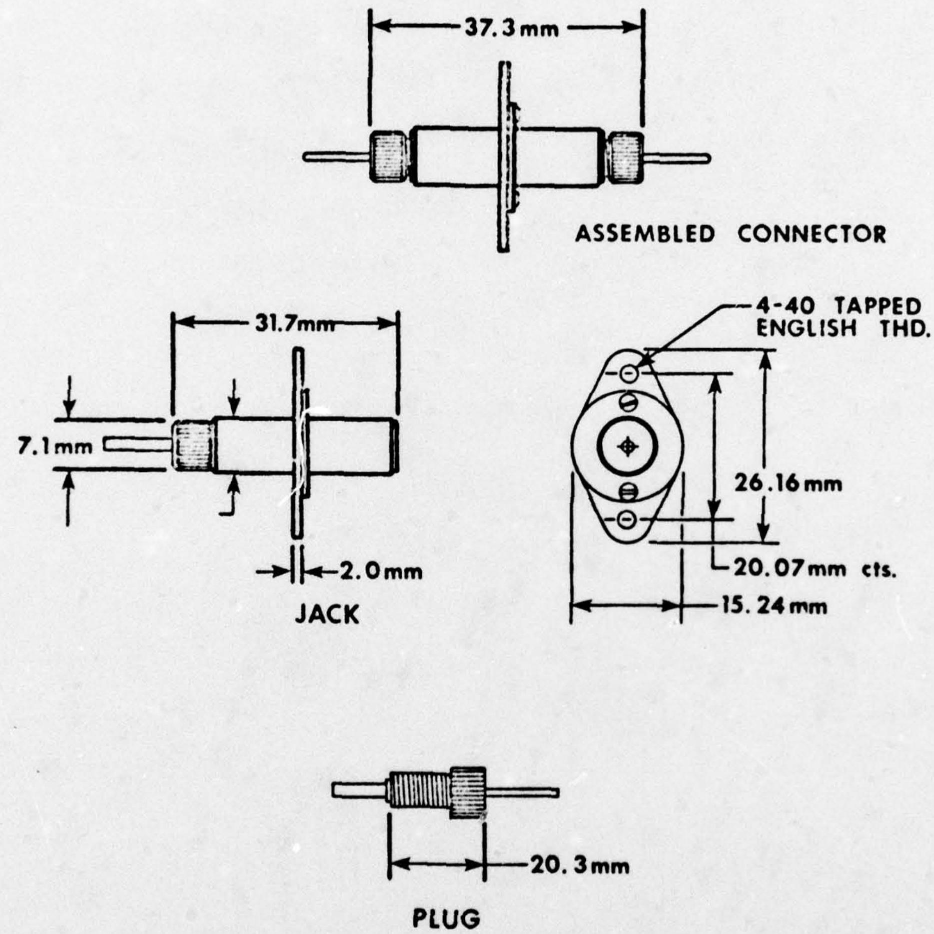

Fig.8 Optical connector physical dimensions

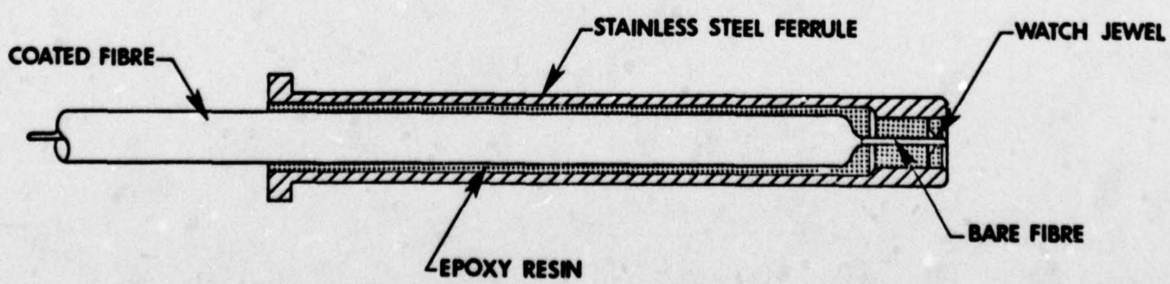

Fig.9 Jewel ferrule assembly

COST MODEL FOR AN OPTICAL FIBRE COMMUNICATIONS SYSTEM

Dr. T.A. Alper

Communications Division
SHAPE Technical Centre
P.O. Box 174, The Hague
The Netherlands

SUMMARY

This study derives a cost model for an optical fibre communications system and presents the normalized cost of such systems for several modulation schemes. Reasonable assumptions are used in developing the model and its application is confined to transmitters that have LED sources and use parabolic-index fibre cables. For the purposes of calculation, a signal-to-noise ratio requirement of 70 dB is assumed for analogue systems, an error rate requirement of 10^{-9} is assumed for digital systems, and modulation rates are assumed not to exceed 100 Mbit/s. The costs per channel per kilometer for a typical short-haul system and for a typical long-haul system are derived to illustrate the use of the model.

1. INTRODUCTION

Optical-fibre communications systems offer many advantages in civil and military applications and most of these advantages are attributable to the optical-fibre waveguide itself. In addition to its small propagation loss and pulse dispersion, this new communications medium also offers the following advantageous properties and features:

(i) Large Transmission Bandwidth

The optical-fibre waveguide is one of the few types of transmission line that can carry extremely broadband information.

(ii) Electrical Isolation

Optical fibres are electrically non-conducting and thus they provide excellent electrical isolation between the transmitter and the receiver. They present no short-circuit or grounding problems.

(iii) Electromagnetic Interference

The optical-fibre waveguide is not susceptible to electromagnetic interference and it does not radiate to any significant degree.

(iv) Physical Factors

Optical fibres and their associated cables are small in size (typical diameters are 0.1 mm and 5 mm respectively) and light in weight. They are easy to transport and to install. (Note, however, their small bending radius demands care in installation).

(v) Environmental Factors

Optical fibres are immune to high operating temperatures. They do not burn, corrode or deteriorate under severe environmental conditions.

(vi) Cost

In addition to their physical advantages, optical-fibre systems also have a cost advantage, since they fall into the medium-cost bracket for electrical communications. Furthermore, the price of the optical fibre cable in the future will depend more or less entirely upon the production rate and consequently they could become relatively cheap.

Although optical-fibre systems are fairly new, they are already being implemented for trial purposes, and they are expected to be widely used in the near future. Cost is one of the important factors that has to be considered in the implementation of any system. The communications system designer has to be able to minimize the system cost by considering trade-offs between repeater spacing, modulation method, modulation rate and system performance, and he can only do this by comparing the cost and the performance of the various available types of optical systems.

In this paper, a cost model for an optical-fibre communications system is presented. The cost of the constituents of an optical-fibre link such as the transmitter, the repeater, the receiver and the cable are represented as functions of the system parameters. These parameters are the overall system length, the repeater spacing, the modulation rate, the output power of the optical source, the sensitivity of the detector and also, of course, the loss and the dispersion characteristics of the cable.

Cost evaluations are carried out separately for short-haul and long-haul systems. In this connection, short-haul systems are considered to be less than one kilometer in length and it is assumed that repeaters are not used in these systems. For both short-haul and long-haul systems, the following modulation schemes are considered:

- Analogue Intensity Modulation (AIM),
- Pulse Position Modulation (PPM),
- Coded Digital Modulation (CDM).

In Chapter 2, the total cost of an optical-fibre communications system is formulated. In this formulation, certain practical engineering assumptions are adopted in order to permit the cost to be expressed in terms of a minimum number of system parameters. In addition, a normalized cost per unit length and bandwidth is defined, and the total system cost is normalized with respect to the sum of the unit prices of a transmitter, a receiver and a repeater.

The performance measure for a modulation scheme is either the signal-to-noise ratio (SNR) or the bit error rate (BER) and in Chapter 2 the appropriate measure is derived for the AIM, PPM and CDM schemes referred to above. By applying suitable assumptions, simplified relationships between the SNR or the BER, and the bandwidth of each modulation scheme are derived.

The numerical results are presented in Chapter 3. The performance measure (SNR or BER) of each modulation scheme is plotted against the bandwidth with the average received optical power as a parameter. The average received power depends on such parameters as the link length or the repeater spacing, the transmitter power, and the cable loss, and it is also given as a function of these parameters.

As examples of the use of the cost model, the normalized costs are derived for a short-haul PPM system, where they are plotted as functions of the link length and information bandwidth, and for a long-haul CDM system, where they are plotted against repeater spacing and the modulation rate.

The final Chapter contains an estimate of the optical-fibre communications system cost per channel per unit length and comments on some of the significant results of the study.

2. COST MODEL AND FORMULATION OF THE SYSTEM PARAMETERS

Consider the optical-fibre communications link shown in Fig. 1, where the overall length of the system is L (km) and the repeater stations are spaced ℓ (km) apart. The cost of such a system depends on the cost of the transmitter unit, the receiver unit, the number of repeaters and the unit cost of each repeater, as well as the total length and the per unit length cost of the fibre cable.

2.1 THE COST MODEL

2.1.1 Transmitter Cost

An optical transmitter consists of a modulator, a light source and associated driver circuitry, and a source-to-fibre connector; its cost is designated C_T. It is reasonable to assume that the cost of an optical transmitter depends on the modulation rate and the output power of the optical source in the following manner (Refs. 2 and 3):

$$C_T = C_{oT} (R/R_o)^{\gamma} (P_t/P_{to})^{\eta} \tag{1}$$

where R_o and P_{to} are respectively the reference value of the modulation rate R and the reference value of the output power of the optical transmitter P_t. The term C_{oT} represents the reference value of the optical transmitter cost corresponding to the reference modulation rate and the reference output power. The values of γ and η depend on the modulation rate as follows:

$$\gamma,\eta < 1 \quad \text{for } R < 100 \text{ Mb/s}$$

$$\gamma,\eta > 1 \quad \text{for } R > 100 \text{ Mb/s}$$

2.1.2 Receiver Cost

The cost of an optical receiver is denoted C_R, and it comprises the costs of a fibre-to-light-detector connector, a light-detector, and a modulator. Although the cost of a light-detector varies as a function of its sensitivity bandwidth, rise-time and quantum efficiency, many of these factors can be combined into a single constant and the cost variation of C_R can be represented as a function of merely the modulation rate. Thus,

$$C_R = C_{oR} (R/R_o)^{\gamma} \tag{2}$$

where C_{oR} is the reference value of the optical receiver cost corresponding to the reference bit rate R_o. Analytical considerations have shown that it is reasonable to express the exponent on (R/R_o) by γ as defined for the transmitter.

2.1.3 Repeater Cost

The repeater cost is referred to here as C_r, and it is dependent upon the sensitivity of the repeater detector, the output power of the repeater transmitter, and the transmission rate. If we assume that the type of optical source and detector used in the repeater have the same cost dependence on bit (or modulation) rate and output power as in the transmitter and the receiver units, the cost of each repeater can be formulated by:

$$C_r = C_{or} (R/R_o)^{\gamma} (P_t/P_{to})^{\eta} \tag{3}$$

where C_{or} is the reference value of the optical repeater cost corresponding to the reference bit rate and the reference transmit power.

2.1.4 Cable Cost

The cable cost is represented here by C_F and it is assumed to depend only upon the transmission loss of the fibre itself. Thus C_F can be written as

$$C_F = C_{oF} (20/\alpha) L \tag{4}$$

where C_{oF} is the reference value of the cable cost corresponding to a 20-dB/km transmission loss and α is the optical fibre cable loss in dB/km.

2.1.5 Link Cost

The total cost of the link is obtained by combining eqs. (1) to (4). Thus

$$C = C_T + C_R + NC_r + C_F \tag{5a}$$

where $N = (L/\ell - 1)$ is the number of repeaters. Eq. (5a) can also be expressed as

$$C = \left[(C_{oT} + NC_{or})(P_t/P_{to})^{\eta} + C_{oR}\right](R/R_o)^{\gamma} + LC_{oF}(20/\alpha). \tag{5b}$$

It is useful to normalize the total system cost in the following manner in order to obtain costs per unit length and per bit/s.

$$\bar{C} = C/\left[LR(C_{oT} + C_{oR} + nC_{or})\right] \tag{6}$$

$$\text{where } n = \begin{cases} 0, & N=0 \\ 1, & N\neq 0 \end{cases}$$

Then

$$\bar{C} = \frac{\left[(1 + N\beta_r)(P_t/P_{to})^{\eta} + \beta_R\right](R/R_o)^{\gamma} + L\beta_F(20/\alpha)}{\left[LR(1 + \beta_R + n\beta_r)\right]} \tag{7}$$

where

$$\beta_R = C_{oR}/C_{oT}$$
$$\beta_r = C_{or}/C_{oT}$$
$$\beta_F = C_{oF}/C_{oT}$$

When $N = 0$, eq. (7) represents the normalized cost of a *short-haul* system, and when $N \gg 1$, it is the normalized cost of a *long-haul* system.

2.2 MODULATION SCHEMES

The cost formulation derived in the previous section can now be used either for a digital or an analogue system with specified system performance. The performance measure for a modulation scheme is either the SNR or the BER. In this study, three types of modulation schemes are considered and in the following sub-sections a relationship between the performance measure, the modulation rate and the detected average optical power is derived.

2.2.1 Analogue Intensity Modulation

In the AIM scheme, the emitting diode is intensity modulated and the SNR at the receiver can be expressed as (Refs 1, 6 and 8).

$$SNR_I = 0.5\left[Q(e/h\nu)\, G\, m\, P_o\right]^2 / \langle i_n^2 \rangle \tag{8}$$

where Q is the quantum efficiency, G is the gain of the optical detector, e and $h\nu$ are the electron charge and the energy per photon respectively, m is the modulation index and $\langle i_n^2 \rangle$ is the total root mean square noise power. P_o is the averaged received optical power and is given by

$$P_o = P_c/\text{anti-log}_{10}\left[(\alpha\ell + \alpha_c)/10\right] \tag{9}$$

where α_c is the fibre-to-optical detector coupling loss, and P_c is the amount of power coupled into the fibre from a source with optical power P_t. The approximate relationship between P_c and P_t is

$$P_c = 0.5\ P_t\ (NA)^2 \tag{10}$$

where NA is the numerical aperture of the fibre.

In eq. (8) $\langle i_n^2 \rangle$ consists of the quantum noise, the thermal noise, the background noise, the leakage and the beat noise (these are discussed in detail in Reference 6). If we assume

$Q = 0.5$,

$\lambda = 0.85\ \mu m$,

$G = 10$,

and $m = 1$,

eq. (8) reduces to

$$SNR_I = 6 \times 10^8\ P_o^2/\left[B_I(2.5 \times 10^{-5}\ P_o^2 + 3.5\ P_o + 3.1)\right] \tag{11}$$

where B_I is the bandwidth of the information source and is taken equal to the channel bandwidth for AIM. Thus, B_I can be expressed as

$$B_I = 6 \times 10^8\ P_o^2/\left[SNR_I(2.5 \times 10^{-5}\ P_o^2 + 3.5\ P_o + 3.1)\right]\ \text{kHz} \tag{12}$$

where P_o is in μW.

2.2.2 Pulse Position Modulation

PPM is an analogue-sampled modulation scheme and the position within the sample period of the leading edge of a short-duration pulse is proportional to the sampled amplitude of the information signal. *The expression for the SNR of such a system can be found in Refs. 6 and 8. If we use the same* values taken for the parameters in the AIM scheme, the expression for the SNR of a PPM system takes the form

$$SNR_P = \frac{6 \times 10^8\ \left[\pi K\ (K - 1)\ P_o\right]^2}{\left[B_N(2.5 \times 10^{-5}\ P_o^2 + 3.5\ P_o + 3.1)\right]} \tag{13}$$

where $K = P_m/2P_o$ and P_m *is the peak pulse power at the receiver, and* B_N *(in KHz) is the noise* bandwidth. The information bandwidth of a PPM system is

$$B_P = B_N/(4K) \tag{14a}$$

and by using eq. (13), the bandwidth is

$$B_P = \frac{1.5 \times 10^7\ \left[\pi K\ (K - 1)\ P_o\right]^2}{\left[K(2.5 \times 10^{-5}\ P_o^2 + 3.5\ P_o + 3.1)\ SNR_P\right]} \tag{14b}$$

where again P_o is in μW.

2.2.3 Coded Digital Modulation

In this scheme, binary pulse code modulation (PCM) is implied and the main requirement would be the achievement of a particular desired error rate, and this is determined mainly by the receiver input power P_o and the pulse rate. If we use the expression given in (9) for the receiver input power with no avalanche gain, we have

$$P_o = h\nu\ q/(QT^{3/2}) \tag{15}$$

where 1/T is the bit rate (and is equal to R) and q is the factor that determines the error rate given by

$$BER = (1/2\pi)^{1/2} \int_q^\infty \exp(-\ x^2/2)\ dx \tag{16}$$

For a digital receiver with additive gaussian noise, the bit rate is obtained from eq. (15) as:

$$R = 100\ (2.2\ P_o/q)^{2/3}\ \ \text{Mb/s} \tag{17}$$

where P_o is in μW.

3. NUMERICAL RESULTS

The study and the application of the model are confined to optical transmitters that have LED sources and use parabolic-index fibre cables. The normalized cost values can be obtained by evaluating eq. (7) as a function of the system length or the modulation rate. The maximum possible value of modulation rate for each scheme is given by eqs. (11), (13) and (16). However, in certain circumstances the information bandwidth can be limited to lower values than those calculated by eqs. (11), (13) and (16) by virtue of the dispersion characteristics of the fibre. It follows from Refs. 4, 5 and 7 that the maximum modulation rate of a parabolic-index fibre is

$$R_p \cong 2\, c\, n_1^3 / [\ell (NA)^4] \tag{18}$$

where c is the velocity of light in vacuo and n_1 is the index of refraction of the fibre core.

3.1 ASSUMPTIONS

With regard to the calculations, there are certain simplifying assumptions concerning the values of the constants and the variables; in brief, the values of the constants are estimated from the small quantity prices of various optical components and the range of values for the variables are constrained to the state-of-the-art. Also, in all the cases considered, the information bandwidth is limited to 100 MHz, since it appears to be the upper limit achievable with LED sources.

The constants in the analysis are:

$\beta_R = 1,\ \beta_r = 2,$ and $\beta_F = 10,$

$\gamma = 0.5$ and $\eta = 0.5,$

$n_1 = 1.5,$

$NA = 0.2,$

$\alpha_c = 4$ dB,

$R_o = 1$ Mb/s

$P_{to} = 1$ mW

The variables in the analysis are:

$1 \text{ mW} \leq P_t \leq 10 \text{ mW}$

$10 \text{ dB/km} \leq \alpha \leq 40 \text{ dB/km}$

3.2 RESULTS

When the assumptions stated above are used in eq. (7), the normalized cost of both short-haul and long-haul systems can be simplified. Thus, for the short-haul systems when N = 0

$$\bar{C}_S = 5 \times 10^{-7} \left[(1 + P_t)^{1/2} / (L\, R^{1/2})\right] + 10^{-4}/\alpha R \tag{19a}$$

and for the long-haul systems when $N >> 1$

$$\bar{C}_L = 5 \times 10^{-7} \left[P_t^{1/2} / (\ell\, R^{1/2})\right] + 5 \times 10^{-5}/\alpha R \tag{19b}$$

where P_t is in mW, R is in Mb/s, α is in dB/km and L or ℓ is in km.

The performance measure of the modulation schemes given in eqs. (11), (13) and (16) are plotted in Figs. 2 to 4 against the information bandwidth or the modulation rate. The average received optical power (P_o), which is used as a parameter, is given by eq. (9) and it can be seen to depend on the link length (or the repeater spacing), the transmitter power, and the cable loss. The values of P_o are plotted in Fig. 5 as a function of link length with transmitter power and cable loss as parameters. One can use Figs. 2 to 5 to select the type of cable and the transmitter power if the system SNR or BER and the information bandwidth are specified.

Equations (19a) and (19b) can now be used to evaluate the normalized cost of the short-haul and the long-haul systems for a range of α and P_t values by varying R and L in the case of the short-haul systems and R and ℓ in the case of long-haul systems. However, instead of presenting the results for all possible cases, the use of the cost model will be illustrated with specific examples; For a short-haul system, the PPM scheme is considered and the normalized cost ($\bar{C}_S$) is plotted in Fig. 6 as a function of the link length and the information bandwidth. For a long-haul system, the PCM scheme is considered and the normalized cost ($\bar{C}_L$) is plotted in Fig. 7 against the repeater spacing and the modulation rate. In the evaluations, P_t and α are used in turn as the parameter.

3.2.1 Short-Haul PPM System

The SNR objective of this system is assumed to be 70 dB and the maximum information bandwidth is plotted against the system length in Fig. 6. By selecting various combinations of α and P_t one can use Fig. 6 to maximise either the information bandwidth or the system length.

The normalized cost of the PPM system ($\bar{C}_S$) is plotted in Fig. 7 against the system length for a constant information bandwidth of 5 MHz. In all the cases shown, the normalized cost decreases as a function of the system length and one can trade-off the cable loss against transmitter power, in order to minimize the cost. For example, for system lengths less than 0.3 km the cost is minimum for a cable loss of 40 dB/km and a transmitter power of 1mW, and for the same transmitter power over system lengths of 0.3 to 0.6 km, the 20 dB/km cable gives the minimum cost. On the other hand, for system lengths greater than 0.6 km, the cost can be minimized by selecting the 20 dB/km cable with a transmitter power of 10 mW. Thus, for shorter lengths, the transmitter-receiver cost dominates and variation of the normalized cost is determined by the system length. However, for longer system lengths, the cable cost dominates and variation of the normalized cost is determined mainly by the type of cable used.

In Fig. 8, the normalized cost $\bar{C}_S$ is plotted against the bandwidth for two different values of L. For a constant P_t and α, the normalized cost is an inverse function of the bandwidth and its slope is dependent on the value of L.

3.2.2 Long-Haul PCM System

The BER objective of this system is taken to be 10^{-9} and the maximum modulation rate is plotted in Fig. 9 against the repeater spacing. As can be seen from Fig. 9, the maximum bit rate decreases as a function of ℓ and it is 0.1 Mb/s for a repeater spacing of 6 km when using the 10 dB/km cable and a transmitter power of 10 mW.

In Fig. 10, the normalized cost of the long-haul PCM system ($\bar{C}_L$) is plotted against the repeater spacing, and the modulation rate is used as a parameter. For low modulation rates, i.e. less than 1 Mb/s, $\bar{C}_L$ is nearly constant and its value is determined mainly by the cable cost. However, for higher bit rates, the repeater cost dominates and the variation of $\bar{C}_L$ as a function of ℓ is more prominent.

$\bar{C}_L$ is also plotted in Fig. 11 against the bit rate for a repeater spacing of 2 km with α and P_t taken as parameters. For a constant α, the normalized cost decreases as a function of the modulation rate, and has almost no dependence on P_t. For example, if baud rates above 2 Mb/s are desired, the 10 dB/km loss cable has to be used, and the difference in $\bar{C}_L$ with ten times more transmitter power is not significant, even though four times faster transmission rate is provided.

4. CONCLUSIONS

In this paper, a cost model for an optical fibre communications system is derived, and the normalized cost curves for a short-haul PPM system with an SNR of 70 dB, and for a long-haul PCM system with a BER of 10^{-9}, are presented. The results obtained in the evaluations are based on reasonable assumptions and are applicable to transmitters with LED sources and graded -index fibre cables.

The data for the short-haul PPM system is shown in Figs. 7 and 8. When the information bandwidth is held constant, the normalized cost is effectively determined by the transmitter-receiver cost for short system lengths (i.e. less than 300 metres) and by the cable cost for longer system lengths. If we consider the system length of 0.5 km in Fig. 8, the minimum normalized cost is 5.5×10^{-6} for 1 MHz bandwidth when using the 40 dB/km cable and a transmitter power of 4 mW. If C_{oT} is assumed to be 500 US dollars, the total cost of this system for a duplex link would be 5500 US dollars (or approximately 50 US dollars per channel per km.). If a 10 dB/km cable is used, the total cost of this system would be 13000 US dollars (or approximately 100 dollars per channel per km.).

The data for the long-haul PCM system is shown in Figs. 10 and 11. At low transmission rates, i.e. less than 1 Mb/s, the normalized cost has almost no dependence on the repeater spacing and the system cost is determined predominantly by the cable cost. At higher transmission rates, the total cost is more dependent on the repeater cost and the number of repeaters, and thus the variation of the normalized cost with the repeater spacing is more evident. Also for long-haul systems, the normalized cost is weakly dependent on the transmitter power.

If a pulse rate of 2 Mb/s is selected for the long-haul PCM system, corresponding to 32-channel PCM, the normalized cost is 2×10^{-6} for a repeater spacing of 2 km and a cable loss of 20 dB/km. Again, if C_{oT} is assumed to be 500 US dollars, the total cost of this system is 8000 US dollars per km (or 270 US dollars per km per channel). However, for a 10 dB/km cable, the total cost would be 12000 dollars per km (or approximately 400 US dollars per km per channel).

The results presented in this study are, of course, only valid for the parameters considered, but we have tried to select values for these parameters that reflect the state-of-the-art. Only data relevant to LED sources are presented, since these are the most reliable optical sources known at present, and the cable-loss values were selected on the basis of current commercially-available products. The exact relationships between the cost, the pulse rate (or bandwidth), the output power of the transmitter and the cable loss naturally have a significant bearing on the results. These relationships are constructed on the basis of the cost analysis of several optical components. We believe the results of the cost calculations given above for the short-haul and the long-haul systems are within the range of commercially-available system costs.

REFERENCES

1. R.M. Gagliardi and S. Karp, "Optical Communications", John Wiley & Sons, New York, 1976. Sections 4-5.

2. R.L. Gallawa, M. Koyama, "A Cost Model for Optical Waveguide Communication Systems", Office of Telecom., Boulder, Colorado, Rep. No. 74-32, March 1974

3. R.L. Gallawa, "A User's Manual for Optical Waveguide Communications", Office of Telecom., Boulder, Colorado, Rep. No. 76-83, March 1976

4. D. Gloge, Appl. Opt., Vol. 10, pp. 2252-2258, October 1971

5. D. Gloge and E.A.J. Marcatili, Bell System Technical Journal, Vol. 52, pp. 1563-1578, November 1973

6. W.M. Hubbard, Bell System Technical Journal, Vol. 52, No. 5, May-June 1973, pp. 731-765

7. D. Marcuse, Bell System Technical Journal, Vol. 52, pp. 1169-1174, September 1973

8. S.E. Miller, T. Li and E.A.J. Marcatili, Proc. IEEE, Vol. 61, No. 12, December 1973, pp. 1703-1751

9. S.D. Personick, Bell System Technical Journal, Vol. 52, No. 6, July-August 1973, pp. 843-874.

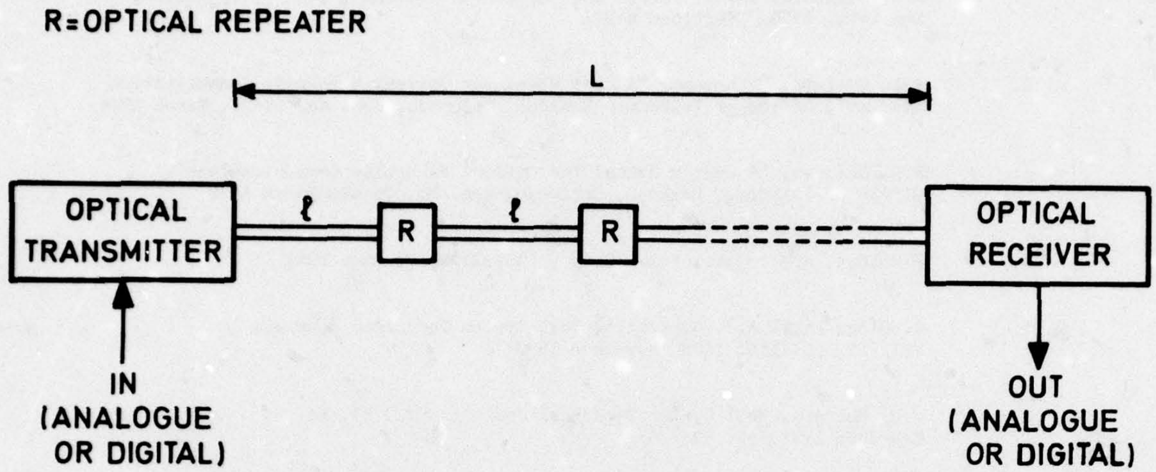

Figure 1: Block Diagram of an Optical Fibre Link

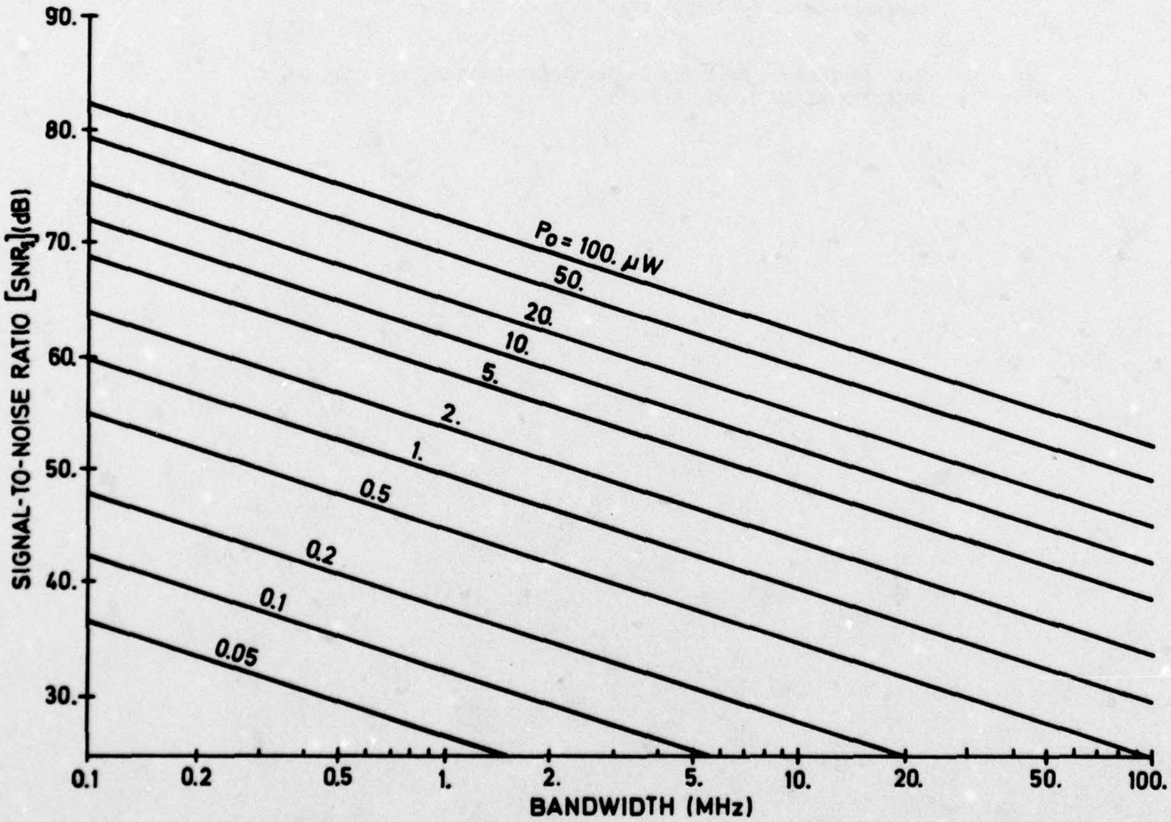

Figure 2: Signal-to-Noise Ratio of an Analogue Intensity Modulation System versus Bandwidth

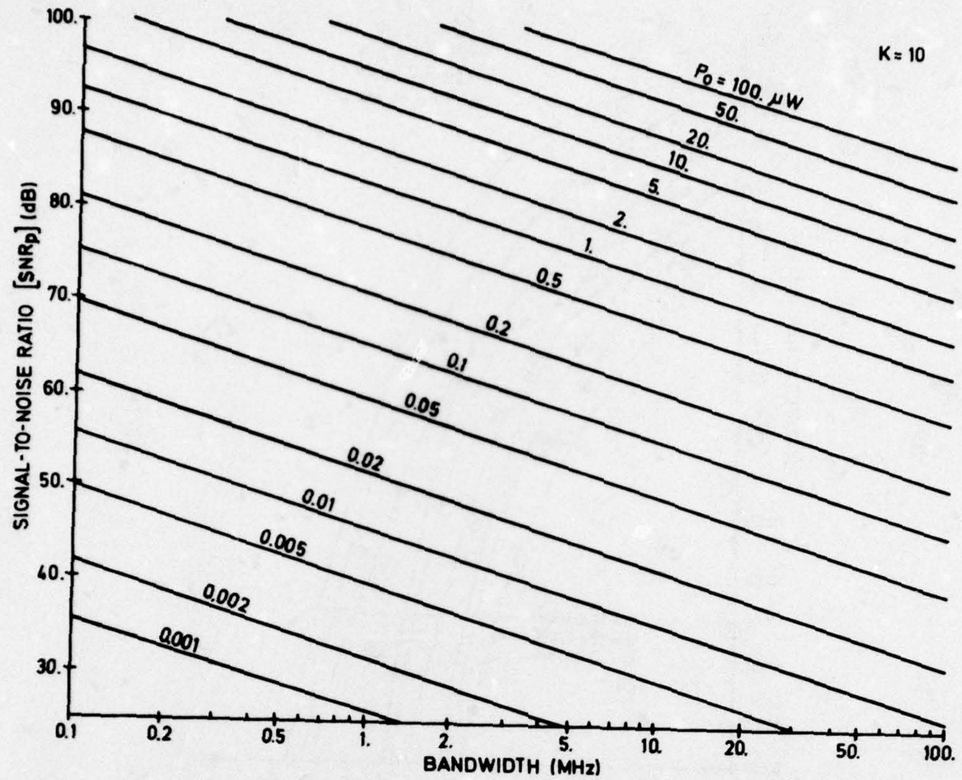

Figure 3: Signal-to-Noise Ratio of an Analogue Pulse Position Modulation System versus bandwidth

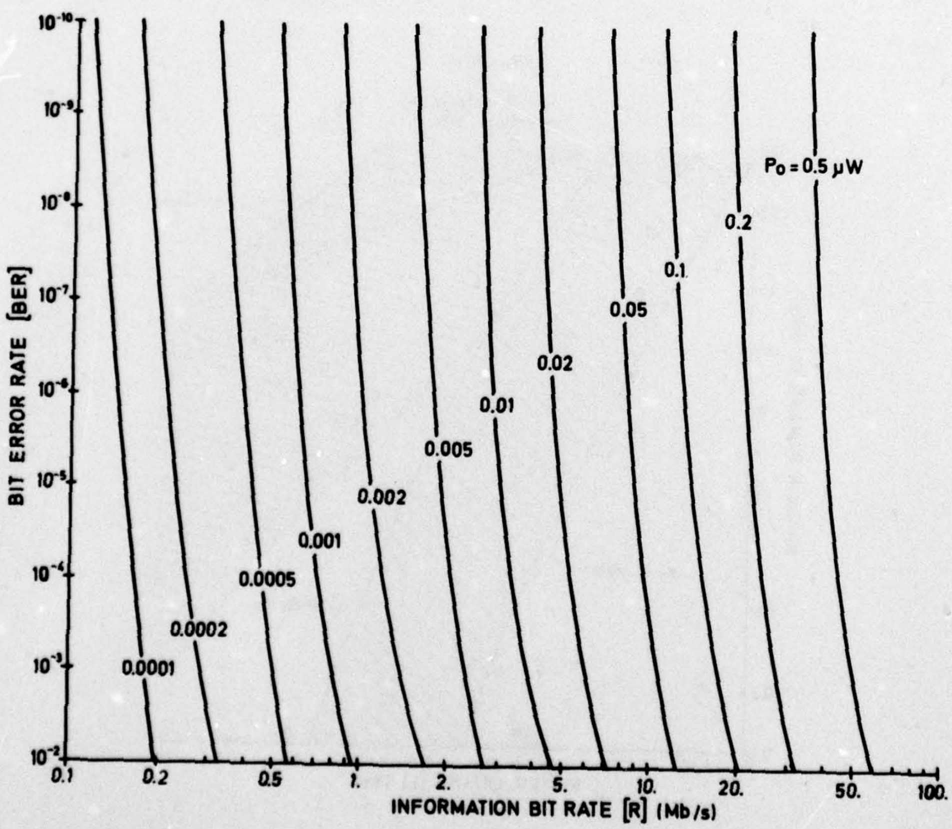

Figure 4: Bit Error Rate of a Pulse Code Modulation System versus Information Bit Rate

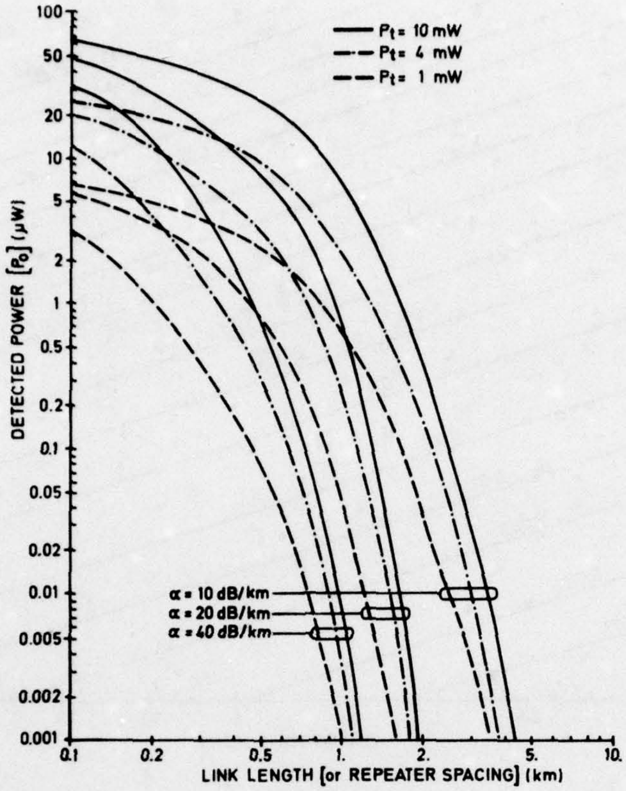

Figure 5: Average Optical Detected Power versus Link Length, with Cable Loss and Transmitter Power as Parameters

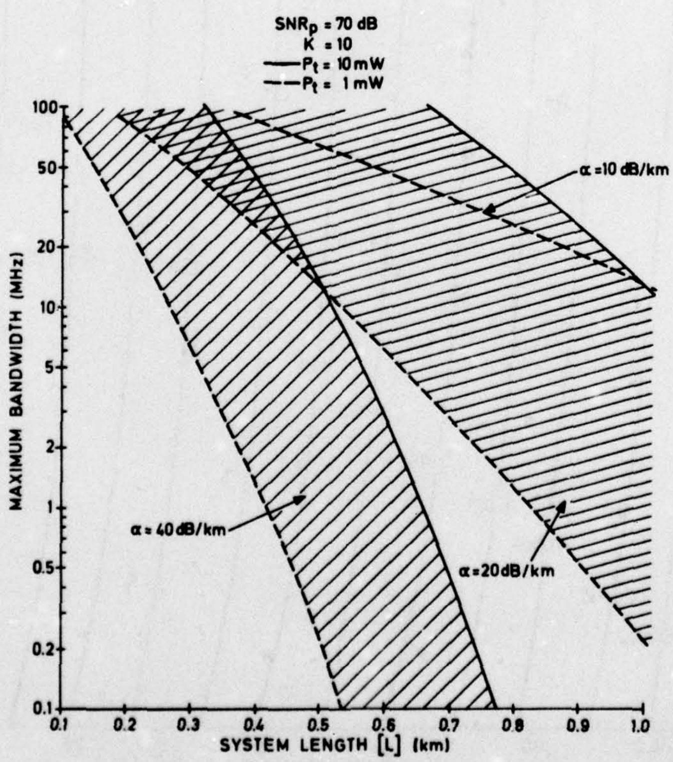

Figure 6: Maximum Bandwidth of the Pulse Position Modulation System versus Link Length for a Signal-to-Noise Ratio of 70 dB

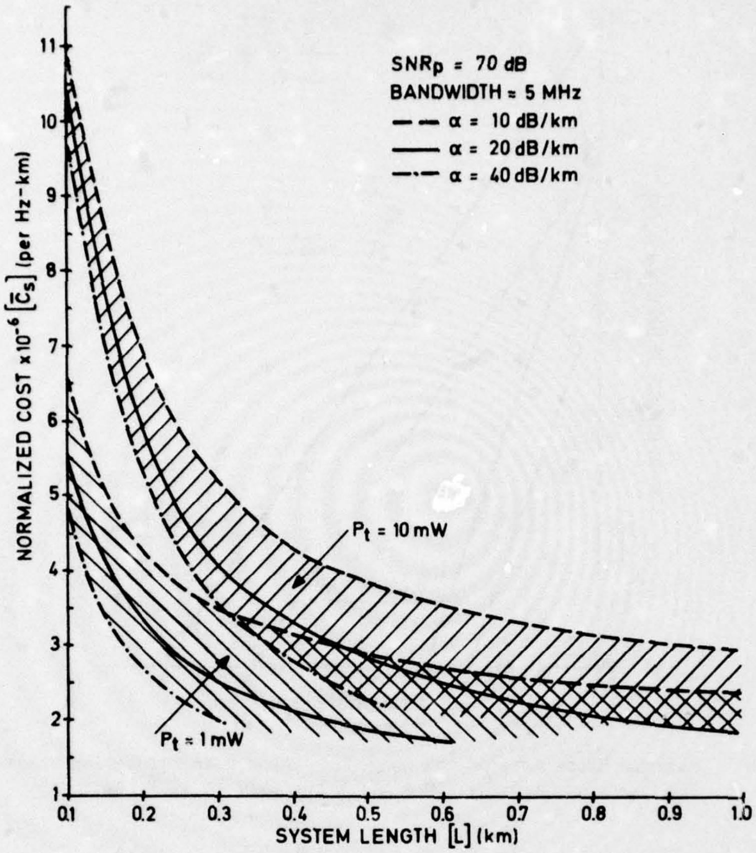

Figure 7: Normalized Cost of the Short-Haul Pulse Position Modulation System versus Link Length

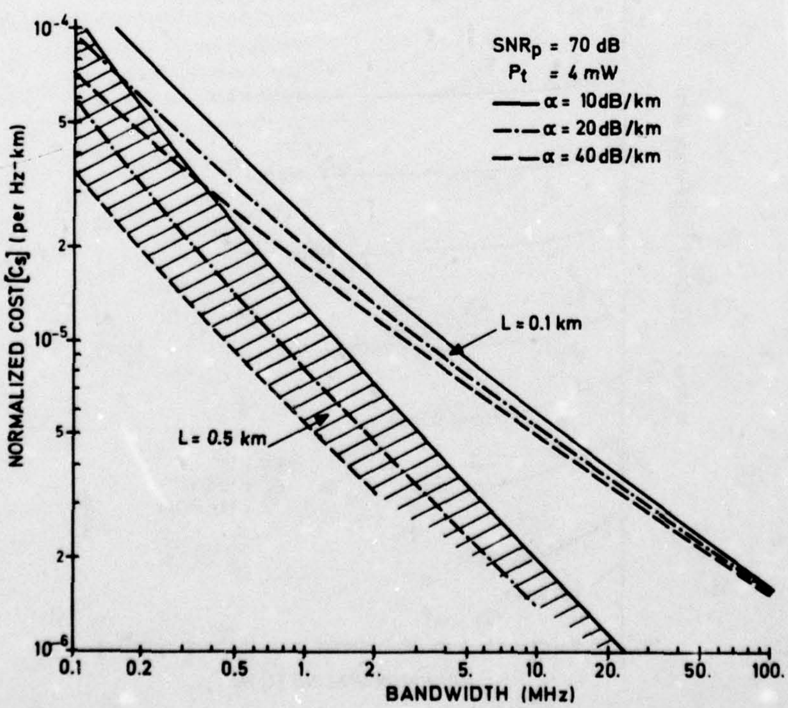

Figure 8: Normalized Cost of the Short-Haul Pulse Position Modulation System versus Bandwidth for a Signal-to-Noise Ratio of 70 dB

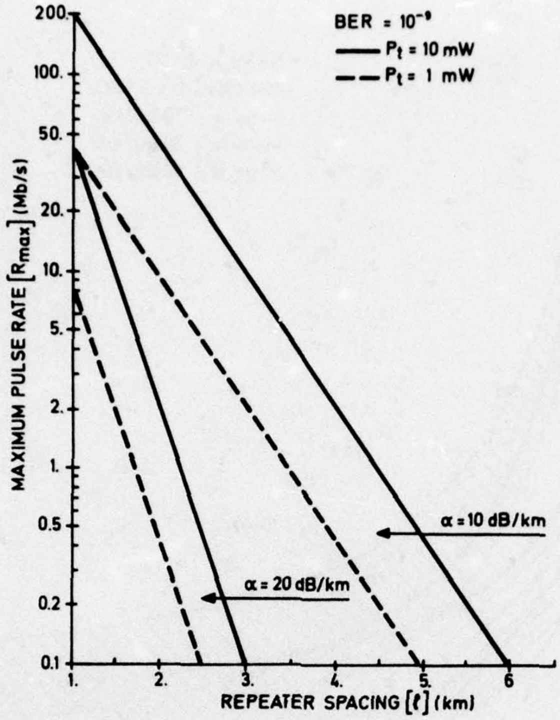

Figure 9: Maximum Pulse Rate of the Long-Haul Pulse Code Modulation System versus the Repeater Spacing, for a Bit Error Rate of 10^{-9}

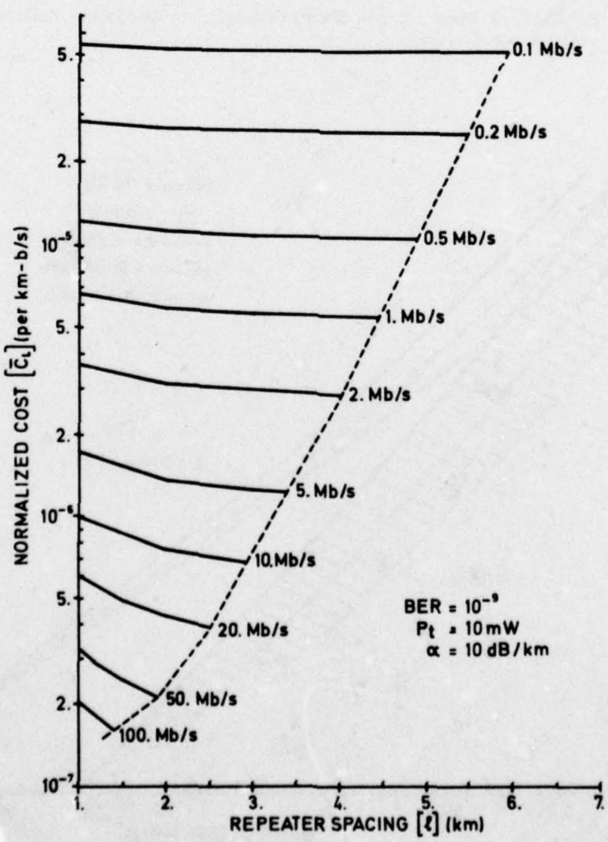

Figure 10: Normalized cost of the Long-Haul Pulse Code Modulation System versus the Repeater Spacing for a Bit Error Rate of 10^{-9}

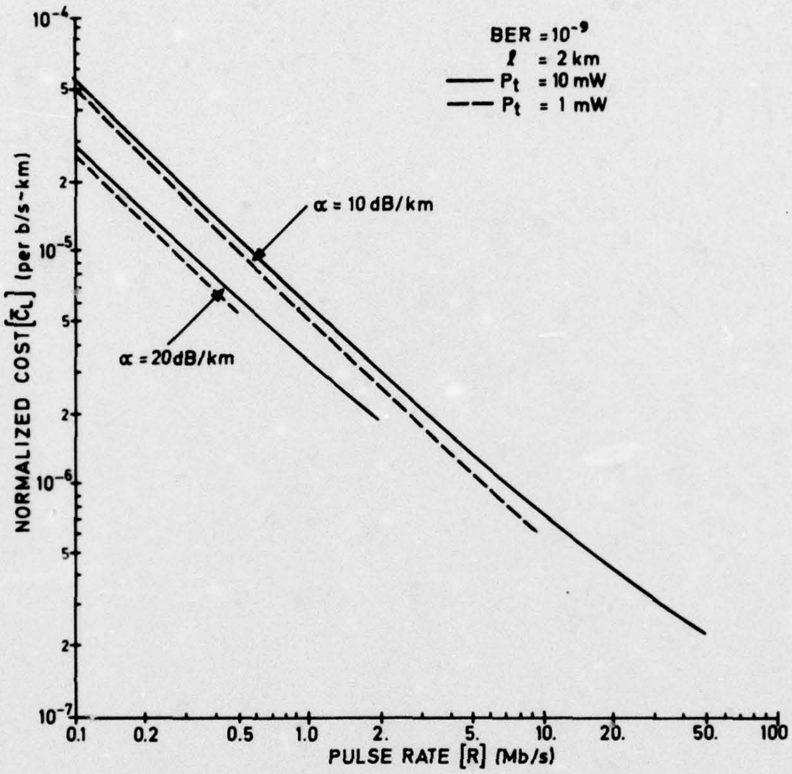

Figure 11: Normalized Cost of the Long-Haul Pulse Code Modulation System versus the Pulse Rate for a Bit Error Rate of 10^{-9}

A-7 ALOFT ECONOMIC ANALYSIS AND EMI-EMP TEST RESULTS

R. A. Greenwell and G. M. Holma
Naval Electronics Laboratory Center
271 Catalina Blvd.
San Diego, CA 92152 USA

Summary

An economic analysis of fiber optics technology for the A-7 aircraft was undertaken in July 1975. The project, Airborne Light Optical Fiber Technology (ALOFT), was assigned to the Naval Electronics Laboratory Center (NELC), San Diego, California, to manage the flight test and evaluate the effectiveness of a fiber-optic interface communication system in an operational aircraft. The purpose of this paper is to present the final results of the economic analysis made of the system and to report upon electromagnetic-interference (EMI) and electromagnetic-pulse (EMP) tests.

The economic analysis developed credible cost projections for three performance-equivalent cable alternatives: coaxial, twisted-shielded pair, and fiber optic. These cost projections were generated by an approach which utilizes two techniques; one which computes very specific costs of research and development (R&D), investment, and operation and support (O&S) for the data-transmission links, and the other which computes total weapon systems cost of R&D, investment, and O&S resulting from the inclusion of the field-operation systems. The results clearly indicated definite economic benefits with fiber optics.

Tests were also performed to determine EMI susceptibility and EMP effects on fiber-optic and wire interconnects for the A-7 navigation and weapon delivery subsystem (NWDS). These tests were performed in the laboratory and on the aircraft. Results from the EMI and EMP tests have shown that the A-7 ALOFT fiber-optic subsystem is less susceptible to EMI and greatly reduces electromagnetic induction from an induced transient pulse.

1.0 INTRODUCTION

The A-7 ALOFT program was assigned to the Air Systems Program Office, NELC, San Diego, California, for management and control of the flight test, evaluation, and economic feasibility of a fiber-optic interface communication system in an operational military environment. This program, sponsored by the Naval Air Systems Command, Washington, DC, provided a meaningful demonstration of fiber-optic systems for use as internal aircraft signal-data transmission links. Signal wiring in the navigation weapon delivery system (NWDS) of a Navy A-7 aircraft was replaced by electronic multiplexing circuits and fiber-optic interface components. The system was first tested in the laboratory and then was installed in the A-7 aircraft in which nearly 150 flight test hours have been conducted on the fiber-optic interconnect configuration. Definitive comparisons have been made of the original A-7 wiring and the improved fiber-optic interconnect configuration to show EMI immunity, reduction in system transient pulses produced by high magnetic induction fields, increased reliability, and total cost offsets.

The requirement for an economic analysis is defined in most program and planning documents. Economic analysis, as defined by the Defense Economic Analysis Council (DEAC) and as explained in DOD Instruction 7041.3 and DOD Directive 5000.28 as well as many others, is "the process which assists the decision maker in the allocation of resources through the determination of the costs and benefits of each future course of action." During the conceptual phase of a program, the chosen alternatives should be compared with total life-cycle costs and total benefits before a decision is made. All the risks and uncertainties should also be addressed prior to this decision.

The requirement for fiber optics was expressed clearly in the Operational Requirement (OR), "Advanced Aircraft Electrical System (AAES)." Future threats dictate a need for an improvement in the quantity and quality of aircraft and their avionics. The threat to avionics must be met with a reduction in radio-frequency interference (RFI), electromagnetic interference (EMI), and electromagnetic pulse interference (EMP). In addition, there exists a need for a dramatic reduction in weight and volume. Coupled with these items is the desire for improved reliability, maintainability, availability, survivability, and capability. Other ORs and Scientific and Technical Objectives (STOs) have the same requirements. These stated requirements are the proven or expected advantages of fiber optics. The economic-analysis effort has compared these desired benefits with other alternative wire-interconnect subsystems and, at the same time, has determined the total life-cycle costs for each subsystem. Life-cycle costs are the total costs, directly or indirectly associated with an alternative during its development, acquisition, and operational time frame.

2.0 ALOFT INTERFACE DESCRIPTION

One hundred fifteen signals which were originally transmitted over a very dense, parallel interface, consisting of 302 wires (twisted-shielded pair, three-wire, and coaxial cables) were multiplexed into 13 data-transfer channels. Data were transmitted via 13 fiber-optic cables and were consolidated into a single optical connector at the computer interface. Such extensive point-to-point multiplexing was possible because of the wide bandwidth available with fiber-optics. Analog, digital, discretes, pulse trains, and switch closures were among the signal types which were transmitted over these 13 fiber-optic multiplexed channels. The ALOFT system was designed to operate up to 10 megabits per second. The signals were time-division multiplexed and were transmitted over the fiber-optic cables using Manchester coding. The maximum transmission distance in the ALOFT configuration was less than 10 metres, with a maximum of 5 passive coupling points from the light source to the detector. The actual worst-case system attenuation losses through this longest link with the greatest number of coupling points, including splice margins, connector losses, and error margin, was less than 45 dB. This was achieved with 1974 technology which consisted of gallium-aluminum-arsenide (GaAs) light-emitting diodes (LEDs), a 45-mil bundle, high-loss, glass-on-glass, fiber-optic cables, PIN silicon photodiodes, and 3 types of connectors along with the appropriate circuitry needed to convert electricity to light and, conversely, light to electrical potentials. Figure 2-1 presents a side-by-side comparison of the amount of copper wiring and connectors displaced in the A-7 aircraft by the 13 fiber-optic cables in the multiplexed ALOFT system. Length, weight, and actual cost comparisons are also presented in this figure.

3.0 COST ANALYSIS METHODOLOGY

The purpose of the A-7 ALOFT Economic Analysis Program was to develop valid cost estimates for performance-equivalent digital-data transfer systems utilizing conventional wire and fiber-optics. The cost estimates were generated by an approach which utilized two techniques: one which computed research and development (R&D), investment, and operating and support (O&S) costs for the fiber optics and wire interconnect data transmission subsystems ("Bottoms-Up" model); and another which computed the total weapon system costs as a result of changes in weight of the respective subsystems ("Top-Down" model). The "Bottoms-Up" model outputs became one of the inputs to the "Top-Down" model which yielded the total life-cycle cost (LCC) results.

The "Bottoms-Up" model was designed to reflect the subsystem cost differences between the fiber-optic and wire-interconnect alternatives. The "Top-Down" model measured changes in weight which affected design options on aircraft LCC. The integration of the two models was conducted in the following manner and is illustrated in figure 3-1:

a. Detailed subsystem LCC differentials for a specifically designed data transmission subsystem were generated from the "Bottoms-Up" model.

b. The delta weight associated with a specific data-transmission subsystem (relative to the baseline A-7 aircraft weights) was utilized to determine the change in total weapon system life-cycle costs through changes in the growth or shrinkage of the airframe, engine, etc., to support the respective changes in subsystem weight ("Top-Down" model).

c. The results from these two models were then consolidated, tested for sensitivity, and evaluated to provide the total LCC for each alternative.

Several basic parameters had to be established before data could be input to the cost models. Production schedules and quantities had to be established for each alternative design configuration. Escalation and strategic-commodity rate increases and experience-curve estimates had to be established for each alternative.

The base year for the economic analysis was established as beginning 1 January 1977 with a 3-year period assigned to perform the research, development, and test and evaluation of a subsystem design. The next 4 years were assigned to the acquisition of the subsystem, and the final 10 years were assigned as anticipated operational life without a service-life extension program (SLEP). The basic A-7 Navigation/Weapon Delivery Subsystem (N/WDS) is the baseline design in a total production schedule of 812 A-7E aircraft. Of these 812 aircraft, 12 are test vehicles, the costs for which are included in RDT&E fabrication costs. The remaining 800 aircraft will meet the following delivery schedule:

1980 – 80,

1981 – 240,

1982 – 240, and

1983 – 240.

It was also assumed that, of the 800 aircraft, 675 will be operational vehicles. The utilization rate was assumed to be 35 hours per month for 9 of the 10 years of operation. The remaining year was considered to be a wartime operational environment and the operation rate was assumed to be 12 hours per day. A-7E aircraft attrition rates in Southeast Asia were also assumed for survivability analysis.

3.1 "Bottoms-Up" Model

NELC had the requirement of obtaining fiber-optic cost information in the development of the A-7 ALOFT Cost Model. Many difficulties arose in the development of the life-cycle cost model. There was no data base for production-unit costs (except for those costs for model-shop work and prototype development). No cost models existed for component-level development such as for cables, connectors, and, particularly, virgin-technology fiber optics. Additionally, no operational fiber-optic system had ever been constructed. All of these factors meant that standard analytical techniques could not be applied to the study and that many uncertainties had to be considered.

Therefore, in order to alleviate some of the overall uncertainties relating to any new technology, the decision was made to consider only those costs which were relevant to the problem at hand. This was accomplished by identifying only those life-cycle cost elements which had significant cost differences between wire-interconnect and fiber-optic configurations. This model was called "Bottoms-Up" and it addressed cost changes between particular data-transmission subsystems. These cost elements were separated into 4 major cost categories: research, development, test and evaluation (RDT&E); nonrecurring investment; recurring investment; and operation and support (O&S). Sixteen cost elements in these 4 categories were determined to have significant cost differences and therefore became the elements of the "Bottoms-Up" cost model.

Initial cost data for fiber-optic, life-cycle cost elements were gathered with the use of questionnaires. Appropriate Delphi questionnaires were distributed to both aircraft and fiber-optic manufacturers. Telephone and personal interviews were then conducted with manufacturers and other organizations, as appropriate, to finalize the data collection. From the data-collection effort, cost factors were calculated for the fiber-optic cost elements. These cost factors are summarized in Table 3-1. Except where noted, the cost factor is the

TABLE 3-1. TABULATION OF DIFFERENTIAL COST ELEMENTS.

Cost Category	Cost Element	Cost Element Description	Cost Factor
RDT&E	1.2.1.2	Design Engineering Cost	0.80
	1.2.1.3	Fabrication Cost (Test aircraft)	0.95 (labor) 1.05 (material)
	1.2.1.4	Development Test Costs	$100 000
	1.2.1.5	Test Support Costs	$100 000
	1.2.1.8	Test Equipment Costs	$100 000
Nonrecurring Investment	2.1.5	Initial Spares & Repair Parts	0.83
	2.1.6.3.2	Maintenance Training (Contractor)	$4000
	2.1.10	Peculiar Support Test Equipment	1.30
	2.2.2.2	Training Devices Costs	2.00
	2.2.2.3.2	Maintenance Training (Government)	$8000
	2.2.2.3.3	Instructor Training (Government)	$8000
Recurring Investment	3.1.1	Manufacturing Costs	0.80
	3.1.2.1	Purchased Equipment & Parts	0.83
	3.1.3	Sustaining Engineering	0.80
Operating & Support	4.2.1.1.1	Organizational Maintenance	0.80
	4.2.1.3	Support Equipment Maintenance	0.80
	4.2.2.3	Spare Parts & Repair Material	0.50
	4.2.2.4.1	Inventory Management Costs	1.60

ratio of the fiber-optic cost relative to the cost of "equal-functions" performance if coaxial cables were used. The coaxial subsystem costs are based upon the component types and quantities specified in NELC Technical Document 435 (ELLIS, J. R. and GREENWELL, R. A., 1975). An example of the cost factor can be explained by observing the cost element number, 1.2.1.2, Design Engineering. The cost factor value of 0.80 signifies that the estimated aircraft design-engineering cost for electrical subsystems using fiber-optics technology would be only 80 percent of the design-engineering cost using coaxial-cable technology. For some cost elements, where coaxial costs are not applicable, the fiber-optics costs are estimated actual dollar values.

Besides the Delphi Technique as a forecasting tool to predict future costs, experience-curve theory was also used as a forecasting technique to estimate the future cost behavior of fiber-optic components. Experience-curve theory predicts cost reductions for all cost elements, including labor, development, overhead, capital, marketing, and administration. Experience-curve theory implies that present costs obtained from industry of components in full-scale production can be expected to reduce by a fixed percentage of previous cost with each doubling of industry's production volume. Past costs of the fiber-optic cable, which constitutes only one of the required building blocks to build interface systems, indicate that the experience-curve slope will be between 70 and 80 percent.

This means that future cost of the required fiber-optic components, which will be determined by the demand placed on industry, should be reduced to 80 percent of the previous cost as industry's production volume doubles. Figures 3-2 and 3-3 are current cost-prediction curves of two fiber-optic components compared with those of coaxial-component counterparts. The fiber-optic component costs are actual dollars, including inflation. The material cost factors in table 3-1 are based upon these estimated cost-prediction curves.

3.2 "Top-Down" Model

The second major effort undertaken was the definition, quantification, and evaluation of system effectiveness. In other words, the determination of what benefits are received for the dollars expended. The comparison of total costs of each alternative subsystem meets only half the requirements for an economic analysis. Benefits such as improved mean-time-between-failure (MTBF) and mean-time-to-repair (MTTR) may result from one alternative or the other. Immunity to EMP, EMI, or RFI may also be achieved by one alternative. Signal-bandwidth capacity may be increased, cable redundancy may be improved, weight and volume may be reduced, and many more benefits may be achieved. Each of these effectiveness parameters must be quantified, ranked, verified, and revised in terms of cost offsets and levels of attainment. An advanced-concept cost model estimates costs and benefits as functions of design and weight requirements. Two effectiveness areas were pursued for total cost impact from the "Top-Down" model: weight and MTBF. In order to relate these effectiveness factors into some quantifiable measures, a direct-cost relationship approach was applied.

3.2.1 Airframe Plus Subsystem MTBF Analysis

Normally MTBF does not vary without some equipment modifications, improvements, etc., that may have resulted from a weight or requirement change. However, to show the effect of MTBF alone, an analysis was performed in which MTBF was varied without considering any accompanying change in weight.

The baseline for this analysis assumed that the MTBF for the A-7E is 0.9 hour. Based upon actual data for the period January 1975 through June 1975, the MTBF of the airframe plus subsystems was 1.5639 hours. For purposes of this study, the airframe plus subsystems was defined as the total aircraft less the propulsion and avionics subsystems. The electrical subsystem is thus part of the airframe plus subsystems. The MTBF of the airframe plus subsystems was varied from 1.550430 hours to 1.584552 hours corresponding to a 15-hour decrease to 60-hour increase, respectively, in the MTBF of each equipment which is affected by a weight change. A baseline MTBF of affected equipment was arbitrarily chosen as 60 hours and is representative of an aircraft such as the A-7. The electrical subsystem MTBF is included in the baseline airframe plus subsystem MTBF since it is beyond the scope of this effort to allocate a separate MTBF to all components of the airframe plus subsystems.

Changing the A-7 airframe plus subsystems MTBF affects 2 fundamental inputs to the "Top-Down" model. The first is the total aircraft MTBF; the second is the airframe plus subsystems MTBF. All other MTBF's remain the same.

Figure 3-4 was developed by combining the procurement and O&S MTBF cost deltas. The baseline cost is the same as for total LCC sensitivity to weight, or 11459.38 millions. The magnitude of the cost delta ranges from plus 6.2 millions for a 15-hour MTBF to a savings of 16.3 millions for a 45-hour MTBF change.

It is important to note that the projected cost deltas do not include cost increases nor decreases due to the RDT&E necessary to achieve the MTBF change since this relationship is unknown and cannot be established from data currently available.

3.2.2 Weight-Impact Analysis

This model will involve changes in aircraft size which will result from possible weight savings which occur when fiber optics are used or the possible weight increases caused by increased wire and airframe shielding required to meet performance requirements. The model will include cost categories normally used with the Advanced Design Level (ADL) studies at McAir for making projected weapon-system cost estimates.

The electrical subsystem weight-analysis phase of the cost benefit evaluation is executed by parametrically increasing and decreasing the electrical subsystem weight of the basic A-7 aircraft to illustrate the effect upon weapon system costs.

The relationship of RDT&E costs to electrical subsystem weight is shown in figure 3-5. Because the baseline cost is so large (1,016.988 millions in constant 1977 dollars), the cost deltas for ±50 kilograms are proportional to the weight. The RDT&E cost delta is, thus, linear over this range of weights. The slope of the cost delta is $\$1.716 \times 10^5$ per kilogram.

The Procurement cost delta was computed from the baseline cost for 800 aircraft of 4,260.198 millions of 1977 dollars. Performing the same type of calculations as previously discussed, yields the results shown in figure 3-6. The cost delta is again linear. The maximum positive delta is 47 millions for the addition of 50 kilograms, while the reduction of 50 kilograms results in a negative delta of 47 millions.

It should be noted that the cost delta shown for procurement includes the cost delta shown for Flyaway and that all the spares are included in procurement costs. The slope of the procurement cost delta is $\$9.6 \times 10^5$ per kilogram.

The cost delta associated with the effect of electrical subsystem weight upon operating cost is shown in Figure 3-7. The baseline operating cost for 675 aircraft for 10 years is 6,182.194 millions in 1977 dollars. The cost delta is piecewise linear and has a slope of $\$6.05 \times 10^5$ per kilogram. The step in the cost delta between -20 and -30 kg is a consequence of the structure of the "Top-Down" model. Integer squadron maintenance staffing is assumed, and realistically so. Thus, at a given input level, staffing must increase or decrease by one unit which is reflected as a substantial increase or decrease of cost delta over the life cycle of the aircraft.

Figure 3-8 is a summation of cost deltas which shows the total life-cycle cost delta for the aircraft due to electrical subsystem weight variations. The plot is piecewise linear and has a slope of $17.22 $\times 10^5$ per kilogram.

MTBF of total life-cycle cost is very small compared to weight. The relation between MTBF and life-cycle cost is non-linear but, by way of example, a life-cycle cost offset of $4 million was realized by either a reduction of 2.3 kilograms of electrical subsystem component weight or an increase of 20 hours to the MTBF of the affected equipments. The aircraft industry believes it is easier to achieve the weight reduction than it is to increase MTBF. Thus, this "Top-Down" model was based only upon changes in aircraft weight. However, when more valid data can be collected for electro-optic systems MTBF, both weight and MTBF cost values will be utilized in future electro-optic economic analyses.

4.0 EMI/EMP TESTS

Several tests were performed to determine the electromagnetic-interference and pulse-induction characteristics of the fiber-optic data link. These series of tests conformed to the procedures of MIL-STD-461/462 and were performed both in the laboratory bench-test environment and with the system installed on the aircraft. The tests performed were: transient (low-level, 2000 amperes) lightning test, radiated susceptibility testing (simulates aircraft carrier EM environment), and wire coupled susceptibility testing (simulates aircraft EMI situations).

4.1 Transient-Analysis Testing

The method currently in use for determining the amplitudes and character of induced transients on aircraft is the Transient-Analysis Test. This test applies a current pulse (similar to lightning in waveshape but much lower in peak current amplitude) to the aircraft under test, while circuits of interest within the aircraft are monitored to record the transients which are induced (figure 4-1). When the induced transient levels the aircraft will experience due to a full-threat lightning strike (200 thousand amperes) are of interest, the results obtained at the lower current levels (300 to 3000 amperes) are linearly extrapolated to the 200 thousand-ampere strike level. This test is non-destructive in that no damage to the aircraft avionics generally results even when the aircraft is repeatedly subjected to pulses of these low amplitudes.

The transient voltages and currents experienced by aircraft avionics systems due to the flow of lightning currents through the skin and structure of an aircraft are considered to be coupled into the avionics, in general, by three different mechanisms: (1) electromagnetic induction into the power-supply wiring within the aircraft, (2) electromagnetic induction into the low-level signal wiring within the aircraft, and (3) electromagnetic induction directly into the device or subsystem from the electric and magnetic fields generated within the aircraft due to the lightning current flowing through the structure. Little information is available to date on the relative importance of these 3 mechanisms.

This test provides a simulation of a natural and expected environment and has been performed in numerous aircraft with valid results. However, it should be noted that previous aircraft used all-wire systems and that energy induced on existing standard signal and power wiring may mask the test results in a hybrid (wire and fiber) configuration.

4.2 Radiated Susceptibility Testing

The fiber-optic data link was exposed to radiation at several discrete frequencies from 15 kHz to 10 GHz as shown in figure 4-2. RF field strength measurements of the radiation incident on the link were made for several frequencies in order to relate test levels to the carrier environment. Transients induced in the conventional wiring and performance factors in the fiber-optic link were measured by interference analyzers which were located in a shielded enclosure away from the test area.

Radiated susceptibility testing is a low-risk, inexpensive method of simulating an aircraft carrier electromagnetic environment.

4.3 Wire-Coupled Susceptibility Testing

This test was performed by applying a noise signal to a test wire which was taped adjacent to the fiber-optic and conventional-wire bundles. The system was then operated in the most susceptible mode and performance was observed for degradation while the amplitude and modulation of the noise signal were varied. The noise signal was generated using a transient generator as shown in figure 4-3 with variable pulse rate and amplitude. Forty-five, 100, and 200 volt spikes were induced on the test wire to determine evidence of degraded system operation.

5.0 EMI/EMP TEST RESULTS

In a benign EMI and lightning environment, the multiplexed fiber-optic system possessed the same accuracy as the non-multiplexed wire system. In an EMI or lightning environment, the multiplexed fiber-optic system was superior to the non-multiplexed wire system. The majority of the induced transients were found to be introduced on the signal wires and not on power wires or box couplings. This indicates that fiber optics will solve many EMI/EMP problems.

5.1 Transient Analysis Test Results

These tests simulated a lightning-strike test as performed by the Flight Dynamics Laboratory, Wright-Patterson Air Force Base. These tests were conducted at NATC, Patuxent River. Various test points in the NWDS computer were monitored while the aircraft was exposed to the simulated lightning strike. In the fiber-optic configuration, the induced voltages within the computer when exposed to a simulated lightning strike, were 85-to-90 percent less than the induced voltages in the wire configuration. Thus, the fiber-optic configuration would be much less susceptible to damage if the aircraft were to be struck by lightning. This is even more significant considering that the A-7 aircraft signal wiring is all double-shielded wire. Since a lightning strike is very similar to an electromagnetic pulse (EMP) in its induced effects on avionics, the same results could be carried over to EMP susceptibility.

5.2 Radiated Emission/Susceptibility Test Results

Radiated emissions in the frequency range of 14 kHz to 50 MHz were far below the limits of MIL-STD-461A. Except for a narrowband signal at about 118 MHz and one at about 210 MHz, no signal was recorded which was above the receiver ambient noise level. Even these signals appeared to be transient in nature and could not be repeated.

No malfunctions of the data link occurred when it was subjected to the following electric fields:

14 kHz to 35 MHz	10 V/m
35 MHz to 1 GHz	5 V/m
1 GHz to 10 GHz	5 V/m

The results of these laboratory bench tests indicate that the fiber-optic cable and its coupling devices for attachment to the electronics units do not emit significant radiation in the specified frequency range.

In addition, the operation of the fiber-optic data link was not affected when exposed to the specified electric fields.

5.3 Wire-Coupled Susceptibility Test Results

The first of these tests were performed at LTV with the ALOFT hardware operating with the A-7 simulator. These tests measured the bit-error rates of the NWDS double-shielded wire interface and the NWDS fiber-optic interface when exposed to EMI. The bit-error rate for the multiplexed fiber-optic interface was 500 times lower than the bit-error rate for the non-multiplexed wire interface when exposed to the same EMI levels. The bit-error rates are shown in table 5-1.

The second series of these tests consisted of quantitative tests performed at McDonnell Aircraft Company, China Lake, California. The HUD (Heads-Up Display) and PMDS (Projected-Map Display System) were monitored for picture quality while the systems onboard the aircraft were exposed to EMI. No interference with the displays could be observed when the fiber-optic cables were exposed to EMI. The display quality was severely degraded when the single-shielded wire was exposed to EMI. It was found, however, that a massive increase in the bit-error rate is required to produce a noticeable decrease in the quality of the displays.

TABLE 5-1. SUMMARY OF BIT ERROR RATE TEST RESULTS.*

	Data Transmission Time Interval (minutes)	Data Transmitted (Number of Bits)	Errors Induced (Number of Errors)	Bit-Error Rate (Errors/Bit)
Fiber optics exposed to EMI	20	2.6×10^7	0	$< 3.9 \times 10^{-8}$
Wire exposed to EMI	1.67	2.1×10^6	42	2.0×10^{-5}
No EMI exposure	52	6.7×10^7	0	$< 1.5 \times 10^{-8}$

*Test levels from RS02, MIL-STD 461/462 were 20 amperes, 100 volts, and 10 pulses per second.

6.0 ECONOMIC ANALYSIS RESULTS

The results indicate, in the comparison between conventional-wire systems and fiber-optic systems, fiber-optics technology clearly provides substantial future benefits of reduced system weight, survivability, improved reliability, increased data transmission, and ease of maintenance at reduced life-cycle costs while meeting or exceeding the future requirements of EMI and EMP.

The results of the economic analysis are summarized by system configuration, electromagnetic environment, and wire-fiber interconnects. These results, of course, must be bounded since they are constrained by the basic assumptions of the program. The major assumptions were:

- All costs are assumed to be applicable to a new program, not to a retrofit program since all the alternative configurations are new design subsystems for the A-7;
- Cost elements will be developed only where differences between conventional wire and fiber-optic costs occur for the "Bottom's-Up" approach; and
- Fiber optics presents no serious development, reliability, nor production problems and the fiber-optic components are environmentally qualified with life expectancy equal to that of comparable conventional wire components.

For the coaxial TSP, and fiber optics, actual costs are used wherever possible. Specifically, costs of materials were requested from several sources although they were not always received. Where actual data were unavailable, engineering judgment was exercised.

The cost data resulting from exercising the "Top-Down" and "Bottoms-Up" life-cycle cost models applicable to the A-7 aircraft have shown that fiber optics is an attractive alternative to conventional wire data-transfer systems in most cases and especially when the EMI environment places severe demands on the amount of protection required.

For the A-7 ALOFT configuration, the cost results conclude that fiber optics is the best choice followed by TSP and then coaxial in all EMI environments except the one case where the "Top-Down" results indicate the positions of TSP and coax are reversed for the 100 volt/metre (baseline) environment. The total LCC of TSP and fiber optics applied to the A-7 ALOFT configuration are similar. Such a result is highly encouraging in that fiber optics must necessarily carry the burden of large RDT&E costs plus nonrecurring investment maintenance and instructor training costs. Assuming reliability objectives for fiber optics can be realized, this investigation concludes that recurring investment and operating and support costs for TSP are greater than those for fiber optics. For the completely multiplexed A-7 aircraft configuration, fiber optics is the only system to show a cost savings over the baseline system in all categories of environment (eg, in the most severe environment (EMP) a TSP system costs more than the baseline system). The weight savings due to multiplexing translate into a significant cost pay off. Savings are realized both by lower total equipment costs and larger weight savings. For the 100 point-to-point data-link case, the use of fiber optics does not appear to be justified for any environmental situation, principally due to the large amount of conversion components. Only if a situation exists where an aircraft system will not function unless a selected number of fiber optic transmission lines are employed in critical areas can the unmultiplexed point-to-point technique be economically justified.

Similarly, the cost data resulting from exercising the top down and bottoms up life cycle cost models applicable to the advanced A-7 (data bus) aircraft have shown that fiber optics is an attractive alternate to conventional wire data transfer. For the baseline system in the 100 volt/metre environment, a 25-percent savings in LCC is realized using fiber optics for data transfer instead of conventional wires. Also, the LCC increases as the environment becomes more severe for both the conventional wire and fiber-optic configurations, but the increases are significantly larger for conventional wire. There is no linear relation between weight increases and LCC increases. These results are summarized in table 6-1. Tables 6-2 through 6-7 provide the total cost/benefit estimates for the basic A-7 NWDS and the complete A-7 Data-Bus configurations.

TABLE 6-1. SUMMARY LCC RESULTS FOR A-7 ALTERNATIVE CONFIGURATIONS.

ALTERNATIVE WIRE/FIBER INTERCONNECTS		A-7 Alternative Electrical Subsystem Configurations												
		N/WDS			Complete			Mission Critical	Point-to-Point			Data Bus		
		Alternative Electromagnetic Environments (volts per metre)												
		100	200+	50K	100	200+	50K	50K	100	200+	50K	100	200+	50K
Baseline or Copper Wire (unmux)	Δ Bottoms Up	not applicable			second lowest	second lowest	second lowest	second lowest	lowest	lowest	lowest	not applicable		
	Δ Top Down				highest	highest	highest	highest	lowest	lowest	lowest			
	Δ Total LCC				highest	highest	highest	highest	lowest	lowest	lowest			
Fiber Optics (mux)	Δ Bottoms Up	second lowest	lowest	lowest	lowest	lowest	lowest	lowest	second lowest	second lowest	second lowest	lowest	lowest	lowest
	Δ Top Down	lowest	lowest	lowest	lowest	lowest	lowest	lowest	second lowest	second lowest	second lowest	lowest	lowest	lowest
	Δ Total LCC	lowest	lowest	lowest	lowest	lowest	lowest	lowest	second lowest	second lowest	second lowest	lowest	lowest	lowest
Twisted-Shielded Pair (mux)	Δ Bottoms Up	highest	second lowest	second lowest	highest	highest	highest	highest	not applicable			second lowest	second lowest	second lowest
	Δ Top Down	highest	second lowest	second lowest	second lowest	second lowest	second lowest	second lowest				second lowest	second lowest	second lowest
	Δ Total LCC	highest	second lowest	second lowest	second lowest	second lowest	second lowest	second lowest				second lowest	second lowest	second lowest
Coax (mux)	Δ Bottoms Up	lowest	highest	highest	not applicable			not applicable	not applicable			not applicable		
	Δ Top Down	second lowest	highest	highest										
	Δ Total LCC	second lowest	highest	highest										

lowest life-cycle cost — second lowest life-cycle cost — highest life-cycle cost

based on a production of 800 aircraft and assumed 675 operationally ready.

TABLE 6-2. A-7 & NWDS COST/BENEFIT EVALUATION FOR A 100 VOLT/METER EMI ENVIRONMENT.

(Constant 1977 dollars, millions)

	Pessimistic	Fiber Optics Most Likely	Optimistic	Coaxial	TSP
RDT&E	$ 1.07	$ 0.32	$ 0.17	$ 0.09	$ 0.20
Investment (Nonrecurring)	0.52	0.46	0.40	0.66	1.08
Investment (Recurring)	0.52	0.46	0.40	0.76	1.27
Operation & Support	0.14	0.13	0.12	0.45	0.88
Total Life Cycle Cost (Current 1977 Dollars)	$ 2.25	$ 1.37	$ 1.09	$ 1.96	$ 3.43

*based on a new production of 800 aircraft and assumed 675 operationally ready.

TABLE 6-3. A-7* NWDS COST/BENEFIT EVALUATION FOR AIRCRAFT CARRIER EMI REQUIREMENTS (IN MILLIONS).

	Fiber Optics	COAX/TRIAX	TSP/TDS
RDT&E	$ 0.32	$ 0.93	$ 0.47
Investment	0.92	6.90	3.79
O&S	0.73	3.58	1.85
Total (1977 Dollars)	1.37	11.41	6.11

*based on a production of 800 aircraft and assumed 675 operationally ready.

TABLE 6-4. A-7* NWDS COST/BENEFIT EVALUATION FOR A TACTICAL EMP ENVIRONMENT (IN MILLIONS).

	Fiber Optics	COAX/TRIAX	TSP/Double Shield
RDT&E	$ 0.32	$ 1.05	$ 0.61
Investment	0.92	7.82	4.56
O&S	0.13	4.02	2.29
Total (1977 Dollars)	1.37	12.89	7.46

*based on a production of 800 aircraft and assumed 675 operationally ready.

TABLE 6-5. A-7 DATA BUS COST/BENEFIT EVALUATION FOR 100 V/M EMI REQUIREMENTS.

Cost Elements (1977 dollars, Millions)	Fiber-Optics	Twisted-Shielded-Pair
RDT&E	$ 4.7	$ 5.4
Investment	115.0	170.4
O&S	21.0	32.7
Total	$ 140.7	$ 208.5

TABLE 6-6. A-7 DATA BUS COST/BENEFIT EVALUATION FOR AIRCRAFT CARRIER EMI REQUIREMENTS.

Cost Elements (1977 dollars, Millions)	Fiber-Optics	Twisted-Shielded-Pair
RDT&E	$ 6.0	$ 12.8
Investment	114.9	243.4
O&S	21.0	57.9
Total	$ 141.9	$ 314.1

TABLE 6-7. A-7 DATA BUS COST/BENEFIT EVALUATION FOR A TACTICAL EMP ENVIRONMENT

Cost Elements (1977 dollars, Millions)	Fiber-Optics	Twisted-Shielded-Pair
RDT&E	$ 6.0	$ 18.6
Investment	120.4	178.2
O&S	21.7	72.8
Total	$ 148.1	$ 269.6

BIBLIOGRAPHY

DIJAK, J. T., Captain USAF, September 1976, "Simulated Lightning Test on the Navy ALOFT A-7 Aircraft", Air Force Flight Dynamics Laboratory, AFFDL-TM-100-FES.

ELLIS, J. R., LCDR, USN, and GREENWELL, R.A., 7 July 1975, "A-7 ALOFT Economic Analysis Development Concept", Naval Electronics Laboratory Center Technical Document 435.

ELLIS, J. R., LCDR, USN, 1 January 1976, "Interim Progress Summary and Description of the A-7 ALOFT System". Naval Electronics Laboratory Center Technical Report 1968.

FARRELL, H.C., and JACKSON, R.N., June 1973, "EMI Tests of a Fiber-Optic Data Link and A-7 D/E Bench-Test Demonstration", IBM Federal Systems Division.

GORDON, T. J., and HELMA, D., September 1964, "Report on a Long-Range Forecasting Study", Rand Corporation Report P-2982.

GREENWELL, R.A., 1 March 1976, "A-7 ALOFT Life-Cycle Cost and Measures of Effectiveness Models", Naval Electronics Laboratory Center Technical Report 1982.

GREENWELL, R.A., 26 July 1976, "Results of A-7 ALOFT "Bottoms-Up" Model and Weight Sensitivity Analysis", Naval Electronics Laboratory Technical Report 1998.

GREENWELL, R.A., and HARDER, R.D., 12 November 1976, "Airborne Light Optical Fiber Technology", SAWE Paper SWR34 (presented at the Third Southwestern Regional Meeting of the Society of Allied Weight Engineers).

HENDERSON, B., 1970, "Perspective on Experience", The Boston Consulting Group.

JOHNSON, R.L., and KNOBLOCH, E.W., December 1975, "The A-7 Cost Model: A Study of High-Technology Cost Estimating", Naval Postgraduate School Thesis.

MCGRATH, S.M., and MICHNA, K.R., September 1975, "An Approach to the Estimation of Life-Cycle Costs of a Fiber-Optic Application in Military Aircraft", Naval Postgraduate School Thesis.

MCDONNELL AIRCRAFT COMPANY, December 1976, "A-7 ALOFT Economic Analysis.

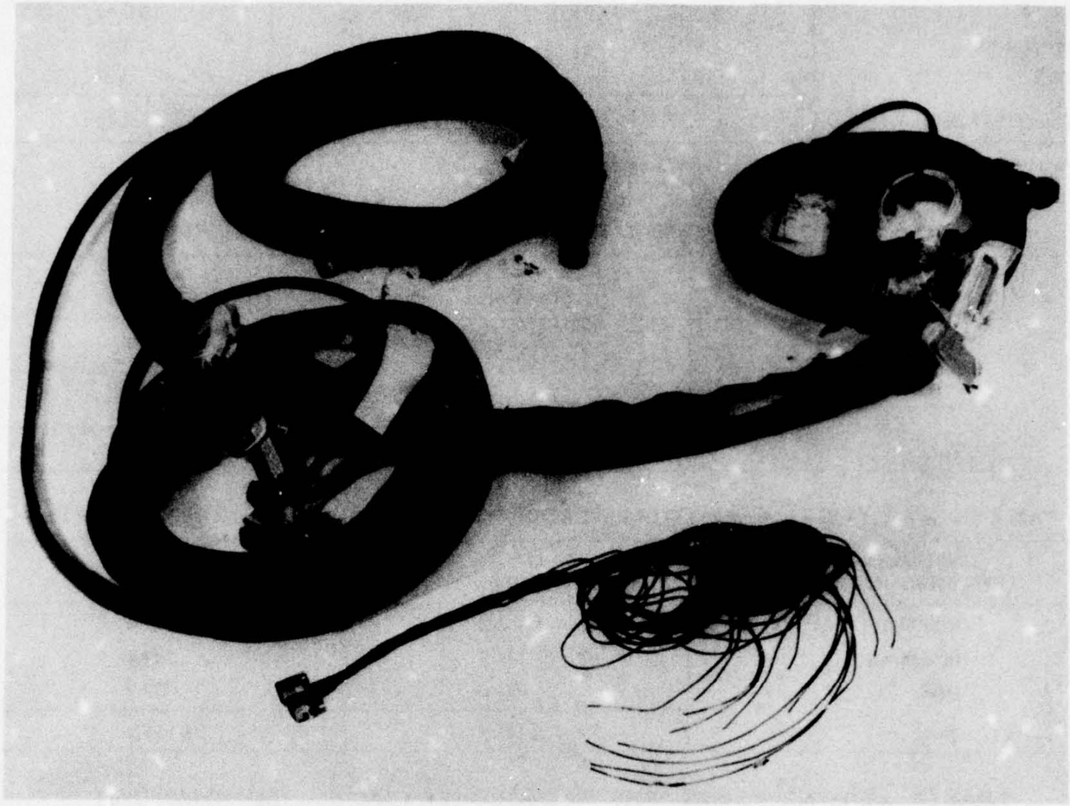

	ORIGINAL WIRE	FIBER OPTICS (MULTIPLEXED)
NUMBER OF WIRES/CABLES	302	13
TOTAL LENGTH	1890 FT (576.07 M)	224 FT (68.27 M)
TOTAL CABLES & CONNECTORS WEIGHT	31.9 LB (14.45 KG)	2.7 LB (1.2 KG)
TOTAL CABLES & CONNECTORS COST	$0.35K	$0.79K
TERMINATION & TEST COST	$1.28K	$0.24K
TOTAL COST	$1.63K	$1.03K

Figure 2-1. Side-by-side comparison, fiber-optic and electrical cables.

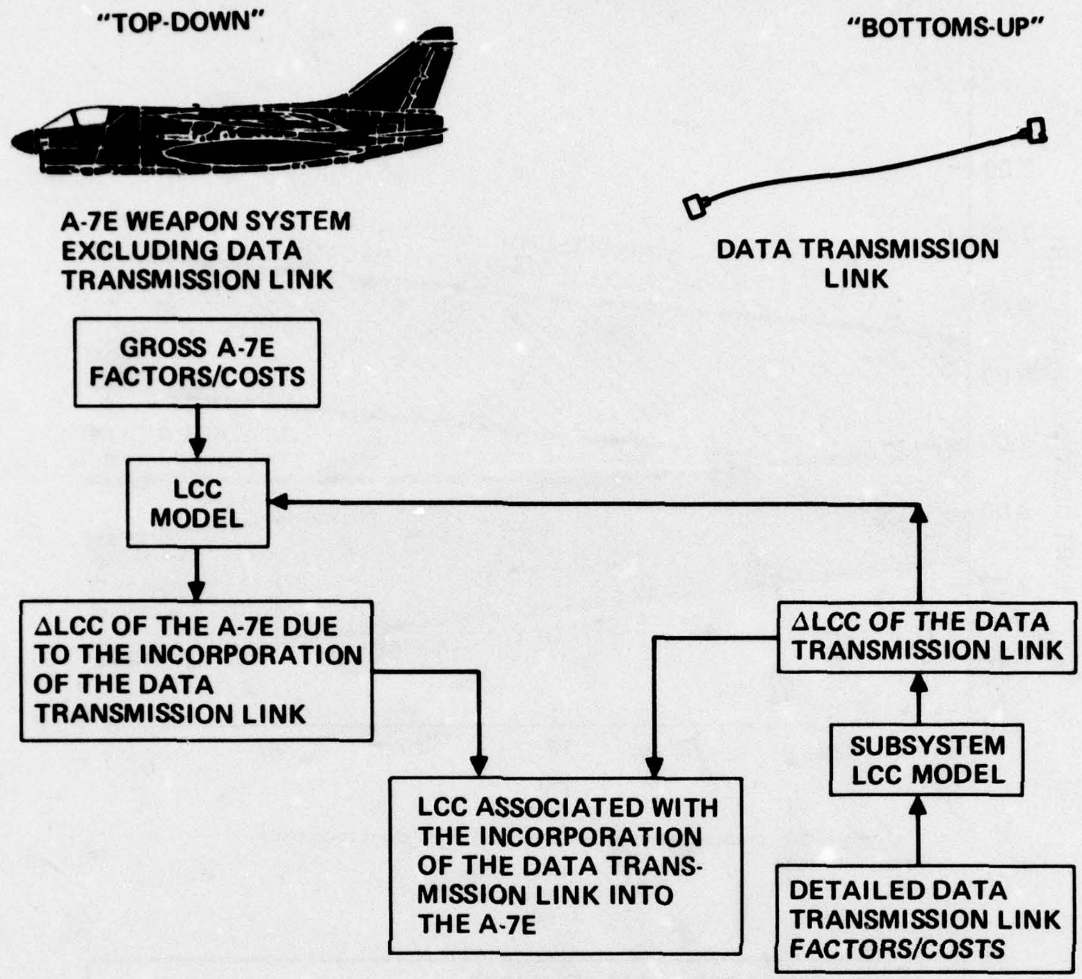

Figure 3-1. Two-level LCC approach.

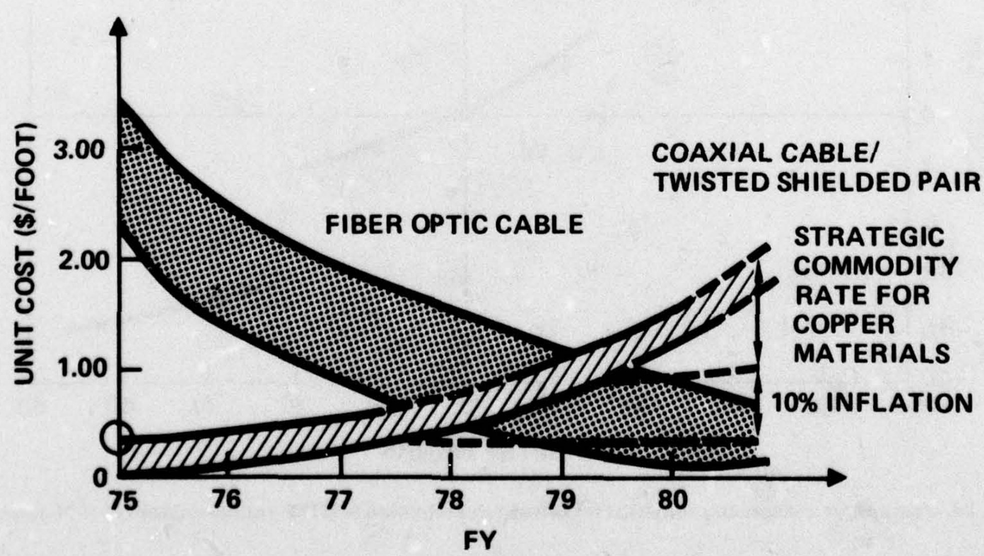

Figure 3-2. Cost-prediction curve: cables.

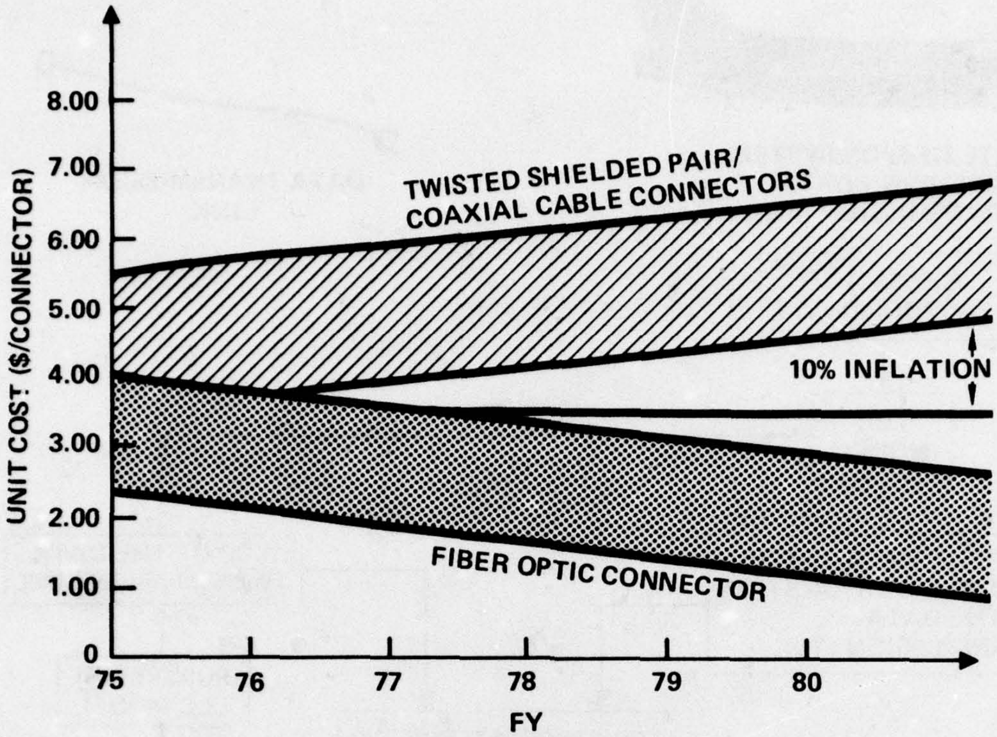

Figure 3-3. Cost-prediction curve: single-channel bulkhead connectors.

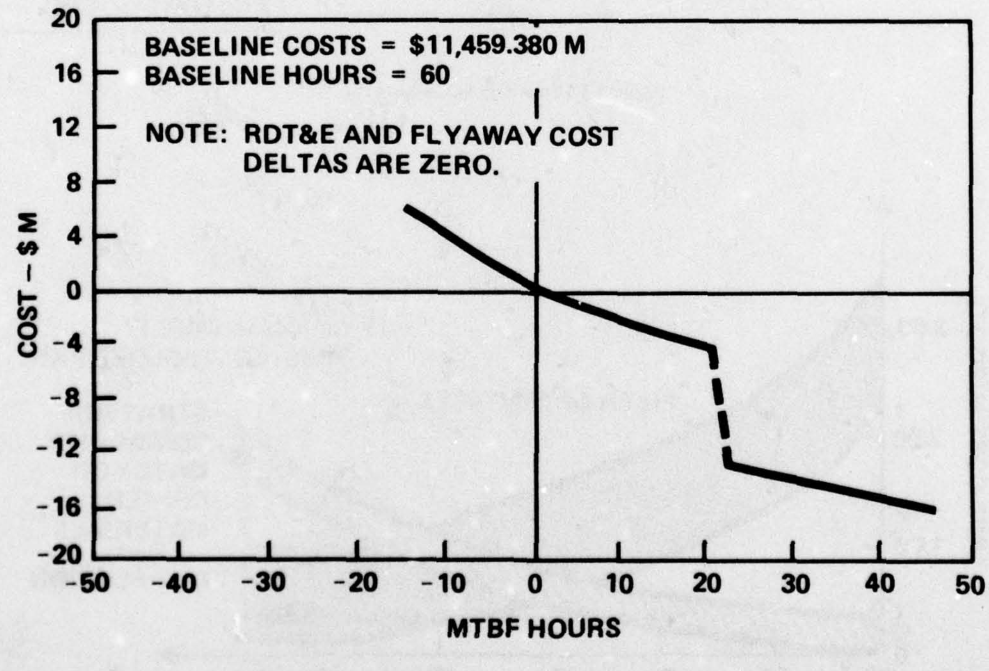

Figure 3-4. Procurement and operating cost deltas for airframe plus subsystem in MTBF analysis (millions of 1977 dollars).

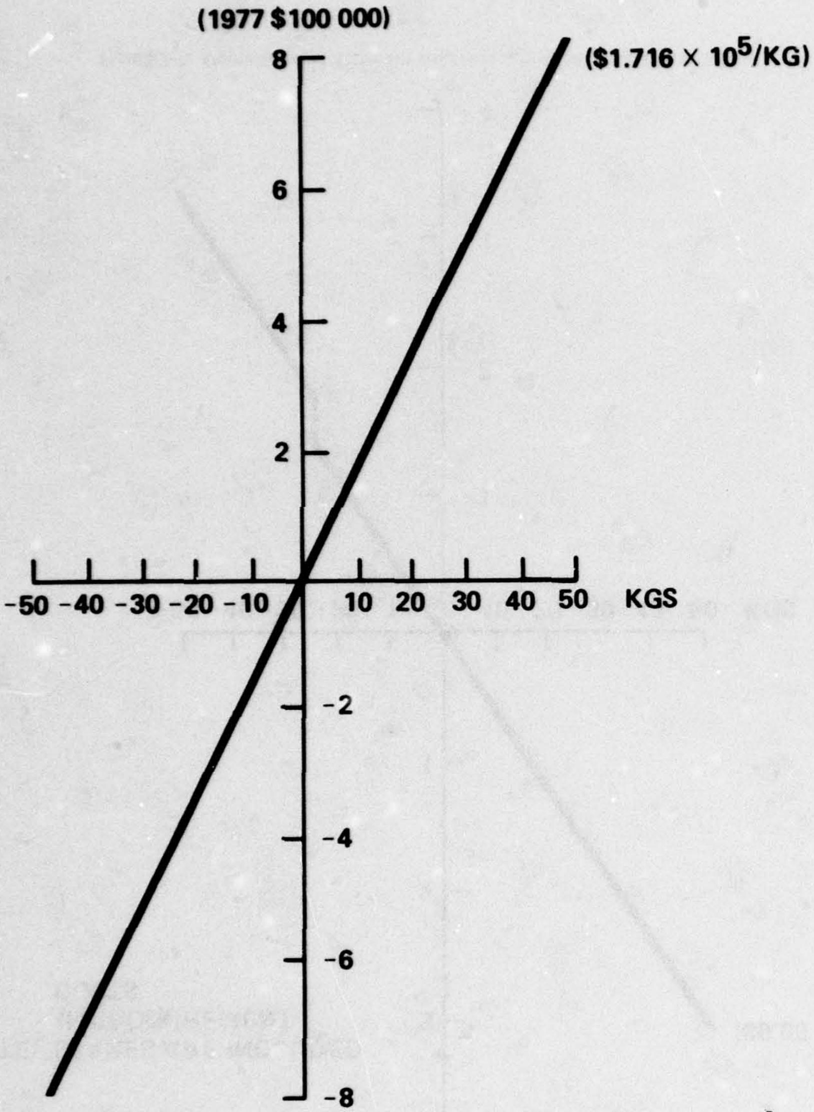

Figure 3-5. RDT&E cost deltas for electrical subsystem weight sensitivity.

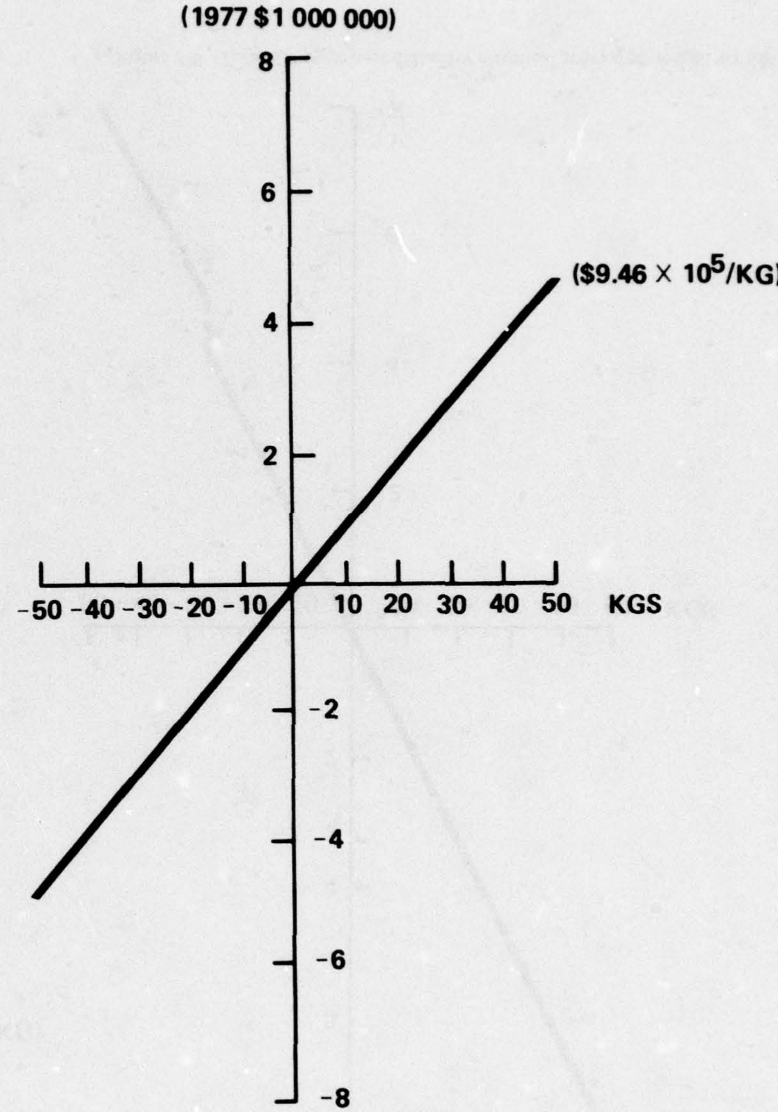

Figure 3-6. Procurement cost deltas for electrical subsystem weight sensitivity.

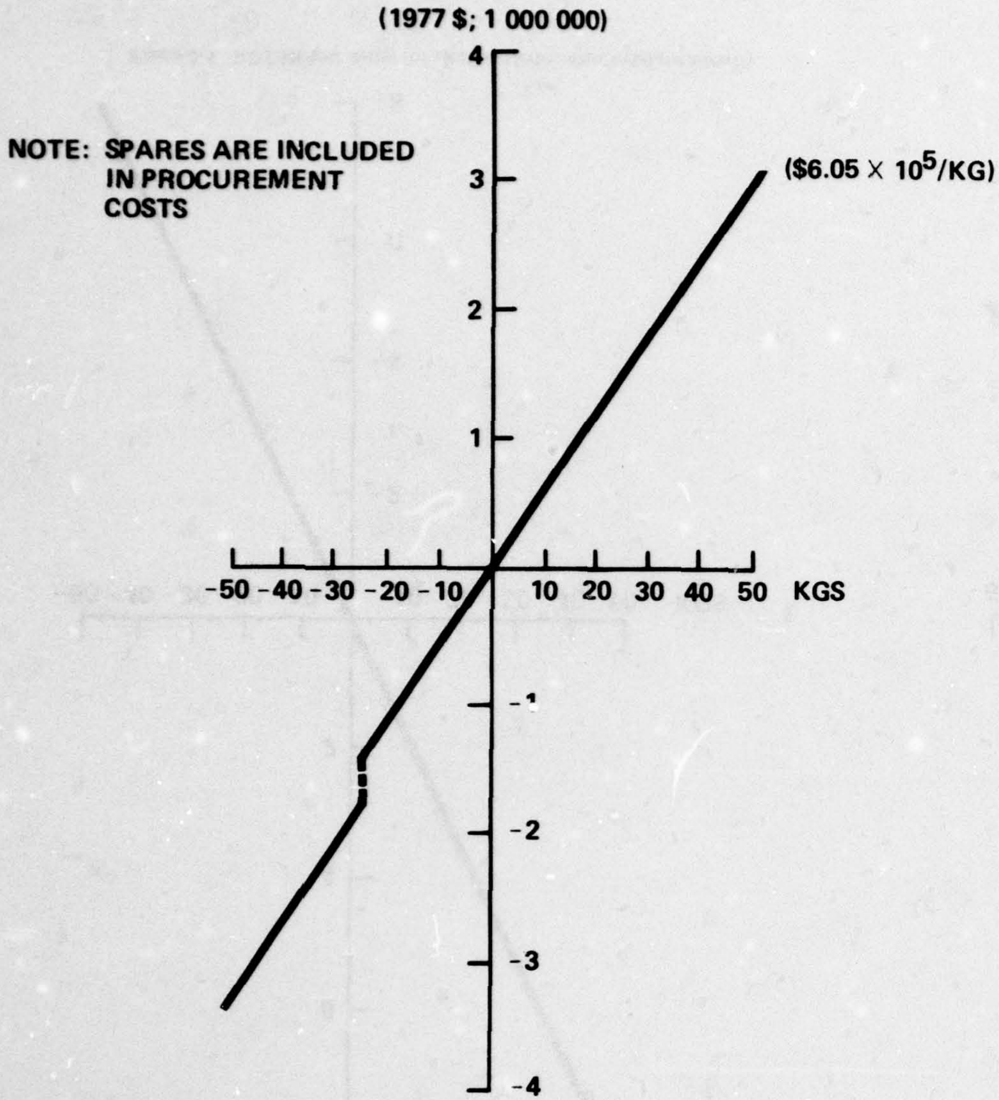

Figure 3-7. Operating cost deltas for electrical subsystem weight sensitivity.

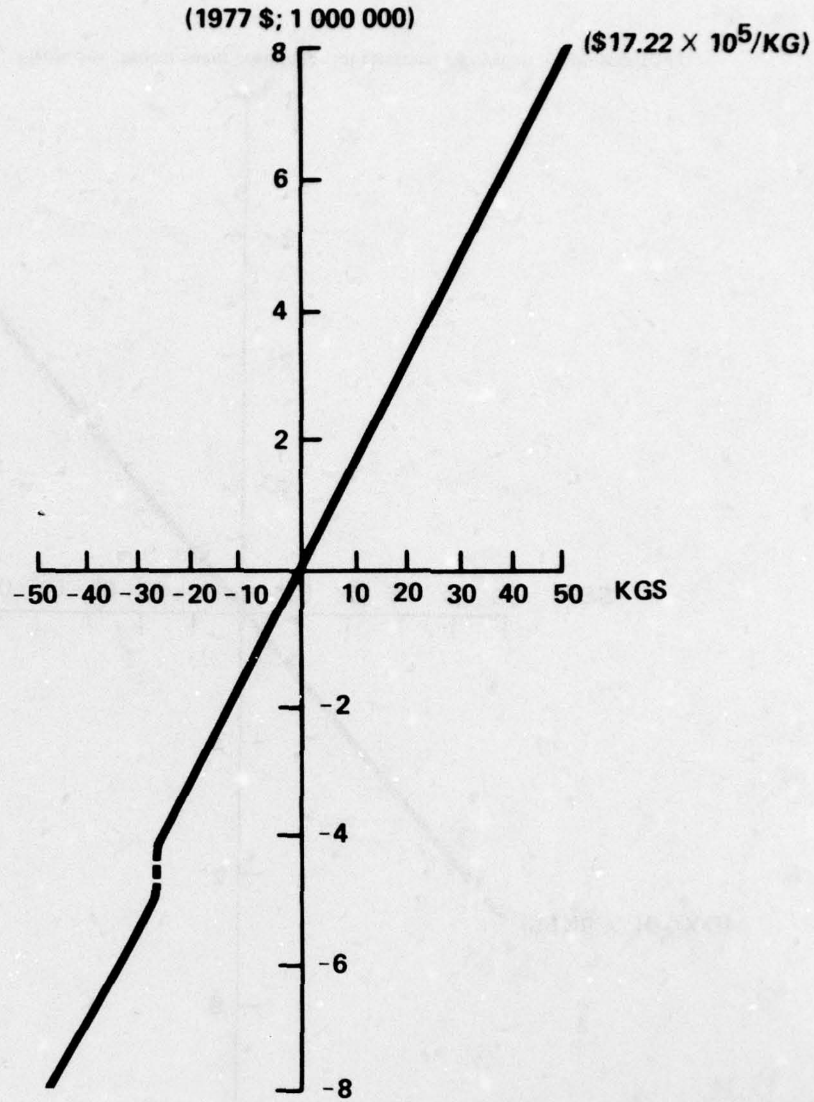

Figure 3-8. Total life-cycle cost deltas for electrical subsystem weight sensitivity.

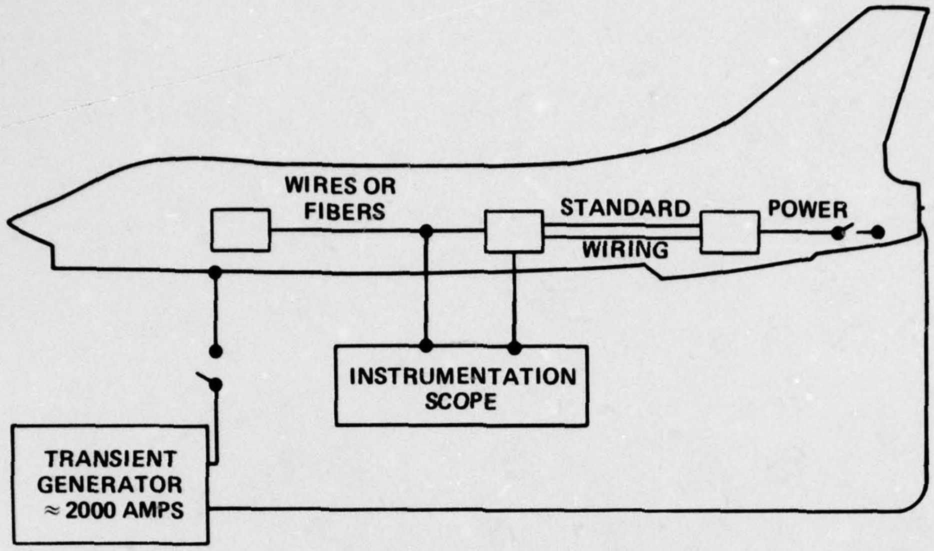

Figure 4-1. Transient (low-level 2000A) lightning test.

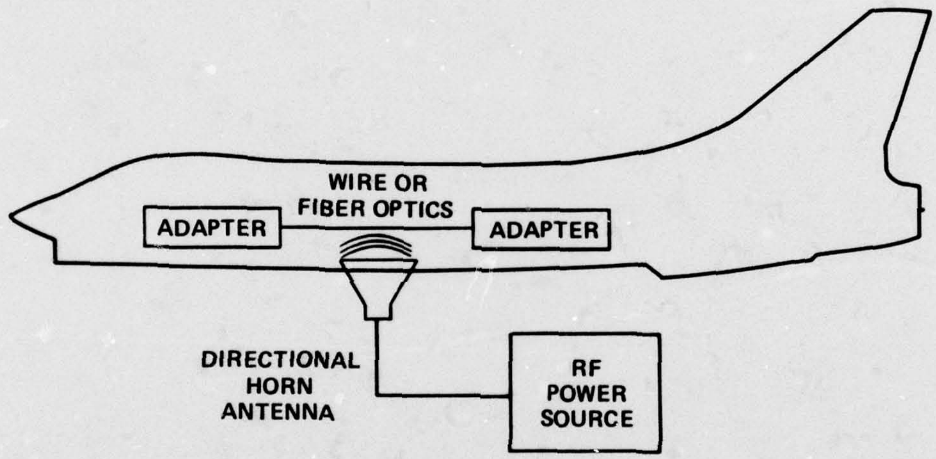

Figure 4-2. Radiated emission susceptibility testing.

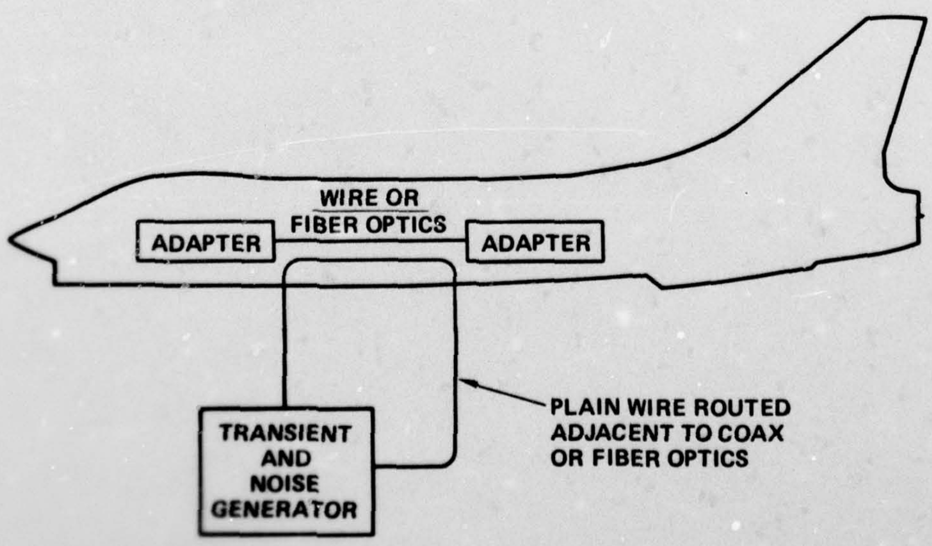

Figure 4-3. Wire-coupled susceptibility testing.

Device and System Concepts for Multimode Single Fiber Optical Data Links

D. H. McMahon and A. R. Nelson
Sperry Research Center, Sudbury, Massachusetts 01776

H. Wichansky
U. S. Army Electronics Command, Fort Monmouth, New Jersey 07703

SUMMARY

The principle of internal reflectance at grazing incidence is being used to create devices for controlling guided multimode light by electro-optic means. The feasibility of multiple switching has been demonstrated through the construction and evaluation of a variety of devices including modulators, couplers and multiplexers. Such devices add impetus to the growth of the multimode single fiber technology by presenting new opportunities for system design.

1. INTRODUCTION

Much of the research and development in the field of optical communication has traditionally been divided into two distinct technologies, fiber bundle links and integrated optics. The advantage of the former lies in its immediate practicality; the advantage of the latter lies in its greater bandwidth over long distances.

While the fiber bundle technology has often been used to demonstrate the feasibility and benefits of simple point-to-point communications systems, it has numerous disadvantage for multi-terminal applications. The principal disadvantage is the packing fraction losses that occur at all passive interconnect points. The effects of such losses can be minimized by employing Star Couplers (HUDSON, M. C., 1974) but only at the expense of increased cable usage. Attendant disadvantages include potentially higher costs for cable and passive interconnect devices and the inability to redirect optical signals electrically except through mechanical or cost-prohibitive means.

Conversely one may cite the disadvantages associated with the single mode technology. It is, of course, recognized that the tremendous amount of research in the development of integrated optics has produced significant progress both in device conceptualization and implementation. However the problems relating to the implementation of this technology to fiber optic systems are severe and largely unsolved. The principal problem is the difficulty of coupling and splicing, not solved after a decade of research on integrated optics. Additional, but less severe problems are fragility, lack of redundancy, and incompatibility with long-lived inexpensive LED sources.

Because of the difficulties associated with single mode and multifiber bundles, an intermediate technology has emerged — multimode single fiber links. Study programs have been undertaken at both USAECOM and at the Sperry Research Center to clarify the comparative merits of the three technologies. A systems analysis performed at USAECOM has indicated clearly the benefits to be derived from the multimode single fiber approach — lower cable costs, relative ease of splicing and interfacing, simpler passive interconnect structures, and compatibility with LED as well as laser sources (DWORKIN, L., 1975; WICHANSKY, H., 1976). Simultaneous analyses carried out at the Sperry Research Center first used thermodynamic arguments to demonstrate that one cannot usefully mix single and multimode components in the same link without incurring overwhelming losses (McMAHON, D. H., 1975). Subsequent studies showed that transformer coupler such as the taper ease positional alignment only at the expense of more ciritical angular alignment (NELSON, A. R., 1975). It now appears that the multimode single fiber technology can be applied to a majority of envisioned military situations and that it offers an optimum mix of benefits for multi-terminal links. Fabrication of passive interconnects is simplified and packing fraction losses eliminated. LED sources already exist capable of coupling more than 300 μW of optical power into 75-μm single fiber channels. Moreover many applications neither need GHz bandwidths nor require communication over very long distances.

Additional benefits would however accrue to the multimode single fiber technology if concepts existed for controlling the routing of optical signals electrically. One could then gain many of the advantages of integrated optics while avoiding the difficulty of coupling single mode fibers.

2. MULTIMODE ELECTRO-OPTIC GUIDING CONCEPTS

A suitable technique for creating active optical switching devices has been found at Sperry. This technique uses the quadratic behavior of Snell's law for light incident at grazing angles onto boundaries containing small refractive index discontinuities to cause electrically controllable amounts of refraction or reflection. Using Snell's law in the small angle approximation, the critical angle for internal reflection θ_c can be expressed in terms of the index of the medium n and the index change Δn across the boundary as $\theta_c{}^2 = 2\Delta n/n$. The importance of this quadratic behavior is readily apparent. Namely, fractional index changes of 10^{-3} suffice to produce a critical angle of 1.7° and hence enable one to reflect or to pass any beam having an angular divergence of less than this amount. The utility of the above observation stems from the fact that index changes of 10^{-3} can be produced electro-optically in a variety of materials, e.g., $Sr_{1-x}Ba_xNb_2O_6$, $KTa_xNb_{1-x}O_3$, $Ba_2NaNb_5O_{15}$, $LiTaO_3$ and $LiNbO_3$.

Of these materials, $LiNbO_3$ (LN) and $LiTaO_3$ (LT) appear most practical at the present time. The crystal growth art for LN and LT has become highly refined in recent years. Large boules 12 cm long and 5 cm in diameter with excellent optical quality and high resistivity are now grown routinely and are commercially available at costs of $9/cm^3. These materials can be polished without introducing significant work strain, have a high Pockel's coefficient, a low loss tangent, are reistant to optical damage, and are stable against depoling over the entire military temperature range.

Given the materials LN and LT to work with, how does one proceed to build practical devices? The principal design criterion, high input and output coupling efficiencies between fibers and electro-optic material, can be met by choosing the thickness of the electro-optic medium to be approximately equal to the core diameter of the fibers. The simplest type of electro-optic multimode device that one may construct consists of a single electro-optic channel. Such a device is shown in Fig. 1. This structure differs from that of Channin (CHANNIN, D., 1971) and Campbell et al. (CAMPBELL, J. C., 1975) in that the upper and lower surfaces of the crystal are used both to confine the injected light to the crystalline layer, and to create perpendicular electric fields through the entire thickness of the crystal.

Although it is readily apparent that the high index of LN or LT (~ 2.2 for both e and o rays) suffices to confine a highly divergent light beam to the crystal, such highly divergent light beams cannot be readily controlled in the plane of the crystal by electro-optic means. Using the structure shown in Fig. 1, an excitation of 400 volts across a 75 μm thick crystal produces a 10^{-3} change in index. As noted above, this change is only sufficient to guide light that diverges by $\approx 1.7^{o}$ in LT or LN or, because of the index change between crystal and air, about $\pm 3.8^{o}$ in air.

A potential problem then arises due to the fact that voltages much in excess of 400 must be avoided in order to prevent breakdown through the crystal and the fact that most multimode fibers have divergence angles appreciably greater than $\pm 4^{o}$ in air. A very simple technique has been developed at Sperry for simultaneously collimating the light while butt coupling the light to the electro-optic crystal, thereby eliminating the need for external lenses. This collimation technique, illustrated in Fig. 2, allows the $\pm 7.5^{o}$ to $\pm 15^{o}$ emission angle of multimode fibers to be controlled electro-optically in LT or LN without exceeding the crystalline breakdown voltage.

In Fig. 2(a), divergent light is incident at angle θ from glass through air onto a crystal having an index greater than glass. Snell's law indicates that rays incident at larger angles are bent to a greater degree than rays incident at more normal angles. Figure 2(b) shows a natural extension of this idea where the intermediate air region has been eliminated by cutting the fiber end at an angle and directly butting the fiber to the crystal. One can readily show for a glass-LT (or LN) interface that fibers terminating at angles of 69^{o}, 76^{o} and 79^{o} yield collimation factors of 2, 3 and 4, respectively.

3. DEVICE APPLICATIONS

By controlling the effectiveness of the electro-optic channel, one can construct the two port modulator shown in Fig. 3. This device uses a 75 μm thick c-cut wafer of LT 1.5 cm long with Cr/Al stripe electrodes. Such a modulator was fabricated at Sperry (NELSON, A. R., 1976). The modulator yielded the response curve shown in Fig. 4. Although the insertion loss from a Corning fiber is relatively large due to the use of normal-incidence butt coupling, 50% and 25% modulation depths were induced with 15 V and 5 V ac rms, respectively. The rise time of this modulator was measured to be less than 3 ns.

Additional improvements in the design of modulators of this type were recently obtained at Sperry (NELSON, A. R., 1976) using the double stripe-electrode geometry shown in Fig. 5 and 2:1 collimation via non-normal incidence butt coupling. Results for both TM polarized and unpolarized light are summarized in Table I. Although significant improvements are demonstrated in Table I, additional improvements, especially in throughput loss, appear possible.

The next device fabricated at Sperry was the electrically controlled directional coupler (SOREF, A. R., 1976) shown in Fig. 6. In this case a 54 μm thick c-cut plate of single crystal LN was used. The branch angle lies at 1^{o} angle with respect to the main channel and has a width that tapers to zero in the interaction region. The gap between the branch and main channels was 75 μm and the total crystal length 1.7 cm. The switch was designed to work with a light beam having an angular divergence of $\pm 2^{o}$ in the crystal (i.e., $\pm 4^{o}$ in air) for which case the 1^{o} branch geometry creates an active 3 dB coupler. LN was chosen because the dielectric anisotropy enlarges the lateral spread of the fringing fields into the interelectrode region of the crystal.

If electrical excitation is applied only to the main channel, the lower index of the crystal in the interelectrode gap acts as a barrier that reflects light incident on this wall back toward the main channel axis. If both branch and main channel electrodes are excited, the barrier is removed and the switch acts as a 3 dB directional coupler. The response of the coupler is shown in Fig. 7 for intermediate voltages applied to the branch channel. With this coupler the achromatic nature of the electro-optic barriers was verified by using white light excitation from an incandescent source.

A more recent project being carried out at Sperry under USAECOM sponsorship is the construction of an optical data link using optical multiplexers to achieve time division multiplexing. Figure 8 shows a block diagram of half of a bidirectional multiplexed data link. Manchester coded, 32 Kbit/s asynchronous light signals of the same wavelength, originating at any oneof 12 LED (or laser) sources are coupled to the multiplexer via optical fibers having core diameters of 75 μm and numerical apertures of .2 to .3. All 12 signals are multiplexed onto 3 single fibers of the same type, are transmitted a distance of up to several kilometers, and are subsequently demultiplexed back into the 12 component signals. Aside from the LEDs and photodetectors, and optical synchronization signals, multiplexer and demultiplexer ends of the link are identical.

Sperry's implementation of this multiplexed link makes use of three 4:1 optical multiplexers of the type illustrated in Fig. 9 at each end of the link for transmission of light in one direction. As shown in Fig. 9, each individual 4:1 multiplexer is fabricated from a 50 to 75 μm thick c-axis oriented crystal of LT and includes electrodes on top and bottom surfaces to create a main channel, four branch channels, and four gates to couple branch channels to the main channel. Here, as in Fig. 5, channels are created by guiding light between two lower index stripe barriers created electro-optically. The two-stripe barrier approach was adopted because 1) optical absorption at metal-crystal interfaces is eliminated, 2) the possibility of optical damage is reduced by propagating light in the low field regions, 3) crosstalk is reduced because light traveling outside a guide is prevented from entering the guide and 4) more ideal 3 dB coupler action is expected because no decrease in index occurs under the gate electrodes when the inhibit voltage is removed.

Demultiplexer action results by sequentially removing the inhibit voltage one at a time from the four gate electrodes thereby producing a junction that permits approximately one-half of the light to propagate down the corresponding branch channel. The reciprocity theorem guarantees that the demultiplexer will work equally well as a multiplexer for light traveling in the reverse direction.

The multiplexer was designed for use with available multimode fibers having core diameters from 50 μm to 75 μm and numerical apertures from .2 to .3. Non-normal incidence butt coupling, not shown explicitly in Fig. 9, was used to achieve a 4:1 collimation factor and compatibility with these fibers. The angularly terminated fiber increases the width of the channels to 355 μm in the plane of the crystal. A branch angle of 1^0 was selected to yield 3 dB switching action with an excitation of 400 volts. From geometric considerations, one can calculate that the length of the multiplexer must be 4.5 cm and the width .25 cm. Clearly three 4:1 multiplexers can be fabricated on a single crystal wafer to achieve 12:3 multiplexing action.

The performance of one 4:1 optical multiplexer design fabricated at Sperry is shown in Fig. 10. A length of fiber (.2 NA, 55 μm diameter) with angular termination was directly butt coupled to the main channel input of the multiplexer. All modes of the fiber were equally excited by illumination with a He-Ne laser and lens arrangement. A similar fiber was butt coupled to the output surface and was moved along the output surface to obtain the results shown in Fig. 10. The figure shows that the input insertion loss for light traveling along the main channel is 8 dB, that the total insertion loss through any one of the branch channels is 15 dB, and the signal to crosstalk ratio is 10 dB.

4. SYSTEM CONSIDERATIONS

Because of excessive weight, bulk, electromagnetic interference and bandwidth limitations of metallic wire cables, investigations have been under way at USAECOM for five years to assess the suitability of optic cable for current and future Army telecommunication systems. Although initial emphasis was on replacing cables on a point-to-point basis, recent efforts have centered not only on the transmission aspects but also on the electronic functions performed in a multi-terminal communications environment. Specifically, an assessment of technologies available for signal routing and signal processing was sought. If functions such as switching, multiplexing, signal addressing, and signal coupling could be performed optically, costs savings might result as well as increases in system reliability.

Recognizing the practicality of present multimode optical links, in particular the compatibility with reliable and low cost LED sources, the relative ease of coupling and splicing, the ability to fabricate low loss and low cost passive interconnect components, and recognizing the incompatibility of the multimode technology with integrated optics, the need for creating multimode switching devices became apparent.

The optical functions required in military telecommunication systems have already been enumerated in some detail (WICHANSKY, H., 1976). The broadest division involves splitting optical link interconnect components into two groups: passive interconnects and electrically controllable interconnects. Additional classifications result by considering the relative power transferred (i.e., coupler vs power divider) at a signal routing intersection. As one illustration of the merits of active vs passive coupling let us consider a 1:N optical power splitter which, used in reverse, becomes a N:1 optical combiner. Since one recognizes that at least an N-fold optical power division must occur in a 1:N coupler, any active switching structure that routes more than 1/N of the light power toward a selected receiver represents an improvement over passive coupling. Conversely, optical reciprocity guarantees that at best only 1/Nth of the power entering a N:1 combiner will propagate down the output channel. Optical reciprocity also then guarantees that a useful 1:N switch offers identical advantages as a N:1 combiner.

There are significant reasons for specifically addressing the design of an optical multiplexer. First, the construction of a multiplexer demonstrates the feasibility of multimode switching. Second, the construction of a time division multiplexed link using optical multiplexers enables one to make an assessment of this approach relative to alternative, better established technologies such as electrical or surface acoustic wave multiplexing. Third, many of theproblems associated with multimode switching are included as part of the construction of a multiplexer. The problems of coupling fibers to electro-optic materials is important and must be handled satisfactorily. The ability to perform switching functions with sufficient rapidity is another. Thus while one might hope optimally that optical multiplexers will supplant other techniques for performing this function, such a result is by no means necessary to gain value from an optical multiplexer program.

The feasibility of routing multimode optical signals has been demonstrated. Device structures are simple and readily fabricated using commercially available electro-optic materials. The approach is compatible with simple, efficient butt coupling procedures, and non-normal incidence butt coupling allows compatibility with the properties of available multimode fibers. Finally, switching voltages are modest and not critical, and device operation is independent of wavelength. Modulators, couplers and multiplexers based on the principle of electro-optically induced reflection barriers have been fabricated and evaluated. In particular the function performed by the Sperry optical multiplexer design appears difficult, if not impossible, to accomplish in any other way optically. The measurement of the performances of these devices already facilitates a comparison with alternative approaches. Moreover the steady stream of advanced concepts which has been forthcoming leads one to believe that significant additional improvements in performance can be expected in the field of multimode optical switching.

REFERENCES

CAMPBELL, J. C., 1975, "GaAs electrooptic channel-waveguide modulator," Appl. Phys. Letters, vol. 26, p. 640, coauthored with Blum, F. A. and Shaw, D. W.

CHANNIN, D., 1971, "Voltage induced optical waveguide," Appl. Phys. Letters, vol. 19, p. 128.

DWORKIN, L., 1975, "The application of optical waveguides to army communications," SPIE Journal, vol. 63, p. 140, coauthored with Coyell, L.

HUDSON, M. C., 1974, "The star coupler: a unique interconnect component for multimode optical communications systems," Appl. Opt., vol. 13, p. 2540, coauthored with Thiel, F. L.

McMAHON, D. H., 1975, "Efficiency limitations imposed by thermodynamics on optical coupling in fiber optic data links," J. Opt. Soc. Am., vol. 65, p. 1479.

NELSON, A. R., 1975, "Coupling optical waveguides by tapers,' Appl. Opt., vol. 14, p. 3012.

NELSON, A. R., 1976, "Electro optic channel modulator for multimode fibers," Appl. Phys. Letters, vol. 28, p. 321, coauthored with McMahon, D. H. and Gravel, R. L.

NELSON, A. R., 1976, "Modulators for multimode single fiber communications systems," Electro-Optics/Laser 76 Conference Proc., New York, New York, Sept. 1976, paper II.4, coauthored with McMahon, D. H.

SOREF, A. R., 1976, "Multimode achromatic electro-optic waveguide switch for fiber optic communications," Appl. Phys. Letters, vol. 28, p. 716, coauthored with McMahon, D. H. and Nelson, A. R.

WICHANSKY, H., 1976, "Multimode optical devices for signal processing," Electro-Optics/Laser 76 Conference Proc., New York, New York, Sept. 1976, paper XVI.8, coauthored with Dworkin, L. U. and McMahon, D. H.

TABLE 1 Summary of modulator performance measured for single and double stripe channel geometries for $LiNbO_3$ and $LiTaO_3$ with and without collimation and polarizer.

MODULATOR TYPE	VOLTAGE FOR 50% MODULATION (V_{RMS})		THROUGHPUT LOSS (dB)		BANDWIDTH (GHz)	
	POLARIZER	NO POLARIZER	POLARIZER	NO POLARIZER	$LiNbO_3$	$LiTaO_3$
SINGLE STRIPE	10	40	18	14	1.2	.6
DOUBLE STRIPE	10	40	18	14	.9	.45
IMPROVED DEVICE DESIGN	5	20	18	14	.6	.3
2:1 COLLIMATION DEVICE	–	23	–	10	.6	.3

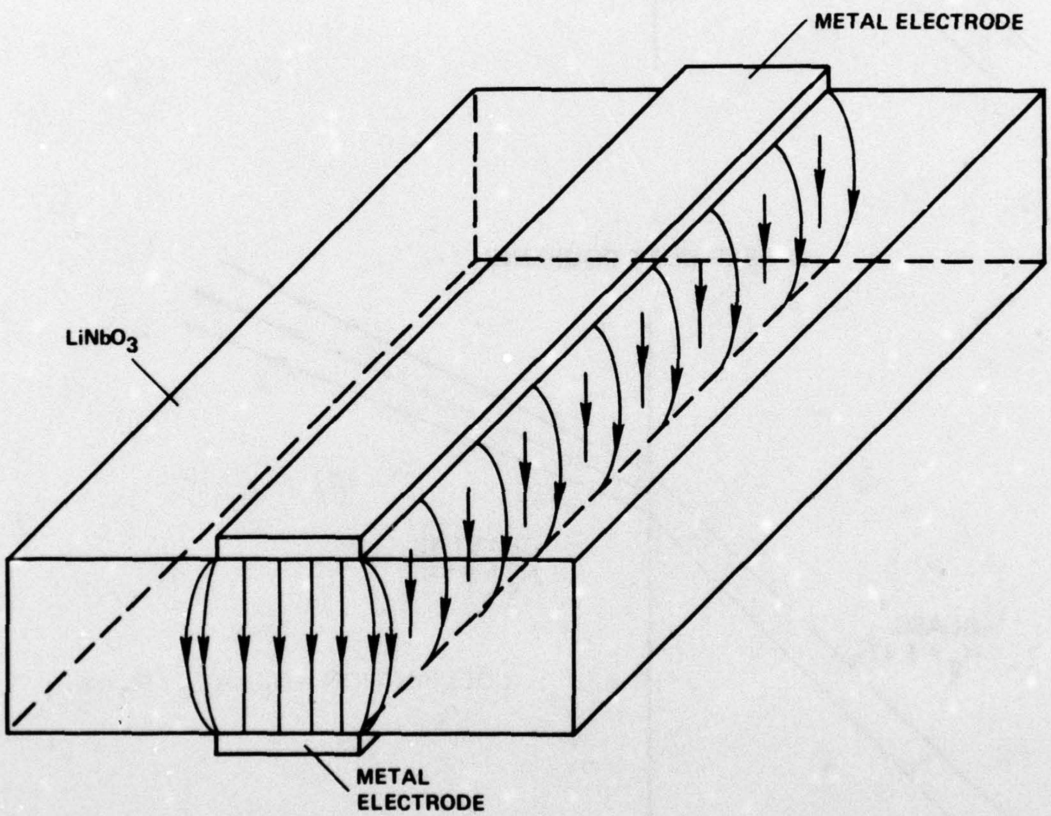

FIG. 1 Electro-optic channel. A voltage applied between the top and bottom surface electrodes produces an increase in index of refraction in the region between the electrodes forcing light to be confined to this region.

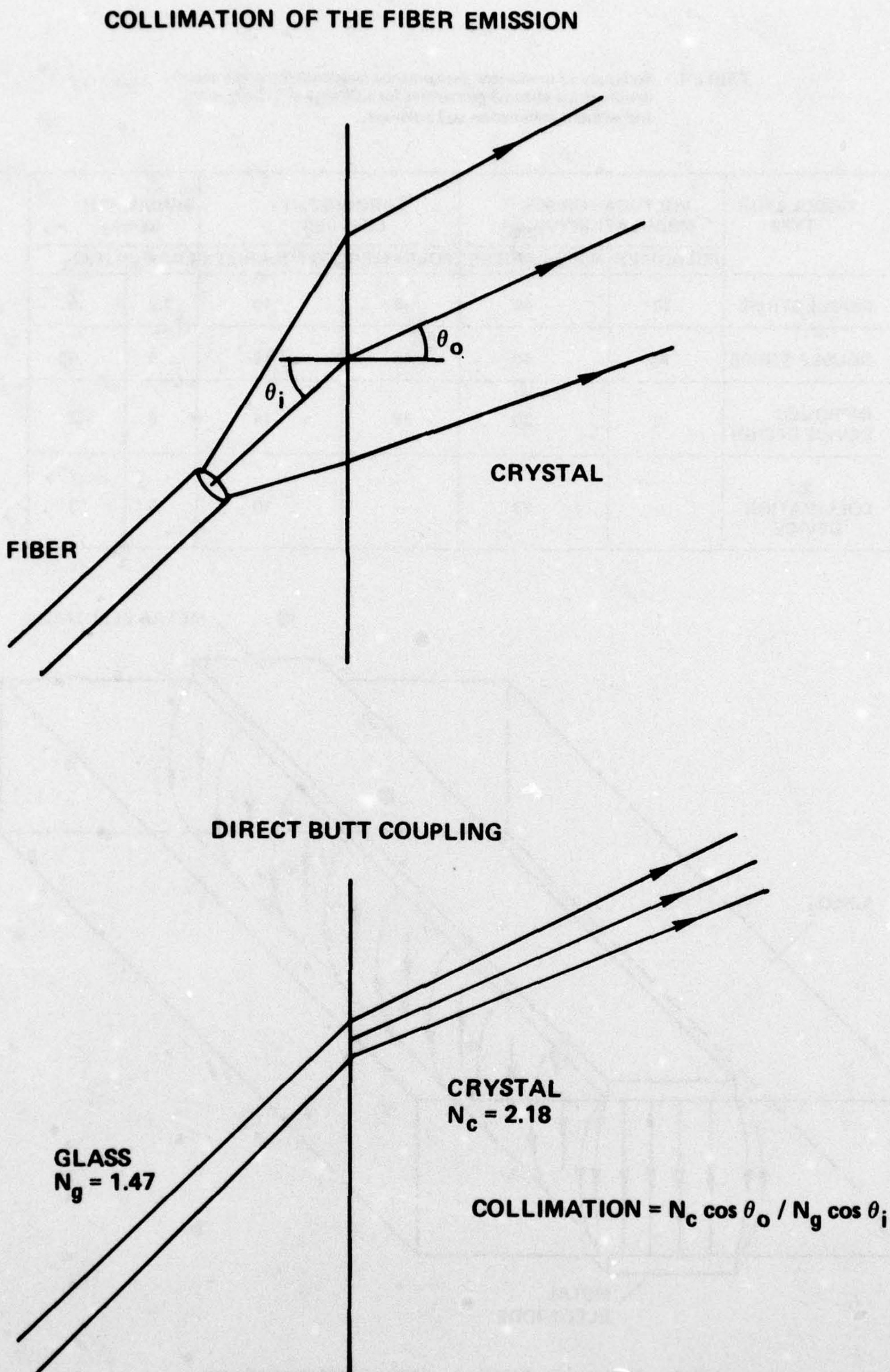

FIG. 2 (a) Principle of collimation via non-normal incidence butt coupling.
(b) A practical example illustrationg collimation via non-normal incidence butt coupling.

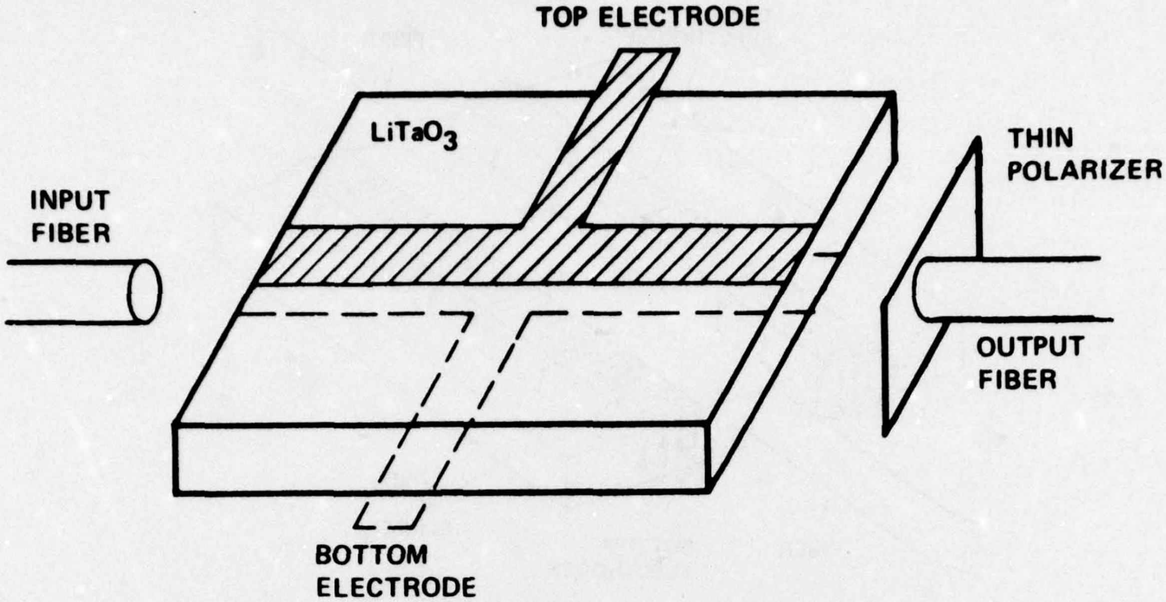

FIG. 3 $LiTaO_3$ channel waveguide modulator.

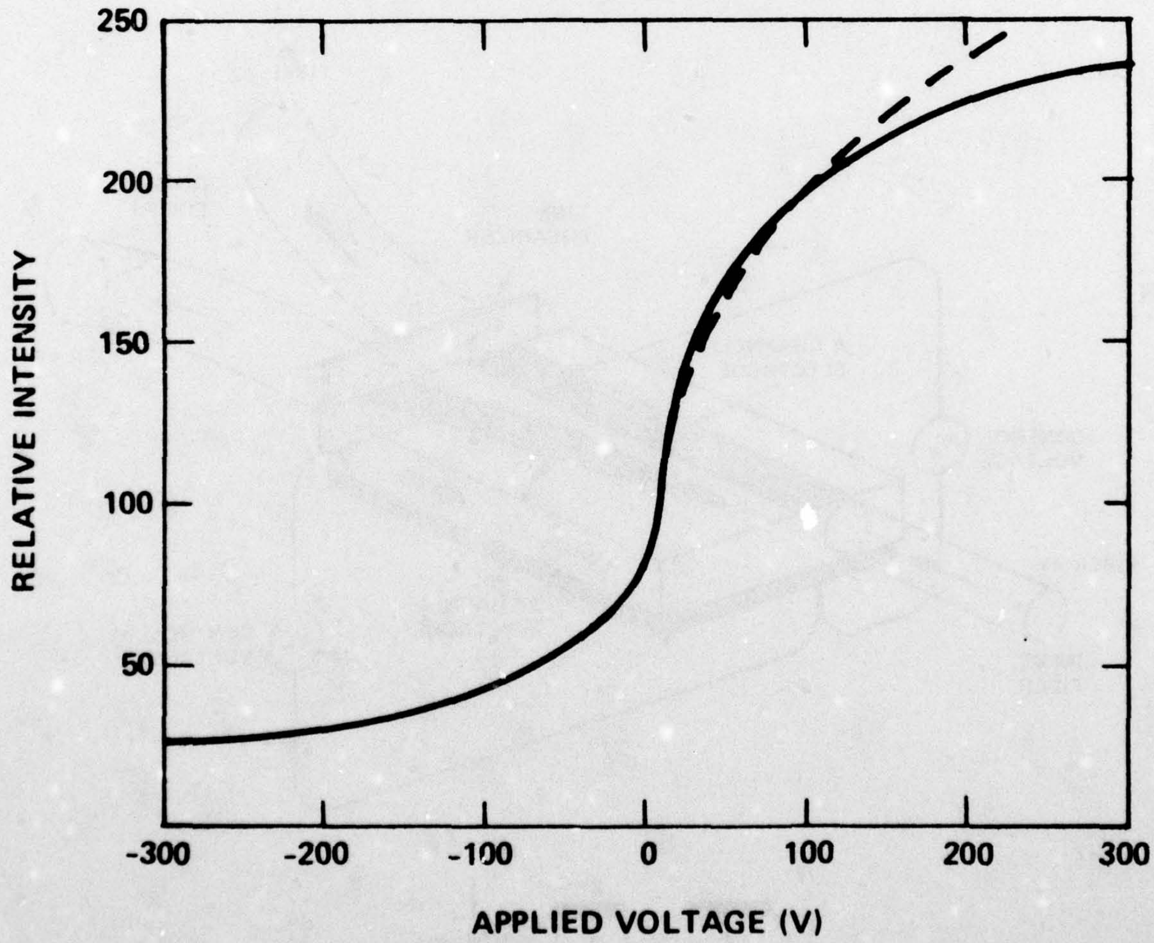

FIG. 4 Relative intensity of output light vs applied dc field. Solid line is experimentally determined output intensity vs applied voltage using multimode fibers. Dashed line for I and V½.

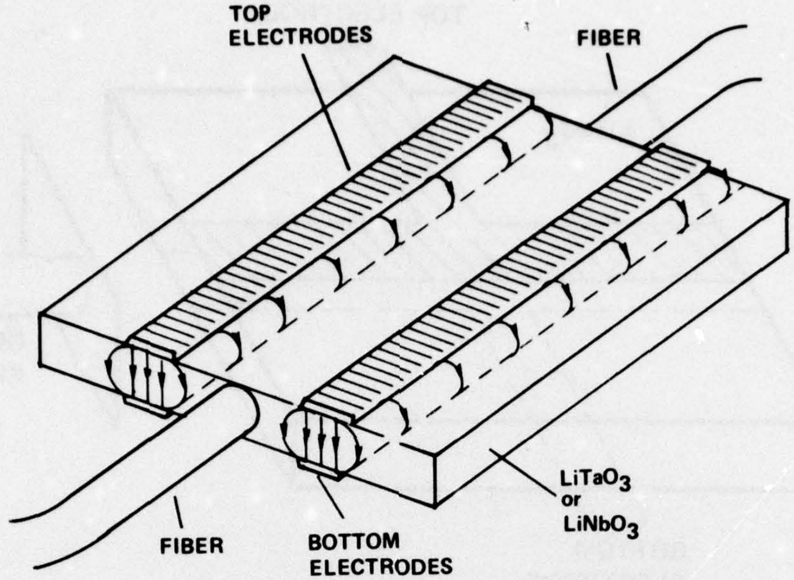

FIG. 5 Electro-optic channels created by double strip electrode geometry. Electric fields applied between top and bottom electrodes create a decreased index between the electrodes *thereby confining the light beam.*

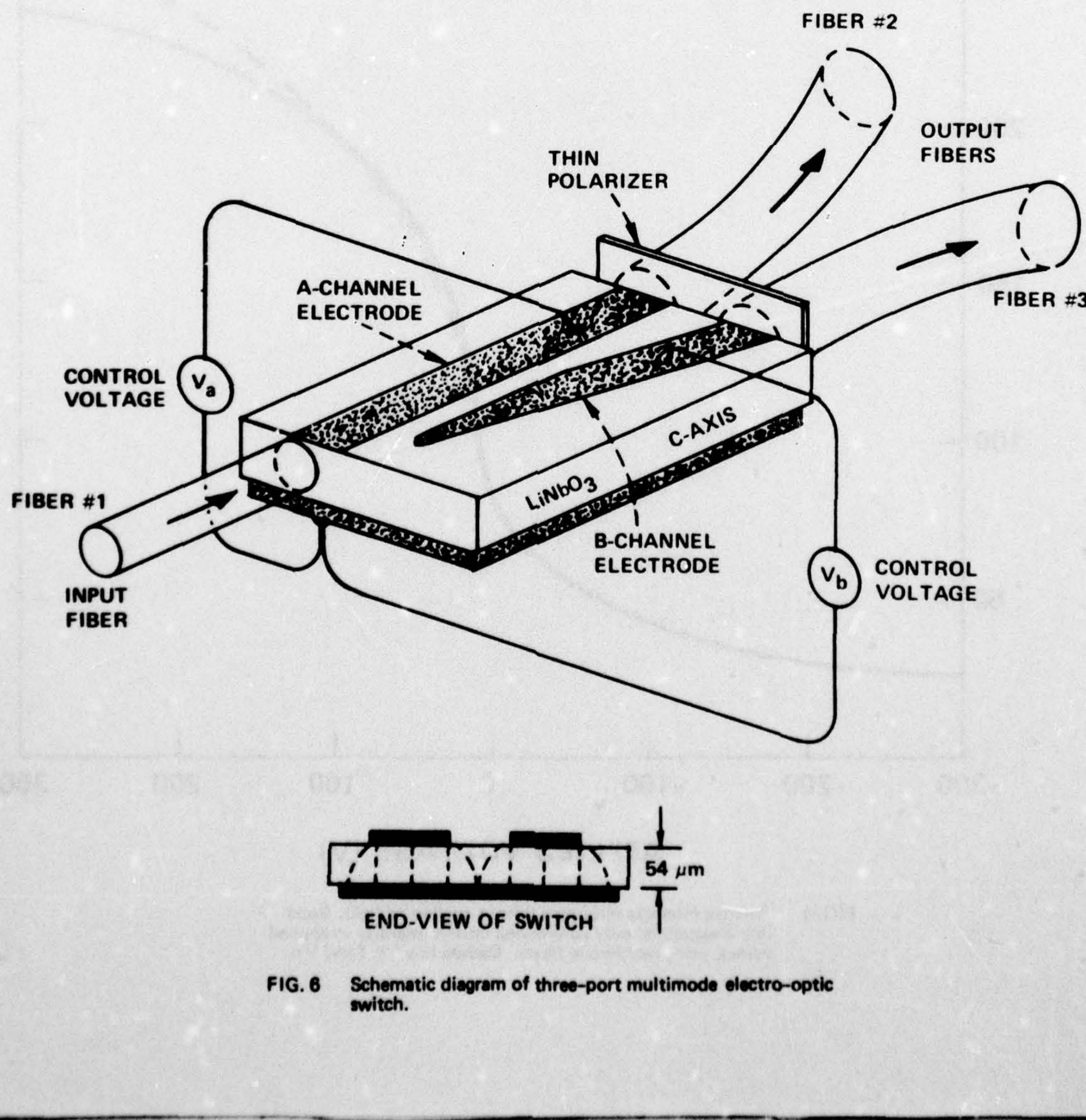

FIG. 6 Schematic diagram of three-port multimode electro-optic switch.

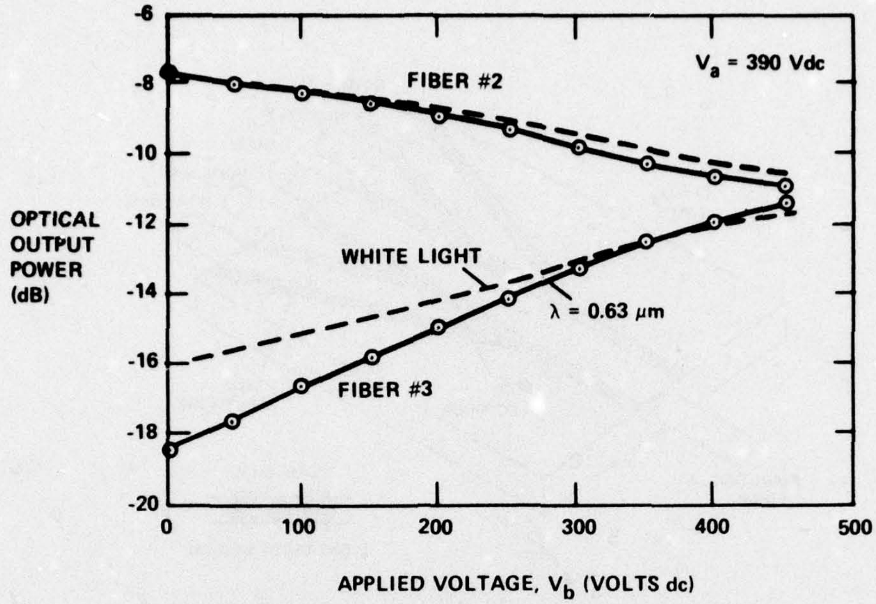

FIG. 7 Optical output power in both fiber channels as a function of branch voltage. Input fiber emission centered on channel A.

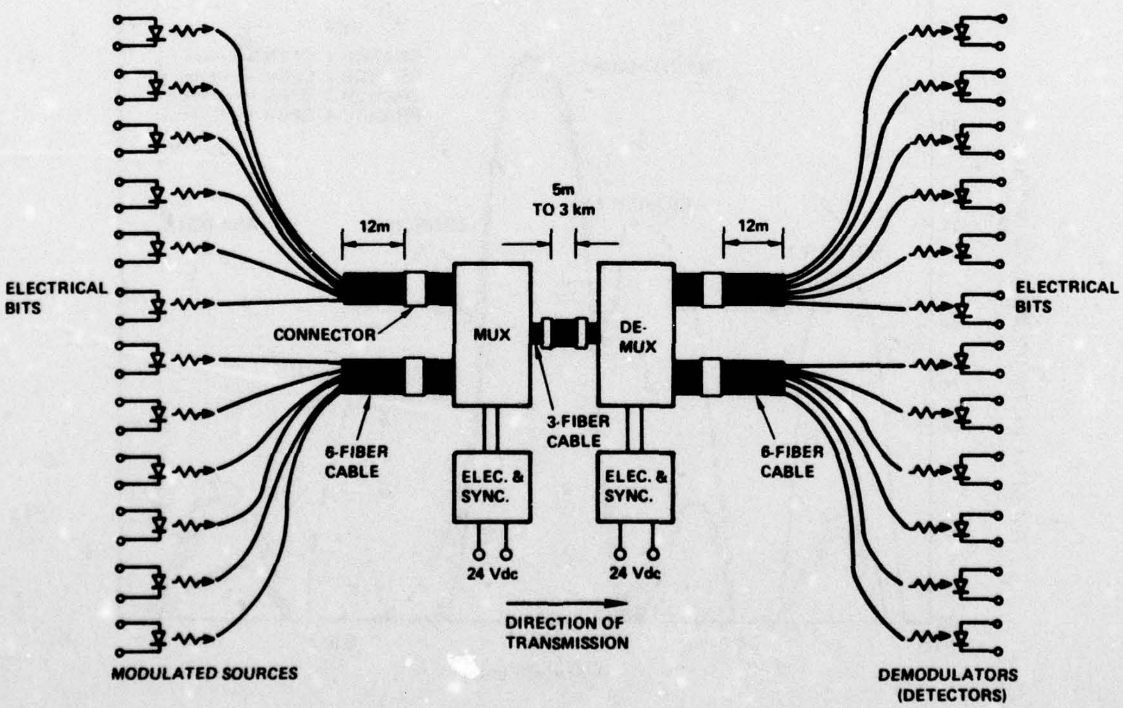

FIG. 8 Block diagram of complete optical data link employing electro-optic multiplexer and demultiplexer.

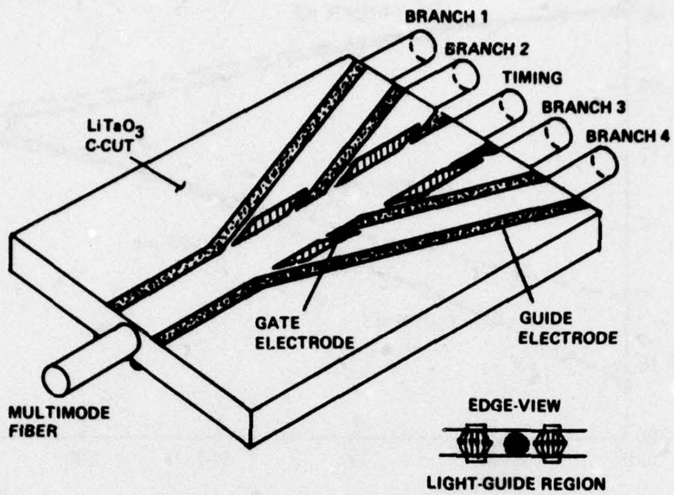

FIG. 9 Structure of a single 4:1 optical multiplexer/demultiplexer containing four 3 dB couplers.

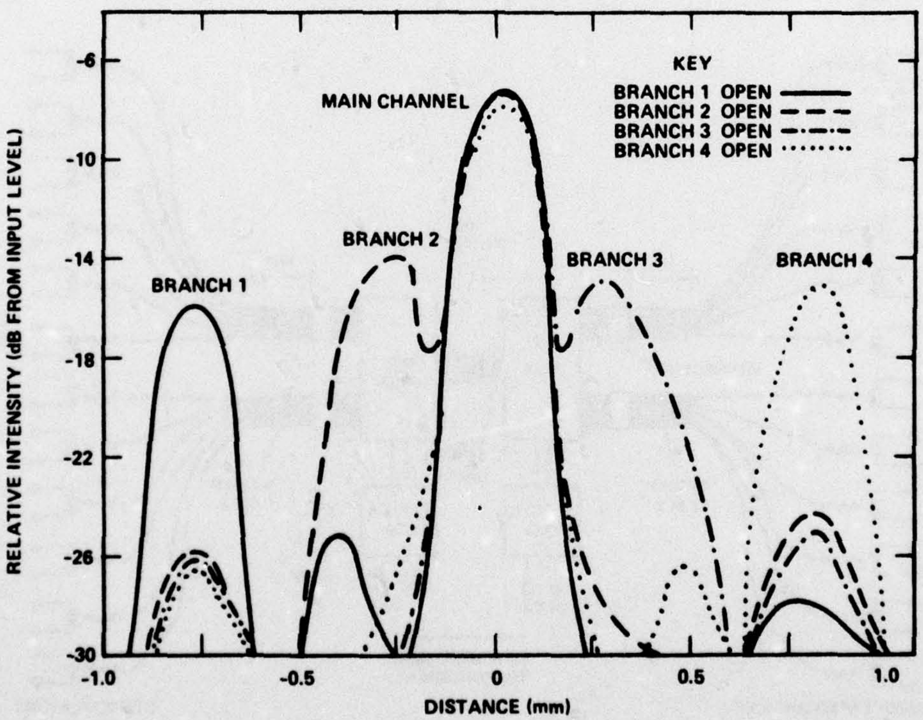

FIG. 10 Performance of 4:1 optical multiplexer.

QUESTIONS AND COMMENTS ON SESSION II

MULTI-CHANNEL FIBER OPTIC SONAR LINK
F. C. Allard, N. S. Bunker

Dr. Elmar H. Hara: I think your system deals with a sonar array and therefore the skewness between channels will be an important factor. What skewness did you achieve?

Dr. Allard: All channels were within 1.5° which corresponds to a skewness of less than 1 microsecond.

COST MODEL FOR AN OPTICAL FIBER COMMUNICATIONS SYSTEM
T. A. Alper

Dr. LeCat: (1) You showed us results of lightning tests. Were they obtained under full scale level of threat, or extrapolated from low-level measurements? (2) When extrapolating results from low-level measurements, can one really assume that phenomenons are linear, since non-linearities such as flashover can occur?

Dr. Alper: Most of the tests are run at low levels. Data is taken at 2000 amps and extrapolated at 200,000 amps. Most theoreticians agree that extrapolation is valid.

Summary of Session II

SYSTEMS

by
Eric Spitz

This session featured 6 conferences which can be classified as follows:

3 on operational systems,
3 on technico-economic surveys,
1 dealing with the design of devices for links via multimode-single fibers.

I. OPERATIONAL SYSTEMS

I.1. The first one of the operational systems, presented by Communication Research Center of Canada, dealt with a link (31 - 10 Mb/s channels) between two display consoles installed on a warship. This experimentation, which does not utilize high performance components, shows that such links can be operational for military applications and resolve problems such as immunity to electromagnetic radiations.

I.2. The second system, presented by Naval Underwater Systems Center, featured a link between a pre-amplifying rack and the processing end for Sonar signals assembled with currently available components and sub-assemblies.

This system, like the former, is mainly of interest to the extent that the choice has been made to process a very large number of channels via optical technologies, even if input and distance are limited.

I.3. The third system, offered by ITT/Roanoke, field-links in the 20 Mb/s - 2 km area. Objective was to exploit available good performance components.

The system comprising a multifiber cable, installable in ducts is designed for field mounting of the connectors.

Their paper shows real care for compatibility of devices utilized.

II. TECHNICO-ECONOMIC SURVEYS

Mr. Alper, SHAPE, THE HAGUE, has proposed a model for computing the cost of optical fibers systems, by involving various parameters related to performance and characteristics of given devices.

However, this model does not take into account the estimated evolution of the cost of components and sub-assemblies nor the cost of installation, the latter being at times nonnegligible.

A thoroughly complete paper was given by NELC, describing after economic analysis and flight testing, an evaluation of ALOFT program on A 7 aircraft of which a technical description was made in several instances and which appears as the most complete program in the field of military applications.

A large number of tests has been carried out (150 hrs of flight testing) in varied environmental conditions (EMI, EMP, lightning) tests that have shown that comparison with classical techniques appears as very favorable to optical fiber links, inasmuch as a technico-economic analysis confirms these indications.

III. DESIGN OF DEVICES FOR LINKS VIA MULTIMODE-MONOFIBERS

Mr. MacMahon of Sperry Research Center has proposed, along with U.S. Army Electronics Command, possibilities to fabricate electrooptic modulators, couplers and multiplexers enabling to design high performance systems based on multimode single fibers.

Proposed concepts rest on ideas developed in the field of integrated optics and aim at resolving the problems encountered in multi-conversational links.

Feasibility of components defined for this goal has been demonstrated but it is to be noted that industrial angle has not been considered.

To summarize, it appears that work, extensive and thorough, is being currently carried out for experimentation of complete operational military systems based on optoelectronic components and sub-assemblies available off-the-shelf.

Single Mode Fiber Optics and Integrated Optics for use in Optical Communications

T. G. GIALLORENZI and A. F. MILTON
Naval Research Laboratory
Washington, D. C. 20375

ABSTRACT

The status of components for use in single mode fiber and integrated optical communication systems is presented in this paper. The single mode coupling problems are stressed because couplers and splicers are the technological items which pace the implementation of single mode data transfer systems.

1. INTRODUCTION

In the past several years, significant progress has been realized in the areas of fiber and integrated optics and attention is now being directed towards using light guiding optical components in high capacity data transfer systems. Graded and step index multimode fibers are being marketed in several countries and many telecommunications and military applications for fiber optics have been delineated. Optoelectronics interfaces (source and detector modules) for use with fiber optic transmission lines have also been developed. With fiber losses below 4 dB/km, it now seems possible to transmit signals over distances of 10 - 20 km without repeaters, an attractive capability. However, multimode fiber dispersion will limit the available signal bandwidths than can be transmitted. As an example, with step multimode fibers with low numerical aperture, bandwidths are limited to about 5 Mbit/sec for a 10 km propagation path. For available graded index fibers in which modal propagation times are almost equalized by a radial fiber index variation, bandwidths on the order of 60 Mbit/sec are possible for repeater spacing of 10 km. Single mode fibers however do not suffer from modal dispersion. For bit rates exceeding 100 Mbit/s, the use of single mode fibers becomes attractive. Although such high data rates (>100 Mbit/sec) are not presently required in the majority of applications, the presence of high capacity lines would permit long term data transfer growth potential in the cables to be installed. Cable replacement is costly and involves considerable inconvenience. Therefore, long term planning suggests one consider the installation of optical cables with excess bandwidth.

A second consideration in favor of single mode communications is the extreme difficulty in switching multimode light; a difficulty manifest by the absence of any useable multimode switches. With a single mode it is possible to efficiently modulate and switch optical power in low crosstalk integrated optical modulators and switches. This capability is particularly attractive in multiterminal data buses where active optical taps would offer increased performance and capabilities. Additionally, integrated optical switches can be cascaded to form optical switchboards for routing signals.

The transition from multimode to single mode fibers, while offering switching capabilities and significantly higher bandwidths (> 10 Gbits/km), does require closer tolerances for splicing and coupling and, when used with integrated optics, requires special techniques for handling the two polarization states.

In this paper, we will describe those considerations which come into play when developing a single mode fiber optic/integrated optical communication system. Coupling tolerance considerations represent the largest technological difficulty to be dealt with. Fiber to fiber splicing and fiber to thin film coupling typically require micron level tolerances. In spite of the low level of development effort in the single mode coupling area, significant progress has already been achieved. Single mode fiber to fiber splicing losses of less than 1/2 dB have been achieved and fiber to film coupling losses of 4 dB have been demonstrated. When considering single mode fibers connected to integrated optical switches, regard must be given to the two states of polarization which normally propagate in single mode fibers. The usual designs for integrated optical switches are optimized for a single polarization so that if both polarizations are present, significant interchannel crosstalk results. The design of polarization insensitive switches thus becomes of prime importance.

In the following sections, we will describe relevant properties of single mode fibers. Description of the various coupling approaches will then be given, and finally, polarization insensitive switches will be described. It will be seen that solutions to the problems associated with single mode fiber optical communications are well along and that extremely high data transfer capabilities will be possible in the next few years.

2. SINGLE MODE FIBER PROPERTIES

Single mode propagation is realized in fibers by designing core sizes to be a few wavelengths in cross sectional dimension and by having small index differences between the core and cladding. The normalized core size which is used in the dispersion relationship to calculate the modal properties of a fiber is defined as (Boerner, M. 1976)

$$V = \frac{2\pi a}{\lambda} (n_c{}^2 - n_o{}^2)^{1/2} \tag{1}$$

where a is the core radius, λ is the free space wavelength and n_c and n_o are the core and cladding indices. For single mode operation, $V \leq 2.4$, i.e. only the doubly degenerate HE_{11} mode propagates for $V < 2.4$. From Eq. (1), one sees that the physical core size a and the core-cladding index differences $\Delta n = n_c - n_o$ may be varied over a considerable range while maintaining $V \leq 2.4$. Figure 1 shows the relationship between normalized core size V and the physical extent ((1/e)points)of the guided HE_{11} mode. By either making Δn or a small, it is possible to have the guided fields extend significantly into the cladding and increase the physical extent of the mode. This feature (Cook, J.S. 1973) is of interest in fiber splicing since it affords a means of relaxing the translational dimensional tolerances.

AD-A050 748 ADVISORY GROUP FOR AEROSPACE RESEARCH AND DEVELOPMENT--ETC F/G 20/6
OPTICAL FIBRES, INTEGRATED OPTICS AND THEIR MILITARY APPLICATIO--ETC(U)
OCT 77 H HODARA
UNCLASSIFIED AGARD-CP-219 NL

3 OF 6
AD A050748

However as V becomes small, the wave in the fiber becomes loosely guided and thus susceptible to bending losses. Reducing the fiber's V number only in the region of splicing by elongating the fiber should reduce the accuracy with which the ends of the fibers to be joined must meet on-center and should not increase propagation losses significantly if the small V number region is limited to the splicing region.

Another feature of single mode fibers is the dependence of propagation loss on wavelength. For a given number, V ~ 2.3 at .85 μm, we plot in Fig. 2 the loss dependence on wavelength. Also plotted here is the wavelength dependence of loss for a multimode fiber. We see that for single mode fibers, loss is a strong function of λ through the dependence of V on λ. On the long wavelength side, scattering into the cladding dominates whereas as the wavelength decreases, the mode fiber is no longer single mode and conversion to other modes dominates the losses suffered by the HE_{11} modes. In multimode fibers, the presence of hundreds of modes leads to an averaging over wavelength of loss for each mode. This results in a very weak dependence of loss on wavelength. Single mode fibers must therefore be designed for the wavelength of interest and large deviations from the design wavelength will lead to excessive losses.

Finally another feature of single mode fibers of interest is their relative insensitivity to the microbending losses; losses often encountered in the cabling of fibers. Olshansky, R. 1976, has shown that for a single mode fiber with a V ~ 2.4, the microbending losses are an order of magnitude lower than those of conventional multimode fibers. Single mode fiber optical cables therefore potentially offer the lowest loss fiber optical data transmission media.

Production of single mode fibers is similar to that used for multimode fibers. Chemical vapor deposition is the most widely used approach and in the case of single mode fibers, this deposition proceeds (Boerner, M. 1976) much more quickly than for multimode fibers since multimode fibers usually require > 40 times more material. For single mode fibers, however, the starting tubes must however be more concentric to ensure accurate core placement. From coupling considerations, it is desired to have the core centered to < ± 1% of the cladding diameter. Fabrication of single mode fibers with the desired tolerances is within the state of the art.

3. SINGLE MODE FIBER SPLICING

Although there are many desired features associated with single mode fibers (low loss, extremely high bandwidth), the disadvantage of using single mode fibers is the tight mechanical tolerances required for low loss interconnects. Besides mode pattern matching, accurate alignment is required. A simple rule of thumb derived from an examination of the propagation of Gaussian beams is that for coupling efficiencies > 50% we need

$$\Delta\theta\Delta x < \lambda_o/n_c \qquad (2)$$

where Δθ is the required angular precision in angle and Δx is the required alignment precision in position. Angular tolerance can be traded off for positional tolerance. At optical wavelengths it would be preferable to work with Δx ~ 15 μm and Δθ ~ 1° which is why there is an interest in large radius (~ 7 μm), small Δn fibers. As discussed in connection with Fig. 1, a wider optical beam can also be realized by reducing the V number of the guide. By drawing the end of a single mode fiber, (Cook, J.S. 1973) the V number of a fiber is reduced and the optical beam size increased. It was shown (Cook, J.S. 1973) that this technique readily permits a factor of two decrease in the required fiber alignment accuracy. The required angular alignment accuracy is increased; however, in general, the angular tolerances do not present as difficult a problem as the displacement tolerances.

Fiber splicing requires a means of physically aligning fibers. A very simple method of fiber alignment was demonstrated by Someda (Someda, C.G. 1972) in which he used embossed grooves in plexiglass. Plexiglass is a thermoelastic material with a glass transition at about 100°C. To form the embossed groove, the fibers to be spliced are pressed into the heated plexiglass (Someda, C.G. 1972) to deform the plexiglass. Upon cooling, precision grooves remain (Fig. 3). Using this approach, splicing efficiencies in excess of 92% are readily achievable. This approach has also been shown to permit low loss interconnections between fibers of different O.D. Someda (Someda, C.G. 1972), using two 3.7 μm core single mode fibers with O.D.'s which differed by 10 μm was able to achieve 90% coupling. The plexiglass deformed elastically and accomodated the fiber O.D. difference in a symmetrical manner which permitted the core axis to remain aligned along the embossed groove. This work demonstrated the O.D. variations can be compensated for in coupler design.

A second approach developed by Hsu and Milton, (Hsu, H.P. 1976), used preferentially etched grooves in silicon to splice fibers. Coupling efficiencies in excess of 90% were again achieved. This coupler was also employed to couple single mode fibers to channel guides and will be discussed in detail in the next section.

If fiber diameter and/or core eccentricity are not controlled, adjustable couplers may be required. A simple coupler using the double-eccentric principle was used to form a detachable fiber-fiber connector, (Guttmann, J. 1975), and fiber to film connector, (Krumpholz, O. 1974), (Fig. 4). To achieve low loss connections, the light scattered into the fiber core must be monitored and minimized. While easily achieveable in the laboratory, field connections will be hampered by the need to monitor scattered light.

The longitudinal separation between fibers is not as critical as the transverse alignment requirements. If the two fibers to be spliced are placed within 15 μm of each other, the loss due to longitudinal displacement is less than 1 dB, (Someda, C. G. 1972).

The ability to readily splice fibers in a low loss fashion favors the use of fiber pigtails on injection lasers and integrated optical circuits. It is envisioned that the more difficult fiber to film coupling will be accomplished in the more controlled environment of the manufacturing plant whereas the demountable coupling of the fiber pigtail to the fiber transmission line can be accomplished in the field using a variety of splicing techniques, some of which have already been outlined.

4. LASER TO FIBER COUPLERS

In order to employ single mode fibers at all, it is required that a source be connected to these fibers. End-fire coupling is the most widely used technique. Single transverse mode operation is required of the laser since in end-fire coupling, one matches the modal fields of the laser with the single mode fiber. Stable single transverse modal operation is routinely achieved in state of the art lasers provided that the active stripe is not too wide ($\leq$ 15 microns) and that the laser is not operated in a current region several times above threshold. With stable laser operation, the coupling problem involves field matching and fiber alignment in a stable manner.

In an early work, Cohen coupled several single mode fibers which possessed cores of about 3.5 microns to double heterojunction lasers. Coupling efficiencies exceeded 40%. Permanent, self-supporting couplers were fabricated by applying suitable epoxies between the structures which supported the fiber and the lasers.

By applying lens to the ends of fibers, it is possible to increase the coupling efficiencies above these reported by Cohen, (Cohen, L. G. 1972). This miniature lens may be fabricated either by melting the ends of the fibers (Kolanzadeh, Y. 1976) or by depositing photoresist on the fiber ends, (Kolanzadeh, Y. 1976). Improvements in coupling efficiencies of a factor of two appear feasible, (Kolanzadeh, Y. 1976), and power launched into single mode fibers should be in excess of 1/2 mW, (Kressel, H. 1976).

Laser-pigtail assemblies are thus feasible with current state of the art devices. It is important now to improve fiber-laser coupling and potting techniques with emphasis on stability and efficiency. Coupling the laser-pigtail assembly to the single mode transmission line will then involve use of the splicing techniques described in Section 3.

5. FIBER TO FILM COUPLING

There exist two basic approaches for fiber to film coupling: end-fire and evanescent field coupling. Evanescent field coupling occurs when the waveguides to be coupled are parallel to each other in the coupling region; whereas the end-fire coupling occurs when the ends of the two waveguides are butted up against each other. Theoretically evanescent techniques offer high coupling efficiency; however, a large number of practical problems have to be solved to make an evanescent single mode fiber to film coupler. In most cases of practical interest a mode liftoff structure must be introduced on the waveguide to avoid mode sinking, (Arnaud, A. 1974). A coupling region which ensures phase matching must be provided after mode liftoff and a single mode fiber arranged to have appreciable modal field at the surface must be aligned on top of the coupling region. End-fire coupling is undoubtedly more straightforward, but it does require preparation of the waveguide ends and precision alignment. Losses due to dissimilarities in mode patterns and reflection at the butt joint interface are inevitable.

5.1 End-fire

End-fire coupling involves bringing the single mode fiber in close proximity to the planar waveguide. Minor reflection losses occur due to dissimilarity in index of refraction between the fiber and the planar guide. Efficiency with an end fire arrangement requires mode pattern matching which can usually be accomplished by matching the cross sectional dimensions of the two guiding regions. If end fire coupling to a fiber with a planar guide were to be attempted, focusing of the light in the planar guide on the coupling end surface would be necessary.

For the case of a high index channel guide a dimensional matching to the size of the core of a low index single mode fiber can be obtained with a small index difference in the channel guide system. Mode pattern matching requires a cross sectional aspect ratio of unity for the channel guide which is hard to achieve with indiffused channel guides due to sideways diffusion. There will therefore always be some mismatch due to the asymmetry of the channel guide and the slightly different geometries.

Besides mode pattern matching, accurate alignment of the two waveguides is required. The discussion of Eq. (2) on angular and spatial accuracies again applies here. With indiffused channel guides the waveguide mode patterns are rarely more than five microns deep so that single mode fibers with small cores will be required for reasonable mode pattern matching. As long as the mode cross sectional dimensions are large compared to a wavelength, the alignment precision in the direction of propagation (z) (how close the waveguides have to be) is not as severe. The rule of thumb derived again from an examination of the propagation of Gaussian beams is

$$\Delta z < \frac{\Delta x^2 n}{\lambda_o} \tag{3}$$

where Δx is the cross sectional dimension. For a fiber to channel waveguide coupler with guide dimension $\Delta x = 2$ µm, the above equation gives an allowable separation $\Delta z = 15$ µm for $n = 1.9$. In other words, as long as the end surface separation between the fiber and the channel guide is kept within 15 µm, there will be no significant reduction on coupling efficiency.

A practical approach to the positioning of a number of single mode fibers for end fire coupling to channel waveguides has been developed by Hsu and Milton, (Hsu, H.P. 1976). Fibers can be accomodated with a separation between fiber and channel waveguide of 1.23 times the fiber outer diameter (O.D.). Figure 5 shows a schematic of how the approach would be used to connect four single mode fibers and a single multimode fiber to a high speed integrated optic channel waveguide switch to form a terminal for a data transfer system.

With the flip chip approach, (Hsu, H.P. 1976), a preferentially etched silicon groove is used to position the fiber core just above the surface of the silicon wafer. By viewing through the transparent $LiNbO_3$ plate (see Fig. 6) and by matching up etched registration grooves in the silicon with indiffused registration stripes in the $LiNbO_3$ (made visible due to the formation of a ridge during indiffusion), fiber alignment within $\pm$ 1 μm over a distance up to several mm has been obtained. In Fig. 7, the fiber positioning accuracy using this approach is shown. A $LiNbO_3$ sample was used which had channel waveguides running perpendicular to the cleaved (10.2) end surface and a 95 μm O.D. single mode fiber with a 4 μm core with its end surface prepared by the score and break under tension method. Since the $LiNbO_3$ plate and the fiber both have square corners and flat end surfaces, the two waveguides could be brought within 10 μm by sliding the fiber along the fiber positioning groove toward the $LiNbO_3$ cleaved end surface.

To understand the effect of misalignment and the effect of channel waveguide diffusion profile and fiber core diameter selection on end fire coupling efficiency, the square of the electric field overlap integral between the modes of a fiber and a channel guide has been plotted in Fig. (8). The indiffused channel waveguide is approximated by a rectangular step index embedded channel guide to facilitate the use of Marcatili's fields, (Marcatili, E. A. 1969), in the calculation. Figure 8 shows the square of the overlap integral as a function of position displacement between the channel waveguide and fiber core. Since after correcting for reflection (about 2.4% in our case) the coupling efficiency is directly proportional to the square of the overlap integral, Fig. 8 indicates that the coupling efficiency is very sensitive to displacement errors; and that the maximum obtainable efficiency could be improved by a better match between fiber core diameter and diffusion depth (channel waveguide mode extent in the y direction).

Another constraint with the flip chip coupler is that in the absence of a good index matching liquid for n = 2.2 the channel waveguide must end with a square corner. Since the fiber is held parallel to the waveguide surface any corner (cleaved or polished) which is not square (90° to the channel waveguide) can cause inefficiencies. Without a index match the beam will tilt away from the fiber axis on exiting the $LiNbO_3$. Convenient index matching fluids exist for indices up to 1.9. Beam tilt angles as a function of the corner angle are plotted from Snell's law in Fig. 9. With an index matching liquid of 1.9 for a waveguide mode thickness of 2 μm, we estimate that the tilt angle w for λ_o = .633 μm must be less than about 5° to avoid serious inefficiency. From Fig. 9 the corner angle thus has to be larger than 65°.

In the couplers demonstrated in Ref. (5), (Hsu, H.P. 1976), cleaving was used to prepare good surfaces. $LiNbO_3$ however only cleaves in a single direction (10.2 cleavage plane) which will place a constraint on device orientation. One alternate edge preparation techniques for $LiNbO_3$ is the use of sputter etching, (Sepori, B. L. 1976). High quality edges suitable for end-fire coupling may be prepared using this method in arbitrary directions. Another alternate technique is polishing. Recently, (Verber, C., et al.), have succeeded in obtaining very high quality polished edges on $LiNbO_3$. Figure 10, a scanning electron micrograph of polished edges in $LiNbO_3$ is shown. Neglectable edge rounding was demonstrated and scattered pit sizes no larger than 1/2 micron were observed. These high quality edges demonstrate that it is within the state of the art to prepare sufficiently high quality edges by polishing.

Figure 6 shows a microscope photograph of the fiber alignment grooves and the single mode channel waveguide in $LiNbO_3$. Experimentally measured coupling efficiencies in excess of 30% have been measured for coupling waveguides and fibers which were not optimized for mode pattern matching. The fibers that are coupled to the channel waveguides represent the desired pigtail couplers. Splicing these pigtails to the transmission line fibers can also be accomplished in the etched alignment grooves.

5.2 Evanescent coupling

With an evanescent approach when the two waveguide material systems have vastly different indices of refraction, as is the case for coupling between metal indiffused $LiNbO_3$ or $LiTaO_3$ waveguides ($n \approx 2.1$) and single mode fused silica fibers ($n \approx 1.5$), severe phase mismatch problems can exist. As long as the index of refraction of the waveguide system substrate is higher than the effective index of the mode in the single mode fiber, phase matching will necessarily exist between a set of substrate modes and the guided mode in the fiber. The phase matching condition applies in the direction of the fiber core leading to a situation similar to output coupling with a high index prism. Unless this unwanted waveguide-substrate coupling which we call mode sinking is impeded, it will dominate and coupling between the waveguide and fiber will not be efficient.

In the pursuit of an evanescent fiber to film coupler we have concentrated most of our efforts on the investigation of an adiabatic mode liftoff structure (Hsu, H. P. 1977), which introduces a low index buffer layer to shield the low index fiber from the high index substrate. It differs from the structure proposed by Dalgoutte, (Dalgoutte, D. G. 1975), in that no low index tunneling layer is included between the indiffused waveguide and the high index top layer.

A full device with the materials we have chosen to use is shown in Fig. 11. The mode liftoff section is followed by a branching section, a transition section and than a tapered velocity coupler. The device is designed to be completely adiabatic, (Hsu, H. P. 1977), (no power transfer between local normal modes) without any mode interference sections so that no critical coupling lengths or field pattern matching sections are involved. Adiabatic operation was achieved; however the experimentally observed losses in the branching section and the transition section were unacceptably high, (Hsu, H.P., 1977). It is believed that for $LiNbO_3$ substrates, these high losses would be difficult to eliminate because of the surface roughness of $LiNbO_3$ and it is concluded that adiabatic evanescent coupling from low index fibers to $LiNbO_3$ waveguides will in general be unacceptably lossy.

This conclusion does not apply for lower index waveguides such as those formed in glasses ($n \sim 1.5$). Dalgoutte et al. (Dalgoutte, D. G. 1975), have achieved 70% coupling efficiencies for evanescent coupling between an externally mounted fiber and a planar glass waveguide. An externally mounted fiber is shown in Fig. 12 and is made single mode by making the thickness t sufficiently small. These fibers generally are multimode in the thicker direction W. By placing this fiber in close proximity to the waveguide, evanescent coupling is achieved.

This work can be extended to higher index waveguides such as $LiNbO_3$ either by developing high index externally mounted core fibers or by using an end-fire coupling technique to get light into a low index transitional guide. Using sputter etching to form a high quality edge, (Sepori, B. L. 1976) demonstrated the fabrication of such a transition guide (Fig. 13). Efficiencies better than 80% have been obtained for end-fire coupling from the $LiNbO_3$ waveguides into the lower index guides. Using the evanescent coupling methods of Dalgoutte, D. G. 1975, one should then be able to couple into a fiber with an externally mounted core.

5.3 Laser to film couplers

Coupling of lasers directly to thin film waveguides involves many of the problems previously discussed. In Fig. 14, we show the direct coupling technique which was studied by (Hunspenger, R. G. 1976). Critical for high efficiency is field matching, accurate device alignment and stable device support. The waveguides employed in Fig. 14 were fabricated of Ta_2O_5 on glass. Coupling into the allowed modes is shown in Fig. 15. Coupling efficiency for the lowest order mode was in excess of 40% and it is seen that the experimental data closely follows the predicted efficiency curves. The structure fabricated by Hughes did show a good deal of mechanical stability and demonstrated the feasibility of rugged laser to waveguide coupling.

6. FIBER COMPATIBLE INTEGRATED OPTICAL SWITCHES

Many of the integrated optical switches demonstrated to date are not suitable for use in a fiber optic transmission system. These switches have been optimized for a single polarization and evidence considerable interchannel crosstalk when both polarizations are simultaneously present. To be used in an optical communication system employing fiber optical transmission lines, switches must be designed to be insensitive to the state of incoming polarization, (Steinberg, R. A. 1976).

In general, linearly polarized light coupled into single mode fibers suffers rapid conversion to other polarization states, so that light emerges from the fiber with some unknown elliptical polarization. The cause of this polarization scrambling is related to core ellipticities and to stress birefringence. Rectangular or strongly elliptical cross sections fibers would prevent polarization conversion; however, no one to date has fabricated useable structures, (Kaiser, P. 1973).

Electrooptical switches and modulators can be made with planar guides or with channel guides. All of these devices work by having change in guide index of refraction caused by an applied electric field produce a phase shift in part of the beam. Various waveguide switch designs are presented in Fig. 16. The planar devices only confines the light in the plane of the film and usually work to deflect the light either by an electrooptically induced prism or by Bragg deflectors from an electrooptical induced grating. The different polarization have slightly different propagation constants in the guide which alters the angle of deflection; however for indiffused waveguide systems this is not enough of a difference to be important. Polarization insensitivity can therefore be achieved by operating with a crystal orientation such that the electrooptic effect is the same for both polarizations, (Steinberg, R. A. 1976). This will assure that waves of different polarization will suffer the same angle of deflection for an induced prism and the same deflection efficiency for a Bragg device.

Channel guides confine the light in both transverse dimensions. With an electrooptic channel device the volume over which an electric field must be applied is therefore less than with a planar device. Electrical drive power for modulation at a given frequency is therefore reduced and channel switches can be remarkably efficient. The channel geometry is also more suitable to coupling to the core of a single mode fiber. Many switch/modulator designs for channel guides however require precision modal interference in a close coupling region where two channel guides come close together. Due to dissimilarities in propagation constant and coupling coefficient this interference usually does not have the same effect on both polarizations and polarization insensitivity is hard to achieve. The modal evolution 3 dB coupler made with branching waveguides on the other hand does not depend on modal interference and a symmetric type II switch made with two of these 3 dB couplers and oriented such that the electrooptic coefficient for both polarizations is the same will be polarization insensitive. An alternative approach is to electrically compensate for fabricational errors in the modal interference class of switches demanding tolerance requirements of earlier modal interference type switches. Steinberg, R. A. 1976, have shown that this switch configuration can also be configured to be polarization insensitive. Electrical compensation of fabricational errors has recently been demonstrated by (Kogelnik, H. 1976) who used multiple electrodes to tune out errors. A three section version of their device is shown in Fig. 17.

Although Bragg switches and channel switches may be made polarization insensitive, the allowable crystal orientations are restricted, (Steinberg, R. A. 1976 and 1977a). This results in the use of non-optimum electrooptic coefficients in the switching and significantly decreased efficiency. In a new design (Steinberg, R. A. 1977b) have found that the use of two electrode types with the crossed β design (Kogelnik, H. 1976) makes it possible to electrically achieve polarization insensitive operation for arbitrary crystal orientations (Fig. 18). As seen in Fig. (18b), the two different types of electrodes result in applied fields in the waveguide region which are either horizontal or vertical. Since the electrooptic effect is a tensor quantity, the use of horizontal fields result in a different electrooptic effect than the vertical fields. As was shown, (Steinberg, R. A. 1977b), this configuration affords a new degree of freedom which permits an electrical means to compensate for different efficiencies in TE and TM modal switching. This design concept permits the use of the largest electrooptic coefficients and thus maximizes device efficiency. Efficient integrated optical switches can thus be made compatible with fiber optical transmission lines for the first time.

7. SINGLE MODE DATA SYSTEMS

With the advent of useable components with which to construct single mode fiber optical data systems, consideration is now being given toward the design of optical data buses and switchboards. In Fig. 19, a schematic of two possible data bus layouts is presented. The terminals for this multiterminal data link consist of high speed four port switching modules similar to those described in Fig. 5. With the arrangement in Fig. 19a, a single centrally located laser can provide the light for all the terminals via a "power line" fiber, (outer loop). Data pulses are put on the communication line (inner loop) by crossing the switch as shown in Fig. 20. Alternatively, CW injection lasers can be used at each terminal as shown in Fig. 19b. In this case, the switch serves as a modulator and input coupler. With these loop designs, terminal throughput loss must be kept low. Various forms of star designs such as shown in Fig. 21 can be used which permit higher terminal throughput losses. In this case, data signals originating from a given terminal pass through a single repeater module before being delivered to the receiver terminals. Here again the basic terminal module shown in Fig. 5 can be used if minor modifications are incorporated. With an optical switching capability, communication systems can be built with remotely located laser sources. This will have advantages for terminal locations where access is restricted and/or where minimizing size and power is important.

Switchboards can be realized using single mode technology simply by cascading a number of integrated optical switches. In Fig. 22, an experimental realization of a four by four switch is shown, (Schmidt, R. V. 1976). In this example, five multiple electrode four port switches (Kogelnik, H. 1976) were cascaded to construct this switching network. -19 dB crosstalk was observed when a signal was inputted into one terminal and the various output terminals were monitored. More elaborate switching networks such as a 10 x 10 switchboard are now within the state of the art thus making many telecommunication architectures possible to fiber optic systems.

Mention should also be made of high capacity point to point data links. With fiber propagation losses below 4 dB/km, high capacity (> 500 Mbit/s) links with repeater spacings between 10-20 km are becoming possible. For this class of applications, lasers and detector modules are the key active elements. Fiber splicers and connectors must still be perfected and engineered; however, the implementation of these links now appears to be within the state of the art.

8. SUMMARY

Single mode fiber optic data transfer systems using integrated optical circuits and single mode fibers appear to offer a viable approach to high data rate communication. While the samll lateral dimensions of single mode structures require higher displacement precision for coupling and splicing than multimode structures, techniques for achieving the required accuracy have been demonstrated. Splicing single mode fibers is more difficult than for multimode fibers; however, acceptable splicing losses have been routinely demonstrated in the laboratory with coupling efficiencies in excess of 90% demonstrated. The relative ease of splicing single mode fibers leads one to favor the integrated optical circuit fiber-pigtail or the laser-fiber pigtail concept in which the more difficult fiber to film coupling is performed in a controlled environment. Laser and integrated optical circuit modules will then all come with suitable fiber pigtail couplers.

The laser or thin film to fiber coupling efficiency has now exceeded 30% and improvements can reasonably be expected. The use of miniature lens on the ends of fibers appears to offer increased coupling efficiencies over the quoted 30%. Since the principals of coupling have been established, rugged, reliable structures now have to be developed. Approaches to compensate for fabricational errors should also be further developed.

Polarization-insensitive integrated optical circuits have been studied and are being developed. Communication terminals such as shown in Fig. 5 are now possible as are optical switching networks using multiple microoptical switches. These terminals will provide fiber optical systems its first active terminal capability for routing, tapping or processing optical data transmission.

References

Arnaud, A., 1974, "Transverse Coupling in Fiber Optics, Part 1. Coupling between two trapped modes," Bell Syst. Tech. J. 53, 217.

Boerner, M. and Masbowski, S., 1976, "Single mode transmission systems for civil telecommunications," Proc. IEEE 123, 627.

Cohen, L. G., 1972, "Power coupling from GaAs injection lasers into optical fibers," Bell Syst. Tech. J. 51, 573.

Cook, J. S., Mannel, W. L., and Grow, R. J., 1973, "Effects of misalignment on coupling efficiency of single mode optical fiber butt joints," Bell Syst. Tech. J. 52, 1439.

Dalgoutte, D. G., Smith, R. B., Achutaramayya, G., and Harris, J. H., 1975, "Externally mounted fibers for integrated optics interconnections," Appl. Opt. 14, 1860.

Guttmann, J., Krumpholz, O., and Pfeiffer, E., 1975, "A single connector for glass fiber optical waveguides," Arch. Elektron. Ubertragungstech 24, 288.

Hsu, H.P., and Milton, A. F., 1976, "Flip chip approach to end fire coupling between single mode optical fibers and channel waveguides," Elect. Lett. 12, 404.

Hsu, H. P., and Milton, A. F., 1977, "Single mode coupling between fibers and indiffused waveguides," (to be published J. Quant. Elect.).

Hunsperger, R. G., 1976, "Optimized thin film light sources," Hughes Technical Report AFRL-TR-76-81.

Kaiser, P., Marcatili, E. A., and Miller, S. E., 1973, "A new optical fiber," Bell Syst. Tech. J. 52, 265.

Kogelnik, H., and Schmidt, R. V., 1976, "Switched directional couplers with alternating $\Delta\beta$," J. Quant. Elect. QE-12, 396.

Kohanzadeh, Y., 1976, "Injection laser coupling to optical waveguides with integral lens," J. Appl. Phys. 47, 177.

Kressel, H., 1976 (private communication).

Krumpholz, O., and Pfeiffer, E., 1974, "Coupling device connecting a glass fiber with an integrated optical circuit," Topical Meeting on Integrated Optics, New Orleans.

Marcatili, E. A., 1969, "Dielectric rectangular waveguide and directional coupler for integrated optics," Bell Syst. Tech. J. 48, 2071.

Olshansky, R., 1976, "Microbending losses in single mode fibers," Fiber Optics Conference, Paris, France.

Steinberg, R. A., and Giallorenzi, T. G., 1976, "Performance limitations imposed on optical waveguide switches and modulators by polarization," Appl. Optics 15, 2440.

Steinberg, R. A., and Giallorenzi, T. G., 1977a, "Design of integrated optical switches for use in fiber data transmission systems," (to be published in J. Quant. Elect.).

Steinberg, R. A., Giallorenzi, T. G., and Priest, R. G., 1977b, "A new electrode design for polarization-insensitive integrated optical switches," (to be published Appl. Optics).

Schmidt, R. V., 1976, "Guided wave optical devices using Ti-diffused $LiNbO_3$," Proc. Electrooptics Systems Design Conference, New York, pp. 557.

Someda, C. G., 1972, "Single, low loss joints between single mode optical fibers," Bell Syst. Tech. J. 52, 583.

Sopori, B. L. , Chang, W. S. C., and Phillips, C. M., 1976, "A new method for the efficient interconnection on high index planar waveguides to low index transitional waveguides," Appl. Phys. Lett. 29, 800.

Verber, C., (private communication).

Weidel, E., 1974, "Light coupling from a junction laser into a monomode fiber with a glass cylindrical lens on the fiber end," Opt. Comm. 12, 93.

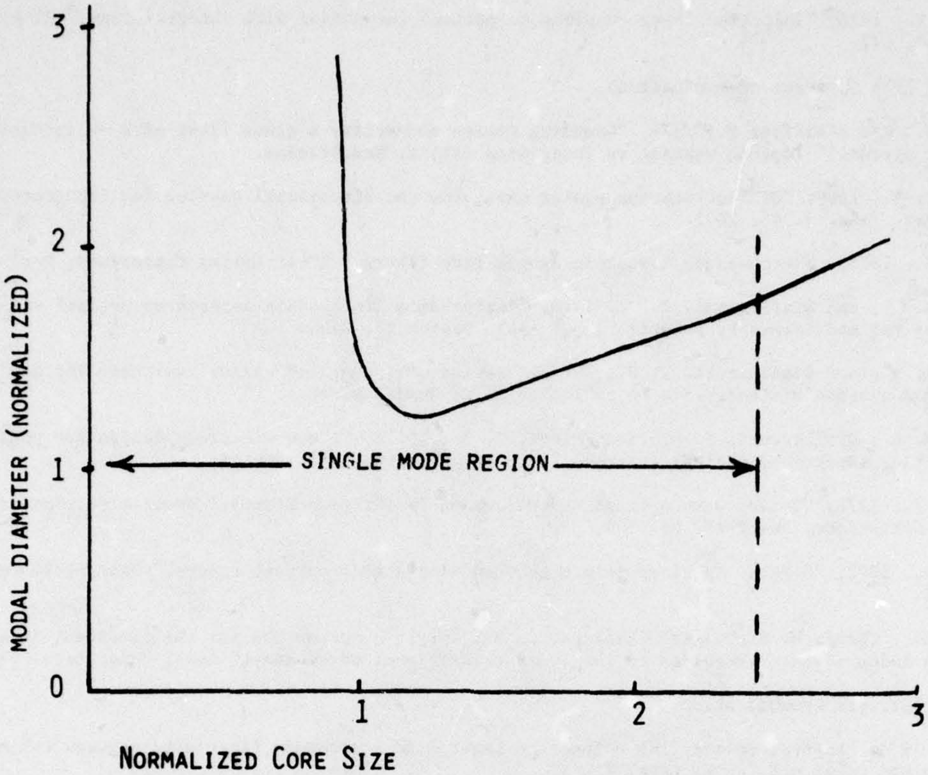

Figure 1 - Normalized beam size versus normalized fiber core size. Single mode HE_{11} propagation occrus when the core size is less than 2.405. The HE_{11} fundamental mode does not cut off as the core size shrinks but becomes less loosely bound. Consequently, the fields spread out beyond the physical core in this region of operation.

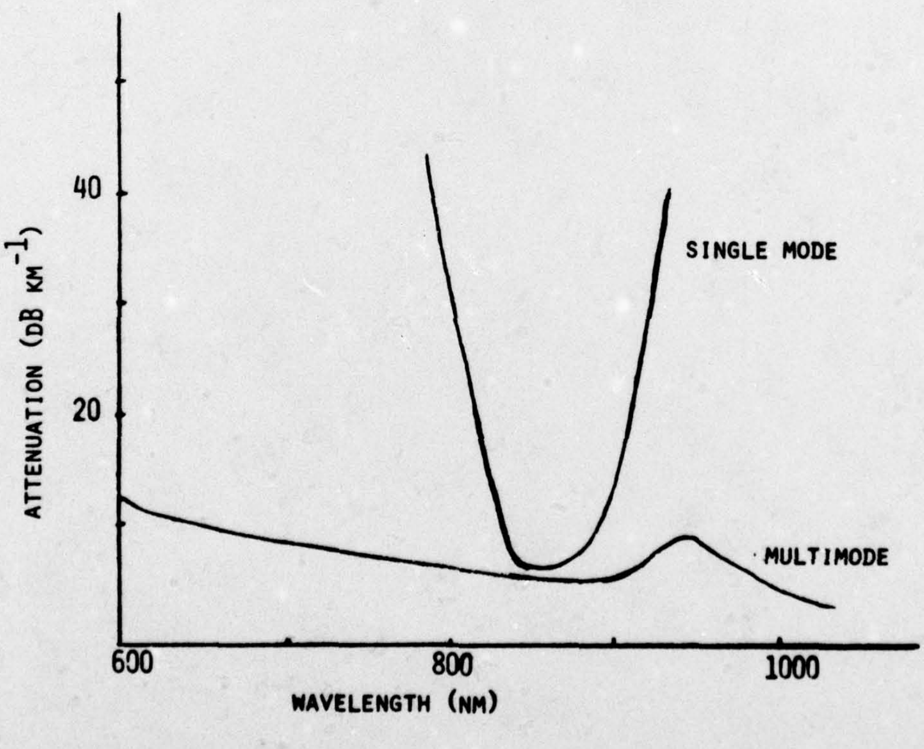

Figure 2 - Fiber attenuation as a function of wavelength. The minimum corresponds to the optimum normalized core size and in this region, the fiber is relatively insensitive to microbending loss. Multimode fibers are not particularly sensitive to the propagating wavelength.

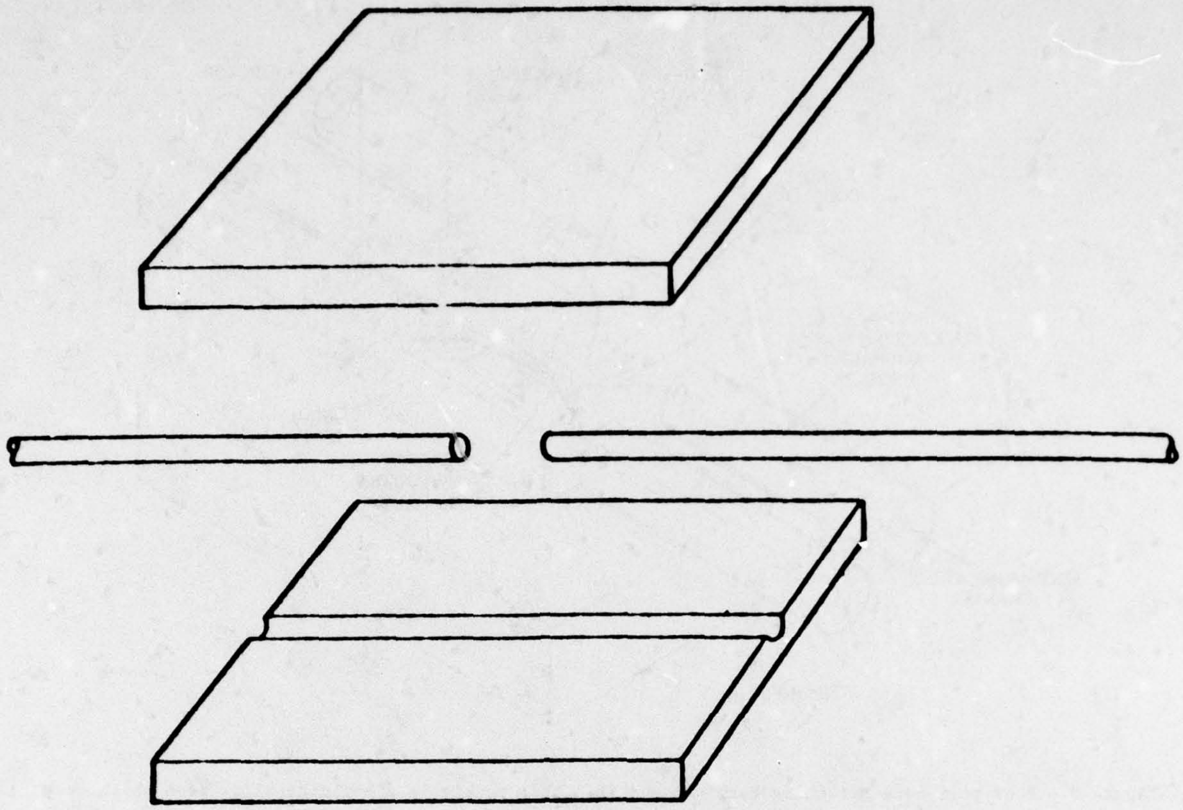

Figure 3 - Embossed groove fiber to fiber splicer.

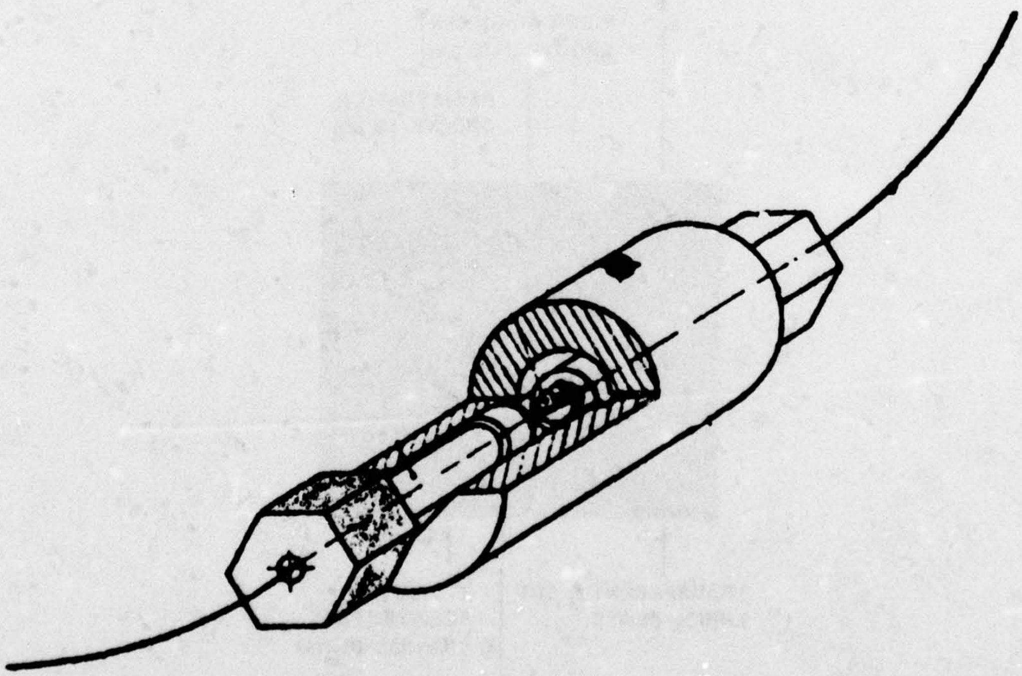

Figure 4 - Asymmetrical fiber to fiber splicer. Fiber alignment is achieved by rotating two eccentric sleeves until the fiber core lines up.

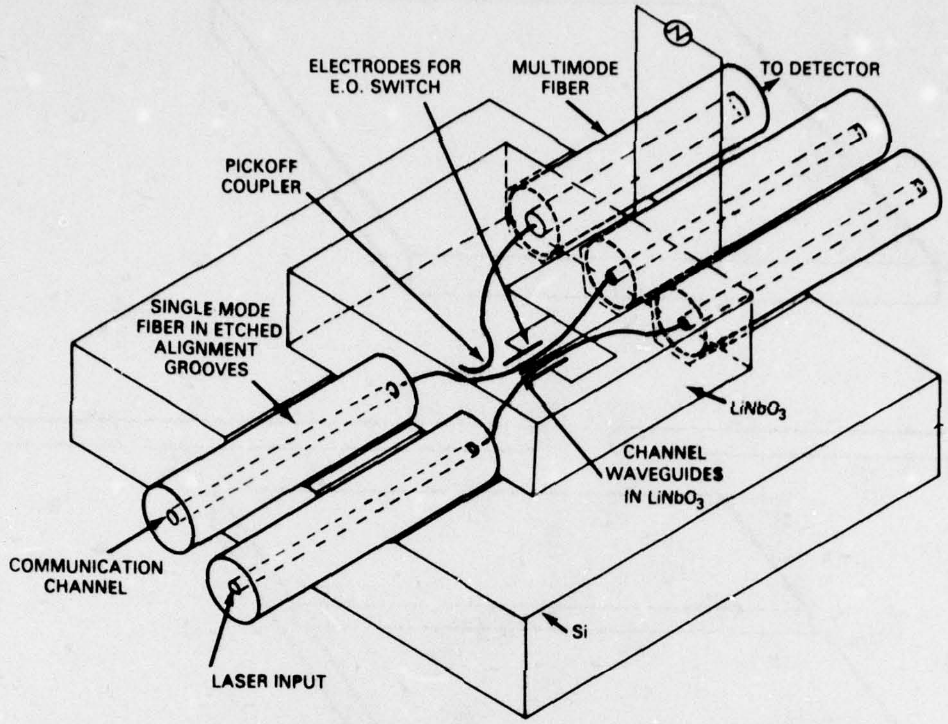

Figure 5 - Four port data switching terminal module. This module is a building block from which many data transfer systems can be constructed.

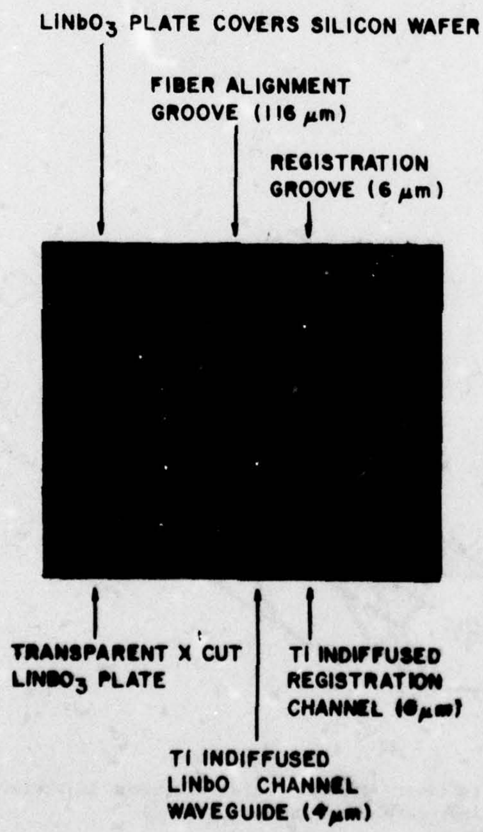

Figure 6 - Photograph of aligned $LiNbO_3$ plate and fiber-positioning silica-wafer assembly as viewed through transparent $LiNbO_3$ plate.

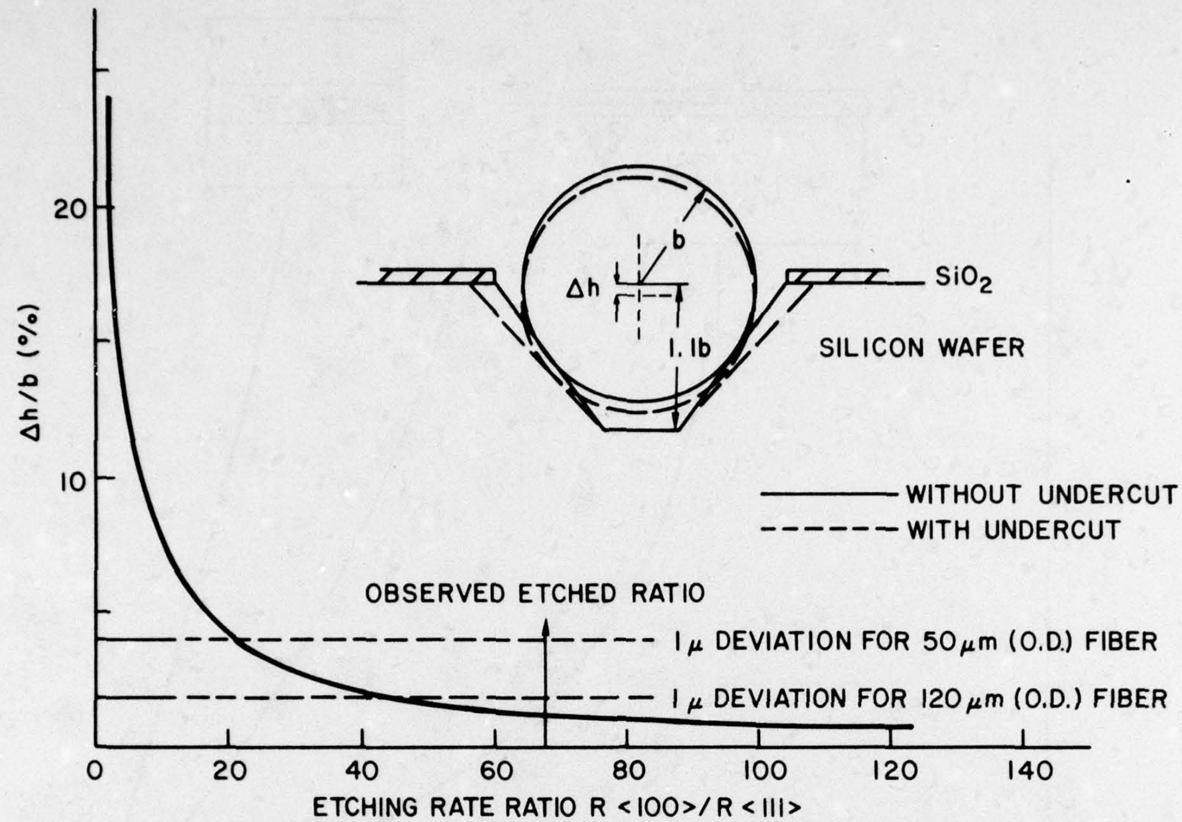

Figure 7 - Percentage error of altitude of center of fiber owing to undercutting as a function of etching rate ratio R(100)/R(111).

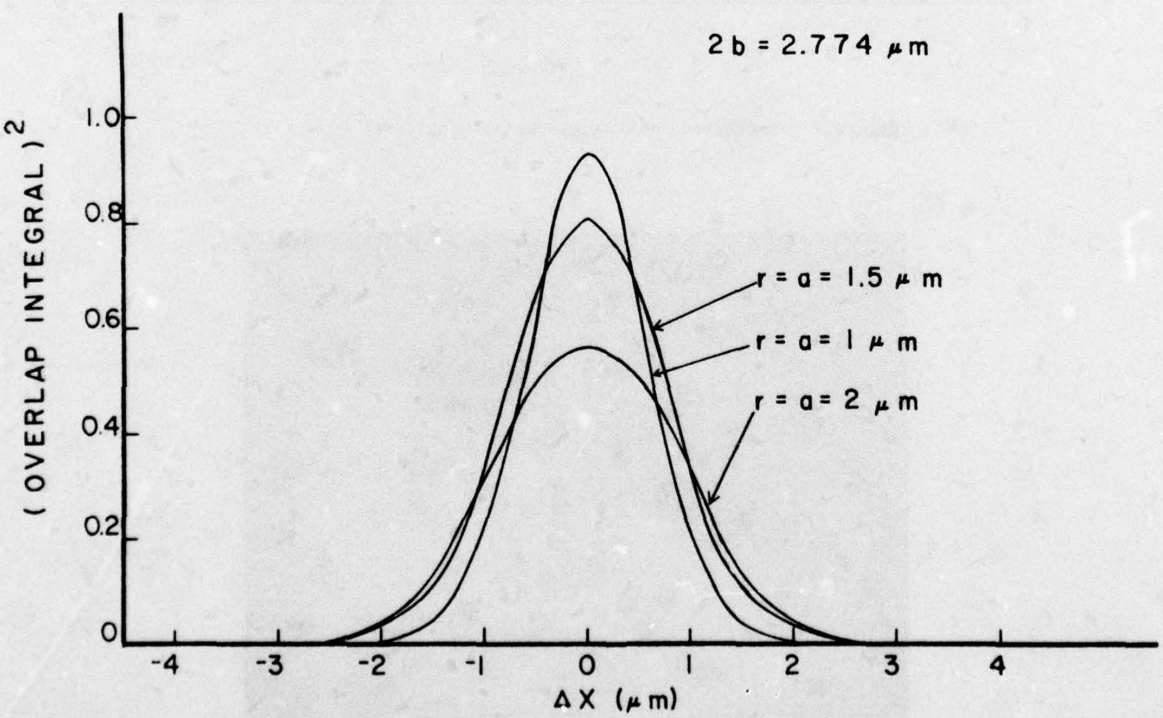

Figure 8 - Fiber-channel waveguide overlap integral as a function of lateral displacement.

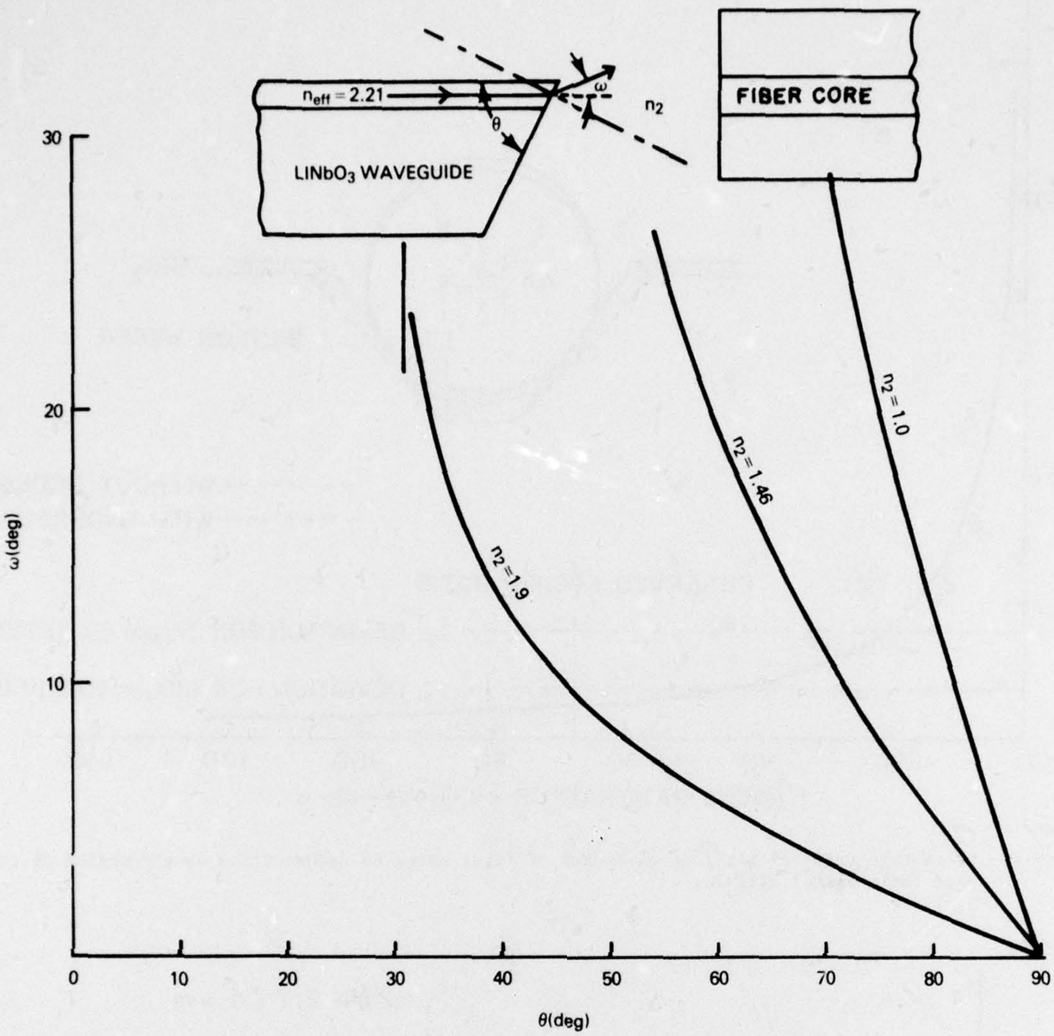

Figure 9 - Refracted light angle as a function of edge tilt.

Figure 10 - Electron micrograph of the edge of a polished $LiNbO_3$ waveguide (5500X).

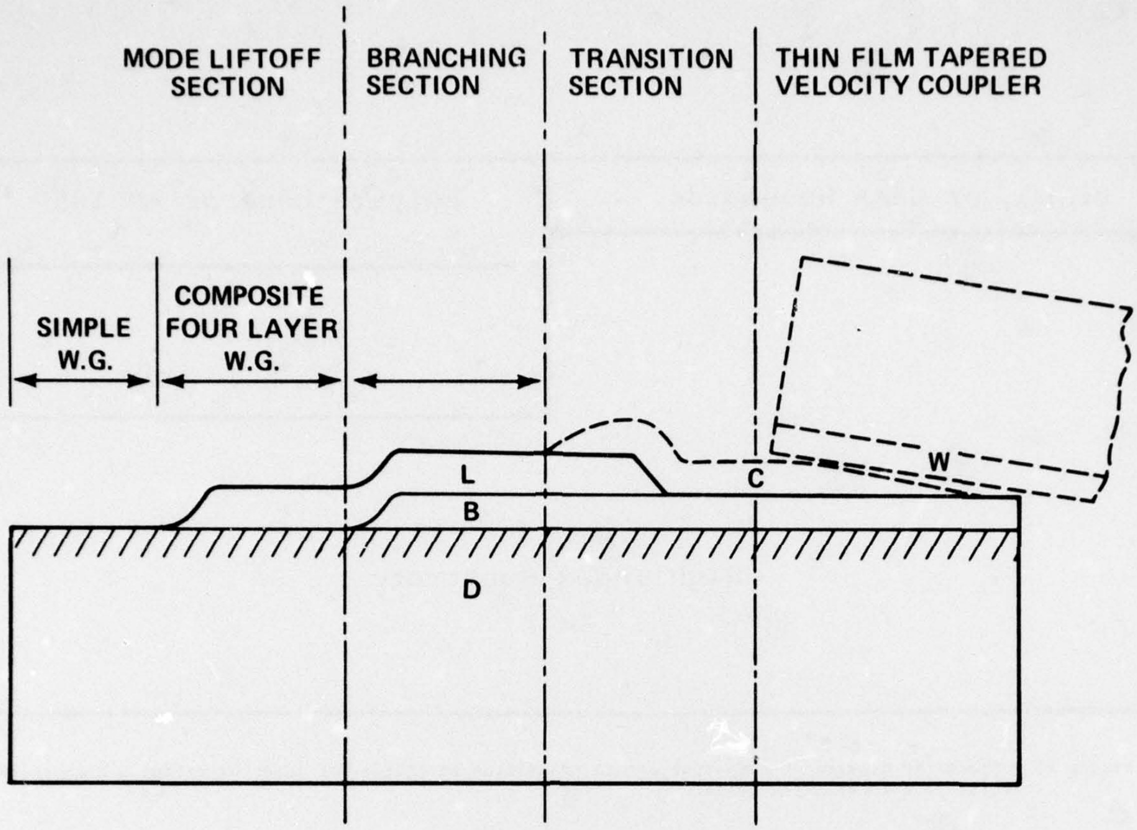

D : HIGH INDEX WAVEGUIDE (IN-DIFFUSED $LiNbO_3$ WAVEGUIDE)

B : LOW INDEX BUFFER LAYER (SiO_2)

L : HIGH INDEX LIFTOFF TOP LAYER (Nb_2O_5)

C : TAPERED LOW INDEX WAVEGUIDE (BARIUM SILICATE)

W : LOW INDEX WAVEGUIDE (EVENTUALLY THE FIBER)

Figure 11 - Modal lift off structure needed to couple a low index fiber to a high index waveguide.

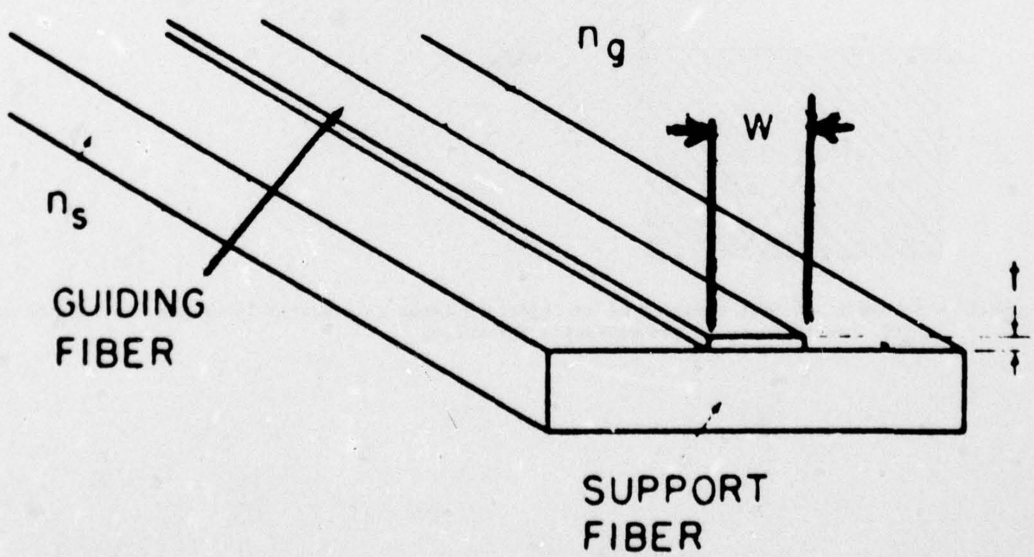

Figure 12 - Schematic of an externally mounted coupling fiber.

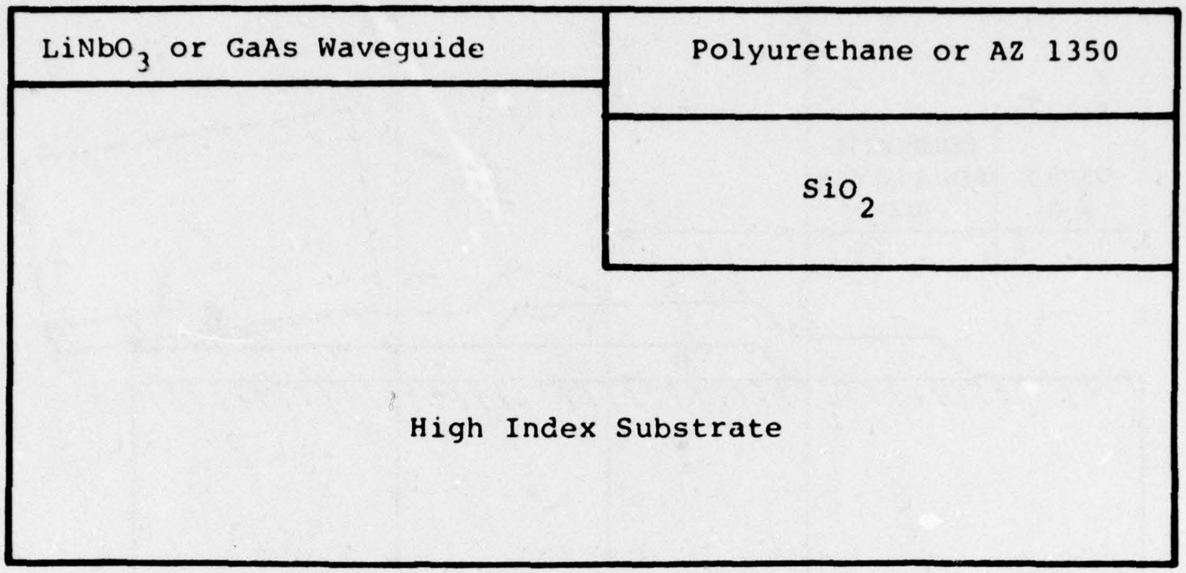

Figure 13 - Schematic diagram of a sputter etched transition waveguide for interconnecting a high index guide to a lower index guide.

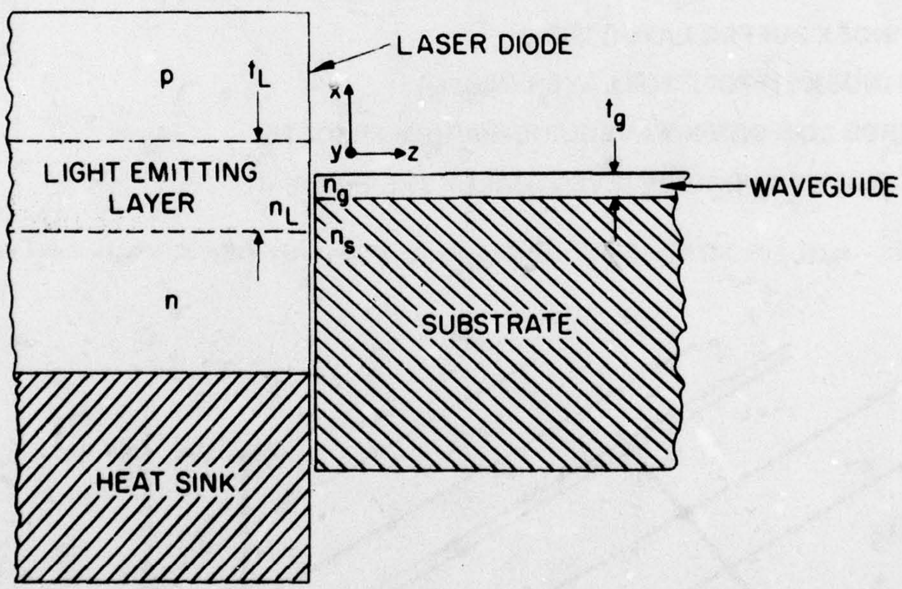

Figure 14 - Schematic of butt coupling of an injection laser to a planar waveguide. t_l is the thickness of the laser and t_g is the waveguide thickness.

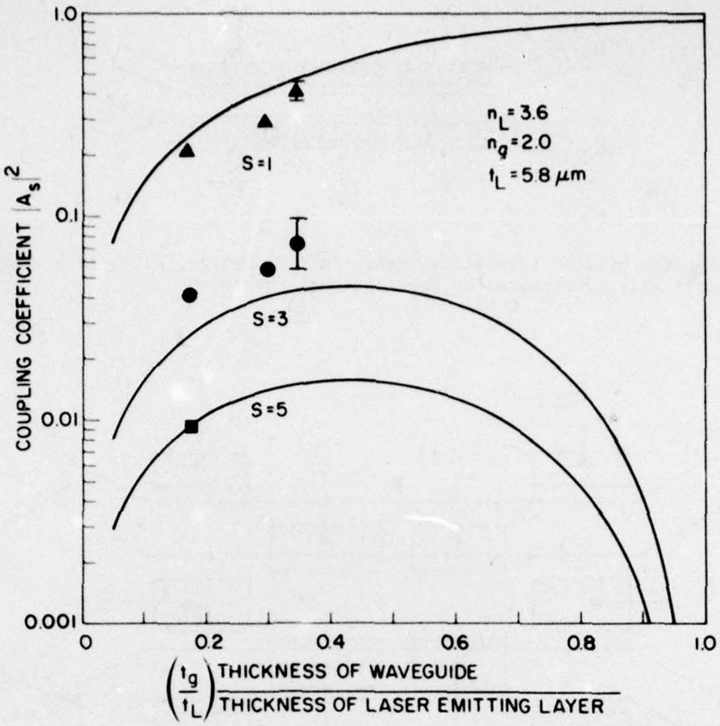

Figure 15 - Comparison of theoretical and experimental coupling coefficient of a laser to a planar guide (Hunsperger, R. G. 1976).

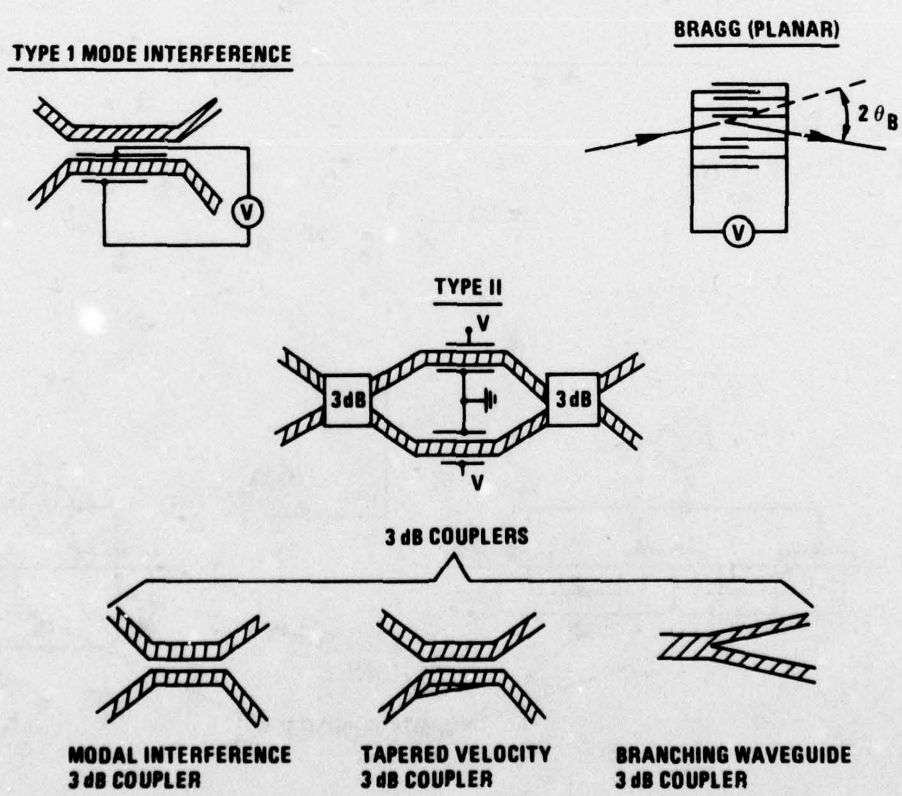

Figure 16 - Commonly used modulator configurations. In type I modulators the coupling and phase shift regions coincide. In type II devices, the channel coupling regions (labeled 3 dB in the figure) are separated from the phase shift region. At the bottom of the figure are three alternative schemes for realizing the 3-dB couplers needed to construct the type II device.

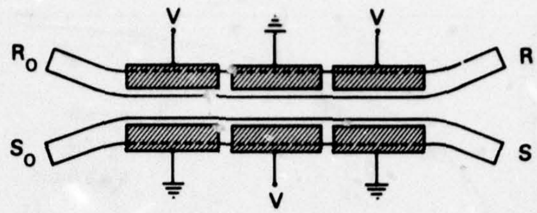

Figure 17 - Schematic of a Δβ reversal switch. In this design, multiple electrodes are used to electrically compensate for fabricational errors.

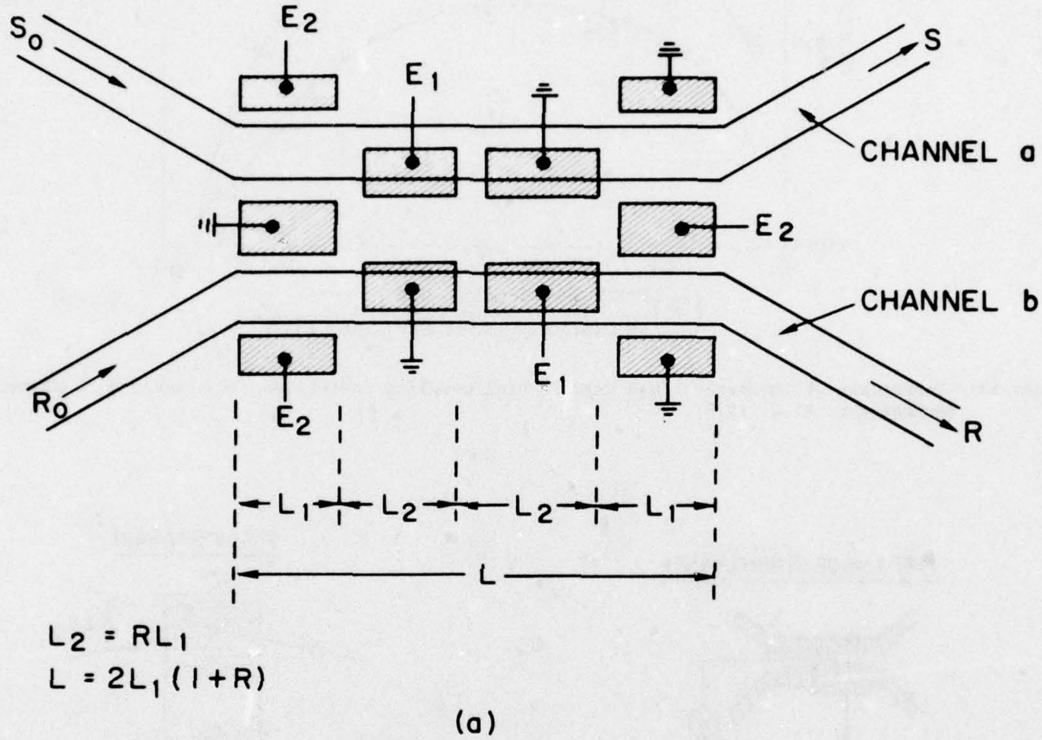

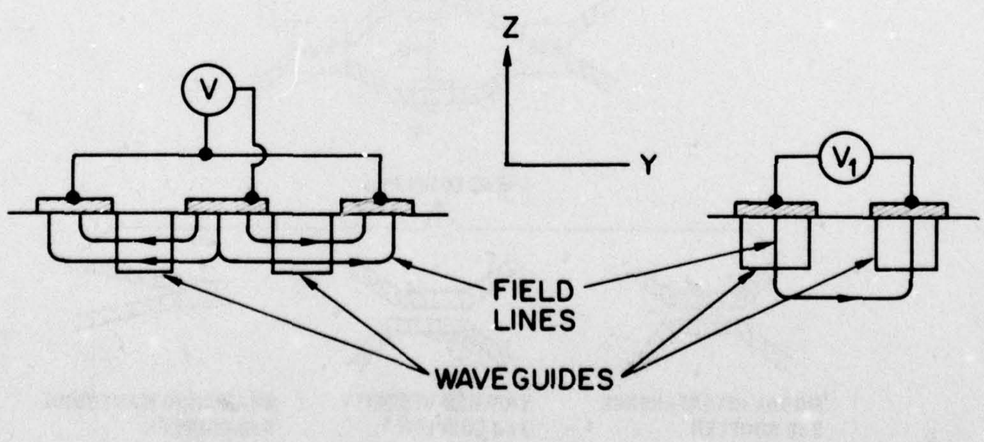

Figure 18 - Schematic of polarization insensitive channel switch design. The use of two different electrode types permits one to tune for polarization insensitive operation.

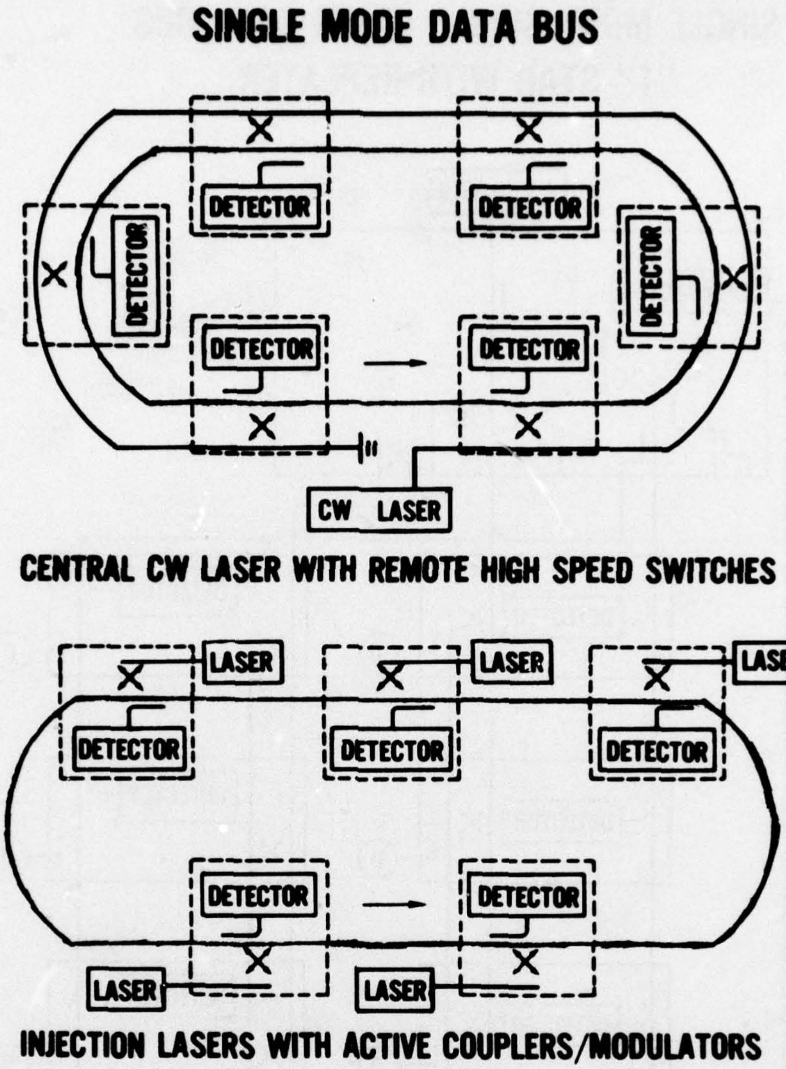

Figure 19 - Loop type single mode optical data bus designs. In the upper figure, a single laser powers every terminal whereas the lower figure utilizes a separate laser at each terminal.

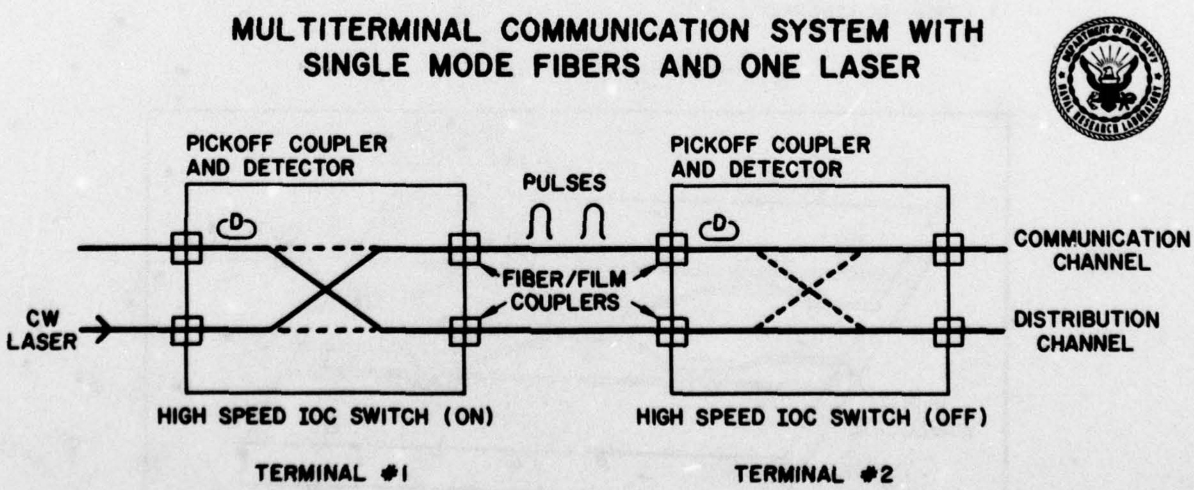

Figure 20 - Single mode data bus terminals. This figure describes the operation of integrated optical switches in a data bus configuration similar to those shown in Fig. 19. To transmit data, a terminal switches light from the distribution channel onto the communication channel.

SINGLE MODE SINGLE LASER DATA BUS "T" STAR WITH REPEATER

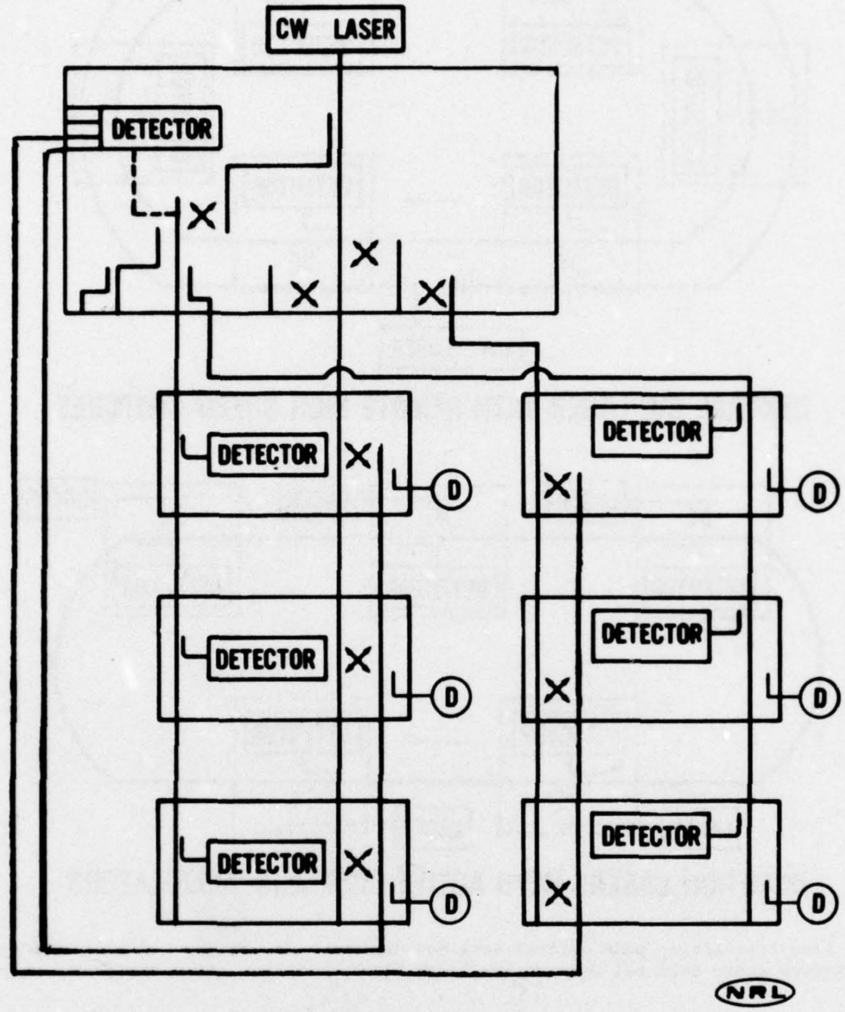

Figure 21 - Single mode, single laser data bus "tee" star configuration. Incorporated in this design is a repeater type star.

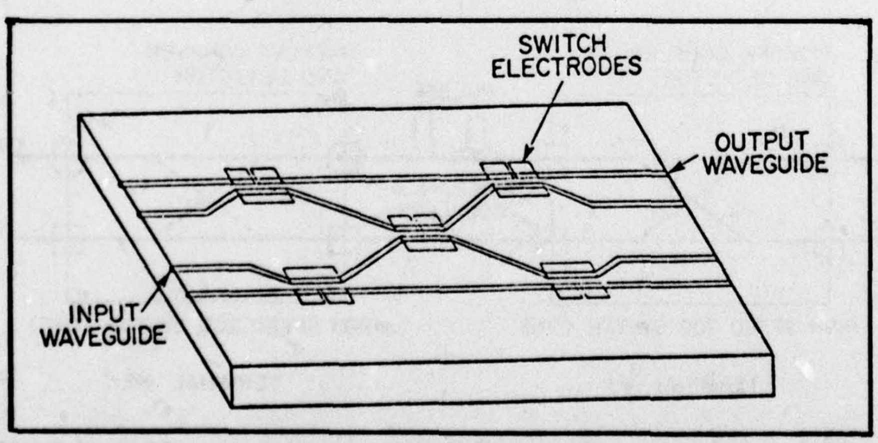

Figure 22 - 4 x 4 switching network (switchboard) (after Schmidt, R. V. 1976).

ELECTROOPTICAL ACTIVE COMPONENTS FOR GUIDED LIGHT

M. Papuchon

THOMSON-CSF
Laboratoire Central de Recherches
B.P 10 - 91401 ORSAY
FRANCE

ABSTRACT.

Modulators and switches are very important components for Integrated Optics. The electrooptical effect is a good candidate to realize them because the geometrical parameters lead to a considerable reduction in the driving powers.

In this paper we shall present the results obtained in the realization of electrooptical active components in Integraded Optics and in particular using the in diffusion of Titanium in $LiNbO_3$ Crystals to create the guides. We shall discuss elements such as phase modulators, amplitude modulators and switches. Recent experimental results concerning their caracterisation and performances will be presented.

I- INTRODUCTION.

Electrooptical components play a very important role in classical optics and since the beginning of integrated optics it has been recognized that modulators or switches that use the electrooptical effect and realized in an optical integrated form would lead to very low drive power and high potential bandwith components. As a matter of fact the basic principle of the electrooptical effect is the induced change in the refractive indices of a material under the application of an electric field.Thus, after an interaction length L the light propagating in the medium undergoes a phase shift that is proportional to L and to the induced refractive index change Δn:

$$\Delta \phi = \frac{2\pi}{\lambda} \Delta n L$$

Where is the wavelength of the light in vacuum. In this paper, we shall consider only the linear electrooptical effect in which Δn is proportional to the applied electric field Thus if the field is created by applying a voltage V to two electrodes spaced by d we get

$$\Delta \phi = \frac{2\pi}{\lambda} B V \frac{L}{d}$$

Where B is proportional to the appropriate electrooptical coefficient of the material used in the experiment.

The voltage used to create a π phase shift :

$$V_\pi = (\lambda/2B) \frac{d}{L}$$

is then proportional to the geometrical factor $\frac{d}{L}$

In classical optics this ratio is limited by light diffraction to values of the order of $\frac{1}{50}$ or $\frac{1}{100}$ but this is not the case in integrated optics where ratios of the order of $1/1000$ or $1/10000$ can readily be obtained (for example a 2 μm wide and 1 cm long waveguide leads to $d/L = 2\,10^{-4}$) leading to very low driving voltages.

These great advantages exist only if channel waveguides are used and so, in this paper we shall consider only modulators realized with these sort of guides.

Another important point is the material problem-Among the electrooptical materials known to day, LiNbO3 crystal seems to be a very good candidate because its very good optical properties, high electrooptical coefficients and the possibility to create relatively easily very good optical waveguides (losses $\leq$ 1 dB/cm) with it. As a consequence we shall concentrate the discussion on the realization of electrooptical components using channel guides in $LiNbO_3$ crystals. To begin with we shall discuss the fabrication problems and then describe practical realization of some electrooptical components namely : a phase modulator, an amplitude modulator and a switch based on the directional coupler configuration.

II - WAVEGUIDE FABRICATION.

Several methods have been proposed to realize waveguides with crystals like $LiNbO_3$ including :

out-diffusion (KAMINOW, I.P, 1973)

hetero-hepitaxy (MIYAZAWA.S, 1973) and the techniques of metal in diffusion which was first demonstrated by Hammer and Phillips, using niobium diffusion in $LiTaO_3$ (HAMMER, J.M, 1974) and then, by KAMINOW in $LiNbO_3$, using various metals (Ti ....)(KAMINOW, I.P,1974)

Metal in-diffusion can lead to monomode waveguides with very low losses and, as it is very easy to mask it, it seems to be the most promising method to-day.

As a consequence, we use it intensively,and all the waveguides used in the diffecent switch/modulator configurations we shall describe in this paper have been realized by Ti in diffusion in $LiNbO_3$ crystals.

The general fabrication process is as follows : 500 Å Titanium film is sputtered on a $LiNbO_3$ substrate. The desired circuit drawing is then realized in the metal film by masking and ion etching. After cleaning, the sample is introduced in an oven to perform the diffusion process for several hours at a temperature of 1000°C and under an oxygen atmosphere. Very good quality (losses $\leq$ 1 dB/cm) monomode waveguides can readily be obtained with such a process, and complex circuitry realized. To apply the electric field in electrooptical components electrodes are needed. They are realized by sputtering 2000 Å of gold on the substrate and by using superposition, optical masking machines and ion etching. The modulator/switch is then ready for electrooptical tests.

Having described the techniques used to create electrooptical channel waveguides in $LiNbO_3$, we shall now give some results obtained in our laboratory during the realization of different electrooptical components. To begin with the simplest one we shall discuss in the next part a phase modulator with low drive power and high electrical bandwidth.

III - PHASE MODULATOR.

In this section, we shall describe the performances of an electrooptical phase modulator. The waveguide configuration is shown on figure 1 and consists of a 5 μm wide and 1,5 cm long waveguide realized with the process described in section II. Larger sections have been realized at the input and output of the guide to facilitate the coupling and recoupling of the light, which is achieved with rutile prisms.

The electric field is applied parallel to the C axis via two gold electrodes spaced by 5 μm and placed on either side of the waveguide. As we have already seen in section I, the application of an electric field induces a change in the index of refraction, and so, the voltage required to make a π phase shift (for a TE polarized guided light in our case) is :

$$V_\pi = \frac{1}{A}\,\frac{\lambda}{n_e^3 r_{33}}\,\frac{d}{L}$$

Where λ is the wavelength in vacuum, n_e the extraordinary index of $LiNbO_3$, r_{33} the electrooptical coefficient used in the experiment, d the spacing between the two electrodes and A the factor that takes into account the effective electric field and the fact that the variation in the propagation constant is no exactly to Δn .By using the numerical values of the experiment, we get :

$$V_\pi = 0{,}6 \text{ Volts} \qquad (\text{If } A = 1 \,,\ \lambda = 0{,}6328\,\mu)$$

To detect the phase modulation of the out-going light we have used the following method : we analyze the frequency spectrum of the modulated light and compare the relative heights of the sidebands created when a sinusoidal voltage is applied to the electrodes. The corresponding set-up shown in fig.2. The optical spectrum analyser is simply a scanning Fabry Perot interferometer and the spectrum is displayed on an oscilloscope after detection with a photomultiplier. This method permits the detection of a high frequency phase modulated light at a very low frequency, which is the scanning frequency of the interferometer. Using this technique, the performances of the phase modulator have been measured :

- the command voltage for a π phase shift is 0,9 volts (indicating a A factor of about 0,66)
- the bandwidth is 600 MHz using a 50 Ω load.

These experiments demonstrate the possibility of realizing high performances phase modulators in integrated optics but, in general, amplitude modulators are preferred. An example of such a circuit is described in the next section.

IV- AMPLITUDE MODULATOR.

When a phase modulator is realized, a simple way of obtaining an amplitude modulator is to make an interferometer. An integrated interferometer configuration, first demonstrated by OHMACHI, is shown in fig. 3. (OHMACHI,Y,1975). The light incident in guide 1 is splitted into two parts by branch B1. Then light propagates in the two arms (guides 2 and 3) Branch B2 combines the light coming from these two arms in guide 4.

If E1 and E2 are the electric fields of the waves at the beginning of the two arms, thus if and are the phase shifts undergone by the guided waves, after recombination in branch 2, the total field is :

$$E_T = E_1 e^{i\phi_1} + E_2 e^{i\phi_2}$$

and the intensity in guide 4 is proportional to :

$$\left| E_1 e^{i\phi_1} + E_2 e^{i\phi_2} \right|^2 = E_1^2 + E_2^2 + 2E_1E_2\cos(\phi_1 - \phi_2)$$

So we can see that, by inducing phase shiffs in the two arms, the output light is amplitude modulated. With this configuration OHMACHI et al get 34% extinction ratio, with 19 Volts using 20 μm wide rigde guide and 4 mm long electrodes.

We have realized such a structure with monomode waveguides having a width equal to 2 μm the length of the arms being 5 mm. Opposed phase shifts are induced in each arm via electrodes spaced by 5 μm . A typical result is shown in figure 4 where we can see the sinusoidal response of the modulator when a linear varying voltage is applied to the electrodes.

In this case a 95% extinction ratio has been measured and the command voltage is 1.1 volt for $\lambda = 0{,}5145\mu$

Up to now, we have described relatively simple and classical circuits realized in an integrated form. But integrated optics permits the realization of more complex components that could even not be imagined in classical optics ; one is described in the next section : the directional coupler switch.

V - THE DIRECTIONAL COUPLER SWITCH.

Components capable of switching the light from one channel guide to another would be of great interest Several configurations have already been proposed to realize that (ZERNIKE, F, 1974 ; MARTIN W E, 1975 ; KURAZONO , S, 1972) but one of the most promising to day seems to be the directional coupler switch the principle and realization of which we shall now describe.

a) Principle of the directional coupler switch.

It is now well kuown that, if two lossless waveguides are coupled (fig 5) and if light is incident in one of them, energy exchange occurs and if the waveguides are resonant (ie if the two propagation constants $\beta 1$ and $\beta 2$ of the coupled modes are equal) 100% of the energy can be coupled from one guide to the other. The minimum length required to achieve this is called the coupling length L_o. If we are able to change the properties of the coupler we can choose the guide by which the light will leave the circuit. To do this it can be shown that the best way is to destroy the resonance between the guides by introducing assymetric changes in the propagation constants of the two modes. This is shown on fig 5 where the energy in the originally excited waveguide has been plotted versus the propagation length in two cases: $\Delta\beta = 0$ and $\Delta\beta = C\sqrt{12}$ where C is the coupling constant . We see from these curves that when $\Delta\beta \neq 0$ the coupling length is shortened and the maximum energy that we can exchange is less than 100%

Therefore by passing from the resonant to the non resonant case and by choosing the correct length of the coupler (L = (2 m + 1) Lo where m is an integer) light can be switch from one guide to the other. The resonance can be destroyed electrooptically by applying opposed electric fields to the two guides (in order to maximise $\Delta\beta$). This can be done by using either the three electrodes or COBRA configuration (PAPUCHON, M, 1975) shown in fig 6. With the latter only two electrodes are needed to create opposed electric fields in the two guides (by using vertical components of the field)

Light switching can readily be achieved in this way (PAPUCHON, M, 1975) but it is very difficult to get one hundred percent switching as we have to control perfectly the different parameters in order to achieve the correct length of the coupling region (L = (2 m + 1) Lo) To overcome this difficulty KOGELNIK and SCHMIDT (KOGELNIK, H 1976) proposed a configuration (fig 7) where the resonance is destroyed with opposite signs in each half of the coupling region , ie , if I and II are the two guides we get :

	first half	second half
guide I :	$-\Delta\beta\ (-\Delta n)$	$+\Delta\beta\ (+\Delta n)$
guide II :	$+\Delta\beta\ (+\Delta n)$	$-\Delta\beta\ (-\Delta n)$

In this way they showed that the two states of the coupler can be adjusted electrooptically in many cases. Having describe the principles of operation of the switch we shall now give some results that we have obtained during its realization.

b) Experiments.

To realize the switch we have used the processes already described in section I the electrodes being the COBRA ones with the Kogelnik configuration to get the two switching states electrically. A C cut plate of $LiNbO_3$ crystal is then used in this case and the r_{33} electrooptical coefficient is used via the vertical components of the field and TM polarized guided waves.

The geometrical parameters of the coupler used in the experiment are :

- width of the guides : 2 µm
- spacing : 3 µm
- length of the coupling, region : 3 mm

The measured switching voltages are :

- 5 volts to switch the light from the originally excited waveguide to the other
- 9 volts to maintain the light in the originally excited waveguide.KOGELNIK configuration has been used in the first case and the normal COBRA configuration in the second one.Crosstalks of 20 dB have been measured in the two states of the switch. When one switch is made we can try to integrate several ones to create more complex functions. In our case two COBRA have been realized in a serial configuration (fig 8) to obtained a 2 input to three output circuit. Crosstalks of 18 dB have been measured in this case.

VI - CONCLUSION.

In this paper, several electrooptical components for integrated optics have been described. The use of channel waveguides realized using Ti : diffusion in $LiNbO_3$ crystals shows that even if much work is required to optimize the different configurations high performances electrooptical components can readily be obtained in an optical integrated form.

REFERENCES.

HAMMER J.M and W. PHILLIPS (1974)
" Lowloss single mode optical waveguides and efficient high-speed modulators of LINbX Ta_1 $-xO_3$ on $LiTaO_3$ " Appl. Phys. Lett. Vol 24 , N° 11

KAMINOW I.P. and CARRUTHERS J.R (1973)
" Optical waveguiding layers in $LiNbO_3$ and $LiTaO_3$ " Appl. Phys. Lett. Vol 22 N° 7

KOGELNIK H. and SCHMIDT R.V (1976)
" Switched Directional Coupler with stepped reversal "
Digest of tech Papers Topical meeting in Integrated Optics Salt Lake City

KURANONO S. IWASAKA K. KUMAGAI N. (1972)
" A nex Optical modulator consisting of Coupled Optical waveguides "
Electron and Comm in Japan , Vol 55 C N° 1

MARTIN W E. (1973)
" A new waveguide Switch/modulator for integrated optics "
Appl. Phys. Lett . Vol 26 N° 10

MIYAZAWA S. (1973)
" Growth of $LiNbO_3$ single crystal film for integrated optics "
Appl. Phys. Lett Vol 23 N° 4

OHMACHI Y and NODA J (1975)
" Electrooptics light modulator with branched ridgewaveguide "
Appl. Phys. Lett .Vol 27 N° 15

PAPUCHON M. COMBEMALE Y. MATHIEU W. OSTROWSKY D B. REIBER L. ROY A M. SEJOURNE B and WERNER M (1975)
" Electrically switched optical directional coupler : COBRA "
Appl. Phys. Lett. Vol 27 N° 5

SCHMIDT R V.and KAMINOW I P. (1974)
" Metal diffused optical waveguides in $LiNbO_3$ "
Appl. Phys. Lett. Vol 28 N° 8

ZERNIKE F. (1974)
" Integrated Optics switch "
Digest of tech Papers Topical meeting on Integrated optics New Orleans

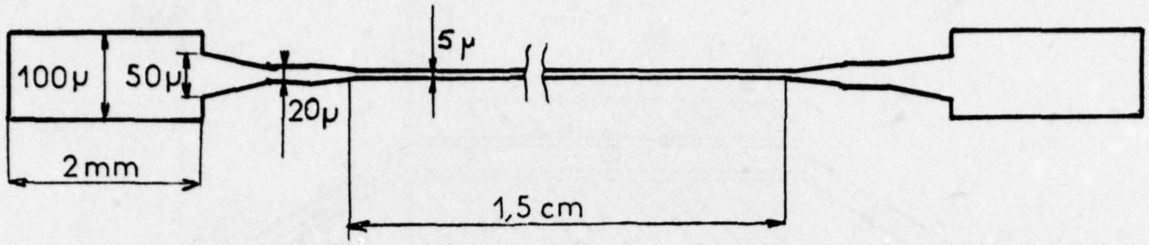

Fig.1- Phase modulator configuration

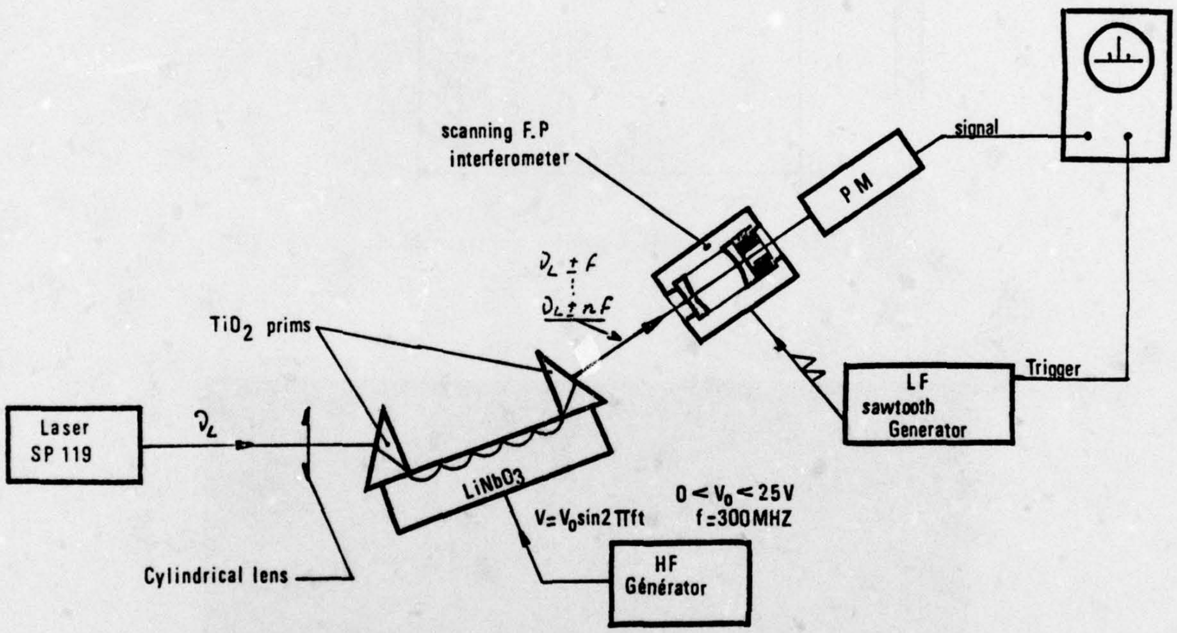

Fig.2- Set up used to test the phase modulator

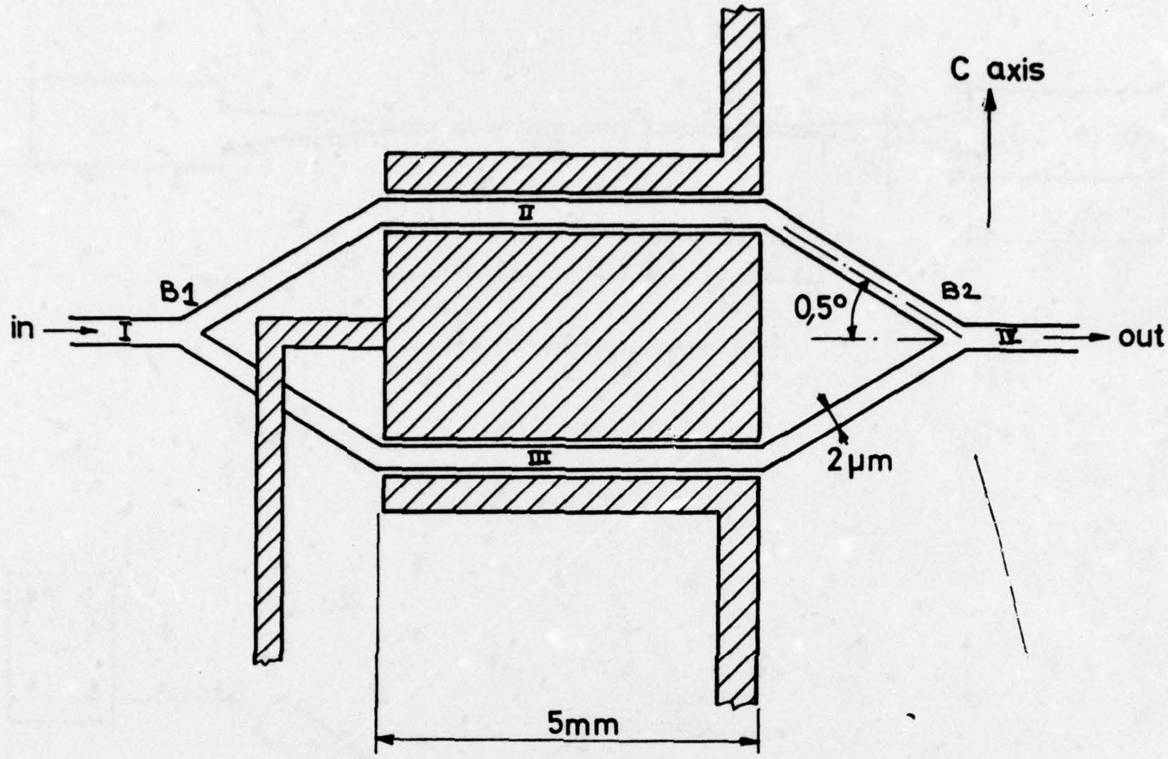

Fig.3- Amplitude modulator configuration

Fig.4- Sinusoidal response of the amplitude modulator when a linearly varging voltage is applied

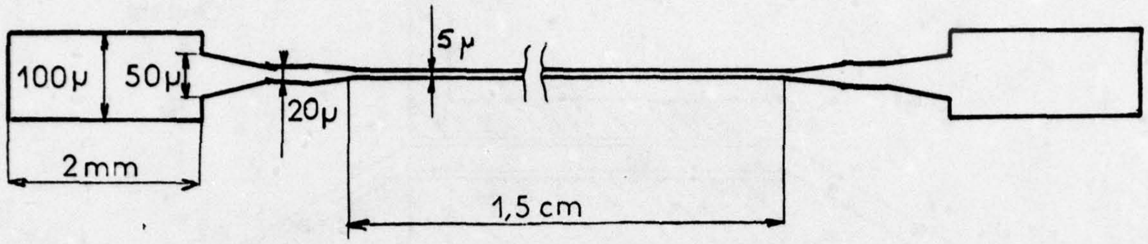

Fig.1- Phase modulator configuration

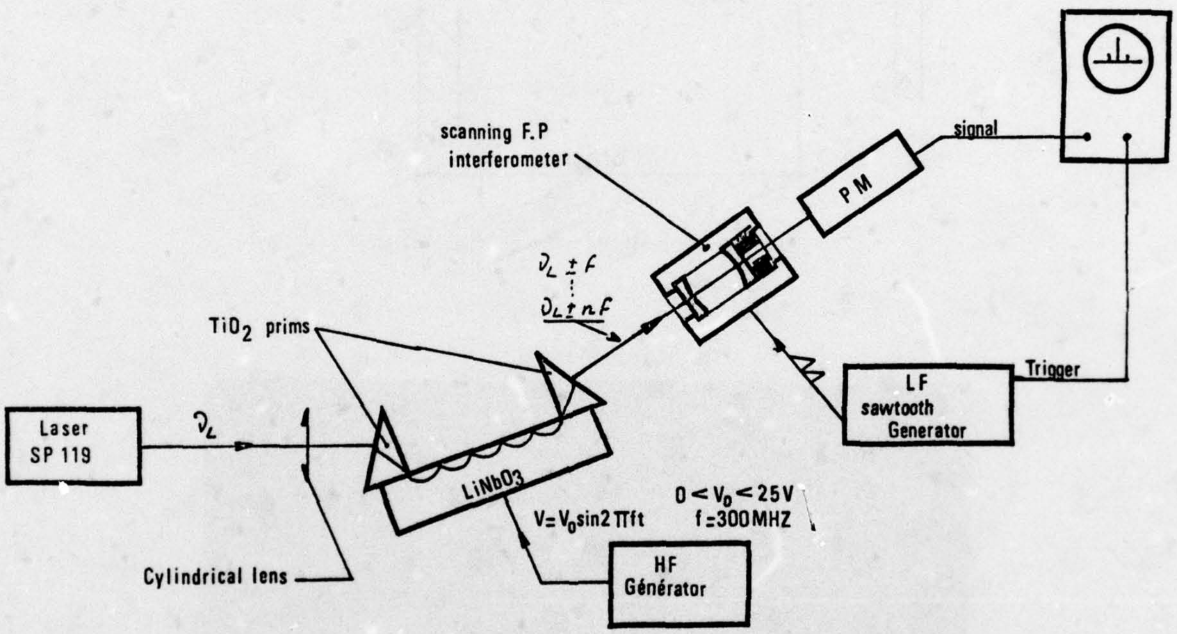

Fig.2- Set up used to test the phase modulator

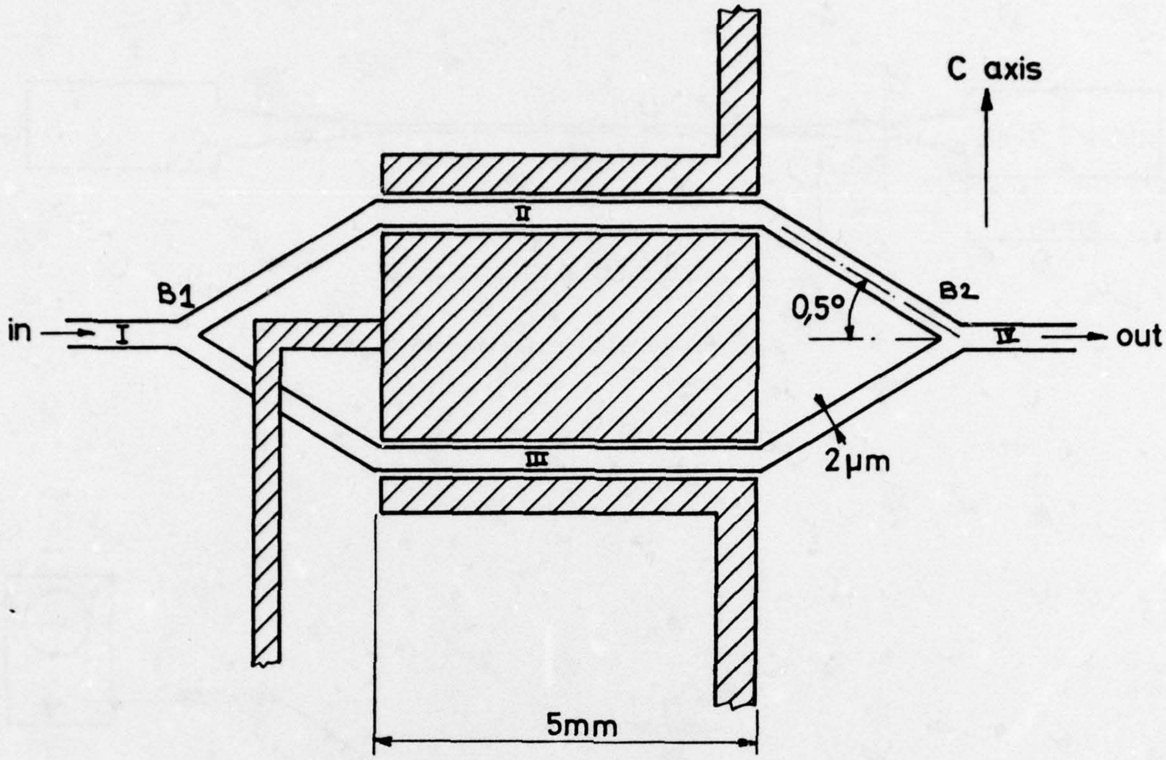

Fig.3- Amplitude modulator configuration

Fig.4- Sinusoidal response of the amplitude modulator when a linearly varging voltage is applied

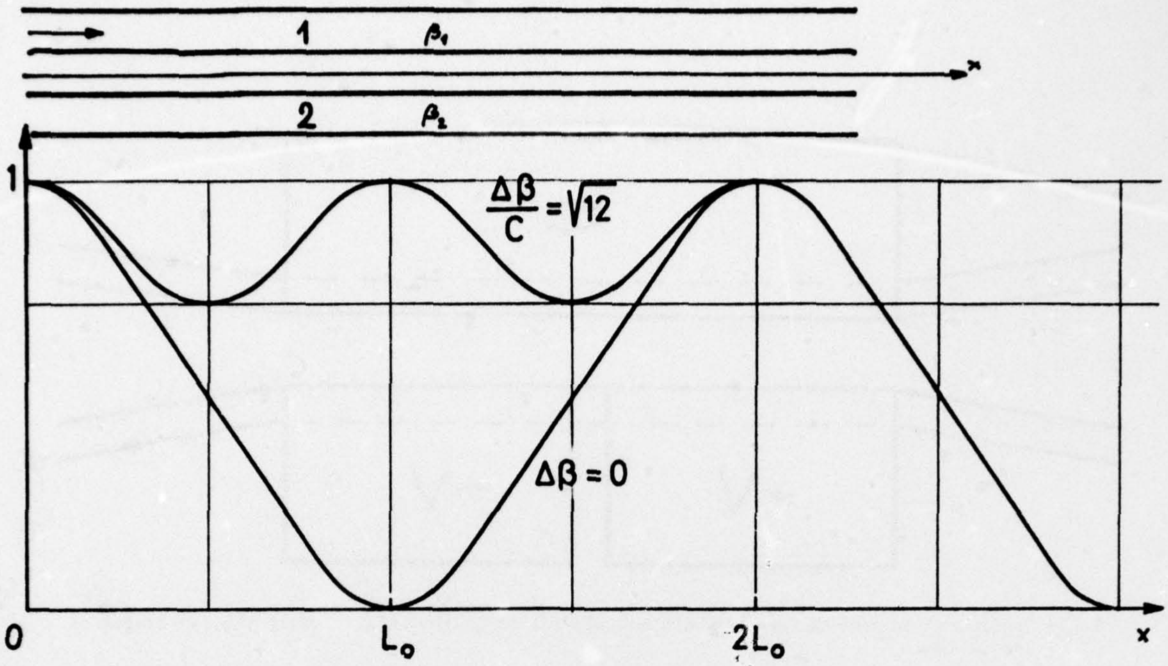

Fig.5- Energy in the originally excited waveguide of a directional coupler versus coupling section length, for $\frac{\Delta\beta}{C} = \sqrt{12}$ and $\Delta\beta = 0$ (C = coupling constant)

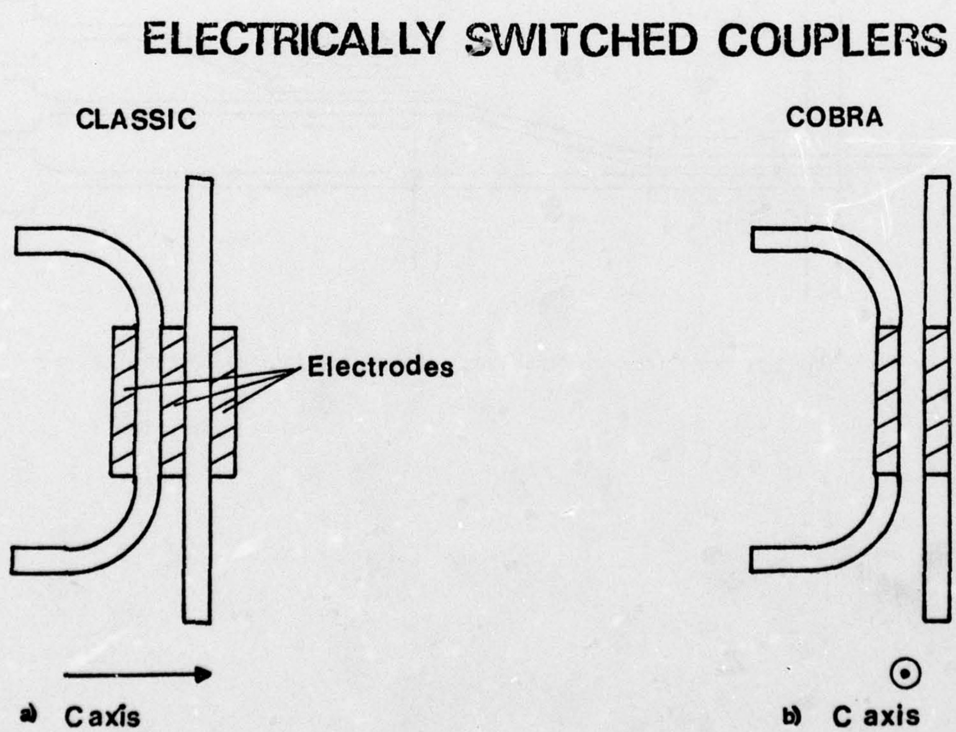

Fig.6- Two possible electrodes configuration to destroy the resonance in the directional coupler : a) three electrodes configuration
b) COBRA configuration

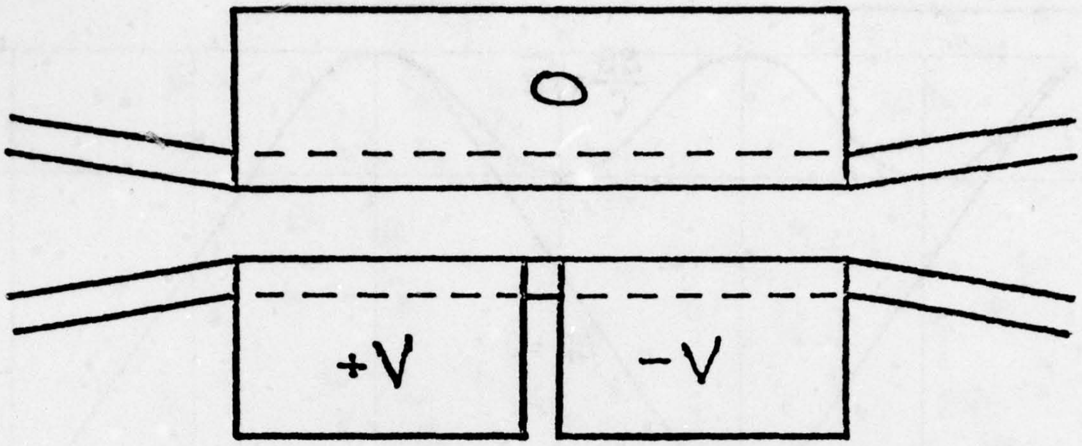

Fig.7- Configuration proposed by KOGELNIK and SCHMIDT to control electrically the two states of the switch

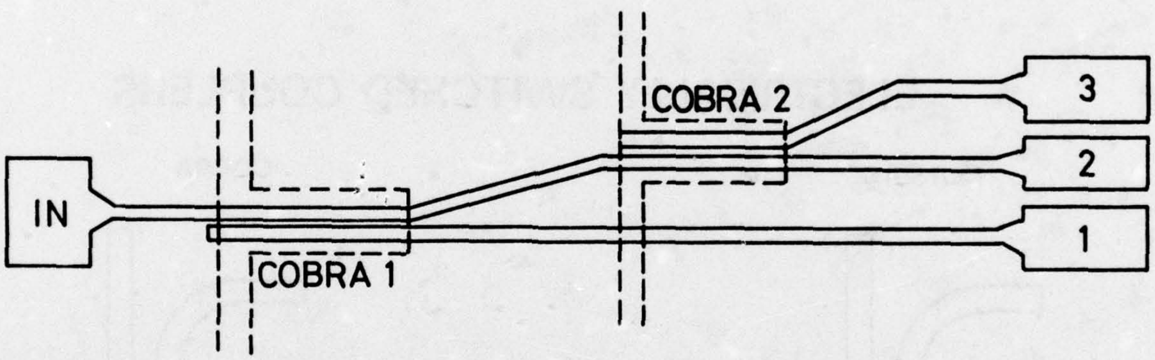

Fig.8- One (or two) input to three outputs circuit using two COBRA in series

GIGA-HERTZ MODULATORS USING BULK ACOUSTO-OPTIC INTERACTIONS IN THIN FILM WAVEGUIDES

Gerald B. Brandt, M. Gottlieb and R. W. Weinert
Westinghouse Research Laboratories
Pittsburgh, Pennsylvania 15235
U.S.A.

SUMMARY

When bulk acoustic waves are applied to an optical waveguide, several modulation effects are observed depending upon the type of wave (longitudinal or shear). Longitudinal sound waves frequency-shift the guided light, thus providing a means of modulating light in a wide variety of waveguide materials. Using thin-film mosaic acoustic transducer technology, we have demonstrated such modulation at frequencies in the gHz region. By segmenting the acoustic transducer electrodes, the same arrangement can be used for deflecting the light since, with this arrangement, the acoustic field sets up a time-varying grating whose spatial frequency is set by the segment spacing. Theoretical frequency limitations on these devices do not appear to be important until approximately 30 gHz is reached, thus they are potentially useful for extremely wide-band data links. Experiments at 1.5 gHz show 30% bandwidth of acoustic modulation using optical heterodyne detection.

1. INTRODUCTION

High data rate modulation of guided light is one of the basic future applications of integrated optical devices. In addition to the obvious use in optical communication links, high speed modulators or deflectors can be expected to contribute to other integrated optic signal processing functions such as heterodyne detection. Acoustooptic modulation possesses a considerable advantage over competing technologies such as electro-optic modulation, particularly when a hybrid fabrication approach is taken (Brandt et al., 1976). Since all optical materials exhibit an acousto-optic effect to some degree, waveguide materials are not limited to those which possess a particular property, possibly one which requires fabrication of a single crystal film. Thin film transducer technology has made possible the fabrication of reasonably high impedance, efficient transducers operating in excess of 5 gHz. At such high frequencies, all materials attenuate acoustic waves by an amount which increases with frequency. This attenuation sets a practical upper limit to the frequency at which bulk and surface acoustic wave modulators and signal processors can operate; typically this limit is on the order of a few hundred mHz. On the other hand, thin film bulk wave modulators are not limited by attenuation until frequencies or the order of tens of gHz are reached, by virtue of the fact that the acoustic path through the waveguide is short (on the order of micro-meters in length). In the following sections we will describe the nature of the interaction, the technology required to make thin film transducers, performance of experimental devices, and promising directions for future applications.

2. BULK ACOUSTIC INTERACTION WITH GUIDED LIGHT

2.1. Phase Modulation

Unlike the more common bulk or surface acoustic wave modulators in which the sound propagation path extends over the full optical aperture of the device, bulk guided waves require only that the sound traverse a relatively short region in the waveguide (Brandt et al., 1973). Figure 1 shows the layout of these devices. Light of wavelength, λ, is confined to a waveguide of thickness, t, deposited on a substrate such as glass. An acoustic transducer is bonded or deposited on the top surface of the guide after an optically insulating layer of low refractive index has been deposited on the guide to eliminate loss caused by the metal ground electrode on the transducer. This layer is not shown in Figure 1, nor is a similar layer between the waveguide and substrate which is required when a conducting substrate (such as Si) is used. For frequencies less than 5 gHz, the acoustic wavelength, Λ, is much longer than the waveguide thickness. Thus, at these frequencies, the sound wave simply modulates the refractive index of the waveguide periodically with the acoustic frequency. The amount of optical phase change, ϕ, caused by the acoustic wave is

$$\phi = 2\pi L\ \Delta\beta/\lambda \qquad 1)$$

where L is the length of the transducer under which the light propagates and $\Delta\beta$ is the change in the propagation constant of the guided light. $\Delta\beta$ is equal to $\partial\beta/\partial n \cdot \Delta n$ where β is the propagation constant in the particular mode of operation. Since the refractive index changes are small, $\partial\beta/\partial n$ will be a constant, b, for any given waveguide and mode. Thus $\Delta\beta$ is proportional to Δn which in turn is a function of the waveguide refractive index, n, the photo-elastic constant, p, and the strain amplitude, e, through the relation

$$\Delta\beta \propto \Delta n = -\ b\ n^3\ p\ e/2\ . \qquad 2)$$

Equations 1) and 2) can be used to calculate the peak value of the phase excursion induced by an acoustic wave on an optical wave contained in a waveguide mode. This phase modulation can be calculated by considering (Christensen et al., 1975) a guided wave with amplitude A of the form

$$A = A_o \exp i\,(\beta x - \omega_\ell t) \qquad 3)$$

where A_o is the amplitude and ω_ℓ is the frequency of the light beam. Acoustic modulation with a bulk wave simply adds a phase term to equation 3) which varies in time with the acoustic frequency ω_a. Now the modulated light is of the form A'

$$A' = A_o \exp i\,(\beta x + \phi \cos(\omega_a t) - \omega_\ell t) \quad . \qquad 4)$$

It is well known (ITT, 1968) that a signal of this form can be described as a carrier at the center frequency ω_ℓ plus an infinite number of sidebands at frequencies, for the m'th sideband, equal to $\omega_\ell \pm m\omega_a$. The amplitude, A_m, of each of these sidebands is given by

$$A_m = A_o\,(-1)^{m-1}\,J_m\,(\phi),\ m < 0;\ A_m = A_o\,J_m(\phi),\ m \geq 0 \qquad 5)$$

where J_m is the Bessel function of the first kind of order m. For small phase excursions corresponding to low depth of modulation, only the first sidebands are important. In this limit, equation 4) can be simplified to the form of a carrier plus two sidebands, namely

$$A' = A_o \exp(i\beta x)[\cos(\omega_\ell t) - \frac{\phi}{2}\cos(\omega_\ell - \omega_a)t + \frac{\phi}{2}\cos\,(\omega_\ell + \omega_a)t] \qquad 6)$$

namely a propagating wave which is time modulated at the carrier frequency ω_ℓ, plus two sidebands at frequencies ω_a from the carrier. Each of the sideband amplitudes is proportional to $\phi/2$ thus ϕ takes on the significance of the modulation index in amplitude modulation. Each sideband, for the small modulation case, has a power relative to that of the carrier which is proportional to $\phi^2/4$ and the light in the downshifted sideband has a phase shift of π relative to that in the upper sideband.

At large values of ϕ (large L or high acoustic fields), many sidebands are present and equation 5) must be used to describe the modulation. In addition, at high fields, the interaction exhibits a geometrical dependence (Brandt et al., 1973, Christensen, 1975). Various portions of the guided light beam experience differing degrees of modulation; this leads to amplitude modulation in the output-coupled spot which is a function of position from the spot center. This effect is observed only at high acoustic fields and its explanation must include the effects of geometrical spreading of the guided light. It is not a particularly useful effect for modulation because of its appearance only at high acoustic powers.

2.2. Deflection with Segmented Transducers

Up to this point, our analysis has assumed that the sound field is uniform in its intensity across the optical aperture. An alternative mode of operation achieves deflection by segmenting the electrode structure as shown in Figure 2. When the top electrode of the transducer consists of a fine bar pattern with spacing, s, the piezoelectric film forming the transducer is excited only in the area under the electrode structure. Thus the incident light beam sees a spatially varying sound field which acts as a time-varying grating of spatial frequency 1/s. This mode is very similar to the Bragg electro-optic modulator (Hammer et al., 1973). When sound is applied to the waveguide with a grating structure, the incident guided wave will be diffracted in the plane of the waveguide into various diffraction orders at angles θ_m where

$$\sin \theta_m = m\lambda/s \quad . \qquad 7)$$

If the transducer is long with respect to the electrode spacing, i.e., if

$$2\pi\lambda L/s^2 >> 1 \qquad 8)$$

the operation is in the Bragg diffraction regime in which most of the light is diffracted into the m'th order when the guided light is incident at θ_m from equation 7). For short L, the diffraction is the same as that from a thin phase grating and analysis is identical to the phase modulation case treated above. A spatial variation of phase replaces the time variation in equation 4), the relative amplitudes of the spatially separated diffraction orders are given by equation 5), and again, the value of ϕ corresponds to a modulation index which gives a quadratic dependence of power in the first orders for small ϕ. If L is large, equation 5) represents the ratio of the amplitude in the m'th order relative to that in the zero order. Experimentally, we have demonstrated this type of deflection in sputtered 7059 glass waveguides using segmented transducers with 25 micro-meter spacing (Gottlieb, 1975).

2.3. Mode Conversion and Anisotropic Diffraction.

When shear acoustic waves are applied to a guided wave, conversion between TE and TM modes is observed (Brandt et al., 1973, Shah, 1973). This effect results from the stress-induced birefringence caused by the shear wave and is consistent with the more familiar bulk case in which diffracted orders take on the orthogonal polarization to that of the incident light. Analysis of diffraction by an acoustic shear wave in birefringent media (Dixon, 1967) leads to the anisotropic Bragg relations between angles of incidence and diffraction which, in contrast to the isotropic case, are different from one another. A waveguide, even if it is fabricated of an isotropic material, is intrinsically birefringent since the TE and TM modes have different propagation constants.

We have extended Dixon's formulation (Gottlieb, 1976) to include the coupling of two orthogonal waveguide modes by the grating induced by a spatially periodic shear acoustic wave. Conservation of momentum dictates a relationship between the incident and diffracted propagation vectors, $\vec{\beta}$, and $\vec{\beta}'$, and the momentum transfer characteristic of the grating, $|\vec{K}| = 2\pi/s$ as

$$\vec{\beta}' = \vec{\beta} + \vec{K} \quad . \tag{9)}$$

Note that $\vec{K}$ is not variable with acoustic frequency but is fixed by the spacing of the transducer elements. For diffraction in a waveguide, the anisotropic Bragg relations are

$$\sin\theta = \frac{K}{2\beta}\left|1 + \frac{\beta^2-\beta'^2}{K^2}\right| \tag{10)}$$

$$\sin\theta' = \frac{K}{2\beta'}\left|1 - \frac{\beta^2-\beta'^2}{K^2}\right| \tag{11)}$$

where θ and θ' are the angles of incidence and diffraction measured from the normal to the grating. A plot of equations 10) and 11) for a typical waveguide (Corning 7059 glass sputtered on a microscope slide substrate) is shown in Figure 3. For large K, the first term in brackets in equations 10) and 11) dominates and diffraction is the same as the isotropic Bragg case and $\theta = \theta'$. For small K (large spacing, s) the second term predominates and there is a minimum value of K for which $\theta = -\theta' = \pi/2$. At this point, the three vectors in equation 9) are collinear and the relationship reduces to a simple scalar one

$$s = 2\pi/(\beta'-\beta) \quad . \tag{12)}$$

At this angle there will be no deflection of the light beam and the effect of the grating is to produce mode conversion between TE and TM modes of the guided light. Operation under these conditions was demonstrated by Shah (Shah, 1973) who observed that there is an optimum spacing between transducer segments for efficient TE-TM mode conversion.

Another interesting point occurs at $\theta' = 0$ where

$$K = \sqrt{\beta^2-\beta'^2} \quad . \tag{13)}$$

At this point there is a minimum in θ and its value is given by

$$\sin\theta = K/\beta \quad . \tag{14)}$$

In some applications it may be useful to operate devices near this minimum value in order to take advantage of the insensitivity of angle to change in grating spacing.

3. TRANSDUCER DESIGN FOR HIGH FREQUENCY PHASE MODULATORS

At giga-Hertz frequencies, transducer design becomes an extremely important part of any acousto-optic or acoustic device. The main problem at these frequencies is that for conventional transducer size and shape, the transducer input impedance at the half-wave resonant frequency is very low ($Z = 0.1 - i1.0$ ohms for a transducer of lateral area = 1 mm^2). Since there is electrical loss in the contacts to the transducer, in the metal films used as electrodes, and in the matching network, if used, a fairly low power conversion from electrical to acoustical energy can be expected from such a low impedance device. In order to increase the input impedance of the transducer at high frequencies without reducing the bandwidth, we use a mosaic transducer design (Weinert et al., 1972).

The geometry of the mosaic transducer is shown schematically in Figure 4. It can be shown (Weinert, 1977) that the input impedance of a transducer goes up as the lateral area goes down. When small lateral area transducers are put into an array as shown in Figure 4, the diffraction spread of the zero order acoustic beam in the far field is that due to the overall size of the transducer and not that of the individual element size. In the near field, the acoustic beam is an array of the small individual beams. By adjusting the element size, number, and interconnection pattern, the input impedance of a mosaic transducer can be tailored to approximately match conventional RF sources.

For our experiments we used a 16 element, series connected mosaic transducer. The piezoelectric film was RF sputtered ZnO approximately 1.25 micro-meters thick. When this structure was fabricated on a glass waveguide, the peak response was at 1.5 gHz and, at this frequency, the calculated value of transducer input impedance is $Z = 20 - i\,40$ Ohms. Also, the calculated resistance of the metal films is 9 Ohms and this resistance is in series with the transducer impedance. A 1.6 micro-meter thick SiO_2 film isolated the bottom Al metal electrode from the guiding layer. Because of acoustic reflections at the SiO_2 boundaries, this film can have an influence on impedance. However at 1.5 gHz, this thickness of SiO_2 is acoustically transparent because it is one-half of an acoustic wave thick. Figure 5 is a photograph of the completed transducer on a sputtered glass waveguide.

4. PERFORMANCE OF DEVICES

4.1. Efficiency and Power Limits

For both acoustic phase modulators and deflectors, the amount of light in either the m'th frequency sideband or the m'th diffraction order is proportional to the square of the Bessel function of order m and argument ϕ, the optical phase excursion induced by the sound wave. In order to define modulation efficiency exactly, it is necessary to specify the mode of operation of the modulator. For example, if the application requires modulation of the zero order, 100% of the light is removed from that order when ϕ takes on a value of 2.4 (that argument for which $J_0 = 0$). On the other hand, if the requirement is to maximize the amount of light in the first order or sideband, then the modulator should operate so that $\phi = 1.8$ where J_1 has its first maximum. At $\phi = 1.8$, 11% of the energy remains in the zero order, 68% of the light appears in the two first orders, and the remaining 21% is in the second and higher orders (sidebands). By comparison, an electro-optic modulator has maximum contrast when the phase shift is equal to a half wave, i.e., $\phi = \pi$. In our analysis we will denote the maximum value of ϕ as r, recognizing that r will take on different numerical values, depending upon the application.

When the bandwidth of the acoustic transducer is not a limitation (in practice bandwidths of 100% of the operating frequency can be obtained with mosaic designs), the transit time of the sound wave across the waveguide thickness, T, will set the bandwidth limit. This frequency, f_{max} is just equal to v/T where v is the acoustic velocity. For a waveguide medium with an acousto-optic figure of merit M_2, the power needed to produce a given phase excursion $\phi = r$ is well known (Damon et al., 1970). Taking this expression and dividing by f_{max}, we get the amount of power per unit bandwidth for an acousto-optic modulator as

$$P_r/f_{max} = \frac{r\ w\ \lambda^2\ T\ b}{4\ L\ k^2\ v\ M_2} \qquad 15)$$

where w is the transducer width and k^2 is the electro-acoustic conversion coefficient (typically $k^2 = 0.1$). Equation 15) shows that once the dimensions of the transducer have been chosen and once the bandwidth has been set by the waveguide thickness, improvements in performance can be made only by using waveguide materials with large M_2. Table I shows the influence of M_2 on modulation power requirements.

TABLE I: POWER REQUIRED FOR PHASE MODULATOR

Material	M_2 (s^3/gm)	P_r/f_{max} (mW/MHz)
Fused quartz	1.56×10^{-18}	19.4
Niobium Oxide	16×10^{-18}	1.9
TeO_2	35×10^{-18}	0.86
As_2S_3	433×10^{-18}	0.16
Tl_3AsS_4	800×10^{-18}	0.10

These efficiencies are estimates for a 1 cm long transducer with a value of r = 1.8. The last material shown in the table, Tl_3AsS_4 (Roland et al., 1972) is an exceptionally good acousto-optic material and we have prepared thin films of it. Unfortunately, they are not yet of waveguide quality; waveguides of the other materials have been prepared successfully.

Figure of merit plays an important role in another limitation of acousto-optic modulators, namely the maximum achievable modulation set by thermal damage to the transducer. A power density greater than approximately 10 to 20 W/cm² on a transducer will damage it due to thermal and electrical breakdown effects. This power density, in turn, sets a limit to the maximum practical value of ϕ which can be generated, which in turn, sets a maximum to the modulation depth. Equations 1) and 2) can be used to predict the maximum phase shift when the transducer is operated at a maximum safe power loading. Phase shift is related to the acoustic power density P_a (Damon et al., 1970) by

$$\phi = 2\pi L\Delta n/\lambda = -\frac{r\ b\ L\ n^3\ p}{\lambda}\left(\frac{2\ P_a}{\rho\ v^3}\right)^{1/2} \qquad 16)$$

which can also be expressed in terms of M_2 and electrical power input P_e as

$$\phi = \frac{\pi L}{\lambda}\,(2\ M_2\ P_e\ k^2)^{1/2} \quad . \qquad 17)$$

Taking values of M_2 from Table I and assuming maximum electrical power loadings of 10 W/cm² and 1 W/cm² we show in Table II the maximum phase shift achievable and the maximum intensity in the first diffraction order or sideband.

TABLE II: MAXIMUM PHASE SHIFT AND 1st ORDER INTENSITY

	$P_e = 10\ W/cm^2$		$P_e = 1\ W/cm^2$	
Material	ϕ_{max}	$J_1^2(\phi_{max})$	ϕ_{max}	$J_1^2(\phi_{max})$
Fused quartz	0.48	0.038	0.16	0.006
Nb_2O_5	1.55	0.316	0.49	0.06
TeO_2	2.29	0.338	0.72	0.11
As_2S_3	8.05	"	2.54	0.338
Tl_3AsS_4	10.95	"	3.46	"

From this table it is clear that quartz and similar glasses are not very good material choices since only 3.8% of the light can be diffracted or frequency shifted even at 10 W/cm^2. On the other hand, materials such as As_2S_3 and Tl_3AsS_4 provide more than enough phase shift to reach the first maximum of J_1 even at 1 W/cm^2. Thus, large M_2 materials for waveguides are important both for wide bandwidth designs and highly efficient designs.

4.2. Heterodyne Detection

Amplitude modulated signals produced in the diffraction mode of operation can be detected directly, however phase modulated signals require that a reference beam be present to mix with the signal in order to detect the modulation. In the laboratory, the reference signal is readily supplied by setting the modulator-waveguide assembly in one leg of a Mach-Zehnder interferometer. With prism coupling into and out of the waveguide, were able to provide satisfactory matching to the relatively small diameter wavefront with non-precision optics to achieve satisfactory heterodyne detection over the detector area. For a detector we used a PIN diode which was connected integrally with an 18 dB gain wideband amplifier. The frequency range of this combination extended from 4 to 600 MHz, thus the 1.5 gHz modulated signal could not be detected directly with this system. As a light source we used a Spectra Physics model 120 He-Ne laser which operates with several longitudinal cavity modes spaced 280 MHz apart. As a result, heterodyne detection could be performed with no frequency shifter in the reference arm; laser cavity modes produced frequency offsets of 280, 560, 840, and 1120 MHz. Using the various combinations of these we were able to verify the operation of the 1.5 gHz modulator over most of its designed 30% bandwidth from approximately 1.2 to 1.7 gHz.

5. CONCLUSION

We have fabricated mosaic bulk acoustic transducers on optical waveguides and have demonstrated phase modulation of guided light at frequencies as high as 1.7 gHz. Using these techniques it appears possible to reach frequencies in excess of 10 gHz before fundamental limitations are met. At higher frequencies, providing that transducer fabrication can be accomplished, transit time across the waveguide will limit bandwidth. Acoustic attenuation does not become a limiting factor until the 30 to 50 gHz range of frequencies. Heterodyne detection is necessary at gHz frequencies because readily available solid state detectors are limited in frequency response to 1 gHz or less. Integrated optical techniques, particularly hybrid fabrication on various electronic substrates such as silicon or GaAs should offer promising solutions to realizing heterodyne detection on a single device. High frequency modulators and detectors will find wide applications in future large bandwidth communications and signal processing systems for aerospace applications.

6. REFERENCES

BRANDT, G.B., Gottlieb, M., & Conroy, J.J., 1973, "Bulk Acoustic Wave Interaction with Guided Optical Waves", Appl. Phys. Lett. 23, p. 53.

BRANDT, G.B., Gottlieb, M., and Marx, G., 1976, "Integration of Deflection and Detection of Guided Light on Silicon Substrates", Technical Digest, Optical Society of America Conference on Integrated Optics January 1976, paper TuA6.

CHRISTENSEN, C.P., Steier, W.H., & Basu, R., 1975, "Guided Wave Acoustooptic F.M. Modulator", I.E.E.E. J. Quant. Elect. QE11, p. 849.

DAMON, R.W., Maloney, W.T., & McMahon, D.H., 1970, "Interaction of Light with Ultrasound" in "Physical Acoustics Vol. VII", W.P. Mason and R.N. Thurston, eds., Academic Press, N.Y., pp. 273-366.

DIXON, R.W., 1967, "Acoustic Diffraction of Light in Anisotropic Media", I.E.E.E. J. Quant. Elect. QE3, p. 85.

GOTTLIEB, M. & Brandt, G.B., 1975, "Integrated Optical Deflector Using Bulk Acoustic Waves", J. Opt. Soc. Am. 65, p. 1222.

GOTTLIEB, M. & Brandt, G.B., 1976, "Anisotropic Diffraction of Guided Light by Bulk Acoustic Waves", Proc. I.E.E.E. Ultrasonics Symposium Sept. 1976, paper BB7.

HAMMER, J.M., Channin, D.J., & Duffy, M.T., 1973, "Fast Electro-Optic Waveguide Deflector Modulator", Appl. Phys. Lett. 23, 176.

I.T.T., 1968, "Reference Data for Radio Engineers", 5th Ed., p. 21-7.

ROLAND, G.W., Gottlieb, M., & Feichtner, J.D., 1972, "Optoacoustic Properties of Thallium Arsenic Sulphide, Tl_3AsS_4", Appl. Phys. Lett. 21, p. 52.

SHAH, M.L., 1973, "Fast Acousto-optic Waveguide Modulators", Appl. Phys. Lett. 23, p. 75.

WEINERT, R.W., & DeKlerk, J., 1972, "A Thin Film Mosaic Transducer for Bulk Waves", I.E.E.E. Trans. Sonics & Ultrasonics SU19, p. 354.

WEINERT, R.W., 1977, "Very High Frequency Piezoelectric Transducers", I.E.E.E. Trans. Sonics & Ultrasonics SU24, to be published.

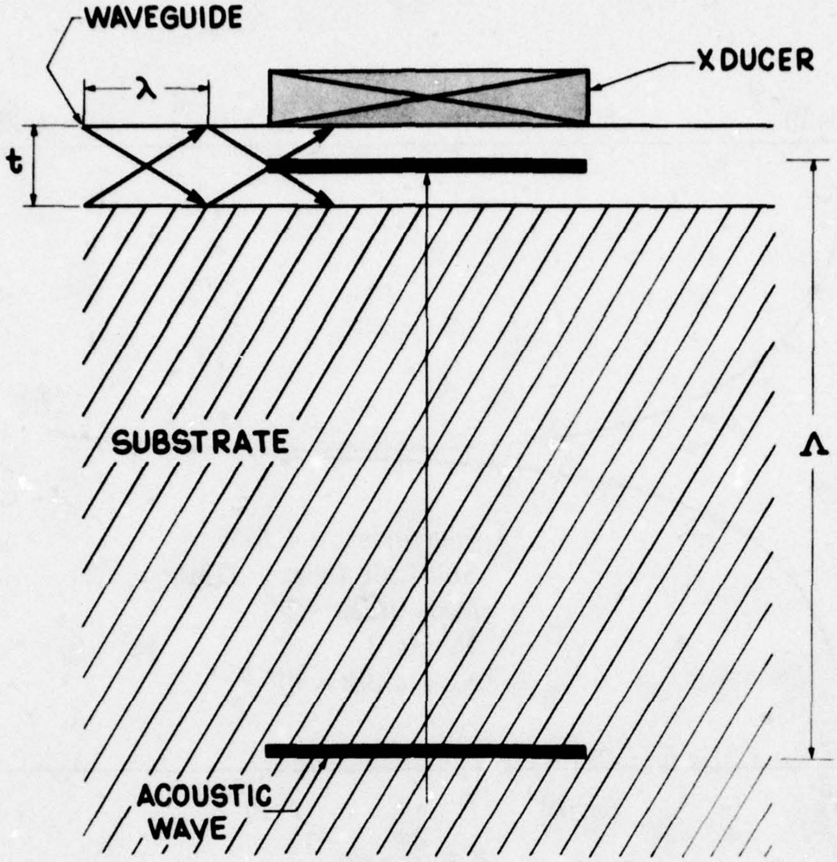

Figure 1. Geometry of the bulk acousto-optic modulation of guided light. Light guided in the waveguide of thickness T is modulated by an acoustic wave imposed by the transducer bonded to the top of the waveguide.

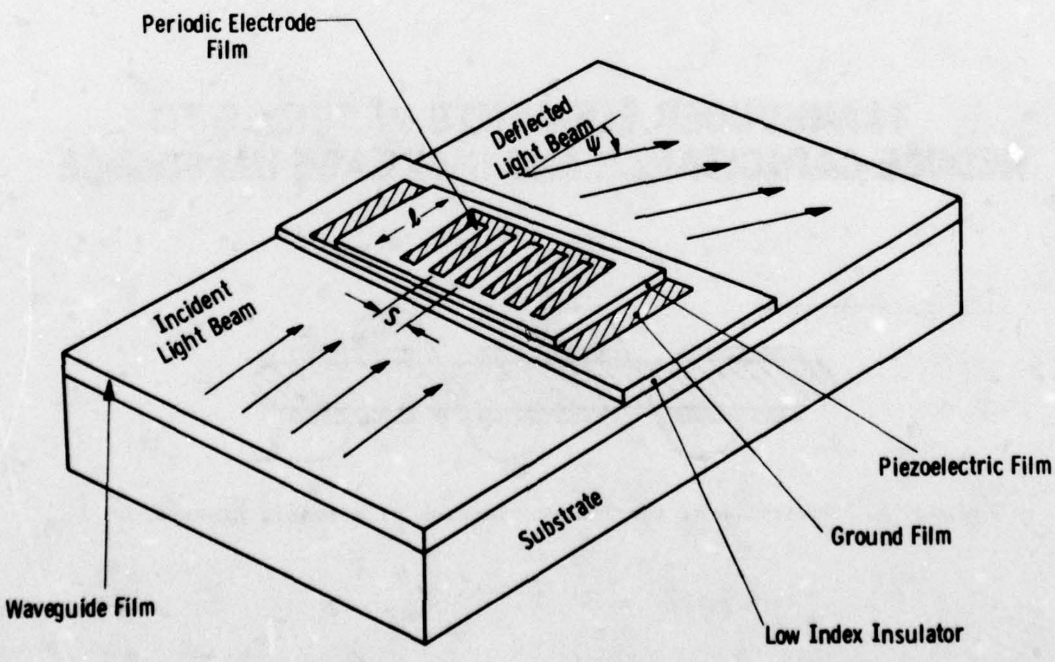

Figure 2. Segmented electrode geometry for deflecting the beam in the plane of the waveguide. The periodic structure sets up a grating sound field which deflects the incident guided light.

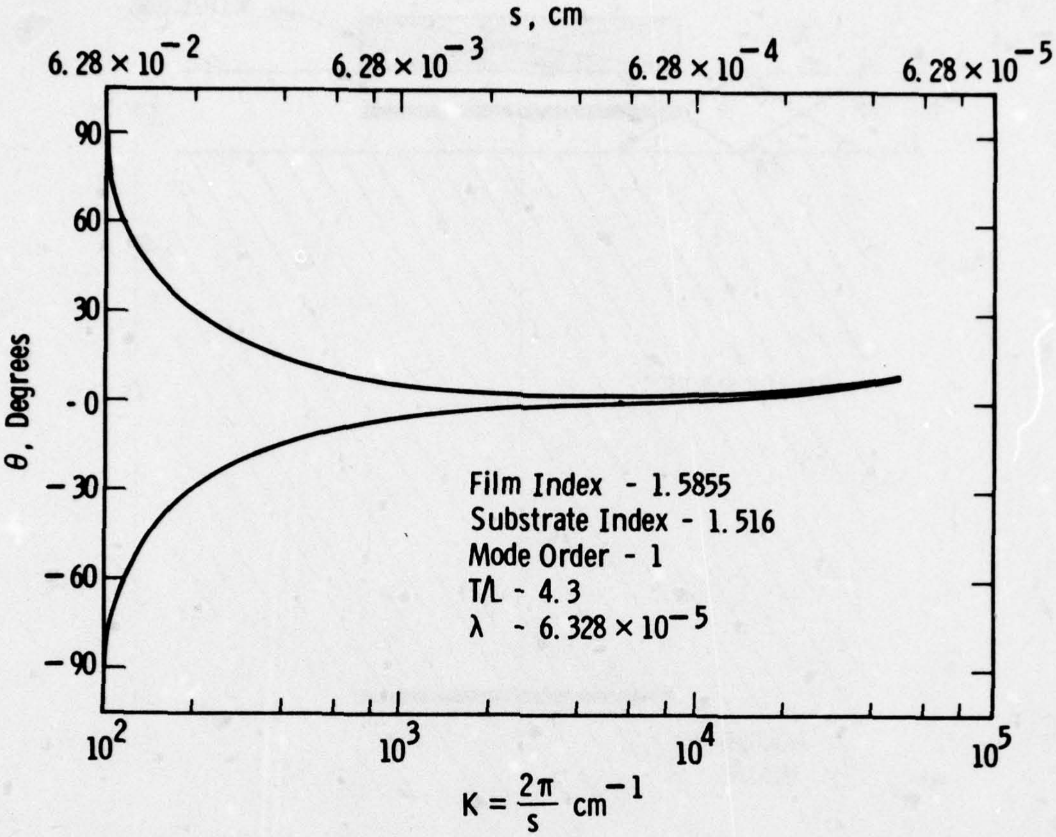

Figure 3. Anisotropic Bragg diffraction by an acoustic grating. Upper curve represents incident angle and lower curve the diffracted angle for the deflected propagation constant larger than the incident.

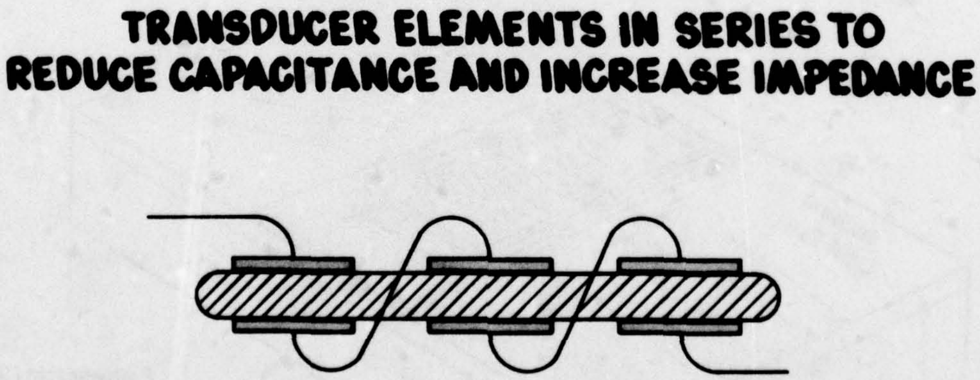

Figure 4. Schematic of the interconnection of a mosaic transducer.

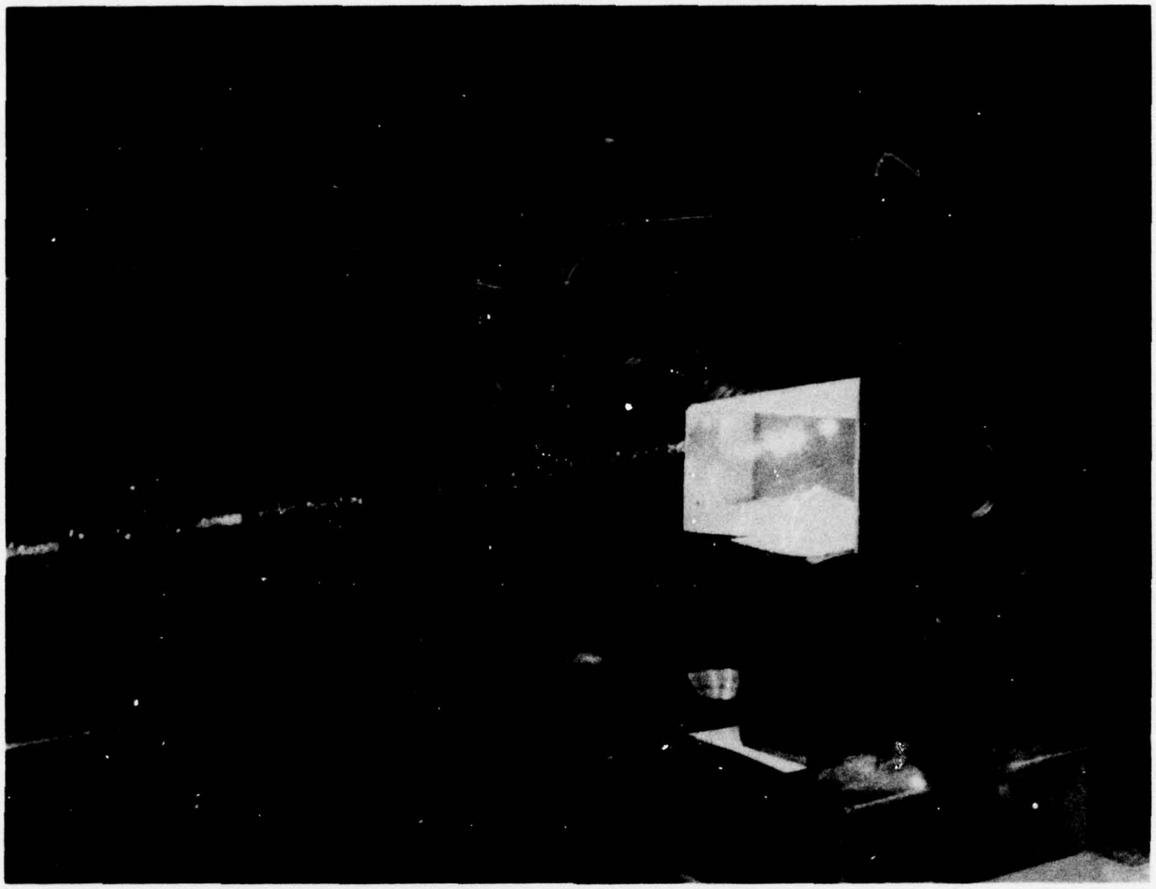

Figure 5. Photograph of a 16 element mosaic transducer on a sputtered glass waveguide.

DISTRIBUTED-BRAGG-REFLECTOR INJECTION LASERS FOR INTEGRATED OPTICS

Shyh Wang
Department of Electrical Engineering and Computer Sciences
and the Electronics Research Laboratory
University of California, Berkeley, California 94720

SUMMARY

We discuss the underlying principles and describe the fabrication and operation of the DBR injection laser, a novel semiconductor laser which shows great promise as a source for integrated optics. The laser uses two corrugated waveguides at the ends as reflectors. First, the effect of periodic thickness variation on wave propagation is reviewed and the dispersion relation for the eigen Bloch wave is presented. This presentation is followed by a derivation of the reflection and transmission coefficients of the periodic-waveguide (or Bragg) reflector. Then the fabrication procedures and the operation of a DBR GaAs-$Ga_{1-x}A\ell_xAs$ laser are described. The performance of the laser is analyzed and ways to optimize the design of the laser for single mode operation with appreciable output power are discussed. Finally, possible schemes for future integration with other optical components and for direct coupling into optical fibers are proposed. Possible ways to fine-tune and to stabilize the laser wavelength are also suggested.

1. INTRODUCTION

The advent of low-loss optical fibers (Maurer, R. D., 1973) has brightened prospects of integrated optical communication systems and given impetus to research in integrated optics (Miller, S. E., 1969). Incoherent light sources such as LED's, light emitting diodes (Bergh, A. A. et al., 1972), are limited in their uses to systems of low information-carrying capacity principally for two reasons. Firstly, LED's are broad-band sources. Light waves of different wavelengths travel in an optical fiber with different velocities because of the variation of index of refraction with wavelength (material dispersion). Secondly, multimode transmission is necessary because the amount of power which can be coupled from a LED into a single-mode fiber is very small. Different modes propagate with different velocities (modal dispersion) even if they are at the same wavelength. Both material dispersion and modal dispersion distort the shape of an optical signal and thus limit the information rate of an optical communication system. Coherent light sources are needed if we are to have an optical signal of a narrow bandwidth to be propagated in a single-mode optical fiber.

There are three important considerations in the selection of a laser for use as the source in fiber and integrated optics: low-loss transmission of the laser beam in optical fibers, suitability of the laser structure for future integration with other optical components and possibility of single-mode, narrow-band operation. Semiconductor double-heterostructure (DH) injection lasers with periodic waveguide structures at the two ends serving as mirrors, known as the distributed Bragg-reflector or DBR laser (Wang, S., 1974), appear most promising in satisfying all the three requirements. A semiconductor DH laser (Hayashi, I., et al., 1971) is one in which the active region is sandwiched between two mixed semiconductors of a different composition so as to have a larger energy gap and a smaller index of refraction in the two outer regions than in the middle region. Therefore, a waveguide is built into the laser structure. Furthermore, the emission from the laser can be made to fall in one of the low-loss regions of optical fibers (Miller, S. E., 1973) by properly choosing the composition of a mixed compound semiconductor such as $Ga_{1-x}A\ell_xAs$.

The waveguiding structure in a DH injection laser, if extended beyond the laser, can be used as a common waveguide upon which other optical devices can be built. To make such a laser suitable for integrated-optics applications, periodic waveguides are incorporated into the structure. The periodic waveguides in a semiconductor DH DBR injection laser will serve the same function as mirrors in conventional lasers, but can be fabricated on a continuous waveguiding structure without disrupting the structure. The name "Bragg reflector" is used because strong reflections from the periodic waveguides take place only when the Bragg condition is satisfied. Such a reflector can have a bandwidth sufficiently narrow for the laser to operate at a single wavelength. In this paper, we first review the underlying principles of the DBR laser, then describe the fabrication and operation of a GaAs-$Ga_{1-x}A\ell_xAs$ DBR injection laser, and finally discuss future directions for further development of the DBR injection laser as a source for use in integrated optics.

2. WAVE PROPAGATION IN PERIODIC WAVEGUIDES

The pioneering work of Kogelnik and Shank (Kogelnik, H. and Shank, C. V., 1971 and 1973) on distributed feedback (DFB) laser has stimulated a great deal of interest in the use of periodic waveguides in different laser structures using various laser-active materials. Among different laser structures, the multi-layer structure using periodic thickness variation as first proposed by Wang (Wang, S., 1972 and 1973) is most suitable for integrated optics because the scheme can be easily implemented in the conventional semiconductor DH injection laser. In this section, we review the essential features of wave propagation in a periodic waveguide and formulate the necessary theoretical background for an analysis of the DBR laser.

First, we consider wave propagation in a uniform planar waveguide which consists of a waveguiding film of thickness W and with refractive index n_f sandwiched between a substrate with index n_s and a superstrate with index n_d. The proper mode of the planar dielectric waveguide is governed by the mode equation (Tien, P. K., et al., 1970):

$$k_x W - \tan^{-1}(e_s p_s/k_x) - \tan^{-1}(e_d p_d/k_x) = m_t \pi \tag{1}$$

where k_x is the transverse wave number, $p_{s,d}$ is the decay constant of the evanescent wave in the substrate and superstrate, respectively, $e_{s,d}$ is a polarization factor with $e_{s,d}=1$ for TE waves and $e_{s,d} = (n_f/n_{s,d})^2$ for TM waves, and m_t is an integer representing the transverse mode number. From Eq. (1), we can solve k_x as a function of W. For each mode, we have a characteristic value for k_x and corresponding values for

k_z and $p_{s,d}$. Wave propagation in the uniform waveguide is described by the wave equation

$$d^2E/dz^2 - (g-i\beta)^2E = 0 \tag{2}$$

where $\beta = k_z$ is the longitudinal wave number and g is a gain constant to account for either amplification (g=+) or absorption (g=-) of a wave in the guide. Each mode propagates with a distinct β. Because all the modes are orthogonal, there is no coupling between the modes in a perfectly uniform dielectric guide.

Next, we consider wave propagation in a waveguide with periodic thickness variation (Fig. 1). A change in thickness from W to W+t produces a corresponding change in transverse wave number from k_x to $k_x+\Delta k_x$. Expanding Eq. (1), we obtain

$$\Delta k_x = (dk_x/dw)t + (d^2k_x/dw^2)t^2/2 = b_1t + b_2t^2 \tag{3}$$

The periodic change in k_x, in turn, results in a correponding change in k_z with $\Delta k_z = -(k_x/k_z)\Delta k_x$. Under the circumstance, the longitudinal wave number β has a periodic component $\Delta\beta$ superposed on the constant value β_0, and Eq. (2) can be rewritten as

$$d^2E/dz^2 - (g-i\beta_0)^2E = 4\beta_0[\Sigma\kappa_q\cos(q2K_Bz)]E \tag{4}$$

where $K_B = \pi/\Lambda$ and Λ is the period of thickness variation. The coefficient κ_q in a Fourier expansion of $\Delta\beta$ is called the coupling constant because it introduces coupling between two waves whose wave numbers differ by $q2K_B$. In a DBR or DFB laser, the two coupled waves have their wave vectors in opposite directions; therefore, the Bragg condition for coupling becomes

$$k_1 + k_2 = q2K_B \tag{5}$$

Since the operational properties of a DBR or DFB laser are dependent on the coupling strength, we devote some discussion to the computation of κ_q. In Fig. 2, we plot the longitudinal wave number β versus W curve computed for three transverse TE modes. The index values chosen as $n_f = 3.60$ and $n_{s,d} = 3.40$ correspond approximately to the values in a typical GaAs DH laser. Knowing the swing in ΔW, that is, t_1 and t_2 in Fig. 1, and the profile of the thickness variation, we can construct the β versus z curve and thus find the coupling constant κ_q for use in Eq. (4). The following general features of the β versus W curves are worth noting. First, the slope of the curve increases with increasing transverse mode number m_t. Therefore, higher order modes have a stronger coupling constant. Second, the curve deviates considerably from a linear relation especially for the $m_t=2$ mode. Therefore, the β versus z curve will not follow exactly the grating profile, that is the W versus z curve. A practical consequence of this nonlinearity is that even harmonics of κ_q will exist even *for gratings with symmetric profiles.*

To gain physical insight as to what factors control the coupling constant, we use Eq. (3) to find an analytical expression for κ_q for two simple grating profiles: rectangular and symmetric triangular. If we write κ_q as

$$\kappa_q = F_q(k_x^2/2\beta_0)(\Delta W/W_{eff}) \tag{6}$$

then we find: for the rectangular profile of width 2a,

$$F_q = (2/q\pi)\sin(q2\pi a/\Lambda) \tag{7}$$

and for the symmetric triangular profile,

$$F_q = 4/(q\pi)^2,\quad q = \text{odd} \tag{8}$$

$$F_q = [4/(q\pi)^2](b_2\Delta W/b_1),\quad q = \text{even} \tag{9}$$

In the above calculation, $t_1 = t_2 = \Delta W/2$ is assumed, that is, the unperturbed waveguide is taken to be midway between the two extremes. In Eq. (6), the quantity $(k_x^2/2\beta_0)(\Delta W/W_{eff})$ is the amplitude (half swing) of the β change produced by the thickness change (half swing = $\Delta W/2$), based on the linear relation $\Delta k_x = b_1t$ alone. The quantity F_q is the Fourier coefficient of the β versus z curve taking into account both linear and quadratic terms.

The proportionality constant b_1 in Eq. (3) and hence the quantity W_{eff} in Eq. (6) can be found by differentiating Eq. (1). We find: for TE waves,

$$W_{eff} = W + p_s^{-1} + p_d^{-1} \tag{10}$$

which is exact and for TM waves,

$$W_{eff} \approx W + (p_s^{-1}+p_d^{-1})[\beta_0^2/(\beta_0^2-k_x^2)] \tag{11}$$

which is a good approximation if $n_{s,d}$ is close to n_f as in semiconductor DH lasers. Based on Eqs. (10) and

(11), we expect the coupling constant to be higher for TE waves than for TM waves. This conclusion is consistent with experimental observations that the DBR laser has a TE polarization. For modes not too close to cut-off, we can approximate k_z by $n_f k_0$, W_{eff} by W, and k_x by $(m_t+1)\pi/W$, and thus estimate the value of the coupling constant from

$$\kappa_q \sim F_q[(m_t+1)^2\pi^2/k_0 n_f][\Delta W/W^3] \tag{12}$$

which clearly shows the dependence of κ_q on m_t and W. The Fourier coefficient F_q is normalized for a unit change in $\Delta\beta$ calculated from the linear term alone in Eq. (3). For the rectangular grating and for the odd harmonics of the symmetric triangular grating, F_q is proportional to $\Delta\beta_1 + \Delta\beta_2$ and for the even harmonics of the symmetric triangular grating, it is proportional to $\Delta\beta_1 - \Delta\beta_2$ where $\Delta\beta_1$ and $\Delta\beta_2$ (Fig. 1) are the swing of β with respect to β_0 of the unperturbed waveguide. Because the contributions to $\Delta\beta_1$ and $\Delta\beta_2$ from the linear term in Eq. (3) have the same sign while those from the quadratic term have opposite signs and because the magnitudes of $\Delta\beta_1$ and $\Delta\beta_2$ depend on the division in $t_1+t_2 = \Delta W$, the quantity F_q is dependent on the choice of the unperturbed waveguide. Equations (7) to (9) are based on $t_1 = t_2 = \Delta W/2$.

In Fig. 3, we plot the values of the coupling constant κ_3 for the third harmonic as a function of the tooth height ΔW from Eq. (6) as curve 2, from Eq. (12) as curve 3 and directly from Fig. 2 as curve 4 for the rectangular and symmetric triangular gratings. For comparison, the curves computed by Streifer, Scifres, and Burnham (Streifer, W., et al., 1975), using an overlap integral involving the index change Δn^2 weighted by the transverse field distribution $E^2(x)$, are shown as curve 1. The agreement is almost perfect in the triangular case, for which $t_1 = t_2$ was assumed in both the present and SSB calculations. A significant discrepancy exists between the results from the two calculations in the rectangular case, for which different divisions in $t_1 + t_2 = \Delta W$ were used. Because the information concerning the field distribution in the transverse plane is already contained implicitly in the mode equation, there is really no need to formulate the problem of wave propagation involving again the transverse field distribution E(x). Therefore, the two methods should yield consistent results if the same assumptions are used about the unperturbed waveguide. The procedure outlined above for computing κ_q is comparatively simple, and can easily be extended to other simple grating profiles such as the sawtooth and sinusoidal profiles. The major uncertainty in computing κ_q is in choosing the unperturbed waveguide, especially at large values of ΔW where the quadratic term in Eq. (3) becomes important.

Now we discuss the eigen modes of the guide. In a periodic medium, the proper solution must be in Floquet-Bloch form

$$E(z) = A\phi_1(z)\exp(\Gamma z) + B\phi_2(z)\exp(-\Gamma z) \tag{13}$$

where $\phi(z) = \phi(z+\Lambda)$ is a periodic function and hence can be expanded in terms of its Fourier components. However, because of the Bragg condition, only the components whose wave vectors are related by Eq. (5) have significant amplitudes. Therefore, the solution of Eq. (13) can be approximated by

$$E(z) = [U_f + U_{f+q}\exp(+iq2K_B z)]\exp(\Gamma z) + [U_b + U_{b-q}\exp(-iq2K_B z)]\exp(-\Gamma z) \tag{14}$$

where $\Gamma = G-iK$ is the effective propagation constant. Physically, the terms U_f and U_b represent the two primary waves propagating in the forward and backward direction, respectively, and the terms U_{f+q} and U_{b-q} represent their respective Bragg-scattered secondary waves. Substituting Eq. (14) in Eq. (4) and collecting terms related by the Bragg condition, we find

$$U_{f+q}/U_f = U_{b-q}/U_b = s \tag{15}$$

where the scattering factor s and other relevant parameters are defined as

$$s = -i\kappa[G + g + i(\delta+\delta_{eff})]^{-1} \tag{16}$$

$$\delta = qK_B-\beta_0, \quad \delta_{eff} = qK_B-K \tag{17}$$

$$P^2 = (G+i\delta_{eff})^2 = (g+i\delta)^2 + \kappa^2 \tag{18}$$

In Fig. 4, we show the wave vectors of the four principal field components of Eq. (14). The reciprocal lattice vector $q2\vec{K}_B$ couples U_{f+q} to U_f and couples U_{b-q} to U_b. In this coupling process, the wave vectors are conserved. However, the wave vectors of U_f and U_b are not connected by the reciprocal lattice vector. Therefore, in Eq. (14), there are two independent waves U_f and U_b which are not coupled. A DBR or DFB laser, like a conventional laser, needs a change of the propagation property at a boundary to couple U_f and U_b. This will be further discussed in Sec. 3. In Fig. 5, we present the dispersion diagram showing the general behavior of $\Gamma = G-iK$ near the Bragg wavelength and defining the various parameters in Eqs. (16) to (18). For comparison, the dispersion diagram for a corresponding uniform waveguide is drawn as curve (I). The other three curves are for periodic waveguides without loss (curve II), with gain (curve III) and with loss (curve IV).

3. REFLECTION AND TRANSMISSION AT BOUNDARIES

In this section, we treat the problem of matching the fields at a discontinuity and derive expressions of the reflection and transmission coefficients for the DBR laser cavity. First we consider the boundary problem between a uniform and a corresponding periodic waveguide made of the same material and of nearly equal waveguide thickness W. The field in the uniform waveguide can be represented by

$$E(z) = A\exp(\gamma z) + B\exp(-\gamma z) \tag{19}$$

where $\gamma = g-i\beta$ is the propagation constant, and the field in the periodic waveguide can be represented by Eq. (14). Continuity of the tangential component of E and H at the boundary (chosen as z=0) requires

$$U_f + U_{f+q} + U_b + U_{b-q} = A + B \tag{20}$$

$$K(U_f - U_{f+q} - U_b + U_{b-q}) \simeq \beta(A-B) \tag{21}$$

In obtaining Eq. (21), we make the approximations that $\gamma \simeq -i\beta$, $\Gamma \simeq -iK$, and $K \simeq qK_B$ near the Bragg wavelength. We also note from Fig. 5 and Eq. (18) that K and β differ by a maximum amount of $\delta = \kappa$ which is of the order of 10^2 cm^{-1} (Fig. 3) whereas the value of K is on the order of $2.5 \times 10^5 cm^{-1}$ in GaAs laser. Therefore, we can further let $K = \beta$ and thus obtain

$$U_f + U_{b-q} = A, \quad U_b + U_{f+q} = B \tag{22}$$

Equation (22) says that at the junction of a periodic and uniform waveguide, we can equate the amplitudes of the waves with their wave vectors in the same direction. This simplification is a direct consequence of the assumption that the two waveguides have approximately the same propagation characteristics. Even though K is different from β, the quantity $(K-\beta)/(K+\beta)$ is too small to cause any appreciable reflection. However, in the periodic waveguide, the proper modes are Bloch waves but not plane waves. In terms of the eigen Bloch waves, there is reflection at the boundary. In Fig. 6, we illustrate two boundary situations: (a) a Bloch wave incident on a uniform waveguide of infinite extent and (b) a plane wave incident on a periodic waveguide of infinite extent. For case (a), we set B=0 and $A=U_t$. Thus, we find $U_b/U_f = -s$ and $U_t/U_f = 1-s^2$ using Eq. (15). For case (b), we set $U_i = A$, $U_r = B$, $U_b = 0$ and $U_{b-q} = 0$. Thus, we find $U_r/U_i = s$. In both cases, the ratio of the reflected wave to the incident wave is equal to the scattering factor s. The value and the phase of s are plotted in Fig. 7 as functions of δ/κ for several values of g/κ. As we can see, a high reflection can be obtained near the Bragg condition ($\delta<\kappa$) if g/κ is small.

The above discussion is for incidence on an infinite waveguide. Now we consider the situation in which a periodic waveguide of length L is connected at the ends to two uniform waveguides as shown in Fig. 8. A wave incident from one of the uniform waveguides may undergo multiple reflections at the two boundaries, and finally be either reflected back to the original uniform waveguide or transmitted through the periodic waveguide to the other uniform waveguide. We refer to the periodic waveguide as a Bragg reflector. The reflection coefficient R and the transmission coefficient T can be found by using the method of multiple reflections (Wang, S., et al., 1974) and are, respectively, given by

$$|R| = \left|\frac{s[1-\exp(2PL)]}{1+s^2\exp(2PL)}\right| \quad , \quad |T| = \left|\frac{(1+s^2)\exp(PL)}{1+s^2\exp(2PL)}\right| \tag{23}$$

In Fig. 9, the value of $|R|$ and $|T|$ are plotted as functions of δ/κ for two lossless (g=0) Bragg reflectors of different lengths. The dimensionless quantities δ/κ and κL are used as parameters. Several features of the curves are worth noting. The relation $|R|^2 + |T|^2 = 1$ is always true as required by the condition for energy conservation. The reflection coefficient has appreciable values only for $\delta < \kappa$, that is, near the Bragg condition. Using $K \simeq 2\pi\, n/\lambda$ and $\delta=\kappa$, we obtain the half bandwidth of a Bragg reflector as

$$\Delta\lambda \simeq \kappa_q \lambda^2/2\pi n_{eff} \tag{24}$$

where n_{eff} is the effective index of the guide taking dispersion into account. The values of $|R|$ and $|T|$ at the Bragg wavelength ($\delta=0$) are given by

$$|R|_B = \tanh(\kappa L), \quad |T|_B = \mathrm{sech}(\kappa L) \tag{25}$$

and those at the edge of the Bragg-reflector band ($\delta=\kappa$) are given by

$$|R|_1 = \kappa L/\sqrt{1+\kappa^2L^2}, \quad |T|_1 = 1/\sqrt{1+\kappa^2L^2} \tag{26}$$

To achieve high reflection, we should choose $\kappa L > 2$, and to have appreciable transmission we should let $\kappa L < 1$.

In Fig. 10, we plot the values of $|R|$ and $|T|$ for a lossy Bragg reflector with $\kappa L = 1$ and $g/\kappa = -0.2$. Because of loss in the periodic waveguide, the sum $|R|^2 + |T|^2 < 1$ is true. From Fig. 7, we see $|s| < 1$ even at $\delta=0$. By letting $|s| = \exp(-A)$, we find at $\delta=0$

$$|R|_B = \sinh(PL)/\cosh(PL+A), \quad |T|_B = \cosh A/\cosh(PL+A) \tag{27}$$

where $P^2 = \kappa^2+\alpha^2$ and α is the loss constant in the periodic waveguide ($g=-\alpha$). For $PL > 2$, Eq. (27) can be approximated by

$$|R|_B \simeq |s| \quad , \quad |T|_B \simeq (1+|s|^2)\exp(-PL) \tag{28}$$

For a loss constant of $\alpha/\kappa = 0.2$, $|s|$ is 0.8 (Fig. 7). Therefore, the relatively low value of $|R|_B$ ($\simeq 0.66$) in Fig. 10 is the combined effects of a lossy reflector and a relatively small value for κL. For PL=1 and $|s| = 0.8$, we find from Eq. (28) $|T|_B \simeq 0.61$ not too far from the value 0.55 given in Fig. 10. Therefore, the value of $|T|_B$ is still mainly determined by the product κL. For practical DBR lasers, it appears desirable that we have two different reflectors: one mirror reflector with $\kappa L > 2$ for high reflectivity and mode selectivity, and one output reflector with $\kappa L < 1$ for appreciable output power.

4. PERFORMANCE AND OPTIMAL DESIGN OF THE DBR LASER

Operation of the DBR injection laser has been reported in the GaAs-$Ga_{1-x}Al_xAs$ system by several groups. (Reinhart, F. K., et al., 1975; Tsang, W. T., et al., 1976; Ng, N., et al., 1976; Kawanishi, H., et al., 1977.) Here we briefly review the experimental results reported by Tsang and Wang, and discuss the performance characteristics and fabrication procedure of the DBR laser as a discrete device. Those aspects of the laser relevant to applications in integrated and fiber optics will be discussed in Sec. 5. Figure 11 shows the experimental structure of the laser. First, a multi-layer structure similar to that of DH injection laser is grown by liquid-phase epitaxial (LPE) growth process. The middle GaAs layer serves both as the recombination layer generating laser radiation and as the waveguiding layer guiding the laser radiation. The two $Ga_{1-x}Al_xAs$ layers which have a larger energy gap and a smaller refractive index than GaAs serve as claddings to confine the laser radiation mainly to or in the vicinity of the GaAs waveguide. The two outmost GaAs materials, the n-GaAs substrate and the p-GaAs cap, are needed for electrical contacts.

After the LPE growth, wide channels are made in the wafer by etching away chemically the two top grown layers to expose the middle GaAs layer. Then periodic gratings are made onto the exposed surface by using laser-interference (Shank, C. V., et al., 1973) and preferential chemical etching (Tsang, W. T., et al., 1976) techniques. Finally, silicon dioxide is sputtered on the whole wafer, windows are opened in the oxide for electric contacts, and the wafer is cut to make individual DBR lasers. The laser is mounted on the cold finger of a dewar and the laser characteristics are studied at 183°K.

Figure 12 shows a high-resolution spectrum of the DBR laser at a current density $J = 1.1\ J_{th}$ above the threshold. Setting $k_1 = k_2 = \beta$ in Eq. (5), we can express the Bragg condition in terms of wavelength as

$$\Lambda = q\lambda/(2n_g) \tag{29}$$

where $n_g = \beta/k_0$ is the equivalent index for a guided mode. The average thickness of the corrugated sections of the guide is 0.94 μ. From Fig. 2, we see that the TE_2 mode is fairly close to cut-off and hence is expected to have a large leakage loss. Therefore, we use the value of n_g for the TE_1 mode, which is 3.53 from Fig. 2. With $\lambda = 8509$ Å and $q = 3$ in Eq. (29), we find the theoretical value for the grating period $\Lambda = 3615$ Å. The value of Λ as determined by SEM and diffraction angle measurements is 3550 ±70 Å.

Two important questions relating to the performance of a DBR laser are the mode selectivity and the output power. To achieve single-mode operation, we must make the longitudinal-mode spacing larger than the bandwidth of the Bragg reflectors. For a laser with an active region of length L_a, the longitudinal mode spacing is

$$\Delta\lambda = \lambda^2/2n_{eff}L_a \tag{30}$$

The value of $n_{eff} = n - \lambda dn/d\lambda$ in bulk (not waveguide) GaAs is 5.5. Corrected for the difference between β and $n_f = 3.6$, the value of n_{eff} for the TE_1 mode is 5.43. For $L_a = 480$ μm and $\lambda = 8509$ Å, the calculated mode spacing is 1.39 Å. The observed mode spacing is 1.36 Å. In the experiment, as the injection current was raised, the mode at 8507.6 Å also became prominent while the background radiation which also displayed an interference pattern due to the gratings remained more or less the same. Obviously, the group around $\lambda = 8514$ Å is outside the bandwidth of the Bragg reflectors. Using Eqs. (24) and (30), we obtain $\kappa_q L_a < \pi$ as the condition for single mode operation. For the experimental unit, the product $\kappa_q L_a = 5.5$. Therefore, two dominant longitudinal modes are expected and were observed.

Figure 13 shows the total power (curve A) and the power (curve B) measured around 8509 Å with a bandwidth of about 5 Å. Both curves give a threshold current density of 890 A/cm^2 at 183°K. The linearity of curve B above threshold indicates the predominance of the two longitudinal modes which are within the bandwidth of the Bragg reflectors, for current densities up to $J = 2.5\ J_{th}$. The slope of curve B gives the differential quantum efficiency which is theoretically given by

$$\eta_{DBR} = \eta_i |T|^2/[\alpha_{fc}L_a + \ln(1/|R|^2)] \tag{31}$$

where η_i is the internal quantum efficiency, and α_{fc} is the loss constant in the active region mostly due to free-carrier absorption. The value of κ for $q = 3$ and the TE_1 mode is estimated to be 115 cm^{-1} (for a rectangular grating of 3 Λ/8 teeth width and 0.12 μm = ΔW teeth height). The loss constant α in the reflector region is estimated to be 80 cm^{-1} (Wang, S., 1977). Using Eqs. (16), (17), (18), and (23), and a value $L = 150$ μm, we find $|R| = 0.51$ and $|T| = 0.16$. Substituting these values and assuming $\eta_i = 0.60$, $\alpha_{fc} = 10$ cm^{-1}, and $L_a = 480$ μm in Eq. (31), we obtain $\eta_{DBR} = 0.66\text{x}10^{-2}$. The output power of the laser is 7 mW (3.5 mW from one reflector) at a current of 300 mA above the threshold. This power yields an experimental value for $\eta_{DBR} = 1.6\text{x}10^{-2}$. Owing to the uncertainties in estimating κ and α, the agreement is considered good.

In the experimental DBR laser, we have used the same length L for both reflectors, a cavity length L_a to allow two longitudinal modes, and lossy GaAs in the reflector region due to re-absorption. The mode selectivity and output power could be greatly improved by using two different κL products, by reducing the cavity length and by using $Ga_{1-x}Al_xAs$ to minimize α in the reflector region. As an example, we keep $\kappa = 115$ cm^{-1} but choose $L_2 = 80$ μm and $\kappa L_2 = 0.92$ for the output reflector, $L_1 = 200$ μm and $\kappa L_1 = 2.3$ for the mirror reflector, and reduce L_a to 240 μm. Further, we assume $\alpha = 10$ cm^{-1} in the passive reflector region. For future reference we label this proposed laser as the "optimally designed" DBR laser. Using these values in Eqs. (16), (17), (18), (23), and (31), we find at the Bragg wavelength $R_0 = 0.693$ and $T_0 = 0.648$ for the output reflector, $R_r = 0.920$ and $T_r = 0.184$ for the mirror reflector, and a differential quantum efficiency $\eta_{DBR} = 12.5\text{x}10^{-2}$ which should raise the output power to 130 mW. Note that both R_0 and R_r are higher than the value 0.565 in cleaved DH lasers. The threshold gain of a laser with two different reflectors is given by

$$g_{th} = \alpha_{fc} + L_a^{-1}\ln(1/|R_0R_r|) \qquad (32)$$

The longitudinal mode spacing in terms of δ is given by $\delta = \pi/L_a$. For $L_a = 240$ µm, the mode next to the one at the Bragg wavelength has a value $\delta = 130\ cm^{-1}$. Thus, we find from Eqs. (16), (17), (18) and (23), $R_0 = 0.617$ for the output reflector and $R_r = 0.736$ for the mirror reflector. Substituting these values in Eq. (32), we obtain a difference of threshold gain $\Delta g_{th} = 14\ cm^{-1}$ for the two modes. Based on the gain-current-density relation of Stern (Stern, F., 1973), we can expect single mode operation from a DBR laser with power up to 60 mW. Therefore, with improved design, a DBR injection laser can operate in single mode with sufficient output power.

5. LASER INTEGRATION AND WAVEGUIDE-FIBER COUPLING SCHEMES

Before we discuss ways how the DBR laser can be integrated into an optical circuit or coupled into an optical fiber, it may be useful to comment on the relative merits of the DBR and the DFB laser from the standpoint of laser fabrication and design. The rapid development of integrated electronic circuits on a large scale is made possible by standardization of processing procedures and simplification and reduction of processing steps. The DBR laser is compatible with this concept. Because the reflectors can be made by photolithographic and etching techniques after the waveguiding structure is fabricated, only one LPE growth step is needed. In contrast, two LPE processing steps are usually needed for the DFB laser. We feel that the one-step LPE growth offers a tremendous advantage.

What we envision for future integrated optical circuits is a basic waveguiding structure common to most, and all if possible, optical devices. This common structure should require only one LPE processing step. Should we need separate and different LPE growth steps for each device, then integration of optical devices would be difficult. Additional pre-LPE or post-LPE processing steps would be introduced to divide the common waveguiding structure into several segments for different device functions so that the devices could be physically separated and electrically isolated from one another. The two reflector regions in a DBR laser could be used for separation and isolation from other optical devices.

The DBR laser structure also offers flexibility in laser design. As discussed in Sec. 4, to maintain high mode selectivity and low laser threshold but at the same time to be able to derive appreciable output power, we must have different reflection and transmission coefficients at the two ends of a laser. This can be done in the DBR laser by making the two reflectors of different lengths. In the DFB laser, the reflection and transmission properties at the two ends are the same because the parameters that we can adjust, for example, the coupling constant and the length, are all those of the one and only active region. The reflectors in the DBR laser also may serve other purposes. For example, if a second-order (q=2) grating is used, the fundamental component of the coupling constant can be used to couple out the laser radiation while the second harmonic component provides the necessary reflection for laser action. The coupled-out beam has extremely low divergence (Alferov, Zh. I., et al., 1974; Zory, P., et al., 1975). The reflector also can serve to provide some optical isolation between the DBR laser and the adjoining optical circuit for preventing parasitic effects. In contrast, a DFB laser is directly connected with the adjoining optical circuit unless special provision is made to separate them.

Now let us examine possible schemes for integration of the DBR or DFB laser into an optical circuit. As mentioned earlier, the first step toward integration is to find a common waveguiding structure. One fundamental problem we face in using semiconductors as the base material for monolithic integration of optical components is absorption losses. The laser radiation emitted from the pumped (active) part of a GaAs waveguide will be re-absorbed in the unpumped (passive) part. In Sec. 4, we estimated $\alpha \sim 80\ cm^{-1}$ in the unpumped reflector region. The same loss constant is expected in the unpumped regions of the common waveguide interconnecting two optical devices. As a discrete device, the DFB laser has the distinct advantage that there are no unpumped regions. In an integrated optical circuit, however, the problem with re-absorption losses in the interconnection regions exists irrespective of whether we use the DBR or DFB laser as the source. For an unpumped distance of 400 µm which we think is a minimum separation between two devices for adequate isolation, the power loss is about 96% if $\alpha = 80\ cm^{-1}$. This power loss is unacceptable. The problem with lossy reflectors in the DBR laser is automatically solved if the loss constant α in the unpumped waveguide region can be substantially reduced.

One way of having a low-loss reflector region is through the use of a tapered coupler whereby the reflector can be made on (GaAℓ)As which has a larger energy gap than GaAs. Such a DBR injection laser has been demonstrated and made by a single LPE step (Reinhart, F. K., 1975). Here we consider a simpler way of solving the problem through the use of separate optical and carrier confinement. The original purpose of the separate confinement scheme (Kressel, H., et al., 1972; Thompson, G. H. B., et al., 1973; Casey, H. C., Jr., et al., 1974) is to lower the threshold current density by reducing the active-layer thickness and at the same time to minimize output-beam divergence by increasing the optical aperture. We propose to use the same scheme to minimize re-absorption losses in the unpumped interconnection regions in integrated optical circuits.

A DBR injection laser with separate optical and carrier confinement is shown in Fig. 14 with the middle p-GaAs layer (layer 3) used as the recombination layer and the neighboring n-$Ga_{1-y}A\ell_{1-y}As$ layer (layer 2) used as the main waveguiding layer. For the separate confinement to be effective, the GaAs layer should be thin (of thickness 0.1 µm or smaller) and the n-$Ga_{1-y}A\ell_yAs$ layer should be comparatively thick (in the neighborhood of 1 µm) so that the GaAs layer can be terminated without much loss of radiation at the termination. The continuing n-$Ga_{1-y}A\ell_yAs$ layer can then be used as a common waveguide on which other optical devices can be built. We should point out that the optical confinement layer has to be below the carrier confinement layer for the common waveguide to continue. The structure proposed in Fig. 14, therefore, would be impractical for the DFB laser for lack of suitable place for the grating. We do not want to place the grating between layers 1 and 2 because this would require a second LPE growth on the $Ga_{1-x}A\ell_xAs$ layer of relatively high Aℓ concentration (x>0.3). We also do not want to place the grating between layers 2 and 3 because the grating would reduce drastically the recombination efficiency and thus stop the laser action.

To find the composition y needed in the waveguiding layer, we set an upper limit of $\alpha = 10\ cm^{-1}$ on the absorption coefficient. This is the value we assumed in Sec. 4 for the passive reflector region of an "optimally designed" (not the experimental) DBR laser. Using the experimental data of GaAs (Casey, H.C., et al., 1976), we find that this value is reached in heavily doped GaAs at an energy 0.065 below the energy gap of pure GaAs. For small y, the band shift in $Ga_{1-y}Al_yAs$ with respect to GaAs is about 12.7 meV for 1% Aℓ concentration. If we assume that the absorption coefficients in GaAs and $Ga_{1-y}Al_yAs$ have similar behavior then a value of 0.06 for y should be sufficient to keep α below $10\ cm^{-1}$. The composition x for the other two $Ga_{1-x}Al_xAs$ layers, on the other hand, should be larger than 0.3 to prevent leakage of laser radiation into the two outmost GaAs regions. The DBR laser labelled as "optimally designed" in Sec. 4 should be realizable with the present technology.

Once we have in mind a suitable common waveguiding structure for integrated optics, we can think of building various optical devices with or on the structure. In Fig. 15 we present our ideas for consideration as possible approaches to building simple integrated optical circuits. In region A, the GaAs cap, the $p\text{-}Ga_{1-x}Al_xAs$ layer (layer 4), and the GaAs layer (layer 3) are removed by chemical etching. Obviously this region can be used for isolation. For some purposes, we may use p-n junctions for better isolation and want to perform a subsequent diffusion or ion implantation to convert the $Ga_{1-y}Al_yAs$ layer from n to π or p^-. This step would make it possible to apply a high electric field and thus enable us to use the electrooptic effect in this region. For example, if region A is a part of the DBR laser, we can use the electrooptic effect to control the laser action. For a field of 10^5 V/cm which is below the breakdown field in GaAs, the shift in laser wavelength [Eq. (29)] is estimated to be 4 Å which is comparable to the bandwidth of the Bragg reflectors. This effect offers several interesting possibilities. If the effect is applied to both Bragg reflectors, then we could fine tune the laser wavelength. If the effect is applied only to one Bragg reflector, then we could modulate the output of the laser by shifting the Bragg wavelength of one reflector with respect to the other. If the effect is controlled by the output of the laser through a detector such as the one shown in region B, we could stabilize the laser wavelength against unwanted drifts through the use of a proper feedback control circuit.

In region B, the structure is the same as that for the DBR laser without the Bragg reflectors. If the diode is forwardly biased, it could be used as an amplifier. Based on the gain relation of Stern (Stern, F., 1973), a gain constant $g = 75\ cm^{-1}$ could be expected at current density of 7 kA/cm^2 at room temperature. Assuming a confinement factor $\Gamma = 0.2$ (fraction of laser radiation in GaAs), this would mean a gain in power by a factor 4.5 in a distance of 1 mm. If the diode is reversely biased it could be used as a detector. Any laser radiation guided in the $Ga_{1-y}Al_yAs$ layer (layer 2) will spread to and hence be absorbed in the GaAs layer (layer 3) upon entering the detector region. If we use the same absorption coefficient $\alpha = 80\ cm^{-1}$ in GaAs as before and assume a confinement factor $\Gamma = 0.2$, then a detector of length 2 mm could have a detection efficiency of 96%.

Finally we present a possible scheme for direct fiber-waveguide coupling. Although several coupling schemes have been proposed, they all have one problem in common, that is, matching the geometry of the fiber and waveguide. Recently, several techniques have been proposed and demonstrated for making two-dimensional GaAs-(GaAℓ)As waveguides (Tsukada, T., 1974; Burnham, R. D., 1975; Kirkby, P. A., et al.; Namizaki, H., 1976). We have independently developed an etch-and-grow technique for making inverted ridge waveguide (Botez, D., et al., 1976). Clean mode excitation and transmission in the guide (Tsang, W.T., et al., 1976) and laser action in optically pumped half rings (Botez, D., et al., 1976) have been reported. One obvious advantage of the inverted-ridge waveguide is that the shape of the laser can be made to approximate that of a fiber and hence direct fiber-waveguide coupling is possible. In direct end coupling, accurate positioning of the fiber with respect to the waveguide is important. We propose to use channels preferentially etched into Si for housing fibers. The three walls of the channel are formed by a set of crystalline planes (Tsang, W. T., et al., 1975). Therefore, once the channel opening and the fiber diameter are chosen, the position of the fiber in the channel is accurately determined and can be held fixed by epoxy. This arrangement is simple and accurate. In Fig. 16, we show schematically the arrangement for a multi-channel system by making a linear array of such channels with fibers individually coupled to lasers in a separate linear array. In principle, if the geometry and dimensions of the lasers and the fibers in the array are properly designed and chosen the alignment procedure should be simple and the laser-fiber coupling assembly could be compact in size even in a multi-channel system. We are presently investigating suitable means of providing adequate isolation between the lasers.

6. CONCLUSION

We have analyzed the operation of the DBR injection laser and compared the theory with experiment. We have shown that with improved design, it should be possible for a DBR laser to operate in a single mode with sufficient power. A common waveguiding structure using separate optical and carrier confinement is proposed for integration of the laser into an optical circuit. Various optical devices which could be built onto the common waveguide are suggested. A simple scheme for direct laser-fiber coupling is also proposed. The proposed laser integration and fiber coupling schemes should be practicable and actual implementation of the schemes is being studied and pursued.

7. ACKNOWLEDGEMENT

Research sponsored by the National Science Foundation Grant ENG76-08292 and the Office of Naval Research Contract N00014-75-C-0420.

8. REFERENCES

ALFEROV, Zh. I., Gurevich, S. A., Kazarinov, R. F., Mizerov, M. N., Portnoi, E. L., Seisyan, R. P., and Suris, R. A., 1974, "Semiconductor Laser with Extremely Low Divergence of Radiation," Sov. Phys. Semiconductor, vol. 8, pp. 541-543.

BERGH, A.A. and Dean, P.J., 1972, "Light-Emitting Diodes," Proc. IEEE, vol. 60, pp. 156-223.

BOTEZ, D., Tsang, W.T., and Wang, S., 1976, "Growth Characteristics of $GaAs\text{-}Ga_{1-x}Al_xAs$ Structures Fabricated by Liquid Phase Epitaxy over Preferentially Etched Channels," Appl. Phys. Lett., vol. 28, pp. 234-237.

BOTEZ, D., Figueroa, L., and Wang, S., 1976, "Optically Pumped GaAs-$Ga_{1-x}A\ell_xAs$ Half-Ring Laser Fabricated by Liquid-Phase Epitaxy over Chemically Etched Channels," Appl. Phys. Lett., vol.29, pp.502-504.

BURNHAM, R.D., and Scifres, D.R., 1975, "Etched Buried Heterostructure GaAs/GaAℓAs Injection Lasers," Appl. Phys. Lett., vol. 27, pp. 510-511.

CASEY, H.C., Jr., Panish, M.B., Scholosser, W.O., and Paoli, T.L., 1974, "GaAs-$A\ell_xGa_{1-x}As$ Heterostructure Laser with Separate Optical and Carrier Confinement," J. Appl. Phys., vol. 45, pp. 322-333.

CASEY, H.C., and Stern, F., 1976, "Concentration-Dependent Absorption and Spontaneous Emission of Heavily Doped GaAs," J. Appl. Phys., vol. 47, pp. 631-643.

HAYASHI, I., Panish, M.B., and Reinhart, F.K., 1971, "GaAs-$A\ell_xGa_{1-x}As$ Double Heterostructure Injection Lasers," J. Appl. Phys., vol. 42, pp. 1929-1941.

KAWANISHI, H., Suematsu, Y., and Kishino, K., 1977, "GaAs-$A\ell_xGa_{1-x}As$ Integrated Twin-guide Lasers with Distributed Bragg Reflectors," to be published in IEEE J. Quantum Electronics.

KIRKBY, P.A., and Thompson, G.H.B., 1976, "Channel Substrate Buried Heterostructure (GaAℓ)As Injection Lasers," J. Appl. Phys., vol. 47, pp. 4578-4589.

KOGELNIK, H., and Shank, C.V., 1971, "Stimulated Emission in a Periodic Structure," Appl. Phys. Lett., Vol. 18, pp. 152-154.

KOGELNIK, H., and Shank, C.V., 1973, "Coupled-Wave Theory of Distributed Feedback Lasers," J. Appl. Phys., vol. 43, pp. 2327-2355.

KRESSEL, H., Lockwood, H.F., and Hawrylo, F.Z., 1972, "Large-Optical-Cavity (AℓGa)As-GaAs Heterojunction Laser Diode: Threshold and Efficiency," J. Appl. Phys., vol. 43, pp. 561-567.

MAURER, R.D., 1973, "Glass Fibers for Optical Communications," Proc. IEEE, vol. 64, pp. 452-462.

MILLER, S.E., 1969, "Integrated Optics: An Introduction," Bell Syst. Tech. J., vol. 48, pp. 2059-2069.

MILLER, S.E., Marcatili, E.A.J., and Li, T.Y., 1973, "Research Toward Optical-Fiber Transmission Systems; Part I: The Transmission Medium," Proc. IEEE, vol. 61, pp. 1703-1726.

NAMIZAKI, H., 1976, "Single Mode Operation of GaAs-GaAℓAs TJS-Laser Diodes," Trans. IECE, Japan, vol. E59, pp. 8-15.

NG, N., Yen, H.W., Katzir, A., Samid, I., and Yariv, A., 1976, "Room Temperature Operation of Distributed Bragg-Reflector Lasers," Appl. Phys. Lett., vol. 29, pp. 684-686.

REINHART, f.k., Logan, R.A., and Shank, C.V., 1975, "GaAs-$A\ell_xGa_{1-x}As$ Injection Lasers with Distributed Bragg REflectors," Appl. Phys. Lett., vol. 27, pp. 45-48.

SHANK, C.V., and Schmidt, R.V., 1973, "Optical Technique for Producing 0.1 μ Periodic Surface Structures," Appl. Phys. Lett., vol. 23, pp. 154-156.

STERN, F., 1973, "Gain Current Relation for GaAs Lasers with n-type and Undoped Active Layers," IEEE J. Quantum Electron, vol. QE-9, pp. 290-294.

STREIFER, W., Scifres, D.R., and Burnham, R.D., 1975, "Coupling Coefficients for Distributed-Feedback Single- and Double-Heterostructure Diode Lasers," IEEE J. Quantum Electron., vol. QE-11, pp. 867-873.

THOMPSON, G.H.B., and Kirkby, P.A., 1973, "(GaAℓ)As Lasers with a Heterostructure for Optical Confinement and Additional Heterostructure for Carrier Confinement," IEEE J. Quantum Electron., vol. QE-9, pp. 311-318.

TIEN, P.K., and Ulrich, R., 1970, "Theory of Prism-Film Coupler and Thin-Film Light Guides," J. Opt. Soc. Am., vol. 60, pp. 1325-1337.

TSANG, W.T., Tseng, C.C., and Wang, S., 1975, "Optical Waveguides Fabricated by Preferential Etching," Appl. Optics, Vol. 14, pp. 1200-1206.

TSANG, W.T., and Wang, S., 1976, "Profile and Groove-Depth Control in GaAs Diffraction Gratings Fabricated by Preferential Chemical Etching in the H_2SO_4-H_2O_2:H_2O System," Appl. Phys. Lett., vol. 28, pp. 44-46.

TSANG, W.T., and Wang, S., 1976, "GaAs-$Ga_{1-x}A\ell_xAs$ Double-Heterostructure Injection Lasers with Distributed Bragg Reflectors," Appl. Phys. Lett., vol. 28, pp. 596-598.

TSANG, W.T., and Wang, S., 1976, "Mode Properties of GaAs-$Ga_{1-x}A\ell_xAs$ Heterostructure Inverted Ridge Optical Waveguides," Appl. Phys. Lett., vol. 28, pp. 665-667.

WANG, S., L972, "Proposal of Periodic Layered Waveguide Structures for Distributed Lasers," Digest of Technical Papers, VIIth International Quantum Electronics Conference, May 8-11, Montreal, Canada p. 29-30.

WANG, S., 1973, "Proposal of Periodic Layered Waveguide Structures for Distributed Lasers," J. Appl. Phys., vol. 44, pp. 767-780.

WANG, S., 1974, "Principles of Distributed Feedback and Distributed Bragg Reflector Lasers," IEEE J. Quantum Electron., vol. EQ-10, pp. 413-427.

WANG, S., 1977, "Design Considerations of the DBR Injection Laser and the Waveguiding Structure for Integrated Optics," to be published in IEEE J. Quantum Electronics.

WANG, S., Cordero, R.F., and Tseng, C.C., 1974, "Analysis of Distributed-Feedback and Distributed-Bragg-Reflector Laser Structures by Method of Multiple Reflections," J. Appl. Phys., vol. 45, pp. 2975-2977.

ZORY, P., and Comerford, L.D., 1975, "Grating-Coupled Double-Heterostructure AℓGaAs Diode Lasers," IEEE J. Quantum Electron., vol. QE-11, pp. 451-455.

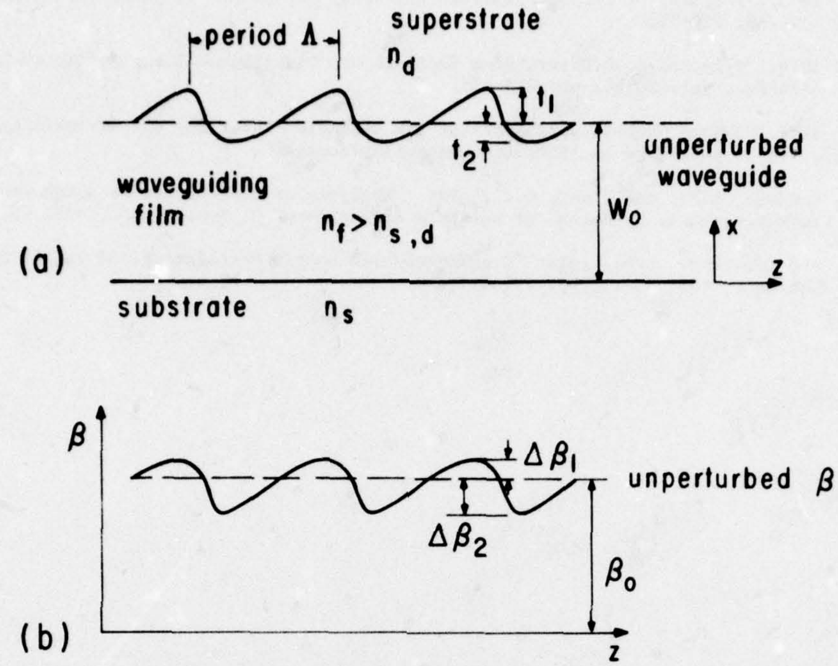

Fig. 1. Schematic diagrams showing (a) a dielectric waveguide ($n_f > n_{s,d}$) with periodic thickness variation and (b) the resultant periodic variation in the longitudinal wave number $k_z = \beta$. Because of the nonlinear dependence of β on waveguide thickness W, the β versus z curve will not follow linearly the W versus z curve.

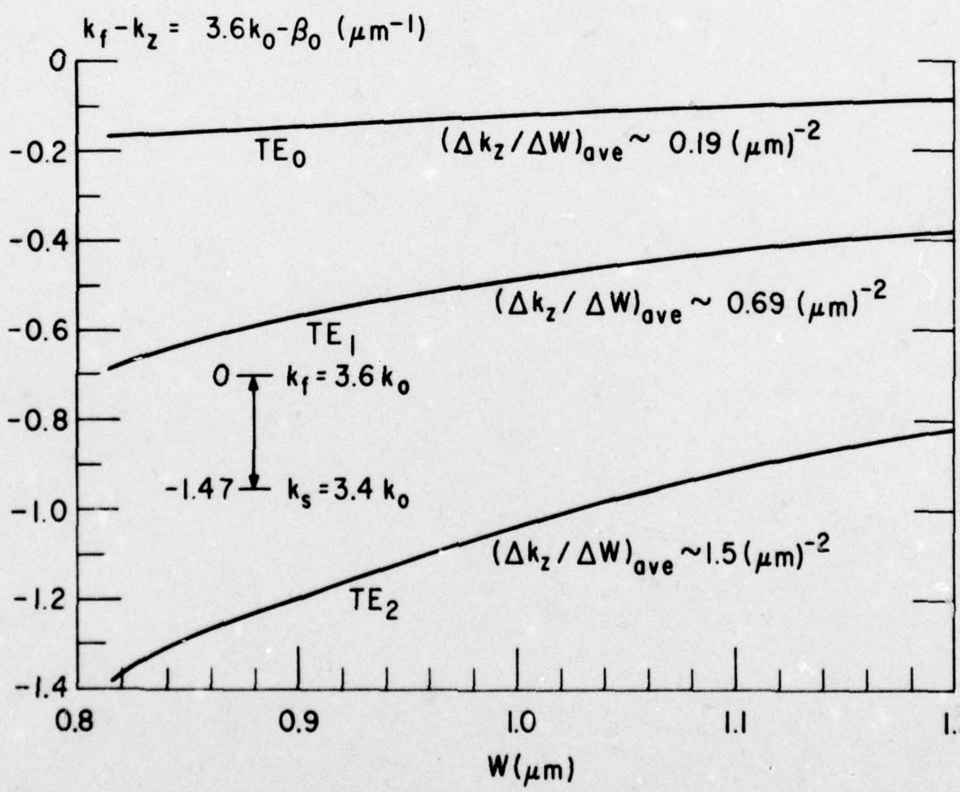

Fig. 2. Curves showing the longitudinal wave number k_z in a uniform waveguide relative to the free space wave number $n_f k_0$ as a function of the waveguide thickness W for three transverse TE modes. The values chosen for the indices of refraction are n_f=3.60 and $n_{s,d}$=3.40.

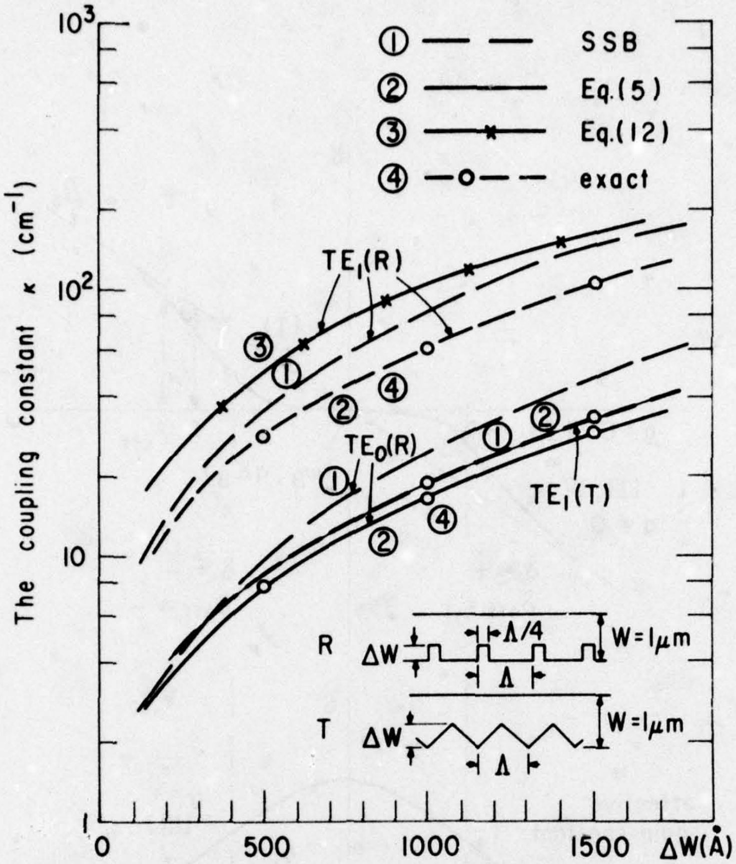

Fig. 3. The third harmonic coupling constant κ_3 as a function of the teeth height ΔW for two grating profiles, rectangular (R) and symmetric triangular (T), and for two transverse TE modes, m_t=0 and m_t=1. The computation is based on the following set of values: W_0=1μm, n_f=3.60, and $n_{s,d}$=3.40.

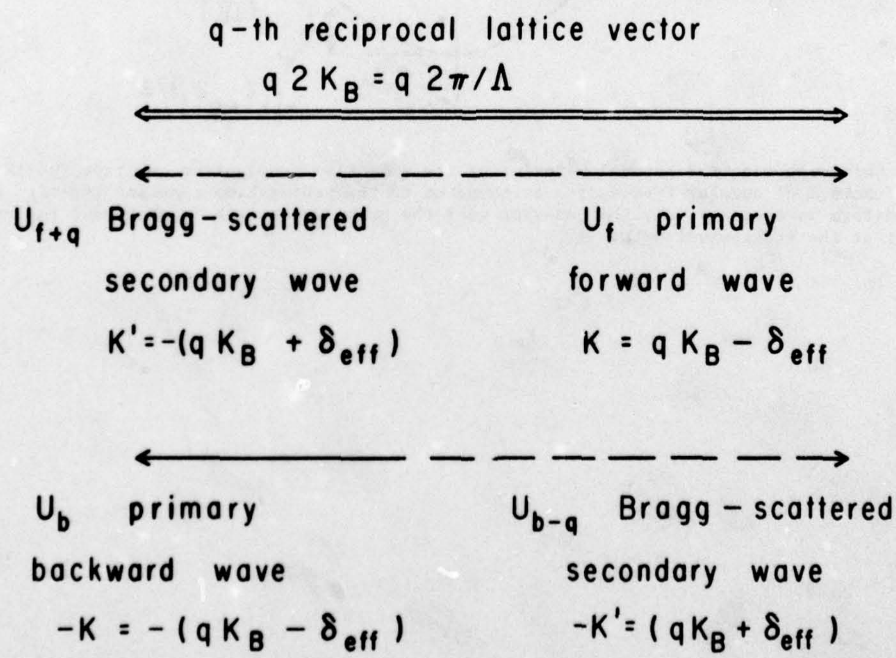

Fig. 4. Wave-vector relations of the principal components of the Bloch waves involved in a Bragg scattering process. The wave vectors are conserved in the process coupling U_{f+q} to U_f and the process coupling U_{b-q} to U_b. However, wave vectors of U_f and U_b are not connected by the wave vector $q2\kappa_B$.

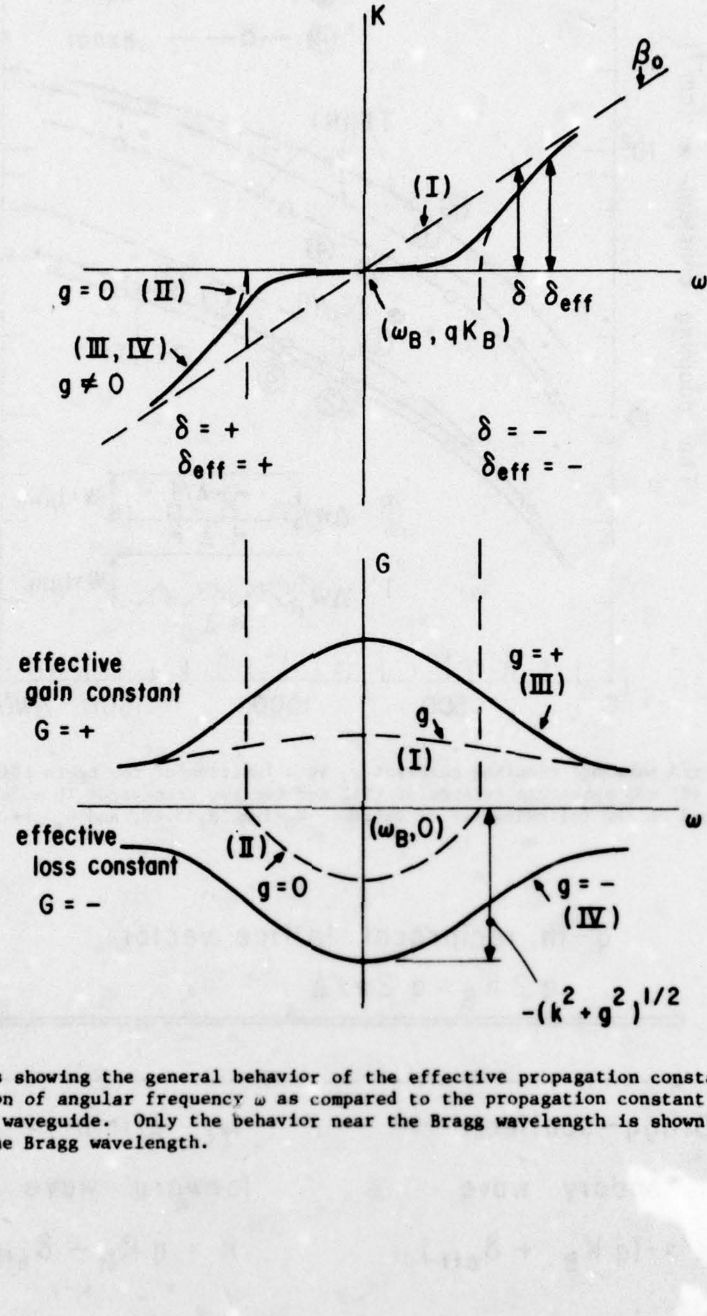

Fig. 5. Curves showing the general behavior of the effective propagation constant Γ=G-iK in a periodic waveguide as a function of angular frequency ω as compared to the propagation constant $\gamma=g-i\beta_0$ in a corresponding uniform waveguide. Only the behavior near the Bragg wavelength is shown and the value of K is relative to that at the Bragg wavelength.

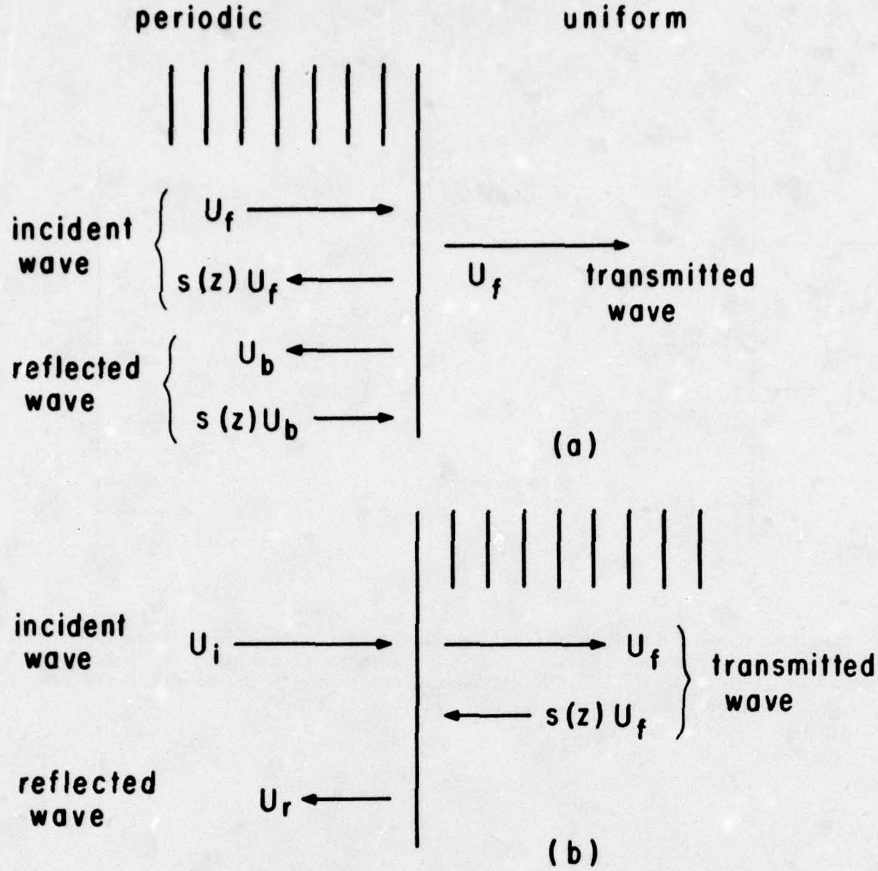

Fig. 6. Diagrams showing the physical situation at a boundary between uniform and periodic media: (a) with the incident beam from the periodic side, and (b) the incident beam from the uniform side.

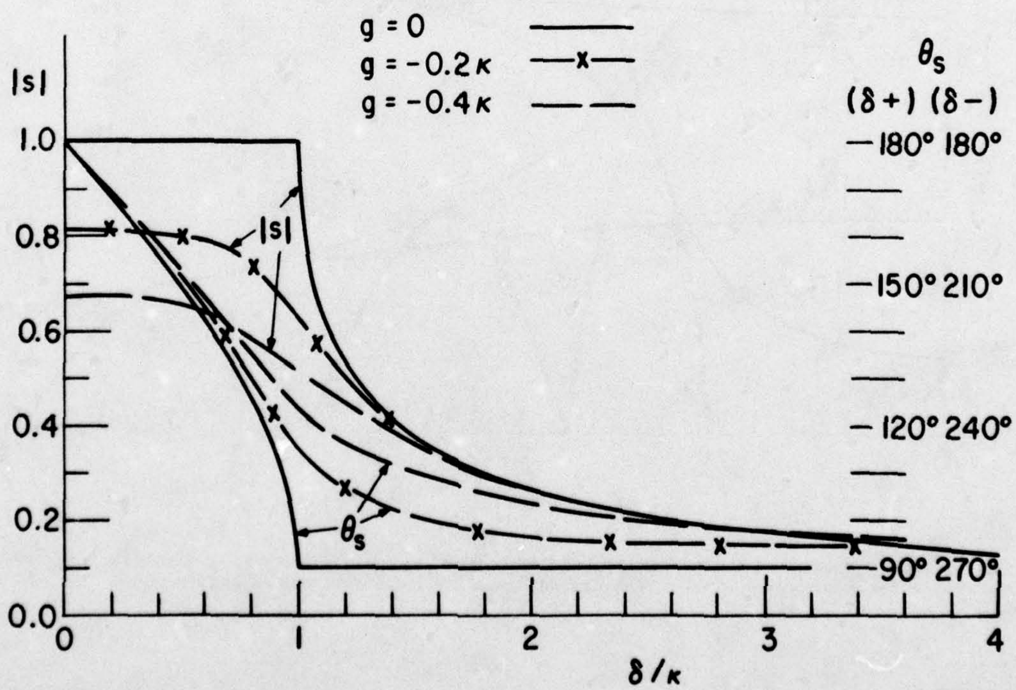

Fig. 7. The magnitude and the phase angle of the scattering factor s plotted as functions of δ/κ for several values of g/κ. The factor s relates the Bragg-scattered secondary wave to the primary wave whereas the parameter δ measures the deviation from the Bragg condition.

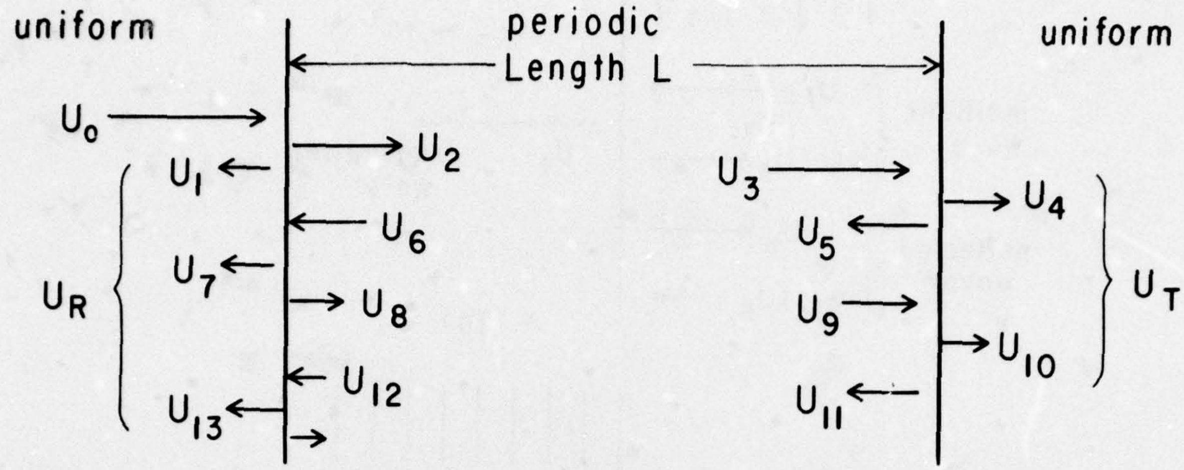

Fig. 8. Diagrams showing multiple reflections inside a periodic waveguide. The relations U_1/U_0, U_2/U_0, U_4/U_3, U_5/U_3, etc. can be found from an analysis as those illustrated in Fig. 6 while the relations U_3/U_2, U_6/U_5, etc. are given by $\exp(\Gamma L)$. The reflection and transmission coefficients are, respectively, given by $R=U_R/U_0$ and $T=U_T/U_0$ by summing U_1, U_7, etc. and U_4, U_{10}, etc.

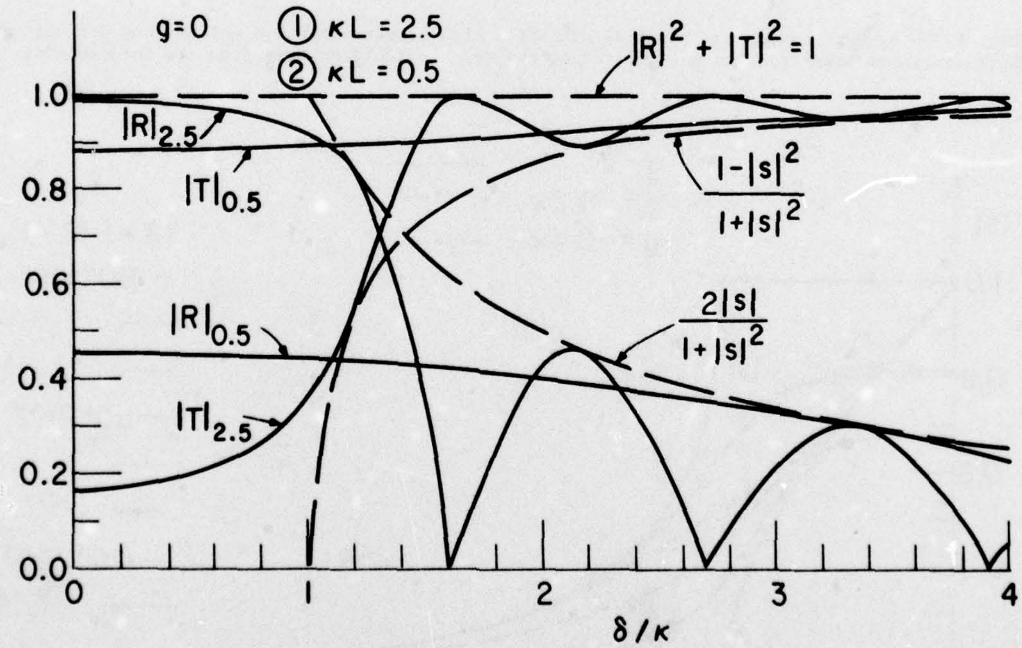

Fig. 9. Curves showing the reflection and transmission coefficients of a lossless Bragg reflector as functions of δ/κ for two values of κL. The dashed lines indicate the ranges within which $|R|$ and $|T|$ lie.

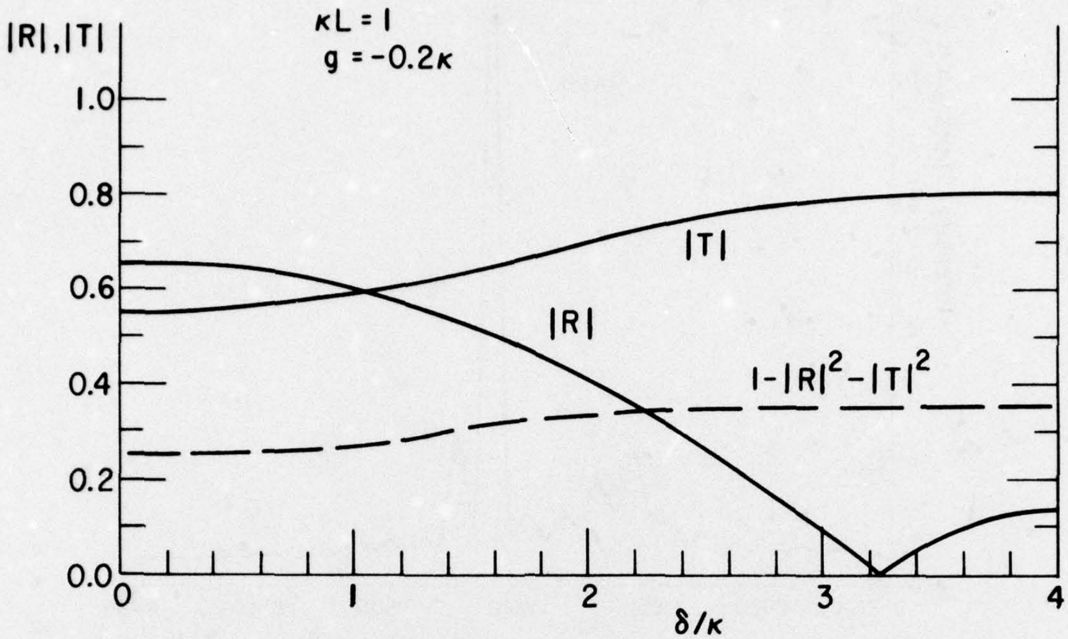

Fig. 10. Curves showing the reflection and transmission coefficients of a lossy Bragg reflector as functions of δ/κ for $\kappa L=1$ and $g/\kappa=-0.2$.

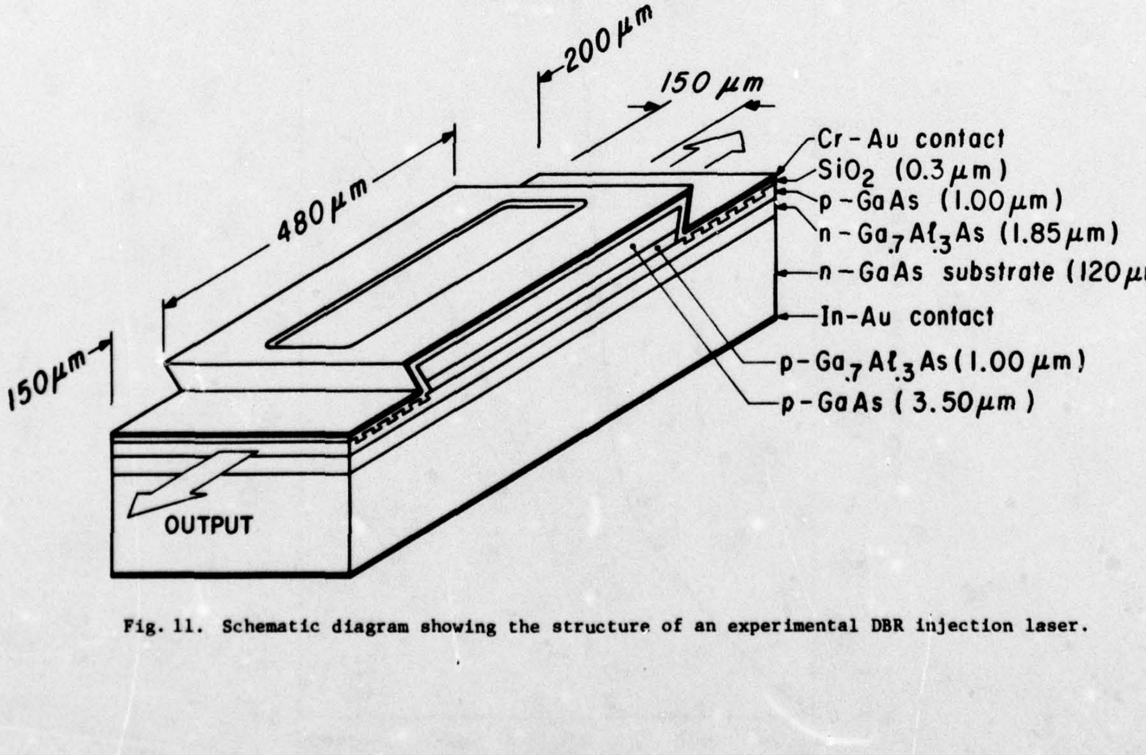

Fig. 11. Schematic diagram showing the structure of an experimental DBR injection laser.

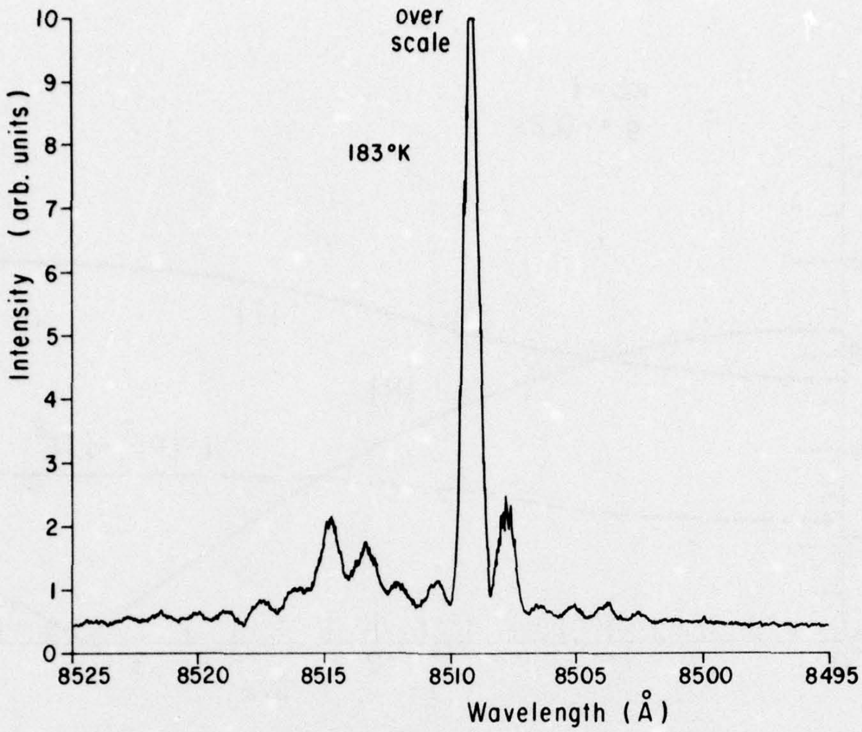

Fig. 12. High resolution spectrum of the DBR laser observed at 183°K. The measured bandwidth of the longitudinal mode at 8509Å is 0.5Å and is resolution limited.

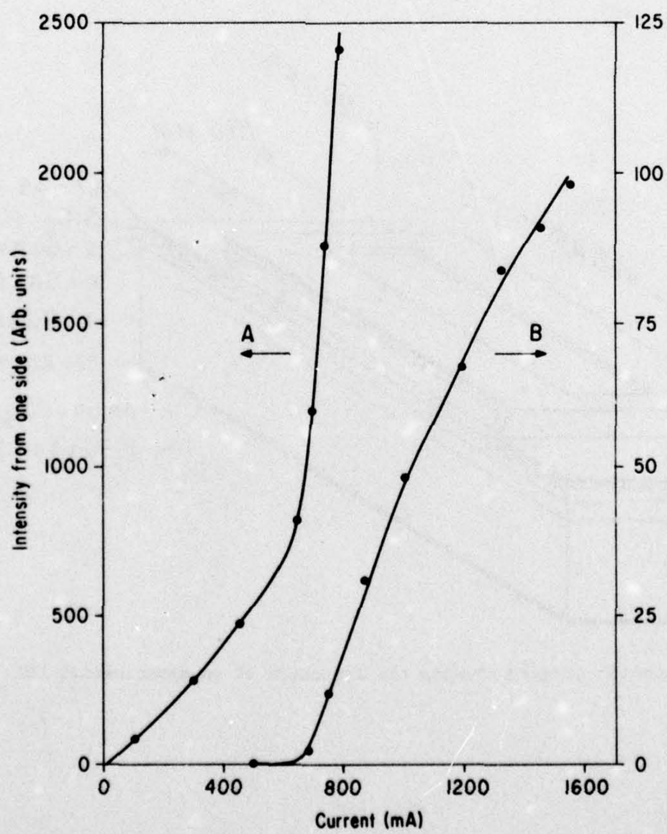

Fig. 13. Output power from one side of the same DBR laser as a function of the injection current. The junction area is about $7.2\times10^{-4}\,cm^2$.

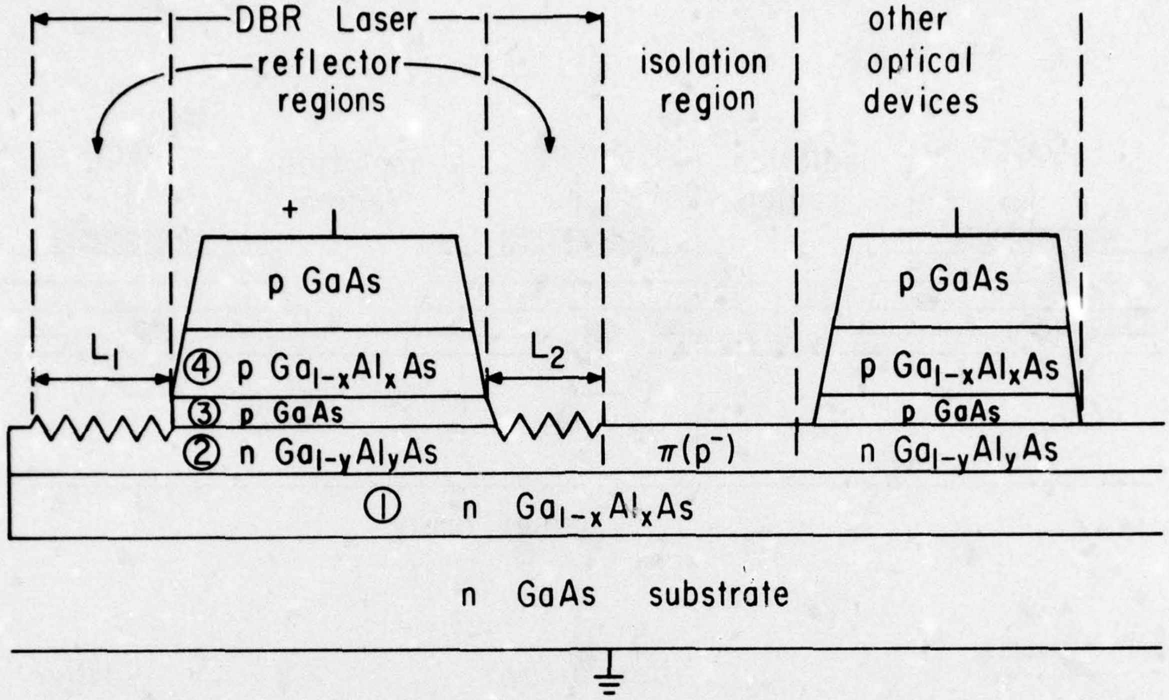

Fig. 14. Schematic diagram showing a DBR laser structure employing separate optical and carrier confinement. The recombination GaAs layer (layer 3) is terminated at the reflectors. The main waveguiding n-$Ga_{1-y}A\ell_yAs$ layer (layer 2) is continued into and beyond the reflector regions.

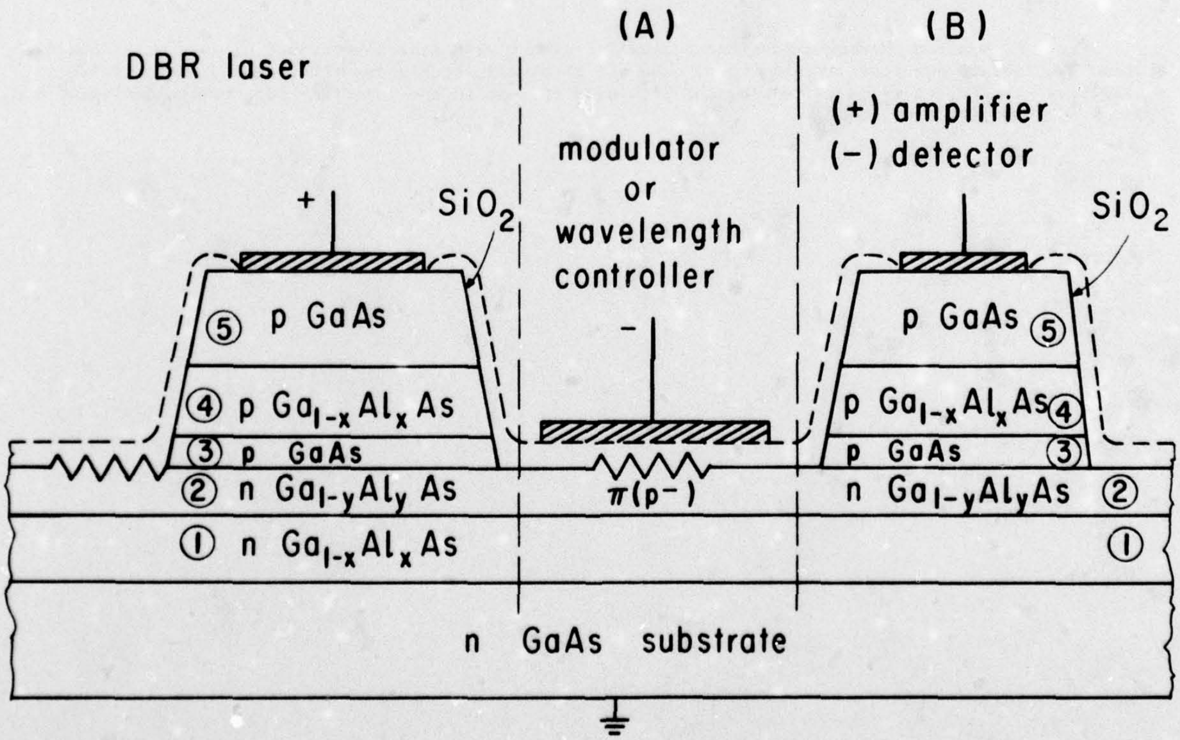

Fig. 15. Schematic diagram showing possibilities of building various optical devices with or on the multi-layer common waveguiding structure.

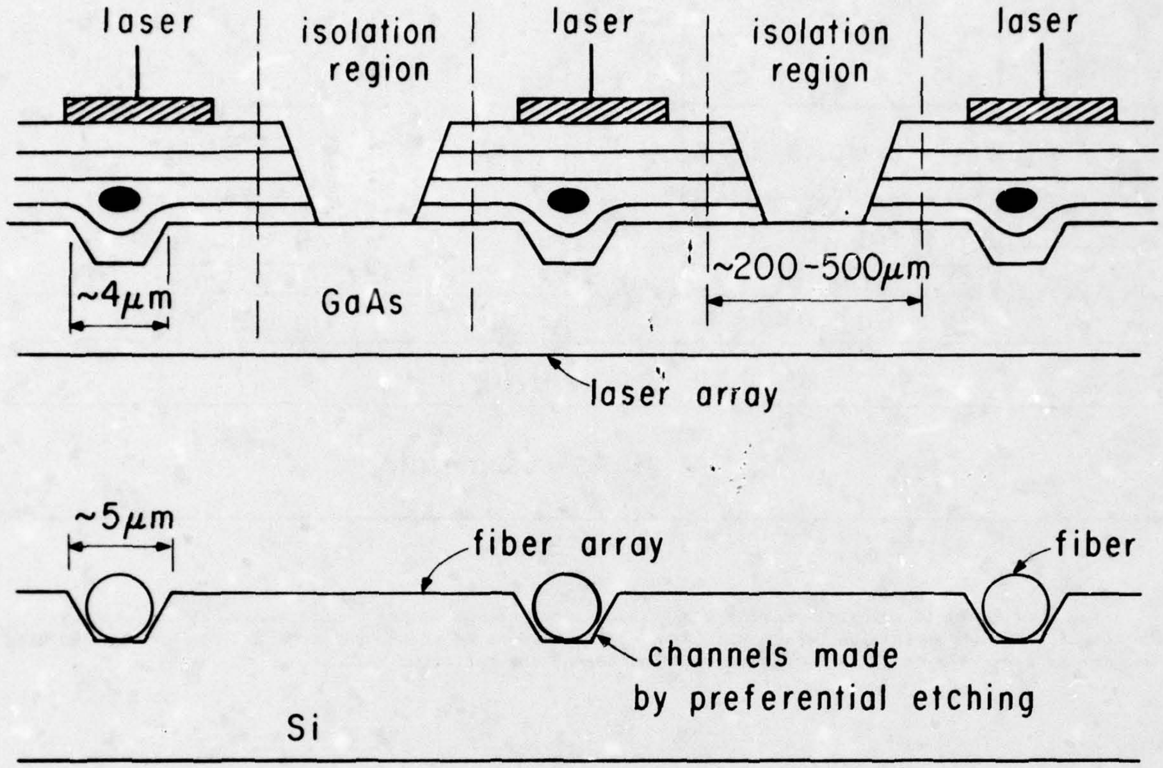

Fig. 16. Diagram showing a possible scheme for direct waveguide-fiber coupling in a multi-channel system. To isolate one laser from another, channels chemically etched into the wafer are a definite possibility. Effective means to confine the injection current to the inverted-ridge waveguide region are under study but yet to be tested.

MULTIMODE OPTICAL SYSTEMS-POWER COUPLING BETWEEN WAVE GUIDES.

M.G.F. Wilson, C.W.Pitt, A.D.de Oliveira
and O. Parriaux,
Department of Electronic and Electrical
Engineering,
University College London,
Torrington Place, London W.C.1.
England.

SUMMARY

Theoretical and experimental results are presented for multimode optical waveguide intersections fabricated by an ion-exchange technique. A simple ray theory is used to derive the power division and mode conversion, both of which are influenced greatly by the geometry in the intersection region.

1. INTRODUCTION

Although there have been rapid advances made during the last few years in the field of integrated optics, the problem of providing efficient coupling between an integrated optical circuit and a fibre still remains largely unsolved. Integrated optics is based almost exclusively on single mode interactions and its full potential can be realised only in conjunction with single mode optical fibre systems. However, for various reasons, interest and effort have been concentrated recently on multimode fibre systems and this has created a demand for new, compact, optical components which can be used to interface the fibre. It is interesting therefore to consider the feasibility of some form of multimode integrated optics.

Certainly the variety of interactions and devices will be severely restricted. Simple functions such as power splitting should not be too difficult to achieve but more sophisticated functions such as switching and modulation may be possible only at the expense of reduced performance. The multimode nature of the problem points strongly to inevitable compromise solutions involving the trading of one performance parameter against another.

The purpose of this paper is to examine the properties of a simple multimode waveguide intersection, fabricated by planar techniques, which might have application as a power splitter/coupler or as a non-coupling waveguide 'crossover' in a multimode communication system.

1.1 BASIC ARRANGEMENT.

The basic arrangement is shown in Fig. 1a. Two wide multimode dielectric waveguides intersect at angle θ. Optical power introduced into arm 1 is transmitted to arms 2 and 4. The proportion of power coupled to arm 4 depends upon the angle θ and the incident mode content in arm 1.

2. THEORY

A simple ray analysis is used to determine the effect of single-mode excitation in arm 1. Each mode in arm 1 is associated with rays oriented at $\pm\alpha$ to the z-axis in the xz plane. For the present case of a highly overmoded guide, *we assume a continous distribution for* α *between zero and* α_c, *the* critical angle. Diffraction effects within the junction are neglected, as are the phase of the rays. The result for multimode excitation can be obtained by summation.

Rays leave the aperture AB at angles $\pm\alpha$ to the z-axis. A fraction p_1 impinge directly on the aperture BC, enter arm 4 with their ray angle reduced to $\theta-\alpha$ and are given by

$$p_1 = \tan\alpha/2\sin\theta \qquad 0 < \alpha < \theta/2$$
$$= \sin(\theta-\alpha)/2\sin\theta\cos\alpha \qquad \theta/2 < \alpha < \theta \tag{1}$$

A fraction of the rays leaving AB impinge directly on the aperture AD and are reflected by the surface DE into arm 4 with their ray angle increased to $\theta+\alpha$. This fraction p_2 reaches its maximum when $\alpha=\alpha_m$, where

$$\tan(\alpha_m+\theta) = \frac{3\tan\theta}{2+\tan\theta\tan\theta/2} \tag{2}$$

and is zero when $\alpha=\alpha_o$, where

$$\tan(\alpha_o+\theta) = 2\sin\theta \tag{3}$$

Thus

$$p_2 = \tan\alpha/2\sin\theta \qquad 0 < \alpha < \alpha_m$$
$$= \frac{\tan\alpha}{2\sin\theta}\left[\frac{2\sin\theta - \tan(\theta+\alpha)}{\tan(\theta+\alpha) - \tan\theta}\right] \qquad \alpha_m < \alpha < \alpha_o \tag{4}$$

The total power P_4 coupled to arm 4 is given by $p_1 + p_2$; the total power in arm 2 is simply $P_2 = 1-P_4$. For small θ, P_4 becomes

$$P_4 = \left.\begin{array}{ll} \alpha/\theta & 0 < \alpha < \theta/2 \\ = 1-\alpha/\theta & \theta/2 < \alpha < \theta \end{array}\right\} \quad (5)$$

The results for P_2 and P_4, for small θ are plotted in Fig. 2a and this shows that a maximum coupling of 50% occurs when the mode angle $\alpha=\theta/2$. It is interesting to examine the mode content of powers P_2 and P_4 and to divide P into components having a particular mode angle α, e.g. P^α Fig. 2b shows that the power transmitted to arm 2 is unchanged in mode, whereas the coupled power P_4 contains equal fractions of power which have been 'upconverted' and 'downconverted' to modes determined by the angles $\theta+\alpha$ and $\theta-\alpha$ respectively.

Radiation, which can occur when the mode angle in arm 1 exceeds $\alpha_c - \theta$ can be taken into account when computing theoretical curves, by using the appropriate Fresnel reflection coefficients. For example, light coupled to arm 2 via the surface DE may suffer two lossy reflections. The length DE is given by

$$\text{length DE} = W\left[1/\tan\theta - 1/\tan(\theta+\alpha)\right] \quad (6)$$

The results shown in Fig. 2. are based on the assumption that the critical angle α_c is nowwhere exceeded.

The simple analysis presented above applies within the range $0<\alpha<\theta$. For $\alpha>\theta$ multiple reflections lead to more complicated expressions. However, numerical results are available for all values of α.

Reduction of cross sectional area in multimode guides can lead to unwanted radiation. The overall effective width of the structure shown in Fig. 1. is 2W except in the region of intersection where it falls to W. Certainly radiation does occur from the length DE (Wilson, M.G.F. et al, 1976) and in an attempt to obviate this one might consider modified geometries. Several modifications have been examined but here we will discuss only one.

Consider the intersection shown in Fig.3. Using a similar analysis to that described above we find that the powers P_2 and P_4 are as shown in Fig. 4a. The peak coupling has been increased to 100% and shifted to $\alpha=\theta$. A breakdown of the mode content, shown in Fig. 4b. shows a more complicated dependence of mode conversion on input ray angles.

3. FABRICATION

Devices have been fabricated by an ion exchange process (Giallorenzi, T.G. et al 1973). Briefly, monovalent sodium ions present in the glass substrate as the metallic oxide, are thermally dissociated from the oxygen and diffuse through the glass into a melt of a metallic salt. The melt consists of a thermally dissociated salt, $AgNO_3$ in our experiments, maintained at a few hundred degrees centigrade, the temperature being sufficiently high to cause thermal diffusion of the monovalent ion Ag^+ into the glass where it replaces the out-diffused Na^+ ion. The larger mass and higher polarisability of the silver ion increase the refractive index of the glass.

The depth profile of the dopant ion concentration below the substrate surface, is controlled by the immersion time and melt temperature. The total number of guided depth-modes produced in a thin film waveguide is dependent only on the maximum temperature that the glass can tolerate without surface damage (250° C) and the immersion time (see Fig. 5). The refractive index depth profile has the form of a half Gaussian / Complementary Error function.

In order to fabricate defined stripe waveguides, the substrate surface was masked with an aluminium film. The stripe pattern was exposed by photolithography and chemical etching of the aluminium film to allow the melt to contact the glass in the desired area. The total number of depth modes in the stripe waveguide depends only on the lifetime of the aluminium mask in the corrosive melt (see Fig. 6).

4. EXPERIMENTAL

4.1 PRELIMINARY RESULTS

Extensive tests were made on intersections of 30 micron wide strip guides of the type shown in Fig.1.

Fabrication was effected by immersion of a microscope slide (refractive index 1.5124), suitably masked with an aluminium film approximately 1 μm thick, into a melt of silver nitrate held at 250° ± 1° for a period of 30 min. The surface refractive index of the guiding layer was measured as 1.593 at the helium-neon wavelength of 0.63 μm. The equivalent-slab-waveguide thickness measured by the prism-coupler technique was 1.8-2.1 μm; the same measurements gave the effective refractive indices for the three modes as $(\beta/k)_{TE_0} = 1.5930$, $(\beta/k)_{TE_1} = 1.5815$, $(\beta/k)_{TE_2} = 1.5725$. These values were used, when $\alpha > \alpha_c - \theta$, to determine the Fresnel reflection coefficients in the modified theory mentioned above.

Helium-neon laser light at $\lambda = 0.63$ μm was injected into one of the three depth modes via a prism (refractive index 1.7) placed over arm 1, and a focusing lens, the latter being necessary to restrict the coupling to a single arm. The laser beam was further oriented in the xz plane so that most power was launched into a particular transverse mode with angle α. The intensity of the light scattered from the waveguide arms was assumed to be proportional to the waveguide power and was determined by two methods. In the first, the scattered light from both output guides was scanned by a photodiode, with a limited aperture of 200 μm, at a distance 1.5mm from the centre of the junction; these precautions being necessary to avoid detecting scattered light from the intersection. In the second method, a photographic exposure was taken and subsequently analysed using a photodensitometer.

Examination of the photographic exposures showed intense scattering in arm 3 along the surface DE, the length of the bright line agreeing very well with the theoretical value given by eqn. 6. The attenuation in arm 4 was considerably greater than in arm 1, since some of the coupled power in arm 4 has been shifted into a higher-order mode with angle $\theta + \alpha$.

The measured variation of power in arms 2 and 4 with angle α was compared with theory and found to be in excellent agreement, due allowance being made for the normal scattering loss of the stripe waveguides. Measurements were made for intersection angles $\theta = 4, 6, 8$ and 12^o.

For one particular case with $\theta = 6^o$ and $\alpha = 3^o$ the loss of the intersection region was estimated to be less than 2.4dB, this being due largely to the scattering from the length DE,(Wilson,M.G.F.et al,1976).

4.2. RECENT RESULTS

An extensive programme of measurements is being carried out on a wide variety of intersections having X, Y or modified X, Y geometries. One object of this programme is to determine the dependence of coupling and mode conversion on the intersection geometry. As was shown in Fig. 2 and 4, significant changes can be effected by relatively small changes in geometry.

Whereas the preliminary experimental work was concerned with shallow waveguides supporting only 3 depth modes, the present programme is concerned with deep guides supporting 30 to 40 depth modes (see Fig 7.) The measured critical angle for width and depth modes is $\alpha_c = 15^o$. A multimode fibre (NA = 0.13) butt-jointed to the polished end face of the stripe guide, excites all modes having ray angles within the range $o < \alpha < 5^o$; the stripe waveguides are therefore not completely 'filled'.

Measured waveguide losses of approximately 1dB/cm are due largely to scattering at the glass/air interface. This loss could be much reduced by suitably cladding the waveguide.

Experimental results for X and modified X intersections are shown in Fig. 8. The intersection loss was too small to be resolved in our experiments but was estimated to be a small faction of a dB.

For large θ the coupling is small and the device operates primarily as a waveguide 'cross-over' having an unwanted cross coupling of less than -30dB. (This figure being limited in the present experiments by the dynamic range of the measuring apparatus).

Similar measurements have been made on Y intersections of the type shown in Fig. 9. Here the coupling is determined by (a) the angle θ, (b) the width ratio W_3/W_2 and (c) the depth of the side arm relative to the depth of the main arm. Results for equi-depth intersections having W_2 = 100 micron, W_3 = 35 micron, supporting 30 to 40 depth modes, are shown in Fig. 10. When excited at port 1, the intersection loss was again estimated to be a small fraction of a dB.

The simple theory described in Section 2 can be modified to treat the case of deep waveguides. Assuming uniform distribution of power with angle α for width and depth modes, the total coupling can be obtained by integration over all α. The result for the Y intersection is shown in Fig. 10. For the X intersection at $\theta = 90^o$, the theoretical radiation loss can be shown to be $- 10 \log (1-4\alpha_m/3\pi)$ dB where $o < \alpha < \alpha_m < \alpha_c$. Thus in the present experiments $\alpha_m = 5^o$ and a loss of 0.16 dB is predicted.

Little attention has yet been directed to the input and output butt joints. It is expected that low loss joints could be fabricated to suitably profiled strip waveguides.

5. CONCLUSIONS

The X intersection has possible application in multimode communication systems as (a) a power divider and (b) a non-coupling waveguide cross-over. The power division is accompanied by mode conversion which might cause difficulties if several devices were operated in series and if the full range of angle α was used. In a single device the performance is determined by the geometry and by the input mode distribution. For fully excited guides the intersection loss can be minimised by appropriate choice of geometry.

The Y intersection could be used in fibre data-highway systems as an access coupler. The coupling is again determined by the geometry and the input mode distribution (in common with other access couplers) the geometry can be reliably reproduced by conventional photo lithographic techniques. The intersection loss is very low, a small fraction of a dB, and the waveguide loss, at present 1dB/cm, could be much reduced by eliminating the waveguide-air interface and introducing a cladding layer.

6. ACKNOWLEDGEMENTS

This work is supported by a Ministry of Defence contract. A NATO Fellowship (A.D. de O) and a Royal Society Fellowship within the European Exchange programme (O.P.) are also gratefully acknowledged.

7. REFERENCES

1. Wilson, M.G.F., Pitt, C.W., Manku R. Oliveira A.D. de and Parriaux O. 1976 "Optical power division in a multimode-waveguide intersection", Electronics Letters, Vol. 12. No. 17. pp 434-435.

2. Giallorenzi, T.G., West, E.J. Kirk, R., Ginther, R. and Andrews, R.A. 1973 "Optical waveguides formed by thermal migration of ions in glass", Appl. Opt., 12, pp 1240-1245.

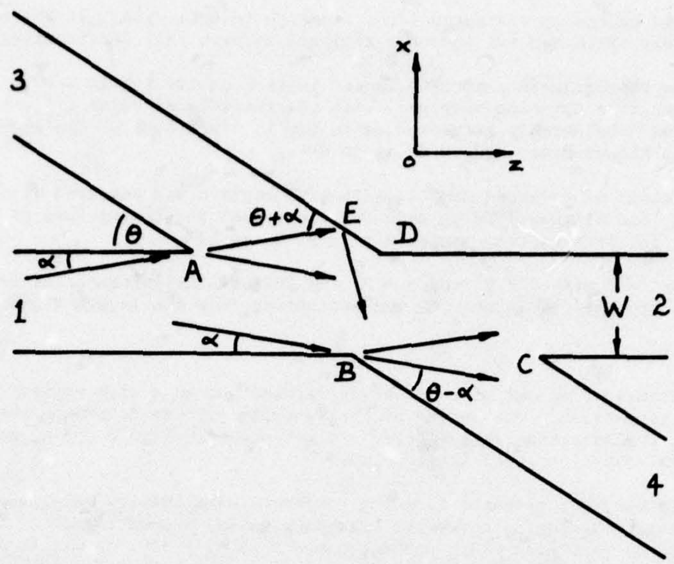

Fig. 1 Plan of simple planar waveguide intersection.

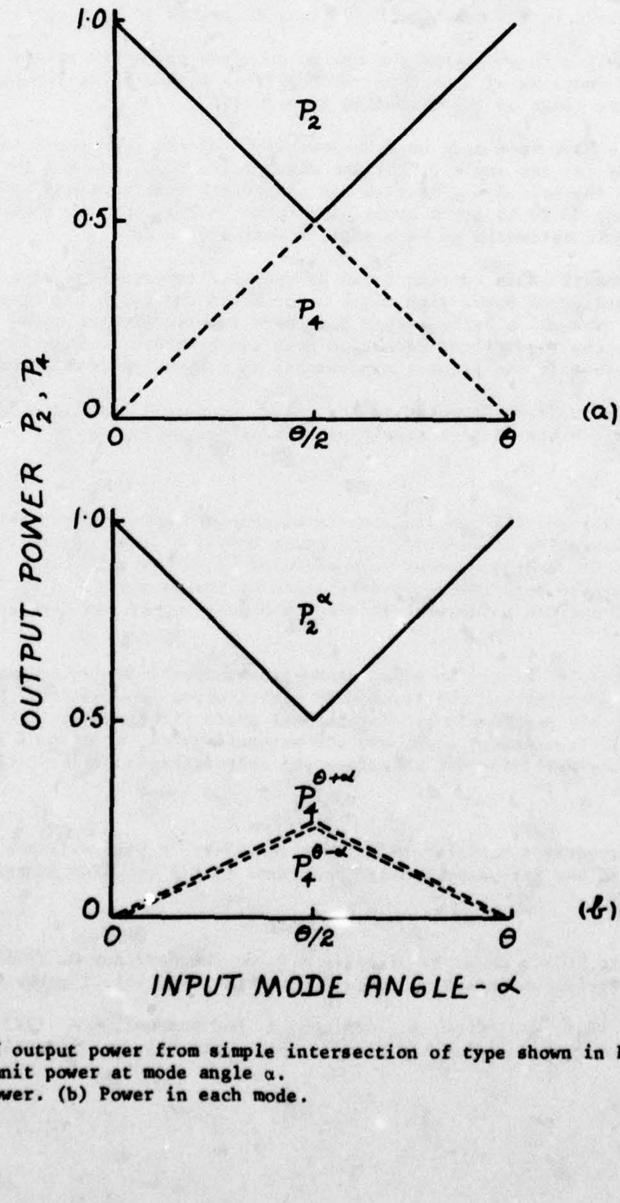

Fig. 2 Variation of output power from simple intersection of type shown in Fig. 1 when excited at input 1 by unit power at mode angle α.
(a) Total power. (b) Power in each mode.

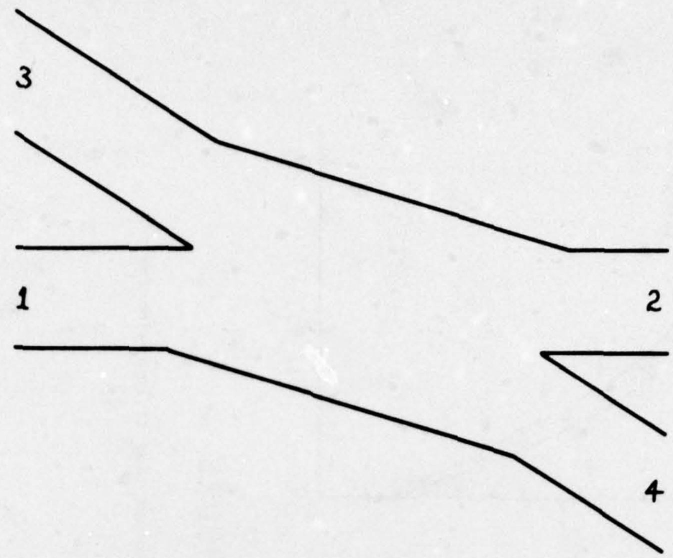

Fig. 3 Plan of modified planar waveguide intersection.

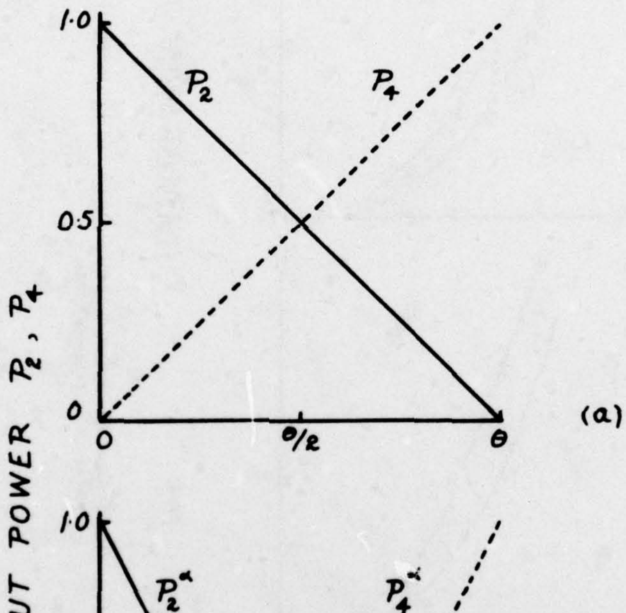

Fig. 4 Variation of output power from modified intersection of type shown in Fig. 3 when excited at input 1 by unit power at mode angle α.

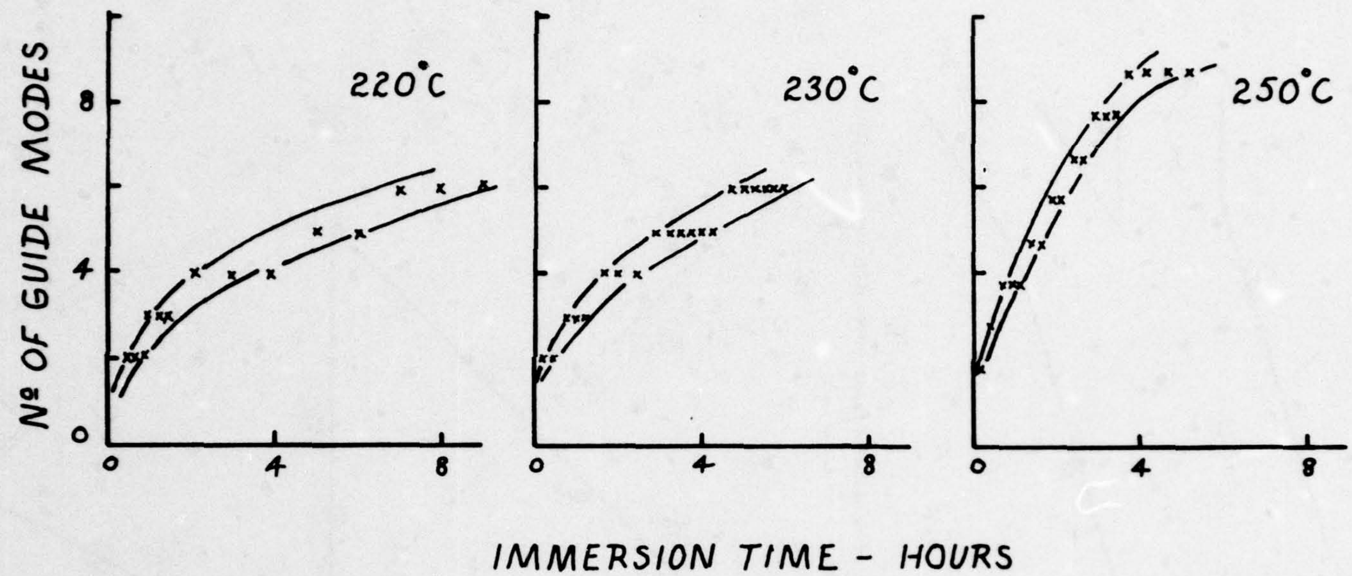

Fig. 5 Number of waveguide modes supported by an ion exchange film against time of immersion for three melt temperatures.

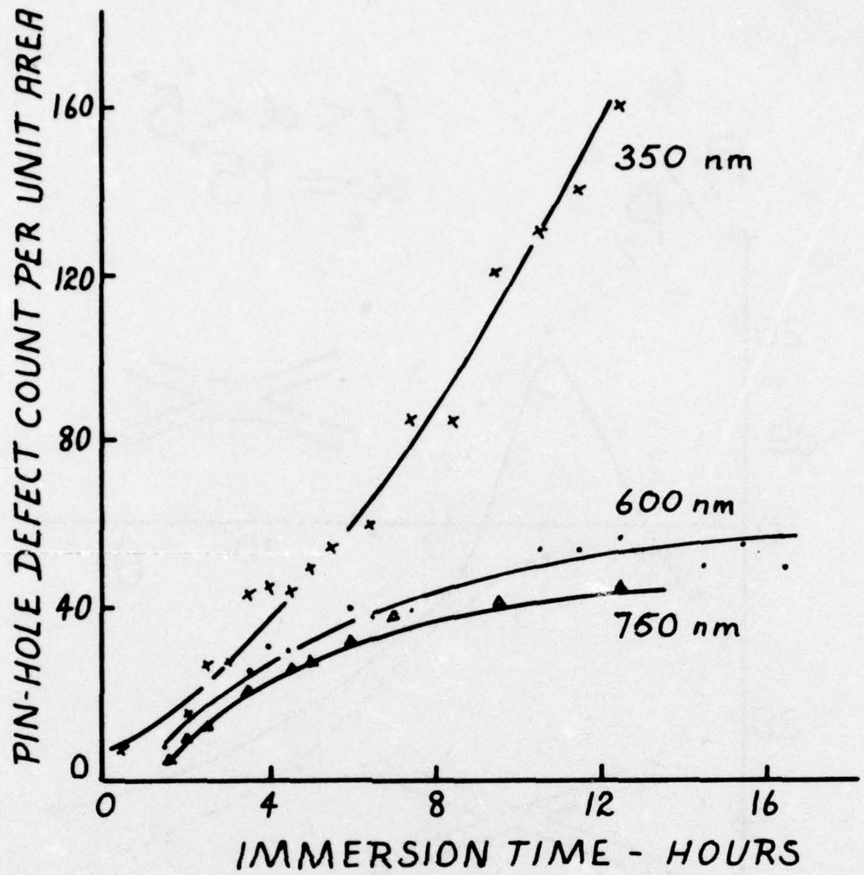

Fig. 6 Density of pinhole defects for 3 aluminium films, against immersion time in melt.

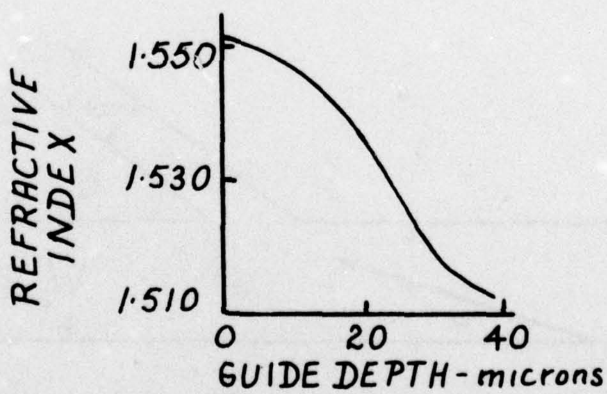

Fig. 7 Refractive-index profile of an ion exchange, (Na:Ag) thin film waveguide supporting 29 modes at $\lambda = 0.6$ micron.
(Data supplied by M. Johnson U.C.L.)

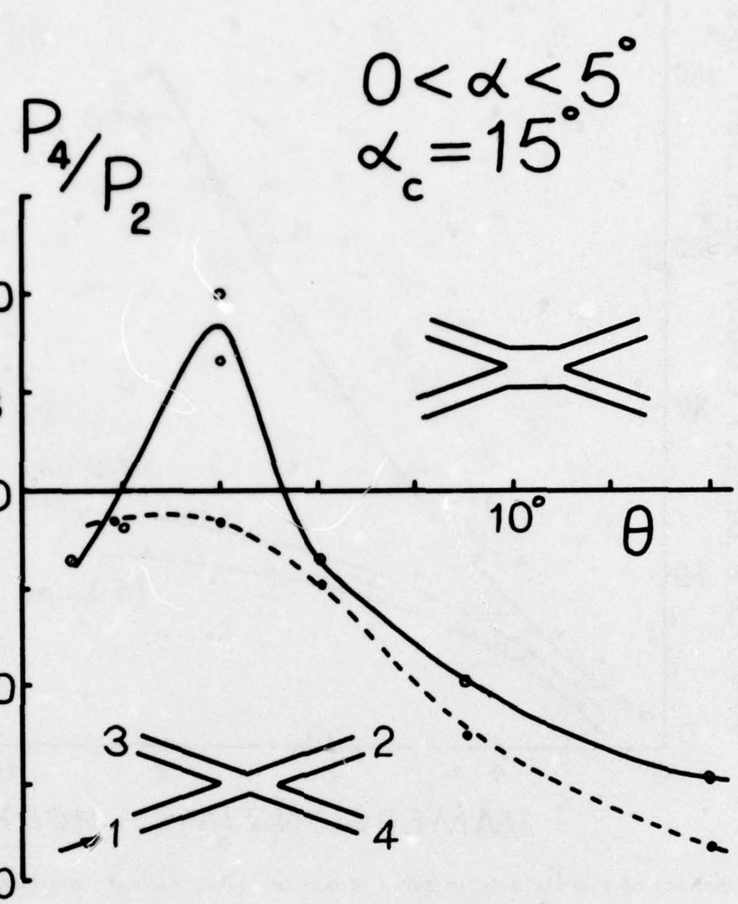

Fig. 8 Experimental values of P_4/P_2 against intersection angle θ for two X structures.

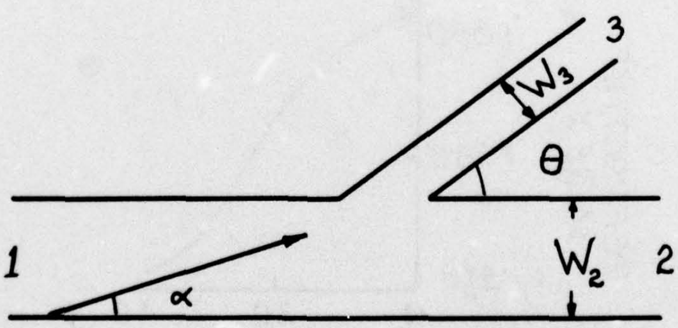

Fig. 9 Plan of Y intersection.

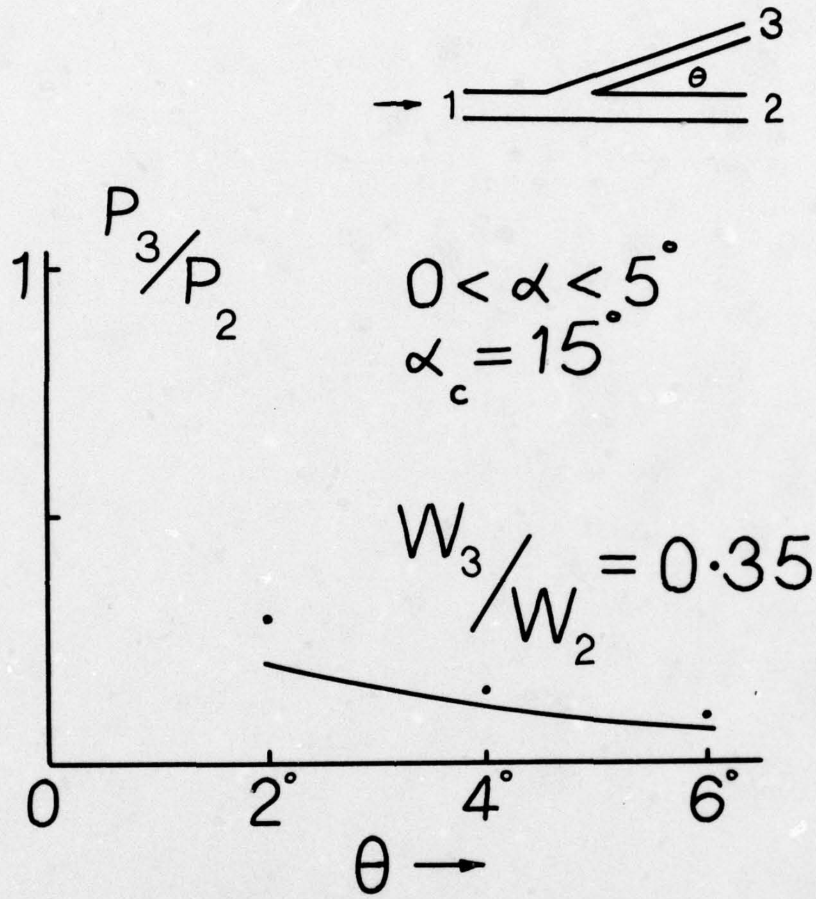

Fig. 10 Output power ratio P_3/P_2 against intersection angle θ for a waveguide width ratio W_3/W_2 = 0.35.
Theoretical ———— Experimental • • • •

LASER-FIBER COUPLING WITH OPTICAL TRANSITION STRUCTURES

by

Gordon L. Mitchell
Department of Electrical Engineering

and

William D. Scott
Department of Mining, Metallurgical, and Ceramic Engineering

University of Washington
Seattle, Washington 98195

ABSTRACT

An optical transition fiber is used to couple between a diode laser and a single-mode fiber. Coupling optimization is detailed in terms of fiber size and refractive index. Fabrication techniques and material-selecting parameters for rectangular fibers used to make the transitions are discussed.

1. INTRODUCTION

Optical components which can be cleaved or cleanly cut are generally well-suited to coupling by butt joints; examples of this sort are glass fibers, semiconductor lasers, and integrated optic components on some crystalline substrates. The loss in butt-joining is in general due to geometrical mismatches. The example of heterojunction laser to circular fiber coupling (illustrated in Figure 1) is inefficient use of butt-joining that can be improved by a geometrical transition between the laser and fiber core. The transition in this case is actually an optical "funnel" which has a rectangular cross section matching the laser active area on one end and a round cross section on the other end.

The transition structure shown in Figure 2 has been formed from a drawn rectangular fiber. The core end cross sections match typical semiconductor laser and single-mode fiber geometries with a transition length of several millimeters. Experimental data indicate coupling greater than 35 percent between the butt joint between a double heterostructure laser and the rounded end of a transition fiber. This (unoptimized) transition coupling efficiency is about five times better than the maximum efficiency obtainable by the direct laser-fiber butt-joining arrangement. Transitions must couple efficiently to conventional round fiber, as well as to the diode laser. Simultaneous optimization of both the laser-transition and transition-round fiber connections is required, however. The maximum overall transition coupling efficiency to single-mode fibers obtained to date has been only 3.5 percent. Improvement of this result involves a careful analysis of the coupling problem in terms of optical field matching at both ends of the transition. Analytical work, presented later in this paper, indicates that total coupling efficiency from the laser to a single-mode round fiber through a transition can be expected to be about 50 percent.

2. COUPLING OPTIMIZATION

The key to efficient coupling between laser and transition and between transition and fiber is matching optical fields. This can be done in the laser-transition case by measuring the near field light intensity distribution for the laser and varying waveguide thickness and numerical aperture to maximize the light-eigenfunction overlap integral. It should be noted that numerical aperture is used only to infer relative fiber indices; for near field coupling situations, a conventional analysis of source divergence angles does not give very useful results.

Laser near field intensity measurements were obtained with the setup shown in Figure 3. A microscope focused onto the laser output facet projects a magnified image of the laser on a masked detector. As the galvanometer-driven mirror moves, the detector responds to different portions of the image. Within the limitations of the optical system, the near field intensity distribution can be accurately plotted. For system adjustments the x-y plotter is replaced with an oscilloscope and scanner speed increased. Typical scans across the active region of the RCA room-temperature CW laser are shown in Figure 4. Since these data were found to fit a Gaussian function well (Figure 5), subsequent computations were based on the Gaussian rather than raw data.

Transition eigenfunctions were calculated from the three-layer symmetric waveguide characteristic equations for the geometry shown in Figure 6.

$$U_2 t_2 - 2\tan^{-1}\frac{K_1}{iK_2} + m\pi = 0 \qquad m = 0,1,2.... \tag{1}$$

where

$$U_i = \frac{2\pi}{\lambda_o}(n_i^2 - n_x^2)^{\frac{1}{2}}$$

$$K_i = \begin{cases} U_i & \text{for TE} \\ \dfrac{U_i}{n_i^2} & \text{for TM} \end{cases}$$

t_2 = core thickness

$n_{1,2}$ = clad, core index

with y components of fields in the various layers of the form

$$A_1 e^{-iU_1 z} \qquad , z < 0$$

$$A_2 \cos\left(U_2 z - \tan^{-1}\frac{K_1}{iK_2}\right) \qquad , 0 < z < t_2 \tag{2}$$

$$A_3 e^{iU_1 z} \qquad , z > t_2$$

if

$$A_2 = iA_1 \frac{\sqrt{K_1^2 - K_2^2}}{K_2}$$

$$A_3 = \frac{iA_1 K_2}{\sqrt{K_1^2 - K_2^2}} \cos\left(U_2 t_2 + \tan^{-1}\frac{K_1}{iK_2}\right)$$

When these fields are fitted to laser output measurements, coupling efficiency can be calculated.

Figure 7 indicates the match for two transition eigenfunctions with calculated coupling efficiency for each. As one might imagine, the best match between laser and transition fiber is obtained when normalized field curves coincide. One measure used (Smith, R. B., 1975) to evaluate the match between these similarly shaped field functions is the width, σ, of each. When the transition σ is equal to the laser σ, coupling efficiency is highest. The optical width of the transition decreases as t_2 decreases, until the guided mode approaches cutoff. At this point the optical width increases (to $\sigma = \infty$ when $t_2 \to 0$). This behavior is shown in Figure 8. If the σ-width for the laser is the dashed line, coupling efficiency would be expected to peak where transition optical width is near this line. Comparing thickness values between Figure 8 and Figure 9, a plot of efficiency indicates that this is true.

One conclusion that can be drawn from Figures 8 and 9 is that, so long as some minimum NA is maintained, efficient coupling between the laser and fiber are possible. Because it is also necessary to efficiently couple the round end of the transition fiber to a conventional single-mode fiber, another factor affects the choice of NA, however. If a 1 x 15 µm rectangular transition is rounded without changing cross section, it produces a five µm core diameter. In order to be a single-mode guide, this fiber must satisfy

$$V = \frac{2\pi}{\lambda_o} a(n_2^2 - n_1^2)^{\frac{1}{2}} < 2.4$$

or

$$N.A. = (n_2^2 - n_1^2)^{1/2} < 0.13$$

for

$$\lambda_0 = 0.83\ \mu m$$

If this end can be coupled to a single-mode fiber with 80 percent efficiency and if the loss within the transition is one dB, the maximum overall coupling efficiency from the laser to the fiber can be as high as 50 percent.

3. FABRICATION TECHNIQUES

The fabrication of the transition (Matsumoto, R. L. K., 1975) is a four-step process: 1) drawing the rectangular core preform; 2) making the core-clad preform; 3) drawing the clad rectangular ribbon; and 4) forming the rounded end of the transition device. The formation of clad rectangular fiber relies on the fact that the aspect ratio of the preform is retained during drawing into a ribbon, while the cross-section dimensions are reduced by factors of 20 to 100. The round end of the transition structure is produced by localized heating and rounding by surface tension forces. The transition structures are quite short (typically one cm), so absorption losses in the transition structures are not critical. This means that any good quality optical glasses with appropriate indicies and fairly close softening points and thermal expansion coefficients may be used.

For initial work, Corning 7740 was used for the cladding material and Corning 7059, for the core. The properties of these glasses are given in Table I. There are several other families of optical glasses available from commercial suppliers which have thermal properties appropriate for transition fabrication. (See Table II.) The optical criteria for selection were developed in the previous section.

The core preform was a 26 x 213 μm ribbon drawn on a fiber-pulling machine from a polished plate 0.5 mm thick and 25 mm wide. One draw produced several hundred meters of core preform. A ten cm length of this ribbon was placed between two strips of cladding glass 0.8 mm thick by 25 mm wide, and the preform sandwich was fused at 780°C in a furnace which was heated and cooled at 14°C/min. The final clad rectangular waveguide was then drawn from this preform in a vertical fiber-drawing apparatus with a resistance furnace at 1100°C. Two or three hundred meters of rectangular waveguide can be made in one draw from a preform. Maintenance of the rectangular cross section during drawing depends on the temperature of the drawing furnace. Figure 10 shows the effect of drawing temperature on waveguide cross section.

The transition is formed by localized heating in the center of a ten to 20 cm piece of rectangular waveguide. Several successful rounding techniques were utilized, ranging from horizontal support and heating with a wooden match to vertical suspension and a platinum heating coil. The vertical system has an advantage, in that the cross section of the round end could be reduced by slight elongation. Figure 11 shows typical small core transition structures.

It was found that the rounding process was controlled by the cladding (Dalgoutte, D. G., 1975). In order to produce round cores, the aspect ratio (width/thickness) of the rectangular core should be one to two times the aspect ratio of the cladding. In one core in which the rectangular core was relatively large (8 x 68 μm), the flow during rounding produced an irregular core cross section, as shown in Figure 12. The flow process during rounding and the shape of the transition core are currently being investigated.

4. EXPERIMENTAL MEASUREMENTS

The first transitions evaluated were made from Corning 7059 and 7740 glasses. Since this combination has a relatively high NA of 0.42, the best coupling can be obtained with a guide thickness of 3.0 μm, as shown in Figure 9. For transitions which had two to three dB internal losses, the best coupling efficiency obtained for diode laser light coupled through a rectangular-to-round transition was -4.6 dB (35 percent). Unfortunately, for reasonable core cross sections the 7059/7740 glass fiber is multimode, and, as a consequence, it does not couple well to single-mode fibers. Measured loss for this laser-transition-single-mode fiber combination is 14 dB (3.5 percent).

Improved transitions have been made from a family of Schott glasses with nearly identical thermal and mechanical properties (Table II). These glasses allow selection of a wide range of fiber NA and should prove to be much more efficient than previously evaluated transitions.

5. ACKNOWLEDGMENT

Fibers used in this study were drawn by Dr. G. Achutaramayya and R. L. K. Matsumoto. Efficiency calculations were done by R. B. Smith. This research was supported by the Naval Electronics Laboratory Center, Defense Advanced Research Projects Agency, and the National Science Foundation.

6. REFERENCES

Dalgoutte,D.G., Mitchell,G.L., Matsumoto,R.L.K., Scott,W.D., August 1, 1975, "Transition Waveguides for Coupling Fibers to Semiconductor Lasers", Applied Physics Letters, 27, p. 125.

Matsumoto,R.L.K., Mitchell,G.L., April 30,1975, Laser Waveguide Coupling Structure Fabrication" AD-A 015318, National Technical Information Service, Springfield, VA, USA, 22151

Smith, R.B., Mitchell,G.L., January 30, 1975, "Analysis of Coupling Efficiency Between Semiconductor Lasers and Dielectric Waveguides, AD-A 022069, National Technical Information Service, Springfield, VA USA 22151

Type	Corning 7040 (cladding) Borosilicate	Corning 7059 (core) Barium-Alumino-Borosilicate
Index of Refraction	1.474	1.530
Coefficient of Thermal Expansion	$35 \times 10^{-7}\ {}^{o}C^{-1}$	$46 \times 10^{-7}\ {}^{o}C^{-1}$
Anneal Point	560°C	635°C
Softening Point	821°C	842°C
Working Point	1252°C	1160°C

Table I. Properties of Glasses Used to Make Transitions

# # # # # # # # # # # #

Schott Glass Type	Index n_D	Expansion Coefficient at -30°C/+70°C	Glass Transition Temperature
SK1	1.61025	$61/71 \times 10^{-7}/{}^{o}C$	650°C
2	1.60738	60/70	654
6	1.61375	62/72	648
8	1.61117	60/70	638
9	1.61405	60/70	641
11	1.56384	65/76	610
12	1.58313	64/75	633
13	1.59181	68/79	620
SSK2	1.62230	62/71	636
3	1.61484	66/76	615
4	1.61765	61/71	639
SSKN5	1.65844	68/79	641

Table II. Optical Glasses

Parameters of interest to fiber designers are listed. This table illustrates the range of refractive index available from glasses having matched mechanical and thermal properties.

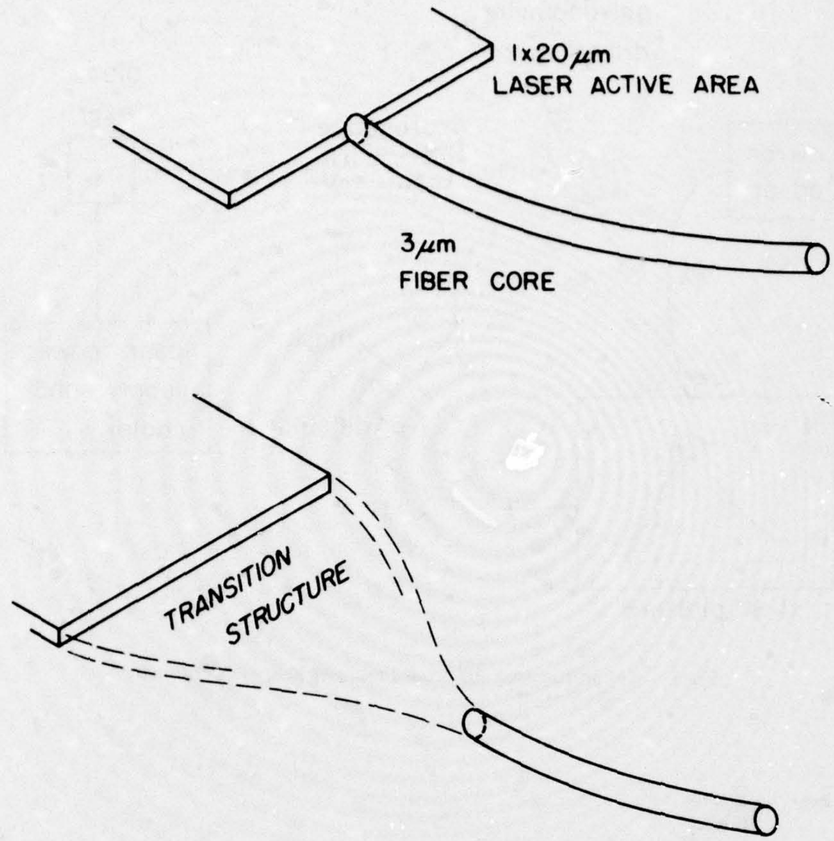

Fig. 1 The rectangular output aperture of a typical double heterostructure laser is poorly matched to the core of a single mode fiber. Coupling between a laser and a fiber can be improved by a transition structure of "optical funnel" shown in the lower drawing

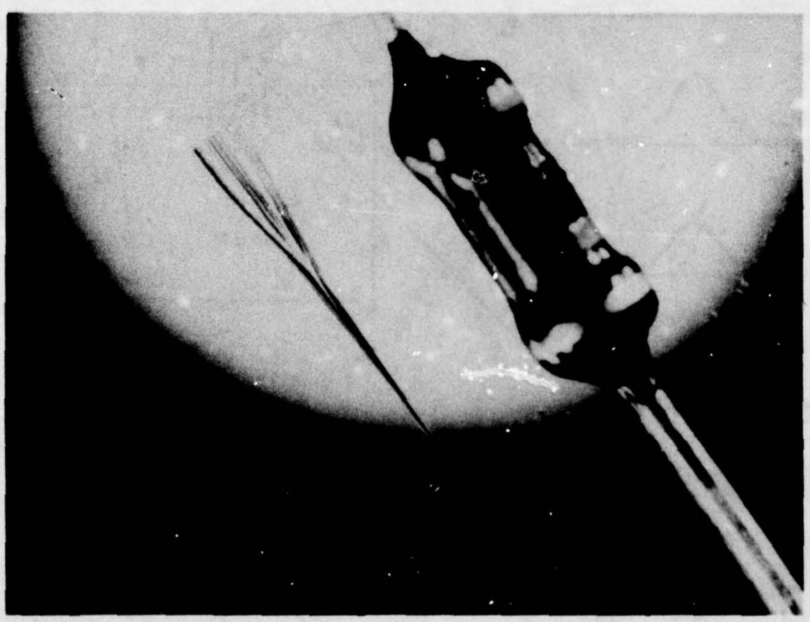

Fig. 2 Transition shown beside a 1/4 watt resistor. The large end of the transition has a rectangular (core and cladding) cross section whereas the small end is circular. This transition was formed by drawing a rectangular preform into a fiber and then rounding the fiber

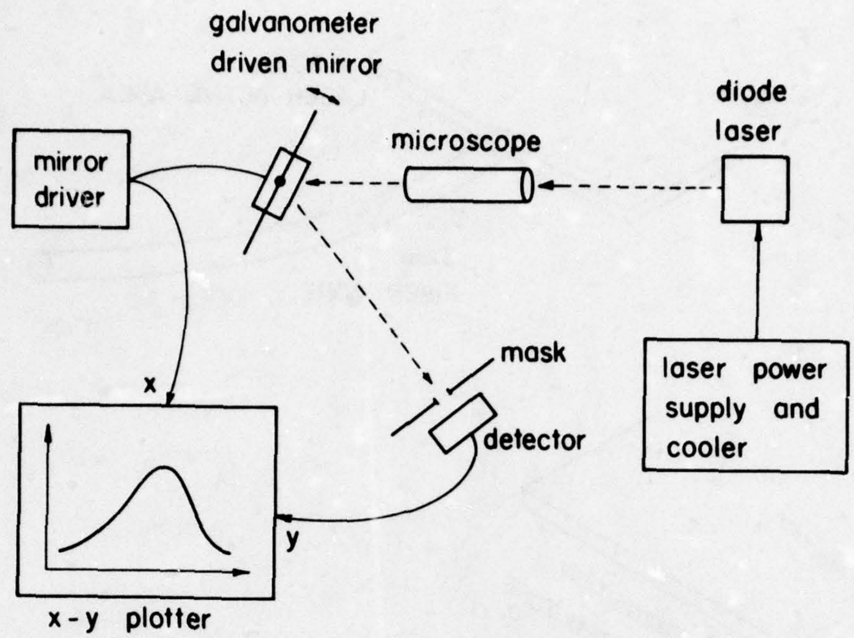

Fig.3 Apparatus used for recording laser near field intensity

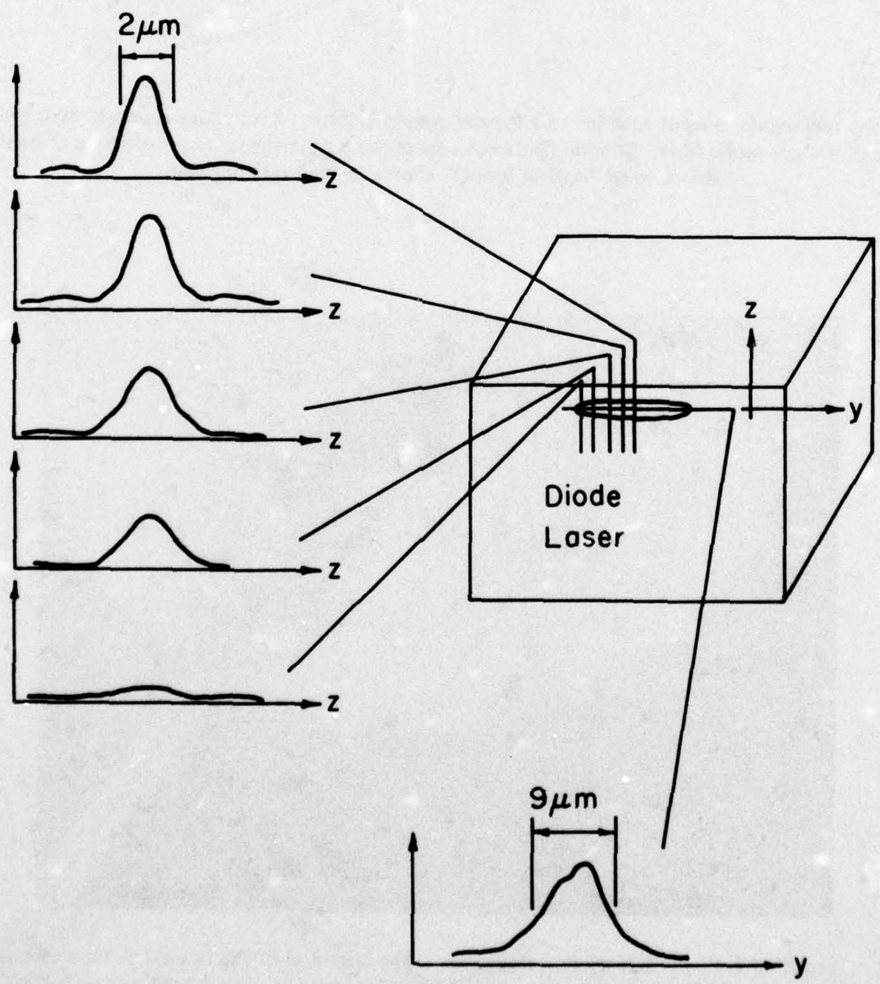

Fig.4 Measured near field intensity for a RCA double heterostructure laser

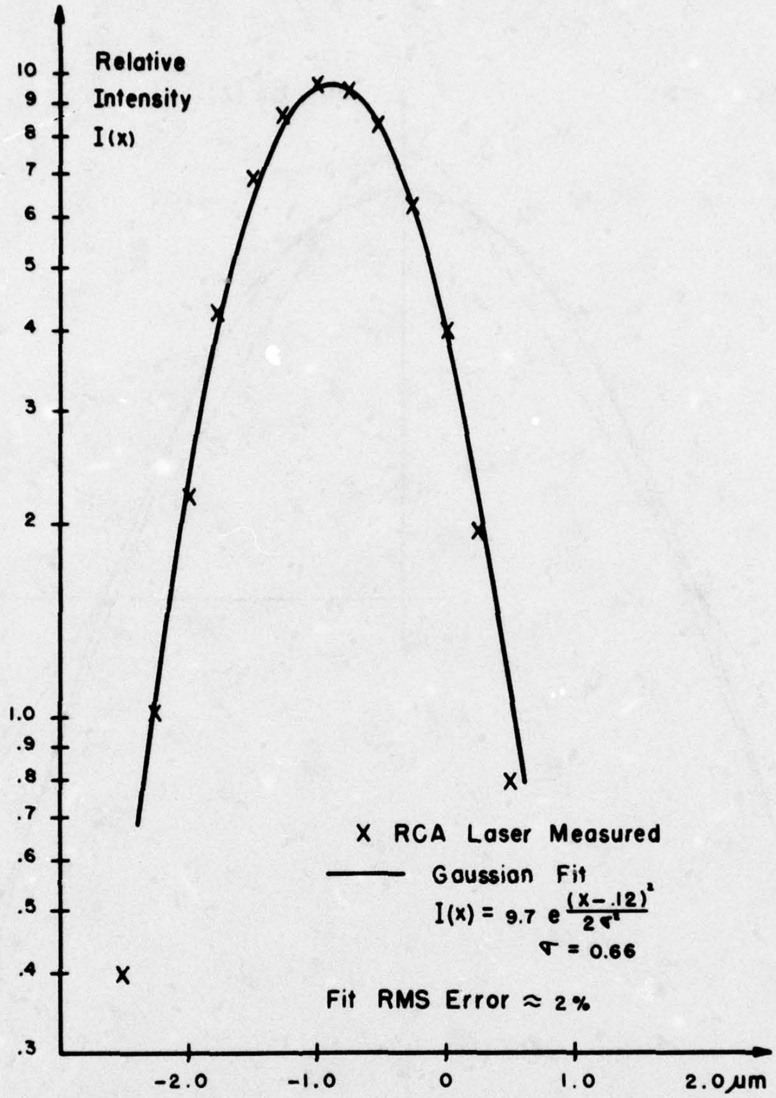

$$I(x) = 9.7\, e^{\frac{(x-.12)^2}{2\sigma^2}}$$

Fig.5 Gaussian fit to data from the upper curve shown in Figure 4. The Gaussian function is used to simplify calculations involving intensity profile data

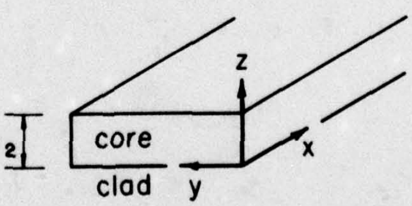

Fig.6 Transition structure presuming infinite thickness clad. For coupling analysis, field variation in the y-direction are not considered

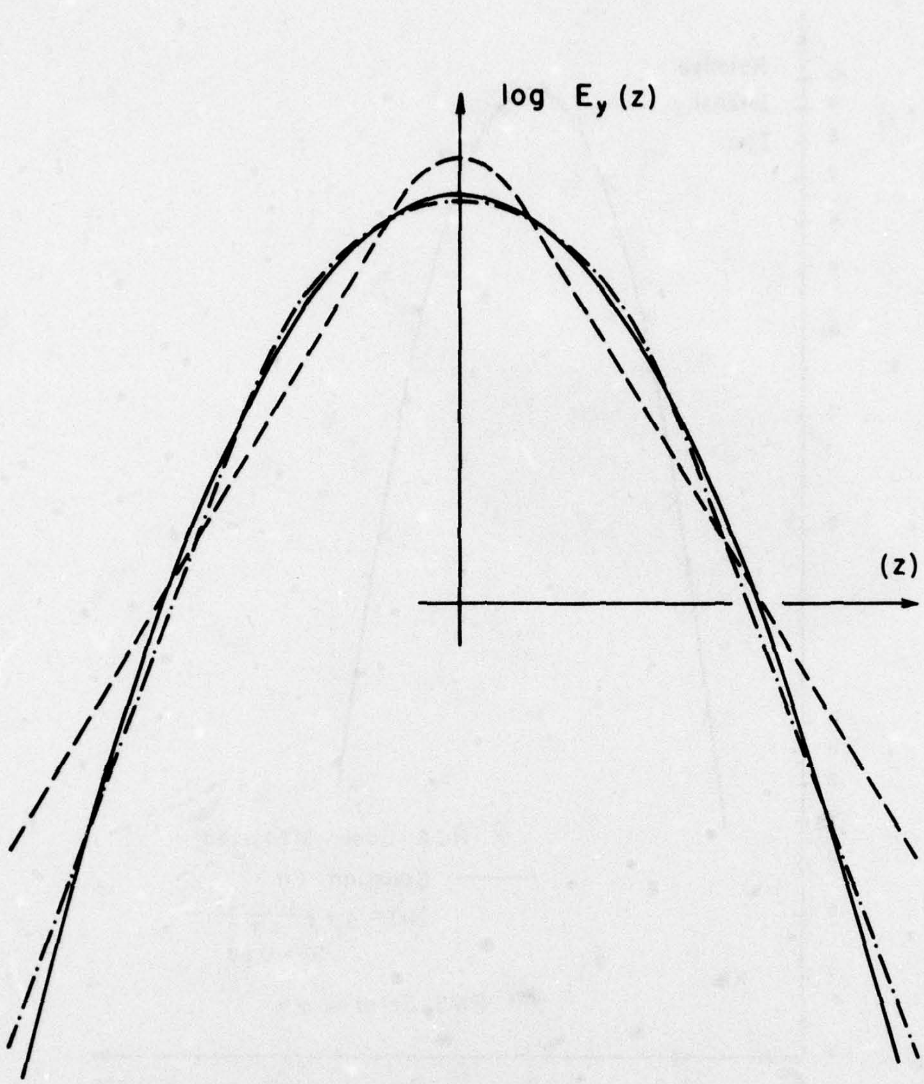

Fig.7 Calculated eigenfunctions for a symmetric waveguide with $\Delta n = 1.0065$.
$t_2 = 1\ \mu m$ (– – –) and $t_2 = 3.4\ \mu m$ (– · – · – ·) compared to a Gaussian with $\alpha = 1$ (——)

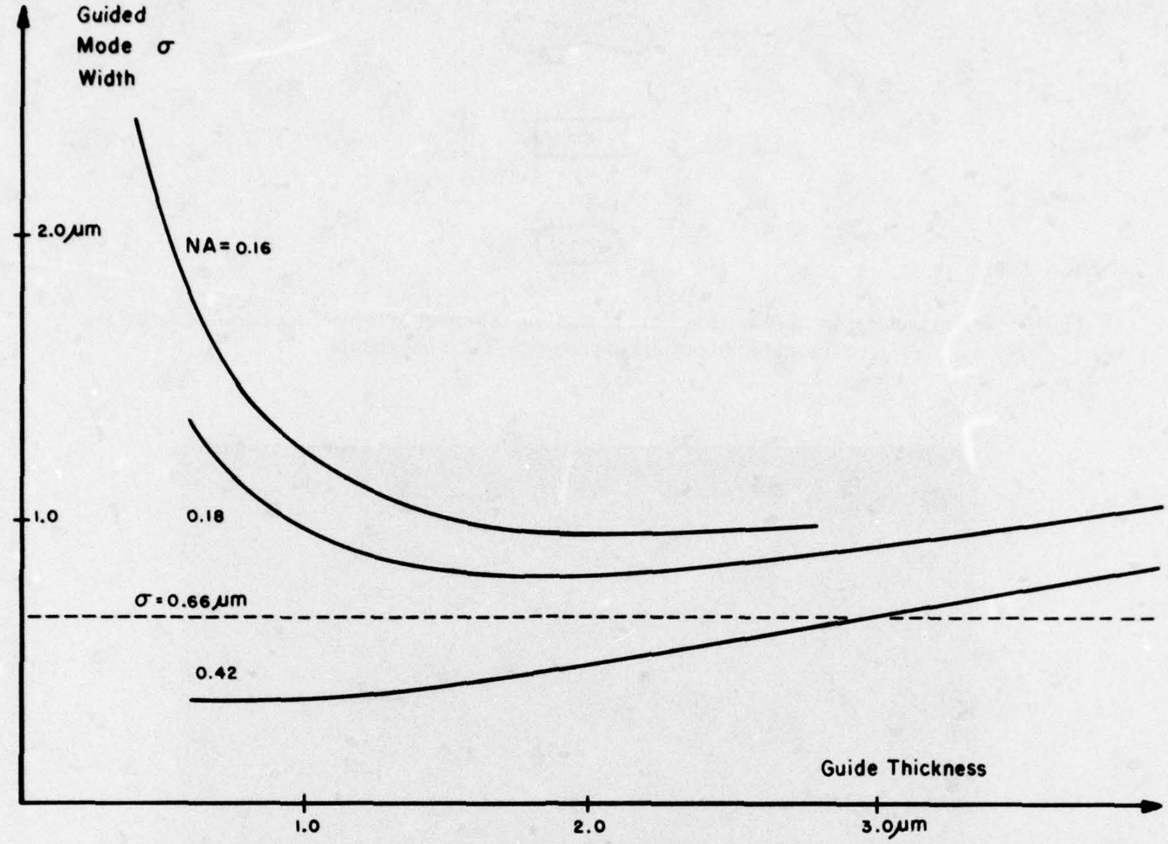

Fig.8 Lowest order guided mode width as a function of waveguide thickness t_2. As t_2 decreases, the guided mode begins to widen as the guide approaches cutoff. For a given laser e.g. $\alpha = 0.66\ \mu m$ best coupling efficiency is expected when the guided mode width approaches the laser width Several values of numerical aperture (NA) are shown

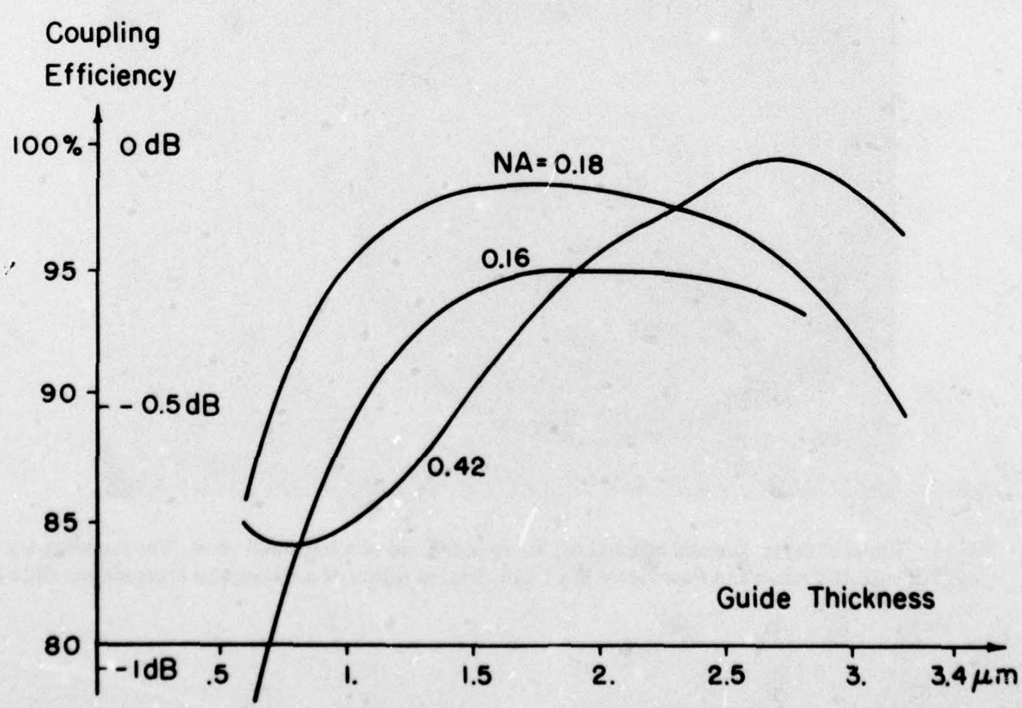

Fig.9 Calculated efficiency from Figure 8

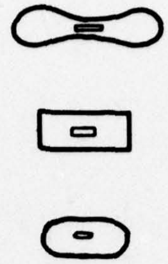

Fig.10 Drawn rectangular fiber cross sections illustrating the effect of furnace temperature variations. From top to bottom low, correct, high temperature

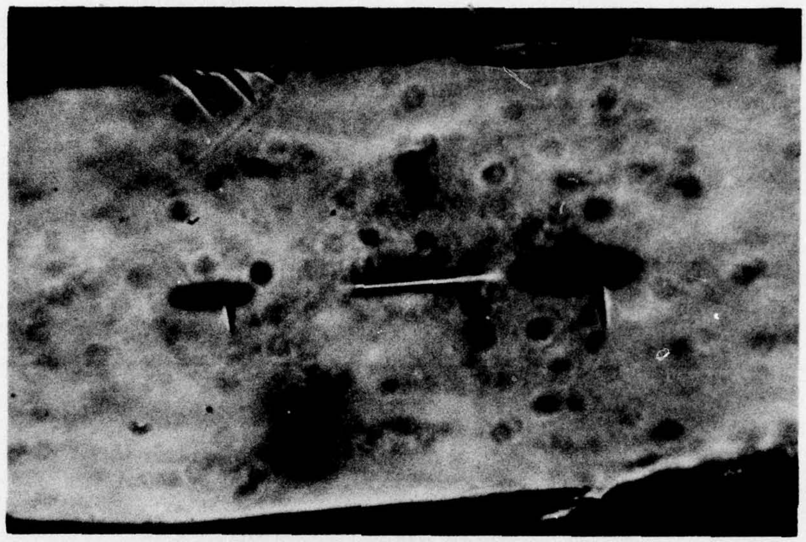

(a)

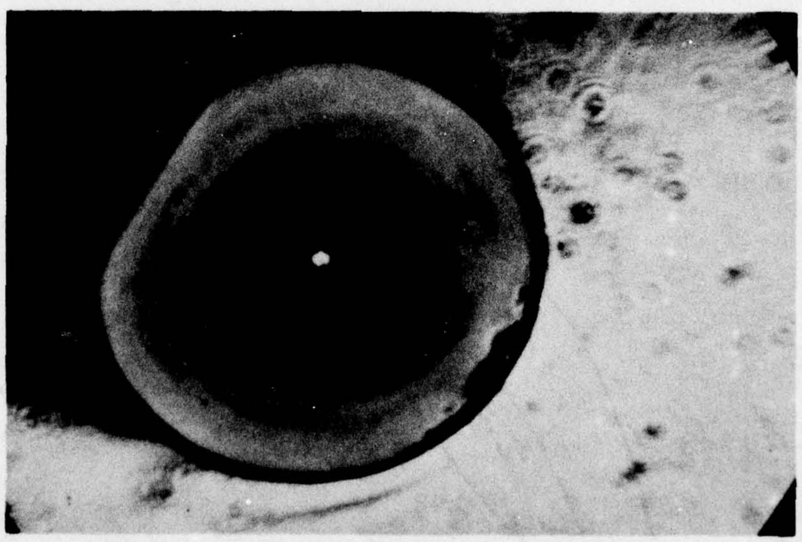

(b)

Fig.11 Views of (a) rectangular end and (b) the rounded end of a transition fiber. The rounding is a result of surface tension and flow forces in a locally heated region of a rectangular cross section fiber

Fig.12 Improperly formed core in the rounded end of a transition fiber

An Integrated Optical Analog-to-Digital Converter

By

D. C. Lewis, Office of Naval Research, Arlington, VA 22217
H. F. Taylor, Naval Electronics Laboratory Center, San Diego, CA 92152

SUMMARY

The purpose of this paper is to analyze an electrooptic A/D converter which promises high speed and is capable of being integrated on one chip. The proposed device utilizes an array of optical branching waveguide modulator channels fa ·icated in a linear electrooptic material. In each channel, light from an appropriate laser source is coupled into a single mode waveguide. The waveguide branches into two parts, in which the light is phase modulated by the input analog voltage signal. Light from the two branches is brought together into another section of single-mode waveguide. The output of this waveguide is detected, and the detector output passed through an electronic analog comparator. The output of the comparator represents one bit in the digital representation of the input signal. Electrode lengths for the modulator channels in an N-bit converter are chosen in the ratio 2^n, n = 0, 1,..., N-1.

It is possible to apply a static (dc) bias voltage to each of the channels to implement various digital coding schemes. The use of a Gray scale for the device output, for example, would eliminate ambiguities which can arise in other binary codes in which two or more bits can change in value simultaneously.

The optical A/D converter would require only N comparators (vs. 2^N for an electronic parallel converter), and each comparator would operate with the same signal level. Furthermore, the use of a repetitively pulsed laser source would provide a "sampling window" to eliminate the need for an electronic sample-hold, or at least relax the drift tolerance for such a device.

The electronic comparator is a limiting factor in determining the speed with which the device could operate. Present commercial comparators are limited to about 400 MHz, but considerable improvement using newer, fast logic can be anticipated. The number of bits of precision is limited by noise-in-signal at the photodetector and comparator overdrive requirements.

The high speed and low power requirements of the proposed A/D converter make it attractive for many military applications including high resolution radar and wideband receivers. Hence, the development of integrated optical signal processing components such as the A/D converter could have a significant impact on the capability of future military systems.

INTRODUCTION

Analog-to-digital (A/D) converters (Hoeschele, D. F., 1968; Sheingold, D. H., and Ferrero, R. A., 1972) are widely used to translate sensor measurements into the digital language of computing, information processing, and control systems. In some instances, the performance of military equipment is limited by the speed with which present A/D converters can function. Guided-wave electrooptic devices provide an alternative to conventional techniques, with the potential for high-speed operation (Wright, S. et. al. 1974; Taylor, H. F., 1975). This paper analyzes an electrooptic technique for A/D conversion based on an interferometric intensity modulator, and indicates the advantages in comparison with present or alternative methods. Potential military applications are also discussed.

DEVICE DESCRIPTION AND ANALYSIS

The basic circuit of the electrooptic A/D converter is shown in Fig. 1. The circuit consists of a branching waveguide interferometric modulator, a laser, a photodetector, and an electronic comparator. The A/D converter makes use of the fact that the output of the optical intensity modulator, the operation of which is based on a linear electrooptic phase retardation (Kaminow, I. P., 1975), varies in a periodic fashion as a function of an applied voltage. Similarly, each bit in the binary representation of an analog quantity is a periodic function of the value of that quantity.

A schematic diagram of the A/D converter is given in Fig. 2. Basically, it consists of an array of circuits, such as that shown in Fig. 1, in which the length of the electrodes on each modulator is tailored such that a binary code is generated as the applied analog voltage varies. The waveguide modulators (Martin, W. E., 1975; Ohmachi, Y. and Noda, J., 1975) are fabricated in a single crystal substrate of a linear (Pockels) electrooptic material. Each waveguide, which can support one guided mode, is excited by linearly polarized light from a CW laser. A signal voltage V is applied across each waveguide.

The electrooptic interaction length L_n for the n'th waveguide, as determined by the length of the signal electrodes, is given by

$$L_n = 2^{n-1}L_1, \; n = 1, 2, 3, \ldots$$

The phase of the light in one branch is retarded with respect to the other branch by an amount $\Delta\Gamma_n$ given by

$$\Delta\Gamma_n = 2^{n-1}KL_1V.$$

The value of the constant K is determined by the electrooptic coefficients of the material, the waveguide parameters, and the electrode spacing. The intensity of light emerging from the nth waveguide modulator is given by

$$I_n = A_n \cos^2(\Delta\Gamma_n/2 + \psi_n) \quad (1)$$

where Ψ_n is a static phase shift and A_n is the modulation amplitude.

The light emerging from each of the modulators is detected and amplified, and a binary representation of V is obtained by electronically comparing the intensity I_n with a threshold I_{nt}, and generating a "one" or "zero" for the n'th bit based on the outcome of the comparison. For example, an offset binary code for a bipolar signal is obtained if $\psi_n = \pi/4$ for each n by generating a "one" for the first bit if $I_{1t} > I_1$ and a "one" for the n'th bit, for the n'th bit, n = 2, 3,... if $I_n > I_{nt}$. The required values for the ψ_n's are obtained by applying a dc voltage V_{Dn} to a short section of waveguide in each modulator. The intensity I_n and the corresponding offset binary code are plotted as a function of V in Fig. 3 for a device with 3-bit precision. It is evident from Fig. 3 that, as V changes, it is possible for two or even all three bits to change in value simultaneously. Significant errors in the conversion are most likely to occur for values of V near these intensity crossover points. One way to avoid this problem is to use a Gray scale instead of a pure binary code. The only change from the offset binary device is in values for the static phase shifts (ψ_n's). Variations in the intensity components I_n for a four-bit Gray-scale converter are illustrated in Fig. 4. Since the value of only one bit changes for small variations in V, the probability of error in one of the most significant bits is greatly reduced. Furthermore, in a device of given length, one more bit of precision can be obtined with the Gray code than with the offset binary code.

The number of bits of precision, N, which can be obtained with a Gray code is related to the length of the waveguides according to

$$N = \log_2(\ell/\ell_\pi) + 2, \quad (2)$$

where ℓ_π is the minimum length required for a pi-radian electrooptic phase retardation. The formula

$$\ell_\pi = \frac{dV}{2V_m}, \quad (3)$$

relates ℓ_π to the electrode spacing d, the half-wave voltage V of the material and the maximum applied voltage V_m. (It is assumed that V varies between $\pm V_m$.) The factor of 2 in that equation arises from the fact that V is applied to both branches of the modulator structure. As a numerical example, the electrooptic material is assumed to be $LiNbO_3$, oriented with the c-axis in the device plane and perpendicular to the waveguide axes (see Fig. 1). The value of V in that material using the r_{33} coefficient, is 2000 V at 6328 A for an applied field parallel to the c-axis and propagation perpendicular to that axis. If V_m = 4.7 volts and d = 5 μm, corresponding to an average field strength of 9600 V/cm between the electrodes, the value for ℓ_π is estimated from (3) to be 1.08 mm. According to (2) the length of a 6-bit A/D converter with these parameters is 1.7 cm.

The electrical power required to drive the modulator is an important parameter of the device. This can be calculated from the formula

$$P = \frac{\pi}{2} CV_m^2B \quad (4)$$

where B is the modulation bandwidth and C is the electrode capacitance. If the widths of the electrodes and the spacing between them are of equal magnitude, the capacitance is approximately given by

$$C = (\varepsilon_o + \varepsilon) L$$

where L is the total electrode length, in this case given by

$$L = 2\sum_{n=1}^{N} L_n$$

But $L_n = 2^{n-N} \ell$, where ℓ is the total length of the interferometric sections of the modulators, so evaluating the sum yields

$$L \sim 4\ell$$

But $\epsilon_o = 8.9 \times 10^{-14}$ f/cm, and, in lithium niobate, $\epsilon \sim 40\epsilon_o$, so if $\ell = 1.7$ cm, then

$$C = 25 \text{ pf}$$

For a signal bandwidth of 500 MHz (corresponding to a Nyquist sampling rate of 1 GHz) the power calculated from these equations, assuming $V_m = 4.7$, is 500 mW.

In terms of overall power dissipation, the optical device offers a substantial improvement over conventional A/D converters, primarily because of the reduction in prime power required to drive the comparators. For conversion at a 1-Gb/s sampling rate, it is estimated that the power dissipation is of the order of 0.5 W per comparator. The 64 comparators in an electronic parallel A/D would therefore dissipate 32 watts, versus only 3 watts for the optical device. Assuming 0.3 watt for a laser source, 0.5 watt for the electro-optic portion of the device, and 0.6 watt each for the 6 photodetector/amplifiers raises the total to only 7.5 watts for the optical device.

A limiting factor in implementing fast A/D converters, either electronic or electrooptic, is the speed of the analog comparator. Present commercial devices operate at a rate of less than 4×10^8 comparisons per second, although continuing improvements in high-speed logic devices encourage us to anticipate faster comparators in the near future. Ultimately, the best solution might be to integrate the comparator by fabricating it in the form of an integrated optical logic device on the same electro-optic substrate as the waveguide modulators.

ALTERNATIVE TECHNIQUES FOR A/D CONVERSION

The most common method for performing high-speed (> 25 megawords/second) A/D conversion is to compare the input voltage V with reference voltages which correspond to different levels in the digital representation of V. This is referred to as the "parallel" method, since all the comparisons are done simultaneously. A three-bit parallel converter is illustrated in Fig. 5. The reference voltages, which are set by a resistor chain, are each supplied as an input to an analog comparator. The input voltage is supplied through a second resistor chain as the other input to each comparator. The high speed results from the fact that all of the comparisons are done in parallel, but a large number of comparators (2^N-1 for an N-bit converter) are needed to accomplish this. Furthermore, electronic logic elements are required to convert the comparator outputs to a binary representation of V.

Open-loop successive approximation is a technique for "pipelining" the conversion process by computing the most significant bits first and determining the reference voltage for each subsequent bit from the comparator outputs for previously computed bits. A time delay is required to allow for the computation of the most significant bits before V is applied to the comparators which compute less significant bits. Only N comparators are required with this method, but the synchronization problems are more severe and the time delay between input and output is considerably greater than with the completely parallel approach.

The fastest devices which are commercially available at the present time perform 10^8 conversions/second with 6-8 bits of precision (Rimmel, A. W., 1975). A device marketed by TRW utilizes two interleaved converters, each of which operates at 5×10^7 conversions/second and utilizes both parallel and serial logic with ECL comparators. Also, Biomation and Phoenix supply converters with conversion rates of 10^8 words/sec; both use parallel conversion schemes. The Biomation device uses TTL comparators while the Phoenix device employs ECL. Aeroflex has developed an 800 MW/sec 6 bit A/D converter. The Aeroflex system uses an interleaved parallel conversion scheme and ECL logic; the system requires roughly 800 watts of prime power.

Several companies have proposed or are developing devices with conversion rates in excess of 10^8/second. Parallel and successive-approximation schemes using ECL comparators are among the most common approaches. TRW is scheduled to deliver a developmental 5-bit, 400-megaword/second (Mw/s) device to an Air Force sponsor in the near future. A novel technique in which the applied voltage V deflects an electron beam in an electron-bombarded semiconductor device is being pursued by the Watkins-Johnson Company. An electro-optic device which uses a phase grating to deflect a guided light beam has been demonstrated at University College, London (Wright, S. et. al., 1974). That device is capable of operating at high speeds, but is inherently limited to only 3 bits of precision. NRL (Giallorenzi, T. G., 1976) has proposed an attractive electrooptic A/D conversion circuit which should be capable of high speed at low powers; however, it will be difficult to integrate that circuit onto one chip. Another novel approach to A/D conversion would utilize superconducting Josephson-junction arrays.

COMPARISON OF ELECTRO-OPTIC A/D CONVERTER WITH PRESENT TECHNIQUES

The electro-optic A/D converter can potentially provide several advantages in comparison with conventional fast parallel A/D converters. First, the number of comparators would be dramatically reduced, from 2^N to N, for an N-bit converter (e.g., from 64 to 6 for a 6-bit converter). This would substantially reduce the electrical power drain of the unit (~200mW each for commercial 200-MHz ECL comparators) and would greatly simplify the timing problems which occur in electronic converters because of the large number of comparators.

Another advantage of the optical device is that the use of a repetitively pulsed (mode locked) laser source could eliminate the need for a sample-and-hold device. The function of a sample-and-hold in an A/D converter is to sample the signal at fixed time intervals and maintain the value of the sampled signal during the time a conversion takes place. The output of the sample-and-hold is the voltage input to the device which actually performs the conversion. The drift of the sample-and-hold must be less than $2^{-(N+1)}$ times the full voltage swing to obtain N bits of precision, and the jitter in the sampling clock must be less than $2^{-(N+1)}$ times the conversion period; e.g., 8 ps for a 1-gigaword/second (Gw/s), 6-bit converter. With a short optical pulse, the width of the pulse would provide a time window for performing a sampling operation. Techniques to provide mode locked pulse widths as short as 5 ps using compact solid state lasers are being studied (Hill, K. O., et al, 1976; Tsukada, T. and Tang, C. L., 1976; Washio, K. et al, 1976). It has been calculated that a 100 ps pulse width would be short enough for a 1-Gigaword/second, 6 bit converter and the pulse repetition interval for these lasers should be stable enough to satisfy the requirements indicated above. Additional work will be needed to perfect mode-locked lasers suitable for use with the optical A/D converter.

A final feature of the optical A/D converter is that the output can be recorded directly upon photographic film. This would make it possible to collect, digitize, and make a permanent record of data at a very high rate. The data could then be processed later at more convenient speeds.

A summary of the critical characteristics of the electrooptic A/D converter is presented in Table 1.

TABLE 1 HIGH-SPEED ELECTRO-OPTIC A/D CONVERTER--SUMMARY

Present method: High-speed electronic logic

Elements of integrated optics device:

- Array of modulators on electro-optic substrate
- Injection laser source
- Sample-and-hold interface
- Avalanche photodiode detectors
- Electronic comparators.

Potential advantages of integrated optics device:

- Fewer comparators (N versus 2^N)
- No sample-and-hold with pulsed light source
- Lower electrical power dissipation
- Optical output can be recorded directly on film.

Disadvantages:

- Development needed
- Not cost competitive at low (25-Mw/s) conversion rates
- Limited to 8 bits of precision for parallel operation

Performance-limiting factors:

- Present comparators operate at 400 MHz
- Speed of avalanche photodiodes limited to ~ 1 GHz.

Potential performance:

- Near-term (1-3 years) 400 megaword/second, 6 bits
- Intermediate term (3-6 years) 1 gigaword/second, 6-8 bits.

Major technology development needed:

- Multichannel modulator fabrication
- Mode-locked lasers
- Laser-modulator coupling techniques
- Faster comparators

POTENTIAL APPLICATIONS

A number of military systems have been identified as potential application areas for an electrooptic A/D converter (Dillard, G. M., et. al., 1977). These are for the most part systems in which signal processing performance is limited by the speed of present electronic converters.

Signal processors for high-resolution radars (HRR) with a bandwidth which is typically of the order of 500 MHz, could make effective use of faster A/D capability in several ways. The range resolution of real-time synthetic aperture radars is inversely proportional to the conversion rate. An increase in conversion rate from 100 MW/s to 500 MW/s, for example, would improve range resolution from about 3 meters to about 0.6 meters. Faster conversion rates would make it possible to perform monopulse HRR imaging on a pulse-by-pulse basis, rather than sampling a large number of successive pulses to reconstruct a single return signal. Target classification would also be aided by the improved resolution available to a digital processor. High-speed A/D's would also be useful as a means of discriminating true returns from those generated by repeater jammers. A final HRR application would involve the use of the optical A/D in conjunction with a fiber delay line for pulse-to-pulse integration as a means of clutter suppression. Such a radar processing technique could be used, for example, for obstacle avoidance for high-speed surface-effect ships.

Two examples of how high-speed A/D converters might be used in electronic warfare (EW) systems are illustrated in Fig. 6 and Fig. 7. The optical analog-to-digital converter operating at gigaword/s rates combined with long recirculating fiber optic delay-line memory loops can store broadband (300 to 500 MHz) signal data excerpts (1000 to 2000 microseconds) for indefinite periods of time (see Fig. 6). This would provide the capability to analyze repetitively a time slice of signal spectrum in an adaptive hypothesis testing manner. Airborne systems could use this technique for fine-grain pulse analysis and signature recognition.

An extension of the recirculating spectrum storage technique utilizing a two-channel receiver (see Fig. 7.) could compute direction of arrival (DOA) on spread-spectrum signals utilizing cross correlation or convolution to derive time difference of arrival. This method has the advantage of substantial signal-to-noise improvement (because of signal autocorrelation) over leading-edge gating and carrier-frequency independence, as well as signal-to-noise improvement over interferometer techniques. The technique would be useful primarily with signals above 500 MHz, with bandwidths in excess of 100 MHz.

Another interesting application of the optical A/D converter is in intelligence data collection. In this case, it might prove expedient to eliminate the photodetectors and subsequent electronics and to record the optical output of the modulator chip directly on fast-moving film.

CONCLUSIONS

The electrooptic A/D converter seems to offer several potential improvements over present techniques: faster conversion rate, fewer comparators, lower electrical power dissipation (if used with an injection laser source), and the opportunity to record the output on photographic film. Military application areas include signal processing for wideband radar and electronic warfare systems.

REFERENCES

Dillard, G. M., et. al., 1977 "Fiber Optics and Integrated Optics Techniques for Signal Processing" Naval Electronics Laboratory Center Technical Report 2013.

Giallorenzi, T. G., 1976. Private communication.

Hill, K. O., et al., "CW Generation of Multiple Stokes and Anti-Stokes Brillouin Shifted Frequencies," Appl Phys Lett, v 29, p 185-187, August 1976.

Hoeschele, D. F., Jr., 1968. "Analog-to-Digital/Digital-to-Analog Conversion Techniques." New York, Wiley.

Kaminow, I. P., "Optical Waveguide Modulators," IEEE Trans. Microwave Theory and Tech., v MTT-23, p 57-70, January 1975.

Martin, W. E., "A New Waveguide Switch/Modulator for Integrated Optics," Appl Phys Lett, v 26, p 562-564, May 1975.

Ohmachi, Y., and Noda, J., "Electro-optic Light Modulator With Balanced Bridge Waveguide," Appl Phys Lett, v 27, p 544-546, November 1975.

Paoli, T. L., and Ripper, J. E., 1969. "Optical Pulses from cw GaAs Injection Lasers," Appl Phys Lett, v 15, p 105-107.

Rimmel, A. W., "State-of-the-Art Analog-to-Digital Conversion Equipment," 1975 Report R-4657, Battelle Columbus Laboratories, Columbus, Ohio.

Sheingold, D. H., and Ferrero, R. A., 1972, "Understanding A/D and D/A Converters," IEEE Spectrum, v 9, no 9, p 47-56.

Taylor, H. F., 1975. "An Electro-optic Analog-to-Digital Converter," Proc IEEE, v63, p 1524-1525.

Tsukada, T. and Tang, C. L.,"Q-Switching of Semiconductor Lasers," IEEE J of Quantum Electronics, v QE-13, p 37-46, February 1977.

Wright, S., Mason, I. M., and Wilson, M. G. F., 1974, "High-Speed Electro-optic Analog-to-Digital Conversion," Electron Lett v 28, p 508-509.

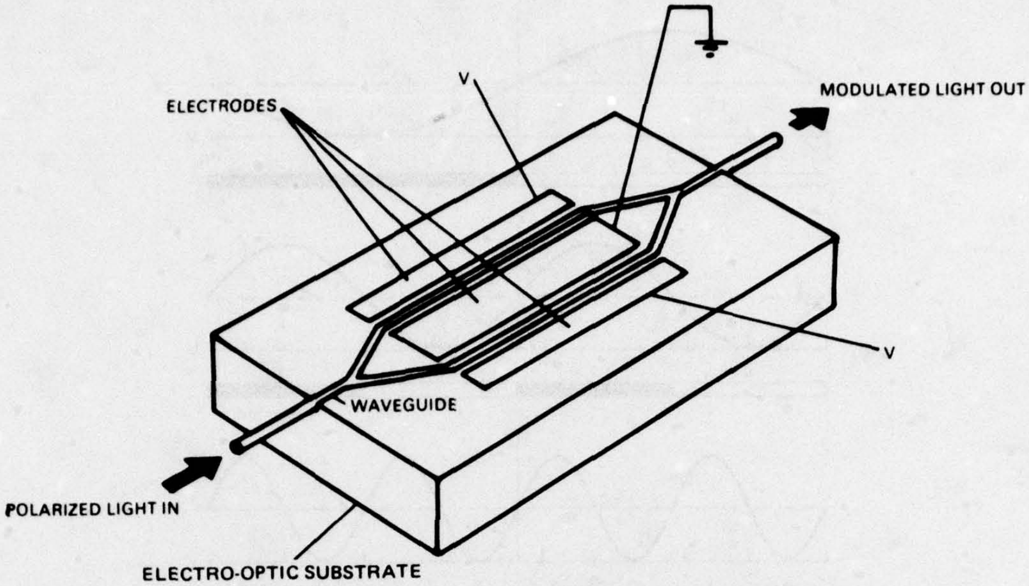

Fig. 1. The basic optical circuit.

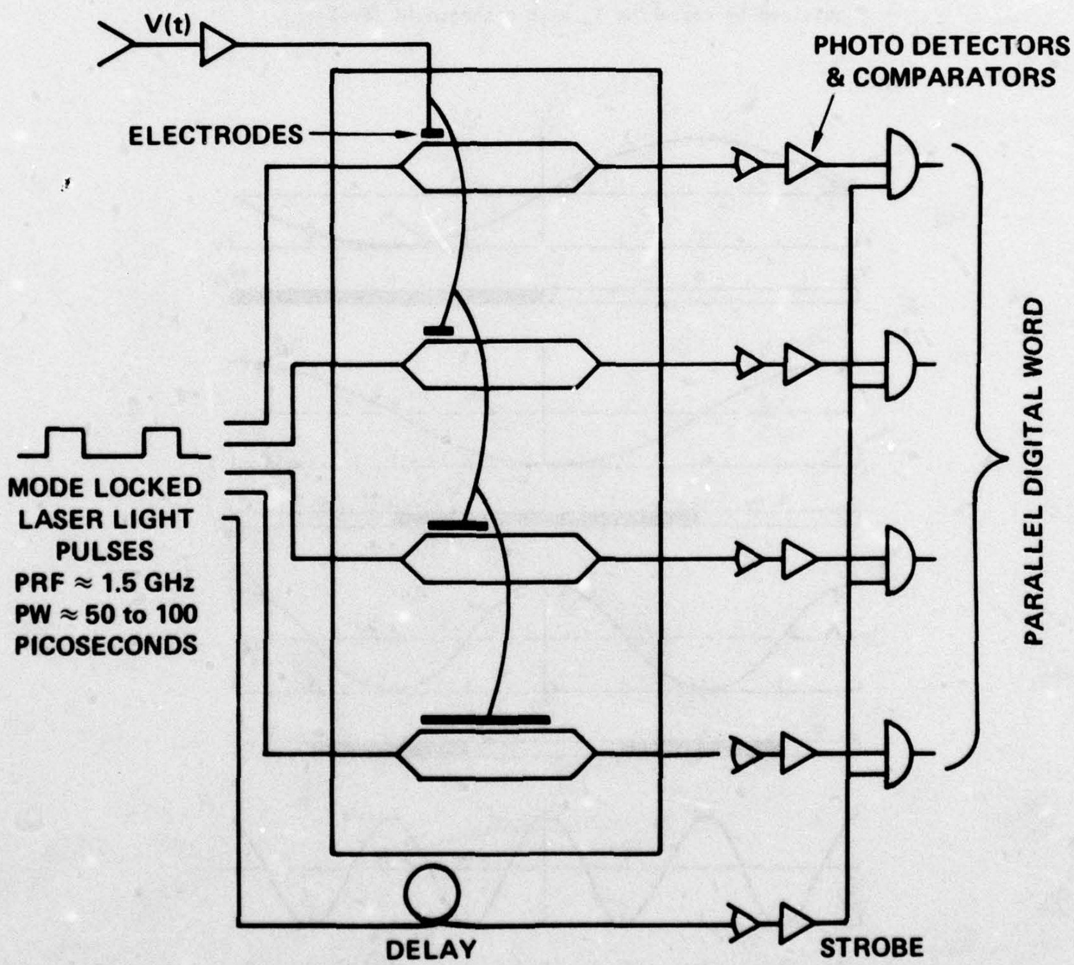

Fig. 2. Schematic diagram of a three-bit electrooptic A/D converter.

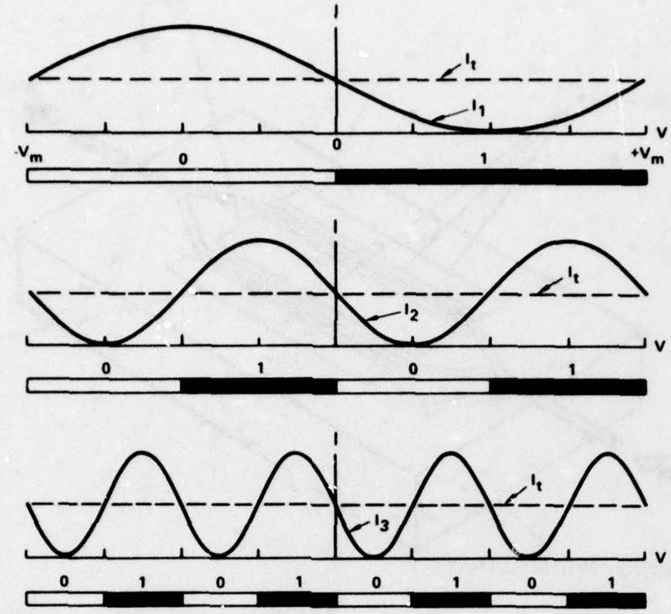

Fig. 3. Variation of the intensities I_n of light emerging from the waveguide modulators as a function of the applied voltage V, which can vary from $\pm V_m$. The offset binary representation of V is obtained by comparing I_n with a threshold level I_{nt}.

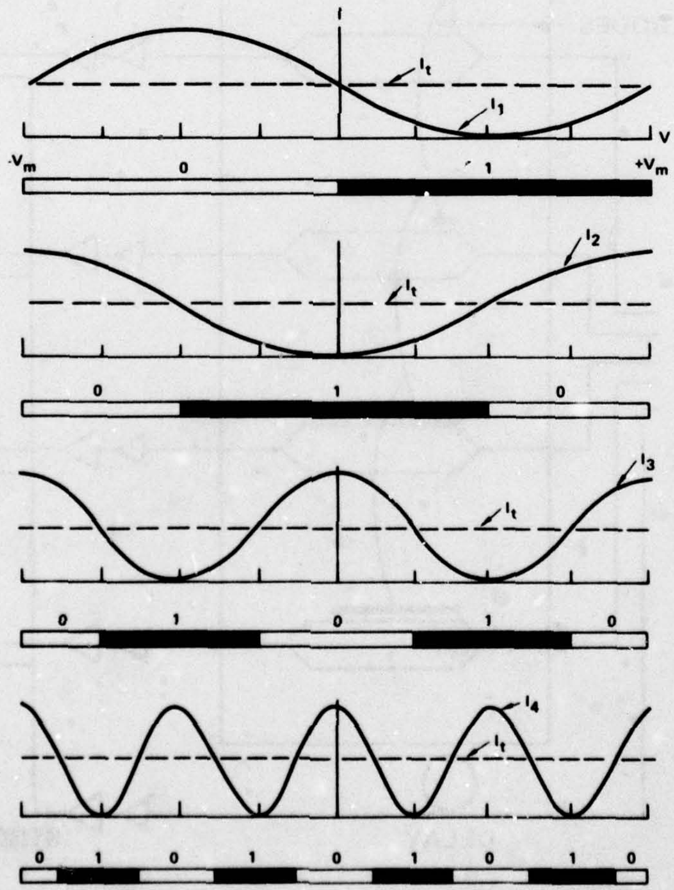

Fig. 4. Intensity vs. voltage plot for a four-bit A/D converter with Gray-scale output.

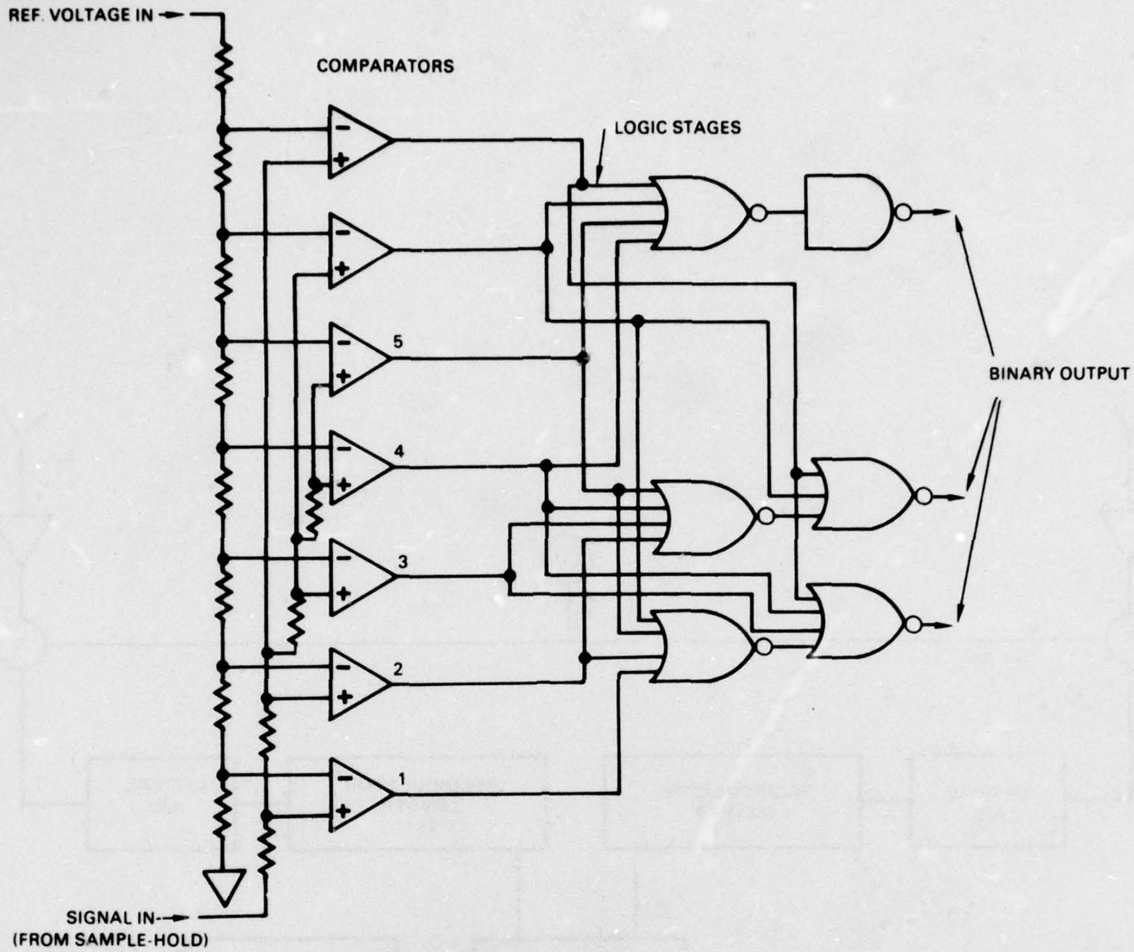

Fig. 5. Schematic diagram of an electronic parallel A/D converter with three bits of precision.

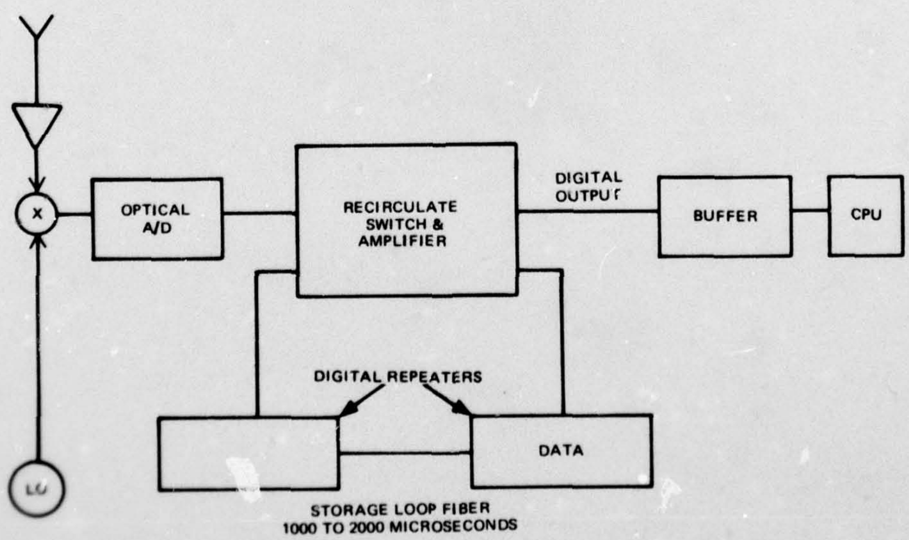

Fig. 6. Recirculating loop fine-grain-analysis ESM receiver.

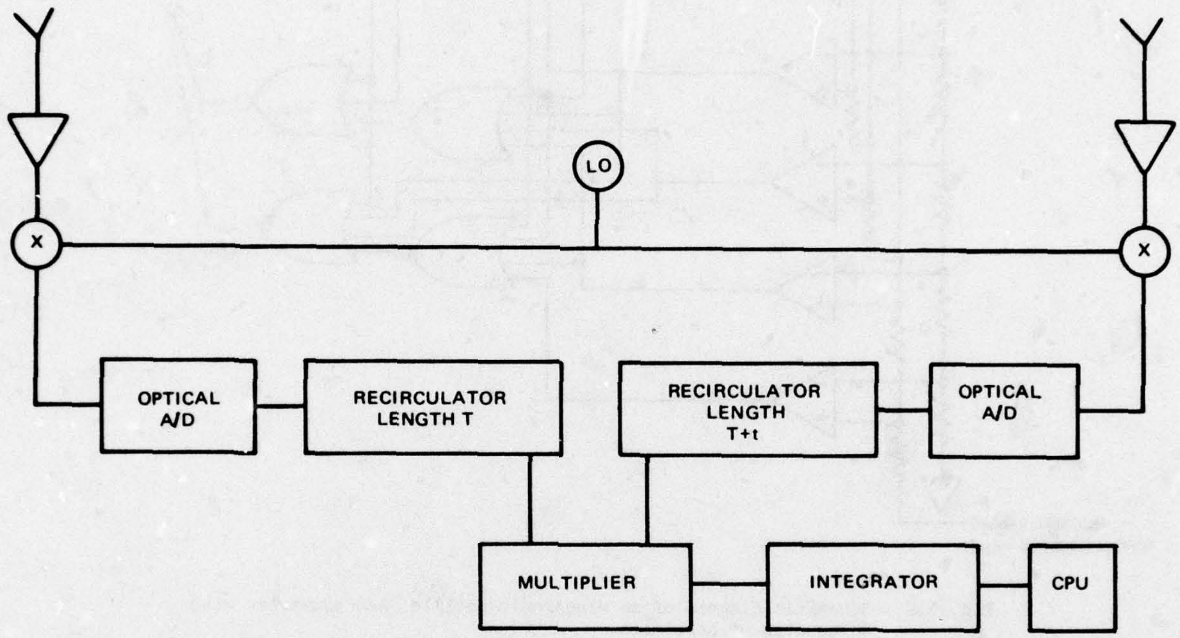

Fig. 7. Time Difference of arrival by broadband cross correlation.

THIN FILM INTEGRATED SIGNAL PROCESSORS

G.C. Righini, V. Russo, S. Sottini
Istituto di Ricerca sulle Onde Elettromagnetiche
50127 Firenze
Italy

SUMMARY

The realization of miniaturized optical analogic processors is expected to allow much higher performances than the bulk counterparts. A two-dimensional optical system is sufficient for processing one-dimensional signals, as for instance radar and communication signals.

Many thin film integrated configurations can be realized with a suitable assembly of integrated lenses, modulators and detectors. This paper is concerned with the applicability of geodesic thin film lenses to integrated convolvers and correlators. Two geodesic systems have been considered. The first one, constituted by a perfect geodesic lens having planar input and output and F/number ∿ 1.3, seems to be particularly suitable to separate, with a good resolution, the beams diffracted by a modulator. Two beams making an angle of 0.7 degrees have been resolved by a lens of 9 mm focal length and 7 mm aperture. The second geodesic system is consituted by a hemispherical surface and it is the analog of the bulk double diffraction processor. The aberrations of this system have been studied and numerical examples have been carried out to verify its Fourier transform capabilities. Two and three-level transmission filters have been considered in the numerical simulation of pattern recognition operations.

1. INTRODUCTION

The integrated optical technique can be applied to the realization of miniaturized optical analogic processors, as suggested by several authors because the two-dimensional processors should have higher performances than their bulk counterparts. A two-dimensional optical system is sufficient for processing one-dimensional signals, as for instance radar and communication signals.

In theory, integrated optical data processors can be achieved by extending to one-dimensional optics the working principles of bulk optical systems. In integrated optics many configurations can be realized with a suitable assembling of integrated lenses, modulators and detectors. Such elementary components are among the most studied in the last few years and a variety of prototypes have been tested, showing high performances and interesting properties.

This paper is concerned with a particular type of thin film lenses, the geodesic lenses, and their applicability to integrated signal processors.

2. GEODESIC LENSES AND APPLICATIONS

A lens which has to be used in a processor must present higher performances than in conventional uses: the tolerated aberrations must be very small over a large field angle. Lenses produced as a variation of the effective refractive index of the film (SHUBERT, R. et al., 1968; ULRICH, R. et al., 1971) suffer from non-negligible spherical aberrations, and mode conversion occurs at the boundary of the lens. In addition they have small focusing power.

A different method can be used to produce high-quality thin film lenses by taking advantage of the two-dimensional geometry of a waveguide. The third dimension is used for obtaining the path-length differences required for a perfect focusing. These lenses are the so-called geodesic lenses which were studied many years ago for application in microwave scanning antennas and which we introduced in two--dimensional optics (RIGHINI, G.C. et al., 1972 and 1973). The working principle of the geodesic lenses is that the propagation occurs along a curved surface in a two-dimensional Riemann space. The simplest geodesic lens consists of a quarter of a spherical surface (Fig.1); it is a perfect lens but it cannot be easily inserted in a planar circuit. On the other hand every portion of spherical surface focuses with strong spherical aberration, as it was founded in acoustics by Van Duzer (VAN DUZER, T., 1970). By combining a spherical depression lens with a mode index lens it is possible to considerably reduce aberrations (SPILLER, E. et al., 1974). These lenses however have F/number of the order of 3.5 and mode conversion can occur.

Let us now consider <u>perfect</u> geodesic lenses with planar input and output, which have large focal power (F/number ∿ 1) and no discontinuity in the mode index. A family of these lenses was described (TORALDO DI FRANCIA, G., 1955 and 1957) as a result of a general theorem on rotation surfaces. These lenses are perfect collimating systems on almost the entire aperture and they have the same properties as the well known variable-index Luneburg lens without any discontinuity on the tangent plane. The meridional curve of a lens of this family is shown in Fig.2, together with its mathematical expression. The radius b gives the maximum aperture of the lens. In other words (Fig. 3) the geodesics that do not cross the parallel with radius b are not collimated. By choosing different values of b/a it is possible to obtain lenses with different apertures. In practice it is necessary to find a compromise between the convenience of choosing b very near to a, in order to increase the aperture, and the necessity of a smooth juncture between the lens and the plane surface. A typical value of $\sin\gamma = b/a$ could be 0.8. This lens was designed to focus a set of plane waves into a corresponding set of points lying on the fundamental parallel A. The focus size is given only by the diffraction of the limited plane wave. Two plane waves with angular separation α focus in two points separated by an arc given by the product $a\alpha$. A geodesic lens of this type seems to be very useful to separate the set of beams diffracted by a modulator. Because the lens is theoretically perfect a very good angular resolution is expected in practice as well.

Several geodesic lenses have been tested in our laboratory either as a protrusion or as a depression in a film waveguide (Fig.4). Figure 5 refers to a geodesic depression lens of diameter 9 mm, focal length 9 mm and $\sin\ \gamma = 0.73$. The useful linear aperture was 7 mm. An epoxy film doped with rhodamine B was deposited on a glass substrate having the desired shape. Figure 6 shows a plane beam 1,5 mm wide which is focused in a focal spot of size 20 ÷ 30 μ; an optical fiber of 140 μ diameter is also shown for comparison. Figure 7 shows two plane waves forming an angle of ∿ 0.7 degrees which are focused in two separate points. As an example, in the case of an acousto-optic modulator (YAG-lithium niobate) such an angle between the two diffracted beams can be obtained with a carrier frequency of only 65 MHz ($\lambda \sim 55\mu$).

Such a geodesic lens can be used in an integrated convolver of the type sketched in Figure 8 (DAS, P. et al., 1976). This device can find application in optical digital communications or for radar signal processing. In both the cases one must detect highly correlated signals (such as Barker codes) used for instance as synchronization patterns, as code words or as pulses in radar technique. The geodesic lens could also be used in devices like the thin film spectrum analyzer already suggested (HAMILTON, M.C. et al., 1976) for microwave signals.

The geodesic lenses have the advantage that they can be prepared in advance, on the same substrate of the remainder of the integrated circuit. The accuracy is that of the glass optics technique. Then, the guiding film can be fabricated with the greatest variety of techniques, without masking problems.

3. HEMISPHERICAL GEODESIC CORRELATOR

Concerning the ability of the above geodesic lens to perform Fourier transformations, it is to be noted that the focal points corresponding to different spatial frequencies (Fig.9) present a phase distribution different from that theoretically expected. In addition, because of the circular symmetry, the Fourier transform locus is a circle which lies on the light-guiding plane. Such a characteristic makes it very difficult to assemble two lenses in order to constitute a thin film correlator analogous to a bulk double--diffraction system.

However, among geodesic lenses, the simplest one, which is the hemispherical surface (RIGHINI, G.C. et al., 1972), shows the interesting characteristic of imaging without aberrations as sketched in Fig.10, and its symmetry properties allow us to expect a suitable Fourier transform locus. Such an imaging system (Fig.11.a) can be compared with the bulk imaging system of Fig.11.b. In bulk optics, forming an image of the object is a sufficient condition for producing the Fourier transform on a plane (VANDER LUGT, A., 1974). We investigated if an analogous property is valid also in the case of an unusual imaging system such as the hemispherical surface. For symmetry reasons, in agreement with the focusing property of a quarter of spherical surface, the Fourier transform locus under investigation must be the great circle that divides the surface into two parts (Fig.11.a).

To verify this assumption, one can evaluate the lack of parallelism on the FT line of the beams diffracted by point sources on the input line. The lack of parallelism or angular aberration δ of the beam from S_1 with aperture α and field angle Ω defined in Fig. 11.a turns out to be

$$\delta = -\frac{1}{2}\,\Omega\,\alpha^2 \tag{1}$$

Analogously the wave aberration turns out to be

$$W = \frac{1}{6}\,\Omega\,\alpha^3 \tag{2}$$

It corresponds to the coma in bulk optics, while no axial aberration exists. The aberrations have been also numerically evaluated (Fig.12). As an example, if we consider, according to Rayleigh, a maximum wave aberration of $\lambda/4$, we can use an aperture of 10° and a field angle of 9°, while the lack of parallelism turns out to be less than 0.1°. It is to be noted, however, that the aberrations are completely corrected by the second part of the correlator because the semispherical surface constitutes a perfect imaging system.

A model of the geodesic correlator has been constructed. In order to easily feed the hemispherical correlator with a parallel beam, it has been superposed on a cylinder which is connected to a planar guide by means of a suitable toroidal junction. Figure 13 shows a sketch of the model constituted by a hemisphere with radius 20 mm superposed on a cylinder 20 mm high. The glass substrate was shaped, polished and then coated with a thin film of doped epoxy (Araldit MY 757). We have not yet carried out any experiment of optical processing with this correlator. However, numerical evaluations have been made in order to clarify the effects of wave-aberration on the complex amplitude of the Fourier transforms and on the auto- or cross-correlations of binary signals.

Let us consider the pulse train shown in Fig.14, constituted by N rectangular pulses. The Fourier transform F(u) actually performed by the first lens (one half of hemispherical surface) must be evaluated by taking into account the wave-aberration W:

$$F(u) = \int_{-\infty}^{+\infty} f(x')\, e^{-jW(x',u)}\, e^{-jux'}\, dx' \tag{3}$$

where W(x',u) is obtained from eq.(2) with the formulas of spherical trigonometry. Let us assume that the radius R of the hemispherical correlator equals 10 mm and that the input signal has a 2.5 mm maximum width. Such a value, which seems to be suitable for integrated optical circuits, is related to the choice of the field angle equal to 9°. Figure 15.a shows the normalized amplitude of the aberrated FT of 5 pulses, 0.2 mm wide, with period b = 0.55 mm, plotted versus the x coordinate along the FT line. The imaginary part turned out to be zero as in the unaberrated case due to signal symmetry reasons. The amplitude differences with respect to the exact FT are shown in Fig.15.b and remain very small ($\sim 3\ 10^{-5}$) up to $|x| \leq 1.4$ mm, that is up to spatial frequencies of $\sim$880 lines/mm. This limit is higher than the $|x|$ value of 0.88 mm corresponding to a maximum wave-aberration $\lambda/4$.

To obtain the autocorrelation pattern on the output line of the correlator, the aberrated FT must be multiplied by the matched filter transmission (equal to the complex conjugate of the signal spectrum) and then again Fourier-transformed. Due to the previous results the FT performed by the second lens has been calculated neglecting the aberration. This FT has been evaluated by means of the Fast Fourier Transform algorithm on an Eclipse S 200 computer. The autocorrelation intensity pattern for the train of 5 pulses plotted versus the coordinate x" of the output line and stopped at x" = 2 mm, is shown in Fig. 15.c.

The practical realization of the filter having an amplitude transmission equal to $F^{*}(u)$ constitutes a difficult problem; it is much more convenient to look for approximated filters with only two or three transmission levels. Figure 16 shows the autocorrelation of the 5-pulse-train obtained in the case of binary filters: obviously the performance of the filter is affected by the choice of the cutoff level corresponding to zero transmission. Three cutoff levels are considered, equal respectively to 5%, 10% and 20% of the central peak amplitude A(o) of the matched filter $F^{*}(u)$. By increasing the cutoff level one simplifies the filter fabrication at the expense of an increase of the lateral lobes of the autocorrelation. A good compromise is a cutoff level equal to 10%; in this case we have almost the same intensity ratio between the central peak and the next two triangles as in the case of the continuous matched filter. Fig.17 shows the binary filter corresponding to this choice (bottom right) and the related autocorrelation pattern (top right). The filter is compared with a three level filter (-1,0,+1) (bottom left). For the three level filter a phase control in the fabrication is required. On the other hand the autocorrelation pattern (top left) obtained in this case shows a higher ratio between the central peak and the next lobes than in the previous case, even if a higher cutoff amplitude (15% of A(o)) has been chosen for this case than for the binary filter.

As a further test, several cross correlation patterns have been evaluated using these filters. Figure 18 shows two crosscorrelation patterns of a 3-pulse input with 5 pulses obtained by using respectively the two filters of Fig.17.

4. CONCLUSIONS

The previous results seem to confirm the possibility of applying the geodesic correlator to communication systems. In particular, for pattern recognition applications, binary filters could often be used with acceptable performances, thus simplifying the practical realization of the matched filters. On the other hand, the input signal must usually be introduced by means of one integrated modulator, for instance of the acoustooptic or electrooptic type. The practical problems to be solved do not seem, however, more complicated in the case of the geodesic correlator than in planar correlators.

In the communication or radar fields, several applications of the geodesic correlator could be suggested. Figure 19 shows, for instance, the sketch of the geodesic analog of a time integrating acoustooptic correlator suggested in bulk optics by Sprague and Koliopoulos (SPRAGUE, R.A. et al., 1976). The comparison with the bulk system shows that even rather complex optical systems can be realized with a spherical surface. This kind of correlator could be particularly interesting for the possibility of coupling it to an optical fiber which brings the input signal.

In conclusion, the hemispherical correlator described above can be used as an optical processor with aperture and field angles suitable for application to integrated optical circuits. The simple shape of the substrate and the usual advantages of geodesic optical systems are further interesting characteristics of this correlator.

REFERENCES

DAS, P., and D.SCHUMER, 1976, "*Optical Communications Using Surface Acoustic Waves*", paper Tu-D.2, Int.Conf. on Applications of Holography and Optical Data Processing, Jerusalem.

HAMILTON, M.C., and D.A.WILLE, 1976, "*Acousto-Optic Diffraction in Optical Waveguides*" in Digest of Technical Papers, OSA/IEEE Topical Meeting on Integrated Optics, Salt Lake City.

RIGHINI, G.C., V.RUSSO, S.SOTTINI, and G.TORALDO DI FRANCIA, 1972, "*Thin Film Geodesic Lens*", Applied Optics 11, 1442.

RIGHINI, G.C., V.RUSSO, S.SOTTINI, and G.TORALDO DI FRANCIA, 1973, "*Geodesic Lenses for Guided Optical Waves*", Applied Optics 12, 1477.

SHUBERT, R., and J.H. HARRIS, 1968, "*Optical Surface Waves on Thin Films and Their Application to Integrated Data Processors*", IEEE Trans. MTT-16, 1048.

SPILLER, E., and J.S. HARPER, 1974, "*High Resolution Lenses for Optical Waveguides*", Applied Optics 13, 2105.

SPRAGUE, R.A., and C.L. KOLIOPOULOS, 1976, "*Time Integrating Acoustooptic Correlator*", Applied Optics 15 89.

TORALDO DI FRANCIA, G., 1955, "*A Family of Perfect Configuration Lenses of Revolution*", Optica Acta 1, 157.

TORALDO DI FRANCIA, G., 1957, "*Un problema sulle geodetiche delle superficie di rotazione che si presenta nella tecnica delle microonde*", Atti Fondaz. Ronchi, XII, 151.

ULRICH, R., and R.J. MARTIN, 1971, "*Geometrical Optics in Thin Film Light Guides*", Applied Optics 10, 2077.

VANDER LUGT, A., 1974, "*Coherent Optical Processing*", Proc. IEEE 62, 1300.

VAN DUZER, T., 1970, "*Lenses and Graded Films for Focusing and Guiding Acoustic Surface Waves*", Proc.IEEE 58, 1230.

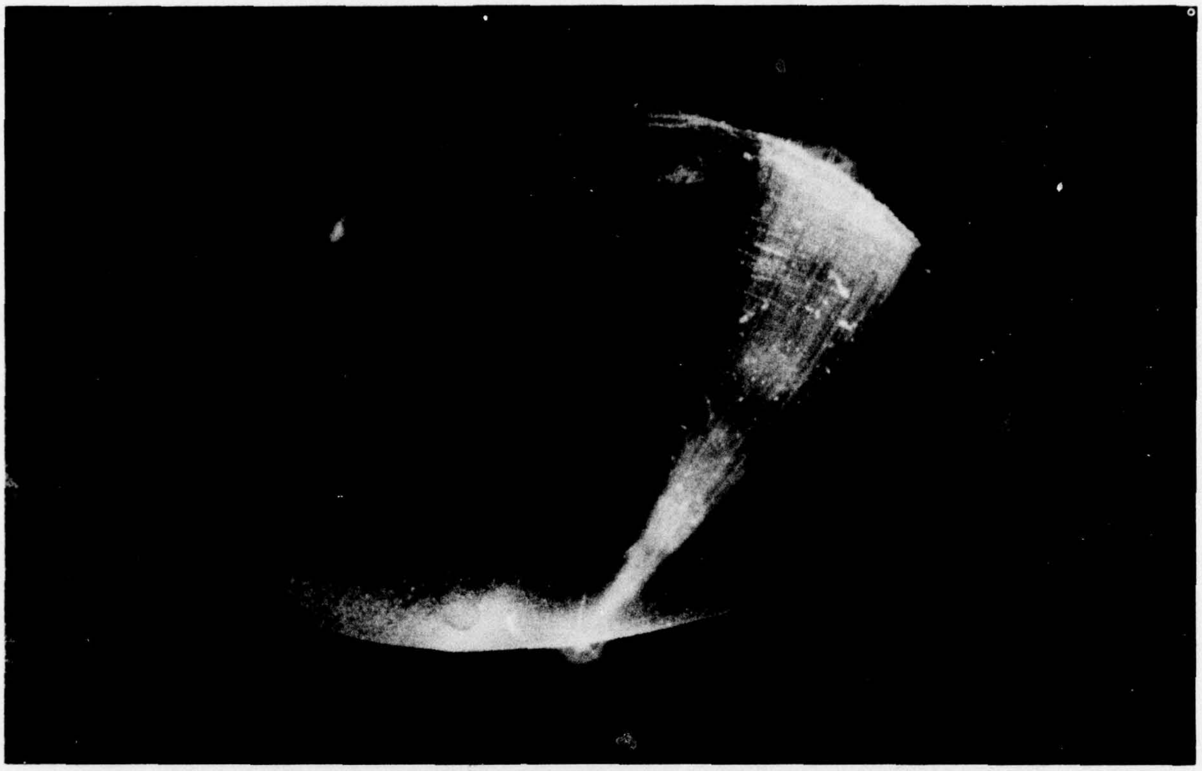

Fig. 1 A geodesic lens, constituted by a quarter of a spherical surface, focusing a plane laser beam.

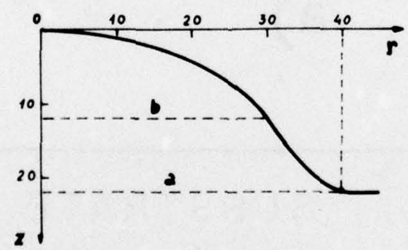

$$z(r) = \int_0^r \left\{ \left[-\left(1 + \frac{a^2 - r^2}{h^2}\right) + \frac{2}{\pi} \frac{\sqrt{b^2 - r^2}\sqrt{a^2 - b^2}}{h^2} + \frac{1}{\pi}\left(1 + 2\frac{a^2 - r^2}{h^2}\right) \operatorname{arcsen} \sqrt{\frac{b^2 - r^2}{a^2 - r^2}} \right]^2 - 1 \right\}^{1/2} dr$$

when $0 \leq r \leq b$

$$z(r) = \int_0^r \left[\left(\frac{a^2 - r^2}{h^2}\right)^2 + 2\,\frac{a^2 - r^2}{h^2} \right]^{1/2} dr$$

when $b \leq r \leq a$

$$h = a\sqrt{\frac{\pi - 2\gamma - \operatorname{sen}^2\gamma}{\gamma}} \quad ; \quad \operatorname{sen}\gamma = \frac{b}{a}$$

Fig. 2 Meridional curve of a geodesic lens belonging to a family of perfect lenses having planar input and output.

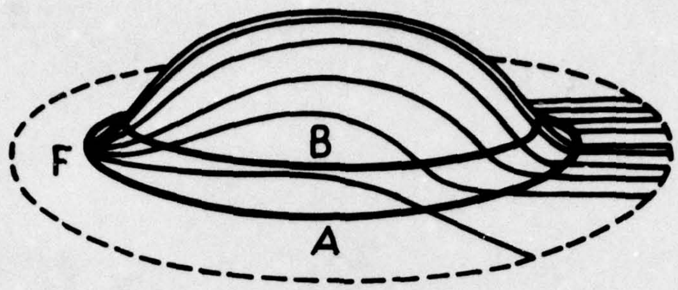

Fig. 3 Sketch of the previous lens showing the maximum aperture for which it constitutes a perfect focusing system.

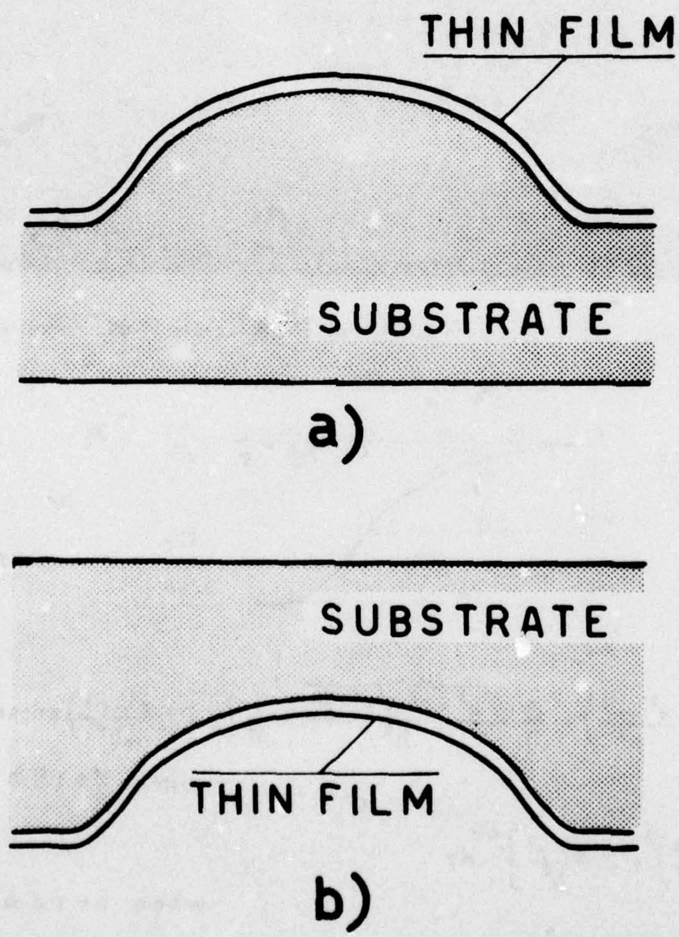

Fig. 4 Sketch of the geodesic lens constructed either as a protrusion with respect to a planar film (a) or as a depression in the planar film (b).

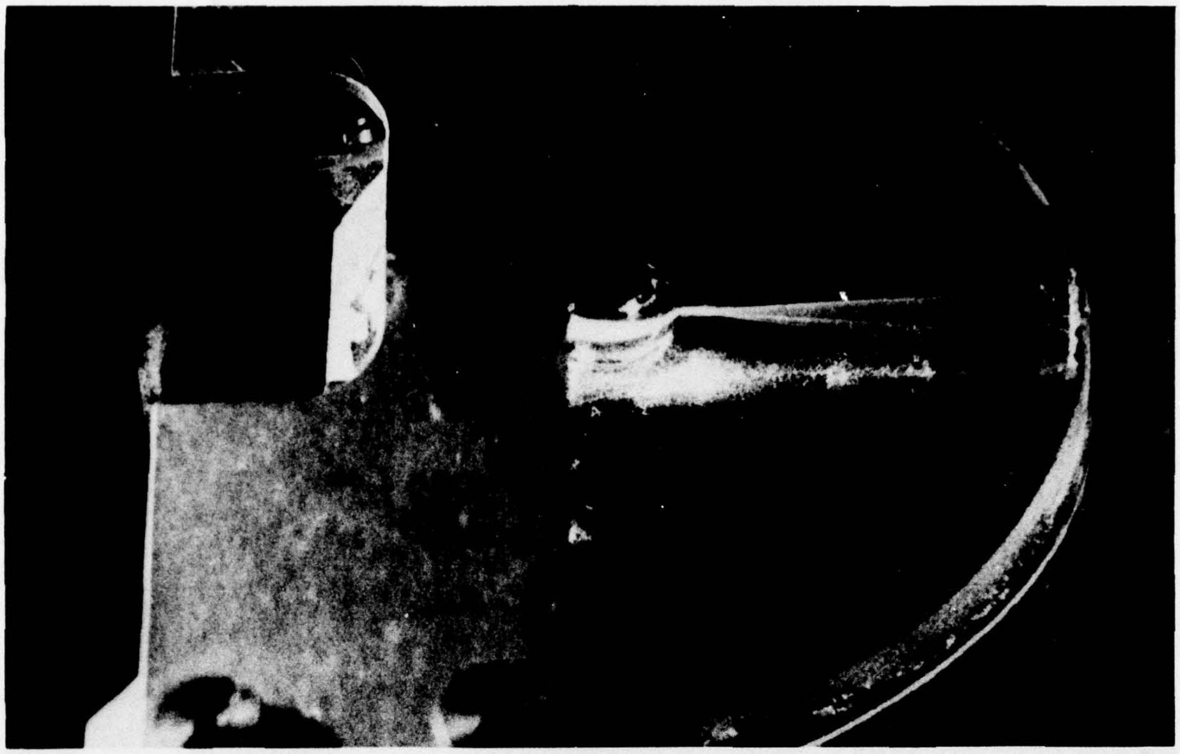

Fig. 5 Depression geodesic lens with 9 mm focal length and 7 mm linear aperture focusing a planar beam.

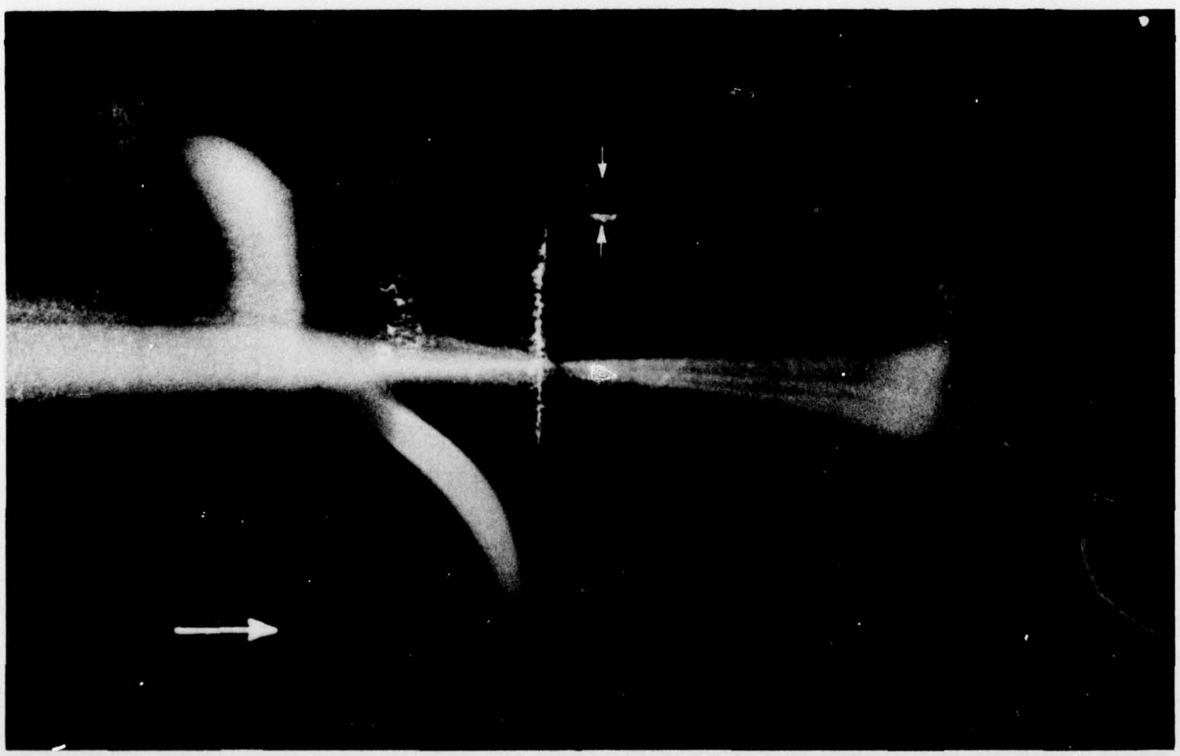

Fig. 6 A plane beam 1.5 mm wide focused in a focal spot of size 20 : 30 μ. For comparison an optical fiber of 140 μ diameter is also shown.

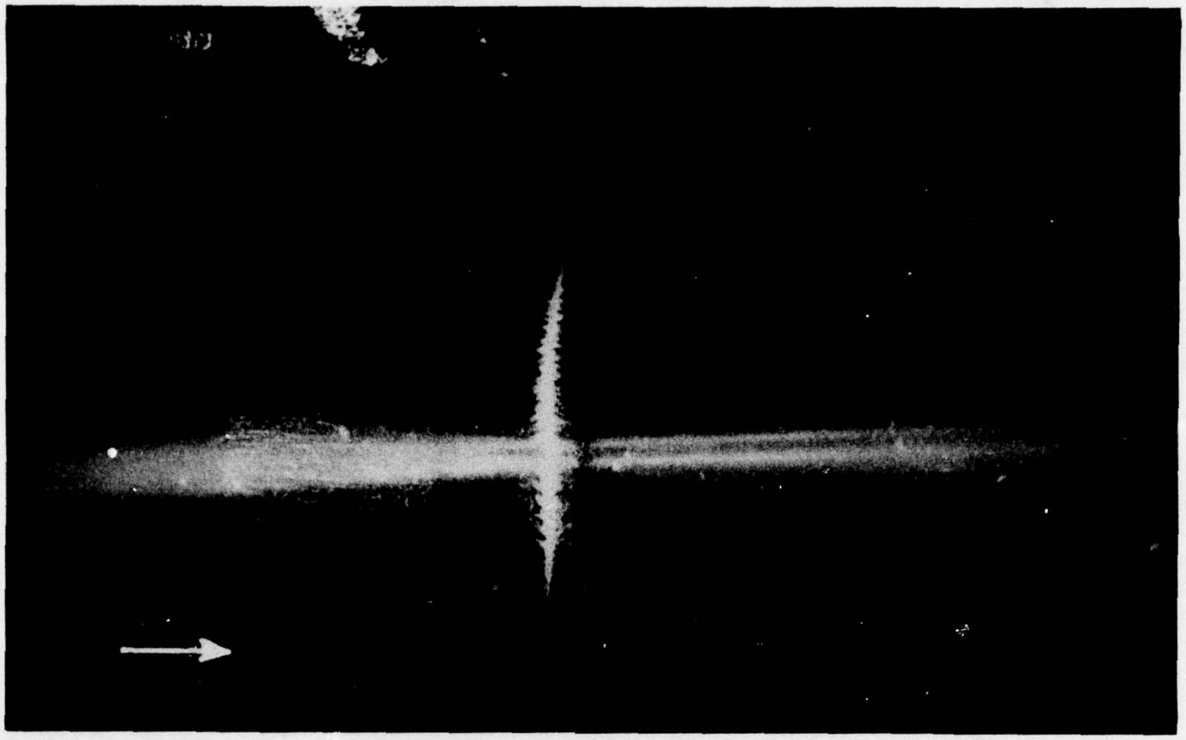

Fig. 7 Two plane waves forming an angle of ∿0,7 degrees are focused in two clearly separated points.

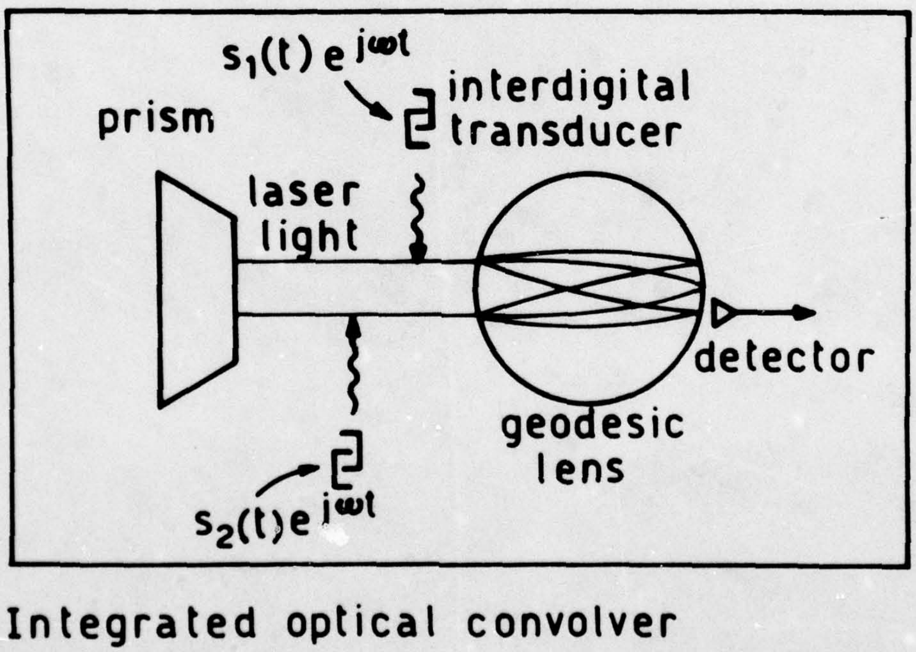

Fig. 8 Sketch of an integrated convolver employing a geodesic lens and two acoustooptic modulators with parallel track configuration.

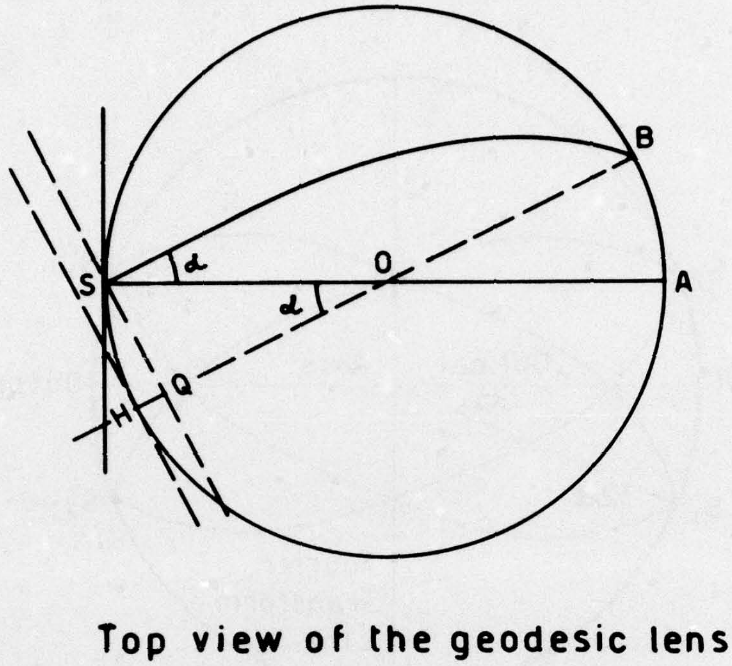

Fig. 9 Top view of the geodesic lens.

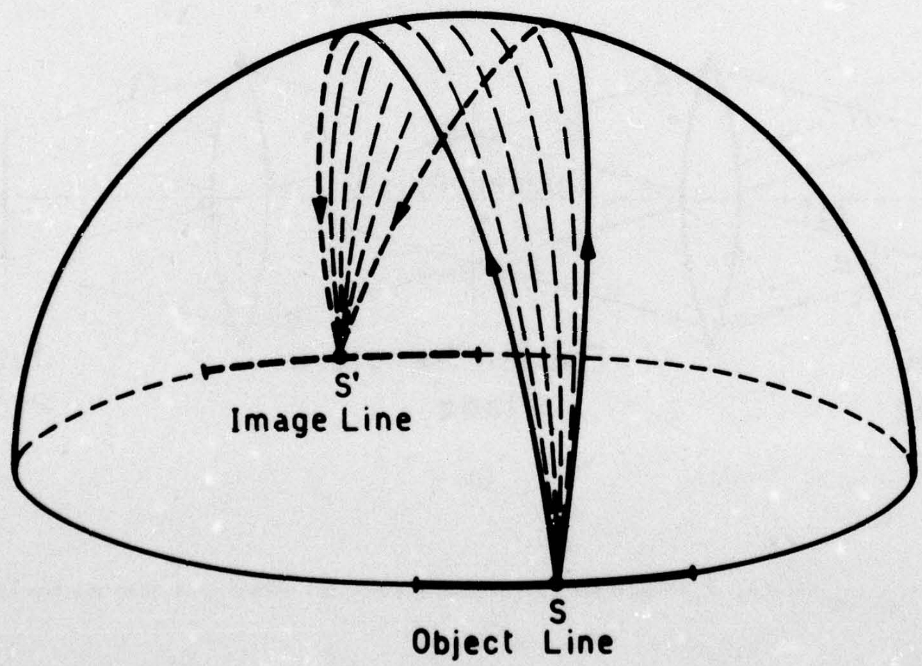

Fig.10 Schematic representation of the imaging properties of a hemispherical surface.

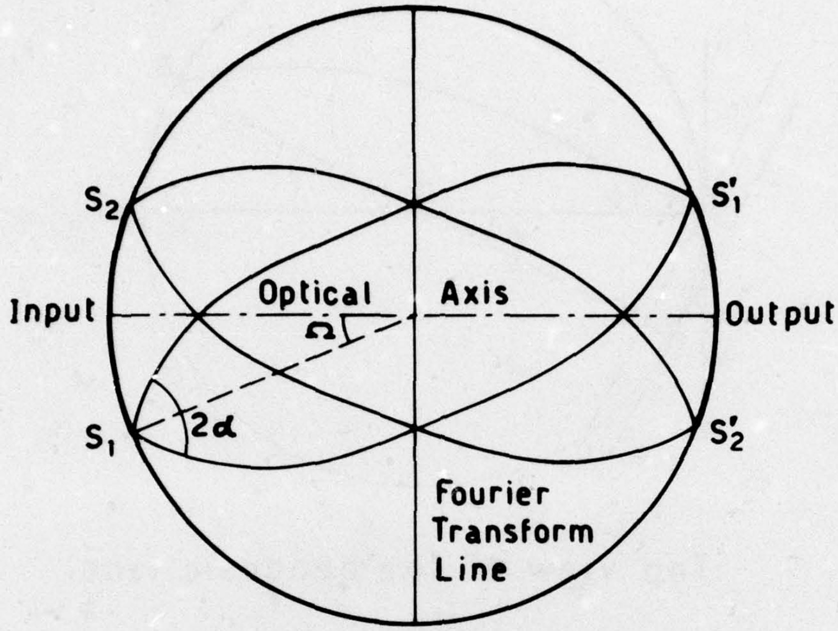

(a)

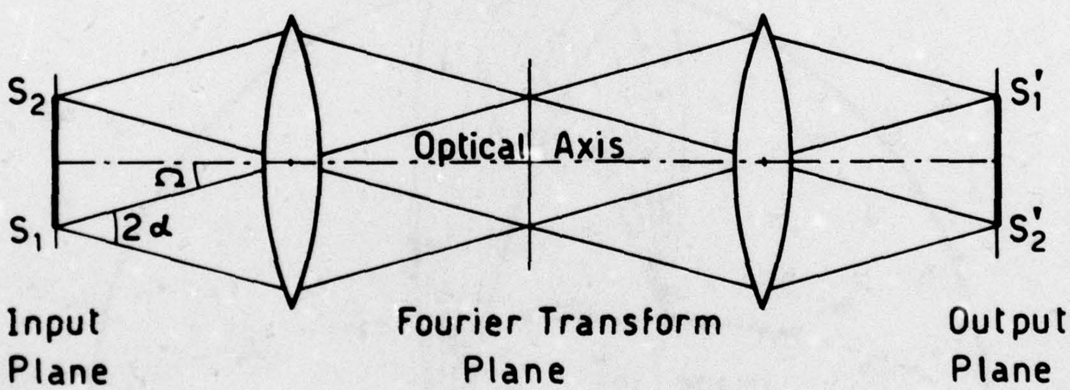

(b)

Fig.11 (a) Top view of a hemispherical imaging system; (b) sketch of a bulk imaging system.

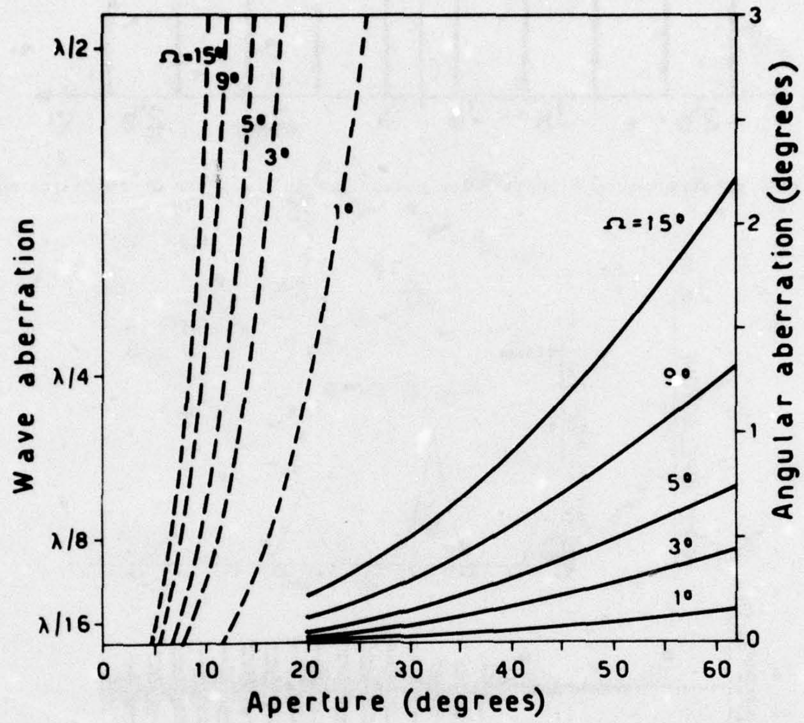

Fig.12 Numerical evaluation of the angular aberration δ and the wave aberration W versus Ω and α.

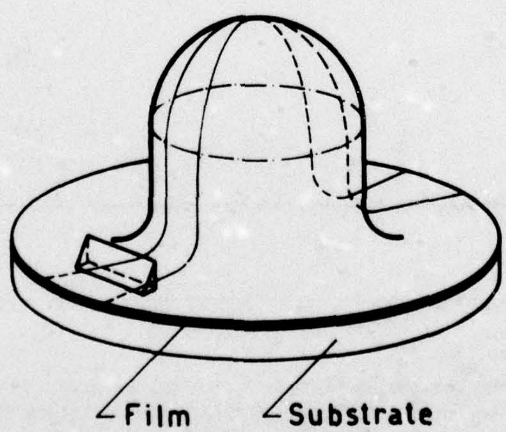

Fig.13 Sketch of the model of the geodesic correlator constituted by a hemisphere with radius 20 mm superposed on a cylinder 20 mm high.

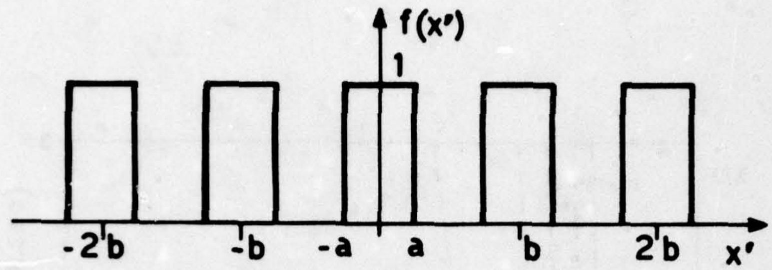

Fig.14 Pulse train constituted by 5 rectangular pulses. 2a is the width of the pulse and b the period.

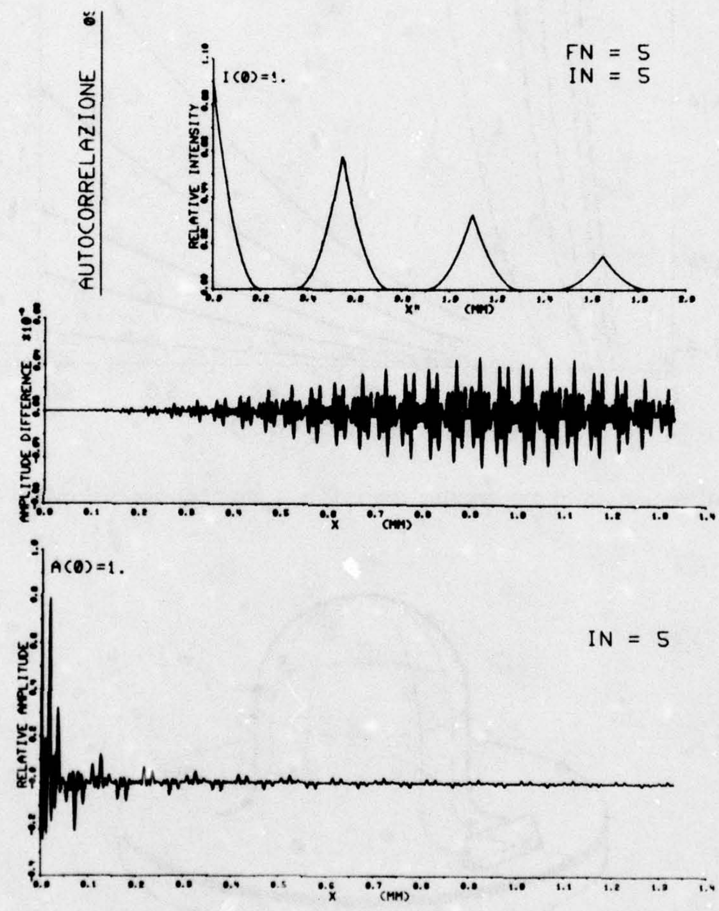

Fig.15 (a) Normalized amplitude of the aberrated FT of 5 pulses with a = 0.2 mm and b = 0.55 mm, plotted versus the x coordinate along the FT line; (b) Amplitude differences with respect to the exact FT. They remain less than $\sim 3\ 10^{-5}$ up to $|x| \leq 1.4$ mm, that is up to spatial frequencies of ~880 lines/mm ; (c) Autocorrelation intensity for the train of 5 pulses plotted versus the coordinate x" of the output line and stopped at x" = 2 mm.

AD-A050 748 ADVISORY GROUP FOR AEROSPACE RESEARCH AND DEVELOPMENT--ETC F/G 20/6
OPTICAL FIBRES, INTEGRATED OPTICS AND THEIR MILITARY APPLICATIO--ETC(U)
OCT 77 H HODARA

UNCLASSIFIED AGARD-CP-219 NL

4 OF 6
AD
A050748

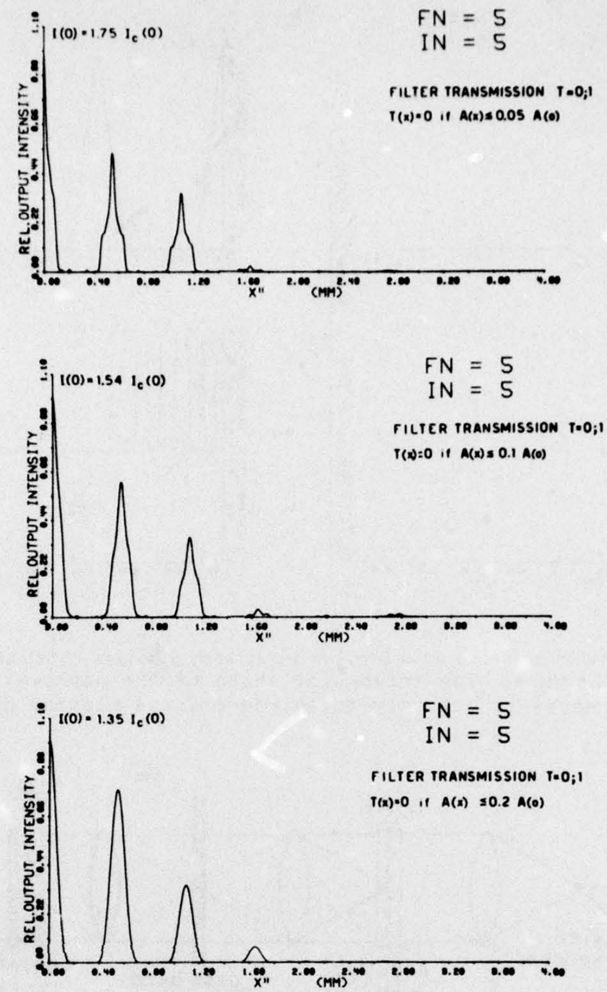

Fig.16 Autocorrelation of the 5-pulse-train obtained by using binary filters. Three cutoff levels are considered, equal respectively to 5%, 10% and 20% of the central peak amplitude A(o) of the matched filter $F^*(u)$.

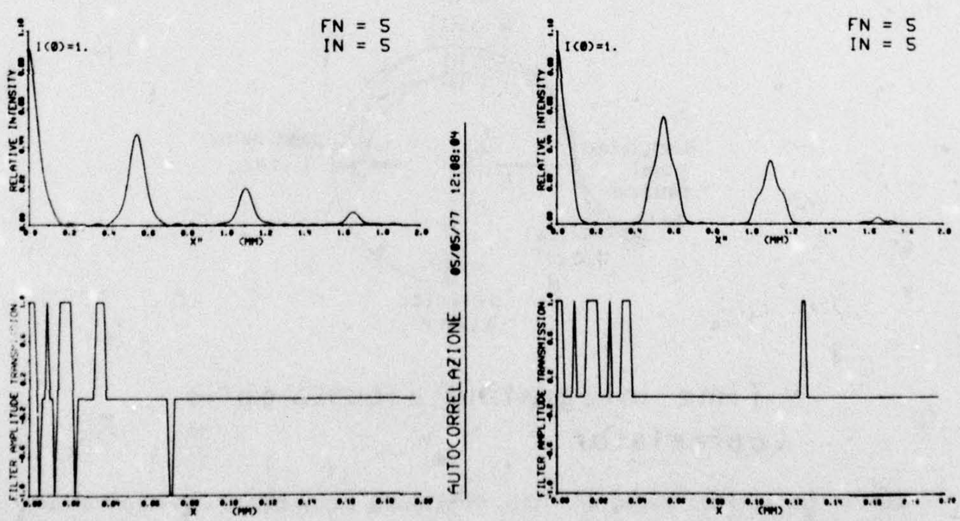

Fig.17 Comparison between the performances of binary (bottom right; 10% cutoff level) and three-level (bottom left; 15% cutoff level) filters. The corresponding autocorrelation pattern for 5-pulse--trains are shown top right and top left respectively.

QUESTIONS AND COMMENTS ON SESSION III

GIGA-HERTZ MODULATORS USING BULK ACOUSTO OPTIC INTERACTIONS IN THIN FILM WAVEGUIDES
G. B. Brandt, M. Gottlieb, R. W. Weinert

Dr. R. De La Rue: What is the number of resolved spots that your deflector device can achieve, compatible with reasonable insertion loss (optical)? The supplementary should have been: What is the actual optical insertion loss of the device?

Dr. Brandt: We have not measured the insertion loss of these deflectors but since we are using prism coupling it is likely to be high. The number of resolvable elements is equal to the number of fingers on the transducer electrode. With conventional photomasking techniques 100 or 200 elements should not be difficult to fabricate; much beyond 200 elements, the transducer size would tend to become too large to qualify as a miniaturized integrated optic device.

LASER-FIBER COUPLING WITH OPTICAL TRANSITION STRUCTURES
G. Mitchell, W. D. Scott

Dr. John Dakin: Did you observe spatial oscillations in coupling efficiency as the relative position of the laser and the light guide were changed? Other workers have reported considerable oscillations of this type.

Dr. Mitchell: The process of adjustment to optimize coupling involved moving the transition structures with respect to the laser, however, we did not observe output fluctuations that could be considered to result from interference between the laser and transition ends.

AN INTEGRATED OPTICAL ANALOG-TO-DIGITAL CONVERTER
D. Lewis, H. F. Taylor

Dr. R. M. De La Rue: Laser was presumably YAG laser at 1.06 μm wavelength? (after discussion) Can GaAs type lasers achieve required power and pulsewidth? What value of optical insertion and output coupling losses assumed in the power calculation?

Dr. Lewis: It appears that there are three questions here: (1) Was a NdYAG laser used, (2) Could a GaAs laser achieve the required powers and pulse widths, (3) What value of optical insertion and coupling losses were assumed in the power calculation?

With regards to the first question, a helium neon laser is being used with the proto-type circuits until the modulators, photodetectors, and comparators are characterized and working together properly.

As regards to the second question, either NdYAG or GaAs lasers could be used depending on the pulse widths required. Hill has demonstrated a laser/fiber optic system that may be capable of providng 5 ps pulses, the laser used in this system was Nd TAG as I recall. GaAs lasers with subnanosecond pulse widths have been prepared and reported on. We anticipate the successful development of the A/D converter will require the development of a suitable picosecond laser source.

Finally, as regards the third question, it is not necessary to assume values for insertion and coupling losses. We have instead assumed what we believe to be reasonable powers to drive each of the components in the circuit.

Summary of Session III
INTEGRATED OPTICS

by
Dr. T. G. Horwath

The third session of this conference, on the subject of Integrated Optics was primarily devoted to single-mode technology. It consisted of presentations covering a broad spectrum of devices, such as sources, modulators, connectors and couplers, as well as two intriguing approaches to the realization of special signal processing functions.

The paper presented by Dr. T. G. Giallorenzi, "Compatibility of Integrated Optics and Single Mode Fiber Optics," discussed the status of interface components for integrated optical data communication systems. Couplers and connectors were identified as the most critical components from the standpoint of systems implementation.

Mr. Papuchon's paper, "Electro-Optical Active Components for Guided Light," presented the results obtained with electro-optical components based on Titanium diffused Lithium Niobate technology. Devices such as phase modulators, amplitude modulators and switches were presented, together with the results of experiments conducted to establish their characteristics.

"Giga-Hertz Modulators Using Bulk Acousto-Optic Interactions in Thin Film Waveguides," was the title of the paper presented by Dr. G. B. Brandt. Interactions of light in optical waveguides with longitudinal waves and shear waves were discussed, leading to frequency shifts or deflection of the light wave respectively. Modulators with 1.5 GHz bandwidth have been realized, and 30 GHz appears feasible as the theoretical limit.

A novel injection laser of great potential was reviewed by Prof. Shyh Wang with his paper "Distributed-Bragg-Reflector Injection Lasers for Integrated Optics." This laser uses waveguides of periodically changing thickness as frequency selective reflectors. Prof. Wang first reviewed the wave propagation in such waveguides, presented the dispersion relation for the Eigen Bloch wave and then derived transmission and reflection coefficients. He then commented on optimization realization and operation of such a laser. Finally, he suggested possible schemes for integration with other optical components, stabilization, fine tuning and most of all an imaginative way of direct coupling into single mode optical fibers. This paper was, in my opinion one of the highlights of the session.

"Multimode Optical Systems -- Power Coupling Between Waveguides," presented by Dr. M. G. F. Wilson was unique in the session, as the title might suggest. Dr. Wilson applied ray theory in order to derive power flow and mode conversion as a function of the geometry of waveguide junctions. In addition, he presented experimental results obtained with waveguide junctions produced by ion-exchange techniques.

The problems of coupling integrated optical components and injection laser sources to single mode fibers were again raised in Dr. G. L. Mitchell's paper "Laser-Fiber Coupling with Optical Transition Structures." A transition section from rectangular to circular cross section was suggested, similar to those well known from microwave technology. Fabrication techniques, material selection as well as optimization of coupling efficiency and index of refraction were discussed by Dr. Mitchell.

Dr. Lewis in his paper "An Integrated Optical Analog-to-Digital Converter" suggested an innovative use of an array of phase modulators, connected in parallel, to convert the common analog electrical drive signal into a digital optical output. The phase modulators used closely resemble the ones discussed by Mr. Papuchon earlier in this session. The analog to digital converter has the potential of 8-bit quantization at a speed of one mega-word per second.

"Integrated Signal Processing" was the title of the last paper given by Dr. Vera Russo-Checcacci. Application of the transform properties of lenses to integrated thin film optics has been suggested in the past. Dr. Russo-Checcacci's contribution, however, is the use of geodesic lenses, taking advantage of their symmetry properties and the asbsence of aberrations. A model of a semispherical correlator was discussed in conclusion.

In my opinion, the session was somewhat deficient in two ways. First, it did not contain a presentation on integrated detectors that are efficiently matched to the thin fiber waveguides. Second, there was no attempt of integration beyond the component level, such as complicated logic functions. It appears, therefore, that a lot remains to be done to advance this technology to the degree of maturity necessary for wider application.

HOW DOES ONE INDUCE LEAKAGE IN AN OPTICAL FIBER LINK?

C. Yeh and A. Johnston
Electrical Sciences and Engineering Dept.
University of California
Los Angeles, California 90024

SUMMARY

Three non-destructive methods to induce the leakage of optical signal from optical fibers will be discussed: (1) The index-matching-fluid method, (2) The temperature method, (3) The bending method. Experiments were performed for these cases. Results show that all three methods are effective in inducing leakage from plastic clad fibers while only the bending method is effective for glass-clad fibers.

INTRODUCTION

It has almost been taken for granted that, because optical fiber transmission line is free of RF leakage and cross-talk problems, it can be used readily as a secure information link. Furthermore, the intrinsic crack propagation characteristic of glass prevents cutting into the glass core to gain access to the optical signal without severing it. This talk is an attempt to discuss several non-destructive ways of tapping an optical fiber link. We are interpreting the word tapping in its broadest sense; i.e., any scheme that would induce the leakage of light from the fiber is interpreted as a viable means of tapping the fiber.

Two families of low-loss multi-mode fiber exist: (a) The plastic-clad fiber family, (b) The glass-clad fiber family which includes the graded-index fibers. The plastic-clad fiber usually consist of a glass core and a plastic sheath as its cladding. The cladding of a small section (say, 5 cm.) of a fiber link (say, longer than 20 m.) can be easily stripped off without noticably affecting the strenght of the transmitted signal. On the other hand the cladding of the glass-clad fiber is usually intimately bonded to the glass core in such a way that removing the glass cladding will usually damage the core structure. Different ways must therefore be devised to tap these fibers. Three non-destructive methods may be used to induce the leakage of optical signal from these fibers: (1) The index-matching-fluid method, (2) The temperature method, (3) The bending method.

THE INDEX-MATCHING-FLUID METHOD

The index-matching-fluid method is particularly suited for tapping plastic clad fiber. After stripping off the plastic cladding the bare glass-core section is immersed in an index-matching fluid whose index of refraction may be so chosen that only a small controlled amount of light is allowed to leak out of the core of the multi-mode fiber.

According to the theory of guided waves along optical fibers,[1] the number of modes N that a fiber may carry can be estimated from a very simple relation:

$$N \simeq \tfrac{1}{2}\left(\frac{\omega a}{c}\right)^2 n_1^2\left(1-\frac{n_2^2}{n_1^2}\right) \tag{1}$$

$$\left(n_1 - n_2\right)/n_2 << 1$$

where $\frac{\omega}{c} = k$ is the free-space wave number, a is the radius of the fiber core and n_1 and n_2 are respectively the indices of refraction for the core and for cladding which is the index-matching-fluid. Therefore the number of modes that can be supported by the fiber guide is directly proportional to the difference of the square of indices of refraction. In other words, when the cladding index approaches the core index, the number of propagating modes approaches a small value. By finely adjusting the value for $(n_1 - n_2)$, the number of propagating modes may be adjusted. If the modes excitation condition is such that all modes are equally excited, one may derive an approximate expression for the fractional power carried in the cladding region. It is

$$\frac{\text{power transmitted in the cladding}}{\text{total transmitted power}} \simeq \frac{8}{3V} \tag{2}$$

$$\text{with } V = \left(\frac{\omega a}{c}\right) n_1 \left(1-\frac{n_2^2}{n_1^2}\right)^{1/2} \text{ and } (n_1 - n_2)/n_2 << 1.$$

By adjusting the cladding index, (in the present case, it is the index-matching-fluid) one may control the amount of power carried in the cladding region which can then be tapped off very easily. Relations (1) and (2) have been plotted in Fig. 1.

To verify the above observation, measurements were carried out. A schematic diagram of the experimental setup is shown in Fig. 2. Results of our measurements are shown in Fig. 1. This experiment shows that one may induce a controlled amount of leakage for the plastic-clad fiber link with this method.

THE TEMPERATURE METHOD

It is well-known that the refraction index of glass or plastic varies as a function of temperature.

For the glass-clad fiber, the index of the glass core or that of the glass cladding varies as a function of temperature in a similar fashion such that the NA of the fiber remains unchanged.[2] Hence, no leakage of light occurs as the temperature changes. As far as the plastic clad fiber is concerned, since the index of the glass core and that of the plastic cladding vary as a function of temperature in a dissimilar manner, the NA of the fiber is significantly changed as the temperature varies. Hence, leakage of light occurs as the temperature changes.

To confirm the above observation, measurements were carried out. The schematic diagram of the experimental setup is similar to that shown in Fig. 2, except the segment where we placed the index-matching fluid is replaced by a dewar which provides a controlled temperature enviornment for a length of fiber. To make the desired measurements it is not necessary to strip the cladding from the fiber as was done for the previous method. Detailed experimental data are shown in Fig. 3 for the plastic-clad fiber and for the glass-clad fiber. As expected no leakage of light is detectable for the glass-clad fiber as the temperature changes. On the other hand, very significant leakage of light occurs for the plastic-clad fiber when the temperature varies through a critical region. Apparently a phase transition for the plastic cladding occurs in this temperature range so that the index for the plastic changes significantly.

So far, it appears that glass-clad fiber is immune to our attempts to induce leakage. It will be shown, however, that the next attempt will be successful.

THE BENDING METHOD

By bending a fiber, radiation or cladding modes may be induced due to the sharp curvature of the fiber. According to a simplified analysis,[3] the fraction of modes lost in a bent step-index type fiber is $2a/(R\delta)$ where a is the core radius, $\delta = 1 - (n_2/n_1)^2$, and R is the curvature radius. The curvature loss as a function of the curvature for the step-index fiber is sketched in Fig. 4. It can be seen that very large curvature loss can be induced.

Measurements were performed using the basic experimental set-up as sketched in Fig. 2. The fiber under examination was tightly wound tem times around a post with predetermined radius of curvature. By using posts of different radius, we can adjust the bending radius of the fiber. Results of our measurements are shown in Fig. 5. It can be seen that, as expected, leakage from the fiber line is very significant when the radius of curvature reaches a certain critical value. One notes that the bending method to induce leakage is equally effective when applied to the glass-clad fiber as to the plastic-clad fiber.

CONCLUSIONS

The fact that the above methods provide "non-destructive" and "recoverable" ways of inducing leakage in an optical fiber is worth noting. We have also shown experimentally that when the distrubances caused by the above schemes were removed, the transmission characteristics of the fiber link returned to normal. The security implication of the above experiments is clear. It appears that the only way to insure that no leakage of information had occured is to monitor continuously the power level of the received signal. Techniques to achieve this will not be discussed here.

REFERENCES

1. C. Yeh, "Advances in Communication Through Light Fibers in Advances in Communication Systems," Vol. 4, Theory and Applications, Academic Press, New York (1975); D. Gloge, Appl. Opt. 10, 2253 (1971).

2. C. J. Parker and W. A. Popov, Appl. Opt. 10, 2137 (1971).

3. D. Gloge, Appl. Opt. 11, 2506 (1972).

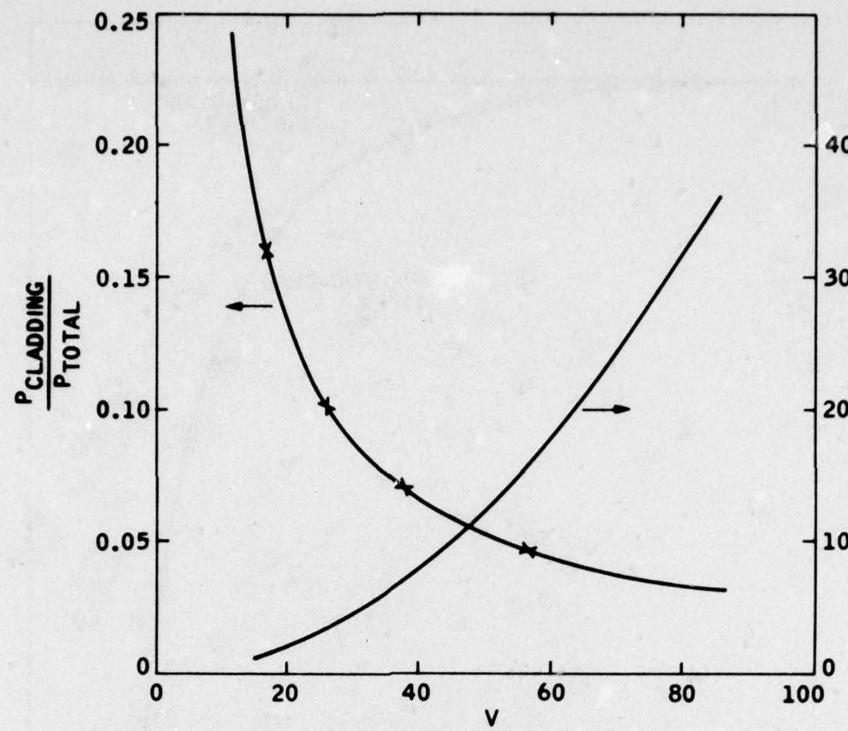

Figure 1 Normalized power in the cladding and the number of modes (N) as a function of $V = k_1a(1 - (n_2/n_1)^2)^{\frac{1}{2}}$. The crosses are experimental points. The arrows indicate the ordinates for the curves.

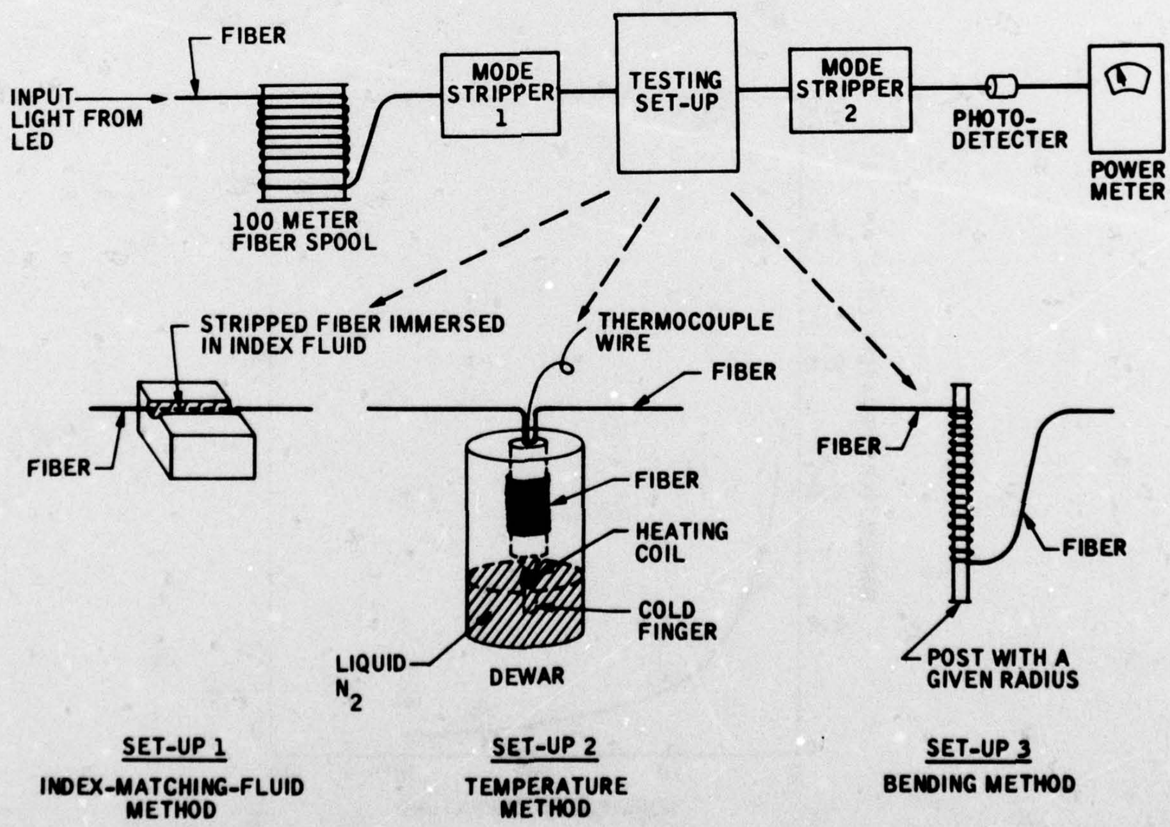

Figure 2 Schematic Diagram for the Experimental Set-Up

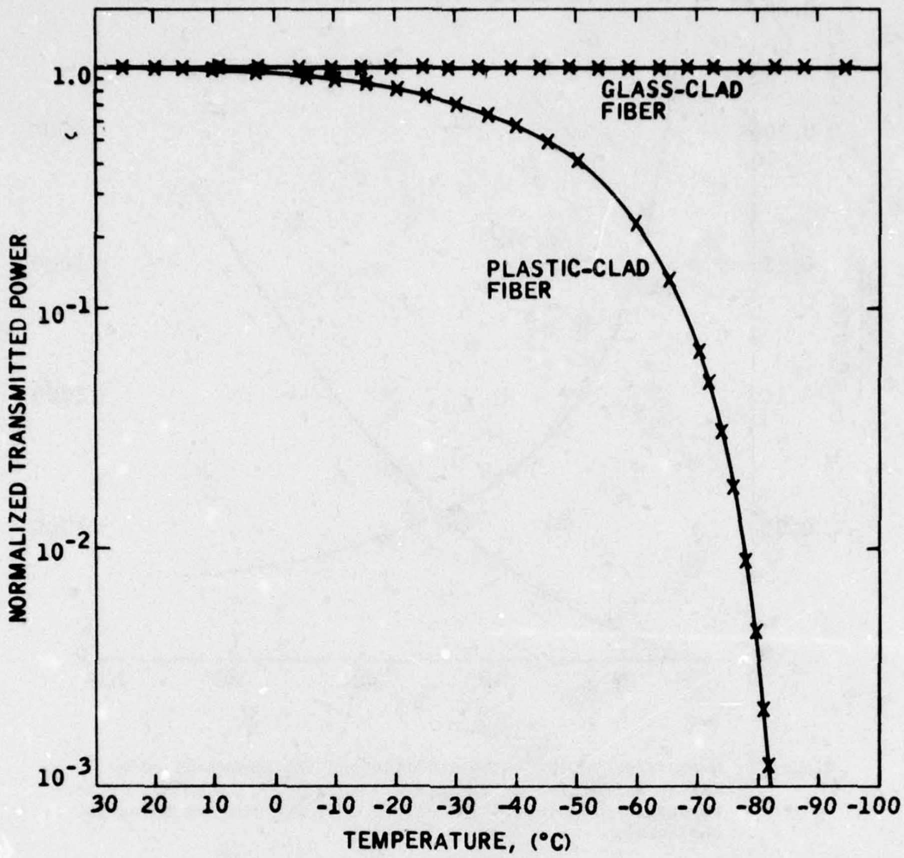

Figure 3 Normalized Transmitted Power vs. Temperature for Plastic-Clad Fiber and Glass-Clad Fiber.

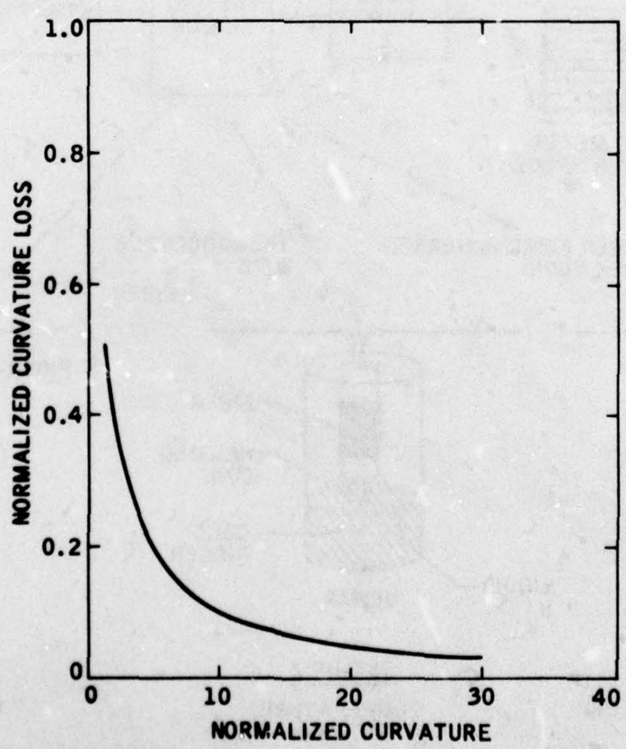

Figure 4 Normalized Curvature Loss vs. Normalized Curvature for Step- Index Fiber.

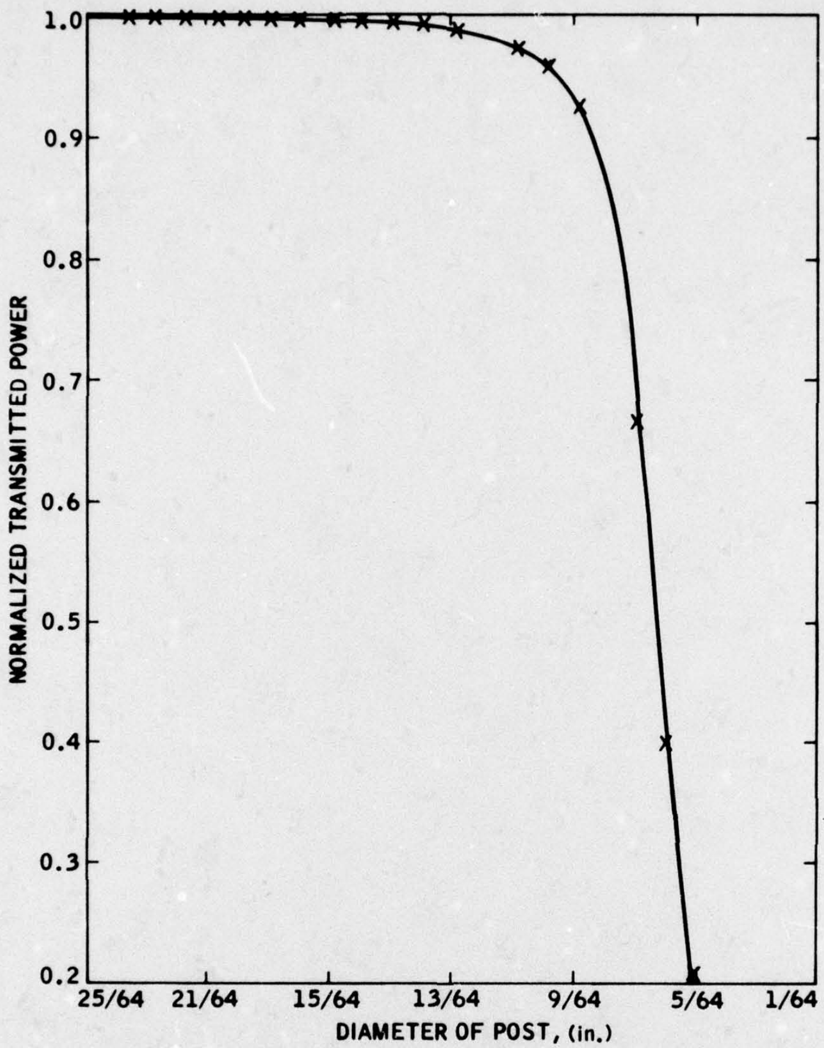

Figure 5 Normalized Transmitted Power vs. Curvature for Glass-Clad Fiber. A length of 1 meter is wound around the post.

ETUDE ET RESULTATS DE LA FONCTION DE TRANSFERT DES FIBRES OPTIQUES

R. BOUILLIE - J.C. BIZEUL - M. GUIBERT
CNET
route de Trégastel
22300 LANNION - France

SOMMAIRE :

Nous donnons dans cette communication un principe d'obtention du module de la fonction de transfert des fibres optiques. Il consiste à utiliser deux transformées de Fourier d'un train d'impulsions lumineuses récurrentes. Ensuite, nous nous attachons à expliquer l'appareillage ainsi que les résultats que nous obtenons sur différents types de fibres (saut d'indice, gradient d'indice, à ouverture numérique différente).

Et en conclusion, nous abordons les possibilités de liaison par fibres optiques selon les divers débits numériques.

I. - INTRODUCTION

La dispersion dans les fibres optiques a été étudiée par de nombreux auteurs. Les techniques les plus anciennes consistent à injecter une impulsion lumineuse de très courte durée dans la fibre et à mesurer l'élargissement à mi-hauteur de cette impulsion après propagation (ref. 1). Si cette mesure est relativement simple avec des fibres à forte dispersion, elle devient plus délicate avec des fibres dont les propriétés de propagation sont nettement meilleures (gradient d'indice quasi parabolique par exemple) ; dans ce cas, un difficile calcul de déconvolution est alors nécessaire. Même si cette technique est utilisée, elle conduit à une valeur caractéristique de la propagation, peu familière aux concepteurs de systèmes, plus habitués à travailler dans le domaine fréquentiel. Depuis quelques années, la mesure de la fonction de transfert des fibres a, peu à peu, remplacé celle de la réponse impulsionnelle (ref. 2). Plusieurs techniques permettent d'arriver à ces résultats (calcul, wobulation etc...), nous décrirons ici la méthode utilisant la transformée de Fourier d'un train d'impulsions lumineuses récurrentes, méthode qui jusqu'à présent a donné les meilleurs résultats.

II. - PRINCIPE ET APPAREILLAGE

II.1. - Principe (Fig. 1)

Si on prend la transformée de Fourier d'un train d'impulsions récurrentes, on obtient, dans le plan des fréquences, un spectre de raies espacées de la fréquence de récurrence du train émis et dont l'enveloppe est la transformée de Fourier de l'impulsion unitaire.

Si on effectue cette mesure avec un train d'impulsions lumineuses avant et après passage dans une fibre optique, on obtient deux spectres de raies, dont le rapport (ou la différence en échelle logarithmique) est le module de la fonction de transfert de la fibre.

II.2. - Appareillage

Il se compose de deux sous-ensembles émission et réception qui peuvent être éventuellement dans des lieux géographiques différents pour des mesures sur des câbles installés par exemple.

II.2.1. - Emission

De nombreuses sources optiques peuvent convenir pour effectuer ces mesures ; nous n'avons retenu que celles susceptibles d'être utilisées dans un système de transmission par fibres, c'est-à-dire les émetteurs semi-conducteurs à base d'Arséniure de Galium dont la longueur d'onde d'émission est de 8300 A°

Dans cette catégorie, nous avons le choix entre la diode électroluminescente, la diode laser à large contact et la diode laser à contact étroit. La diode électroluminescente, du fait de son diagramme de rayonnement ne présente guère d'intérêt pour l'appareillage et de ce fait, nous n'utilisons que les diodes à effet Laser : le laser à large contact utilisé est le LBA 185 du STL dont la largeur du spectre d'émission est d'environ 50 A°, le laser continu provient également du STL et possède une largeur spectrale de 4A°. Ces diodes sont excitées par un générateur d'impulsions réglables en fréquence, en largeur et en niveau. Les impulsions lumineuses générées peuvent être aussi courtes qu'une nanoseconde et pour le LBA 185 avoir une puissance lumineuse de quelques watts crête.

II.2.2. - La réception

La réception est composée d'un photorécepteur et d'organes de mesures et de traitement.

Le récepteur est une photodiode à avalanche, de type PΠPN (< 1 GHz) ou une diode PIN-RTC > 1 GHz. Pour mesurer la courbe affaiblissement/fréquence d'une fibre, il faut émettre de l'énergie dans les fréquences où l'on veut montrer que la fibre va les atténuer ; il faut donc éviter de choisir une diode qui coupe avant la fibre. Le choix du photodétecteur doit donc se faire en fonction du morceau de fibre à mesurer.

Le détecteur chargé sur 50 Ohms est directement connecté à un analyseur de spectre, lui-même relié à un calculateur qui enregistre le spectre de raies et traite les résultats.

L'utilisation des diodes à avalanche nécessite certaines précautions, parmi lesquelles nous noterons :

- avoir de bonnes cassures des extrémités des fibres
- positionner parfaitement la sortie de la fibre devant la diode, afin d'éviter tout filtrage spatial qui fausserait les résultats.
- travailler à puissance optique incidente constante, pour éviter les non-linéarités.
- ajuster la tension d'alimentation afin d'éviter les phénomènes de saturation.

Après avoir rappelé les principes et l'appareillage utilisé, nous allons discuter l'influence des conditions d'injection de la lumière dans les fibres, sur le résultat obtenu.

III. - INFLUENCE DES CONDITIONS D'INJECTION

La figure n°2 montre l'influence des conditions d'injection sur la fonction de transfert ; entre un pinceau très faiblement divergent, un faisceau divergent et une autre fibre prise comme source, on obtient pour certaines fibres des résultats très différents. Pour pouvoir comparer les différentes fibres entre elles, il faut assurer des conditions d'injection absolument répétitives.

D'autre part, dans un système de transmissions longue distance, l'ensemble du câble optique sera constitué par n tronçons de câble connectés bout à bout. Dans ces conditions, seule la moitié des fibres constituant le premier tronçon et la moitié des fibres constituant le dernier tronçon seront excitées par un émetteur optoélectronique, toutes les autres le seront par une autre fibre du tronçon précédent.

Dans ces conditions, pour assurer des injections répétitives et faire des mesures proches de l'application système, nous sommes amenés à mesurer toutes nos fibres à partir d'une "fibre d'injection".

Cette façon de procéder permet des mesures ne nécessitant pas la destruction du câble, la fibre d'injection servant alors de référence.

Cette fibre d'injection a des caractéristiques voisines de celles de la fibre à mesurer (diamètre intérieur et extérieur, ouverture numérique), sa longueur est de quelques mètres et l'on y créée un fort couplage de modes par microcourbures.

De nombreux résultats ont déjà été publiés sur les fibres à saut d'indice (ref. 3 et 4) ; dans la suite nous reprendrons quelques uns des plus importants et nous développerons ceux obtenus plus récemment sur les fibres à gradient d'indice.

IV. - RESULTATS SUR LES FIBRES A SAUT D'INDICE

Dans ce chapitre, nous donnerons des résultats obtenus sur des fibres à saut d'indice susceptibles d'être utilisées dans des systèmes de télécommunications à longue distance ; Ceci suppose une atténuation très basse (4dB/km) donc un matériau très pur (silice - silice dopée). Dans ces conditions, l'ouverture numérique des fibres est généralement comprise entre 0,10 et 0,25. Il est bien évident que pour d'autre type de fibre à ouverture numérique nettement plus grande, le principe des mesures reste toujours valable. (fibre Schott en verre).

IV.1. - Allure et expression mathématique de la fonction de transfert

La figure 3 donne la courbe de réponse d'une fibre de un kilomètre et d'ouverture numérique 0,146. On peut caractériser cette courbe par une ou plusieurs valeurs caractéristiques, telles que fréquence à -3dB ou -6dB.

Pour déterminer la fonction temporelle dont cette courbe est la transformée de Fourier, nous aurons repris les résultats théoriques exprimés dans la ref. 5.

La figure 4 qui présente la transformée de Fourier de la fonction

$$f(t) = \frac{1}{\tau}\left(\tau - \frac{t}{2}\right) \quad \text{pour } t \leqslant 2\tau$$

$$f(t) = 0 \qquad t \geqslant 2\tau$$

et la figure 5 qui présente la comparaison d'une de nos courbes expérimentales à la courbe théorique f(t) pour τ = 6ns montrent que la coïncidence est très bonne. Les considérations théoriques (en particulier l'utilisation de l'optique géométrique) présentées ref. 5 se trouvent ainsi pleinement validées : Ce résultat montre de plus qu'il n'y a pas conversion de modes pour les fibres à saut d'indice sur des longueurs de l'ordre du kilomètre.

IV.2. - Mesure de l'ouverture numérique

La mesure ci-dessus permet, en principe, de mesurer l'ouverture numérique, mais dans la pratique elle s'avère délicate à réaliser avec une bonne précision. Une autre façon de procéder consiste à désaxer d'un certain angle la fibre à mesurer par rapport à la fibre source. La fig. 6 montre l'évolution de la courbe de transfert en fonction de l'angle de désaxage ; il apparaît dans cette caractéristique des trous à certaines fréquences. On démontre théoriquement que la fréquence du premier trou créé dépend de l'ouverture numérique de la fibre et de sa longueur.

La figure 7 montre cette dépendance et peut être utilisée pour la détermination de l'ouverture numérique.

IV.3. - Influence de l'ouverture numérique sur la bande à -6dB

Etant en possession d'un grand nombre de pièces de un kilomètre de fibres, dont l'ouverture numérique varie entre 0,1 et 0,35 nous avons regardé l'influence de cette ouverture numérique sur la fréquence à -6dB ; Le tableau 8 présente ces résultats.

On vérifiera que si pour une fibre donnée, on connait son ouverture numérique N_1 et sa fréquence à -6dB. On déterminera la fréquence f_2 d'un autre kilomètre d'ouverture numérique ON_2 par :

$$f_2 = \left(\frac{ON1}{ON2}\right)^2 \cdot \quad f1$$

Ce résultat découle directement de l'analyse théorique dont la référence a été donnée précédemment et qui conduit à une réponse impulsionnelle f(t) dont la valeur de τ est donnée par :

$$\tau = \frac{kL}{n.C} \quad (ON)^2$$

où n, est l'indice du coeur

L la longueur du guide

C la vitesse de la lumière

k une constante de proportionalité

IV.4. - Association de fibre à saut d'indice

Nous avons connecté bout à bout plusieurs pièces de un kilomètre et à chaque nouveau kilomètre, nous avons relevé la fonction de transfert (fig. 9). Les connecteurs sont constitués de simple rainure en V et ont une perte moyenne d'environ 0,5dB avec liquide adaptateur d'indice.

Si on étudie le comportement du module de la fonction de transfert, on s'aperçoit que plus on ajoute de longueurs, plus on modifie l'allure de la réponse, jusqu'à obtenir une stabilité à la courbe 5. Cette courbe limite est une gaussienne, transformée de Fourier, d'une fonction temporelle gaussienne. La réponse impulsionnelle des fibres connectées est donc différente de la réponse des fibres individuelles. Une réponse gaussienne est due à une importante conversion de modes dans le guide ; dans le cas présent, cette conversion est due aux connecteurs qui font une redistribution aléatoire de l'énergie des modes d'une fibre dans l'autre.

De ce résultat, on en déduit que la bande passante par exemple à -3dB décroît en fonction de l'inverse de la racine carrée de la longueur.

V. - RESULTATS SUR FIBRE A GRADIENT D'INDICE

V.1. - Influence du profil d'indice

Dans cette expérience, nous cherchons à corréler la valeur de f_o (valeur de la fréquence à -6dB) à celle du paramètre α, proposé par GLOGE-MARCATILI, comme décrivant correctement le profil d'indice. La figure 10 montre qu'on obtient une bande passante (à -6dB) optimale pour une valeur de comprise entre 2 et 2,1 comme le prévoient les études théoriques faites pour les fibres dopées au germanium.

V.2. - Expression de la fonction de transfert

La fig. 11 montre la fonction de transfert d'une fibre à gradient d'indice d'une longueur égale à 1km et qui a comme paramètre α une valeur de 2 - 2,1. On vérifie que l'allure de cette courbe est identique à une courbe de Gauss de la forme :

$$e^{-k\left(\frac{f}{f_c}\right)^2}$$

Le paramètre f_c est une valeur caractéristique dépendant de la nature de la fibre et de sa longueur.

Pour plus de commodités, nous identifions chacune des fibres par sa valeur f_c comprise à - 3dB bien que toute autre valeur puisse convenir.

V.3. - Association de fibres à gradient d'indice

Pour les fibres à saut d'indice dont nous avons parlé précédemment, nous avons remarqué qu'il fallait avoir un nombre de pièces connectées pour pouvoir dire que la forme de la courbe représentant le module de la fonction de transfert devenait guaussienne ; pour les fibres à gradient d'indice, dès le premier kilomètre, nous avons déjà cette forme et comme pour les sauts d'indice, nous pouvons donc écrire pour une liaison de pièces connectées

$$F_c \quad \frac{f_c}{\sqrt{L}}$$

F_c fréquence caractéristique à -3dB de la liaison réalisée

f_c fréquence caractéristique à -3dB d'une pièce de la liaison

L longueur totale de la liaison

VI. - CONCLUSION

Dans le tableau ci-dessous (fig. 12) nous allons rassembler différents résultats sur des fibres à saut d'indice dont on connaît l'ouverture numérique O.N. et sur des fibres à gradient d'indice dont on connait le paramètre α .

Cette figure permet de savoir la longueur maximale réalisable avec certaines fibres. Pour un système de débit numérique déterminé, la fréquence de coupure à -3dB est fonction du code en ligne utilisé. Les possibilités de codes sont considérables;ici nous prendrons les hypothèses minimum et maximum pour la bande de fréquence nécessaire en réception, c'est-à-dire 0,5 et 1,5 fois la fréquence rythme du débit en ligne choisi.

Dans ce tableau, la représentation est réalisée à 1 x fr (fr étant la fréquence rythme)

Nous avons repéré la valeur de la fréquence rythme des débits : 2 ; 8 ; 34 ; 52 ; 140 Mbit/s. Sur cette figure, nous n'avons pas tenu compte de l'atténuation propre de la fibre ou du cable , mais en toute rigueur, si l'on se fixe une perte de 6dB par km avec les connecteurs, nous sommes limités par la dynamique des systèmes laser-photodiode (ref 6).

- BIBLIOGRAPHIE -

1. - R. BOUILLIE - J. ANDREWS
Electronics Letters, 16 mai 1972
Measurements of broadening of pulses in glass fibres

2. - K. STEINER - M. TREHEUX - R. BOUILLIE
Applied Optics, Vol. 12 n°11, novembre 1973
"Multimode Waveguide : a lax pass filter"

3. - R. BOUILLIE - M. TREHEUX
Topical meeting on optical fibers
Williamsburg, janvier 1975

4. - G. LE NOANE - R. BOUILLIE
First European conference on optical fibre communication
Londres, septembre 1975

5. - R. BOUILLIE, K.H. STEINER, M. TREHEUX
On the pulse broadening in dielectric multimode waveguides
Opto Electronics 5 1973

6. - C. BOISROBERT, R. BOUILLIE , M. TREHEUX
Echo des Recherches - Octobre 75, page 41

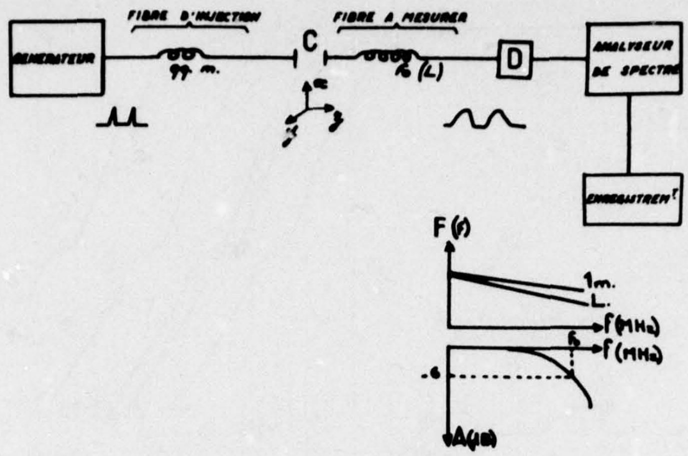

Fig. 1 Principe

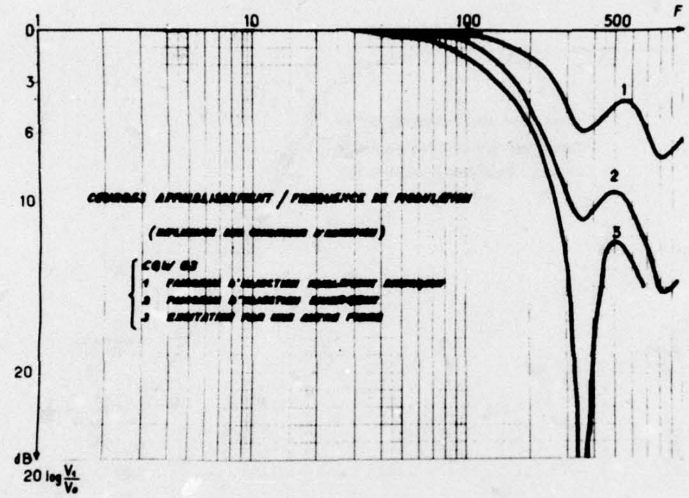

Fig. 2 Allure de la réponse en fonction des conditions d'injection

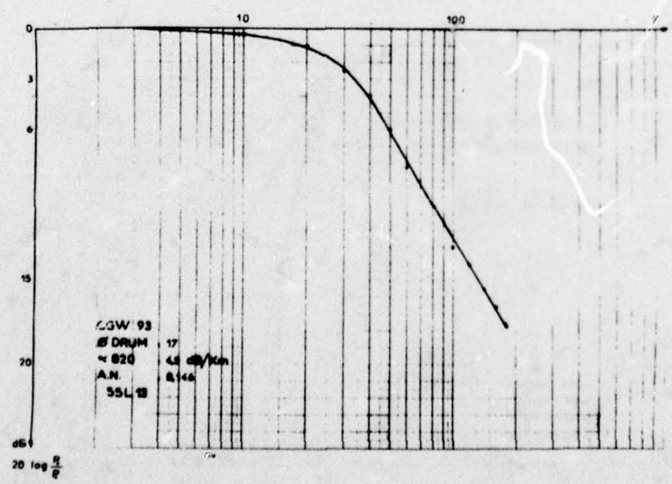

Fig. 3 Allure de la réponse d'une fibre à saut d'indice (CGW 93)

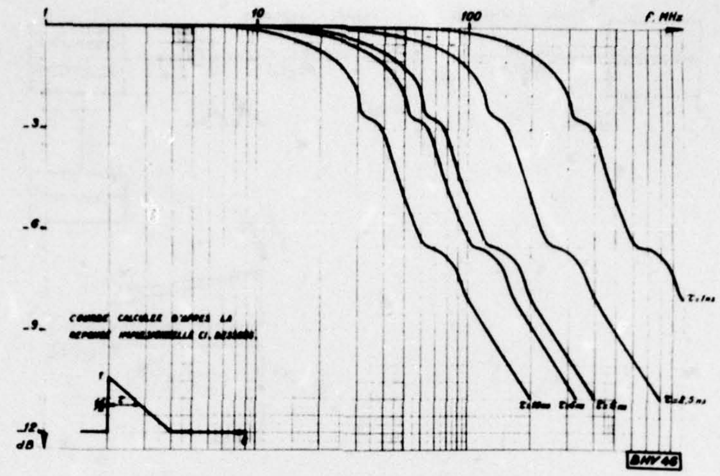

Fig. 4 Réponse fréquentielle théorique

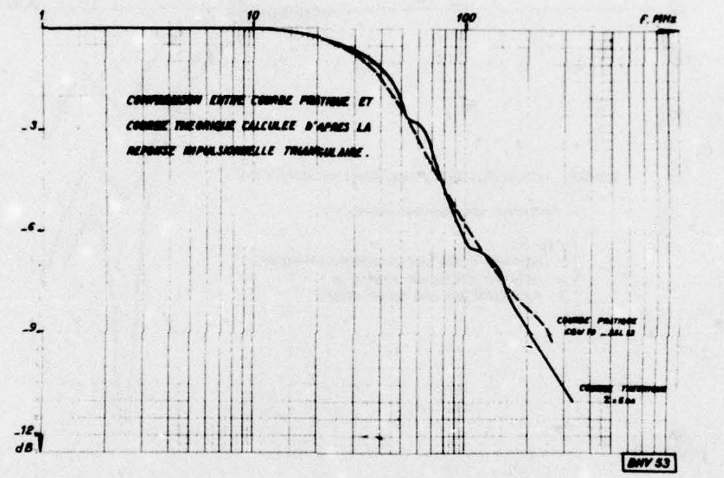

Fig. 5 Comparaison entre courbe pratique et courbe théorique

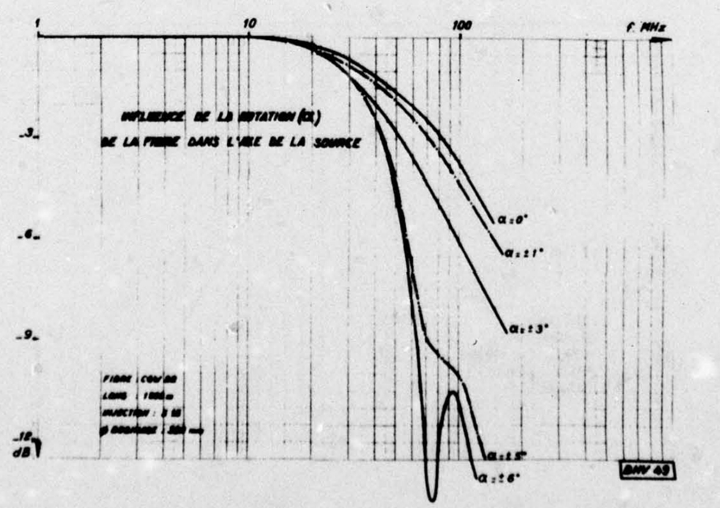

Fig. 6 Influence de la rotation

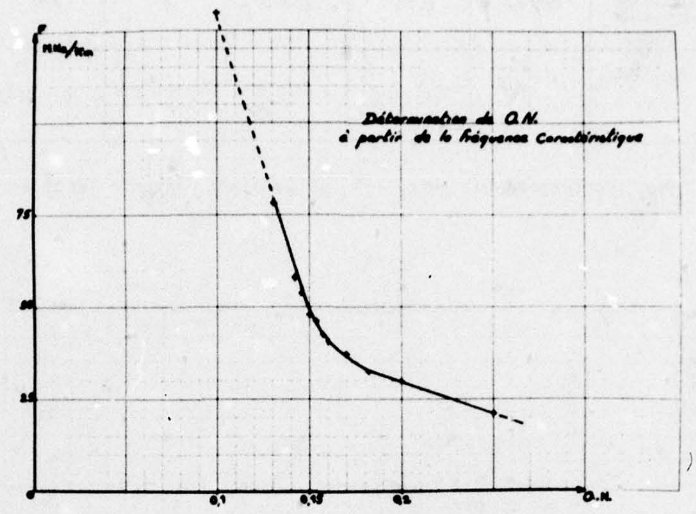

Fig. 7 Détermination de l'ouverture numérique

Désignation	CNET	CGW 22	CGW 65	CNET	CNET	CNET	SCHOTT (verre)
Ouverture Numérique O.N	0,1	0,13	0,16	0,20	0,25	0,30	0,35
Bande Passante à - 6dB (MHz)	100	60	40	25	17	11	8,4

Fig. 8 Correspondance entre l'ouverture numérique et la bande passante (saut d'indice)

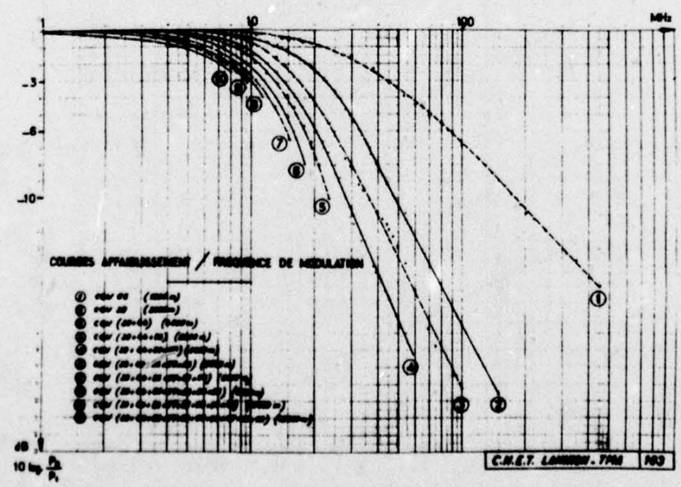

Fig. 9 Composition de pièces connectées (saut d'indice)

Bande Passante à -6dB (GHz)	0,220	0,425	0,750	1	1,5
Paramètre α	1,3	1,6 - 1,7	1,8 - 1,9	1,9 - 2	2 - 2,1

Fig. 10 Correspondance entre α et la bande passante (gradient d'indice)

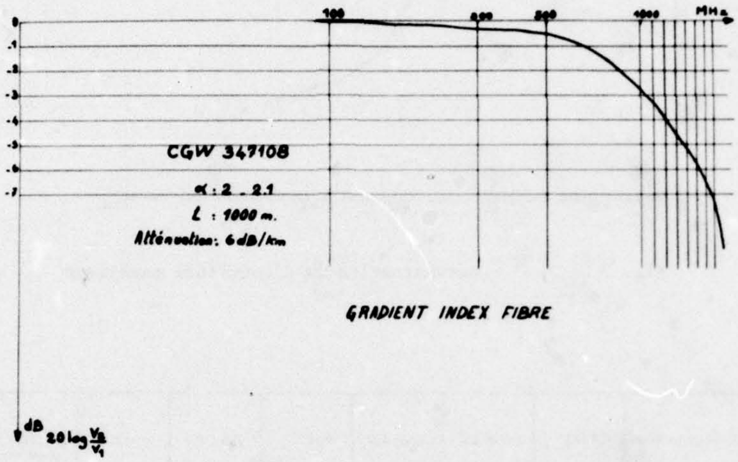

Fig. 11 Allure de la réponse d'une fibre à gradient d'indice

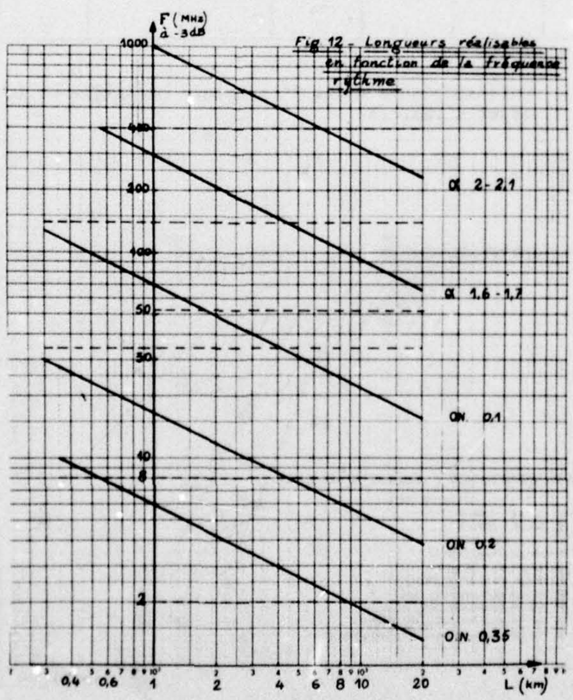

Fig. 12 Longueurs réalisables en fonction des caractéristiques de chaque fibre et de la fréquence rythme.

DETAIL RESOLUTION IN OPTICAL FIBRE INDEX PROFILING METHODS

W. J. Stewart

Allen Clark Research Centre
The Plessey Company Limited
Caswell Towcester Northants.
U.K.

The resolution of fine structure in fibre refractive index profiles by near-field profiling methods has been investigated experimentally and theoretically. The standard near-field method and a new improved method are treated. The significance of this structure in affecting fibre bandwidth is described and the results qualitatively explained in resolution terms. The concept of mode volume is introduced.

The measurement of refractive index within optical fibre cores, and particularly the measurement of index profiles in graded fibres, has always proved difficult. One of the simplest methods is the 'near-field' profiling technique originally described by Payne, Sladen and Adams(1). Variants of this method have been devised by other workers (2,3). All these methods suffer from the need to correct for the effect of leaky modes(1). A new method, based on similar principles but avoiding this effect has been devised, and will be described in full at IOOC in Tokyo. All these methods show very fine structure in the index profile, although it can also show false structure(4). We have done a series of experiments in which a test object known to be of step refractive index structure has been examined using a system similar to that employed in references 2 and 3, except that no guiding structure was involved. The apparatus consisted of a microscope objective that focussed a spot from a laser onto the surface of a silica or glass plate that had been partially cracked. The crack had been filled with liquid of slightly lower refractive index than the plate, and covered with a coverslip. This formed a thin slab with its surface parallel to the axis of the microscope objective, a few microns thick. Liquid refractive indices higher than that of the plate were not used because of losses expected in the liquid. This layer simulates a thin layer within a larger fibre core. The profiling action in near-field methods arises because the fibre core filters the radiation input to it according to the angle of propagation, this angle in turn being determined by the refractive index in the immediate vicinity of the point of launch. In this resolution experiment and also in the new profiling method, the angle filtering action of the fibre is performed using an external stop behind the plate. This has two important advantages. Firstly the stop is so large that all modal effects are eliminated, and secondly the effective NA that it gives can be varied at will. Experiments have been performed at filtering aperture NA's from 0.5 down to near zero, at input objective NA's of 0.5 and 0.25, and for index differences from 10^{-2} to 10^{-4}. The results show fringing at the edges of the objects (known of course to be step index) whose wavelength is characterised by the filtering aperture NA. The amplitude of the fringing is constant for smaller aperture NA's at about 10% of the amplitude of the intensity step, in agreement with ref. 2, but appears to fall for NA's greater than 0.3, possibly due to the finite size of the scanning spot. Neither the fringe amplitude relative to the intensity step nor the wavelength show any dependence upon the size of the index step or the NA of the launching objective.

It is possible to explain these data for some objects in terms of the summation of modes, as was done in reference 2, or indeed on a mode density/information content basis for more general structures, but a simpler method applicable to all near field methods can be devised. This describes the fringes as due to interference between the original launched wave and light Fresnel reflected from the index step. It is not difficult to show that fringes produced in this way satisfy all the requirements of the experimental data and show no significant differences with polarization. They vary in fact exactly as the intensity step predicted by geometrical optics varies, and it seems possible that all near-field imaging might be explained in this way, though this has not proved possible to date. The fringing is also, except for phase changes, independent of whether the index step is up or down. These results are especially significant as it can easily be shown that normal coherent or incoherent imaging theory(5) shows quite incorrect dependencies. This has been confirmed experimentally using both phase and amplitude test objects.

In standard near field methods the observing NA is fixed by the fibre NA - the fibre local NA that is, which falls off towards the edge in graded fibres. This effectively limits the resolution obtainable, especially near the edge of graded fibres where the local NA is very small, and this effect and the lack of available test objects of known structure makes testing this theory impossible. However, the new method mentioned earlier uses radiation modes to profile the fibre and its resolution is controlled using an external stop. Since this stop has of necessity to filter at about twice the fibre NA the resolution should be improved by about this factor. In order to test the theory for an object with a higher refractive index than its surroundings a single mode fibre was profiled using both standard and new methods. The standard method of course gives a curve very similar to the intensity profile of the fibre mode, whereas the new method clearly shows the shape of the fibre index profile, albeit not very clearly.

Much effort has been devoted to the problem of defining the optimum index profile. Less attention has been paid to the effects of errors from this profile. Nevertheless two important papers have appeared on this subject, by Olshansky(6) and Arnaud(7). Both are complex and make resort ultimately to numerical methods to calculate the results. The former treats (among others) sinusoidal perturbations about an optimum profile, and the latter treats a staircase approximation to the optimum. The theoretical approaches also differ considerably. So, unfortunately do the methods of presenting the results and the parameters of the fibres treated numerically. Nevertheless it is possible by examining the equations developed to deduce dependencies, or likely dependencies on the fibre parameters - primarily on the fibre radius 'a', the index difference parameter 'Δ' and the well-known parameter 'V'. Olshansky's equations show that for constant V the degradation in bandwidth produced by a given perturbation is linearly dependent upon Δ, and his numerical results (and comments upon them) appear to suggest that the effect of a sinusoidal perturbation depends upon (n/V), where 'n' is the number of periods radially. Arnaud's results show an approximate dependence on Δ^2 for constant a. Using these to adjust the numerical results so that they apply to the same fibre shows that the results are actually very similar, except that Arnaud's include the effect of the residual second order dispersion and Olshansky's do not. Considering the different nature of the perturbations agreement is quite close. Examination of the results shows that they are consistent with the effect of a sinusoidal perturbation varying as (Δ F(n/V)) where F is a function of u/V that is near-constant for low n/V but shows a cut-off behaviour at higher values. In the vicinity of this cut-off the Δ^2 dependence shown by Arnaud's results is found. The resolution of detail that would be expected from the standard near field profiling method, that is the ability of the fibres' modes to resolve the detail actually shows very much this dependence, so that the effect of a perturbation depends upon it being resolved. This simple picture explains the general features of the calculated results, but, as Arnand pointed out, perturbations at wavelengths down to less than half the resolution limit still have a significant effect, albeit somewhat reduced, and in this context the extra resolution of the new profiling method is useful.

It might also be deduced that small core fibres of low V value will be less sensitive to the inevitable errors from the ideal profile than larger fibres. This is probably true and 'low-mode' fibres with V values less than 10 may be useful as alternatives to single mode fibres for high bandwidth lines. Assuming longer source wavelengths were used this gives a core diameter of about 25 microns. However, care must be exercised in choosing such designs; for example at any given V value optimum insensitivity, and hence maximum bandwidth, is achieved at minimum Δ , but this will also involve highest microbending loss. In this context it seems opportune to introduce a new fibre parameter the effective V value V_e. This is defined as the square root of the integral of the index difference across the core of the fibre. With appropriate choice of constants this gives the usual V value for step-index fibres, but a new value for graded fibres. For doped silica fibres it is simply dependent upon the quantity of dopant per unit length. Ve^2 is also directly proportional to the number of modes in a fibre and therefore the light coupled from an LED. It is defined for any fibre regardless of gradient and cross-sectional shape, and a remarkable range of parameters lose their gradient dependence if expressed in these terms. For example the single mode cut-off in graded and slab guides, and the microbending loss. The dependence of jointing loss on gradient is somewhat reduced.

Thanks are due to the directors of The Plessey Company Limited for permission to publish this paper.

References

1. D. N. Payne, F. M. E. Sladen and M. J. Adams, First European (IEE) Conference on optical fibre communication, London 1975.

2. J. A. Arnaud, B.S.T.J. 55, 10 (1976) p. 1489.

3. J. Midwinter, private communication.

4. E. Bianciardi and V. Rizzoli, to be published.

5. e.g. Born and Wolf, 'Principles of Optics'.

6. R. Olshansky, Applied Optics, 15, (1976) p. 782.

7. J. A. Arnaud, Electronics Letters 12 (1976) no. 1, p. 6.

NOVEL TECHNIQUE FOR MEASURING THE INDEX PROFILE OF OPTICAL FIBERS

by

J.A. Arnaud[(T)]
and
R.M. Derosier
Bell Laboratories
Crawford Hill Laboratory
Holmdel, N.J. 07733

SUMMARY

A novel technique for measuring the refractive index profile of optical fibers is demonstrated, which offers substantial advantages over alternative methods. The method consists of illuminating a small area of the fiber core and measuring the total transmitted power. The transmission of leaky modes is accounted for in the manner reported previously by other authors. The index profiles of germania-doped fibers obtained by this technique are compared to interferometric measurements. The resolution is shown to be limited by wave optics effects to about $\lambda_o\,(4n\sqrt{2\Delta}\,)^{-1}$, where $\Delta \equiv \Delta n/n$. The distorsion of the index profile as the wavelength varies and wave-optics effects are investigated.

1. INTRODUCTION

The accurate measurement of index profiles at various wavelengths may help design multimode fibers whose transmission capacity would go well beyond what has been presently achieved. Indeed, numerical calculations and theoretical analyses (Marcatili 1977, Arnaud 1976a) show that there exists index profiles (usually no power-law profiles) which, for quasi-monochromatic sources, provide transmission capacities of about $1.6/\Delta^2$ Mbit/s x km, where $\Delta \equiv \Delta n/n$. Measured transmission capacities are about 10 times smaller. In order to determine the optimum profiles, it is indispensible to know the variation of $dn/d\lambda_o$ as a function of n for the class of materials considered, with an accuracy of about 1%. The required variation of $dn/d\lambda_o$ as a function of n can be obtained, in principle, from measurements on bulk samples (e.g., Arnaud and Fleming, 1976). One may question, however, whether measurements on bulk samples are applicable to the fiber material with sufficient accuracy. For that reason, and also because the fabrication and measurement of bulk samples is time consuming, the direct measurement of index profiles at various wavelengths is highly desirable. Once the optimum profile applicable to the class of materials considered has been determined, oneneeds measure the departures of the profile $n(r)$ of the fabricated fiber from optimum. Very small deviations may degrade considerably the transmission capacity.

An interesting experimental technique for measuring circularly symmetric index profiles has been proposed by Gloge an Marcatili, 1973. The index profile is obtained by measuring with a pin hole the radial distribution of intensity in fibers excited by Lambertian (e.g., thermal) sources. In a series of careful measurements, Sladen, Payne and Adams (1975) have shown that good agreement can be obtained between the intensity in the fiber core and the index profile obtained be interferometry provided the non-zero transmission of the leaky modes is accounted for. If this correction is made, the fiber samples need not be larger than about 1 meter, and may be as small as 1 cm.

The technique that we describe in the present paper, henceforth called the transmission technique, is related to the near-field technique discussed above, but it differs from it in may significant ways. Arnaud (1976b) has shown that, if one illuminates a small area of the fiber core (perhaps of the order of λ_o^2) at x, y, the total transmitted power is, for sufficiently long fibers, proportional to $n^2(x,y) - n_s^2$, where $n(x,y)$ denotes the refractive index at x,y , and n_c the cladding index. The proof is straight-forward : The rays radiated from the illuminated area have an almost uniform distribution in the plane k_x , k_y , where k_x, k_y denote the transverse components of the wave vector $\underline{k}$. Because of the relation $k_x^2 + k_y^2 + k_z^2 = k^2(x,y) \equiv (\omega/c)^2 n^2(x,y)$ which holds between the rectangular components of $\underline{k}$, and because only rays whose k_z is larger than k_s are transmitted without loss, the power transmitterd through long fibers is proportional to

$$k_x^2 + k_y^2 = k^2(x,y) - k_s^2 \equiv \text{index profile} \tag{1}$$

(see Fig. 1). The rays in the dotted area in Fig. 1b leak away if the fiber is sufficiently long. Otherwise their contribution to the total transmitted power needs to be subtracted in the manner reported by Sladen and others (1975). If the spot size is less than λ_o , one may use as a source either a (coherent) laser or a (spatially incoherent) LED. If, however, the spot size is significantly larger than λ_o , it is essential to use near-Lambertian sources such as LEDs. Indeed, coherent beams of large cross-section would excite predominantly paraxial rays. This would require introducing additional correction factors.

In the present paper we discuss the principles and limitations of the method, and present experimental results(*). The transmission method gives results that are, in principle, identical to the near-field measurements described in Sladen ant others (1975).

(T) On leave of absence at the Laboratoire des Signaux et Systèmes, E.S.E., Gif s/Yvette 91190 FRANCE
(*) After submission of this paper, the authors were informed that similar experiments were being conducted by J. Midwinter and others at the British Post Office, and J.P. Hazan et L.E.P., France (Private communications).

The main advantage of the transmission method, compared with alternative methods, including the near-field technique, is that it is extremely easy to implement. The results are highly reproducible, to better than on part in one thousandth.

2. EXPERIMENTAL CONDITIONS

To implement the proposed technique, all what one needs is an ordinary microscope, a high-radiance LED or a laser and a detector. The numerical aperture (NA) of the microscope objective should be at least twice as large as that of the fiber. One end of the fiber is properly broken or polished, and centered approximately under the microscope objective at focus. When the microscope eye-piece is replaced by a LED, a small spot of infrared radiation illuminates the fiber end. As we have indicated in the introduction, the power detected at the other end of the fiber is proportional to $n^2(x,y) - n_c^2$, where $n(x,y)$ denotes the index at the point x,y of the fiber where the light is focused, and n_c the cladding index. To obtain the index profile, one may scan either the fiber, with a total motion of about 100 μm, or the source, with a total motion of about 3mm. The arrangement shown in Fig. 2 incorporates a beam splitter (# 1) to allow the fiber to be observed during scanning. (A second beam-splitter, which combines the light from two LEDs, is shown in the figure. It is used only for dispersion measurements.) Some infrared LEDs radiate red light with sufficient intensity for direct observation. To obtain a good resolution, it is desirable that the LED act as a point source, that is, that the apparent size of the LED, demagnified by the microscope objective, be smaller than the diffraction-limited spot $\approx \lambda_0/NA$, defined by the numerical aperture NA of the microscope objective. An apparent emissive diameter of 25 μm (before demagnification) is adequate. The angular orientation of the fiber under the microscope objective can be varied. A gauge measures its displacement with respect to the microscope objective.

The advantages of the proposed technique, compared to the more conventional near-field technique, are manyfold.

2.1. In the near-field method, the source is required to be Lambertian and uniform over the full cross-section of the fiber core. As pointed out by Sladen and others (1975), this condition is in fact difficult to achieve with LEDs. It is necessary to use thermal sources instead of LEDs. Thermal sources (e.g., tungsten wires) provide poor signal-to-noise ratios when the spectral width is restricted by narrow-band interference filters. In the transmission method, one does require the NA of the microscope objective to be significantly larger than that of the fiber (at least for coherent sources), but the requirement concerning the spatial uniformity of the source is relaxed. In some sense, the requirement of spatial uniformity is transferred from the source, where it is difficult to achieve, to the detector, where the condition is easily met.

2.2. The optics is much simplified. One needs only one microscope objective instead of (typically) three. Thus, the signal-to-noise ratio is improved.

2.3. Near-field measurements provide the shape of the index profile but not the absolute value of $\Delta n(r) = n(r)-n_c$, where n_c denotes the cladding index. In the transmission method, one can calibrate Δn by measuring the intensity radiated axially by the microscope objective. This calibration technique will be discussed in more detail in the next section.

2.4. The transmission method can be combined with the Fresnel-reflection technique (for a recent report of the Fresnel-reflection technique, see, for example, Stone and Earl (1976). To implement this modification, one replaces the microscope eye-piece in Fig. 2 by a detector.

An important drawback, that applies to both the transmission and near-field methods, is encountered when the fiber exhibits a low-index region near the cladding. In that case, some modes (besides the so-called weakly leaky modes) are leaking very slowly, and the interpretation of the measurements becomes ambiguous. The resolution offered by these methods may be marginal when the fiber profile exhibits very fast fluctuations. Note also that, for non-circularly symmetric profiles, the corrections factors for leaky rays have not been worket out. If the deviation from perfect circular symmetry is small, however, the usual correction factor may be used.

3. INCIDENT BEAM PATTERN AND INDEX CALIBRATION

In order to make precise measurements, the radiation from the microscope objective should obey approximately the Lambert's law, at least for angles α to the axis that are less than $\sqrt{2\Delta}$. To verify that this law is approximately obeyed, one translates the detector in front of the microscope objective at some distance $d \gg \lambda_0$ from the focal point. Ideally the variation of the detected power as a function of the distance r from axis should be

$$P(r) = \cos^4\alpha = (1 + r^2/d^2)^{-2} \qquad (2)$$

The desired variation of P with r in (2) is shown in fig. 3. The maximum value of r/d corresponding to a particular Δ is given by

$$r/d = (NA^{-1}-1)^{-1/2} \qquad (3a)$$

$$NA = n_0\sqrt{2\Delta} \qquad (3b)$$

The values of r/d are shown in Fig. 3 for typical values of Δ and $n_0 = 1.45$.

Let us now consider the problem of calibrating Δn. This is done by measuring the intensity radiated axially by the microscope objective. Let the power detected in front of the microscope objective be denoted P_c and the power transmitted through the fiber for near-axial excitation be denoted P. If the detector radius is denoted ρ , and its distance from the microscope objective focal point is d, the

$NA = n_0 \sqrt{2\Delta}$ of the fiber is given by

$$NA = (\rho/d)\sqrt{P/\eta P_c} \tag{4}$$

where

$$\eta = \left[4n_0/(n_0 + 1)^2 \right]^2 \tag{5}$$

accounts for the Fresnel reflection at both ends of the fiber. This expression for η is not rigorous but it is sufficiently accurate for our application. With sufficient accuracy, we can set $n_0 = 1.45$. Then $\eta = 0.93$. Convenient values for d and ρ are $d = 10$ mm and $\rho = 1$ mm respectively. We thus obtain, from (4) and (5)

$$NA = 0.104\sqrt{P/P_c} \tag{6a}$$

$$\Delta = 0.00255(P/P_c) \tag{6b}$$

It is of course necessary to have good breaks at both ends of the fiber. We have assumed that the fiber loss is negligible; this is the case for most fibers if the length is of the order of 1m or less.

4. REFRACTIVE-INDEX PROFILE MEASUREMENTS

The measurement technique described in previous sections has been applied to graded-index fibers. The results obtained are highly reproducible, to better than one part in 1000, even after a few hours, if the fiber tip is protected by a glass plate and an index matching fluid. The axial index dip characteristic of germania (or phosphor-oxide) doped fibers is very useful to define the fiber center and achieve optimum focusing.

The (uncorrected) transmission profile of a germania-doped fiber ($\Delta = 0.0104$, core radius = 24μm) was measured in two perpendicular aximuthal directions, labeled 0° and 90° respectively. These two profiles are shown in fig. 4 as plain lines and dashed lines, respectively. We conjecture that, for the small deviations from circular symmetry exhibited by the fiber investigated, the usual correction factor is applicable. However, it turns out that interferometric measurements agree better with uncorrected than with corrected profiles. It is not clear at the moment whether this is due to fiber irregularities, lack of perfect circular symmetry of the fiber, or systematic errors in experimental techniques.

The theoretical result in (1) shows that the transmission technique is applicable, in principle, to non-circularly symmetric profiles, as well as to circularly symmetric profiles. A preform that accidentally collapsed flat (MacChesney an O'Connor, private communication) has been pulled at our request into a fiber, and measured. The uncorrected profiles are shown in fig. 5.

One of the most interesting and intriguing question is whether index profiles get significantly distorted as the wavelength varies (independently of possible changes of scale). Fleming's measurements on bulk samples of germania doped-silica clearly indicate that profiles should get distorted significantly as the wavelength varies. This effect, however, has not been observed before on fibers. We report here preliminary measurements of profile distortion.

The profiles of a germania doped fiber were measured with the transmission method at two wavelengths : $\lambda_0 = 0.79$ μm and $\lambda_0 = 0.9$ μm. The resolution (indicated by the depth of the central dip) is slightly poorer at the longer wavelength. When the scanning is made slightly off-center to avoid the central dip, the difference between the two profiles (normalized to unity on axis) are found to be extremely small, yet significant. To exhibit this difference with good accuracy, we have combined the light from the two LEDs with a beam splitter as shown in fig. 2 (# 2). Square pulses are applied to the LEDs. The positive parts of the pulses drive one LED and the negative parts drive the other. The levels are adjusted to have equal detected powers on the fiber axis, and therefore, zero signal on the lock-in amplifier. The difference between the two normalized profiles is plotted in fig. 6 (curve b). More precisely, we have plotted in fig. 6 the "profile distorsion" $d \equiv \lambda_0 dn/d\lambda_0$, where $n \equiv N/2\Delta$ and $N \equiv 1 - n^2/n_0^2$, as a function of r/a.

CONCLUSION

Index profiles can be obtained in about 1 minute (fiber end preparation and testing). The agreement between our technique and interferometric measurements leaves something to be desired. The discrepency, however, may be attributed to the lack of perfect circular symmetry of the fiber investigated. Theoretical considerations show that the resolution is about $\lambda/4\sqrt{2\Delta}$. For a typical value $\Delta \approx 0.015$, this resolution is about the free-space wavelength $\lambda_0 \approx 1$ μm. This appears to be sufficient for most practical purposes.

Comparison of depths of central index dips suggests that the transmission technique (and the near-field techniques as well) provide better resolution than interferometric techniques. We have presented preliminary evidence for the distorsion of the index profile as the wavelength varies (profile distortion), an effect that was infered previously only from measurements on bulk samples. Theories that neglect profile distorsion may be in considerable error.

We shall now make a few suggestions for improvement of the measurement technique. Immersed microscope objectives would be useful to prevent interference effects between the objective and the fiber tip when monochromatic laser sources are used. The processing of the experimental data can be considerably improved if the lock-in amplifier and the gauge have digital read-outs. The correction factor of leaky rays should be calculated for the apparent measured profile (rather than for a square-law profile) and iterated. Non-circularly symmetric profiles can be corrected, in principle, but the correction problem has not been solved yet. Finally, one may attempt to deconvolve the wave-optics effects that are most conspicuous in regions where the index varies rapidly. The possibility of performing this deconvolution is intriguing, but the analytical problem remains, to our knowledge, unresolved. The case of fibers with an index barrier between the core and the cladding requires further analysis.

Among all the index-profile measurement techniques that have been proposed so far, the transmission technique that we have described here appears to be the easiest to implement and the most reliable. Improvement in data processing should make the results quite accurate in most cases.

ACKNOWLEDGMENTS

The authors express their thanks to H. Presby for providing interferograms, to J. MacChesney and P. O'Connor for supplying fibers, to C. Burrus for supplying the LEDs, and to J. Stone and E. A. J. Marcatili for useful discussions.

REFERENCES

Arnaud J.A., 1976a, "Optimum Profiles for Dispersive Multimode Fibers", Electr. Letters, 12, N° 25, 9th Dec. 1976, p. 654.

Arnaud J.A., 1976b, Beam and Fiber Optics, Acad. Press (New York) 1976.

Arnaud J.A., 1977, "Numerical Evaluation of the Impulse Response of Multimode Optical Fibers", Fiber and Integrated Optics, Vol 1, (to appear).

Arnaud J.A. and Fleming J.W., 1976, "Pulse Broadening in Multimode Optical Fibers with Large $\Delta n/n$ Numerical Results" Electr. Letters, 12, n° 7 (April 1976).

Gloge D. and Marcatili E.A.J., 1973, "Multimode Theory of Graded-Index Core Fibers", Bell Syst. Tech. J., 52, 1563.

Marcatili E.A.J., 1977, Bell Syst. Tech. J., Jan 1977, (to appear).

Sladen F.M.E., Payne D.N. and Adams M. J., 1975, "Determination of Optical Fiber refraction Index Profiles by a Near-Field Scanning Technique", Appl. Phys. Letters, 28, N° 5, p. 255, March 1, 1975.

Stone J. and Earl H.E., 1976, "Surface Effects and Reflection Refractometry of Optical Fibers", Opt. and Quant. Elec. (to appear).

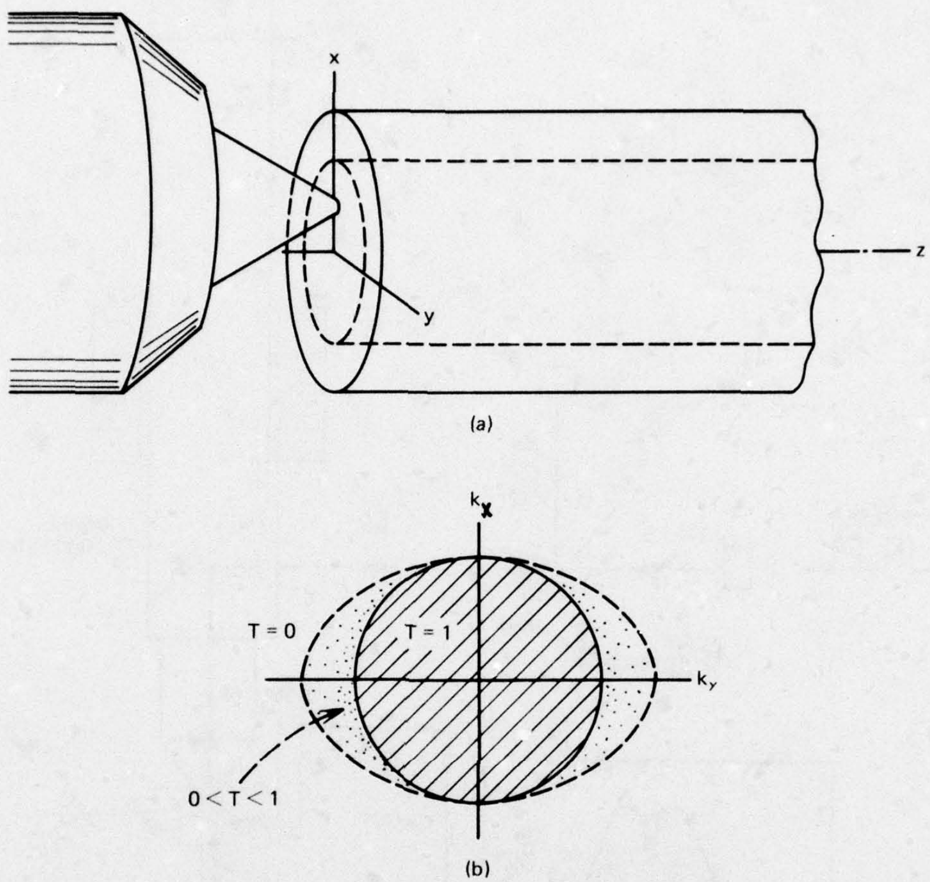

Fig. 1 (a) In the transmission method, the microscope objective illuminates a small area of the fiber end, of the order of λ_0^2 .

(b) The intensity is assumed uniform in the k_x, k_y space. For long fibers, only the rays in the shaded area are transmitted. For short fibers, the rays in the dotted area may also be transmitted (leaky rays). T denotes the power transmission.

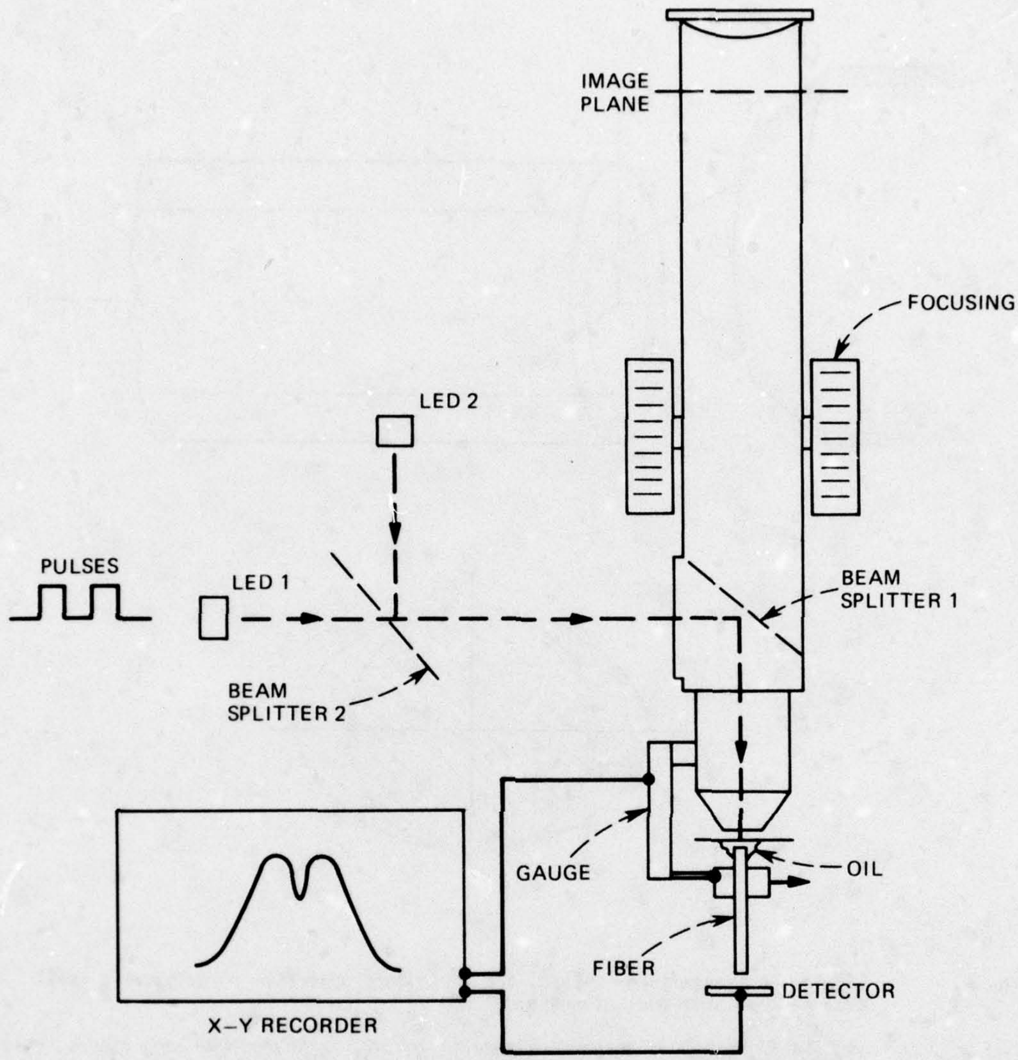

Fig. 2 Experimental set-up of the transmission technique. The fiber is scanned mechanically and its motion is recorded with a gauge. Two LEDs are used for dispersion measurement.

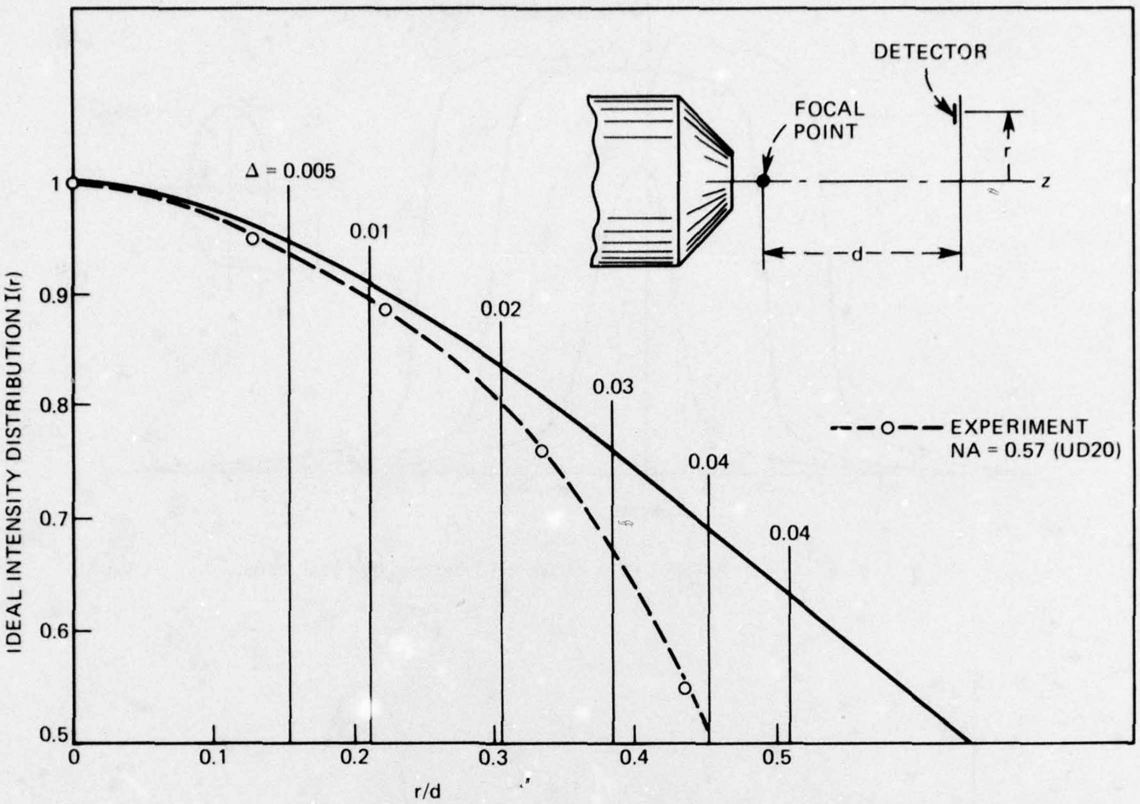

Fig. 3 The curve shown is the desired radiation pattern from the microscope objective. It is sufficient that this law be obeyed from $r/d = 0$ to the value corresponding to the Δ of the fiber (e.g., $r/d < 0.3$ if $\Delta = 0.02$). The experimental points are from a UD20, NA = 0.57, microscope objective.

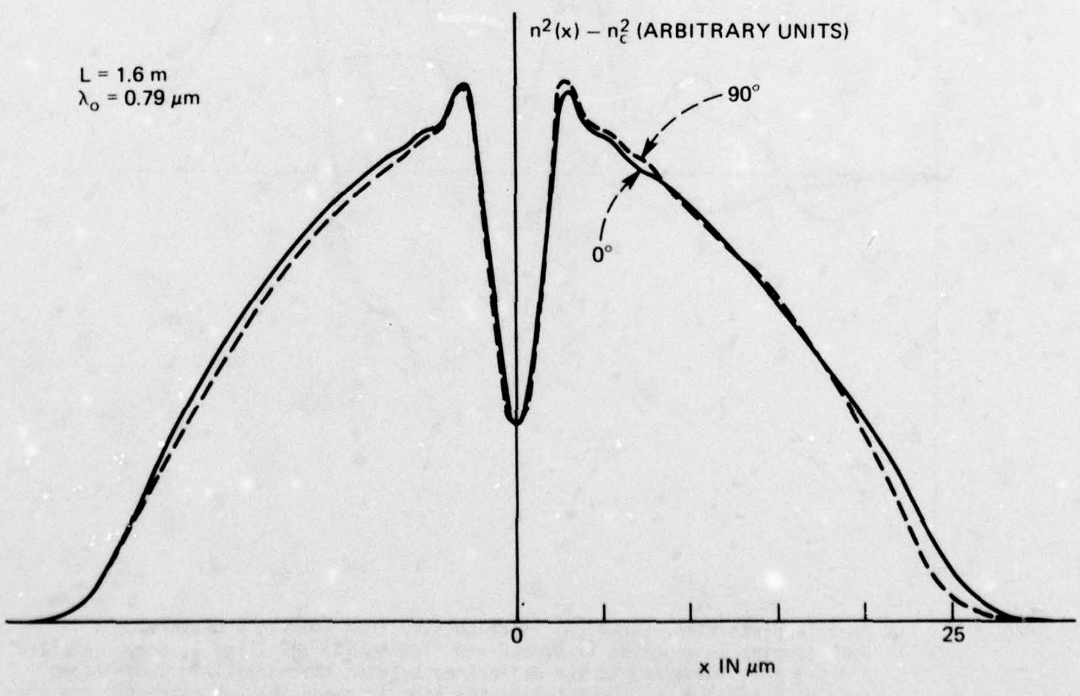

Fig. 4 Profile of a germania-doped fiber in two azimuthal planes (0° and 90°). The measured NA is 0.202, $\Delta = 0.00974$, L = 1.6m.

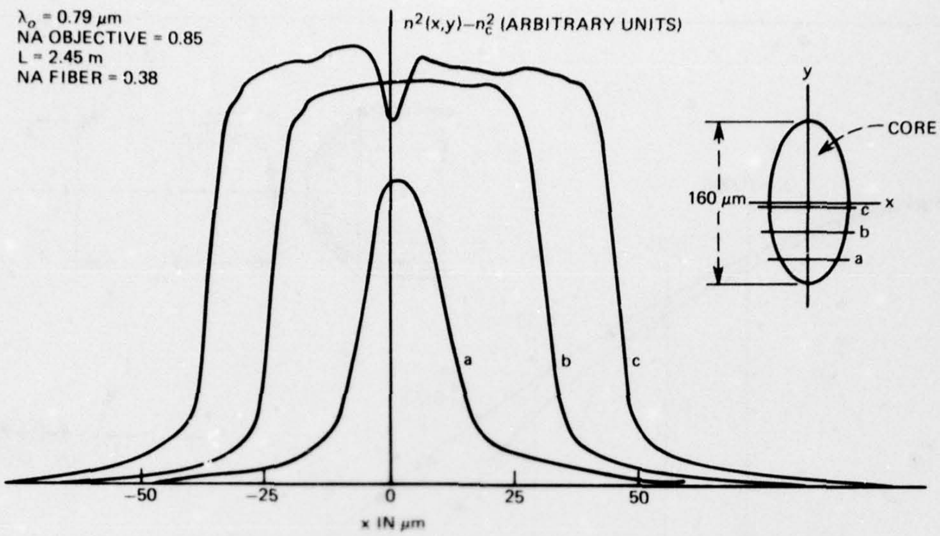

Fig. 5 Profile of a fiber with near-elliptical core.

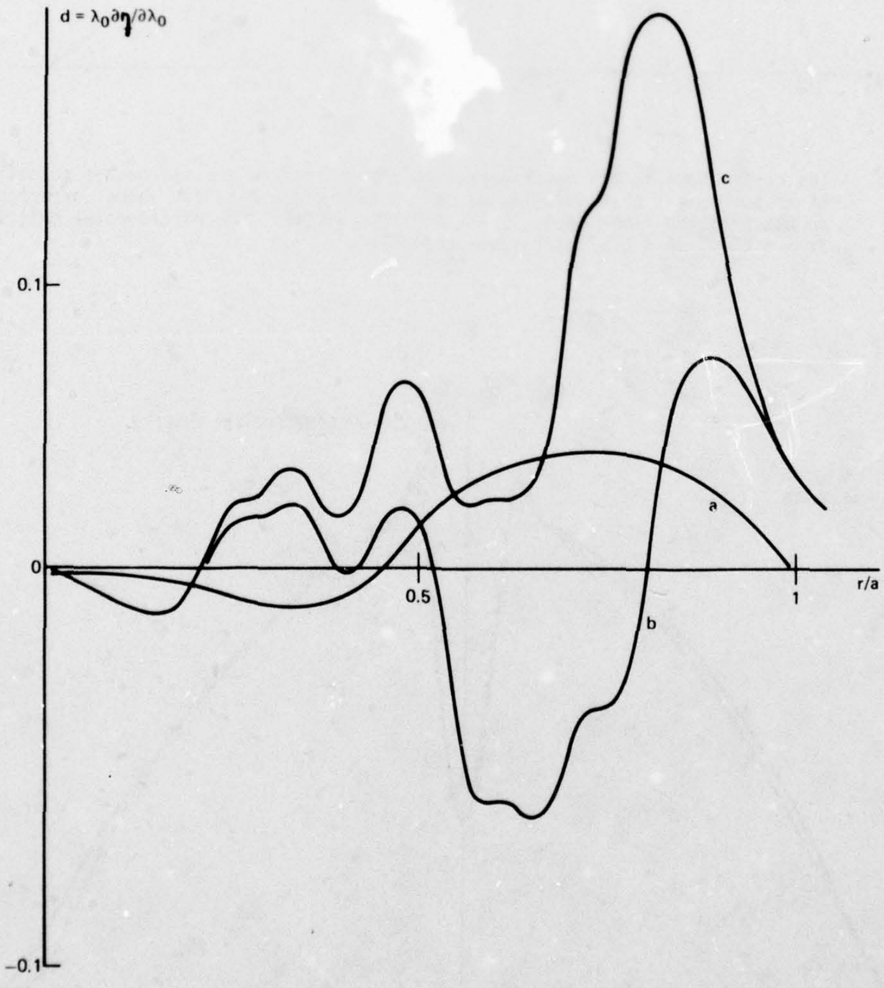

Fig. 6 Profile distorsion. Curve (a) is calculated from Fleming's measurements on bulk samples as reported in Arnaud and Fleming (1976) (Fig. 1, curve labelled λ = 0.9 μm). Curve (b) is the difference between the normalized profiles at λ_0 = 0.79 and 0.9 μm. Curve (c) is the same as curve (b) but corrected for the leaky rays.

INFLUENCE OF THE REFRACTIVE INDEX PROFILE ON THE TRANSMISSION QUALITY OF GRADIENT INDEX OPTICAL FIBRES

G. Gliemeroth, D. Krause, N. Neuroth, F. Reitmayer
Jenaer Glaswerk Schott & Gen., 6500 Mainz, West-Germany

SUMMARY

The problems occurring in the manufacture and investigation of fibres with the refractive index profile, required by theory, are described. The fibre core consists of multi-component-glasses and is produced by the method of inside coating of a glass tube and subsequent collapsing and drawing. The refractive index profile is determined by an interferometric method and by measuring the near field intensity distribution. The pulse broadening is measured directly. The influence of different profiles on the pulse broadening is demonstrated. Typical properties of the fibres: total loss: $<$ 5 dB/km at the wavelength 850 nm; pulse broadening: 1...3 ns/km; numerical aperture: 0,2...0,3.

THEORY OF OPTIMAL REFRACTIVE INDEX PROFILE

Two effects are responsible for the pulse broadening of a gradient index fibre: a) rays with different angle of incidence have different transit time (modal dispersion), especially if the profile is not optimal; b) rays with different wave length have different transit time, caused by the optical dispersion of the core glass (material dispersion). The first effect was investigated by GLOGE and MARCATILI, 1973. The transit time difference is minimized if the core index is formed according to a parabolic profile with the exponent $\alpha = 2 - 2 \cdot (\Delta n/n)$. In figure 1 the pulse broadening of 1 km long fibres is given as function of the exponent α representing the refractive index profile. The minimum difference of transit time depends on the difference Δn of the refractive indices on the axis and at the edge of the fibre core. The value of the delay difference is

$$\Delta\tau = \frac{L}{8\,c\,n_o}(\Delta n)^2$$

with L = fibre length, c = light velocity, n_o = refractive index of the fibre axis. In table 1 $\Delta\tau$ values are computed for different values of the numerical aperture $A = \sqrt{n_o^2 - n_c^2}$. These values are valid for monochromatic light. In practice the light source is radiating in a spectral region of about 20 - 40 nm for a light emitting diode (LED) or about 2 nm for a semiconductor laser. Therefore we have to take into account the wave length dependence of the refractive index of the core glass. The transit time of light pulses in glass is governed by group velocity

$$v_g = \frac{c}{n\left(1-\frac{\lambda}{n}\frac{dn}{d\lambda}\right)} = \frac{c}{n \cdot D}$$

The expression $D(r) = 1 - \frac{\lambda}{n(r)}\frac{dn(r)}{d\lambda}$ is called dispersions-factor (ARNAUD, 1975). It is depending on the distance r from the fibre axis because of the varying glass composition in the fibre core. The behavior of the local wave vector

$$k = \frac{2\pi\, n(r)}{\lambda}$$

is governing the pulse broadening of the fibre. The inhomogeneity of the material dispersion is described by

$$D_k = \frac{k_o^2}{k_k^2}\,\frac{d\,k_k^2}{d\,k_o^2}$$

If the refractive index n(r) depends linearly on composition and varies according to

$$n(r)^2 = n_o^2\left[1-2\Delta\left(\frac{r}{a}\right)^{\alpha}\right]$$

with $2\Delta = (n_o^2 - n_c^2)/\,n_o^2$ and a = core radius, one gets the expression

$$D_k = 1 + \frac{n_c^2}{D_o}\,\frac{D_o - D_c}{n_o^2 - n_c^2}$$

The index $_o$ designes the fibre axis, the index $_c$ the boundary of the core. The variation of D_k in glasses ranges approximately from 0,9 to 1,1. If the material dispersion of the fibre core does not change with r the parameter D_k is unity. For D_k-values smaller than 1 the optimal α-value is lower than 2, for D_k-values greater than 1 the optimal α-value is greater than 2. In figure 2 the pulse broadening is given as a function of the exponent α for the limiting D_k-values 0,9 and 1,1. The other parameter is the aperture of the fibre. The higher the aperture, the narrower is the slope and the larger is the minimum value. If the fibre should have a limited pulse broadening (for instance 3 ns/km) the tolerance for the α-region decreases with increasing aperture. This behavior is already known from figure 1. We suppose it would be possible to generate the optimal α-value with an accuracy of $\pm$ 0,1. Table 2 shows calculated values of the pulse broadening which result from this α-tolerance. It can be seen that the pulse broadening becomes higher than

3 ns/km if the aperture of the fibre is higher than 0,3. In order to increase the bandwidth of fibres with such high apertures the accuracy for making and measuring the profile has to be improved.

PRODUCING THE FIBRE

We use the inside coating technique. The inside of a glass tube is coated directly with layers of multi-component-glasses, consisting of the oxides of Si, Ge, B, P, Sb and others. The first layers have a refractive index lower than that of the substrate tube. So the core of the fibre is optically separated from the tube material. After these layers with low refractive index the coatings with successively higher refractive index follow, which will represent the fibre core after collapsing the tube to a rod and drawing it to a fibre.

MEASUREMENT TECHNIQUES

The refractive index profile is determined by two different methods: a) interferometrically: a thin (several 10 μm) plane polished and parallel sample of the fibre is investigated with an interference microscope; b) the near field intensity distribution of a 3 m long peace of the fibre is measured in the following way (figure 3). The beam of a HeNe-laser is focused as a spot with 1 μm diameter on the end face of the fibre. The fibre is moved in the focal plane. The total transmitted light is collected by a detector. The space between fibre end and detector is filled up with immersion liquid to reduce reflection losses. The intensity is recorded as a function of the distance of the illuminating light spot from the fibre axis. The intensity distribution is proportional to the refractive index profile. The measurement of the far field gives the numerical aperture and thus the refractive index difference between axis and boundary of the fibre core. The index profile can be given quantitatively by evaluation of the two data. The results of both methods are not identical because the excitation of leaky modes can be different in both cases. We will always give the smaller values got by the interferometric measurement.

The pulse dispersion can be measured at two wave lengths: 850 and 904 nm (figure 4). The input pulses are about 0,2 ns wide (half width). They are generated by semiconductor lasers. With a first objective the enlarged image of the light emitting area is produced. With a second objective the light is focused on the fiber entrance surface so that the whole core is illuminated with an aperture greater than that of the fibre. The output pulse is detected by an avalanche diode and a sampling oscilloscope. The half width can be taken directly from the recorded diagram. The transfer function can be analysed by a computer. The measurement at the different wave lengths gives the material dispersion of the fibre. With two highly reflecting mirrors the light is sent many times through the fibres. By this shuttle pulse technique a greater length of the fibre can be simulated and mode coupling effects can be observed.

RESULTS

In figure 5 the index profile (interferometrical measurement) of fibres with different types of profile are shown. The fibre N 217 has an α-value of 1,2, the fibre N 204 has α = 3,97. In both cases the pulse broadening is higher than that of the fibre N 329, which has α = 2,00 and $\Delta\tau_{1/2}$ = 1,1 ns/km. This is according to the theory. These fibres have an aperture between 0,1? and 0,22. The Heinrich-Hertz-Institut in Berlin has made a 1,6 km long digital transmission line with two of our fibres with a capacity of 1,12 Gb/s. Our measurement of pulse broadening (with excitation of all modes) has the result 1,7 ns/km. The transfer function of this fibre is given in figure 6. This analysis gives a nominal capacity of 250 MHz · km. This is valid for full illumination of the fibre. If the fibre is illuminated by a light beam with smaller aperture than the aperture of the fibre the capacity of information can be improved as the experiment of the Heinrich-Hertz-Institut shows. This is expected, if the fibres have no mode coupling which was proved before.

We have tried to increase the fibre aperture. In table 3 the results are summarized. We have got A-Values up to 0,3. The exponent of the parabola of the profile deviates stronger from the optimal value than for fibres with smaller aperture. In figure 7 the refractive index profile is shown. The dip in the center of the fibre is caused by evaporation during the collapsing process. It is not important for the pulse broadening.

Figure 8 shows the spectral loss of fibres with higher aperture. In the short wave length region the curves decrease proportional to λ^{-4}. That shows the loss to be mainly due to scattering. The higher refractive index causes higher scattering loss,because of the greater composition fluctuations. The absorption band at 950 nm is caused by an OH overtone vibration. The independence of fibres with high aperture from the influence of mechanical stress can be demonstrated by the loss measurement. The fibre with A = 0,31 was wound on a drum with weak drawing force and the loss was measured under this tension. The loss remained unchanged after deloading the fibre by cooling the drum. Another advantage of fibres with higher aperture is the increased coupling efficiency between an incoherent light source and the fibre. The efficiency can be increased by approximately 10 dB by increasing the aperture from 0,15 to 0,50, independent of the radiation characteristics of the source.

LITERATURE

GLOGE, D. and MARCATILI, E. A. J., 1971, "Multimode theory of graded core fibres", Bell Syst. Techn. Journ. 52, 1563-1578

ARNAUD, J. A., 1975, "Pulse broadening in multimode optical fibres", Bell Syst. Techn. Journ. 54, 1179-1205

TABLE 1: Calculated pulse broadening of fibres with optimal exponent of the parabola describing the refractive index of the fibre core

Numerical aperture:	0,15	0,20	0,25	0,30	0,35
Pulse broadening (ns/km):	0,015	0,056	0,14	0,29	0,53

TABLE 2: Calculated pulse broadening (ns/km) of fibres with deviation of the optimal exponent $\alpha = (\alpha_{opt} \pm 0{,}1)$

Aperture	Inhomogeneity parameter D_k 0,9	1,0	1,1
0,2	1,3	1,15	1,0
0,3	2,9	2,6	2,4
0,4	5,3	4,7	4,4
0,5	> 10	> 8	> 7

TABLE 3: Properties of fibres with increased numerical aperture

Fibre No.	Aperture	Exponent	Pulse broadening (ns/km)	Core diameter (µm)
347	0,31	2,9	9,1	46
343	0,28	3,4	5,6	50
350	0,23	2,2	3,2	40
319	0,15	2,00	1,1	30

FIGURES

1. Calculated pulse broadening caused by modal dispersion as function of the exponent α of the parabola describing the refractive index profile of the fibre core
2. Calculated pulse broadening as function of α for fibres with different material dispersion; curves on the left side for $D_k = 0{,}9$, curves on the right side for $D_k = 1{,}1$
3. Device for measuring the near field intensity distribution
4. Device for measuring the pulse broadening
5. Refractive index profile of fibres, α-value of the approximating parabola and pulse broadening
6. Transfer function of the gradient index fibre N 360
7. Refractive index profile of fibres with increased numerical aperture
8. Spectral loss of fibres with increased numerical aperture

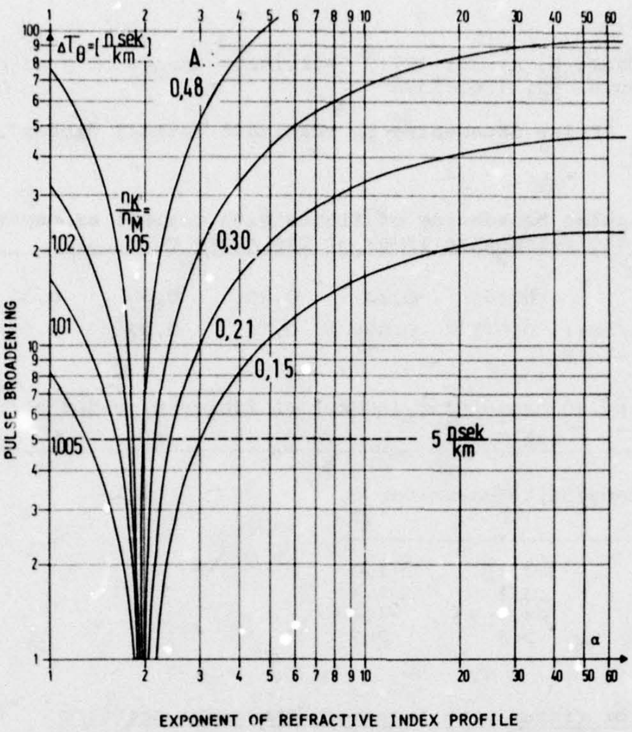

Figure 1

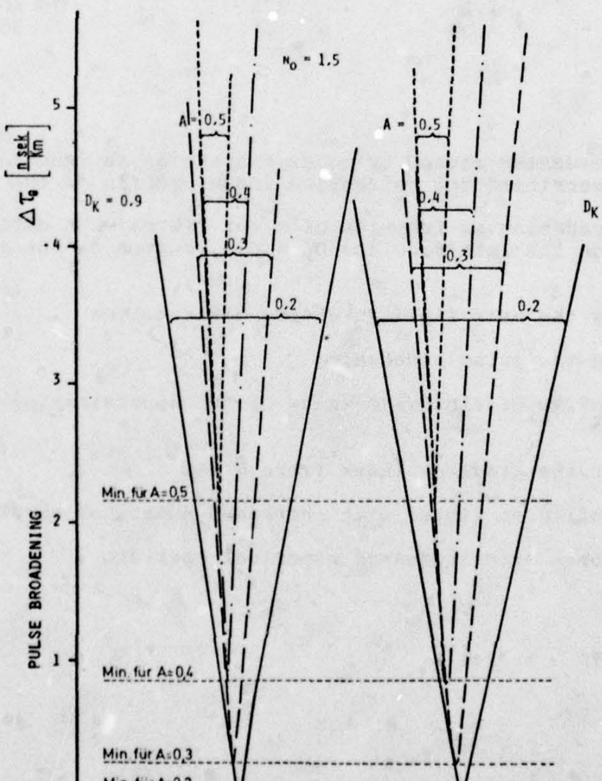

Figure 2

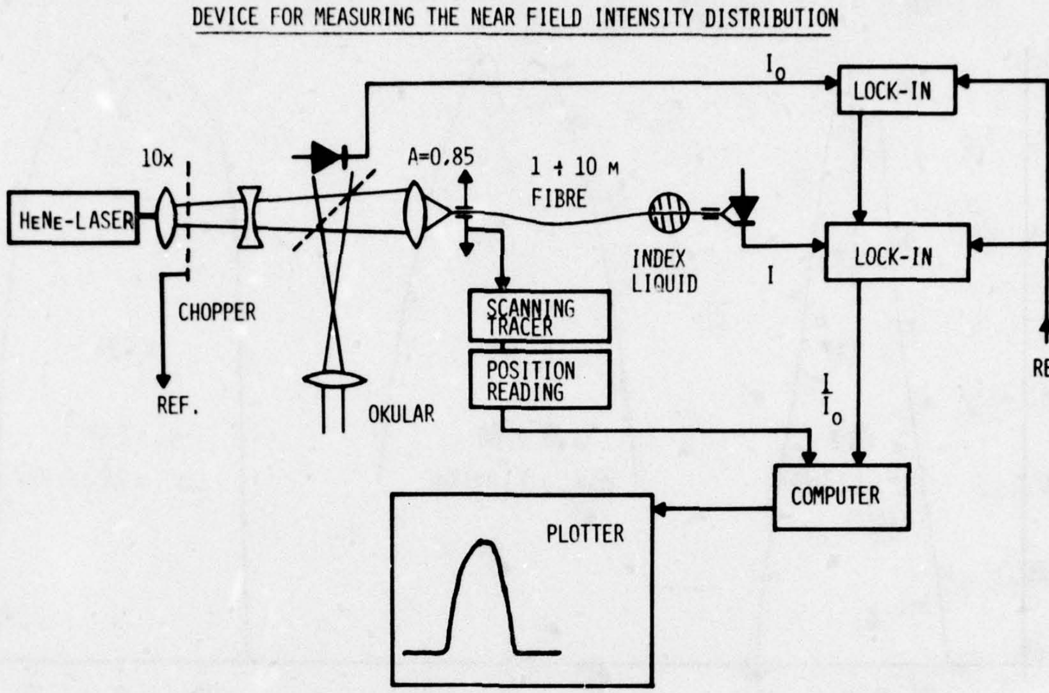

Figure 3

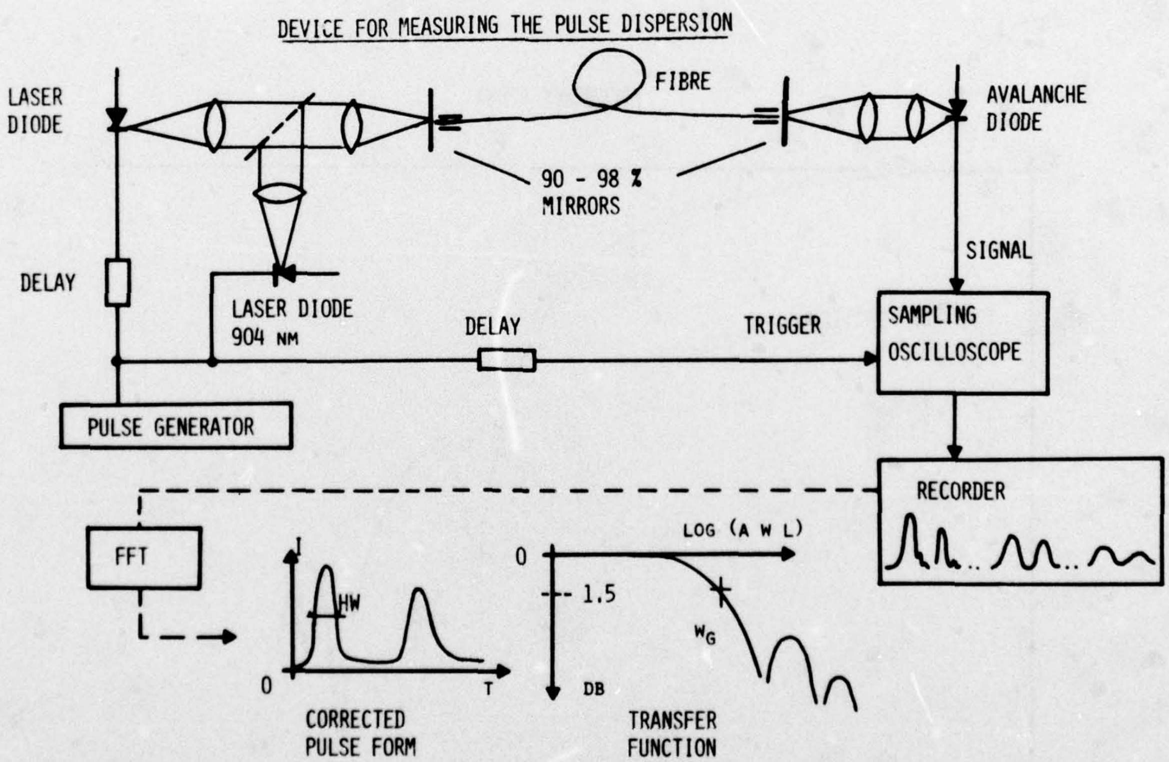

Figure 4

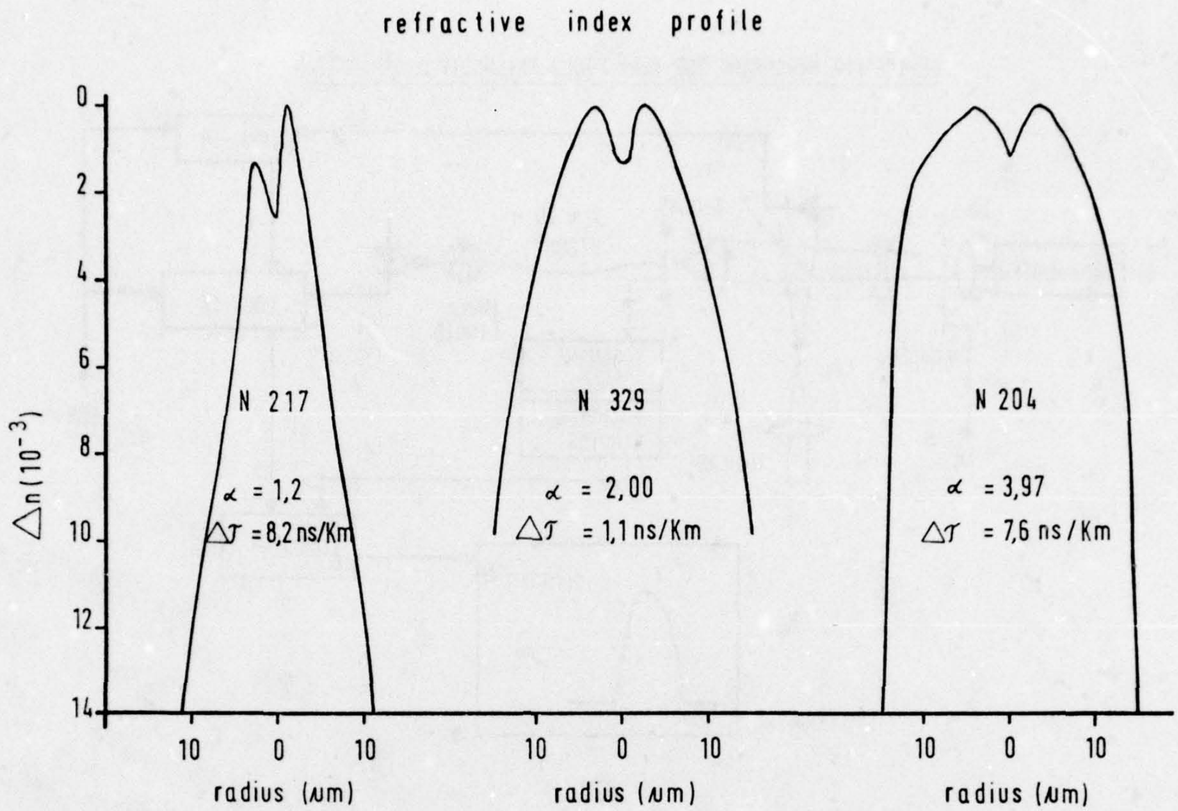

Figure 5

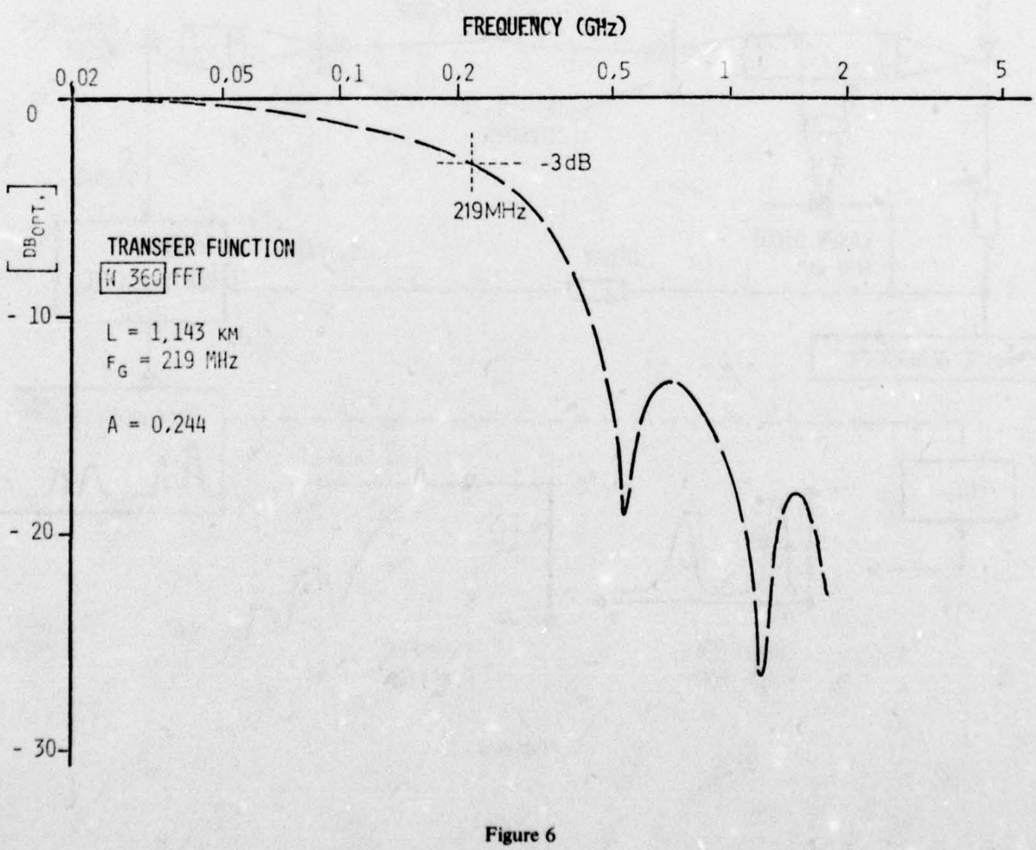

Figure 6

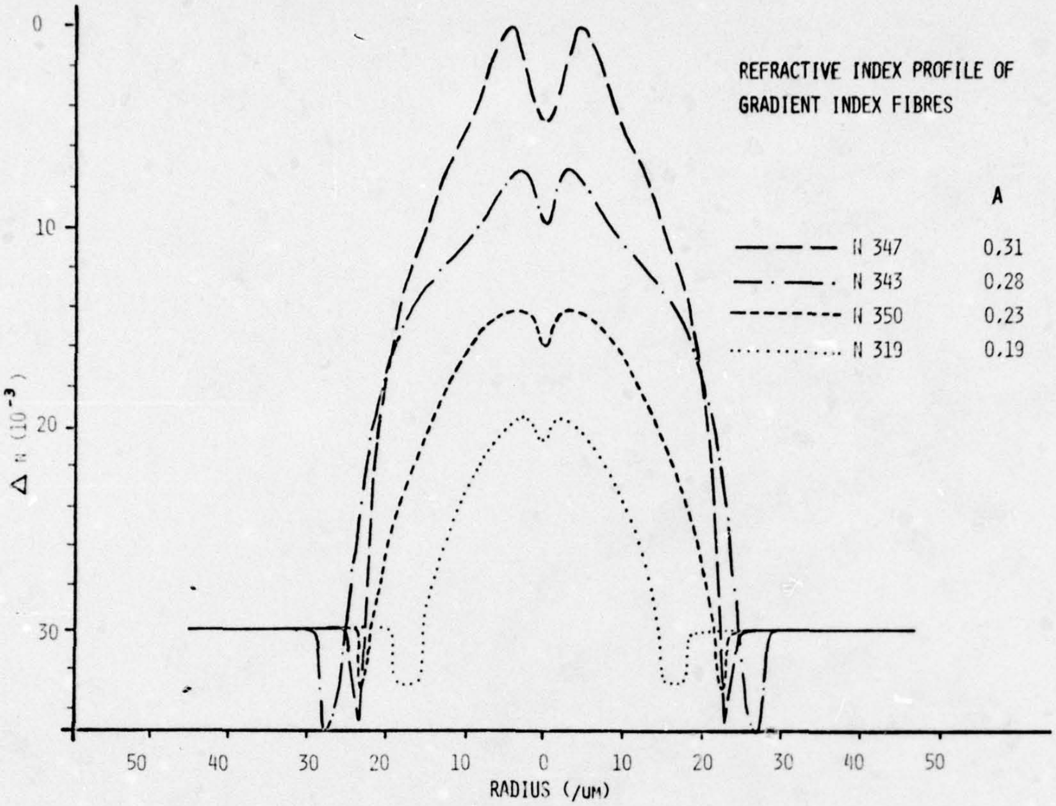

Figure 7

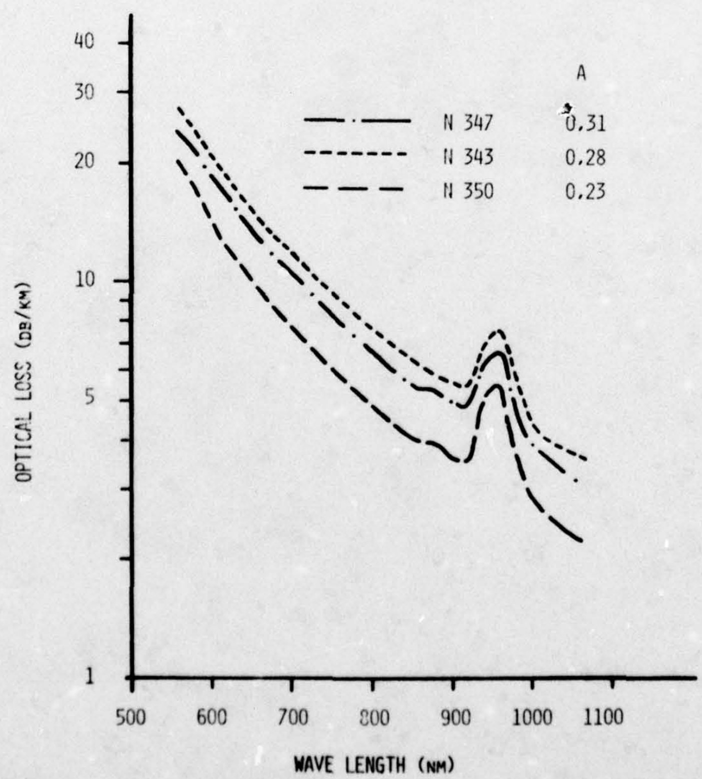

Figure 8

TRANSMISSION CHARACTERISTICS OF GRADED INDEX FIBRES

P.J.B. CLARRICOATS, J.M. ARNOLD and G. CRONE

QUEEN MARY COLLEGE, UNIVERSITY OF LONDON

1. Introduction

The use of graded-index fibres for optical communication systems is now under consideration for numerous civil and military applications, and in these either LED or LASER sources can be deployed. The bandwidth of the system depends on the source linewidth, the dispersion of refractive index in the fibre, the strength of excitation of the modes by the source and upon the extent of mode mixing caused, for example, by microbending. In fibres with refractive index profiles which have a nearly parabolic dependence upon radius, pulse broadening is slight but, small departures from an optimum profile can cause a dramatic decrease in bandwidth. It is of considerable importance to predict the bandwidth of fibres from a knowledge of the refractive index profile and source geometry.

The purpose of the first part of this paper is to compare two computational methods by which the propagation characteristics of a fibre, hence the impulse response and system bandwidth may be determined. In the second part, we shall describe a computer program which determines for a model of a LASER source, the excitation of modes in an arbitrarily graded refractive index fibre.

2. Propagation Characteristics of Graded Index Fibres

2.1. Background

Fig. 1.a) shows the radial variation of refractive index in a graded fibre. Other than for certain special cases, the propagation characteristics of the modes cannot be determined by essentially analytical means and resort must be made to numerical techniques. In 1970, Clarricoats and Chan (1) proposed the replacement of the continuous profile by a staircase approximation, as shown in Fig.1.b). They were then able to compute the propagation coefficient, group velocity, etc, by treating the fibre as if it were a multilayer dielectric. For the case of a fibre with a truncated parabolic refractive index profile, their results agreed precisely with those obtained by an analytic method developed by Kirchhoff (2). However, in 1975 Arnaud and Mammel (3) described results of an alternative numerical method of solution and challenged the reliability and usefulness of the staircase approximation for studying practical fibres.

Subsequently Bianciardi and Rizzoli (4) have described an improved computational method for solving the staircase approximation of Clarricoats and Chan (1) but they have left open the question as to whether the method is more efficient than that of Arnaud and Mammel (3) in its use of computer time. In the next section we describe briefly the two methods and compare results which we have obtained and which appear to demonstrate the superiority of the numerical integration method.

2.2. The Determination of Propagation Characteristics using the Staircase Approximation

In the original method of solving the propagation problem using a staircase approximation, Clarricoats and Chan (1) used the exact vector Helmholtz differential equation to represent the fields in each of the layers shown in Fig.1.b). Subsequently many authors have demonstrated that when the refractive index difference between layers is small, a scalar approximation leads to accurate solutions in the case of step refractive index profiles. Thus, following Bianciardi and Rizzoli (4), we have used a scalar differential equation to represent the field in the p^{th} cylindrical region:

$$\frac{d^2E_x}{dr^2} + \frac{1}{r}\frac{dE_x}{dr} + (k^2n^2{}_p - \beta^2 - \frac{m^2}{r^2})E_x = o \qquad (1)$$

Equation 1 leads to solutions of the form

$$E_x = [A_p\, J_m(K_p r) + B_p\, Y_m(K_p r)]\begin{bmatrix}\cos m\phi\\ \sin m\phi\end{bmatrix} \qquad (2)$$

$$\text{if } \omega^2\varepsilon_p\mu_o > \beta^2 \qquad \text{where} \qquad K_p{}^2 = \omega^2\varepsilon_p\mu_o - \beta^2$$

When $\beta^2 > \omega^2\varepsilon_p\mu_o$ $I_m(k_p r)$ and $K_m(k_p r)$ replace $J_m(K_p r)$ and $Y_m(K_p r)$ respectively.

In the interior region p = 1 and $B_1 = 0$ while in the cladding region, $A_N = 0$. Similar equations apply to the linearly polarised transverse magnetic field components.

Our objective is to obtain the propagation coefficient β. Continuity of E_x and $\frac{dE_x}{dr}$ at each cylindrical boundary yields 2(N-1) independent equations. This leads to a matrix equation of the form

$$[D]\ \{X\} = 0 \qquad (3)$$

where [D] is a (2N-1)(2N-1) square matrix containing Bessel functions, their derivatives and unfilled elements,{X} is a one dimensional vector of (2N-1) arbitrary constants. For a non-trivial solution the determinant of [D] must vanish. To obtain a solution, the characteristic matrix is first transformed into an upper triangular matrix by Gaussian elimination so that its determinant is ultimately given by the product of the diagonal elements. By this procedure, and utilizing the sparse nature of the matrix, the computing time is proportional to the number of layers N, in contrast with the method originally deployed by Clarricoats and Chan (1).

A flow-diagram for the program to compute the normalised propagation coefficient $\bar{\beta}$, the normalised group velocity $\bar{v}_g$ is shown in Fig.2. Table 1 lists the data required to run the program.

Experience shows that quite accurate starting values are required if the program is to run successfully. These are obtained from a knowledge of starting values of $\bar{\beta}$ obtained either for a homogeneous core profile or for an unbounded parabolic profile. Beginning with one or other of these, the profile is gradually deformed until it ultimately corresponds to that of the given distribution.

2.3. The Determination of Propagation Characteristics from a Numerical Solution of the Differential Equation

Following Arnaud and Mammel (3), we convert equation (1) to a pair of first-order differential equations thus :

$$\frac{d\psi_o}{dr} = \frac{1}{r}[K_o - m\psi_o] \tag{4}$$

$$\frac{dK_o}{dr} = rA(r)\psi_o - \frac{mK_o}{r} \tag{5}$$

where $\psi(r)$ is the r-dependent part of E_x in equation (1) and,

$$\psi(r) = r^m\psi_o(r) \tag{6}$$

$$K(r) = r^m K_o(r) \tag{7}$$

The initial conditions at r=o are

$$[\psi_o]_{r=o} = 1 \qquad [K_o]_{r=o} = m \tag{8}$$

$$\left[\frac{d\psi_o}{dr}\right]_{r=o} = 0 \qquad \left[\frac{dK_o}{dr}\right]_{r=o} = 0 \tag{9}$$

At the core-cladding boundary r_c,

$$\psi(r_c) = A\,K_m(W) \tag{10}$$

$$\psi'(r_c) = AW/r_c K_m'(W)$$

$$\text{where} \quad W = (\omega^2\varepsilon_{CL}\mu_o - \beta^2)^{\frac{1}{2}} r_c$$

The above first order differential equations are solved using a 4^{th}-order Runge-Kutta procedure. Trial values of W are iterated until the boundary conditions are satisfied to within a prescribed tolerance. The flow-diagram for the program is shown in Fig.3. The input data differs from that of Table 1 only in that the number of integration points replaces the number of layers used in the staircase approximation.

2.4. Comparison of the Methods

To effect a comparison, (we have determined $\bar{\beta}$ and $\bar{v}_g$) by the two methods of computation. We have also investigated both the convergence of the above quantities as a function of the number of layers, or points selected in the model and the corresponding mill time on an ICL 1904 S computer. We have conducted comparisons for a number of representative modes of a parabolic index fibre. The results of this study are contained in Figures 4-7.

The results show clearly that for LP_{om} modes the advantage lies with the method by which the differential equation is solved numerically (direct method) when convergence is obtained in an order of magnitude less time than for the stratification method. For higher-order modes, convergence using the direct method requires more points than layers in the stratification method but, as Fig.4 shows, the time taken to obtain a solution for a point is smaller by more than one order of magnitude than for a layer, so again the direct method appears more efficient.

3. Excitation of Modes in a Graded Index Fibre

The configuration under study for modal excitation is shown in Fig.8.a) while Fig.8.b) shows the electric field assumed for the laser. The investigation extends the earlier work of Clarricoats and Chan (5) who determined the modal excitation coefficients when a uniform cylindrical region of excitation impinged on the end of a homogeneous fibre. In the present extension, the shape of the laser cross-section can, in principle, be made arbitrary and the fibre refractive index profile is not restricted.

The calculation of the modal amplitudes follows closely the method described previously by Clarricoats and Chan (5) and only an outline is presented here.

Fig.9. shows the cross-section of the fibre end. As a first step the modal fields are obtained following the procedure of section 2. The laser field is assumed to have gaussian variations in x and y directions as shown in Fig.8.b). The field over the end of the fibre excited by the laser, is expanded in terms of the normal modes of the graded fibre and the coefficients calculated after application of orthogonality integrals. Fig.10 contains a flow-diagram for the program "Excitation", while Table 2 specifies the data required. Use is made of the program of section 2 in order to obtain the power flow and field distribution of the modes. An integral which effectively forms the convolution of the laser field with that of the modal field is evaluated by numerical integration using a 5 point Bode rule.

The program has been verified for known cases and excitation coefficients are being computed for lower order modes of graded index fibres and for various laser configurations.

4. Conclusions

The paper has described two computational methods for determining the propagation characteristics of an arbitrarily graded index fibre. Comparison of the methods on an ICL 1904 S computer, shows that the method which employs numerical integration of the scalar differential equation, is superior to the stratification technique.

Program details are given for each method also for the determination of modal excitation when a laser illuminates the fibre end.

5. References

1. CLARRICOATS,P.J.B. and CHAN,K.B. Electromagnetic-Wave Propagation along Radially Inhomogeneous Dielectric Cylinders. Electronics Letters,1970, 6 (22) p.694-695.

2. KIRCHHOFF, H. 'Optical Wave Propagation in self-focussing fibres' IEE Conference Publication "Trunk Telecommunication by Guided Waves", 1970 No.71, p.69.

3. ARNAUD, J.A. and MAMMEL, W. Dispersion in Optical Fibres with Stairlike Refractive Index Profiles. Electronics Letters 1976, 12 (1) p.6.

4. BIANCIARDI, E. and RIZZOLI, V. Propagation in graded-core fibres. A unified numerical description. To appear in Journal of Quantum Electronics.

5. CLARRICOATS, P.J.B. and CHAN, K.B. Propagation behaviour of Cylindrical-Dielectric-Rod Waveguides. Proc IEE, 1973, 120 (11) pp1371-1378.

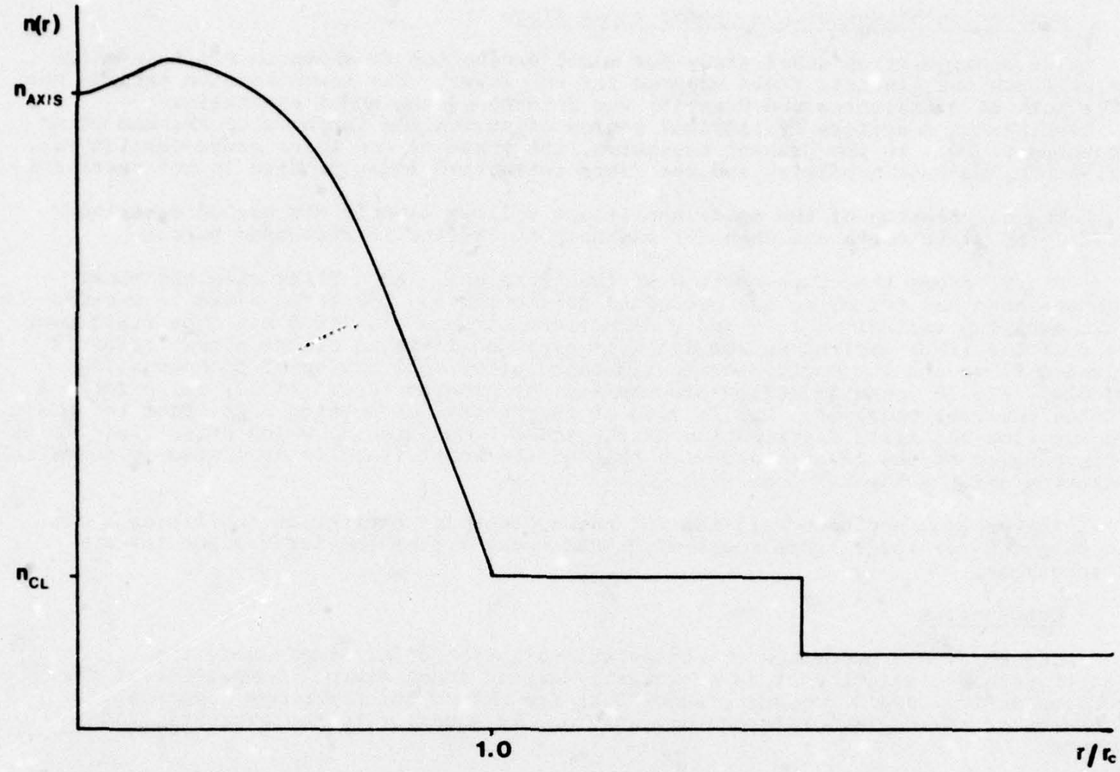

FIG. 1(a) GRADED REFRACTIVE INDEX PROFILE

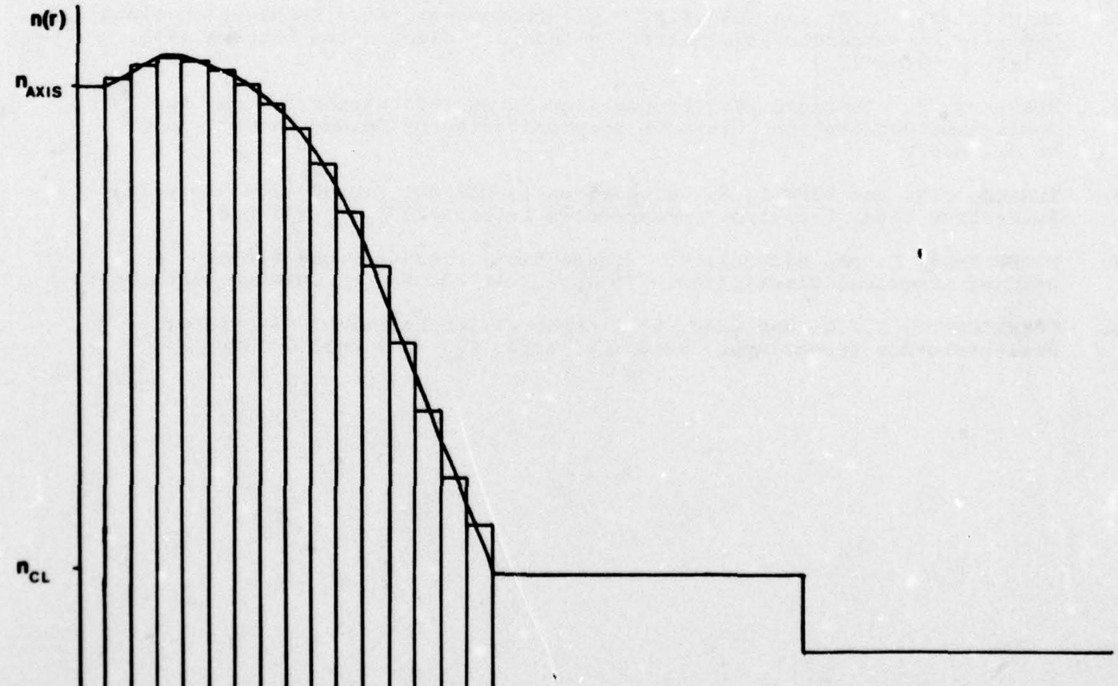

FIG. 1(b) STAIRCASE APPROXIMATION

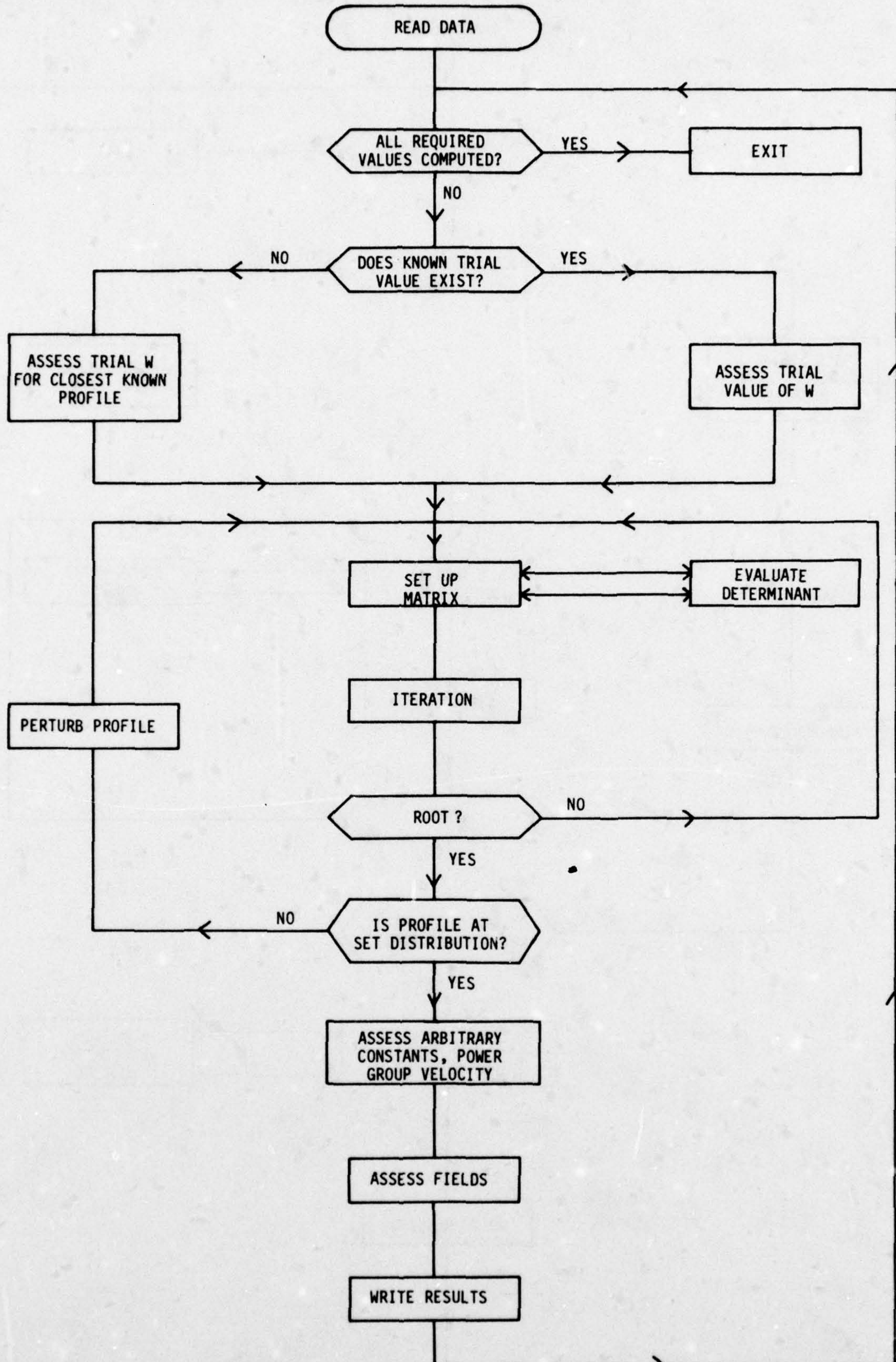

Fig 2. FLOW CHART OF PROGRAM "STAIRCASE"

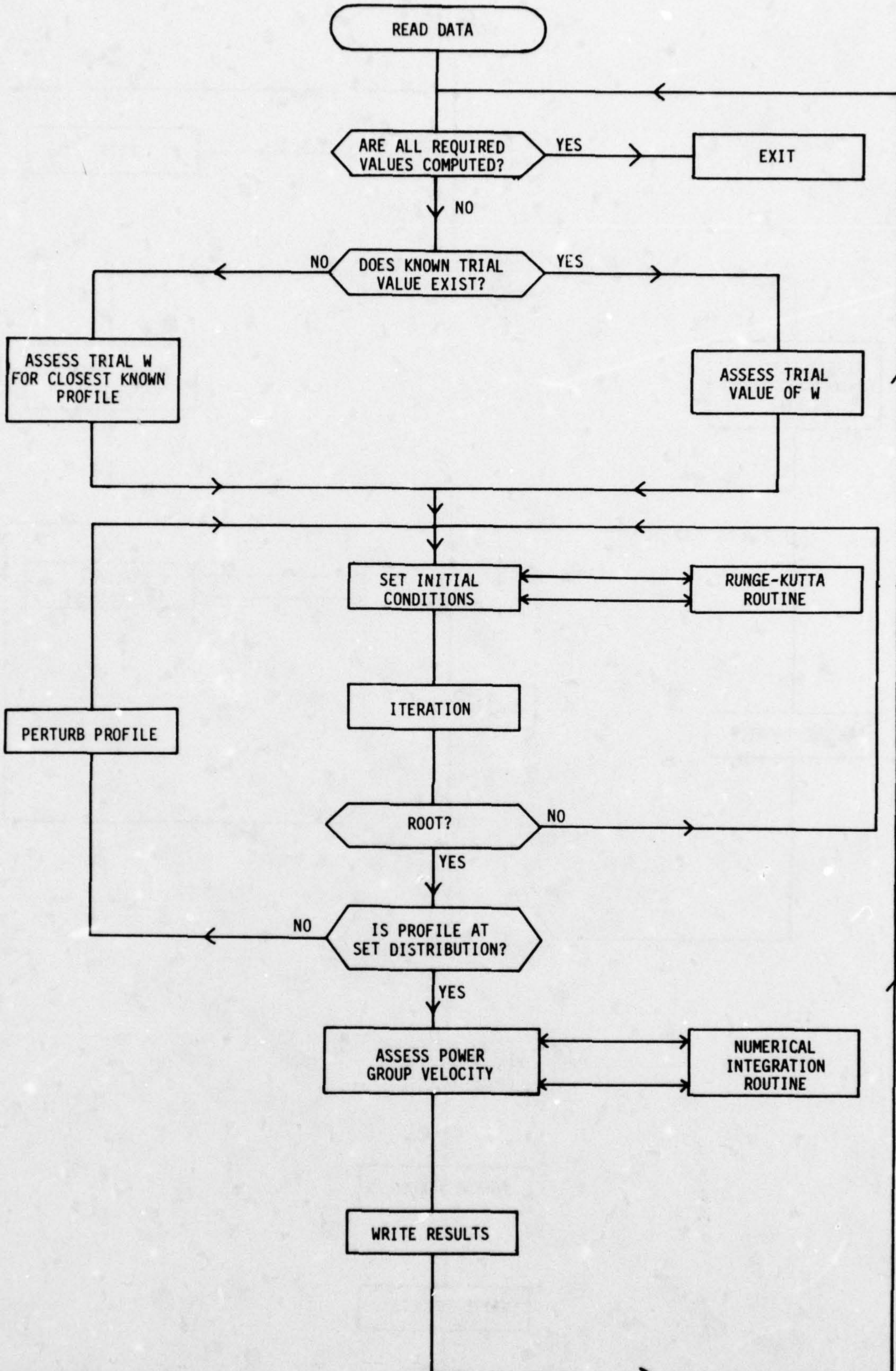

Fig.3. FLOW CHART OF PROGRAM "DIRECT".

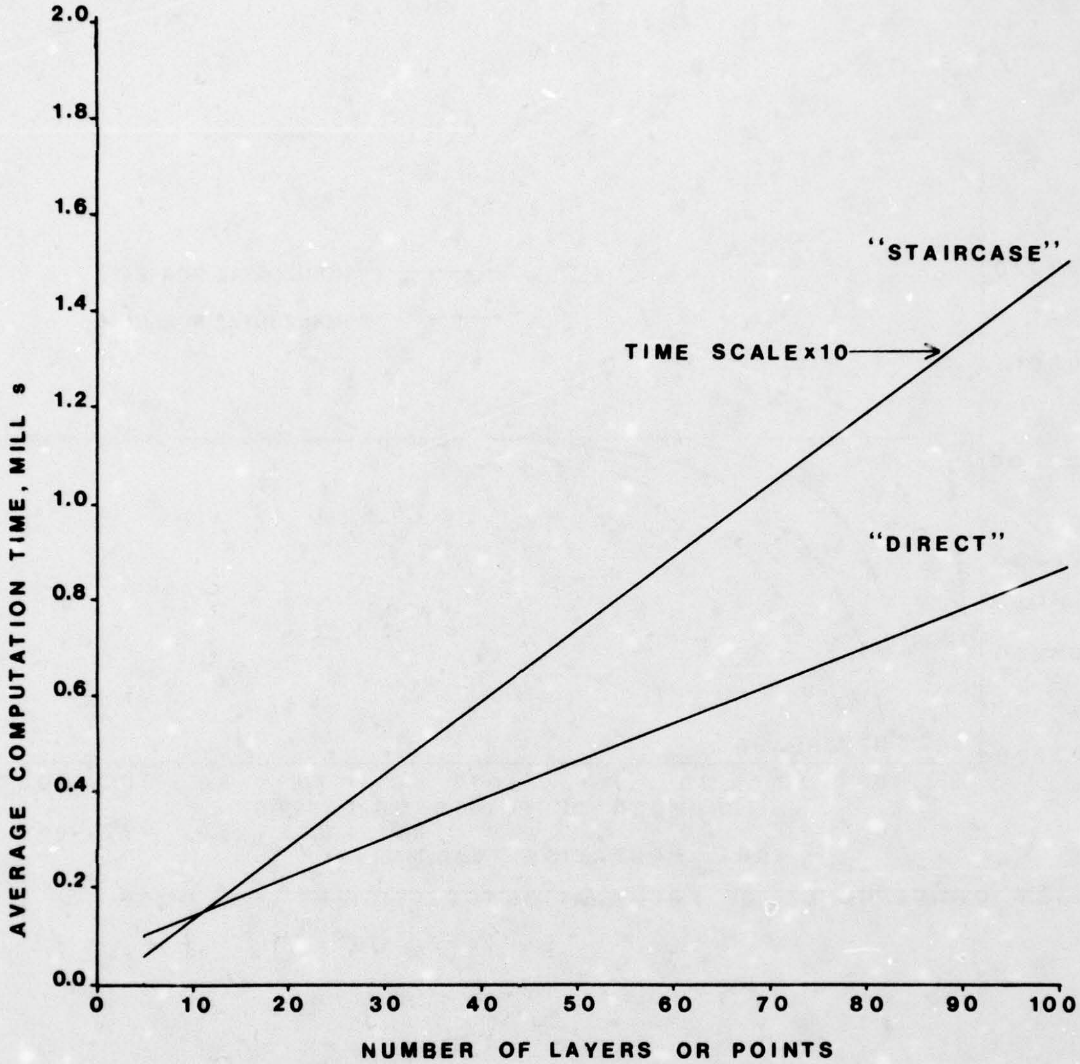

FIG.4 AVERAGE COMPUTATION TIME TO OBTAIN ONE POINT ON THE DISPERSION CURVE V. NUMBER OF LAYERS OR POINTS

REFERENCES

BURRUS, C.A., CHINNOCK, E.L., GLOGE, D., HOLDEN, W.S., TINYGE LI, STANDLEY, R.D., KECK, D.B., 1973; "Pulse Dispersion and Refractive Index Profiles of Some

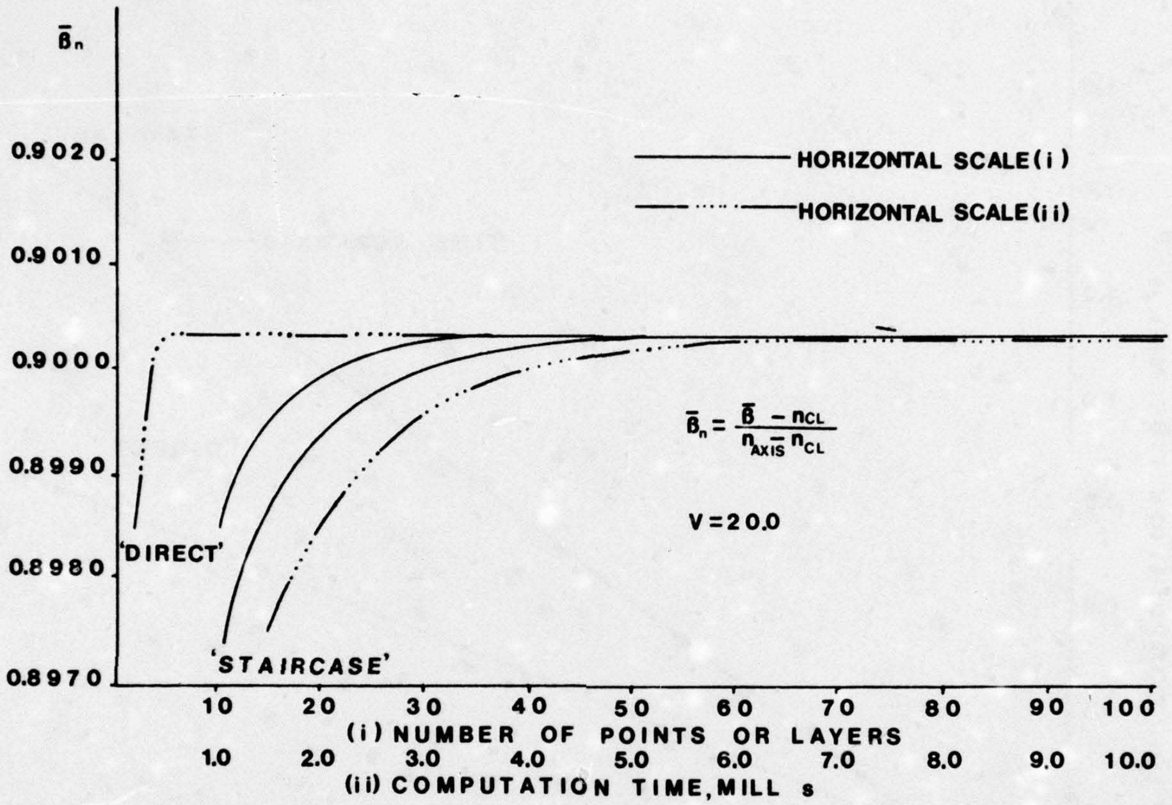

FIG.5 CONVERGENCE OF PROPAGATION COEFFICIENT LP_{01} MODE

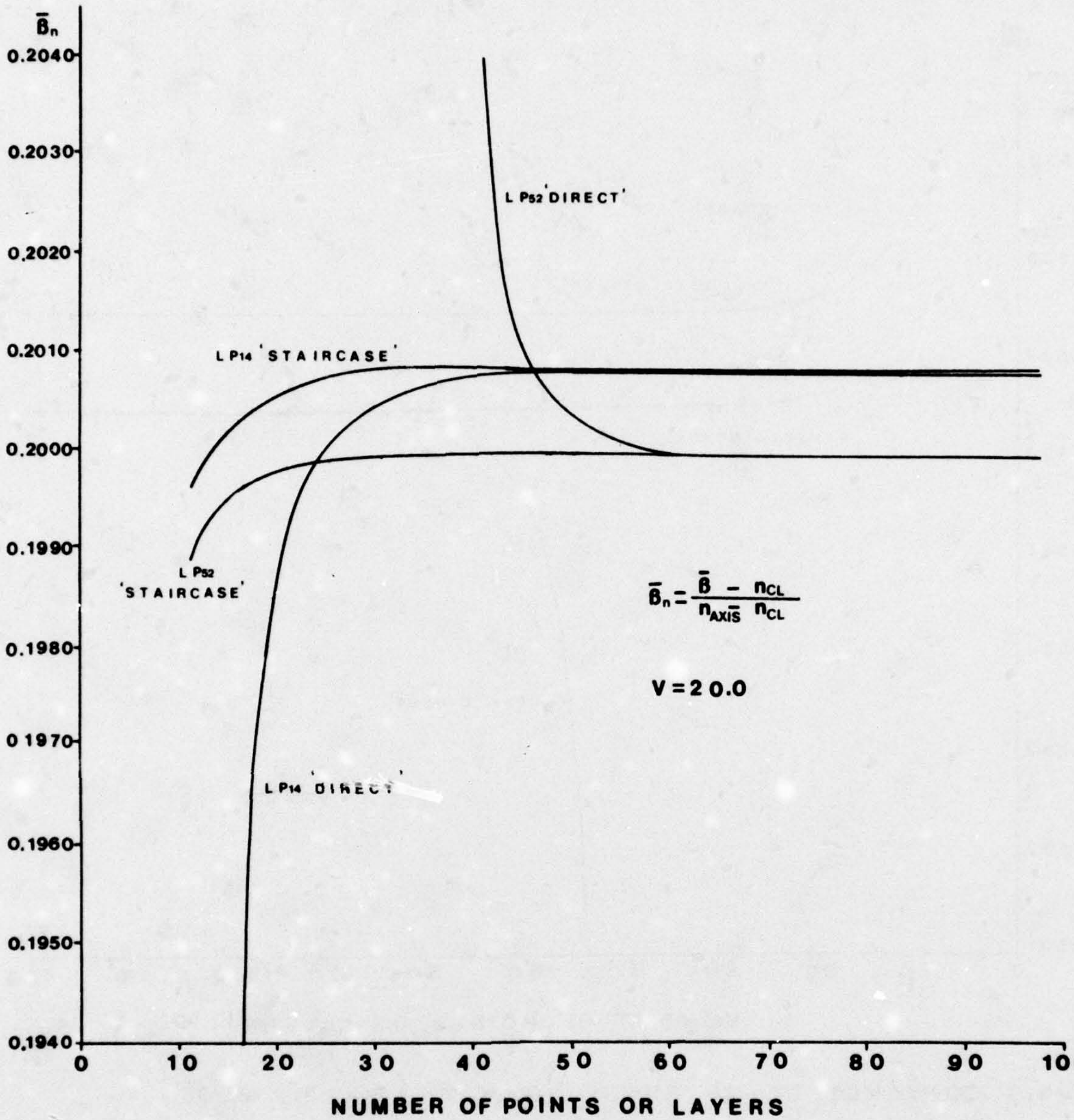

FIG.6 CONVERGENCE OF PROPAGATION COEFFICIENT LP_{14}, LP_{52} MODES

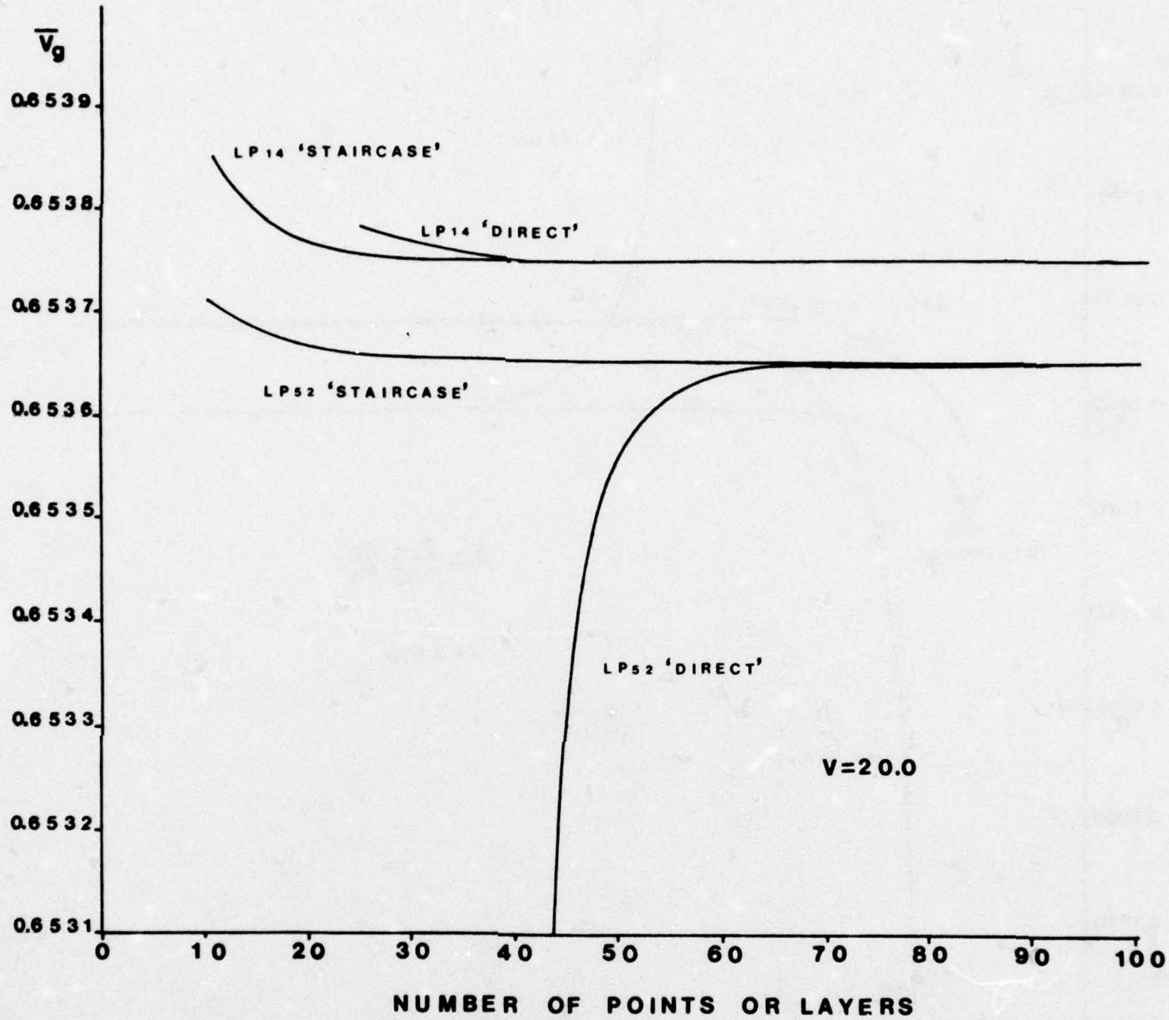

FIG. 7 CONVERGENCE OF GROUP VELOCITY LP14, LP52 MODES

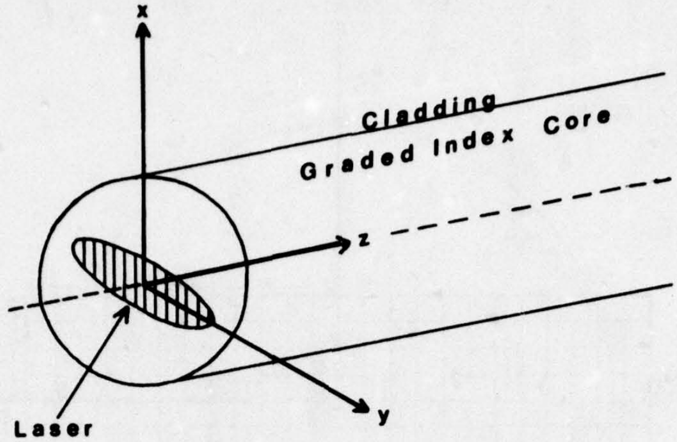

FIG.8(a) SOURCE—FIBRE CONFIGURATION

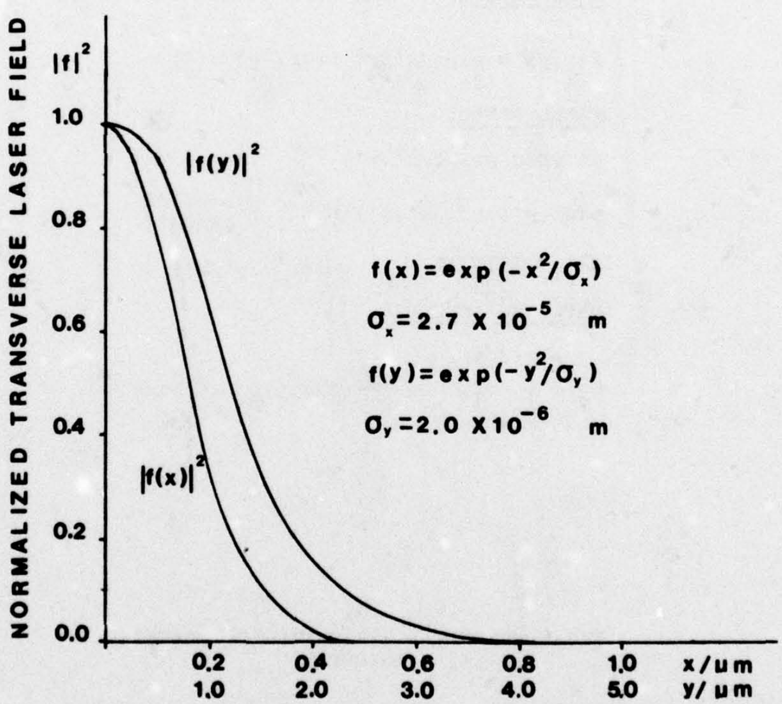

FIG. 8(b) TRANSVERSE LASER FIELD VARIATION

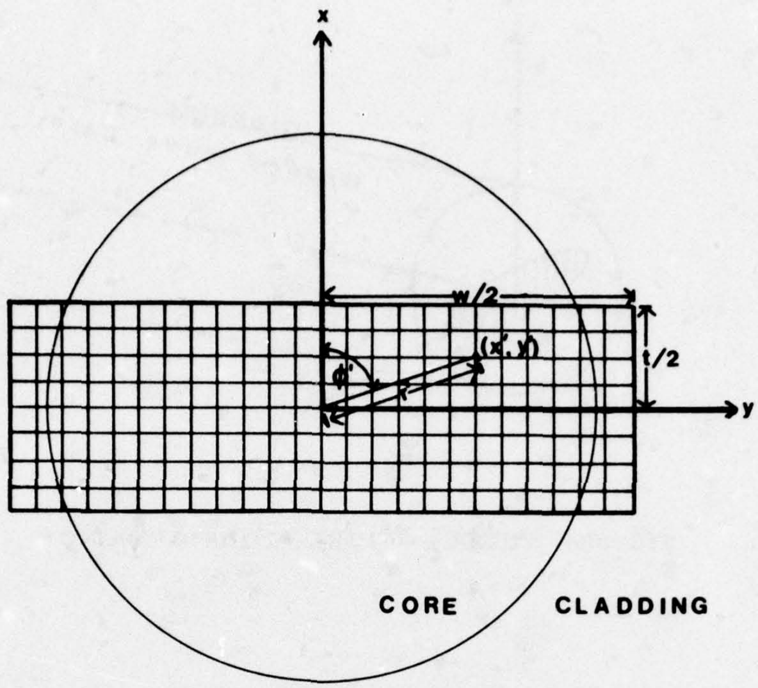

LASER FIELD

$$f(x,y) = \exp(-x^2/\sigma^2_x)\exp(-y^2/\sigma^2_y)$$

MODAL FIELD

At grid point x', y'

$$\psi(x',y') = \psi(r',\phi') = \psi(r')\begin{Bmatrix}\cos m\phi' \\ \sin m\phi'\end{Bmatrix}$$

$$r' = \sqrt{x'^2+y'^2} \qquad \phi' = \tan^{-1}(y'/x')$$

MATCHING INTEGRAL

$$P_o = \int_{-t/2}^{t/2}\int_{-w/2}^{w/2} \frac{n(x,y)}{Z_o} f(x,y)\psi(x,y)\,dxdy$$

FIG.9 NUMERICAL EVALUATION OF MATCHING INTEGRAL

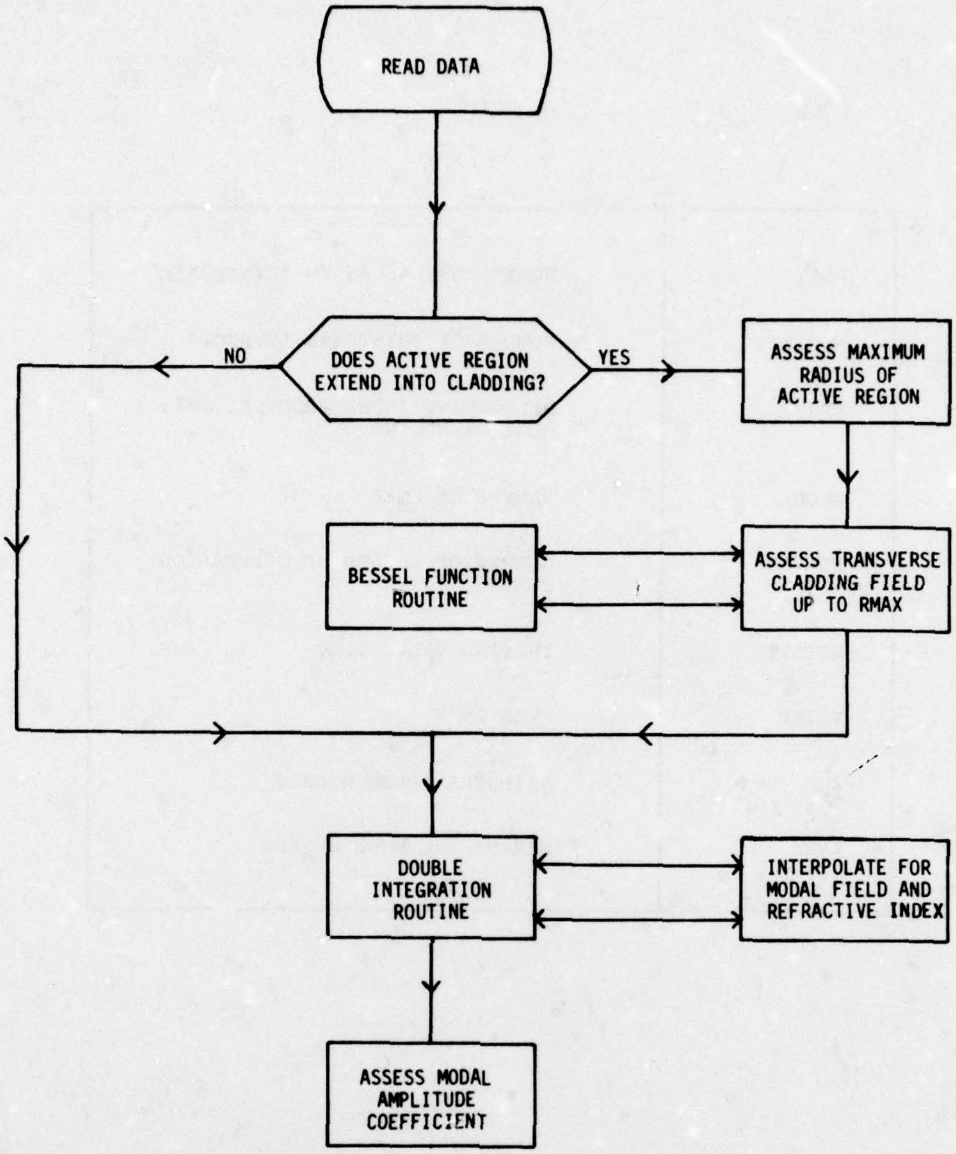

Fig.10 FLOW CHART OF PROGRAM "EXCITATION".

NLAY	NUMBER OF LAYERS IN "STAIRCASE"
NPOINT	NUMBER OF POINTS IN "DIRECT"
EN(J)	REFRACTIVE INDEX PROFILE, J=1, NLAY OR NPOINT
RCORE	RADIUS OF CORE
NUMV	NUMBER OF POINTS ON DISPERSION CURVE
VSTART	INITIAL VALUE OF V
VSTEP	STEP IN V
LJJ	AZIMUTHAL MODE NUMBER
LKK	MERIDIONAL MODE NUMBER

TABLE 1. DATA FOR PROGRAMS "STAIRCASE" AND "DIRECT"

AW,BW	HALF THICKNESS AND HALF WIDTH OF THE ACTIVE REGION
QX,QY	VARIANCES OF LASER FIELD FUNCTIONS
NXP,NYP	NUMBER OF INTEGRATION POINTS OVER ACTIVE REGION IN X AND Y DIRECTIONS
NPOINT	NUMBER OF POINTS AT WHICH TRANSVERSE MODAL FIELD IS SPECIFIED
F(I)	TRANSVERSE MODAL FIELD OVER THE CORE REGION, I=1, NPOINT
R(I)	RADIAL POINTS AT WHICH TRANSVERSE MODAL FIELD IS SPECIFIED, I=1, NPOINT
EN(I)	REFRACTIVE INDEX PROFILE, I=1, NPOINT
LJJ	AZIMUTHAL MODE NUMBER
PQ	MODAL POWER FLOW
W	CONVERGED EIGENVALUE = $r_c k(\bar{\beta}^2 - n_{CL}^2)^{\frac{1}{2}}$

TABLE 2. DATA FOR PROGRAM "EXCITATION".

DISPERSION EVALUATION IN MULTIMODE FIBERS BY NUMERICAL TECHNIQUE: APPLICATION TO RING SHAPED AND GRADED INDEX WITH A CENTRAL DIP

A.M. Scheggi, P.F. Checcacci, R. Falciai
Istituto di Ricerca sulle Onde Elettromagnetiche
C.N.R.
Via Panciatichi, 64 - Firenze, Italy

SUMMARY

A method is described which utilizing ray tracing technique and modal relations allows to evaluate the dispersion characteristics of multimode optical fibers with various refraction index distributions. The possibilities offered by the method are shown by application to fibers with index distribution ranging from the quasi step to the quasi parabolic shape. Then the method is applied to cases of practical interest such as ring profiles and graded index profiles with a central dip.
Dispersion equalization properties are observed for some types of ring profiles, while the effect on the dispersion due to a central dip in a graded profile is examined by varying the depth and width of the dip.

1. INTRODUCTION

Dispersion of multimode fibers with continuously varying refractive index can be investigated either by geometrical optics or by wave optics. We set up a numerical method which utilizing ray tracing technique and modal relations allows to evaluate the dispersion characteristics of multimode fibers with different index profiles.

The feasibility and limits of validity of the method were first proved by application to lossless slab waveguides and by comparing the results with those obtained from the analytical solution of the wave equation in the case of a particular index profile (Scheggi, A.M., et alii, 1975). The method was then applied to slab waveguides having a transverse index distribution varying from the nearly parabolic to the quasi step shapes (Scheggi, A.M., et alii, 1975) and finally extended to cylindrical fibers with the same radial index distributions (Checcacci, P.F., et alii, 1975).

The method constitutes a valid tool for evaluating dispersion characteristics of multimode fibers with different index profiles and presents a practical interest because it can be applied for designing fibers with optimum characteristics as well as for performance predictions. Further, as it will be seen in the sequel, it allows to point out the existence of "tunnelling" or "leaky" modes which are not easily predictable by solely applying either mode theory or geometrical optics.

The present paper is concerned with the description of the method and with its application to practical cases such as ring shaped profiles and nearly parabolic profiles with a central depression. Fibers with ring index profile can present some interest for their particular dispersion characteristics (Glogc, D., et alii, 1973; Stolen, R.H., 1975; Nakahara, T., et alii, 1976) while graded index fibers with a central depression resemble more closely the profiles obtained in practice in the production of preforms by C.V.D. technique. Such a depression, which is usually considered to be a defect (Burrus, C.A., et alii, 1973) is a common phenomenon occurring during the collapse process due to evaporation of the dopant in correspondence with the central region of the preform. In this work two types of ring profiles will be examined, precisely quasi step and quasi parabolic profiles with different central depressions. Finally the effect on the fiber dispersion of a central dip of various sizes in a quasi parabolic index distribution will be investigated.

2. DESCRIPTION OF THE METHOD

It is well known that ray optics technique is an effective tool for studying complex propagation and diffraction problems of high frequency waves in terms of local plane waves and their associated trajectories (the ray paths). In regions exterior to the sources and in a regime where the properties of the medium change slowly over a distance equal to the local wavelength, high frequency fields can be expressed in terms of local plane waves of the form $A(\bar{r})\exp[ik_oS(\bar{r})]$ where A and S are spatially dependent amplitude and phase functions, respectively, and k_o is the wave number in vacuum. The phase function S is obtained by solution of the eikonal equation (Felsen, L.B., et alii, 1973)

$$(\nabla S)^2 = n^2(\bar{r}) \qquad 1)$$

where $\bar{r}$ is the radius vector and n is the refractive index, which must satisfy the condition that its relative variation is small in comparison with the local wavelength or in other terms

$$|\nabla n|/nk_o \ll 1 \qquad k_o = 2\pi/\lambda_o \qquad 2)$$

The local plane waves propagate along trajectories that are tangent to ∇S. The amplitude function A can be determined from a transport equation but will be not considered in this paper.

Starting from the eikonal equation 1) it is possible to derive the ray equation

$$\frac{d}{ds}\left(n \frac{dr}{ds}\right) = \nabla n \qquad 3)$$

where s represents the distance along the ray. In a cylindrical coordinate system ρ, φ, z (Fig.1-a) and for an index distribution depending only on the transverse coordinate ρ, such equation can be written in component form

$$\frac{d}{ds}\left(n \frac{dz}{ds}\right) = 0$$

$$\frac{d}{ds}\left(n \frac{d\rho}{ds}\right) - n\rho \left(\frac{d\varphi}{ds}\right)^2 = \frac{dn}{ds} \qquad 4)$$

$$\frac{d}{ds}\left(n\rho^2 \frac{d\varphi}{ds}\right) = 0$$

For a graded index distribution the rays, which in a cylindrical fiber are nearly all skew to the fiber axis, are trapped by refraction and result tangent to an internal and to an external caustic whose projections on the normal cross section (Fig.1-b) are two circles of radii R_1 and R_2 respectively. R_1 corresponds to the minimum distance from the axis and R_2 to the "turning point". R_1 decreases for rays less skew to the axis and becomes zero in correspondence with meridional rays.

In order to evaluate the dispersion characteristics it is necessary to take into account the radial and azimuthal resonance conditions (Fig.2):

$$\int_{R_1}^{R_2} k_\rho \, d\rho = (\mu + \tfrac{1}{2})\pi \qquad 5)$$

$$\int_0^{2\pi} k_\varphi \rho \, d\varphi = 2\pi\nu \qquad 6)$$

where μ and ν denote two integer numbers which identify each mode. Note that in the radial resonance condition a phase shift of $\pi/2$ produced by each caustic has been taken into account.

Equations 5) and 6) can be joined to give a modal dispersion relation

$$\int_{R_1}^{R_2} \left[k^2 - k_z^2 - \nu^2/\rho^2\right]^{1/2} d\rho = (\mu + \tfrac{1}{2})\pi \quad ; \quad k^2 = k_o^2 n^2(\rho) = k_\rho^2 + k_\varphi^2 + k_z^2 \qquad 7)$$

Obviously when $\nu = 0$ such relation leads to the transverse resonance condition for the bidimensional case (Scheggi, A.M., et alii, 1975). Hence modes with $\nu = 0$, which correspond to meridional rays, represent the modes of a slab waveguide.

Once the trajectory of a generic ray is evaluated it is possible to determine through eqs. 5), 6), for each pair of values μ, ν, k_o and hence the propagation constant $\beta = k_z$ and the group delay $\tau_{gr} = L/c(d\beta/dk_o)$ (L is the fibre length and c the light velocity in vacuo).

3. QUASI-STEP, QUASI PARABOLIC PROFILES

Let us consider a cylindrical waveguide of radius a and an index profile of the form (Ikeda, M., 1974)

$$n(\rho) = n_2 + \frac{n_1 - n_2}{1 + \exp\left[C(\rho/a - 1)\right]} \qquad 8)$$

which for different values of the parameter C ranges from the quasi parabolic to the quasi step shape (Fig.3).

After substitution of expression 8) for the index distribution, system 4) has been numerically solved by the Runge-Kutta-Gill's method for C = 40 and C = 4, thus obtaining the ray trajectories which allow to evaluate the integrals representing the resonance relations in explicit form:

$$k_o \int_{R_1}^{R_2} n \sin\theta_z \cos\theta_\varphi \, d\rho = (\mu + \tfrac{1}{2})\pi \quad ; \quad k_\rho = k_o n \sin\theta_z \cos\theta_\varphi \qquad 9)$$

$$k_o \int_{0}^{2\pi} n \rho \sin\theta_z \sin\theta_\varphi \, d\varphi = 2\pi\nu \quad ; \quad k_\varphi = k_o n \sin\theta_z \sin\theta_\varphi \qquad 10)$$

from which k_o, $k_z = k_o n \cos\theta_z$ and τ_{gr} are obtained for each pair of values of μ and ν. Note that for a given ray k_z results simultaneously proportional to μ (when $\mu \gg 1/2$) and ν. Consequently once the curves of β and τ_{gr} versus k_o are obtained, for a given mode, corresponding to a pair of values μ, ν, the curves for other modes can be obtained by the same simply multiplying the k_o scale by a constant factor. However in plotting the results we will use the well known normalized Gloge notations (Gloge, D., 1971) that is:

$$v = k_o a \sqrt{n_1^2 - n_2^2} \qquad \text{normalized frequency}$$

$$b = (\beta/k_o - n_2)/(n_1 - n_2) \qquad \text{normalized propagation constant} \qquad 11)$$

$$\frac{d(vb)}{dv} = \frac{\frac{c}{L}\tau_{gr} - n_2}{n_1 - n_2} \qquad \text{normalized group delay}$$

Fig.4 shows as an example the normalized group delay and propagation constant of a set of modes (μ = 10, ν = 0,5,10,25,50,100) plotted versus normalized frequency v for a quasi step index profile (C = 40). For large values of v, β tends to $k_o n_1$ while b and d(vb)/dv tend to 1; at cut off where $\beta = n_2 k_o$ b = 0, while $d(vb)/dv \neq 0$ and tends to zero for $\nu \to 0$. The cut off condition ($\beta = n_2 k_o$) corresponds to a launching angle with the generatrix $\theta_z = \arccos(n_2/n_1) = \theta_c$, which constitutes the cut off angle that is the angle below which the rays (and the corresponding modes) remain trapped. However it turns out, from the computations, that for $\theta_z > \theta_c$, b can assume negative values corresponding to $\beta < n_2 k_o$ and the rays remain still trapped before being completely radiated outside the fiber. They constitute the so called "leaky or tunnelling rays" (Marcuse, D., 1973; Snyder, A.W., 1974). Such rays (and the corresponding modes) propagate in the fiber but with attenuation, because they undergo an optical tunnelling through an evanescent region beyond which they emerge as external radiation. Modes with ν = 0 which correspond to meridional rays do not present the tunnelling regions.

Analogous dispersion curves for the same set of modes are shown in Fig.5 for the quasi parabolic profile. As it was to be expected the dispersion in this case is very low. The three trapping, tunnelling and radiating regions are present also here, but the tunnelling region results reduced with respect to the preceding case.

The propagation in the three regions can be also examined by plotting the square magnitudes of the various components of the wave vector <u>k</u> as a function of the radial coordinate ρ (Gloge, D., et alii, 1973). Fig.6 shows such a plot for the quasi-step profile (C = 40) and for the quasi-parabolic profile (C = 4) for the mode μ = 10, ν = 50 and for three values of v chosen in the trapped, tunnelling and radiating regions respectively. In the first case (v = 89) the curve ν^2/ρ^2 intersects the curve $k_o^2 n^2(\rho) - \beta^2$ at two points $\rho = R_1$ and $\rho = R_2$ where $k_\rho = [k_o^2 n^2(\rho) - \beta^2 - \nu^2/\rho^2]^{1/2} = 0$. For $R_1 < \rho < R_2$ k_ρ is real and propagation occurs in the anular region defined by the two caustics of radii R_1 and R_2 respectively. For $\rho < R_1$, $\rho > R_2$, k_ρ is imaginary and the field is evanescent. In the second case (v = 69 for the quasi-step profile and v = 75 for the quasi-parabolic profile) the curves intersect also at a third point for $\rho = R_3$ where again $k_\rho = 0$; k_ρ is real for $R_1 < \rho < R_2$, $\rho > R_3$ and is imaginary for $\rho < R_1$, $R_2 < \rho < R_3$. R_3 represents the radius of a third caustic and defines an evanescent region through which the mode energy tunnells before re-emerging (for $\rho > R_3$) as free radiation. In the third case (v = 54 for the quasi-step profile and v = 70 for the quasi-parabolic profile) only one intersection occurs at $\rho = R_1$ and k_ρ is imaginary for $\rho < R_1$ or real for $\rho > R_1$. The field is evanescent within the caustic and radiating external to that. Note that the values chosen for v in the tunnelling and radiating regions are different for the two profiles because the tunnelling region in the quasi-parabolic case is narrower; in fact the two curves ν^2/ρ^2 and $k_o^2 n^2(\rho)-\beta^2$ are almost parallel when ρ increases ($\rho > R_2$) so that their crossing occurs only in a restricted range of frequency after which the tunnelling region disappears.

The behavior of the caustics bounding the trapping region for the different modes can be easily obtained from the ray tracing computations. Figs.7-a,b show the radii R_1 and R_2 of the two caustics for modes with different azimuthal numbers plotted versus v for the two examined profiles which are sketched at the right hand side. In the quasi-step case (Fig.7-a) the internal caustics are spaced depending on the azimuthal number ν. On the contrary the external caustics are all concentrated in correspondence with the high index gradient at the boundary of the fiber. Consequently the regions bounded by pairs of caustics corresponding to different modes have different widths, so that the ray paths and hence the optical paths (as n is constant) result different with a consequent large differential group delay. For the quasi parabolic case (Fig.7-b) also the external caustics are spaced due to the low gradient of the index, so that the bounded regions exhibit the same behavior with the frequency for the different modes. Further when ν increases such zones are shifted towards a region of lower index: as a consequence the ray paths increase with ν but the optical paths result again practically equal for the different modes and the group delay differences very small.

4. RING SHAPED PROFILES

We considered two sets of ring shaped profiles: quasi-step and quasi-parabolic ring profiles with variable dimensions of the central region (Fig.8). In both cases we utilized the index distribution given in expression 8) with suitable modifications. For what concerns quasi-step index profiles we considered the case corresponding to C = 40 modifying the central region by means of an analogous but reversed profile (Fig.8-a). The quasi-parabolic ring was obtained by joining two identical profiles corresponding to C = 4 in expression 8) and varying the distance $2l$ between the vertexes of the two profiles, which on turn implies a variation in the depth of the central depression (Fig.8-b). By applying the method precedingly described the propagation constant and group delay were evaluated in a number of cases. Fig.9 shows the group delay curves plotted versus frequency for a family of modes (μ= 10, ν = 1,5,10,25,50) in three cases corresponding to different values of the central depression width $2a_1$ and depth d. The case of quasi-step profile is also reported for comparison. The most relevant effect is the equalization of dispersion for a number of modes. When the width $2a_1$ decreases the number of equalized modes decreases and, if for a fixed value of $2a_1$ the depth d decreases, such modes result still equalized but only down to a certain frequency, below which the dispersion increases again. This effect can be better understood if one observes the behavior of the caustics defining the region of trapping for the propagating rays or modes. The radii R_1 and R_2 of the internal and external caustics respectively have been plotted in Fig.10 versus v for the four cases shown in Fig.9. The corresponding profiles are plotted at the right hand side. In the cases of maximum depth ($d = n_1 - n_2$) one can observe in correspondence with the internal step of the index an overlapping of all those caustics which in the absence of central depression are located just in that region, so that the modes remain confined in a small region, that is in the anular region between the internal and external steps of the index. The corresponding optical paths result equalized with reduction of group delay differences. When the depression depth decreases the internal caustics still overlap but only down to a certain value of v below which the rays can again penetrate the central region with a consequent spreading of the caustics and hence of the dispersion. The group delay curves are shown in Fig.11 for the same set of modes in two cases of quasi-parabolic ring profiles. These profiles are inferior from the dispersion equalization point of view with respect to the quasi-step ring profile. This was to be expected if one thinks in terms of location of the caustics, which in this case cannot result concentrated neither in the vicinity of the internal depression nor at the boundary of the fiber due to the slow index gradients.

5. QUASI-PARABOLIC PROFILE WITH A CENTRAL DIP

To the purpose of examining the effect on the dispersion characteristics of a central dip in a graded profile we applied again our numerical method to a quasi-parabolic profile (C = 4 in expression 8), where the central region is matched with a curve of the type sin x/x (Fig.12). A plot of the normalized group delay versus v is shown in Fig.13 for three different cases corresponding to different values of the depth d and width w of the central depression. Also here the case of graded profile without central dip is shown for comparison. The dispersion increases when either d or w increase, and the number of perturbed modes increases with w. Again this effect can be better seen if one observes in Fig. 14 the behavior of the caustics. For the sake of simplicity only the caustics corresponding to the most perturbed modes are shown. The continuous line correspond to the depressed profile while the dashed lines correspond to the unperturbed profile. As already noted in section 3. in the case of a graded profile the zones defined by the caustics present a width varying with frequency in the same way for the different modes but shifted when increases towards lower index regions so that the optical paths result practically equal with consequent minimum group delay differences. In the presence of a central depression such regions tend to overlap when the frequency varies down to a certain value of v below which there is a spread of the caustics with a differentiation in the bounded region widths. As a consequence the optical paths and hence the group delays result equalized in the overlapping region, although presenting a value different from the previous unperturbed one, due to the different index region occupied. The group delays result differentiated for the different modes in correspondence with the region of caustic spreading. Obviously the effect is less evident for smaller depressions. In order to have an idea of the orders of magnitudes let us consider a fiber with $n_1 = 1.46$ $n_2 = 1.45$ and having a diameter 2a of 50 μm.

Table 1 shows the values of the dispersion obtained from the curves of Fig. 14 at a wavelength $\lambda = 1$ μm.

$n_1 = 1.46$; $n_2 = 1.45$; $20 = 50$ μm ; $\lambda = 1$ μm		
$d/(n_1 - n_2)$	w/2a	dispersion (ns/km)
0	0	0.6
0.25	0.1	0.9
0.9	0.1	1.2
0.9	0.2	1.9

These values indicate that there is an increase of the dispersion due to the central dip in the index profile; however the case of minimum depression we considered is closer to realistic cases and gives rise to an increase in dispersion which may be negligible especially if one takes into account also the material dispersion which in the present treatment has not been considered.

6. CONCLUSION

The results described in the preceding sections have shown that the reported method whose feasibility had previously been shown (Scheggi, A.M., et alii, 1975) is suitable for application to a variety of index profiles. In particular it was possible to examine, from the dispersion point of view, types of profiles which find interest in the practice, such as ring profiles and graded profile with central depression. The most relevant results are that ring profiles present equalizing properties, while a central dip in a graded profile can affect differently the dispersion depending on the width and depth of the dip itself. With dimensions closer to realistic cases, such as obtained with good CVD preform production process, the dispersion increase can be neglected, also in comparison with the material dispersion.

REFERENCES

BURRUS, C.A., CHINNOCK, E.L., GLOGE, D., HOLDEN, W.S., TINYGE LI, STANDLEY, R.D., KECK, D.B., 1973, "Pulse Dispersion and Refractive Index Profiles of Some Low Noise Multimode Optical Fibres", in Proc. of the IEEE, 61, 1498.

CHECCACCI, P.F., FALCIAI, R., SCHEGGI, A.M., 1975, "Ray Tracing Technique for Evaluating the Dispersion Characteristics of Graded-Index Cylindrical Fibres", in Electronics Letters, 11,

FELSEN, L.B., MARCUVITZ, N., 1973, "Radiation and Scattering of Waves", Prenctice-Hall, Englewood Cliffs N.J., Secs. 1.7-b and 5.8.

GLOGE, D., MARCATILI, E.A.J., 1973, "Impulse Response of Fibers with Ring-Shaped Parabolic Index Distribution", in Bell Syst. Techn. Journ., 52, 1161.

GLOGE, D., 1971, "Weakly Guiding Fibers", in Applied Optics, 10, 1022.

GLOGE, D., MARCATILI, E.A.J., 1973, "Multimode Theory of Graded Core Fibers", in Bell Syst. Tech. Journ., 52, 1563.

IKEDA, M., 1974, "Propagation Characteristics of Multimode Fibers with Graded Core Index", in IEEE Journ. Quantum Electronics, 10, 362.

MARCUSE, D., 1973, "Cut Off Condition of Optical Fibers", in Journ. Opt. Soc. Am., 63, 1369.

NAKAHARA, T., HOSHIKAWA, M., YOSHIDA, M., SUZUKI, S., 1976, "Transmission Properties of Ring Type Optical Fibers", Second European Conference on Optical Fibre Communication, Paris, September 1976, Part 2, p.149.

SCHEGGI, A.M., CHECCACCI, P.F., FALCIAI, R., 1975, "Dispersion Characteristics in Quasi-Step and Graded Index Slab Waveguides by Ray Tracing Technique", in Journ. Opt. Soc. Am., 65, 1022.

SNYDER, A.W., 1974, "Leaky-ray Theory of Optical Waveguides of Circular Cross Section", in Applied Physics, 4, 273.

STOLEN, R.H., 1975, "Modes in Fiber Optical Waveguides", in Applied Optics, 14, 1533.

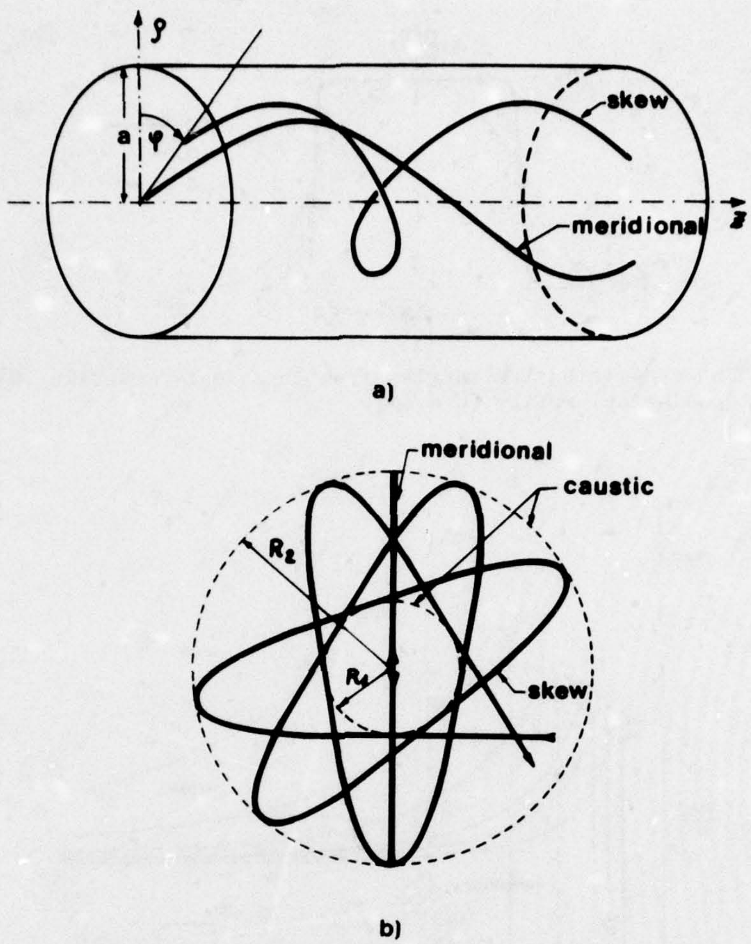

Fig. 1-a The cylindrical coordinate system and two generic trapped rays: a meridional and a skew ray.

-b Cross sectional projections of a skew and of a meridional ray along with the internal and external caustics.

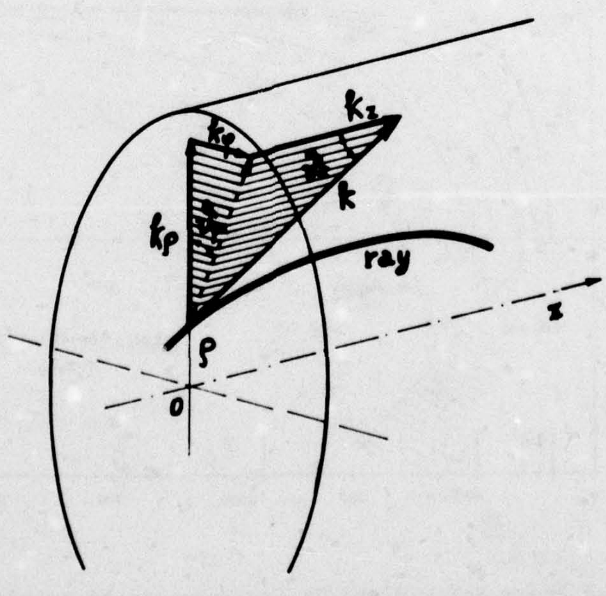

Fig. 2 The wave vector $\underline{k}$ and its components along ρ, φ, and z directions.

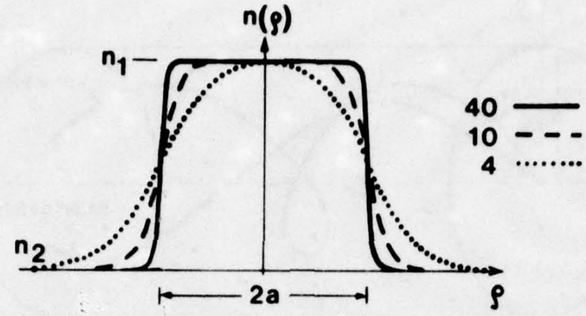

Fig. 3 Index distribution ranging from the quasi-parabolic (C = 4) to the quasi-step profile (C = 40).

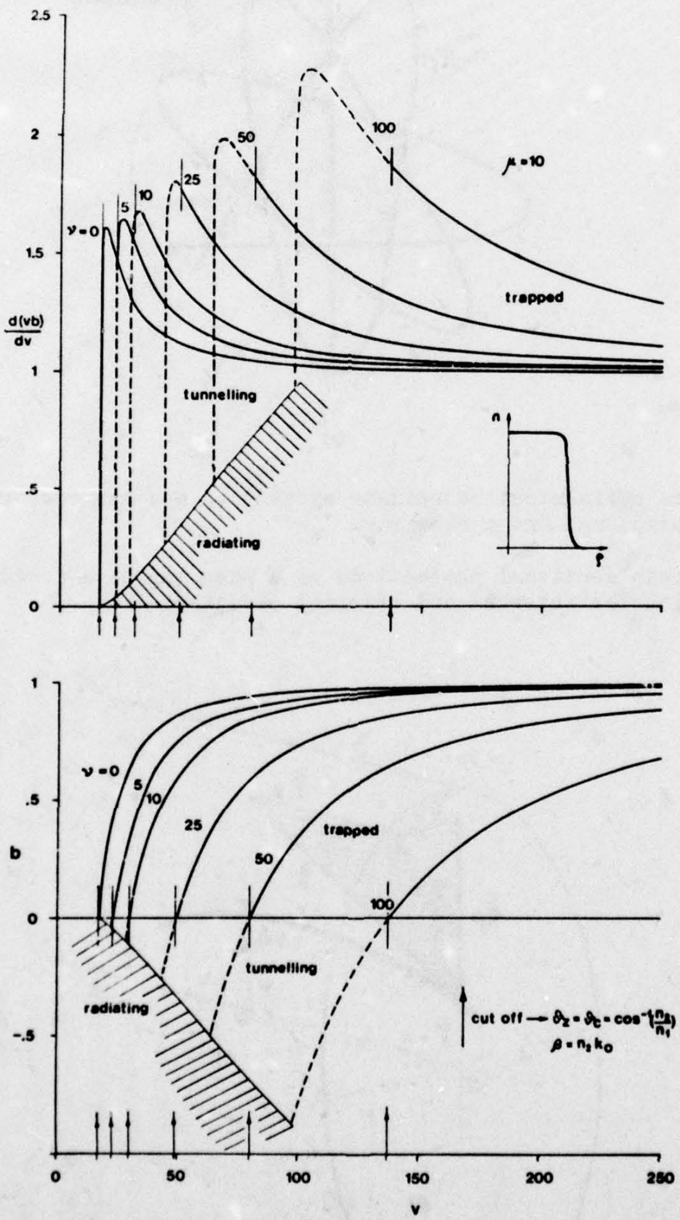

Fig. 4 Normalized group delay d(vb)/dv and propagation constant b versus normalized frequency v for a set of modes (μ = 10, ν = 0,5,10,25,50,100) for a quasi-step index profile (C = 40).

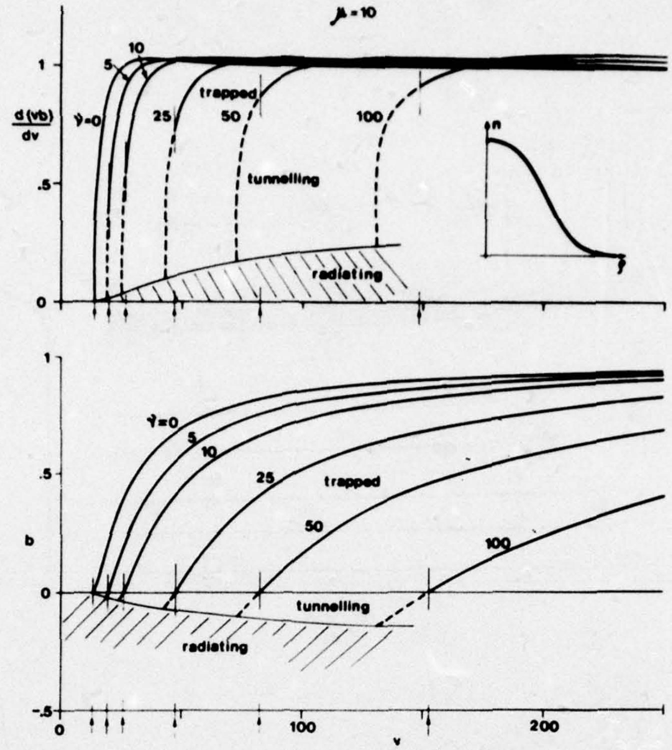

Fig. 5 Normalized group delay d(vb)/dv and propagation constant b versus normalized frequency v for a set of modes ($\mu = 10, \nu = 0,5,10,25,50,100$) for a quasi-parabolic index profile (C = 4).

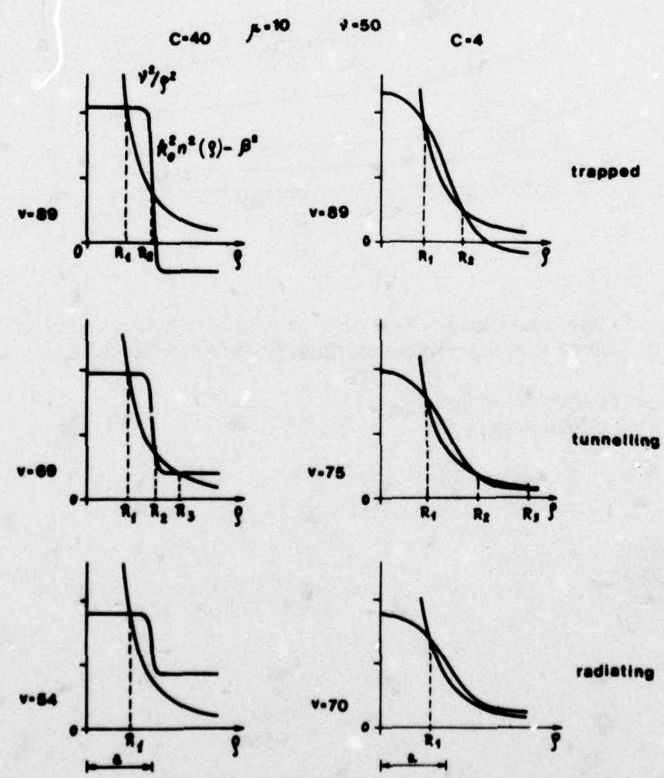

Fig. 6 Sketch defining trapped, tunnelling, radiating regions for particular examples for the quasi-step (C = 40) and quasi-parabolic profile cases (C = 4).

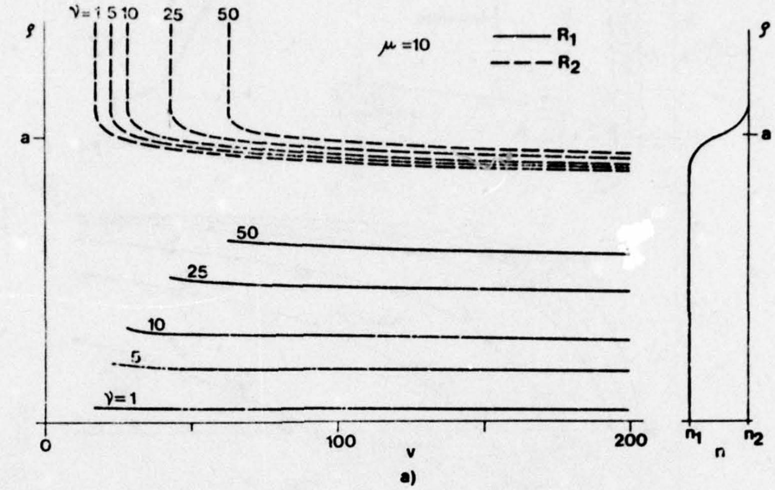

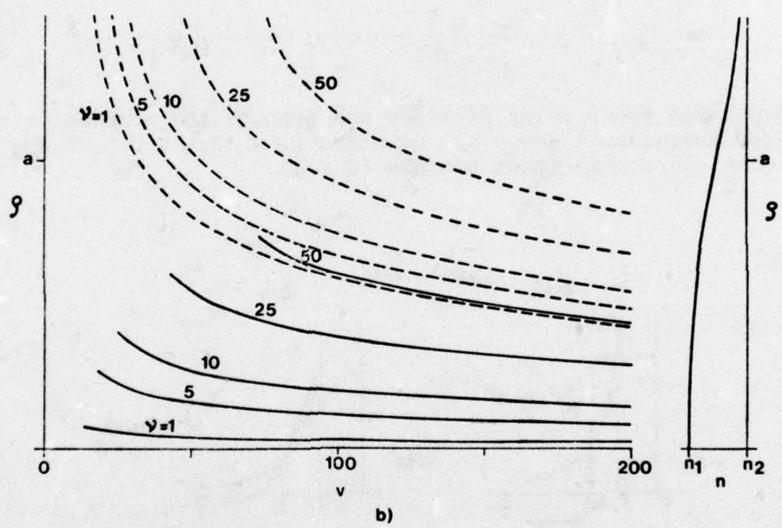

Fig. 7 Radii of the internal (R_1) and external (R_2) caustics bounding modes with different azimuthal numbers plotted versus v.

-a Quasi-step profile

-b Quasi-parabolic profile

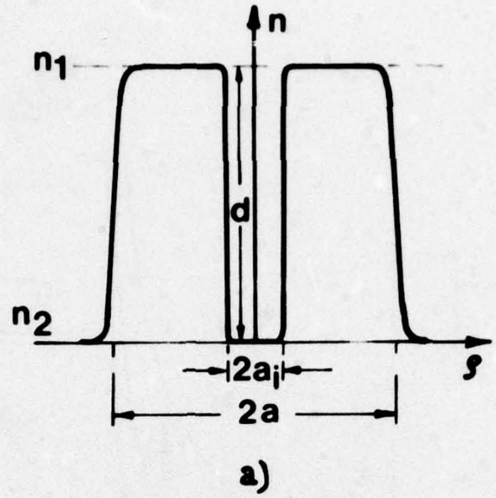

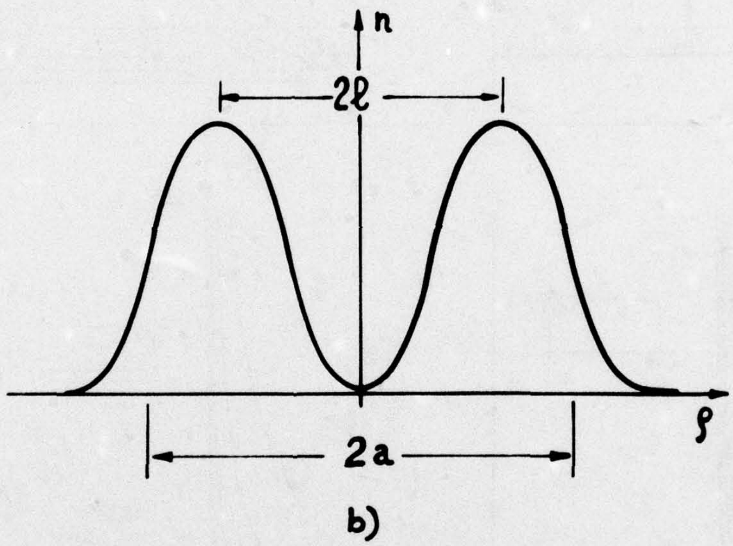

Fig. 8-a Ring quasi-step index profile

-b Ring quasi-parabolic index profile

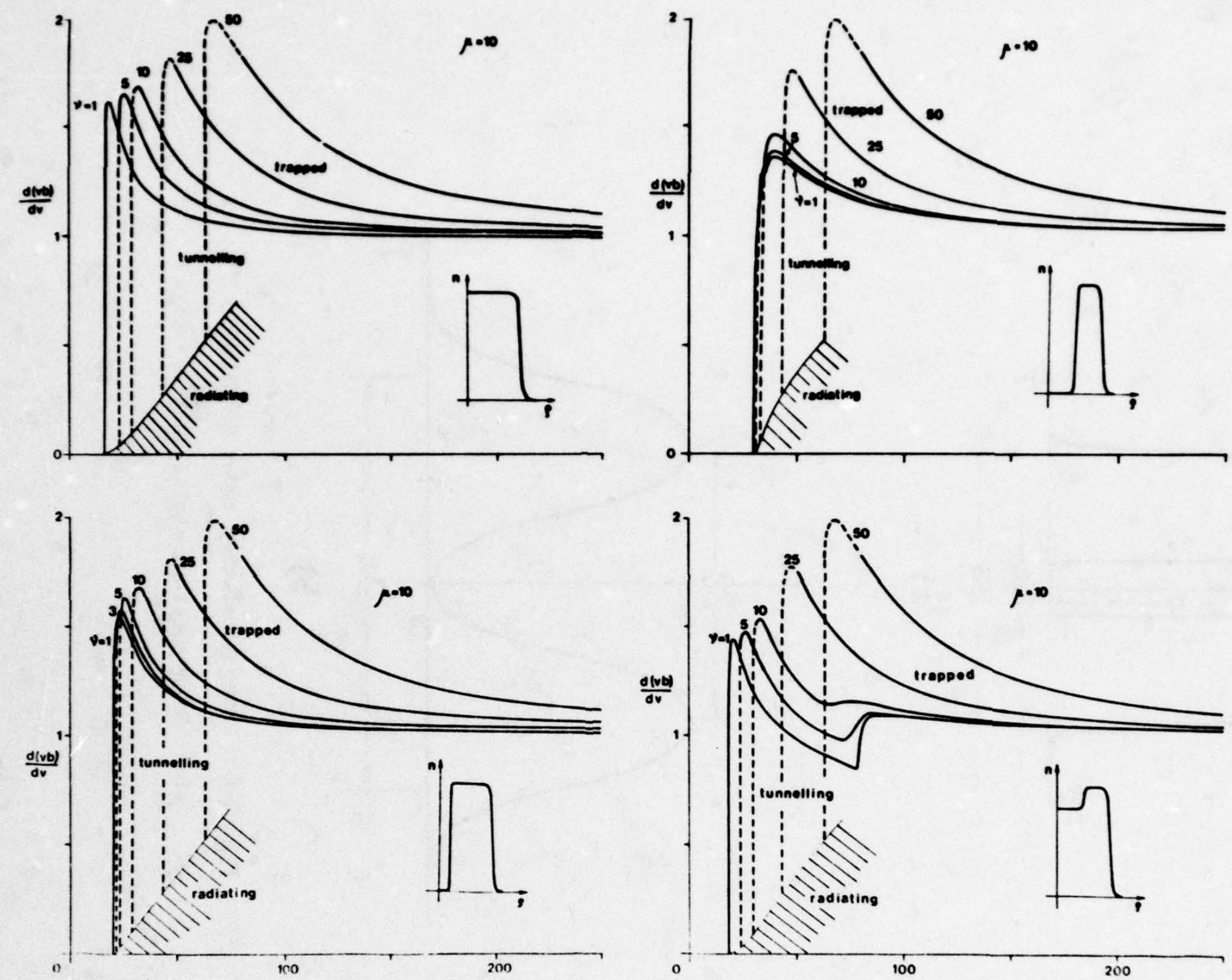

Fig. 9 Normalized group delay versus normalized frequency for a set of modes ($\mu = 10, \nu = 1,5,10,25.,.50$) for three cases of quasi-step ring profile: $a_i = 0.5a$, $d = n_1 - n_2$ (upper right); $a_i = 0.2a$, $d = n_1 - n_2$ (lower left); $a_i = 0.5a$, $d = 0.2(n_1 - n_2)$ (lower right).
The case $a_i = 0$, $d = 0$ (quasi-step case) is shown in the upper left curves.

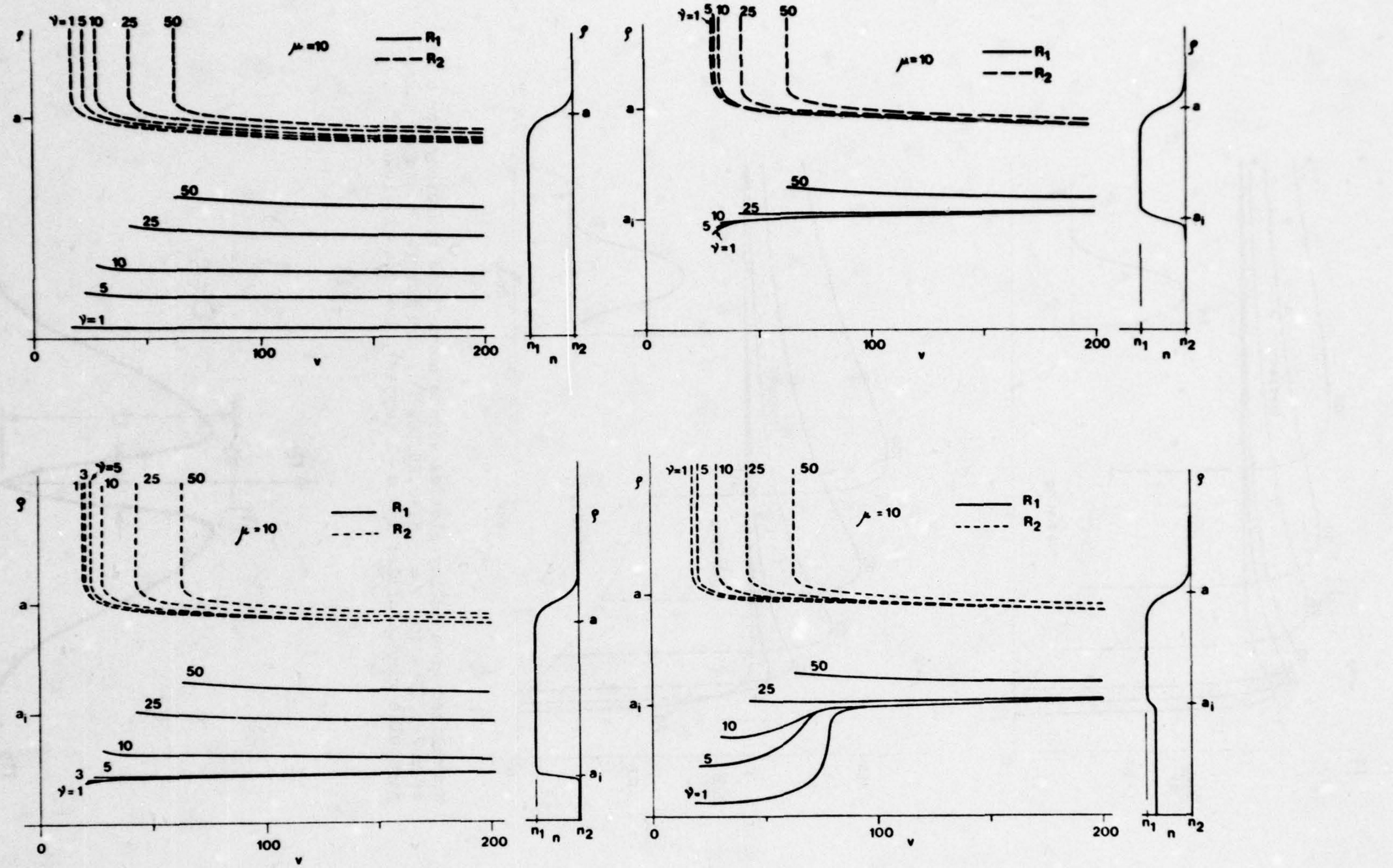

Fig. 10 Radii of the internal (R_1) and external (R_2) caustics versus v for a set of modes ($\mu = 10$, $\nu = 1,5,10,25,50$) in the same cases as in Fig.9. The corresponding profiles are sketched at the right hand sides of each plot.

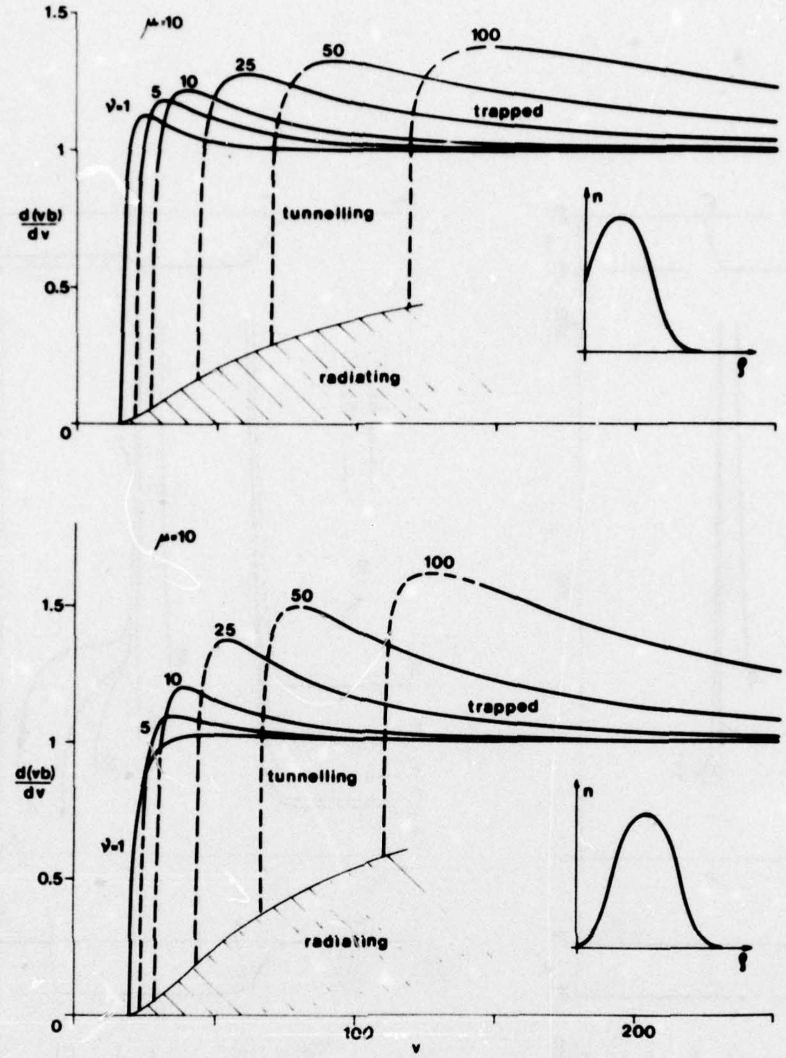

Fig. 11 Normalized group delay plotted versus normalized frequency for a set of modes (μ = 10, ν = 1,5,10,25,50,100) and for two cases of quasi-parabolic ring profile: l = a - 1 (upper), l = 2(a - 1)(lower).

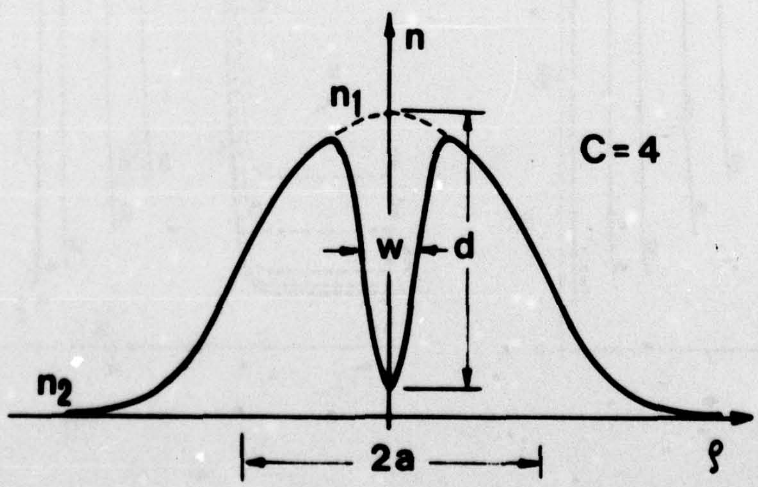

Fig. 12 Quasi-parabolic index distribution with a central depression.

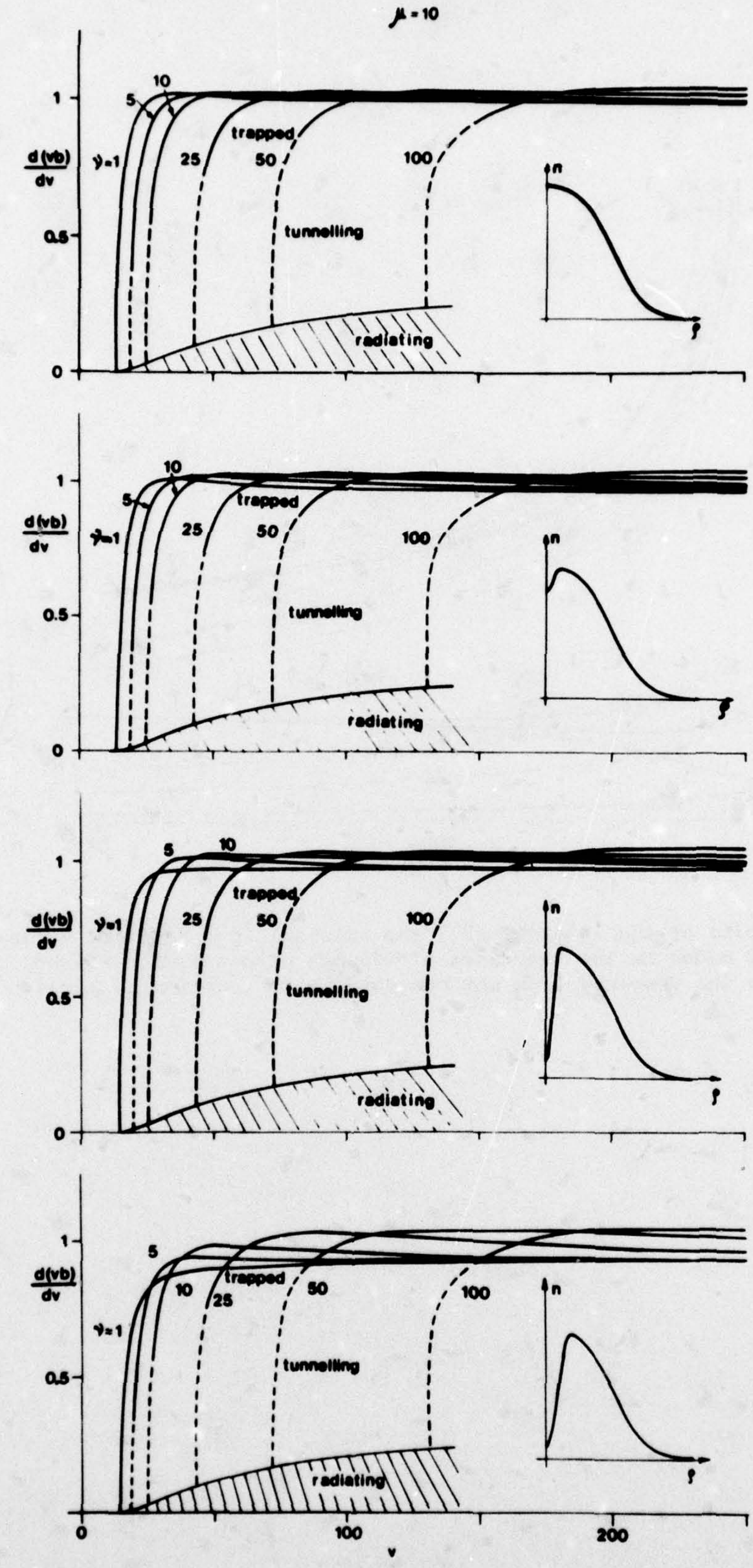

Fig.13 Normalized group delay of a set of modes versus normalized frequency for the quasi-parabolic profile and for three cases of different depressions.

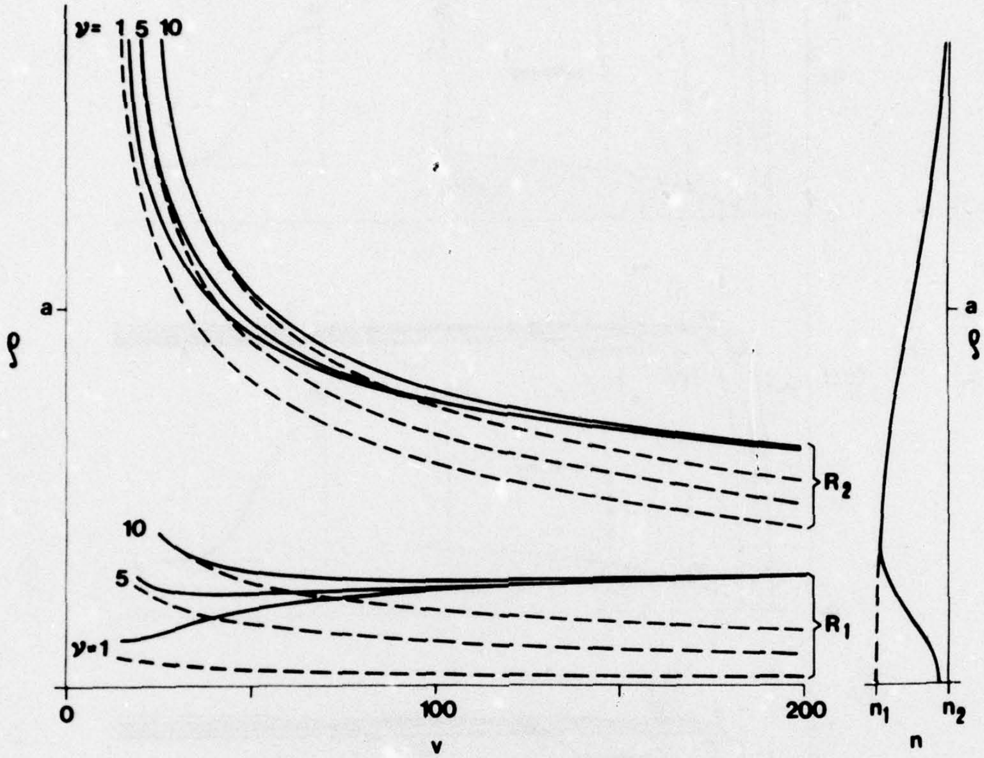

Fig.14 Radii of the internal (R_1) and external (R_2) caustics versus v for a set of modes in the two cases of absence of depression (dashed lines) and in the presence of a maximum depression (continuous line).

FINITE-BANDWIDTH PROPAGATION IN MULTIMODE OPTICAL FIBERS

B. Crosignani, P. Di Porto
Fondazione Ugo Bordoni, Istituto Superiore P.T.,
Viale Europa, Roma, Italy
and
California Institute of Technology, Pasadena,
Cal. 91125, U.S.A.

and

C.H. Papas
California Institute of Technology, Pasadena,
Cal. 91125, U.S.A.

SUMMARY

The propagation in a multimode optical fiber of a finite-bandwidth optical carrier modulated by a nonstationary signal is investigated. The fluctuations of the field due to random mode-coupling are considered and the set of coupled equations describing their evolution is derived. In particular, this allows us to investigate the propagation of a frequency-modulated signal and to obtain a general theorem concerning the asymptotic behavior of mode-power fluctuations.

1. INTRODUCTION

The propagation of a stationary monochromatic carrier in a multimode optical fiber in the presence of mode-coupling has been extensively studied by Marcuse (1), in the frame of a statistical approach based on the introduction of an ensemble of similar fibers slightly differing from a common ideal structure for the presence of random imperfections. The procedure allows one to write two closed systems of differential coupled equations for the single-mode powers averaged over the ensemble of fibers $\langle P_m \rangle$ and for the correlations $\langle P_m P_n \rangle$ (1),(2). The extension to the nonstationary nonmonochromatic case has been accomplished, for what concerns the average powers $\langle P_m \rangle$, on an intuitive basis by Marcuse (1) and by means of more rigorous treatments by Personick (3) and Steinberg (4).

We generalize the statistical approach to furnish the evolution of the quantities $\langle \overline{c_m(z,\omega)c_r^*(z,\omega')} \rangle$ and $\langle \overline{c_m(z,\omega)c_n^*(z,\omega')}\ \overline{c_r(z,\omega'')c_k^*(z,\omega''')} \rangle$, where the c_m's are the slowly varying mode-amplitudes and the bar denotes the averaging operation over the source fluctuations. The knowledge of these quantities allows us in turn to describe the behaviour of the field and of its fluctuations in the general situation in which a finite-bandwidth carrier is amplitude or frequency-modulated.

An other significant result concerns the asymptotic behavior of the single-mode power fluctuations, which tend to vanish as a consequence of the finite carrier-bandwidth, so that, in the lossless case, power equipartition among modes takes place not only on the average, but over each fiber of the ensemble (5).

2. DESCRIPTION OF ELECTROMAGNETIC PROPAGATION IN A FIBER

The transverse part of the electric and magnetic fields excited in a fiber by means of a finite-bandwidth source can be approximately written in terms of the forward traveling guided modes $\underline{E}_m$, $\underline{H}_m$ as (1)

$$\underline{E}(\underline{r},z,t) = \sum_m \underline{E}_m(\underline{r},\omega_o) \int c_m(z,\omega)\, e^{i\omega t - i\beta_m(\omega)z}\, d\omega \quad , \qquad (1)$$

$$\underline{H}(\underline{r},z,t) = \sum_m \underline{H}_m(\underline{r},\omega_o) \int c_m(z,\omega)\, e^{i\omega t - i\beta_m(\omega)z}\, d\omega \quad , \qquad (2)$$

where $\underline{r}$ and z are the transverse and longitudinal coordinates, $\beta_m(\omega)$ represents the propagation constant of the mth mode at the (angular) frequency ω, and the realistic relation between the bandwidth $\delta\omega$ and the central frequency ω_o of the signal

$$\delta\omega/\omega_o << 1 \qquad (3)$$

allows one to evaluate the mode configurations $\underline{E}_m(\underline{r},\omega)$ and $\underline{H}_m(\underline{r},\omega)$ at ω_o. The z-depen_ dence of the slowly-varying mode amplitudes c_m is associated with the departure of the fiber structure from the ideal one to which the configurations $\underline{E}_m$, $\underline{H}_m$ pertain. The electromagnetic power carried through an arbitrary portion of area σ of any given fiber section z = const. can be expressed in terms of the complex Poynting vector $\underline{S}$ (6)

$$\underline{S} = \tfrac{1}{2}\,\overline{\underline{E} \times \underline{H}^*} \quad , \tag{4}$$

where the bar indicates the averaging operation over the source fluctuations, as

$$P^{\sigma} = \mathrm{Re} \int_{\sigma} \underline{e}_z \cdot \underline{S}\ d\underline{r} \quad . \tag{5}$$

Here "Re" means "real part of" and $\underline{e}_z$ is the unit vector in the positive z-direction. By means of Eqs.(1),(2) and (4), Eq.(5) yields

$$P^{\sigma}(z,t) = \tfrac{1}{2} \sum_m \sum_r A^{\sigma}_{mr}(z,t) \quad , \tag{6}$$

where

$$A^{\sigma}_{mr} = \int_{\sigma} d\underline{r}\ \underline{E}_m(\underline{r},\omega_o) \times \underline{H}^*_r(\underline{r},\omega_o) \cdot \underline{e}_z \int d\omega \int d\omega'\ e^{i(\omega-\omega')t - i\left[\beta_m(\omega) - \beta_r(\omega')\right]z}\ \overline{c_m(z,\omega)c^*_r(z,\omega')} . \tag{7}$$

The total power P_t carried by the field is obtained by integrating $\underline{e}_z \cdot \underline{S}$ in Eq.(5) over the whole plane z = const. . This operation furnishes, with the help of the orthogonality relation between the modes (1)

$$\int_{-\infty}^{+\infty} dx \int_{-\infty}^{+\infty} dy\ \ \underline{e}_z \cdot \underline{E}_m(\underline{r},\omega_o) \times \underline{H}^*_n(\underline{r},\omega_o) = 2\,P\,\delta_{mn} \quad , \tag{8}$$

where P is a positive normalization constant and δ_{nm} is the usual Kronecker symbol,

$$P_t(z,t) = \sum_m P_m(z,t) \quad , \tag{9}$$

where

$$P_m(z,t) = P \int d\omega \int d\omega'\ e^{i(\omega-\omega')t - i\left[\beta_m(\omega) - \beta_m(\omega')\right]z}\ \overline{c_m(z,\omega)c^*_m(z,\omega')} \tag{10}$$

can be interpreted as the power carried by the mth mode. It is worthwhile to note that the interference terms between the various modes disappear in the expression of the total power P_t, while they are present in that of P^{σ}.

3. STATISTICAL DESCRIPTION OF PROPAGATION

The random nature of the imperfections unavoidably present in a real fiber suggests some statistical procedure as the most natural way for describing the propagation in optical fibers. This is accomplished by introducing an ensemble of similar fibers, each of which differs from a common ideal model for the presence of random imperfections, and to evaluate the average of the significant quantities, e.g. P^{σ}, P and P_m, over this ensemble, which in turn is equivalent to consider $\langle \overline{c_m(z,\omega)c^*_r(z,\omega')} \rangle$ as the basic quantity.

In order to test the relevance of this approach for what concerns practical situations, in which a single fiber is usually employed, one has to investigate the statistical fluctuations around the average values. This leads to consider higher order averages of the kind $\langle \overline{c_m(z,\omega)c^*_r(z,\omega')}\ \overline{c_m(z,\omega'')c^*_r(z,\omega''')} \rangle$, $\langle \overline{c_m(z,\omega)c^*_r(z,\omega')}\ \overline{c_r(z,\omega'')c^*_m(z,\omega''')} \rangle$.

One starts from the system of equations describing the evolution of the c_m's in the single fiber, which reads (1)

$$\frac{dc_m(z,\omega)}{dz} = \sum_k A_{mk}(z,\omega)\ c_k(z,\omega) \quad , \tag{11}$$

with

$$A_{mk}(z,\omega) = K_{mk}(z)\, e^{i[\beta_m(\omega) - \beta_k(\omega)]z} \quad , \tag{12}$$

the K_{mk}'s being suitable coupling coefficients, vanishing in the case of an ideal fiber. By using Eq.(11) one can easily derive the following equations

$$\frac{d}{dz}\left[\overline{c_m^*(z,\omega')c_n(z,\omega)}\right] = \sum_k \left\{ A_{nk}(z,\omega)\, \overline{c_m^*(z,\omega')c_k(z,\omega)} + A_{mk}^*(z,\omega')\, \overline{c_n(z,\omega)c_k^*(z,\omega')} \right\} \quad , \tag{13}$$

$$\begin{aligned} \frac{d}{dz}\left[\overline{c_m(z,\omega)c_r^*(z,\omega')}\ \overline{c_p(z,\omega'')c_n^*(z,\omega''')}\right] = \\ \sum_k \Big\{ & A_{mk}(z,\omega)\ \overline{c_r^*(z,\omega')c_k(z,\omega)}\ \overline{c_p(z,\omega'')c_n^*(z,\omega''')} \\ + \ & A_{rk}^*(z,\omega')\ \overline{c_m(z,\omega)c_k^*(z,\omega')}\ \overline{c_p(z,\omega'')c_n^*(z,\omega''')} \\ + \ & A_{pk}(z,\omega'')\ \overline{c_n^*(z,\omega''')c_k(z,\omega'')}\ \overline{c_m(z,\omega)c_r^*(z,\omega')} \\ + \ & A_{nk}^*(z,\omega''')\ \overline{c_p(z,\omega'')c_k^*(z,\omega''')}\ \overline{c_m(z,\omega)c_r^*(z,\omega')} \Big\} \quad , \end{aligned} \tag{14}$$

which have to be averaged over the fiber ensemble. The resulting equations can be put in the form of closed systems under the homogeneity assumption

$$< K_{mn}(z) > \ = 0 \quad , \tag{15}$$

$$< K_{mn}(z)K_{rp}(z-\zeta) > = F_{mnrp}(|\zeta|) \quad , \tag{16}$$

provided that the coupling is small enough that the c_m's do not significantly vary over the correlation length of the statistical variables K_{mn}. In this way one obtains (see also Ref.(7)), as a first significant result,

$$\frac{d}{dz} < \overline{c_m(z,\omega)c_r^*(z,\omega')} > \ = - g_{mr} < \overline{c_m(z,\omega)c_r^*(z,\omega')} > \quad , \ m \neq r \quad , \tag{17}$$

$$\begin{aligned} \frac{d}{dz} < \overline{c_m(z,\omega)c_r^*(z,\omega')}\ \overline{c_m(z,\omega'')c_r^*(z,\omega''')} > \ = \\ - (2g_{mr} + f_{mr}) < \overline{c_m(z,\omega)c_r^*(z,\omega')}\ \overline{c_m(z,\omega'')c_r^*(z,\omega''')} > \quad , \ m \neq r \quad , \end{aligned} \tag{18}$$

with

$$\begin{aligned} g_{mr} = & \sum_k \int_0^{+\infty} < K_{mk}(\zeta)K_{km}(0) > e^{-i[\beta_k(\omega_o) - \beta_m(\omega_o)]\zeta}\, d\zeta \\ & + \sum_k \int_0^{+\infty} < K_{rk}^*(\zeta)K_{kr}^*(0) > e^{-i[\beta_r(\omega_o) - \beta_k(\omega_o)]\zeta}\, d\zeta \\ & + \int_{-\infty}^{+\infty} < K_{mm}(\zeta)K_{rr}^*(0) > d\zeta \end{aligned} \tag{19}$$

and

$$f_{mr} = \frac{1}{2} \lim_{L\to+\infty} < \left| (1/L)^{\frac{1}{2}} \int_{-L/2}^{L/2} \left[K_{mm}(z) - K_{rr}(z) \right] dz \right|^2 > \quad . \tag{20}$$

The real part of g_{mr} can be shown to be a positive quantity (7), so that

$$\langle \overline{c_m(z,\omega)c_r^*(z,\omega')} \rangle = \overline{c_m(0,\omega)c_r^*(0,\omega')}\; e^{-g_{mr}z} \quad , m \neq r , \tag{21}$$

and

$$\langle \overline{c_m(z,\omega)c_r^*(z,\omega')}\;\overline{c_m(z,\omega'')c_r^*(z,\omega''')} \rangle =$$

$$\overline{c_m(0,\omega)c_r^*(0,\omega')}\;\overline{c_m(0,\omega'')c_r^*(0,\omega''')}\; e^{-2g_{mr}z - f_{mr}z} \quad , m \neq r , \tag{22}$$

vanish for z large enough (or are identically zero if they are such at z=0).

The lowest-order equations, concerning single-mode powers, read (see also Refs.(3) and (4))

$$\frac{d}{dz} \langle \overline{c_m(z,\omega)c_m^*(z,\omega')} \rangle = -\left(\sum_{k\neq m} h_{mk}\right) \langle \overline{c_m(z,\omega)c_m^*(z,\omega')} \rangle$$

$$+ \sum_{k\neq m} h_{mk} e^{i[\beta_m(\omega)-\beta_m(\omega')+\beta_k(\omega')-\beta_k(\omega)]z} \langle \overline{c_k(z,\omega)c_k^*(z,\omega')} \rangle \quad , \tag{23}$$

with

$$h_{mk} = \int_{-\infty}^{+\infty} \langle K_{mk}(\zeta)K_{mk}^*(0) \rangle\, e^{i[\beta_k(\omega_0) - \beta_m(\omega_0)]\zeta} d\zeta \quad , \tag{24}$$

which constitutes a closed set of equations.

The higher-order terms, concerning mode-power fluctuations and mode-mode correlations, cannot be considered separately since they form together a closed set of equations, which reads

$$\frac{d}{dz} \langle \overline{c_m(z,\omega)c_m^*(z,\omega')}\;\overline{c_n(z,\omega'')c_n^*(z,\omega''')} \rangle =$$

$$-\left[\sum_k (h_{km}+h_{kn})\right] \langle \overline{c_m(z,\omega)c_m^*(z,\omega')}\;\overline{c_n(z,\omega'')c_n^*(z,\omega''')} \rangle$$

$$+\sum_k h_{mk} e^{i[\beta_m(\omega)-\beta_m(\omega')-\beta_k(\omega)+\beta_k(\omega')]z} \langle \overline{c_k(z,\omega)c_k^*(z,\omega')}\;\overline{c_n(z,\omega'')c_n^*(z,\omega''')} \rangle$$

$$+\sum_k h_{nk} e^{i[\beta_n(\omega'')-\beta_n(\omega''')-\beta_k(\omega'')+\beta_k(\omega''')]z} \langle \overline{c_k(z,\omega'')c_k^*(z,\omega''')}\;\overline{c_m(z,\omega)c_m^*(z,\omega')} \rangle$$

$$-(1-\delta_{nm})h_{mn}\Big[e^{i[\beta_m(\omega)-\beta_m(\omega'')+\beta_n(\omega'')-\beta_n(\omega)]z} \langle \overline{c_n(z,\omega)c_m^*(z,\omega')}\;\overline{c_m(z,\omega'')c_n^*(z,\omega''')} \rangle$$

$$+e^{i[\beta_m(\omega''')-\beta_m(\omega')+\beta_n(\omega')-\beta_n(\omega''')]z} \langle \overline{c_m(z,\omega)c_n^*(z,\omega')}\;\overline{c_n(z,\omega'')c_m^*(z,\omega''')} \rangle\Big]$$

$$+\delta_{nm}\Big\{\sum_{k\neq m}\Big[h_{mk} e^{i[\beta_m(\omega)-\beta_k(\omega)+\beta_k(\omega''')-\beta_m(\omega''')]z} \langle \overline{c_k(z,\omega)c_m^*(z,\omega')}\;\overline{c_m(z,\omega'')c_k^*(z,\omega''')} \rangle$$

$$+h_{mk} e^{i[\beta_m(\omega'')-\beta_k(\omega'')+\beta_k(\omega')-\beta_m(\omega')]z} \langle \overline{c_m(z,\omega)c_k^*(z,\omega')}\;\overline{c_k(z,\omega'')c_m^*(z,\omega''')} \rangle\Big]\Big\} \tag{25}$$

and

$$\frac{d}{dz} \langle \overline{c_m(z,\omega)c_r^*(z,\omega')}\;\overline{c_r(z,\omega'')c_m^*(z,\omega''')} \rangle =$$

$$-\left(\sum_{k\neq r} h_{kr} + \sum_{k\neq m} h_{km}\right) \langle \overline{c_m(z,\omega)c_r^*(z,\omega')}\;\overline{c_r(z,\omega'')c_m^*(z,\omega''')} \rangle$$

$$+\sum_{k\neq r} h_{rk} e^{i\left[\beta_r(\omega'')-\beta_r(\omega')+\beta_k(\omega')-\beta_k(\omega'')\right]z} < \overline{c_m(z,\omega)c_k^*(z,\omega')}\;\overline{c_k(z,\omega'')c_m^*(z,\omega''')} >$$

$$+\sum_{k\neq m} h_{mk} e^{i\left[\beta_m(\omega)-\beta_m(\omega''')+\beta_k(\omega''')-\beta_k(\omega)\right]z} < \overline{c_k(z,\omega)c_r^*(z,\omega')}\;\overline{c_r(z,\omega'')c_k^*(z,\omega''')} >$$

$$- h_{mr} e^{i\left[\beta_m(\omega)-\beta_m(\omega'')+\beta_r(\omega'')-\beta_r(\omega)\right]z} < \overline{c_r(z,\omega)c_r^*(z,\omega')}\;\overline{c_m(z,\omega'')c_m^*(z,\omega''')} >$$

$$- h_{mr} e^{i\left[\beta_r(\omega''')-\beta_r(\omega')+\beta_m(\omega')-\beta_m(\omega''')\right]z} < \overline{c_m(z,\omega)c_m^*(z,\omega')}\;\overline{c_r(z,\omega'')c_r^*(z,\omega''')} >, m\neq r. \tag{26}$$

4. SOME APPLICATIONS

The set of equations governing the behavior of the average mode-power $< P_m(z,t) >$ can be easily obtained by taking advantage of Eqs.(10) and (23), thus getting (3),(4),(7)

$$\frac{\partial}{\partial z} < P_m(z,t) > + \frac{1}{V_m}\frac{\partial}{\partial t} < P_m(z,t) > = \sum_k h_{mk}\left[< P_k(z,t) > - < P_m(z,t) >\right] , \tag{27}$$

where

$$V_m = \left(\frac{d\beta_m}{d\omega}\right)^{-1}_{\omega=\omega_o} \tag{28}$$

is the group velocity of the mth mode. On the other hand, Eqs.(6),(7) and (10) allow one to write

$$< P^{\sigma}(z,t) > = \sum_m < P_m^{\sigma}(z,t) > + \frac{1}{2}\sum_{m\neq r}\sum < A_{mr}^{\sigma} > , \tag{29}$$

where the $< P_m^{\sigma}(z,t) >$ possess the same space-time dependence as the $< P_m(z,t) >$. Since a frequency modulation of the signal does not affect the $< P_m >$'s, the dependence on this modulation of $< P^{\sigma}(z,t) >$ is contained in the $< A_{mr}^{\sigma} >$'s, which vanish when considering the power transmitted through the whole section of the fiber. From Eqs.(7) and (17) it follows that (7)

$$< A_{mr}^{\sigma}(z,t) > \propto e^{-g_{mr}z}\,\overline{\underline{F}(t-z/V_m)\underline{F}^*(t-z/V_r)} , m\neq r , \tag{30}$$

where

$$\underline{F}(t) = \underline{E}(z=0,t)\, e^{-i\omega_o t} . \tag{31}$$

Equation (30) shows that mode-coupling affects the propagation of a frequency-modulated signal in an ensemble of fibers only for the presence of a spatial damping factor characteristic of each couple of modes. More precisely, if one excites at the fiber input only two modes m and r, all interference terms but $< A_{mr}^{\sigma} >$ vanish throughout the fiber (see Eq.(17)), while the surviving term propagates as in the absence of coupling but for the spatial attenuation.

The set of Eqs.(23) and the set of Eqs.(25) and (26) allow one in principle to determine the quantities $< P_m(z,t) >$, $< P_m^2(z,t) >$ and $< P_m(z,t)P_n(z,t) >$, and thus the fluctuations whose magnitude furnishes a criterion for the applicability of the statistical theory to a single fiber. While the general solution of Eqs.(25) and (26) is a formidable task, an important particular result can be obtained. If one introduces the energy $I_m(z)$ pertaining to the mth mode

$$I_m(z) = \int_{-\infty}^{+\infty} P_m(z,t)dt = 2\pi P\int \overline{c_m(z,\omega)c_m^*(z,\omega)}\, d\omega , \tag{32}$$

it can be shown (7), by means of Eqs.(25), that, under the condition

QUESTIONS AND COMMENTS ON SESSION IV

DISPERSION EVALUATION IN MULTIMODE FIBERS BY NUMERICAL TECHNIQUE: APPLICATION TO RING SHAPED AND GRADED INDEX WITH A CENTRAL DIP

A. M. Scheggi, P. F. Checcacci, R. Falciai

Dr. L. Felsen: The ray method employed in the paper is equivalent to the WKB procedure, which is known to be inaccurate for the very low order modes. Could you comment on how well your results compare with exact solutions *for the low order modes for* those special cases where exact solutions are available?

Dr. Checcacci: The condition which must be fulfilled for the application of the method is that $|\nabla n|/k_o n^2 \ll 1$. In principle such a condition is not satisfied for very low radial order modes. Comparisons with some special cases for which the exact solutions are available (see Scheggi A.M., Checcacci P.F., Falciai R., 1975 "Dispersion Characteristics in Quasi-Step and Graded Index Slab Waveguides by Ray Tracing Technique" in Journ. Opt. Soc. Am. 65, 1022) show that the method in those cases is quite valid down to modes with radial number μ of the order of some units. Hence we can surmise that for slowly varying index distributions the method is correct at least down to modes having such radial order numbers.

$$z \gg \left| \left(\frac{1}{V_m} - \frac{1}{V_n} \right)^{-1} \right| \frac{2\pi}{\delta\omega} \quad , m \neq n , \tag{33}$$

and provided that z exceeds the equipartition distance beyond which $\langle I_m \rangle = \langle I_n \rangle$, the following relation holds

$$\frac{\langle I_m^2 \rangle - \langle I_m \rangle^2}{\langle I_m \rangle^2} \ll 1 \quad , \tag{34}$$

which implies that the statistical uncertainty of the quantity $I_m(z)$ over the fiber ensemble is negligible, so that mode-energy equipartition takes place over each fiber. This last consideration holds true in the absence of losses or, more in general, if losses are not effective over the characteristic length after which Eq.(34) is verified.

REFERENCES

1) D. Marcuse, "Theory of Dielectric Optical Waveguides", Academic Press, N.Y. 1974.

2) B. Crosignani, B. Daino, and P. Di Porto, IEEE Trans.Microwave Theory Tech. MTT-23, 416 (1975).

3) S.D. Personick, Bell Syst.Tech.J. 54, 47 (1975).

4) R. Steinberg, IEEE Trans.Microwave Theory Tech. MTT-23, 121 (1975).

5) B. Crosignani, B. Daino, and P. Di Porto, Opt Commun. 18, 551 (1976).

6) C.H. Papas, "Theory of Electromagnetic Wave Propagation", McGraw-Hill, N.Y. 1965.

7) B. Crosignani and C.H. Papas, Caltech Antenna Laboratory Report No. 76, 1976.

INJECTION LASER TRANSMITTER FOR LONG DISTANCE FIBER OPTICS COMMUNICATION

Ernst Schiel and Gerald Talbot
US Army Electronics Command, Fort Monmouth, NJ

Henry Kressel
RCA Laboratories, Princeton, NJ

SUMMARY

The design and development of an Injection Laser Transmitter for a tactical long distance fiber optics communication link are described. The double heterostructure GaAlAs Laser is configured in a "triple-stripe" geometry which can feed the optical output power into a linear array of three fibers. The laser structure was grown by the liquid phase epitaxial method and optimized for high peak power operation at a duty factor of ten percent. (Average pulse repetition rate is 10 MHz and pulsewidth is 10 nsec.) The laser chip is mounted in a prototype pill package, which is placed on a thermoelectric heater/cooler keeping the operational temperature of the laser at 15°C. A special drive circuit utilizing a high power field effect transistor (FET) in the last stage was designed to drive the laser at a peak current of 2 A to obtain 250 mW peak output power. Efficient coupling into graded index fibers was accomplished by lensing the fibers by a new technique. Life tests on three lasers showed no degradation after 7000 hours of operation. The feasibility of a high power injection laser transmitter has been proven by the development of an operational prototype.

An important military application of Fiber Optics Technology planned for a long distance data link which connects the switch with a radio site in an Army command post. This full duplex data link can extend to a maximum length of 8 km (5 miles) and the repeater spacing in the presently used coaxial cable link is 0.8 km (0.5 miles). Four parallel coax cables each carry approximately 5 Mbits/sec for a total of 20 Mbits/sec. The large number of repeaters affects adversely the mean-time between failure (MTBF) of the presently used coax link, which is also not electro-magnetic pulse (EMP) and electro-magnetic interference (EMI) proof.

The design of a fiber optic link to replace the coax link is based on graduated index fibers with low attenuation and dispersion. Six fibers are packaged in the fiber optics cable, three fibers carry information in one direction and the other three in the opposite direction.

To compensate for fiber and connector losses and maintain a high signal-to-noise ratio, even under adverse conditions (high loss connector or breaking of a fiber), a sensitive silicon avalanche photodetector is used in the receiver and a high power transmitter is also required.

A laser transmitter was designed for this special requirement. The same signal has to be launched into three fibers. Therefore, a configuration of a triple-stripe geometry was chosen which can feed power into a linear array of three fibers (Figure 1). Since there are no stringent limitations on power consumption on the end points of this fiber optic (F.O.) link (switch and radiosite), the temperature of the injection laser can be stabilized by a thermoelectric heater/cooler.

The complete injection laser transmitter consists of the triple-stripe laser (Lockwood, H., 1976), a high current pulse drive circuit and the thermoelectric heater/cooler, and a three fiber pigtail which leads to an optical bulkhead connector of the modem.

GaAlAs double heterojunction lasers designed for this program combined the following characteristics:

(1) Lasing emission at 820 μm in the region for low loss fiber transmission;

(2) Minimal beam divergence;

(3) Low thermal resistance to minimize the thermal gradient in the device;

(4) Long lifetime (10,000 hours minimum).

To achieve long lifetime, the laser is used in pulsed operation (pulsewidth $\tau \approx 10$ nsec). At an average pulse rate of 10 Mbits/sec (half of 20 Mbits/sec), the duty factor is ten percent. Pulse power can be increased compared to a CW laser biased at threshold. The short pulse duration also allows for pulse dispersion in the long distance link. The triple stripe DH laser was developed to meet the following significant performance characteristics:

(1) Peak power output - 250 mW;

(2) Drive conditions - 2A current pulse, 10 nsec pulsewidth at a pulse repetition rate of 10 Mbits/sec;

(3) Emission wavelength - 820 nm at 300°K;

(4) Laser configuration in a "triple-stripe" geometry for coupling into three fibers spaced 125 μm center-to-center in a linear array;

(5) Laser output must be coupled efficiently into a multimode fiber with a NA = 0.15 and 75 μm core diameter;

(6) Minimum lifetime - 10,000 hours.

The laser structures were grown by the liquid-phase epitaxial technique as developed by RCA Labs. The triple-stripe lasers are a variation of the CW laser designs. Figure 2 is a schematic cross section of the laser showing the dimensions and doping specific to the triple-stripe device. The composition of the active region yields a lasing wavelength of approximately 820 μm. The oxide-defined contacting stripes are 25 μm wide, separated by 125 μm, and have common metallization. Due to current spreading under the contact, the width of the lasing region is approximately 50 μm per stripe for a total emitting width of 150 μm. The diodes are mounted using pure In, with the p-type GaAs cap layer nearest the heat sink.

Each laser has both a reflective and anti-reflective coating on the back and front facets, respective. The anti-reflective coating is approximately 1200 Å of Al_2O_3, while the reflective coating is a composite of 2400 Å of Al_2O_3 followed by 300 Å of Cr, 100 Å of Au, and 2400 Å of Al_2O_3. The net effect of the coatings is to increase the end losses and to raise the threshold by perhaps 20 percent above that of uncoated lasers from the same wafer. However, we have shown in the past that a low-reflectivity facet coating decreases the susceptibility to catastrophic damage (Ettenberg, M., 1971).

The threshold current density of the diodes is approximately 2500 A/cm^2. Figure 3 shows the output power as a function of current for 10 nsec pulses at a repetition rate of 1 kHz where self-heating would be negligible and at 10 MHz where the maximum temperature rise would occur. There appears no significant change in output between these extremes.

The behavior of the threshold current as a function of temperature is shown in Figure 4. The corresponding change in both the coherent and the incoherent peak emission energy appears in Figure 5. Since the temperature interval is rather small, the latter relationship is essentially linear with a slope of 0.51 meV/°K. These data were taken at sufficiently low duty cycles so that internal heating was completely negligible. If the average power is increased so that there is considerable self-heating of the laser, the spectral shift can be used to calculate the thermal impedance. With a power dissipation of 0.52 W, the spectrum was observed to shift by 3.69 meV, corresponding to a temperature rise of 7.24°K and a thermal impedance of 14° K/W. For comparison, the range of thermal impedance measured on well-heat sunk CW type diodes is 10 to 20° K/W.

A typical far-field pattern for a triple-stripe laser is shown in Figure 6. In the plane perpendicular to the junction, the beam width full-width-half-maximum (FWHM) is 49°; in the parallel plane it is 11°, and is operating in the second-order lateral mode. The beam is strongly polarized with a transverse electric (TE) to transverse magnetic (TM) ratio of about 11 dB. (The usual degree of polarization for narrow DH lasers is in the range of 10 to 20 dB). With the beam of Figure 6, the coupling loss into a numerical aperture of 0.14 was measured to be approximately 7 dB. Therefore, of the 250 mW output power, 50 mW is available to the three fibers or 17 mW per fiber. This figure can be improved by designing the laser with a lower degree of optical confinement. Figure 7 is the far-field distribution of a triple-stripe laser with a modified cavity. The beam is 37° FWHM perpendicular to the p-n junction and only 6° in the lateral plane. The coupling loss, at NA = 0.14 is 5 dB for this device compared with 7 dB for the previous example. However, the reduced optical confinement results in an elevated threshold current and drive current to achieve the same total output power of 250 mW. For a given drive current, the proper optimization from the system point of view, of course, would be to optimize the power coupled into the fiber rather than the total power.

The observed values of the threshold current density and beamwidth correlate closely with theoretically predicted values. On the basis of the difference in Al concentration, Δx, between the active region and the bounding regions of 0.27, the estimated step in the refractive index $\Delta n = 0.62\ \Delta x = 0.17$. With an active region of 0.21 μm and emission wavelength of about 0.8 Δm, the following calculated values follow from the theory of Butler (Butler, J. K., 1977)

Confinement factor $\Gamma = 0.6$,

Beam width $\Theta = 47^{\circ}$

QUESTIONS AND COMMENTS ON SESSION IV

DISPERSION EVALUATION IN MULTIMODE FIBERS BY NUMERICAL TECHNIQUE: APPLICATION TO RING SHAPED AND GRADED INDEX WITH A CENTRAL DIP

A. M. Scheggi, P. F. Checcacci, R. Falciai

Dr. L. Felsen: The ray method employed in the paper is equivalent to the WKB procedure, which is known to be inaccurate for the very low order modes. Could you comment on how well your results compare with exact solutions for the low order modes for those special cases where exact solutions are available?

Dr. Checcacci: The condition which must be fulfilled for the application of the method is that $|\nabla n|/k_o n^2 \ll 1$. In principle such a condition is not satisfied for very low radial order modes. Comparisons with some special cases for which the exact solutions are available (see Scheggi A.M., Checcacci P.F., Falciai R., 1975 "Dispersion Characteristics in Quasi-Step and Graded Index Slab Waveguides by Ray Tracing Technique" in Journ. Opt. Soc. Am. 65, 1022) show that the method in those cases is quite valid down to modes with radial number μ of the order of some units. Hence we can surmise that for slowly varying index distributions the method is correct at least down to modes having such radial order numbers.

Summary of Session IV

PROPAGATION

by
H. G. Unger

Chairman's review and conclusions

Most of the papers were addressed to fibre characteristics and their characterization. Methods of measuring the index profile were presented and critically evaluated, and the influence of the index profile on the transfer function and on pulse dispersion were discussed. Particular emphasis was given to fibres of low and intermediate values of the fibre parameter, v.

It is expected that fibres with low v-values have dispersion characteristics which do not degrade quite as critically with deviations from an optimum index profile as do ordinary gradient index fibres. They are however still large enough in core size to allow easy splicing and coupling.

Problems which are still to be solved for low v-value fibres are the optimum profile with respect to delay dispersion, the degrading effects of imperfections such as microbending on multimode signal transmission in such fibres, and the fabrication of such fibres as well as the experimental verification of the theoretical conditions.

The calculated threshold current density based on the theory for undoped active regions yields an expression of the form (for $g_{th} = 30 - 100\ cm^{-1}$) (Stern, F., 1973)

$$J_{th} = \frac{d}{n_s} \left(\frac{g^{th}}{\beta_s} + J_1 \right)$$

where $\beta_s = 0.038$ cm/A at 300 K and $J_1 = 4100\ A/cm^2$. For a diode with a reflective coating,

$$g_{th} = \frac{\alpha_{out}}{\Gamma} + \alpha_{fc} + \frac{1}{\Gamma} \left(\frac{1}{2L} + Ln\,\frac{1}{R} \right) .$$

For the facet coating used, R = 0.05, L = 15 mils, $\alpha_{out} = 10\ cm^{-1}$, and $\alpha_{fc} \sim 10\ cm^{-1}$. Hence, $g_{th} \sim 90\ cm^{-1}$, and $J_{th} = 1460$. With η_i assumed to be ~ 0.7, we calculate $J_{th} = 2000\ A/cm^2$, in good agreement with the experimental results.

The coupling efficiency from an injection laser into a flat cut fiber with low numerical aperture (NA = 0.14) is rather low, as the measured values demonstrate. Coupling can be improved by lensing the fiber end (Benson, W., 1975), however, the method of melting the fiber end by a microtorch or focussed CO_2 lasers to form a hemispherical lens, produces a lens surface which has too large a radius and therefore does not provide optimum coupling. We are now applying a new technique for highly efficient coupling into step or graded index fibers (Timmermann, C., 1976). The cladding of the fiber is etched to reduce the fiber diameter to nearly the core diameter. Then, the fiber end is cut and dipped into a low melting glass to form a small lens. Three fibers prepared in this way are arranged in a linear array so that the lenses are positioned opposite the emitting faces of the triple stripe laser. Coupling efficiencies exceeding 60 percent, corresponding to a peak power of approximately 150 mW, from the laser into three graded index fibers with a core diameter of approximately 80 μm and NA = 0.2 can be obtained.

A prototype pill package (Figure 8) was designed which first was closed by a thin (approximately 100 μm) glass window in front of the laser. In the final assembly the window is replaced by a block of molded plastic in which the linear array of three fibers is imbedded. The best alignment is achieved by operating the laser and moving the plastic block mounted on a micropositioner until optimum coupling has been achieved. Then, the plastic block is affixed to the package by a thin UV-curable epoxy preform.

Life tests on three lasers were performed under the specified operating conditions (P_o = 250 mW, τ = 10 nsec, PRR = 10 MHz). The power output was continuously monitored and no change observed after 7000 hours operation at room temperature in a laboratory environment. This is a strong indication that the 10,000 hours lifetime goal is quite reasonable.

A drive circuit was first designed to utilize a high power VHF bipolar transistors in the last amplifier stage, but problems with regard to ringing and pulse-to-pulse stability were encountered. The reproducibility of these circuits was also not completely satisfactory due to the variation of transistor characteristics. High power junction FETs (VMP-1 manufactured by Siliconix Inc.) were tested and proved to be capable of high speed operation (τ = 10 nsec). These devices provided stable operating conditions at peak current levels of 2-3A and were finally utilized in the last drive stage. The complete schematic of the drive circuit is shown in Figure 9. For convenience in testing, a crystal controlled 10 MHz oscillator consisting of a NAND-gate and a 10 MHz quartz crystal were included in the design. The second NAND-gate, which can be addressed from the 10 MHz oscillator or from an outside source, is used to generate a short pulse which is then amplified in a transistor stage. In the final drive stage, using the high power FET, the injection laser is protected from D.C. overload by capacitive coupling.

The injection laser package is mounted on a one-stage thermoelectric heater/cooler (model ST 1046 manufactured by Marlow Industries, Inc.), which is designed to cool or heat the laser diode to a preset temperature over an ambient temperature range of +71°C to -40°C. The heat pumped by the thermoelectric cooler is passed through a finned heat sink and removed by forced air convection. The blower (Rotron Aximax 1) providing forced air for heat sink cooling also provides additional air for downstream cooling of the drive circuit. The cooler is capable of maintaining a 0.5 W load at 15° C with a controlled surface accuracy of ± 3°C, which is more than sufficient for stable operation of the laser.

The temperature is sensed by a thermistor mounted to the controlled surface which is part of a bridge network. The temperature set-point can be varied by increasing or decreasing the resistance of a potentiometer in the bridge. A voltage divider network supplies a constant voltage level to one input of a differential amplifier, the other input is supplied by the voltage divider network formed by the thermistor and potentiometer. When the bridge is in balance, the two voltage levels from the divider are the same. The differential amplifier amplifies the difference between the voltage levels from the two signals of the bridge, and the output of the differential amplifier drives a transistor network which regulates the power to the thermoelectric cooler.

Figure 9 shows a sideview and Figure 10 a topview of the laser transmitter. The injection laser mounted on the thermoelectric heater/cooler is in close proximity to the output pads of the drive circuit and connected to them by copperbands. This arrangement provides neglible inductive losses and minimizes distortion of the pulse shape. The laser and cooler are heat insulated by foam, in which a channel for the three fiber pigtail is cut. The laser transmitter is RF shielded by a metal housing covering the complete laser transmitter including the drive circuit.

In summary, the feasibility of a high power injection laser transmitter for long distance, tactical fiber optics communication has been proven by the development of an operational prototype. During the development of the prototype transmitter, numerous improvements based on availability of new components (e.g., fast high power FET) and new technologies (e.g., coupling techniques) were incorporated into the design.

References

1. BENSON, W.W., et al., 1973, Appl. Opt. 14, 2815.

2. BUTLER, J. K., 1977, Private communication, to be published.

3. ETTENBERG, M., SOMMERS, H.S., KRESSEL, H. and LOCKWOOD, H., 1971, Appl. Phys. Letters 18, 571.

4. LOCKWOOD, H., ETTENBERG, M., KRESSEL, H., 1976, "GaAlAs and Injection Laser Diodes," Final Report, ECOM-76-0779-F.

5. ETTENBERG, M., SOMMERS, H. S., KRESSEL, H., and LOCKWOOD, H., 1971, Appl. Phys. Letters 18, 571

6. TIMMERMANN, C.C., 1976, Appl. Opt 15, 2432.

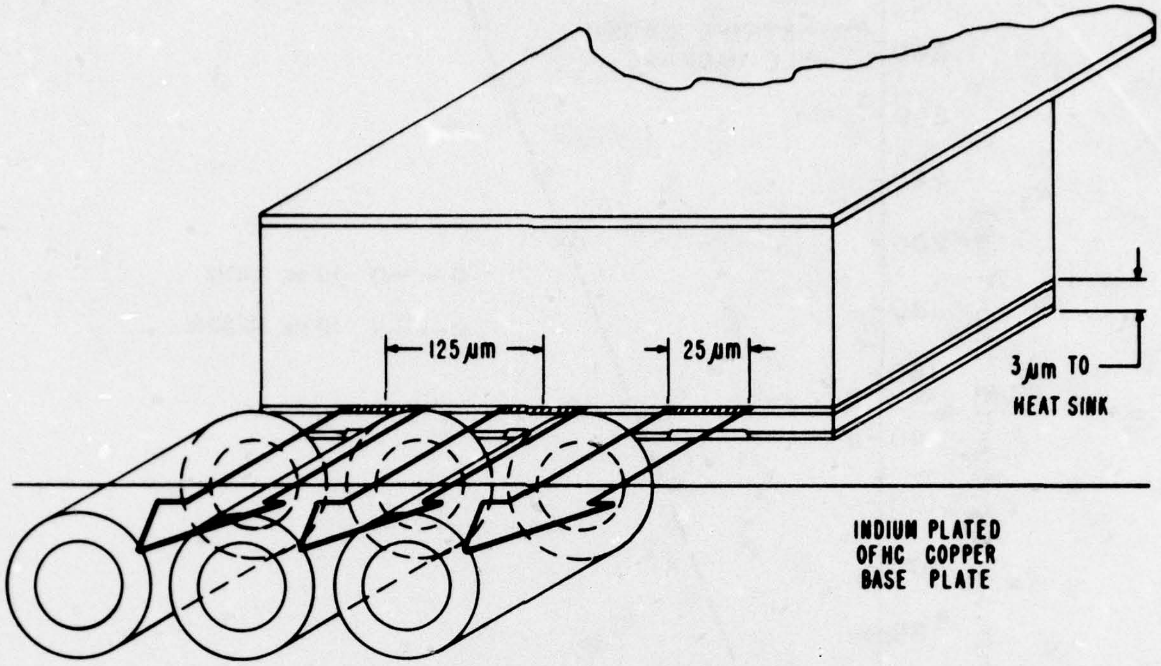

Fig.1 Triple stripe laser configuration and fiber array

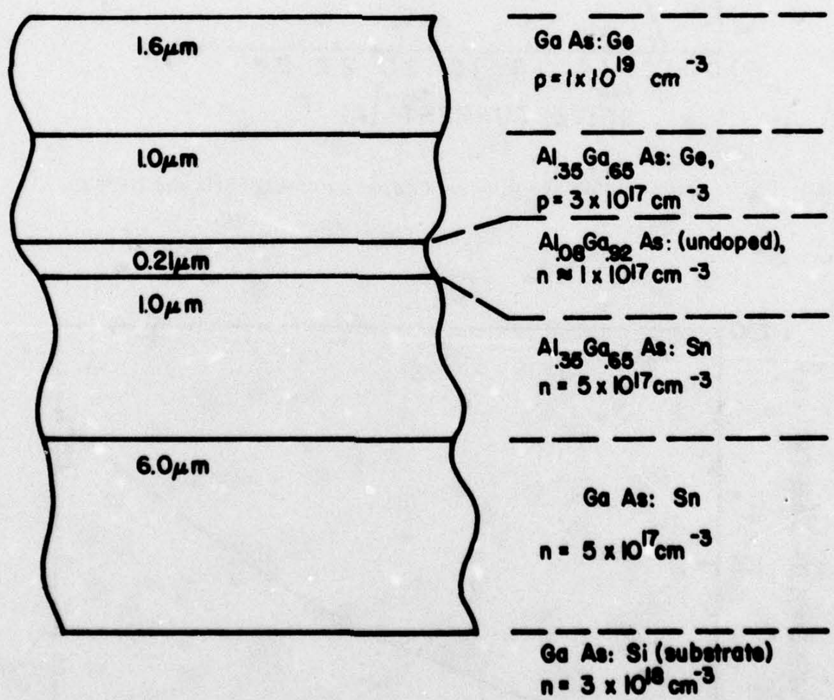

Fig.2 Compositional cross section of the triple-stripe laser

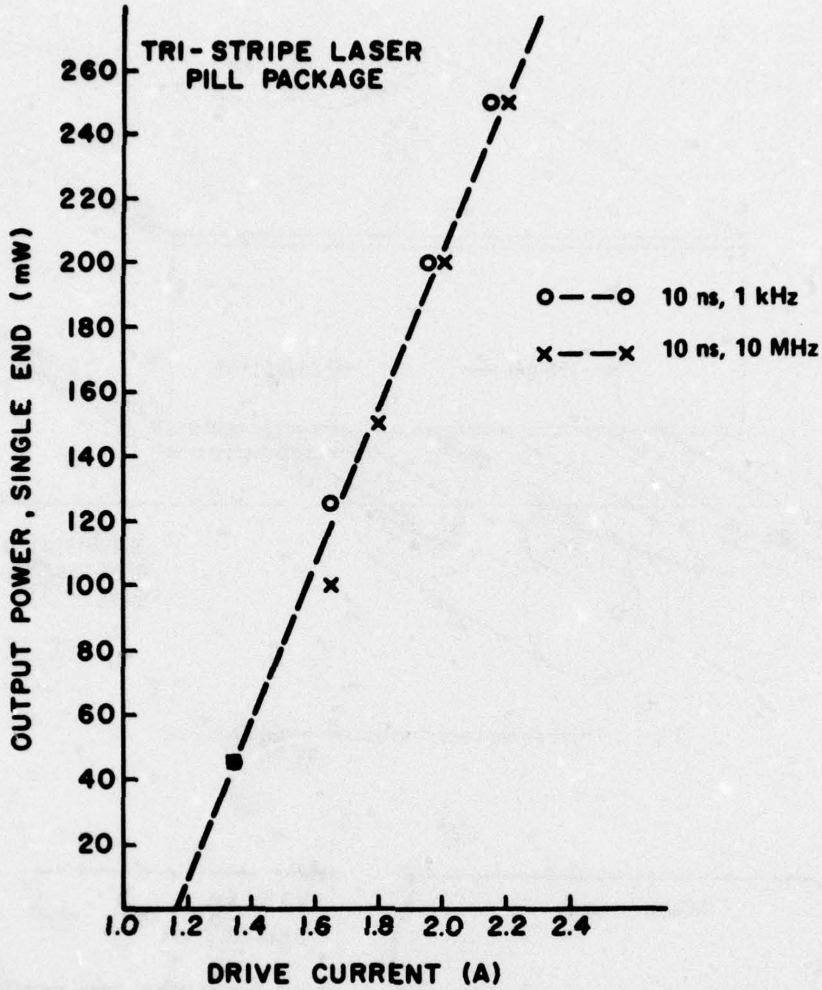

Fig.3 Output power as a function of drive current at 1kHz and 10 MHz

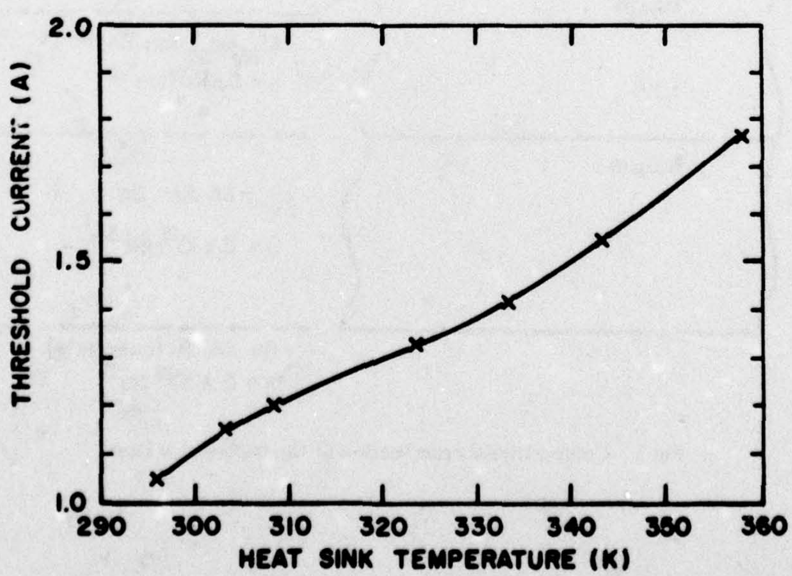

Fig.4 Threshold current as a function of heat sink temperature

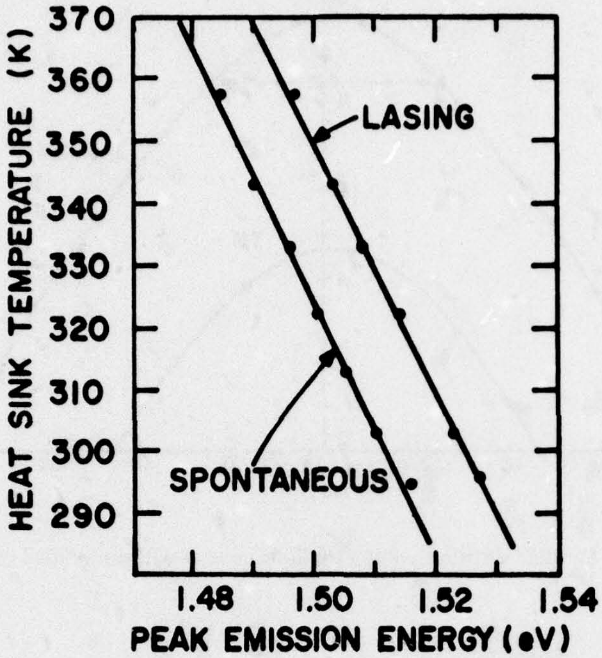

Fig.5 Heat sink temperature as a function of peak emission energy for both coherent (lasing) and incoherent (spontaneous) energy

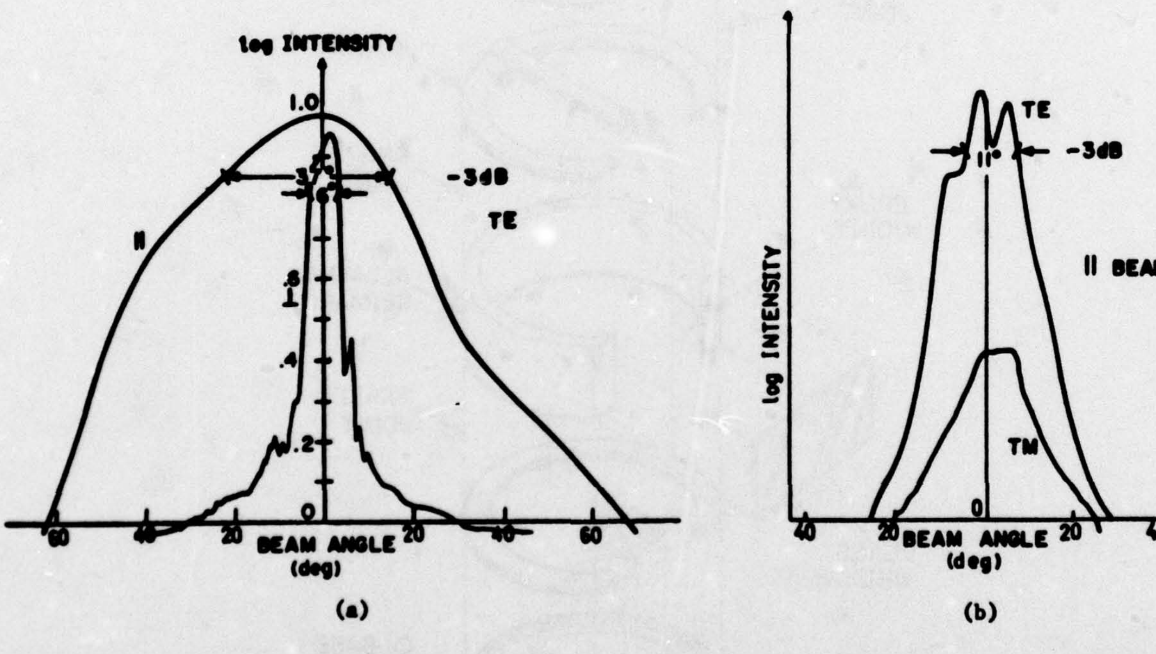

Fig.6 Typical far-field pattern for a triple-stripe laser: (a) perpendicular beam and (b) parallel beam

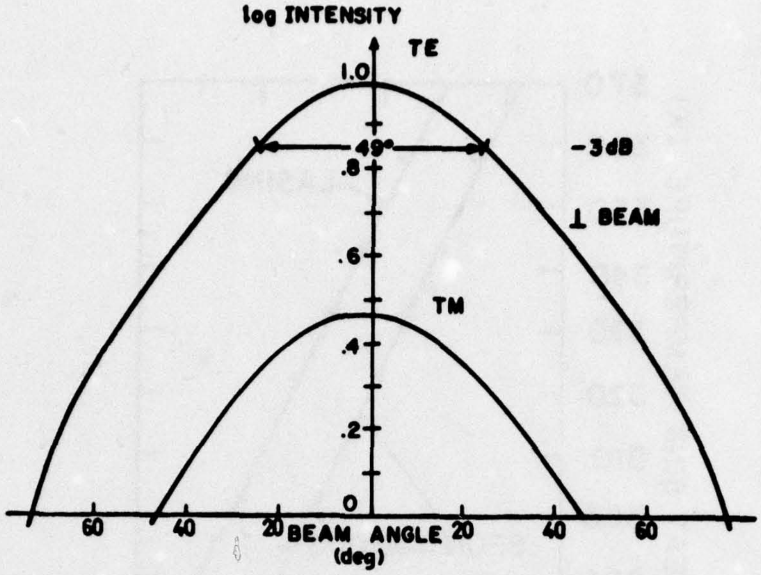

Fig.7 Far-field distribution of a triple-stripe laser with a modified cavity

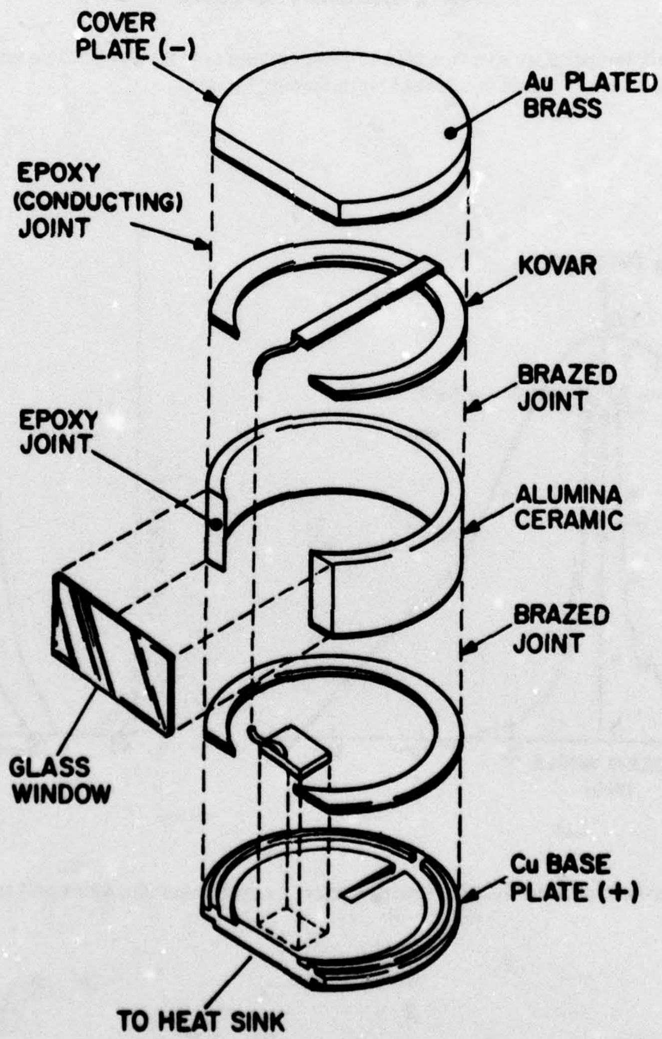

Fig.8 RCA prototype "Pill" package with window

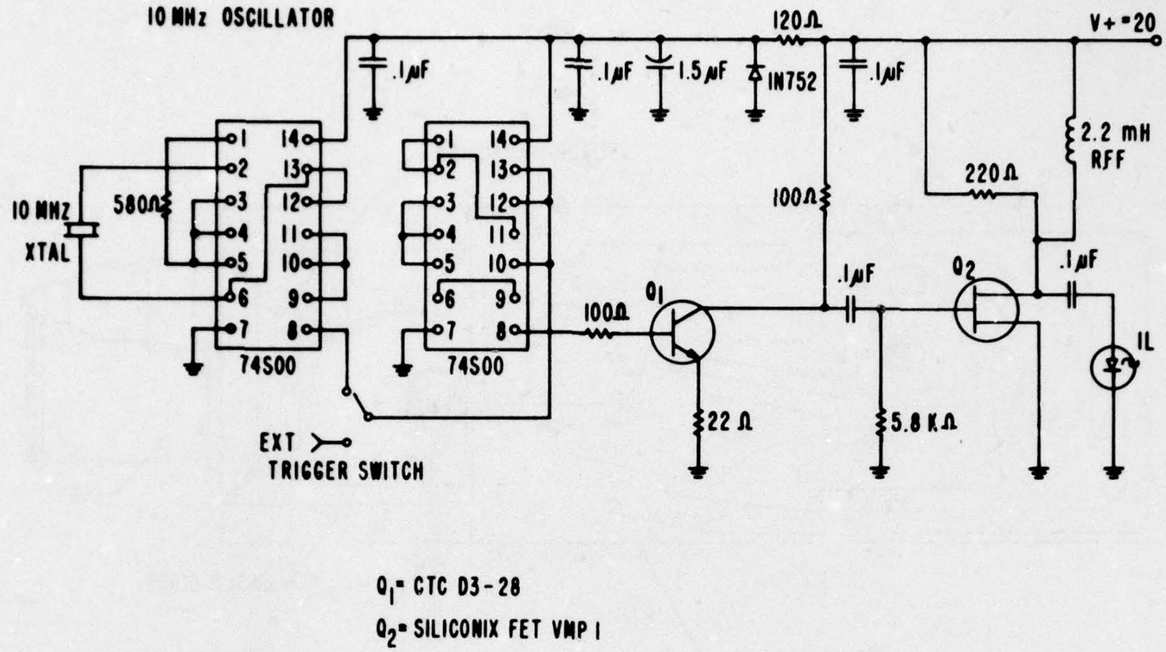

Fig.9 Drive circuit for triple stripe injection laser

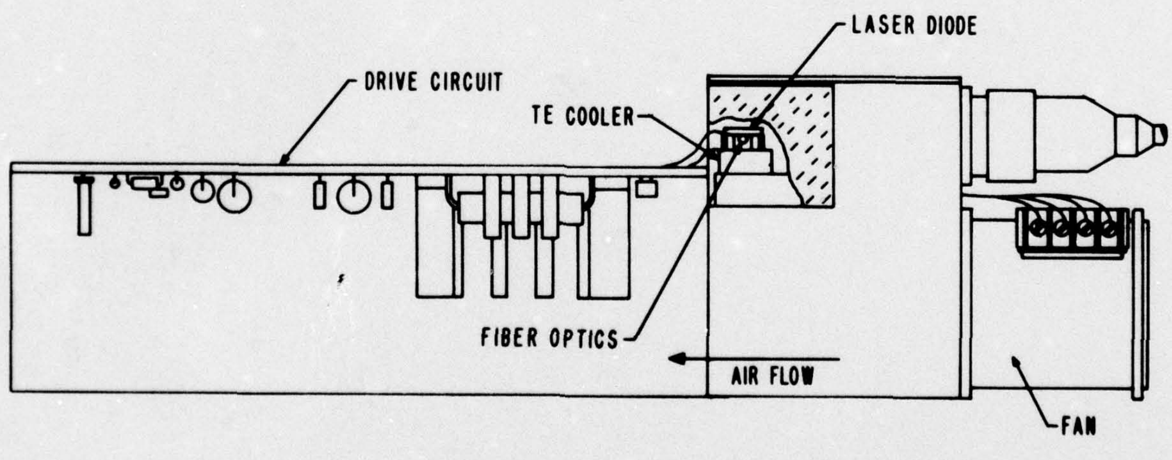

Fig.10 Side view of laser transmitter (cover removed)

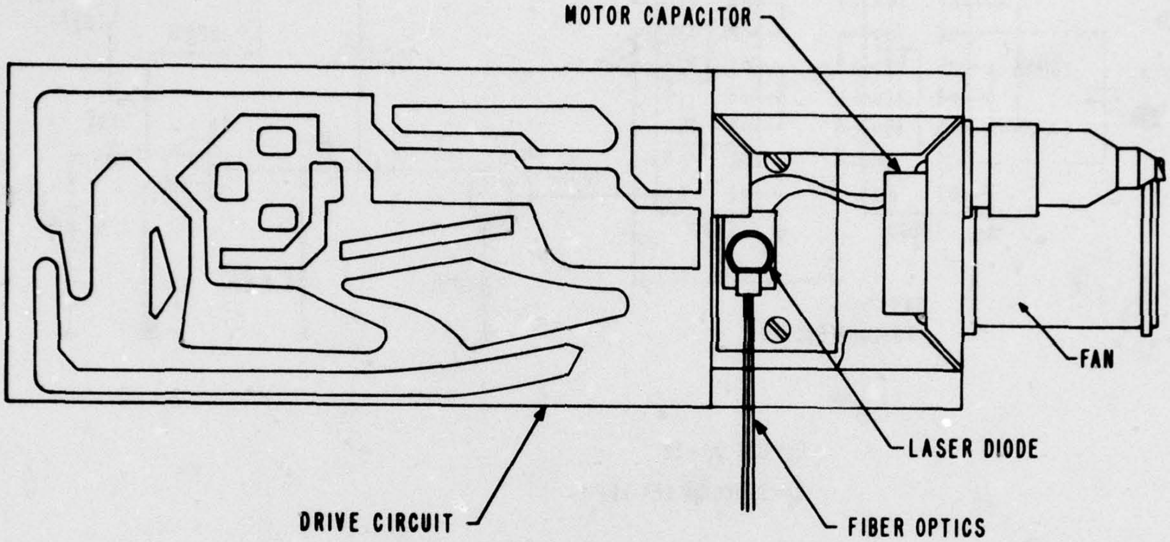

Fig.11 Top view of laser transmitter (cover removed)

GaInAsP/InP DOUBLE-HETEROSTRUCTURE LASERS FOR FIBER OPTIC COMMUNICATIONS*

J. J. Hsieh
Lincoln Laboratory, Massachusetts Institute of Technology
Lexington, Massachusetts 02173, U.S.A.

SUMMARY

This paper reports the performance of broad-area and stripe-geometry GaInAsP/InP double-heterostructure diode lasers prepared by liquid-phase epitaxy. These lasers have the advantage that exact lattice-matching between the GaInAsP active region and the InP substrate is possible for quaternary alloy compositions giving emission wavelengths over a range that includes 1.1-1.3 μm, the optimum region for optical communication systems utilizing fused silica fibers. Continuous operation at room temperature has been achieved in this region both for proton-defined stripe (PDS) and junction-defined, buried-stripe (JDBS) lasers. Near-field observations of the JDBS lasers show total optical confinement, with no spreading of the radiation outside the buried stripe for cw operation at 20% above threshold or for pulsed operation at 8 times threshold. Three PDS devices, the only GaInAsP/InP lasers to be life-tested so far, have already logged over 2000, 1600, and 1200 hours, respectively, of cw operation at room temperature without any degradation in output power, threshold current, or emission spectrum.

Diode lasers have a number of characteristics that make them very promising sources for use in optical communications: they are small, efficient, conveniently modulated at high rates, and capable of being fabricated into integrated optical (I/O) circuits on a single chip. However, conventional double-heterostructure (DH) GaAs/GaAlAs lasers have emission wavelengths in the range between 0.7 and 0.95 μm, which is not ideal for optical communication systems utilizing fused silica fibers. In addition, the yield of these lasers with operating lifetimes long enough to be practical has been low. We will show in this paper that DH GaInAsP/InP quaternary lasers are likely to be a much better choice for use in fiber optic systems.

Optical communication using fibers has recently become practical because of a marked reduction achieved in the attenuation of silica fibers. Figure 1a shows the attenuation of state-of-art laboratory fibers (HORIGUCHI, M., 1976) which has a minimum value of about 0.5 dB/km between 1.1 and 1.3 μm, compared with about 1 dB/km for the emission wavelength range of GaAs/GaAlAs lasers. The material dispersion (PAYNE, D. N., 1975) of silica fibers, as shown in Fig. 1b, approaches zero near 1.25 μm but is ~ 70 ps/nm/km in the GaAs/GaAlAs laser wavelength range. Furthermore, experiments with certain silica fibers indicate considerably more resistance to neutron and gamma radiation at 1.1 μm than at shorter wavelengths (MAURER, R. N., 1973). Therefore the ideal diode lasers for fiber optic communications should have their emission wavelengths in the 1.1-1.3 μm range. In addition they should be both reliable and easy to fabricate. The GaInAsP/InP lasers satisfy all these requirements.

In DH diode lasers close lattice matching between the active region and the adjacent barrier layers is necessary for efficient device operation. However, in the other two types of alloy lasers being investigated as possible sources for the 1.1-1.3 μm range -- GaInAs/GaInP (NUESE, C., 1976) and GaAsSb/GaAlAsSb (SUGIYAMA, K., 1972 and NAHORY, R. E., 1976) -- there is a significant difference in lattice constant between the alloy active region and the GaAs substrate used for epitaxial growth. As a result of this mismatch the fabrication process is made considerably more complicated (and laser reliability most probably reduced) because it is necessary to grow intermediate buffer layers, graded either continuously or step-wise in composition, between the substrate and the barrier layer just below the active region. The alloy compositions of the buffer and barrier layers, as well as that of the active region, must all be carefully controlled.

In contrast to the other alloy lasers, GaInAsP/InP lasers have the important basic advantage that the GaInAsP active region can be exactly lattice-matched to the InP substrate. In Fig. 2 the room-temperature bandgap and corresponding wavelength of alloys in the $Ga_{1-x}In_xAs_{1-y}P_y$ system are plotted against lattice constant. The portion of the dashed vertical line lying within the shaded area represents GaInAsP alloys that have the same lattice constant as InP, giving a possible wavelength range from 0.95 to 1.7 μm at room temperature for lattice-matched GaInAsP/InP lasers. Since InP has a higher energy gap and lower refractive index than any of these alloys, in principle both carrier and optical confinement can be achieved by simply growing successive GaInAsP and InP epitaxial layers on an InP substrate. In practice, an InP buffer layer is first grown on the substrate in order to smooth the irregularities caused by thermal etching of the substrate during pre-growth heating. Figure 3 is a photomicrograph of a cleaved cross section through a heterostructure, grown by liquid-phase epitaxy, that incorporates such a buffer layer. It should be noted that even in this somewhat more complex structure only the composition of the GaInAsP active region needs to be controlled, since the composition of InP layers is practically independent of the composition of the In-P growth solutions.

Diode laser operation in the GaInAsP/InP system has been obtained for active-region compositions spanning the entire lattice-matched range shown in Fig. 2, although laser action has been observed only at 80 K for the two extremes of the range, InP itself (ISMAILOV, I., 1975; WEISER, K., 1964) and the P-free limit ($Ga_{0.465}In_{0.535}As$) (NAGAI, H., 1976; HSIEH, J. J., 1976). Our attention has been concentrated on compositions yielding room-temperature emission in the 1.05-1.3 μm wavelength region. For this reason, Fig. 4 shows the lowest values of threshold current density, J_{th}, obtained for room-temperature pulsed operation of broad-area DH GaInAsP/InP diode lasers grown on either (111)B- or (100)-oriented InP substrates. Most of these values lie between 2 and 4 kA/cm^2. As in the case of DH GaAs/GaAlAs lasers, J_{th} is not sensitive to active-layer carrier concentration over the lower -10^{17} to 10^{18} cm^{-3} range. The lowest J_{th}, 1.5 kA/cm^2, was observed for a laser emitting at

*This work was sponsored by the Department of the Air Force.

1.1 μm with a cavity length of 380 μm and active-region thickness of 0.4 μm. For this laser the reduced threshold is 3.8 kA/cm^2-μm, comparable to the values of 3.5-4 kA/cm^2-μm reported (PANISH, M. B., 1976) for DH GaAs/GaAlAs lasers. The gain and loss values for this laser are about 15 cm/kA and 38 cm^{-1}, respectively, and the beam divergence is about 40° in the plane perpendicular to the junction. These characteristics are also similar to those of GaAs/GaAlAs lasers.

Continuous room-temperature operation of DH GaInAsP/InP diode lasers emitting at wavelengths between 1.1 and 1.25 μm has been achieved by using various device configurations in which current flow is confined to a narrow stripe in the plane of the junction. Initially cw operation was obtained for stripe-geometry lasers in which proton bombardment is used to define the width of the active region by strongly increasing the resistivity of the InP barrier layer outside the stripe (HSIEH, J. J., 1976). Figure 5 is a schematic diagram of such a proton-defined stripe (PDS) device. For PDS lasers with a stripe width of 13 μm, we have obtained cw output power of 8 mW per facet at a dc current of 240 mA and an external quantum efficiency, η_d, of 26% per facet at emission wavelengths of 1.1-1.5 μm. We have also prepared oxide-defined stripe (ODS) lasers in which contact windows in an oxide layer are used to define the active-region width, although cw operation has not been achieved for these devices.

For both the PDS and ODS lasers, as the stripe width decreases below about 15 μm the threshold current density rises rapidly due to lateral spreading of the injected carriers and the stimulated radiation from the sides of the stripe. However, for efficient coupling of a diode laser to an optical fiber the width of the laser active region should be matched to the diameter of the fiber core, which is only about 5 μm for some single-mode fibers. To reduce lateral spreading we have recently fabricated two types of buried-stripe lasers, designated as junction-defined (JDBS) and oxide-defined (ODBS) devices. In these lasers the GaInAsP active region is entirely surrounded by InP, thereby providing lateral as well as vertical carrier and optical confinement. As in the case of GaAs/GaAlAs buried-stripe DH lasers (TSUKADA, T., 1974), such confinement has produced a marked reduction in total threshold current for narrow stripe widths.

For all four types of stripe-geometry lasers the variation of room-temperature pulsed threshold current density, $J_{th}(s)$, as a function of stripe width, s, is shown in Fig. 6, where the ratio of $J_{th}(s)$ to the threshold current density for broad-area devices from the same wafer, $J_{th}(\infty)$, is plotted against s. Note that the relative increase in $J_{th}(s)$ with decreasing s is greatest for the ODS lasers and becomes progressively smaller for the PDS, ODBS, and JDBS devices. For the JDBS lasers $J_{th}(s)$ is only 65% higher for s = 5 μm than for broad-area devices.

Figure 7 is a photomicrograph of a cleaved cross section through a JDBS laser structure with a stripe 5 μm wide, to which the current is restricted by means of an InP p-n homojunction that is reverse-biased when the InP-GaInAsP p-n junction over the stripe is forward-biased. With this structure we have achieved room-temperature cw operation at emission wavelengths of 1.21 and 1.25 μm, with an output as high as 17 mW per facet at a dc current of 500 mA and η_d of 10% per facet. Near-field observations of these lasers show total optical confinement, with no spreading of the radiation outside the buried stripe for cw operation at 20% above threshold or for pulsed operation at 8 times threshold.

It should be mentioned that cw operation of JDBS lasers has been obtained with either the grown side or the substrate side soldered to the heat sink. When the latter configuration was used the total thickness of the device was reduced to 50 μm by lapping down the substrate side before mounting. In this case the cw J_{th} was found to be only about 25% higher than the pulsed J_{th} for the same laser. This scheme should facilitate the light extraction and simplify device fabrication procedure for future I/O applications.

Because the development of GaInAsP/InP lasers has been so recent, life-test results are necessarily quite limited. However, these results are perhaps the most striking so far obtained for these devices. In the initial tests, three PDS lasers prepared from the same DH wafer are being operated continuously at room temperature, and the dc operating current is adjusted periodically to keep the output power constant to within ± 20% at a level of 2 to 4 mW per facet. Figure 8 shows the operating current as a function of time for these three lasers over their first 1400, 1000 and 600 hours, respectively. No significant changes in current are observed; the small changes shown were due to changes in heat sink temperature, not to device degradation. These three lasers are still in operation, having so far logged over 2000, 1600 and 1200 hours, respectively, without any significant change in operating current, threshold current or emission spectrum. These results provide a very encouraging indication that it will be possible to obtain a high yield of GaInAsP/InP lasers with sufficiently long operating lifetimes for practical applications, and they strongly suggest that these devices do not suffer from the reliability problems that have seriously plagued GaAs/GaAlAs lasers (PANISH, M. B., 1976).

In summary, we have fabricated lattice-matched GaInAsP/InP DH diode lasers that exhibit room-temperature cw emission between 1.1 and 1.25 μm. The simplicity of fabrication, appropriate wavelength range, excellent operating characteristics, efficient heat dissipation, and probable reliability of these lasers make them leading candidates as sources for fiber optic communication systems.

REFERENCES

HORIGUCHI, M., 1976, "Spectral Losses of Low-OH-Content Optical Fibers", Elec. Lett. 12, 310.

HSIEH, J. J., 1976, "Double-Heterostructure GaInAs/InP Diode Lasers", Solid State Research Report, Lincoln Laboratory, M.I.T., No. 4, 39.

HSIEH, J. J., ROSSI, J. A., and DONNELLY, J. P., 1976, "Room-temperature cw Operation of GaInAsP/InP Double-heterostructure Diode Lasers Emitting at 1.1 μm", Appl. Phys. Lett. 28, 709.

ISMAILOV, I., SADIEV, A., ALTYNBAEV, R., and SHOKHUDZHAEV, N., 1975, "Characteristics of Diffused InP and InP_xAs_{1-x} Laser Diodes", Sov. J. Quant. Elec. 5, 451.

MAURER, R. N., SCHIEL, E. J., KRONENBERG, S., and LUX, R. A., 1973, "Effect of Neutron and Gamma-Radiation on Glass Optical Waveguides", Appl. Opt. 12, 2024.

NAGAI, H. and NOGUCHI, Y., 1976, "Crack Formation in InP-$Ga_xIn_{1-x}As$-InP Double-heterostructure Fabrication", Appl. Phys. Lett. 29, 740.

NAHORY, R. E., POLLACK, M. A., BEEBE, E. D., DEWINTER, J. C., and DIXON, R. W., 1976, "Continuous Operation of 1.0 μm-Wavelength $GaAs_{1-x}Sb_x/Al_yGa_{1-y}As_{1-x}Sb_x$ Double-heterostructure Injection Lasers at Room Temperature", Appl. Phys. Lett. 28, 19.

NUESE, C., OLSEN, G. H., ETTENBERG, M., GANNON, J. J., and ZAMEROWSKI, T. J., 1976, "CW Room-temperature $In_xGa_{1-x}As/In_yGa_{1-y}P$ 1.06-μm Lasers", Appl. Phys. Lett. 29, 807.

PANISH, M. B., 1976, "Heterostructure Injection Lasers", Proc. IEEE 64, 1512.

PAYNE, D. N. and GAMBLING, W. A., 1975, "Zero Material Dispersion in Optical Fibers", Elec. Lett. 11, 176.

SUGIYAMA, K. and SAITO, H., 1972, "GaAsSb-AlGaAsSb Double Heterojunction Lasers", Japan J. Appl. Phys. 11, 1057.

TSUKADA, T., 1974, "GaAs-$Ga_{1-x}Al_xAs$ Buried-Heterostructure Injection Lasers", J. Appl. Phys. 45, 4899.

WEISER, K., LEVITT, R. S., NATHAN, M. L., BURNS, G., and WOODALL, J., 1964, "InP Laser Characteristics", Trans. Metall. Soc. AIME 230, 271.

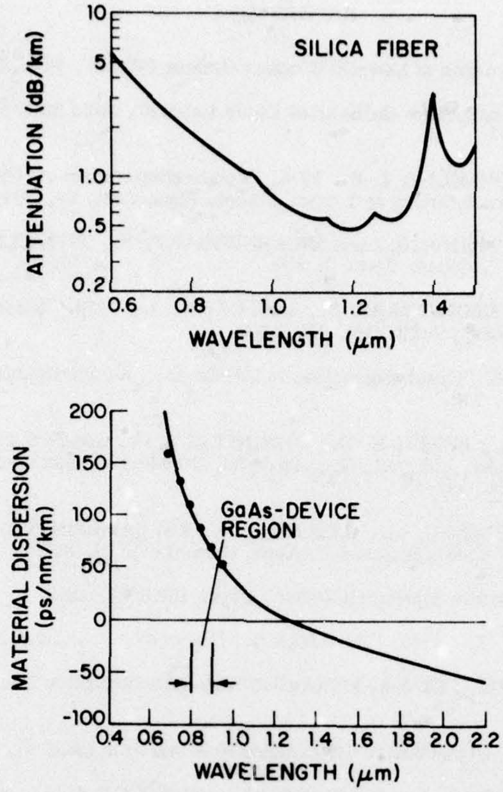

Fig.1 (a) Optical attenuation as a function of wavelength for state-of-art fused silica fibers (Horiguchi, 1976)
(b) Material dispersion as a function of wavelength for fused silica fibers (Payne, 1975)

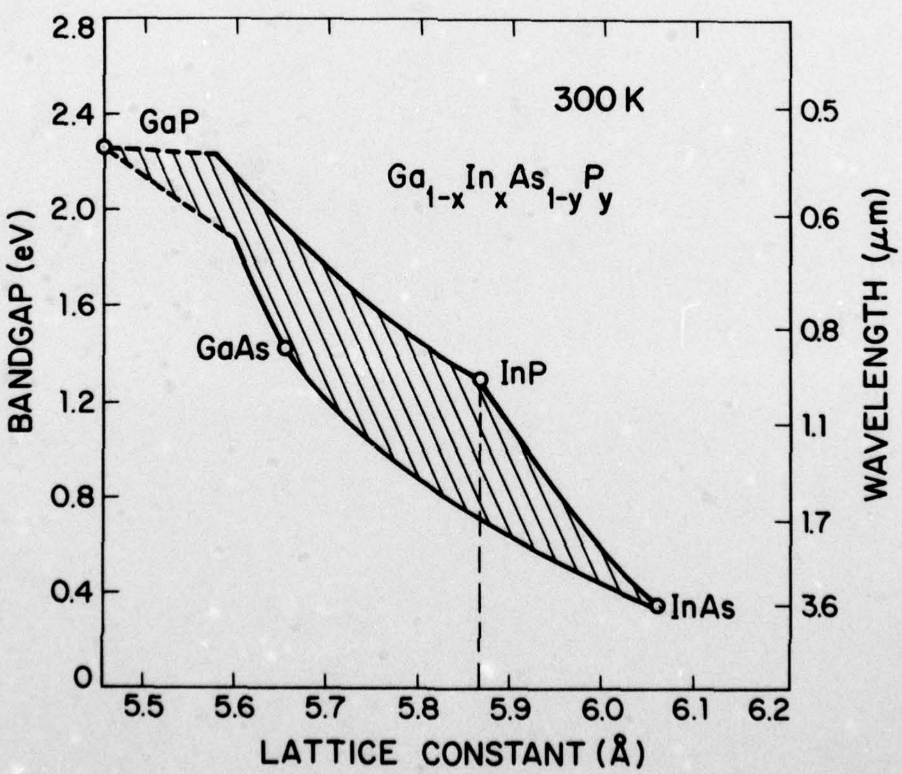

Fig.2 Room-temperature bandgap and corresponding wavelength as a function of lattice constant for $Ga_{1-x}In_xAs_{1-y}P_y$ alloys

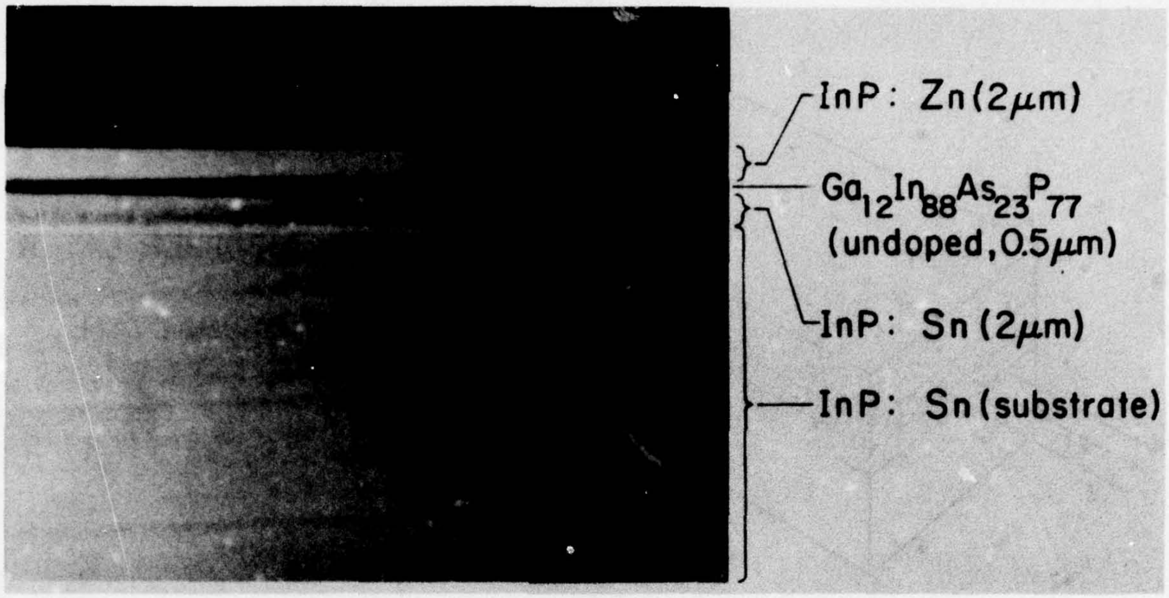

Fig3 Photomicrograph of cleaved cross section through GaInAsP/InP double heterostructure

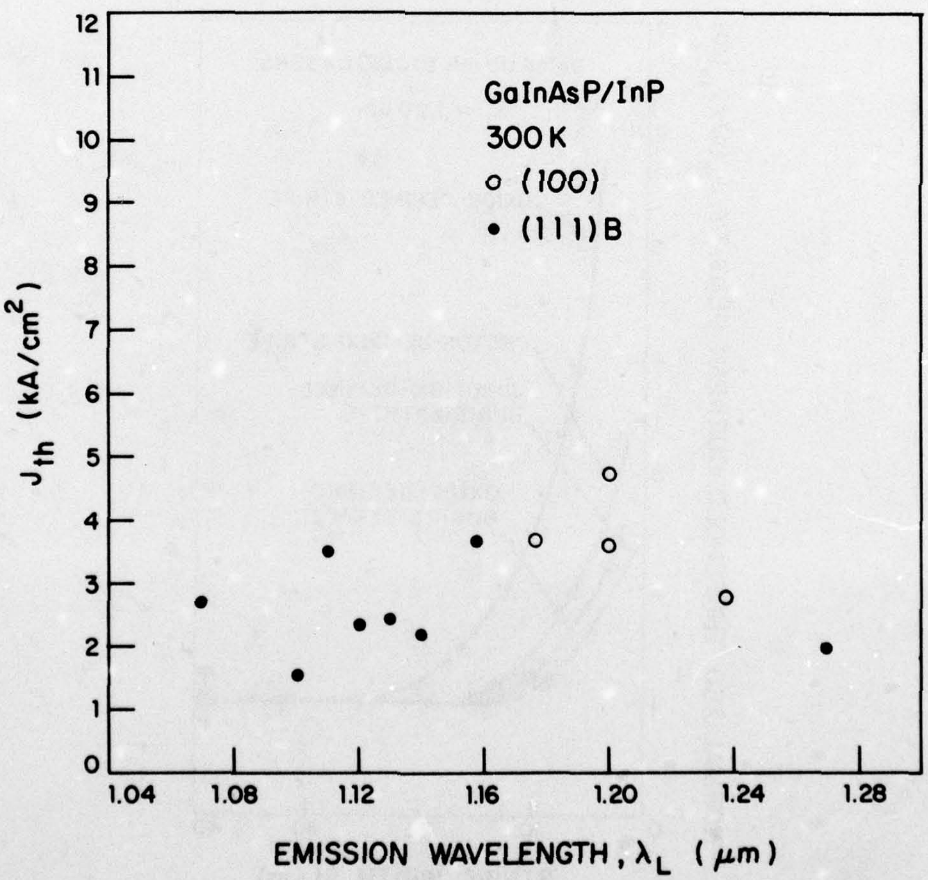

Fig.4 Lowest values of threshold current density, J_{th}, for room-temperature pulsed operation of broad-area DH GaInAsP/InP diode lasers at wavelengths of 1.07–1.27 μm

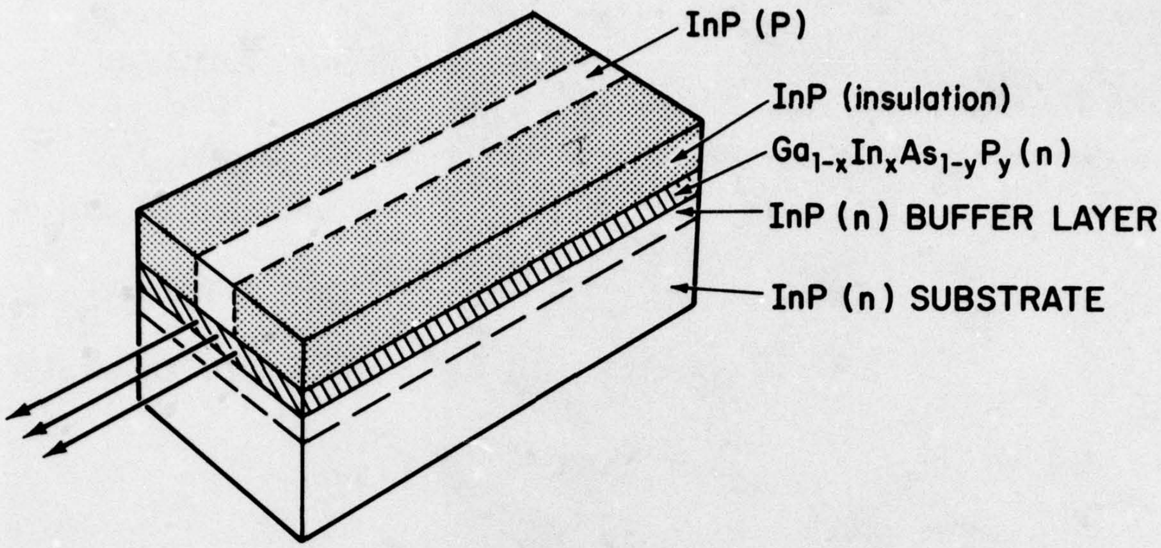

Fig.5 Schematic diagram of proton-defined, stripe-geometry DH GaInAsP/InP diode laser

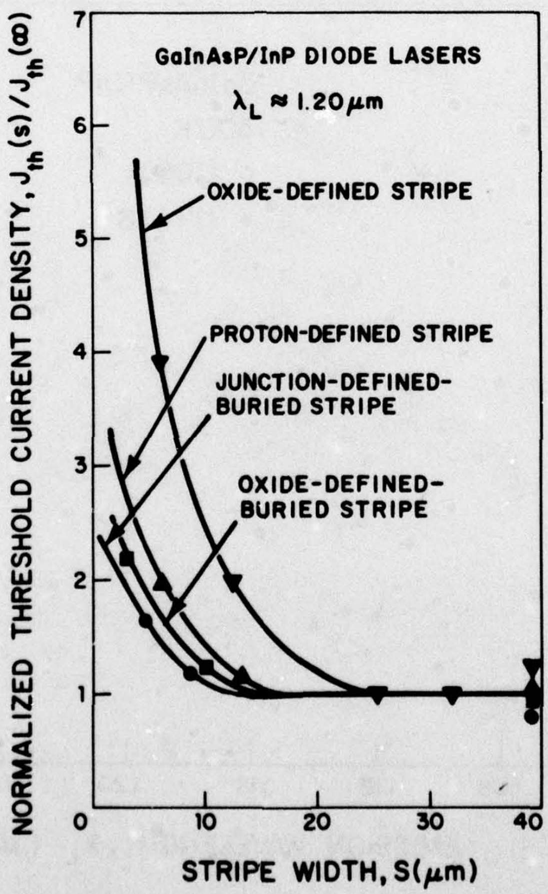

Fig.6 Variation of room-temperature pulsed threshold current as a function of stripe width for four types of stripe-geometry DH GaInAsP/InP diode lasers

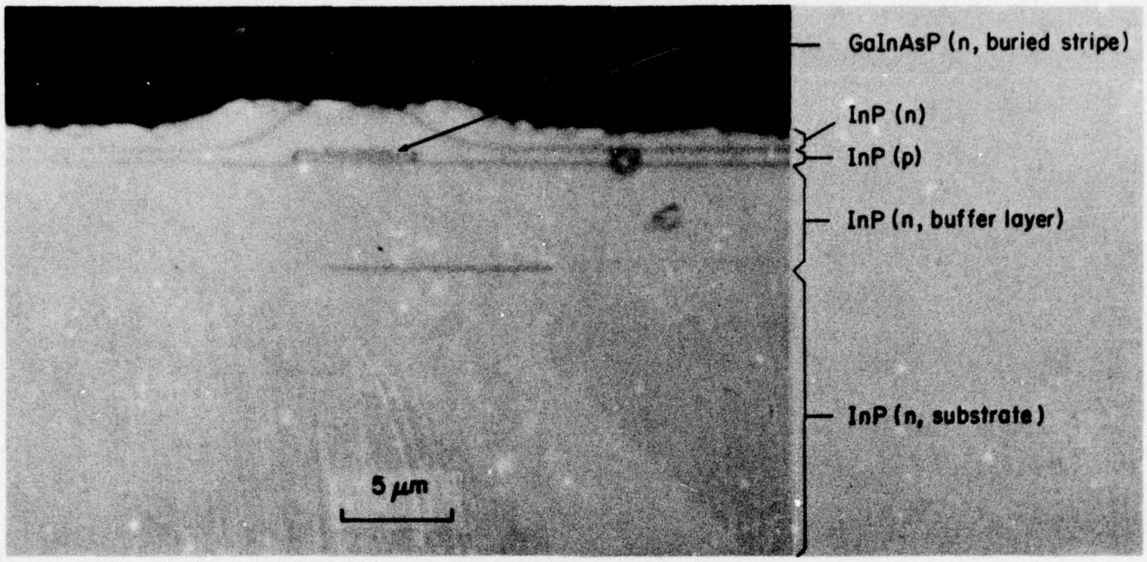

Fig.7 Photomicrograph of cleaved cross section through junction-defined, buried-stripe DH GaInAsP/InP diode laser

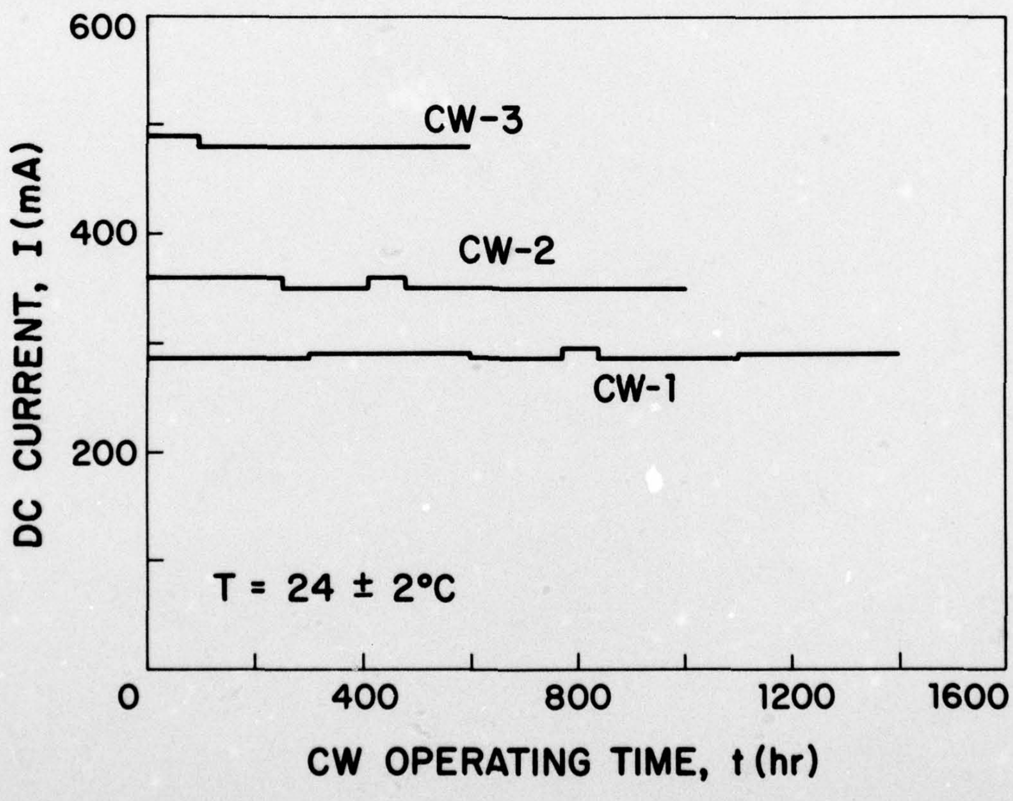

Fig.8 Operating current required to maintain constant output power as a function of time for proton-defined, stripe-geometry DH GaInAsP/InP diode lasers. The small changes observed in current are due to changes in heat sink temperature

REPRODUCTIBILITE DE FABRICATION DES DIODES LASERS

E. Duda, J.C. Carballès, J. Apruzzese
THOMSON.CSF
LABORATOIRE CENTRAL DE RECHERCHES
Domaine de Corbeville
91401 Orsay, France

RESUME

Un problème important rencontré lors de la fabrication des diodes lasers est lié à la difficulté de reproduire de façon satisfaisante leurs caractéristiques. Les diodes lasers fabriquées dans notre laboratoire sont du type double hétérostructure, de zône émettrice 12 µm localisée par implantation protonique peu profonde.

A chaque étape importante de la fabrication (dépôt des contacts ohmiques, clivage, sciage, soudure) des tests sont effectués de façon à vérifier la qualité de l'opération. L'influence de chacune de ces opérations sur les caractéristiques des lasers a été étudiée. En particulier le rôle des contraintes induites au cours du processus a été mis en évidence.

D'autre part, des critères de sélections ont été déterminés de façon à éliminer, aussi rapidement que possible au cours de la fabrication les éléments dont les caractéristiques seraient insuffisantes pour les applications communications optiques.

On a obtenu ainsi une réduction notable de la dispersion des caractéristiques des lasers.

SUMMARY

The most important problem encountered for the production of lasers diodes is the difficulty to reproduce satisfactory performance for these light emitters.

In this paper, we present the main results of a study performed with the aim of improving the reproducibility of these components.

The lasers diodes designed in our laboratory are of double heterostructure type, grown on GaAs substrates; they have an emitting stripe of 12 µm wide formed by a shallow proton implantation.

At each important step of production (deposition of ohmic contact, cleaving, sawing, bonding) tests have been set up to check the quality of the operation. The influence of these operations on the characteristics of the lasers is discussed. The influence of the stresses induced during the process is pointed out.

On the hand, criteria have been derived to eliminate at early stage the chips which would have exhibit insufficient characteristics for optical communication applications.

As a general result of this study, a reduction in the dispersion of the performances has been achieved for the lasers produced through these tests set up along the production line.

I. INTRODUCTION

Des progrès considérables ont été réalisés ces dernières années dans le domaine des lasers à semi-conducteurs. Un certain nombre de laboratoires ont obtenu des lasers ayant fonctionné en continu pendant plus de 10 000 heures[(1) (2) (3)]. Nous avons également obtenu, au laboratoire, de tels lasers. Toutefois s'il est relativement aisé, actuellement, de réaliser quelques lasers présentant de bonnes caractéristiques optiques et une durée de vie de cet ordre, il est plus difficile d'avoir une bonne reproductibilité de fabrication et surtout de prévoir, à priori, la durée de vie de ces composants.

Ce manque de reproductibilité peut être attribué aux défauts existants dans les couches épitaxiales et à ceux introduits par le procédé de fabrication.

Nous avons précédemment[(4)] abordé le problème de la reproductibilité de fabrication. Dans le présent article nous précisons l'influence de certains paramètres et plus particulièrement des contraintes développées lors de la fabrication.

II. FABRICATION DES LASERS

Les lasers utilisés sont du type double hétérostructure, à géométrie ruban, permettant un fonctionnement en continu à température ambiante.

Les épaisseurs et compositions des couches épitaxiales sont données dans le tableau I.

Les contacts ohmiques sont constitués d'un dépôt métallique allié (AuSnTe/Au) côté substrat et d'un dépôt non allié (Ti/Pt/Au) côté épitaxie. Aucune diffusion de zinc n'est effectuée car cette opération ne s'avère pas indispensable à l'obtention de bons contacts. La résistance de contact, côté épitaxié, reste dans ces conditions inférieure à 10^{-5} ohm.cm^2.

La zône active est localisée par implantation protonique peu profonde. Les plaquettes sont alors clivées au pas de 400 µm puis les barrettes obtenues sont sciées en puces élémentaires de 400x300 µm. Les puces sont ensuite soudées à l'indium sur un radiateur de cuivre doré. Le contact supérieur est constitué d'un ruban d'or.

La fig. 1 montre un laser réalisé au laboratoire.

Le processus de fabrication ainsi que les contrôles effectués sont résumés dans le tableau II.

III. CRITERES DE SELECTION EN COURS DE FABRICATION

1. Caractérisation des plaquettes épitaxiales

Pour chaque plaquette, environ dix lasers larges (sans structure ruban) sont soudés sur le support usuel de façon à tester ses propriétés : densité de courant de seuil, rendement externe différentiel (η_D) et résistance série. Les propriétés thermiques sont évaluées en étudiant les variations du courant de seuil I_s en fonction de la température. Nous avons vérifié, en accord avec Hayashi[5] que la loi de variation de I_s en fonction de la température moyenne T de jonction est : $I_{s(T_2)} = I_{s(T_1)} \cdot \exp(\frac{T_2 - T_1}{T_o})$. T_o est une constante homogène à une température qui caractérise la thermique.

Après un certain nombre d'expériences préliminaires nous avons retenu les critères de sélection suivants :

- densité de courant de seuil $J_s \leqslant$ 1800 A/cm^2
- résistance série $\leqslant$ 0,4 ohm (lasers 400 x 125 μ)
- $T_o \geqslant$ 120° K.

2. Contrôle du clivage et sciage

Ces opérations ne posent plus de problèmes importants. Seulement 0 à 5 % des puces sont éliminées à ce stade par tri visuel.

3. Tri sous pointe des puces lasers avant soudure

Ce test consiste en un tracé, en régime impulsionnel, de la caractéristique Puissance optique = F(courant de polarisation). La fig. 2 représente un histogramme des courants de seuil (I_s) des lasers 12 μm.

Au cours de ce tri, les lasers dont I_s est trop élevé ($I_s >$ 200 mA pour les lasers 12 μm) sont éliminés. Les puces sont également triées visuellement; celles qui présentent des défauts tels que protubérances, rayures, trous dans les contacts ohmiques, etc ... sont considérées comme mauvaises. Au total 10 à 20 % des puces sont éliminées au cours du tri sous pointe.

4. Caractérisation des lasers après montage

Nous contrôlons de façon systématique sur chaque laser les paramètres suivants : courant de seuil, rendement externe différentiel (η_D) en régimes impulsionnel et continu, résistance série, diagrammes d'émission en champ proche et lointain et la résistance thermique R_{th}.

Pour une couche épitaxiale donnée, R_{th} est déterminé à partir du décalage en longueur d'onde du spectre d'émission. R_{th} est compris en général entre 20 et 35° CW^{-1} pour les lasers 12 μm. Les études de durée de vie décrites au paragraphe suivant ont montré que les lasers dont $R_{th} >$ 50° CW^{-1} sont à éliminer à cause d'une durée de vie insuffisante.

5. Tests de durée de vie

Un test de prévieillissement est effectué de façon systématique sur les lasers à structure ruban. La puissance lumineuse initiale est fixée à 5 mW et le courant est maintenu constant.

Ces tests ont montré que certains lasers ont des durées de vie inférieures à 200 heures environ. Par contre ceux qui ne sont pas dégradés de façon significative au terme de ces 200 heures ont des durées de vie supérieures à 1 000 heures en général. Des tests de plus longue durée, actuellement en cours, ont montré pour certains lasers des durées de vie supérieures à 10 000 heures.

Certains des lasers à faible durée de vie présentent des défauts tels que protubérances, trous dans les contacts, bavures, etc .... qui s'accompagnent d'une augmentation de la résistance thermique, donc de la température moyenne de jonction en fonctionnement continu.

Cette élévation de température ne suffit pas à expliquer complètement une dégradation aussi rapide. Un autre mécanisme de dégradation doit intervenir à ce stade. Nous pensons que ce sont les contraintes associées au processus de fabrication qui accélèrent la dégradation.

Nous pensons que même pour les lasers qui dégradent rapidement sans défaut d'aspect apparent, une des causes prépondérantes de cette dégradation peut être la contrainte induite au cours du processus.

Il paraît donc comme très important afin de pouvoir optimiser notre processus de fabrication et dans le but de vérifier cette hypothèse d'étudier l'influence des différents types de contraintes sur le comportement des lasers.

REPRODUCTIBILITE DE FABRICATION DES DIODES LASERS

E. Duda, J.C. Carballès, J. Apruzzese
THOMSON.CSF
LABORATOIRE CENTRAL DE RECHERCHES
Domaine de Corbeville
91401 Orsay, France

RESUME

Un problème important rencontré lors de la fabrication des diodes lasers est lié à la difficulté de reproduire de façon satisfaisante leurs caractéristiques. Les diodes lasers fabriquées dans notre laboratoire sont du type double hétérostructure, de zône émettrice 12 µm localisée par implantation protonique peu profonde.

A chaque étape importante de la fabrication (dépôt des contacts ohmiques, clivage, sciage, soudure) des tests sont effectués de façon à vérifier la qualité de l'opération. L'influence de chacune de ces opérations sur les caractéristiques des lasers a été étudiée. En particulier le rôle des contraintes induites au cours du processus a été mis en évidence.

D'autre part, des critères de sélections ont été déterminés de façon à éliminer, aussi rapidement que possible au cours de la fabrication les éléments dont les caractéristiques seraient insuffisantes pour les applications communications optiques.

On a obtenu ainsi une réduction notable de la dispersion des caractéristiques des lasers.

SUMMARY

The most important problem encountered for the production of lasers diodes is the difficulty to reproduce satisfactory performance for these light emitters.

In this paper, we present the main results of a study performed with the aim of improving the reproducibility of these components.

The lasers diodes designed in our laboratory are of double heterostructure type, grown on GaAs substrates; they have an emitting stripe of 12 µm wide formed by a shallow proton implantation.

At each important step of production (deposition of ohmic contact, cleaving, sawing, bonding) tests have been set up to check the quality of the operation. The influence of these operations on the characteristics of the lasers is discussed. The influence of the stresses induced during the process is pointed out.

On the hand, criteria have been derived to eliminate at early stage the chips which would have exhibit insufficient characteristics for optical communication applications.

As a general result of this study, a reduction in the dispersion of the performances has been achieved for the lasers produced through these tests set up along the production line.

I. INTRODUCTION

Des progrès considérables ont été réalisés ces dernières années dans le domaine des lasers à semiconducteurs. Un certain nombre de laboratoires ont obtenu des lasers ayant fonctionné en continu pendant plus de 10 000 heures(1) (2) (3). Nous avons également obtenu, au laboratoire, de tels lasers. Toutefois s'il est relativement aisé, actuellement, de réaliser quelques lasers présentant de bonnes caractéristiques optiques et une durée de vie de cet ordre, il est plus difficile d'avoir une bonne reproductibilité de fabrication et surtout de prévoir, à priori, la durée de vie de ces composants.

Ce manque de reproductibilité peut être attribué aux défauts existants dans les couches épitaxiales et à ceux introduits par le procédé de fabrication.

Nous avons précédemment(4) abordé le problème de la reproductibilité de fabrication. Dans le présent article nous précisons l'influence de certains paramètres et plus particulièrement des contraintes développées lors de la fabrication.

II. FABRICATION DES LASERS

Les lasers utilisés sont du type double hétérostructure, à géométrie ruban, permettant un fonctionnement en continu à température ambiante.

Les épaisseurs et compositions des couches épitaxiales sont données dans le tableau I.

Les contacts ohmiques sont constitués d'un dépôt métallique allié (AuSnTe/Au) côté substrat et d'un dépôt non allié (Ti/Pt/Au) côté épitaxie. Aucune diffusion de zinc n'est effectuée car cette opération ne s'avère pas indispensable à l'obtention de bons contacts. La résistance de contact, côté épitaxié, reste dans ces conditions inférieure à 10^{-5} ohm.cm^2.

La zône active est localisée par implantation protonique peu profonde. Les plaquettes sont alors clivées au pas de 400 µm puis les barrettes obtenues sont sciées en puces élémentaires de 400x300 µm. Les puces sont ensuite soudées à l'indium sur un radiateur de cuivre doré. Le contact supérieur est constitué d'un ruban d'or.

La fig. 1 montre un laser réalisé au laboratoire.

Le processus de fabrication ainsi que les contrôles effectués sont résumés dans le tableau II.

IV. INFLUENCE DES CONTRAINTES SUR LA REPRODUCTIBILITE

Les puces lasers sont soumises essentiellement à deux types de contraintes :

- les contraintes d'épitaxie développées pendant la croissance des couches.
  Elles ont été calculées à partir des différences de coefficients de dilatation thermique des couches. Elles sont pour nos plaquettes de l'ordre de 0,5 à 1.10^8 dynes cm^{-2} (au niveau de la zone active).
- Les contraintes dues à la soudure
  Les mesures de photoélasticimétrie effectuées au laboratoire[6] ont montré qu'elles étaient fonction du type de soudure utilisée. Elles sont, dans le cas d'une soudure Or-Etain, par exemple, de l'ordre de 10^9 dynes cm^{-2}. L'utilisation de l'indium, plus ductile que l'or-étain permet de réduire cette contrainte d'un ordre de grandeur.

Les valeurs des différentes contraintes ainsi que quelques propriétés mécaniques de l'AsGa sont portées dans le tableau III.

La pression utilisée lors de la soudure (0,1 à 0,2 10^8 dynes cm^{-2} a été choisie de façon à être inférieure aux autres contraintes existantes. L'effet de l'application d'une contrainte plus importante lors de la soudure est illustré sur la fig. 3. On remarque que les contraintes supérieures à 2.10^8 dynes cm^{-2}, c'est-à-dire supérieures à la limite de glissement des dislocations évaluée par NANNICHI[7], entraînent une modification de la courbe P(I), qui caractérise une dégradation importante des lasers.

Dans les conditions où sont réalisés les lasers les contraintes existantes sont inférieures à 2.10^8 dynes cm^{-2}, cependant l'existence de défauts superficiels (protubérances, rayures, etc ...) ou de poussières peut induire localement des contraintes très élevées.

L'influence des contraintes localisées a été mise en évidence en dégradant volontairement au moyen d'une pointe de diamant d'un microduromètre Vickers des lasers de 12,25 et 50 μm de large.

Les forces appliquées (1 à 4 g.) sont telles que la pointe de diamant perturbe les couches superficielles GaAs et GaAlAs sans pénétrer dans la couche active.

Les courbes P(I) ont été tracées en régime impulsionnel avant et après dégradation.

On peut résumer les observations de la façon suivante :

- Lasers 12 μm
  L'application de la pointe sur le ruban laser modifie considérablement la courbe P(I) (voir fig. 4). Pour les lasers présentant une caractéristique P(I) linéaire il y a apparition de non linéarité ou "coudes". Pour ceux présentant déjà des "coudes" il y a modification de leurs position et amplitude. L'application de la pointe même en dehors du ruban entraîne une modification notable de la courbe P(I). Sur la fig. 5 on peut voir l'effet d'une dégradation localisée à 12 μm du ruban.
- Lasers 25 et 50 μm
  Les mêmes contraintes localisées appliquées aux lasers 25 et 50 μm ne perturbent pas d'une façon significative les courbes P(I); voir fig. 6.
  Il semble par conséquent que les lasers 12 μm soient extrêmement sensibles aux contraintes localisées. Notons qu'un grand nombre de lasers 12 μm (ou d'une manière plus générale 10 à 20 μm ont une caractéristique non linéaire[8] [9]. On peut donc penser que l'existence de ces non-linéarités est liée aux contraintes localisées dues aux défauts des couches épitaxiées.
  Afin de vérifier l'effet des contraintes localisées à 180° C lors de la soudure à l'indium, nous avons interposé entre la puce laser et le dissipateur thermique des poussières de corindon de 10 μm environ. La répartition et l'amplitude des contraintes sont moins bien définies que dans le cas des essais précédents; toutefois les phénomènes observés (voir fig. 7) sont analogues. La durée de vie de tels lasers est très courte. On peut donc conclure que ce sont les défauts des couches et éventuellement les poussières qui sont essentiellement responsables des dégradations rapides des lasers.

V. CONCLUSION

Pour une couche épitaxiale donnée, l'opération qui affecte le plus la reproductibilité, et surtout la durée de vie, est l'opération de montage des lasers.

En effet, au moment de la soudure des puces sur le radiateur celles-ci sont soumises à des contraintes homogènes (pression sur la puce) et souvent à des contraintes localisées dues aux défauts.

Ces contraintes

- modifient le courant de seuil,
- entraînent l'apparition de non-linéarités ("kinks") dans la courbe Puissance = F (intensité), surtout pour les lasers à structure ruban de 12 μm de largeur.

- diminuent la durée de vie des lasers.

La réduction des contraintes tout au long du procédé de fabrication (pression de soudure faible 0,1.10^8 dyne/cm^2, élimination des poussières et des défauts, etc ...) associée à un contrôle étroit des opérations effectuées permet de diminuer notablement la dispersion des caractéristiques des lasers.

L'ensemble des précautions prises lors de la fabrication permet, après élimination par tri visuel, tri sous pointe, pré-vieillissement, d'obtenir de façon reproductible des lasers présentant des durées de vie garanties supérieures à mille heures.

REFERENCES

1. W.O. BOURNE, A.R. GOODWIN, M. PION, P.R. SELWAY, "Lasers continus à l'arséniure de gallium et à l'arséniure- aluminure de gallium pour télécommunications optiques", Revue des Télécommunications (1976) 51/3, pp. 152-157.
2. W.B. JOYCE, R.W. DIXON and R.L. HARTMAN, "Statistical Characterization of Lifetimes of Continuously Operated (Al,Ga)As Double-hèterostructure Lasers", Applied Physics Letters (1976) 28/11 pp. 684-686.
3. H. KAN, H. NAMIZAKI, M. ISHII and A. ITO, "Continuous Operation over 10 000 h of GaAs/GaAlAs Double-heterostructure Laser Without Lattice Mismatch Compensation", Applied Physics Letters (1975) 27/3 pp. 138-139.
4. J.C. CARBALLES, M. CANTAGREL, "Reproducibility of the Manufacturing Process of C.W. GaAs Lasers", 2ème Colloque Européen sur les transmissions par fibres optiques Paris Sept. 1976.
5. I. HAYASHI, M.B. PANISH and F. REINHART,"GaAs-AlGaAs Double-heterostructure Injection Lasers", Journal of Applied Physics (1971) 42/5 pp. 1929-1949.
6. F. GROSVALET, "Influence des contraintes sur la dégradation des émetteurs électroluminescents à l'arséniure de gallium", Thèse Université Paris Sud Mars 1977.
7. Y. NANNICHI, J. MATSUI and K. ISHIDA, "Rapid Degradation in Double-heterostructure Lasers", Japanese Journal of Applied Physics (1975) 14/10 pp. 1561-1568.
8. T.L. PAOLI, "Nonlinearities in the Emission Characteristics of Stripe-geometry (AlGa)As Double-heterostructure Jonction Lasers", IEEE Journal of Quantum Electronics (1976) QE-12/12 pp. 770-775.
9. R. LANG, "*Horizontal Mode Deformation and Anomalous Lasing* Properties of Stripe Geometry Injection Lasers - Theoretical Model", Japanese Journal of Applied Physics 1977 16/1 pp. 205-206.

Couche	Epaisseur typique /um	Composition	Dopage cm^{-3}
Substrat n	100	GaAs	Si 2.10^{18}
1 couche n	2	GaAs	Sn 6.10^{17}
2 couche n	1	$Ga_{0,7}Al_{0,3}As$	Sn 10^{17}
3 zone active	0,3	$Ga_{0,95}Al_{0,05}As$	Si 3.10^{17}
4 couche p	1	$Ga_{0,65}Al_{0,35}As$	Ge 2.10^{17}
5 couche p	1	GaAs	Ge 2.10^{19}

Tableau I

TABLEAU II

Opérations effectuées	Contrôles
Croissance épitaxiale des couches	Vérification optique des couches. Sciage des parties présentant des défauts
Contacts ohmiques Ti/Pt/Au (côté épitaxie) AuSnTe/Au (côté substrat)	Réalisation de lasers larges - densité de courant de seuil - résistance série - qualité contacts ohmiques - propriétés thermiques
Réalisation de la structure ruban (implantation protonique)	
Clivage	Vérification de la qualité du clivage
Sciage	Tri sous pointe Distribution des courants de seuil
Soudure à l'indium	Défauts tri visuel
Contact supérieur	Caractérisation P(I), V(I) Résistance thermique Diagrammes de rayonnements
Pré-vieillissement	Spectre optique Durée de vie

TABLEAU III

Nature des contraintes	20° C	180° C
	dynes cm^{-2}	
Résistance à la rupture	2.10^{10}	
Limite de glissement des dislocations	10.10^{8} (+)	2.10^{8}
Contraintes résiduelles dans la couche active	0,5 à 1.10^{8}	0,4 à $0,8.10^{8}$
Contrainte exercée lors de la soudure (pression sur la puce)	0,1 à $0,2.10^{8}$	0,1 à $0,2.10^{8}$
Contrainte de soudure liée à la différence de coefficients de dilatation : In	10^{8}	
Contrainte de soudure liée à la différence de coefficients de dilatation : Au-Sn	10^{9}	

(+) valeur estimée par Nannichi et col.[7]

AD-A050 748 ADVISORY GROUP FOR AEROSPACE RESEARCH AND DEVELOPMENT--ETC F/G 20/6
OPTICAL FIBRES, INTEGRATED OPTICS AND THEIR MILITARY APPLICATIO--ETC(U)
OCT 77 H HODARA

UNCLASSIFIED AGARD-CP-219 NL

5 OF 6
AD
A050748

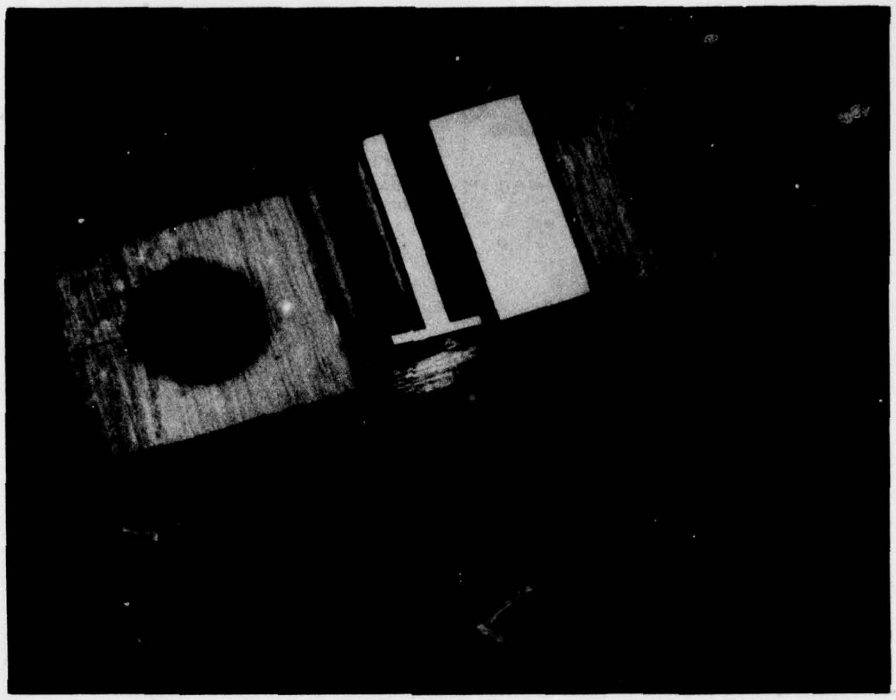

Fig. 1 Photographie d'un laser.

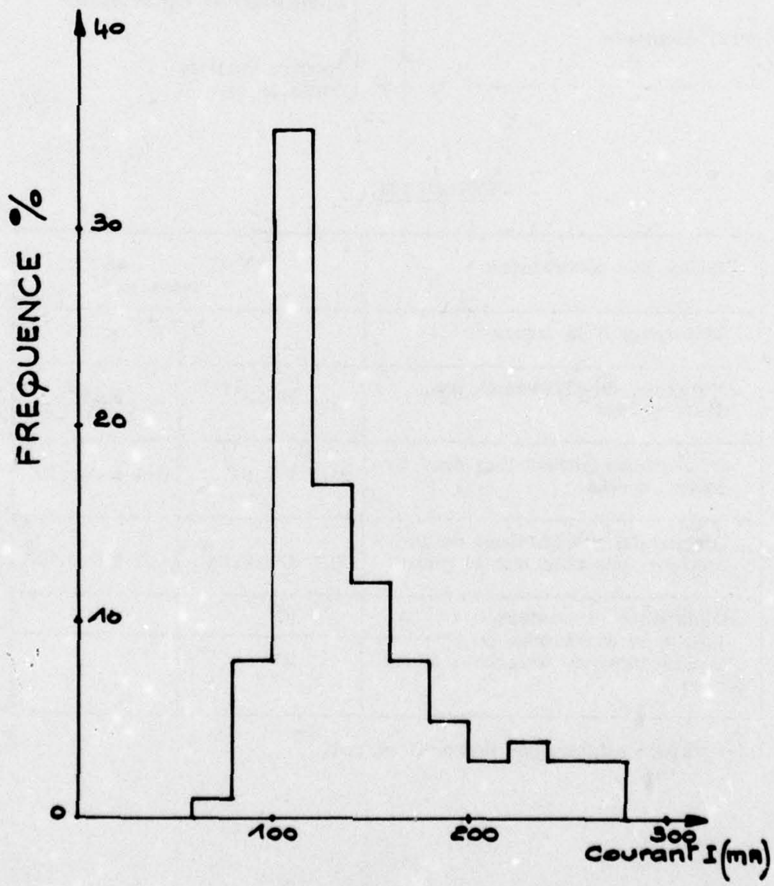

Fig. 2 Histogramme des courants de seuil des lasers à structure ruban de 12 µm.

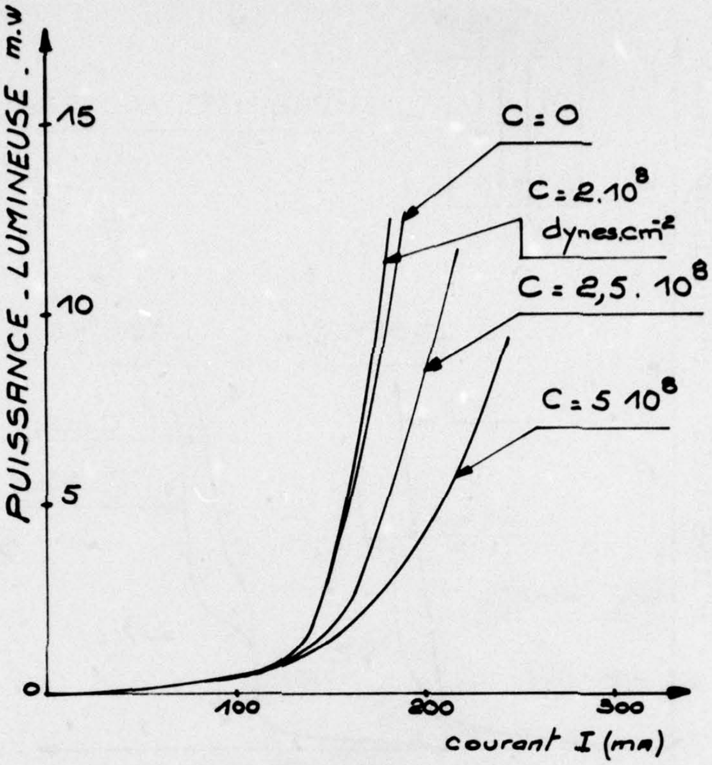

Fig. 3 Influence des contraintes appliquées (c) lors de la soudure des lasers.

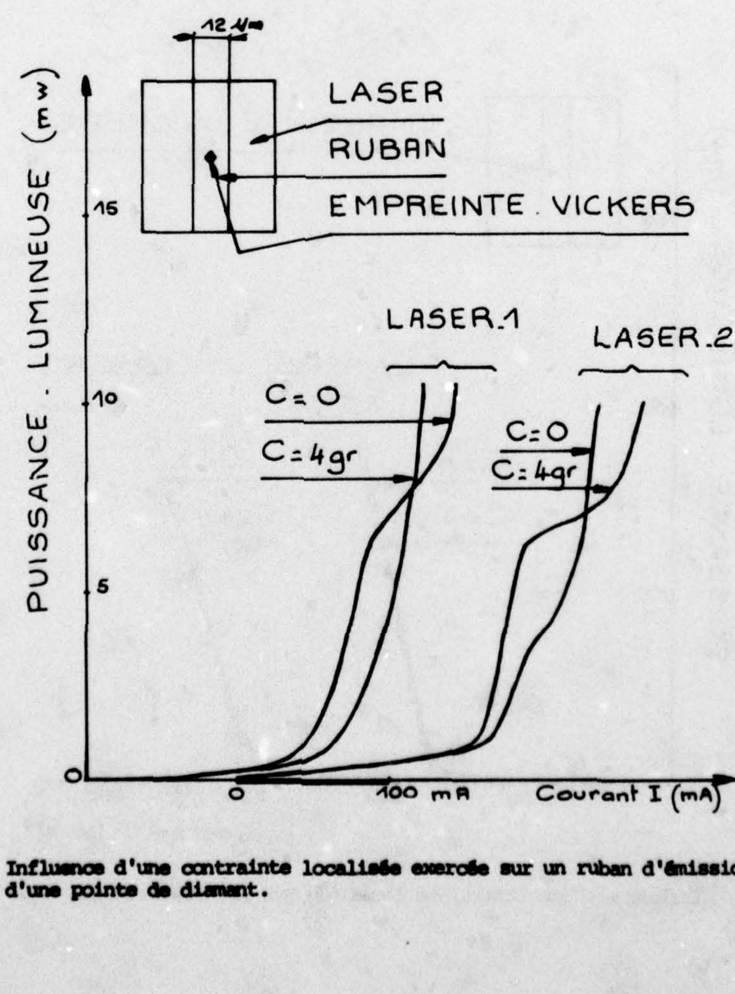

Fig. 4 Influence d'une contrainte localisée exercée sur un ruban d'émission, au moyen d'une pointe de diamant.

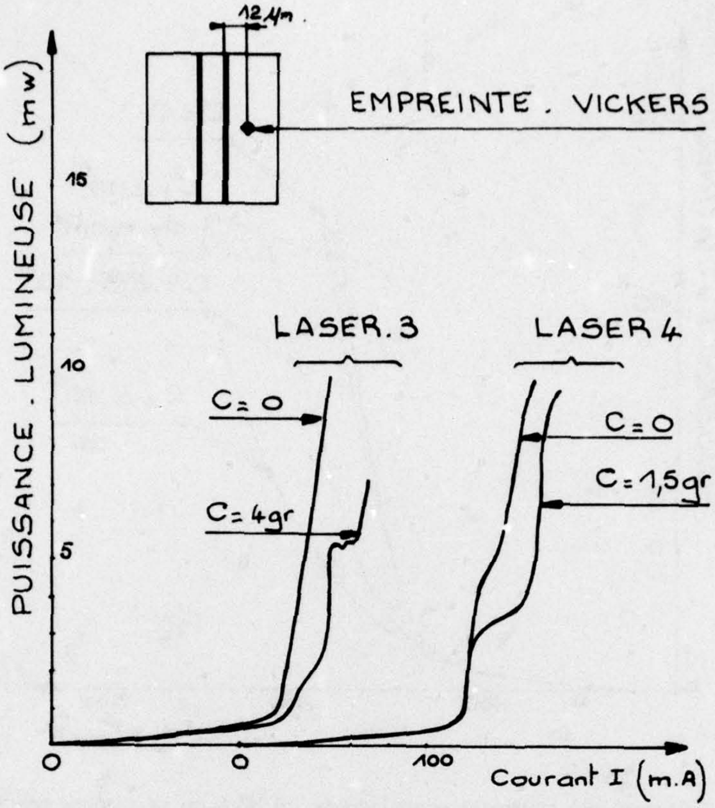

Fig. 5   Influence d'une contrainte localisée appliquée en dehors du ruban d'émission.

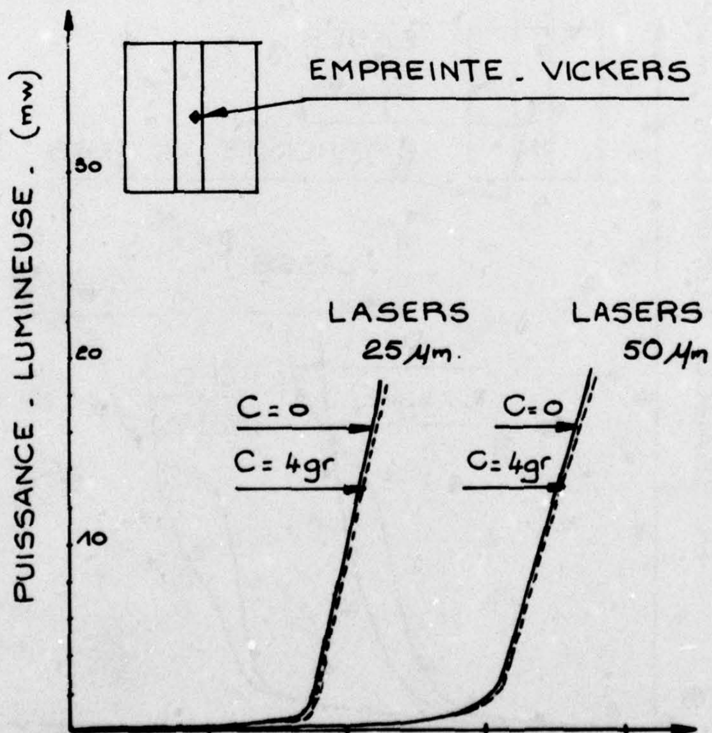

Fig. 6   Influence d'une contrainte localisée sur des lasers 25 μm et 50 μm.

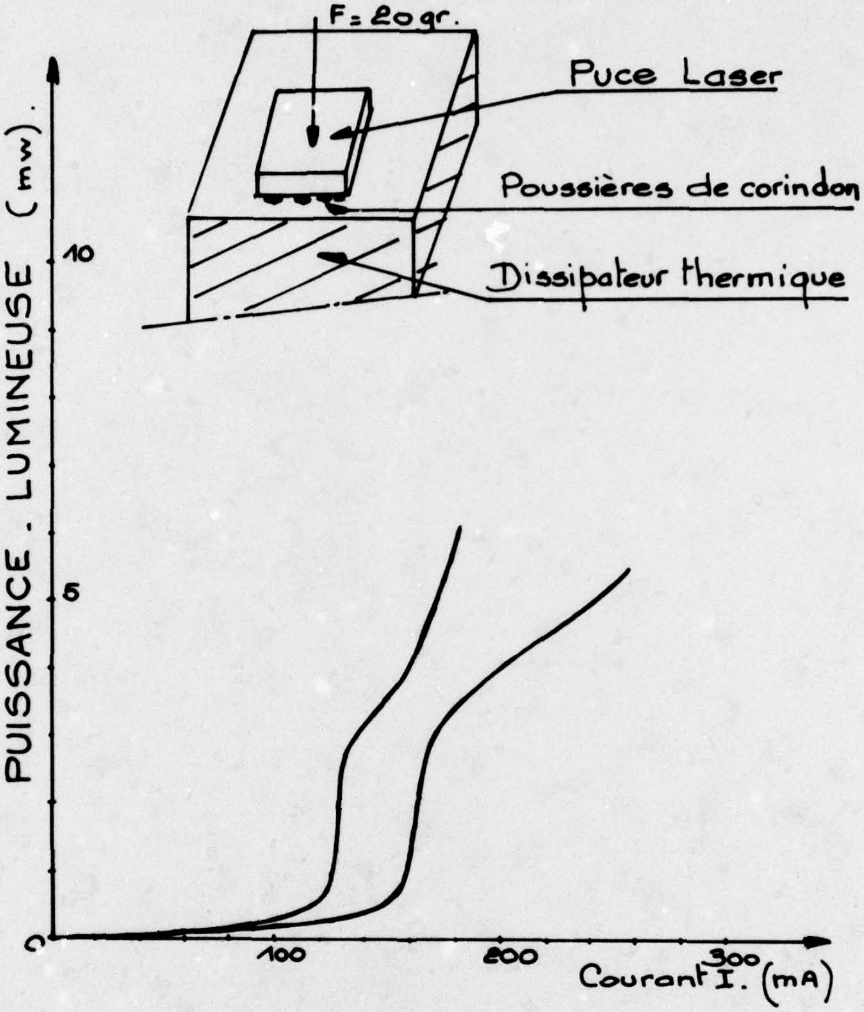

Fig. 7 Influence des contraintes provoquées par des poussières de corindon, lors de la soudure des lasers.

PHYSICS AND TECHNOLOGY OF DEGRADATION IN GaAs LIGHT EMITTING DIODES

G. Zaeschmar
Naval Ocean Systems Center
San Diego, California 92152

Creep-induced lattice defects caused by thermal stress in the junction area have long been believed to be a possible source for light emitting diode (LED) degradation. The increased number of lattice defects causes an increase in nonradiative recombination centers, resulting in a shunt path which decreases the efficiency at constant current. This presentation is an attempt to cast these ideas into a quantitative theory and report the results of novel experiments relating to the matter.

In 1973, Reinhart and Logan [1] extended Timoshenko's calculation [2] of the bimetal strip to a heterojunction. The result is a stress level of approximately 10^8 dyne/cm^2 caused by the different thermal expansion coefficients at the interface. No assessment of the stress at the junction caused by the spatial thermal gradient from the hot junction to the heat sink has been reported. Since the bulk of the heat is generated in or near the junction whose thickness is much less than the thickness of the chip, we may approximate the temperature distribution by a linear function throughout. The chip in the heated and nonheated situation looks like figure 1.

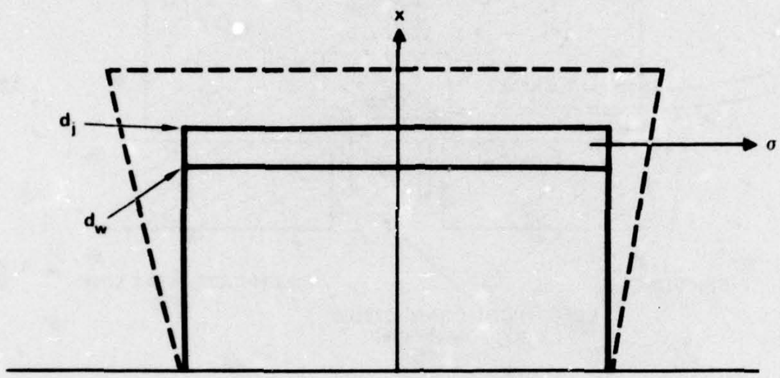

Figure 1

The stress is calculated by making use of the fact that for a linear temperature distribution free of stress, the body bends. The x component of the displacement, u, is in our case given as [2]

$$u = \alpha \left\{x(PFR_{sp} + T_a) + \frac{P}{2\lambda}(x^2 - y^2 - z^2)\right\} \tag{1}$$

where

u = x component of displacement

α = thermal expansion coefficient

P = electrical power/unit area dissipated between $d_w \leqslant x \leqslant d_w + d_j$

R_{sp} = thermal spreading resistance, F = area of chip

T_a = ambient temperature, λ = thermal conductivity

From this we get the bending radius r:

$$\left|\frac{1}{r}\right| \cong \frac{\partial^2 u}{\partial y^2} = \frac{\partial^2 u}{\partial z^2} = \frac{\alpha P}{\lambda} \tag{2}$$

This result is rigorous. The approximations of the theory of plates and shells are implied if we connect the bending radius with the desired stress: [3]

$$\sigma_y = \sigma_z = \frac{1}{r}\frac{Ex}{1-\nu} = \frac{\alpha P}{\lambda}\frac{Ex}{1-\nu} = \frac{\alpha E \Delta T(x)}{1-\nu} \tag{3}$$

E = modulus of elasticity, ν = Poisson ratio, σ = stress

The result is correct if diodes are mounted p side down. The last term in equation (3) gives the stress in terms of the temperature difference ΔT. A typical number would be a stress of 10^9 [dyne/cm^2] at a temperature difference of 100°C. We refer to reference [4] for discrepancies in junction temperature determination. Higher temperatures and stresses have to be anticipated if the diode works in pulsed operation. Indeed, enhanced degradation has then been observed. [5], [6] Based on these results it can safely be inferred that thermal stress-induced creep is a serious possibility in GaAs diodes, although the critical resolved shear stress at these temperatures is not exactly known. [7]

Recently, Brantley and Harrison [8] as well as Eliseev and Khaidarov [9] demonstrated experimentally that additional externally-applied mechanical stress increases the degradation of a LED. Their work was incomplete in the sense that the junction temperatures were not given and no attempt was made to separate the applied stress from the influence of current and heat. Nevertheless, the reported precipitous onset of accelerated degradation at a threshold level of approximately 2×10^8 dyne/cm^2 furthermore underlines strongly the role of creep in degradation.

As for the experimental part of this work, done by Dr. S. Speer at Spectronics Inc., figure 2 shows the apparatus for the uniaxial stress experiment. Figure 3 gives some degradation curves obtained with it. The results confirm qualitatively the work cited above. [8,9] As seen in figure 4, we find for the time derivative of the normalized light output the rule:

$$\frac{d}{dt}\left[\frac{L(t)}{L_o}\right] \propto \sigma^3 \tag{4}$$

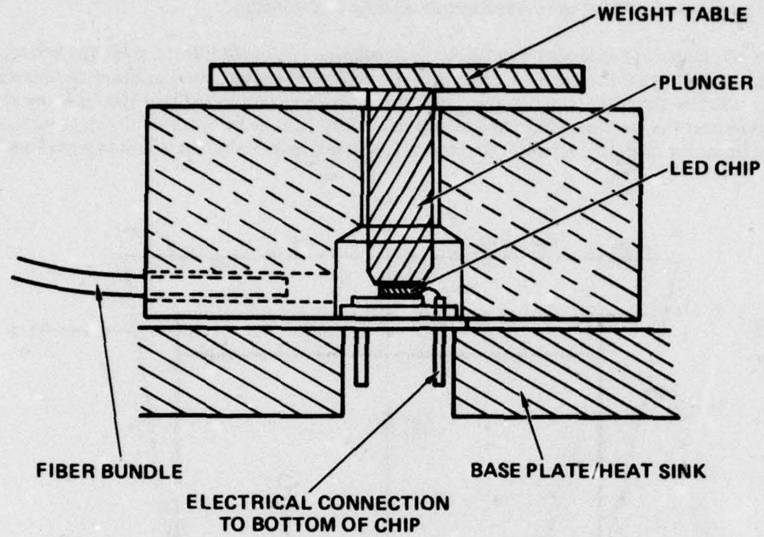

Figure 2. Uniaxial Stress Fixture.

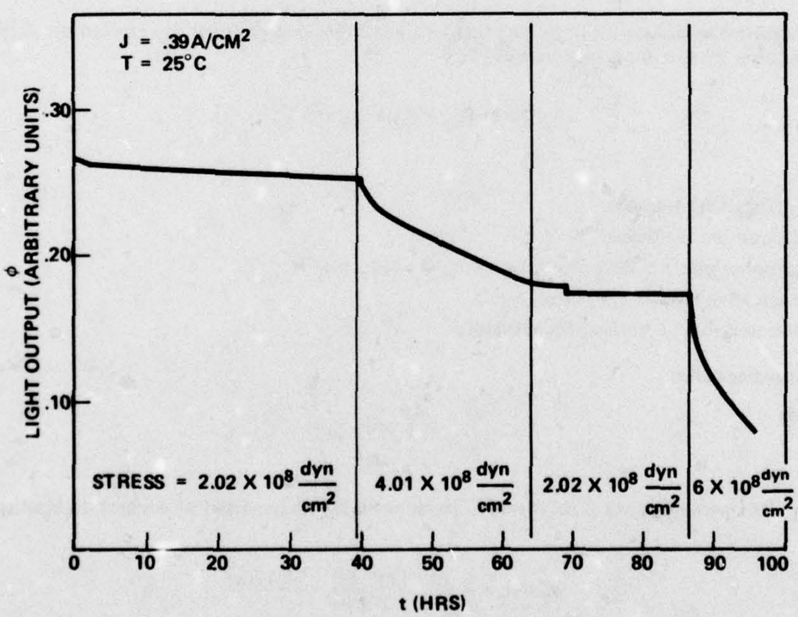

Figure 3. Light Output versus Time with Uniaxial Stress.

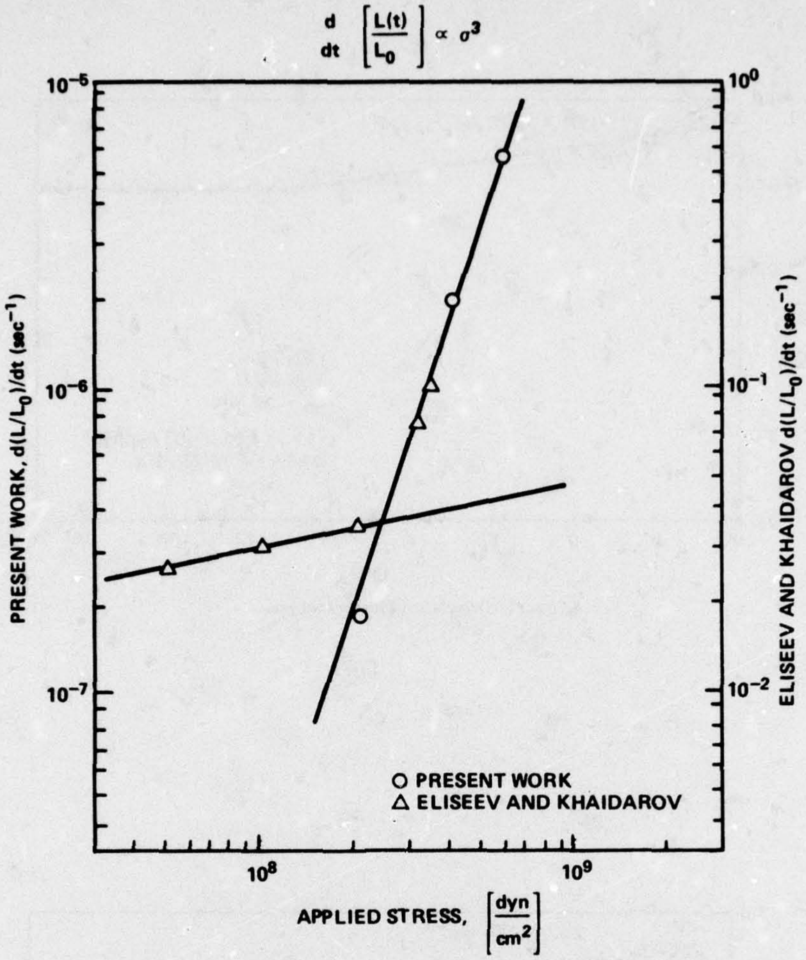

Figure 4. Degradation Rate versus Applied Stress in GaAs LED.

The current density employed in this study is very low, ~ 50 A/cm^2. That means the applied external stress is not obscured by an additional thermal stress. This may be a reason for the somewhat more complicated results of Eliseev and Khaidarov. [9] The break in their curve indicates the effect of a critical stress. Unfortunately, they do not report their current levels either.

Our next step was to find out if degradation occurs if diodes are subjected only to external mechanical stress. The results shown in figures 5 and 6 represent the degradation in light output of two identical LEDs subjected to the same uniaxial stress, the only difference being that LED No. 7-1 had no current flowing except for the brief period during which the light output was measured. **That means, for the chosen stress and temperature, an equivalent degradation can be produced by stress alone, i.e., in the absence of electron-hole recombination.**

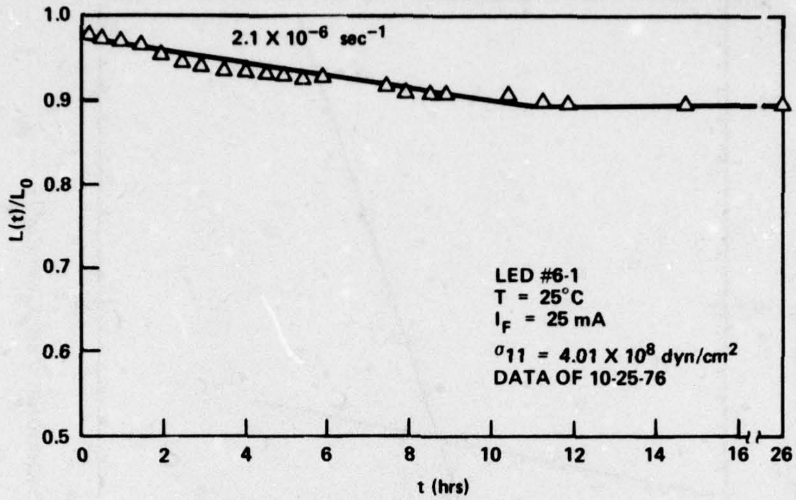

Figure 5. Degradation with forward bias.

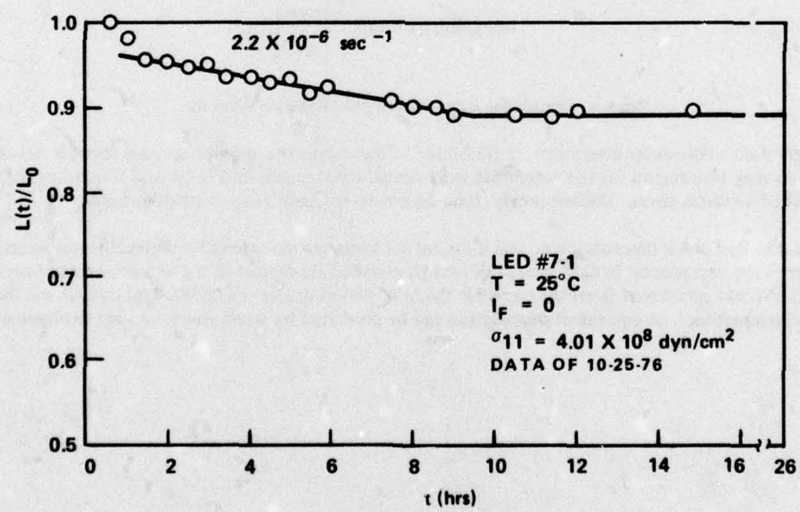

Figure 6. Degradation without forward bias.

Theory of Degradation

One assumption is that the stress induced increase in lattice defects gives rise to a non radiative shunt path by increasing the number of nonradiative recombination centers, leaving the number of radiative centers constant. The natural starting point is the simple two path model for the quantum efficiency $\eta(t)$: [10]

$$\eta = \frac{1}{1 + \frac{\rho_{nr}(t)}{\rho_r} \frac{\alpha_0}{\beta} \frac{p}{n} \exp\left(-\frac{E_{nr} - E_r}{kT}\right)} = \frac{1}{1 + a\rho_{nr}(t)} \tag{5}$$

where

$\rho_{nr}(t)$ = density of non radiative recombination centers

ρ_r = density of radiative recombination centers, assumed constant

E_{nr}, E_r = their respective energy levels

α_0, β = nonradiative, radiative capture rates

n, p = electron, hole densities

The constant a is the product of all the factors in the second term of the denominator except $\rho_{nr}(t)$

An expression connecting the increase of stress-induced lattice defects with time t can be found from the work by Peissker, Haasen, Alexander: [11]

$$dN = Nv\delta dt \tag{6}$$

where

$N(t)[cm^{-2}]$ = density of dislocation lines

v $= K_2(\sigma - A\sqrt{N})^m e^{-Q/kT}$ the dislocation velocity

δ $= K_1(\sigma - A\sqrt{N})^n$ the dislocation multiplication factor

$\sigma - A\sqrt{N}$ = effective shear stress acting on the dislocation

$A\sqrt{N}$ $= \frac{Gb\sqrt{N}}{2\pi(1-\nu)}$ = work hardening term,

G = shear modulus, B = Burgers vector, n, m = empirical kinetic parameters, not necessarily integer

In order to make use of equation (5), we have to connect the density of dislocation lines with the density of nonradiative recombination centers. In the assumed nonconservative climb motion, a trail of point defects is left behind the moving dislocation [12]. We therefore connect N with ρ_{nr} by:

$$\rho_{nr}(t) = N(t)/a_0 \tag{7}$$

where

a_0 = atomic diameter

Integration of (6) therefore leads to:

$$t = \frac{1}{Ke^{-Q/kt}} \int_{N_0}^{N(t)} \frac{dN}{N(\sigma - A\sqrt{N})^{n+m}} = \frac{e^{Q/kt}}{K} \int_{a_{o\rho nr}(0)}^{a_{o\rho nr}(t)} \frac{dN}{N(\sigma - A\sqrt{N})^{n+m}} \tag{8}$$

From purely mechanical, plastic deformation measurements the kinetic parameters n and m were determined for GaAs by Osvenskii et al. [13], [14] as:

$$n + m = 3 \tag{9}$$

Using (5) and (7), the light output L(t) can be written as:

$$L(t) = \frac{B}{1 + a_{\rho nr}(t)} = \frac{B}{1 + \frac{a}{a_o} N(t)} \tag{10}$$

where B = constant of proportionality. Substituting (10) in (6) gives:

$$t = \frac{e^{Q/kT}}{K} \cdot \int_{N_0}^{\frac{a_o}{a}\left[\frac{B}{L(t)} - 1\right]} \frac{dN}{N(\sigma - A\sqrt{N})^{n+m}} \tag{11}$$

which is a degradation formula with several adjustable parameters suitable for a least-square fit. Figure 7 shows a characteristic example.

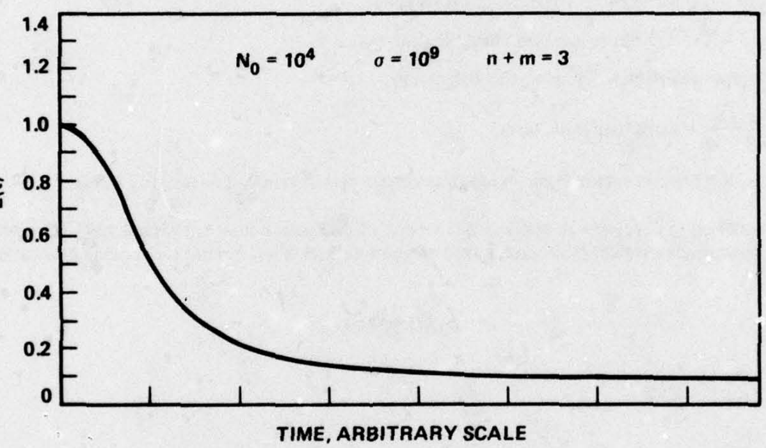

Figure 7

No attempt for a least square fit will be made unless all but two parameters are determined with sufficient accuracy. Of greater importance is the dependence of dL/dt on stress: By differentiating (8) and (10) with respect to time, eliminating $\dot{N}$, we receive:

$$\frac{dL}{dt} = \frac{\text{const } e^{-Q/kT}}{\left[1 + \frac{a}{a_o} N(t)\right]^2} N[\sigma - A\sqrt{N}]^{n+m} \tag{12}$$

which, using (9), renders the important result:

$$\frac{dL}{dt} \sim \sigma^3 \tag{13}$$

in agreement with our measured result (4). That means, we established a quantitative link with the measured change in light output as a function of stress and dislocation kinetic properties measured independently by purely mechanical means.

Acknowledgment

I express my thanks to Dr. S. Speer from Spectronics Inc. for carefully designing and executing the experiments.

References

1. F. K. Reinhart and R. A. Logan, J. Appl. Phys. 44, No. 7, 3171 (1973).

2. B. A. Boley and J. H. Weiner, Theory of Thermal Stresses, New York: John Wiley & Sons, Inc., 1960, p. 273.

3. S. Timoshenko and S. Woinowsky-Krieger, Theory of plates and shells, New York: McGraw-Hill Book Co., Inc., 1959, p. 38.

4. L. G. Walshak and W. E. Poole: Thermal Resistance Measurement by IR Scanning. Microwave Journal, (Feb. 1977), 62.

5. Koyama, Kohisa and Suzuki: Reliability of $GaAs_{1-x}P_x$ LED's, 1973 Proceedings Reliability and Maintainability Symposium, page 203.

6. Private communication by J. M. Ralston.

7. P. A. Kirkby, "Dislocation Pinning in GaAs by the Deliberate Introduction of Impurities," IEEE. J. of Quantum Electronics, QE-11, No. 7, 562 (1975).

8. W. A. Brantley and D. A. Harrison, "Degradation Studies of Diffused GaAs LEDs Subjected to Mechanical Stress: Proc. IEEE Reliability Physics Symposium, April 1973.

9. P. G. Eliseev and A. V. Khaidarov, "Role of Mechanical Stresses in Gradual Degradation of Light-Emitting Diodes and Injection Lasers," Sov. J. Quant. Electron., 5, No. 1, 73 (1975).

10. S. M. Sze, Physics of Semiconductor Devices, New York: Wiley-Interscience, 1969, p. 632.

11. E. Peissker, P. Haasen and H. Alexander, "Anisotropic Plastic Deformation of Indium Antimonide," Phil. Mag. 7, 1279 (1962).

12. P. M. Petroff and L. C. Kimerling, "Dislocation climb model in compound semiconductors with zinc blende structure," Appl. Phys. Letts. 29, No. 8, 461 (1976).

13. V. B. Osvenskii, *et al*, "Effect of charged additions on the plasticity of semiconducting $A^{III}B^{V}$ compounds," Soviet Physics-Solid State, 10, No. 11, 2540 (1969).

14. V. B. Osvenskii, *et al*, "The effect of alloying additions on the creep of GaAs single crystals," Soviet Physics-Crystallography, 12, No. 9, 718 (1969).

RELIABLE SEMICONDUCTOR LASERS FOR WIDE BAND OPTICAL COMMUNICATION SYSTEMS

A.R. Goodwin
P.R. Selway
M. Pion
W.O. Bourne

Standard Telecommunication Laboratories Limited
London Road, Harlow, Essex, CM17 9NA
England

SUMMARY

Semiconductor lasers have now largely overcome the early problem of unreliability following intensive investigations into the degradation mechanisms. Now, SiO_2 stripe geometry GaAs/(GaAl)As lasers have consistently shown that they are capable of providing a c.w. output of 3 to 5 mW for more than 10 000 hours, making them ideal sources for wide band optical communications systems.

1. INTRODUCTION

Semiconductor lasers are rapidly being developed to a stage at which they will make ideal sources for wide band optical communications systems. Despite early concern about reliability, recent investigations of degradation mechanisms have led to considerable improvements in working life, and many laboratories have reported 10 000 hours continuous wave (c.w.) operation. Extrapolations now predict lives in excess of 100 000 hours (HARTMAN, R.L. and DIXON, R.W. 1975).

Although many of the proposed optical communications systems can operate satisfactorily with a simple light emitting diode (LED) or high radiance LED (GOODFELLOW, R.C., 1974), the advantage of a laser's much higher radiance frequently makes it a more attractive proposition even in relatively narrow bandwidth or short distance systems. For example, if a higher power can be launched, more loss can be tolerated in cables and connectors, perhaps leading to an overall cost advantage. However, it is in wide band, long distance systems that the higher power output, higher modulation efficiency, narrower spectral line width, and narrower emission patterns of the laser make it the only practical source.

This paper describes the fabrication and performance characteristics of stripe geometry lasers, suitable for use with small core single mode or graded-index fibres in systems requiring modulation at rates in excess of 250 Mbit s^{-1}.

2. LASER STRUCTURE

A stripe geometry SiO_2 insulated laser is shown in Figure 1. The junction structure is a conventional double heterostructure with $Ga_xAl_{1-x}As$ passive layers containing about 35% Al and an active region with about 5% Al. This latter quantity minimizes the strain in the active layer caused by thermal expansion mismatch between the GaAs substrate and the $Ga_xAl_{1-x}As$ passive layers. The junction is produced by liquid phase epitaxy using a multiple bin sliding graphite boat. Layer dopings are shown in Table 1. One important design consideration is that the p-GaAl/As layer should be doped sufficiently to prevent electron leakage at high temperatures (GOODWIN, A.R. et al 1975) but not so highly doped as to cause excessive transverse conduction of current away from the stripe region.

Table 1 - Layer compositions of a typical double-heterostructure $Ga_xAl_{1-x}As$ wafer.

Layer	1-x	Dopant Concentration in Melt	Carrier Concentration Estimate (cm^{-3})
Substrate	0.0		$\sim 10^{18}$
n-passive	0.35	5 at % Sn	$\sim 10^{17}$
Active	0.05	0.3 at % Si	$\sim 10^{17}$
p-passive	0.35	0.2 at % Ge	$\sim 10^{17}$
p-contact	0.0	0.2 at % Ge	4×10^{17}

After growth the epitaxial wafers are carefully selected for freedom from crystallographic defects such as dislocations and stacking faults because they cause rapid degradation during c.w. operation (De LOACH, B.C. et al 1973 and YONEZU, H. et al 1974). Suitable wafers are coated with SiO_2 using radio frequency plasma deposition and 15 µm wide stripes are then opened using conventional photolithography. A shallow Zn diffusion produces a highly doped p^+ surface in the stripe region which assists the formation of a low resistance ohmic contact by subsequent evaporation of Ti-Au layers. After forming the contacts, the wafer is cleaved into strips to produce the reflecting surfaces, then cleaved again to form dice approximately 400 µm square with an active stripe area in the centre of each die. Dice are bonded to a copper heat sink using indium solder; a soft metal such as indium is used to minimize residual strain in the chip.

3. OUTPUT CHARACTERISTICS

Provided that the basic junction structure has a low threshold current density (1000 to 2000 A cm^{-2}) and reasonable temperature coefficient (GOODWIN, A.R. et al 1975), and that the thermal resistance of the bond is low (10 to 20 KW^{-1}), c.w. operation is easily achieved at heat sink temperatures up to 353K. Figure 2 shows the measured variation of threshold current with temperature for a typical device.

The light versus current characteristics of two lasers are shown in Figure 3. Laser (a) is a well behaved device with an output that increases smoothly to about 10 mW at a current 25 mA above the threshold. The steep region just above the threshold is probably caused by saturation of the optical absorption in the fringe regions on either side of the stripe. Here the carrier density is below that required for gain at threshold but the regions become 'bleached' causing a reduction in the required gain, thus reducing the apparent threshold as the light intensity increases.

Laser (b) in Figure 3 is a less perfect device in which significant kinks or changes of slope occur in the output characteristics at powers well below 10 mW. This type of behaviour is thought to be due to non-uniformities in the active layers; in uniform material a high proportion of stripe lasers behave like laser (a).

In semiconductor lasers a significant noise amplitude is always superimposed on the dc light level. This noise is due to amplification of quantum fluctuations and shows a resonance-like frequency variation related to the small signal modulation response where the peak amplitude occurs at a frequency f_R determined by the overdrive above threshold. In the lasers described here, f_R varies from about 100 MHz just above threshold to 1000 MHz at the drive current corresponding to the maximum output of 10 mW.

In Figure 3 the rms noise power is plotted against the vertical (light) axis for the two lasers. To represent noise as it would affect a real system, the bandwidth of the noise detection system was limited to 150 MHz. This gives a noise peak near the threshold where the peak of the noise spectrum lies within this bandwidth, and a much lower measured noise at higher currents where the peak is outside the detection bandwidth. In lasers with poor output characteristics, such as (b) in Figure 3, high noise levels or self-pulsing are frequently observed at higher drive currents. Although usually at a high frequency, this noise shows in Figure 3 partly due to poor rejection by the 150 MHz filter at frequencies approaching 1000 MHz. Lasers operating in this region are not suitable for communications applications and are not considered any further. In a well behaved laser the noise amplitude depends on the steepness (incremental efficiency) of the output characteristics and for good devices, such as (a) in Figure 3, is of the order of 10 μW rms at power levels from 1 to 10 mW.

4. LASING SPECTRA

Figure 4 shows the spectrum of a good SiO_2 insulated stripe laser operating c.w. with a power output of a few milliwatts. Although a few minor peaks occur, the main power is concentrated in a single longitudinal mode. This behaviour is typical of good uniform devices although frequently 2 or 3 modes may be present in some current ranges. Non-uniform or self-pulsing lasers often exhibit a broad spectrum but this is not typical.

When the bias current is increased the junction temperature changes and the predominant mode(s) shift to longer wavelengths at about 0.3 nm K^{-1}. There is also a slower wavelength shift of about 0.05 nm K^{-1} by the individual modes but this is insignificant for most systems.

5. LASER EMISSION PATTERNS

In the plane parallel to the junction the controlling factor is the optical guiding by the stripe. Guiding is provided by a combination of gain guiding and carrier concentration profile guiding (KIRKBY, P.A. et al 1977) as indicated by the beam astigmatism; the beam waist in the plane of the junction is displaced outside the laser mirror for 20 μm wide stripes and inside for 10 μm wide stripes because the nature of the emission is not that of a plane wave. An experimentally measured far-field pattern is shown in Figure 5. The full width to half intensity is about 5° in this sample and over the power range up to 10 mW the emission is all in the zero order mode.

6. MODULATION

6.1. Analogue Modulation

When a laser is biased continuously above threshold and a small modulation signal is applied to the current drive, the response can be calculated from the rate equations (IKEGAMI, T. et al 1970). The response is expected to show a resonance-like behaviour as a result of the interaction between the photon population and injected carrier concentration. The resonance frequency f_R at a drive current I is approximately given by

$$f_R = \frac{1}{2\pi}\left(\frac{1}{\tau_n\,\tau_s}\,\frac{(I-I_t)}{I_t}\right)^{\frac{1}{2}} \qquad \text{.... (1)}$$

where

τ_n - electron lifetime

τ_s - photon lifetime

I_t - threshold current.

An experimentally determined modulation response is shown in Figure 6. The laser, which had a threshold current of 190 mA, was driven with a constant current of 205 mA and superimposed on this was a 12 mA peak-to-peak sinusoidal modulation, swept in frequency from 10 to 1000 MHz. The output was detected using a pin photodiode with a response time of less than 200ps and displayed on a spectrum analyzer. The shape of the response curve is as expected with a flat frequency response up to 500 MHz and a resonance at 700 MHz. The output level is of the order of 1 mW peak-to-peak at lower frequencies.

The frequency of the resonance varied from 100 MHz at 1 to 2 mA above threshold (measured, of course, with a much smaller input signal) to 900 MHz at 215 mA (25 mA above threshold), and the value closely followed the theoretically expected variation given in Equation (1).

Due to the non-linearity of the output characteristic of the SiO_2 insulated stripe laser, significant second harmonic distortion was observed. However, by carefully choosing the operating point this could be kept to -17dB (optical power ratio of 2%) with 1 mW output and -20dB (1%) at lower power levels. Much better linearity would be obtained from different structures such as wider SiO_2 insulated stripe lasers or, for example, the new buried stripe lasers (SELWAY, P.R., 1976).

6.2 Pulse Modulation

Although many modulation techniques have been proposed, the one of most practical interest is that of directly driving the laser with a pulse code modulation (pcm) current.

When a laser is pulsed from below threshold the most significant feature is the appearance of damped oscillations (spiking or ringing) in the light output . This has been treated theoretically and experimentally (IKEGAMI, T. et al 1970 and OZEKI, T. and ITO, T. 1973), and the main results are that:
- oscillation frequency depends on the final degree of overdrive and is related to the small signal resonance at that overdrive level
- for currents near threshold, the decay time of the oscillation is approximately the electron recombination time ($\sim$ 3 to 5 ns)
- amplitude of the output spikes is determined mainly by the change in current imposed by the modulating signal
- lasing delay between the application of a current step and the appearance of the first spike is decreased by increasing the bias current.

The principal features can be seen in the experimental results shown in Figure 7 for an SiO_2 insulated stripe laser driven with a variable dc bias upon which was superimposed a 250 Mbit s^{-1} non-return-to-zero pcm signal. The c.w. threshold was 190 mA and the drive pulse amplitude 24 mA. The top trace, with a bias of 170 mA, shows that lasing only occurs in the longer pulses; the first spike appears with a delay of 5 ns. At 177 mA, spikes are just appearing in the shorter pulses and the delay is reduced to 2 ns. At 183 mA, two spikes can be seen in the shorter pulses and at 200 mA, above threshold, the modulated light output is an excellent replica of the input signal.

Modulation at higher frequencies requires care since spiking will occur at frequencies comparable to the modulation frequency. Under these conditions it may be possible to use the spiking phenomenon to obtain the required response (FARRINGDON, J.C. and CARROLL, J.E. 1975).

6.3. Effect of Modulation on Lasing Spectrum

It has been reported (IKEGAMI, T., 1975) that lasers show a very broad spectrum during the first few nanoseconds of the output pulse when modulated with a step increase in current from below threshold. This is due to the considerable upward swing in electron density in the time intervals between the output spikes which causes a larger number of longitudinal modes to have above threshold gain than would occur during steady lasing.

Figure 8(b) shows the lasing spectrum measured during an output pulse obtained by applying a 2 ns, 40 mA pulse superimposed on a dc bias just below threshold. At least 15 modes are excited giving a spectral band width of 3 nm. Figure 8(a) shows the spectrum obtained with the same input pulse superimposed an a dc bias current slightly above threshold. The spectrum in Figure 8(a) is almost identical with the normal c.w. spectrum, except that the mode intensity is increased by the increase in drive current. With a real code modulation drive, transients and short term temperature drifts cause some broadening and variation in the peak wavelength. Experiments show that with present lasers, the broadening and drift are contained within an envelope about 1 nm wide, the maximum variation being observed between a long sequence of 1's and a sequence of 0's. These results show that, for wide band systems, careful control of the bias level is necessary to ensure that the laser is always just above threshold to avoid serious broadening of the spectral bandwidth during fast pulsing. Since this condition is also necessary to eliminate variable delay and patterning effects it would appear that a bias control loop based on the measured laser output will be necessary.

7. LASER RELIABILITY

Over the past few years, the degradation mechanisms which seriously limited the life of early c.w. lasers have been widely studied. Much has been written about degradation effects and it is now clear that the main cause of the short lives of earlier devices was the formation and growth of dark line defects, or related effects. These are areas which appear dark when the device is operated as a spontaneous emitter and viewed with an infrared microscope.

Present evidence indicates that dark line defects are initiated at crystal defects in the active region and that their rate of growth depends, among other things, on residual mechanical strain in the device. In the devices life tested at STL, every effort has been made to eliminate crystal defects and to use processing techniques that minimized any residual mechanical strain. The main factors in avoiding crystal defects are:
- choice of low dislocation substrates
- avoidance of scratching or other damage during processing and epitaxial growth
- avoidance of oxygen contamination during epitaxy.

The techniques used to minimize residual strain are:
- use of 5% Al in the active layer
- avoidance of alloyed metal contacts near the junction
- use of a soft metal (indium) for heat sink bonding.

Using these measures many batches of lasers have been made and representative samples were life tested. Figure 9 shows the variation in threshold currents with c.w. operation time; the laser currents were adjusted to give a constant 3 to 5 mW output. The consistency of the results is indicated by the fact that 85% of all the lasers tested to date with the exception of early unoptimised samples have shown degradation rates $\frac{dI_t}{dt}$ of between 0.3% and 5% per 1000 hours.

The longest running life tests have reached 15 000 hours and, with one laser excepted, an entire batch of twenty lasers has now exceeded 10 000 hours with typical threshold increases of from 10 to 20%. A reasonable estimate of time to failure is taken to be the time for threshold to increase 50% assuming a linear variation with time. On this basis it is tentatively predicted that half of all lasers made will exceed 23 000 hours operation at room temperature.

These results show that, by careful materials growth and processing, it is already possible to make lasers with lives consistently greater than 10 000 hours. Considerable work is still required to identify the residual slow degradation mechanisms but the devices are already reliable enough for many systems.

8. CONCLUSIONS

This paper has described the fabrication and operating characteristics of SiO_2 insulated stripe geometry double heterostructure GaAs/(GaAl)As lasers. These devices were designed specifically for coupling to optical fibres of 10 to 20 μm core diameter and are particularly suitable for pcm modulation at bit rates greater than 100 Mbit s^{-1}. Within certain limitations on linearity they are also suitable for analogue modulation up to about 500 MHz. By carefully selecting the substrates and using the latest growth and processing techniques a high proportion of these lasers have operating lives of 10 000 hours or more, and are thus suitable for many existing applications.

9. REFERENCES

DE LOACH, B.C., HAKKI, B.W., HARTMAN, R.L., and D'ASARO, L.A., 1973, "Degradation of CW GaAs Double-Heterojunction Lasers at 300K", Institute of Electrical and Electronics Engineers Proceedings volume 61, no 7, pp 1042-44.

FARRINGDON, J.C. and CARROLL, J.E., 1975, "Trappatt Modulation of GaAs Stripe Lasers", Conference on Active Semiconductor Devices for Microwaves and Integrated Optics, School of Electrical Engineering, Cornell University, 19-21 August. (No proceedings published.)

GOODFELLOW, R.C., 1974, "High Radiance, Small Area Gallium Arsenide Lamps", Proceedings of the Electro-Optics International Conference, Brighton, 19-21 March, pp 168-172.

GOODWIN, A.R., PETERS, J.R., PION, M., THOMPSON, G.H.B., and WHITEAWAY, J.E.A., 1975, "Threshold Temperature Characteristics of Double-Heterostructure $Ga_xAl_{1-x}As$ Lasers", Journal of Applied Physics, volume 46, No 7, pp 3126-3131.

HARTMAN, R.L. and DIXON, R.W., 1975, "Reliability of DH GaAs Lasers at Elevated Temperatures", Applied Physics Letters, volume 26, no 5, pp 239-242.

IKEGAMI, T., 1975, "Spectrum Broadening and Tailing Effect in Directly Modulated Injection Lasers", Proceedings of the Conference on Optical Fibre Communication, London, 16-18 September. London, Institution of Electrical Engineers, Conference Proceedings No. 132, pp 111-113.

IKEGAMI, T., KOBAYASHI, K., and SUEMATSU, Y., 1970, "Transient Behavior of Semiconductor Injection Lasers", Electronics and Communications in Japan, volume 53-B, No 5, pp 82-89.

KIRKBY, P.A., GOODWIN, A.R., THOMPSON, G.H.B., and SELWAY, P.R., 1977, "Observations of self-focussing in Stripe Geometry Lasers, to be published in IEEE-QE Special Issue on Lasers.

OZEKI, T. and ITO, T., 1973, "Pulse Modulation of DH-(GaAl)As Lasers", Institute of Electrical and Electronics Engineers Journal of Quantum Electronics, volume QE-9, no 2, pp 388-391.

SELWAY, P.R., 1976, "Semiconductor Lasers for Optical Communications", Institution of Electrical Engineers Proceedings, volume 123, no 6, pp 609-618.

YONEZU, H., SAKUMA, I., KAMEJIMA, T., UENO, M., NISHIDA, K., NANNICHI, Y., and HAYASHI, I., 1974, "Degradation Mechanism of (Al.Ga)As Double-Heterostructure Laser Diodes, Applied Physics Letters, volume 24, no 1, pp 18-19.

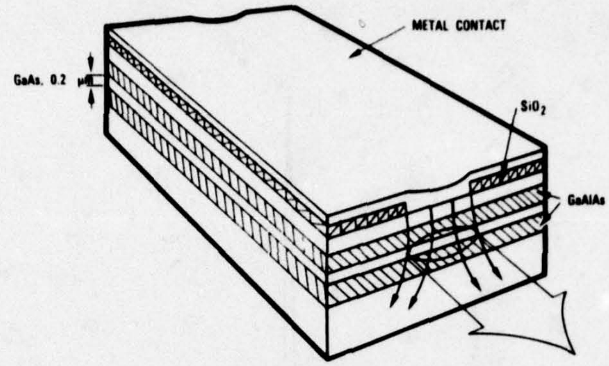

Figure 1 - Structure of an SiO_2 insulated stripe geometry double-heterostructure laser.

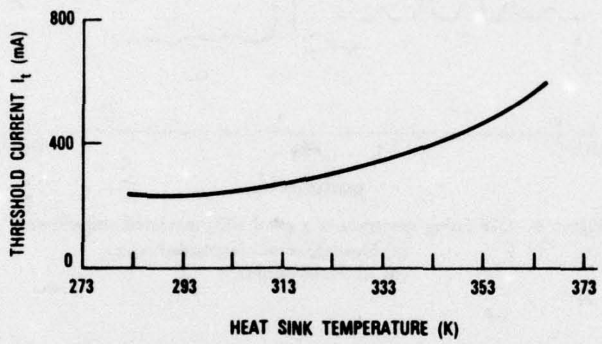

Figure 2 - Variation of CW *threshold current* with heat sink temperature for an SiO_2 insulated stripe laser.

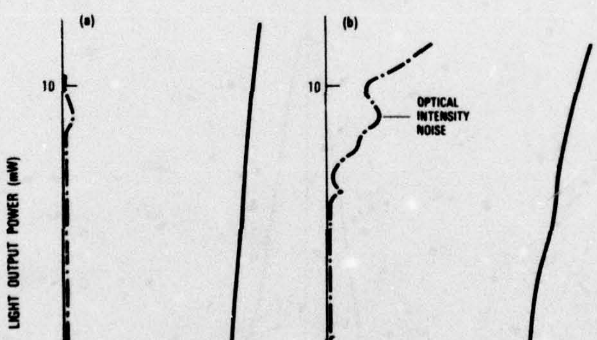

Figure 3 - Light-current characteristics of CW stripe lasers. Also shown is the noise amplitude measured as a function of CW light output: the detection bandwidth was 150 MHz.
(a) Well behaved device
(b) Nonuniform device.

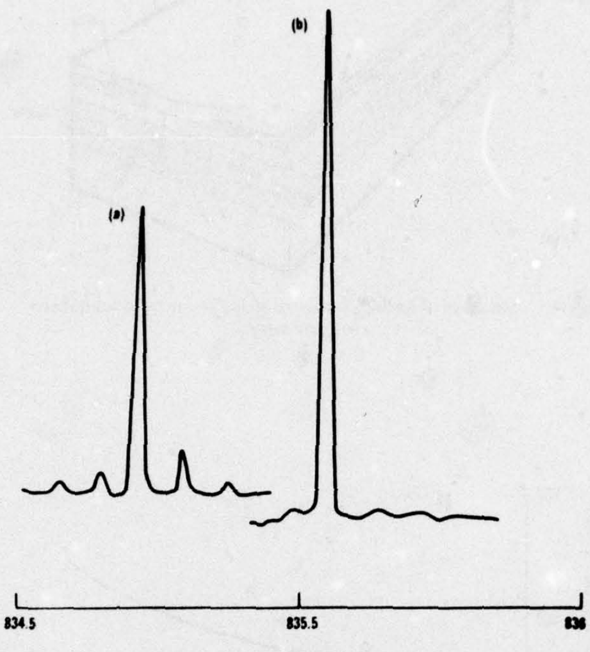

Figure 4 - CW lasing spectrum of a good SiO_2 insulated stripe laser.
(a) Near threshold (expanded scale)
(b) At 5 mW output.

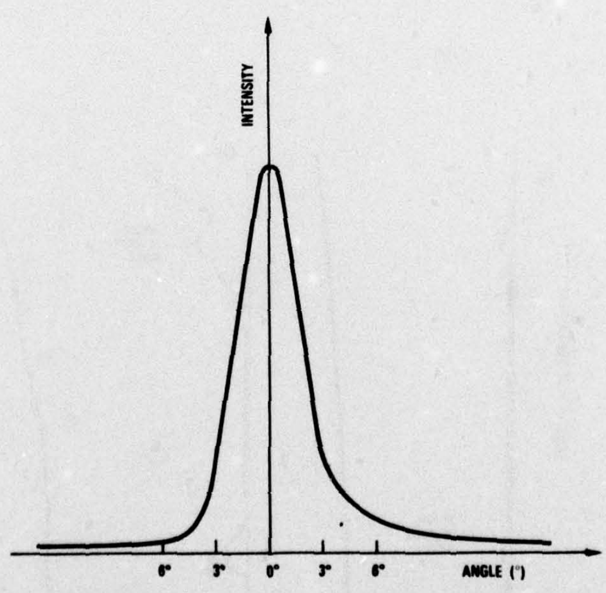

Figure 5 - Emission polar far field pattern parallel to the junction. In the power range up to 10 mW the emission is all in the zero order mode.

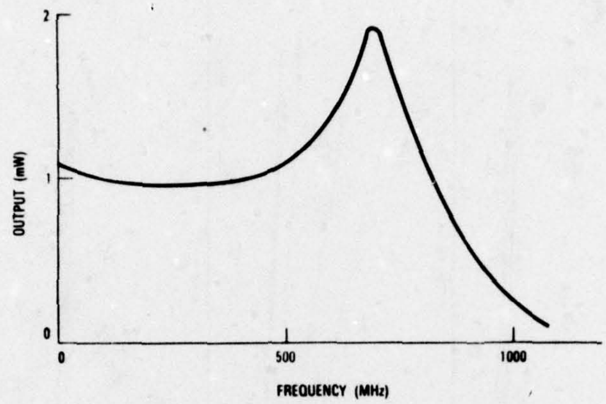

Figure 6 - Experimental frequency response of an SiO_2 stripe laser with a sinusoidal modulation of 12 mA peak-to-peak and a 205 mA bias.

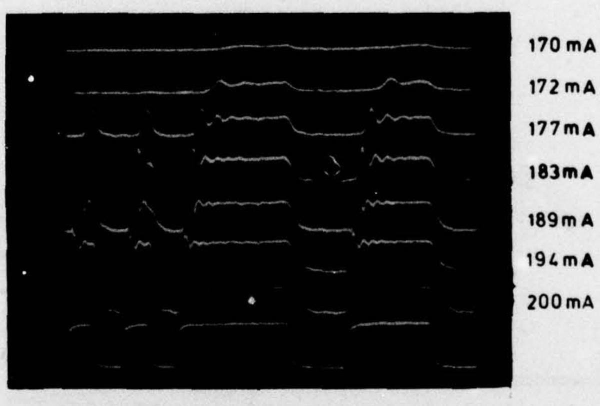

Figure 7 - Response of an SiO_2 stripe laser to 250 Mbit s^{-1} modulation for various DC bias levels. Modulation current is 24 mA (shown on bottom trace). Horizontal scale is 5 ns per division and the vertical scale 5 mW per division.

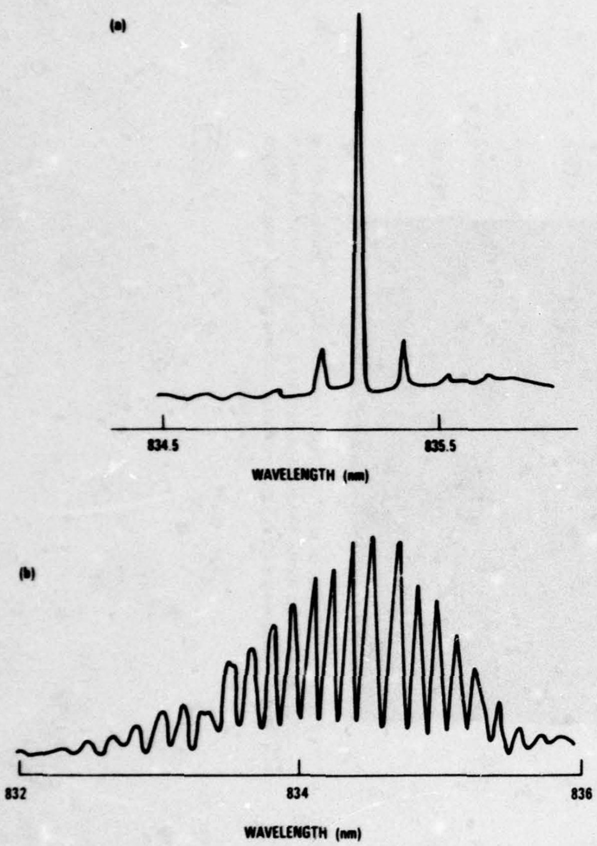

Figure 8 - Lasing spectrum of an SiO_2 stripe laser measured during a 2 ns pulse: 40 mA pulse amplitude.
(a) DC bias just above threshold
(b) DC bias just below threshold.

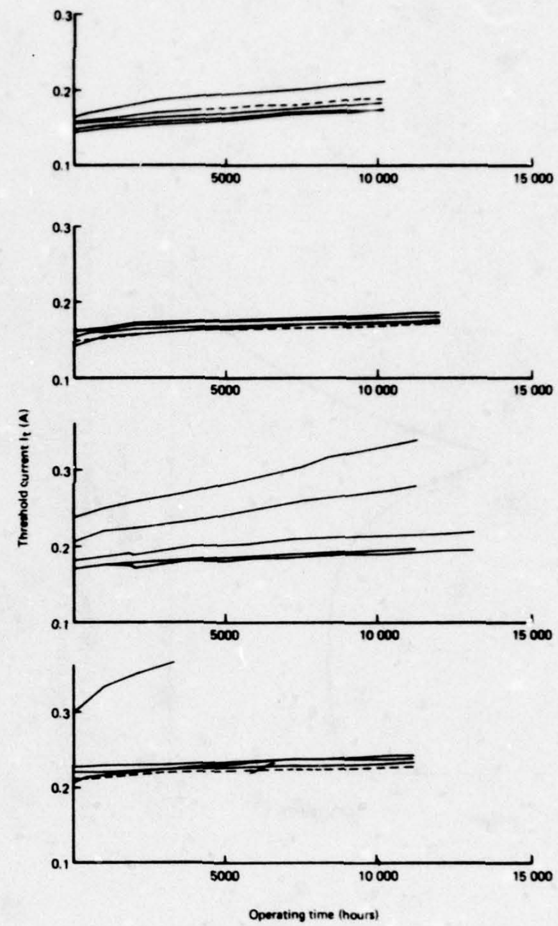

Figure 9 - Variation of threshold current with operating time for a number of SiO_2 stripe lasers. The laser currents were continuously adjusted to maintain a CW power output of 3 to 5 mW.

Design and fabrication of GaAs light emitting diodes for optical communication systems with high transmission capacity

W. Huber, J. Heinen, W. Harth
Lehrst. f. Allg. E.-technik, TU München, Arcisstr. 21, D-8000 München, W. Germany

Abstract

The physical mechanism of the time and frequency behaviour of LED's is investigated. As a result, it is demonstrated that two time constants, the electron life-time and the time constant due to the diode's space-charge capacitance, govern the high frequency performance of a LED. A model is presented which describes the influence of the relevant technological LED parameters (layer structure, active area, active layer width and doping) on the time and frequency behaviour by means of these time constants. The technological and physical factors, which represent the ultimate limitation of the modulation bandwidth, are discussed. Based upon this model, the design concept of a practical LED with a very high modulation bandwidth is described. Measurements of the frequency characteristic, the light power output and the spectral characteristic have been carried out. In addition the AM-noise behaviour is investigated. The transmission rate and the maximum length of an optical communication system using such high speed LED's is estimated.

Light emitting diodes (LED's) are already employed as directly modulated light generators in practical fiber-optic communication systems. Until now the transmission capacity of these systems is still moderate, mainly because of the restricted bandwidth of the LED's. In this paper the theoretical and technological principles of high speed LED's will be shown. Also the properties of a diode, which can be modulated up to the GHz-range, are given. The transmission rate and the maximum length of an optical communication system using such a high speed device are estimated.

According to theoretical and experimental investigations the time and frequency response of light emitting diodes is governed by two time constants: the electron lifetime τ_n in the active volume and a time constant τ_{sp} due to the space-charge capacitance C_{sp}. The frequency dependence of the light amplitude ϕ_1 can be expressed as

$$\phi_1 \sim \frac{1}{1 + j\omega\tau_n\left(1 + \frac{\tau_{sp}}{\tau_n} G\sqrt{1+j\omega\tau_n}\right)} \qquad (1)$$

G is an impedance factor considering the finite active layer width of the diode and τ_{sp} is given by

$$\tau_{sp} = \frac{kT}{qI_o} C_{sp} \qquad (2)$$

where kT is the thermal energy and, I_o is the bias current. Equ. (1) in this form is valid only for single- and double-heterostructure LED's. In diodes with homostructure the nonradiactive recombination at the active layer surface and at the interface between active layer and the contact reduces the effective electron lifetime

$$\tau_{eff} = F(w/L_n)\,\tau_n \qquad (3)$$

as compared with the bulk lifetime τ_n. The reduction by the factor

$$F(w/L_n) = 1 - \mathrm{sech}(w/L_n) \quad (4)$$

depends on the ratio of the thickness of the active layer w to the elctron diffusion length L_n. If w is small compared to L_n a considerable reduction of the effective lifetime τ_{eff} is achieved. For example, at a doping level of the "active region" of $10^{19}cm^{-3}$ which corresponds to a bulk electron lifetime of about 1ns, the effective lifetime becomes only a few hundred picoseconds, if the layer thickness is reduced to 1µm. It can be deduced from this theoretical considerations that modulation in the GHz-range is possible if the negative influence of the space-charge capacitance can be suppressed.

However, it should be pointed out that the light power output of homostructure diodes is decreased by the same factor F.

For the design of a high-speed LED two requirements can be deduced from equ. (1)-(4). It is that both time constants τ_{eff} and τ_{sp} must be kept small. A short electron lifetime τ_n is achieved by using a high doping level in the active region. But a limitation is given at about $2 - 3 \cdot 10^{19}cm^{-3}$ because of the essential broadening of the halfwidth of the light spectrum and the decreasing efficiency at higher doping levels. As mentioned earlier, further reduction of the effective electron lifetime is achieved by using a homostructure with a thin active layer. The layer thickness is limited to a few tenth of a micron in using a liquid phase epitaxy. However, with respect to reasonable light power output an active layer thickness less than half a micron is undersirable.

A low value of τ_{sp} which corresponds to a low space-charge capacitance is achieved by keeping the diode area small. Technologically areas corresponding about 20µm in diameter should be possible. But very small areas lead to high current densities and therefore severe heatsinking problems. An area corresponding to a diameter of about 40 - 60µm seems to be realistic. For better heattransfer an upside down technique must be used where the p, n-junction is near the heatsink.

The space-charge capacitance is also kept small by widening the space-charge region by using low doping levels both in the n- and the active p-layer. However, a low doped active layer is disadnantageous with respect to short electron lifetime. Therefore, only the doping level in the n-region can be lowered. To prevent undesired hole injection at low doping levels of the n-region a wide-gap emitter consisting of $Al_xGa_{1-x}As$ can be choosen. By these means an electron injecting layer with a doping level of only $10^{16}cm^{-3}$ can be used.

Liquid phase epitaxy two layer structures n-$Al_{0,4}Ga_{0,6}As$: p-GaAs with doping levels $n = 5 \cdot 10^{16}cm^{-3}$ and $p = 1,5 \cdot 10^{19}cm^{-3}$ respectively have been grown. The layer-thickness of the active p-layer was 1,2µm and 2µm. From these wafers LED's were fabricated having a geometry as shown in Fig. 1. This is a wellknown typ of LED proposed by Burrus[1] using an upside down technique with an integrated heatsink. An etched hollow at the substrate side minimizes the absorption losses and allows an easy coupling of the diode with the fibre. The small active area corresponding to a diameter of 50 µm has been formed by using proton bombardment. During the bombardment of protons with an energy of 300 keV at a dosis of $2 \cdot 10^{15}cm^{-2}$ the active area is protected by a goldmask. Outside the active area the crystal becomes isolated within a depth of about 3µm. This means that the isolation reaches throughout the p-n junction. Therefore, proton bombardment is a suitable technique to meet the requirements concerning small junction areas with respect to small space-charge capacitance.

These diodes as above were mounted into a microwave package and allow contineous operating with current densities up to 20 000A/cm^2. At a current of 100mA the emitted light power output becomes about 350µW and 200µW for a active layer thickness of 2µm and 1,2µm, respectively. As can be seen from these data light power output strongly depends on the active layer width for this typ of high speed LED's.

Optical transmission of high data rates over a relatively long distance require not only reasonable high light power output of the LED. Also the spectral halfwidth of the emitted light should be as small as possible because of the fibre dispersion to avoid severe limitation in transmission length or data rate. The typical linewidth of these diodes was 35nm.

Measurements of the time and frequency behaviour showed that the high speed characteristic of these diodes is considerably improved by reducing the thickness of the active layer. The rise time (0 - 80%) in light power output was about 1ns at a thickness of 2µm and was only a few hundred picoseconds at a thickness of 1,2µm. The corresponding 3dB cutoff frequencies were 500MHz and 1100MHz, respectively. The modulation measurements were performed with a current amplitude of 30mA superimposed on a bias current of 60mA. Furthermore, these results show that for both diodes the product of light power output and bandwidth is nearly constant.

The AM noise behaviour of these LED's has also been investigated. The optical fluctuations of there light output have been measured at frequencies between 100Hz and 100kHz. For measurement, the diodes were biased with a filtered battery. The emitted light P_o = 100µW was detected by a PIN-photodiode. The result is shown in Fig. 2. The measured noise, which exhibits a 1/f-type frequency dependence, becomes equal to the shot noise limit of the detector below 1kHz. This means that for application the LED noise behaviour is uncritical. For comparison the typical 1/f-noise characteristic of a cw double heterostructure laser reaches up to 100kHz.

By using a $Al_xGa_{1-x}As$ crystal with various Al-content for the active region LED's with wavelengths in the range of 780nm to 870nm have been realized. These diodes nearly show the same time behaviour as compared with GaAs diodes at 890nm ($x = 0$). But as will be shown below it is not necessary to adapt the emitted wavelength of the LED to the minimum attenuation of the fibre (at about 840nm), because the limitation in the transmission capability is primarily caused by fibre dispersion and not by fibre attenuation.

For application it is interesting to know the transmission rates and distancos which can be achieved by these high speed LED's. A limitation is given by the attenuation and dispersion of the fibre. Using a pulse modulated system the following assumptions are made: The halfwidth of the emitted light is 35nm. The diodes are pulsed by 150mA current peaks. The fibre is of gradient index type with an attenuation of 5dB/km and a material dispersion of 1,7ns/km. The coupling efficiency of light into fibre is 5%. A fast photo avalanche diode is used as detector. The signal to noise ratio at the detector should be 30dB. Under these conditions a transmission rate of 1Gbit/s is possible for distance up to 250m. A 1km system could be opertated up to 300Mbit/s.

The calculations show that the capability of the fibre system is not limited by the light power output of the diode but by its linewidth together with the fibre dispersion. To improve the transmission rate diodes with smaller emission lines and fibre with lower dispersion are necessary.

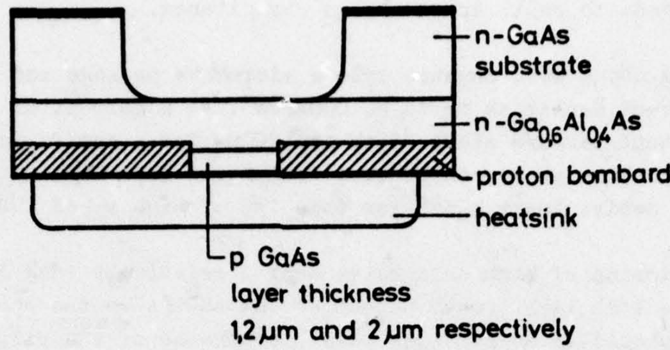

Fig. 1: Cross-sectional view of LED

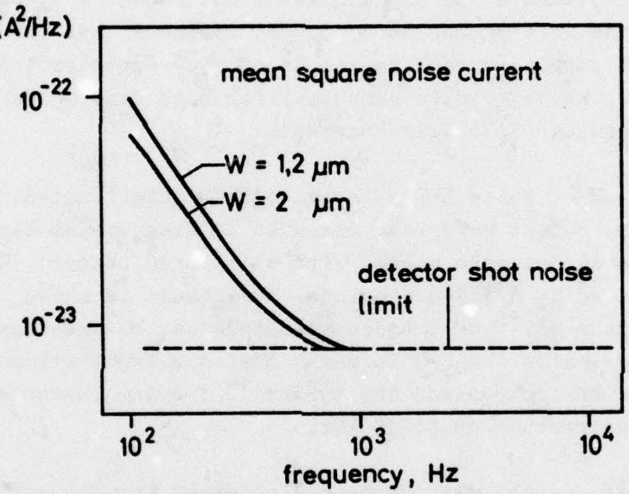

Fig. 2: AM-noise of light power output

Reference:

/1/ Burrus, C.A., Miller, B.I.: "Small-area, double-heterostructure GaAlAs-electroluminescent diode sources for optical-fibre transmission lines", Opt. Commun., 1971, 4, pp. 307 - 309

PHOTODIODES A AVALANCHE AU SILICIUM A GRANDE RAPIDITE POUR SYSTEMES DE COMMUNICATIONS OPTIQUES

G.RIPOCHE, M.BRILMAN
Laboratoires de Marcoussis, Centre de Recherches de la COMPAGNIE GENERALE D'ELECTRICITE.

Route de Nozay

91460 - MARCOUSSIS
FRANCE

RESUME

Les photodiodes à avalanche au silicium sont actuellement les détecteurs les mieux adaptés pour répondre aux besoins des communications optiques aussi bien dans la bande spectrale 800 - 900 nm qu'à 1060 nm. Deux structures de diodes ont été étudiées : la structure $P^+\pi PN^+$ classique et la structure $P^+\pi P\pi N^+$ à couche P enterrée obtenue par implantation ionique à haute énergie, chaque structure pouvant être réalisée sur substrat homogène ou sur substrat épitaxié en fonction des performances recherchées. Après la description du procédé de réalisation des deux structures, les résultats obtenus concernant le gain utile, la sensibilité et la rapidité seront présentés. La comparaison des résultats montre que la structure $P^+\pi P\pi N^+$ à couche P enterrée permet d'obtenir sur substrat épitaxié des dispositifs très performants dans la bande spectrale 800 - 900 nm (gain utile $\sim$ 50, temps de montée et temps de descente $<$ 0,5 ns, sensibilité globale à λ = 850 nm : S = 25 A/W) selon un procédé de réalisation très simplifié.

1. INTRODUCTION

L'intérêt croissant porté aux systèmes de communications par fibres optiques, dû aux progrès effectués dans la réalisation des fibres optiques à faible perte et à faible dispersion et dans celle des sources émettrices continues (DEL, diodes laser), a entraîné un besoin en photodétecteurs particulièrement bien adaptés pour répondre aux exigences d'un domaine encore en pleine évolution. Actuellement, les détecteurs au silicium sont les mieux placés grâce à l'avance technologique dont ils bénéficient. Pour les applications à faible niveau et faible débit d'informations (2 Mb/s et 8 Mb/s), les photodiodes PIN permettent de réaliser des modules récepteurs à hautes performances. Mais pour les applications à faible niveau et à moyen ou grand débit d'informations (30 Mb/s, 140 Mb/s et au-delà), l'emploi des photodiodes à avalanche rapides s'impose en raison de l'amélioration importante du rapport signal sur bruit due au gain interne de la diode (MILLER, S.E., 1973).

Les photodiodes à avalanche de structure $P^+\pi PN^+$ (fig 1) sont présentement les plus performantes car elles cumulent les avantages des photodiodes à avalanche N^+P classiques (le gain) et ceux des photodiodes PIN (sensibilité intrinsèque élevée, grande rapidité) (RUEGG, H.W., 1967). La zone de charge d'espace de telles diodes se compose de deux régions adjacentes : l'une relativement étroite où règne un champ électrique intense dans laquelle prend place la multiplication des porteurs injectés, l'autre plus ou moins étendue à champ faible où les porteurs sont collectés. C'est cette séparation des rôles de multiplication et de collection qui assure des produits gain-largeur de bande élevés à ces dispositifs.

Après un bref rappel des principales propriétés de ces photodiodes à avalanche et de leur principe de fonctionnement, nous présenterons les structures étudiées et décrirons leurs procédés de réalisation. Enfin, la comparaison des résultats expérimentaux permettra de choisir la structure de diode la mieux adaptée pour une application donnée.

2. PROPRIETES DES PHOTODIODES A AVALANCHE $P^+\pi PN^+$

L'utilité des photodétecteurs à avalanche dans un système de communications optiques est déterminé par les propriétés suivantes :

- la sensibilité intrinsèque
- le temps de réponse
- le facteur de multiplication
- le bruit apporté par le détecteur.

Nous allons maintenant reprendre chacun de ces points en cherchant à faire apparaître les problèmes posés par l'optimisation du détecteur.

2.1. Sensibilité intrinsèque

La sensibilité intrinsèque d'une photodiode dépend avant tout du coefficient d'absorption du rayonnement détecté et de la longueur du trajet lumineux dans la zone active. Il est généralement admis que celle-ci doit avoir une largeur au moins égale à la longueur d'absorption du rayonnement incident pour assurer une bonne sensibilité intrinsèque. Or, cette longueur d'absorption qui est d'environ 15 µm à λ = 850 nm passe à environ 250 µm pour λ = 1060 nm (DASH, W.C., 1955.) Il en résulte que la réalisation de dispositifs très sensibles sera rendue plus aisée pour les applications dans la bande 800-900 nm que pour celles à 1060 nm.

Enfin, dans tous les cas, le dépôt d'une couche antireflet au nitrure de silicium centrée sur la longueur d'onde utilisée permet une réduction importante des pertes à l'interface air-silicium, pertes qui sont de 30% en l'absence d'une telle couche.

.../

2.2. Temps de réponse

Les limitations du temps de réponse des photodiodes à avalanche sont les suivantes :

- le temps de transit des porteurs dans la zone de charge d'espace.
- le temps de diffusion nécessaire aux porteurs créés hors de la zone de charge d'espace pour atteindre celle-ci.
- enfin, le temps de mise en avalanche lié au phénomène de multiplication des porteurs.

Généralement, cette dernière limitation n'intervient qu'aux fortes valeurs de multiplication (KANEDA, T., 1975). Les derniers résultats expérimentaux conduisent à un temps de mise en avalanche inférieur à 100 ps pour un facteur de multiplication M = 100.

Pour obtenir des dispositifs performants, il faut absolument rendre négligeable la contribution des porteurs qui atteignent la zone de charge d'espace par diffusion, ce dernier processus étant particulièrement lent. D'où la nécessité de travailler en régime de déplétion totale.

Enfin, le temps de transit des porteurs dans la zone de charge d'espace sera rendu minimum si le champ électrique dans la zone de collection des porteurs est suffisamment élevé pour entraîner les porteurs à leur vitesse de saturation qui est d'environ 10^7 cm/s. Une estimation grossière permet d'évaluer le temps de transit à environ 1 ns pour 50 µm d'épaisseur de zone active.

Dans de telles conditions, il sera possible de réaliser des photodiodes à bonne sensibilité et grande rapidité dans la bande spectrale 800 - 900 nm avec une épaisseur de zone active égale à 20 µm. L'utilisation de substrats à zone active d'épaisseur $\leqslant$ 50 µm conduira à une sensibilité élevée mais à une rapidité moyenne. Par contre, à λ = 1060 nm, la sensibilité intrinsèque sera faible si l'on cherche à obtenir des temps de réponse inférieurs ou de l'ordre de 1 ns.

2.3. Facteur de multiplication

Sous l'action d'un champ électrique intense, les porteurs primaires traversant la zone de charge d'espace peuvent acquérir une énergie suffisante pour ioniser lors de chocs les atomes du réseau cristallin créant ainsi des paires électron-trou secondaires. Celles-ci à leur tour peuvent être accélérées suffisamment et provoquer des ionisations en cascade..Par conséquent, un seul photon absorbé dans la zone active peut ainsi donner naissance à un photocourant important par effet d'avalanche. Le facteur de multiplication croît rapidement avec la tension appliquée dans le cas d'une jonction N^+P car les coefficients d'ionisation des porteurs varient exponentiellement avec le champ électrique. De plus, dans le silicium, le pouvoir ionisant des électrons étant beaucoup plus grand que celui des trous, le facteur de multiplication sera d'autant plus élevé que la proportion des électrons dans le courant primaire injecté sera importante.

Aussi, pour assurer une multiplication élevée, la zone d'avalanche s'étendra-t-elle seulement dans la couche P, la zone de collection occupant toute la couche π . Pour les longueurs d'onde utilisées ici, l'injection du rayonnement incident peut se faire indifféremment côté N^+ ou côté P^+ dans le cas de couches N^+ et P^+ superficielles.

Enfin, la séparation de la zone active en deux régions adjacentes, la zone d'avalanche et la zone de collection, entraîne une variation moins rapide de la multiplication en fonction de la tension appliquée, comme on le verra plus loin.

2.4. Bruit de multiplication

Le bruit de multiplication lié au caractère statistique du phénomène d'avalanche dépend de la valeur du champ électrique et de sa distribution dans la région d'avalanche. L'analyse du comportement en bruit des photodiodes à avalanche a été faite par Mc INTYRE, R.J., 1966. Il a montré que le rapport $k = \frac{\beta}{\alpha}$, où α, β sont respectivement les coefficients d'ionisation des électrons et des trous, joue un rôle essentiel. En particulier, le facteur d'excès de bruit F, défini par la relation (1) :

$$i^2 = 2\,q\,I_o\,M^2\,F \qquad (1)$$

où I_o est le courant primaire injecté, est le plus faible si les porteurs injectés ont le plus fort coefficient d'ionisation. Ainsi, dans le cas du silicium, le facteur d'excès de bruit s'exprime par la relation (2) pour une injection d'électrons seuls :

$$F = M \left[1 - (1-k)\left(\frac{(M-1)}{M}\right)^2\right] \qquad (2)$$

Cette relation montre que pour diminuer F pour une valeur de multiplication donnée M, il est nécessaire de réduire la valeur de k. Ceci peut être obtenu par un abaissement du champ électrique dans la région d'avalanche.

3. PRINCIPE DE FONCTIONNEMENT

Le fonctionnement des photodiodes à avalanche de structure $P^+\pi PN^+$ classique est illustré sur la figure 2 où sont représentés le profil de concentration, la distribution du champ électrique pour 3 tensions de polarisation et une courbe de multiplication typique. Aux faibles tensions de polarisation la zone de charge d'espace est confinée dans la couche P. Lorsque la tension augmente, l'extrêmité de la zone de charge d'espace se déplace jusqu'à atteindre la couche π pour une tension appliquée V_o, juste avant le claquage par avalanche de la jonction N^+P. Le facteur de multiplication atteint typiquement une valeur de 10 à 30 en ce point. Pour toute tension supérieure à V_o, la zone de charge d'espace s'étend à travers toute la couche π faiblement dopée. Tout accroissement de tension par rapport à V_0 se trouve pratiquement réparti aux bornes de la couche π et y établit un champ électrique presque constant.

Si l'épaisseur de la couche π est grande par rapport à celle de la couche P, le champ électrique à la jonction N^+P variera peu pour toute tension appliquée supérieure à V_0. La caractéristique de multiplication M (V) présente ainsi un "palier", typique du fonctionnement d'une telle structure.

Il faut remarquer que généralement le point de fonctionnement d'une telle diode est situé bien au-delà du "palier" afin de bénéficier d'une multiplication élevée.

L'obtention de façon reproductible des caractéristiques de multiplication M (V) souhaitées suppose que l'on sache contrôler avec une bonne précision ($\pm$ 10%) les profils de concentration des couches N^+ et P. En effet, si la couche P est trop large, le claquage de la jonction N^+P intervient avant l'extension de la zone de charge d'espace dans la couche π (fig 2 c, courbe 1) ; si elle est trop étroite, l'extension dans la couche π intervient trop tôt et la multiplication reste faible jusqu'à des valeurs de tension très élevées (fig 2 c, courbe 3).

4. STRUCTURES $P^+\pi PN^+$ ETUDIEES

Le technologue dispose de nombreuses possibilités quant à la réalisation des diodes de structure $P^+\pi PN^+$. Entre le choix de la nature de la jonction N^+P et celui des divers profils de concentration permis par les moyens de dopage actuels, il existe de nombreuses combinaisons possibles, même si actuellement l'implantation ionique est pratiquement l'unique technique employée pour le dopage des couches P. En effet, l'implantation ionique présente par rapport aux techniques conventionnelles de diffusion ou d'épitaxie des avantages d'intérêt primordial : la reproductibilité et le contrôle suffisamment précis de la quantité de charges d'une part et de l'énergie d'implantation d'autre part.

La recherche de dispositifs à faible [illegible]it généralement à adopter des structures à champ électrique maximum le plus faible possible, comp[illegible]ec les techniques de dopage disponibles. Pour notre part, nous avons opté pour les solutions su[illegible] :

- couche P à profil de concentrati[illegible]n gau[illegible]g 3) obtenu par implantation suivie d'une diffusion longue.
- couche P enterrée (fig 4) obtenue par implantation à haute énergie

avec des jonctions N^+P abruptes dans les deux cas.

La structure $P^+\pi PN^+$ classique a donné lieu à des réalisations très variées. Citons, parmi d'autres celles de WEBB, P.P, 1974, de BERCHTOLD, K., 1975, de BOCH, R., 1976, qui présentent chacune leur propre intérêt. Cherchant à réaliser un dispositif travaillant sous une tension moyenne ($<$ 200 V) nous avons été amenés en conséquence à choisir une valeur de tension $V_0 \simeq$ 50 V . Une simulation sur ordinateur nous a ensuite permis de préciser les conditions expérimentales de l'implantation et de la diffusion. Cependant, l'abaissement de la valeur de la tension V_o entraîne un accroissement du champ électrique d'avalanche et donc une dégradation du facteur d'excès de bruit.

La structure $P^+\pi P\pi N^+$ à couche P enterrée (LECROSNIER, D., 1975) offre l'avantage d'une région d'avalanche très étendue où règne un champ électrique constant relativement faible ($\sim 3.10^5$ V/cm). Cette couche P enterrée est très avantageusement réalisée par une implantation ionique à haute énergie ($\sim$1 MeV), la position et la concentration maximale de la couche ne dépendant respectivement que de l'énergie d'implantation E_0 et de la dose implantée Q.

Les simulations effectuées sur ordinateur avec un profil caricatural (fig 4 c) montrent l'influence des divers paramètres sur la caractéristique M (V) : profondeur xj de la jonction $N^+\pi$, énergie d'implantation E_o, dose implantée Q, concentration N_0 du substrat (fig 5 et 6). On remarquera qu'il suffit d'une variation de $\pm$ 10% de la dose implantée, les autres paramètres restant fixes, pour passer d'une bonne caractéristique à une caractéristique sous-diffusée ou surdiffuée.

Les caractéristiques M (V) calculées pour différentes doses implantées dans le cas d'un substrat épitaxié ne présentent plus de "palier" de multiplication (fig 7).

Cette structure est l'aboutissement d'essais réalisés avec une couche P à concentration constante obtenue par des implantations multiples à différentes énergies. Mais les tolérances sur le couple concentration-épaisseur de la couche P étaient si critiques qu'elles interdisaient toute reproductibilité, ce qui nous a conduit à abandonner ce procédé.

.../

5. REALISATION

Les composants de forme circulaire sont réalisés sur des substrats homogènes de type P faiblement dopés ($N_A \leqslant 2.10^{13}$ atomes. cm^{-3}) ou sur des substrats épitaxiés dont la couche épitaxiale P de concentration $N_A \approx 5.10^{14}$ atomes.cm^{-3} et d'épaisseur 20 μm est déposée sur un substrat P^+. La jonction $N^+\pi$ jouant le rôle d'anneau de garde permet d'éviter les claquages périphériques. L'anneau stoppeur P^+ a pour but de limiter sensiblement les courants de fuite superficiels dus à la couche d'inversion qui se développe à la surface des substrats P faiblement dopés.

Tous les composants sont réalisés en technologie planar pour éviter les problèmes de passivation inhérents à la technologie mésa (BOLLEN, L.J, 1976).

Enfin, les substrats homogènes subissent un amincissement localisé par une attaque chimique avec masquage par résine photosensible afin de ramener la zone active à une épaisseur inférieure à 50 μm.

5.1. Structure $P^+\pi PN^+$ classique

La réalisation de cette structure se fait selon le procédé suivant : après oxydation et diffusion de l'anneau stoppeur P^+, la zone active (couche P) est ouverte par photogravure, puis implantée localement (ions bore, dose $Q = 5.10^{12}$ ions.cm^{-2}, énergie E_o = 100 keV), l'oxyde servant de masque. Puis les charges sont redistribuées par une diffusion de 30 heures à T = 1100°C. Enfin, la jonction N^+P est obtenu par une diffusion phosphore d'une durée plus ou moins longue de façon à obtenir la caractéristique M (V) souhaitée.

5.2. Structure $P^+\pi P\pi N^+$

Après oxydation et diffusion P^+ de l'anneau stoppeur et la couche de reprise de contact, la zone N^+ est diffusée superficiellement (xj $\sim$ 0,3 μm). Puis un film épais ($\sim$10 μm) de résine photosensible servant à masquer l'implantation à haute énergie est déposé sur toute la surface. Après ouverture des zones actives, les plaques sont implantées à la dose souhaitée ($1,2 - 1,8.10^{12}$ ions.cm^{-2}) sous forte énergie (E_o = 1 MeV). Les plaques sont alors nettoyées et les charges implantées sont rendues électriquement actives par un recuit (T = 900°C, 20 mn). Enfin si cela s'avère nécessaire, la tension de claquage est amenée à la valeur souhaitée par des recuits successifs à T = 950°C.

L'emploi de l'implantation à haute énergie simplifie beaucoup le procédé de fabrication en supprimant un traitement thermique à haute température de longue durée.

Des structures analogues ont été récemment décrites dans la littérature, mais leur réalisation fait appel soit à une canalisation dans le direction <110> (KANEDA, T., 1976) peu reproductible, soit à une implantation suivie d'une épitaxie à basse température (KANBE, H., 1976) aboutissant à un dispositif en technologie mésa avec les inconvénients d'une telle technologie.

6. RESULTATS EXPERIMENTAUX

Les conditions expérimentales définies à partir des simulations sur ordinateur nous ont permis de réaliser de façon reproductible des composants d'un diamètre de zone active $\varnothing$ = 150 μm aussi bien sur matériau homogène creusé que sur substrat épitaxié selon les deux structures. La comparaison des résultats obtenus permet de séparer les composants en deux catégories : ceux réalisés sur matériau homogène creusé à forte sensibilité et moyenne rapidité et ceux réalisés sur substrat épitaxié à grande rapidité mais moyenne sensibilité.

6.1. Matériau homogène creusé

Le tableau 1 résume les performances obtenues sur matériau homogène aminci localement (épaisseur de la zone active : < 50 μm).

	$P^+\pi PN^+$	$P^+\pi P\pi N^+$	
Zone active (diamètre)	150	150	μm
Tension de claquage V_B	150 - 200	120 - 180	V
Tension V_o	50	30	V
Courant d'obscurité (0,9 V_B)	< 10	< 10	nA
Capacité	1,0	1,0	pF
Multiplication utile Mu	> 100	> 100	
Sensibilité globale 850 nm	50	50	A/W
1060 nm	7	7	A/W
Temps de montée τ_m	1	1	ns
Temps de descente τ_d	1	1	ns

.../

TABLEAU I.

La figure 8 présente les caractéristiques de multiplication M (V) typiques de chaque structure étudiée. Pour des performances équivalentes, la structure $P^+\pi P\pi N^+$ à couche P enterrée permet d'obtenir des dispositifs à plus faible tension. En effet, on peut aisément obtenir une tension V_0 faible (par exemple V_0 = 30 V) avec un gain Mo relativement élevé (entre 30 et 50) pour une valeur comparable de la pente du "palier" de multiplication. Dans une telle structure, la tension V_0 sur un substrat donné dépend uniquement de l'énergie d'implantation. Soit V_0 = 30V pour E_0 = 1 MeV et V_0 = 50 V pour E_0 = 2 MeV.

La structure à couche P enterrée offre aussi l'avantage d'un champ électrique d'avalanche faible, en raison de la largeur de la région d'avalanche (1,5 µm pour V_0 = 30 V). Aussi, le facteur d'excès de bruit espéré de telles diodes est-il plus faible que celui des diodes de structure $P^+\pi PN^+$ classique.

La sensibilité globale est indépendante de la structure des diodes. Pour une multiplication M_u =100, la sensibilité globale est égale à S = 50 A/W à λ = 850 nm. Cette sensibilité chute à S = 7 A/W à λ = 1060 nm. Cette dernière valeur peut être amenée à S = 10 A/W en centrant bien la couche antireflet. En outre, la sensibilité globale peut être augmentée en métallisant la face opposée à la face par laquelle pénètre le rayonnement.

Le cliché 1 montre une réponse typique de photodiodes creusées localement à une impulsion émise par un laser DHJ $Ga_{1-x}Al_xAs$. Pour une épaisseur de zone active inférieure à 50 µm, les temps de montée τ_m et de descente τ_d sont sensiblement égaux à τ_m, τ_d = 1 ns.

Les courants d'obscurité à la tension de fonctionnement sont inférieurs à $I_0 < 10$ nA. Ces courants sont avant tout d'origine superficielle.

6.2. Substrat épitaxié

Les performances obtenues sur substrat épitaxié sont rapportées dans le tableau 2.

TABLEAU 2.

	$P^+\pi PN^+$	$P^+\pi P\pi N^+$	
Zone active (diamètre)	150	150	µm
Tension de claquage V_B	150 - 200	150 - 300	V
Courant d'obscurité (0,9 V_B)	~ 200	~ 200	pA
Capacité	1,0	1,0	pF
Multiplication utile M_u	80	60	
Sensibilité globale 850 nm	32	25	A/W
1060 nm	2	1,5	A/W
Temps de montée τ_m	< 500	< 500	ps
Temps de descente τ_d	≤ 1000	≤ 500	ps

Les caractéristiques de multiplication M (V) typiques relevées sur les diodes réalisées sur substrat épitaxié (fig 9) ne montrent pas de "palier" de multiplication. Les multiplications utiles sont actuellement plus élevées pour les diodes de structure $P^+\pi PN^+$. Cependant pour les diodes de structure à couche P enterrée, la tension de claquage V_B peut être ajustée dans une très large gamme en jouant sur la dose implantée sans nuire aux performances.

Le facteur d'excès de bruit des structures $P^+\pi P\pi N^+$ est plus faible que celui des structures $P^+\pi PN^+$ comme l'ont confirmé des travaux récents effectués sur des structures très voisines (KANBE, H, 1976) (KANEDA, T., 1976). On peut raisonnablement espérer des valeurs de k proches de k_{eff} = 0,03.

Le cliché 2 présente la réponse à une impulsion émise par un laser DHJ $Ga_{1-x}Al_xAs$ d'une photodiode de structure $P^+\pi P\pi N^+$. Ces diodes remarquablement rapides (τ_m, τ_d < 500 ps) ne présentent pas de composante lente à la descente. Le cliché 3 montre une réponse à une impulsion émise par un laser YAG, de largeur à mi-hauteur de 320 ps. Ces rapidités peuvent être obtenues même à faible valeur de polarisation ($V_p \gg 50$ V).

Pour réaliser des photodiodes de structure $P^+\pi PN^+$ à grande rapidité, il faut conserver la transition à l'interface P/P^+ du substrat épitaxié aussi abrupte que possible et donc limiter au minimum la durée des traitements thermiques à haute température. Les performances obtenues sont alors légèrement inférieures à la descente à celles des diodes de structure $P^+\pi P\pi N^+$. Pour des diffusions très longues (30 heures à T = 1100°C), la descente présente une composante lente d'environ 6 à 8 ns rendant leur utilisation impropre aux applications à grande rapidité.

Les sensibilités globales obtenues à λ = 850 nm sont respectivement S = 32 A/W et S = 25 A/W pour la structure $P^+\pi PN^+$ et la structure $P^+\pi P\pi N^+$. A λ = 1060 nm, les sensibilités tombent à des valeurs faibles (≤ 2 A/W) à cause de la faible épaisseur de la zone active. Une amélioration de la sensibilité par augmentation de l'épaisseur de la couche épitaxiée entraînerait un accroissement de la tension de claquage et un allongement du temps de réponse.

Enfin, les courants d'obscurité à la tension de fonctionnement pour les composants réalisés sur substrat épitaxié sont typiquement de 200 - 300 pA.

.../

7. CONCLUSIONS

Deux types de photodiodes à avalanche pour les applications aux systèmes de communications optiques ont été réalisés selon deux structures différentes. Le premier type réalisé sur substrat homogène creusé est destiné aux applications à faible niveau et moyenne fréquence alors que le second type obtenu sur substrat épitaxié est particulièrement bien adapté aux applications à haute fréquence. Les performances en sensibilité sont très attrayantes dans la bande spectrale 800 - 900 nm où se situent la majorité des sources utilisées dans les communications optiques. La faible sensibilité des diodes à $\lambda = 1060$ nm limite leur utilisation à cette longueur d'onde aux applications à fort niveau. Cependant, une amélioration importante de la sensibilité pourrait être obtenue sur une structure à couche active mince en augmentant le parcours de la lumière dans la zone active par des réflexions multiples (MULLER, 1976).

L'expérience a montré que la réalisation de dispositifs performants était plus aisée sur substrat épitaxié que sur substrat homogène creusé, l'opération d'amincissement localisé étant alors supprimée. Ceci nous a conduit à réserver, sauf cas particuliers, la réalisation des photodiodes à avalanche sur substrat homogène aux applications telles que la télémétrie par laser YAG nécessitant une sensibilité très élevée mais une faible rapidité.

Enfin, les avantages présentés par la structure $P^+\pi P\pi N^+$ à couche P enterrée obtenue par implantation ionique à haute énergie ($E_o = 1$ MeV) : meilleur facteur d'excès de bruit d'une part, simplicité de fabrication d'autre part, nous ont amenés à préférer cette structure à la structure $P^+\pi PN^+$, malgrè la meilleure sensibilité globale offerte par celle-ci.

REMERCIEMENTS

Nous exprimons nos remerciements à Mrs G.PELOUS et D.LECROSNIER du CNET-LANNION qui proposèrent l'idée de la structure $P^+\pi P\pi N^+$ et réalisent les implantations ioniques à haute énergie.

8. BIBLIOGRAPHIE

- BERCHTOLD, K, 1975, "Avalanche photodiodes with a gain-bandwidth product of more than 200 GHz", Appl. Phys. Lett, vol 26, p.585,
- BOCH, R, 1976 " Contribution à l'étude et à la réalisation par implantation ionique de photodiodes à avalanche", Thèse, Grenoble.
- BOLLEN, L.J., 1976, "The avalanche photodiode", Philips Tech Rev, vol 36, p.205
- DASH, W.C., 1955 "Intrinsic optical absorption in single crystal Ge and Si at 77°K and 300°K", Phys. Rev, vol 99, p.1151.
- KANBE, H., 1976 " Silicon avalanche photodiodes with low multiplication noise and high-speed response", I.E.E.E. Trans. Electron Devices, vol ED-23, p.1337,
- KANEDA, T., 1975," Avalanche buil-up time of silicon avalanche photodiodes", Appl. Phys. Lett, vol 26, p.642
- KANEDA, T., 1976, "Excess noise in silicon avalanche photodiodes", J.Appl. Phys, vol 47, p.1605,
- LECROSNIER, D, 1975, "Optimization of avalanche silicon photodiodes:a new structure", Tech. Dig. Int. Electron Devices Meet, p.595, Washington D.C.
- Mc INTYRE, R.J, 1966, "Multiplication noise in uniform avalanche diodes", IEEE Trans. Electron. Devices, vol ED-13, p.164.
- MILLER, S.E., 1973 "Research toward optical fiber transmission systems. Part II : Devices and systemps considérations", Proc IEEE, vol 61, p.1726
- MULLER, J., 1976 "Double-mesa thin film reach-through silicon avalanche photodiodes with large gain-bandwidth product", Tech. Dig.Int.Electron Devices Meet, Washington D.C.
- RUEGG, H.W., 1967 "An optimized avalanche photodiode", IEEE Trans. Electron Devices, vol ED-14,p.239.
- WEBB, P.P., 1974 "Properties of avalanche photodiodes", RCA Rev, vol 35, p.234.

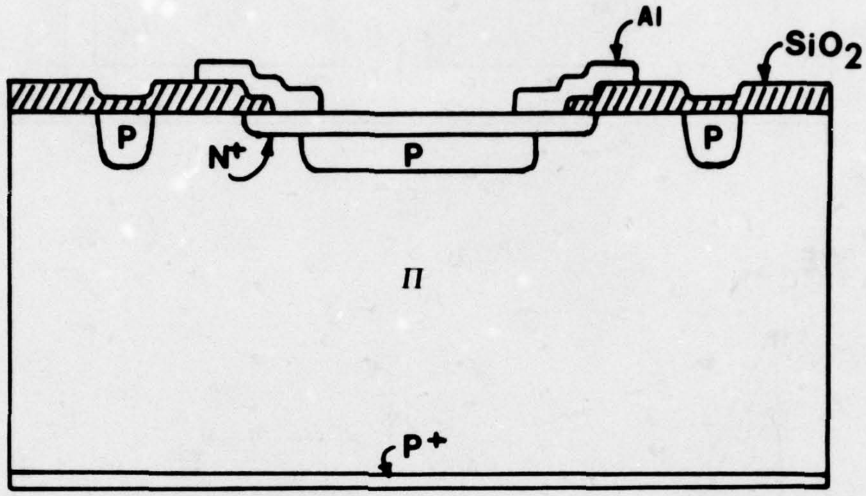

Fig.1 Structure $P^+\pi\ PN^+$

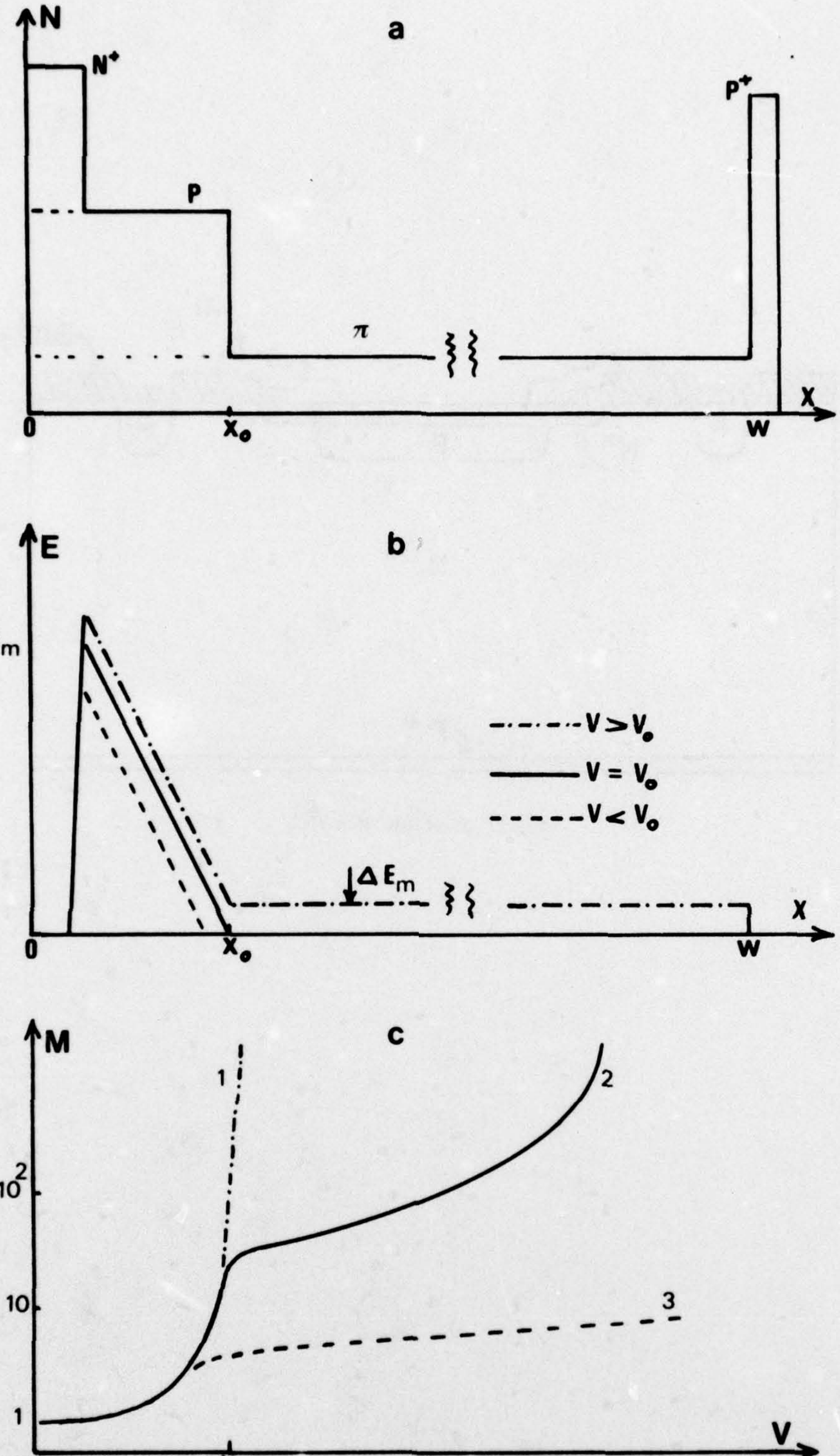

Fig.2 Principe de fonctionnement des photodiodes de structure $P^+\pi PN^+$
(a) profil de concentration
(b) distribution du champ électrique
(c) caractéristique de multiplication M(V)

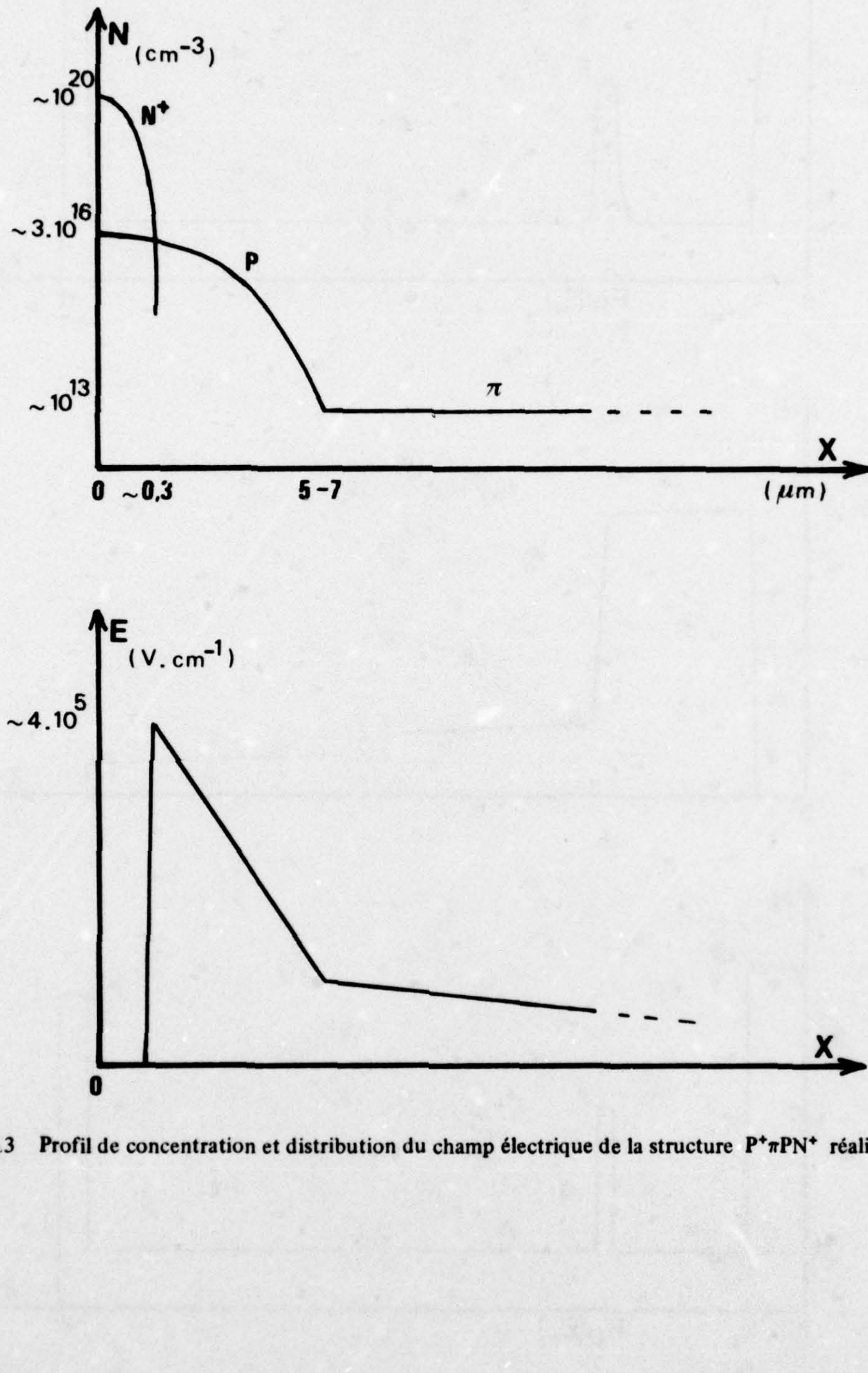

Fig.3 Profil de concentration et distribution du champ électrique de la structure $P^+\pi PN^+$ réalisée

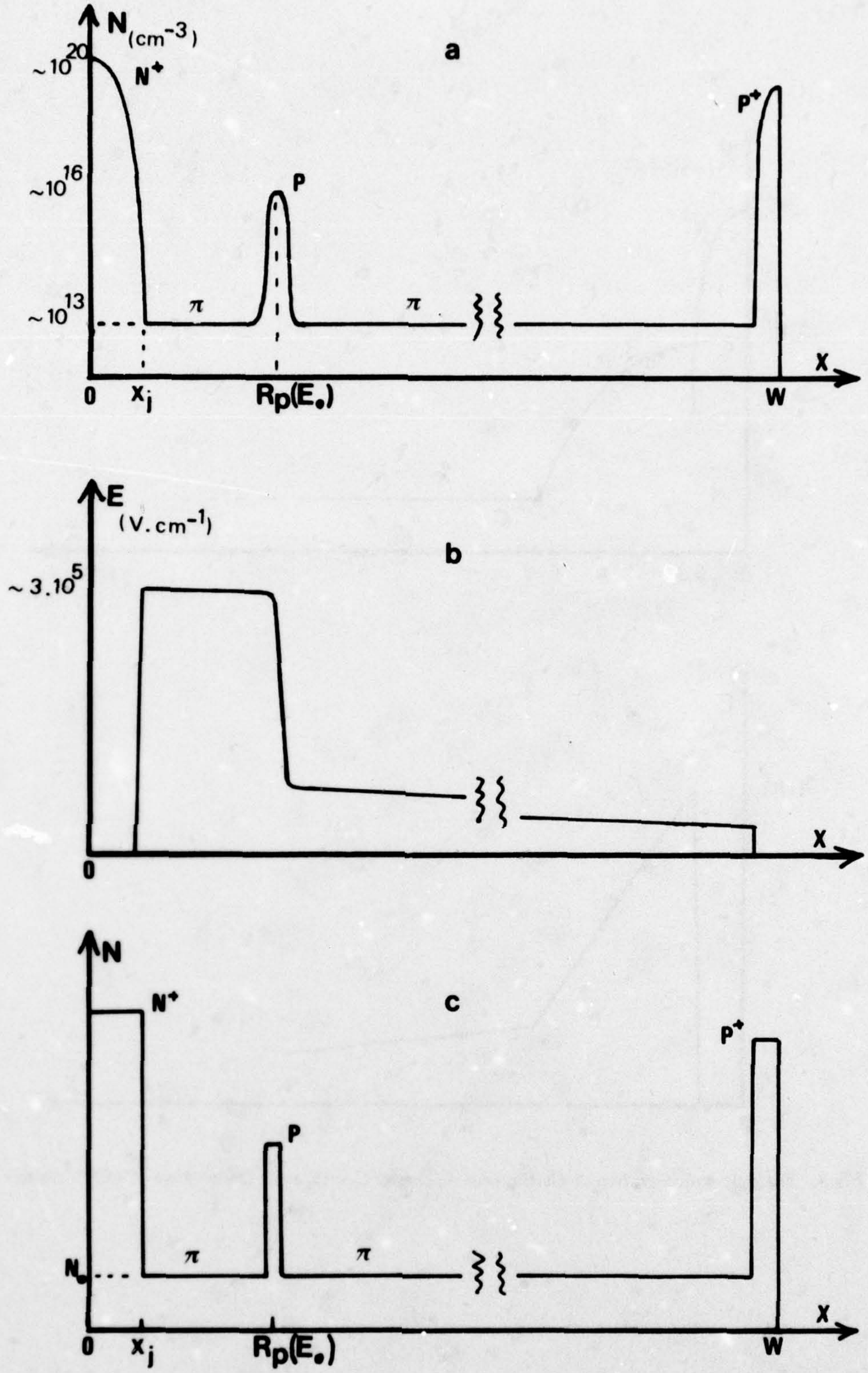

Fig.4 Profil de concentration et distribution du champ électrique de la structure $P^+\pi P\pi N^+$ à couche P enterrée. Profil caricatural

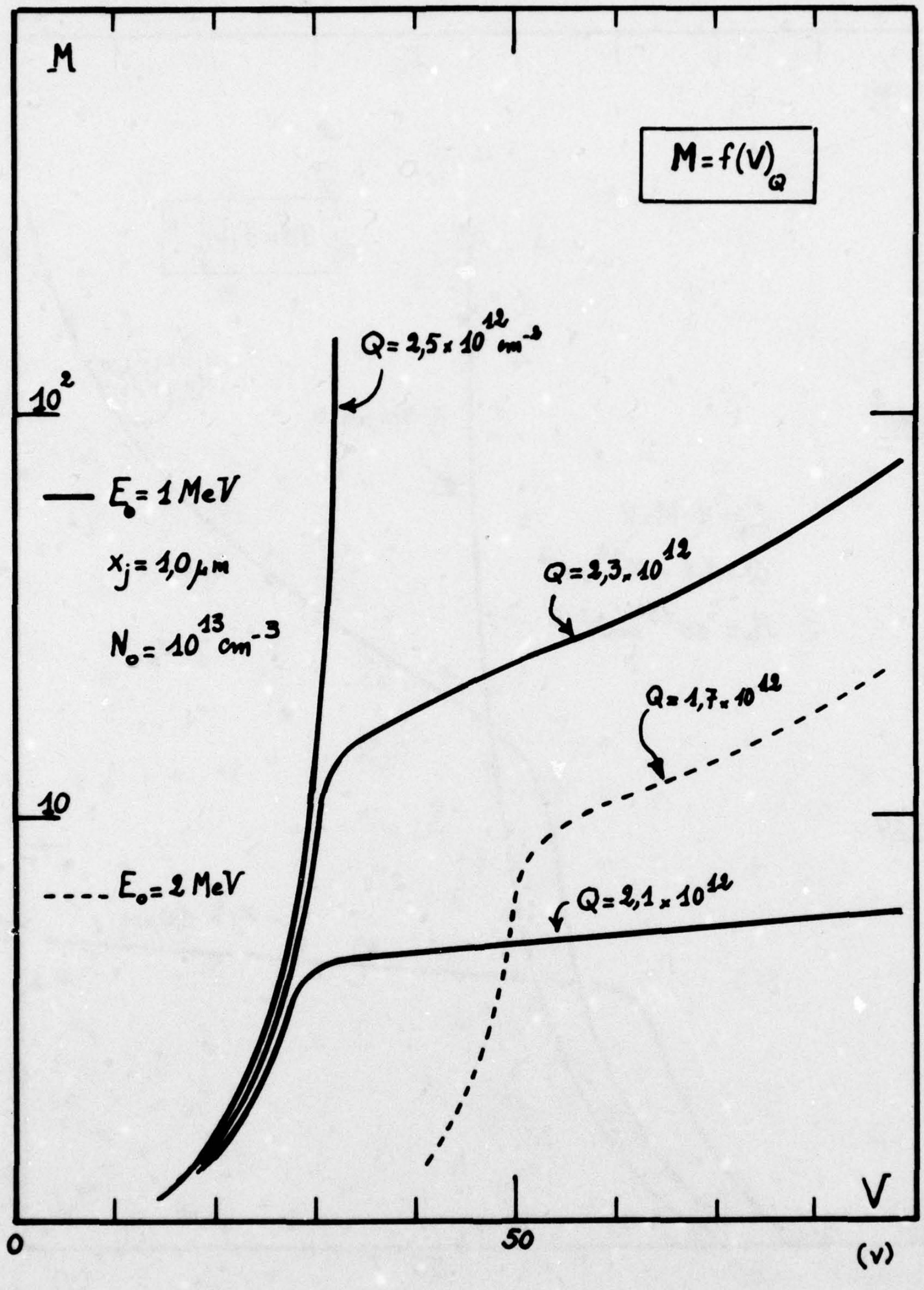

Fig.5 Structure $P^+\pi P\pi N^+$ sur substrat homogène. Influence de la dose implantée Q sur les caractéristiques M (V)

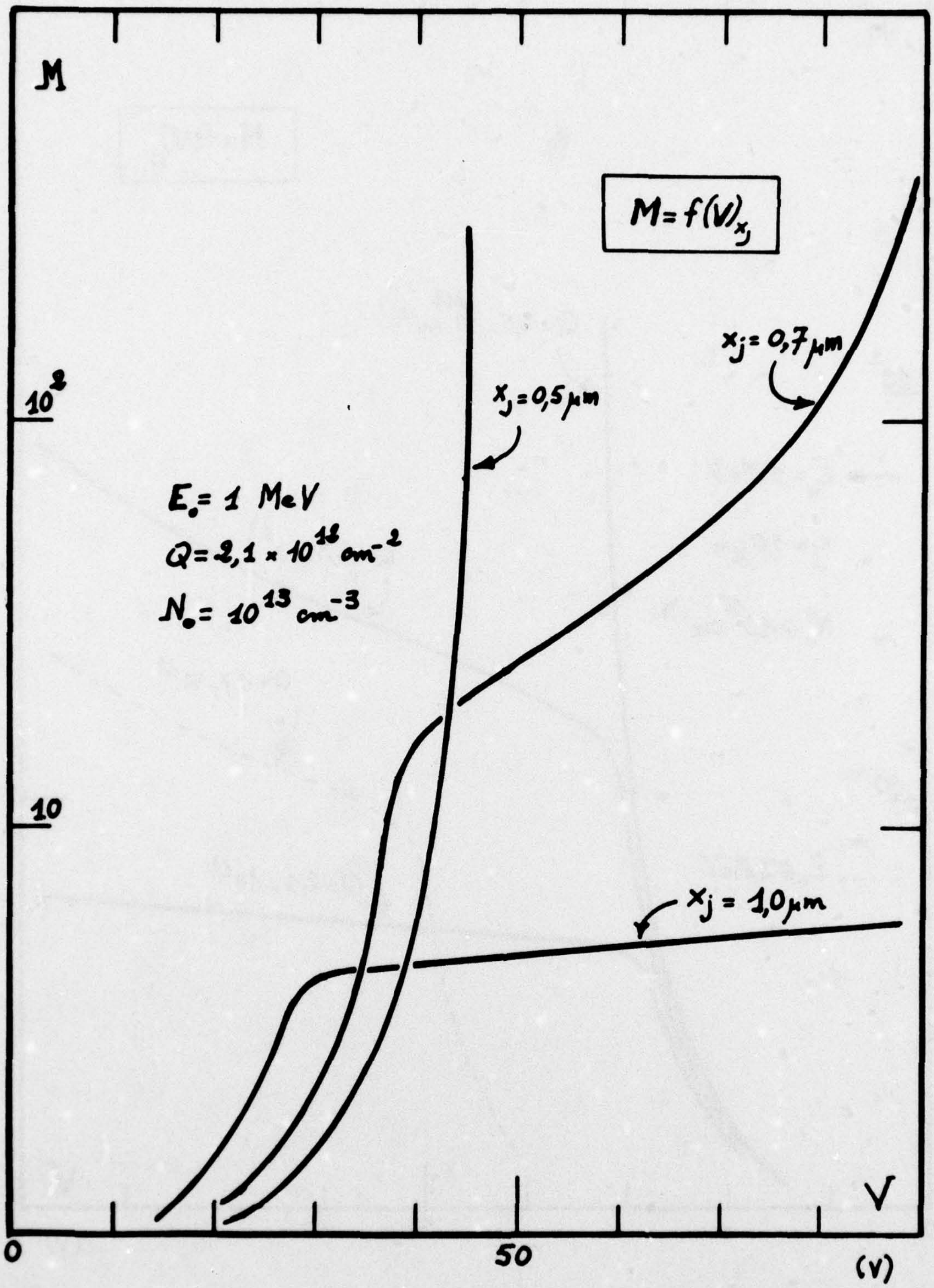

Fig.6 Structure $P^+\pi P\pi N^+$ sur substrat homogène. Influence de la profondeur de jonction xj sur les caractéristiques M(V)

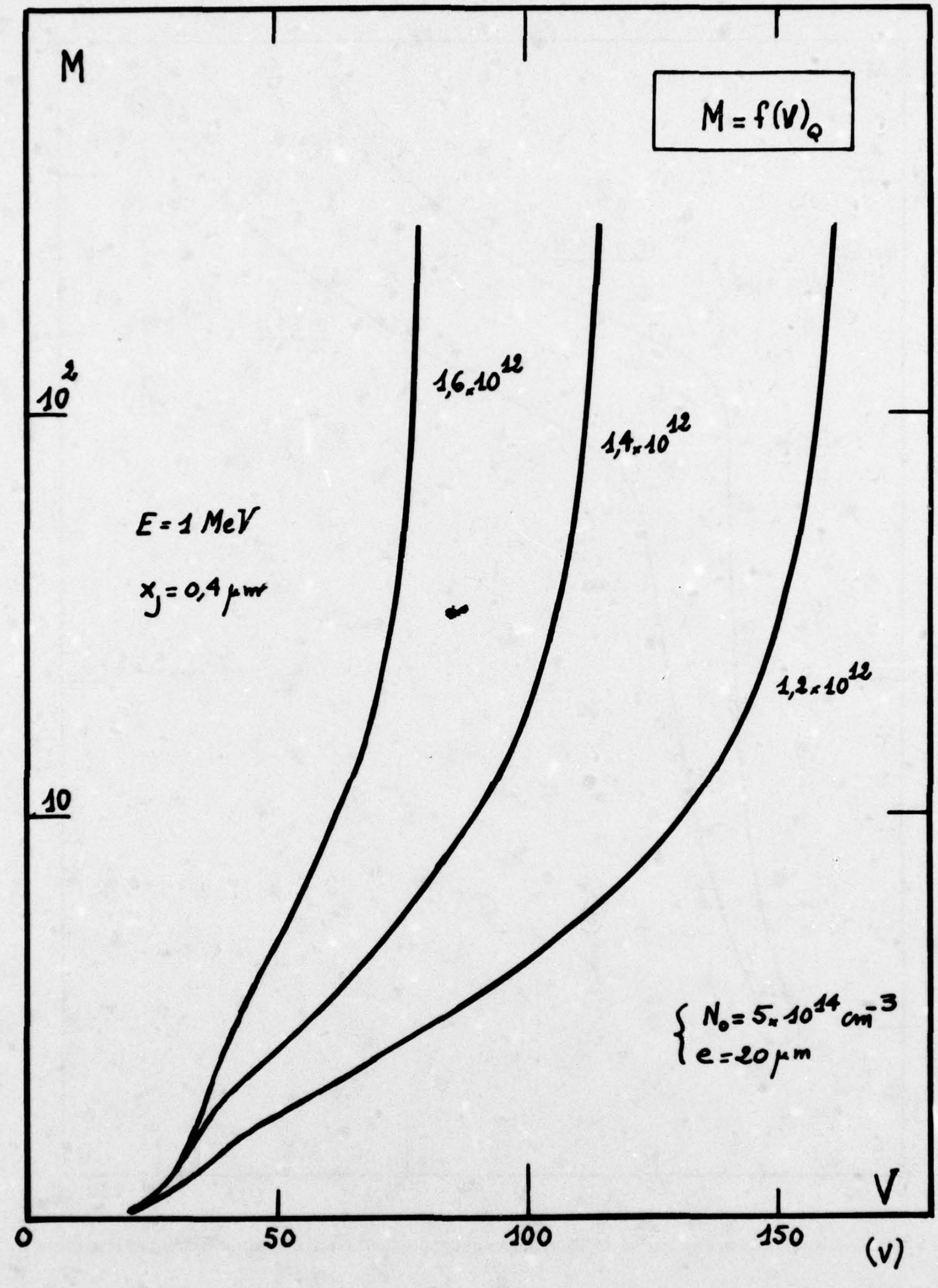

Fig.7 Structure $P^+\pi P\pi N^+$ sur substrat épitaxié. Caractéristiques M(V) en fonction de la dose implantée Q

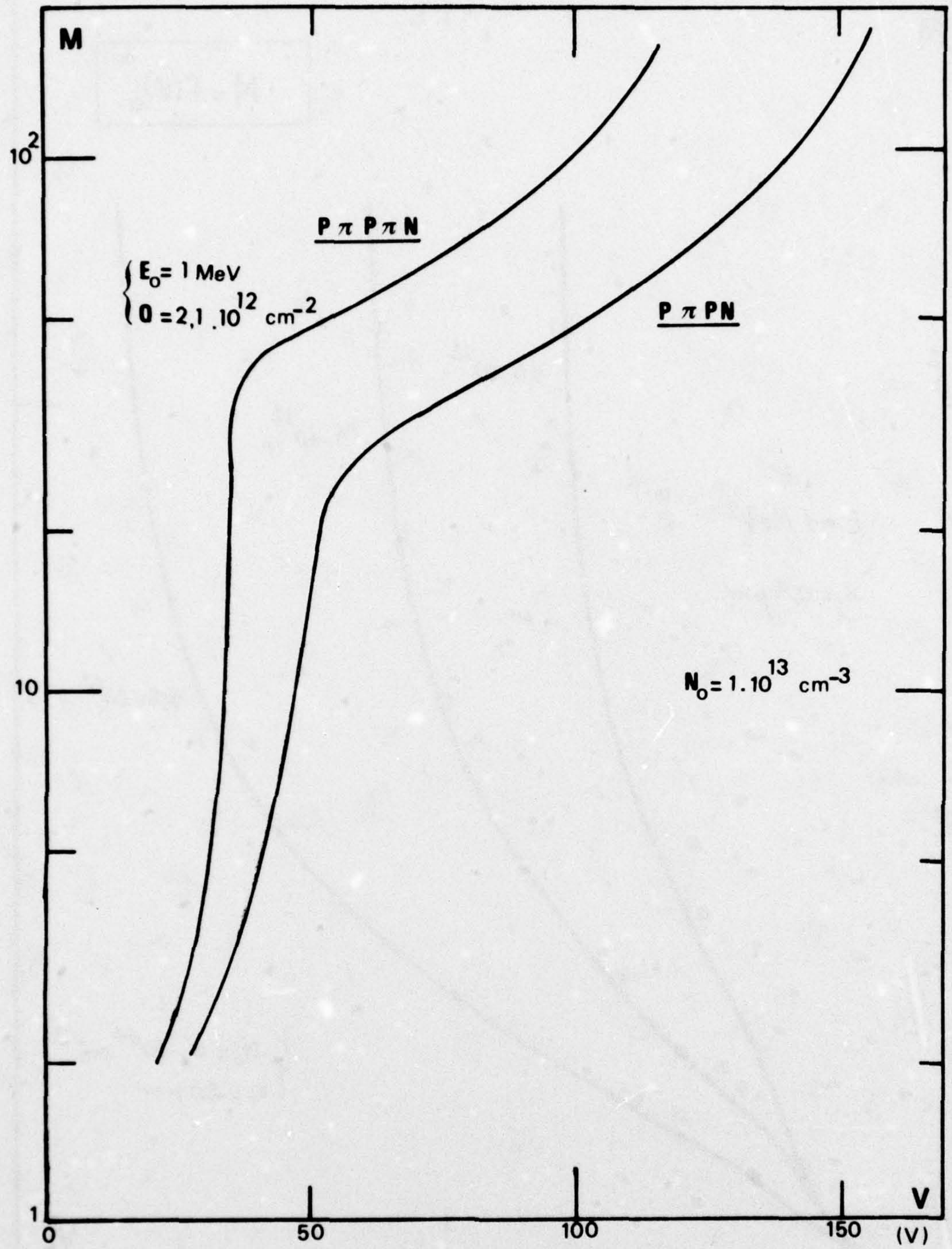

Fig.8 Caractéristiques de multiplication M(V) typiques des photodiodes réalisées sur substrat homogène creusé

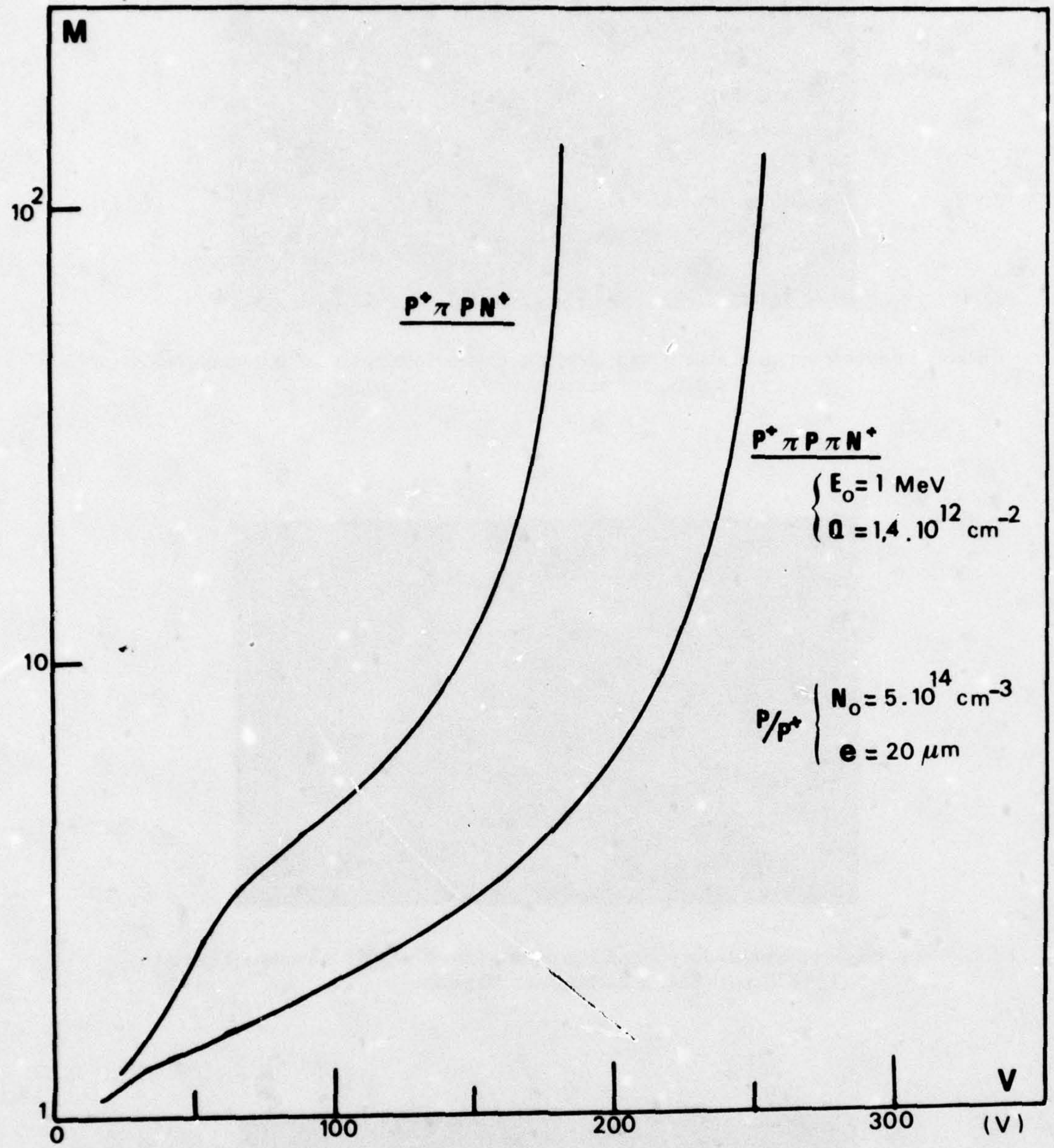

Fig.9 Caractéristiques de multiplication M(V) typiques des photodiodes réalisées sur substrat épitaxié.

Cliché 1 Réponse impulsionnelle typique des photodiodes réalisées sur substrat homogène creusé (λ = 870 nm). Echelle horizontale: 1 ns/div

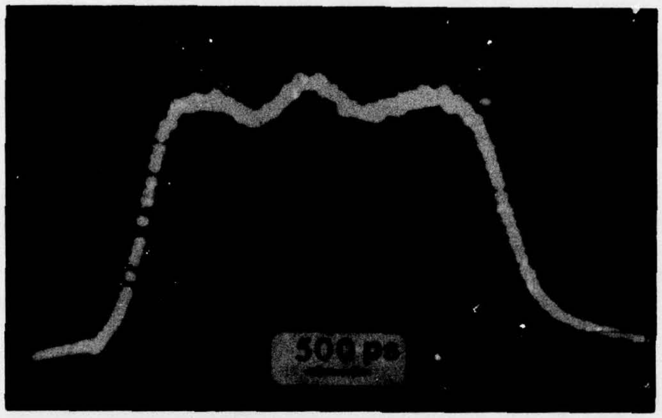

Cliché 2 Réponse impulsionnelle typique des photodiodes de structure $P^+\pi P\pi N^+$ sur substrat épitaxié (λ = 870 nm). Echelle horizontale: 50 ps/div

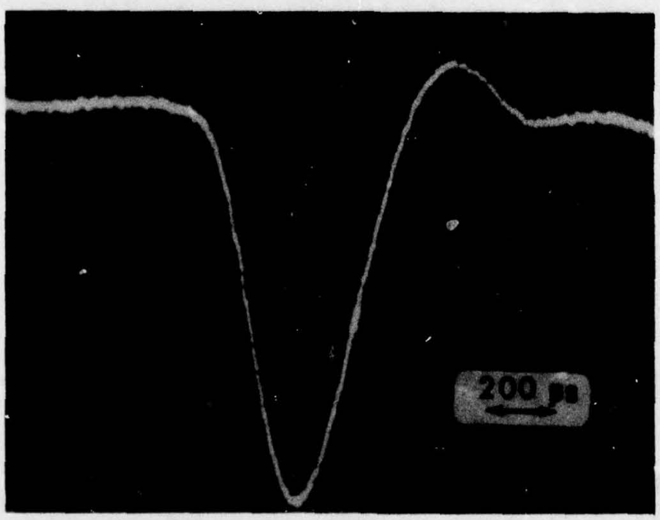

Cliché 3 Réponse impulsionnelle d'une photodiode de structure $P^+\pi P\pi N^+$ sur substrat épitaxié (λ = 1060 nm). Echelle horizontale: 200 ps/div

THE RELIABILITY OF HIGH RADIANCE GaAs LEDS

S. D. Hersee

Allen Clark Research Centre
The Plessey Company Limited
Caswell Towcester Northants.
U.K.

ABSTRACT

Extended lifetesting of diffused junction LED's has revealed that degradation is due to two apparently independent processes. Evidence is presented which indicates that both of these processes are diffusion controlled.

On the basis of these results the room-temperature lifetime of a typical LED is predicted to be approximately 10^6 hours.

INTRODUCTION

The LED's which were studied were of the Burrus (1970) type with the addition of an integral heat sink. The p-n juctions were formed by zinc diffusion into a silicon-doped (2×10^{18} cm^{-3}) GaAs substrate. The emitting region was defined either by silicon dioxide isolation as shown in fig. 1 or by proton bombardment, in which case the material outside the required emitting region was made semi-insulating.

Devices, with emitting diameters of 50 microns, have been produced with radiances of up to 100 W $st^{-1}cm^{-2}$ (at 300 mA) and with a typical bandwidth of 30 to 50 MHz.

Degradation rates at room temperature were in general found to be very low thus in order to accelerate the process most of the experiments were performed at elevated temperatures of between 35°C and 215°C. However, there is some doubt as to the relevance of those experiments performed at temperatures in excess of 150°C for we have found that a thermal strain exists at the metal/semiconductor interface on the p-side. In LED's of a different geometry this strain was sufficient to generate misfit dislocations after extended operation at 154°C.

Therefore only experiments performed at temperatures lower than 150°C are reported here.

It was only after extended lifetesting at high temperature that the complete form of the decay characteristic emerged. This characteristic showed four well defined stages which are illustrated in fig. 2.

Most of the devices lifetested showed a rapid initial drop in output power (STAGE 1 decay) in which between 0% and 35% of the output was lost. During the second stage of decay, in clear devices, the decay rate was lower and decreased continuously until it was zero within the measurement accuracy (±2%). This second stage of decay generally lasted in excess of 10^3 hours even at elevated temperatures.

Devices which showed dark spot defects (DSD's) or dark line defects (DLD's) showed an initial drop which was identical to that for clear devices. However, the decay rate during the second stage of degradation was generally much higher than for clear devices and as a result the 'dark defect' device generally reached its half output during this stage. In this paper only the degradation of clear devices is considered.

Clear devices, in particular devices with proton bombardment isolation, showed a stable plateau or stage III decay which was again of long duration, e.g. greater than 10^3 hours at 130°C or greater than 10^4 hours at 100°C.

The third stage of degradation was terminated by the onset of a degradation process in which the decay rate slowly increased with time. This fourth stage in the life of these originally clear devices was accompanied by the appearance of new DSDs in the device emitting area. At the end of its useful life a large proportion of the emitting area of each device was found to contain dark structure.

One other process which occurred during degradation was the appearance of dark patches in the vicinity of the emitting region perimeter. These patches occurred after extended operation, e.g. 800 hours at 100°C, yet their appearance did not significantly reduce the device output.

The shape of the characteristic, see fig. 2, strongly suggested that there were two independent decay mechanisms operating in these LEDs. The first mechanism was believed to give rise to the first and second stages of decay. There was then an interim period (stage III) during which the first mechanism had ceased yet the second mechanism had not begun to affect the device output. The fourth stage of decay was observed when the second mechanism began to significantly reduce the output.

The characterisation of each of these stages of degradation and the processes which cause them, will now be discussed.

STAGE I DECAY (INITIAL DECAY)

Most of the devices lifetested initially displayed a rapid decay in output. The amount of power lost and the decay rate during this first stage of degradation were found to be functions of temperature and current density.

During this decay the fractional decay rate per unit time was constant thus the decay curve followed an exponential relationship of the form; $P_t = P_o \exp(-\lambda t)$ .... (1)

where P_o and P_t are the output power at times t = 0 and t = t respectively and λ is the fractional decay rate (hr^{-1}).

This relationship was revealed by subtracting the subsequent part of the decay curve from the total curve, as in fig. 3. For each stage I decay this curve fitting procedure was carried out and a value of decay rate was obtained.

The variation in decay rate with reciprocal temperature is plotted in fig. 4. The large scatter of decay rates within a group of devices was due to real differences in this rate rather than inaccuracies in fitting the relationship of equation (1) to the data. This plot yielded an activation energy of between 0.54 eV and 0.86 eV for the stage 1 degradation process.

The variation of decay rate with current for 50 micron, SiO_2 isolated devices from batch D104B is shown in fig. 5. This curve showed that the decay rate was approximately proportional to current density.

The amount of output power lost in the initial drop was also found to be a function of temperature, see fig. 6. There was a large variation in the initial drop, even between devices from the same batch, however, the initial drop was shown to increase with temperature possibly levelling out at temperatures above 50°C.

The variation of size of the initial drop with current density is shown in Table 1.

TABLE 1

Fall in Output for 50 microns, SiO_2, LED's

Bias Current mA	Decay as a fraction of initial output %
300	6.5
100	16
50	21.8
13	28.5

The real loss of output was largest for devices which were operated at the higher currents (300 mA and 100 mA). However, the fractional initial drop increased with decreasing current. This strongly suggested that the initial decay was primarily associated with recombination in the depletion region, as the space-charge recombination-component of the total current was dominant at low operating currents.

Burrus (1970) also found an initial drop in a similar type of LED. He showed that if the diodes were operated in a pulsed mode, in which the normal forward bias was periodically interrupted by a reverse bias pulse, then the initial drop could be removed. He suggested that this degradation mechanism involved the diffusion of an electrically active "killer" species.

We have repeated this experiment using a reverse bias pulse of -4V, duty factor 15% and pulse rep. rate of 10 kp.p.s to interrupt the forward bias. Significant reductions in the initial drop were achieved as shown in table 2.

TABLE 2

Temperature °C	Net Forward Current mA	Initial Drop %	
		Pulsed Operation	D.C. Operation
181	300	7	14
100	300	0	15

It should be noted, however, that on returning to normal D.C. operation the pulsed devices displayed the typical initial drop.

Devices were found not to degrade under zero bias, or reverse bias conditions, e.g. our devices have been held unbiassed at 215°C for 250 hours with no loss of efficiency. However, the requirement of a forward bias for degradation could either mean that the degradation process was assisted by the device electric field or that the power dissipation at the junction (typically 450 mW under forward bias) established temperature gradients that provided the driving force for the decay process.

The reverse-bias pulse experiment in fact removed this ambiguity as in this experiment the junction temperature was the same as under normal forward bias operation yet a much smaller initial drop was observed.

Thus the mechanism responsible for this decay was believed to involve a charged species which was influenced by the junction field.

Knibb et. al. (1976) found an initial drop in GaP LED's and showed that this drop was signicantly reduced when the device slices were sawn on an aluminium rather than a copper base. They suggested that copper had contaminated the devices and had later diffused into the junction region where it provided non-radiative recombination centres.

There was no obvious source of copper contamination in the processing of our devices other than in the substrate material. With the exception of MCP and Litronix substrates the copper concentration in the substrate was generally undetectable by mass spectrograph, i.e. $\leqslant$ 0.003 p.p.m. atomic. In MCP material the copper level was typically 0.1 ppm atomic while in the Litronix material the level was unknown, however neither of these two types of substrate gave devices with a consistently high initial drop.

Both the n and p side contacts on these LEDs contained gold which is known to give rise to deep levels in GaAs, see Boltaks (1963). On certain devices a thin palladium layer was therefore interposed between the Ti and Au metallisation layers of the p-side contact. (Palladium is known to inhibit the diffusion of gold). However no correlation was found between devices showing a low initial decay and those containing a palladium layer.

STAGE II and STAGE III behaviour

The duration of this decay was typically 10^3 hours even at high temperatures, and during this time typically 5% of the LED output was lost. This duration was difficult to measure accurately as the decay rate was small and continuously decreasing. However, the second stages of decay in proton implanted devices and silicon dionide type devices were found to be significantly different, see fig. 7.

The behaviour of these LED's during the first, second and third stages of decay can be explained on the basis of a diffusion model similar to that proposed by Longini (1962) which will now be described.

A Diffusion model for LED Degradation

Longini (1962) proposed that the degradation of tunnel diodes was due to the diffusion of zinc (the p-dopant) across the junction where the resulting compensation reduced the device efficiency. This diffusion was normally retarded by the 'built-in' field at the junction, however under forward bias the retarding potential was removed.

For the reasons given earlier the stage I decay process was believed to be influenced by the junction field. Thus the degradation would be expected to be most severe in the high field region of the device, i.e. in the depletion region. This was the case, for the highest fractional stage I decay occurred at the lowest bias currents, see table 1, where most of the carrier recombination was in the vicinity of the depletion layer.

A field aided mechanism tends to rule out the possibility that this decay was caused by the diffusion of a 'killer' species, e.g. copper, from the p-side contact. For even if this species were charged the diffusion would be largely unaffected by the junction field. Also it would give rise to concentration gradients such that a larger fractional initial decay would be expected at higher currents rather than lower currents as was observed experimentally.

There is no shortage of evidence showing that the stage I and stage II decays are due to the introduction of non radiative recombination centres in the junction vicinity, see for example Schade(1971), Yang (1971), Fabre (1974). However, there has always been some doubt as to whether such centres have arrived by diffusion or have been created by the 'phonon kick' mechanism that was postulated by Gold and Weisberg (1961).

As a result of these measurements, in which the complete form of the decay characteristic has been established, we believe that the phonon-kick mechanism could not be responsible for the first and second stages of decay. The 'phonon kick' principle is that certain non-radiative recombination events can give enough energy to the lattice to create Frenkel defects (an interstitial and a vacancy) which might then act as non-radiative recombination centres. If this were the case then the decay rate would be expected to increase with time, as the number of non-radiative events increased. Experimentally, see fig. 2, the decay rate was observed to decrease with time.

There are two likely diffusion processes which might account for the observed decay, these are firstly, the diffusion of zinc across the junction or secondly, the diffusion of a negatively charged species from the n-side of the junction into the recombination region. Both of these processes will be shown to give a degradation behaviour that is in qualitative agreement with the observed behaviour. For the diffusion of zinc to be enhanced by the forward bias the diffusing species would require a positive charge. It has been suggested by Tuck (1974) and others, that the highly mobile zinc interstitial atom, which is believed to be the dominant diffuser of the zinc species, does in fact act as a donor and therefore has a positive charge. Also the measured activation energy of between 0.54 eV and 0.84 eV was not thought to be unreasonable for the zinc diffusion process.

The second process involved the diffusion of a negatively charged "killer" species across the junction. At this time it is only possible to speculate as to the nature of such a species. However, Schade (1971) and Fabre (1974) have found that defects with energy levels in the range 0.2 eV to 0.55 eV (from either band) are created during the degradation of ternary-compound LEDs. In one case the level at 0.55 eV was associated with copper.

Using either model the first three stages of degradation can be predicted.

Diffusion will only occur in the forward biassed (reduced junction field) regions. The application of a forward bias therefore defines a finite volume of material i.e. a finite diffusion source, from which diffusion can occur. The diffusion rate from such a source will decrease continuously with time eventually reaching zero. This was observed experimentally as the first and second stages of decay. The extremely long stage II decay was believed to arise from diffusion at the periphery of the emitting region where the bias was less, thus the diffusion was inhibited by the larger junction field. In support of this belief was the comparison between the proton implanted and silicon dioxide isolated devices, see fig. 7. In the implanted device the peripheral region was more sharply defined than in the SiO_2 device and the duration of the stage II decay was shorter. The majority of the devices lifetested have shown the first two stages of decay and have now reached their plateau or stable output region, see figures 8, 9, and 10. From figure 6 it can been seen that for operating temperatures around room temperature a small initial drop of up to 10% can be expected. Allowing for a 5% loss of output during the second stage of decay the device therefore reaches the plateau or stage III with probably greater than 85% of its' original output power. In the absence of any other degradation process it is believed that the LED output will then remain constant.

STAGE IV DECAY

In our lifetests only one device has shown a stage IV decay, see figure 10. Lifetests at higher temperature, Wakefield (1977), have shown that the stage IV decay begins after typically 2000 hours at 135°C (bias current 300 mA, 50 microns LEDs). These devices all exhibited new dark spot defects in their emitting areas. In our experiments, although we do not yet have a significant number of devices at their fourth stage of decay, some dark defect growth has been observed.

During the second and third stages of decay faint dark patches, see figure 11, appeared in the emitting regions of most LEDs. With subsequent operation these patches darkened and in some devices distinct dark spot defects were produced in the dark patch regions, see figure 12. The production of these defects was not accompanied by a corresponding loss of output and indeed many of these features have appeared during the stable stage III period. As the LED output remained constant it was concluded that these dark defects were conducting little or no current.

At this time we do not have enough evidence to conclusively determine the cause of these dark defects and the associated fourth stage of decay. However, a likely process is the diffusion of a 'killer' species from the p-side contact.

On several occasions we have removed the p-side contact from degraded devices and have found that part of the contact has alloyed with the GaAs. The alloy particles were oriented in $\langle 110 \rangle$ direction and were similar in appearance to Au-Ga precipitates which have been observed by Magee et. al (1975) after heating a gold/GaAs structure.

After heating device chips 400°C for 5 minutes and then removing the p-contact we have detected gold in the GaAs surface using X-ray microprobe analysis. On one occasion we have found features at the contact/semiconductor interface that correspond with the DPD and DSD features in the degraded devices.

If gold is responsible for the final degradation of these LED's then from knowledge of the gold diffusion coefficient the time before a significant amount of gold reaches the junction can be calculated. The diffusion coefficient of gold in GaAs at room temperature is given by Mochanova (1972) at $10^{-16} cm^2 s^{-1}$. Taking $D = 10^{-16}$ and $X_J = 8$ microns (therefore recombination at ~ 6 microns) then the time (T) taken for significant amount of gold to reach the recombination region is approximately given by:

$$T = \frac{X^2}{D} = \frac{3.6 \times 10^{-7} cm^2}{10^{-16} cm^2 s^{-1}} = 3.6 \times 10^9 \text{ secs.} \qquad (3)$$

$$= 10^6 \text{ hours}$$

At 135°C ambient the fourth stage of decay began after approximately 2,250 hours, in 50 micron, SiO_2, LED's operated at 300 mA D.C. Using eqn. (3) a value of the diffusion coefficient at 135°C was calculated (again assuming a 6 micron diffusion).

$$D_{135^oC} = \frac{3.6 \times 10^{-7}}{2.25 \times 10^6 \times 3.6} = \underline{4.4 \times 10^{-14} cm^2 s^{-1}}$$

Using this value and the value quoted by Molchanova (1972) for D at room temperature ($10^{-16} cm^2 S^{-1}$) an activation energy of 0.55 eV was calculated using the Arrenhius relationship, see Tuck (1974).

$$D = D_o \exp \frac{-Q}{kT} \qquad (4)$$

where A = activation energy
k = Boltzmann's const.
T = absolute temperature
D_o = constant

The activation energy for gold diffusion in GaAs is unknown, however in other III-V compounds (in which a similar diffusion process would be expected) this value varies between 0.32 eV and 0.65 eV. Thus the evidence which is available to date indicates that the diffusion of gold from the p-contact is the probable cause of the stage IV decay in LED's. On this basis the lifetime of these devices (with Ti/Au contacts) will be limited to approximately 10^6 hours at room temperature.

CONCLUSIONS

It has been shown that the species responsible for the initial stages of degradation eventually becomes exhausted and that during normal operation the LED output then remains constant at approximately 85% of its original level.

The stage IV decay process is believed to be due to gold diffusing from the Ti/Au p-side contact. This decay is not thought to present a serious limitation to LED lifetime as work on contacts for IMPATT devices (Purcell, J., 1977) has shown that a much greater contact stability can be achieved by the deposition of a palladium or platinum layer between the titanium and gold regions of the contact.

REFERENCES

1. Boltaks, B.I., "Diffusion in Semiconductors" Cleaver Hume Press Ltd., London, (1963).
2. Burrus, C.A. and Dawson, R.W., App. Phys. Letts. 17, No. 3, (1970) 97-99.
3. Fabre, E., and Bhargara, R.N., App. Phys. Letts. 24, (1974), 322-324.
4. Gold, R.D. and Weisberg, L.R., I.R.E. Trans. electronic devices 8, (1961), 428.
5. Knibb, T.F. (Plessey Co. Ltd.) private communication (1976).
6. Longini, R.L., Solid State Electronics, 5, (1962), 127-130.
7. Magee, T.J. and Peng, J., Phys. Stat. Sol. (a) 32, (1975), 695.
8. Molchanova, S.A. Zh. Fiz. Khim. 46, No. 9 (1972), 2373-4.
9. Purcell, J. J. (Plessey Co. Ltd.) private communication.
10. Schade, H., Nuese, C.J. and Gammon, J.J., App. Phys. 41, (1971) 5072-5075.
11. Tuck, B., "Introduction of diffusion in semiconductors", Peter Peregrinns Ltd. (IEEE Monograph Series 16) 1974, 125, 164.
12. Wakefield, B.W. (P.O.R.C. Martlesham) private communication.
13. Yang, E.S., IEEE. J. or Quantum Electronics, QE-7, No. 6, 1971, 239-244.

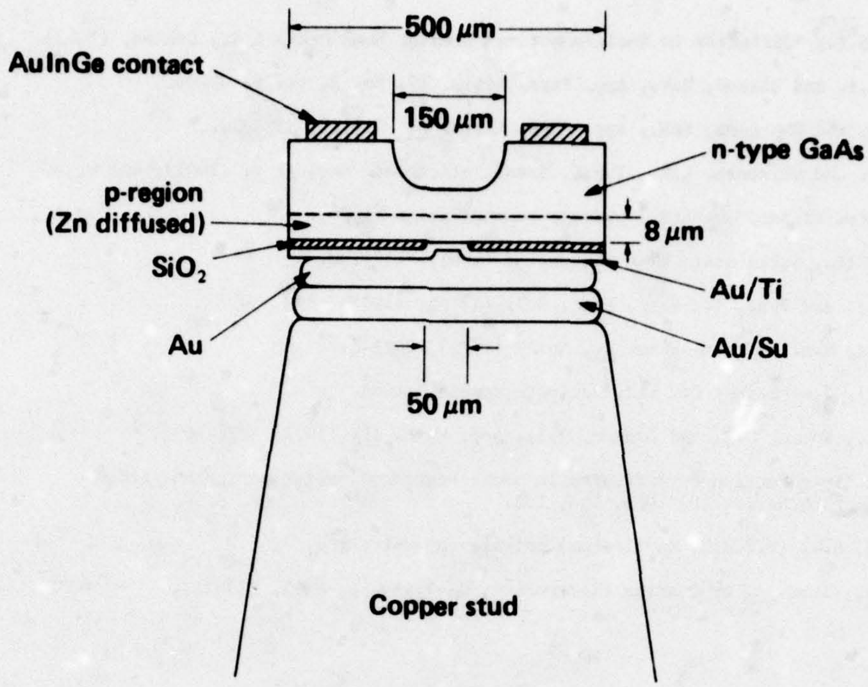

Fig.1 The silicon-dioxide isolated LED

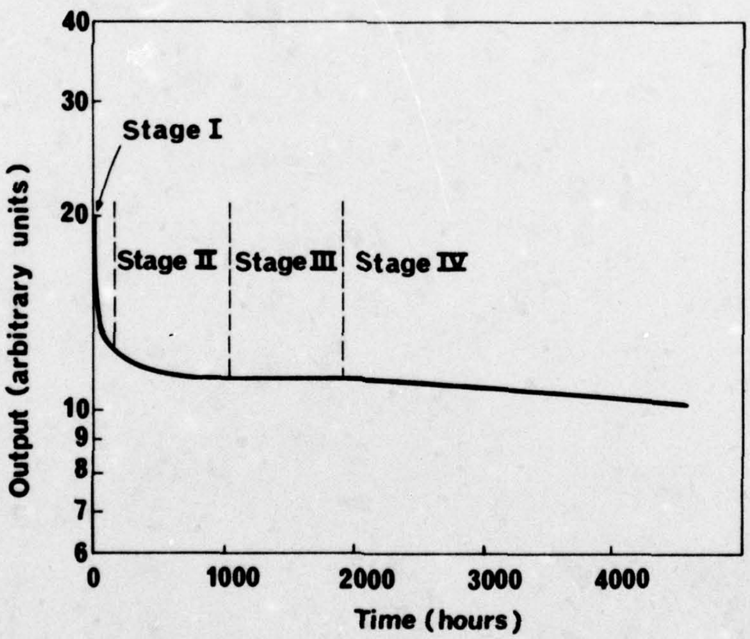

Fig.2 The characteristic form of decay of an LED

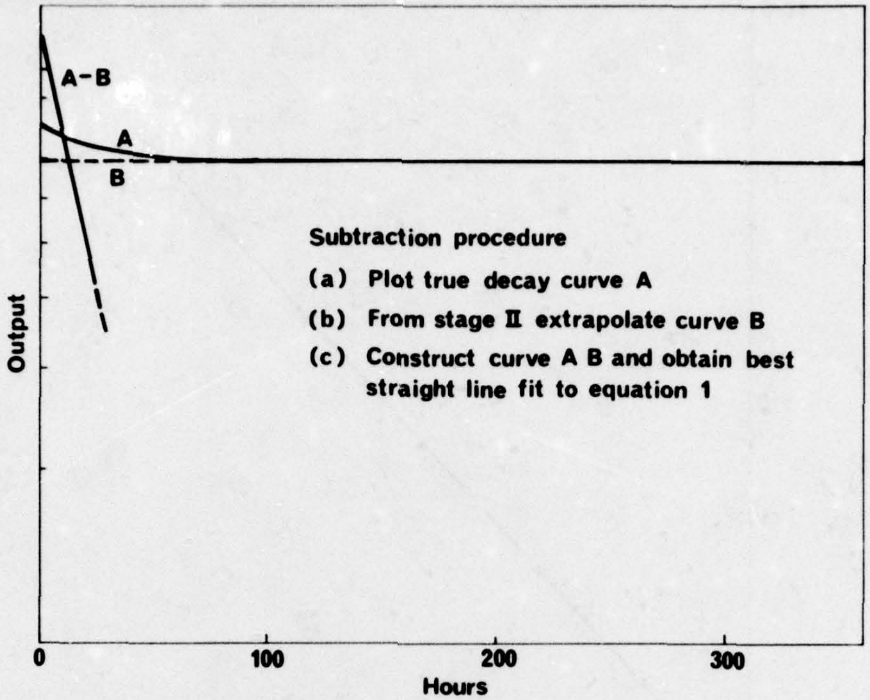

Fig.3 Subtraction to obtain the stage I decay rate

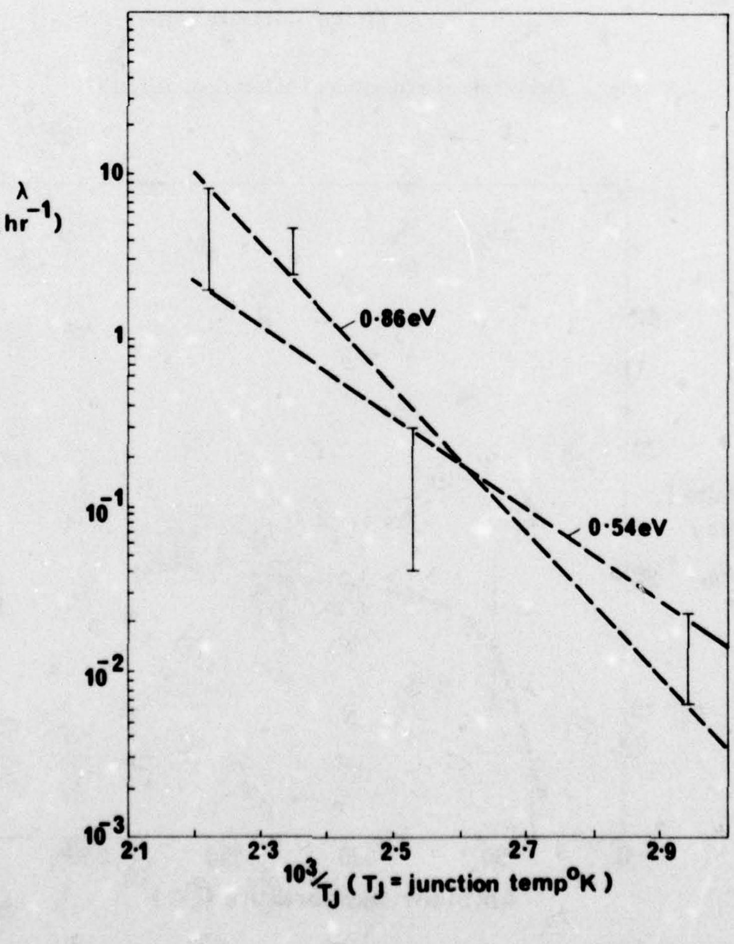

Fig.4 Decay rate as a function of reciprocal temperature

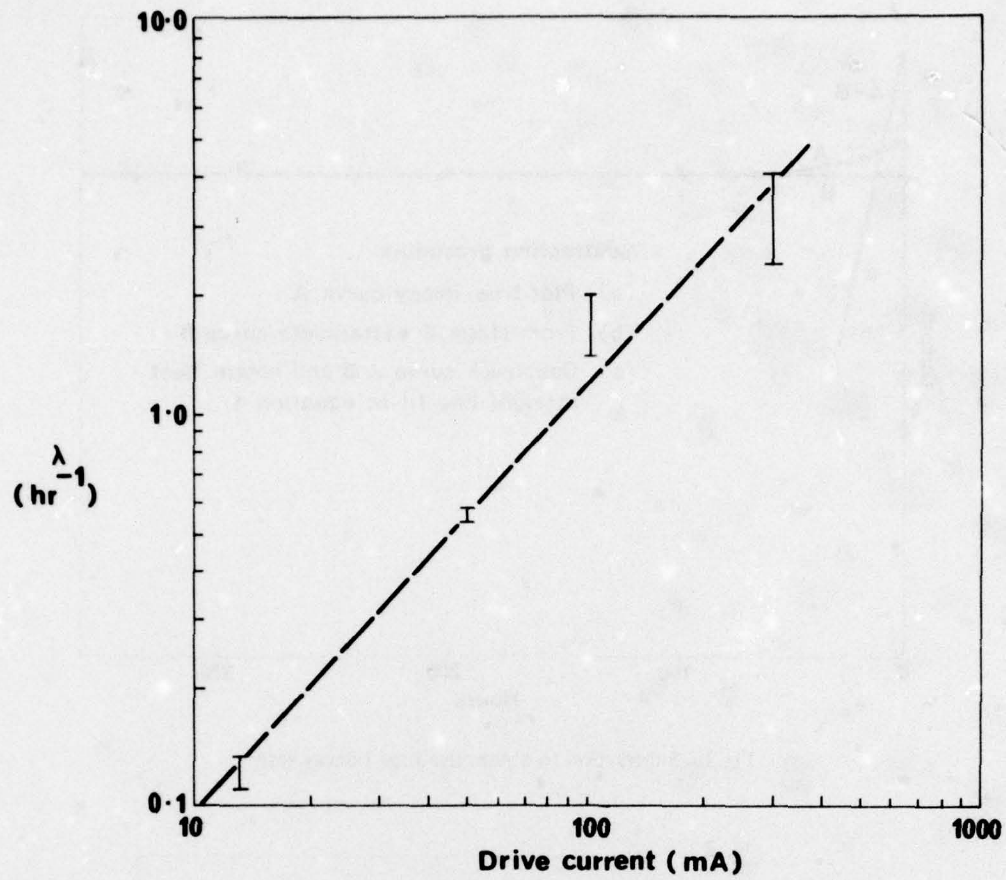

Fig.5 Decay rate as a function of bias-current at 130°C

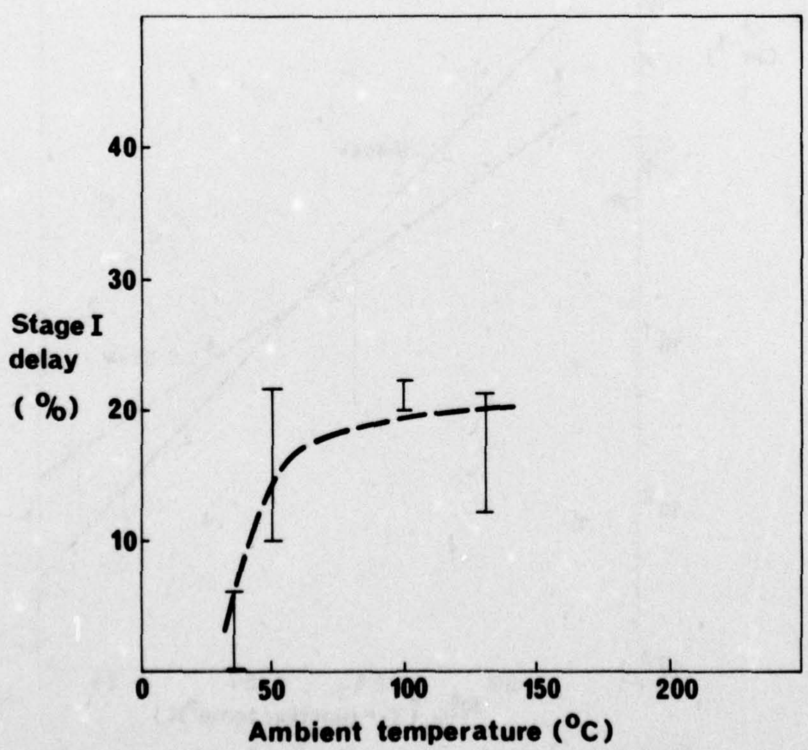

Fig.6 Amount of stage I decay as a function of temperature

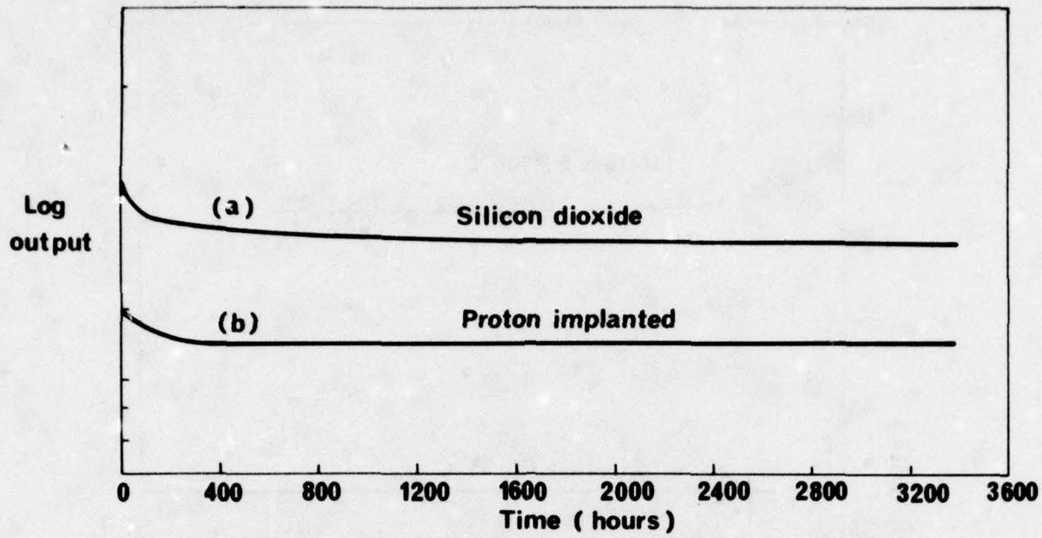

Fig.7 Comparison of decays in a proton implanted and silicon dioxide LED

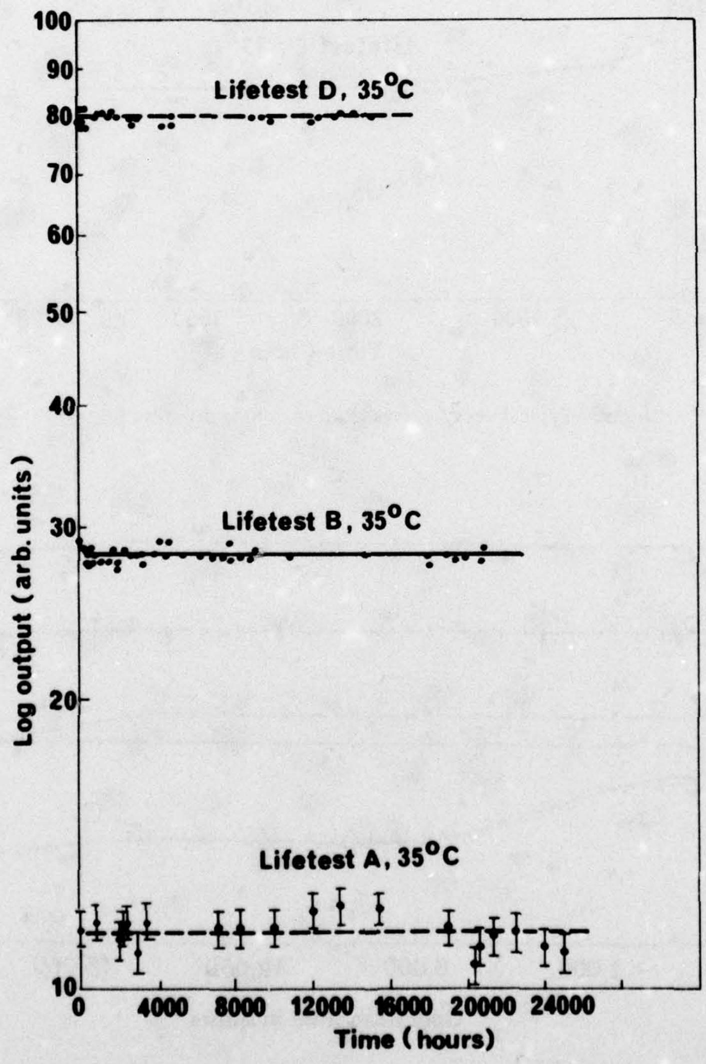

Fig.8 Typical decay curves from each long duration lifetest

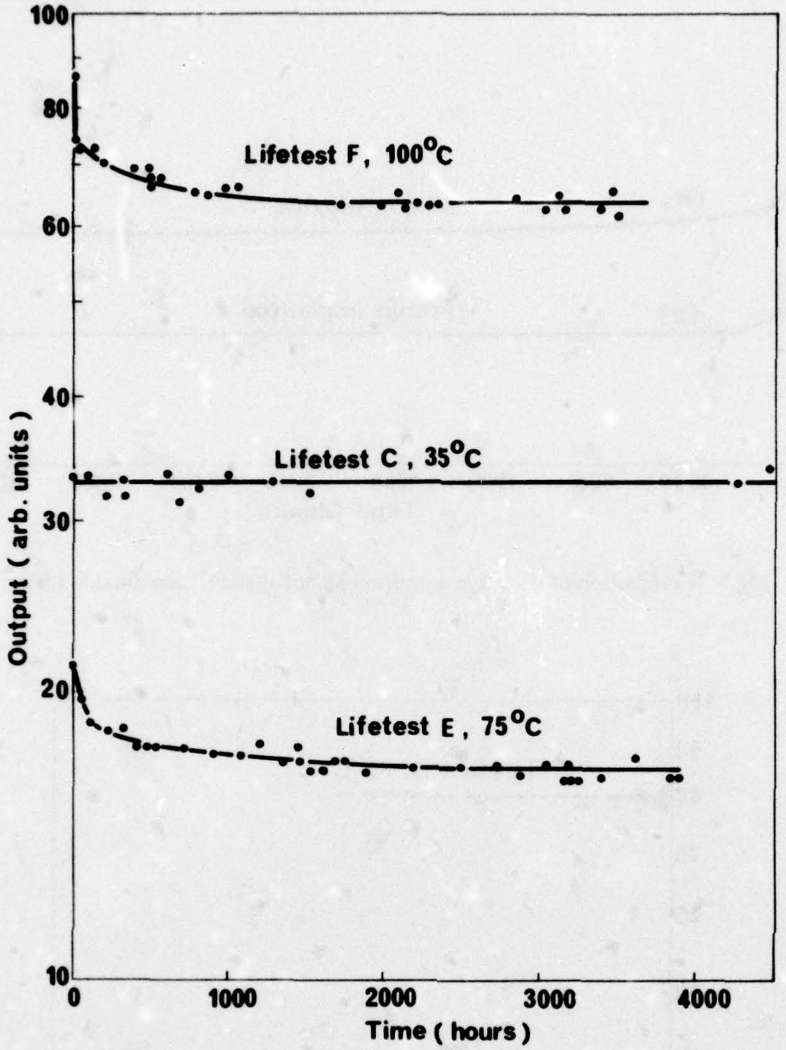

Fig.9 Typical decay curves from each long duration lifetest

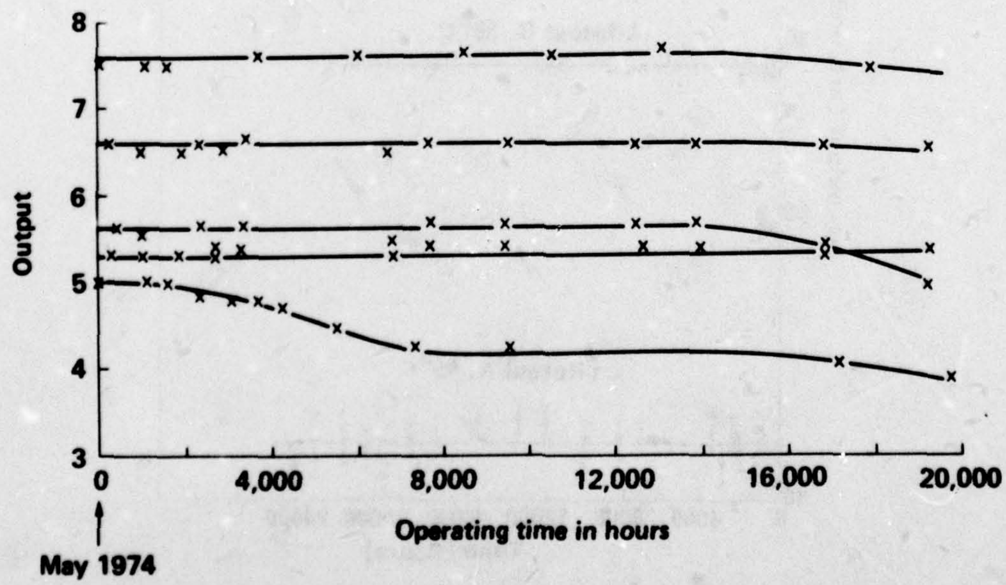

Fig.10 Typical decay curves from each long duration lifetest at 35°C

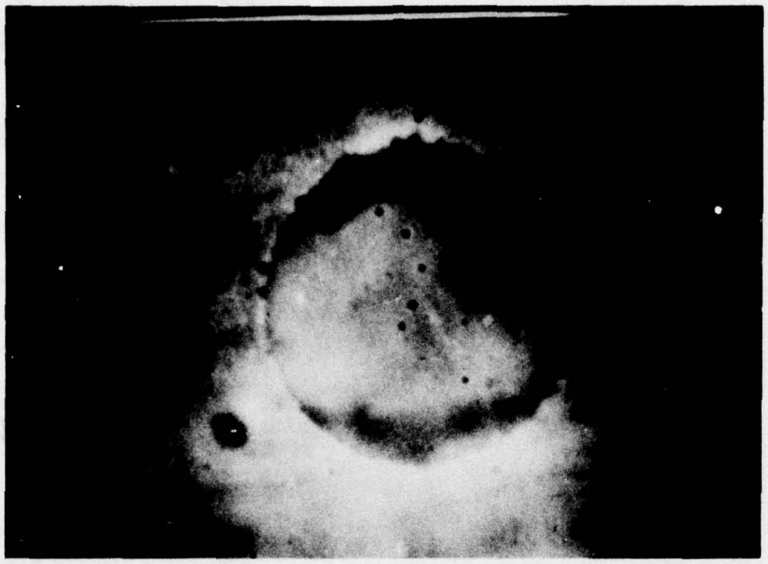

Fig.11 Dark patch defects

Fig.12 Dark patch defects and new dark spot defects

MODULE D'EMISSION A LASER SEMICONDUCTEUR

A. Jacques - L. D'Auria
THOMSON-CSF
Laboratoire Central de Recherches
B.P. 10 - 91401 . Orsay
(France)

RESUME

Nous examinons quelques uns des principaux problèmes qui se posent lors de la conception ou de la réalisation d'un module d'émission à laser semiconducteur. Nous étudions successivement :

- L'embase émettrice constituée de :
  . la puce laser et son support radiateur,
  . la "tête optique" de couplage laser/fibre,
  . la fibre optique intermédiaire et son conditionnement d'extrèmité,
  . les moyens de contrôle du fonctionnement de l'embase.
- Les circuits de commande et de contrôle de l'embase :
  . circuit élémentaire de commande,
  . régulation en température du boîtier laser,
  . contrôle de la puissance optique de sortie.

SUMMARY

We discuss some of the most important problems regarding the design and the realization of an injection laser transmitter module. We consider successively :

- The emitter unit consisting of :
  . the laser chip and its heat sink,
  . the "laser-to-fiber coupling optical head",
  . the intermediate optical fiber and its termination,
  . the working tests of the emitter unit.
- The driving and control circuits :
  . elementary driving circuit,
  . temperature regulation of the laser case,
  . optical power output control.

Le module d'émission à laser semiconducteur constitue une interface entre le signal électrique et le signal optique en vue de sa transmission par une fibre optique. Le module d'émission que nous étudions ici (Figure 1) comprend un composant essentiel qui est l'embase émettrice à laser semiconducteur et des circuits fondamentaux de régulation (température de fonctionnement du laser et contrôle du signal optique de sortie).

Nous allons examiner dans ce qui suit quelques problèmes, parmi les plus importants, que l'on rencontre lors de sa conception ou de sa réalisation. Des problèmes qui seront liés à la nature du laser semiconducteur ou à l'état d'avancement des travaux dans ce domaine ou des problèmes directement issus des premières exigences d'un pré-développement industriel futur.

1 - EMBASE EMETTRICE A LASER SEMICONDUCTEUR

Le laser semiconducteur, par lui-même, ne constitue pas un composant directement manipulable et utilisable lors de l'élaboration d'un module d'émission. A cette notion de composant doit être associée celle d'embase émettrice à laser semiconducteur qui est essentiellement constituée par (Figure 2) :

- la puce laser et son support radiateur,
- la "tête optique" de couplage laser/fibre supportant l'optique de couplage et l'extrèmité d'entrée de la fibre intermédiaire,
- la fibre optique intermédiaire qui achemine le signal lumineux à l'extérieur de l'embase. Cette fibre est choisie (diamètre de coeur, épaisseur de gaine, ouverture numérique) et compatible avec la fibre de transmission de la liaison envisagée. Son extrèmité est munie d'un connecteur,
- les moyens de contrôle du fonctionnement de l'embase : contrôle de la puissance optique émise à l'aide d'un photodétecteur situé en regard de la face arrière du laser et contrôle de la température du boîtier laser, par exemple, au moyen d'une thermistance introduite dans celui-ci.

Chacune de ces parties est positionnée avec précision et scellée sur une semelle rigide commune en bon contact thermique avec le boîtier laser. L'ensemble est placé dans un boîtier et l'embase émettrice se présente avec une entrée de commande du laser, une sortie du signal optique en bout de fibre intermédiaire et deux sorties électriques de contrôle (contrôle de la puissance optique et contrôle de la température).

Nous allons dans ce chapitre examiner les différentes parties constituantes de l'embase émettrice à laser semiconducteur.

1.1 - Le laser semiconducteur

La puce laser semiconducteur opérant en régime continu est du type double hétérostructure $Ga_{1-x}Al_xAs/Ga_{1-y}Al_yAs$. La zone active localisée par implantation protonique se présente sous la forme d'un ruban de 12/um delarge , 400/um de long et 0.3/um d'épaisseur. Pour les lasers considérés ici, les valeurs de x et y sont respectivement 0.35 et 0.08, la longueur d'onde d'émission étant de 830 nm avec une largeur spectrale de l'ordre de 2 nm. Les courants de seuil sont voisins de 150mA et les puissances lumineuses utiles sont de l'ordre de 5mW par face. Après un tri sous pointe des puces laser (1), celles-ci sont soudées côté couche épitaxiale sur le boîtier en cuivre précédemment doré et indié et ce avec une bonne reproductibilité au niveau de la thermique. Enfin le contact est pris à l'aide d'un ruban d'or. Une courbe de la puissance optique émise par la face avant en fonction du courant d'injection en régimes impulsionnels et continus est donnée en exemple à la Figure 4.a.

Une photographie de lasers montés sur leur boîtier est montrée à la Figure 3. Les dimensions typiques du boîtier sont 20x6x3 mm . Des caractéristiques plus précises des lasers sont données au cours des paragraphes suivants.

1.2 - Le couplage laser/fibre

Les propriétés optiques d'un laser semiconducteur sont obtenues, pour un courant d'injection donné, d'une part en mesurant la largeur de la zone émissive (champ proche) et d'autre part en mesurant la répartition angulaire de la puissance optique issue du laser dans les plans parallèle et perpendiculaire à la jonction (champ lointain). Un exemple est donné à la Figure 4 pour un laser dont la largeur de la zone émissive est d'environ 11/um et les demi-angles à 1/e sont 30° (plan perpendiculaire à la jonction) et 5° (plan parallèle à la jonction). Le faisceau laser présente donc, du fait de la géométrie de la zone émissive, un astigmatisme important dont une forte divergence dans le plan perpendiculaire à la jonction qu'il faut corriger si nous voulons obtenir un bon rendement de couplage avec une fibre multimode de faible ouverture numérique.

Hormis le couplage direct (2) qui est intéressant (faibles tolérances de positionnement) dans le cas de fibres à larges ouvertures numériques ($\gtrsim$ 0.3) et qui de plus fournit une référence pour l'évaluation comparée des performances des différents types de couplage, un grand nombre de méthodes de couplage ont été proposées. L'ensemble de ces méthodes fait généralement appel à une microoptique de couplage constituée :

- soit d'une lentille hémisphérique ou hémicylindrique réalisée en bout de fibre par fusion (3-6), par dépôt de résine hepoxy (7), par photolithographie (8) ou par usinage ionique (9).
- soit d'une lentille hémicylindrique hyperbolique réalisée par abrasion (10, 11).
- soit d'une fibre lentille cylindrique placée à 90° devant la face d'entrée de la fibre de transmission (13)
- soit d'une fibre conique. Le cône étant obtenu par attaque chimique ou par étirage à chaud (14).

Les performances de ces différentes solutions sont très variables et dépendent très fortement des conditions expérimentales dont la divergence du faisceau laser et l'ouverture numérique de la fibre. Le facteur de qualité (P couplée avec une optique/P couplée en direct) peut varier de 2 à 5 suivant les cas. Pour le couplage direct, son rendement, si on suppose le faisceau gaussien et le cône d'acceptance de la fibre uniforme (fibre à saut d'indice) est donné par (2) :

$$\eta \approx \mathrm{erf}(tg\theta / tg\alpha_{\perp}) \times \mathrm{erf}(tg\theta / tg\alpha_{/\!/}) \times (1-R)$$

où $\sin\theta$ = ouverture numérique de la fibre.

$\alpha_{\perp,/\!/}$ = demi-angle, à 1/e dans la puissance, dans le plan perpendiculaire ($\perp$) ou parallèle ($/\!/$) à la jonction.

R = réflexion de Fresnel ($\sim$ 5%).

La fonction $\mathrm{erf}(tg\,\theta / tg\,\alpha)$ est représentée à la Figure 5.

On peut voir sur cette courbe que pour une fibre d'ouverture numérique 0.3 et pour un laser de 30°x5° le rendement de couplage sera déjà voisin de 50%. Or on s'aperçoit, sur le tableau ci-après, que si l'adjonction d'une optique de couplage améliore le rendement elle nécessite en revanche un positionnement très précis. De ce fait, pour des fibres de grandes ouvertures numériques il ne sera pas nécessairement utile, dans l'esprit d'une industrialisation éventuelle, d'améliorer le rendement de couplage au prix de tolérances sévères. Il n'en est plus de même, comme on peut le voir sur le tableau comparatif ci-après, dans le cas des fibres à faibles ouvertures numériques.

- Voir Tableau page suivante -

. Les conditions sont :	-Fibre optique	O.N. = 0.1 diamètre coeur = 100/um
	-Laser S.C.	30° x 5° 0.7 x 5/um
	-Indice optique	1.6

OPTIQUE DE COUPLAGE	n_2	$\eta_{\parallel}$ (%)	$\eta_{\perp}$ (%)	η (%)	A (μm)	Y (μm)	X (μm)	$\varphi_{\parallel}$ (degré)	$\varphi_{\perp}$ (degré)
Sans		89	19	17	0 → 500	± 50	± 47	± 3	± 15
Cylindrique	1	89	90	80	7.5 ± 7.5	± 4	± 30	± 3	± 4
Hémicylindrique	1.6	89	78	69	50 ± 5	± 2.5	± 30	± 3	± 1.5
Hémisphérique	1.6	100	78	78	50 ± 5	± 2.5	± 8	± 4.5	± 1.5

A = distance laser - Optique de couplage

Y = déplacement dans le plan perpendiculaire à la jonction

X = déplacement dans le plan de la jonction

$\varphi_{\parallel}$ et $\varphi_{\perp}$ correspondent respectivement aux rotations dans le plan de la jonction (axe de rotation perpendiculaire au plan de la jonction) et perpendiculairement au plan de la jonction (axe de rotation confondu avec la face de sortie du laser). Les tolérances correspondent à 90% de l'efficacité maximale. Il n'est pas tenu compte dans ce tableau des réflexions de Fresnel que l'on peut estimer à 5% par interface.

La tolérance la plus sévère porte sur le déplacement perpendiculaire au plan de la jonction (Y) et il faut envisager, lors de la conception de l'embase, d'utiliser soit des pièces mécaniques sévèrement tolérancées, soit d'avoir recours à des méthodes de couplage en dynamique.

Nous présentons ici une solution que nous avons étudiée au laboratoire et qui est basée sur le principe proposé par Weidel (13). Cette solution qui utilise une fibre placée à 90° de la fibre intermédiaire (Figure 6) comme microlentille cylindrique de couplage, présente un certain nombre d'avantages dont : la reproductibilité, la facilité de mise en oeuvre (possibilité d'un montage collectif de la fibre intermédiaire et de la fibre lentille) et la possibilité d'extension au couplage simultané de plusieurs fibres intermédiaires à une barette de lasers semiconducteurs par exemple.

La "tête optique" représentée à la Figure 6 est constituée d'un plan de référence et de tiges dont le but est de guider et positionner automatiquement les fibres lentille et intermédiaire. La tête optique support des éléments de couplage est alors aisément manipulable et on vient la prépositioner devant le boîtier laser semiconducteur.

Au moyen de micromouvements de rotation et de translation, on optimise le couplage laser/fibre en contrôlant la puissance optique en sortie de la fibre intermédiaire. Ayant atteint la position optimale on scelle la tête optique de couplage sur la semelle de cuivre sur laquelle avait été préalablement soudé le boîtier laser. Des facteurs de qualité de 2 à 3 ont été ainsi obtenus de façon répétitive avec des fibres à saut d'indice, de faible ouverture numérique ($\sim$ 0.12). Bien sur, ceci suppose que la puce laser semiconducteur ait été soudée au bord de son boîtier et que l'axe mécanique de ce dernier ne s'écarte pas de plus de quelques degrés de l'axe optique du laser.

Notons enfin que le facteur de qualité de l'optique choisie dépend également du niveau de courant d'injection dans le laser, les champs proche et lointain ainsi que la proportion de fluorescence étant liés à ce dernier paramètre (13).

1.3 - L'embout de fibre intermédiaire : le connecteur fibre/fibre

L'extrèmité de sortie de la fibre intermédiaire doit être conditionnée de telle sorte qu'elle soit directement connectable à la fibre de transmission. De ce fait, son mode de conditionnement est directement lié à la connectique envisagée.

La connexion des fibres optiques contrairement aux contacts électriques se fait en butée. L'alignement des fibres à connecter doit se faire avec une très grande précision. A la Figure 7.a sont schématisées trois sources mécaniques de pertes : le mésalignement axial δ , la distance d entre les connectés et le mésalignement angulaire ϕ . En plus des pertes mécaniques il faut tenir compte des pertes dues à l'état de surface des faces des fibres et aux réflexions de Fresnel sur celles-ci. Notons que la connexion sera améliorée en disposant un diélectrique adaptateur d'indice entre les deux faces des fibres. La connexion reste néanmoins extrèmement sensible au paramètre δ . A la Figure 7.b sont tracées les pertes en dB à la connexion en fonction du mésalignement axial normalisé δ/D_c. (D_c = diamètre du coeur de la fibre). On peut voir que pour un mésalignement de 10% on obtient une perte voisine de 0.6dB.

Pour une fibre de 50 μm de diamètre de coeur et de 0.2 d'ouverture numérique, les tolérances de connexion sont pour 90% de transmission (sans adaptateur d'indice).

$$\delta = \pm 4 \mu m$$

ou $$d \leq 30 \mu m$$

ou $$\phi = \pm 2°$$

Plusieurs configurations de connecteurs monovoies détachables ont été proposées. Pour la plupart elles se répartissent dans deux groupes : l'un où le positionnement des fibres se fait dans un sillon (15-19), l'autre où chacune des fibres est centrée dans un embout de référence (20-24). Les performances obtenues dépendent des fibres utilisées (ouverture numérique, diamètre du coeur, nature de la fibre ...) mais les pertes à la connexion détachable restent toujours inférieures à 1dB sans liquide adaptateur d'indice.

Nous avons étudié au laboratoire deux embouts appartenant au deuxième groupe évoqué ci-dessus.

Le premier dont on peut voir la photographie de la face de sortie (Figure 8.a) utilise trois tiges rigides parfaitement calibrées dont le diamètre est 6,4 fois celui de la fibre à conditionner. Ces trois piges ont un double rôle le premier est de centrer la fibre optique par rapport au cercle circonscrit au trois piges et le second est de fournir trois génératrices de référence pour la pièce intermédiaire de connexion qui peut être une simple bague fendue. Cette solution à l'avantage d'assurer un positionnement automatique et précis de la fibre ($\leqslant 3\,\mu m$) au centre d'une référence mécanique. Elle est deplus reproductible. La forme de la cavité recevant la fibre permet une introduction aisée de celle-ci (guidage sur trois génératrices) et constitue éventuellement une réserve pour les produits de scellement. Des connexions à moins de 1dB de perte sans liquide adaptateur d'indice ont été aisément réalisées dans ces conditions. Néanmoins l'étroite dépendance du diamètre des piges envers le diamètre extérieur de la fibre rend cette solution laborieuse quant à la sélection des pigesdès lors que le diamètre extérieur de la fibre peut varier de plusieurs microns.

Le deuxième èmbout étudié au laboratoire est un embout à pincement. On peut voir une photographie de sa face de sortie à la Figure 8.b. Il s'agit d'une pièce centrale percée suivant son axe et fendue dans laquelle passe l'extrémité de la fibre à conditionner. Par l'action d'un fourreau coulissant on referme les fentes ce qui a pour effet de centrer la fibre par rapport à la surfaceextérieure du fourreau (non visible sur la photographie) et d'assurer le maintien de la fibre dans l'embout.Une telle solution, outre les avantages de facilité de mise en oeuvre et de reproductibilité, ne nécessite aucun scellement de la fibre (même dans le cas d'un polissage ultérieur) et dans une très large mesure est indépendant du diamètre de la fibre à connecter. De plus, elle permet de conditionner aussi facilement les fibres à gaine optique souple (fibre silice/siliconepar exemple) même si le coeur n'est pas centré dans la gaine puisque le serrage s'effectue alors sur le coeur même de la fibre.

Pour les fibres à gaine optique rigide nous obtenons les mêmes résultats que pour l'embout précédemment décrit. Dans le cas des fibres à gaine optique souple nos premières mesures nous ont donné de façon répétée des pertes inférieures à 2dB sans liquide adaptateur d'indice, les pertes supplémentaires étant essentiellement dues à la perturbation des caractéristiques optiques de la fibre dans les deux embouts connectés. Ces pertes ont été estimées à 0.7dB par embout. Nous pensons améliorer ce résultat notamment en contrôlant précisément la pression de serrage exercée sur la fibre.

Concernant la position de l'embout relativement à l'embase émettrice on peut envisager deux configurations suivant que l'embout est fixé directement sur le boîtier de l'embase (dans ce cas la fibre intermédiaire assure un découplage mécanique entre la tête optique et le connecteur) ou qu'il est indépendant du boîtier de l'embase et situé au bout d'une fibre intermédiaire de 5 ou 10cm de long. Cette dernière éventualité confère plus de souplesse au composant lors de la réalisation du module émetteur mais présente des risques accrus de détérioration lors de son utilisation et de sa manipulation sur le terrain. Ces deux options ont été envisagées et son représentées aux Figures 9 et 10.

1.4 - Les moyens de contrôle du fonctionnement du laser

Dans l'embase émettrice doivent également prendre place les moyens de mesure susceptibles de permettre un contrôle permanent des conditions de fonctionnement du laser semiconducteur :

- contrôle de la température du boîtier laser, par exemple au moyen d'une thermistance introduite dans le boîtier.
- contrôle de la puissance optique issue de la face arrière du laser. Pour ce faire, plusieurs possibilités sont envisageables :
  - Mise en place d'une fenêtre à l'arrière de l'embase.
  - Utilisation d'une fibre optique relais de large ouverture numérique pour collecter efficacement la lumière et la véhiculer à l'extérieur de l'embase. Dans ce cas toute liberté est donnée lors de l'élaboration du module émetteur, quant au choix du photodétecteur et de son emplacement (contre réaction rapide). Comme pour la fibre intermédiaire, l'extrémité conditionnée de sortie de la fibre relais peut être fixée sur une paroi de l'embase.
  - Une photodiode peut être positionnée à distance convenable de la face arrière du laser. Dans ce cas la sortie de contrôle sera une sortie électrique et des précautions particulières sont à prendre pour éviter toute interférence avec les courants d'injection destinés au laser.

Ainsi constituée l'embase émettrice est caractérisée par la donnée de la puissance optique issue d'une fibre connue (diamètre du coeur et ouverture numérique) en fonction des conditions d'injection du courant (régime continu ou impulsionnel) et des valeurs des paramètres de contrôle.

2 - LA COMMANDE ET LE CONTROLE DE L'EMBASE EMETTRICE

Le composant embase émettrice à laser semiconducteur peut être inséré dans un module dont les caractéristiques sont pré-déterminées par l'utilisateur et sont indépendantes des phénomènes de dégradation et des fluctuations de température dans un intervalle connu. Le module comprend alors en plus de l'embase émettrice un circuit élémentaire de commande et les régulations en température et en puissance optique de sortie. Nous allons examiner dans ce chapitre ces différentes fonctions et les problèmes qui leurs sont liés.

2.1 - Le circuit élémentaire de commande

Ce circuit a pour but d'adapter les signaux électriques aux conditions d'utilisation d'un laser semiconducteur. C'est un simple transformateur d'impédance qui d'un signal d'entrée modulé en tension délivre un signal modulé en courant avec éventuellement un gain en puissance. Ce circuit peut être compatible TTL, ECL ou peut être spécifique d'un système particulier (Haut débit d'information).

2.2 - La régulation en température du boîtier laser

Pour illustrer les principaux effets de la température sur le comportement microscopique du laser, nous avons tracé à la Figure 11 la caractéristique P(I) d'un laser à diverses températures. Les courbes de la Figure 12 représentent les variations du courant de seuil Is et du courant Io nécessaires à l'obtention d'une puissance optique de 5mW en fonction de la température.

Lorsque la température du boîtier augmente on constate :

- Une augmentation du courant de seuil du laser et de la proportion de lumière incohérente à puissance globale émise constante.
- Une diminution du rendement différentiel et une accélération des processus de dégradation du laser.

Il est donc nécessaire lorsque les conditions opératoires l'exigent de thermostater le boîtier laser à une température déterminée par les normes adoptées.

Une solution que nous avons étudiée au laboratoire consiste à utiliser pour la régulation en température des microfrigatrons commandés par la sonde de température issue du boîtier et dont la face froide est en contact thermique avec la semelle de l'embase émettrice et la face chaude est pressée contre la semelle du module d'émission. Les puissances nécessaires à la régulation sont typiquement de l'ordre de quelques centaines de milliwatts et les corrections ne s'effectuent que sur les variations lentes de la température. Remarquons qu'une grande précision sur la température n'est pas nécessaire ($\sim$ quelques degrés) les contre-réactions sur les courants de seuil et de modulation pouvant compenser ses effets.

2.3 - Contrôle de la puissance optique de sortie

De même que la température, la dégradation du laser influe sur ses caractéristiques. L'élèvation progressive du seuil diminue la puissance optique continue Po due à la pré-polarisation et la puissance optique modulée P_M et la dégradation du rendement différentiel diminue l'amplitude de modulation du signal optique P_M.IL s'agit donc de contrôler ces deux paramètres et la détection de la puissance optique émise par la face arrière du laser nous en fournit les moyens. Comme l'a montré Epworth (25) une contre-réaction optique lente réalisée à partir du signal détecté fournit des résultats satisfaisants. Dans notre schéma (Figure 1) cette contre-réaction s'applique au courant de seuil et à l'amplitude en tension du signal. Reste à pré-sélectionner Po et P_M. Le courant de pré-polarisation sera choisi juste au-dessus du seuil de façon à limiter le retard indésirable entre l'impulsion de courant et l'impulsion lumineuse. Une pré-polarisation trop élevée serait préjudiciable à la durée de vie du laser et à l'amplitude de modulation disponible. En effet, la puissance optique modulée est limitée soit par la puissance crête permise par le laser ($\sim$ 10mW par face), soit par la présence de"kinks"encore souvent présents au-dessus de 5mW par face.

Notons que le choix de Po et P_M nous amènera à fixer par module un niveau de pré-polarisation et une amplitude de modulation qui diffèrera suivant les embases d'émission, corrigeant ainsi les différences des caractéristiques d'un boîtier laser à l'autre.

L'utilisation de la puissance optique issue de la face arrière du laser comme référence de contre-réaction suppose que celle-ci est proportionnelle à la puissance optique couplée dans la fibre intermédiaire. Cette supposition n'est pas toujours vérifiée soit que le rendement de couplage varie avec le courant d'injection (variation du champ proche, du diagramme de rayonnement, de la proportion d'incohérent ...), soit que la puissance émise par la face arrière n'est pas proportionnelle à la puissance issue de la face avant.

Nous avons réalisé au laboratoire deux premières maquettes de module d'émission dépourvues des circuits de régulation. A la Figure 9 est présentée la photographie d'un module destiné à une liaison ayant un débit de 100 Mbits/s. Le circuit de commande est compatible ECL. La fibre intermédiaire a un coeur de 200/um de diamètre et une ouverture numérique de 0.3. Elle est comme on peut le voir sur la photographie couplée directement au laser semiconducteur. Le connecteur d'extrèmité est fixé sur la face avant du module.

La Figure 10 représente la photographie d'un module d'émission destiné à une liaison télévision. L'entrée est adaptée 75 Ω . Le circuit de codage (ici PWM) est inclus dans le module. Le circuit élémentaire d'attaque est inclus à l'embase. Son temps de montée est de 1ns. Le couplage laser/fibre est fait au moyen d'une fibre lentille. On peut voir la tête optique de couplage et les piges de positionnement. La fibre intermédiaire est terminée par un embout à pincement.

- **REFERENCES** -

1 - J.C. CARBALLES et M. CANTAGREL
"Résultats sur la reproductibilité de fabrication de séries de diodes laser fonctionnant en continu à température ambiante".
Deuxième Colloque Europ. sur les Transmissions par Fibres- Paris 1976

2 - L.G. COHEN
"Power coupling from GaAs injection lasers into optical fibers"
BSTJ, Vol 51, n°3 - 1972

3 - D. KATO
"Light coupling from a stripe-geometry GaAs diode laser into an optical fiber with spherical end"
J. Appl. Phys., Vol 45, n°6 - 1974

4 - C.A. BRACKETT
"On the efficiency of coupling light from stripe-geometry GaAs lasers into multimode optical fibers"
J. Appl. Phys., Vol 45, n°6 - 1974

5 - W.W. BENSON and al
"Coupling efficiency between GaAlAs lasers and low loss optical fibers"
Appl. Optics, Vol 14, n°12 - 1975

6 - C.C. TIMMERMAN
"Highly efficient light coupling from GaAlAs lasers into optical fibers"
Appl. Optics, Vol 14, n°12 - 1975

7 - J. WITTMANN
"Contact-bonded epoxy resin lenses to fibre endfaces"
Electronics Letters, Vol 11, n°20 - 1975

8 - L.G. COHEN and M.V. SCHNEIDER
"Microlenses for coupling junction lasers to optical fibers"
Appl. Optics, Vol 13, n°1 - 1974

9 - E. WEIDEL
"Light coupling from a junction laser into a monomodefibre with a glass cylindrical lens on the fibre end"
Opt. Comm., Vol 12, n°1 - 1974

10 - K. KUROKAWA and E.E. BECKER
"Laser fiber coupling with hyperbolic lenses"
IEEE Trans. Microwave, Theory and Technique, - 1975

11 - Y. KOHANZADEH
"Injection laser coupling to optical waveguides with integral lenses"
J. Appl. Phys., Vol 47, n°1 - 1976

12 - S. SUGIMOTO and al
"Light coupling from a DH laser into a selfoc fiber using slab selfoc lenses"
Techn. Digest., Optical fiber Trans. Conf. - Williamsburg WO 1 - 1975

13 - E. WEIDEL
"Light coupling problems for GaAs laser-multimode fibre coupling"
Optical and Quantum Electronics 8 - 1976

14 - T. OZEKS and B.S. KAWASAKI
"Efficient power coupling using taper-ended multimode optical fibers"
Elect. Letter, Vol 12, n°23 - 1976

15 - C.G. SOMEDA
"Simple, low loss joints between single-mode optical fibers"
BSTJ, Vol 52, n°4 - 1973

16 - C.M. MILLER
"Loose tube splices for optical fibers"
BSTJ, Vol 54, n°7 - 1975

17 - J.F. DALGLEISH and H.H. LUKAS
"Optical fiber connector"
Elect. Lett., Vol 11, n°1 - 1975

18 - J. GUTTMANN, O. KRUMPHOLZ, E. PFEIFFER
"Multipole optical-fibre connector"
Electronics Letters, 27^{th} November 1975, Vol 11, n°24

19 - F. AURACHER
"Planar branching network for multimode Glass Fibers"
Optics Communications, Vol 17, n° 1 - April 1976

20 - M.L. DAKSS and A. BRIDGER
"Plug-in fibre-to-fibre coupler"
Elect. Letters, Vol 10, n°14 - 1974

21 - BREVET N° 74 21 506

22 - R. HAWK and F. THIEL
"Low loss splicng and connection of optical waveguide cables"
SPIE, Vol 63 - 1975

23 - J.S. COOK and P.K RUNGE
"An exploratory fiberguide interconnection system'
IIème Colloque Europ. sur les Transmissions par Fibres - Paris 1976

24 - H. MURATA
"Broadband optical fiber cable and connecting"
IIème Colloque Europ. sur les Transmissions par Fibres - Paris 1976

25 - R.E. EPWORTH
"Subsystems for high speed optical links"
IIème Colloque Europ. sur les Transmissions par Fibres - Paris 1976

26 - P.R. SELWAY and al
"Semiconductor lasers for optical communication"
L'onde Electrique, Vol 56, n°12.bis - 1976

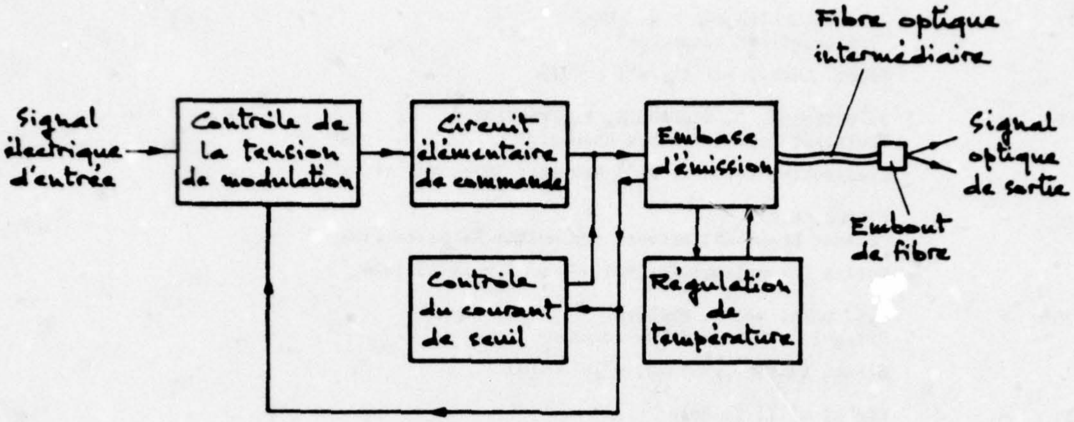

FIG. 1

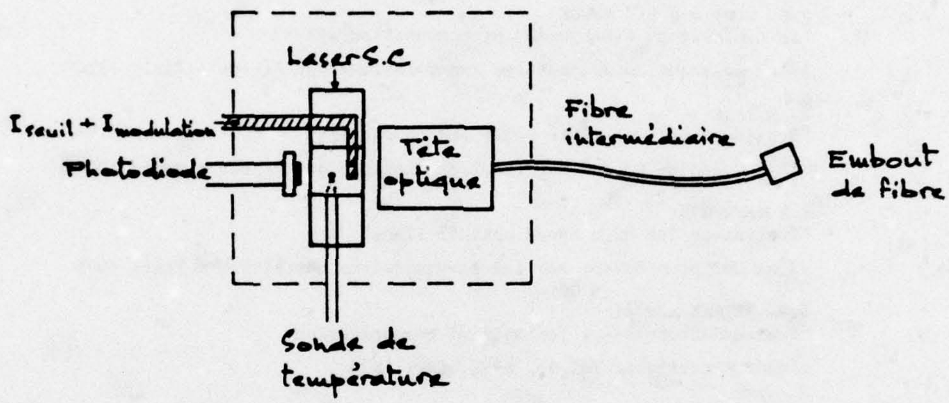

FIG. 2

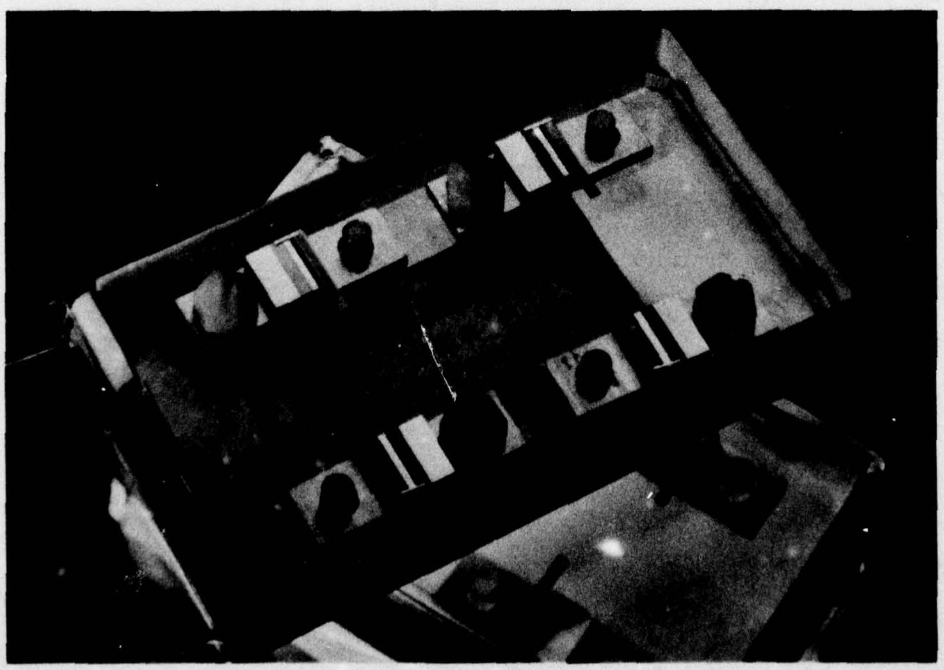

- Figure 3 -

FIG. 4a

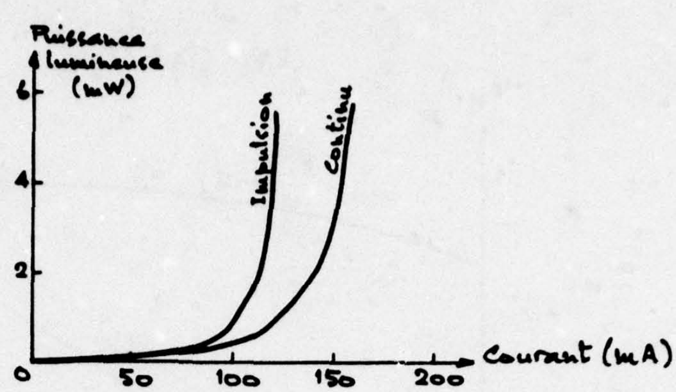

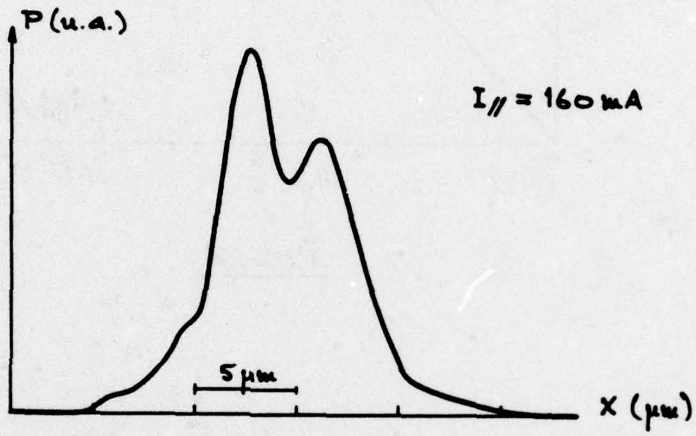

FIG. 4b

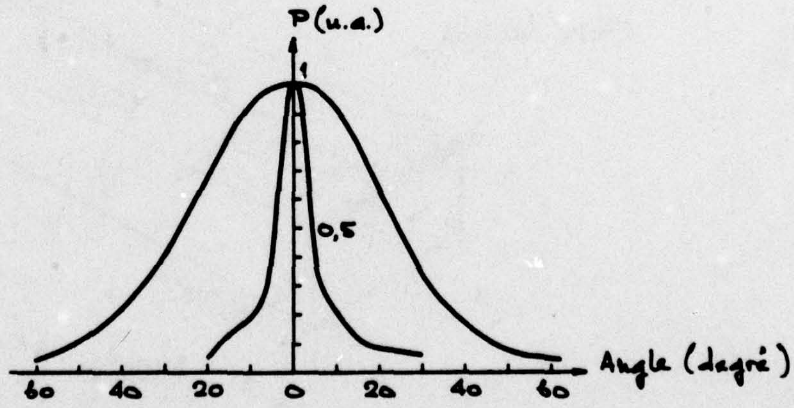

FIG. 4c

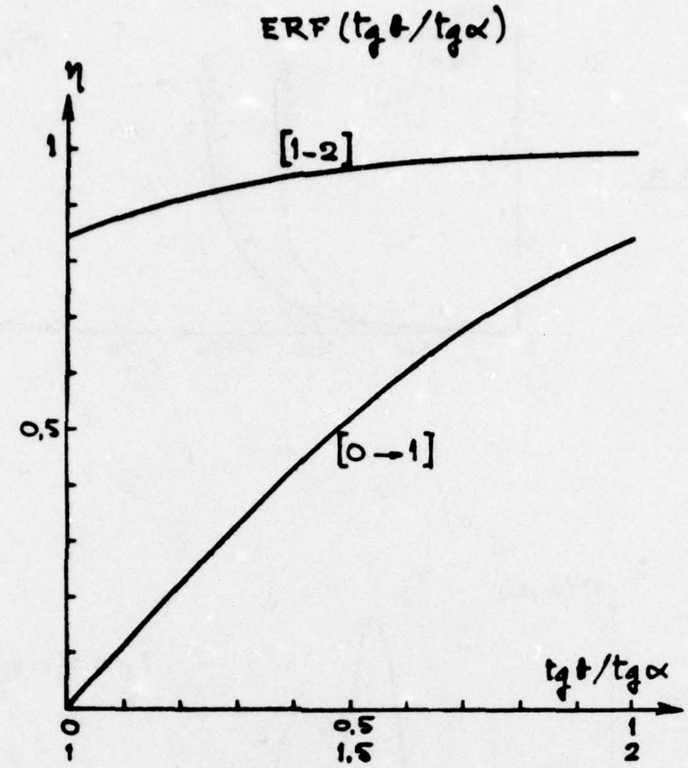
ERF (tgθ/tgα)
η
1
[1-2]
0,5
[0→1]
tgθ/tgα
0
1
0,5
1,5
1
2

FIG. 5

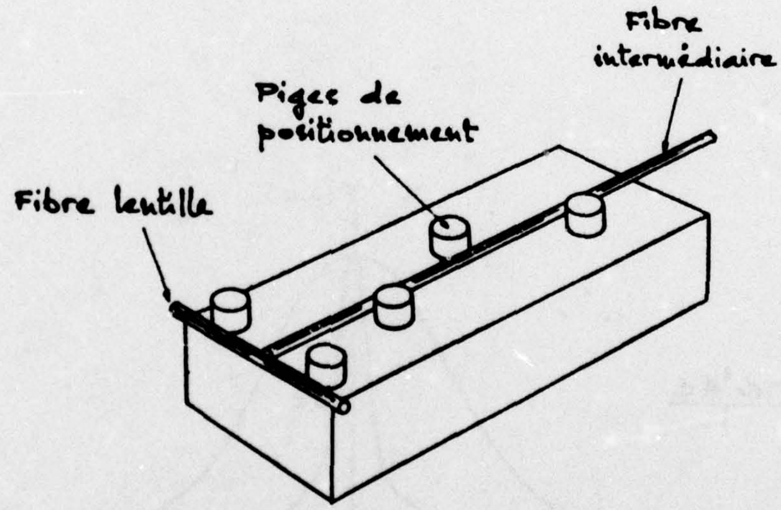
Fibre intermédiaire
Pigee de positionnement
Fibre lentille

FIG. 6

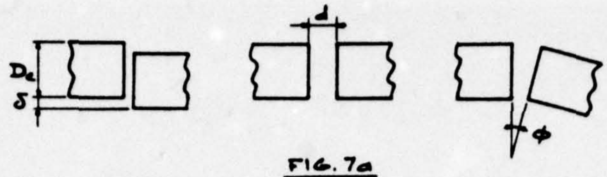

FIG. 7a

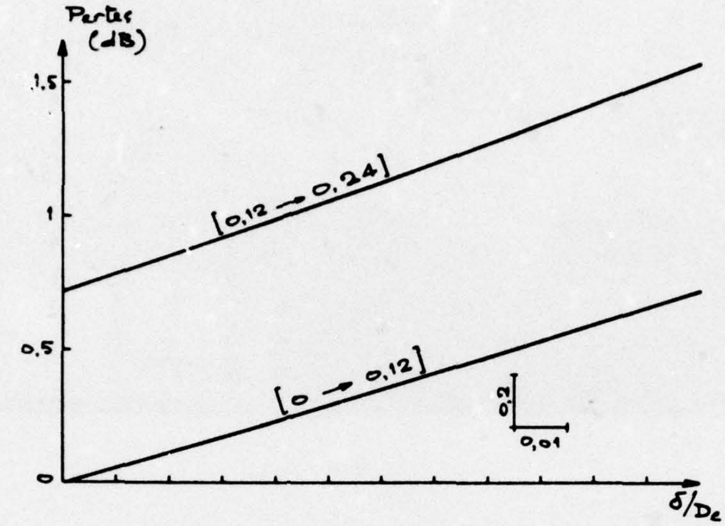

FIG. 7b

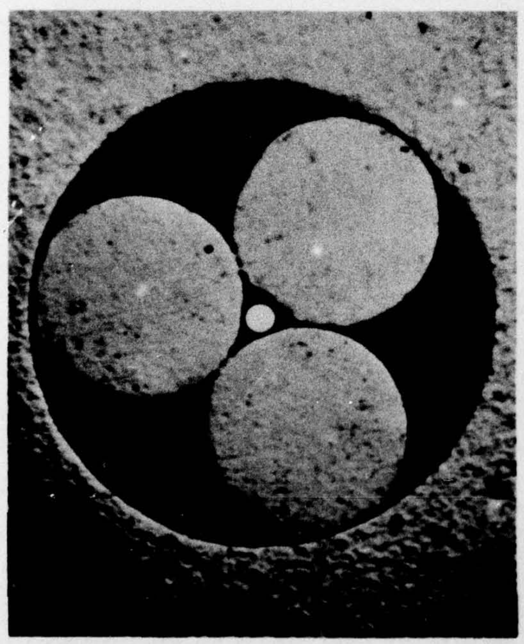

- Figure 8.a -

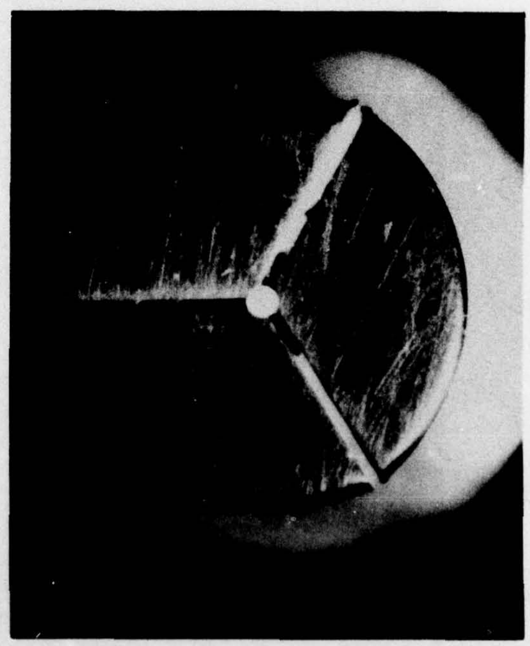

- Figure 8.b -

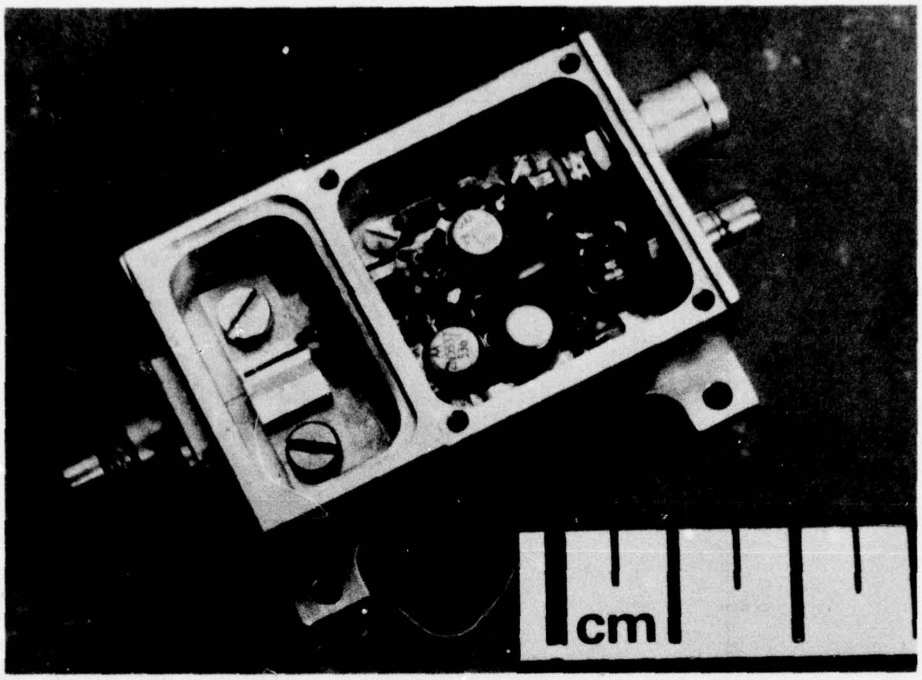

- Figure 9 -

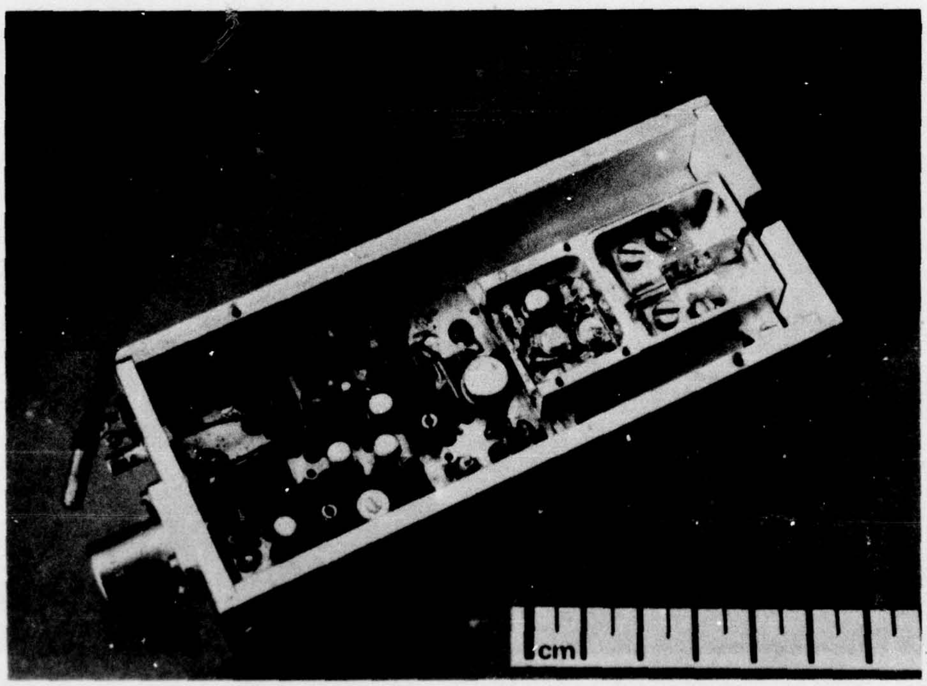

- Figure 10 -

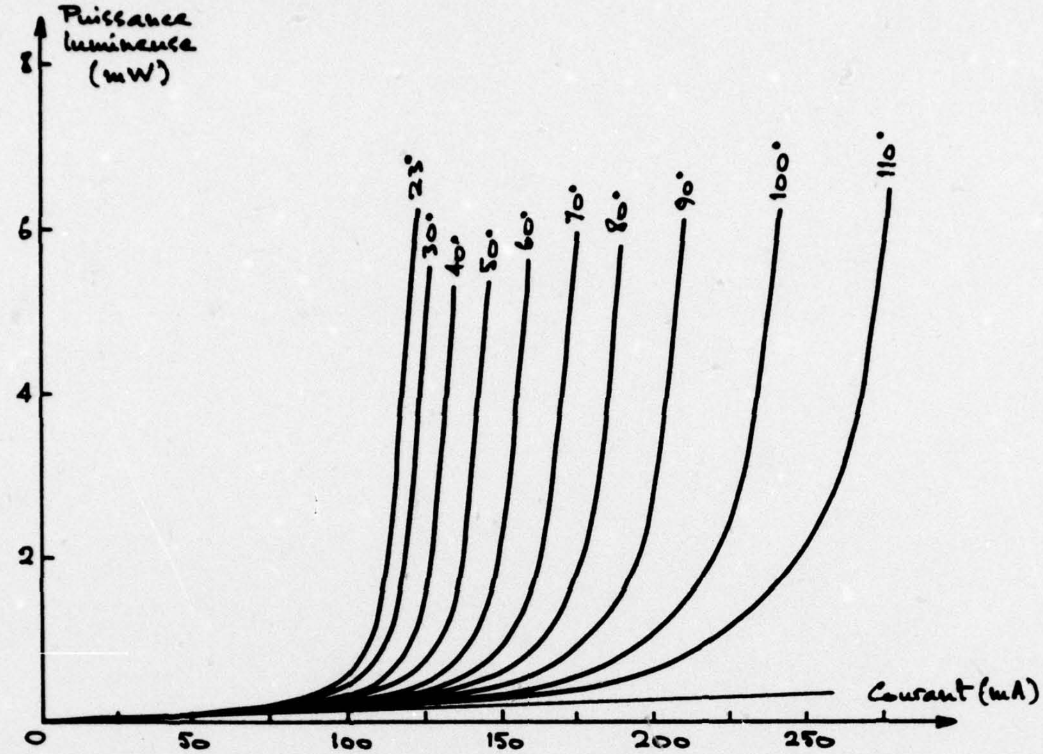

Puissance lumineuse (mW)
8
6
4
2
0
50
100
150
200
250
Courant (mA)
25°
30°
40°
50°
60°
70°
80°
90°
100°
110°

FIG. 11

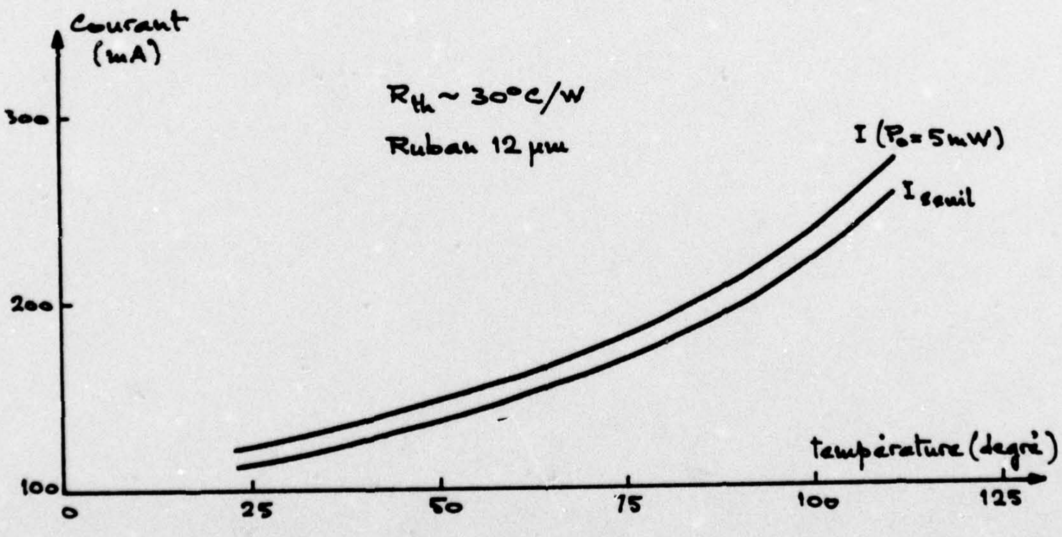

Courant (mA)
300
200
100
0
25
50
75
100
125
température (degré)
$R_{th} \sim 30°C/W$
Ruban 12 µm
$I\ (P_o = 5\,mW)$
I_{seuil}

FIG. 12

INJECTION LASER SOURCES
FOR
FIBER OPTIC COMMUNICATIONS

Robert B. Gill
Laser Diode Laboratories, Inc.
205 Forrest Street
Metuchen, New Jersey 08840

SUMMARY

Over the past seven years there has been substantial effort directed towards the development of reliable injection laser diodes that operate continuously at and above room temperature. This work which produced numerous improvements in laser design, epitaxial and wafer processing, laser assembly techniques and an understanding of the various laser degradation mechanisms has lead to the fabrication under laboratory conditions CW laser diodes which have exhibited over ten thousand hours of operating lifetime at room temperature as well as commercially available CW lasers which exhibit lifetime of several thousand hours. This paper describes some of the laser designs and GaAs and GaAlAs epitaxial and wafer processing technology currently used in the fabrication of laser diodes which are intended for incorporation into fiber optic communication or data link systems. Two classes of laser diodes are described; CW laser diodes emitting up to 75mw and devices emitting in excess of 200mw peak pulsed power at 27°C at duty cycles up to 10%. Both groups of devices are fabricated from double heterojunction GaAs and GaAlAs liquid phase epitaxial structures as first proposed by Hayashi in 1970. In addition, these devices all contain monolithic stripe geometry emitting regions similar to those described by Itoh in 1974. The processing utilized in the fabrication and assembly of these devices is presented in detail with particular emphasis on liquid phase epitaxy and monolithic stripe generation. The problems encountered in the transfer of these processes from a research environment to a manufacturing operation are discussed.

Data is presented showing laser emitted power both pulsed and continuous, the angular distribution of emitted power, emission wavelength and bandwidth, optical coupling efficiency to various fibers and laser lifetimes. In addition, the interaction between laser threshold current density, thermal impedance, emitted beam distribution and fiber optic coupling is described. Several fiber optic laser coupling schemes are described with particular emphasis on device concepts currently either in commercial production or pilot production.

Finally, the results of qualification testing pulsed laser diodes to standard military environmental and performance test requirements are described with specific data presented showing the value of burn-in testing to eliminate from test lots lasers which exhibit abnormally short lifetimes.

This paper describes the fabrication and performance characteristics of injection lasers and light emitting diodes currently being developed for use in fiber optics communication or data link systems. Emphasis is directed on device design and GaAs and GaAlAs epitaxial and wafer processing technology currently in use for the routine manufacture of commercial light emitting diodes and high duty cycle or CW room temperature injection laser diodes. Therefore, the device performance results which are discussed are typical of manufactured devices rather than the best results observed in our laboratory. While the processing technology which is described is based on the fabrication of CW room temperature laser diodes, the processing techniques detailed are also applicable to the manufacture of double heterojunction light emitting diodes as well as large optical cavity, high power, high duty cycle laser diodes.

The approach to CW injection laser fabrication follows a design originally proposed by Hayashi in 1970 and extended to a monolithic striped geometry configuration by Itoh in 1970. A detailed schematic representation of this device structure is shown in Figure 1.

The substrate wafer, region 1, is n-type, Si Doped GaAs having a net donor concentration of about $2x10^{-18}cm^{-3}$ and a dislocation density of about $1000cm^{-2}$. The use of this low dislocation substrate, which is grown at Laser Diode Laboratories by the gradient freeze technique, has been shown to be crucial for routinely obtaining devices which exhibit reduced gradual performance degradation due to dislocation migration and/or growth from the substrate to the active region of the device during the epitaxial growth or actual operation. To further decrease these effects an attempt is made to terminate existing dislocation networks or substrate surface imperfections by the growth of at least one n-type Te Doped GaAs buffer layer which is shown as Region 2.

Regions 3 and 5 are n-type and p-type GaAlAs layers which contain approximately 35% Aluminum. These two layers act to confine the light generated in the active layer, Region 4, to that layer. Light is confined to that region by the waveguiding effects of the interfaces between Regions 3 and 5 and Region 4. These effects arise due to slight index of refraction decrease at these boundaries with the lower bandgap active layer, Region 4. The actual peak laser emission wavelength is determined by the bandgap of the active layer. In practice an 8% Aluminum concentration corresponds to an emission wavelength of about 820 nanometers at room temperature. This particular emission wavelength is found to have an absorption loss of about 5db per kilometer in typical low loss glass fiber. In order to obtain the low threshold current densities required for CW laser operation the total recombination volume must be minimized. For typical CW lasers, d, the thickness of Region 4 is maintained between 0.25 and 0.3μm.

Region 6 functions as a contact gap with a small amount of Aluminum incorporated into it to minimize lateral current flow by increasing its resistivity. Typically, this p-type layer is Ge Doped.

Stripe geometry fabrication permits room temperature CW operation by limiting the current to the portion of the laser pellet located under the narrow stripe and thereby activating only a small portion of the junction width. This allows the heat generated in the 25μm lasing region beneath the contact stripe to be distributed throughout the bulk of the laser pellet. This fact together with the close proximity of the active region to the heat sink results in laser diodes which are capable of sustained CW operation to temperatures in excess of 70°C.

Stripe geometry was first accomplished by masking Region 6 with an oxide insulator and chemically etching open contact stripes perpendicular to the cleaved laser cavity end mirrors. Ohmic contacts were then evaporated over the entire wafer, forming a selectively contacted stripe which allows current to flow through the cavity only in the region directly beneath the contact stripe. Since its inception the concept of striped current isolation has been modified to include such sophisticated formation techniques such as: proton bombardment, diffused and mesa stripe geometries. One approach however employs a monolithic isolation technique which fully exploits the capability of liquid phase epitaxy to generate material to which stripe geometry contacts can be applied without the need for complex or sophisticated wafer processing techniques. In this approach the oxide insulator is replaced by a lattice matching GaAs blocking layer. The layer consists of lightly doped n-type GaAs or semi-insulating Cr Doped GaAs. Following photolithographic definition of the contact stripe array, 20μm wide contact channels are etched through the blocking layer. Under conditions of laser die forward bias, current is restricted to flow through the active region only beneath the etched channel. Elsewhere because the p/n junction formed at the interface between Regions 6 and 7 is backbiased, the laser cavity remains unpumped. Using this technique, high power CW laser diodes which emit up to 75mw have been produced. The forward current versus power output characteristics for one of the highest power 15μm wide striped lasers manufactured at Laser Diode Laboratories is shown in Figure 2. The device which contained no reflective optical mirror coating exhibited a single ended output of over 70mw at 400ma forward drive. The single ended external differential quantum efficiency was 23%.

The monolithic stripe geometry formation technique used in the fabrication of this device offers several advantages over the oxide isolation or other alternative stripe formation approaches.

1. The high device thermal impedance due to the presence of the poor thermally conducting oxide insulator is eliminated thereby improving device thermal conduction and high temperature performance.
2. The surface stress induced by the presence of the oxide film which has different thermal expansion characteristics from the GaAs pellet is eliminated.
3. The danger of lattice damage and dislocation formation present in diffused stripe geometry lasers is eliminated.
4. The simplicity of the blocking layer isolation technique lends itself to high volume, high yield production.

In view of the previously demonstrated association between laser and ligh emitting diode reliability, four criteria have been considered to be of primary importance in establishing epitaxial wafer and die assembly processes, to achieve an as-grown wafer surface that is flat and free of both melt residue and pinholes in order to permit uniform wafer thinning, stripe formation and contacting, to maximize the yield per wafer of devices having identical structural, electrical and optical properties over the desired operating temperature range, and finally, to establish processes compatible with a production operation to insure that continuous process adjustments are not required to achieve process repeatibility.

Figure 3 shows an etched cross-section of a typical double heterojunction structure used in the manufacture of monolithic stripe geometry injection laser diodes. Similar structures are used in the fabrication of high speed striped light emitting diodes or in broad area LED's. For the latter devices the final n-GaAs layer is eliminated.

The fabrication of CW lasers follows the process sequences shown in Figure 4. After expitaxial growth the wafer is cleaved along its perimeter on all four sides to create mutually perpendicular <110> reference edges for channel alignment. Photolithographic definition of the stripe contact channels is accomplished by aligning the photo-mask reference with the <110> direction as indicated in b. Photolithographic definition is followed by an etch which removes the n-GaAs blocking layer, forming an array of 15μm wide contact channels to the p-GaAlAs contact cap. Channel separation is on 325μm centers. After removing the masking resist the wafer is thinned to a 75μm thickness and ohmic contacts applied to both sides of the wafer. The wafer is then cleaved and optical coatings applied to the mirror facets. Finally, the individual laser die is formed by wire sawing the coated slivers. Figure 5 shows an etched cross-section of a typical 15μm stripe. This illustrates the excellent stripe definition and uniformity achieved using this monolithic approach. After formation of the laser or LED die, the die is screened for performance characteristics prior to package mounting. The pretesting of the die prior to mounting assures that no defective or substandard die reaches final testing. The cost reduction achieved by pretesting is significant in assembly, packaging, burn-in and final test. Each completed device assembly is burnt in to eliminate unstable devices from final acceptance.

Typical performance characteristics of 15μm stripe contact in commercial CW room temperature lasers are shown in Figure 6. These devices which emit 5 and 10mw minimum average power can be fabricated with emission wavelengths ranging from 790 to 890nm at 27°C. The characteristics of the two devices shown here are typical of devices which emit at about 820nm at 27°C. Shorter wavelength devices will exhibit a slightly higher threshold current, while longer wavelength devices will have somewhat lower threshold currents. The single ended differential quantum efficiency of the LCW-5 which emits between 5 and 10mw continuous power generally lies between 6 and 12% while the efficiency of the LCW-10 which typically emits between 10 and 20mw at room temperature lies between 11 and 20%. The variation in threshold current with increasing temperature for a typical LCW-5 laser diode is shown in Figure 7. Operation at temperatures up to 65°C results in typically lasing threshold current increases of up to 50%. This level of increase in threshold current appears to be independent of the device's emission wavelenth and efficiency. Therefore we observe a similar result for the LCW-10 lasers. Similar relative changes in threshold current versus temperature are also observed in the high power pulsed room temperature lasers such as Single Heterojunction, LOC or TH lasers. If we then operate a device at a constant drive current above threshold we obtain a power characteristic similar to that shown in Figure 8. Using a current DC over drive of 50ma above threshold we obtain nearly constant power output up to at least 65°C. This indicates that the device quantum efficiency is not strongly affected by temperature over this range. The slight rolling off of output observed near 65°C is probably associated with local device heating due to the higher drive current rather than fundamental change in lasing characteristics. This type of result again appears to be similar to that observed in highly efficient pulsed multiheterojunction devices and seems to be independent of wavelength from 790nm to 890nm. The complete performance characteristic of a typical LCW-5 laser at 27°C and 70°C is shown in Figure 9. Here again we see results similar to those just described; namely, a threshold current increase of about 50% and little or no change in quantum efficiency or slope of the output characteristic above threshold. Typical devices show a full angle to 50% intensity distribution of about 40-45 degrees. In practice this distribution is effected by the Al content of the optical cavity bounding layers, the width of the optical cavity and to a lesser degree by the emission wavelength. In the plane parallel to the junction plane, devices typically show a full angle to 1/2 power emission distribution of about 4 to 7 degrees. This characteristic is generally far superior to the 14 to 16 degree distribution observed for typical broad area high power pulsed devices.

One area that has been of great concern to potential users of CW injection laser diodes has been device lifetime. Early in the technology of CW lasers, it was found that most devices exhibited extremely erratic operating lifetimes, typically in the order of a few hours. Over the past five years, considerable research effort has been expended in understanding the sources of service instability and improving device processing techniques to surpress or eliminate the numerous sources of device degradation. This work has resulted in several laboratories reporting CW devices with operational lifetimes in excess of 15,000 hours and in projected operational lifetimes of about 100,000 hours. While these lifetimes have not yet been demonstrated to be characteristic of all commercial production devices, a key question that arises is what can be expected of present commercial manufacturing technology. Figure 10 shows a typical life characteristic obtained from a standard commercial CW laser. Prior to entry into life test or acceptability into commercial sale, all CW lasers are burnt-in to eliminate unstable devices from the test or acceptable population. This initial burn-in generally screens from the product run unstable devices which would degrade after the first few hundred hours operation. However the screening system still remains to be further perfected to permit both more accurate screening, a pre-conditioning and accelerated life testing to permit routine and accurate extrapolation of commercial device performance characteristics and assurance to lifetimes in excess of 10,000 hours.

Another area that the stripe laser technology can be extended to, is in the development of more reliable high performance, high power pulsed lasers for operation at and above room temperature. Figure 11 shows the performance characteristic of a 3 mil wide stripe geometry TH laser diode designed for high pulsed power operation at room temperature. In practice this size device has been one of the most difficult to manufacture reproducibly using standard wire cutting techniques due to die size variations associated with the cutting process as well as the penetration of cutting damage at the laser sides to a depth which is significant when compared to the lasers width. The use of striped laser technology in the manufacture of these devices largely eliminates these two problems with the result that both laser reproducibility and reliability can be significantly improved. Devices of this type have been reliably operated at output emission densities of over 1 watt/mil of facet while broad area wide saw devices made of similar epitaxial materials have failed at power densities of less than 3/4 watt per mil of facet. In addition, these devices have exhibited reliable operation at duty cycles of 1 to 10% making them potentially extremely useful in fiber optic data link applications which require high peak power.

The performance characteristics of a typical high power, high duty cycle injection laser is shown in Figures 12 and 13. This particular device which is intended for a redundent fiber optics communication application consists of a monolithic array of three 25μm striped lasers on 125μm centers which are operated in parallel. These devices have been operated at duty cycles exceeding 10% with little change in performance over several thousand hours.

As discussed earlier, the room temperature CW or high duty cycle injection lasers utilize variations of the narrow optical cavity double heterojunction (DH) structure to achieve the low threshold current densities required to support these levels of operation.

Because of the small recombination region thickness, the beam divergence perpendicular to the plane of the junction in this device is excessive. Beam divergence can exceed 50° FWHM for CW laser structures with narrow cavities. The divergence results from diffraction of the emitted beam as it passes through the output aperature of the

Fabry-Perot cavity. Excessive beam divergence occurs since the wavelength of light in the $Ga_{1-x}Al_xAs$ active region is roughly the same size as that of the diffraction slit (exit aperature d). The divergence parallel to the P/N junction is not determined by diffraction effects because $s \gg \lambda/n$. Beam divergence in the transverse parallel direction is more strongly related to the mode structure of the laser diode. The intensity distribution of the emitted beam parallel to the plane of the P/N is typically less than 10° FWHM. Figure 14 shows schematically the main features of the beam pattern for a typical CW injection laser diode.

Unfortunately, the angular intensity distribution of the room temperature CW injection laser diode poses a major problem for fiber optic applications. Because of low loss graded index fiber types have small numerical aperatures, (n.a. 2.25), the acceptance angle of the fiber is much less than the half intensity angle of the laser's beam distribution. This results in extremely low coupling efficiencies for the laser-fiber interface when butt coupling is employed. The laser diode fiber interface is illustrated schematically in Figure 15 for three coupling configurations:

a) Butt coupling
b) Butt coupling with index matching
c) Lensed fiber coupling

To date both butt coupling with an air gap and with index matching agents have been utilized in prototype laser products. However, coupling with these two techniques is generally inefficient due to the low n.a. generally observed in low loss fibers. Depending on the fibers selected, coupling efficiencies in the range of 10 to 25 percent are generally observed.

An alternative technique for increasing the collection efficiency of the fiber involves the use of a hemispherical lens affixed to the input end of the optical fiber pigtail. The lens, when properly designed and fabricated, collinates the divergent laser beams so as to increase the amount of light which enters the fiber at an angle less than the acceptance angle of the fiber. The function of the lens is illustrated schematically in Figure 15 c. The concept of using lensed fibers to increase the coupling of laser output into the fiber was first proposed by Kato et al in 1973. He suggested forming the lens by careful melting of the cleaved fiber and to form a hemispherical lens whose radius of curvature is determined primarily by the fiber radius and the surface tension of the molten glass. More recently, C. C. Timmerman has pointed the way toward further improvements in collection efficiency by improving on Kato's original concept. Figure 16 shows segmented views of two lensed fibers:

a) thin core step index
b) thin cladding step index

The lens is formed on each fiber by melting the cleaved end with a micro-torch (after Kato et al). In a) the lens formed a small radius of curvature compared to the radius of the fiber core. In Figure 16 b, the cladding wraps around the core during formation of the lens. In both cases, the lenses are inefficient in collimating the divergent output of the laser diode. Timmerman has demonstrated experimentally, that the properly designed lens must have a radius of curvature approximately equal to the radius of the fiber core. This applies not only to step index but also to low loss graded index fiber of the type commonly used for fiber optic communications.

His solution to the problems of lens formations shown in Figure 16 c, requires the removal of all or part of the fiber cladding by chemical etching prior to forming the lens. This technique guarantees that the lens will have approximately the same radius as the fiber core. In addition, a technique other than melting the fiber end was demonstrated. Using lenses formed by dipping the core in optical epoxy or low melting point high index glass,C.Timmerman achieved efficiencies up to 80% with standard commercial CW injection coupled to low loss fibers with an n.a. of .16.

Work is now underway to extend this work to standard commercial products. Figure 17 shows an outline of a fiber coupled injection laser intended for introduction into commercial sale later this year. The diamond based TO-5 or TO-39 package was chosen for the base outline because of its improved heat sinking over the conventional TO-5 stud packages. In addition, stripline leads are provided as well as a floating case to make the device more compatible with the requirements of high frequency drive circuitry. The internal structure of the device is shown in Figure 18. This figure presents the laser-fiber interface as it appears in the completed device. The lensed fiber coupling scheme shown requires a separate mounting ledge to provide mechanical stability to the fiber. Alignment of the fiber to the laser is accomplished using a micromanipulator and photodetector and peaking the fiber output by adjusting the position of the fiber with the manipulator. After peaking the lensed end of the fiber is tacked to the supporting ledge and the ferrule support sleeve expoxied in place. Using commercially available 0.2 n.a. graded index fiber with 50μm core diameter and less than 5db per kilometer loss laser outputs in excess of 5mw can be achieved at drive currents less than 30ma.

Work directed toward the qualification of injection laser diodes for military applications has to date utilized device configurations which do not include optical fibers within the device package. This work has included successful qualification of injection laser assemblies to high temperature storage 150°C, temperature shock (-55°C to 150°C), acceleration (20,000g), mechanical shock (1,500g) and vibration. No particular problems have been encountered to date in routinely qualifying monthly manufacturing lots to these requirements. During the near future work will be initiated toward the qualification of a fiber optic coupled device similar to that just described to similar environmental and mechanical requirements.

In summary, both striped geometry and broad area double heterojunction CW lasers and light emitting diodes have been developed for application in fiber optic data and communication links. The processing required for the manufacture of these devices has been demonstrated to be compatible with a manufacturing environment. Using these process devices with operational lifetimes in excess of 3000 hours can be routinely manufactured.

Finally, these devices are currently being integrated with fiber optic pigtails and connectors to provide device designs suitable for effective applications in fiber optic data and communication links.

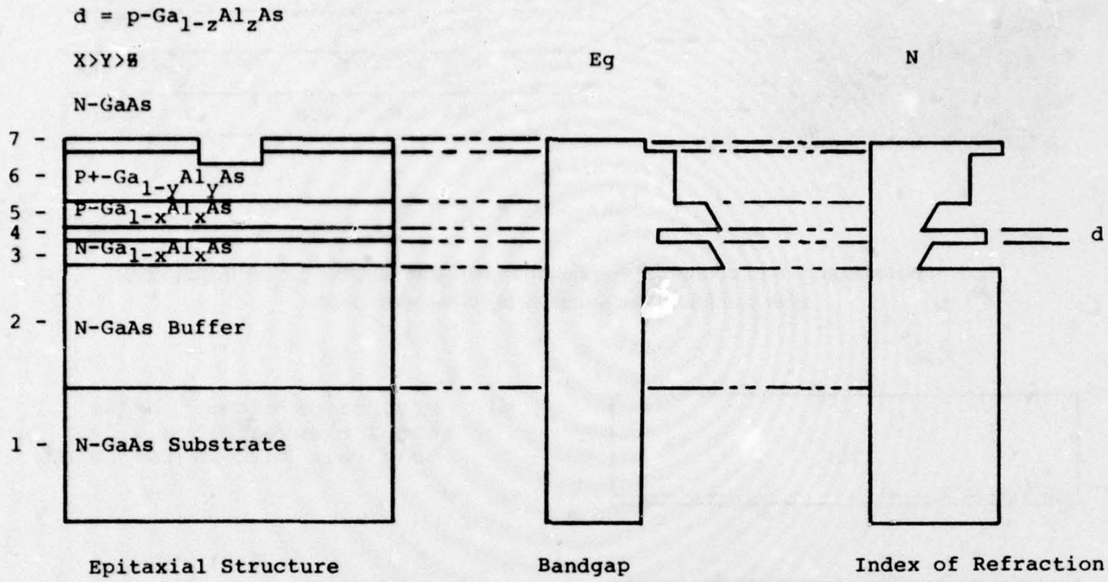

Fig.1 Schematic representation of the epitaxial structure for fabrication of stripe geometry double heterojunction injection laser diodes

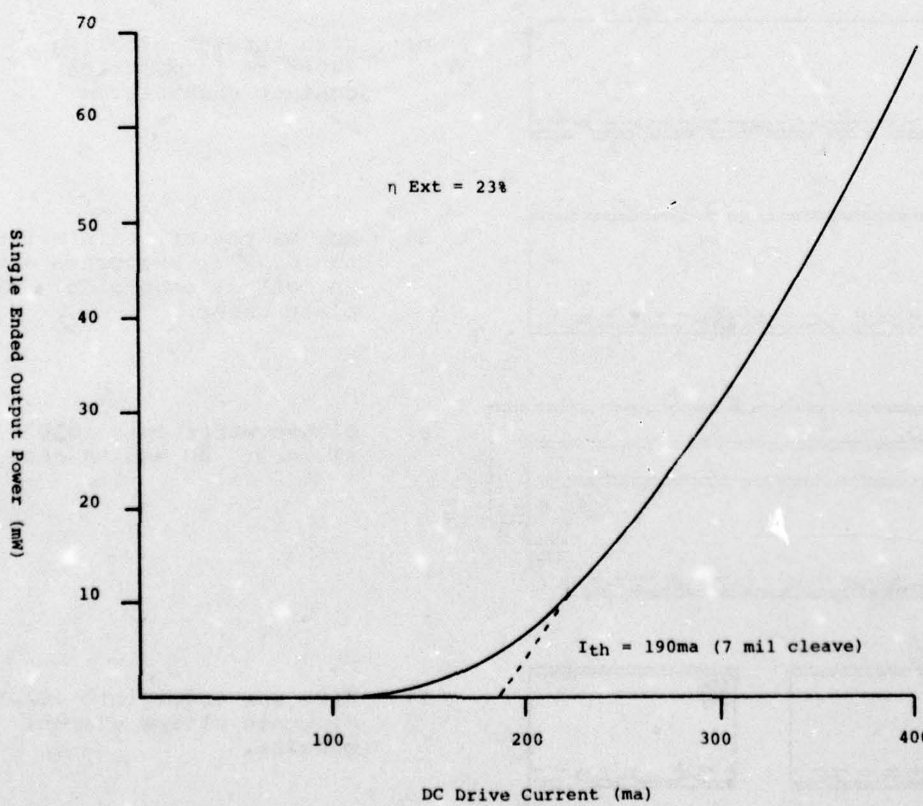

Fig.2 Output power versus current for 15 μm stripe geometry room temperature CW lasers

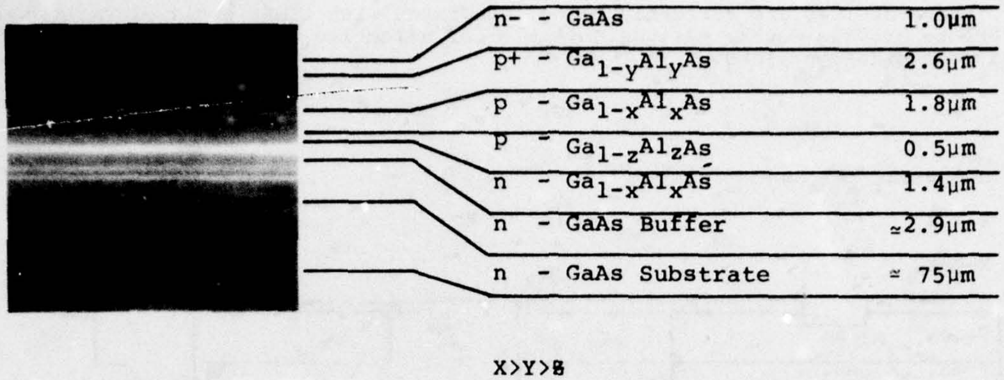

Fig.3 Photograph of typical double heterojunction structure required for the manufacture of monolithic stripe geometry injection laser diodes

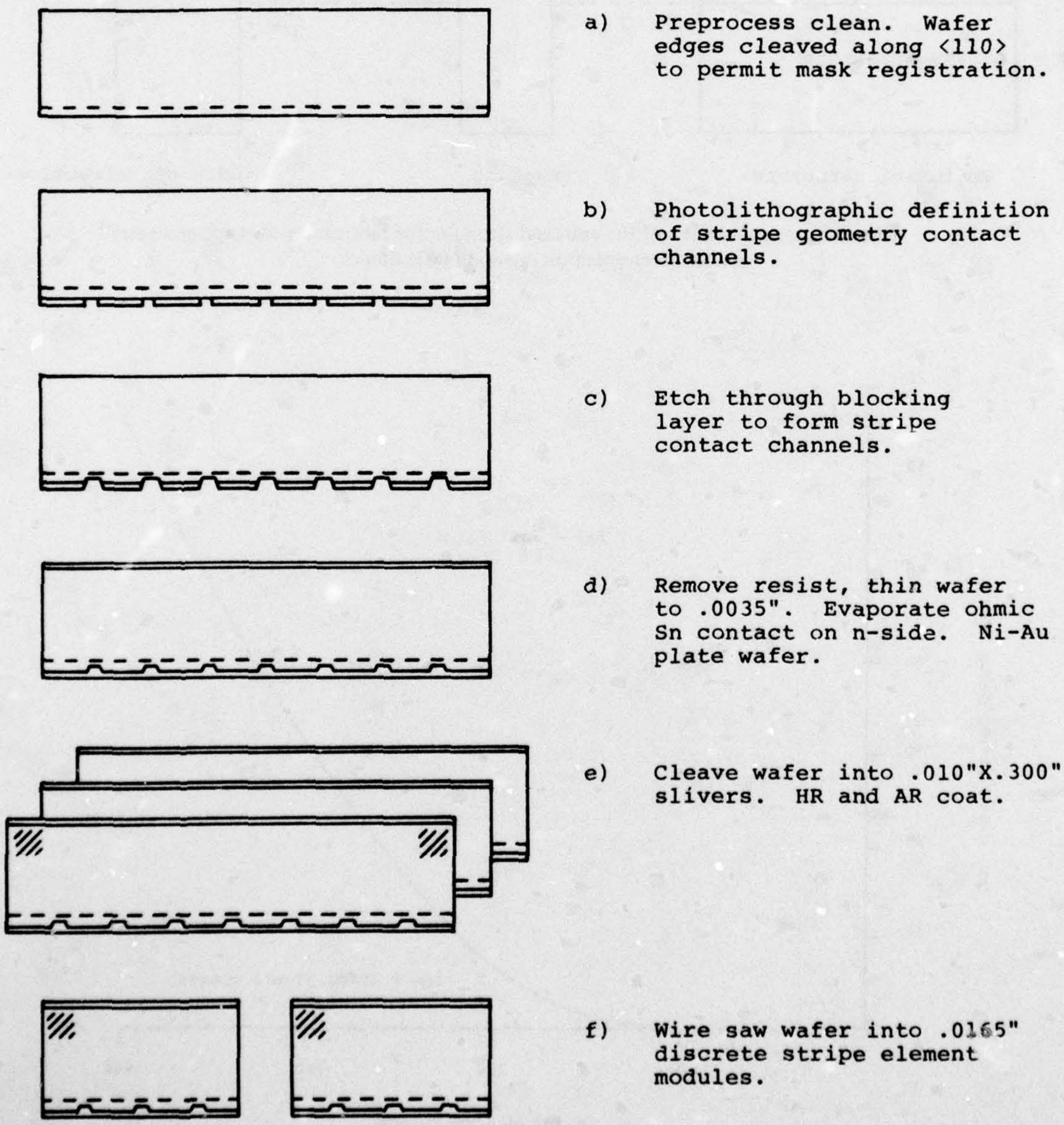

Fig.4 Process flow diagram for the fabrication of monolithic stripe geometry injection laser arrays

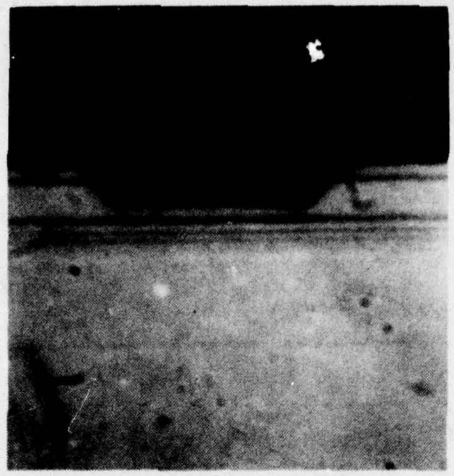

Fig.5 Etched cross-section of a 15 μm etched stripe geometry DH laser structure

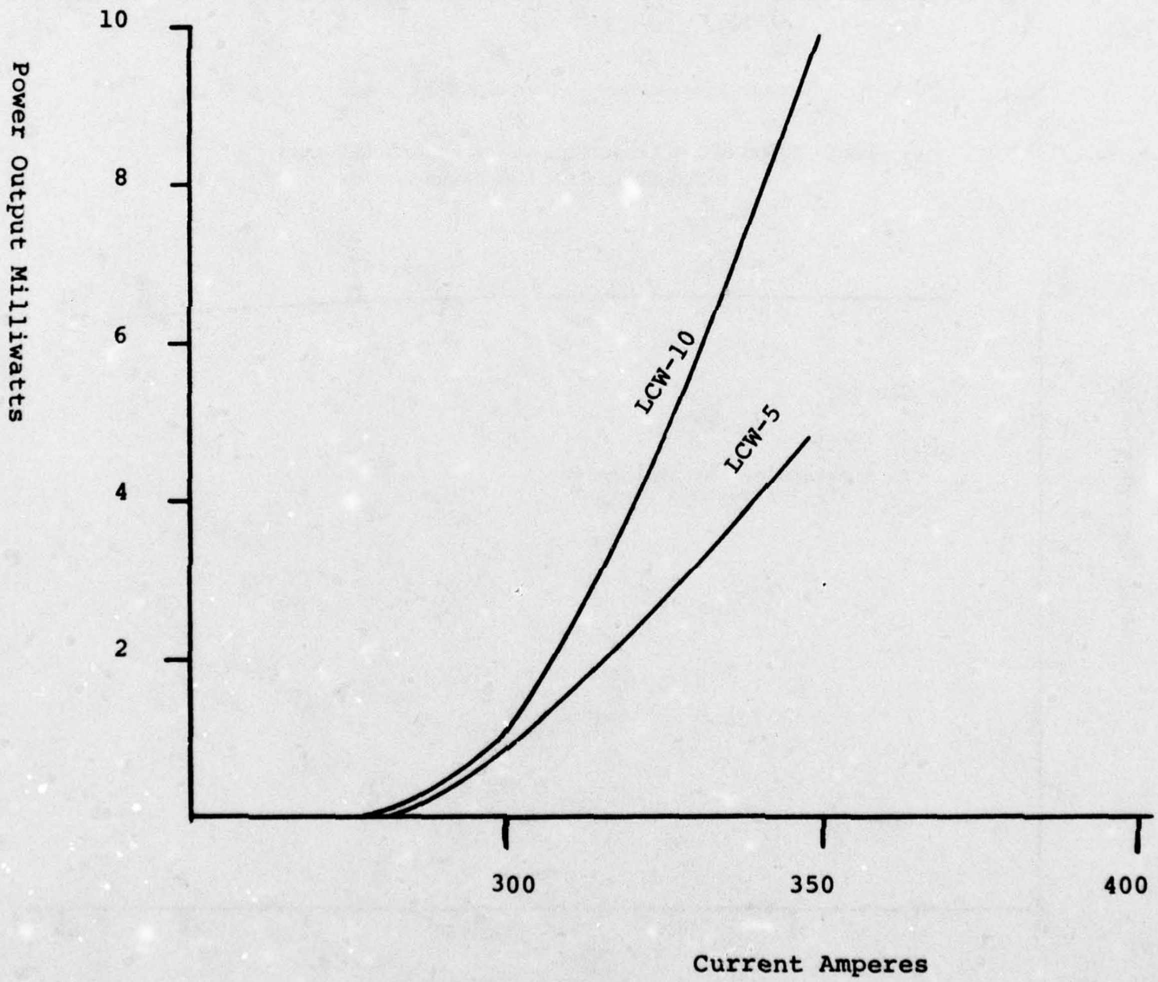

Fig.6 Output characteristics of typical commercial CW laser diodes

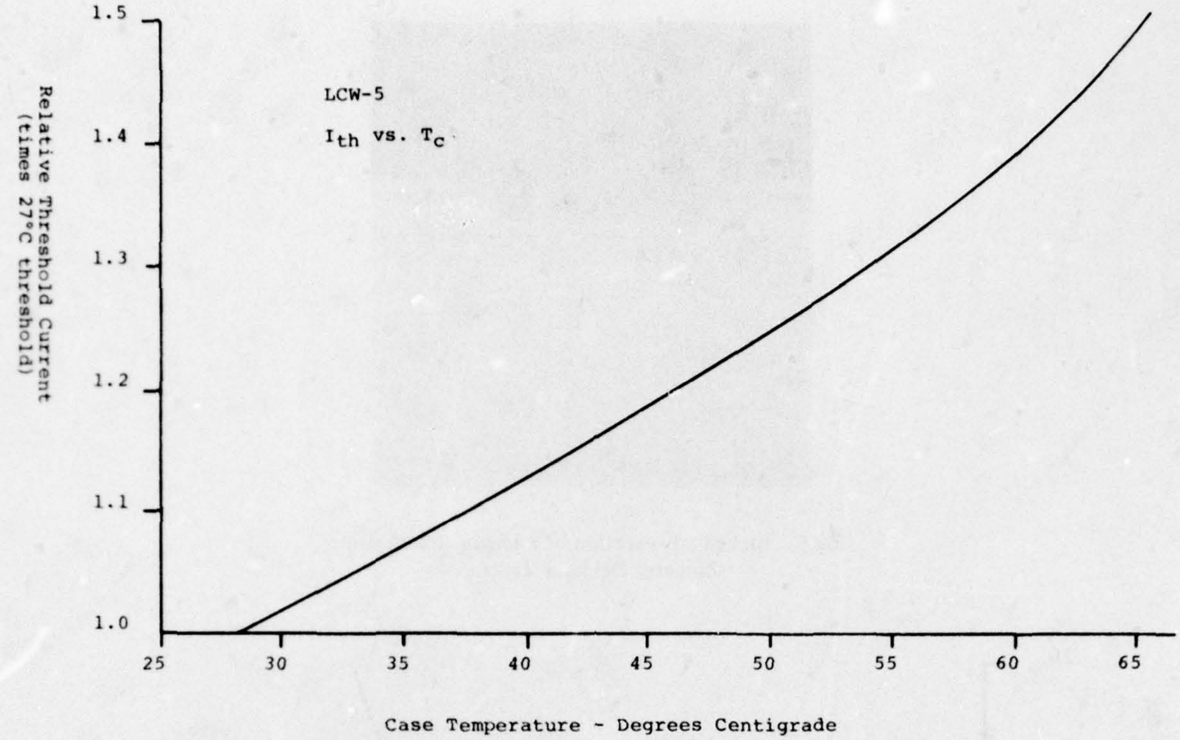

Fig.7 Effect of case temperature on lasing threshold current for commercial CW laser diodes

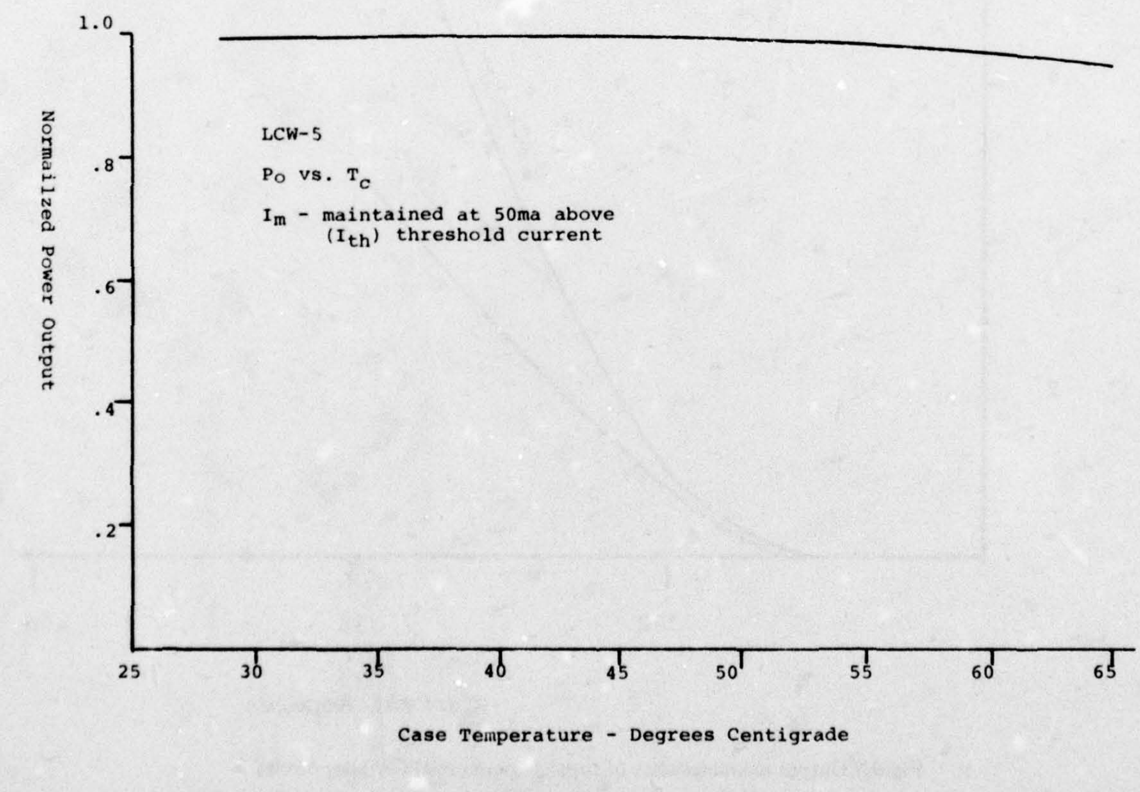

Fig.8 Output characteristics of CW laser diodes as a function of case temperature at constant drive current above threshold

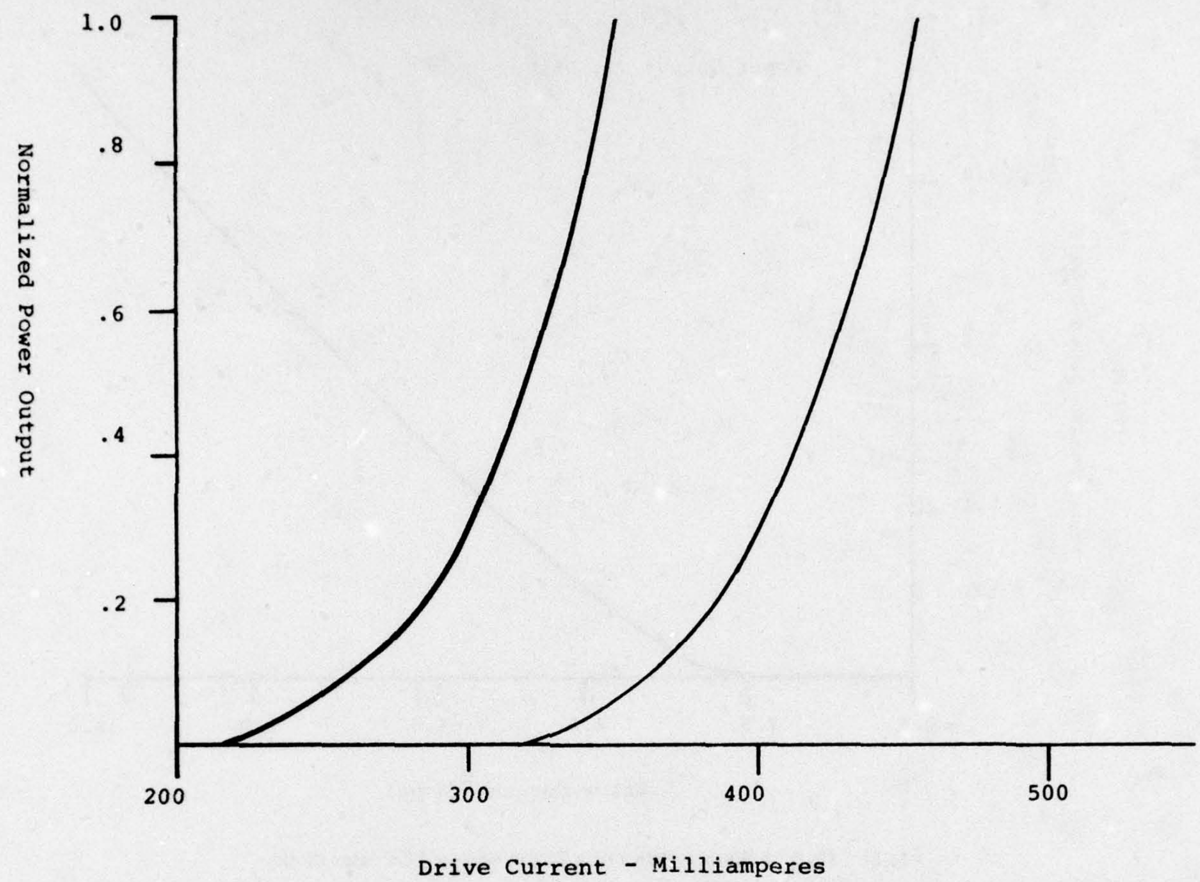

Fig.9 Output characteristics of CW laser diodes at 27°C and 70°C

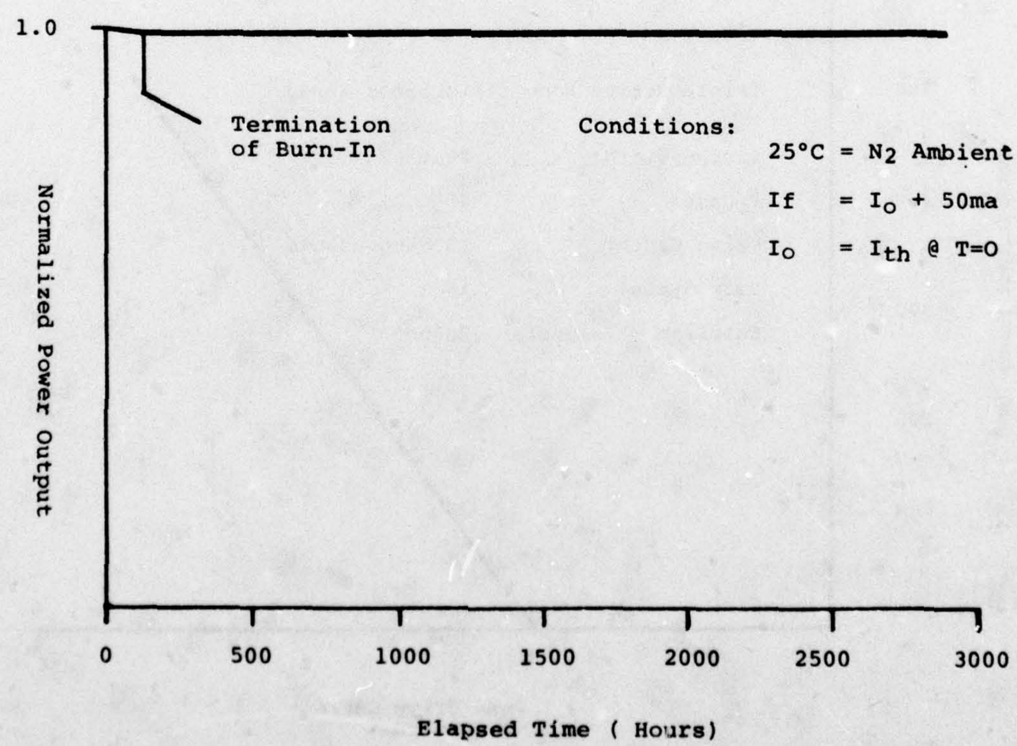

Fig.10 Room temperature CW laser diode lifetime stability

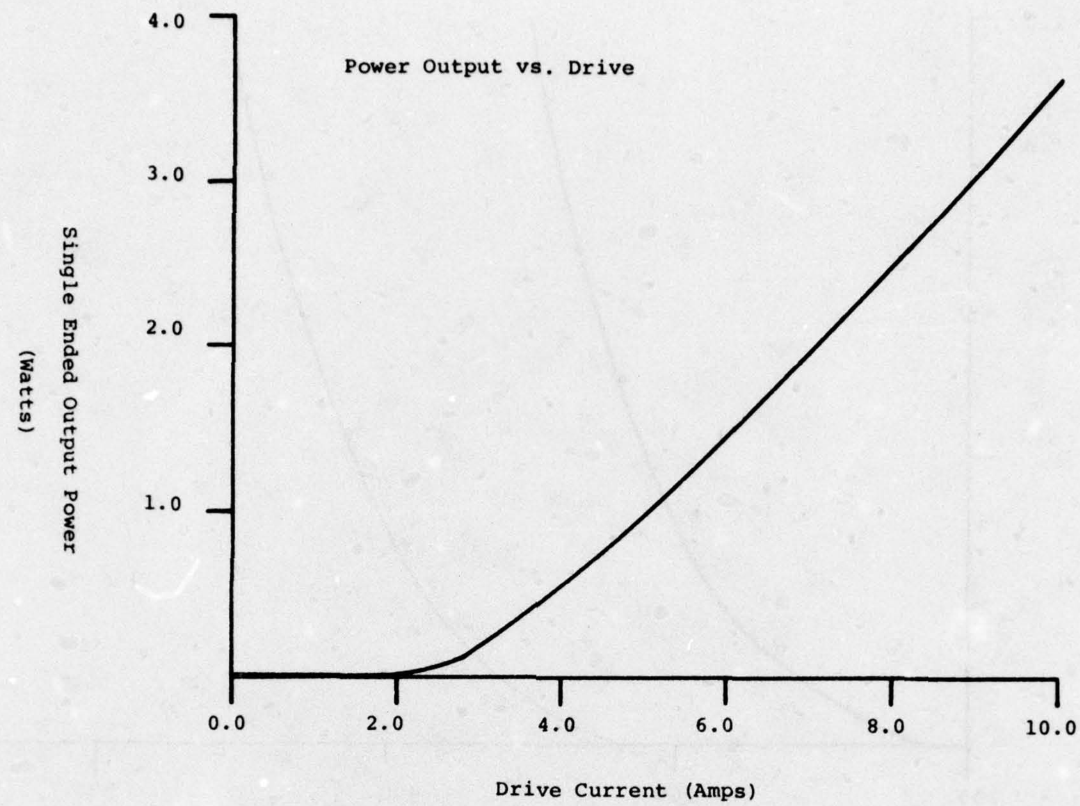

Fig.11 Output characteristics of a 75 μm striped LOC laser diode

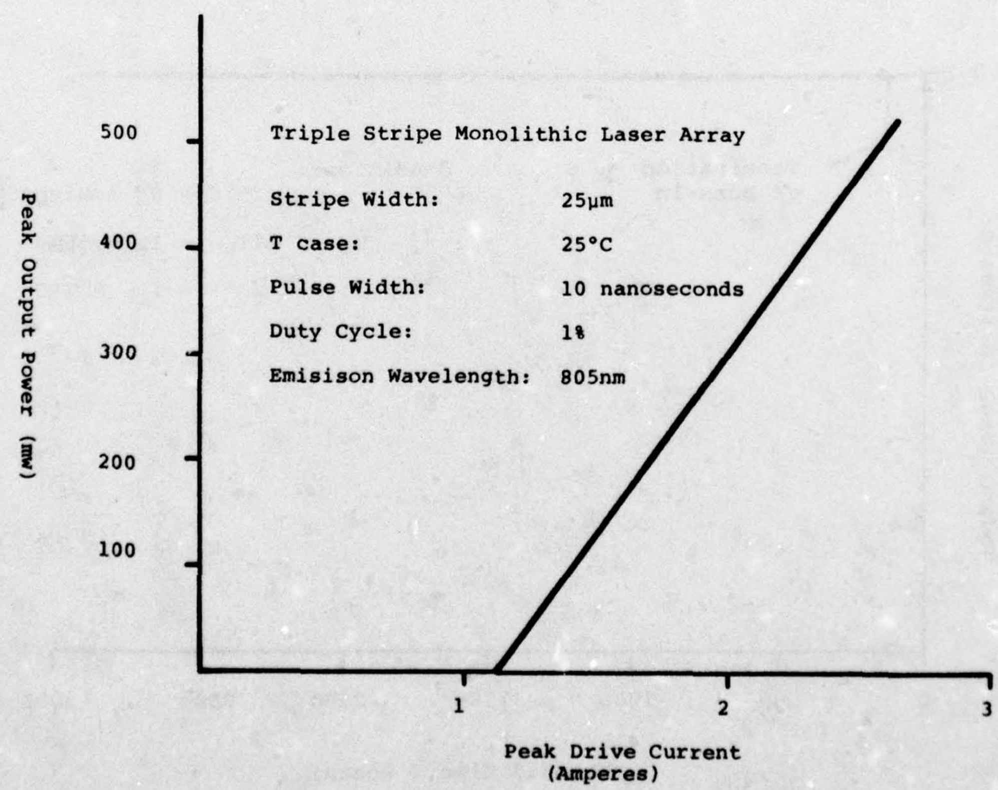

Fig.12 Emission characteristics of a monolithic triple striped laser array

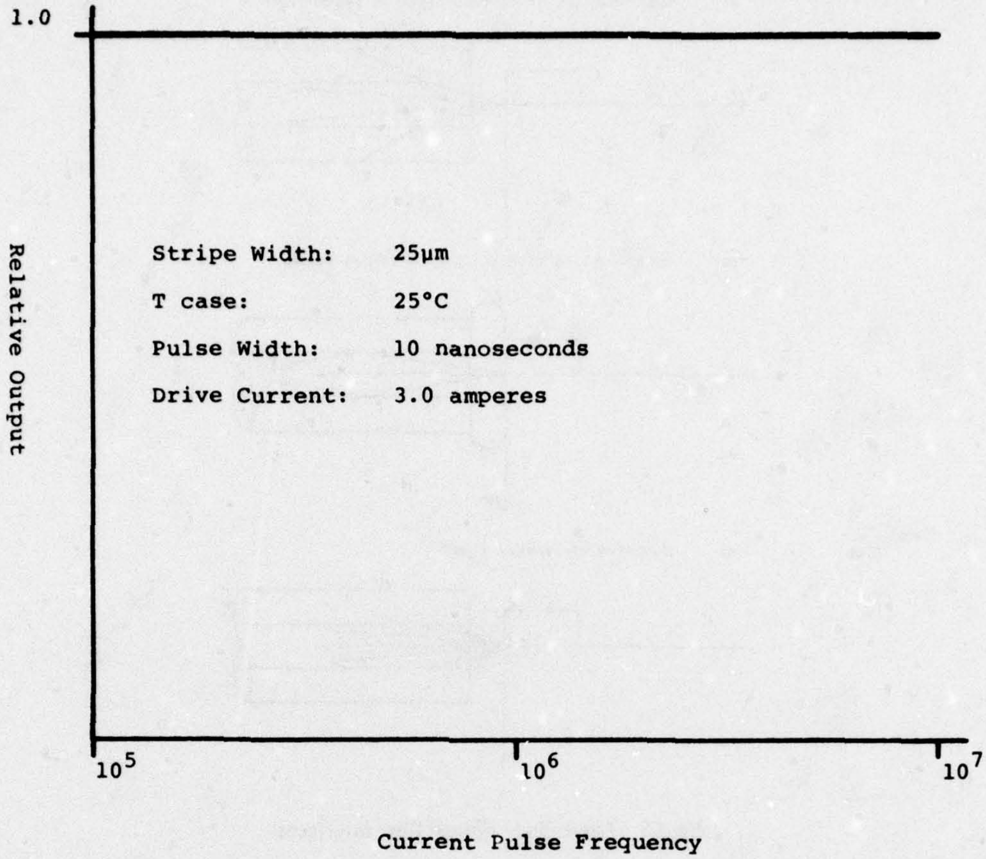

Fig.13 Output of a triple striped laser array as a fraction of pulse frequency

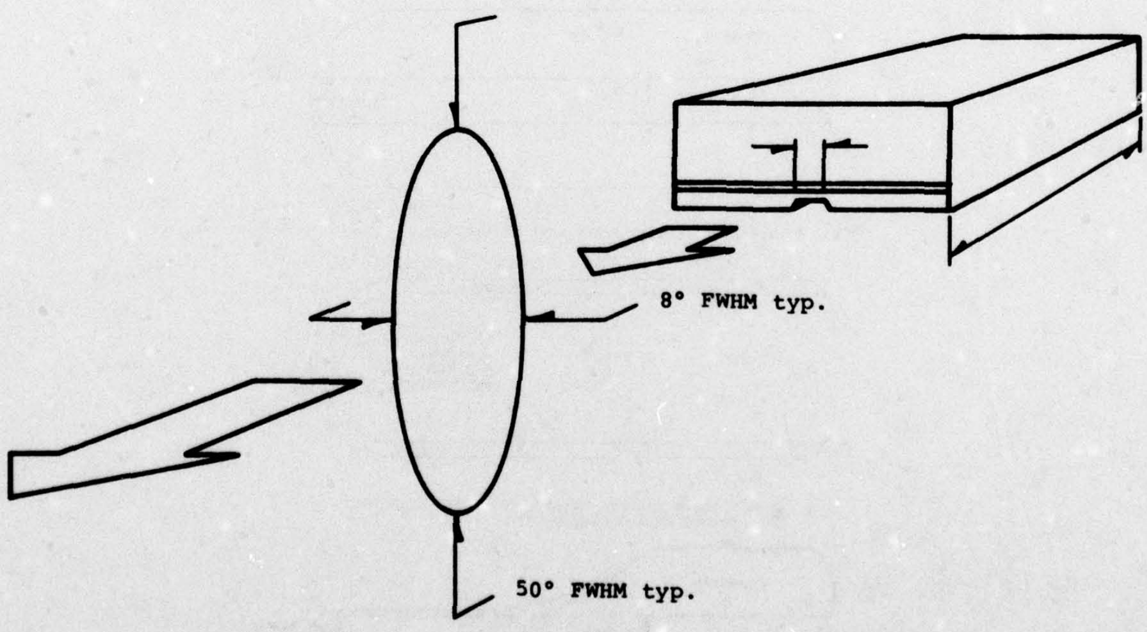

Fig.14 GaAs-GaAlAs stripe geometry room temperature CW injection laser diode

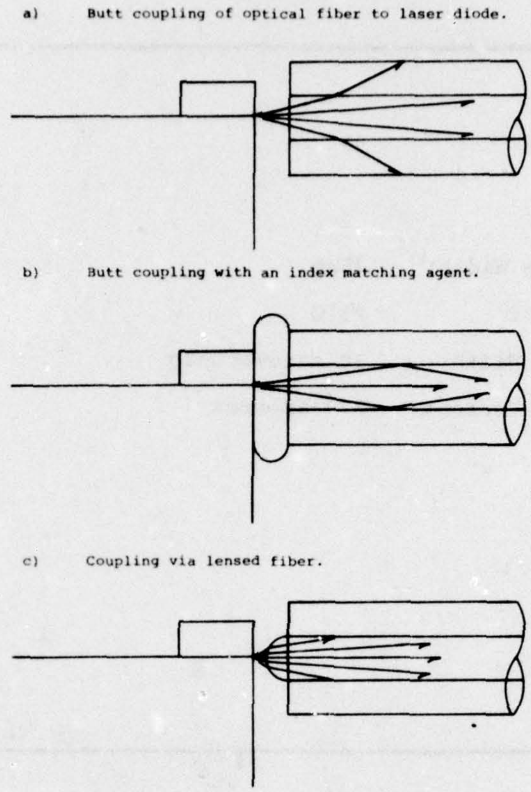

Fig.15 Laser diode optical fiber interfaces

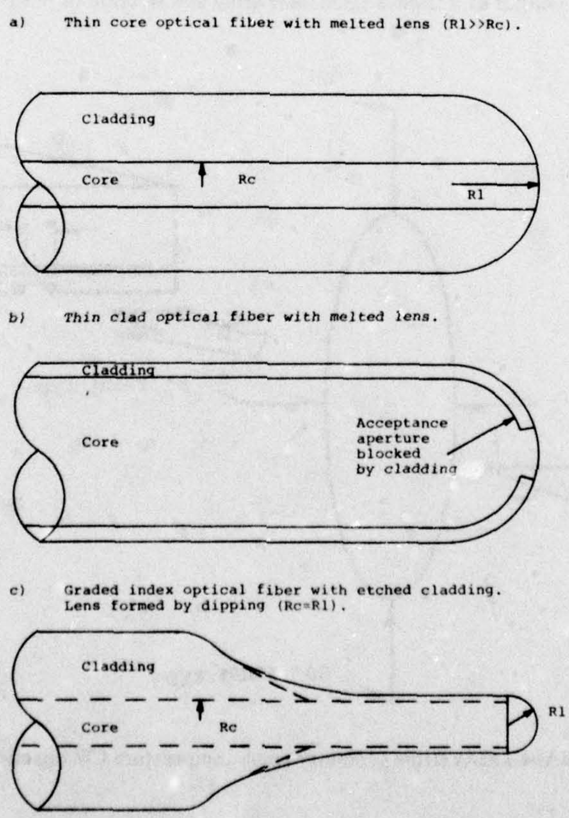

Fig.16 Techniques for fiber lens formation

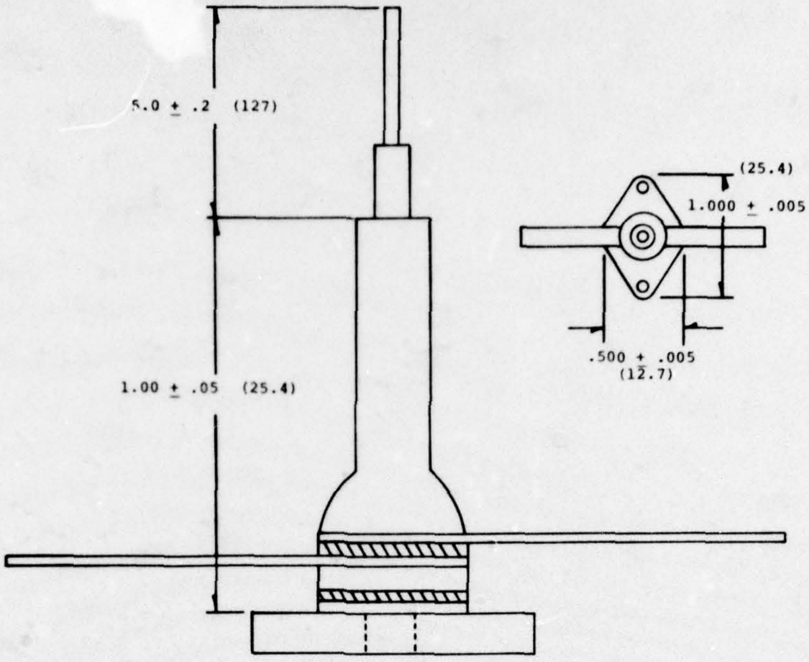

Fig.17 Outline of fiber optic coupled injection laser package. (Dimensions nominal.)

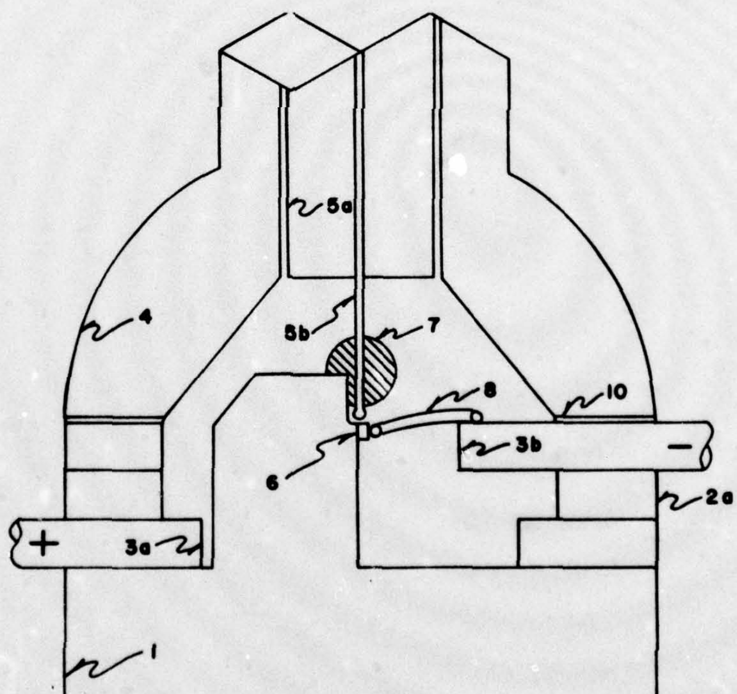

Fig.18 Internal structure of the fiber coupled CW injection laser diode

QUESTIONS AND COMMENTS
ON SESSION V

GaInAsP/InP DOUBLE-HETEROSTRUCTURE LASERS FOR FIBER OPTIC COMMUNICATION
J. J. Hsieh

Dr. Dworkin: Relative to temperature, (a) What variation in threshold has been observed with temperature? (b) Can you speculate on lifetime of laser above room temperature?

Dr. Hsieh: We have operated CW at about 40 C. If you pulse, the threshold current density almost doubles up to about 65 C. We haven't done any other temperature test.

RELIABLE SEMICONDUCTOR LASERS FOR WIDE-BAND OPTICAL COMMUNICATION SYSTEMS
A. R. Goodwin, P. A. Kirkby

Dr. Visser: Using pulse modulation, measurements were made from just below threshold level to above. From power consumption and circuit simplicity view, total (100%) current modulation would be preferable. (1) Are there any specific reasons for not doing so? (2) Using 100% current modulation, do you think that temperature cycling introduced by this kind of modulation may shorten laser diode life and reliability?

Dr. Goodwin: No recorded answer.

Dr. Elmer H. Hara: What was the peak modulation depth in terms of optical power for the analogue intensity modulation experiments?

Dr. Goodwin: No recorded answer.

Summary of Session V
SOURCES AND DETECTORS

by
W. S. Nicol

1. **Summary**

In summarising Session 5 we highlight the following:

1) Interest in complete modules.
2) 1 GHz response achieved for LEDs now stimulating interest in LED bandwidth reduction.
3) 10000 to above 25000 hours CW lifetime for gallium aluminium arsenide lasers.
4) The shift in semiconductor laser wavelength to the 1.2 micron region with potential low cost and reliability.
5) The detector situation. Is there a reliability problem?

2. **Paper 34 - Laser Transmitter for Long Distance Communications**

The important point in this paper was that we are progressing to the complete module stage where we no longer consider the laser in isolation but also consider electrical drive, thermal aspects and optical output coupling as integral parts. An important point was made of how new components and coupling techniques were being incorporated.

3. **Paper 43**

The paper by Dr. Gill of Laser Diode Labs continued the theme of the complete device package covering various ways of fibre shaping to increase collection efficiency.

The current status of the GaAlAs CW room temperature laser produced by liquid phase epitaxy was presented; with routinely available devices of 3000 hr lifetimes and lifetimes over 10000 hrs achieved together with a great deal of investigation of degradation this structure is becoming well characterised.

I felt that consistency of results amongst various groups in this work is now seen.

4. **Paper 35**

The paper by Dr. Hsieh certainly lived up to its reputation as being very significant and created widespread interest. Points which were brought out were that we have:

1) A more stable structure, being less demanding on low dislocation density than the gallium aluminium arsenide systems.
2) A simpler and potentially lower cost structure because of only one critical layer.

In addition Dr. Hsieh seemed confident that we now have the optimum composition for this type of structure.

As regards the impressive CW lifetime performance we can perhaps now give fibre optics conference dates as 5000 hrs to AGARD London, another 720 hrs and we will be in Munich, 6500 hrs to Tokyo and so on! We all wish him well in this work. (Dr. Hsieh wasn't at this session so I couldn't ask him what voltage drop there is across the laser).

5. **Paper 36**

This paper on reproducibility of diode lasers clearly brought out the importance of stress, especially point stress, when it was shown that the operation influencing laser life most is the laser mounting.

6. **Paper 37**

This presentation by Dr. Zaeschmar of NELC on the physics of degradation in LEDs was certainly entertaining. He was confident that we can directly relate optical properties to mechanical stress. I won't attempt to reopen the lively discussion which took place on point defects, (since we must all know that m + n = 3!).

One question does, however, remain in finding the number of batches which he used.

7. **Paper 38**

The paper on reliable GaAlAs lasers by Dr. Goodwin of STL reinforced the results that lifetimes in excess of 10,000 hrs can certainly be achieved and indeed can be considered beyond 25000 hrs with reasonable expectancy.

8. **Paper 39**

In some ways this paper was comparable with the Plessey high speed LED results in that there is agreement in response to beyond 500 MHz with a cut-off around 1 GHz. Current state is that we are now limited by fibre dispersion and LED linewidth so that future LED research should be concerned with reducing linewidth.

9. Paper 40

This paper gave a state of the art summary of avalanche photodiodes which have no difficulty with 1 GHz response. An interesting question was raised by Dr. Chown concerning reliability. It does seem that it is difficult to obtain APD reliability data from manufacturers. Although basically only silicon technology is involved and so APD reliability might not be considered different from other silicon devices, there is still the question of operation under high reverse bias.

10. Paper 41

Dr. Hersees paper from Plessey Caswell highlighted 1 GHz LED response and 20,000 hr lifetimes. Obviously we shall follow stage 4 degradation which begins at 2000 hrs. However we shall forget the Au diffusion process he suggested if it does indeed turn out to be 10^6 hours.

11. Paper 42

Finally the Thomson CSF paper on a laser transmitter module again showed the complete sub-system approach which has to be taken.

An interesting comment was made by the speaker in pointing out that module characteristics were really determined by the user.

12. Additional Comments by C. P. Sandbank

1) This session was one of the first at the conference to bring into perspective first of all the important potential of a GaInAsP/InP system, not only as a longer wave length source, but offering a number of other advantages (identified by Mr. Nicol in his comments on paper 35).

2) The identification of some degradation properties in LEDs including some mechanisms which appear to show up fairly late in life, e.g. after 7,000 hours. This is particularly interesting, since one tends to look for degradation processes which can be "weeded out" in early life, but it is unusual to find a situation where the performance is stable for a substantial period and then an identifiable degradation process appears. Several papers made some comment about this.

I support Mr. Nicol's concern about the statistical significance of Zaeschmar's results but Hersee's paper 41 presented some very clear and significant data on this "stage 4" degradation which is not noticeable until at least 2,000 hours, and I personally had not come across this type of data at previous conferences. It was also new to several of my reasonably experienced colleagues.

HOLOGRAPHIC ELEMENTS FOR PRACTICAL FIBRE BUNDLE COUPLERS

O.D.D. Soares *
A.M.P.P. Leite **
E.A. Ash ***

* formerly with Department of Electronic and Electrical Engineering
University College London
Torrington Place
London W.C.1, England.

now with Departmento de Fisica
Universidade do Porto
Portugal.

** Department of Electronic and Electrical Engineering
University College London
on leave of absence from Departmento de Fisica
Universidade do Porto
Portugal.

*** Department of Electronic and Electrical Engineering
University College London.

SUMMARY

The difficulty of realizing effective couplers for single-mode fibres, imposes a significant obstacle to their application. The paper is concerned with the use of a holographic element, which substantially reduces the sensitivity to tolerance errors in the manufacture of such a coupler. The approach is based on the use of a hologram output window for the cable end, the coupling between the two windows proceeding by means of pseudo-plane waves. The effect is to transfer the need for precision to the factory, the coupler to be assembled in the field being relatively undemanding. The system is applicable to bundles of fibres; preliminary experimental results for the coupling between one pair of fibres to another pair are described.

1. INTRODUCTION

The main thrust of the development in optical telecommunications is concerned with the use of multimode fibres. The bandwidth capability of the graded index fibre which has now become apparent, has reduced the previously perceived need for a single-mode fibre. Nevertheless there are considerations which would favour the exploitation, even in the relatively near future, of the single mode fibre. The case for this development has recently been made by Maslowski, 1976; most of the needed technology exists and suitable small-source lasers are being developed. The use of single-mode systems would also greatly facilitate the incorporation of switches and modulators which can now be realized, with impressive performance in integrated optical form (Ash, 1976). One obstacle in the path of this development, which we believe to be significant, is the absence of fibre to fibre couplers which do not require adjustment, and which one could contemplate using in the field. The problems of mechanical tolerances which are encountered in the direct realization of such a coupler are formidable even for a single connector, and appear quite unattainable for a multiple connector which is required for bundles of fibres. It is the primary aim of the present paper to describe an approach based on holography which, whilst it does not eliminate the requirement for high precision, transfers this requirement to a factory environment. The demands made on the actual connector, to be assembled in the field, are very greatly reduced.

The basic principle of the method has been previously desribed (Ash, 1974; Soares, 1976; Nishihara, 1975). Figure 1. A hologram is associated with each fibre or waveguide. A hologram of the output of the fibre is recorded using a plane reference beam, the two reference beams making complementary angles with the plane of the hologram. The output from the hologram when excited by the waveguide is then in the form of a pseudo-plane wave, which in turn generates the required coupling wave for the second fibre. The holograms are separately prepared, rigidly and permanently attached to their respective fibres in the factory. The key consideration is the fact that the coupling between the two holograms proceeds by means of a plane wave. It is therefore intuitively obvious that the system will be extremely insensitive to lateral displacements of the holograms. The tolerance requirements are essentially confined to the maintenance of parallelity,which is achieved by the use of a simple spacer. The form sucn a coupler could take is indicated in Figure 2.

The basic operation of the coupler emerges directly from the elementary theory of holography. Let U_{F1} and U_{F2} be the intensity of the waves radiated by fibres one and two respectively and let U_{R1} and U_{R2} be the corresponding reference waves used to encode the fibre waves. When fibre one is switched on, the coupling wave U_C generated by hologram one is given by

$$U_c = U_{R1} \, |U_{F1}|^2 \tag{1}$$

If U_R1 had a plane wave front, U_C will again have a plane wave front. It will however be amplitude modulated by $|U_{F1}|^2$. Provided however that one arranges for U_{F1} to give a reasonably constant illumination over the hologram, this effect will not be large. Under these conditions,

$$U_c \simeq U_{R2}^{*} \tag{2}$$

which is of course the input required to generate U^*_{F2} and which completes the coupling into the second fibre. Other than the need for $U_{F1,2}$ to provide sensibly uniform illumination over the hologram, there is no other constraint on its form. It is not therefore necessary to prepare the fibre ends in any particular way. Indeed there may be advantages in making them deliberately rough - a technique which has previously been demonstrated in the context of planar waveguides (Ash, 1974). Nor is there any important constraint on the position of each fibre relative to its hologram. The only requirement is that this position, once established, shall be maintained after the hologram has been recorded.

These simple considerations apply in the first instance to a thin hologram. However, the same results apply approximately also to thick holograms (Kogelnik, 1969), in which the recording medium may extend for many tens of wavelengths, provided that the thickness is still very small compared with the lateral dimensions of the hologram. This is important, as the attainment of high efficiencies - essential for our purpose - depends on the use of such thick holograms. The use of thick holograms rises also another consideration: We have shown the basic concept in Figure 1, for the case of a simple fibre-to-fibre coupler. If however we wish to couple a bundle of fibres, we will need to record multiple holograms, using a set of different reference waves U_{Rj}, each making a different angle with respect to the hologram plate. The question then arises, how much angular spacing do we require between the U_{Rj}. The answer is provided in the paper by Kogelnik already cited. The minimum angular space is, approximately, inversely proportional to the thickness. Increasing the thickness also has a further desirable consequence, in that the total volume of sensitive material is increased, and this increases the total number of holograms which can be stored. There is however a limit to the thickness which one can use; beyond a certain point the simple imaging properties indicated in equations 1 and 2, no longer hold (Solymar, 1976 a) and b)). However it would appear that this regime applies to a thickness far greater than one would, for other reasons, wish to use.

The efficiency of phase holograms can be very high (Biedermann, 1975) with reported figures approaching 90%. Unfortunately these results have only been achieved in the visible, and not as yet in the near infra-red. There is less information on the maximum efficiency which is attainable for multiple holographic recording. We will return to this issue in the discussion, where we attempt to estimate the size of the bundle which one could hope to couple with acceptable efficiency.

In assessing the holographic coupler, we are, in the first instance, concerned with its performance, in the absence of tolerance errors. In particular we must determine the errors in the final coupling field, and the consequential reduction in efficiency arising from diffraction effects, and from the amplitude modulation error embodied by the factor $|U_{F1}|^2$ in equation 1. We will briefly portray the relevant theory, and some results in section 2, to find that this basic performance, for physically realizable situations, is in fact highly encouraging. As we have seen, the main motivation of this work is to overcome tolerance errors. It is therefore pertinent to extend the theory to allow an assessment of the resulting reduction of efficiency. This analysis will be summarized in section 3. Section 4 is devoted to an account of a preliminary experiment in coupling a "bundle" of two fibres, to a second set of two fibres. Finally in section 5 we will attempt to assess the applicability of the holographic coupler to situations which are likely to be encountered in optical fibre telecommunications

2. THEORY OF COUPLER

We will concern ourselves with a scalar theory, in which the field at a point is represented by a single quantity U. This is of course an approximation, which however is entirely adequate for our purpose, though it is important to appreciate the implied assumption, that all the waves we consider have the same polarization. As we will see later, this restriction can be removed by regarding two orthogonal polarizations as separate modes - which accordingly have to be separately recorded on the hologram.

The experimental work has used two-mode fibres, and we have obtained some results which bear on the mode cross-coupling. In the following we will however confine ourselves to describing the treatment of a single mode in each fibre; the more general case is not in any essential way different. A further restriction is to treat only the case of a slab guide - i.e. a guide in which the mode can be described in terms of a single spatial variable. Again this restriction is imposed simply to reduce the complexity of the algebra; the extension to the two dimensional case, which we have also carried out does not involve any essentially new problems.

We will concern ourselves with the geometry indicated in Figure 3. The two holograms are assumed to be thin and in contact, located at z=0. Distance from an arbitrary axis is measured by y_h. We define a reference output plane for the object fibre, located at $z=-z_o$, and similarly for the image fibre at $z=z_i$, with distances at right angles to the z axis being denoted by y_o and y_i respectively. We will begin by calculating the image field U_i in response to point sources located in the object and image planes at $y_o=\eta_o$ and $y_i=\eta_i$ respectively (thus defining point source holograms):

$$U_{Fo}(y_o) = [\delta(y_o-\eta_o)]^{1/2}$$
$$U_{Fi}(y_i) = [\delta(y_i-\eta_i)]^{1/2} \tag{3}$$

where $\delta(y - \eta)$ is the delta function at η. With this definition we ensure that the source is normalized, i.e.

$$\int_{-\infty}^{+\infty} U^2(y)\, dy = 1 \tag{4}$$

We adopt a paraxial approximation so that we can use the Fresnel approximation - i.e. describe the cylindrical wave radiated by the point source in terms of a wave having a parabolic phase front. We assume further that the reference beam is plane, and for the moment also that we can neglect the variation of the amplitude of the wave from the point source over the effective area of the hologram. This enables us to calculate the transmission of the holograms after exposure, assuming t-E linearity. The reconstructed wave is then obtained by calculating the transmission of the object wave through the two holograms and again using a Fresnel approximation to calculate the wave distribution U_i which appears in the image plane.

In practice the lateral extent of the hologram is limited to a region $y = \pm H/2$. As in any optical system we have a finite aperture. In computing the transmissions of the wave through the holograms, we must include the effect of this finite aperture by means of a pupil function $P(y_H)$, so defined that it has unity transmission for $-H/2 \leq y_h \leq H/2$, and zero outside this range. With these assumptions we find,

$$U_i(y_i) = A \exp\left\{j\frac{k}{2z_i}(y_i^2-\eta_i^2)\right\}\int_{-\infty}^{+\infty} P(y_H)\exp\left\{j\frac{k}{z_i}y_H(y_i-\eta_i)\right\}dy_H \qquad (5)$$

where A is constant.

We note that we can regard the integral in equation 5 as the Fourier transform of the pupil function, where the transform frequency f_t is given by

$$f_t = \frac{y_i - \eta_i}{\lambda z_i} \qquad (6)$$

If now instead of point sources at $y_o = \eta_o$ and $y_i = \eta_i$ we have distributed functions $U_o(y_o)$ and $U_i(y_i)$, we must consider the summation of all elementary sources in these distributions. However in the present approximation, the coupling between the two holograms is in the form of a plane wave; this will be as true for the distributed source as it was for the point source, so that the distribution in the image plane is not affected. This conclusion can be readily confirmed formally. The result of equation 5 therefore still holds, provided only that the source field is normalized - i.e. provided equation 4 holds. The situation is however quite different if the image waveguide source is now regarded as finite, which will of course modify the second hologram. Our aim will be to couple to a specific mode of the image fibre $U_{fi}(\eta_i)$, which we will again assume to be normalized,

$$\int_{-\infty}^{+\infty} U_{fi}(\eta_i)\,U_{fi}^*(\eta_i)\,d\eta_i = 1 \qquad (7)$$

We can recalculate the expression for $U_i(y_i)$ and find,

$$U_i(y_i) = B \exp\left\{j\frac{k}{2z_i}y_i^2\right\}\int_{-\infty}^{+\infty} U_{fi}(\eta_i)\exp\left\{-j\frac{k}{2z_i}\eta_i^2\right\}\mathcal{F}_{f_t}(P)\,d\eta_i \qquad (8)$$

where $\mathcal{F}_{ft}$ represents the Fourier transform, with a transform frequency f_t as given by equation 6. It is readily shown that equation 8 is in accord with equation 5 for the special case when U_{fi} is a delta function. The constant B is again chosen to normalize U_i.

The wave incident on the image fibre will be partially reflected. However this effect amounts in practice to a loss of only a few percent and will for the moment be disregarded. If we can assume that the holograms per se are 100% efficient, it is then readily shown that the overall coupler efficiency is given by

$$\rho = \left|\int_{-\infty}^{+\infty} U_i(y_i)\,U_{fi}(y_i)\,dy_i\right|^2 \qquad (9)$$

If we no longer make the assumption of a uniformly illuminated hologram, the expression for U_i becomes a little more complicated. We have incorporated this additional effect in all the results presented in this paper.

As an example of the application of the formulation which we have developed in this section, we have calculated the predicted performance of a coupler between two identical slab waveguides, shown in Figure 4. At the wavelength considered the guides can support two TE modes, TE_0 and TE_1. The calculated efficiency for the TE_0 to TE_0 coupler is 86%. Our formalism also allows the spurious coupling to the TE_1 mode. For this case the predicted power to this mode was more than 100 db below the power into the desired mode. We have also calculated the efficiency of the coupler when designed deliberately to couple the TE_0 mode of one guide to the TE_1 mode in the other. In this case, the efficiency was only 60%. The reduced power transfer is primarily due to the amplitude modulation arising from the object waveguide wave. In this case the mode has a symmetry opposed to that of the image waveguide, and it is intuitively clear that this will lead to reduced coupling. In practice one could largely overcome this effect by using a rough waveguide end, so that the distribution is scrambled before recording on the hologram.

3. SENSITIVITY OF COUPLER PERFORMANCE TO TOLERANCE ERRORS.

In the last section we have investigated the performance of the coupler under geometrically ideal conditions. In practice we will encounter a number of tolerance errors, including the following:

(i) Displacement of object fibre with respect to its hologram between recording and usage, by amounts $\delta\eta_0, \delta z_0$ and $\delta\eta_i, \delta z_i$ respectively.
(ii) Lateral displacement by δy_H of one half of the coupler with respect to the other.
(iii) *Departure from parallelity of one hologram with respect to the other by an angle* $\delta\theta$.

We have evaluated all of these, and some typical results will be presented following a brief outline of the formulation. In addition to these constructional tolerances there is one other possible defect which we have considered, arising from non-uniformity in the hologram plates. We will *give some results on the* required degree of parallelity.

As one example let us consider the case when an object point source is laterally displaced by $\delta\eta_0$ after recording the hologram. The expression for the image field now takes the form

$$U_i(y_i) = A' \exp\left\{j\frac{k}{2z_i}\left(y_i^2-\eta_i^2\right)\right\} \cdot \mathcal{F}_{f_t'}\left[P\right]$$

$$f_t' = \frac{y_i-\eta_i}{\lambda z_i} + \frac{\delta\eta_0}{\lambda z_0} \qquad (10)$$

where, to facilitate comparison with equation 5, we have retained the approximation of uniform object field illumination. If we now wish to consider the case of a finite object, we must carry out an integration over this distribution using equation 10 as the impulse response function. In contrast to the case of zero error this integration will now affect the image field distribution. The result can be expressed in the form

$$U_i(y_i) = B' \exp\left\{j\frac{k}{2z_i}y_i^2\right\}\int_{-\infty}^{+\infty} U_{f_i}(\eta_i)\exp\left\{-j\frac{k}{2z_i}\eta_i^2\right\}\mathcal{F}_{f_t'}\left[P\right]d\eta$$

$$f_t' = f_t + \frac{\delta\eta_0}{\lambda z_0} \qquad (11)$$

The efficiency is of course still correctly given by equation 9. We have calculated the effect of a number of different tolerance errors, using the arrangement of Figure 4. Figure 5 shows the effect of an error $\delta\eta_0$ and also of the "worst case" situation when both fibres are displaced equally in the same direction, $\delta\eta_0 = \delta\eta_i$. We see that for a single fibre misalignment of one half guide width the efficiency has dropped to 50%. For equal displacements of the same magnitude by both fibres the efficiency is reduced to a few percent. Thus the stability of the position of the fibre relative to its hologram is paramount, and would have to be maintained with an accuracy of around 0.5 μm.

Of fundamental interest to the concept is the effect of a relative lateral displacement between the two halves of the holographic coupler. This is shown in Figure 6. It is seen that displacements of as much as 1 mm have very little effect on the efficiency. The effect we see here is primarily the change in overlap area between the two holograms. In assembling the structure of Figure 2 in the field, we clearly need not fear any difficulties from lateral alignment tolerances. There is however a vital need to maintain parallelity as indicated in Figure 7, which shows the degradation as a result of a tilt angle $\delta\theta$. *We see that the required tolerance here is of the order of* 5.10^{-5} rad. corresponding to a non-uniformity in the spacer of 0.5 μm over a diameter of 1 cm. Fortunately this is an entirely feasable engineering tolerance.

Even in the absence of any mechanical tolerance errors, we must contend with deviation from parallelity and uniformity of the hologram plates themselves. We can describe this error in terms of a phase function $k\,\delta t_H$ where t_h is the plate thickness. The simplest case corresponds to a wedge error $(\delta t_H = \text{const.} \times y_H)$, and this is of course identical in form to that already discussed in terms of a tilt between the two holograms. For more complicated cases, we must incorporate the phase function in the calculation of the transmittance of the holograms. This has been done, and we can therefore readily compute the situation for various specific functional forms. However there is one case which leads to a more direct estimate of the damage which such phase errors can cause - that of a sinusoidal phase error. If the spatial frequency f_H is sufficiently high, the effect of this phase error will be to generate grating orders which fall outside the region occupied by the image waveguide. To calculate the loss of efficiency we need therefore only estimate the power diverted into higher orders. A well known result from grating theory shows that the fraction of the power diffracted into the first order lobe is simply J_0^2. We have, in Figure 8 shown computed results for a phase error, as a function of f_H for two different depths of modulation. We have also indicated the asymptotic result which derived from the above simple argument. We find that the computed curves approach this limiting value for $f_h \gtrsim 1$. It would appear that phase errors should be maintained under about 0.1 wavelength - a figure which is however achieved in available precision plates.

4. EXPERIMENTAL INVESTIGATION AND RESULTS.

The purpose of the experiments was to demonstrate the principle of the coupler, and to explore the discrimination against unwanted couplings which one might achieve in a multiple-fibre coupler. Further we wished to obtain some experimental confirmation of the predicted tolerance sensitivities.

In the realization of a practical coupler it is essential that the holograms should have the highest possible efficiency; if the insertion loss due to the holograms themselves is to be less than 1 db, this demands an efficiency of around 90%. Whilst such efficiencies for thick phase holograms have been observed we made no attempt to duplicate such results; rather we used simple amplitude holograms, in some cases bleached, their efficiency being of the order of 20%, leading to an insertion loss from this cause of around 14 db. Since the dynamic range of our measurement system exceeded 60 db, this fact did not however present any obstacle to the measurements of interest.

There was one further way in which we simplified our experiments relative to the demands which would be made if one were to implement a complete coupler. Rather than exposing the holograms in two separate systems, and then bringing them together, we placed both holograms spaced by a small distance in a frame, so that after exposure and development they could be replaced into their original position. This procedure greatly simplified the provision of the two complementary reference beams; it was necessary only to provide two contra-propagating accurately collinear beams. The collinearity is achieved by the use of a cyclic interferometer. Figure 9 shows the basic arrangement which we adopted. The system shows an arrangement of beam splitters to allow the excitation of each of the four fibres, two in each half of the coupler. The heavy lines indicate the path of the reference beam and the form of the cyclic interferometer. This was adjusted so as to produce an alignment fringe pattern on the screen. It is seen that with additional beam splitters it was possible to generate two reference beam directions (and their complements), to allow the separate recording of the outputs from each one of the two pairs of fibres.

After recording the holograms, it was possible to reposition the plates by making slight adjustments on the precision XYZ support for the plate carrier (-though it was not possible to adjust the relative positions of one hologram with respect to the other). The repositioning was greatly aided by the ability to observe interference fringes between the reference beams and their respective reconstructions, produced by the holograms when illuminated by the fibres' beams. Figure 10 shows typical results obtainedusing a double-cladded step index fibre with a 10.6μm core, $\delta n = .00104$. The fibre supported two modes at the HeNe wavelength; however it was possible to excite selectively the lowest mode, and the mode conversion in the lengths used (of the order of 1m) was not significant. No great care was taken to minimize the lens-fibre coupling efficiency and it is estimated that the loss going into the fibre was of the order of 5 db, and the loss coming out of the order of 3db. This would suggest that the inherent coupling loss for this experiment was of the order of 7db. However the possible errors imply that this result must be bracketed by $\pm$ 2db. A series of similar measurements confirm that the results lie in this range. It should be emphasized that in achieving these results there was no provision for separately adjusting the position of each fibre with respect to the hologram. It is therefore likely that a substantial part of the loss of efficiency is attributable to a displacement of the image, arising from gelatine shrinkage or small errors in the angular repositioning of the hologram. There are grounds for expecting that with better holographic materials the coupling efficiency, ρ , (quite apart from the basic hologram efficiency) could be substantially enhanced.

Of more immediate concern was an investigation of the cross-coupling encountered in a multiple fibre coupler. In typical experiments this was found to be at least 40db below the wanted signals. This figure was achieved even when the two fibres, on one half of the coupler, were side by side and in contact. This result is readily understood in terms of the formulation presented in section 3.

In order to investigate the tolerance to angular misalignment of one hologram with respect to the other, experiments were conducted using the undiffracted component of a reference beam incident on the pair of holograms as shown in Figure 11. Tilting the mirror and using the undiffracted beam between the two holograms is equivalent to a tilt of one hologram with respect to the other in normal operation. A typical experimental result is shown in Fig. 12. It confirms the order of magnitude of the sensitivity calculated for the different - but related - case, Figure 7. The system can also be used to effect a displacement of the beam by means of a tilted optical flat; this is approximately equivalent to a relative lateral displacement between the two holograms, Figure 13. The lack of degradation in coupling even for displacements as large as 0.5mm, effectively confirms one of the main objectives sought in this study.

5. ASSESSMENT AND CONCLUSIONS.

We have analysed the operation of a fibre coupler to be built on the basic scheme of Figures 1 and 2. The results indicate that the tolerances which have to be met are, as expected, tight, but that those which relate to the realization of the final coupler between two cables, factory-fitted with holographic end windows, are readily attainable. The experiments confirm the basic predictions of the theory. Nevertheless, it is far from clear whether, and if so where, such a coupler could be implemented in a fully operational system. In this section we will briefly discuss some of the relevant considerations.

The insertion loss of couplers is the primary measure of performance. If we can anticipate the emergence of a phase holographic material technique allowing the attainment of 90% efficiency - in the visible this is only a small extrapolation from the present situation - we could anticipate a loss (attributable only to the action of the holograms) of around 1db. The inherent coupling efficiency will depend primarily on the size of the fibre; it will be substantially less for a small index step large core diameter fibre than for the relatively small core sample used in our experiments. However it would to us seem unduly optimistic to assume that the inherent coupling loss could be reduced below 1db. This suggests an overall insertion loss for the coupler of not less than 3db. In this we have so far considered the case of a single fibre-to-fibre coupler. For fibre bundles, the situation would not however be drastically changed. The use of a multiplicity of fibres does imply using a larger volume of active holographic material, if we are to attain the same efficiency, for a given dynamic range as we do for a single fibre. In the above we have for the moment disregarded the absence, at this time, of good holographic materials in the wavelengths range which is currently of greatest importance - 0.9 μm to 1.3μm. Let s however take the further leap of faith in assuming that such materials will be found.

We can then still come rapidly to one negative conclusion: It does not seem likely to us that such a holographic coupler could serve as the primary splicing means, for jointing trunk cables. With fibre losses which are now well under 1db/km, a loss of 3db in the coupler would represent an intolerable deficit. These considerations do not however apply with comparable impact at a terminal to a fibre system. One can envisage that at such a terminal there will be the need to join rapidly a bundle of fibres to one of a different set of other bundles. One can also envisage the need for patch boards, which allow flexible redirection of traffic, or permit rapid testing of combinations of route fibres. In this area, we believe that the chances for applying the holographic coupler are very much more favourable.

It is of interest to consider how many fibres in a bundle one might be able to combine in a single coupler. We can immediately conclude that the limit will not be set by lack of space. We have shown that crosstalk in addressing one of a pair of touching fibres is less than -40db. If one were to take a bundle in contact, one could readily accommodate 100 fibres in an area of less than 2mm square. The limit must therefore be set by the dynamic range of the hologram, and the available hologram volume. Since it is the product of modulation index and the thickness of the hologram which determines the efficiency (Kogelnik, 1969), one can argue that in order to store N high efficiency holograms on a single plate, the photosensitive material must be N times thicker than for a single hologram. Typical thicknesses for high efficiency bleached emulsion holograms are of the order of 6μm. Thus for 50 holograms, one would, on this simple argument, require a thickness of the photosensitive layer of 300 μm. In practice, it is necessary to record two holograms per fibre, to allow for the fact that the direction of polarization is not known. A storage of 50 holograms therefore allows the coupling of two 25 fibre bundles. -These considerations are speculative; however, it is clear that the number can certainly be in excess of 10, and also that it would prove very difficult to contemplate a number as large as 100.

6. ACKNOWLEDGMENTS.

The authors are grateful to Dr. J.C. Williams of Bell Telephone Laboratories for supplying the fibre used in the experiments.

One of the authors, A.M.P.P. Leite, is the recipient of a Calouste Gulbenkian Foundation fellowship.

REFERENCES

Ash E.A., Seaford E., Soares O., Pennington K.S., 1974, "Holographic Coupler for Integrated Optics", Appl. Phys. Lett., 24, pp.207-208.

Ash E.A., Pitt C.W., Wilson M.G.F., 1976, "Integrated Optical Circuits for Telecommunications", Nature, 261, pp.377-381.

Biedermann K., 1975, "Information Storage Materials for Holography and Optical Data Processing", Optica Acta, 22, pp.103-124.

Kogelnik H., 1969, "Coupled Wave Theory for Thick Hologram Gratings", Bell Syst. Tech. J., 48, pp.2909-2945.

Maslowski S., 1976, "High Capacity Communications Using Monomode Fibres", 2nd. European Conf. Optical Fibre Communications, pp.373-376.

Nishihara H., Inohara S., Suhara T., Koyama J., 1975, "Holocoupler : A Novel Coupler for Optical Circuits", IEEE J. Quant. Elect., QE-11, pp. 794-796.

Soares O.D.D., Ash E.A., 1976, "Holographic Selective Mode Coupling to Integrated Optical Waveguides", Elect. Lett., 12, pp.239.

Solymar L., 1976, "Power Conservation Theorem for 2-Dimensional Volume Holograms", Elect. Lett., 12, pp.606-607.

Solymar L., Jordan M.P., 1976, Private Communication.

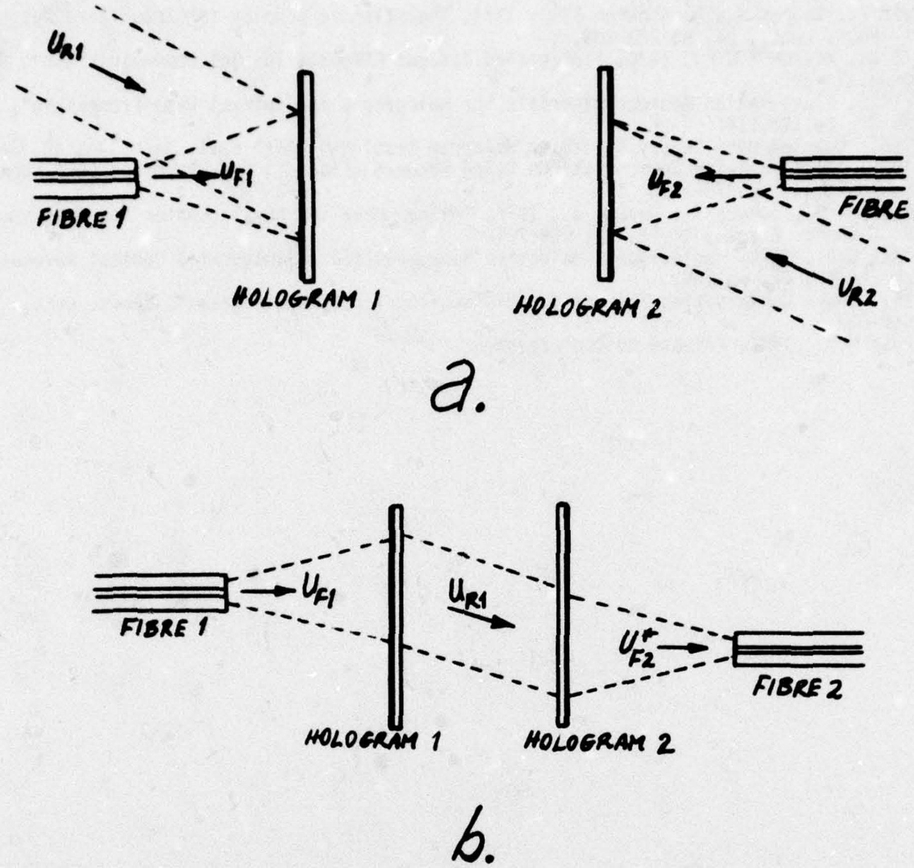

Figure 1 Basic holographic coupler system
(a) Recording geometry. The holograms are separately recorded, with $U_{R1} = U^*_{R2}$.
(b) Reconstruction geometry to effect fibre-fibre coupling. The wave between the holograms is approximately plane.

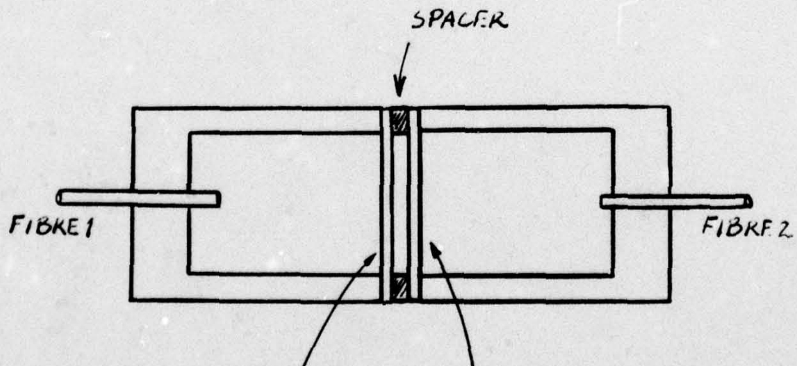

Figure 2 A possible form of the holographic coupler.

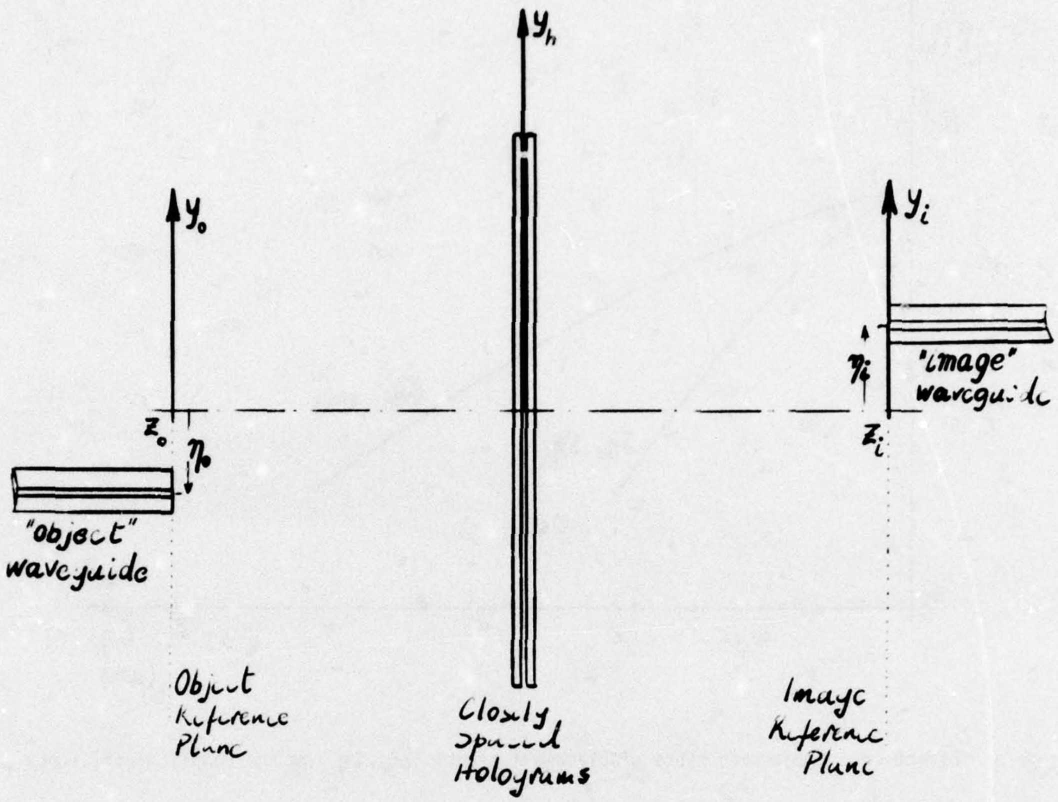

Figure 3 Basic coupler geometry. The quantities η_o and η_i are coordinates for the source distributions.

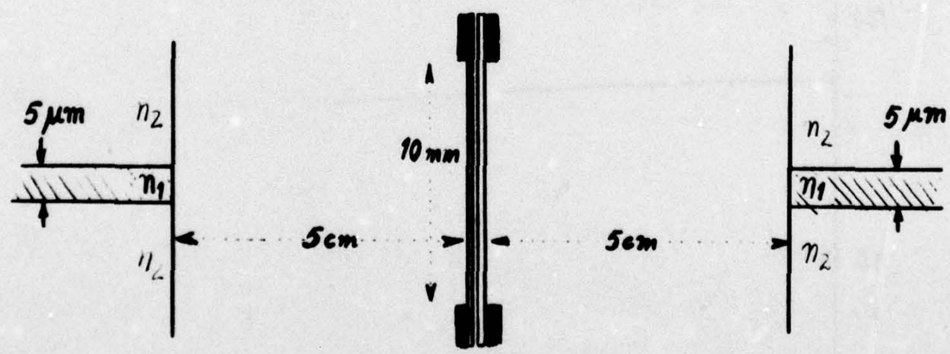

Figure 4 Model used for calculations. The refractive indices are n_1 = 1.5 and n_2 = 1.495.

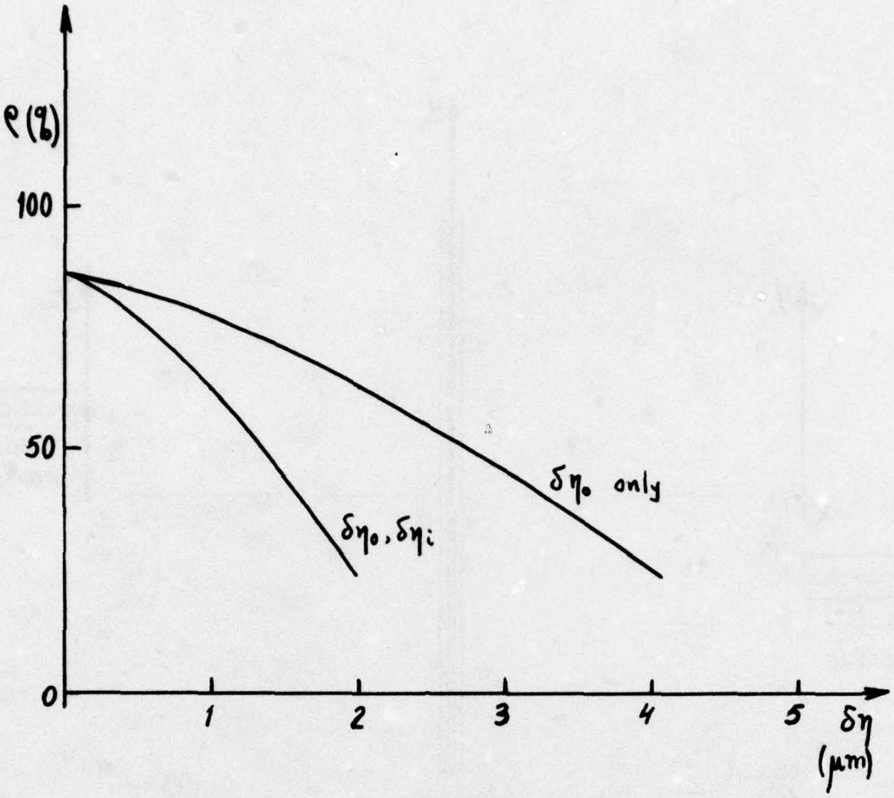

Figure 5 Effect of transverse fibre displacement errors $\delta\eta_o$, $\delta\eta_i$ on the coupling efficiency ρ.

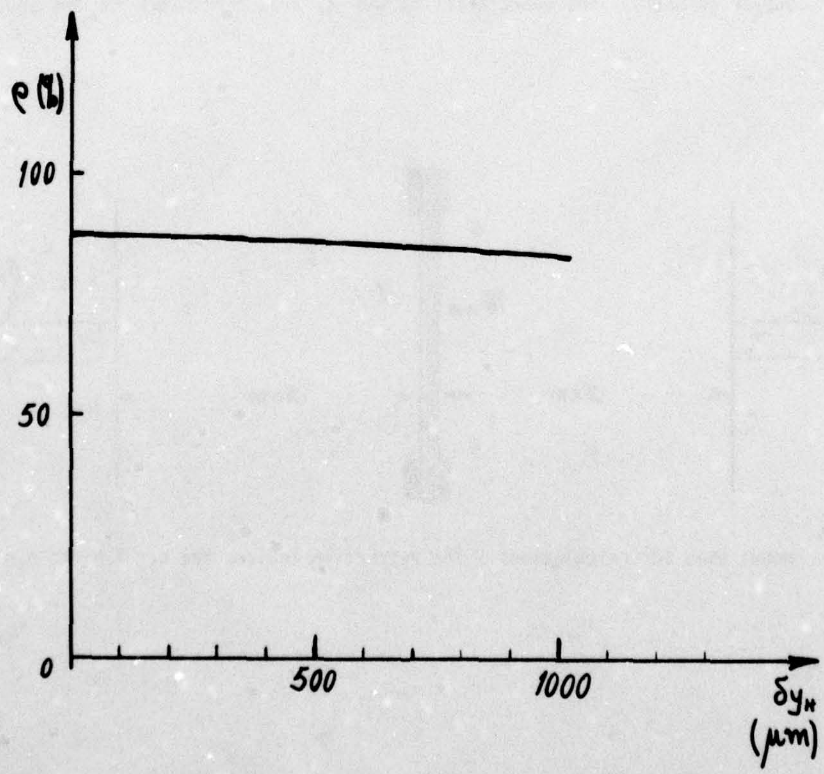

Figure 6 Effect of a lateral misalignment δy_H of one half coupler relative to the other half coupler, on the coupling efficiency ρ.

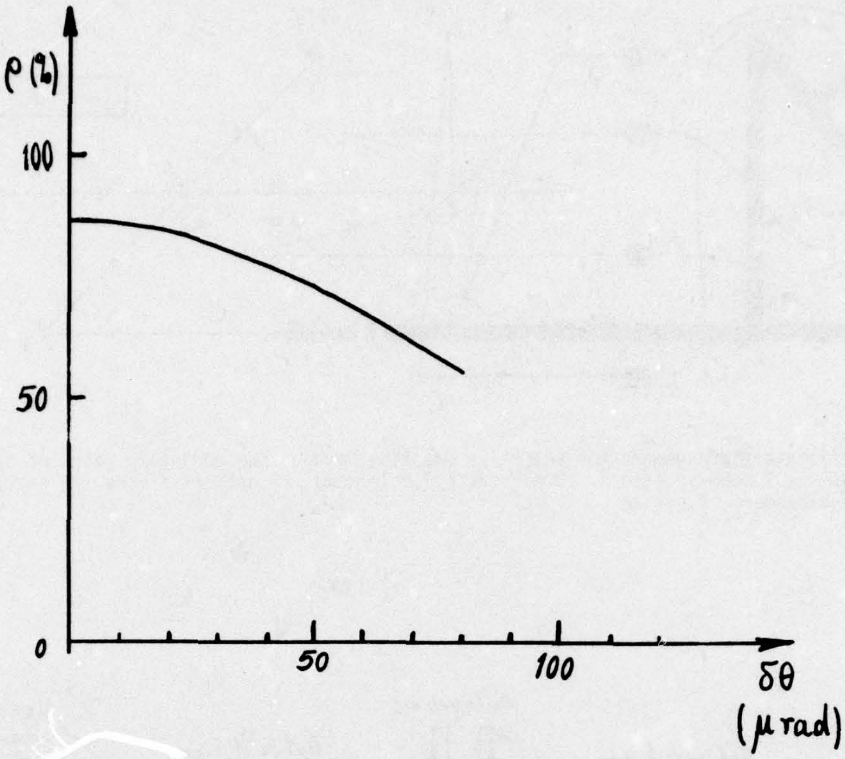

Figure 7 Effect of an angular error δθ in the alignment of the halves of the coupler on its efficiency ρ.

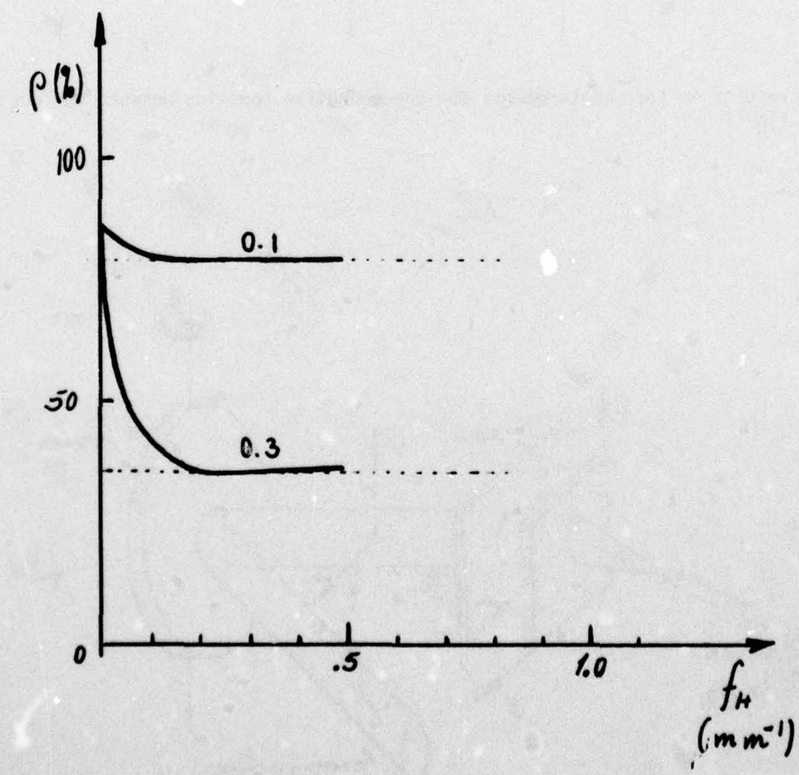

Figure 8 Effect of a sinusoidal roughness in the hologram substrate, with amplitude δt_H and frequency f_H, on the coupling efficiency ρ.

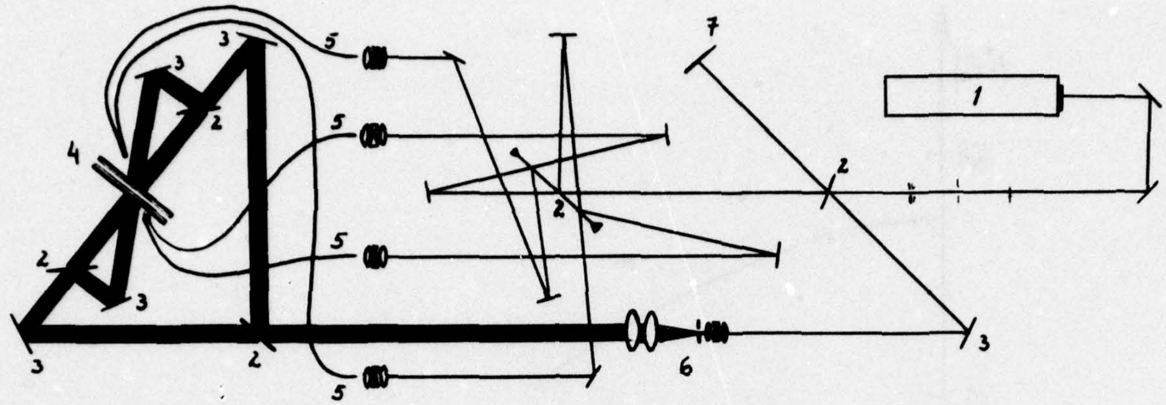

Figure 9 Experimental arrangement for selective coupling between two conjugate pairs of optical fibres. 1.laser 2.beam-splitters 3.mirrors 4.holograms 5.optical fibres 6.spatial filter, beam expander 7.screen.

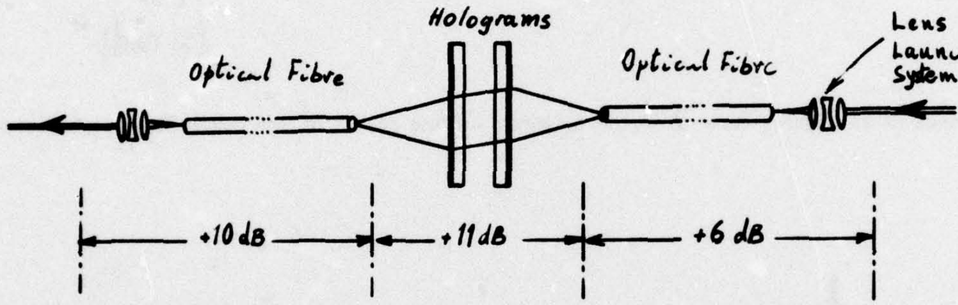

Figure 10 Typical results on loss measurements for the selective coupling between two conjugate pairs of optical fibres.

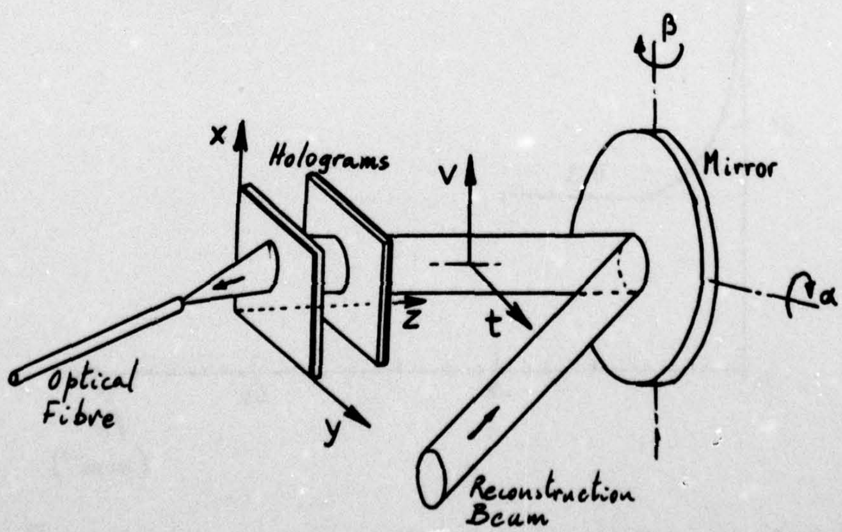

Figure 11 Experimental arrangement for tolerance evaluation.

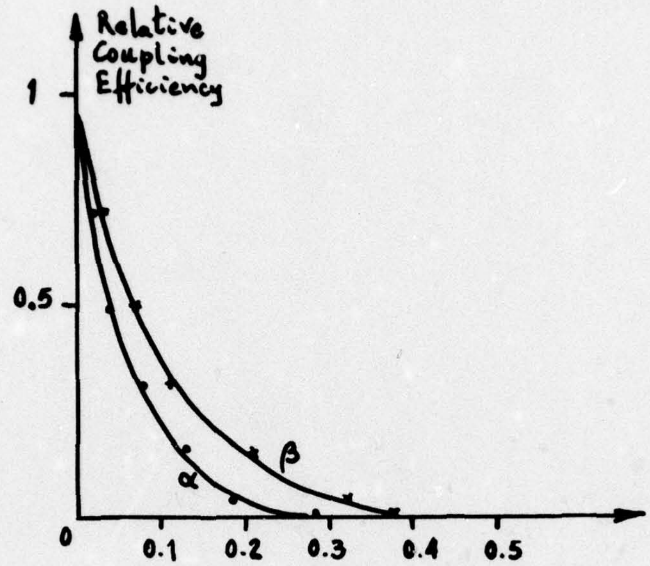

Figure 12 Tolerances on the holograms' angular relative misalignment.

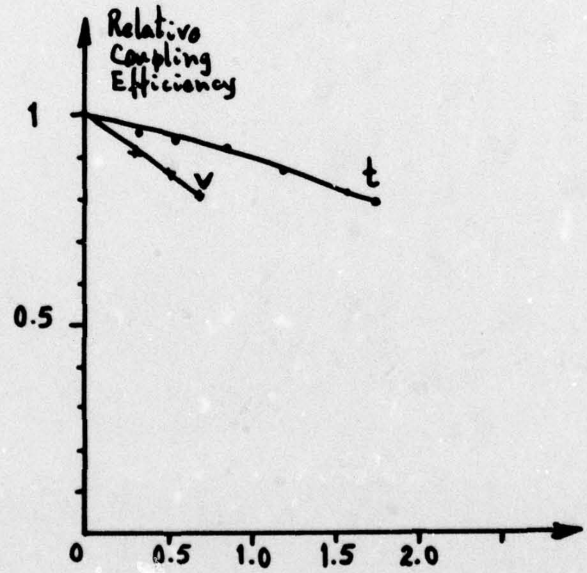

Figure 13 Tolerances on lateral shift of one half of the coupler with respect to the other.

STRUCTURE DE CABLE POUR FIBRES OPTIQUES ET PROCEDE DE RACCORDEMENT

par : G. LE NOANE

CNET/LANNION
France

RESUME

Après une présentation sommaire des trois grandes familles de structures envisageables pour des câbles optiques à conducteurs monofibres et l'exposé des résultats opto-mécaniques obtenus après la pause d'un câble à structure "classique", nous décrivons un support de transmission composé d'un élément de câble à structure cylindrique compartimentée et d'un système de raccordement. Nous abordons le mode de réalisation en continu d'un tel élément et rapportons les résultats expérimentaux obtenus sur un raccordement effectué entièrement dans une chambre de raccordement. Nous mettons d'autre part l'accent sur le caractère modulaire d'une telle solution qui doit permettre son adaptation à différentes applications.

INTRODUCTION

Les nombreuses applications envisagées pour les fibres optiques justifieront certainement l'utilisation de différentes structures de support de transmission. Dans tous les cas, cependant, il importe de profiter des qualités essentielles de la fibre pour obtenir, à la différence des câbles actuels, des câbles légers, peu encombrants, économiques et utilisables pour divers débits d'informations. Les premiers prototypes de câbles à conducteurs monofibres ont montré qu'il était possible de rendre ces câbles très fiables et très résistants. En fait, les performances mécaniques et optiques de ces supports pourront être très variables en fonction du nombre de fibres requis, de la qualité des fibres nécessaires, des contraintes de pose et d'exploitation et des performances recherchées aux raccordements. Nous décrivons une structure d'élément de câble cylindrique compartimentée et un procédé de raccordement constituant la base d'un système modulaire capable de répondre aux exigences de multiples applications.

STRUCTURES DE CABLES

On peut classer les structures de câbles ou d'éléments de câbles formés de conducteurs monofibres en trois grandes familles :

- les structures "rubans"(M.J. SCHWARTZ, 1976) qui assemblent les fibres en matrice constituée par empilage de rubans et assurent la protection mécanique par la gaine extérieure. Elles présentent surtout un grand intérêt pour les supports de transmission nécessitant un grand nombre de fibres (systèmes de télécommunications numériques à bas débits par exemple)(fig.1)
- les structures "classiques" (fig. 2) basées sur la protection individuelle de la fibre par gainages et l'utilisation des techniques habituelles d'assemblage. ELles peuvent conduire à des performances intéressantes en atténuation et à une tenue mécanique remarquable. Nous disposons de tronçons de ce type de câbles (R. JOCTEUR, 1976) posés en conduites sur 700m au CNET. L'atténuation moyenne est de 6,3dB/km (valeurs extrêmes 5 dB/km et 9dB/km) et n'a pas évolué après un an de pose. Les tests mécaniques de traction (fig. 3) effectués jusqu'à présent sur courtes longueurs (points d'ancrage distants de 1,20m pour un câble de 30m de long) ont montré qu'un tel câble, grâce à sa gaine aluminium peut supporter une traction de 300 daN (allongement 8/1000) sans risque de modification de son atténuation et bien entendu sans rupture de fibre (fig. 4). On peut cependant craindre pour de telles structures un encombrement important, un processus de fabrication compliqué et coûteux et des difficultés importantes pour le raccordement (dégainage des fibres, repérage...) dans le cas d'un grand nombre de fibres.
- les structures cylindriques "compartimentées"(G. LE NOANE, 1976) dont le principe est d'éviter la protection individuelle de la fibre grâce à un profilé adapté. Ce type de structure modulaire peut répondre à une gamme importante d'applications en faisant varier le nombre de fibres par élément, le diamètre de cet élément et le nombre d'éléments dans le câble.

La structure de chaque élément repose sur quelques principes fondamentaux :

- obtenir une unité ayant les qualités mécaniques de résistance et de souplesse compatibles avec l'assemblage et facilitant les raccordements
- protéger et repérer les fibres par un profilé adapté ce qui évite l'utilisation de gainages complexes
- éviter les traitements délicats de la fibre (extrusion - enrobage) qui pourraient nuire aux qualités optiques en utilisant la fibre munie d'un revêtement très fin et régulier, ce qui facilite aussi le raccordement

- définir un processus de fabrication en continu qui rende économique la réalisation des éléments de câble

Chaque élément comprend (Fig. 5)

a - une âme cylindrique qui comporte à sa périphérie une série de cannelures hélicoïdales recevant chacune une fibre.

b - les fibres munies d'un revêtement fin (2 à 3μm d'épaisseur) et régulier appliqué au cours du fibrage. Elles conservent ainsi leurs qualités d'origine et ont une tenue mécanique compatible avec les opérations de câblage (souplesse, résistance à la traction > 1 daN pour une fibre de diamètre 125 μm)

c - un gainage qui assure la fermeture des alvéoles. Comme dans tous les cas de structures ce gainage pour des applications à faible nombre de fibres peut à lui seul assurer une excellente résistance mécanique au câble. (ce gainage peut aller d'un simple enrubannage à une gaine aluminium...)

Les caractéristiques des rainures ou des alvéoles (hauteur environ 6 fois le diamètre d'une fibre, pas d'environ 200mm) ont été établies afin que la fibre, grâce à des degrés de liberté suffisants, ne subisse pas les effets des phénomènes de dilatation, d'allongement sous effort de traction, de torsion, de flexion de l'âme centrale.

L'extrusion de polyéthylène H.D. ou de polypropylène autour d'un porteur central permet d'obtenir les qualités essentielles du profilé, qui sont la régularité géométrique et la tenue mécanique, (chocs, écrasements, flexion, traction). Nous étudions actuellement différentes possibilités de fabrication en continu d'un tel élément de câble, afin de simplifier l'opération de pose des fibres.

PROCEDE DE RACCORDEMENT

Nous avons développé une méthode dont le principe de base consiste à remplacer, à chaque extrémité des éléments à raccorder, le support cablier des fibres (porteur central, profilé rainuré..) par un profilé parfaitement calibré (fig. 6). Lorsque l'objectif essentiel est de rechercher les très faibles atténuations (application aux télécommunications) les deux profilés employés au raccordement sont issus d'une seule pièce et les performances dépendent alors principalement des écarts de dimensions et de profils d'indices entre les fibres à raccorder. Dans le cas ou les performances optiques recherchées sont moins sévères, (transmissions courtes distantes) on peut envisager la production indépendante des deux profilés par moulage. Indépendamment de l'adaptation d'un tel procédé à une structure de câble qui permet d'éviter le dégainage des fibres, l'application d'une technique industrielle de sciage (sans polissage) pour la préparation des faces évite les opérations de positionnement longitudinal, simplifie la partie mécanique du raccordement et permet d'effectuer toutes les préparations sur le chantier de pose (fig. 7).

Le procédé de raccordement consiste donc à :

- remplacer le support cablier par un profilé rainuré en matériau tel que l'alumine après épanouissement de l'élément de câble.
- dégainer les fibres si besoin est, et les placer dans les rainures : les centrer et les coller en appliquant une pression à l'aide d'une gaine thermorétractable.
- scier les fibres dans un plan perpendiculaire à l'axe du profilé
- nettoyer les deux extrémités et les enduire d'une graisse assurant la protection et la continuité d'indice, puis assembler les deux embouts ainsi préparés à l'aide d'un montage mécanique (fig. 8) dont la fonction essentielle est de reconstituer aussi fidèlement que possible le profilé initial - l'alignement axial est assuré par deux demi-coquilles pressées contre les surfaces cylindriques des profilés et le positionnement angulaire par deux clavettes - D'autres solutions mécaniques peuvent être adoptées pour assurer ces fonctions mais l'ensemble constitue un montage mécanique rigide et étanche (joints d'étanchéité) ce qui permet d'assurer une excellente stabilité.

RESULTATS EXPERIMENTAUX

Les résultats présentés sur les fig. 9 et fig. 10 ont été obtenus à partir de profilés en alumine comportant cinq rainures et d'un montage mécanique analogue à celui utilisé pour un élément de câble complet. Les résultats portent sur 40 raccordements effectués avec deux types de fibres (step-index - 4dB/km - 115-65 μm et 125 - 85μm). Bien que les fibres appartiennent à des lots de fabrication différents, il est difficile de préjuger de la valeur exacte que prendraient ces résultats au stade industriel en fonction de la qualité des fibres employées.

Nous avons d'autre part appliqué cette méthode au raccordement de deux câbles à structure classique posés sur 700m en conduite et obtenu des résultats analogues à ceux des échantillons de laboratoire. Cette opération nous a permis de tester la stabilité du connecteur (fig.11) qui après 9 mois d'exploitation a gardé les mêmes performances malgré de grandes variations de température (-5 à +30°C). Elles nous a confirmé les avantages de la méthode : positionnement des fibres en une opération à l'aide d'une gaine thermorétractable, préparation des faces d'extrémités par sciage, positionnement longitudinal rigoureux. Elle nous a montré d'autre part, qu'il peut être très important de disposer d'une structuee de câble bien adaptée, telle que la structure cylindrique compartimentée permettant d'éviter les opérations délicates de dégainage et assurant le repérage des fibres, surtout dans le cas d'un grand nombre de fibres.

CONCLUSION

Nous avons défini un support de transmission sur fibres optiques composé d'un élément du câble à structure cylindrique compartimentée et d'un système de raccordement. Nous pensons que les possibilités de variation de la taille de l'élément, du nombre d'alvéoles, de la nature de la gaine en fonction des contraintes imposées permettront à un tel support de satisfaire à de nombreuses applications.

REFERENCES :

M.I. SCHWARTZ, R.A. KEMPF, W.B. GARDNER - 1976
"Conception et caractérisation d'un câble expérimental à fibres optiques"
Deuxième colloque Européen sur les transmissions par fibres optiques

R. JOCTEUR, 1976
"Réalisation d'un câble à conducteur optiques pour les transmissions numériques dans les systèmes de télécommunications"
Deuxième colloque Européen sur les transmissions par fibres optiques

G. LE NOANE - 1976
"Structure de câble pour fibres optiques et procédés de raccordement"
Deuxième colloque Européen sur les transmissions par fibres optiques

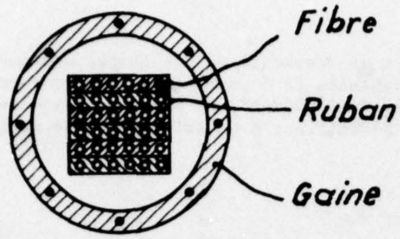

Fig. 1 Schéma d'un élément de câble à structure ruban

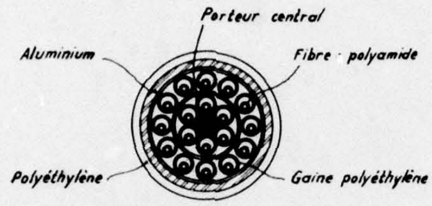

Fig. 2 Schéma d'un élément de câble à structure classique réalisé par les "Câbles de Lyon"

Fig. 3 Appareillage de tests opto-mécaniques de câbles

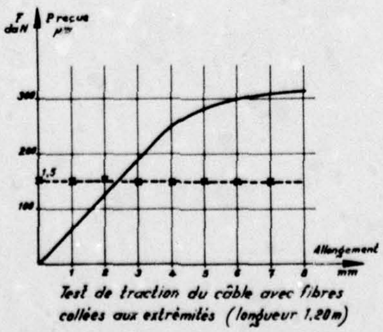

Fig. 4 Courbe de traction - atténuation sur câble à structure classique

AD-A050 748 ADVISORY GROUP FOR AEROSPACE RESEARCH AND DEVELOPMENT--ETC F/G 20/6
OPTICAL FIBRES, INTEGRATED OPTICS AND THEIR MILITARY APPLICATIO--ETC(U)
OCT 77 H HODARA

UNCLASSIFIED AGARD-CP-219 NL

6 OF 6
AD
A050748

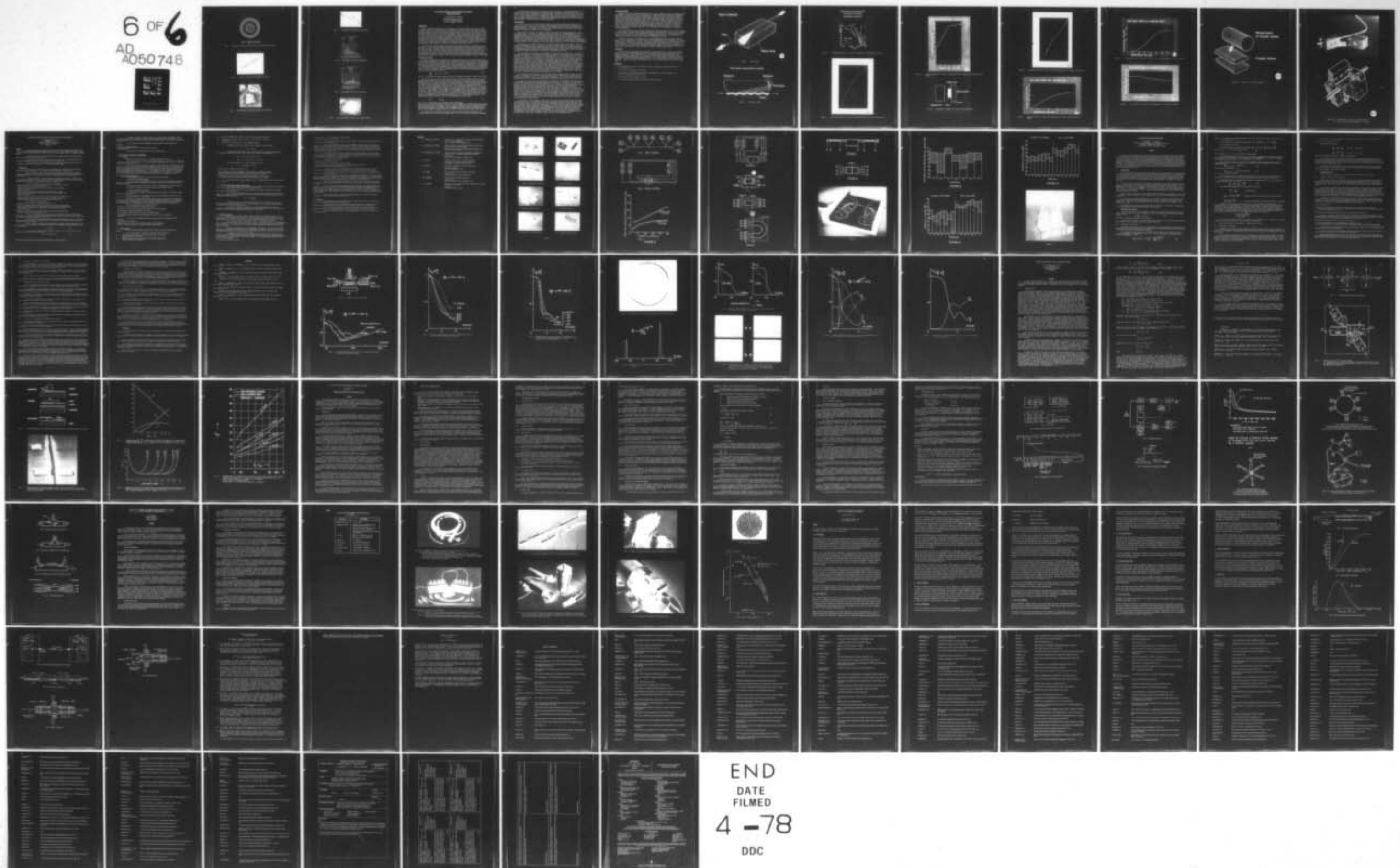

END
DATE
FILMED
4-78
DDC

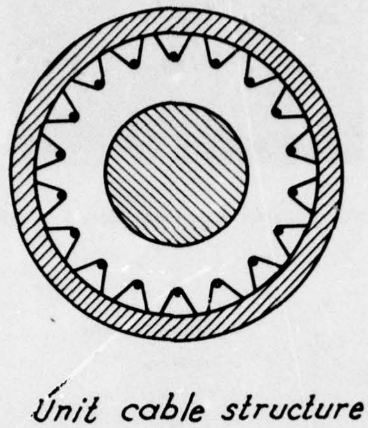

Fig. 5 Schéma d'un élément de câble à structure cylindrique compartimentée

Fig. 6 Profilé en alumine pour raccordement des câbles

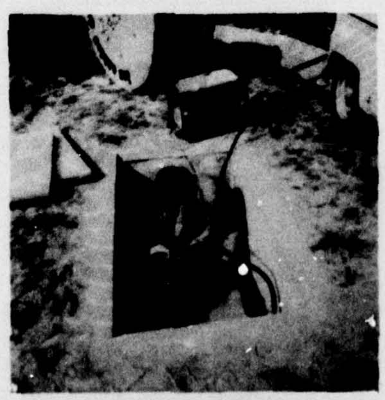

Fig. 7 Préparation de la jonction en chambre de raccordement

Fig. 8 vue éclatée du raccordement de deux câbles

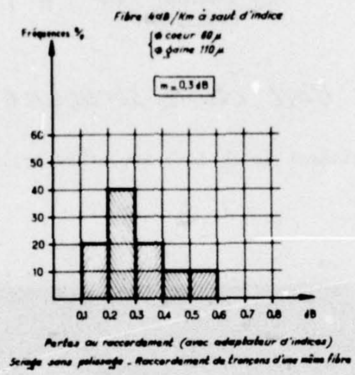

Fig. 9 Histogramme des pertes au raccordement

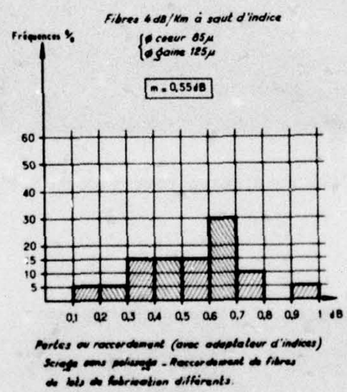

Fig.10 Histogramme des pertes au raccordement

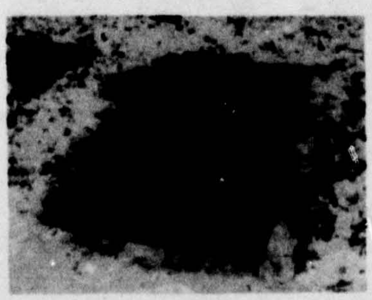

Fig.11 Vue du raccordement de deux câbles à fibres optiques

AN ADJUSTABLE BRANCHING COUPLER/ATTENUATOR FOR MULTIMODE SINGLE FIBRE SYSTEMS

C. Stewart and W. J. Stewart

Allen Clark Research Centre,
The Plessey Company Limited,
Caswell, Towcester, Northants.
U.K.

INTRODUCTION

There is currently growing interest in directional or T-coupling components for use with single multimode optical fibres. Perhaps there has been somewhat less interest in the development of variable and fixed attenuators. These will, however, probably be required for system testing. The devices which are described in this paper are essentially directional couplers or fibre taps, which, because of their principle of operation, could also be used as attenuators. The essential property of the device is that it is non-invasive; that is, the fibre is not permanently changed or damaged in any way when the device is in use. This means that the degree of coupling or attenuation achieved, and indeed, whether there is any coupling at all can be externally controlled in a simple manner. The non-invasive property is very important since it enables the other desirable features of the device to be realised. These features are very low insertion loss, and the elimination of the need for any connectors or splicer which would in turn introduce a further source of overall loss. Furthermore, the inherent mechanical simplicity of this component permits easy fabrication in quantity and therefore potentially low cost.

Two forms of the coupler/attenuator are presently under study. The first is illustrated in fig. 1 and consists of a block of clear plastic material with an amplitude grating on one surface against which the fibre is pressed. The fibre assumes the shape of the grating which is approximately sinusoidal. Power from the fibre is coupled out into the plastic medium and may be detected at the end face. We refer to this type of coupler as a 'bulk' coupler. The second form of the device (fig. 2) which is in many ways more attractive, consists of a thin glass plate of about the same thickness as the fibre with a grating formed on one edge. The plate is shaped such that the emerging radiation from the coupling region is focussed on to a detector or another fibre. We report results for both types of coupler in this paper.

PRINCIPLE OF OPERATION

Although we have described the operation of this device previously (1), its unique features justify a more detailed explanation. The coupler may be conveniently considered to operate via a two stage process. Firstly, power is converted from low order, well confined modes to much higher order, poorly confined modes. These high order modes are then extracted from the fibre to complete the coupling process. The phenomenon of induced coupling between waveguide modes due to a periodic perturbation of the guide is well-known and it is this effect which is used to implement the conversion of optical power from low to high order modes. This is achieved by pressing the fibre in intimate contact with the mechanical grating which has a wavelength such that phase matching of the propagation constants of adjacent fibre modes becomes possible. The phase matching condition is given by

$$\frac{2\pi}{\Lambda} = \beta_1 - \beta_2 = \Delta\beta \tag{1}$$

where Λ is the grating wavelength and β_1 and β_2 are the propagation constants of adjacent fibre modes.

This approach makes use of the highly multimode nature of currently available communication fibres. Although for a step-index fibre $\Delta\beta$ varies with β the variation is sufficiently small for a highly multimode guide of small refractive index difference between core and cladding to make operation possible. Nevertheless, there is still no single value of coupling wavelength Λ which can produce coupling over the complete range of propagation constants. We refer now to the graph of azimuthal mode number ν as a function of normalised propagation constant β/kn_o for a multimode step index fibre shown in fig. 3. k is the free space propagation constant and n_o is the refractive index of the core. All the bound, leaky and radiating modes of the fibre can be represented on this diagram. The bound modes lie between the line $R = \infty$ (i.e. $\beta/kn_o = 1-\Delta$) and $\beta/kn_o = 1$. The parameter R is a radius, normalised to the fibre core radius, at which a mode becomes radiative. Since bound modes have no radiative part in this case $R = \infty$. The region of the graph to the left of the line $R = \infty$ represents leaky and radiating modes. The line $R = 1.47$ corresponds to modes which become radiative at the cladding radius for this fibre. Superimposed on the graph are lines of constant coupling wavelength Λ in mm calculated subject to the experimentally determined selection rule for this coupling process, which is (3)

$$LP_{\nu\mu} \qquad LP_{\nu\pm 1,\mu} \tag{2}$$

where ν, μ are the azimuthal and radial mode numbers respectively.
We see that it is possible to choose a value of Λ (in this example $\Lambda \sim 1.9$mm) which will couple together pairs of bound and pairs of leaky modes. In fact, because the grating has a finite interaction length the resulting 'Fourier spread' of wavelengths about the central wavelength ensures that coupling can occur between adjacent mode pairs over a range of value of propagation constant. Gloge (2) has shown that this type of nearest neighbour coupling results in a diffusion of power from lower to higher order modes.

The coupling action is completed when power in modes of sufficiently high order leaks at the individual bends of the grating into the coupler medium. This is the well-known bending loss phenomenon.

An important practical parameter in the description of the coupler is the mechanical amplitude of the grating. Coupled mode theory has been used (4) to calculate the coupling coefficient between pairs of modes for various types of deformation of a multimode fibre. However, the overall behaviour of the coupler as a function of grating amplitude will naturally also depend on the particular mode distribution on the fibre. A detailed analysis will not be attempted here and we therefore restrict our consideration to the assertion, based on intuition, that for a quasi-stable mode distribution coupled power will be a smoothly varying function of grating amplitude, for small deformations.

'BULK' COUPLERS

In order to arrive at the necessary design criteria for a given application the properties of the coupler and the way in which they are affected by fibre parameters must be determined. Experiments were therefore performed to investigate the relationship between coupling efficiency and attentuation and the mechanical amplitude of the grating. The insertion loss, or more usefully, the incremental (or excess) system loss introduced by the device was also determined.

Figure 4 shows the variation of coupling efficiency as a function of grating amplitude for a very short system length. This data was obtained using five bulk couplers of different amplitudes to which the experimental points refer. The results suggest a sharp initial increase in coupling efficiency with amplitude followed by a more well behaved, smoothly varying region. In order to check this behaviour an experiment was performed with the 16 micron amplitude coupler. The fibre was pressed gradually into contact with the grating until the full depth of the coupler was impressed on the fibre, while simultaneously monitoring the power from the coupler. Figure 5 shows that a sudden rise of coupled power at low amplitude is again followed by a more well-behaved section and eventual saturation as the fibre becomes fully contracted.

The labelling of the abscissa on this and some subsequent graphs merits further comment. The actual experimental arrangement is shown in figure 6. The coupler is rigidly fixed and the fibre is loosely attached to a rubber pad soaked in index matching liquid. The pad is mounted on a rigid plate which may be translated by a micrometer stage with an electrical output facility. While the exact mechanical behaviour of this arrangement is not simple, for the very small displacements involved we infer that the micrometer displacement is roughly proportional to the effective grating amplitude produced.

These experiments were repeated for longer lengths of two different step index fibres. In the first case, shown in figure 7, for the same fibre as before, the sudden rise in coupled power is not present. The absence of the effect is also apparent on a measurement made on a single coupler (fig. 8). We explain this result by noting first that for the case of the coupler very close to the source the fibre will contain a sizeable proportion of leaky modes (5), many of which are very lossy and would not be present further from the source even if the coupler were not applied. Also as we showed in a previous paper (1), the action of the coupler is such that power is extracted predominantly from the outer fibre modes. The initial application of the coupler, therefore, causes the high order modes to be stripped rapidly and detected at the coupler output. The resulting fibre mode distribution is then narrower and more representative of the distribution further from the source. Applying a greater amplitude to the fibre therefore merely enhances the power diffusion from low to high order modes to produce coupled power in the expected manner. In this region therefore an increase in grating amplitude has the primary effect of increasing the coupling coefficient between adjacent fibre modes. In the experiments using the longer length of fibre the extremely high loss modes have been removed before the coupler is encountered. No rapid rise in output power is therefore expected on initial application of the coupler.

The second longer length experiment used a step index fibre of slightly smaller core size (63 micron as opposed to 85 micron). The behaviour is substantially the same as before with no apparent transient effects, as illustrated in fig. 9, for a single coupler measurement. In this instance the output power from the fibre end was also monitored and decreases in a moothly continuous manner as shown in fig. 10.

We consider now the effect of the application of the coupler on the incremental (or excess) system loss introduced for a short and intermediate distance of the coupler from the source. The output power of the fibre end was monitored before and after application of the coupler. The coupled power was also measured. The fibre was broken a short distance from the input end and the input power measured. Cladding power was stripped at both the launch end and the termination. In the short length experiment the arrangement consisted of about 1.5m of fibre followed by the coupler and a further 3.5m of fibre. The measured fibre loss was of course very small for such a short length. Assuming all of the fibre loss to occur between the source and the coupler - that is the total fibre loss is referred to the input end of the coupler - then the excess loss introduced by the coupler calculated on this basis represents a worst case figure. Thus the transmission of the fibre with the coupler applied was 87.2% with 11.5% of the unit input power appearing at the coupler output. The total losses were therefore 1.3%. If the loss in the fibre is not referred to the input end of the coupler, but treated as occuring all along the length of the fibre then the measured excess loss was 1.3%. As might be expected for this very short length of fibre the difference is very slight.

A longer length of fibre arranged with 30m prior to the coupler and 10m afterwards gave performance data (with normal fibre losses referred to the coupler input) of transmission 72.4%, coupled power 23.6% and total losses of 4%. By assuming fibre loss to occur throughout the system the excess loss was about 3%. It should be noted that these loss figures refer to the total losses for a system to which a coupler is applied. They consist in general of two components. The first is due to imperfections of the coupler itself resulting in loss of light after it has been extracted from the fibre. This loss component is expected to be very small and has been reported previously (1) to be of the order of 0.5%. The other loss component is due to light which has been converted by the coupler into high order modes but not extracted before the end of the interaction region. This high order mode power is subsequently lost in the fibre itself. This effect is thought to account for most of the measured power loss.

THIN PLATE COUPLERS

Recently we have made preliminary measurements on thin plate couplers which have the advantages over bulk couplers of small size and only a one dimensional focussing requirement. They are also potentially cheap items since many may be fabricated simultaneously. While there are several possible methods of fabrication which could be investigated we have chosen a polishing technique which allows the grating profile to be formed simultaneously on a stack of about 100 coupler blanks. The blanks are prepared by waxing together about 100 circular glass cover slips. The resulting cylindrical block is then cut and polished to form two blocks of coupler blanks (see fig. 11). It is naturally essential that all the plate edges are of good optical finish and this is checked by inspection. The blanks are polished on a wheel which resembles a caricature of a gramophone record except that the grooves have a sinusoidal profile. After a time the blanks assume the same profile and are finally polished to a good optical finish. Separation of the plates results in a set of couplers more or less identical in geometry and therefore properties.

Preliminary measurements have been made on these devices and these compare well with results obtained with bulk couplers. For a thin-plate coupler which usefully extracted 14% of the input light, for example, a loss of 2.5% was recorded. This measurement did not fully take account of the excess loss discussed earlier and is thought to be almost entirely due to imperfections of the plate. With improvements in manufacturing tolerances this loss may be expected to be substantially reduced.

A prototype assembly for a thin plate fibre to detector coupling device has also been constructed. Figure 12a shows a photograph of the device and fig. 12b a cut away view of the arrangement. The plate is held in a slot at the bottom of a V-block. The fibre is located at the bottom of the V and pressed on top of the plate by a flexible pad operated via an adjusting screw. The coupled light is focussed on to a detector attached to a miniature electrical connector which is screwed to the bottom of the block. The outer metallic casing serves to protect the bared fibre and to clamp the cable. We have demonstrated the operation of this assembly and work is proceeding to improve the design and performance.

CONCLUSIONS

We may say that the reasonably well behaved nature of the coupled power as a function of grating amplitude for realistic fibre lengths and the small incremental loss penalty introduced show that this device is capable of effective operation both as a directional coupler and as an attenuator. The important non-invasive property, which is responsible for the low loss, allows the coupling fraction or attentuation to be made continuously variable from zero to the device maximum, a feature which would be difficult to achieve with alternative invasive schemes. We have made prototype devices which are now undergoing practical assessment and development and we hope to present details of this work at a later date.

REFERENCES

1. C. Stewart and W. J. Stewart, 2nd European Conference on Optical Fibre Communication, Part 27 - 30th September, 1976.
2. D. Gloge, B.S.T.J. 1972, 51, pp. 1767-1783.
3. W. J. Stewart, I.E.E. Conference on Optical Fibre Communication, 16th-18th September 1975. Conference Publication No. 132, pp. 21-22.
4. D. Morcuse, B.S.T.J. 1973, 52, pp. 817-842.
5. W. J. Stewart, Electronics Letters 11 (24th July 1975) pp. 321-322.

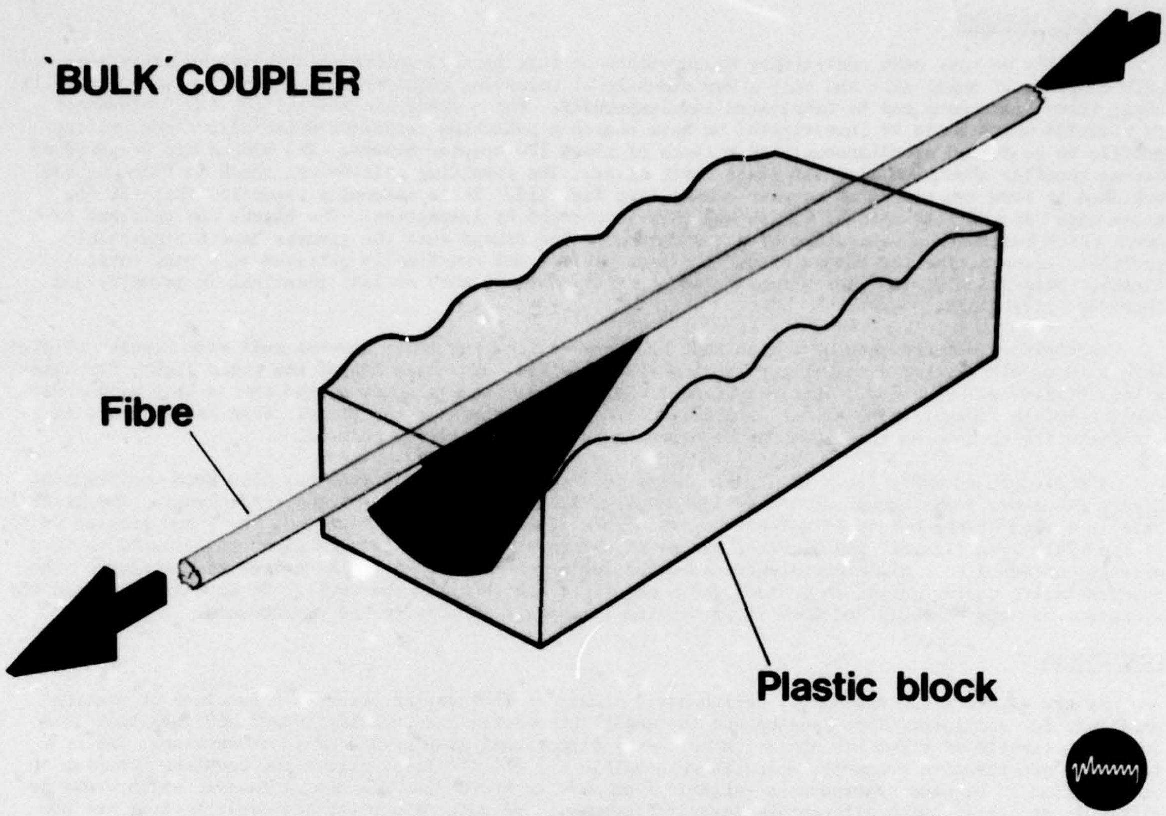

Figure 1. 'Bulk' Coupler

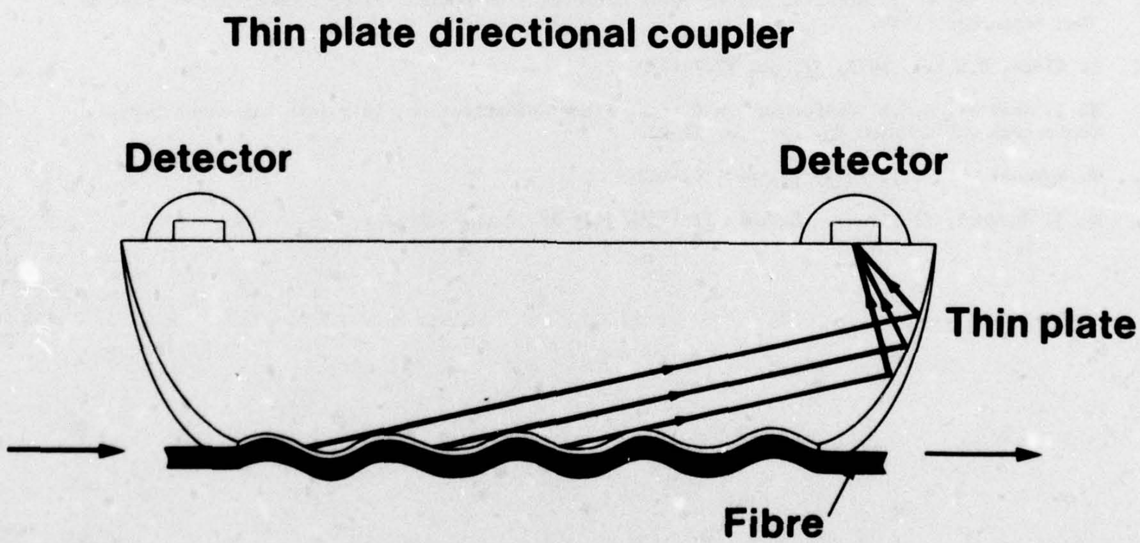

Figure 2. Thin plate coupler

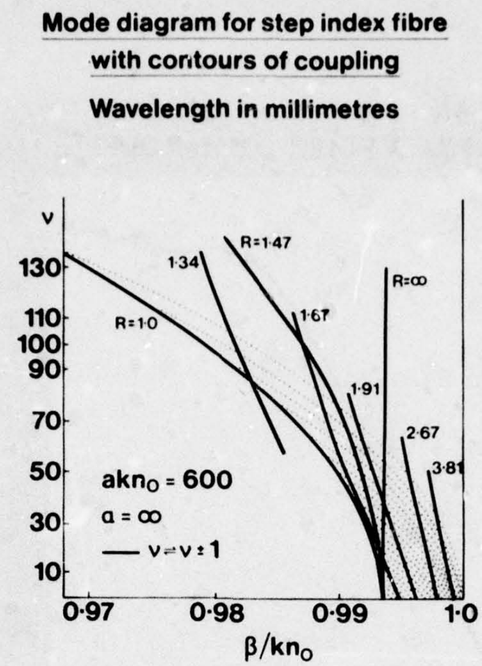

Figure 3. Azimuthal mode number ν as a function of β/kn_o for a multimode step index fibre.

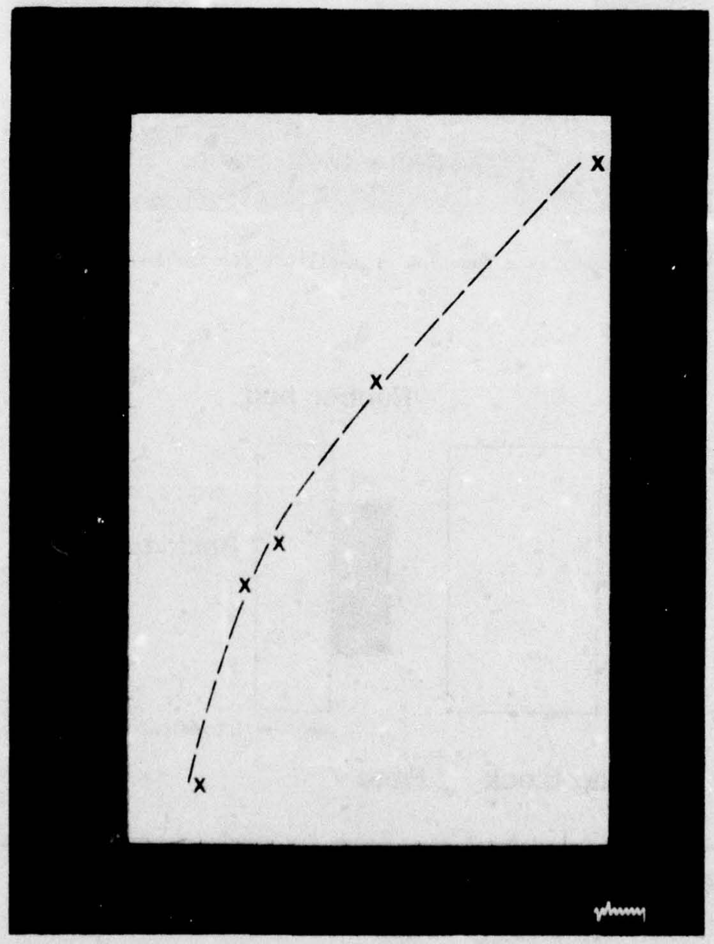

Figure 4. Coupling efficiency as a function of grating amplitude for a short system length.

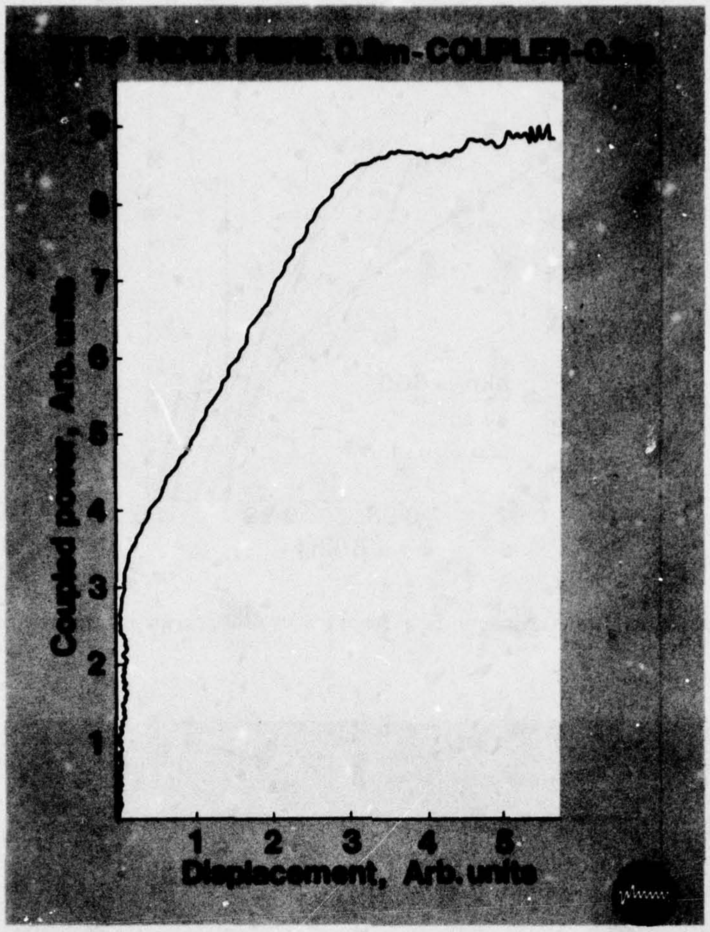

Figure 5. Coupling efficiency as a function of amplitude for the 16 micron grating and short fibre length.

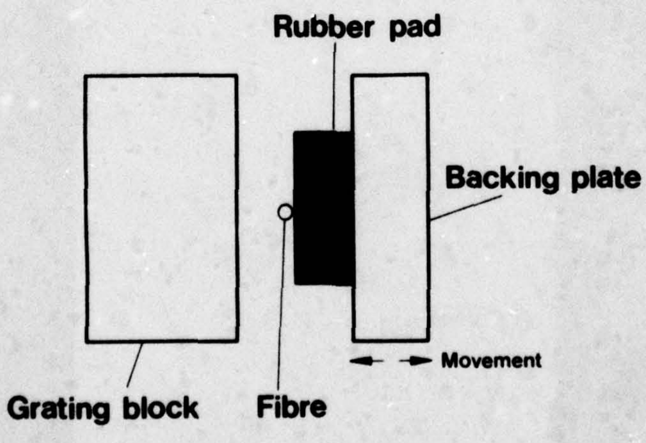

Figure 6. Experimental arrangement for single grating measurements.

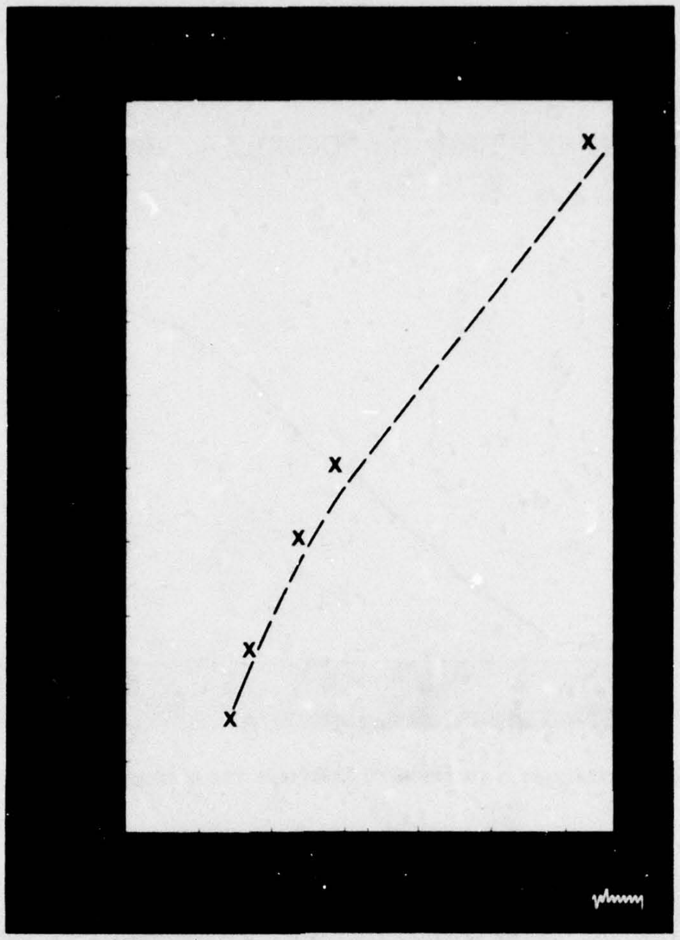

Figure 7. Coupling efficiency as a function of grating amplitude for intermediate system length.

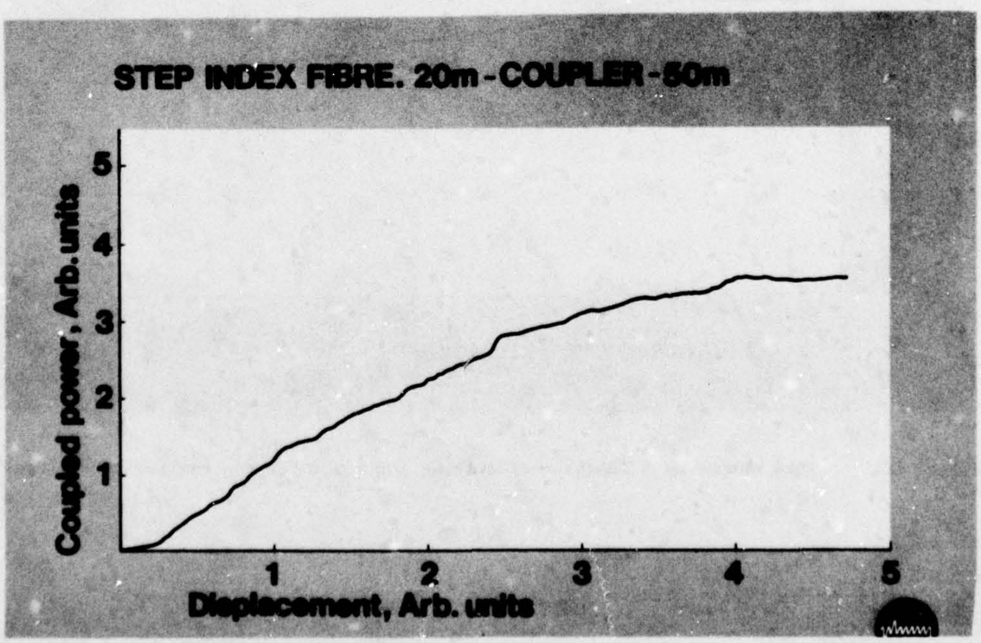

Figure 8. Coupling efficiency as a function of amplitude for a single grating and intermedia
length.

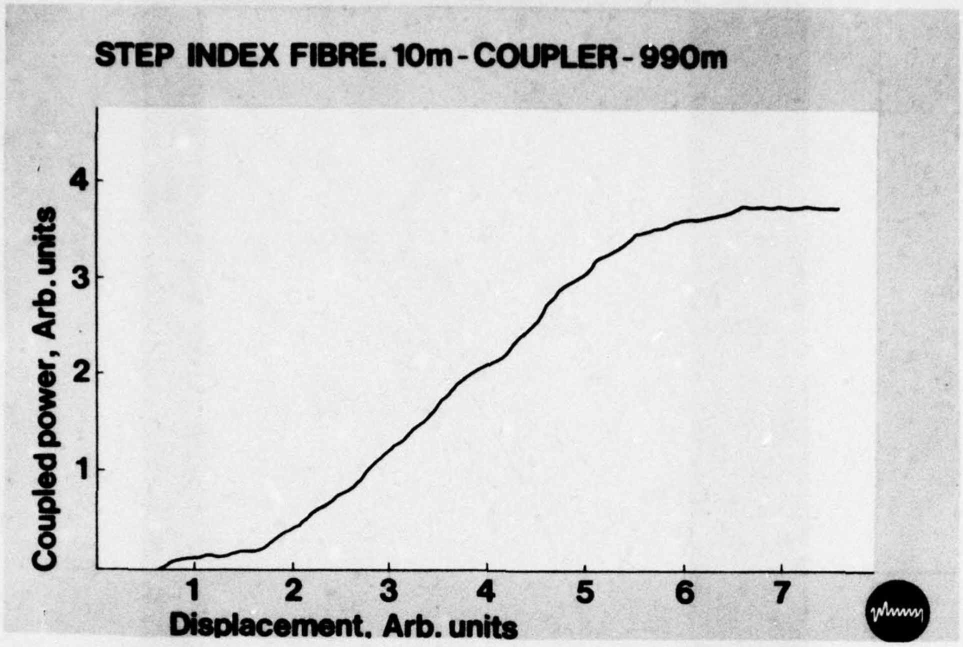

Figure 9. Coupling efficiency as a function of amplitude for a single grating with a smaller core fibre.

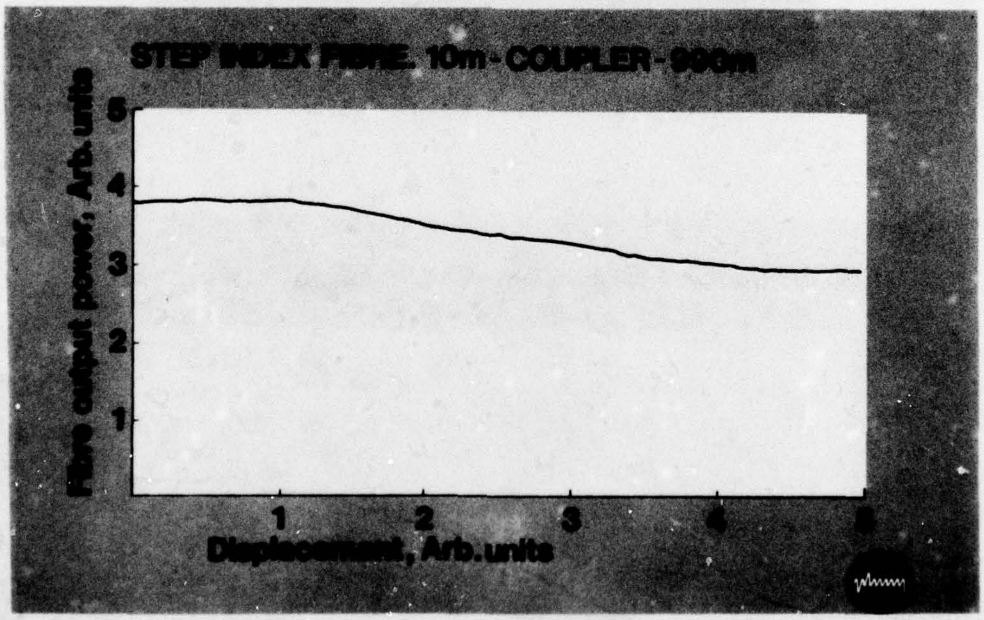

Figure 10. Fibre output as a function of grating amplitude for the smaller core fibre.

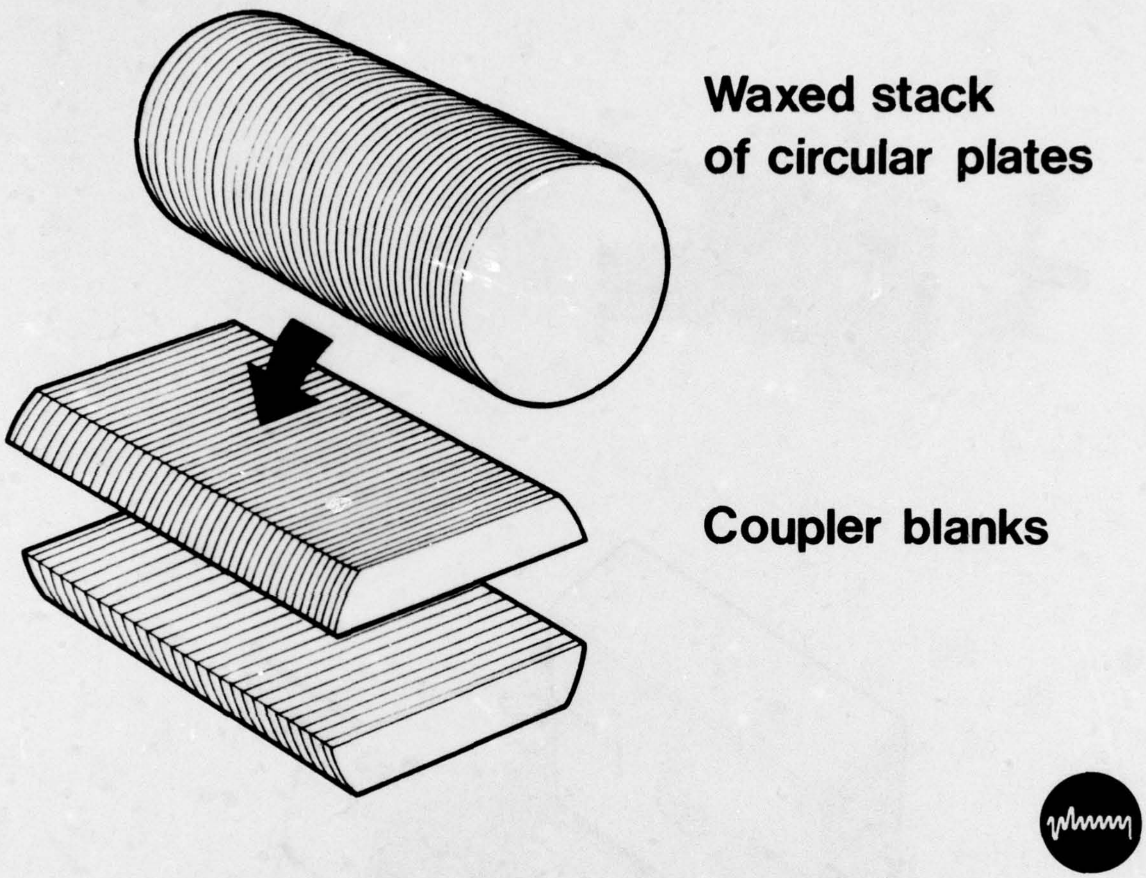

Figure 11. Fabrication of thin plate couplers.

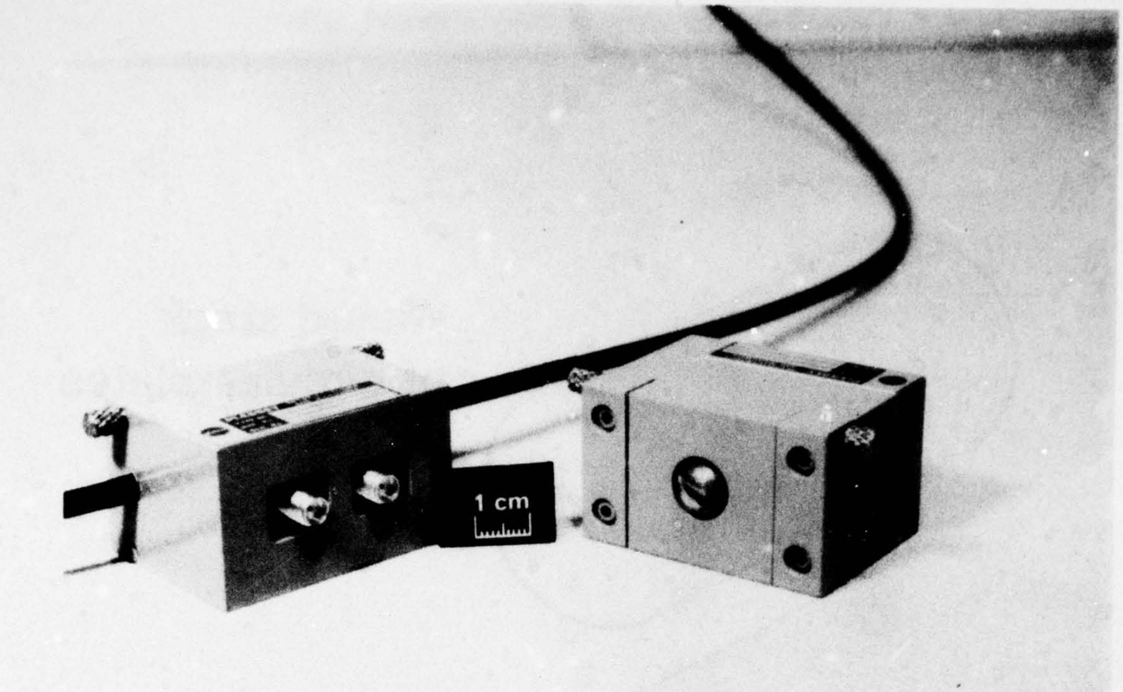

(a)

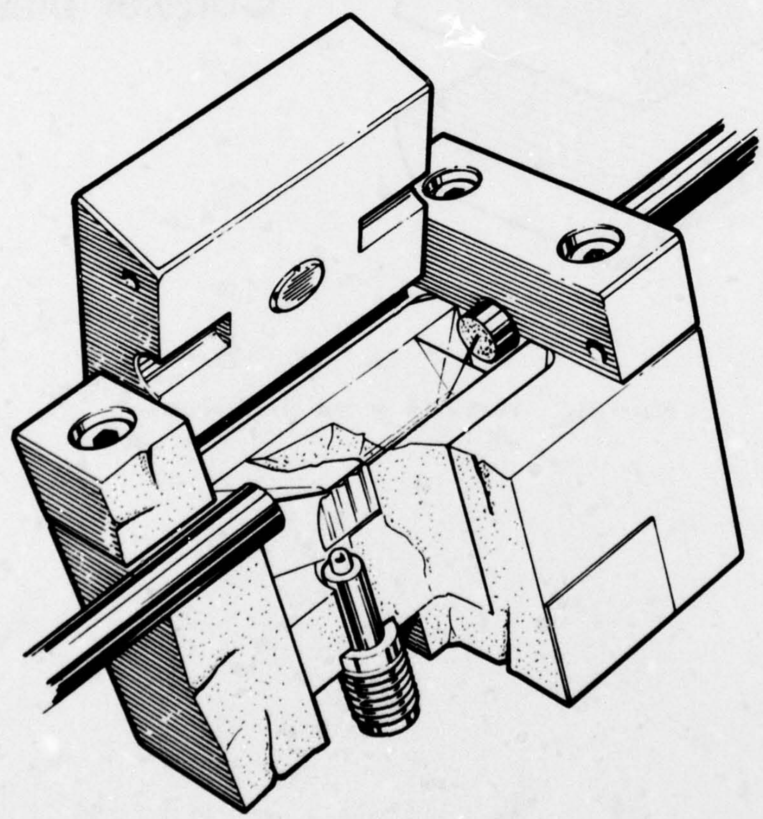

(b)

Figure 12a) Prototype packaged thin plate directional coupler.
b) Cut away view of internal arrangement of prototype.

BIDIRECTIONAL CENTRAL COUPLERS FOR LINKS WITH OPTICAL FIBER BUNDLES*

L. D'Auria and A. Jacques
THOMSON-CSF
Laboratoire Central de Recherches
B.P. 10 - 9140. . Orsay
(France)

SUMMARY

A range of compatible and detachable devices for links with optical fiber bundles have already been developed including both components for point to point links (transmitter, receiver, connectors ...) and data distribution devices (3dB splitter, electrically tapped connector, mechanical multiple switch).

In this paper we describe bidirectional central couplers having seven input/output terminals, compatible with all realized devices.

Construction of two types of central couplers is described : assembled bundle coupler and separable bundle coupler (with linear central fiber and U central fiber).

A technique using a central diffuser allows a significant and reproductible decrease of the maximum variation of the detected levels on the same detecting channel.

1 - INTRODUCTION

The optical fiber bundles with low active diameter ($< 600\,\mu m$) have been retained for operational links with medium rates ($\sim$ 40 Mbits/s) on short distances ($\sim$ 100 meters).

The use of several optical fibers transmitting the same signal achieves transmission security by redundancy, connection simplicity related to large mechanical tolerances and the reliability of electroluminescent emitters, adapted to the bundle size and working with low current densities (< 100 A/cm^2).

A range of detachable, active and passive devices have been developed ; these devices are specifically adapted for use with optical fiber bundles containing 37 or 19 fibers, 85 μm in diameter, with high numerical aperture (0.5) and medium losses ($<$ 100dB/km) [1, 2] .

The family includes devices for point to point links :

- Emitter and detector units including LED's, PIN silicon photodiodes and optical couplers enclosed with flange mounting (Figure 1.a).
- Complete transmitter and receiver modules with analogic on TTL compatible output/input (Figure 1.b).
- Bundle to bundle mixing connectors permitting standardization of cable terminals and reducing random coupling variations due to fiber breakage and positioning (Figure 1.c).
- Multiple connectors for cables containing six optical fiber bundles (Figure 1.d).
- Feedback regulated emitter permitting optoelectronic feedback linearization, constant peak power emission or built in test functions (Figure 1.e).

And devices for data distribution :

- 3dB passive splitter made with single fibers (Figure 1.f).
- Electrically tapped connector performing two functions : bundle to bundle mixing connection and taking a fraction of the signal circulating in the link and allowing optoelectronic splitting with low leakage factors and localization of faulty bundles (Figure 1.g).
- Mechanical multiple switch allowing the passage of the optical information from one bundle to any of six bundles (Figure 1.h).

To realize conversational links between several terminals with optical fiber bundles (see Figures 3.a and 2.b), Tee and Star systems have been examined and specific devices (Tee couplers and Star couplers) have been proposed [3, 4, 5, 6, 7, 8] .

It has been further demonstrated that, although requiring greater length of fiber bundles, the Star configuration is more advantageous than the Tee configuration concerning the optical power attenuation between two terminals.

Indeed, assuming that the insertion losses and the connexion losses are negligible ; in a star system with N terminals, the theoretical attenuation As, expressed in dB, between any two terminals is given by :

$$A_s = 10 \operatorname{Log} N \qquad (1)$$

In a Tee system, using for example, identical couplers with a 10dB coupling ratio the attenuation A_T in the worst case is given by :

$$A_T = 0.46\,(N-3) + 13 \qquad (2)$$

* This work is supported by the "Direction des Recherches et Moyens d'Essais".

The curves in Figure 2.c show clearly that the possible number of terminals for the same attenuation between two terminals is higher in the Star system than in the Tee system ; this difference is emphasized when the insertion losses and the connection losses are introduced in the formulas (1) and (2).

In the following, various configuration of bidirectional central couplers are described :

- Coupler with assembled bundles.
- Coupler with detachable bundles with linear central fiber and U central fiber.

These couplers are compatible with already existing devices.

2 - DESCRIPTION AND THEORETICAL CONSIDERATIONS

2.1 - General

Figure 3 diagrams the principle of a bidirectional multiport coupler.

The coupler is constituted by a central optical fiber F_o, on the input face of which are assembled all the emitter bundles F_1, F_2 ... F_n ; the assembled detecting bundles F'_1, F'_2 ... F'_n being issued from the output face of F_o.

The optical information coming, for example, from the emitter E_1 and circulating in the bundle F_1 is injected in the central fibre F_o whose numerical aperture is the same as that of the fibers constituting the bundles and which core area is at least equal to the area of the central bundle constituted by the assembling of the bundles F_1, F_2 ... F_n. The length of F_o is at least such that the optical energy coming from any of the bundles F_1, F_2 ... F_n covers all the output face of F_o ; the information from emitter F_1 will be then distributed to the receiver R_1, R_2 ... R_n through the bundles F'_1, F'_2 ... F'_n. The same holds true for the information emitted by any of the emitters F_2 ... F_n.

2.2 - Central coupler configuration

Two main types of seven-port central couplers have been examined.

-a- Coupler with assembled bundles

This type of coupler is schematized on Figure 4.a. The optical fiber bundles coming from the emitter (and detector) units are assembled into a single ferrule and all the fibers of the seven bundles are solidary.

The detachable connections are located at the two extremities of the central fiber F_o.

An additional detachable connector may exist on each elementary bundle.

-b- Coupler with detachable bundles

It seems desirable to dispose of independent *detachable bundles on the central coupler* realized in a monoblock form.

Two types of coupler with detachable bundles have been examined (see Figure 4.b and 4.c) : with linear central fiber and U central fiber.

The transition between the detachable connection and the central fiber is ensured by intermediate single fibers, linear or curved with two bends according to the position of the terminal. If the central fibre is U-shaped, notice that the detachable connections are set in the same plane (P) as the interface between the intermediate single fibers and the central fiber in the plane (P').

The main advantages of such a configuration are :

- Utilization of standard bundles and standard connections.
- Possible location of the coupler on the front panel of monitoring equipment.
- The monoblock concept gives robustness to the device.
- The intermediate single fibers are polished in a single operation.
- The components and the technology used are simple, insuring a low cost in industrial production.

The bolting of the connections between the bundles and the intermediate fibers can be made :

- Independently as in Figure 4.c.
- Simultaneously on the seven ports using for instance classical bolting of multiport electrical connectors ; the bundles being strand assembled.

2.3 - Loss evaluation

The loss evaluation below is applied in the case of couplers with detachable bundles.

Let N be the number of terminal and, expressed in dB (see Figure 5).

P_c : LED-monofiber coupling loss in the emitter Unit (due to the limited numerical aperture of the fiber).

P_E : Monofiber-bundle coupling loss (due to the detachable connection and the filling factor of the bundle).

P_d : Bundle-intermediate fiber coupling loss (due to the detachable connection).

P_s : Central fiber-intermediate fiber coupling loss (including the N terminals separation).

P_t : Loss due to the filling factor of the intermediate fibers.

Assuming an uniform distribution to the N terminals it can be written :

$$P_s = P_t + 10 \text{ Log } N$$

Neglecting the bundle lineic losses, the attenuation A_{ED}, expressed in dB, between the optical power emitted by the LED and the optical power detected by the photodiode, is :

$$A_{ED} = P_c + P_E + P_d + P_S + P_E + P_d$$

$$A_{ED} = P_c + 2(P_E + P_d) + P_t + 10 \text{ Log } N$$

If optical fibers with 0.5 numerical aperture are used :

$$P_c = 10 \text{ Log } \left(\frac{1}{0.5}\right)^2 = 6\text{dB}$$

The other causes of losses are principaly [1] :

- The losses due to mechanical misaligments in the detachable connections (axial and angular misaligments, distance between the optical faces, optical surface quality, perpendicularity defects, Fresnel losses) combined are between 1 and 2dB.
- The losses due to the filling factor of the utilized bundles (2 to 3dB) and the filling factor of the central fiber-intermediate fibers interface (1 to 2dB).

Under these conditions A_{ED}, expressed in dB, is comprised between (15 + 10 Log N) and (22 + 10 Log N).

2.4 - Problems of variation of the detected levels

One of the problems encountered using central couplers is the variation of the detected level on the same detecting channel with the different emitter ports.

This variation is due to the non-uniformity of the light distribution on the output core surface of the central fiber.

One can define the maximum variation D as the difference, expressed is dB, between the maximum optical power P_M and the minimum optical power P_m detected on the same detecting channel considering all the emitting channels :

$$D = 10 \text{ Log } \frac{P_M}{P_m}$$

A technique to make the light distribution uniform on the central fiber output face, while ensuring the coupler reproducibility in a serie fabrication, is to introduce a light diffuser in the middle of the central fiber (see Figure 6).

This diffuser rearranges the angular optical power distribution in the fiber and favourises the power mixing , decreasing the variation D. It introduces obviously some losses and a trade off has to be done between the maximum variation D and the extra losses.

3 - EXPERIMENTAL RESULTS

We have made a seven-port central coupler prototype with assembled bundles. Each of the input/output bundles contains 37 fibers, giving a central bundle with 259 fibers. The diameter of the central bundle after packing in the ferrule is 1.5mm. The bundles assembled on each side of the central fiber, which length is 17.5mm, are detachable and connected with modified Conhex connectors.

The photograph of Figure 7 represents a coupler with assembled bundles on a testing Bench specially designed for the characterization of central couplers. The bundles coming from the input/output faces of the coupler are connected to seven emitter units and seven detector units with modified subminiature connectors.

On Figure 8 is summarized the loss measurement and shown for every channel the maximum variation in the attenuation between the optical power emitted by the emitter unit and the optical power detected by the detector unit. In the worst case, a 5dB maximum range is seen on channel 2, due to patterning effects on the output face of the central fiber.

A randomization procedure for the arrangement of the fibers in the central bundle can be used in order to reduce partially the magnitude of the variation ; Nevertheless it should be note that this procedure is not reproducible and causes some breakage 3 . The average terminal-to-terminal attenuation is 18dB including :

- The seven port separation (8.5dB).

- The filling factor of the input/output bundles (2x3dB).
- The detachable connections (3.5dB).

Two prototypes of central couplers with detachable bundles have been made with a linear central fiber and a U-central fiber.

The seven intermediate fibers at the two extremities of the central fiber have a core diameter of 535/um corresponding to the active diameter of 37 fiber bundles. Among the intermediate fibers, one is linear and six have two bends. The seven fibers are introduced in an optical head whose one face contains the intermediate fibers in a surface of 1.9mm diameter corresponding to the active diameter of the central fiber ; the other face of the optical head includes seven independent connectors corresponding to the seven channels.

The filling factor of the seven intermediate fibers with regard to the core diameter of the central fiber corresponds to 2dB loss. In this type of coupler the insertion loss P_i is defined as the attenuation between the optical power coming into an intermediate input fiber and the optical power detected at the output of an intermediate fiber.

The insertion loss includes :

- The seven port separation (8.5dB).
- The filling factor of the output optical head ($\sim$ 2dB).
- The proper losses due to the passage through the intermediate fibers and the central fiber (with and without diffusing interface).

In the case of the linear central fiber, the diagrams of Figure 9 give, for every detecting port, the maximum variation of the insertion loss with and without interposed diffuser.

The total length of the central fiber is 24.6mm and the diffuser is characterised by a diffusion angle of 25° (half power).

Under these experimental conditions, the greatest maximum variation of the insertion loss occurs on the central port (number 7) and is equal to 5.4dB without diffuser and to 2.7 dB with diffuser ; the average insertion loss is equal to 11.5 dB or 14.5 dB according to the absence or the presence of the diffuser. Similar results have been obtained with various lengths of the central fiber.

An other prototype has been realized with a U central fiber. The two optical heads are in a same plane and are separated from 5cm. The central fiber has a length of 8cm and a bending radius of 17.5mm.

As in the previous case, the diagrams of figure 10 give for every detecting port, the maximum variation of the insertion loss with and without interposed diffuser. The maximum variation is equal to 1.9dB (channel number 5) without central diffuser and to 1.5 dB (channel number 3) with a central diffuser, the average insertion loss passing from 12.5dB to 14.5dB. We note a decreasing of the maximum variation due to mixing effects in the curved central fiber and then a lower relative efficiency of the diffuser.

The prototype of Figure 11 shows a mounting possibility of a central coupler with independently detachable bundles and U central fiber.

4 - CONCLUSION

Various structures of bidirectional central couplers with seven ports for links with optical fiber bundles have been analyzed and realized.

The working principle of a central fiber has been verified for an assembled bundle structure and a detachable bundle structure with a linear central fiber and a U central fiber.

In the case of a linear central fiber, the utilization of a central diffuser allows a significant decrease of the maximum variation in the detected level of the same output channel.

Conventional technology allows an easy reproducibility of the central coupler with detachable bundles.

REFERENCES

1 - L. D'AURIA et A. JACQUES — "Composants pour liaisons par faisceaux de Fibres Optiques"
Revue Technique THOMSON-CSF,
Vol 7, n°4, pp.651-675 - Décembre 1975

2 - L. D'AURIA and A. JACQUES — "Specific Devices for point to point links and data distribution with optical fiber bundles"
Second European Conference on Optical Fibre Communication
Paris 27-30 Septembre 1976

3 - M.C. HUDSON and F.L. THIEL — "The star coupler : A unique interconnection component for multimode optical waveguide communications systems".
Applied Optics,
Vol 13, n°11, pp.2540-2545 - November 1974

4 - F.L. THIEL — "Coupling considerations in optical data buses"
Topical Meeting on Optical Fiber Transmission,
Williamsburg, Virginia, January 7-9, 1975

5 - F.L. THIEL — "Coupling considerations in optical data buses"
Electronic Components
pp.17-18 - February 11, 1975

6 - F.L. THIEL — "Coupling considerations in optical data buses"
Alta Frequenza,
Vol XLV, n°2, pp.144-146 - Febbraio 1976

7 - M.K. BARNOSKI — "Data distribution using fiber optics"
Applied Optics,
Vol 14, n°11, pp.2571-2577 - November 1975

8 - M.K. BARNOSKI — "Coupling : in systems with 20 or more terminals, star couplers out perform "tee" types"
Electronics
pp.102-104 - August 5, 1976.

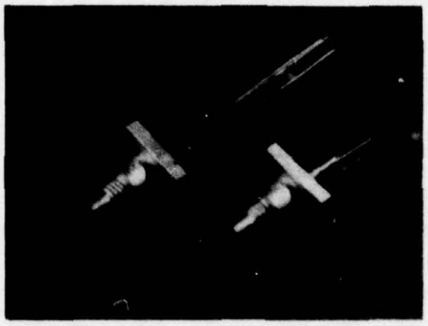

1.a - Emitter/Detector Units

1.b - Emitter/Detector Modules

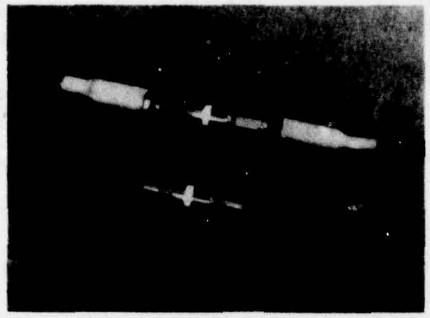

1.c - Bundle-to-bundle mixing connector

1.d - Multiple connector

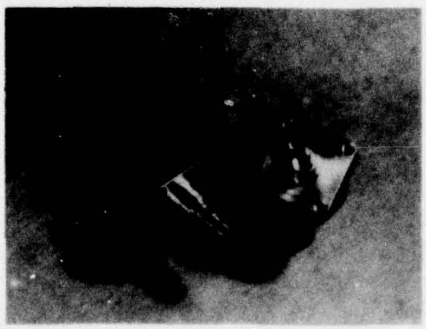

1.e - Feedback regulated emitter

1.f - 3dB passive splitter

1.g - Electrically tapped connector

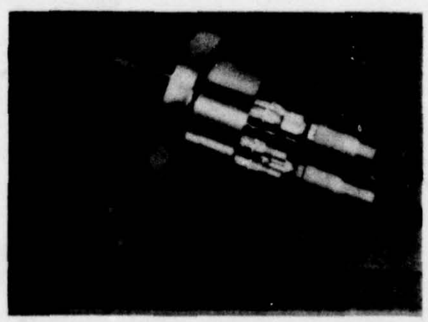

1.h - Mechanical multiple switch

- Figure 1 -

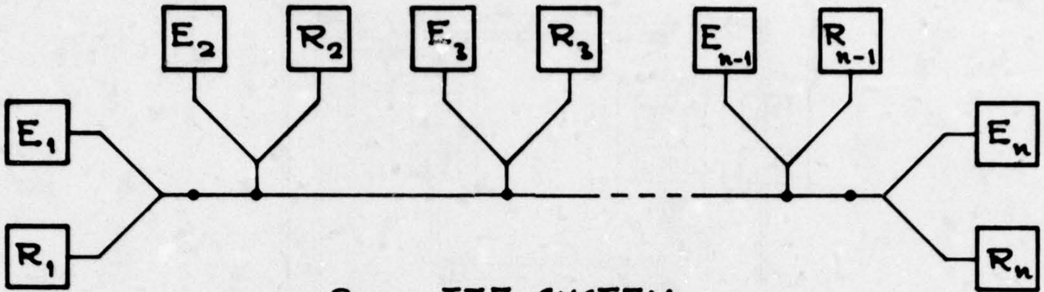

2a - TEE SYSTEM

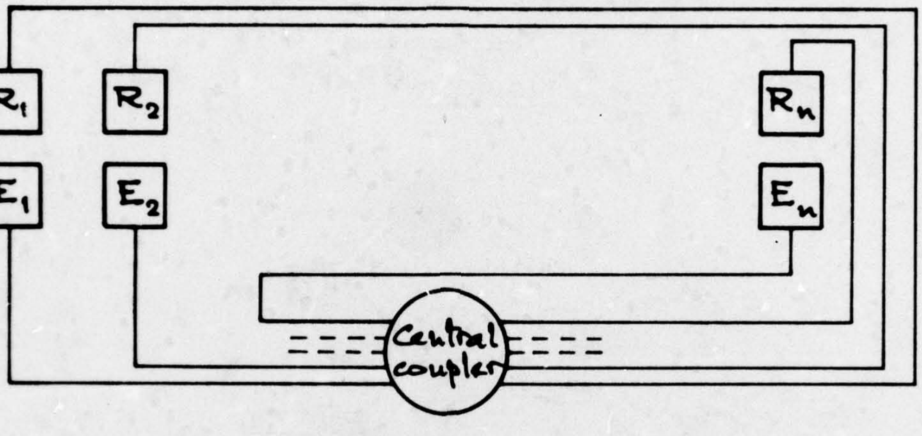

2b - STAR SYSTEM

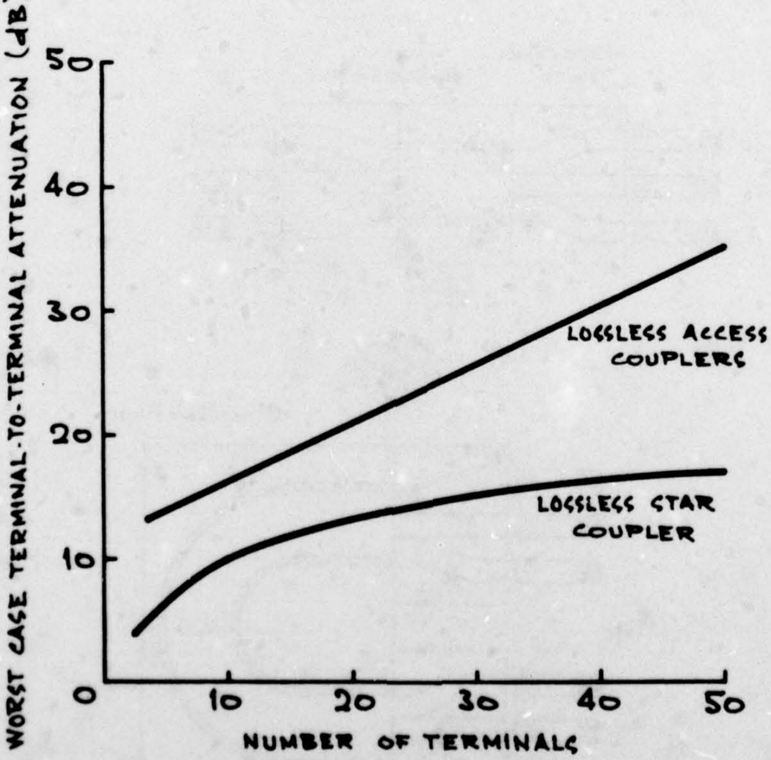

2c. -

FIGURE 2

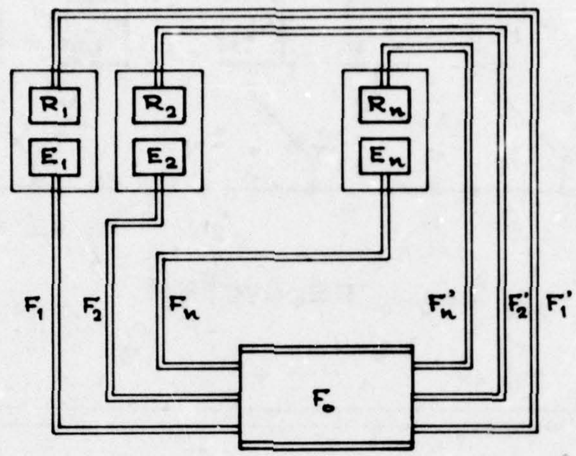

FIGURE 3

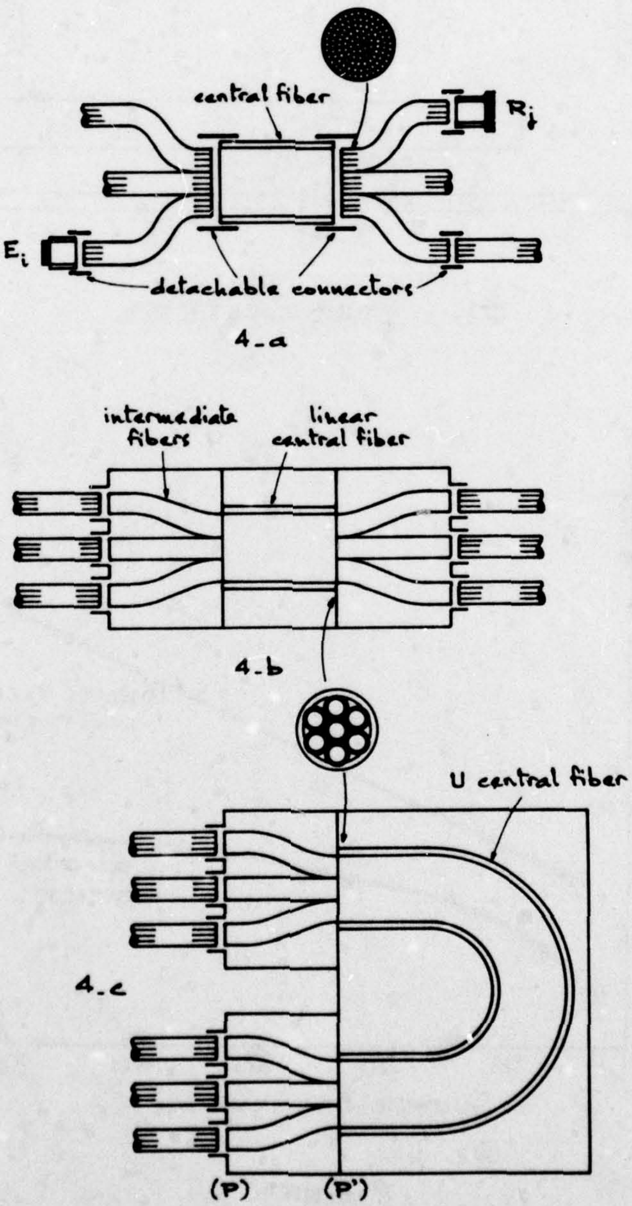

FIGURE 4

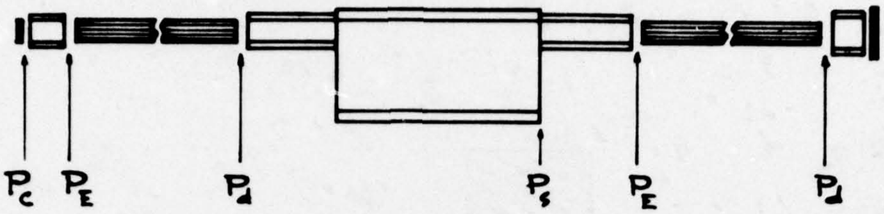

FIGURE 5

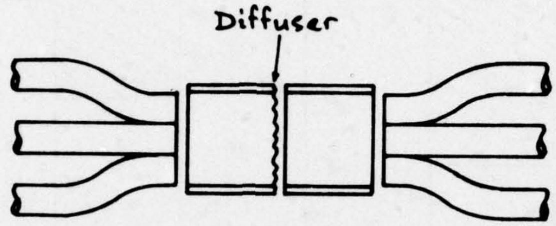

FIGURE 6

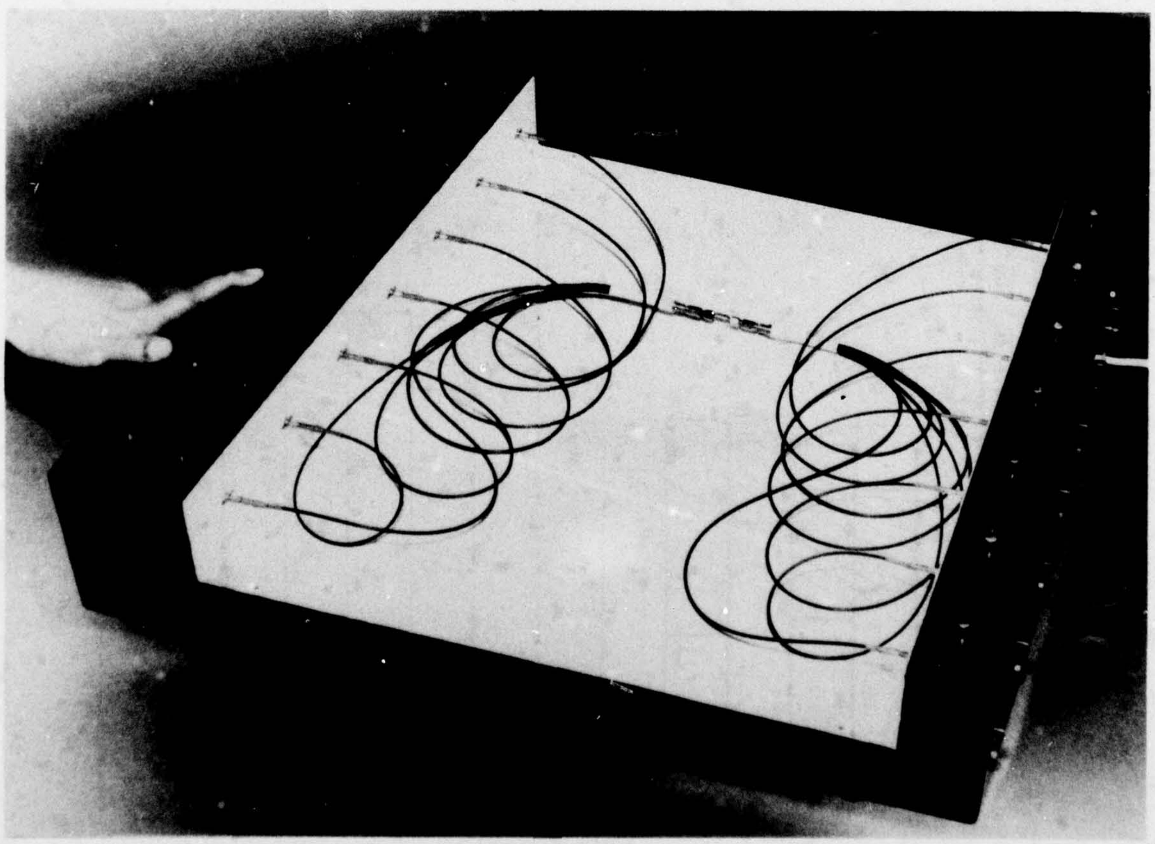

- FIGURE 7 -

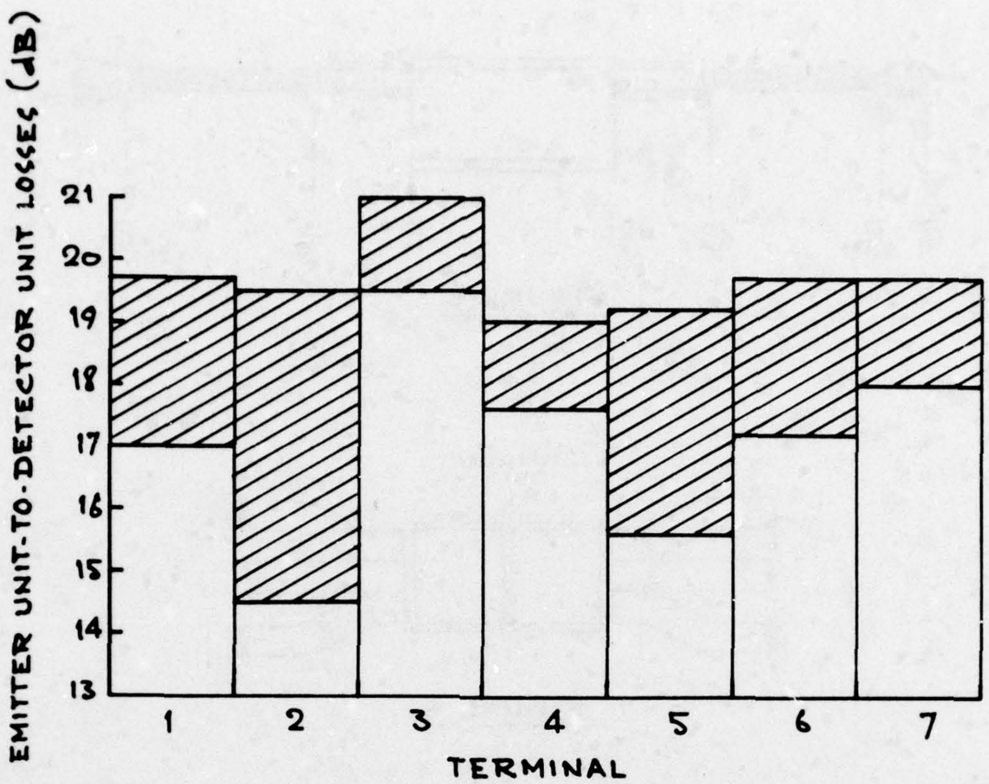

FIGURE 8

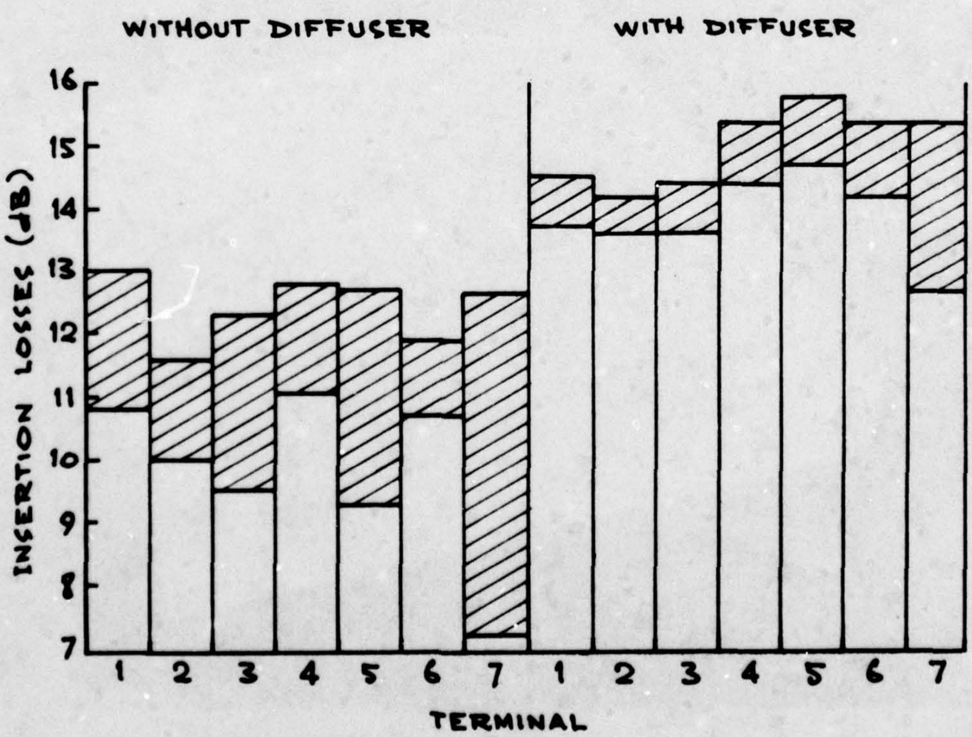

FIGURE 9

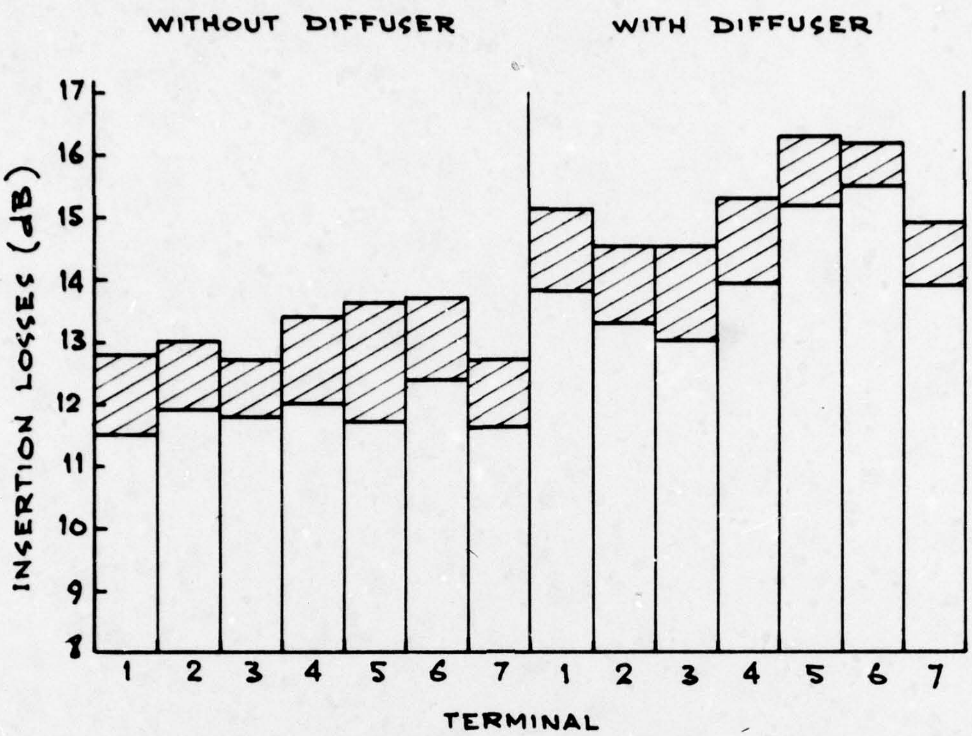

FIGURE 10

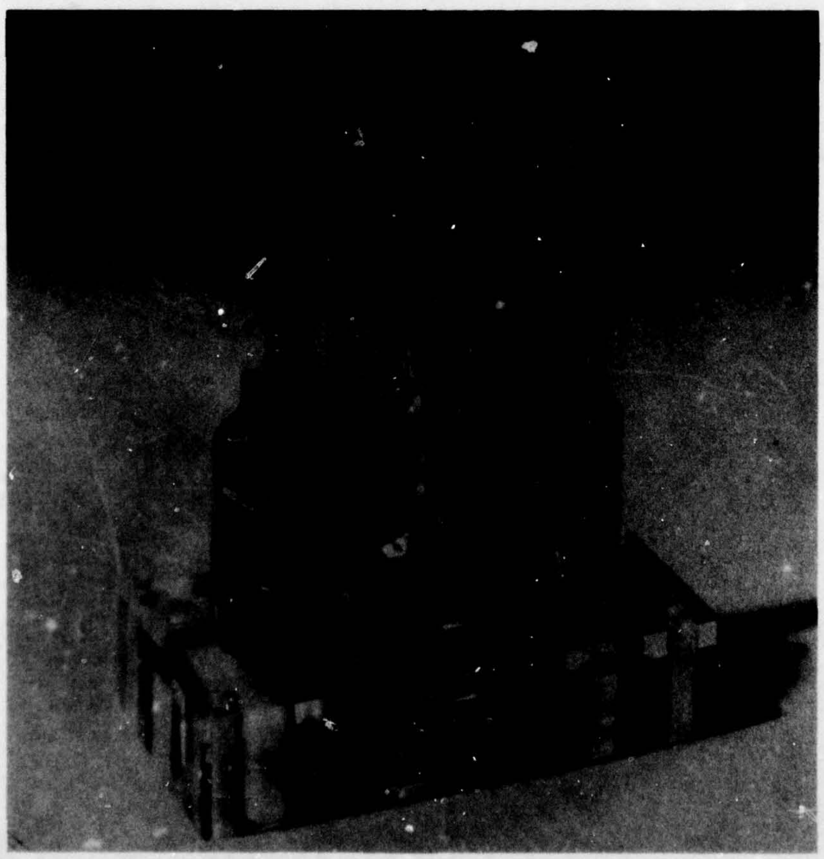

FIGURE 11

T - COUPLER FOR MULTIMODE OPTICAL FIBERS

L. JEUNHOMME, J.P. POCHOLLE
Laboratoires de Marcoussis, Centre de Recherches de la
COMPAGNIE GENERALE D'ELECTRICITE
Route de Nozay, 91460 - Marcoussis - FRANCE

SUMMARY

The device to be described here allows the derivation of a variable amount of the light travelling in a multimode optical fiber without interruption of the transmission link. The principle of this optical fiber tap is to induce well controlled mode conversion between guided and radiation modes of the fiber, which can then leak out in a higher-index surrounding medium and reach a photodetector. The mode conversion is induced by bending the fiber in a sinusoïdal way and the derivation ratio is adjusted by varying the amplitude of the sinusoïdal deformation. The results presented here concern the influence of the mechanical wavelength of the deformation, the radiation pattern of the power derivated from the fiber and the influence of the device on the propagation characteristics of the fiber (far-field radiation pattern and impulse response). Results concerning the derivation ratio achievable with this device are also presented for both step-index and graded-index fibers.

1. INTRODUCTION

Since the advent of low-loss multimode optical fibers, there is a great interest in the realisation of optical fiber data buses, especially for military applications. For this purpose, it is necessary to use T - couplers which allow (i) the extraction of a part of the light travelling in the optical link and/or (ii) the insertion of a signal into the main opticla link. In the case of data buses achieved with fiber bundles, many possible schemes have been proposed, but it recently appeared that single fiber data buses could also be of interest. It is thus necessary to solve the problem of the T - coupler for the single fiber case.

We restrict here our interest to the problem of the optical fiber tap, which allows only the extraction of a part of the power travelling in a single multimode optical fiber. Some authors have recently proposed different solutions to this problem, such as using a tapered section of fiber (OZEKI, T. and KAWASAKI, B.S., 1976), etching the cladding of the fiber (PAN, J.J., 1976), fusing two fibers to one other fiber (FUJITA, H., SUZAKI, Y. and TACHIBANA, A., 1976), inserting and fusing a microprism between three fibers (SUZUKI, Y. and KASHIWAGI, H., 1976) or using the lateral displacement of a fiber incident on two other fibers (WITTE, H.H., 1976).

However, none of these devices can be inserted without interrupting the transmission, in most cases it is difficult to adjust the amount of power extracted from the fiber and the coupling efficiency is often very small.

On the other hand, we have demonstrated that it is possible to achieve an optical fiber tap which can be inserted without interrupting the transmission and for which the derivation ratio can be easily adjusted up to -3 dB with a very good coupling efficiency and small insertion loss (JEUNHOMME, L. and POCHOLLE, J.P., 1976).

The purpose of this paper is to further describe the principles of this coupler, the influence of the important parameters and the performances which can be reached.

2. PRINCIPLE OF THE COUPLER

It is well known from the work of MARCUSE, D. (1973), that inducing a periodic distortion (for example a periodic bending) in an optical fiber will couple pairs of modes with propagation constants β_1 and β_2 such that :

$$\beta_1 - \beta_2 = \pm\ 2\pi / \Lambda \qquad (1)$$

where Λ is the mechanical wavelength of the distortion.

It should thus be possible, by suitably choosing the value of Λ, to couple guided and radiation modes together ; this is the basic idea which is used in our coupler.

2.1. Theoretical considerations

We consider here multimode fibers with a high number of modes. These modes are characterized by two indices μ and ν which, respectively, count the number of radial and azimuthal nodes in the field intensity of that mode. Each mode has a propagation constant $\beta_{\mu,\nu}$

If we restrict interest to fibers for which the refractive index profile is described by an α - power law (GLOGE, D. and MARCATILI, E.A.J., 1973), it can be shown that the propagation constant is given by (OLSHANSKY, R., 1975) :

$$\beta_{\mu,\nu} = k_1 \left\{ 1 - 2\Delta \left[\frac{\alpha+2}{\alpha} \quad \frac{(2\mu+\nu)^2}{a^2 k_1^2 \Delta} \right]^{\frac{\alpha}{\alpha+2}} \right\}^{1/2} \qquad (2)$$

where . k_1 is the free-space propagation constant of the light x the refractive index on fiber axis (n_1) : $k_1 = 2\pi n_1 / \lambda$

. Δ is the relative index difference between axis (n_1) and cladding (n_2) : $\Delta = \frac{n_1 - n_2}{n_1}$

. a is the radius of fiber core.

All the guided modes have propagation constants $\beta_{\mu,\nu}$ such that $\frac{2\pi n_2}{\lambda} \leq \beta_{\mu,\nu} \leq \frac{2\pi n_1}{\lambda}$

which means also : $$0 \leq (2\mu + \nu)^2 \leq \frac{\alpha}{\alpha + 2} a^2 k_1^2 \Delta \qquad (3)$$

For other values of $(2\mu + \nu)$, we have leaky or radiation modes.

It has been experimentally observed that, when a fiber is sinusoïdally bent, there exists an additional selection rule to relation (1) for coupling pairs of modes (STEWART, W.J., 1975), which expresses that coupling occurs from a mode (μ , ν) to a mode (μ , $\nu \pm 1$) only.

We are thus able to compute the difference in propagation constants of the modes which can be coupled together through a periodic distortion of the fiber axis. For two particular cases of practical interest, we obtain :

$$\Delta\beta_{(\mu,\nu)(\mu,\nu+1)} = (2\Delta)^{1/2} / a \qquad (4)$$

for the parabolic index fiber (α = 2).

$$\Delta\beta_{(\mu,\nu)(\mu,\nu+1)} = \frac{1}{a^2 k_1} \left(1 + 2(2\mu + \nu) \right) \qquad (5)$$

for the step index fiber. ($\alpha \to \infty$)

It can thus be seen that for parabolic index fibers, either all the modes are coupled together if the mechanical wavelength of the distortion verifyes relations (1) and (4), or they are uncoupled.

For step-index fibers, by considering the minimum and the maximum value of $(2\mu + \nu)$ given by (3), it appears that $\Delta\beta$ varies in the range :

$$\frac{1}{a^2 k_1} \leq \Delta\beta \leq \frac{1}{a^2 k_1} + \frac{2\sqrt{\Delta}}{a} \qquad (6)$$

If the mechanical wavelength Λ of the distortion is such that :

$\frac{2\pi}{\Lambda} < \frac{1}{a^2 k_1}$ no coupling occurs

$\frac{1}{a^2 k_1} \leq \frac{2\pi}{\Lambda} < \frac{1}{a^2 k_1} + \frac{2\sqrt{\Delta}}{a}$ coupling occurs only between some particular guided modes

$\frac{2\pi}{\Lambda} \geq \frac{1}{a^2 k_1} + \frac{2\sqrt{\Delta}}{a}$ coupling occurs between some guided, leaky and radiation modes.

It appears thus clearly that, for coupling a part of the guided light to radiation modes, in a step-index fiber, it is necessary that Λ verifyes this last inequality. It appears also that, if the distortion of the fiber is purely sinusoïdal on an infinite length, only a few particular guided modes will be coupled to radiation modes. This would, of course, limit the interest of such a coupler. In practical cases, however, the induced distortion of the fiber will occur only on a finite length and this fact allows all the modes to be coupled together and to radiation modes : let us take Λ as the mechanical wavelength and 2 l as the length of distortion, then the mechanical spectrum of the distortion is :

$$\left[\frac{\sin\left(\frac{2\pi}{\Lambda} - \Delta\beta \right) l}{\left(\frac{2\pi}{\Lambda} - \Delta\beta \right) l} \right]^2$$

Thus, all the modes which have $\Delta\beta$ in the range were this spectrum is not too small will be coupled together, and shorter the deformation, wider the range of coupled modes.

We can now define the way in which such a coupler should be built.

2.2. Definition of the coupler

The simplest way to achieve a quasi sinusoïdal deformation of fiber axis is to press it between two gratings, with the convenient mechanical wavelength and sufficiently deep to allow strong deformation of the fiber, as shown on figure 1. The displacement of the upper grating can be controlled through a precise translation stage.

For the experiments to be described here, we dispose after the gratings a glass hemisphere of higher refractive index than the cladding and a mirror plate, between which the fiber passes, immersed in an index matching oil. This device allows the light transferred to radiation modes by the gratings to leak out and to reach a photodetector. In the definitive coupler both functions, deformation and index matching should be combined in order to get a better efficiency.

The fiber used in the experiments is a step index CGW fiber with the following characteristics :

$n_1 = 1.46$, $a = 42.5\ \mu m$, $\Delta = 6 \times 10^{-3}$

From relation (6) we obtain :

$$\frac{2\pi}{164} \leq \Delta\beta \leq \frac{2\pi}{1.72} \quad mm^{-1} \text{ for } \lambda = 0.633\ \mu m$$

$$\frac{2\pi}{127} \leq \Delta\beta \leq \frac{2\pi}{1.72} \quad mm^{-1} \text{ for } \lambda = 0.82\ \mu m$$

which are the wavelengths which will be used in the experiments.

For efficiently coupling light from many guided modes to radiation modes, we shall thus use a grating with a mechanical wavelength slightly higher than 1.72 mm and a finite length such that the mechanical spectrum extends above 1.72 mm. On the other hand it is clear that decreasing the length of the gratings will decrease the amount of power that can be coupled out from a particular mode, and we have thus to find a trade off between both effects.

It should be noticed that the upper limit of $\Delta\beta$ is nearly independent of the light wavelength (since $2\sqrt{\Delta} >> 1/ak_1$, in multimode fibers) and thus the optimum value of the mechanical wavelength is also nearly independent of the light wavelength.

3. EXPERIMENTAL RESULTS

The first point to be examined is the optimum mechanical wavelength of the gratings.

3.1. Influence of the mechanical wavelength

The light source used in this experiment is a He-Ne laser weakly focused onto the input plane of the two meter long fiber. This ensures that only low-order modes are launched (the far field radiation pattern after two meters of fiber has a base line semi angle of 5° compared to 9° for the maximum guiding angle of the fiber) and thus the conditions are particularly difficult because we need a wide mechanical spectrum.

We use two sets of gratings pairs, mechanically manufactured on circular perspex plates. The first set has a mechanical wavelength of 1.4 mm and the second one of 2 mm, the diameter of the plates is 42 mm and the depth of the gratings is 1 mm and 1.4 mm respectively. The angle between the fiber axis and the grooves of the gratings, in the horizontal plane, is varied through a precise rotation stage so that the effective mechanical wavelength of the induced distortion can be varied from 1.4 mm to 2.8 mm for the first set and 2 mm to 4 mm for the second set. It should be noticed that varying the mechanical wavelength in this way let the distortion length fixed, so that the mechanical spectrum bandwidth is constant.

We measure the total transmitted power P_2 at port 2, as a function of the rotation angle, with a constant amplitude of deformation of the fiber. This experiment has been carried out with three different amplitudes of deformation (weak, medium and strong) and the curves P_2/P_2° (P_2° = transmitted power without deformation) as a function of the mechanical wavelength are shown on figure 2.

It can be observed that :

(i) increasing the deformation increases the insertion loss (or equivalently decreases P_2/P_2°)
(ii) there exists an optimum for the mechanical wavelength which varies from 2 mm to 2.6 mm when the amplitude of the deformation decreases.

These values are in good agreement with the theorical predictions of section 2.2..

In order to have a more complete insight into the influence of the mechanical wavelength, we have also made detailed investigations of P_2/P_2° as a function of the displacement d of the grating (or amplitude of the deformation) for several mechanical wavelengths in the range 1.8 to 2.6 mm.

The results are presented on figure 3 where it is seen that :

(i) for strong deformations, the optimum mechanical wavelength is 2 mm
(ii) when the amplitude of the deformation decreases, the optimum mechanical wavelength becomes higher.

These observations confirm the preliminary constatations made on figure 2, and in the subsequent experiments, we will use the 2 mm wavelength.

We can also conclude from this experiment that this wavelength and length of gratings combination allows even the low order modes to be coupled to radiation modes.

Similar measurements made with an L.E.D. butt joined to the fiber instead of the He-Ne laser, and using a cladding mode stripper at the input show that 2 mm is also the optimum mechanical wavelength under these conditions (light wavelength 0.82 μm and all modes excitation).

3.2. Influence of the length of the gratings

For this experiment, we use the same experimental arrangement as in section 1 with little changes : For the launching conditions, in addition to the low order modes excitation, we use also an all modes excitation by pressing the first 20 cm of fiber between elastomer and sandpaper ; under these conditions the far-field radiation pattern has a base-line semi-angle of about 12°.

Two sets of gratings are used : the first one has a mechanical wavelength of 2 mm and a length of 42 mm and the second one has the same mechanical wavelength but a length of 10 mm, in order to widen the mechanical spectrum.

Figure 4 shows the curves P_2/P_2° for both launching conditions and both grating lengths.

Results indicate that this change has little effect on the maximum extinction ratio achievable and confirm the fact that the broadening of the spectrum is compensated by the smaller coupling strength.

3.3. Radiation pattern of the derivated light

In order to design the best shape for the higher index surrounding medium, for focusing the derivated light onto a photodetector, we look now to the radiation pattern of the derivated light.

For this purpose, we use the He-Ne laser with the low order modes excitation, a 2 meters length of fiber and the gratings with 2 mm wavelength and 42 mm length. After the gratings, the fiber passes between two glass hemispheres of index 1.486 and diameter 35 mm, with an index matching paste.

The fiber is black painted on its total length, excepted a small element, 2 mm in length, which is carefully positioned at the center of the sphere, so that rays are emitted only from this point and are not deviated at the glass-air interface.

The far-field is then scanned by a photodetector moving on a 160 mm radius circle centered on the emitting element, with an angular resolution of 0.2°.

Figure 5 shows a photograph of this far-field, where it is seen that there is a circular symetry in the emission (the black points correspond to the plane where the hemispheres are not exactly contacting).

Figure 6 represents the corresponding far-field which shows a strong directivity, as all the light is emitted between 11.9° and 14.8°, the angle corresponding to the peak beeing 12.6°.

These results will enable us to design a convenient higher index medium for refocusing this light onto a photodetector.

However, this has not been done yet and the other experiments reported here are always carried out with the glass hemisphere and the mirror plate.

3.4. Influence on the propagation characteristics of the fiber

The next point to be examined is how the insertion of such a coupler in a transmission link will affect its transmission characteristics.

We look first at the modification of the far-field radiation pattern (or power distribution among the modes) of a fiber, when the coupler is inserted.

Figure 7 shows the far fields at the output of a 2 meter long fiber, with low order modes excitation (He-Ne) and with all modes excitation (L.E.D. with a cladding mode stripper) : comparisons are made between the far-field without distortion and with the maximum distortion induced through the 2 mm/42 mm gratings.

It is observed that the far-field is strongly broadened when a low order modes excitation is used, and much less with the all modes excitation. In fact, the resulting far-field with the distortion are similar and include both some leaky modes.

As it is generally observed that leaky modes disappear after a few meters of fiber, we can conclude that introducing this coupler in a practical system with L.E.D. excitation, will not strongly affect the transmission characteristics of the link since the power distribution among the modes is not significantly altered by the introduction of the coupler. For the same reason, each coupler in a link with several couplers will be independent of the other ones, and thus introducing or removing one coupler in the link will affect very slightly the performances of the system.

In order to confirm these observations, we now look at the pulse spreading in a 1.2 km long step index fiber, with a small amount of mode coupling, excited by a Ga As laser. The pulses are detected by a high speed avalanche photodiode and observed on a sampling oscilloscope ; the measured FWHM of the output pulse of a 2 meter long fiber (response of the measurement system) beeing 300 ps.

We use two different launching conditions, either a low order modes excitation by just focusing the laser beam onto the input plane of the fiber or an all modes excitation by pressing the first 20 cm of fiber between sandpaper and elastomer. The 2 mm/42 mm gratings and the glass hemisphere are disposed 1 meter after the input end of the fiber. Figure 8 (a) shows the output pulse with the low order modes excitation and no deformation, and the FWHM is 13 ns. Figure 8 (b) shows the output pulse with the same launching conditions and the maximum deformation of the fiber, and the FWHM is increased to 18.5 ns. Figures 8 (c) and 8 (d) show the output pulses with the all modes excitation and no deformation or the maximum deformation respectively : the FWHM changes from 17 ns to 19 ns.

We can deduce from these measurements that the frequency response of a link with an L.E.D. excitation (all modes) will not be affected by the presence of couplers, but that with a Ga As laser, there might be an alteration of the frequency response when introducing the first coupler. It is also likely that introducing more and more couplers in a link will increase the apparent mode coupling coefficient of the fiber and thus increase the bandwidth once a sufficient number of couplers are used.

3.5. Performances of the coupler

Having determined all the important features which concern the action of this coupler, we have now to look at the coupling efficiency. For this purpose, we have made several experiments : we use the 2 mm/42 mm gratings followed by a glass hemisphere and a mirror plate. A large area photodetector is disposed at port 3, in order to measure the amount of derivated power. It should be noticed that this arrangement is not optimised, because the gratings and the glass hemisphere are separated by several centimeters along which the fiber radiates a significant amount of the light coupled to radiation modes.

The first measurement is carried out with a 2 meter long step index fiber excited by the He Ne laser with or without the sandpaper. Figure 9 shows the transmitted power $P_2/(P_2^\circ + P_3^\circ)$ and the derivated power $P_3/(P_2^\circ + P_3^\circ)$ as a function of the amplitude of the deformation d for both low order and all modes excitations.

Several observations are made :

(i) with the low order modes excitation, it is possible to extract up to 70 % of the power travelling in the fiber, while this value is only 55 % with the all modes excitation. The corresponding values of the transmitted power are 7 % and 25 % respectively, about 20 % of the total power being lost.

(ii) a -10 dB coupler can be achieved with an insertion loss of 1.1 dB for the low order modes excitation and of 0.55 dB for the all modes excitation, while the theoretical limit of the insertion loss is 0.46 dB for a -10 dB coupler.

(iii) an equal power coupler can be achieved with 40 % or 42 % of the total power, at each port, for the low order and the all modes excitation, respectively.

The efficiency of this coupler is thus very good, and the amount of derivation can be varied in a great range without important losses.

Another experiment has been carried out, using a 2 meter long graded index CGW fiber, with the same coupler and a low order modes excitation. The results are presented on figure 10 and show that the -10 dB coupler is achieved with an insertion loss of 0.55 dB and an equal power coupler with 42 % of the total power, at each port. These results are very similar to those obtained with a step index fiber and indicate that such a coupler can also be used with graded index fibers.

In order to get an evaluation of the directivity of this coupler, we return to the step index fiber and launch the light through port 2, towards port 1. With the maximum deformation applied to the fiber, the ratio of the power detected at port 3 to the power launched at port 2 is -24 dB, showing that the power detected at port 3 is only function of the power propagating from port 1 towards port 2.

In that sense, this coupler has a strong directivity but it should be noticed that in practical systems, the power propagating in both directions are similarly affected by the presence of the grating, an important length of fiber allowing the leaky and radiation modes to disappear. The directivity is bidirectionnal because it is clear that a higher index medium can be disposed on both sides of the grating.

4. CONCLUSION

We have examined here the optimisation and the performances of a coupler based on deformations induced in the fiber.

An optimum mechanical wavelength, independent of the light wavelength and of the launching conditions, has been found and it has been seen that the length of the deformation has little effect in the range 1 to 5 cm.

The light emitted by the fiber at the tap can be easily focused onto a photodetector and a definitive coupler can be molded in clear epoxy resin in order to enhance the efficiency of the device.

The influence of the coupler on the transmission characteristics of a practical L.E.D. step index fiber system is negligible and successive couplers will be independent one from the others. The performances (derivation ratio, insertion loss) of the coupler are very good and will probably improve in the definitive version of the coupler.

This work is carried out with the financial assistance of Délégation Générale à la Recherche Scientifique et Technique.

REFERENCES

FUJITA, H., SUZAKI, Y. and TACHIBANA, A., 1976, "Optical fiber wave splitting coupler", Appl. Opt. 15, p 2031

GLOGE, D. and MARCATILI, E.A.J., 1973 "Multimode theory of graded core fibers", Bell Syst. Tech. J. 52, p 1563

JEUNHOMME, L. and POCHOLLE, J.P., 1976, "Directional coupler for multimode optical fibers", Appl. Phys. Lett. 29, p 485

MARCUSE, D., 1973 "Coupled mode theory of round optical fibers", Bell Syst. Tech. J., 52, p 817

OLSHANSKY, R., 1975, "Mode coupling effects in graded index optical fibers", Appl. Opt. 14, p 935

OZEKI, T. and KAWASAKI, B.S., 1976, "Optical directional coupler using tapered sections in multimode fibers", Appl. Phys. Lett. 28, p 528

PAN, J.J., 1976, "Fiber optic directional coupler", Conference on laser and electrooptical systems, San Diego, paper THE 3.

STEWART, W.J., 1975, "Mode conversion due to periodic distortions of the fibre axis", IEEE Conference on Optical Fibre Communications, London, p 19

SUZUKI, Y. and KASHIWAGI, H., 1976, "Concentrated type directional coupler for optical fibers", Appl. Opt. 15, p 2032

WITTE, H.H., 1976, "Optical tapping element for multimode fibers", Opt. Commun. 18, p 559

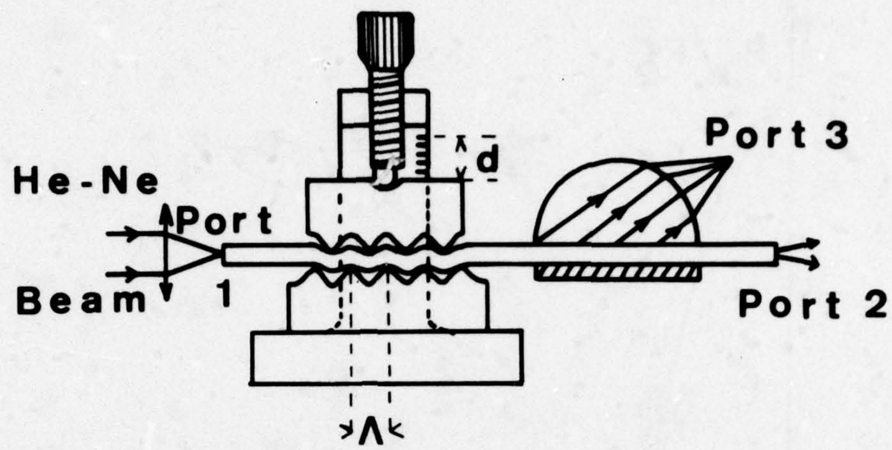

Figure 1 : Schematic diagram of the coupler

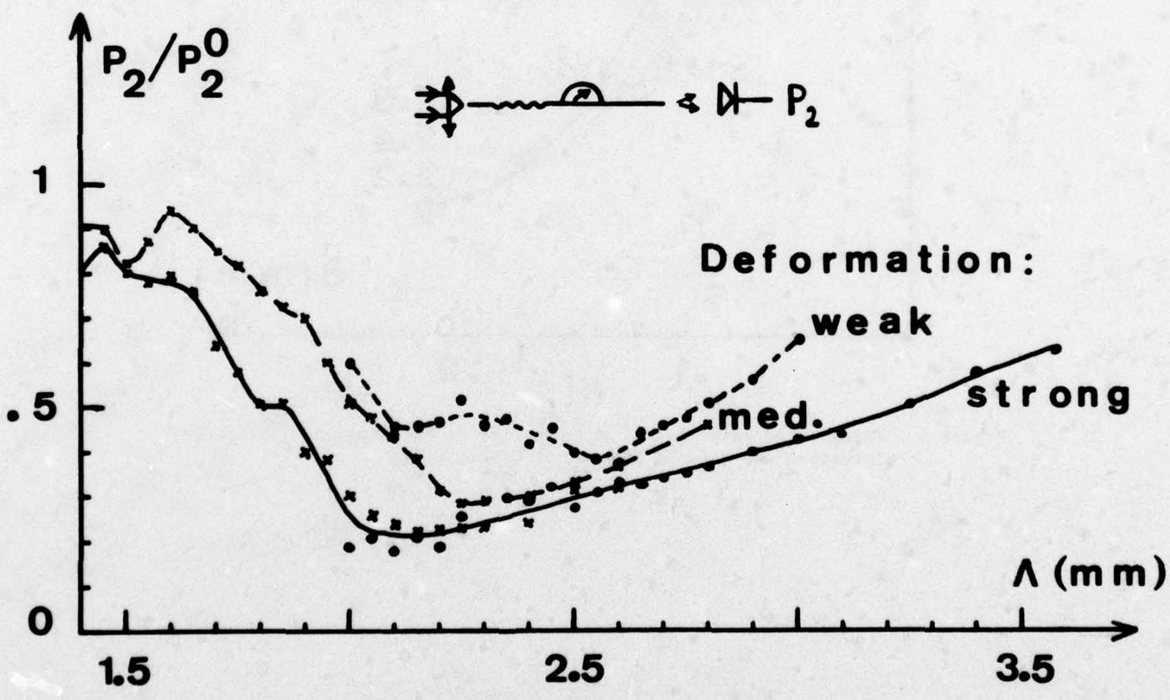

Figure 2 : Transmitted power P_2/P_2° as a function of the mechanical wavelength for different deformation amplitudes

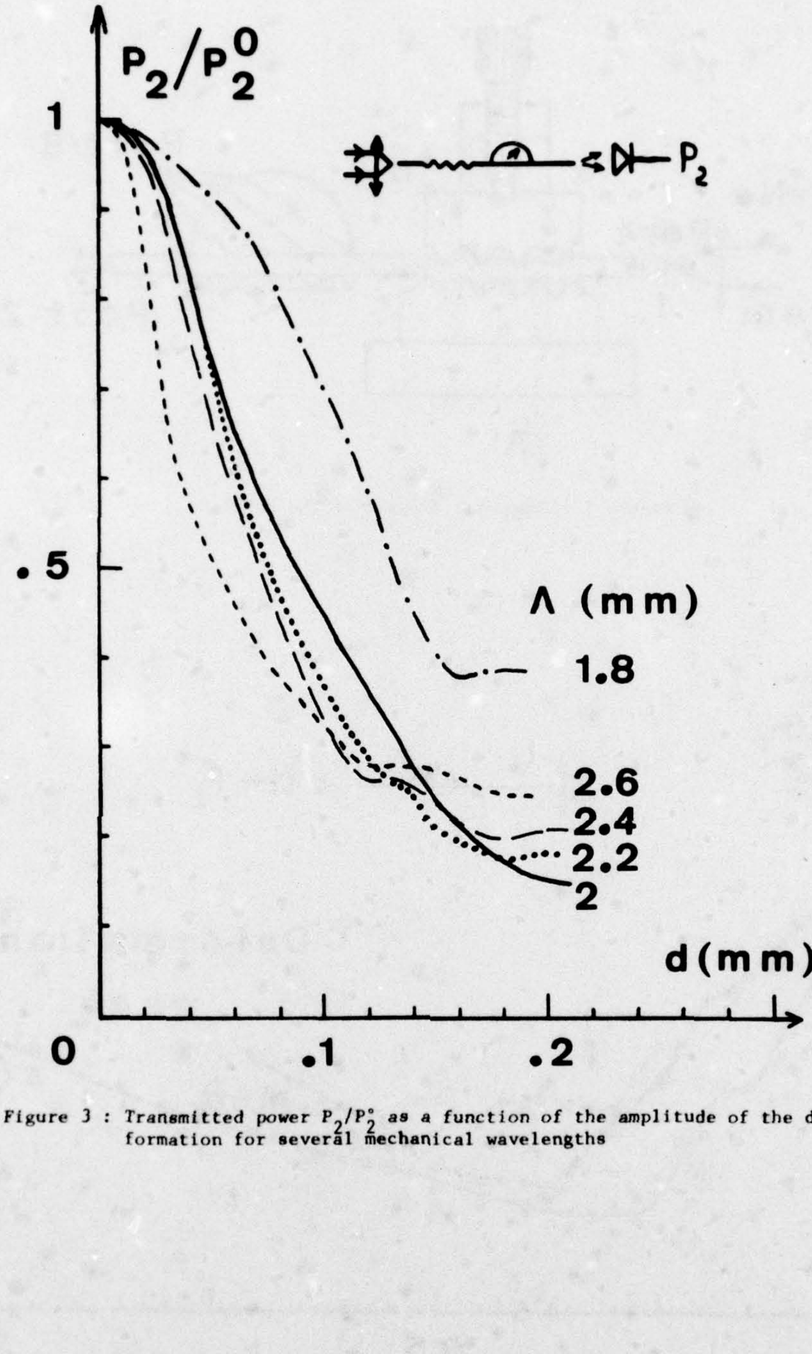

Figure 3 : Transmitted power P_2/P_2° as a function of the amplitude of the deformation for several mechanical wavelengths

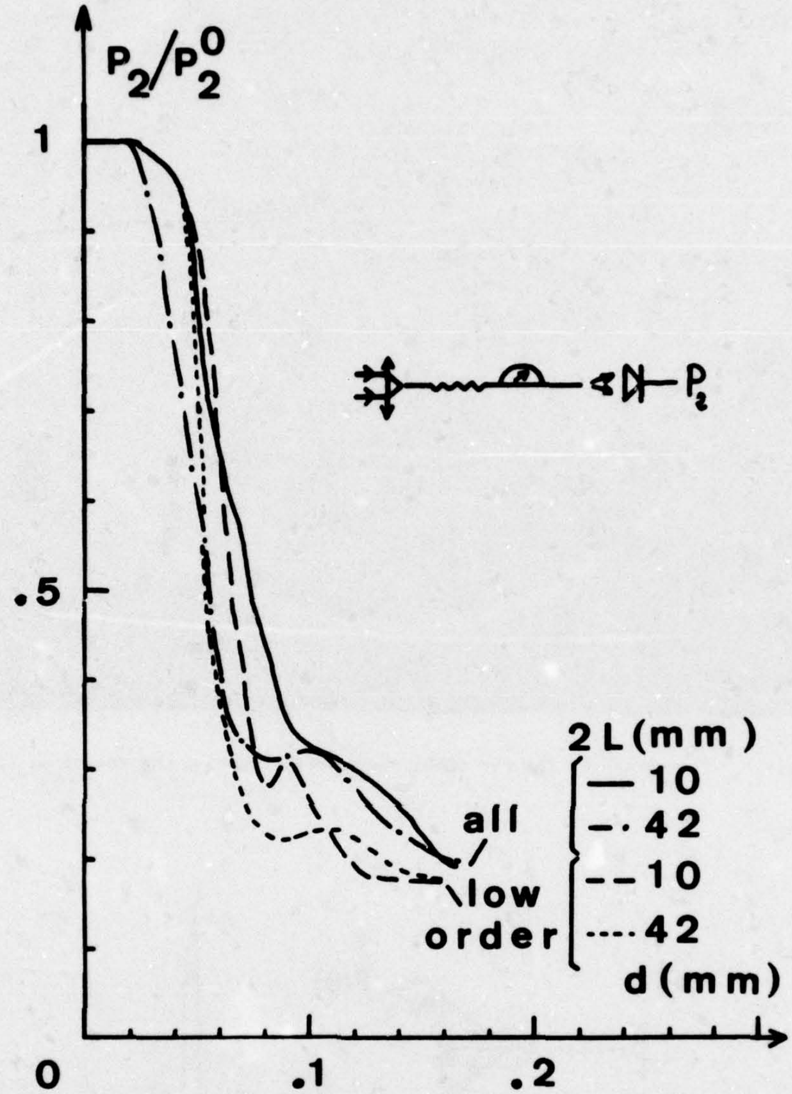

Figure 4 : Transmitted power P_2/P_2° as a function of the amplitude of the deformation for two different grating lengths (2L) and for all-modes and low order modes excitation (= 2 mm)

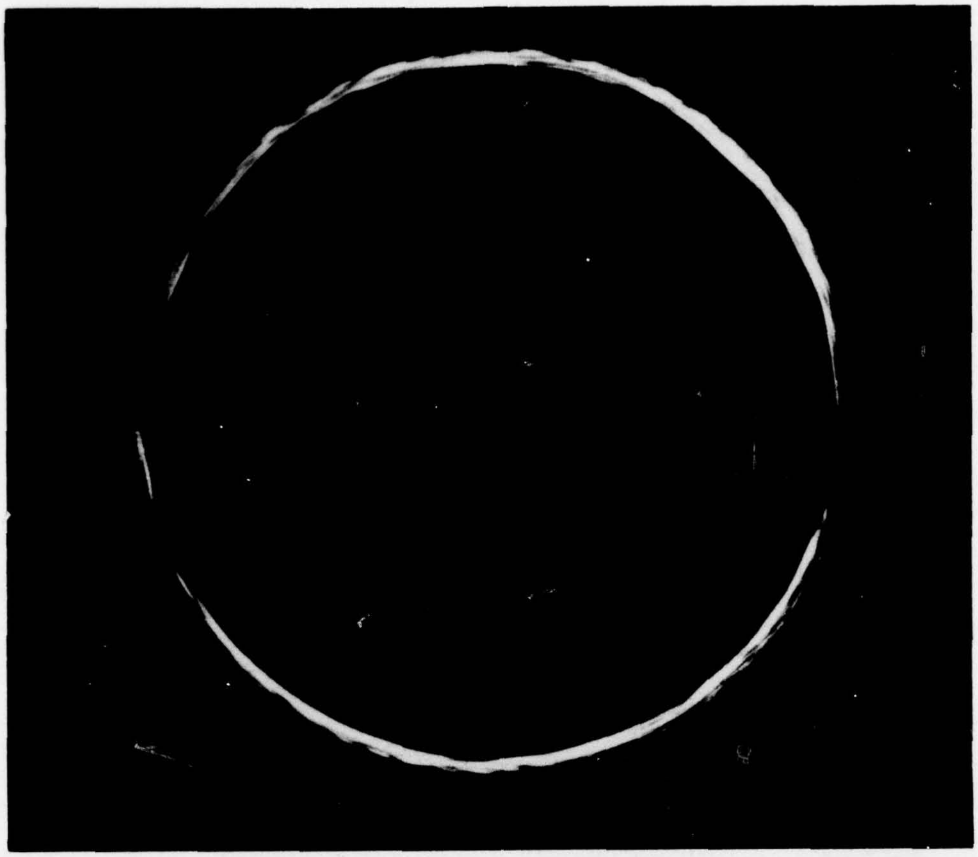

Figure 5 : Photograph of tne far field radiation pattern of the derivated light

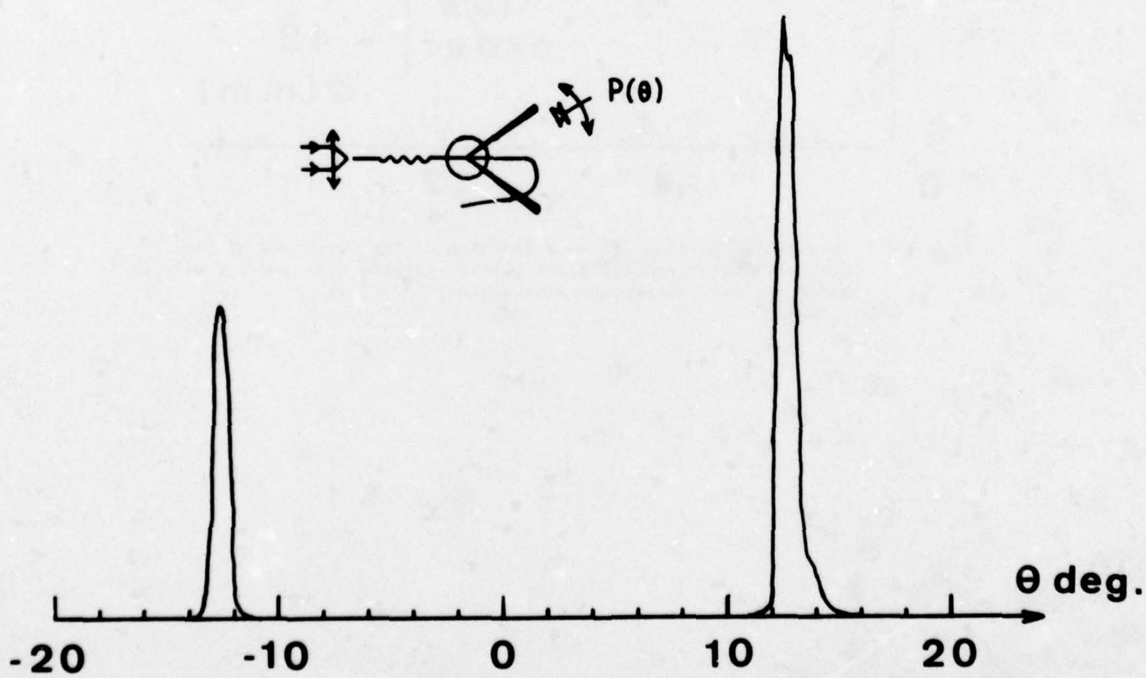

Figure 6 : Radiation pattern of the derivated light, emitted from one point of the fiber

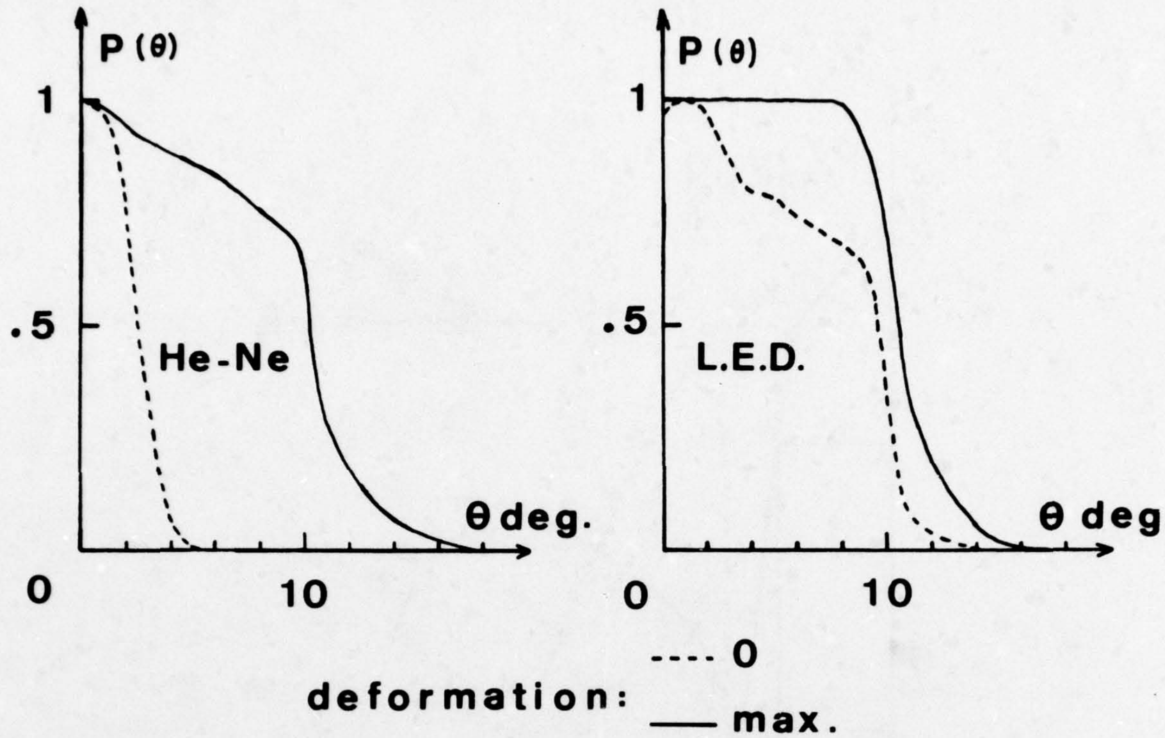

Figure 7 : Far field radiation pattern at the output of the fiber with different light sources and different deformations.

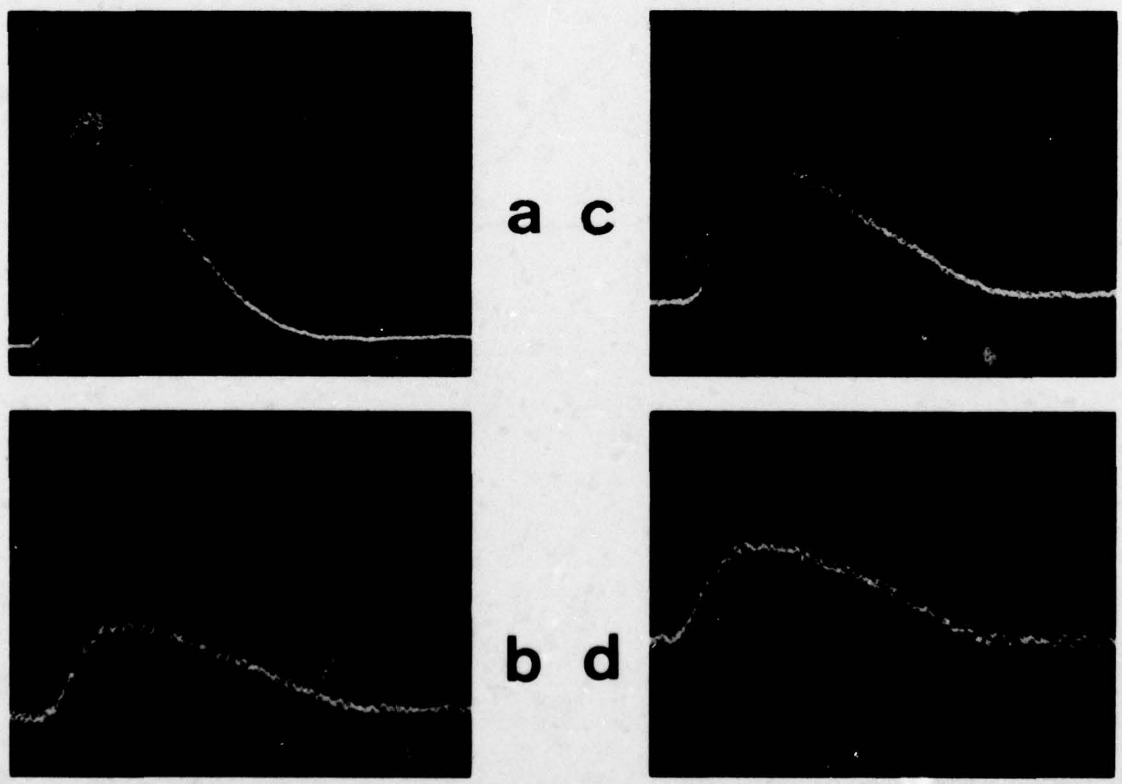

Figure 8 : Output pulse of a 1.2 km long step index fiber with a Ga As laser (a) low order modes, no deformation ; (b) low order modes, strong deformation ; (c) all modes, no deformation ; (d) all modes, strong deformation. (Vertical scales are different)

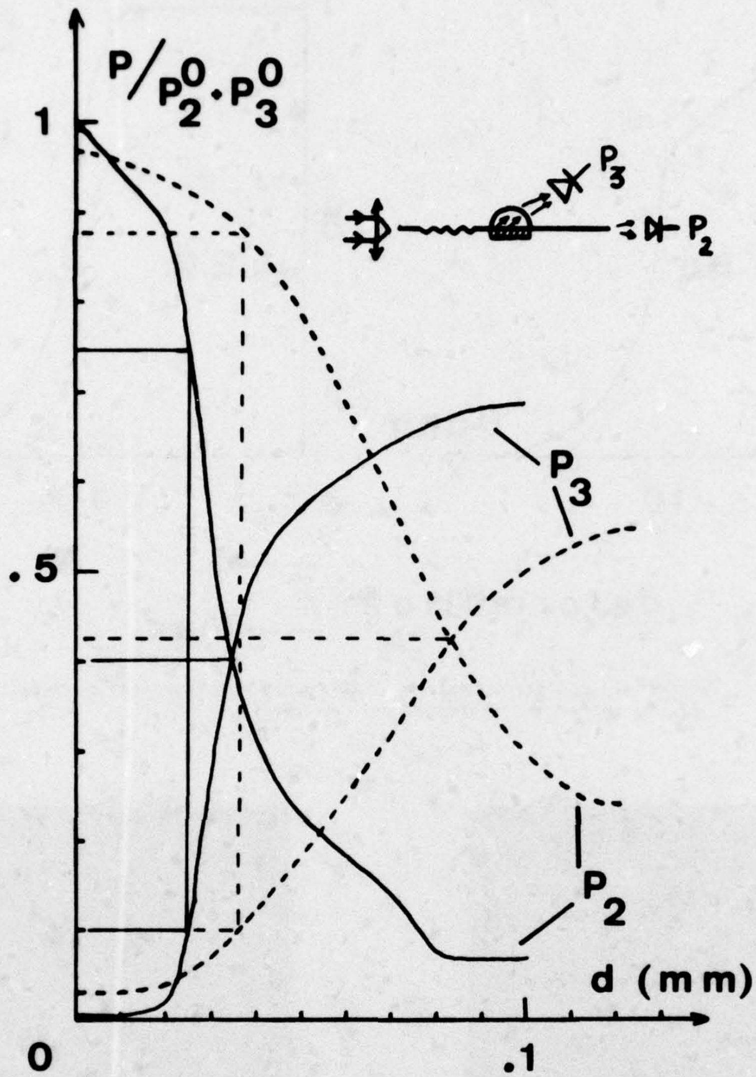

Figure 9 : Transmitted and derivated power as a function of the deformation for low order modes (-) and all modes excitation (----)

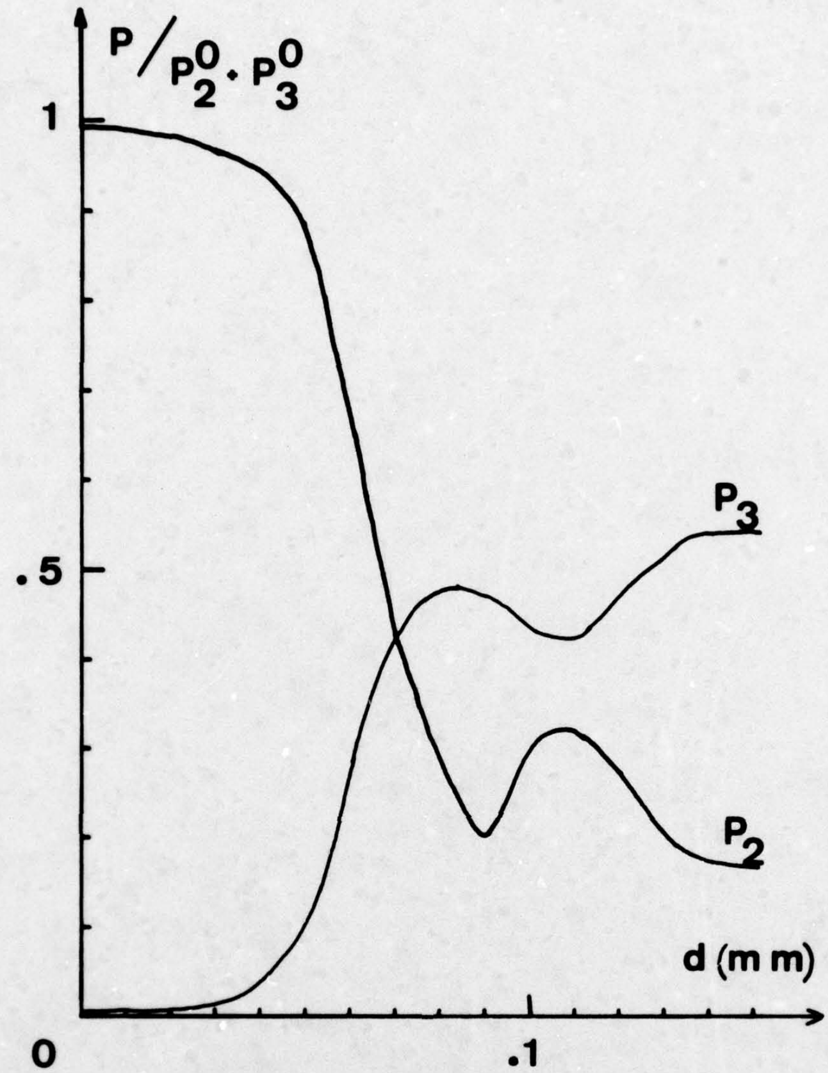

Figure 10 : Transmitted power and derivated power as a function of the deformation for a graded index fiber.

DATA BUS SYSTEM WITH SINGLE MULTIMODE FIBERS

F. Auracher, H.-H. Witte
SIEMENS AG
Research Laboratories
D-8000 Munich 70
Germany

SUMMARY

We report on the concept of a single fiber data bus-system in T-structure based on a new access coupler which is easy to fabricate and has a low insertion loss. We also calculate the maximum possible number of terminals that can be supplied with an optimized system.

1. INTRODUCTION

Fiber optics technology offers much promise for data communication systems. Advantages of optical fibers over conventional transmission lines are lack of electromagnetic interference and ground loop problems, high bandwidth as well as flexibility, small size and weight. Special requirements of military data transmission lines are often small volume and weight, flexibility and electromagnetic isolation of the terminals. Lately the concept of the data bus system, where many spatially distributed terminals are served with the same multiplexed signal, has become very important. The two principal approaches to optical data bus systems are the Star- and the T-system using fiber bundles containing a large number of fibers for data transmission (Andrews, R.A. et al., 1973; Hudson, U.C. et al., 1974; Taylor, H.F. et al., 1975; Milton, A.F. et al., 1976). Such fiber bundles require great fiber lengths and are rather stiff. In addition, scrambler rods (mixers) are needed as part of the coupler. The coupling losses at the interface bundle-mixer rod and also in the fiber bundle connectors are very high. In the star system only a single mixer is necessary, so that the associated loss is by far not as high as in the T-system, where each of the terminals requires mixers and where all insertion losses add up along the transmission line for the worst case signal path. Another practically unsolved problem is the fabrication of connectors (splices) which ensure the alignment of the individual fibers of the fiber bundle.

We propose a data bus T-system with a single multimode fiber as a transmission line. Such a system does not require mixers and there are also low-loss connectors available. Fig. 1 shows an unidirectional data bus T-system (a second identical system would be necessary for the opposite signal direction). We also describe a new coupler suitable for single-fiber data bus systems. This access coupler has comparatively low insertion loss and is very easy to fabricate. Fig. 2 shows a schematic drawing of our new access coupler. In the access coupler fibers 1 and 2 of the main transmission line are butt joined with a small lateral off-set. Light can be coupled out or in at the butt joint via the curved waveguides 3' and 4', respectively. The insertion loss and the out (in) coupling efficiencies depend, of course, on the lateral off-set of the main fibers as well as on the thickness of the fiber cladding.

With a fiber of 100 µm o.d. and 5 µm cladding thickness we have actually measured an insertion loss of about 25 % to 30 % (1-1,5 dB) with a lateral off-set of 15 µm to 20 µm which is within a few percent of the theoretical value (Witte, H.-H., 1976). Typical fractions of the power coupled out for this range of lateral off-set were of the order of several percent.

The fabrication of our coupler is very simple, it is based on a thick-film planar technology using a standard photolithographic process (Auracher, F., 1976). Fig. 3 briefly shows the fabrication steps. A sheet of light sensitive material of about the thickness of the fiber is laminated onto a fused quartz substrate; then it is exposed through a suitable mask and developed thereafter. Thus we obtain in a single photolithographic step the alignment grooves of the fibers as well as the plastic waveguides. Moreover, the planar process assures the required reproducible tight alignment tolerances. Fig. 4 shows a fabricated device (in this particular device no in-coupling waveguide 4' was provided).

In order to find out the limitations of a data bus system based on our access coupler we have calculated the number of terminals N for different values of light power coupled into the fiber and for different sensitivity limits of photo-detectors. We give the results for the case of an optimized data-bus system where the coupling factors of the T-couplers vary along the main trunk line and for comparison, also for a T-bus system consisting of identical T-couplers. If the mode spectra of fibers 1 and 4 and waveguides 3' and 4' (see Fig. 2) are identical, then the efficiencies for coupling out and coupling in are identical, too, because of reciprocity. Assuming that waveguides 3' and 4' have a thickness equal to the core diameter plus one cladding thickness and that they have a single curved boundary which is perpendicular to the substrate surface we find for the transmission from waveguide 1 to waveguide 2 in %

$$\tilde{T}_{12} = 100\,\frac{\frac{\pi}{180}\beta - \sin\beta}{\pi}\,,\qquad \text{where}$$

β=2 arccos $\varepsilon/(2r_c)$, with ε being the lateral off-set of the main fibers 1 and 2 and r_c the core radius. Similarly, we find for the transmission from waveguide 1 to 3' in %

$$\tilde{T}_{13'} = 100\,\frac{\frac{\pi}{180}\alpha - \sin\alpha}{\pi}\,,\qquad \text{where}$$

α=2 arccos$((r_c - W)/r_c)$ and $W = \varepsilon - \delta$, with δ being the thickness of the cladding (see Fig. 2). In Fig. 5 we show as an example the calculated values of $\tilde{T}_{12}$, $\tilde{T}_{13'}$, and the total loss L defined by L = 1-($\tilde{T}_{12} + \tilde{T}_{13'}$) for r_c = 45 µm as a function of ε. The total transmission $\tilde{T}_{13}$ from waveguide 1 to 3 is lower than the above calculated value for $\tilde{T}_{13'}$, due to absorption, radiation and scattering losses in the curved plastic waveguide 3' (see Fig.2). We have also calculated the radiation losses for our curved single boundary waveguide and found that they should lie below 0,5 dB if $(W_{eff}/R) < 0.006$, where W_{eff} is the effective width of the curved waveguide 3' given by $W_{eff} = R - (R - W)\cos\gamma$, with R being the radius of curvature and γ the maximum ray angle with respect to the fiber axis. There are also additional losses at the butt joint between the fibers and the plastic waveguides. We take these additional losses into account by subtracting a value of 1.6 dB from the transmission in dB $T_{13'} \equiv 10\lg \tilde{T}_{13'}$, i.e. $T_{13} = T_{13'} - 1.6$ dB. Neglecting the transmission losses of the fiber itself (the fiber lengths in data bus systems are usually small and one can use low-loss fibers in single fiber data-bus systems) we can calculate now the optimized parameters for the data bus system shown in Fig. 1. For ease of calculation we introduce the following normalized variables:

- P_S : source-power level coupled into fiber in dBm
- P_{min}: minimum required power level at detector in dBm
- $P^{(n)}$: power level in main line between coupler (n-1) and n in dBm
- $P_D^{(n)}$: power level delivered to detector n in dBm
- $T_T^{(n)} = P^{(n+1)} - P^{(n)}$, which includes twice the connector loss L_c = 0.2 dB each, i.e. $T_T^{(n)} = T_{12}^{(n)} - 2L_c$
- $T_{out}^{(n)} = T_{in}^{(n)} = P_D^{(n)} - P^{(n)}$, which includes again twice the connector loss L_c = 0.2 dB, i.e. $T_{out}^{(n)} = T_{in}^{(n)} = T_{13}^{(n)} - 2L_c$

Starting with the last element in the direction of the signal flow we require (Fig. 1) $P_D^{(n)} = P_{min}$. We find from Fig. 1

$$P^{(n)} = P_{min} + L_c \tag{1}$$

Going back from the last element we find with the above definitions

$$P^{(n)} = P^{(n+1)} - T_T^{(n)} \tag{2}$$

Requiring again that the nth detector also obtains at least P_{min} for all signal sources lying to the left of the nth element, we find from Fig. 1

$$T_{out}^{(n)} = P_{min} - P^{(n)} \tag{3}$$

From (2) and (3) we obtain

$$T_{out}^{(n)} = P_{min} + T_T^{(n)} - P^{(n+1)} \tag{4}$$

Replacing n by (n+1) in (3) we can rewrite (4)

$$T_{out}^{(n)} - T_T^{(n)} = T_{out}^{(n+1)} \tag{5}$$

where $$T_{out}^{(N+1)} = 0$$

With the aid of the equation (3) and (1) the initial value $T_{out}^{(N)} = -L_c$ follows. Thus we can successively determine from (5) $T_{out}^{(n)} - T_T^{(n)}$. Having calculated $T_T^{(n)}$ as a function of $T_{out}^{(n)}$ for our element we can determine $T_{out}^{(n)}$ and $T_T^{(n)}$ uniquely. As we move to the left in Fig. 1 we find ever smaller values for $T_{out}^{(n)}$. This means the required off-set of the main fibers becomes smaller for decreasing n and consequently the transmission $T_T^{(n)}$ of the coupler higher. Because $T_{in}^{(n)} = T_{out}^{(n)}$ this implies also ever smaller values for $T_{in}^{(n)}$, i.e. an ever smaller part of the source power P_S is coupled into the main line for decreasing n. The above shown recursive calculation (eq. 5) can therefore only be continued until the power level $P_S + T_{in}^{(n)}$ coupled into the main line from the nth source becomes smaller than $P^{(n)} + T_T^{(n)}$ coming from the left. From this point on we have to replace (3) by

$$P_s + T_{in}^{(n)} = P^{(n+1)}$$

and $T_{in}^{(n)}$ ($T_{out}^{(n)}$) increases then for decreasing n. One can then show that $T_{out}^{(N-n)} = T_{out}^{(n+1)}$ and, consequently, also $T_T^{(N-n)} = T_T^{(n+1)}$ i.e. all elements are symmetric with respect to the above mentioned point. In order to limit variations of $T_{out}^{(n)}$ due to manufacturing tolerances in ε to reasonable values (we can guarantee a reproducible off-set to within ± 1 µm at best), we restricted the excited width of the curved plastic waveguide to $W \geq 4$ µm.

A typical result of our calculations is shown in Fig. 6 assuming r_c = 45 µm and a cladding thickness δ of 5 µm. The figure shows the required off-set ε as a function of the terminal-address number n for various combinations of input power and detector sensitivity. To obtain the maximum possible number of terminals that can be supplied in the data bus system one has to add 1 to the highest address number in Fig. 6 for the particular input power chosen. One can see that ε varies rapidly for the first and last few elements in the data-bus system whereas it is limited to 9 µm (W=4 µm) for all terminals that lie about halfway along the main transmission line. It is only necessary to optimize the first and last 3-5 couplers, all the other couplers can be made identical without decreasing the maximum number of terminals considerably. This is very important because one of the main advantages of a data-bus system in T-structure, namely the ease with which an existing T-system can be expanded, depends heavily on the use of many identical couplers.

In Fig. 7 we show the maximum number of terminals as a function of the available difference in power level between source and detector, $P_s - P_{min}$, for three different thicknesses δ of the cladding for an optimized system (full lines). For comparison we also show in Fig. 7 the maximum number of terminals for the same parameters when only identical couplers are used exclusively (dashed lines). One can see the considerable increase in the number of terminals in the case of the optimized system as compared to a system with identical T-couplers.

We have shown that with an optimized T-bus system based on a new planar coupler and a single multimode fiber for each signal direction one can supply a reasonable number of terminals. Moreover, one could install several such systems in parallel increasing the number of terminals and the safety against failure due to a cable fracture, especially when the individual cables are guided along different cable ducts and are only combined at the terminals.

This work has been supported under the Technological Program of the Federal Department of Research and Technology of the FRG. The authors alone are responsible for the contents.

References

ANDREWS, R.A.; MILTON, F.; GIALLORENZI, 1973, "Military Applications of Fiber Optics and Integrated Optics", IEEE Trans. on Microwave Theory and Techniques, Vol. MTT-21, No. 21, 763-769

HUDSON, U.C.; THIEL, F.L., 1974, "The star coupler: A unique interconnection component for multimode optical waveguide communication systems", Appl. Opt. 13, 2540-2545

TAYLOR, H.F.; CATON, W.M.; LEWIS, A.L., 1975, "Data Busing with Fiber Optics", Nav. Res. Rev. 28, 12-15

MILTON, A.F.; LEE, A.B., 1976, "Optical access couplers and a comparison of multiterminal fiber communication systems", Appl. Opt., Vol. 15, No. 1, 244-255

WITTE, H.-H., 1976, "Optical Tapping Element for Multimode Fibers", Opt. Commun., Vol. 18, No. 4, 559-562

AURACHER, F., 1976, "Planar Branching Network for Multimode Glass Fibers", Opt. Commun., Vol. 17, No. 1, 129-132

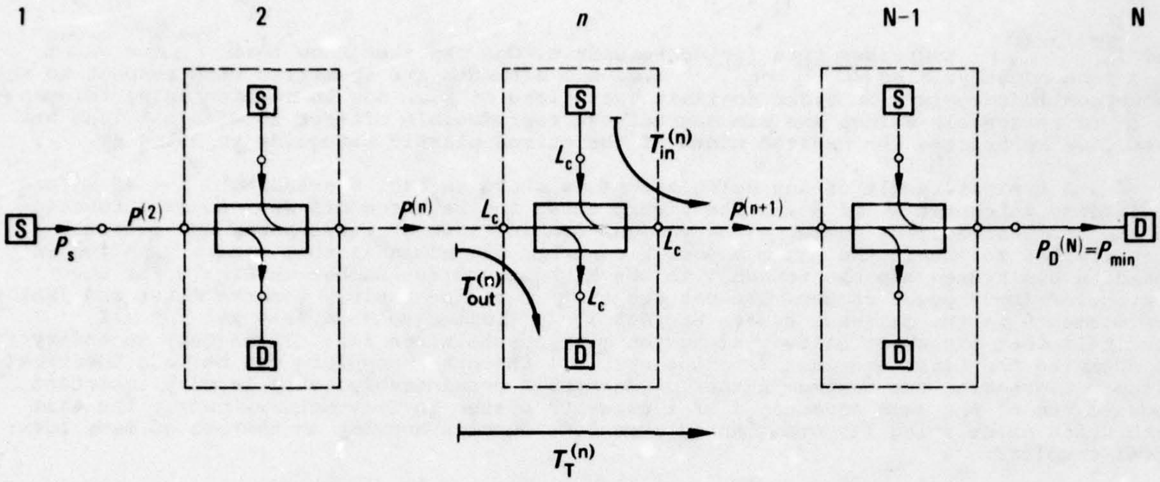

Fig. 1 Unidirectional data bus T-system.

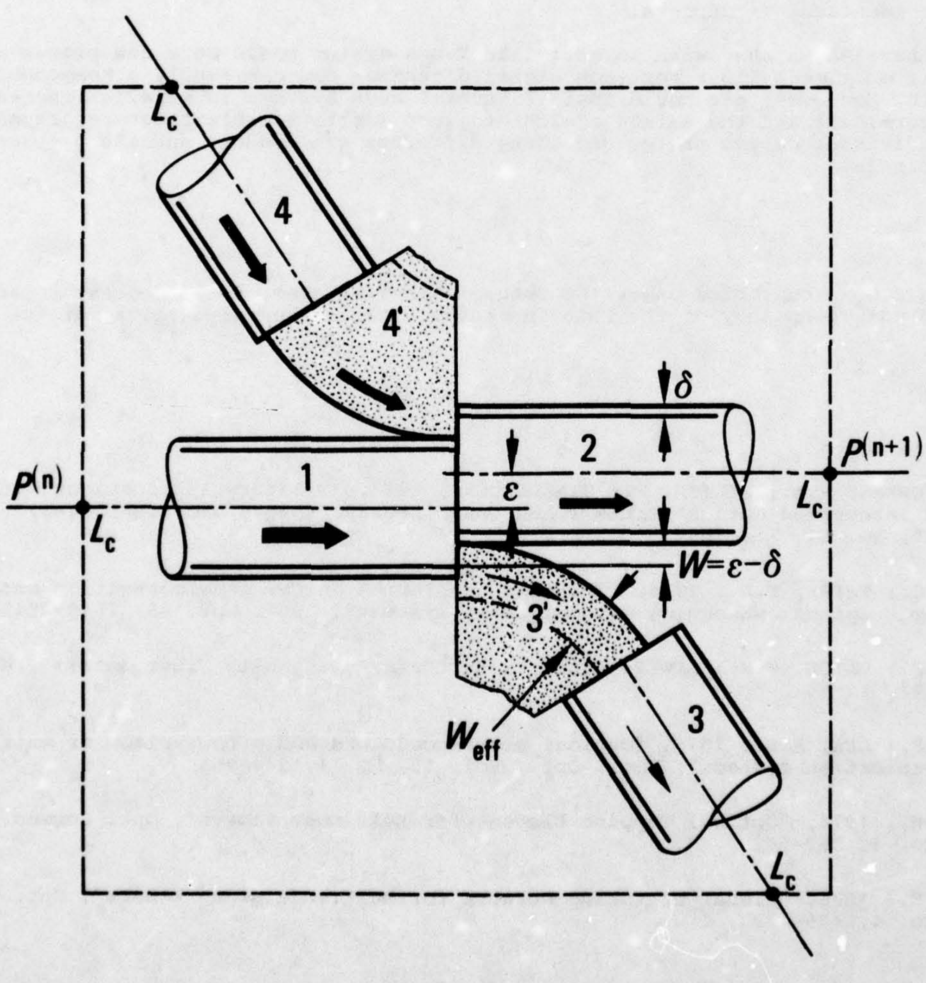

Fig. 2 Schematic of the nth coupling element.
L_c: connector loss; ε: lateral off-set of the main trunk fibers 1 and 2; δ : thickness of the fiber cladding; W_{eff} : effective width of the single boundary-curved waveguide 3'.

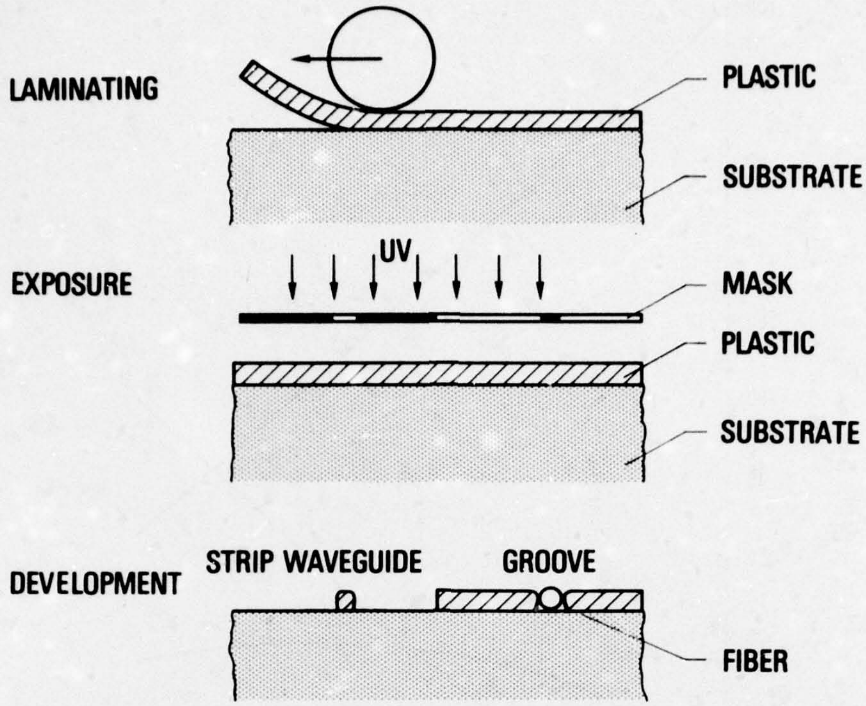

Fig. 3 Processing steps for fabricating the structures in the light sensitive material.

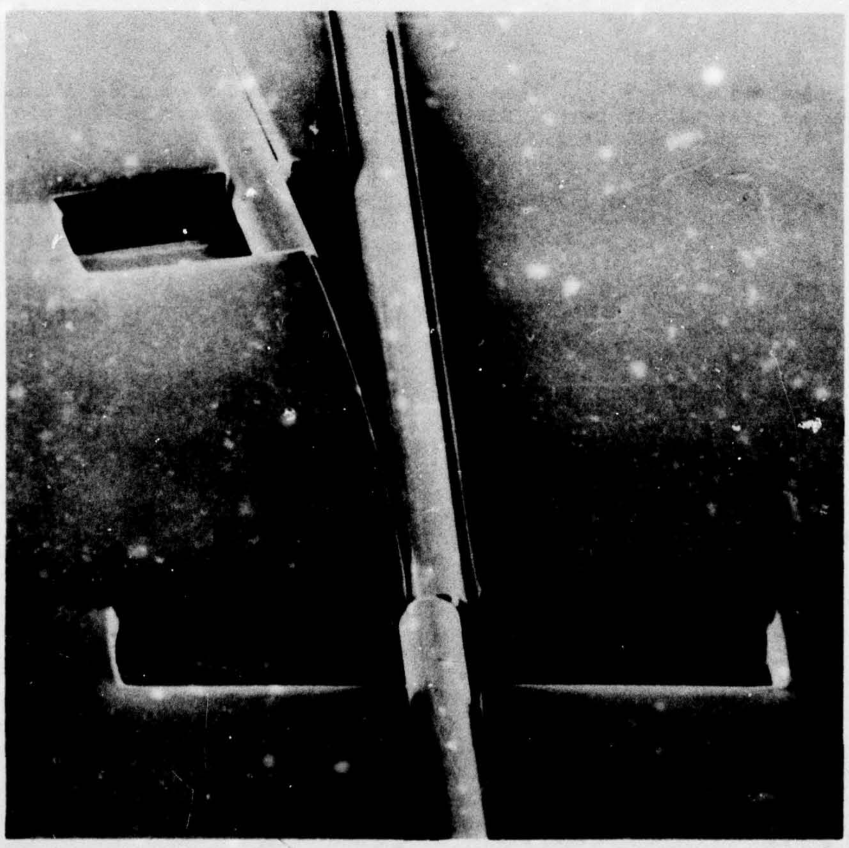

Fig. 4 SEM picture of the tapping element with two main trunk fibers, and curved single-boundary plastic waveguide between the butt joint of the main fibers and the output fiber.

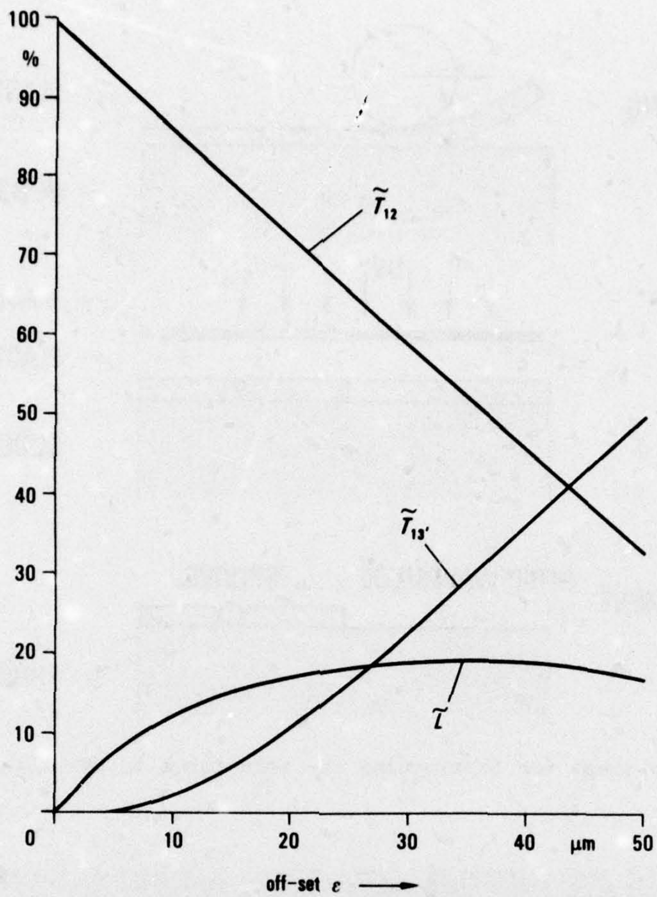

Fig. 5 Transmissions $\tilde{T}_{12}$, $\tilde{T}_{13'}$ from fiber 1 to fiber 2, waveguide 3', respectively, versus lateral off-set ε for a fiber with an outer diameter of 100 μm and a cladding thickness of 5 μm. $\tilde{L}$: total loss of the coupler at the butt joint.

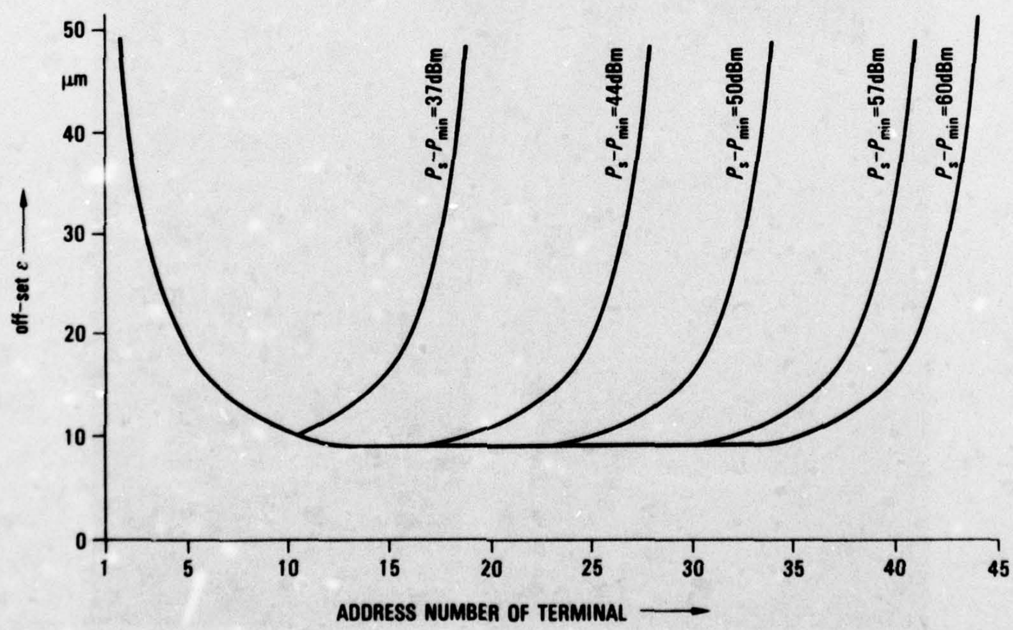

Fig. 6 Required off-set ε for the couplers in an optimized data T-bus system as a function of the address number n and for various power level differences $P_s - P_{min}$. Assumed thickness of fiber cladding δ = 5 μm.

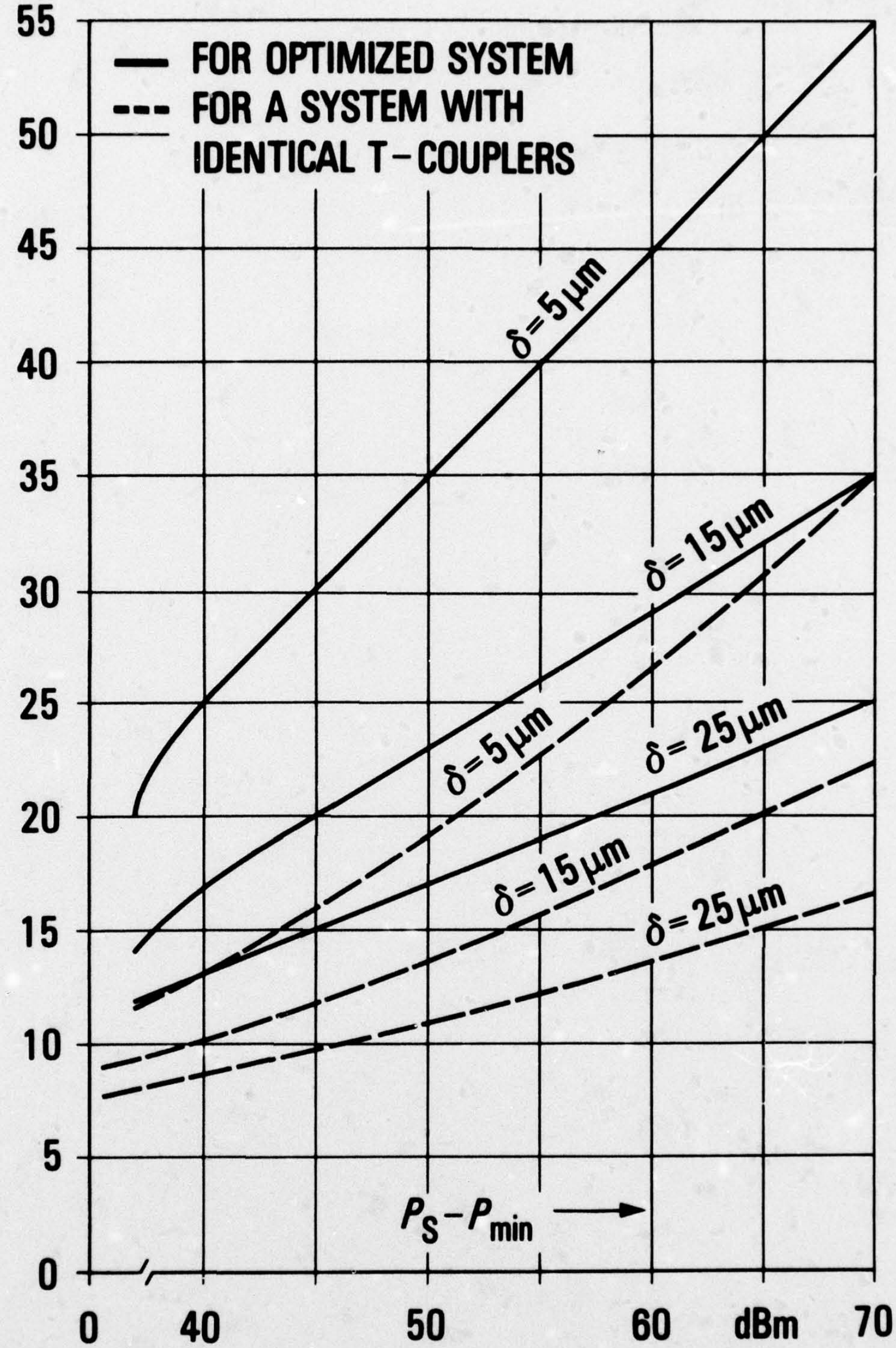

Fig. 7 Maximum number of terminals as a function of the difference between the source power level coupled into the fiber and the detector sensitivity limit $P_s - P_{min}$ for three different thicknesses of the cladding.
Full lines: for optimized system.
Dashed lines: for a system with identical T-couplers.

AN OPTICAL FIBRE, MULTI-TERMINAL DATA SYSTEM FOR AIRCRAFT

J.G. Farrington
M. Chown

Standard Telecommunication Laboratories Limited
London Road, Harlow, Essex, CM17 9NA, England

SUMMARY

As a result of a study on the potential of optical fibre multi-terminal data systems for avionics, a design approach has been chosen which is expected to be a suitable basis for a wide range of applications. This is a time division multiplexing system, which has features of being highly immune to problems of optical loss and multipath effects in optical highways having redundant paths, and of avoiding the need for any master terminal. This system approach is taylored to characteristics of optical fibres, and should lead to good integrity and ruggedness.

A breadboard model of a terminal has been demonstrated, and the construction of functional models is currently underway.

1. INTRODUCTION

It is becoming widely accepted that optical fibre data transmission will find applications in avionics because of its electrical isolation, wide bandwidth and immunity to crosstalk and RFI. The principle has already been proved and advantages demonstrated for avionics applications in point-to-point links, much of this preliminary work having been carried out with fibre bundles. (Belcher, G., Marshall, D., 1975) (Biard, J.R., 1975).

There are even more potential advantages for multi-terminal optical highway or data bus systems, since the problems for a corresponding electrical system would be greater than for point-to-point links. (Altman, D.E., 1975).

A study on optical fibre multi-terminal systems for avionic applications is currently underway at STL (Farrington, J.G., Chown, M., Dalgoutte, D.G. 1976), and is supported by DRASA (MoD). One aim of the study is to produce an initial demonstration (functional model) of a system based on principles which may be expected to have wide avionic applications. This paper describes design principles of the demonstration system which is currently under construction.

The extreme complexity and variety of avionic data links is making it necessary for the industry to undertake long-term rationalization programmes. These should help clarify and perhaps standardize requirements for data bus systems (electrical or optical). In the meantime, there is no clear choice of requirement specifications against which a demonstration optical bus system should be designed. Whereas there are immediate applications for optical point-to-point links to replace existing electrical links, there is currently little use of electrical highways in avionics, so there are no immediate requirements for replacing wire systems by multi-terminal optical systems.

In the longer term, there appears to be definite and widespread applications for optical highways. For example, telemetry, display systems, or stores management could be suitable choices for first applications. The Flight Control system is an example which would have to wait until the high integrity and reliability of fibre systems had been thoroughly proved in practice.

The key optical components - tee pieces, star couplers, etc - are at an early stage of development, so a system cannot be fully optimized in terms of these components.

While it is thus too early to attempt to optimize a multi-terminal system for any particular application, it is nevertheless vital to start experimental work on multi-terminal systems at this stage. This will ensure that the possibilities of the new technology are included in the long-term data management plans. Otherwise, a framework set up on the basis of conventional technology, with fibre systems designed to fit in at a later stage, would fail to make full use of the potential.

The other reason for undertaking immediate experimental work is to help direct the development of key optical components such as tee pieces and star couplers. In addition to using fibre systems to meet conventional requirements more efficiently, there must be new opportunities which would not be considered for electrical systems. Direct optical sensoring, without electrical interfaces, is a possible example.

The system approach to be described in which any number of terminals up to a given maximum (ten in our example) with no requirement for a master terminal, and with great flexibility for the system designer to arrange redundancy, self-checking etc., is likely to be widely applicable. (It can even be used for point-to-point tests, simply by connecting any two terminals). No clear preferred optical highway configuration emerged, and so initial experimental systems should allow this to be flexible.

The system is designed to be compatible not only with a "star" configuration optical harness which is well behaved from the point of view of the terminals, but with almost any complex highway configuration which may have advantages of considerable redundancy and be adaptable to constraints on layout, maintenance etc. Such complex highways may be prone to optical echo pulses and other problems outlined in Section 7 below.

It is important to emphasise that the terminal design outlined here is considerably more complex than is envisaged in a typical system. The reason is that this is an experimental system, not an optimized communication link for a particular application, and many of the facilities can be implemented or switched out at will, in order to gain experience.

2. GENERAL MULTI-TERMINAL DESIGN

The choice of multiplexing technique depends on the capabilities and limitations of the transmission medium, and on the use that is to be made of the entire system. For an optical fibre several alternatives exist and several possible solutions are listed below:

1. Time division multiplexing, TDM, where each transmitter in turn has sole use of the optical highway.
2. Frequency division multiplexing, FDM, where each transmitter uses an optical source, amplitude modulated at a different frequency. This carrier can be amplitude or frequency modulated with information. The total received signal is filtered electrically.

   Pulse frequency modulation is a version of FDM where a train of short pulses is used instead of the carrier signal.
3. Colour multiplexing - each transmitter uses a different wavelength source, and filters at the photodiodes separate the signals.

These solutions fall into two broad groups: a) those that are most suitable for replacing point-to-point links, because they require duplication of receiving and decoding equipment to receive from more than one other terminal and b) those suited to random data interchange between the terminals.

The former group includes all systems except TDM as it will always be necessary to use duplicated receiving equipment if at any one time more than one transmitter can be sending to the same terminal. Of these systems FDM would appear to be most suitable for development using existing components. The technology of FDM is well developed for other fields, e.g. telecommunications, and systems can be made small and reliable.

The wide bandwidths offered by the optical fibre would make them particularly suitable for this type of approach. The independence of the data paths would make this an ideal solution to problems requiring the replacement of many point-to-point links between existing equipment. It should be possible to produce very small, simple terminals for this system as very little circuitry is needed.

Where data transfer is required between any pair of terminals the most suitable choice would seem to be a TDM system with only a single transmitter active at any one time. A single receiver will then be able to receive messages from all other terminals. To select destinations, an address can be included in the message, and the receiver itself can decide whether to accept or reject the message that follows.

It was decided that the latter approach was most suitable for development and so the TDM system will now be discussed in more detail.

3. THE TDM SYSTEM

3.1 Synchronisation.

For a TDM system where only one transmitter is allowed to send information at any one time, the timing arrangements are of crucial importance. The most straightforward timing arrangement is to use a master terminal, where a single master unit has responsibility for absolute timing, and sends whatever information is needed to the other terminals to maintain the synchronisation of the system. In the extreme, the master terminal can make all decisions about timing and send a short message to each terminal in turn to start its transmission. This approach can give a very flexible system, where time can be allocated by the master terminal in a way that varies with the amount of information needing transfer, and this leads to very efficient use of the data bus. Unfortunately this arrangement gives a single vulnerable point in the master terminal where damage or a fault can disrupt the whole system. This situation can be improved by having several terminals, ready to take over from the master if it should fail. This needs a system of priorities to define which terminal will take over first, and involves many problems in deciding whether the first unit has failed or not. To avoid this situation it is preferable that there should be no master terminal, and to achieve this each terminal must do its own timing and some means must be found to keep all the terminals in synchronism. One possible means of achieving this is described in Section 4 of this paper.

One consequence of this is that the data transmission capacity of the terminals must be predetermined, and cannot easily be changed to meet different network loadings. This approach is acceptable for a fibre optic network as the high bandwidth available means that excess data capacity can be made available at low cost.

3.2 Coding.

The choice of coding in an optical system can considerably effect the rest of the design. For example the choice of a PPM code would enable a low duty cycle optical source to be used, or a code with no low frequency content allows an AC coupled receiver. Because of the rapid changes of signal level expected at a receiver, it is desirable that the chosen code should allow fast AGC to be applied. Another requirements is that the data clock can be easily extracted from the data, preferably without the use of a phase locked loop. This is necessary because each received message will be at a different phase due to the different path lengths involved. A short preamble can be included on each message to allow the receiver decoder to settle down, but if this is too long then the system becomes very inefficient.

The most appropriate code would seem to be bi-phase (Manchester) (see Fig. 1) as this offers several advantages. There is a data transition at the centre of every clock interval which makes clock extraction easy, it only being necessary to time from one cycle to the next with a delay element such as a monostable. The bi-phase code is also arranged to have very little low frequency content, whatever the data being sent. This occurs because the code has a constant average value for ones and noughts. This allows fast AGC and AC coupled receivers to be used.

This code is most ideally suited to bipolar appoications where differential signalling is employed. Unfortunately this is not possible with a single optical fibre, and so a unipolar version must be used. This has the disadvantage of needing a threshold shift if the signal strength changes, also shown in Fig. 1, and ways of overcoming this difficulty will be discussed in Section 4.

4. THE ADOPTED SYSTEM DESIGN

4.1 General Principle.

A time division multiplex approach has been chosen where each transmitter in turn has complete use of the optical highway, for a burst period. See. Fig. 2. It sends a fixed length message in that period, complete with an address code to specify the terminal that is to receive it. The transmitters send in strict rotation, and if a terminal is inoperative, or if no information is available for sending, then that period is either left empty or a dummy message is sent. Each terminal contains its own clock oscillator and divider chain which provides all the timing information within the terminal. These clocks must be kept approximately in step so that the transmission periods do not overlap. This can be achieved if each transmitted message contains the address of the sending terminal. This can be received by all other units and used to correct small timing errors that have developed. Special attention should be given to the problems of synchronisation from switch-on and to the effects of a single faulty terminal.

Bi-phase coding has been adopted as this offers several advantages. With this code there is a data transition at the centre of each clock interval, and the direction of this transition (low to high or high to low) defines whether a 1 or 0 is being sent. (See Fig. 1). The advantages of the code are described in Section 3.2, but briefly it allows the use of an AC coupled receiver, rapid AGC and simple clock extraction circuitry.

4.2 Terminal Design.

The block diagram of a terminal design that is being developed is shown in Fig. 3. It consists of three main sections. The receiver, transmitter and timing.

4.2.1 The Receiver.

The optical signal is detected by a photodiode and the signal is then amplified. For bi-phase signals the amplifier can be AC coupled and limiting, so reducing the amount of AGC necessary in following circuitry. This amplifier can be disabled during the terminals own transmission period if this is desirable. This received signal is decoded from bi-phase and then fed via a serial - parallel converter to two comparators. These act as word recognition circuits and detect the transmitter address and receiver address in the message. These addresses are protected by redundancy so that they are not falsely decoded from data or each other.

When a comparator recognises the terminals own address in the received message the following data is gated into the terminals store for output to the external equipment.

4.2.2 The Transmitter.

Data to be transmitted is clocked to the transmission store by the external equipment. During the transmission burst period, defined by the timing circuit, the data is clocked out of the store, and transmitted as a bi-phase signal at a data rate fixed by the terminal clock. Before the actual data certain service data is inserted into this message. This service data consists of:

1. A preamble to enable the received decoder and AGC to settle.
2. An address code for the transmitting terminal for checking and timing purposes.
3. The address of the terminal to receive the message. This part may be preset, or may be part of the input data.

The optical transmitter must handle the 50% duty cycle bi-phase signal, and so a high duty cycle source must be used.

4.2.3 The Timing Section.

The timing for the terminal is carried out by a crystal clock oscillator and divider chain. The various waveforms needed in the terminal such as the transmission burst period can be derived from this divider chain by simple gating.

Every time a transmitter address is received by the word recognition circuit, this is compared with the divider chain and the difference used to correct errors that may exist due to signal delays or clock oscillator differences.

Large discrepancies may occur at switch-on before all the terminals have reached synchronism or if a terminal develops a fault in its timing system and both of these possibilities should be catered for. To do this a type of majority voting has been used. If large errors are consistently detected between the internal clock and the received transmitter addresses, the terminals transmitter is disabled.

4.3 Dynamic Range.

An important parameter for a receiver in a system such as this, is the dynamic range that can be tolerated from one message to the next.

The received bi-phase signal has a DC component that is proportional to the average received power, and in a simple receiver this will be removed by the AC coupling before the signal is passed to the level detector. See Fig. 4. This process will limit the dynamic range as the recovery after a large signal is exponential. The time available for recovery is limited to the intermessage gap and the preamble before each message, and if these are lengthened a greater change in message amplitude can be tolerated. For an intermessage gap of 10 bit periods, a dynamic range of greater than 40 dBs can be expected.

The capacity to tolerate a large dynamic range for received messages would only be needed for certain optical harness configurations. If necessary these configurations could be avoided in practice; however, more flexible and redundant harnesses should be possible if they are allowed.

4.4 Data Input and Output.

Data for transmission is supplied from external equipment and stored in a buffer store until the transmission burst period. Only if there is a complete message in the store is the transmission made. For synchronisation purposes, however, it is still necessary to send the service data, perhaps with a dummy receiver address. The true data section of the message can be left blank.

The receiver address to which data is to be sent may be preset or may be taken as the first word of the input data. This would allow the external equipment to select the destination of the message.

Received data may also be stored in a buffer store to allow the external equipment to take the information whenever it is ready. Unfortunately the terminal has no control over when data is going to be received and so no action can be taken to prevent store overflow. For this reason it may be preferable to output received data as it arrives.

4.5 Fault Protection.

The multi-terminal system as described is very flexible, and various self checking features could be built into the terminals. The timing section as described in Section 4.2.3 ensures that a terminal with a faulty clock divider will shut down its own transmitter as it will continually find large errors between its own clock and the other terminals. This is probably the most serious type of fault that could occur as it might result in transmission at incorrect intervals, so corrupting other terminals data.

Another form of protection is the maximum transmission time limit. The period that the transmitter is active for should never exceed a certain limit. This can be timed independently, and if the limit is exceeded the transmitter can be shut down.

Parity checking is incorporated into the system by inserting one parity bit after every 16 bits of data. This is checked by the receiver so that a message with a parity fault can be rejected.

Message confirmation could be incorporated to provide protection against random errors. This could take the form of an added service data section in which a terminal can acknowledge receipt of messages in the last frame. If receipt was not acknowledged the message could be retransmitted by the sending terminal. A suitable code for this is suggested as a ten bit word (for ten terminals in the system). All bits would normally be zero with one bit in the sequence to represent each terminal. This bit would be one to indicate that a parity correct message had been received from that terminal in the last frame. Alternatively this type of message checking can be built into the external equipment as it may only be required over limited paths.

A more general checking system could consist of a special purpose terminal which monitors all information on the bus. By checking for parity correct messages, and correct transmitter sequence, etc., it should be possible for the monitor to isolate faulty terminals. The monitor could then be given the power to shut down faulty units. If this was implemented, care would have to be taken that the overall reliability was not reduced as faults in the monitor could result in operating terminals being shut down.

4.6 Computer Simulation.

To investigate the behaviour of the system under various start up and fault conditions, a computer simulation has been developed. The simulation works on an event stepping basis, which leads to efficient use of computer time. The simulation program allows the systems behaviour to be predicted starting from any set of initial conditions. It is hoped that by careful choice of initial conditions, worst case situations can be found.

A simple system model has been assumed initially with sufficient flexibility for the simulation of areas of interest to be expanded in more detail in the future. For example, the initial system assumes a simple uni-directional ring harness, with uniform attenuation properties.

5. TRADE-OFFS IN DATA FORMAT PARAMETERS

Consider the data format described above and shown in Fig. 2. The peak bit rate, B_m, which is required to be carried by the optical fibre depends primarily on the mean data rate, $\bar{B}$, per terminal, and on the maximum number of terminals to be accommodated, M. Ideally, $B_m = M\bar{B}$, but in practice B_m will be higher because there are periods where useful data cannot be sent. These consist of the interburst gap periods, and the periods where service data is being sent.

A further increase in B_m will occur when redundancy is built into the message, but this is considered to depend on the user and will not be considered here.

The significance of these periods is clearly reduced as the message length in each burst is increased, but this requires increased data storage capacity, and increases the update period for each terminal.

These trade-offs will be considered in broad outline here. Define:

To	interburst gap period which depends on maximum fibre length
n	number of bits of service data per burst period
N	number of message data per burst period
T	frame period = update period for each terminal

Then, considering the uniform data output of any one terminal:

$$T = N/\bar{B} \qquad \ldots(1)$$

Alternatively, by summing the elements of a frame:

$$T = M \left(\frac{n}{B_m} + \frac{N}{B_m} + To \right) \qquad \ldots(2)$$

Eliminating T, we have

$$\frac{B_m}{\bar{B}M} = \left(\frac{n+N}{N} \right) \cdot \left(\frac{1}{1 - \frac{M}{N} \bar{B}\, To} \right) \qquad \ldots(3)$$

A plot of this function for some typical parameters is shown in Fig. 5.

For the experimental model, we chose N = 128, n = 52, $\bar{B}$ = 100 kbit/s, M = 10 and To = 8 µs.

Equation (3) leads to

$$B_m = 1.406 \times 1.071\ \bar{B}M$$

$$= 1.50\ \bar{B}M$$

$$= 1.50 \text{ Mbit/s.}$$

The factor of 1.071 occurs because To is much larger than it need be in an optimized system. For example, in order to tolerate an optical delay in 200 metres of fibre the gap period need only be 1 µs. and the factor on the RHS of Eqn (3) would only be 1.004. Except for much larger systems than this, or when the burst length N is reduced, this factor can be neglected and Eqn. (3) approximated by

$$\frac{B_m}{\bar{B}M} = \frac{n+N}{N} \qquad \ldots(4)$$

This represents simply the ratio of total to useful message data.

The frame period T is also the update period for each terminal, and represents a message delay between any two terminals. In the experimental model, T = 1.28 ms from Eqn. (1). This can be reduced if a lower value of N is chosen, at the expense of requiring a higher peak bit rate B_m. A reasonable alternative design for M=10 and $\bar{B}$ = 100 kbit/s would be n = 32, N = 16, To = 1 µs, which leads to a frame period of T = 160 µs and peak bit rate of 3.2 $M\bar{B}$ = 3.2 Mbit/s.

6, ELECTRO-OPTIC COMPONENTS

Several types of photodetectors and optical sources are available which are suitable for this application, and the chief advantages and disadvantages of some of these will be discussed here.

6.1 Sources.

The requirement for duty cycles of up to 50% to transmit bi-phase signals means that only a device capable of continuous operation is really suitable. These fall into two major groups: light emitting diodes and CW double heterostructure lasers.

These in general show marked differences in optical power outputs when small core low loss transmission fibres are used. It is normally the case that the greater launched power the higher the loss that can be accepted in the optical highway, and so in general higher powers are preferable.

As well as the power output differences between the LED and the lasers, there are important differences in driving techniques. The laser has a current threshold, below which it only emits a low level of spontaneously generated light. Above threshold the incremental efficiency can be very high and feedback is normally needed to stabilise the operating point.

CW stripe geometry lasers can be damaged by excess light levels, and this means that the peak light output must be closely controlled, even under transient conditions, such as switch-on. This increase in complexity needs to be traded against the improved performance offered by these devices.

6.2 Detectors.

There are two main classes of solid state photodetector currently available: the PIN photodiode and the avalanche photodiode. The avalanche device utilises internal multiplication to give low noise amplification and this should lead to a significantly more sensitive receiver. Unfortunately avalanche devices require accurate control of bias voltages for stable operation, and this would probably lead to the need for some type of feedback bias circuit especially for wide temperature range operation. Again this increase in circuit complexity must be traded against the improved performance.

7. THE OPTICAL HIGHWAY

7.1 Optical Highway Configuration.

The multiple access fibre optical data highway considered here is an optical interconnection network in which an optical signal injected to any access point appears at all other access points. Therefore, no optical switching is necessary.

Two well known configurations for such a highway are the star or ring systems, illustrated respectively in Figs. 6 and 7. The relative merits of these are well documented (Hudson, M.C., Thiel,F.L. 1974). Briefly, the star system has the advantages to the system designer of low optical loss, freedom from echo pulses and can easily be designed to give loss and delay which is the same for all pairs of terminals. The restrictions on configuration, and the vulnerability to the star component itself are, however, unacceptable for some applications. The ring system suffers from high and variable loss, variable delays and echoes, but the configuration itself is sometimes preferable, especially if access points can be added at will.

More complex configurations, which can be thought of as hybrids between the ring and the star can readily be conceived to avoid the very high loss of ring systems or the vulnerability and inflexibility of the star configuration. (Porter, D.R., Reese, I.R., 1976).

A hypothetical configuration is shown in Fig. 2, which combines several concepts for illustration. It shows that a hybrid can consist of a ring of star subgroups or the reverse, and it also shows how two- or three-way fibre mixers can be used as couplers for ring configuration. The use of extra optical paths is illustrated which provides redundancy and greatly reduces the loss between the most distant terminals. There are considerable opportunities for tailoring the configuration to meet constraints on layout, installation and redundancy to suit the particular requirements but only if the terminals are well able to tolerate a wide range of optical loss, delay and echo pulses. These considerations have guided the terminal design described above.

Flexible, redundant highway configurations of this sort can clearly be developed round either access couplers (tee pieces) or star couplers (which may be of the transmission type). While it will naturally be desirable to have a wide range of components to choose from, one of the most useful devices for initial work for the system described here is a simple two or three-way transmission star mixer.

7.2 Coupling Devices.

Figure 9 shows an idealized three point tee-piece (Y-junction) used for combining or dividing optical power. This representation indicates a wastage of optical power, and it may be thought that this could be avoided by suitable design. Under conditions of a uniform transmission fibre whose numerical aperture is always filled, however, such an improvement is not available, and the loss is fundamental. This is simple to prove by considering optical sources of the same brightness completely filling ports A and B. If the loss indicated did not occur, the power at C would be greater than that at A, which would mean a greater brightness at C than at either A or B, contradicting the Law of Brightness (a corollary of the Second Law of Thermodynamics). The device shown can obviously be used as a divider or combiner, and the foregoing has shown that ideally the transmission loss between A and C is the same for a combiner as for a divider.

The four-port devices indicated in Figs. 10 and 11 are applicable for transmit/receive access points, and in effect make use of the otherwise wasted power referred to above. Mixing devices (Fig.12) can either be used as star couplers (e.g. in Fig. 6) or can replace access couplers in bus or ring configurations.

A number of approaches to realizing these devices for single-strand multimode fibre are being pursued. One is to bring two or more fibres in close proximity with cladding removed, and an index matching material applied. An alternative to removing the cladding is to taper the fibres and place together in the presence of a high index medium. Either approach requires means of supporting the fibres, and providing a low loss connection to the transmission fibre, unless the transmission fibre itself is to form part of the coupler.

Another approach is to use planar optics techniques, in which planar waveguides are formed in a substrate. Photolithography can be used to define the transverse dimensions. Many techniques are being developed, including ion exchange in glasses. Coupling between fibre and waveguide requires close attention.

Expanded Beam Techniques offer an alternative coupler approach to the waveguide approaches described in the previous paragraphs. Built-on lenses or tapers at each fibre termination, designed to expand and collimate the optical-beam, are a possible means for demountable coupling between two fibres. The lateral alignment of the two terminations is less critical than in a straight butt joint because of the larger diameter of the collimated beams.

If expanded beam terminations are available, they should ease the task of developing tee-pieces.

For example, four collimating fibre-terminations could be offered to a beam-splitting cube, with the coupling ratio controlled by the reflection coefficient of the beam-splitter. In principle this device would be equivalent to the four port of Fig. 10.

8. THE BREADBOARD MODEL

A breadboard model of a single terminal has been constructed, and based on the satisfactory results with this model, construction of several functional models is now underway. The model uses TTL technology and the general design is on the lines described above, and the basic parameters are:

Number of terminals	-	10
Baud rate of transmission	-	1.5 Mbit/s
Transmission data rate per terminal	-	100 kbit/s

It has been found possible to demonstrate the correct functioning of almost all parts of the circuit in spite of the fact that only a single terminal is available. This is because of the basic independence of the receiver and transmitter sections of the terminal, so the transmitter can be optically connected to the receiver. By arranging for the transmitter to address data to its own receiver, the correct functioning of the address recognition circuits, parity checkers, stores, etc., were demonstrated.

In order to demonstrate the wide dynamic range of the receiver a separate experiment was carried out in which two simple bi-phase optical transmitters are alternated and the combined signal fed to a single receiver. With different attenuations in the paths from the two transmitters, large and rapid changes in signal amplitude were simulated.

These experiments do not deal with the synchronisation behaviour of the whole network, and for this the computer simulation is used. Results so far indicate that rapid synchronisation can be expected from random start conditions.

9. CONCLUSIONS

It seems certain that future aircraft systems will make use of multi-terminal optical highways. To make the best use of the optical fibres, data bus systems should be designed to take advantage of the particular opportunities offered, and this will not be the case if networks are designed for electrical and then converted to optical.

The system described here has proved to be a very flexible approach, easily modified to fit a wide range of applications. It should be insensitive to optical harness imperfections, and so should be suitable for use with a wide range of harness configurations, including hybrid star/ring combinations. The system should also be tolerant of limited fault conditions within the terminals, the remaining portion of the network continuing to function.

REFERENCES

1. Belcher, G., Marshall, D., Sept. 1975, "Use of Fibre Optics in Digital Automatic Flight Control Systems", IEEE Trans. Aerospace and Electronic Systems, Vol. AES-11, No. 5, p 841-850
2. Biard, J.R., "Opto-electronic Aspects of Avionic Systems II", AFAL Report TR-75-45
3. Altman, D.E., Nov. 1975, "Bidirectional Fibre Optic Trunk Data Bus", NELC Technical Report 1969
4. Barnoski, M.K., Nov. 1975, "Data Distribution using Fibre Optics", Applied Optics, Vol. 14, No. 11 p 2571-2577
5. Milton, A.F. Lee, A.B., Jan. 1976, "Optical Access Couplers and a Comparison of Multiterminal Fibre Communication Systems", Applied Optics, Vol. 15, No. 1, p244-252
6. Hudson, M.C., Thiel, F.L., Nov. 1974, "The Star Coupler: A Unique Interconnection Component for Multimode Optical Waveguide Communications Systems", Applied Optics, Vol. 13, No. 11, p 2540-2545
7. Porter, D.R., Reese, I.R., 1976, "A Hybrid Configured Fibre Optic Data Bus System", 2nd European Conference on Optical Fibre Communication - Paris, p 421-429
8. Farrington, J.G., Chown, M., Dalgoutte, D.G., 1976, "Multi-terminal Data System for Aircraft", Final Technical Report on Feasibility Study, STL-1083-FR

ACKNOWLEDGEMENTS

The authors would like to acknowledge the help and advice of numerous colleagues within STL, and in particular Dr. D.G. Dalgoutte for his advice on optical coupler components. They would also like to thank Standard Telecommunication Laboratories Limited for permission to publish this material.

This work has been carried out with the support of Procurement Executive, Ministry of Defence.

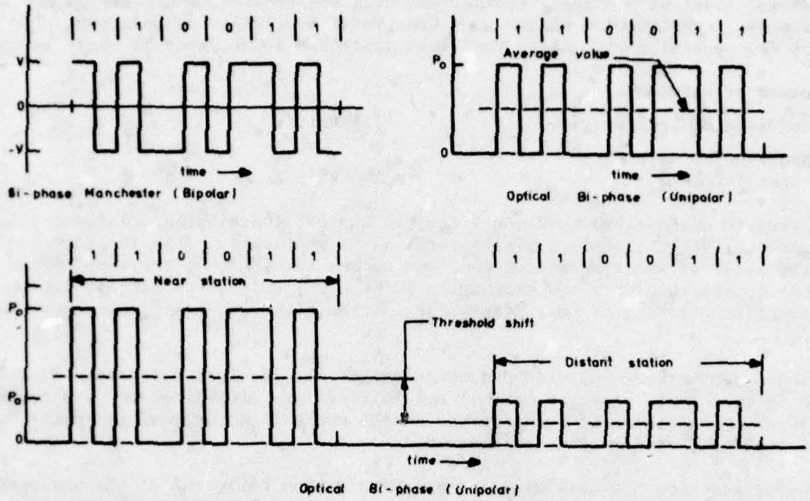

Fig.1 Bipolar and unipolar bi-phase (after J.R.Biard Ref.2)

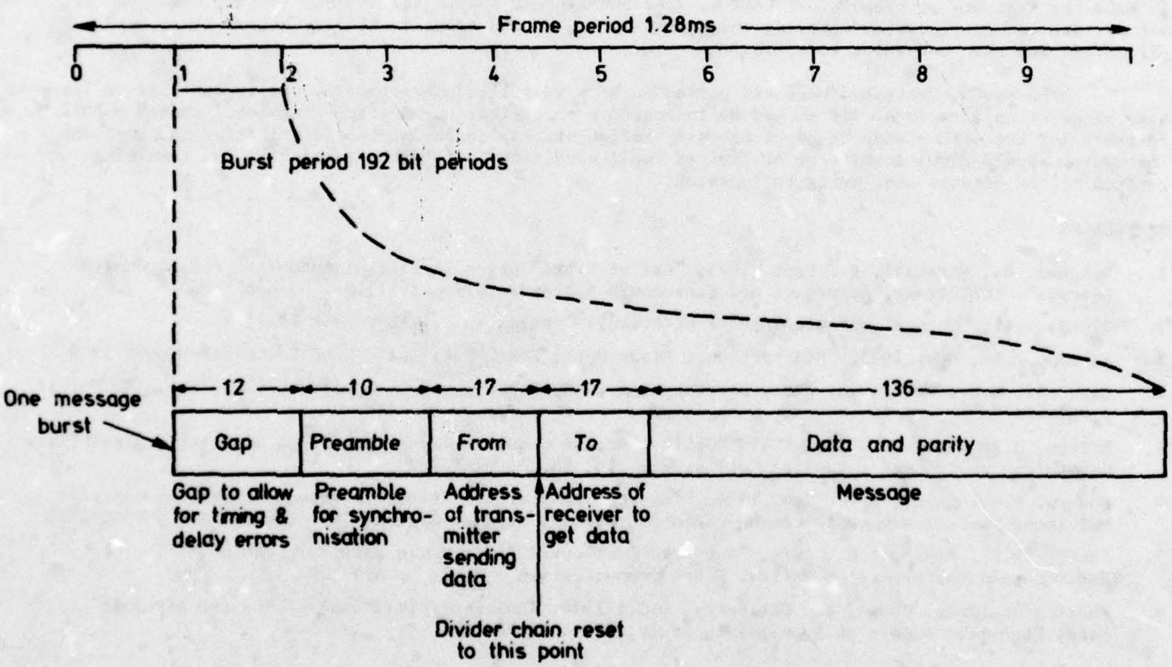

Fig.2 Timing diagram for ten terminal system

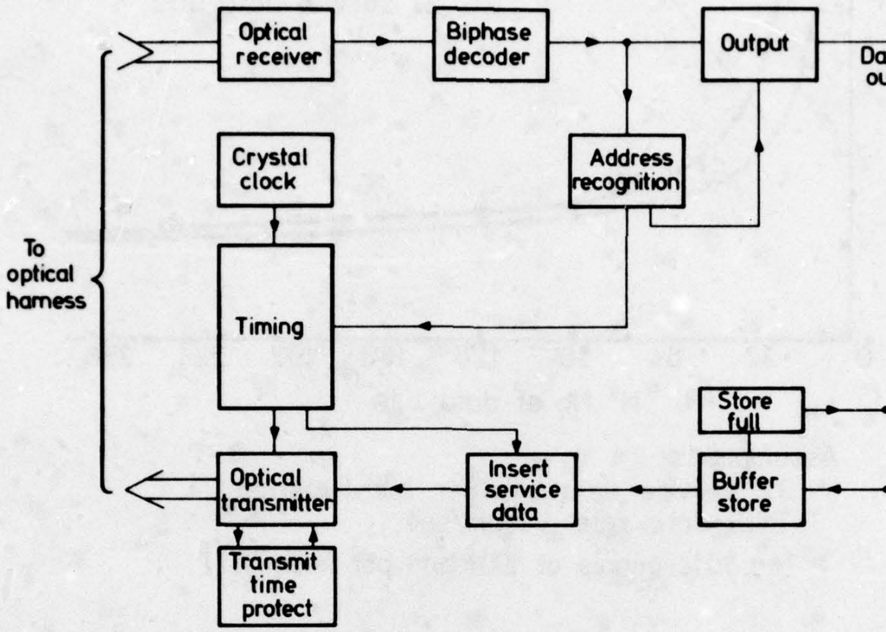

Fig.3 Terminal block diagram

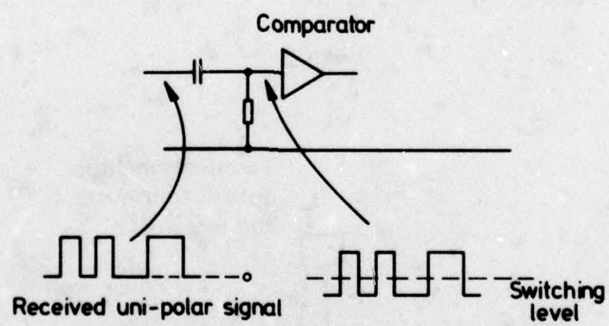

Fig.4 Uni-polar signal AC coupled to comparator

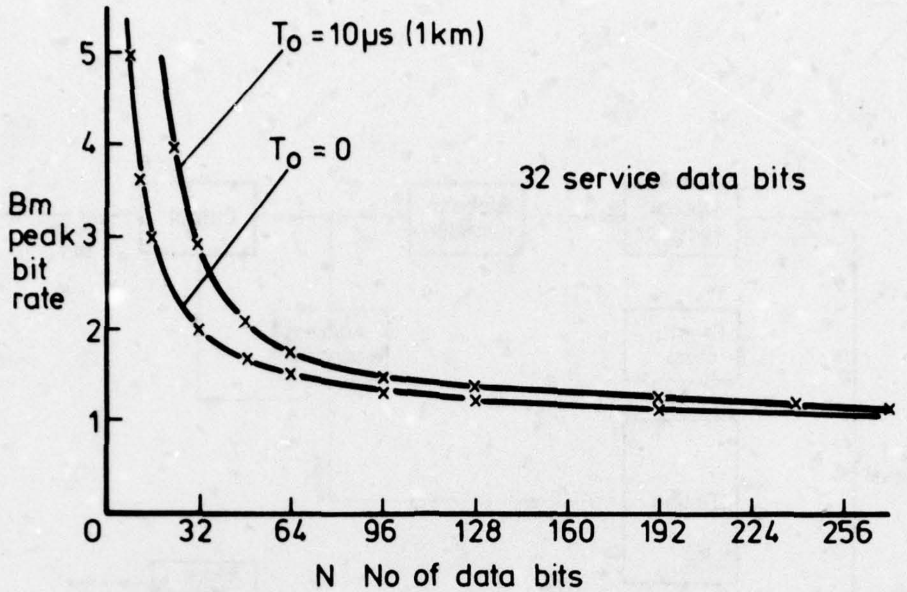

Assumptions
32 service data bits per burst period.
Total data rate 1 Mbit/sec.
(eg. 10 terminals at 100 kbits per terminal)

Peak bit rate as a function of the number of message data bits per burst period, for a 1Mbit/s system

Figure 5

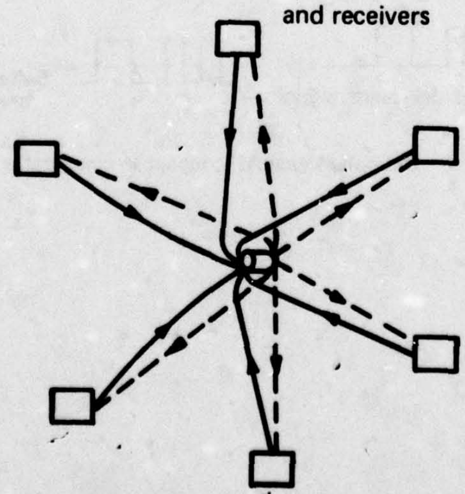

Fig.6 Multi-terminal optical data system – star
An example of an optical fibre highway configuration.
Each optical transmitter sends to all terminals simultaneously.
In this star configuration loss and delay may be equalized.

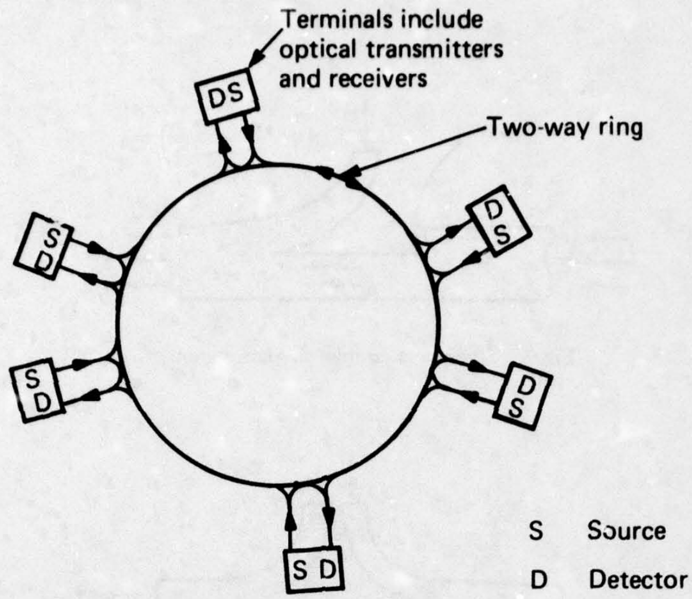

Fig.7 Multiterminal optical data system – ring
Each transmitter sends to all terminals simultaneously, but loss and delay between pairs of terminals will vary considerably. Also, multiple echos will be present. Optical terminals are being designed to tolerate this, to reduce constraints on the highway design.

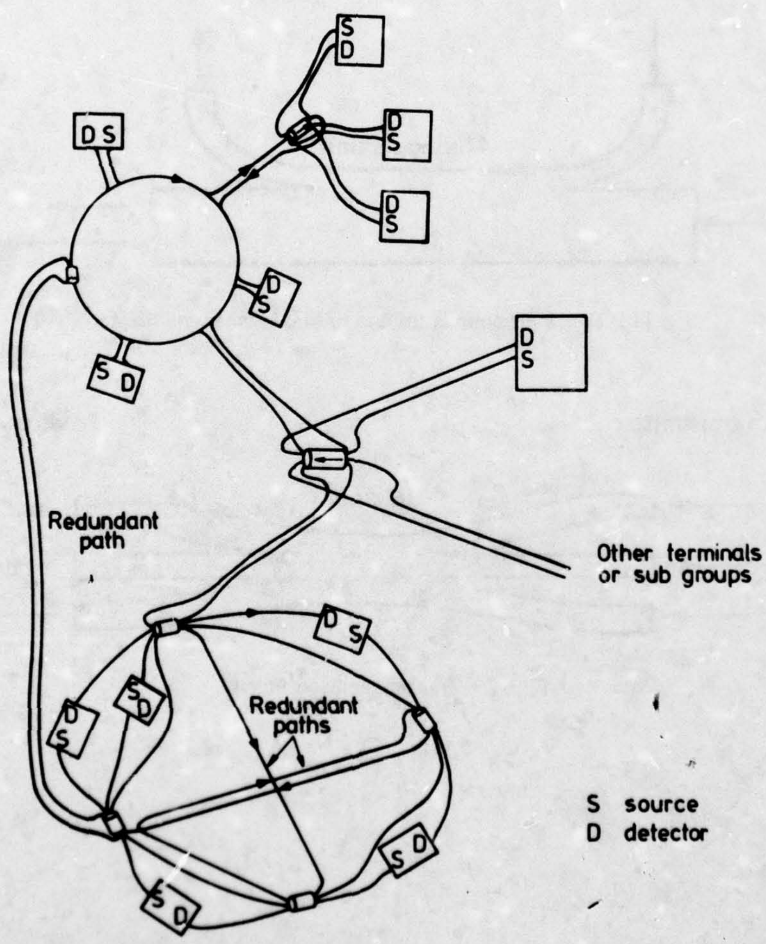

Fig.8 A hypothetical optical highway configuration to illustrate several concepts including redundancy and the use of a range of coupling components

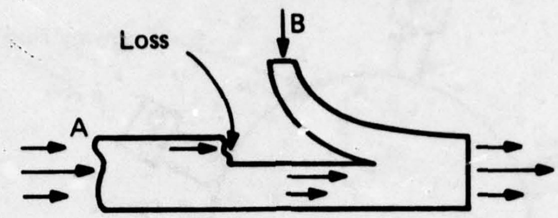

Fig.9 Three-port coupler used as combiner

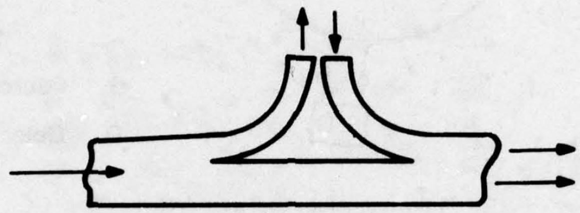

Fig.10 Alternative configuration for a four-port coupler

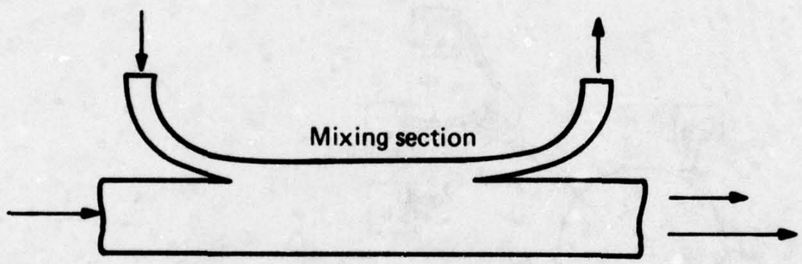

Fig.11 Four-port coupler used as both combiner and divider

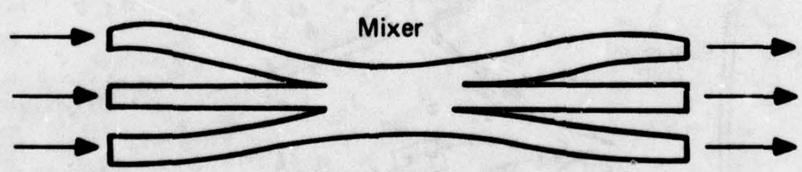

Fig.12 Transmission star mixer

FIBRE OPTICS CONNECTORS : HOT FORMING VERSUS EPOXY BONDING OF BUNDLES AND NEW TECHNIQUES WITH SINGLE FIBRES

R.B. Quarmby,
Hellermann Deutsch,
East Grinstead,
Sussex, England.

SUMMARY

The requirements of fibre optics for military use are reliability, ease of maintenance and speed of both installation and repair. Various single and multichannel connectors and systems for cable-cable and cable-diode coupling can be made, and with suitable design will withstand temperature cycling, humidity, vibration and shock to military standards.

Until now fibre bundle cables have been terminated by epoxy resin bonding, but this technique has been inconvenient to apply in the field. A new dry technique has now been developed for hot forming the cable ends and details are given. The new process results in junctions of higher optical efficiency and it can be carried out with only a few minutes' training in the use of the portable tools now available.

Butt jointed single fibre connectors have been made and have coupling losses in the order of 3dB. Work is proceeding on an alternative design in which a matching fluid is used to reduce losses. Further work is needed to bring these single fibre connectors to a state of development suitable for military applications.

1. MILITARY REQUIREMENTS

In designing fibre optic components and systems for military use, the main emphasis is placed on the following factors: (a) operational reliability in the intended function, (b) ease of maintenance, (c) speed of installation and repair.

1.1 For operational reliability, the fibre optic components and systems must meet the same mechanical and environmental test specifications as the electrical and electronic units they replace. For example, the diode-cable assemblies and fibre optic harness shown in Fig.1, which are fitted into the Boeing YC - 14 STOL transport aircraft, are capable of meeting the aircraft environmental test specification shown in abridged form in Table I.

The illustration shows the transmitting LED in its housing, with a Y - junction cable attached. This arrangement permits a single transmitting diode to send simultaneous signals along separate paths to two receivers, thereby providing a system redundancy which is an operational requirement; a receiving diode-cable assembly is shown on the right. The main harness is a four channel system of 10ft length, terminated in fully sealed, bayonet coupled quick release connectors.

A secondary sheath has been provided to give the fibre optic cables the additional protection they need, the junctions of this with the connector shells being protected by heat shrink boots. Protective caps are provided to maintain the environmental sealing of the harness when disconnected from the system.

1.2 Ease of maintenance results from the use of connectors to divide systems into modules, so that every component part is removable for replacement. Dimensional standardisation of cable terminations and connectors is essential to ensure every cable-cable or cable-diode interface gives an identical optical performance (see Fig.2). The exception occurs in "buried" cable systems where the fibre optic cables themselves are inaccessible once installed. In such cases it is usual to provide redundant circuits, and various junction units are available for their construction, typically Y - junctions and star coupled multiway junctions (Quarmby, R.B., 1976).

1.3 Speed of installation is facilitated by the use of system modules and quick release bayonet connectors. There are, however, other considerations which must be taken into account in selecting the most suitable system. For example, by making the retention features of the termination ferrules the same dimensionally as those of standard electrical contacts, it is possible to make use of the same plastic insertion and removal tools, (see Fig.3). In the same way as soldering has been superseded as a technique by crimping for the termination of electrical cables, so now epoxy bonding of bundle fibres into ferrules is superseded by hot forming. The reasons for going to a new method are much the same, being the abandonment of a wet technique needing specific skills on the part of the operator, in favour of a dry technique calling for no special skills, but relying instead on factory produced portable tools and components, (see Fig.4). These can also be used to make in-field repairs.

2. BUNDLE FIBRE SYSTEMS

Multimode bundle fibre cables are the current preference in military equipment applications. Their losses are not too great for the short distances which are usual, their flexibility makes them easy to install without risk of breakage and their light weight makes them rugged in use. Because of a relatively large diameter, they can be coupled directly to light emitting and detecting diodes, and to each other, with a high level of efficiency.

As already stated, the techniques for terminating and polishing fibre bundle cables have until now been suitable for use in a factory or workshop environment but inconvenient to apply in the field. Epoxy resin bonding of the cable ends into metal ferrules prior to polishing is a process requiring careful control of resin mixing and application to achieve good results. It is, moreover, a lengthy process to apply as time must be allowed for the resin to cure before the fibre ends are polished.

The use of epoxy processes during installation can be avoided by procuring the exact lengths of terminated cable required in advance, based on system design calculations. Maintenance of equipment in the field has been achieved by providing a number of finished cables for use as spares.

In regard to repair in the field, and if advance procurement of exact lengths is impossible, the epoxy resin bonding technique can be used, although as a process it has the drawbacks which have already been stated. The new techniques described in this paper are a significant improvement in this regard and facilitate the use of cut-and-fit techniques for the installation of long runs of fibre optic cable.

3. HOT FORMING AND POLISHING

The new method of cable termination is based on the development of hot forming techniques for securing the cable ends in their ferrules, prior to polishing. Only dry components are used, and the entire process of preparing and polishing a cable end is completed in three to four minutes using specially developed portable tools. Training in the use of the tools can be given in only ten minutes.

The hot forming process requires the use of a factory made composite ferrule (see Fig.5). This is assembled from three components: an outer or driving ferrule, the internal bore of which tapers inwardly at its extremity, a glass bead and an inner ferrule. The three parts are pre-assembled to facilitate the process of threading it over the fibre bundle end of a stripped back cable. After threading, the cable sheathing is retained in the bucket of the inner ferrule by crimping.

The hot forming tool is shown in Fig.4 and is used to seal the cable end into the ferrule. The termination is inserted into the tool and is clamped into position. Operation of a control knob on the side of the tool releases an internal spring, which pushes a heating element against the driving ferrule. The termination becomes heated by its contact with the element and the heat softens the glass bead, which begins to flow into the tapered portion of the driving ferrule under the driving force of the spring. At the same time, the ends of the cable begin to soften and are deformed under the radial compression of the glass bead, the interstices between fibres being virtually eliminated. As a result, the fibres end up tightly packed within the ferrule. Thus total peripheral support is provided for each and every fibre during the subsequent polishing operation.

Compared with a resin bonded termination, the resulting cross section has a much reduced dark area, as shown in Fig.7. In a test of both methods with a nominally 100 - fibre cable, the insertion loss of the connection was reduced from 2.75 to 1.5 dB. The degree of compression applied during the hot forming process depends upon the original size of the gap and the size of glass bead. Various ferrules have been designed to accommodate a range of cables, up to 3.5mm diameter.

The termination is finished off by crimping the inner and outer ferrules together, and using the second portable tool for polishing. The tool houses a geared electric motor which drives a polishing disc covered with a suitable grade of carborundum paper. An internal reservoir holds fluid to wet the disc during polishing, the motor shaft being sealed to keep it out. A clamp is provided which holds the ferrule normal to the plane of the polishing disc, but allows it to be moved radially in and out during rotation. Polishing a hand held termination always leads to a domed end which is inefficient in use. This is avoided in the design of this tool.

4. SINGLE FIBRE CONNECTORS

Light can be transmitted from one single fibre to another by the arrangement of a butt-joint between them, but, because of the small sizes involved in connectors of this type, major losses can occur unless fibre misalignment, end separation of fibres and angular misalignment of fibres are avoided. The connector components must therefore be made to a very high degree of accuracy and matching fluid is used to eliminate the air space between butting ends, wherever possible.

A single fibre connector made in this straightforward way has been developed. As with bundle fibre connectors, the essential factor in the repeatability of performance between one connection and another is in the provision of ferrules and housings of accurately controlled dimensions. Termination of the cables in the ferrule is still based on the use of epoxy resin bonding techniques and factory polishing of ends.

To facilitate cleaning of the polished ends prior to connection, the complete system utilizes two plugs to interconnect to a central receptacle. Each plug is attached to an optical cable, and a retention nut holds the ferrule and plug firmly together. Only single channel versions have been considered and the insertion loss achievable is of the order of 3dB, without matching fluid to reduce Fresnel reflections. Work is proceeding on an alternative design in which a matching fluid is used to reduce losses. Further work is needed to bring these connectors to a state of development suitable for military applications.

5. REFERENCES

QUARMBY, R.B., 1976 "Data Highway Devices and Systems", Conference Proceedings, Electro-Optics/ Laser International '76 UK, IPC Science and Technology Press.

TABLE I

ABRIDGED FORM OF ENVIRONMENTAL TEST SPECIFICATION

FOR BOEING YC - 14

CONDITION	REQUIREMENT
Temperature Range	-65 to + 160°F
Temperature Shock	Temperature (°F) cycled four hourly in the following sequence: ambient, +160, *0, +130, -20, +130, -65, +130, 0, 150, 0, ambient. (*power applied 30 minutes before change from 160 to 0)
Altitude	8000 ft, continuous operation 50,000 ft, 30 minute operation
Humidity	0 - 100% R.H.
Sand and Dust	As MIL-STD-810B method 510
Vibration	As Test Envelope of Fig.8
Shock and Crash	As MIL-A-8865 A Amendment 1
Abrasion	As MIL-W-22759 Paragraph 4.7.5.12

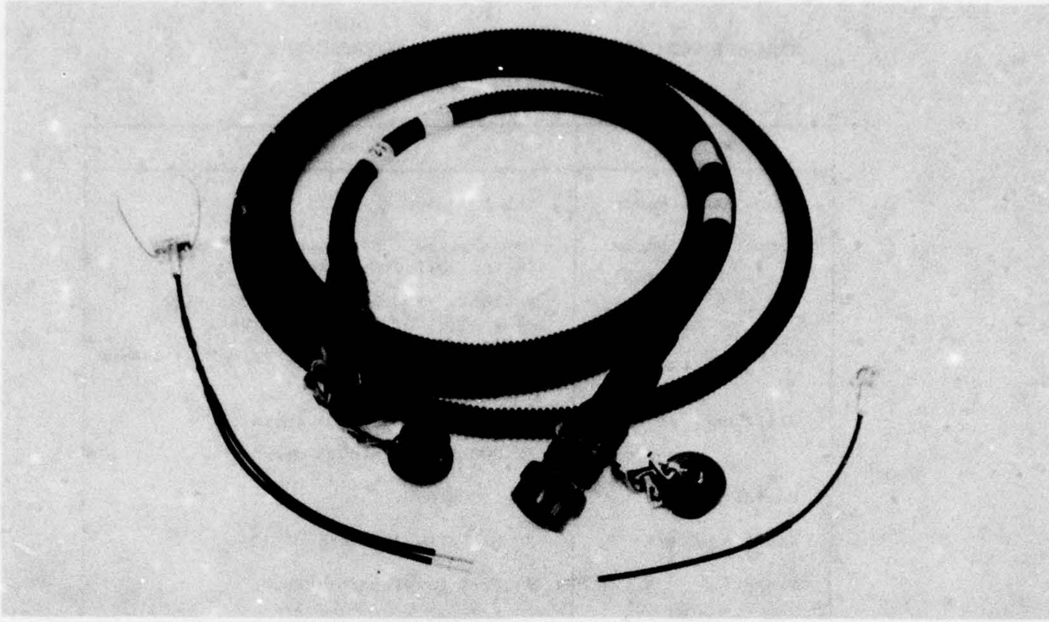

FIG.1 Fibrocon components fitted to the Boeing YC - 14 STOL transport aircraft.
(a) Light emitting diode housing with Y Junction Cable.
(b) Harness comprising FRR bayonet coupled quick release connectors, based on Pattern 602 (EL 2112) aircraft types, and secondary sheathing in the form of corrugated plastic conduit, for extra protection of the fibre optic cables themselves. Note caps which are supplied to protect the harness from the environment when disconnected.
(c) Light receiving diode housing and cable.

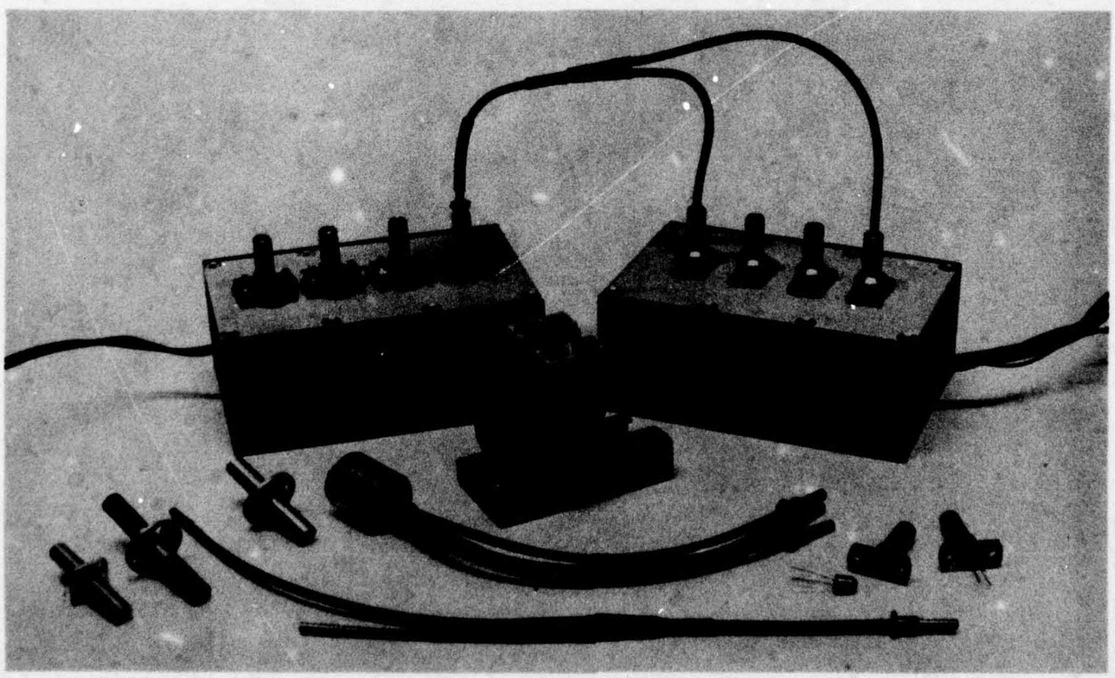

FIG.2 Fibre optic connector and cable modules.

Back row: Modulator unit driving 4 LED's; rail mounted screw-coupled optical connector with two electrical rail mounted blocks; demodulator unit with 4 Pin diode housings.

Front row: Single channel square flange connector; environmentally sealed single channel snap-in connector; single channel snap-in connector; 3-way star coupled junction; diode housings.

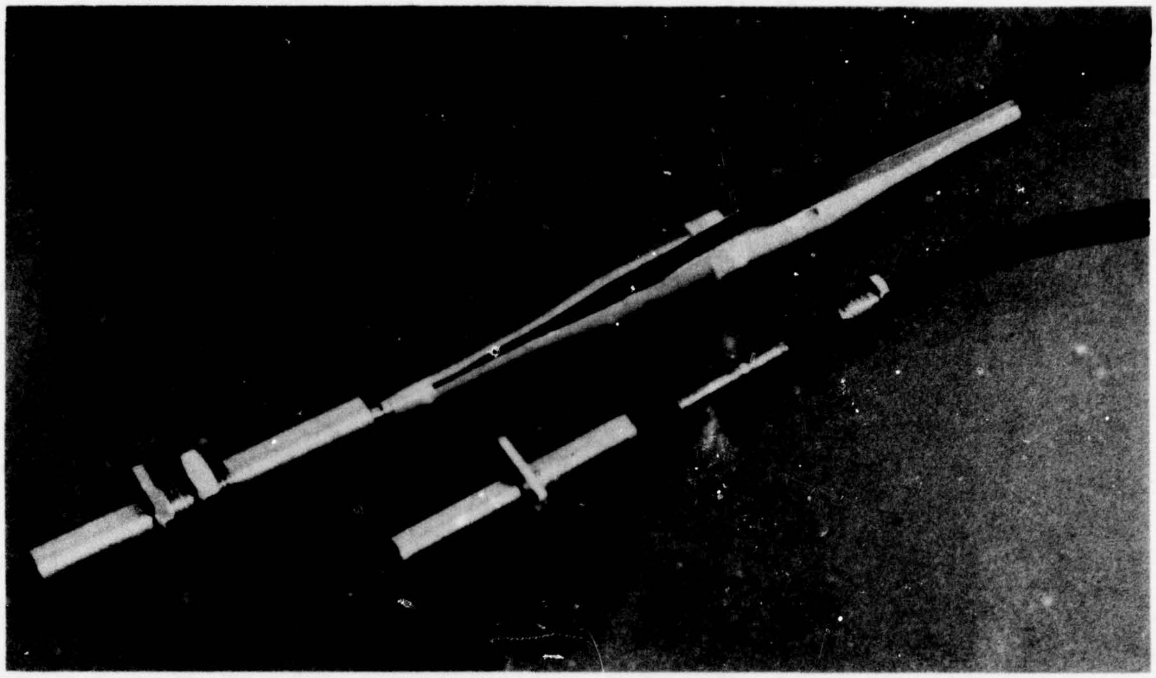

FIG.3 (a) Insertion and extraction tool with single channel clip type connector.
(b) Single channel bulkhead connector with screw retained cable termination.

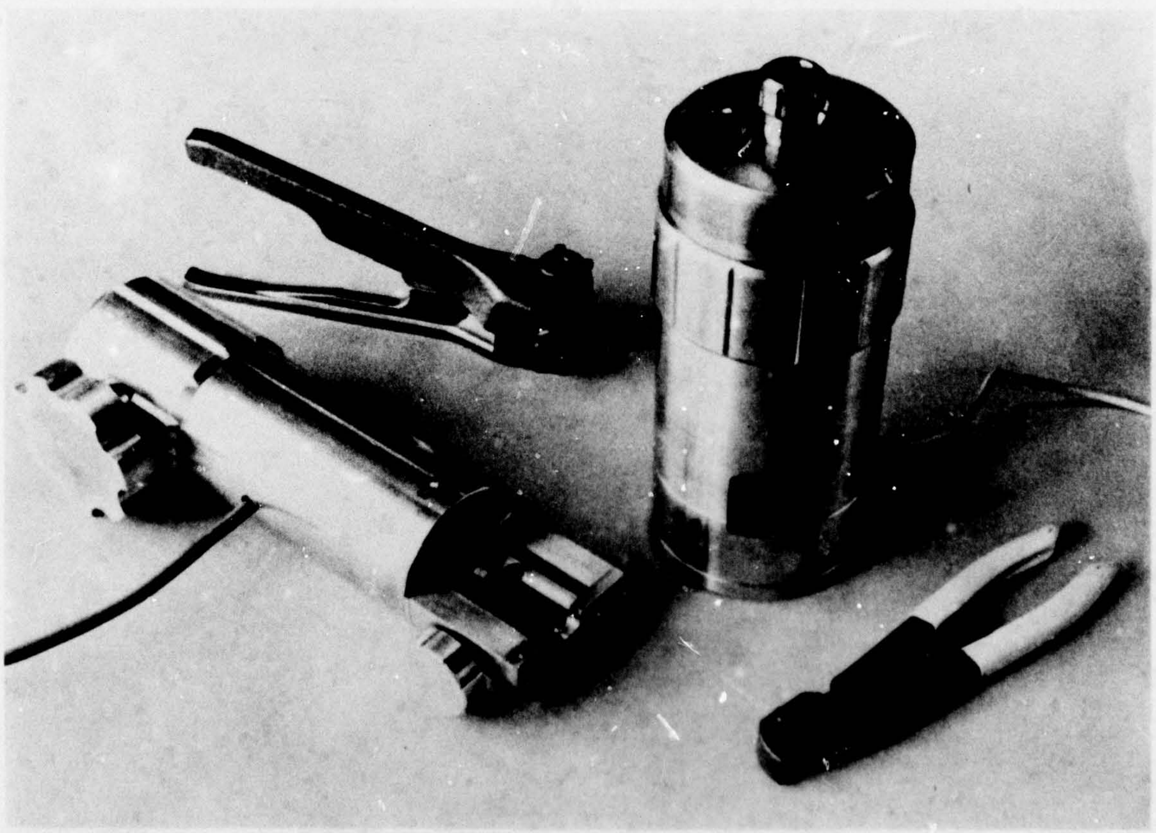

FIG.4 Portable tool kit, showing from left to right, hot forming tool, crimp tool for attaching outer to inner ferrule, polishing tool and crimp tool for attaching inner ferrule to cable cladding. By use of these tools it is possible to achieve terminations of factory made quality with portable tools used by unskilled staff in the field.

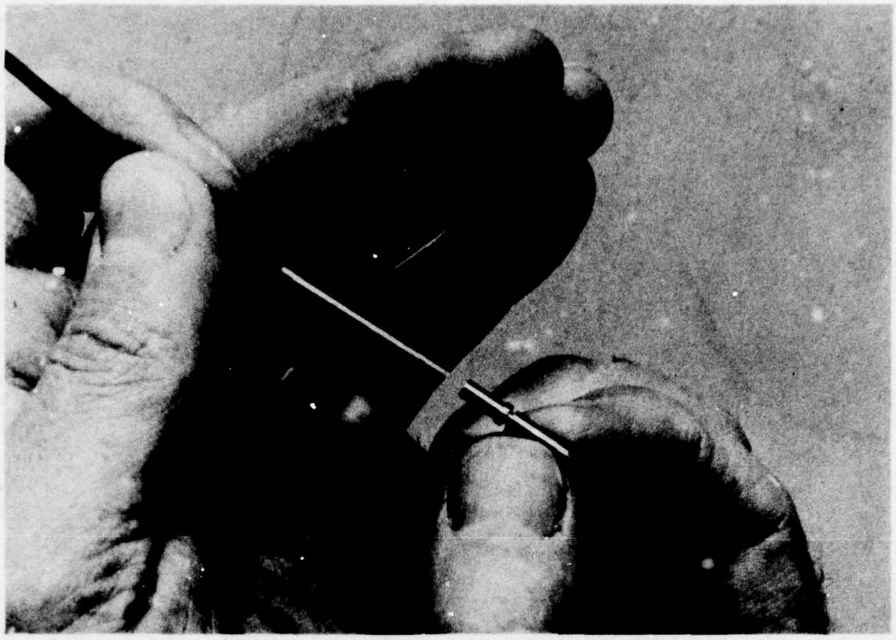

FIG.5 Threading of fibre bundle through composite ferrule prior to hot forming.

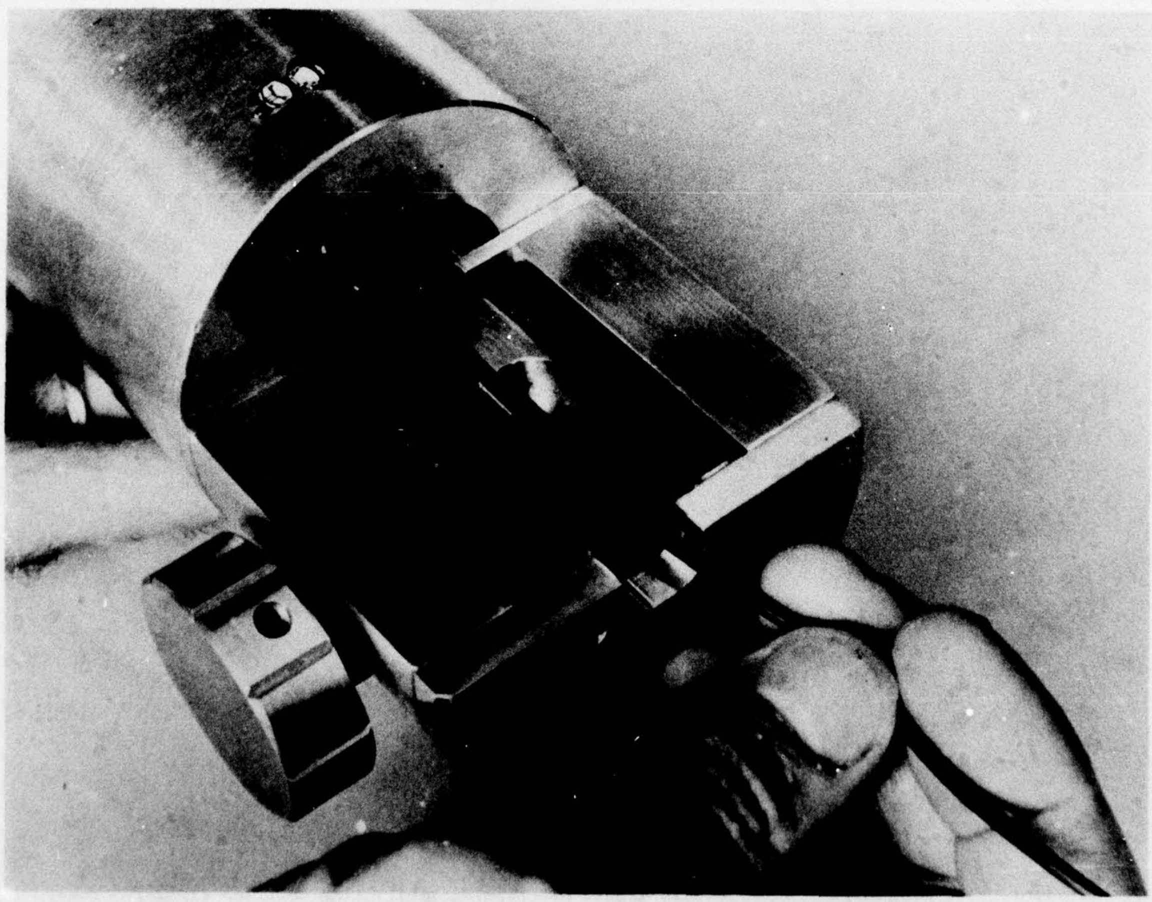

FIG.6 Application of termination to hot forming tool.

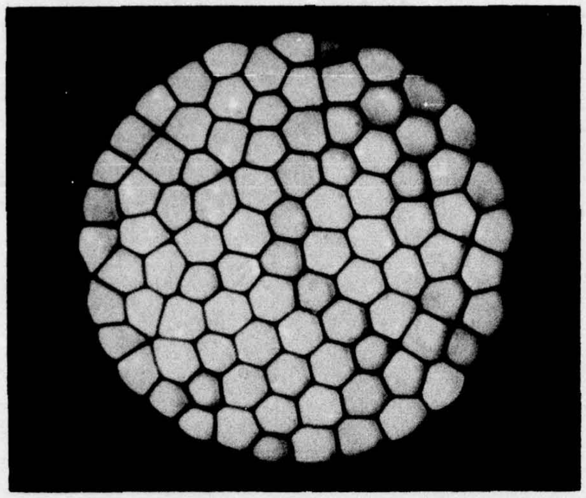

FIG.7 Hot formed cross section.

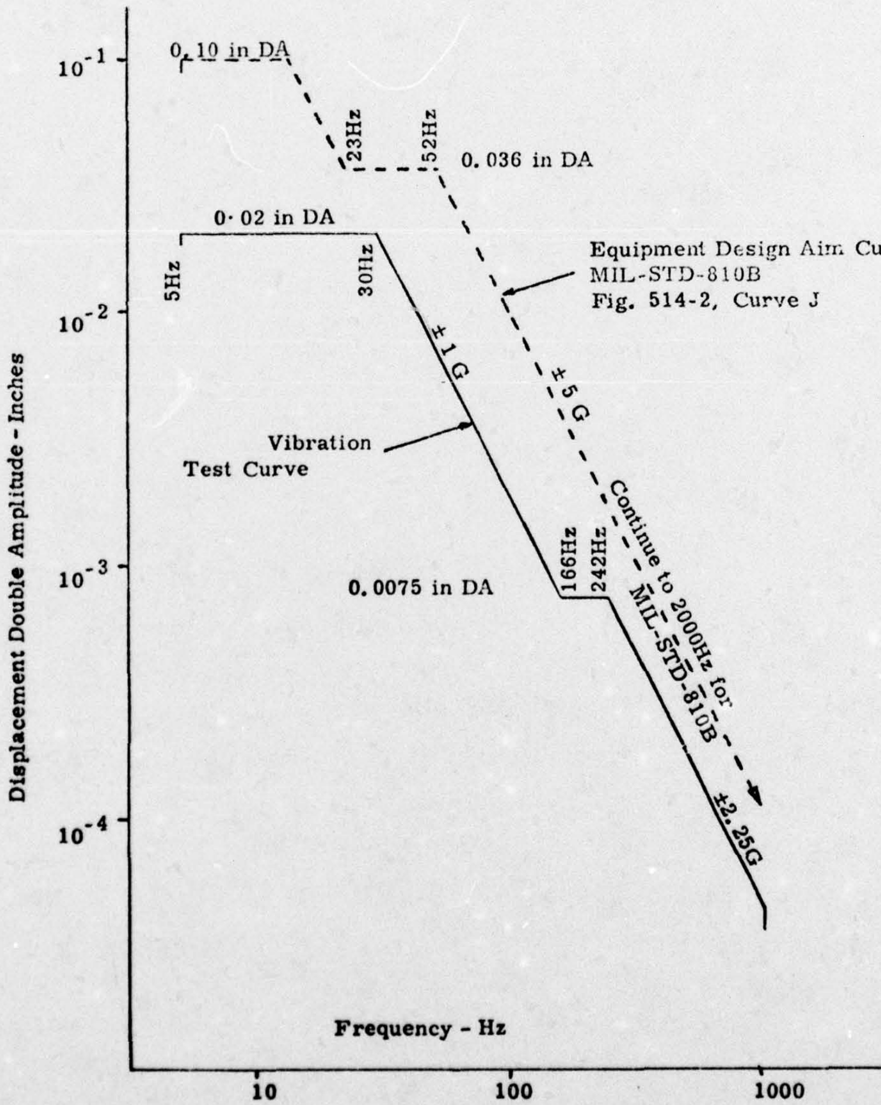

FIG.8 Vibration Test Envelope YC - 14.

FIBRE OPTICS INTERCONNECTION COMPONENTS

J.D.Archer, B.Tech.

ITT Components Group Europe,
Leeds, Yorkshire, UK.

SUMMARY

This paper describes a range of single fibre demountable connectors and active devices, and compares measured performances with theoretical predictions.

1. INTRODUCTION.

Although the original aim of fibre optics communications has been the establishment of cheap long haul high bandwidth links for the telecommunication industry, many of the earliest systems have been for military and other short range applications, where the main advantages accrued have been in terms of low weight, freedom from EMI and electrical isolation. Many of these systems have employed fibre bundles as the transmission media, due, perhaps, to availability, and to the relative ease with which they can be coupled to one another, and to existing large area sources and detectors.

However, there is growing interest in these areas in the approach of using a single fibre per information channel, thus gaining from the expertise of the telecommunications industry which is already committed to single fibre operation on economic grounds. In addition, the military user can expect to reap benefits from the potential ruggedness of well protected single fibres, together with good theoretical coupling characteristics, and the availability and life of small area sources and detectors. A general comparison of single fibre versus fibre bundle operation is beyond the scope of this paper, but has been well documented elsewhere.

One key factor in the acceptance of single fibres for military and other non-telecommunications applications has been the development of demonstrable coupling techniques between fibres and to terminal devices. In these areas, requirements part company from the telecommunications field where the emphasis has been placed on extremely low loss permanent or semi-permanent joints or splices. Whilst the need for splicing techniques does exist in the military field as a repair facility, the primary means of coupling is likely to be by means of demountable connectors, capable of being mated many times by non-specialist personnel, ofter under arduous environmental conditions, with repeatable rather than the ultimate optical performance.

As the first step towards this goal, ITT have developed a range of rugged demountable single and multiway connectors, and a compatible family of sources and detectors. The remainder of this paper will describe these devices, and compare experimental results with theoretical predictions.

2. FIBRE TERMINATION.

Whilst direct alignment of bare fibres in a suitable guide probably represents the ultimate solution in terms of optical performance, being limited only by intrinsic fibre defects and Fresnel reflections, this principle is fraught with difficulties when applied to practical connectors due to the extreme fragility of unprotected fibres. Admittedly, such techniques have been successfully demonstrated, particularly in the telecommunications field, where the cost of skilled assembly can be offset by a saving in repeaters as a result of the low insertion losses obtained.

However, the military requirement is for a more rugged device, often in applications where a margin of system performance exists and slightly higher insertion losses can be tolerated. For such cases it is desirable to protect the fibre end in a concentric ferrule, thereafter aligning the two ferrules rather than the bare fibres. Care can be taken to ensure that the exposed fibre is polished flush with the end of the ferrule, so that provided dirt is excluded, the risk of damage during mating is greatly reduced.

The price to be paid for protecting the fibre in this way is in the exacting tolerances which have to be applied to the component parts in order to prevent fibre misalignment raising the insertion loss to unacceptable levels. This has necessitated the development of techniques which not only realise the pieceparts with the required degree of accuracy, but which are sufficiently flexible to accommodate a wide range of fibre diameters. This is particularly important as there has not yet been any standardisation of fibre diameters, although there does appear to be a convergence towards the range 100-150 um. In addition there are difficulties in achieving tight process control, and CVD fibres in particular often exhibit considerable diameter fluctuations.

Thus the ferrule termination has to be manufactured to a high order of accuracy, yet be versatile in accepting various fibre diameters. This goal has been economically achieved by making the ferrule in two parts; an accurately ground stainless steel body, relatively expensive, but common to all sizes; and a cheap watch jewel insert, to adapt the ferrule to suit the relevant fibre size. This latter item is available with holes ranging from 70 um to in excess of 200 um, incrementing by 10 um steps, and costing only a few pence, can economically be held as stock items, ready to be pressed into the ferrule bore as requirements dictate (figure 1).

Despite its low cost, the jewel insert is manufactured to a high degree of accuracy, and its addition only impairs the overall concentricity by a maximum of 1.5 um. Each ferrule-jewel combination is permitted a maximum total eccentricity of 5 um, although new techniques are being developed which promise to substantially reduce this figure. In addition, the possible clearance caused by a worst case fibre-jewel fit can contribute a further 5 um eccentricity, although in many cases the fibre diameter falls between two jewel sizes, thus reducing this error also.

One particularly useful feature of the watch jewel is the hemispherical "oil retaining recess", which, being highly polished, acts as a fibre guide, and enables the potentially difficult task of threading the bared fibre to become an almost trivial operation, so that even inexperienced visitors usually become adept at this process with a few minutes practice. The actual fibre termination is accomplished by first removing a few millimetres of the protective plastic coating with proprietry wire strippers, followed by threading the bared fibre through a ferrule loaded with epoxy resin. After curing, the protruding fibre is polished flush with the ferrule end by a simple hand process and visually inspected for defects using a portable microscope which has been developed for this purpose.

3. FERRULE ALIGNMENT.

The type of alignment guide currently used in ITT optical connectors is a precision cylindrical bore. This is attractive in its simplicity and reliability, and is relatively easy to manufacture to the required tolerances using conventional maching techniques. In addition it is readily adaptable to suit a variety of connector configurations. The major disadvantage of this method of alignment is that a minimum clearance must be maintained between the ferrules and the bore in order to permit a sliding fit, which, together with the inevitable machining tolerances can lead to a further fibre eccentricity of 5 um maximum. Other alignment principles which substantially eliminate this clearance are currently being investigated as part of a general programme to improve the overall connector performance.

4. OPTICAL PERFORMANCE.

It will be evident from the previous discussion that fibre misalignment in this type of connector can be attributed to three major sources, each currently being limited by tight manufacturing control to a maximum value of about 5 um. To recap, these are:-

a) Fibre O/D - Jewel I/D clearance.

b) Jewel I/D - Ferrule O/D eccentricity.

c) Ferrule O/D - Alignment bore I/D clearance.

Each of the above occurs quite independently and in both halves of the connector so that a worst case estimate of the resulting misalignment leads to a figure of 30 um, which even with the relatively large core fibres (~85 um) favoured for many applications leads to a high insertion loss.

However, it will also be obvious that this will be a very rare occurence, since random selection of components will lead to better individual fits, and the equally random orientation of the contributing eccentricities will cause some degree of self cancelling. Thus, it is apparently impossible to predict an individual connector performance even with a calibrated set of components. However it is possible to define confidence levels for achieving a desired optical specification.

This is achieved by regarding the six contributing eccentricities as a system of rotating vectors, each with its own angular velocity and initially considered to have the maximum permitted value, ie. 5 um. By calculating the value of the resultant at a sufficient number of random instants in time, a probability distribution can be built up, from which the confidence levels are determined. Figure 2 demonstrates the result of this procedure, along with the corresponding curve for a smaller number of vectors.

Two conclusions can be drawn from these predictions; firstly that a high confidence level can be attributed to achieving a relatively low nett fibre misalignment; and secondly that reducing the number of sources of error does not reduce the resultant by an equivalent proportion as is illustrated by the 2 vector curve in figure 2. The effect of a random selection of tolerances can also be evaluated, since it has been found that, whilst those eccentricities caused by unavoidable clearances have average values equal to their arithmetic mean, the eccentricity of the jewel hole within the ferrule exhibits an average very close to its maximum, due to the extreme difficulty of achieving low values. Thus, these two eccentricities (one for each ferrule) predominate and at best the system will only revert to the 2 vector curve. The actual distribution will lie between the two, and the curve most likely to be obtained from random selection of components has been included in figure 2.

In addition to fibre misalignment, other losses are caused by separation of the fibres due to inclination of the ferrules within the clearance in the bore, and to Fresnel reflections, the latter typically adding a fixed 0.45dB for glass fibres without index matching.

A considerable number of single way connectors have been built in the last few months, and the losses obtained between a small number of 85 um test fibres have been measured as an inspection procedure. These results have been plotted as a histogram in figure 3, together with the theoretical predictions obtained from figure 2, including an allowance for Fresnel reflections.

5. PRACTICAL COMPONENTS.

Figure 4 represents a schematic layout of typical multichannel data links that have been supplied for evaluation purposes. Admittedly this may not represent the optimum solution in many instances, but it does demonstrate the need for various interconnection components.

In particular, each end of the multichannel cable is terminated with a panel mounted connector, which also serves as a convenient junction box between the cable and the individual fibre tails leading to discrete transmitter and receiver modules. Depending on the length of the link and the physical layout, there may be a requirement for free connectors within the length of the cable.

Inside the terminal units, single way connectors are provided as internal maintenance joints, and finally each fibre can be disconnected from its corresponding source or detector package. Strictly speaking, there is no need for both these joints and there is some controversy as to whether devices should incorporate permanently attached fibre tails in order to eliminate the additional loss. However, permanently attached fibres pose an additional and unnecessary hazard to the survival of an expensive device, and the alternative solution of eliminating the single way maintenance connector is preferable if both joints cannot be tolerated.

5.1 Multiway Connectors.

These connectors, the first of the range to be developed by ITT, have been based on the PVX pattern 602 miniature circular LF connectors of ITT Cannon, Basingstoke, and are currently offered in either 4 or 8 way versions. The conventional electrical pin and sockets have been replaced by externally compatible optical contacts, internally modified to provide the necessary alignment facilities. Figure 5 shows a sectioned view of one mated pair of contacts, illustrating the alignment principle of the jewelled ferrules and precision bore. One of the ferrules is allowed axial freedom under spring pressure in order to eliminate tolerancing problems.

This type of connector is particularly suitable for use with cables of a circular construction employing a central strength member, and provision is made for securing this mechanically to an extension tube fitted to the rear of the connector body.

5.2 Single Way Connectors.

As discussed earlier, many single way connector applications are envisaged as internal maintenance joints, and as such the mechanical and environmental requirements are less severe. A prime requirement however, is that the connector should be small and light weight, compatible in fact with individual fibres protected only with a thin plastic coating. Some degree of environmental protection is required, but only as far as protecting the optical interface from the ingress of dirt and moisture.

The design of a single way connector to these requirements has enabled a considerable degree of compatibility to be achieved with device packages, which has considerable advantages for the user by allowing flexibility of installation and testing. Thus it is not by chance that the devices have very similar external appearances.

Figure 6 illustrates the single way connector, showing the alignment principle which is similar to the multiversion, except that the precision bore is allowed to 'float' between the two identical terminations. Two 'O' rings provide a degree of sealing and help to minimise vibration effects.

5.3 Device Connectors.

The layout of the pulsed laser assembly is very similar to the single way connector (figure 7) with many components being common to both.

The major difference is that one of the terminations has been replaced by a flanged ferrule containing a short fibre terminated at both ends in watch jewels. This provides an optical window which enables good collecting efficiency to be maintained, whilst isolating the semiconductor from the outside world. Since epoxy resin is used in the construction of this device, it cannot be claimed that the seal is truy hermetic, but it is considered adequate for many existing applications.However, investigations are being carried out into other techniques which will achieve a hermetic seal.

The short flanged ferrule now represents one half of a single way connector, and is aligned with a demountable fibre termination in the same manner. Pulsed double heterostructure lasers are currently being made which will typically launch 100mW peak power into an 85 um fibre, with a maximum duty cycle of 10%. These same devices can be operated continuously below threshold as LEDs, launching 50uW mean power with 100mA forward current.

Pulsed laser assemblies currently exhibit limited lives measured in terms of a few hundred hours. However, CW lasers have been developed which promise to extend this to in excess of 10,000 hours, and modifications are underway to permit these to be fitted in the same package. The major requirement is the need for a rear window to permit optical feedback, which is necessary to stabilize the working point of this device against long term drift.

Detectors, both Pin and Avalanche, have been fitted into the same outline package, with minor modifications. In particular, the inside surface of the short fibre window is cleaved, and allowed to protrude thus enabling very close coupling to be achieved to small, very fast devices. Typical sensitivities achieved have been in the range 0.3 - 0.4 A/W depending on the actual detector used. With the larger devices, the possibility has arisen of using a large core fibre (~150 um) as the optical window, which permits better coupling with the free fibre, without sacrificing coupling efficiency at the detector.

6. BACK-UP FACILITIES.

With any new technology, it is essential to provide the potential user with back-up services and equipment. Terminating optical cables is not yet as simple as is desirable, but it can be achieved by a competant technician give the correct facilities and a small amount of training.

ITT have attempted to satisfy this need by offering packaged termination kits, together with one day training courses during which practical experience is obtained. The termination kit includes, as an optional extra, a portable microscope, complete with incident illumination and a dry battery pack. The microscope has been specifically designed to accept ITT ferrules, but will accommodate others of the same overall diameter. While not to the same standard as a laboratory instrument, a magnification of x 150 and a field of view of 1mm makes this a useful tool for both single fibre and bundle servicing.

7. CONCLUSION.

ITT have developed a range of optical connectors and terminal devices which will satisfy many existing requirements and whose performance is not too far removed from theoretical predictions (fig.3). Naturally, development is continuing in order to improve optical performance and environmental properties, but only by receiving feedback from a substantial number of first generation applications can sufficient information be obtained to design products which meet the necessary specification.

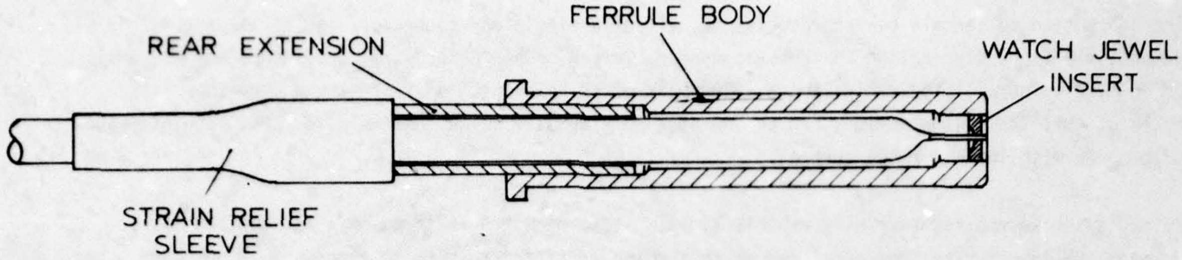

Fig.1 Jewelled ferrule termination

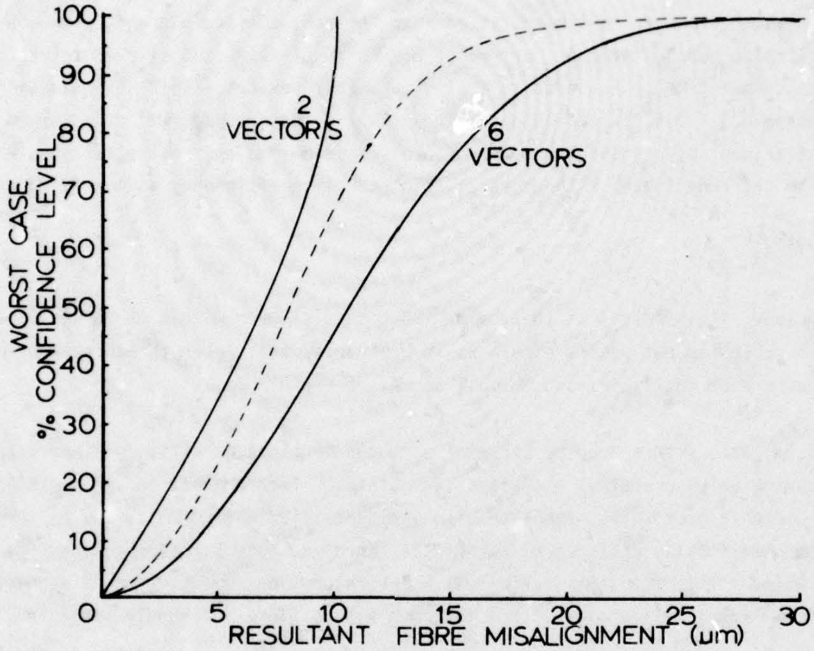

Fig.2 Fibre misalignment distribution

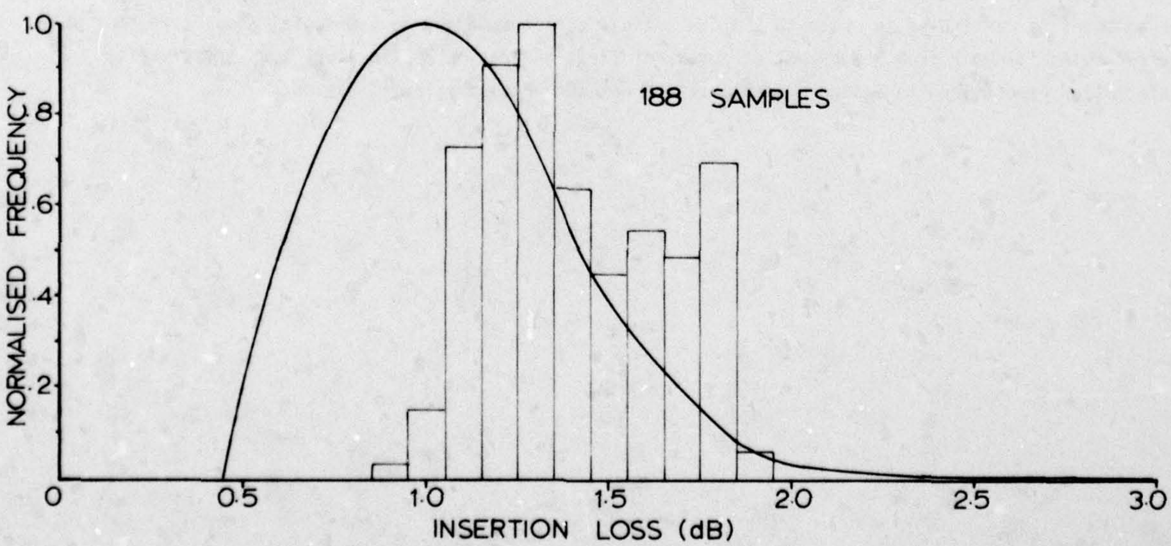

Fig.3 Connector loss histogram (with predicted distribution)

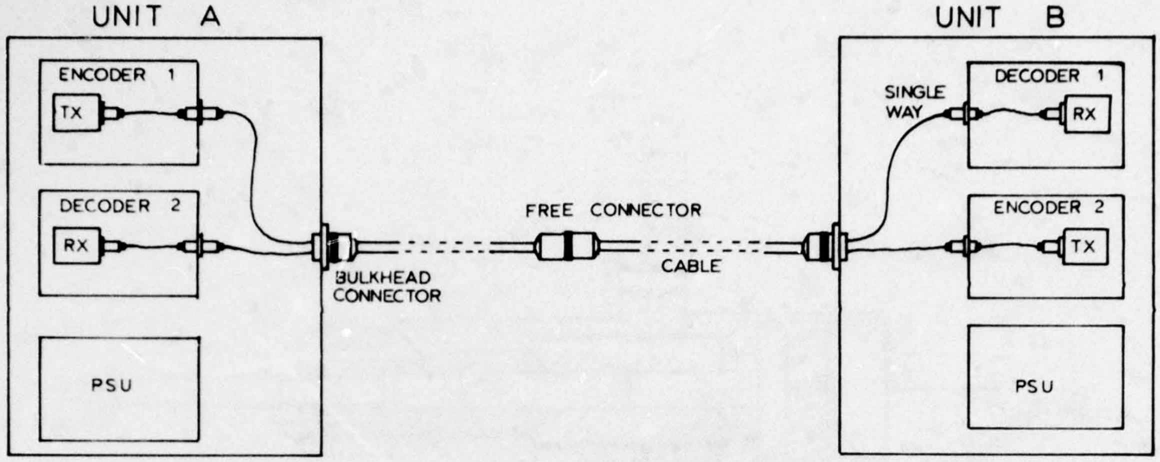

Fig.4 Typical multichannel point-to-point F.O. data link

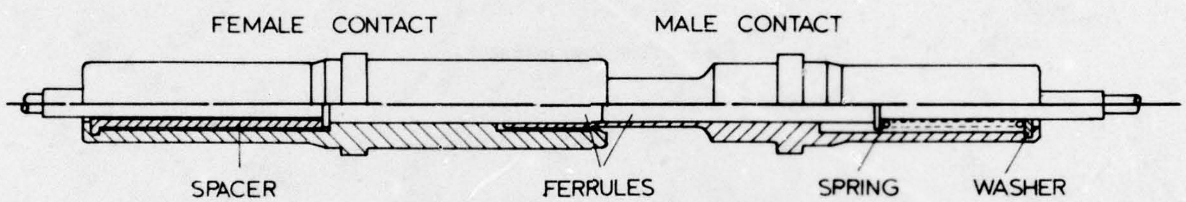

Fig.5 PVX connector optical contacts

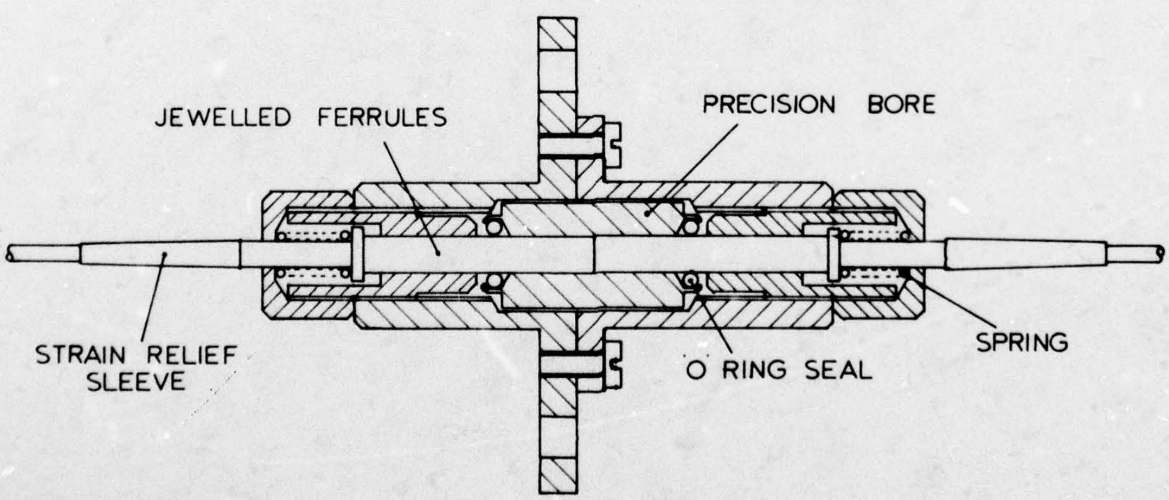

Fig.6 Single way connector

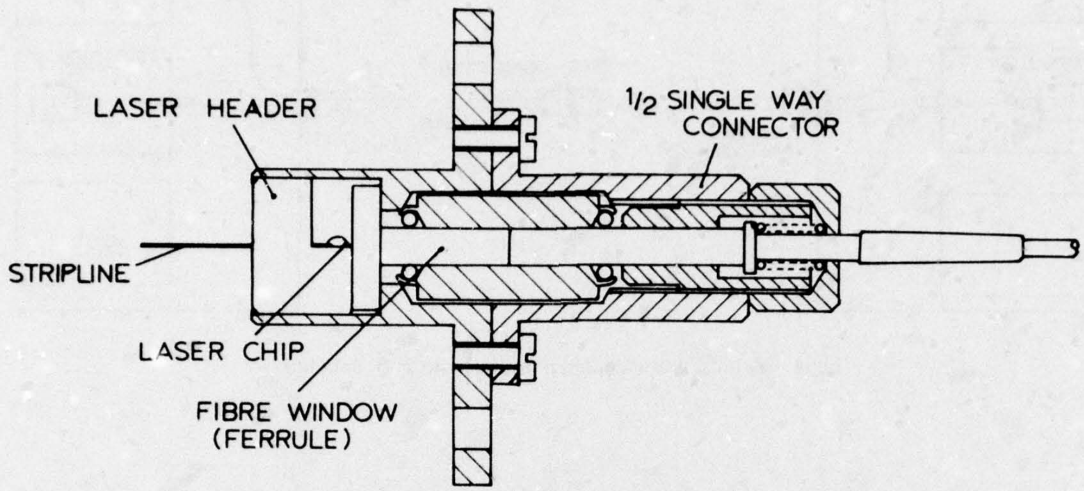

Fig.7 Pulse laser package

QUESTIONS AND COMMENTS ON SESSION VI

HOLOGRAPHIC ELEMENTS FOR PRACTICAL FIBER BUNDLE COUPLERS

O.D.D. Soares, A.M.P.P. Leite, E. A. Ash

Dr. H. J. Frankena: How can you, using normal holograms, attain a 100% efficiency for the image-forming beams? Is the system sensitive for lateral dispositions in the case that the fibre ends are irregular?

Dr. Leite: High efficiencies are only to be obtained using thick phase holograms. The holograms are "adapted" to the fields radiated by the fibres; as long as the recording and reconstruction field are the same, after traversing the first hologram there will be a quasi-plane-wave in all cases.

AN OPTICAL FIBER MULTITERMINAL DATA SYSTEM

J. G. Farrington, M. Chown

Dr. R. S. Hopkins: (1) Please give any information on error rate, especially the design assumptions about noise in the transmission link which guided your choice of the type of redundant codes used. (2) Would the simple input circuit to the comparator receiver be vulnerable to unequal rise and fall times of the pulses?

Dr. Farrington: (1) Because the trade-off between signal to noise ratio and error rate is very sharp, with a system naving a reasonable safety margin in the power budget, error rates should be so low as to be unmeasurable. The use of redundant coding is principly to ensure that valid address codes cannot be recognized in data messages. (2) Unequal rise and fall times would have the effect of slightly increasing error rates, but if these are already very low this probably doesn't matter. Unequal rise and fall times due to photodiode imperfections should not have an effect on the time rates involved in most avionic applications.

Dr. Steve Brandt: The paper concludes that "to make the best use of the optical fibres, data bus systems should be designed to take advantage of the particular opportunities offered [by optical fiber technology], and this will not be the case if networks are designed for electrical and then converted to optical." It appears, however, that the network under construction was indeed designed for or patterned after electrical (MIL-STD-1553A, Manchester Bi-phase Coding converted to optical, fixed length message) and that no attempt was made to take advantage of the particular opportunities offered by optical fiber technology, such as higher data signaling rates than possible with shielded-twisted-pair wire (>10 MHz) or low crosstalk between adjacent parallel conductors.

Dr. Farrington: The system was the result of an attempt to re-think the requirements of an avionic data bus, but starting with the use of optical fibres. No attempt was made to use any specific properties of the fibre for example very high bandwidth, but rather the system was designed around a best estimate of existing requirements, (i.e. <10 MHz). The system does in fact differ in several important ways from MIL-STD-1553A and was not based on this standard. Extra bendwidth has been used to simplify the system design instead of offering higher data rates.

FIBER OPTICS INTERCONNECTION COMPONENTS

J. D. Archer

Dr. R. B. Dyott: I would like to suggest a possibly more precise method of locating the fiber than by using jewels with a range of discrete bore sizes. If a large glass or silica tube is first accurately ground and polished to size and then pulled down to a much smaller diameter, the bore can be made to fit the fiber exactly; the radio of outer to inner diameters being maintained accurately during the drawing process.

Dr. Archer: This principle is being used by STL in a slightly different form. However, the overwhelming advantage of the watch jewel is that it is readily available, cheap (approx 10p) and highly accurate. At the moment there does appear to be some difficulty in controlling fibre geometry, and the slightly reduced insertion loss of your suggestion has to be weighed against the disadvantage of selecting to suit a particular size. However I very much appreciate your suggestion.

Dr. D. A. Kahn: Have any tests of your demonstrable connector been carried out in non-laboratory, i.e. unclean environments and what use the results if so.

Dr. Archer: The honest answer to your question is No in a controlled sense. However, feedback has been received from various customers with generally favorable comments. Our own exhibition displays have suffered minor increases in insertion losses, but these have been recovered by simple cleaning technique, e.g. cleaning with aerosol degreaser.

In fact degradation by dust does not appear to be as severe as might be expected. Of course, severe dirt will probably be a very different matter, and some embryo ideas are being generated on automatic shuttering techniques etc, but this is a very difficult nut to crack, as I'm sure you will agree.

Summary of Session VI

COUPLERS

by
Prof. P. F. Checcacci

Connectors and couplers are key components of an operational optical system, especially the first ones. Any operational system requires, for installation and maintenance, a number of fixed and movable connections. It is also well known from the past, that the realibility of electronic equipments is largely influenced by connectors.

In the section of the conference dedicated to this subject, papers were presented describing operational connectors with some ancillary tools for assembling it with the optical cable. This indicates that the development stage is well advanced. Of course only after some operation time we can gain confidence in such solutions and experience for future development. Splicing techniques for long distance optical cable at present under evaluation were also presented. In this case the main problem is to develop techniques suitable for field use by the existing skilled cable laying personnel.

A well promising coupling technique for connecting fiber to fiber and fiber to source or to detector by means of a matching hologram was also described. This was at the experimental stage and needs further development.

In the field of coupler, used largely as branch in the optical data bus line, a number of simple T or X branch was described either using transparent bulk material or using integrated optics technique. All of these couplers are substantially a crude power divider and do not use technique similar to those applied in millimeter waveguide couplers. Perhaps future monomode fibers will allow to use such well known waveguide technique.

Variable couplers using perturbation on the main optical conductor to provide leakage were also described, as well as those using more simple power splitting by offset of the main optical conductor. Both are at present in the experimental stage.

In conclusion it seems that the field although being still open, exhibits a substantial amount of devices which, overcome the development stage, are now in evaluation in operational systems. It is expected to have soon some results of the realibility of such components.

LIST OF ATTENDEES

AARONS, J. Dr EPP Panel Member	Air Force Geophysics Lab. L.G.Hanscom Field, Bedford, Mass. 01731, USA
AARONSON, G.	GTE Sylvania Incorporated, Communication Systems Division, 189 B. Street, Needham, Mass. 02194, USA
ADDA, J.	Laboratoires de Marcoussis, C.G.E., Route de Nozay, 91460 Marcoussis, France.
ADLER, E.E.	Standard Elektrik Lorenz AG, Research Center CS-FZNG, Hellmuth-Hirth-Str. 42, D-7000 Stuttgart 40, Germany
AITKEN, J.E.	Electronics Branch, Royal Military College of Science, Shrivenham, Swindon, Wilts, SN6 8TB, UK
ALBER, K.	Elektro Spezial der Philips, GmbH, D-2800 Bremen, Hans Bredow Strasse 20, Germany
ALBRECHT, H.J. EPP Panel Deputy Chairman	FGAN, Konigstrasse 2, 5307 Wachtberg-Werthhoven, Germany
ALEXANDER, A.S.	Marconi Elliott Avionic Systems Ltd. FARL, Airport Works, Rochester, Kent ME 1 2XX, UK
ALLARD, F.C.	Naval Underwater Systems Center, New London, CT 06320, USA
ALPER, T.A.	Shape Technical Center, P.O. Box 174, The Hague, Netherlands
AMAUDRIC DU CHAFFAUT Mrs	CEA-DAM, Centre S4, B.P. 561, 92542 Montrouge CEDEX, France
ANASTASSIADIS, M. Prof. EPP Panel Member	Skoufa Street 71A, Athens, 144, Greece
ANDERSEN, J.P. Mr AVP Panel Member	Chief Aeronautical Systems Programs Division, Transportation System Center, Kendall Square, Cambridge, MA 02142, USA
ARCHER, J.D.	ITT Components Group, Westfield Mill, Broad Lane, Bramley, Leeds 13, UK
ARNAUD, J.	CNRS, E.S.E. Plateau du Moulon, 91190, Gif-sur-Yvette, France
ARNOLD, J.	Dept. of Electrical Engineering, Queen Mary College, Mile End Road, London EI 4NS, UK
ARNOLD, L.J.	GEC Hirst Research Center, East Lane, Wembley, Middx, HA9 7PP, UK
AURIA D', L.	Thomson CSF, Lab. Central de Recherches, B.P. No.10, 91401, Marcoussis, France
AZE, P.D.T.	BAC, Filton, UK
BAKER, P.D.	Smith Industries Ltd., Aviation Div., Winchester Road, Basingstoke, Hants, RG22 6HP, UK
BAKER, P.W.	R.S.R.E. St Andrews Road, Malvern, Worcs, WR14 3PS, UK
BALDWIN, M.	ASWE (MOD-PE) Portsdown, Cosham, Portsmouth, PO6 4AA, UK

BALL, W.F. Mr AVP Panel Member	Code 3141, Naval Weapons Center, China Lake, CA. 93555, USA
BALL	Electrical Engineering Dept., University College, Torrington Place, London WC1E 7JE, UK
BAQUE, F.	LMT, 46 Quai A. Le Gallo, 93103, Boulogne, France
BARELLI, A.	Via Antonio Gramci, N.7 00197 Roma, Italy
BARNETT, J.A.	Standard Telephones & Cables Ltd (Hydrospace), Christchurch Way, Greenwich, SE10 AG, UK
BARRÉ, P. Ing. en Chef AVP Panel Member	STTA, 129, rue de la Convention, 75015 Paris, France
BARTHEL, K.	FFO-(FGAN) Schloss Kressbach 7400, Tubingen, Germany
BEASLEY, R.D.	Marconi Elliott Avionic Systems Ltd. FARL, Airport Works, Rochester, Kent ME1 2XX, UK
BEDWELL, P.J.	SBAC – Aeronautical & General Instruments Ltd., 40 Purley Way, Croydon, CR9 3BH, Surrey, UK
BEGER, H.	CERN – CH 1211, Genève 23, Division SPS, Switzerland
BELROSE, J.S. Dr EPP Panel Member	Dept. of National Defence, Communication Research Center, Ottawa, K1A OK2, Canada
BERG, A.	ELAB – 7034 Trondheim, Norway
BIZEUL, J.C.	TMA du CNET, Route de Tregastel, 22301, Lannion, France
BIZE, D.	CERT, ONERA, 2 Av. E Belin, B.P. 4025, 31055 Toulouse, France
BLACK, P.W.	Standard Telecommunications Lab. Ltd., London Road, Harlow, Essex, CM17 9NA, UK
BLACHMAN, N.M.	Office of Naval Research Branch Office, London, 223, Old Marylebone Road, London, UK
BLACKMORE, R.W.	Plessey Telecommunications Ltd., Taplow Court, Berks, UK
BLADEL, VAN J. Prof. AVP Panel Member	Directeur Laboratorium voor Electromagnetisme en Acustica, St Pietersniewstraat, 41, B-9000, Gent, Belgium
BLACKWELL, J.F.	Standard Telephones & Cables Ltd, (Hydrospace), Christchurch Way, Greenwich, SE10 AG, UK
BLOK, H.	Delft University of Technology, Mekelweg 4, Delft, 2208, Netherlands
BLOOM, J.N. Mr AVP Panel Chairman	CRC P.O. Box 11490 Station H, Ottawa Ontario, Canada, K2H 8S2
BLYTHE, J.H. Dr EPP Panel Member	Marconi Research Lab., West Hanningfield Road, Great Baddow, Essex CM2 8HN, UK
BOOSMAN, J.C.H.	Royal Netherlands Navy, Directorate Materiel Navy, Koningin Marialaan 17, Den Haag, Netherlands
BOSMAN, D. Prof. AVP Panel Member	Twente University of Technology, P.O. Box 217, Enschede, Netherlands
BRADNAM, R.B.	GEC Marconi Electronics Ltd, Great Baddow Research Laboratories, West Hanningfield Road, Great Baddow, Chelmsford, Essex CM2 8HS, UK
BRAID, J.M.	ESD Ferranti Ltd., Ferry Road, Edinburgh EH5 2XS, UK

BRANDT, G.B.	Westinghouse R & D Center, 1310 Beulah Road, Pittsburgh, PA 15235, USA
BRANDT, S.A.	IBM/FSD 9500 Godwin Drive, Building 400/041, Manassas, VA 22110, USA
BRATAAS, T.	A/S Standard Telefon og Kabelfabrikk, P.B.60 Okern, Oslo 5, Norway
BRAULT, Y. Mr AVP Panel Member	Division Equipements Avioniques & Spatiaux, 178 Bld Gabriel Peri, 92240 Malakoff, France
BRIGHT, A.G.	Hellerman Deutsch, Imberhorne Way, East Grinstead, Sussex, RH19 IRN, UK
BRILMAN, R.	Laboratoire de Marcoussis, CGE, 91460, Marcoussis, France
BROOKFIELD, M.J.	Cambridge Consultants Ltd, Bar Hill, Cambridge, CB3 8EZ, UK
BROSCH, B.	AEG Telefunken, Elisabethenstr. 3, D-7900 Ulm, Germany
BULMAN, J.	OCA2 Team, EEW – CSDE, RAF Swanton Morley, Dereham, Norfolk, NR20 4IJ, UK
BURGESS, B. Dr EPP Panel Member	RAE, Farnborough, Hants, UK
BURKE, P.F.C.	ITT Components Group Europe, Optical Equipment Div., Westfield Mill, Broad Lane, Leeds 13, UK
BURT, D.J.	Hellerman Deutsch, Imberhorne Way, East Grinstead, Sussex, RH19 IRN, UK
CAIN, P.S.	Rank Optics, 200 Harehills Lane, Leeds, West Yorks, LS8 5QS, UK
CANNELL, G.G.	Standard Telecommunications Lab Ltd., London Road, Harlow, Essex, CM17 9NA, UK
CAREALLES	L.C.R. Thomson CSF, Domaine de Corbeville, 91401, Orsay, B.P. No.10, France
CARLIER, Ing. en Chef AVP Panel Member	Centre d'Essais en Vol, B.P. No.2, 91220, Bretigny-sur-Orge, France
CARPENTER, R.	Allen Clark Research Centre, The Plessey Co Ltd., Caswell, Towcester, Northants, UK
CHADWICK, K.J.	NDHQ, 101 Colonel By Drive, Ottawa, Ontario, K1A OK2, Canada
CHECCACCI, P.F.	IROE, CNR, Via Panciatichi, 64 Firenze, Italy
CHENON, F.P.	Laboratoire Central de Télécommunications, 18/20 rue Grange Dame Rose, 78140 Velizy-Villacoublay, France
CHOWN, M.	Standard Telecommunications Lab Ltd., London Road, Harlow, Essex, CM17 9NA, UK
CLARRICOATS, P.J.B.	Department of Electrical and Electronic Engineering, Queen Mary College, University of London, Mile End Road, E1, UK
COLEMAN, D.R.	ITT Components Group Europe, Edinburgh Way, Harlow, Essex CM20 2DE, UK
COLLINSON, R.P.G.	Marconi Elliott Avionic Systems Ltd., FARL Airportworks, Rochester, Kent, ME1 2XX, UK
CONCORDIA, J.J.	GTE Sylvania Incorporated, Communication Systems Division, 189 B. Street, Needham, Mass. 02194, USA
COULSON, E.J.H.	Ferranti Ltd., Western Road, Bracknell, Berks, UK
COX, A.A.	ITT Components Group, Brixham Road, Paignton, Devon, TQ4 7BE, UK
COYNE, V.J. Mr EPP Panel Member	Chief, Strategic Surveillance Branch, Rome Air Development Center (AFSC), Griffiss AFB, N.Y. 13441, USA

CRABTREE, R.	MOD (PE), Room 371, St Giles Court, St Giles High Street, London WC2 H8LD, UK
CRAMIER	Thomson CSF, 178 Bld Gabriel Péri, 92240 Malakoff, France
CHRISTOPHOULOS, A.	Royal Military College of Science, Shrivenham, Wilts, UK
CROME, E.D.	Rikelstr. 31, 5205, St Augustin, 1, Germany
CRONE, G.	Dept of Electrical Engineering, Queen Mary College, Mile End Road, London E1 4NS, UK
CROSIGNANI, B.	Italy
CULSHAW, B.	University College London, Gower Street, London WC1, UK
CUNDY, S.L.	GEC Hirst Research Center, East Lane, Wembley, Middx, HA9 7PP, UK
CURRAN, H.	Hawker Siddeley Aviation, Systems Group Design Div., Hatfield Aerodrome, Barnet Bypass, Hatfield, Herts, UK
CUTOLO, M. Prof. EPP Panel Member	University of Naples, Via G Santacroce 60, Napoli 80129, Italy
DAKIN, J.P.	Plessey Radar Ltd., Southleigh, Park House, Eastleigh Road, Havant, Hampshire, UK
DALGOUTTE, D.G.	Standard Telecommunications Lab Ltd., London Road, Harlow, Essex, CM17 9NA, UK
DAMM, K.	Army Materiel Command, Electronics Division, Arsenalvej 55, DK 9800 Hjoerring, Denmark
DAVIDSON, J.N.	Rank Precision Industries, 34 Hither Chantlers, Langton Green, Kent, TN3 0BL, UK
DAVIES, E.N.	University College London, Torrington Place, London WC1E 7JE, UK
DAVIES, K. Dr EPP Panel Member	NOAA/ERL R-43, Boulder, Colorado, 80302, USA
DAVIS, P.	Allen Clark Research Center, The Plessey Co Ltd., Caswell, Towcester, Kent ME1 2XX, UK
DECAUDIN	DRME, 26 Bld Victor, 75015 Paris, France
DE LA RUE, R.	Dept. Electronics & EE, The University, Glasgow G12, Scotland, UK
DEMOSTHENOUS, G.	SBAC – Aeronautical & General Instruments Ltd., 40 Purley Way, Croydon, CR9 3BH, Surrey, UK
DENNIS, R.W.	MOD (PE) ASA7, Room 842A, The Adelphi, John Adam Street, London WC2 N6BB, UK
DESORMIERE, B.	L.C.R. Thomson CSF, Domaine de Corbeville, 91401, Orsay, P.P. No.10, France
DIAMOND, F.I. Dr AVP Panel Member	Communications & Control Div., Rome Air Development Center, Griffiss AFB, N.Y. 13441, USA
DIGBY, P.R.	Marconi Elliott Avionic Systems Ltd. EOSD, Christopher Martin Road, Basildon, Essex, UK
DI PORTO, P.	Italy
DOES, van der R.D.	Netherlands Standard Electric ITT, le van der Kunstraat 292, Postbus 1013, Den Haag 2077, Netherlands
DORE, A.	SAGEM, 70 rue de la Tour Billy, 95101, Argenteuil, France

DRUMMETER, L.F. Dr EPP Panel Member	Associate Superintendent, Optical Sciences Division, US Naval Research Laboratory, Washington D.C. 20390, USA
DUNSMUIR, R.	Dept. Electronics & EE, The University, Glasgow G12, Scotland, UK
DWORKIN, L.U.	ECOM-NL-RM1, Ft Monmouth, N.J. 07703, USA
DYKE, R.D.	EMI Electronics Ltd, Victoria Road, Feltham, Middx. TW13 7DZ, UK
DYOTT, R.B.	Dept. of Electrical Engineering, Imperial College, Exhibition Road, London SW7, UK
EDWARDS, M.P.	BAC, Warton Aerodrome, nr Preston, Lancs, UK
EKRE, H. Mr AVP Panel Member	Kongsberg Vapenfabrikk, c/o NCRE, P.O. Box 25, N-2007 Kjeller, Norway
ELLIS, B.	RAE, Farnborough, Hants, UK
EMERY, A.J.	c/o Technical Training Office, EQD, MOD/PE, Room 2D25, Aquila Golf Road, Bromley, Kent, UK
ENGELHARDT, R.	SEL, AG 7000 Stuttgart, 40, Helmuth Hirth Str. 42, Germany
EPPES, T.	ITT Electro Optical Products Division, P.O. Box 7065, Roanoke, Va 24019, USA
FAIRFULL, D.	EOARD, 223-231 Old Marylebone Road, London NW1 5TH, UK
FARRINGTON, J.G.	Standard Telecommunications Lab. Ltd., London Road, Harlow, Essex, CM17 9NA, UK
FAULTLESS, M.	Allen Clark Research Center, The Plessey Co Ltd., Caswell, Towcester, Northants, UK
FELSEN, L.B.	Polytechnic Institute of N.Y., 333 Jay Street, Brooklyn, N.Y. 11201, USA
FERGUSON, S.G.	UK
FILBY, J.D.	DCVD, Room 320, Empress State Bldg, Lillie Road, London SW6 1TR, UK
FOUCARD, J.	CROUZET S.A., B.P. 1014, 26010 Valence, France
FRANKENA, H.J.	Delft University of Technology, Physics Department, Lorenzweg 1, Delft, Netherlands
FREEDMAN, J. Mr AVP Panel Member	MIT Lincoln Laboratory, P.O. Box 73, Room A-175, Lexington, MA 02173, USA
FREEMAN, G.S.P.	EMI Electronics Ltd., Radar & Equipment Div., 248 Blyth Road, Hayes, Middx, 4B3 1BP, UK
FULLER, J.N.	MEL Equipment Co Ltd, 475 Godstone Road, Whyteleaf, Surrey, UK
GADSDEN, P.	Royal Military College of Science, Shrivenham, Wilts, UK
GAFFNEY, W.M.	National Defence Headquarters, Ottawa, Ontario, KTAOK4, Canada
GAME, C.A.	STC, Optical Communications Unit, London Road, Harlow, Essex, UK
GARETT, I.	Post Office Research Centre, Martlesham Heath, Ipswich, IP5 7RE, UK
GERBI	Aeritalia, CEA, Settore Avionica, Caselle Torinese, Torino, Italy
GERRITY, K.P.	BAC, Warton Aerodrome, Preston, PR4 1AX, UK
GIBBONS, G.	Allen Clark Research Center, The Plessey Co Ltd., Caswell, Towcester, Northants, UK

GILL, R.B.	Laser Diode Laboratories, Inc., 205, Forrest Street, Metuchen, N.J. 08840, USA
GIRARD	Thomson CSF, B.P. No.10, 91401, Orsay, France
GLEAVE, A.	RAE, Farnborough, Hants, UK
GOEDMAN, F.	Delft University of Technology, Van Hasseltlaan 486, Delft, Netherlands
GOOCH, C.H.	RSRE, MOE, PE, Baldock, Herts, 6G7 6NG, UK
GOODFELLOW, R.C.	Allen Clark Research Center, The Plessey Co Ltd, Caswell, Towcester, Northants, UK
GOODWIN, A.R.	Standard Telecommunication Lab. Ltd., London Road, Harlow, Essex, UK
GOODWIN, R.J.	Plessey Co Ltd., Avionics Commercial Div., Roke Manor, Romsey, Hants, UK
GOMPERTS, R.J.	Canada
GREENWELL, R.A.	Naval Electronics Lab., 271 Catalina Bld., San Diego, CAL 92152, USA
GREER, D.	MEL Equipment Co Ltd., Manor Royal, Crawley, UK
GROTJOHANN, H.H.	Philips Telecommunicatie Industrie, P. O. Box 32, Hilversum, Netherlands
HALL, G.K.	Mullard Ltd., Mullard House, Torrington Place, London WC1E 7HD, UK
HALLEY, P. Ing. en Chef EPP Panel Chairman	C.N.E.T., 38, 40, rue du Général Leclerc, 92131, Issy-les-Moulineaux, France
HANDSFORD, D.J.	MOD (PE), Salisbury Square, London, EC4Y 8AT, UK
HARA, E.H.	C.R.C. P.O. Box 11490, Station H, Ottawa, Ontario, Canada K2H 8S2
HARDENBOL, A.G. Associate AVP Panel Member	HQ AFCENT, Scientific Advisor, Brunsumm, Netherlands
HARDING, J.H.	Ferranti Ltd., Western Road, Bracknell, Berks, UK
HARPER, D.W.	Pilkington P.E. Ltd., Glascoed Road, St Asaph, CLWYD, UK
HARRIS, M.S.	EOARD, 233, 231, Old Marylebone Road, London NW1 5TH, UK
HART, D.A.	US Navy, Office of Naval Research, Branch Office, 223, 231 Old Marylebone Road, London NW1 5TH, UK
HARTH, D.	Tech. Universitat Lehrstuhl fur Allgelektrotecknik, Arcisstr. 21, Munchen, 2, Germany
HARTL, M.	Rue FO3, Bundesministerium der Verteidigung, Postfach 1328, 53, Bonn, Germany
HAUPT, H.	Standard Elektrik Lorenz AG, D-7000 Stuttgart 40, Hellmuth Hirth Str. 42, Germany
HEATH, C.E.J.	Cambridge Consultant, Bar Mill, Cambridge, CB3 8EZ, UK
HEINEN, J.	Tech. Universitat Lehrstuhl fur Allg-Elektrotechnik, Arcisstr 21, Munchen 2, Germany
HERSEE, S.	Allen Clark Research Center, The Plessey Co Ltd., Caswell, Towcester, Northants, UK
HESKETH, T.G.	BAC (MAD) Ltd., Warton Aerodrome, Preston, PR4 1AX, UK
HEUVEN van, J.H.	Philips Research Laboratory, Eindhoven, Netherlands
HOBSON, M.P.	Hawker Siddeley Aviation Ltd., Woodford, Bramhall, Stockport, Cheshire, SK7 1QR, UK
HODARA, A. Dr EPP Panel Member	Tetra Tech. Inc., 630 North Rosemead Bld., Pasadena, CA 91107, USA

HOFMANN, A.	Firma MBB, Pommernstr. 14, 8012 Ottobrunn bei Munchen, Germany
HOLLAWAY, B.	RAE, Farnborough, Hants, UK
HOPKINS	Sperry Gyroscope, UK
HORSLEY, A.W.	Standard Telecommunication Lab. Ltd., London Road, Harlow, Essex, UK
HORWATH, T.G.	Office of Naval Research, 800 No. Quincy Street, Arlington, VA 22217, USA
HORST, ter J.A.M.	Royal Netherlands Navy, Navy Navigational Equipment, Molenstraat 33, Ter Aar, Netherlands
HOWARD, D.	University College London, Gower Street, London WC1, UK
HOWARD, R.W.	Marconi Elliott Avionics Systems Ltd., Airport Works, Rochester, Kent, ME1 2XX, UK
HSIEH, J.J.	MIT Lincoln Lab., Lexington, MA 02173, USA
HUMPAGE, J.	Allen Clark Research Center, The Plessey Co Ltd., Caswell, Towcester, Northants, UK
HURST, I.L.	MOD, A.S.W.E. Cosham, Hants, UK
INCE, A.N. Dr EPP Associate Panel Member	Communications Division, S.T.C., P.O. Box 174, The Hague, Netherlands
IVELAND, T.D.	ELAB, N-7034, Trondheim, NTH, Norway
JACKSON, J.Q.	NDHQ, 101 Colonel By Drive, Ottawa, Ontario, K1A OK2, Canada
JACOBSEN, M. Mr AVP Panel Member	AEG-Telefunken N14/v6, D-79 Ulm, Postfach 1730, Germany
JACQUES, A.	Thomson CSF, Domaine de Corbeville, B.P. No.10 91401, Orsay, France
JEUNHOMME, L.	Laboratoire de Marcoussis, Route de Nozay, 91460, Marcoussis, France
JOHNSTON, A.R.	Jet Propulsion Lab., (NASA) California Institute of Technology, 4800 Oak Grove Drive, Pasadena, CA 91103, USA
JUDEINSTEIN	Laboratoire Central de Télécommunications, 18, 20 rue Grange Dame Rose, 78140, Velizy-Villacoublay, France
KAHN, D.A.	Plessey Radar Research Centre, Southleigh Park House, Havant, Hants PO9 2PE, UK
KENT, A.H.	Plessey Telecommunications Ltd., Taplow Court, Taplow, Maidenhead, Berks, SL6 OE9, UK
KINGSLEY, S.A.	Dept. of Elect. Eng. University College, London, Torrington Place, London WC1, UK
KISTER, H.	VDO Luffahrtgerate Werk, An der Sandelmuhle 13, 6000 Frankfurt/Main, Germany
KOCH, R.	Italy
KOGELNIK, H.	Bell Laboratories, Room 4E, Holmdel, N.J. 07733, USA
KOOPMAN, K.	RNLAF, Chief Ground Systems Division, Directorate Materiel Air, Prins Clauslaan 8, Den Haag, Netherlands
KOSTKA, M.H.	EMI Electronics Lab., Radar & Equipment Div., Radar House, Dawley Road, Hayes, Middx, UB3 1HN, UK
KRUGER, W.	S.T.C., P.O. Box 174, The Hague, Netherlands

KRUMPHOLZ, O.	AEG Telefunken, Forschungsinstitut, Elisabethenstr. 3, 7900 Ulm, Germany
LAMB, J.	University of Glasgow, Glasgow G12 8QQ, Scotland, UK
LANGE-HESSE Dr EPP Panel Member	Max-Planck-Institut für Aeronomie, Post Box 20, D3411, Lindau-Harz, Germany
LEATHER, R.A.	Ferranti Ltd., Dunsinane Ave., Dundee, Angus, DD2 3PN, UK
LECAT, P.	STTA, 129, rue de la Convention, 75731 Paris CEDEX 15, France
LEES, R.	R.S.R.E., Malvern, UK
LEITE, A.	Dept. of Elect. Eng., University College, London, Trorrington Place, London WC1, UK
LEMMERS, L.J.	Netherlands Standard Electric ITT, le van der Kunstraat 292, Post bus 1013, Den Haag 2077, Netherlands
LEVIN, H.J.	Rank Optics, 200 Harehills Lane, Leeds, West Yorks, LS8 5QS, UK
LEVY, Y.	Faculté des Sciences, Batiment 503, Orsay, France
LEWIS, E.L.	Marconi Elliott Avionic Systems Ltd., FARL, Airport Works, Rochester, Kent, ME1 2XX, UK
LEWIS, D.C.	Office of Naval Research, 800 North Quincy Street, Arlington, VA 22217, USA
LEY, J.M.	Electro-Optics Developments, 117 High Street, Brentwood, Essex, UK
LOCK, J.M.	R.S.R.E., St Andrews Road, Malvern, Worcs, WR14 3PS, UK
LUEG, H. Prof. AVP Panel Member	Institut für Technische Elektronik, RWTH, Aachen, Templergraben 55, D-5100 Aachen, Germany
LYON, I.	P.B. 244, British Aircraft Corporation, Stevenage, Herts, SG2 7HW, UK
MADGER, E.R.	Raytheon Overseas Co. Ltd., UK
MAIDMENT, H.	UK
MAKLAD, M.	ITT, Electro Optical Products Division, P.O. Box 7065, Roanoke, VA 24019, USA
MAGNE	Centre de Prospective et d'Evaluation, 10/14 rue St Dominique, 75997, Paris ARMEES, France
MARIANI, A.F.	UK
MATHEWSON, D.	Royal Military College of Science, Shrivenham, Wilts, UK
MARTIN, J.T.	Ferranti Ltd., Western Road, Bracknell, Berks, UK
MATTHEWS, M.A.	ITT Cannon Electric (GB) Ltd., Lister Road, Basingstoke, Hants, RG22 4AS, UK
McCREE, A.D.	RARDE, Fort Halstead, Sevenoaks, Kent TH14 7BP, UK
McMAHON, D.H.	Sperry Research Center, Sudbury, MA 01776, USA
MEISTRING, R.	Messerschmitt-Bolkow-Blohm, 8000 Munchen 80, Postfach, Germany
MIDWINTER, J.E.	Post Office Research Center, Martlesham Heath, Suffolk, UK
MILLER, J.	ITT Cable – Hydrospace Div., P.O. Box 81446, San Diego, CA 92138, USA
MILNER, J.G.	R.S.R.E., St Andrews Road, Malvern, Worcs, WR14 3PS, UK

MITCHELL, G.L.	University of Washington, Dept. of Electrical Engineering, Mailstop FT 10, Seattle, WA 98195, USA
MITCHELL, J.	Electro Optics Dev. Ltd., 117 High Street, Brentwood, Essex, UK
MANCALVO, A.	CSELT, Via Reiss Romoli, 274, 10148 Torino, Italy
MOORE, J.	UK
MOREAU, R.	ONERA, 92320 Châtillon, France
MOSSMAN, P.	UK
MUIR, N.	BAC, P.B. 244, Stevenage, Herts, SG2 7HW, UK
NEUROTH, N.	Jenaer Glaswerk Schott & Gen. Abt ZFO, D-65 Mainz 1, Germany
NEWNS	Post Office Research Centre, Martlesham Heath, Ipswich, IP5 7RE, UK
NICIA, A.	Philips Research Laboratory, Eindhoven, Netherlands
NICOL, W.S.	DCVD-MOD (PE), Room 330, Empress State Building, Lillie Road, Fulham, London SW6 1TR, UK
NORBY, H.O.	Norwegian Telecommunication Adm. Res. Est., Postboks 83, N-2007 Kjeller, Norway
OLIVEIRA de, A.D.	Department of Electronic and Electrical Engineering, University College, London WC1E 7JE, UK
OSBORNE, C.S,	ITT Cannon Electric (GB) Ltd., Lister Road, Basingstoke, Hants, RG22 4AS, UK
PAPUCHON, M.	Thomson CSF, Laboratoire Central de Recherche, 91401, Orsay, France
PARRIAUX, O.	Department of Electronic and Electrical Engineering, University College, London WC1E 7JE, UK
PATTERSON, L.R.	ONR, 223/231 Old Marylebone Road, London NW1 5TH, UK
PAYNE, R.	US Air Force, Hanscom AFB, Bedford, MA 01731, USA
PEARSON, R.F.	Mullard Research Lab., Cross Oak Lane, Salfords, Redhill, Surrey, RH1 5HA, UK
PENHALE, L.G.	Royal Military College of Science, Shrivenham, UK
PERBET	SFENA, B.P. 59, 78140 Velizy, France
PERTICONE, U.	Aeritalia, 52 Via Panama, Roma, Italy
PETERSEN, K.H.	Air Materiel Command, Post Box 130, 3500 Vaerloese, Denmark
PHILIP, M.A.	STC, Optical Communications Unit, London Road, Harlow, Essex, UK
POELMAN, E.E.P.	St Paulus Str. 4, Leidschendam, Netherlands
PONT, W.	Physics Lab. TNO, Oude Waalsdorperweg 63, P.O. Box 2864, Den Haag, Netherlands
PORTAS, D.	Dunlop Ltd., Aviation Division, Holbrook Lane, Coventry, CV6 4AA, UK
PRESNER, K.	BICC Ltd., 38 Wood Lane, Shepherds Bush, London W12, UK
PRETIOUS, D.W.	SBAC, 40 Purley Way, Croydon, Surrey, UK
PRUTZER, H.	AEG Telefunken, N22/E13, Gerberstrasse D-7150, Backnang, Germany

QUARMBY, R.B.	Hellermann-Deutsch, East Grinstead, Sussex, UK
RAVENSCROFT, I.A.	Post Office Research Centre, Martlesham Heath, Ipswich, IP5 7RE, UK
REID, J.P.	Sperry Gyroscope Ltd., Downshire Way, Bracknell, Berkshire, UK
ROBERTS, L.W. Mr Panel Member	Code 600, Transportation System Center, Kendall Square, Cambridge, MA 02142, USA
ROBERTSON, J.W.	Marconi Radar Systems, West Hanningfield Road, Great Baddow, Chelmsford, Essex, UK
ROUGNY	UER de Sciences, 23 rue du Dr Paul Michelon, 42100 St Etienne, France
ROUSSEAU	Laboratoires de Marcoussis, DEO/EP Route de Nozay, 91460, Marcoussis, France
RUGGLES, R.	Marconi Elliott Avionic Systems Ltd., FARL, Airport Works, Rochester, Kent ME1 2XX, UK
RUMMLER, D.C.	US Navy, Office of Naval Research Branch, Branch Office, 223 Old Marylebone Road, London NW1 5TH, UK
RUSH, D.A.	Smiths Industries Ltd., Aviation Division, Bishops Cleeve, Cheltenham GL52 4SF, UK
RUSSO, V.	IROE, Via Panciatichi 64, 50127 Firenze, Italy
RYEN, N.	Elab. 7034 Trondheim, Norway
SADLER, A.	BICC General Cables Ltd., Helsby, UK
SANDBANK, C.P.	Standard Telecommunication Laboratories Ltd., London Road, Harlow, Essex, UK
SAVAGE, J.A.	RSRE, St Andrews Road, Malvern, Worcs, WR14 3PS, UK
SCUDELLARI, A.	CSELT, Via Reiss Romoli, 274, 10148, Torino, Italy
SHAW, P.A.	MOD, Room 241, St Giles Court, 1–13 St Giles Court, High Street, London WC2, UK
SHRUBB, K.F.	Hawker Siddeley Aviation, 12 Speer Road, Thames-Ditton, Surrey, KT7 0PW, UK
SHUTTLEWORTH, R.	Technical Training Office, EQD, MOD/PE, Room 2D25, Aquila Golf Road, Bromley, Kent, UK
SIMMONS, M.G.	Hawker Siddeley Aviation, Brough, N. Humberside, MU15 1EQ, UK
SINGLETON, J.	UK
SLAUGHTER, R.J.	BICC Ltd., 38 Wood Lane, Shepherds Bush, London W12, UK
SLETVOLD, O.	A/S Norsk Kabelfabrik, P.O. Box 369, N-3001 Drammen, Norway
SMILEY, V.N.	ONR, 223 Old Marylebone Road, London NW1 5TH, UK
SMITH, K.W.	Drasa, Adelphi, John Adam Street, London WC2, UK
SMITH, P.W.	MOD (PE), Room 842, John Adam Street, London WC2, UK
SOARES, O.D.D.	University of Porto, Praca Gomez Teixeira, Porto, Portugal
SOICHER, H. Dr EPP Panel Member	US Army Electronics ATTN: DRSEL-NL-RH4, Ft Monmouth, N.J. 07703, USA
SPOONER, A.M.	Redifon Flight Simulation Ltd., Gatwick Road, Crawley, Sussex, UK

STEEN, A.	EMI Electronics Ltd., Radar & Equipment Div., 248 Blyth Road, Hayes, Middx, 4B3 1BP, UK
STEWART, C.	Allen Clark Research Centre, The Plessey Co Ltd., Caswell, Towcester, Northants, UK
STEWART, W.J.	Allen Clark Research Centre, The Plessey Co Ltd., Caswell, Towcester, Northants, UK
STREHL, H.	Siemens AG 8000 Munchen 70, Hofmanstr. 51, Lab. 533, Germany
STRINGER, F.S. Mr AVP Panel Member	MOD (PE), Room 802 Adelphi, John Adam Street London, WC2, UK
SUETA, T.J. Mr AVP Panel Member	Deputy Director, US Army Avionics Laboratory, Fort Monmouth, N.J. 07703, USA
SUTHERLAND, N.	Plessey Connectors, P.O. Box 30, Kingsthorpe, Northampton, NN2 6NA, UK
SZCZEPANEK, P.	Laboratory for Physical Sciences, 4928 College Avenue, College Park, Maryland 20740, USA
TAILLET, J. Dr AVP Panel Member	ONERA, 92320, Châtillon, France
TATE, C.E.	Plessey Telecommunications Ltd., The Lodge, Roke Manor, Romsey, Hampshire, UK
TARBATT, M.A.	BICC General Cables Ltd., Leigh, UK
TAYLOR, H.	Naval Electronics Lab., 271, Catalina Bld., San Diego, CA 92152, USA
TEWS, H.J.	MBB Hamburger Flugzeugbau, 2103 Hamburg 95, Germany
THEOPHANOUS, N.	Electronics Lab., Athens University, Solonos 104, Athens, Greece
THOMASON, R.	Cranfield Institute of Technology, Cranfield, Beds, UK
TIMMERS, H.A.T. Ir AVP Panel Deputy Chairman	NLR, Anthony Fokkerweg 2, Amsterdam 1017, Netherlands
TRABAUD	CEA DAM Centre S4, B.P. 561, 92542 Montrouge CEDEX, France
TREBER, N.	Heraeus Quarzschmelze GmbH, D6450 Hanau/Main, Germany
TRIBOULET, M.	Thomson CSF, LCR, Domaine de Corbeville, 91401, Orsay, France
TRUMBLE, K.C.	AF Avionics Lab., Wright-Patterson AFB, OH 45433, USA
TURLEY, W.H.	Plessey Connectors, P.O. Box 30, Kingsthorpe, Northampton, NN2 6NA, UK
TYSON, A.	Pilkington P.E. Ltd., Glascoed Road, St Asaph, CLWYD, UK
UNDERWOOD, G.W.	Hawker Siddeley Aviation Ltd., Richmond Road, Kingston-upon-Thames, KT2 5QS, UK
UNGER, H.G.	Technische Universitat, Postfach der TU 3329, D-3000 Braunschweig, Germany
VAGNARELLI, F. Lt Col AVP Panel Member	Ufficio del Delegato Nazionale all'AGARD, 3 Ple Adenauer, Roma EUR, Italy
VERBEEK, C.J.	Delft University of Technology, Insulindeweg 9, Delft, Netherlands
VERET, C.	ONERA, 92320 Châtillon sous Bagneux, France
VISSER, J.M.P.C.M.	NLR, Anthony Fokkerweg 2, Amsterdam 1017, Netherlands

VOGEL, M. Dr AVP Panel Member	DFVLR, D-8031, Oberpfaffenhofen, Germany
VOLES, R. Mr AVP Panel Member	EMI Electronics Ltd, 135 Blyth Road, Middx, UB3 1BP, UK
WAINMAN, H.	A & AEE, Boscombe Down, Salisbury, Wilts, UK
WAIT, J.R.	ERL/NOAA, US Department of Commerce, Boulder, COL. 80302, USA
WAMSTEKER, P.J.	RNLAF, Chief Scientific Research Division, Directorate Materiel Air, Ypenburg Air Base, Building A 16, Rotterdamseweg 35, Rijswijk, Netherlands
WANG, G. EPP Panel Member	N.D.R.E., P.O. Box 25, No. 2007, Kjeller, Norway
WANG, Shyh	Electronics Research Laboratory, College of Engineering, University of California, Berkeley, CA 94720, USA
WATSON, D.H.	RAE (AW2), Y20 Bldg, Farnborough, Hants, GU14 6TD, UK
WESKETH, T.G.	BAC (MAD) Ltd., Warton Aerodrome, Preston, Lancs, PR14 1AX, UK
WHITTON, R.L.	UK
WILKINS, G.A.	Naval Undersea Center, Hawaii Laboratory, Code 605302, P.O. Box 997, Kailua, Hawaii 96734, USA
WILKINSON, F.	BICC Telecom. Cables Ltd., Prescott, Merseyside, Lancs, UK
WILKINSON, D.	Dept. Electronics & EE, The University, Glasgow G12, Scotland, UK
WILLIAMS, D.	Naval Electronics Lab., Code 220, San Diego, CA 92152, USA
WILLIS, A.	BICC General Cables Ltd. Helsby, UK
WILLIAMS, G.A.	Room 200, AUWE, HM Naval Base, Portland, Dorset, UK
WILLIAMS, J.S.	Hawker Siddeley Aviation Ltd., Richmond Road, Kingston-upon-Thames, KT2 5QS, UK
WILLIAMS, R.G.	ITT Electro-Optical Products Div., P.O. Box 7065, Roanoke, VA 24019, USA
WILSON, M.G.F.	Department of Electronic and Electrical Engineering, University College, London WC1E 7JE, UK
WIMPENNY, J.C.	Hawker Siddeley Aviation Ltd., Richmond Road, Kingston-upon-Thames, KT2 5QS, UK
WINDUS, G.G.	Marconi Research Lab., West Hanningfield Road, Great Baddow, Essex CM2 8HN, UK
WIRTZ, C.C.	Philips Research Laboratory, Eindhoven, Netherlands
WITTE, H.H.	Siemens AG, 8 Munchen 70, Hoffmanstr. Raum Nr 13345, Germany
WRIGHT, R.E.	Ferranti Ltd., Western Road, Bracknell, Berks, UK
YARKER, C.A.	Pilkington P-E Ltd., Glascoed Road, St Asaph, CLWYD, UK
YEE, H.	BAC Electro-Optics Dept., P.B. 244, Gunnels Wood Road, Stevenage, Herts, SG1 2DA, UK
ZAESCHMAR, G.	Naval Ocean Systems Center, Electronic Material Sciences Division, 271 Catalina Bld, San Diego, CA 92152, USA

REPORT DOCUMENTATION PAGE

1. Recipient's Reference	2. Originator's Reference	3. Further Reference	4. Security Classification of Document
	AGARD-CP-219	ISBN 92-835-0206-X	UNCLASSIFIED

5. Originator	Advisory Group for Aerospace Research and Development North Atlantic Treaty Organization 7 rue Ancelle, 92200 Neuilly sur Seine, France
6. Title	OPTICAL FIBRES, INTEGRATED OPTICS AND THEIR MILITARY APPLICATIONS
7. Presented at	the Electromagnetic Wave Propagation Panel/Avionics Panel Joint Symposium held in London, 16–20 May 1977.

8. Author(s)	9. Date
Various Editor: Dr H.Hodara	October 1977
10. Author's Address	**11. Pages**
Various	594

12. Distribution Statement	This document is distributed in accordance with AGARD policies and regulations, which are outlined on the Outside Back Covers of all AGARD publications.

13. Keywords/Descriptors

Optical fibres	Optical couplers	Integrated optics
Multimode optical fibres	Optical propagation	
Semiconductor lasers	Index profiling	

14. Abstract

Rapid developments in laser semiconductors and low-loss optical fibres have revealed many new applications. The obvious advantages of a high degree of communication security, freedom from electronic interference, large length-bandwidth product, and system miniaturization possibilities have led to new concepts and applications in military systems.

This conference provided a forum to review and discuss the latest developments in fibre and integrated optics, with emphasis on military applications.

AGARD Conference Proceedings No.219
Advisory Group for Aerospace Research and Development, NATO
OPTICAL FIBRES, INTEGRATED OPTICS AND THEIR MILITARY APPLICATIONS
Editor: Dr H.Hodara
Published October 1977
594 pages

Rapid developments in laser semiconductors and low-loss optical fibres have revealed many new applications. The obvious advantages of a high degree of communication security, freedom from electronic interference, large length-bandwidth product, and system miniaturization possibilities have led to new concepts and applications in military systems.

P.T.O.

AGARD-CP-219

Optical fibres
Multimode optical fibres
Semiconductor lasers
Optical couplers
Optical propagation
Index profiling
Integrated optics

AGARD Conference Proceedings No.219
Advisory Group for Aerospace Research and Development, NATO
OPTICAL FIBRES, INTEGRATED OPTICS AND THEIR MILITARY APPLICATIONS
Editor: Dr H.Hodara
Published October 1977
594 pages

Rapid developments in laser semiconductors and low-loss optical fibres have revealed many new applications. The obvious advantages of a high degree of communication security, freedom from electronic interference, large length-bandwidth product, and system miniaturization possibilities have led to new concepts and applications in military systems.

P.T.O.

AGARD-CP-219

Optical fibres
Multimode optical fibres
Semiconductor lasers
Optical couplers
Optical propagation
Index profiling
Integrated optics

AGARD Conference Proceedings No.219
Advisory Group for Aerospace Research and Development, NATO
OPTICAL FIBRES, INTEGRATED OPTICS AND THEIR MILITARY APPLICATIONS
Editor: Dr H.Hodara
Published October 1977
594 pages

Rapid developments in laser semiconductors and low-loss optical fibres have revealed many new applications. The obvious advantages of a high degree of communication security, freedom from electronic interference, large length-bandwidth product, and system miniaturization possibilities have led to new concepts and applications in military systems.

P.T.O.

AGARD-CP-219

Optical fibres
Multimode optical fibres
Semiconductor lasers
Optical couplers
Optical propagation
Index profiling
Integrated optics

AGARD Conference Proceedings No.219
Advisory Group for Aerospace Research and Development, NATO
OPTICAL FIBRES, INTEGRATED OPTICS AND THEIR MILITARY APPLICATIONS
Editor: Dr H.Hodara
Published October 1977
594 pages

Rapid developments in laser semiconductors and low-loss optical fibres have revealed many new applications. The obvious advantages of a high degree of communication security, freedom from electronic interference, large length-bandwidth product, and system miniaturization possibilities have led to new concepts and applications in military systems.

P.T.O.

AGARD-CP-219

Optical fibres
Multimode optical fibres
Semiconductor lasers
Optical couplers
Optical propagation
Index profiling
Integrated optics

This conference provided a forum to review and discuss the latest developments in fibre and integrated optics, with emphasis on military applications.

Papers presented at the Electromagnetic Wave Propagation Panel/Avionics Panel Joint Symposium held in London, 16–20 May 1977.

ISBN 92-835-0206-X

This conference provided a forum to review and discuss the latest developments in fibre and integrated optics, with emphasis on military applications.

Papers presented at the Electromagnetic Wave Propagation Panel/Avionics Panel Joint Symposium held in London, 16–20 May 1977.

ISBN 92-835-0206-X

This conference provided a forum to review and discuss the latest developments in fibre and integrated optics, with emphasis on military applications.

Papers presented at the Electromagnetic Wave Propagation Panel/Avionics Panel Joint Symposium held in London, 16–20 May 1977.

ISBN 92-835-0206-X

This conference provided a forum to review and discuss the latest developments in fibre and integrated optics, with emphasis on military applications.

Papers presented at the Electromagnetic Wave Propagation Panel/Avionics Panel Joint Symposium held in London, 16–20 May 1977.

ISBN 92-835-0206-X

AGARD

NATO OTAN

7 RUE ANCELLE · 92200 NEUILLY-SUR-SEINE

FRANCE

Telephone 745.08.10 · Telex 610176

DISTRIBUTION OF UNCLASSIFIED AGARD PUBLICATIONS

AGARD does NOT hold stocks of AGARD publications at the above address for general distribution. Initial distribution of AGARD publications is made to AGARD Member Nations through the following National Distribution Centres. Further copies are sometimes available from these Centres, but if not may be purchased in Microfiche or Photocopy form from the Purchase Agencies listed below.

NATIONAL DISTRIBUTION CENTRES

BELGIUM
Coordonnateur AGARD – VSL
Etat-Major de la Force Aérienne
Caserne Prince Baudouin
Place Dailly, 1030 Bruxelles

CANADA
Defence Scientific Information Service
Department of National Defence
Ottawa, Ontario K1A OZ2

DENMARK
Danish Defence Research Board
Østerbrogades Kaserne
Copenhagen Ø

FRANCE
O.N.E.R.A. (Direction)
29 Avenue de la Division Leclerc
92 Châtillon sous Bagneux

GERMANY
Zentralstelle für Luft- und Raumfahrt-dokumentation und -information
Postfach 860880
D-8 München 86

GREECE
Hellenic Armed Forces Command
D Branch, Athens

ICELAND
Director of Aviation
c/o Flugrad
Reykjavik

ITALY
Aeronautica Militare
Ufficio del Delegato Nazionale all'AGARD
3, Piazzale Adenauer
Roma/EUR

LUXEMBOURG
See Belgium

NETHERLANDS
Netherlands Delegation to AGARD
National Aerospace Laboratory, NLR
P.O. Box 126
Delft

NORWAY
Norwegian Defence Research Establishment
Main Library
P.O. Box 25
N-2007 Kjeller

PORTUGAL
Direccao do Servico de Material
da Forca Aerea
Rua de Escola Politecnica 42
Lisboa
Attn: AGARD National Delegate

TURKEY
Department of Research and Development (ARGE)
Ministry of National Defence, Ankara

UNITED KINGDOM
Defence Research Information Centre
Station Square House
St. Mary Cray
Orpington, Kent BR5 3RE

UNITED STATES
National Aeronautics and Space Administration (NASA),
Langley Field, Virginia 23365
Attn: Report Distribution and Storage Unit

THE UNITED STATES NATIONAL DISTRIBUTION CENTRE (NASA) DOES NOT HOLD STOCKS OF AGARD PUBLICATIONS, AND APPLICATIONS FOR COPIES SHOULD BE MADE DIRECT TO THE NATIONAL TECHNICAL INFORMATION SERVICE (NTIS) AT THE ADDRESS BELOW.

PURCHASE AGENCIES

Microfiche or Photocopy
National Technical
Information Service (NTIS)
5285 Port Royal Road
Springfield
Virginia 22151, USA

Microfiche
Space Documentation Service
European Space Agency
10, rue Mario Nikis
75015 Paris, France

Microfiche
Technology Reports
Centre (DTI)
Station Square House
St. Mary Cray
Orpington, Kent BR5 3RF
England

Requests for microfiche or photocopies of AGARD documents should include the AGARD serial number, title, author or editor, and publication date. Requests to NTIS should include the NASA accession report number. Full bibliographical references and abstracts of AGARD publications are given in the following journals:

Scientific and Technical Aerospace Reports (STAR),
published by NASA Scientific and Technical
Information Facility
Post Office Box 8757
Baltimore/Washington International Airport
Maryland 21240, USA

Government Reports Announcements (GRA),
published by the National Technical
Information Services, Springfield
Virginia 22151, USA

Printed by Technical Editing and Reproduction Ltd
Harford House, 7–9 Charlotte St, London W1P 1HD

ISBN 92-835-0206-X